PROCEEDINGS

of the 4:th CEAS Conference in Linköping, 2013

Editors:

Tomas Melin
Petter Krus
Emil Vinterhav
Knut Övrebö

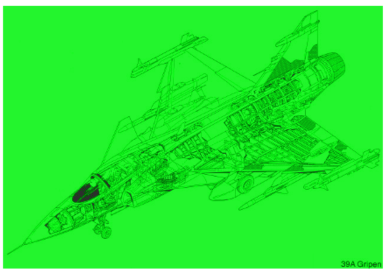

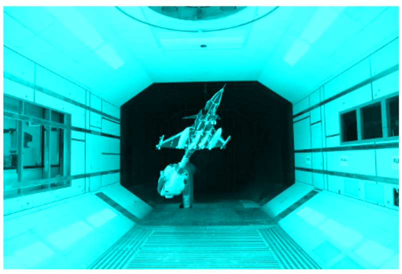

Proceedings of the 4:th CEAS Conference in Linköping, 2013.

Editors:

Tomas Melin	Linköpings Universitet
Petter Krus	Linköpings Universitet
Emil Vinterhav	SCC ECAPS
Knut Övrebö	SAAB AB

Place of publication: Linköping, Sweden
Publisher: Linköping University Electronic Press
SWEDEN

ISBN: 978-91-7519-519-3
First Edition, October 2013.

Copyright

Linköping University Electronic Press Linköping, Sweden, 2013

Proceedings

The full length papers presented in this book are the scientific contributions presented at the conference. For abstracts of the technical contributions, please review the book of abstracts for the CEAS2013 conference.

PROCEEDINGS

of the 4:th CEAS conference in Linköping, 2013

Editors:

Tomas Melin
Petter Krus
Emil Vinterhav
Knut Övrebö

Welcome

We welcome you to the fourth Council of European Aerospace Societies (CEAS) Air and Space Conference. We have chosen the theme 'Innovative Europe' for the gathering of Europe's most qualified professionals in air and space technologies.

Europe has a leading role in research, engineering and manufacture of aerospace systems. Today, development of new concepts and systems are increasingly dependent on cooperation and mutually beneficial relationships, such that meetings and networking between professionals become even more important. Those are the basics for this conference, and the necessary elements for the air and space industries of Europe to take innovative and leading steps into the future. We are very happy to have received so many high quality contributions in such a wide range of topics. We are also proud to have a number of very high profile keynote speakers and thematic sessions with invited speakers, to reflect the overall theme of the conference.

There are contributions from more than twenty countries, also from outside of Europe. Integrated in this conference are also a great number of national contributions in line with our regular national conference on aviation and space technologies. We feel confident that this range of presentations will firmly establish the CEAS Air & Space conference as one of the most important events among the community of air and space professionals.

The city of Linköping has a background of more than one hundred years in aviation, and is the locus of many emerging companies in the air and space arenas. Additionally, Linköping is situated in a beautiful rural district with many lakes, channels and rivers. The city was founded in the 12th century and is the fifth largest city in Sweden, where you can find many places and buildings of historical interest.

We wish you a fruitful meeting and a pleasant stay in Linköping.

Petter Krus
Chairman of programme committee
Professor in Fluid and Mechatronic
Systems, Linköping University

Roland Karlsson
Chairman of the organizing committee
Chairman of the Swedish Society of
Aeronautics and Astronautics

Index sorted by page number

Index sorted by page number

Index sorted by author name

Index sorted by author name

Index sorted by title

Index sorted by title

Index sorted by paper number

Index sorted by paper number

4:th CEAS Air & Space Conference
FTF Congress: Flygteknik 2013

Micro T-strips to save cost and fuel

George R Seyfang BSc.
Formerly with BAE Systems, UK

georgeseyfang@supanet.com

Keywords: T-strip, Aerofoil, Divergent Trailing-edge, Gurney Flap

Abstract

This paper re-examines the ubiquitous T-strip which has been previously used at the trailing edge of aerofoils to increase their lifting capability at both positive and negative AoAs. In particular it examines the potential of very small (Micro) T-strips to increase the aerodynamic efficiency of symmetric aerofoils.

An example is shown of how Micro T-strips might be used on a new airliner design to allow smaller tail surfaces to be fitted and so reduce operating costs and save fuel. Several research topics are suggested to enlarge the limited data base of T-strips.

1. History of T-strips

The T-strip, applied to the trailing edge of an aerofoil, is a double-sided version of the well-known L-strip which was originally called a Zaparka flap, but is now more commonly called a Gurney flap. The key advantage of the T-strip is that it is effective in increasing the lift slope, maximum lift and control power of aerofoils at both positive and negative angles of attack.

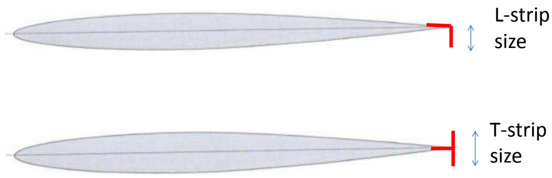

Fig. 1 The T-strip and L-strip compared

A visit to any aircraft museum shows that various sizes of T-strip have been used on many older aircraft as shown in Fig.2. Sometimes they are large metal plates, other times as small, fabric-covered ‘cording’. Although they are seldom described in technical documents, it is known that these T-strips were applied as economy ‘fixes’ to correct some problems of stability, control power or handling qualities identified during flight testing. The inevitable small drag penalty was presumably accepted in exchange for a speedy and simple solution to a more serious stability or control problem.
T-strips of various sizes are still being fitted to the vertical tails of some new aircraft of the business and general aviation types.

Fig. 2 Examples of T-strips on aircraft

2. T-strip data and analysis

In general the T-strip was not 'designed in' to these older aircraft and very little effectiveness data exists in the literature. The current author has found only one recent report having a comprehensive set of wind tunnel tests of both T-strips and L-strip / Gurney flaps, and in this case on a non-symmetric aerofoil [1]. There are similarities to T-strips in the nautical world with 'staukeils' [2] and Schilling rudders [3], which feature wedge-shaped, blunt trailing edges on symmetric underwater sections.

The very limited amount of published T-strip data [1] does show some very interesting trends, especially at very small T-strip sizes. Figure 3 extracted from ref.1, shows the most relevant lift and drag data from that report, covering a range of T-strip sizes from 0.4% to 5.0% chord.

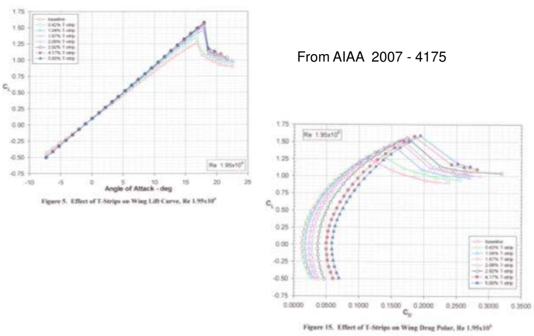

Fig.3 Extracts from published T-strip data

The data shown in Fig. 3 has been analysed here to explore how different sizes of T-strip can affect the aerodynamic efficiency of an aerofoil. One useful efficiency parameter is the ratio of increments of maximum lift and minimum drag, as shown in the left side of Fig.4. It is seen that this ratio becomes increasingly large at smaller T-strip sizes and it is difficult to estimate values for the smallest T-strip sizes. A simple way to interpolate for data at very small T-strip sizes is to plot the inverse parameter as shown on the right of Fig.4. Here the measured data is seen to lie on a straight line to the origin, enabling interpolation to very small, Micro T-strips.

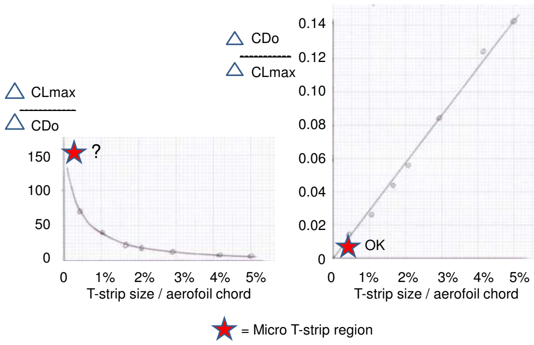

Fig.4 Efficiency of Micro T-strips

This analysis of the data for T-strips on a cambered aerofoil in Fig. 3 has encouraged the current author to make additional low-speed wind tunnel tests of T-strips, mounted on other aerofoils and also on flapped control surfaces. Results of some of these unpublished tests are shown in Fig 5.

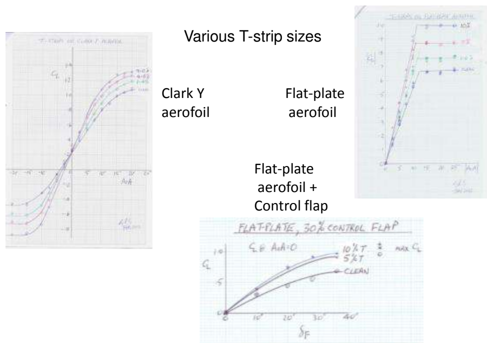

Fig.5 Author's T-strip data

The author's measurements shown in Fig.5 tended to confirm that T-strips can be equally effective on symmetric aerofoils and on flapped control surfaces.

A correlation of all available T-strip test data has been attempted and the major data trends have been identified. These correlations were needed to allow robust interpolation down to the very small, high efficiency, T-strip sizes, much smaller than those sizes tested to-date.

The increase of maximum lift, lift-slope and control power were found to average about 14% for a 1% chord T-strip. These lifting increments were also found to be proportional to T-strip size to the power 0.5, as indicated in Fig.6.

Correlation of T-strip Lift Results

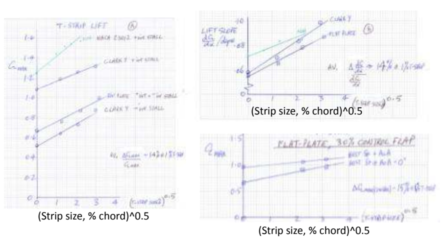

** 1% chord T-strip increases lift and control by about 14%
** lift effectiveness with small T-strips varies as (size)^0.5

Fig. 6 Correlation of T-strip data – Lift

The profile drag increments from [1] are shown on the left side of Fig. 7. A 1% chord T-strip is seen to have a drag increment of about 0.005 for a 1% chord T-strip, approximately doubling the clean aerofoil drag. This drag increment was found by examination to be proportional to T-strip size to the power 1.5, as shown in the right side of Fig. 7.

Correlation of T-strip Drag Results

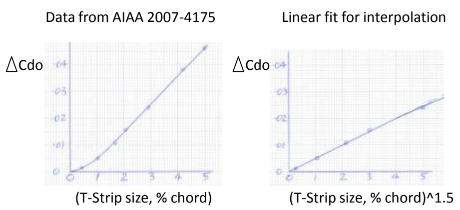

** 1% chord T-strip increases section Cdo(tail) by 0.005
** section drag with small T-strips varies as (size)^1.5

Fig.7 Correlation of T-strip data – Drag

The key finding of these correlations is that, as the T-strip size is reduced, the drag penalty reduces more quickly than the lift benefit. This means that very small, Micro T-strips can be very efficient for many other applications, as was first seen in Fig.4.

Very similar results have also been observed for the single-sided L-strip.

3. Concept to use T-strips on Airliner Tails

The high efficiency of very small T-strips inspired the author to explore ways in which they might be used. One possibility is to add T-strips to the horizontal and vertical tails of a new airliner during the early design stage.

T-strips would increase the effectiveness of the symmetric tails in both stability and control. More effective tails can be made smaller and lighter, and this would allow an increase of payload and/or a fuel burn reduction, Fig.8.

An approximate evaluation of these benefits has been made by a project-level design study combining the aerodynamic data for T-strips described in section 2 with open-source data for airliner aerodynamics, structures and economics.

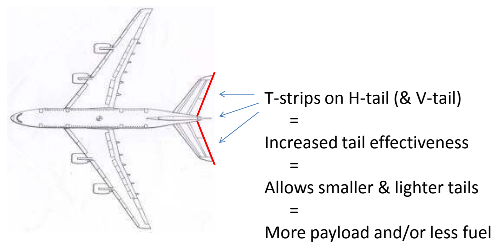

Fig.8 The concept to use T-strips on airliner tails

However there is a small profile drag penalty due to even the smallest T-strips and it is necessary to find the optimum size to best balance the T-strip's lift and drag effects to maximise the reduction of Direct Operating Cost and Fuel Burn. Fig. 9 shows the various parameters considered in this concept trade study.

- T-strip effects on Tail's aerodynamic parameters
  (Lift Slope, Max. Lift, Profile Drag, Max. Control, Lift Centre)
- Reduction of Tail size & weight ......more payload
  ......less capital cost
  ......less fuel
- Increase of Tail profile drag ......more fuel
- Combined effects of payload, fuel & capital on D.O.C.
- Identify optimum T-strip sizes, D.O.C. saving and Fuel saving

Fig.9 Parameters included in the T-strip trade study

4. Optimum T-strips for Airliner Tails

The concept trade study described in section 3 has been applied to notional replacements of two important classes of airliner, the small, short-range type such as A320 or B737, and the large, long-range type such as A380 or B747, shown in Fig.10.

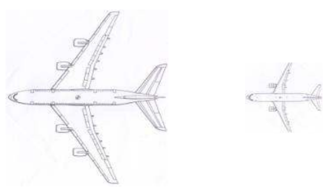

	A-380 / B747	A-320 / B737
Passengers	600	150
Design Range	15,000km	5,000km

Fig. 10 Two major classes of airliner studied

For each class of aircraft, the structure weight and cruise drag of the tails were estimated from generic and open-source data. The several contributions to Direct Operating Costs were similarly estimated.
Some results of this study of different T-strip sizes are shown in Fig. 11. At the optimum T-strip size, the D.O.C. might be reduced by 1.6% on the larger, long-range aircraft and by 0.8% on the smaller, short-range types.

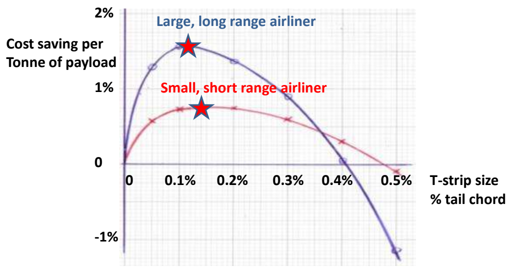

Fig.11 Effect of tail T-strip size on D.O.C.

The study also showed that fuel burned per tonne of payload would be reduced by similar percentages and at similar optimum T-strip sizes, Fig 12.

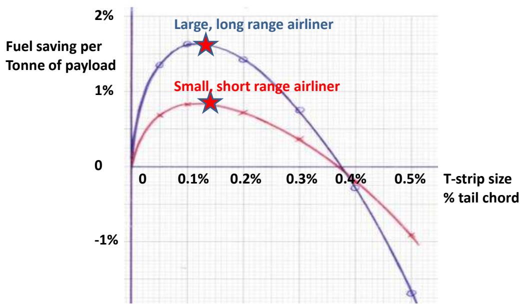

Fig. 12 Effect of tail T-strip size on Fuel Burn

The optimum size of T-strip required to achieve these savings is seen in Figs. 11 and 12 to be between 0.1% and 0.2% of the tail chords. These optimized Micro T-strips equate to less than 10mm at full-scale, and allow the horizontal and vertical tails to be about 5% smaller.
The potential to save about 1% cost and fuel may seem to be rather small. However, based on forecasts for future airliner production [4], [5] and jet fuel usage [6], there would be an industry-wide operating cost saving of over $4Bn per year, together with a jet fuel saving of over 2 million tonnes per year.

5. Other Applications of Micro T-strips

Similar design and trade studies could be performed for the use of Micro T-strips on other new-design aircraft including combat aircraft, UAVs, general aviation aircraft and even space-planes. It is expected that similar savings would emerge. There may also be some potential for applications in the nautical world, on the underwater fins and rudders of ships, submarines and torpedoes, and above water on the tails of wing-sails.

If T-strips are applied to the tails of existing aircraft then there is the historically-proven potential to widen the safely-allowable CG range. This occurs because the tails will have extra stabilizing effect, allowing a further aft CG limit, and extra control power, allowing a further forward CG limit. This wider CG range would be particularly useful for military aircraft with unusual external loads or during conversion of passenger airliners to cargo operations.

6. Caveats

There are two caveats to the conclusions drawn in this paper.
Firstly, there is very little published test data or CFD data for T-strips. This is in sharp contrast to the physically similar L-strip or Gurney flap which has a large literature data-base of tests and CFD covering the effects of aerofoil section, Reynolds Number, Mach Number and surface sweep angle. Examples are to be found in [7], [8] and [9].
The simple L-strip has also been refined over the years into a Divergent Trailing Edge, [10] and [11], to increase physical robustness and reduce its profile drag. There will probably be advantages from similar refinements to the simple T-strip as indicated in Fig. 13.

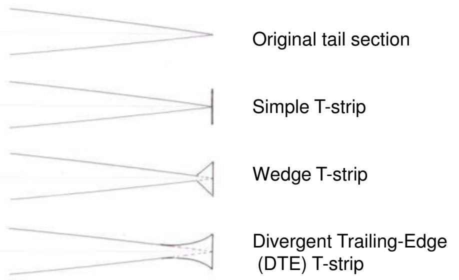

Fig. 13 Some T-strip shape options

It is recommended that the research community should explore the T-strip in detail, both with CFD and wind tunnel testing, and in particular at very small T-strip sizes. The results of this new work would help to better quantify the potential for Micro T-strips to reduce cost and fuel burn.
Secondly, the T-strip trade study presented here was done using fairly simple, concept-level, first-order methods and did not consider all of the second-order terms which a full industry-standard MDO method would include.

7. Summary

The limited test data for T-strips has been augmented, analysed and correlated to allow interpolation down to very small sizes……the Micro T-strip. The author would be happy to receive other T-strip data.

An example is shown of how Micro T-strips might be used on a new airliner design to allow smaller tail surfaces and so reduce operating costs and fuel burn by up to 1.6%. The simple trade study results reported here need to be confirmed using industry methods.

It is suggested that the Micro T-strip would be a suitable research topic for both CFD and wind tunnel testing at high speed….perhaps as part of the EU Clean Sky programme?

References

1. Cavanaugh, M. A., Robertson, P. and Mason, W. H., "Wind tunnel test of Gurney flaps and T-strips on an NACA 23012 wing", AIAA 2007 - 4175

2. Thieme, H. "Design of Ship Rudders" US Department of the Navy, Translation 321, 1965 pp 53. (staukeil or rudder wedge)

3. Schilling Rudder, " www.wiki.schilling_rudder "

4. Global Market Forecast, " www.airbus.com "

5. Current Market Outlook, " www.boeing.com "

6. World Jet Fuel Production, " www.indexmundi.com "

7. Jeffrey, D. R. M. and Hurst, D. W. "Aerodynamics of the Gurney Flap" AIAA 96-2418

8. Blow, A.W., Tsioumanis, N. and Mellor, N. T., "Enhanced aerofoil performance using small trailing-edge flaps", Journal of Aircraft Vol 34, 1997, pp 569 – 571.

9. Richter, K. and Rosemann, H. "Experimental investigation of trailing-edge devices at transonic speeds", The Aeronautical Journal April 2002, pp 185 – 193

10. Henne, P.A. and Gregg, R.D. "A new airfoil concept", AIAA 89-2201

11. Thompson, B.E. and Robert. D.L. "Divergent-Trailing-Edge airfoil flow" Journal of Aircraft, Vol. 33, No. 5, 1996, pp 950–955

4:th CEAS Air & Space Conference
FTF Congress: Flygteknik 2013

Study on the influence of deflected strake on the rocket plane aerodynamic characteristics.

A. Kwiek, M. Figat
Warsaw University of Technology, Poland

Keywords: *CFD, Applied Aerodynamics, Wind Tunnel Test, Strake.*

Abstract

The paper presents the research on the influence of the movable strake on the basic aerodynamic characteristics of aircraft in tailless configuration. Concept of the movable strake includes deflection of the whole strake (Hinged Strake) and conception of the strake forward flap (SFF) which is attached to leading edge of the strake. The shape of flap and its deflection are considered. The research includes two method of investigation: numerical and experimental.

1 Introduction

Nowadays the number of commercial space technology applications are continue to grow. A new era of the universe exploration was begun, visiting the outer space by an average people as a tourist [1].

Now on the market are many private space companies, which are non-governmental entities. One of the proposed services is space tourism. Ansari X Prize competition encourages to investing money for this kind of branch industry. The competition was dedicated to non-governmental entities and consists in design and built a spacecraft for a human space suborbital flight. The vehicle should be able to take three persons on board and perform two flights in two weeks and obtain altitude 100 kilometres above sea level. Scaled Composite was the winner of the mentioned competition. They design Tier One which consists of the mother plane (White Knight) and the rocket plane (Space Ship One).

A multistage configuration is popular in a space technology, especially in rockets design. However the concept of a coupled airplane is also utilized in aviation for example Zveno project, S.20 Mercury & S.21 Maia, Mistel and X-15& B-52.

Currently, a few companies take the race on the first privet vehicle for commercial manned space tourism flights.

2 MAS – Modular Aeroplane System

Due to a market demand on a vehicle to space suborbital human flights [1], WUT team beginning working on an airplane system to space tourism [2]-[4]. The concept is inspire by White Knight & Space Ship One but consists of some interesting improvements. WUT concept assumes that both vehicles are design as a tailless airplane but bonded together create a conventional plane where the rocket plane is use as a tail of the whole system. This system is called Modular Aeroplane System – MAS and is presented in Fig. 1.

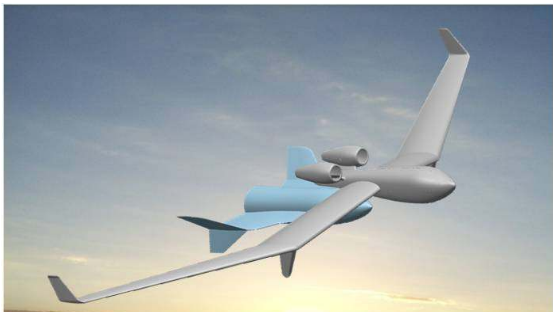

Fig. 1 Modular Aeroplane System – MAS.

The concept of MAS mission profile assumes five flight phases. In the first phase the rocket plane is lifted by the carrier on the 15 kilometres above sea level. The next part of the mission includes vehicles separation and the engine flight of the rocket plane. In the third phase the suborbital flight is performed. During the re-entry the rocket plane is glides and vortex flow is generated by the strake [5]. This phenomenon supports aerobraking which prevents excessive accelerating of the rocket plane.

MAS main requirements are determined by mission profile. Especially the geometry parameters of the rocket plane are defined by flight conditions of re-entry. The paper focused only on the rocket plane. Fig. 2 presents the layout of the vehicle geometry.

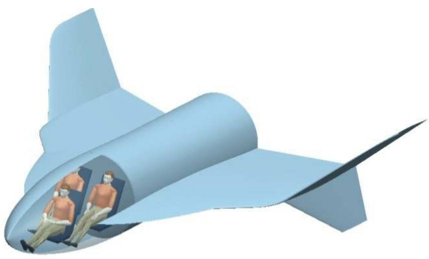

Fig. 2 The rocket plane layout.

The rocket plane is the most important part of the MAS. Previous research was mainly focused on aerodynamic investigation of the rocket plane [2]-[4]. Especially, to find the optimal geometry of the rocket plane: main wing, all moving tail and strake which fulfil requirements of the mission. A lot of numerical calculations were made by different software and for a few configurations of the rocket plane.

Due to providing proper aerodynamic force and ensure stability of the rocket plane investigation on possibility improvement of aerodynamic characteristic has been undertaken and below is presented.

3 Concept of the rocket plane aerodynamic performance improvement

3.1 Basic Consideration

Generation of the vortex lift [6] by the strake is very important issue to provide the proper flight condition of the rocket plane. It allows generating an additional component of the lift force and allows controlling descending speed of the vehicle. Moreover aircraft with a strake usually have problem with instability part of pitching moment characteristic. Motivation to consider influence of strake forward flaps on aerodynamic characteristic is to find possible improvement of the rocket plane performance. Moreover, the deflected flaps may be a tool to control the initialization, generation and intensity vortices. This solution may be a efficient solution to control the vortex breakdown phenomenon too [7] .

3.2 Geometry of the strake-wing configuration

The research consists of numerical aerodynamic calculation and wind tunnel test too. Investigated configurations can be divided on two groups. The first included numerical models of the strake and theirs geometry is described in this chapter. Results of numerical analysis are presented in chapter 4.

The second group is experimental models. All results and detail information of the test are presented in chapter 5.

Mentioned numerical group can be distinguished on two kinds of strake configuration. The first consider concept of the strake is called hinged strake (see Fig. 3). This idea assumes that whole strake is deflected, detail information is included in chapter 3.2.1. Second type of aerodynamic characteristic improvements consist in Strake Forward Flaps (SFF) is an integral part of the strake, detail information is presented in chapter 3.2.2.

3.2.1 Hinged Strake

The hinged strake concept is not new idea [7]. It assumes that whole surface of the strake is deflected. The rotation axis is parallel to the rocket plane symmetry axis and is target to the body surface. The shape of leading edge of the strake was optimized, but during this process assumed that the strake is fixed component. The optimization is not a part of presented study.

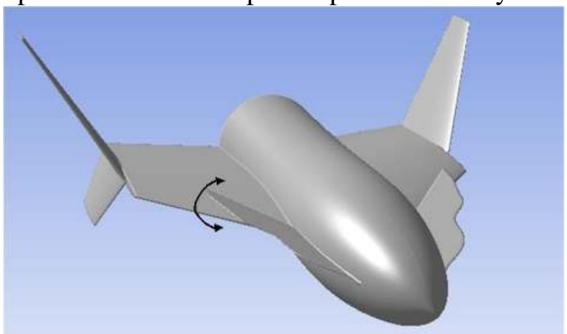

Fig. 3 The model of hinged strake.

3.2.2 Strake Forward Flap

The concept of Strake Forward Flap - SFF assumes that the triangular shape strake (Fig. 4 - baseline configuration in gray) will be equipped with forward flap (Fig. 4 black). The hinge line is presented in Fig. 7 and was assumed that is the same for all considered cases of SFF.

A few cases of SFF geometry are presented. Some of them are inspired by experience some are results of previous numerical investigation.

The first investigated case SFF 2, assumes use of simple straight flap with constant chord in span-wise direction (see Fig. 4). The flap is spanned along all leading edge of the strake.

The next flap concept presented in Fig. 5 is called SFF 8. The main modification according to the previous one is span wise variable chord. The taper ratio of presented flap is equal 1/3. It is used for provide a changeable sweep angle of the SFF along span.

Fig. 6 presents SFF 4, the flap consist of two the same segments, both flap segments has the same geometry and the taper ratio is equal 1/3.

The last considered case is SFF 7. Fig. 7 presents the geometry of this flap. The shape of the flap is a results of analyses of previous solutions and was experimental investigated in wind tunnel too.

Both models presented in Fig. 7 and Fig. 8 are used to wind tunnel test only. Two group of strake were tested. The first group consists of SFF attach to leading edge of the triangular strake. In this case the rotation axis is collinear with the hinge line.

The second group consists of the concepts of retractable flap. The main idea of this kind of flap is modify a sweep angle of the strake by retractable flap. Two cases of retractable flap are presented in Fig. 9 and Fig. 10. The rotation axis is attached to strake apex and perpendicular to strake face. In first case a whole leading edge of the strake is retraceable. However in second case only a half of the strake leading edge is retraceable.

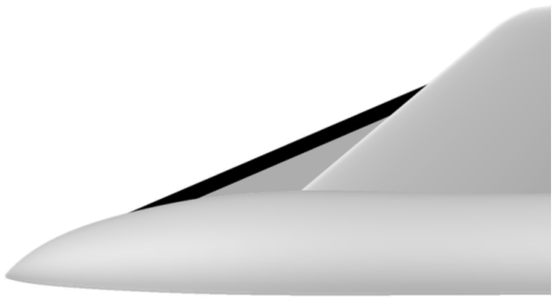

Fig. 4 Top view of SFF 2.

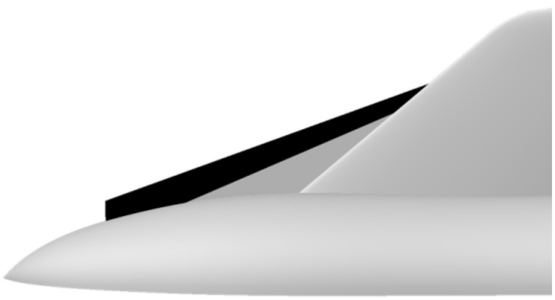

Fig. 5 Top view of SFF 8.

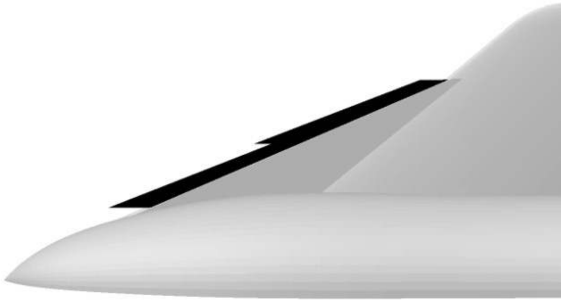

Fig. 6 Top view of SFF 4.

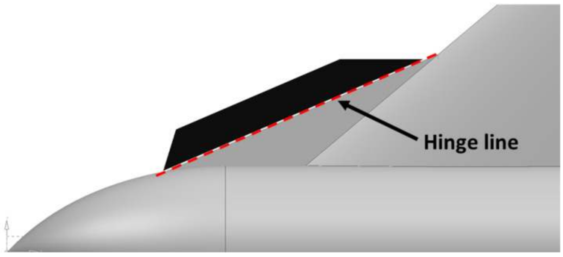

Fig. 7 The strake with attach SFF 7.

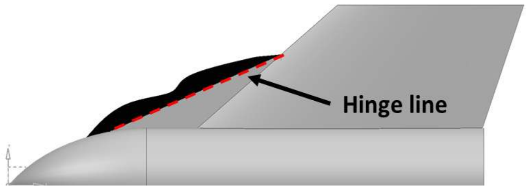

Fig. 8 The strake with attach ogee forward flap.

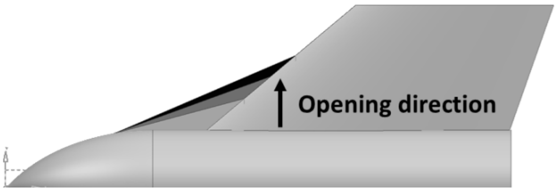

Fig. 9 Retractable flap 1.

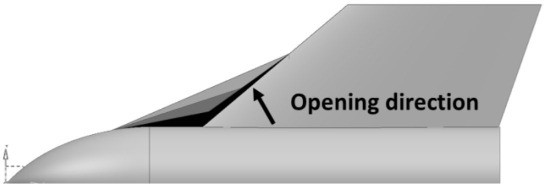

Fig. 10 Retractable flap 2.

4 Numerical calculation

Numerical aerodynamic calculations were computed only for Mach number Ma=0.1 and for wide range of angle of attack. Especially the high angles of attack were deeply investigated. Calculations were conducted by two kind of software.

4.1 Numerical method

The first software is MGAERO [10] which use multi-grid scheme [11] and Euler equations to flow simulation. This program can be used for vortices flow computation but the vortex breakdown is not considers due to inviscid flow. However previous results were validated in wind tunnel test and confirm that this software can be used to preliminary design. A lot of computations were conducted by MGAERO software. The main goal was prepare a quick evaluation of usefulness of a few concepts of the SFF's.

Second software was Fluent which can solve Navier-Stokes equations. This software allow to make a more accurate calculations

4.2 Results

The calculation was conducted for Mach number Ma=0.1. Numerical model for MGAERO software includes seven level of grid. However the mesh for Fluent consists of 5.4 million of elements and k-ε turbulence model was applied. Results for the hinge strake and SFF includes diagram of lift coefficient and pitching moment coefficient versus angle of attack and flap deflection. Moreover pressure distribution (Fig. 12) and vortex visualization by path line (Fig. 11) are presented.

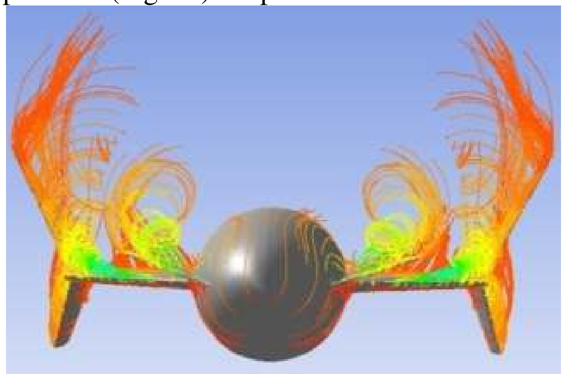

Fig. 11 Model of the rocket plane with the strake deflected – visualization of path lines.

All results are referred to the same reference area. The pitching moment coefficient was measured according to 21% of mean aerodynamic chord. The positive angle of SFF deflection means that flap was deflected down.

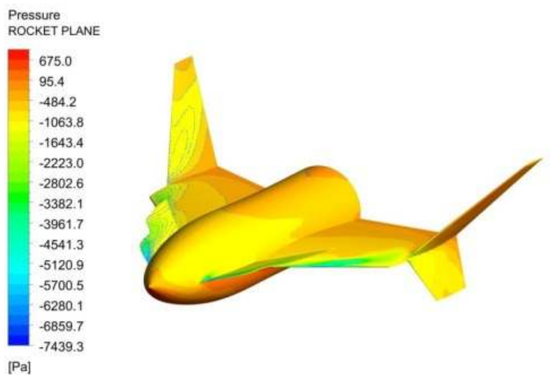

Fig. 12 Pressure distribution for the rocket plane with the strake deflected for Re=10.5M and AoA =22 [deg.].

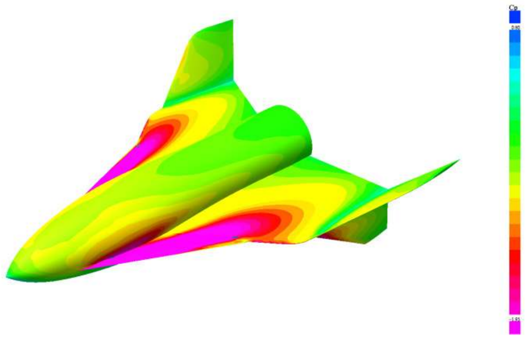

Fig. 13 SF Flap v22 Cp distribution for Ma=0.1 and AoA =24[deg.].

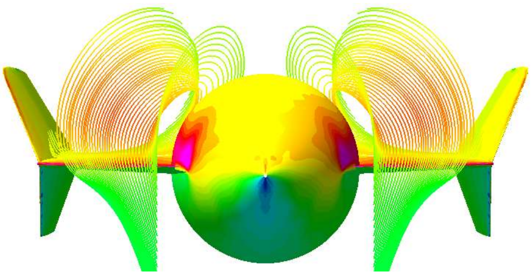

Fig. 14 Streamlines visualization for SSFv23 for Ma=0.1 and AoA =30 [deg.].

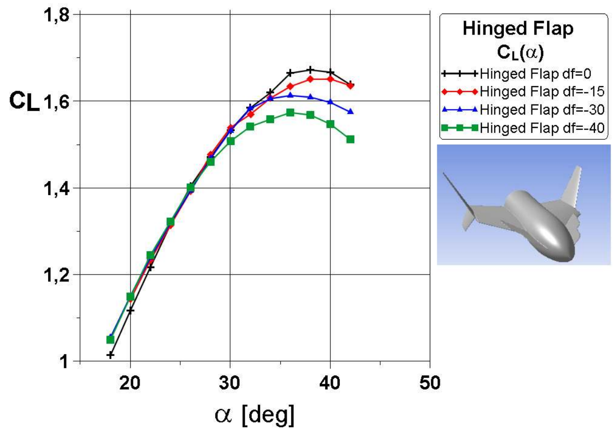

Fig. 15 Lift coefficient vs. angle of attack and deflection angle of strake for hinged flap case.

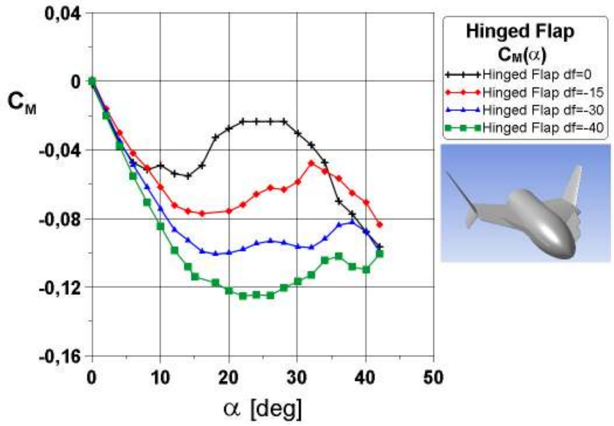

Fig. 16 Pitching moment coefficient vs. angle of attack and deflection angle of strake for hinged flap case.

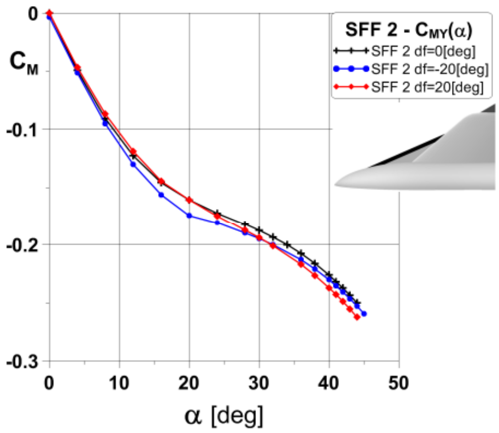

Fig. 17 SFF 2 pitching moment coefficient vs. AoA.

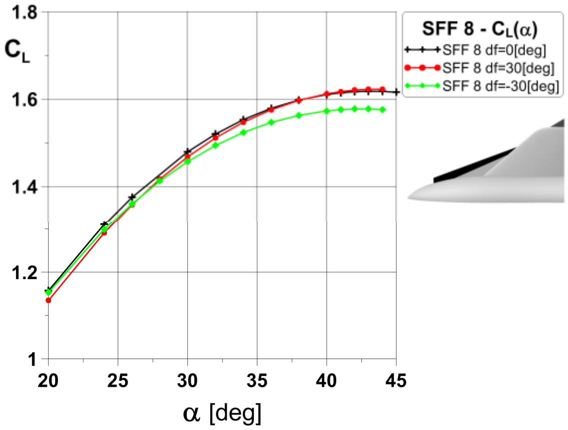

Fig. 18 SFF 8 – Lift coefficient vs. AoA.

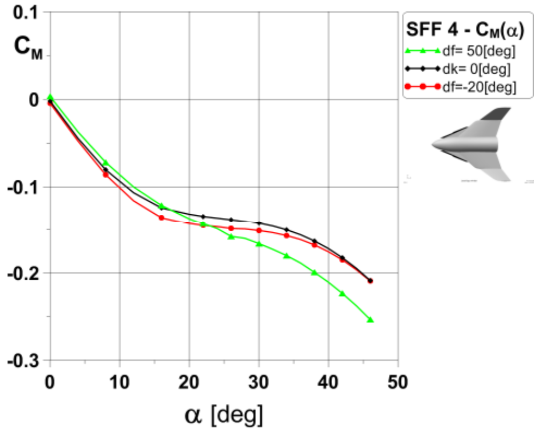

Fig. 21 SFF 4 - Pitching moment coefficient vs. AoA.

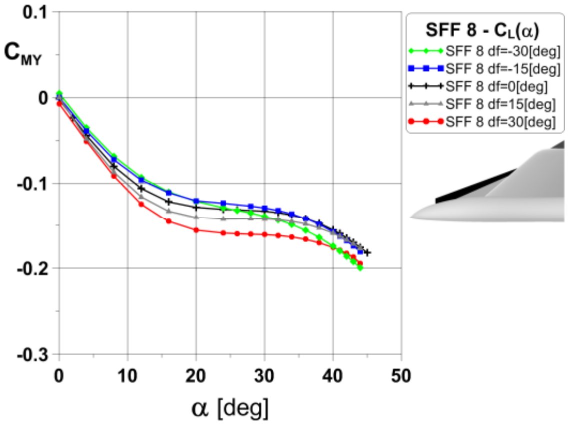

Fig. 19 SFF 8 - Pitching moment coefficient vs. AoA.

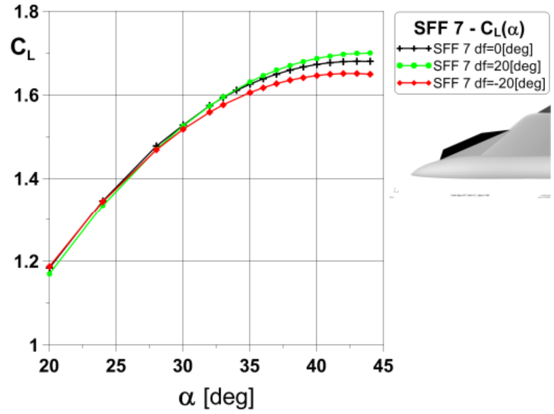

Fig. 22 SFF 7 - Lift coefficient vs. AoA.

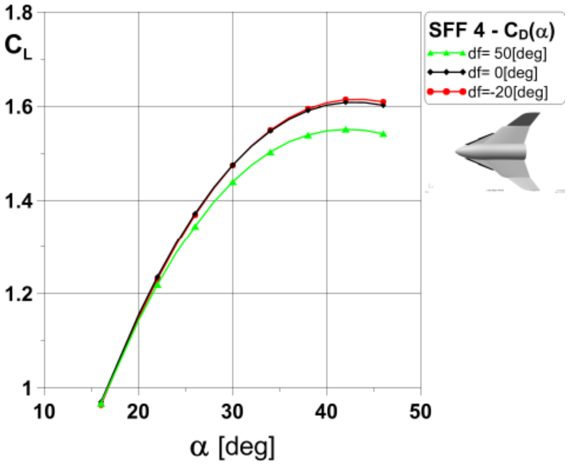

Fig. 20 SFF 4 - Lift coefficient vs. AoA.

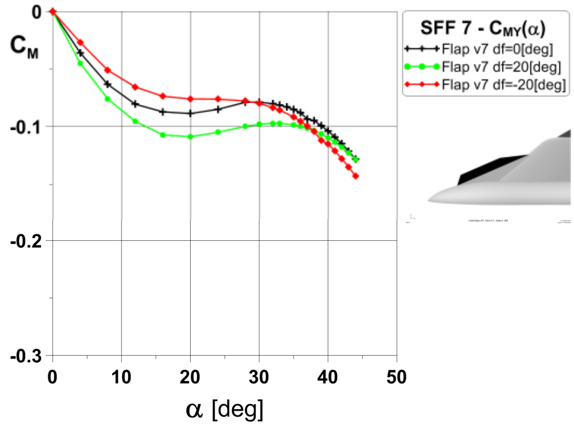

Fig. 23 SFF 7 – Pitching moment coefficient vs. AoA.

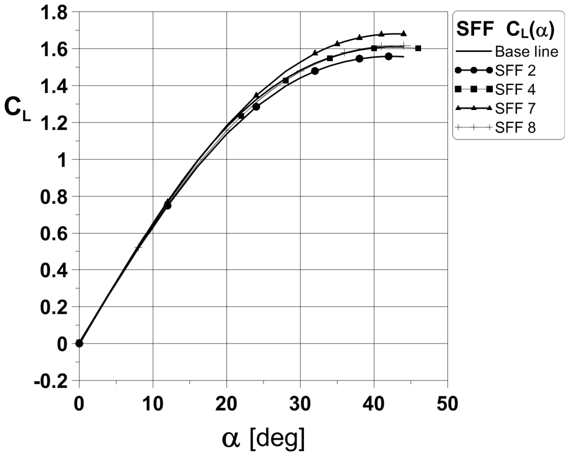

Fig. 24 Comparison of lift force coefficient for all cases of SFF.

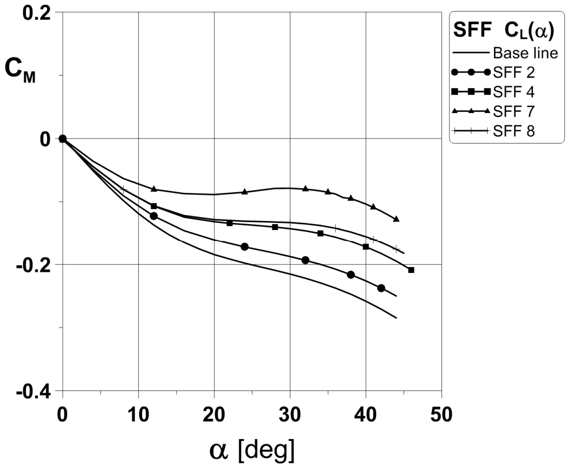

Fig. 25 Comparison of pitching moment coefficient for all cases of SFF.

4.3 Conclusions

Numerical analysis of the hinged flap and SFF reveal that the shape and deflection has an important impact but mainly on the pitching moment of aircraft. The derivative and value of coefficient were changed. The lift coefficient is rather low but change is not significant and is observed only on the high angle of attack.

Fig. 15 and Fig. 16 present the basic aerodynamic characteristics for hinged flap, the calculation were conducted by Flunet for Re=10.5M. This concept improves stability of the rocket plane especially for angles of attack 18 to 24 degree. The lift force coefficient is slight change due to hinged flap deflection.

The most disadvantage of this solution is the deflected area of the strake. Probably, it will be a problem to implementation and design a proper control system.

The SFF concept seems to be easier to implementation then previous solution. Results of computation reveal that impact SFF is similar for hinged strake concept. All presented outcomes for SFF concept were computed by MGAERO.

The lowest impact was observed for SFF 2. The change of lift and pitching moment coefficient caused by flap deflection is low (Fig. 17). For this case the highest value of pitching moment was obtained.

Application of two segmented flap concept – SFF 4 is not change the aerodynamic characteristics significantly (see Fig. 20 and Fig. 21).

The most impact on the aerodynamic characteristics and obtained the highest value of the lift coefficient was observed for SFF 7 (see Fig. 22 and Fig. 23). Moreover, the minimal value of pitching moment (the absolute value) was reached.

For all SFF cases non linear change of pitching moment versus flap deflection was observed (Fig. 17, Fig. 19, Fig. 21, Fig. 23).

Downward deflected flap increase in the maximum lift coefficient slightly, but upward deflected flap reduce the maximum lift coefficient significantly. Probably, it is caused by shifting the vortex flow from wing and reduced its influence on it.

Fig. 24 and Fig. 25 present the comparison of all considered SFF cases without deflection.

5 Wind Tunnel Test

Second part of presented research is results of wind tunnel experiment. A few concepts (presented in chapter 3) of Forward Strake Flaps were examined in subsonic wind tunnel. Main purpose of this experiment was investigation on influence of SFF on main aerodynamic characteristic for low Reynolds number.

5.1 Wind tunnel description

The research was carried out in wind tunnel placed at Aerodynamic Department Faculty of Power and Aeronautical Engineering Warsaw University of Technology. The test focused only on longitudinal cases. The wind tunnel facilities is equipped with devices which is able to measurement the drag force, the lift force and force cause the pitching moment. The campaign was carried out for free stream speed equal V=40m/s, Re=705 000 and for range of angles of attack from 0^o to 45^o.

5.2 Model

The model was built in 1:15 scale. The baseline configuration consist of the axis symmetrical fuselage, the sweep wing, all moving tail placed on the wing tips and the triangular strake.

Two group of strake were tested. The first group consists of SFF attach to the leading edge of triangular strake. The flap was rotated around the same hinge line. Fig. 26 and Fig. 27 presented two shapes of flaps which were tested.

Second type was the strake retractable flap. Fig. 28 to Fig. 31 presents wind tunnel model of this kind of flap.

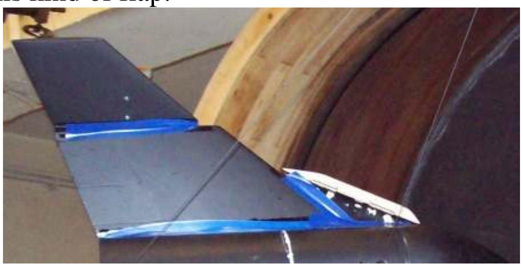

Fig. 26 Trapeze flap attach to the triangular strake.

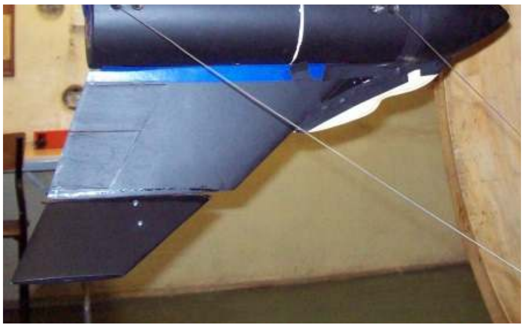

Fig. 27 Ogee flaps attach to the triangular strake.

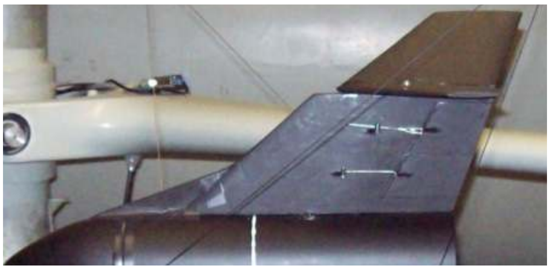

Fig. 28 The strake retractable flap for full leading edge rotation.

Fig. 29 The strake retractable flap for full leading edge rotation.

Fig. 30 The strake retractable flap for half leading edge rotation.

Fig. 31 The strake retractable flap for half leading edge rotation.

5.3 Results

Results of wind tunnel test include chart of lift force versus angle of attack and chart of pitching moment coefficient versus angle of attack for some of investigated configuration.

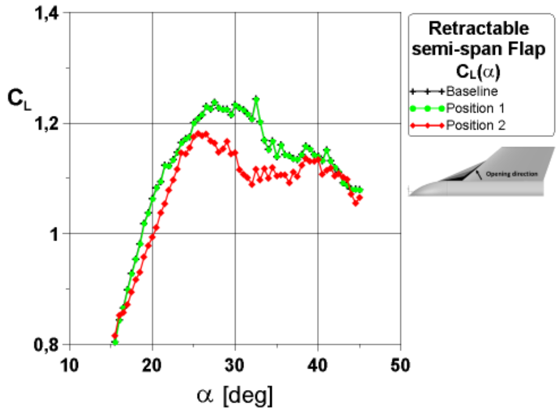

Fig. 32 Retractable semi-span flap - Lift coefficient vs. AoA.

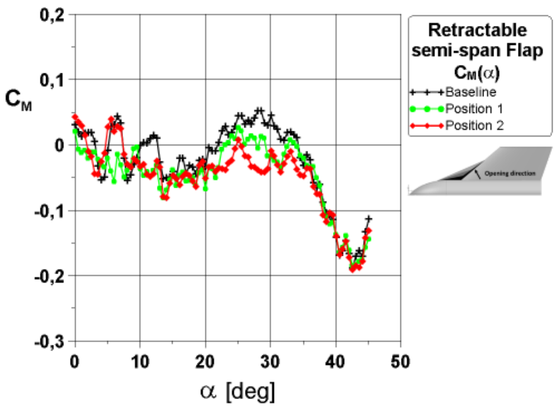

Fig. 33 Retractable semi-span flap – Pitching moment coefficient vs. AoA.

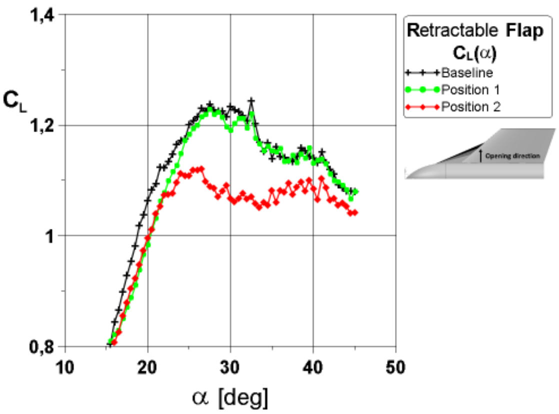

Fig. 34 Retractable full-span flap - Lift coefficient vs. AoA.

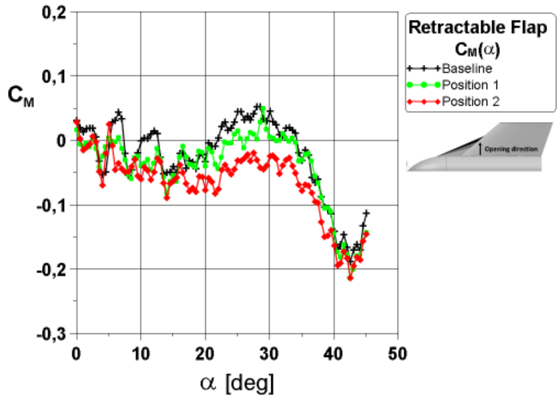

Fig. 35 Retractable full-span flap – Pitching moment coefficient vs. AoA.

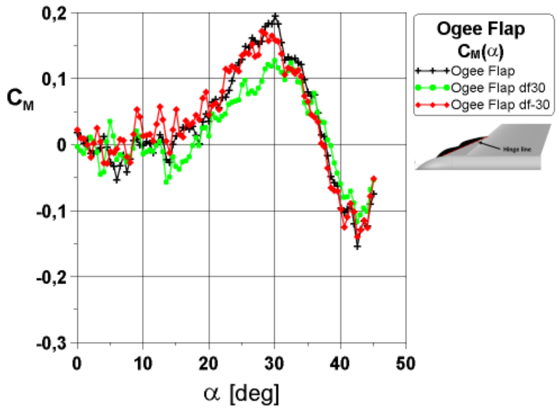

Fig. 36 Ogee flap – Pitching movement coefficient vs. AoA.

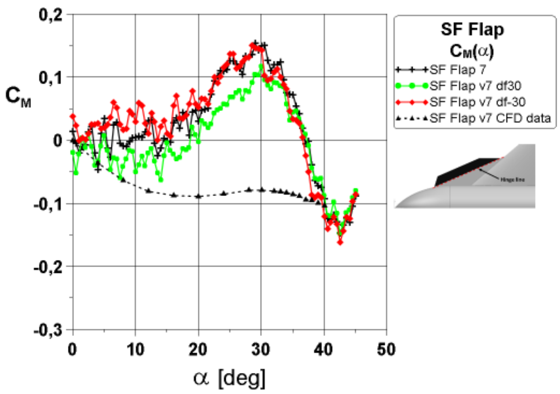

Fig. 37 Trapeze SFF – Pitching moment coefficient vs. AoA.

5.4 Conclusions

According to experimental results all presented type of flaps a little improves the pitching moment coefficient. However the most effective solution is full span retractable flaps (see Fig. 35) but this configuration has the lowest value of lift coefficient (see Fig. 34).

Additionally, the result of computation for SFF 7 was validated by wind tunnel test (see Fig. 37). The difference between numerical and experimental data is connected with method of numerical calculation (inviscid flow), different configuration of all moving tail in wind tunnel model compare to numerical model and precision of define reference point during experiment.

6 Summary and Conclusions

The main goal of this paper was to research the influence of movable strake on the aerodynamic characteristics of aircraft in tailless configuration. Two concepts of movable strake were considered: hinged strake and Stake Forward Flap. .

Results of computation reveal that the concept of hinged strake is promising, but the some problems with implementation may occur. It is connected with quite large area of strake which will be deflected.

Conception of SFF reveals that it will be very useful but only to control the pitching moment. The increase of lift coefficient caused by flap deflection is rather low.

The wind tunnel test was used to validate the numerical computation and to check other concept of flap. Results reveal small improvement of aerodynamic coefficient by presented cases.

Usually tailless configuration of aircraft designed with a strake has a big problem with pitching moment. Results of presented investigation show that for triangular strake with the simple straight flap deflected obtain stability for full range of angle of attack is possible. Moreover, the lost of lift coefficient caused by deflected flap is slight.

Research presented in this paper includes only preliminary analysis of the movable strake. It is planned to continue the further research on presented problem.

Acknowledgements

Authors would like to express our thank for Aerodynamic Department for access to wind tunnel. Moreover, the baseline configuration of the wind tunnel model was built by students of WUT: P. Felczyński and M. Milewska as part of their thesis.

References

[1] Report prepared by The Tauri Group "Suborbital Reusable Vehicles: A 10 Years Forecast of Market Demand" http://space.taurigroup.com/reports/FAA_SRV_2012.pdf
[2] Galiński C., Goetzendorf-Grabowski T., Mieszalski D., Stefanek Ł., „A concept of two-staged spacepalne for suborbital tourism", *Transactions of the Institute of Aviation,* Vol. 191 No.4/2007, pp.33-42
[3] Figat M., Galiński C., Kwiek A., „Modular Aeroplane System. A Concept and Initial Investigation", *Proceeding of ICAS 2012 Conference*, Brisbane, paper number ICAS 2012-1.3.2
[4] Figat M., Galiński C., Kwiek A., „Modular Aeroplane System to space tourism", *Progress in Aeronautics* Vol. 32, No. 1, 2011, pp. 24-37
[5] Lamar J.E., Frink N.T., "Aerodynamic Features of Designed Strake-Wing Configurations", *Journal of Aircraft,* Vol. 19, No. 8, 1982 pp. 639-646
[6] Polhamus E.C., „A Concept of the vortex lift of sharp-edge delta wing based on a leading-edge-suction analogy", *NASA technical note*, Washington D.C. 1966
[7] Mitchell A. M, Delery J., „Research into vortex breakdown control", *Progress in Aerospace Sciences,* Vol. 37, pp. 385-418, 2001
[8] Rao D. M., "Vortical Flow Management for improved configuration aerodynamic- recent experiences" Vigyan Research Associates. Inc.
[9] Zahao W., Kwak D., Rinoie K., „Studies on Improvment of Nonlinear Pitching Moment Charactersitics of Cranked-Arrow Wing" *Proceeding of ICAS 2012 Conference*, Brisbane, paper number ICAS 2012-3.2.1
[10] MGAERO A Cartesian Multigird Euler Code for Flow Around Arbitrary Configuration User's Manual Version 3.1.4
[11] Mavriplis D.J., "Three-Dimensional Unstructured Multigrid for the Euler Equations", *Journal of Aircraft*, Vol. 30, No 7, July 1992

Fluid-Structure Interaction Analyses of Wings with Curved Planform: Preliminary Aeroelastic Results

M. R. Chiarelli, M. Ciabattari, M. Cagnoni and G. Lombardi
Aerospace Unit, Department of Civil and Industrial Engineering, University of Pisa, Italy

Keywords: *curved wing, drag polar curves, FSI analyses, stall of wings*

Abstract

The paper shows preliminary results of aeroelastic analyses of two half-wing models, having curved and swept planform, carried out at the Aerospace Unit of the Department of Civil and Industrial Engineering of Pisa University. For a wing with a curved planform, as demonstrated in previous papers regarding rigid models of wings, the wave drag effects are strongly reduced in the transonic flight conditions.

In the paper some results obtained by using Star-CCM+® 6.04.14 and Abaqus® 6.11 in "co-simulation" are summarized: for this reason the present numerical comparison, between a curved wing and a swept wing, includes the effects of structure's deformability (the wings have the same aspect ratio). The beneficial effects of the planform shape on drag polar curves are confirmed.

Moreover the curved planform configuration improves the wing's aeroelastic behavior: for a fixed value of CL the reaction moments and stress values at the root of the curved wing are reduced by about 5%÷8% with respect the data obtained for the swept wing at the same flight conditions.

Finally, preliminary numerical analyses carried out at high angles of attack show that, as expected, the centers of pressure of the wings move forward with percentage variation of their longitudinal positions that are quite similar. These results indicate that the curved planform shape does not change in a drastic fashion the performances of a wing when the stall condition are reached.

1 Introduction

It is well known that a method to reduce the effect of a shock wave over wings, flying at high subsonic conditions, concerns the increase of the sweep angle of the leading edge. Modern aircrafts have high value of this angle and also high levels of tapering. To obtain the same effects, that is a reduction of both shock wave effects and drag for the aircraft, the curved wing concept has been introduced and discussed by the authors in some previous papers ([1], [2], [3]). To get a confirmation of the good aerodynamic behaviour of such a wing configuration, a new comparative analysis has been executed, at the Aerospace Unit of the University of Pisa, adopting a fluid-structure interaction technique: this analysis provides obviously the effects of the elastic deformation of the wings' structure, representing in a more realistic fashion the loading condition of a flying wing.

In the research development the two wings shown in Figure 1 have been considered [4], [5].

The two wings have the same aspect ratio (half span and chords' distribution are similar:

the sheared wing method has been adopted to draw the curved wing), and the same airfoils. In the present case, swept and curved wings have the aspect ratio equal to AR=7.53. The two wing's models have not twisted profiles along the half span.

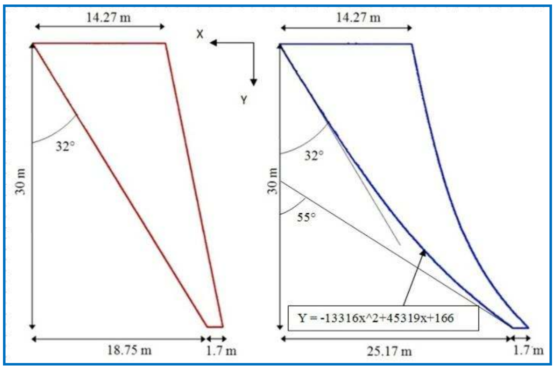

Fig. 1 Geometry of the Wings (Swept and Curved).

Previous campaigns of numerical analyses has shown that, in the case of rigid wing-body models the first with a traditional swept wing and the second with a curved planform wing geometry, a CD (drag coefficient) reduction of 4% can be reached for altitude equal to 10,000 m, Mach number equal to 0.85 and a CL (lift coefficient) equal to 0.4, i.e. a condition representing a transonic cruise flight [2].

The shape of the leading edge of the curved wing have been defined by fixing the values of the slope at root and tip sections and by assuming a second order law in the span direction (in the Figure 1 the mathematical expression of the curve which defines the shape of the l.e. has been inserted).

Both in the swept and in the curved wing configurations the geometry of the airfoil, used to create the CAD models, have been introduced in the X-Z plane according to the adopted reference system (Figure 1): in this way, the selected supercritical airfoil lies on planes parallel to the longitudinal plane of the wing half models. The origin of the reference system coincides with the leading edge of the root section profile.

It is well known that the drag estimation for real configurations of aircrafts, especially in the non-linear transonic conditions or at high angles of attack, represents a challenge for the aerospace engineers and aerodynamic scientists ([7], [8], [9]).

Even thought at the first step the models used in the present research work were not so refined, due to the limitation in the available computational resources, the numerical results obtained allow to assess, with a satisfactory level of reliability, the feasibility of the novel curved wing concept.

2 Results of the Co-Simulation Analyses

The models of the swept wing and of the curved wing has been constructed assigning the properties to the structural components (skin, stringers, ribs, spars) in Abaqus® 6.11. As example a sketch of the structural model for the curved wing is shown in Figure 2. Both structural models of wings have the same dimensions for all their characteristic components. The non-linear large displacement option has been activated to carry out the coupled FE analyses.

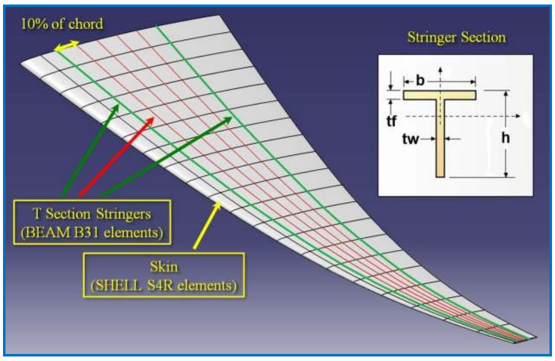

Fig. 2 View of the Curved Wing FE Model.

The results shown in the present work (relevant only to static aeroelastic analyses) do not take into account the distributions of structural weight and non structural weight. From a practical point of view it has been demonstrated that the structural weight has a very little influence on the deformed shape of the wing models at the examined flight conditions.

To carry out the co-simulation analysis is necessary that the CFD and the structural model are perfectly complementary in the areas where take place the exchange of the nodal forces and the nodal displacements. For this reason, in Catia® V5 R20 the complete aerodynamic field that surround the wings has been constructed in such a way that the surface describing the upper and lower skin of the wings are correctly defined and coupled between aerodynamic and structural models.

The object of the present FSI (fluid structure interaction) analyses is a comparative study between two elastic models of wings. The drag polar curves, the CD-Mach curves, the distributions of pressure coefficient along the wings chords, the comparison of both shape and dimensions of the sonic zone around the wings (the so called bubble zone), and the stress values by Von Mises rules have been computed and drawn under the following hypothesis:

Standard Air
Altitude = 10,000 m
CL = 0.4 (to draw the CD-Mach curves)

To execute the comparison the following Mach numbers have been chosen: 0.80, 0.85, 0.875. The drag polar curves have been drawn interpolating the calculated data and an estimation of the drag coefficient per cent reduction has been obtained. In this case an implicit unsteady analysis technique and the k-ε turbulence model have been selected to activate the CFD code; they have been necessary about 500 hours of CPU simulation to obtain the results.

The drag polar curves (H=10,000 m, Mach=0.85) and the CD-Mach curves (H=10,000 m, CL=0.4), represented respectively in the Figure 3 and Figure 4, have been obtained for the two compared wing configurations: swept elastic wing and curved elastic wing.

In the Figure 5 and Figure 6 the distribution of the pressure coefficient for the two wing models, at section planes having the same y coordinate along the half span direction (y = 60% of the half span B and @ y =80% of B), are shown. Looking at the gradient of the pressure coefficient along the chord it can be said, as discussed in [2] and [4], that the intensity of the shock wave for the curved wing is much lower than the intensity of the shock wave for the swept wing: so the wave drag for the curved wing model reduces respect to the swept wing model. From a physical point of view, the reduction of the adverse pressure gradient across the shock wave on the wing surface (in the X-Z plane) should provide also a retardation of the boundary layer separation, and then an increase of the whole aerodynamic efficiency of the wing. This phenomena, which depends on the interaction between the boundary layer and the shock waves, need to be investigated within a suitable and much expensive experimental tests campaign.

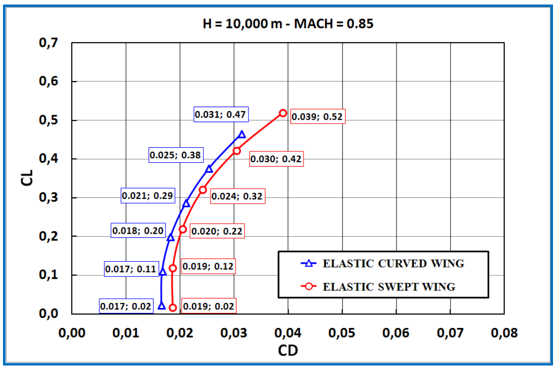

Fig. 3 Drag Polar Curves of the Two Elastic Wings.

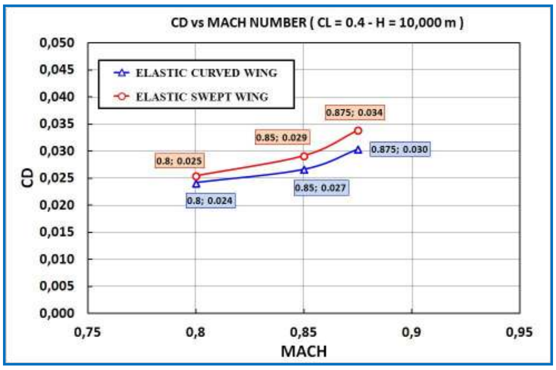

Fig. 4 CD-Mach Curves of the Two Elastic Wings.

In the Table 1 the numerical values of the drag components for each part of the wings' surfaces and the drag coefficient per cent reduction are shown (CL=0.4 and Mach=0.85).

A comparison of the in plant shape and position of the wave front (the shock wave) on the upper surfaces of the two wings proves that, towards the tip of the wings, the area of subsonic flow downstream of the wave front is greater for the curved wing. This phenomena is highlighted in the Figure 7 and Figure 8.

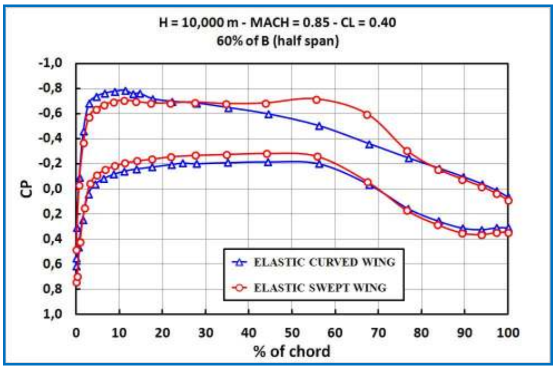

Fig. 5 Comparison of the CP Distribution on the two Wings (Section @ 60% of the Half Span).

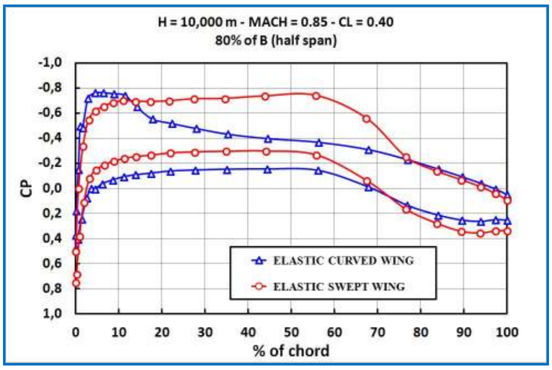

Fig. 6 Comparison of the CP Distribution on the Two Wings (Section @ 80% of the Half Span).

ELASTIC CURVED WING	CD PRESSURE	CD SHEAR	CD TOT
NOSE SURFACE	0.0081	0.0006	0.0087
UPPER SURFACE	0.0164	0.0019	0.0183
LOWER SURFACE	-0.0015	0.0017	0.0002
Total	**0.0230**	**0.0042**	**0.0272**
ELASTIC SWEPT WING	CD PRESSURE	CD SHEAR	CD TOT
NOSE SURFACE	0.0111	0.0005	0.0116
UPPER SURFACE	0.0158	0.0018	0.0176
LOWER SURFACE	-0.0015	0.0016	0.0001
Total	**0.0254**	**0.0039**	**0.0293**
	ΔCD PRESSURE %	ΔCD SHEAR %	ΔCD TOT %
NOSE SURFACE	-27.0	20	-25.9
UPPER SURFACE	3.8	5.6	4
LOWER SURFACE	0	6.2	0
Total	**-9.4**	**7.7**	**-7.2**

Table 1 CFD Results – CD Data for the Elastic Models (Drag Components Reduction: CL=0.4 & Mach=0.85).

In these figures the sonic boundary, the red surfaces which enclose the supersonic region around the wing, has a different shape and different dimensions comparing the swept wing with the curved wing, especially towards the tip of the two wings.

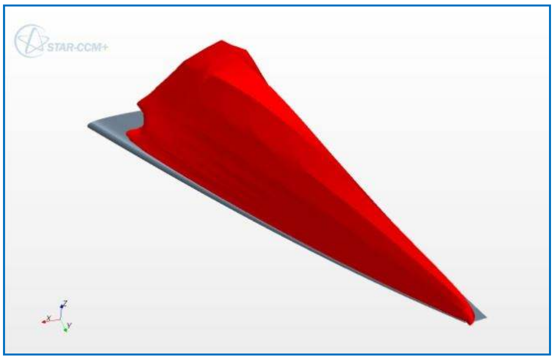

Fig. 7 Swept Wing – Front View of the Supersonic Zone (H=10,000 m, Mach=0.85, CL=0.4).

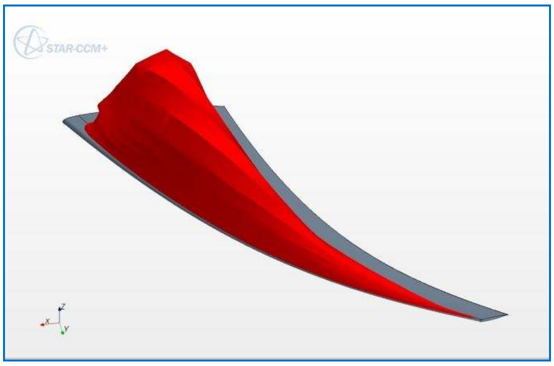

Fig. 8 Curved Wing – Front View of the Supersonic Zone (H=10,000 m, Mach=0.85, CL=0.4).

This fact demonstrates that the perturbation induced in the aerodynamic field by the curved wing is much less intense: that is a lower quantity of the overall asymptotic energy is dissipated in the flow around the curved wing (for a fixed transonic flight condition).

3 Comparison of Results Between Rigid and Elastic models

As an example in the Figure 9 has been represented the comparison between the **CL-CD** curves computed for the rigid and elastic swept wings. As can be seen the two curves overlap perfectly for low values of CL [4], [5], [6].

A similar situation occurs also for the curved wing models.

On the other hand it is to be observed that the **CD_0** value, that is the value of the drag coefficient corresponding to zero value of the lift, as expected, is not influenced by the deformation effects, due to the reduction of the aerodynamic loads along the span of the two wings (looking at the Figure 9 the two couples of drag polar curves overlap perfectly as CL tends to zero). This result is a proof of the goodness of the FSI analysis.

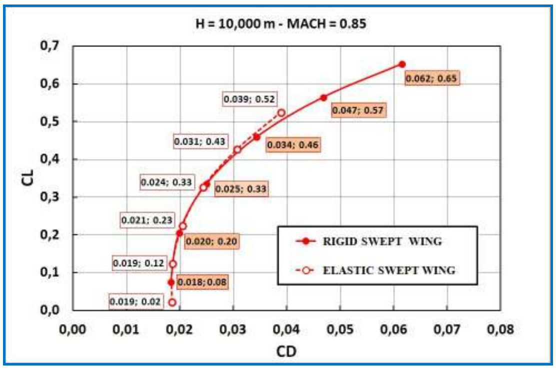

Fig. 9 CL-CD Curves (Rigid vs. Elastic).

Finally observing the results provided by the structural FE models of wings, at the clamped section for the curved wing model the stresses are reduced respect the swept wing model (a reduction of about 5% has been obtained). This fact depends on the reduction of both the bending moment and the torque at the root of the curved wing as a consequence of the in plant shape of this wing [4]. In fact, the resultant lift force for the curved wing tends to move inwards and this causes, as a consequence, the reduction of the bending moment characteristic at the root of the wing.

In the Figure 10 the distributions of the equivalent stress on the upper surface of the two FE models have been shown (reference condition: h=10,000 m, Mach =0.85, CL=0.4). As said these results do not take into account the gravity effects but only the aerodynamic loads acting on the two wings. These results have been obtained adopting a similar structural layout for the two wing models according to works [4], [5], [6]. For these reasons, it can be asserted that the results obtained depend only on the in plant shape of the wings.

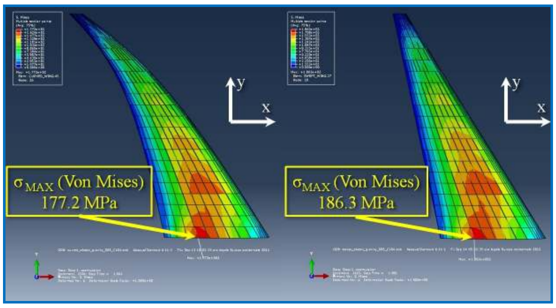

Fig. 10 Comparison of stress on the upper skin of the wings (h=10,000 m, Mach=0.85, CL=0.4).

4 Comparison of the Stall Characteristics for a Swept and a Curved wing

To compare the aerodynamic behavior of a curved and a swept wing at high angles of attack a novel campaign of suitable numerical analyses has been set up. For these analyses new highly refined grids have been constructed: two parametric three-dimensional grids of about 9 million cells. A steady state physical model has been used to carry out preliminary analyses and the k-ε turbulence model, available in the commercial code Star-CCM+, has been adopted. In Figure 11 a sketch of a section of the grid has been shown.

The geometry of the two wings is similar to that used in the previous analyses (Figure 1).

The grids have been constructed following a procedure that is not available in the CFD code. Only hexagonal regular cells have been used to construct the grids around the models of the wings. For the sake of simplicity, the CFD analyses have been carried out without the elasticity effects (rigid wing models).

A low subsonic flight condition has been assumed, that is:

Standard Air
Mach = 0.2
Altitude = 0,0 m (sea level)

As made in the previous works, the drag polar curves of the curved and swept wings have been constructed: these curves are shown in the Figure 12. The data refer to mean values of the converged solutions for both CL and CD.

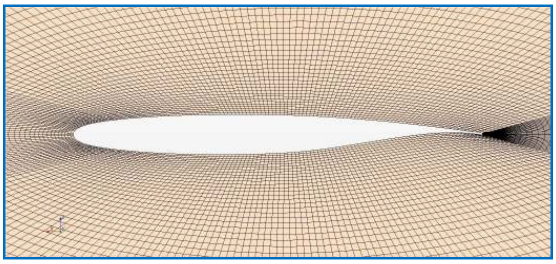

Fig. 11 View of the Plane Grid Around a Section of Wing Models (Structured Grid).

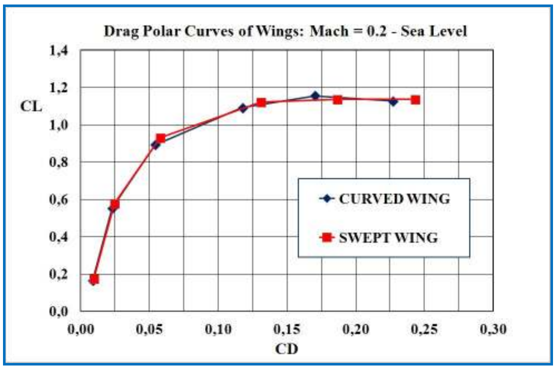

Fig. 12 Drag Polar Curves of the Two Rigid Wing Models (Mach=0.2, Sea Level).

As a first result it can be observed that at low subsonic flight conditions the planform shape does not affect the polar drag of the wings: that is a swept and a curved wing (having the same aspect ratio, same profiles and same value of the angle of sweep of the leading edge at the root section) have same value of efficiency for each physical value of the lift coefficient.

In other words, the curved planform does not modify the aerodynamic performances of a swept wing, having the same aspect ratio, at low subsonic flight conditions. But, as above demonstrated, in the transonic regime the curved planform improves markedly the aerodynamic efficiency of a wing.

A technical aspect that must be investigated concerns the behavior at high angles of attack that is the behavior of a curved wing near the stall condition. To carry out this type of study the longitudinal position of the center of pressure has been computed for the two wing models (for each value of the angle of attack considered). The position of the center of pressure has been measured respect to the leading edge of the root section (that is: the origin of x and y axes in Figure 1) following the approximated formulas (that does not take into account the vertical position of the center of pressure):

$$X_{0-1} = \frac{\int_{wing} (P \cdot X \cdot n_z + S \cdot X \cdot t_z)\, dA}{\int_{wing} (P \cdot n_z + S \cdot t_z)\, dA} \qquad (1)$$

$$X_{0-2} = -\frac{\int_{wing} (P \cdot Z \cdot n_x + S \cdot Z \cdot t_x)\, dA}{\int_{wing} (P \cdot n_z + S \cdot t_z)\, dA} \qquad (2)$$

$$X_0 \approx X_{0-1} + X_{0-2} \qquad (3)$$

where P and S represent respectively the modules of normal and tangential vector forces acting at a generic point point on the wings surface, n_z , t_z , n_x , t_x represent respectively the components of the normal and tangential unit vectors at a generic point on the wings surface along z and x axes (Figure 13).

The quantity X in the integrals represents the distance of a generic point on the wing with respect to the leading edge of the root section, measured in the chord direction as shown in Figure 13. In the same manner the quantity Z represents the vertical coordinate of the generic point on the surface of wings.

In the equation (3) are shown also the effects of horizontal components of vectors $P \cdot \boldsymbol{n}$ and $S \cdot \boldsymbol{t}$: the quantity X_{0-2} contains these effects.

As can be demonstrated this last term can be neglected also for angle of attack of about 20 degree. For this reason the following numerical computation does not take into account this contribution and it is assumed $X_0 \approx X_{0-1}$.

In the Figure 14 have been represented the approximated values of X_0 for the two wing models as a function of the angle of attack. The centers of pressure tend to move forward from their initial positions corresponding to the angle of attack equal to zero (the angle of attack is measured respect to the x-y plane defined in the

Figure 1: this plane that does not contain the zero lift axis of the wing). From the Figure 14 it can be seen that for both the wings the minimum value of X_0 is equal about 10 m.

Computing the percentage variation of X_0 respect to its initial value, the graphs of Figure 15 has been obtained.

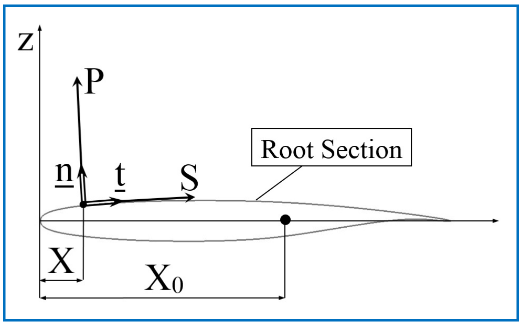

Fig. 13 Notations Used for the Computation of X_0.

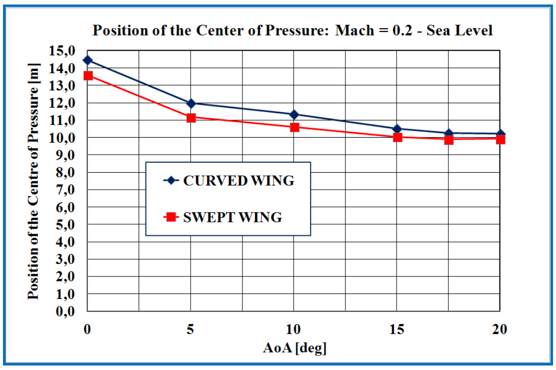

Fig. 14 Values of X_0 for the two wings.

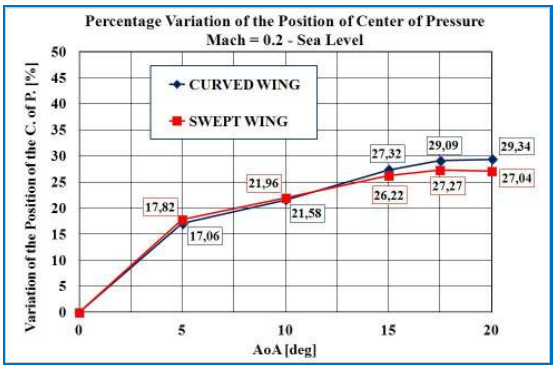

Fig. 15 Percentage Variation of X_0 for the Two Wings.

The numeric data reported in the Figure 14 indicate that for the curved planform wing the percentage variation of the position of the center of pressure reaches a maximum difference respect to the swept wing that is less than 2,5% (curved 29,34% vs. swept 27,04%).

These preliminary results indicate that for low speed and high angles of attack the aeromechanical behavior of a curved wing is similar to the aeromechanical behavior of a swept wing having similar design parameters (aspect ratio, aerodynamic profiles, twist distribution, etc …). In other words, according to these last results, the curved planform wing does not modify in a negative manner the mechanics of flight of an aircraft and, in particular, the stall phenomena will be quite similar to those of a traditional swept wing configuration. On these basis, the well known deep stall phenomena, which typically concerns wings with high sweep angles, can be easily avoided adopting standard methods in the preliminary design phase of a curved wing aircraft configuration.

5 Conclusion

In the paper it has been shown that also taking into account the elasticity effects of the wing-box structure the curved planform of a wing favourably influences the distributions of both pressure coefficient and Mach along the wing span: the results discussed in the present paper, available also in [4], [5] and [6] with much more details, agree with previous results published by the authors and confirm that the feasibility of the examined novel wing configuration can be reached also adopting standard design technology for the wing-box structure.

More in particular, analyzing the co-simulation results it can be said that for the same flight condition (h=10,000 m, CL=0.4 and Mach=0.85) the drag coefficient of the curved elastic model is less of 7% than the same of the swept elastic model (see Figure 4 and Table 1). Moreover the bending moment and torsion moment computed for the curved elastic model are less of about 5% than the computed moments on the swept elastic model. Consequently also the stresses in the skin of the curved wing are less of about 5% than the same of the swept wing (Figure 10).

Analysing the graphs of the distribution of the pressure coefficient at some control sections, see Figure 5 and Figure 6, it can be concluded that the pressure rise across the shock wave is less intense and smoother in the curved wing, and consequently, the adverse pressure gradient towards the trailing edge is reduced. It can be expected that the separation of the boundary layer of the curved wing is delayed with respect to the swept wing in the transonic regime, with consequent beneficial effects on the drag (the aerodynamic efficiency tends to increase).

The plant shape of the shock wave front and the shape and dimensions of the supersonic zone around the wing (the bubble zone) are strongly influenced by the shape of the wings: from a physical point of view it means that the perturbation induced by a curved wing is less intense and then the energy dissipated in the transonic phenomena around it reduces with respect a swept wing flying at the same values of CL and Mach.

Because of the limits of the computational resources a non optimised modelling of the boundary layer has been set up, and certainly absolute values of the drag coefficient are affected by errors, but within the limits of a comparative study the results obtained confirm that, also adopting a fluid structure interaction procedure, the effects of the curved planform configuration of a wing is not negligible from the aerodynamic point of view in the transonic regime.

Further research will be carried out in the future to draw, by the use of FSI procedure, the flutter boundary of a curved wing configuration and to study the vibrations of the tip of wings that can be induced by the turbulent unsteady flow that develops around the wings at high angles of attack.

Preliminary analyses about the aerodynamics at low speed and high angles of attack have demonstrated that for the curved wing configuration the aeromechanical properties are quite similar to that of a traditional swept wing.

In fact both the polar drag curves and the computed position of the centers of pressure are quite identical for the two type of wings.

References

[1] Chiarelli M.R., Cagnoni M., Ciabattari M., De Biasio M., Massai A., "Preliminary analysis of a high aspect ratio wing with curved planform", *XX Congresso AIDAA*, Milan, Italy, 2009, CD-Rom ISBN 978-88-904668-0-9.

[2] Chiarelli M.R., Cagnoni M., Ciabattari M., De Biasio M., Massai A., "High aspect ratio wing with curved planform: CFD and FE analyses", *27th Congress of the International Council of the Aeronautical Sciences*, Nice, France, 2010, CD-Rom ISBN 978-0-9565333-0-2.

[3] Chiarelli M.R., Lombardi G., Nibio A., "A straight wing and a forward swept wing compared with a curved planform wing in the transonic regime", *International Conference of the European Aerospace Societies*, Venice, Italy, 2011, CD-Rom ISBN 978-88-96427-18-7.

[4] Ciabattari M. and Cagnoni M., "Effetti della forma in pianta sul comportamento aeroelastico di ali di elevato allungamento: confronto fra un'ala a freccia e un'ala con forma in pianta curva", Master Degree in Aerospace Engineering, Department of Civil and Industrial engineering, University of Pisa, Italy, 2012. Ref. http://etd.adm.unipi.it/t/etd-09132012-114137/

[5] Chiarelli M.R., Ciabattari M., Cagnoni M. and Lombardi G., "The effects of the planform shape on drag polar curves of wings: fluid-structure interaction analyses results". *STAR Global Conference 2013*, Orlando, Usa, 2013. Ref. http://www.cd-adapco.com/presentation.

[6] Chiarelli M.R., Cagnoni M., Ciabattari M., Lombardi G., "A comparison of the drag polar curves of wings using the fluid-structure interaction analyses", *XXII Congresso AIDAA*, Naples, Italy, 9th – 12th September 2013.

[7] Cole J.D. and Malmuth N.D., "Wave drag due to lift for transonic airplanes", *Procedings of The Royal Society*, A 2005, 461, pp. 541-560, doi: 10.1098/rspa.2004.1376.

[8] Antunes A.P., da Silva R.G. and Azevedo J.L.F., "A Study of Different Mesh Generation Approaches to Capture Aerodynamic Coefficients for High-Lift Configurations", *27th Congress of the International Council of the Aeronautical Sciences*, Nice, France, 2010, CD-Rom ISBN 978-0-9565333-0-2.

[9] Gur O., W.H. Mason W.H. and Schetz J.A., "Full-Configuration Drag Estimation", *Journal of Aircraft*, Vol. 47, No. 4, 2010, pp. 1356-1367.

Acknowledgements

The authors wish to thank the Research Coordination Department of the Tuscany Region for the granted financial support used to carry out the last part of the research work.

4:th CEAS Air & Space Conference

FTF Congress: Flygteknik 2013

Design and Construction of a Silent Wind Tunnel for Aeroacoustic Research

Roberto Putzu, Davide Greco, David Craquelin, Fabien Crisinel

hepia - University of Applied Sciences of Western Switzerland, Switzerland

Keywords: aeroacoustics, silent wind tunnel, anechoic room

Abstract

The anechoic chamber of "hepia - Genève" was modified with the purpouse to host a removable wind tunnel for aeroacoustic research. This paper describes in detail the design and construction of this small scale, low Mach number, silent wind tunnel. Special attention is given to a detailed description of the technical challanges faced.

1 Introduction

Due to the growing interest in aeroacoustics from the side of *"hepia - Genève"* (Haute école du Paysage d'Ingénierie et d'Architecture de Genève - hereafter *hepia*), its pre-existing anechoic chamber was modified in order to host a wind tunnel which can be used for aeroacoustic research. The anechoic chamber, still having to be used for classical acoustic measurements, could not host a permanent facility. A choice has been made to design and construct a removable wind tunnel inside the anechoic chamber.

2 Scope of the work

This paper presents the design and the construction of a small-scale, low Mach number and silent wind tunnel for aeroacoustic research. The presented work was realized in the anechoic chamber of *hepia*. The technical challenge of this project rises due to the fact that any new installation in the anechoic chamber should not prevent its further use for purely acoustical measurements. This led to the choice of a silent wind tunnel that does not introduce relevant structural modifications to the anechoic chamber and that can be easily removable.

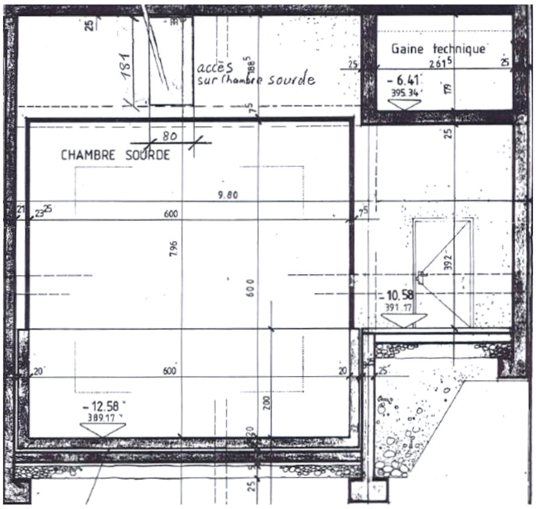

Figure 1: Schematic drawing of the hepia anechoich chamber.

The silent wind tunnel test section is an open test section where flow is provided by an horizontal square jet. The open jet test section is particularly suitable for acoustic testing because the surrounding plenum chamber can be equipped with acoustc linings [2]. In fact, the test section is positioned inside the anechoic chamber, so that aeroacoustic experiments can be performed with a very low background noise

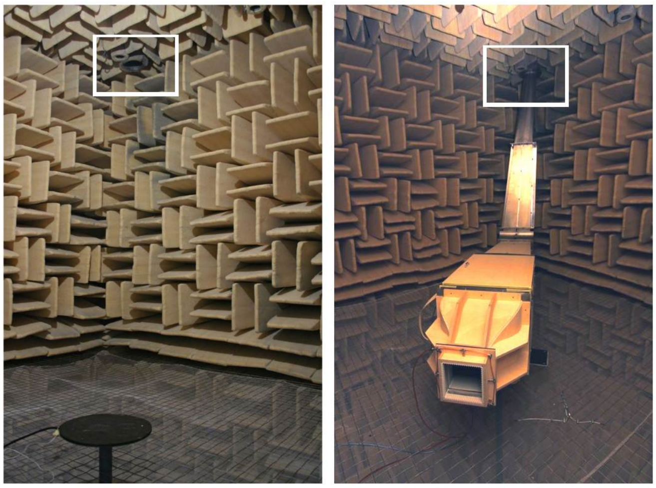

Figure 2: Internal pictures of the *hepia* anechoic chamber. The left figure shows the empty chamber. The right figure shows the wind tunnel setup inside it. The figures highlight the aperture used for the ventilation of the room.

level.

3 The *hepia* anechoic chamber

The *hepia* anechoic chamber, presented in Fig. 1, is a 6 m side cubic chamber lined with sound absorbing wedges (prisms 860 mm long) on the walls, ceiling and floor. The chamber is mounted inside a room that is located underground, to minimize the noise transmitted from the surroundings to the anechoic chamber. Several omega-shaped springs suspend the chamber with respect to the room where it is housed and prevent acoustic-vibrational coupling of the two structures. Above the ceiling of the anechoic chamber, an empty space exists, providing room for technical inspections and for housing a ventilation system. This system is used to blow air from outside into the test chamber, with the purpose of reducing the moisture level in the acoustic facility. The ventilation system discharge (highlighted by the white square in the left picture of Fig. 2) is a 200 mm circular aperture placed near the upper corner of the chamber opposite to the chamber door.

In order to obtain a low background noise the test section of the silent wind tunnel is housed inside the anechoic chamber. To keep this low noise level during the aeroacoustic experiments, the wind tunnel was designed such that it does not introduce additional noise (silent wind tunnel). To achieve such an objective, the fan of the wind tunnel was housed outside of the chamber, in the empty space above the ceiling of the anechoic chamber.

The main issue to be addressed in the wind tunnel design and construction was the identification of a flow entry within the anechoic chamber without massive, expensive and destructive actions on the structure of the room. As shown in Fig. 2, the flow entry was decided to be the already existing aperture previously used for ventilation purposes. Since this hole is placed on the opposite top corner of the room entrance, the layout of the room suggested the possibility of using the open door as air outlet during the aeroacoustic experiments. Fig. 3 shows the configuration of the silent wind tunnel.

4 Aerodynamic design

The design goal of the wind tunnel is to perform aeroacoustic measurements at low Mach numbers. For this purpose, the target maximum flow velocity in the test section was set to 20 m/s.

According to the geometrical dimensions of the anechoic room, we found that a suitable configuration is to have a square nozzle of 20 cm edge with a contraction ratio of 6.25. The settling chamber is then a square cross section chamber with 50 cm edge. This nozzle design leads to a volume flow rate in the test section of 2900 m^3/h (at 20 m/s). With the 20 m/s of airflow speed and nozzle dimensions of 400 cm^2, is possible to guarantee the Strouhal similarity for a wide range of aeroacoustic applications of technical interest.

The design value of the volume flow rate, together with the overall pressure drop of the wind tunnel, governs the aerodynamic choice of the driving fan [3]. The pressure drop Δp was computed as the summation of the individual pressure losses estimated for each component of the wind tunnel.

After comparing our design requirements with the data given by different fan manufacturers, the best solutions in terms of pressure increase and noise emission (Table 1) with the Helios GigaBox 560 4/4. It consists of a centrifugal fan driven by a three-phase motor (400 V, 50 Hz) which absorbs a maximum power of 2.5 kW. A frequency regulator was adopted to vary the fan speed.

5 Acoustic design

An essential requirement of an open jet wind tunnel for aeroacoustic measurements is that the background noise level should be significantly smaller (at least 10 dB) compared to a reference test noise that could possibly be investigated in the test chamber [1], for instance the jet noise. The acoustic design of the wind tunnel was conducted according to the technique proposed by Sarradj et al. [11]. Considering the fan as the main source of acoustic disturbances, the acoustic calculation aimed at predicting the background noise induced by it inside the test section all through the wind tunnel conduits [11, 9]. The background noise level was then compared to the reference jet noise.

In general all the fan contributions to the background noise have to be considered in the acoustic design of a silent wind tunnel: upstream, downstream and casing radiation noises.

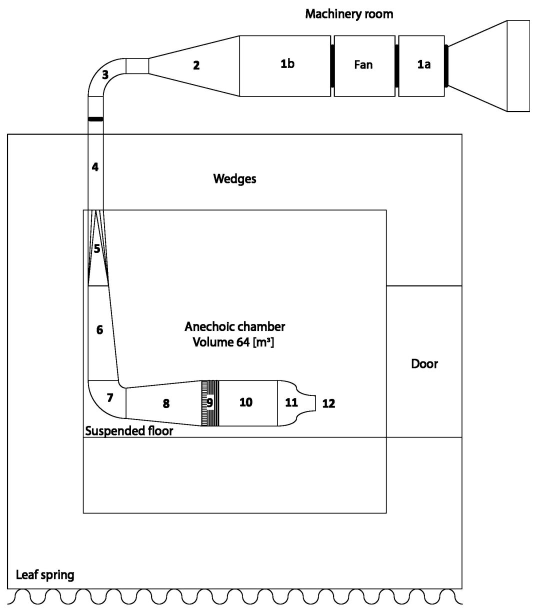

Figure 3: Configuration of the silent wind tunnel housed in the *hepia* anechoic chamber. The elements composing the wind tunnel are: a centrifugal fan, two cylindrical mufflers (1a - 1b); a convergent muffler (2); an elbow (3); a straight unlined duct (4); a round-to-square diffuser (5); a square diffuser (6); a lined absorbing elbow (7); a square diffuser (8); a section with honeycomb and screens (9); a settling chamber (10); and a convergent (11). The test section of the wind tunnel is the open-jet discharge (12).

Especially, in a closed loop wind tunnel, both upstream and downstream sections would need to be designed to damp the noise produced by the fan in both directions. Nevertheless, in our specific case there is no return circuit from the test chamber to the fan. The fan and its aspiration port are placed in the machinery room right above the anechoic chamber avoiding a direct contact with the test section. For these reasons, their contribution to the background noise was neglected and only the downstream fan noise reaching the test section by the nozzle was considered. Furthermore, the transmission of structural vibrations from the fan casing to the test chamber is prevented by the use of soft connections with the adjacent ducts and by

Sound Power Level	**125**	**250**	**500**	**1k**	**2k**	**4k**	**8k**	
$L_{W,Fan}$ (@ max speed)	78.1	82.6	78.2	75	72.8	69	62.1	Given by the manufacturer

Table 1: Fan SWL in octave bands

Figure 4: Wind tunnel setup in the machinery room above the anechoic chamber.

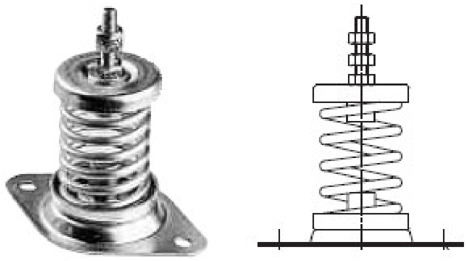

Figure 5: Fan casing silent block - Helios catalog.

silent block connections on its base.

In order to damp the noise propagated downstream from the fan (Fig. 3), a cylindrical muffler (Fig. 3-1b) and a convergent muffler (Fig. 3-2) are used. Similar silencer arrangements have been already introduced in many acoustic wind tunnel facilities as describerd by Mueller [8]. In particular, the convergent downstream of the fan (Fig. 3-2) is necessary to reduce the duct section to size of the aperture used for the ventilation of the room (Fig. 2). The vertical conduit (Fig. 3-3,4,5,6) presents: a narrow corner, high flow velocities and a diffuser. These elements introduce new flow-generated noise that needs to be damped. On this purpose, the last components of the wind tunnel before the open jet were acoustically treated. The elbow downstream of the diffuser (Fig. 3-7) is lined both on the walls and on its turning vanes; In a similar manner, the settling chamber walls (Fig. 3-10) are acoustically lined.

6 Mechanical design

As shown in Fig. 4, all the elements installed in the machinery room were hung on the room ceiling (room's top wall) in order to preserve the modal separation of the anechoic camber from the rest of the bulding. Moreover, as better explained in the following sections, the fan was assembled in the structure carefully avoiding rigid connections in order to avoid solid noise transmission.

When possible, commercial sound absorbers have been used, but when particular shapes were necessary the acoustic damping elements were manufactured at the *hepia* workshop. In all these cases a dynaphon absorbing material panel was used, which was held in place by a perforated stainless steel plate. The perforation pattern of this plate was chosen according to Mueller [7] and Schultz [12] in order to guarantee a reasonable transparency index to the acoustical radiation.

In most of the sections of the wind tunnel, static pressure probes were installed for troubleshooting purposes. This enables the investigation of the experimental head losses all along the tunnel.

As shown in the right picture of Fig. 2, at present only the bare wind tunnel construction materials were left in the anechoic chamber without absorbing coating. In the future work, all the rigid sections exposed to the test room will be covered to limit the acoustic reflections.

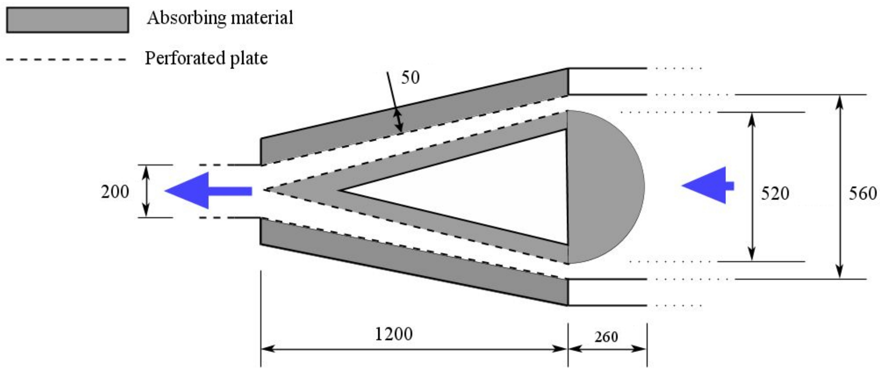

Figure 6: Convergent muffler's schematic drawing, units are in mm.

6.1 The Fan and the cylindrical silencers

In order to avoid the propagation of vibrational solicitations from the motor, the centrifugal fan (Helios GigaBox 560 4/4) and the cylindrical silencers (Helios RSD series, elements 1a and 1b in Fig. 3) were assembled together by means of flexible junctions, represented in Fig. 3 by thick black lines. Moreover, for the same purpose, the fan casing was connected to the hanging frame by means of spring silent blocks (Fig. 5).

6.2 The convergent muffler

Downstream of the commercial muffler (Fig. 3-1b), a convergent section (Fig. 3-2) had to be installed to fit the dimension of the old ventilation duct and to enter the anechoic chamber. To increase the acoustical damping of the wind tunnel, the external wall of this contraction cone was lined with a 5 cm thick layer of absorbing material (Dynaphon B810 50). In order to further increase the acoustic damping of the section and to avoid the direct radiation of the fan noise past the convergent, an absorbing cone was manufactured and was installed in the convergent as shown in Fig. 6.

6.3 The first elbow

Downstream the convergent silencer, the flow has to bend downwards, in the direction of the anechoic chamber. To limit the flow losses due to the reduced duct diameter and to the small curvature radius, three panels were installed inside the elboe as flow separators. Downstream of the first elbow, a straight duct section enters inside the anechoic chamber, where a divergent section slows down the flow and changes the cross section shape from circular to square.

6.4 The second elbow

The second elbow, necessary to redirect the flow towards the exit door, has a square cross section bending with concentric radii. To reduce the head losses and generate an uniform flow downstream, it has two flow separators [3] shaped as airfoils and installed with respect to the elbow rotation center at the distances imposed by Eq. (1) [3]:

$$r_i = 1.26 r_{i-1} + 0.07 b_0 \tag{1}$$

where b_0=400 mm is the size of the square section.

The second elbow is an acoustically absorbing element. As shown in Fig. 7, both the external casing and the turning vanes were lined with absorbing material (Dynaphon B810 50).

In order to insure the stiffness of the absorbing flow separators, the leading and trailing edges were manufactured in wood. Moreover, the foils' upper and lower surfaces, riveted to the wooden elements, were made in bent perforated stainless steel, holding together a shaped Dynaphon panel.

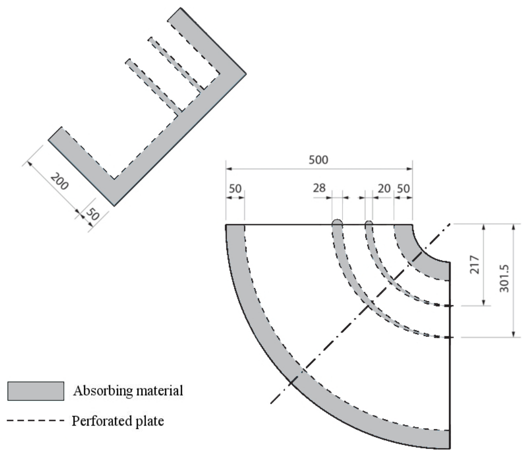

Figure 7: Second elbow section's schematic drawing, units are in mm.

6.5 The settling chamber

Downstream of the second elbow lays the last diverging element, bringing the dimension of the duct to the size of the settling chamber, which is 1 m long with a 500 mm side square cross section.

The settling chamber walls were covered with 40 mm thick Dynaphon B810 foam, using the same technique as for the other wind tunnel's absorbing elements. Inside the settling chamber, a honeycomb and several screens were installed to insure the flow quality in the test section [10, 4]. The screens were installed on wooden frames housed between the absorbing elements. As shown in Fig. 8, the settling chamber can be easily opened and the wooden frames are easy to change. This modular design was chosen to simplify the aerodynamic tuning of the facility once the construction was finished.

The mainframes of the last divergent and of the settling chamber (elements 8 and 10 in Fig. 3) were manufactured in wood to limit the vibrations induced by the flow instabilities. Moreover, the use of wood has simplified the subsequent modification operations necessary for the commissioning of the facility. Nevertheless, the use of wood in a removable facility is to be done with caution, since the wood can't withstand several mounting and unmounting operations. For this reason, stainless steel flanges were installed at the extremities of the wooden elements and rubber joints were used to insure the air-tightness.

Figure 8: Settling chamber assembly.

6.6 The nozzle

Since the settling chamber and the test section were designed to have respectively the sides of 500 mm and 200 mm, the contraction ratio of the wind tunnel nozzle was fixed to 6.25.

The profile of the contraction cone was chosen according to Morel and Su [5, 6, 13], aiming at minimizing its length without generating flow separations and turbulence in the test section.

The side walls of the nozzle were built in 7 mm thick aeronautic flexible plywood, that could be bent in one direction. Moreover (Fig. 9), the nozzle's surfaces were designed to be held in place by a wooden external frame and by a steel flange connecting it to the previous element.

A second metal flange was installed at the nozzle exit. On both (inlet and outlet) metal structures, rings of static pressure probes were mounted. These pressure rings were correlated to pitot tube measurements and are currently used to measure the wind speed in the test sec-

Figure 9: Wind tunnel nozzle.

tion.

7 Conclusions

After the design of the wind tunnel, the aeroacoustic facility was built. Today the authors are working on the stabilisation of the flow in the vertical diffuser. Moreover, the wind tunnel's surface exposed to the anechoic chamber still needs to be lined in absorbing foam.

A preliminary characterisation of the wind tunnel was conducted after its construction, but a complete investigation will be carried out in the next future.

Acknowledgements

The authors aknowledge Devis Tonon, Antoine Pittet, Franois Bugnon (hepia Geneva) and Renzo Arina (Politectico di Torino), for their valuable contribution to this project.

References

[1] Chong T.P., Joseph P.F. and Davies P.O.A.L., "Design and performance of an open jet wind tunnel for aero-acoustic measurements", *Applied Acoustics*, No. 70, 2009, pp. 605-614.

[2] Helfer M. and Wiedermann J., "*Experimental aeroacoustics*", Von Karman Lecture Series, 2007-01.

[3] Idel'cik I.E., "*Handbook of Hydraulic Resistance*", Jaico Publishing house, 3rd edition, 2005.

[4] Loehrke R.I. and Nagib H.M, "Control of Free-Stream Turbulence by Means of Honeycombs: A Balance Between Suppression and Generation", *Journal of Fluids Engineering*, No. 98, 1976, pp. 342-351.

[5] Morel T., "Design of Two-Dimensional Wind Tunnel Contractions", *ASME - Journal of Fluids Engineering*, No. 99, 1977, pp. 371-377.

[6] Morel T., "Comprehensive Design of Axisymmetric Wind Tunnel Contractions", *ASME - Journal of Fluids Engineering*, No. 97, 1975, pp. 225-233.

[7] Mueller T.J., "*Aeroacoustic Measurements*", Springer Editions, 2002.

[8] Mueller T.J., Scharpf D.F., Batill S.M., Strebinger R.B., Sullivan C.J. and Subramanian S., "The Design of a Subsonic Low-Noise, Low-Turbulence Wind Tunnel for Acoustic Measurements", 17^{th} *Aerospace Ground Testing Conference*, 1992, AIAA 92-3883.

[9] Munjal M.L., "*Acoustics of ducts and mufflers*", John Wiley and Sons Inc., 1987.

[10] L. Prandtl, "*Attaining a steady air stream in wind tunnels*", NACA Technical Memorandum No. 726, 1933.

[11] Sarradj E., Fritzsche C., Geyer T., Giesler J.B. and Brown J.,"Acoustic and aerodynamic desing and characterization of a small-scale aeroacoustic wind tunnel", *Applied Acoustics*, No. 70, 2009, pp. 1073-1080.

[12] Schultz T.J., "Acoustical uses for perforated metals: Principles and applications", Industrial Perforators Association, Inc.

[13] Y. Su,"Flow analysis and design of three-dimensional wind tunnel contractions", *AIAA Journal*, No. 29, 1991, pp. 1912-1920.

An Experimental Study of a Separation Control on the Wing Flap Controlled by Close Loop System

A. Krzysiak
Institute of Aviation, Poland

Keywords: *applied aerodynamics*

Abstract

Flow control by using an additional blowing has been a subject of many experimental and computational works. The main task of an additional blowing is to increase the flow velocity in the airfoil boundary layer to delay the flow separation phenomenon and in result to improve the airfoil aerodynamic performance. This paper presents the results of wind tunnel tests of flow control using an additional blowing on the airfoil segment equipped with the movable flap. Blowing was realized through the set of nozzles located on the trailing edge of the main body of the airfoil. Air flow through the nozzles was controlled by a set of the electromagnetic valves located inside the model. Pressures, measured by sensors mounted on the flap surface, created a control signal for a feedback system, regulating flow through the nozzles. The work was performed under the European project "ESTERA".

1 Introduction

Active flow control became widely used in many fields of science and technology and continues to be the subject of intense experimental and numerical studies in a number of research centers [1-7]. Improvement of the efficiency of currently used aircraft control systems or replace them by unconventional flow control methods, can be a source of measurable benefits. These benefits can still be significantly enhanced by the use of flow control operating in the Close Loop Control (CLC) System .

The literature describes a number of different flow control methods [1], One of the methods of active flow control is an additional blowing on a wetted surface. In this method, properly targeted additional air jets increase energy of the flow. Boundary layer supplied with additional energy becomes less susceptible to separation, even at angles of attack higher than the critical (for the condition without blowing). Postponed flow separation contributed to the increase of maximum lift and simultaneously to drag decrease. This in turn, can improve the airplane aerodynamic performance.

In flow control process important issue is to minimize air mass flow rate necessary to use. So air mass flow rate blown to keep flow attached, should be changed respectively to the actual flow conditions. These conditions may change due to deflection of the airplane control surfaces, as well as due to change in external flow conditions. To avoid flow separation during changes in flow conditions it is required to keep track of a boundary layer state. This means you need to define a parameter, whose change in value would indicate the possibility of the appearance of flow separation. Minimization of air flow rate necessary to maintain the desired state of the boundary layer, basing on an analysis of its current state, requires the implementation of such process in control loop

Flow control operating in the feedback loop was the subject of several numerical and experimental studies [8, 9]. In the presented investigation, the numerical simulations were conducted to develop a general aerodynamic concept of the proposed Close Loop Control System for fluidic active flow control. Several different concepts were considered [10]. Finally, as a subject of the research, the high-lift wing segment, based on airfoil NACA0012 with the 30% slotted flap and equipped with air blowing system situated at the airfoil main body trailing edge, has been chosen. In proposed, developed and tested CLC System as a fluidic actuators the electromagnetic valves were applied. Pressure on flap trailing edge as a control parameter was used.

Work has been carried out in the framework of the European Project "ESTERA - CLEAN SKY" (Multi-level Embedded Closed-Loop Control System for Active Flow Control Fluidic Actuation Applied in High Lift and High Speed Aircraft Operations).

2 Experimental Setup and Instrumentation

2.1 Low speed wind tunnel T-1

The experimental tests described in this paper were performed in the low speed wind tunnel T-1 (with 1.5 m diameter open test section) in the Institute of Aviation (IoA), Warsaw for Mach numbers M = 0.1, 0.075 and 0.05. The model of segment of the NACA 0012 airfoil with movable flap was mounted in the wind tunnel test section in a vertical position between two stationary endplates (1495 x 1495 mm), Fig. 1. The bearings placed in stationary endplates made possible the change of the model angle of attack in the range $\alpha = \pm 45\,°$.

Fig. 1 Model of NACA 0012 airfoil with movable flap in the wind tunnel T-1 test section.

The airfoil aerodynamic characteristics (lift and moment) were determined by measuring pressure distribution on the model surface. To calculate the total drag coefficient of the airfoil wake rake measurements were taken. Mach number, Reynolds number and the velocity of undisturbed flow obtained in the wind tunnel test are presented in Table 1.

Table 1 Mach number, Reynolds number and velocity of undisturbed flow.

M	0.05	0.075	0.1
Re	$0.6*10^6$	$0.84*10^6$	$1.12*10^6$
V_∞	18.3 m/s	25.9 m/s	34.4 m/s

2.2 Model of NACA 0012 airfoil

The NACA 0012 airfoil segment model of 0.5 m chord, 1 m span and 30% flap (without optimization of the gap between flap and airfoil main body) was used, Fig. 2. The two spar model was made of composite and equipped with a number of removable upper covers and the free space inside the model.

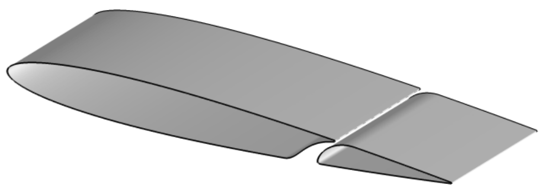

Fig. 2 Model of NACA 0012 airfoil with movable flap.

Movable 30% slotted flap was installed to the main airfoil body on four consoles to allow it deflection in the range from $\delta = 0^0$ to $\delta = 45^0$, Fig. 3. Flap motion with defined angular speed was provided by system of four synchronized electronically servos. The current angular position of the flap has been recorded by the encoder.

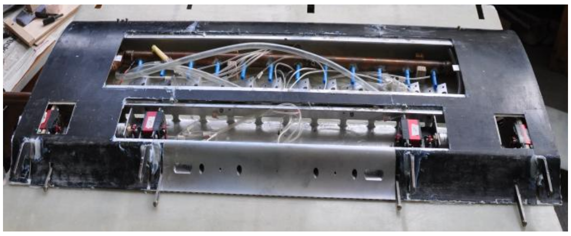

Fig. 3 Model main body with open covers.

To measure pressure distribution on the model surface, approximately one hundred measurement orifices of 0.5 mm diameter were distributed, on the upper and lower surfaces of the airfoil, along its chord (on the flap in four cross sections). The pressures from airfoil and rake were measured by pressure system “INITIUM”, which consists of three pressure electronic scanners ESP-32HD.

The main airfoil section was equipped with the row of the 12 nozzle’s sets situated in its trailing edge. They were arranged in such way, that blowing was directed into the boundary layer on the flap upper surface, Fig. 4. Additional blowing increased the energy of the boundary layer making it more stable and resistant to separation.

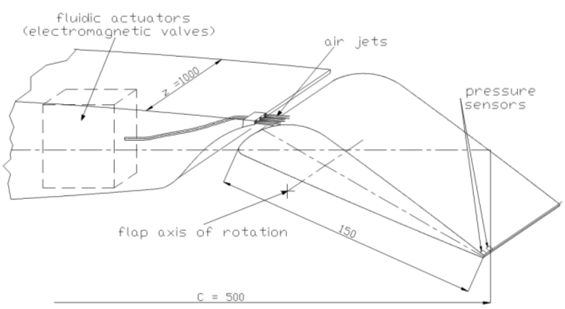

Fig. 4 Blowing on the airfoil flap.

Each of the nozzle’s sets consisted of three nozzles (outlet dimensions 5.6 mm x 1 mm) supplied with air from one chamber. The chambers have optimized internal geometry allows a uniform flow through each of the three nozzles (the solution protected by the patent), Fig. 5.

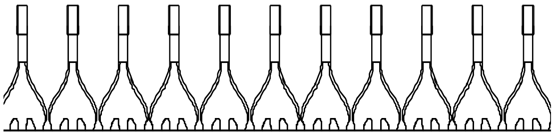

Fig. 5 The shape of the nozzle’s sets.

The nozzles outlet had a rectangular shape with rounded corners (5.6 mm x 1 mm). The flow through the nozzles was controlled by set of the twelve double position electromagnetic valves (MHE4-MS1H type with controlled operating frequency) mounted inside the model. The compressor with a maximum volume flow rate 1100 L / min. supplied air to the model pneumatic system. The air supplying system consist also with an expansion tank (with a capacity of 1000L), proportional electro-magnetic valve and flow-meter, Fig. 6.

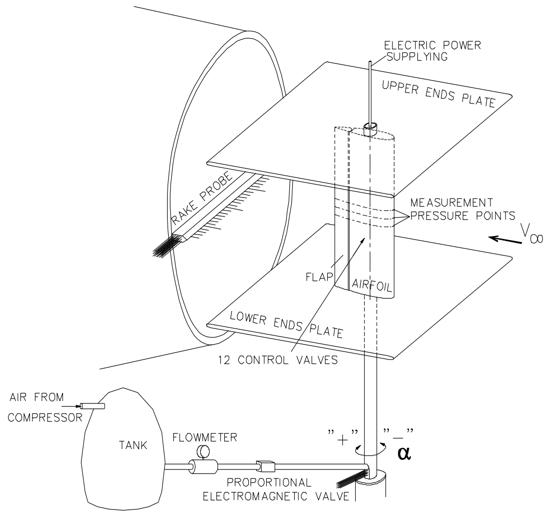

Fig. 6 Air supplying system.

3 Aerodynamic concept of the CLC-System

The main task of the described in this paper CLC System for fluidic active flow control was to keep flow attached on the upper flap surface during its movement. Presented experimental studies were preceded by numerical calculations, which showed, that in order to keep flow attached during the flap deflection, in the range from $\delta = 0^0$ to $\delta = 45^0$, the total air jets flow rate of about $\dot{m}$ = 0.075 kg/s is necessary.

Electromagnetic valves used for flow control were double position so they can be completely closed or provide full air flow rate (which was controlled by a proportional valve). To keep flow attached on the upper flap surface during its movement needed continuous testing of the boundary layer state. Many years of experimental tests and numerical calculations performed at the Institute of Aviation has shown, that the appropriate parameter, which can determine the state of the boundary layer on the upper airfoil surface (i.e. whether the flow is attached or separated), it can be a static pressure (or its pressure coefficient Cp) measured on the upper airfoil surface close to flap trailing edge. In the case of attached flow the pressure coefficient Cp has a positive value, while in the case of a detached flow, negative. Comparison of pressure distribution on the NACA 0012 airfoil ($\delta = 40^0$, $\alpha = 12^0$) for blowing system used (attached flow) with blowing system unused (flow detached) is shown in Fig. 7. This drawing shows mentioned differences in the pressure coefficient Cp measured close to the flap trailing edge.

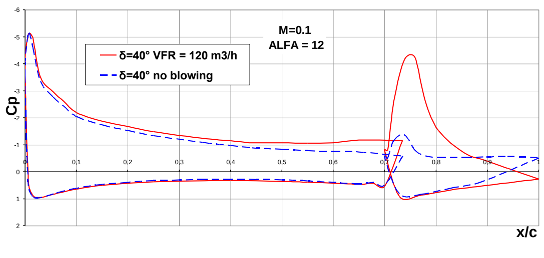

Fig. 7 Comparison of pressure distribution on the airfoil with the flow attached and separated.

Operation of the proposed Closed Loop Control System for fluidic active flow control was as follows:

- At certain constant angle of attack of the airfoil, the flap was deflected with constant angular velocity. Simultaneously the static pressure distribution (on the surfaces of the airfoil main body and flap), as well as the parameters of undisturbed flow (i.e. total pressure and static pressure) were measured.
- The value of static pressure measured at the flap upper surface, close to its trailing edge, as well as parameters of undisturbed flow, were transmitted to the electronic control system (made by Tech-Design). Such a single measurement lasted 2 ms.
- From the specified number of samples (usually from a 10-th or 20-ies) the control system calculated the average value of the pressure coefficient measured close to the flap trailing edge and compared it with the set value of the Cp (usually, it was Cp = 0).
- If the calculated value was less than the set point, which indicated that flow separation had occurred on the flap, the controller sent a signal to open the electromagnetic valves.
- Opening of the valves results in the out-flow of the air jets from the nozzles located on the trailing edge of the airfoil main body. The jets directed to the upper flap surface provided an additional energy to the flap boundary layer, causing flow attachment and thus the increase of the airfoil lift coefficient.
- Flow attachment on the airfoil flap resulted in increase of the static pressure measured close to the flap trailing edge.
- If the comparison carried out by the control system showed that the calculated value of the pressure was higher than the set point, the system sends a signal to close the valves. Closing the valve caused the suspension of air jet blowing and velocity drop in the flap boundary layer. This creates conditions leading to flow separation, manifested by a decrease of the static pressure measured close to the flap trailing edge.

In Fig. 8, general idea of Closed-Loop Control System for fluidic active flow control is presented.

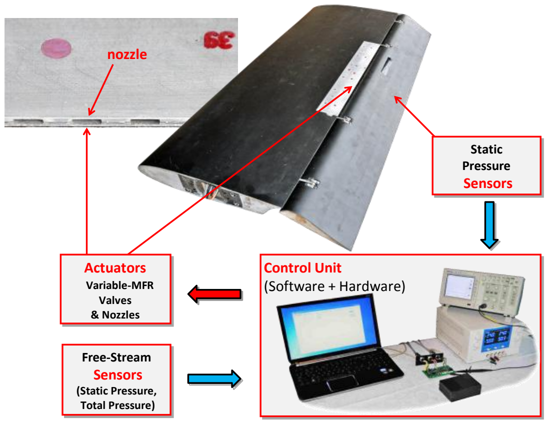

Fig. 8 The general concept of CLC-system.

4 Results

Experimental investigation of flow control by using additional blowing on the NACA 0012 airfoil flap was carried out in two stages. In the first step, the effect of continuous blowing on the airfoil aerodynamic characteristics for the flap deflected at a defined angle was tested. The tests were performed for the following flap deflection $\delta = 10^0$, 20^0, 30^0 and 40^0 and at various total volume flow rates of the air jets, VFR = 60 ÷ 140 m^3 / h.

In the second stage of the study, the CLC System for flow control was used. With this arrangement, the air jets, flowing out from the nozzles were controlled (by opening or closing the electromagnetic valves), depending on the state of the boundary layer on the airfoil flap (separated flow or attached). During these tests the airfoil flap had been deflecting with a constant angular velocity, changing its position from the angle of deflection $\delta = 0^0$ to $\delta = 40^0$, then back again to the angle $\delta = 0^0$. These tests were carried out for a number of selected airfoil angles of attack from the range $\alpha = 0^0 \div 20^0$ and at speeds corresponding to the undisturbed flow Mach numbers M = 0.05, 0.075 and 0.1.

4.1 Effect of continuous blowing on the airfoil aerodynamic characteristics

In Fig. 9 the effect of continuous blowing on the pressure distribution on the NACA 0012 airfoil is presented. The tests were performed for the airfoil angle of $\alpha = 10^0$, flap deflection $\delta = 40^0$, Mach number M = 0.1 and for few chosen total volume flow rate of the air jets from the range VFR = 0 ÷ 140 m^3/h.

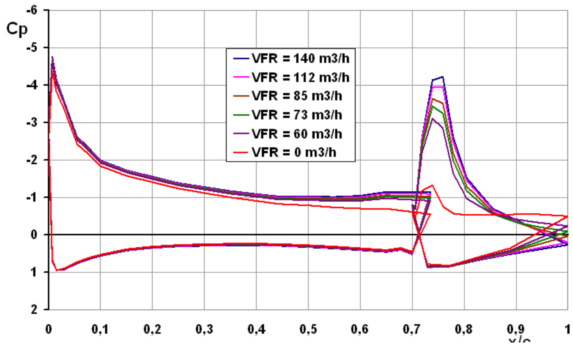

Fig. 9 Effect of continuous blowing on the pressure distribution on the NACA 0012 airfoil.

The wind tunnel tests showed, that blowing on the airfoil flap results in increase of the suction, both on the upper surface of the flap (especially near its leading edge) as well as close to the airfoil main body trailing edge. Before blowing the flow on upper flap surface (deflected at $\delta = 40^0$) was separated. In effect of blowing supplied with additional energy, boundary layer began to attach to the flap surface. With increase of air jet velocity, the area of separated flow on the upper flap surface becoming to diminish. As a result, the lift force generated on the whole airfoil increases, as well as increases the coefficient of the static pressure measured close to the trailing edge of the flap. As it was mentioned above, this coefficient was a parameter used by CLC System. During the study it was also found, that the increase in volume flow rate of the air jets above VFR = 75 ÷ 85 m3/h eliminates completely the flow separation on the upper flap surface deflected at $\delta = 40^0$ and the pressure coefficient measured at the at the flap trailing edge had positive value. As a result of the elimination of the flow separation on the airfoil flap, significantly increases the airfoil coefficient of lift. In Fig. 10 the influence of air blowing (VFR ≈ 120 m^3/h) on the lift coefficient versus airfoil angle of attack at the flap deflection $\delta = 20^0$, 30^0 and 40^0 is presented.

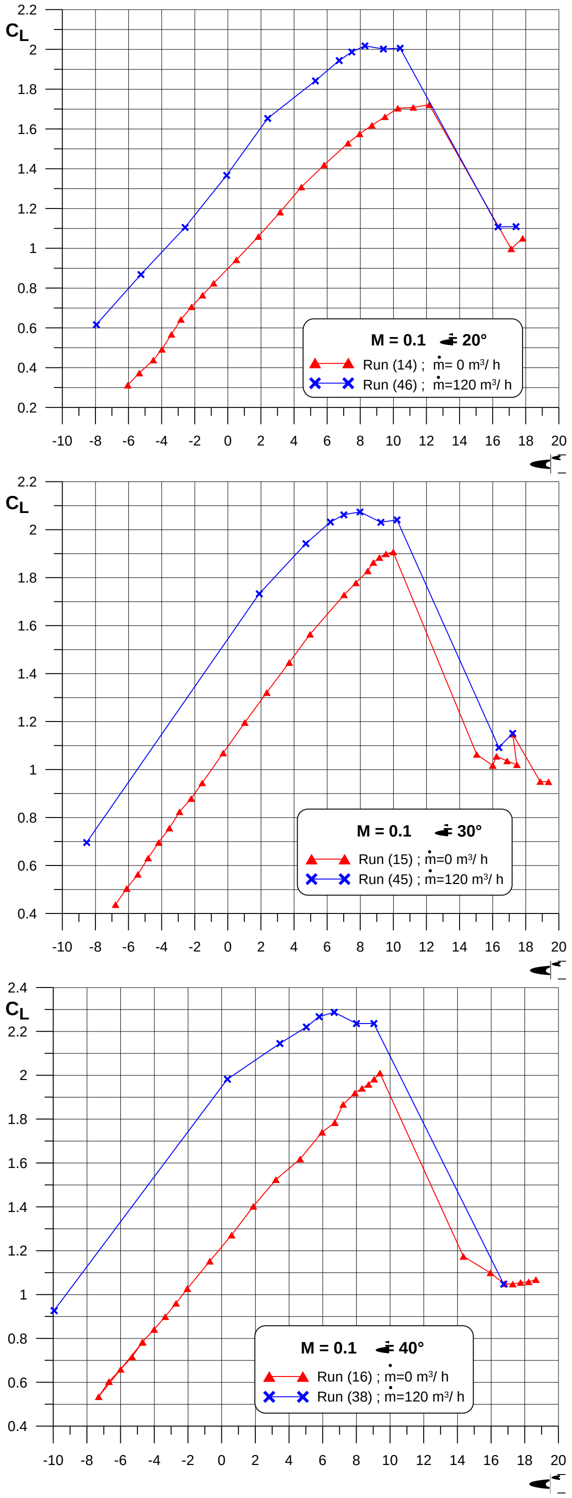

Fig. 11 Effect of air jet blowing on the airfoil lift coefficient versus angle of attack for δ = 20^0, 30^0 and 40^0.

Experimental tests have shown high efficiency of air jet continuous blowing on the airfoil flap. For example, the flap deflection at δ = 20^0 and 30^0 and continuous blowing with a total flow rate VFR = 120 m^3/h caused, the increase in the lift coefficient at ΔCl ≈ 0.45 and for the flap deflection δ = 40^0, increase in the value of this coefficient of ΔCl ≈ 0.7.

4.2 Wind tunnel tests with using CLC-system

Wind tunnel tests program with using the CLC-System for active flow control included the following issues:

- Influence of the value of pressure coefficient (Cp_c) used by the CLC-System as a signal for opening or closing the valves, on the pressure distribution along the airfoil chord, on the airfoil aerodynamic characteristics and on the air jets volume flow rate.
- Influence of the airfoil angle of attack and undisturbed flow velocity on the airfoil aerodynamic characteristics.

All the wind tunnel tests were performed with the same sequence of changes in the angle of flap deflection, i.e. initially the flap was deflected from the δ = 0^0 up to δ = 40^0 with angular speed δ = 1.4-1.5 deg/s, then was kept deflected (δ = 40^0) for about 20 seconds and finally restored to the starting position (δ = 0^0) with approximately same angular speed. During all these studies CLC System operated and control the opening or closing the valves. With a fully open electromagnetic valves, the proportional valve (contained in air supplying system, Fig. 6) was so positioned, that total (from 36 nozzles) air volume flow rate was VFR ≈ 120 m^3/h (which correspond to air jet velocity Vj ≈ 90 m/s).

The example of wind tunnel test results with usage of the CLC-System for active flow control are presented in Fig. 12. This figure shows changes in the total airfoil lift coefficient during the flap deflection. The next 10 plots (Fig. 13) present the changes in the pressure distribution on the upper and lower surface of the flap and rear part of the airfoil main body over time (during the CLC-System operation at δ = 40^0) . These plots are shown in the order, that first presents the moment, when due to CLC System operation, it begins to growth the negative pressure on the upper flap surface in the leading edge area. The last plot presents approximately the same moment after one full cycle of the CLC System operation (i.e. plots cover the entire cycle of the CLC-System action).

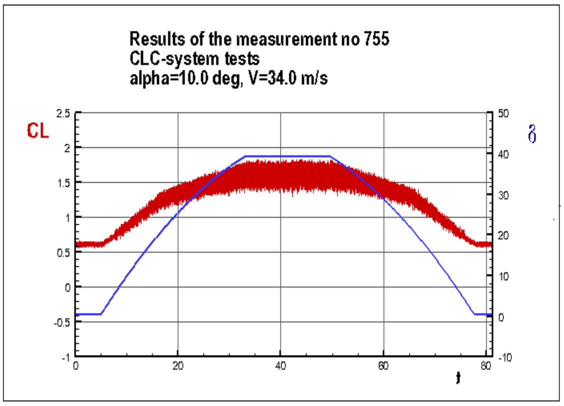

Fig. 12 Airfoil lift coefficient during the CLC-System operation.

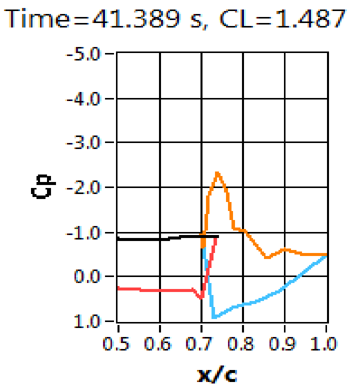

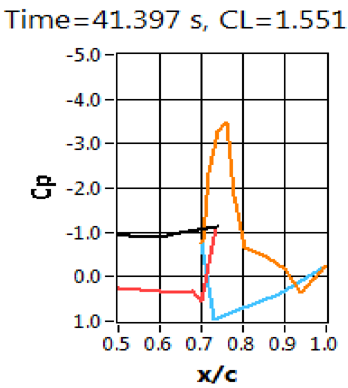

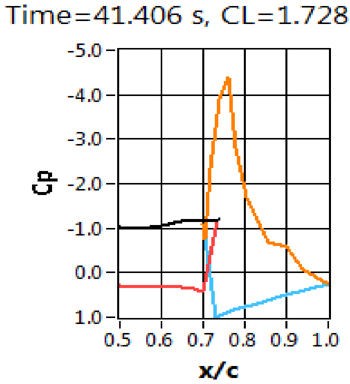

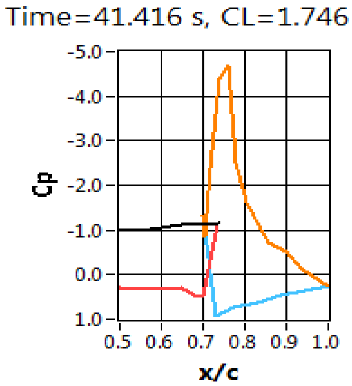

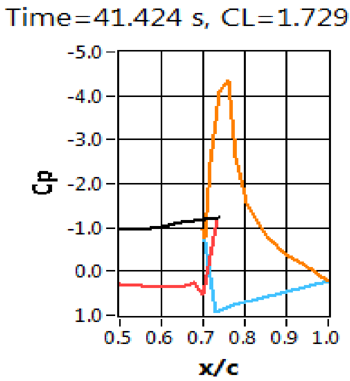

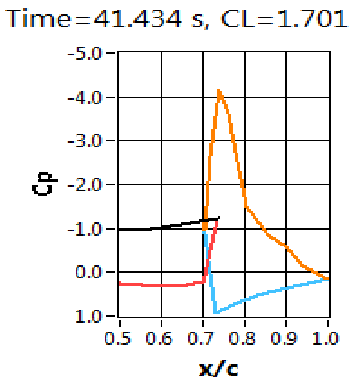

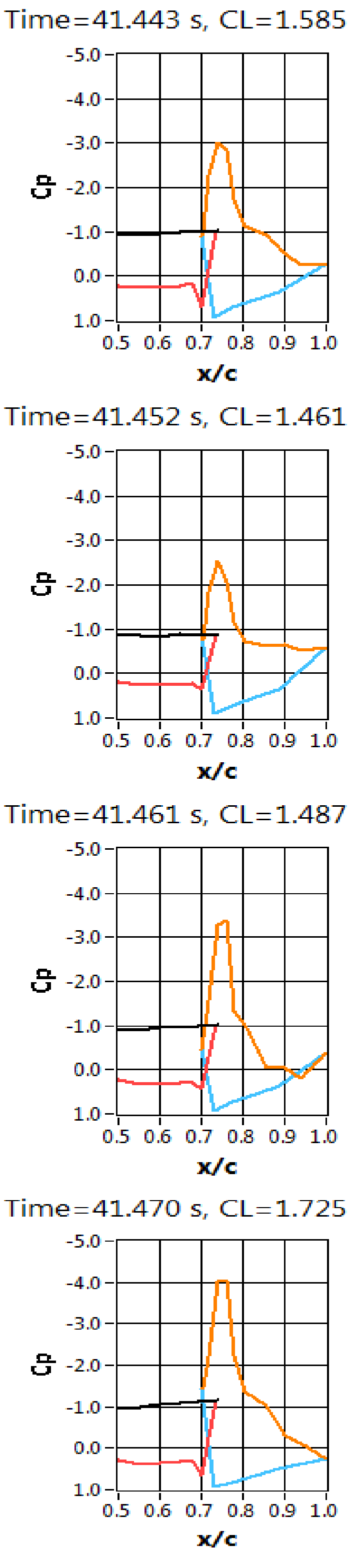

Fig. 13 Changes in the pressure distribution over time.

5 Conclusion

In the project ESTERA complete Closed Loop Control System for fluidic active flow control was designed and manufactured together with the necessary controller unit. The CLC System prototype has been tested experimentally on a two dimensional airfoil model NACA 0012 equipped with movable flap. The tests were performed in the low speed wind tunnel T-1 in the Institute of Aviation for Mach numbers M = 0.1, 0.075 and 0.05.

Performed wind tunnel tests of the CLC-System prototype showed the following:

- Blowing is an effective way to increase the lift coefficient achieved by the airfoil with strongly deflected slotted flap. It was recorded maximally 30% increase in the lift coefficient. The lift increased not only due to reduction at a separation zone on the flap but also due to increasing a negative pressure on the upper surface of the main airfoil body (suction effect of the air blowing).
- The tests confirmed hypothesis, that the measurement of the pressure on upper-aft part of the flap (in one point only) allows to detect the separation.
- The investigation confirmed an efficiency of the CLC System as a way to increase lift with relatively low volume flow rate of the compressed air. Using a pulsed jets controlled by CLC System, the volume flow rate was diminished from VFR ≈ 120 m^3/h (steady blowing) to VFR ≈ 68 m^3/h (for $Cp_c = 0.0$) and to VFR ≈ 33 m^3/h (for $Cp_c = -0.4$).
- The increase in airfoil C_L value due to CLC System operation was generally independent of the value of pressure coefficient, used by the CLC-System as a signal for opening or closing the valves, i.e. Cp_c.
- Duration of the one complete cycle of the CLC-System operation was about Δt ≈ 65 ms. Since the opening of the valves to the full flow attachment on the flap passes about 12 ÷ 14 ms. On the other hand since the closing of the valves to the full flow

separation on the flap passes about 27 ÷ 28 ms.

- During the flap deflection (the increase of the flap deflection from $\delta = 0^0$ to $\delta = 40^0$ and decrease from $\delta = 40^0$ to $\delta = 0^0$ was tested), the angle of attack significantly affects the beginning and end of the CLC System operation. The increase in the airfoil angle of attack delays the start of the CLC-System operation.

References

[1] Gad-el-Hak M., *Flow Control – Passive, Active, and Reactive Flow Management*, Cambridge University Press, 2000.

[2] Gad-el-Hak M., "Flow control - The future", *Journal of Aircraft*, No. 38, 2001, pp. 402-418**.**

[3] Nishri A., Wygnanski I., "Effects of periodic excitation on turbulent flow separation from a flap", *AIAA Journal*, No. 36**,** 1998, pp. 547–556.

[4] Melton L., Yao C. and Seifert A., "Active control of separation from the flap of a supercritical foil", *AIAA Journal*, No. 44, 2005, pp. 34–41.

[5] Seifert A., Greenblat D., Wygnanski I., "Active Separation Control: an Overview of Reynolds and Mach Numbers Effects", *Aerospace Science and Technology*, No. 8**,** 2004, pp. 569–582.

[6] Seifert A., Pack L., "Compressibility and Excitation Location Effects on High Reynolds Numbers Active Separation Control", *Journal of Aircraft*, No. 40, 2003, pp. 110–126.

[7] Krzysiak A., Narkiewicz J., "Aerodynamic Loads on Airfoil with Trailing-Edge Flap Pitching with Different Frequencies", *Journal of Aircraft*, No.2, 2006, pp. 407-418.

[8] Alam M., Liu W., Haller G., "Close-Loop Separation Control - An Analytic Approach", *Physics of Fluids*, No. 18, 2006, (043601)

[9] Bright M., Culley D., Braunscheidel E., Welch G., "Closed Loop Active Flow Separation Detection and Control in a Multistage Compressor", NASA/TM 213553, 2005.

[10] Krzysiak A,. Hanzlik A., Ruchała P., "Final report of the ESTERA project", Institute of Aviation, Poland, 2013.

Navier-Stokes Simulations of Store Separation

Torsten Berglind and Shia-Hui Peng
FOI, Sweden

Lars Tysell
FOI, Sweden

Keywords: *unsteady aerodynamics, store separation*

Abstract

CFD has become increasingly important in the design of systems for store separation. It offers opportunities to investigate complex flow physics interacting with the separated store, which is a basis for the design of the store release unit (ERU). An integrated system for numerical simulation of store separation by solving, quasi-steady or unsteady, Euler or Navier-Stokes equations is presented. The flow computations are coupled to a 6-DOF rigid body motion module. The grid is deformed in order to conform to the moving boundaries and remeshed when the grid deformation module fails to achieve sufficient grid quality. The computational method is assessed against experimental data for an AGARD test case, separation of a generic finned-store shape at transonic speed from a wing-sting-pylon configuration. The computational results compares well with wind tunnel measurements.

1 Introduction

In the last decades, computational fluid dynamics coupled to 6-DOF simulation have been applied to analyze store separation scenarios. The three main components of the computational model consists of flow solver, grid system and flight mechanics model.

Quasi-steady Euler computations have been successfully applied to simulate separation of external weapons Ref. [1-3]. If stores are separated from weapons bays, the flow around the weapons is unsteady and the computations must be time accurate viscous simulations in order to capture relevant flow physics, Ref. [4-5].

1.1 Flow solver

The CFD computations are carried out with FOI in-house tool Edge, Ref. [6]. The Navier-Stokes equations in integral form are solved with convective fluxes approximated with a second-order central scheme. Explicit artificial scalar dissipation is added, using combined second and fourth order differences. The time-dependent simulation is advanced using dual-time stepping, where a global physical time step is employed and the local time step is used in the sub-iterations based on explicit three stage Runge-Kutta scheme.

In this study both URANS and hybrid RANS-LES approaches are applied to model time accurate flow. The RANS-LES approach is the HYB0 model, Ref. [8], the turbulent stress tensor, is modeled using the eddy viscosity concept for RANS and LES modes. The HYB0 model has been thoroughly examined for fundamental and industrial applications including wall bounded and separated flow, see Ref [7].

1.2 Grid System

Different approaches to handle the necessary grid dynamics have been applied: deforming meshes, Chimera grids and various Cartesian approaches. The Chimera grid approach readily addresses the problems of moving grids but the inter-grid interpolation stencils for viscous flow are computationally demanding. The Cartesian approach, see Ref. [8], implies the use of non-body-fitted volume meshes, enabling fully automated grid generation. However, the extension to viscous flows encounters substantial difficulties. In this work, grid deformation of unstructured grids is utilized. The main advantage is the use of coherent grids requiring a minimum overhead of memory and computational costs.

All grids in this paper are generated by TRITET, FOIs in-house general purpose grid generation code TRITET, Ref. [9]. TRITET is a complete tool for generation of hybrid unstructured grids in two and three space dimensions. Grids are generated using the advancing front algorithm. Modules for adaptation and moving grids are also included.

The grid assembly process to handle dynamic domain problems requires: grid deformation, hole cutting, hole filling and grid check. The computational grids presented in this paper are deformed by Laplacian smoothing. As objects move further away from its original position, the quality of the grid will inevitably degrade until it finally becomes too poor to be used. In some cases volumes of elements will be negative and in other cases the grid will simply be too sparse in some regions.

Local remeshing implies that the grid is modified locally, in this case in the vicinity of the moving objects, thereby retaining the original grid properties elsewhere. The local remeshing procedure, Ref. [10], starts from a reference grid around the main object and separate grids around the moving objects, see Figure 1a. The grid between the inner boxes and the body surface will remain fixed, defining a near wall grid region that moves with the body. In cases of solving Navier-Stokes equations, the prismatic layers should be contained within the inner boundary of the hole. The inner boundary is not allowed to intersect solid walls, which sets a limit to how far from the solid boundary it can be located.

The outer boxes define an outer boundary for which the grid will be removed. The outer boundary may intersect objects. The domain between the inner and the outer boundaries is gridded with the advancing front method, Figure 1b. The different parts of the grid are thereafter merged to a complete grid. This technique implies that the original grid is modified locally, thereby minimizing effects of grid dependency.

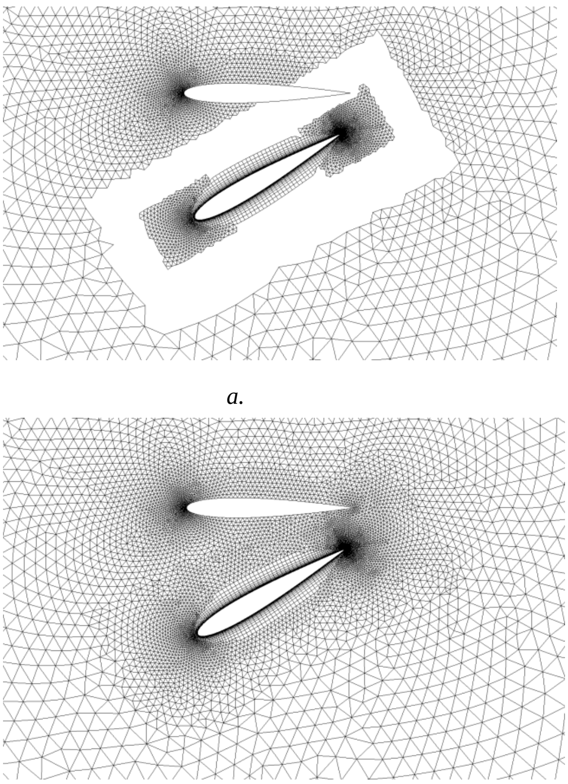

a.

b.

Fig. 1 Illustration the process of local remeshing: a. a hole in the reference grid with the moving object and the inner grid in a new position, b. the complete grid with the hole filled.

1.3 Flight Mechanics Model

The flight mechanics model in EDGE is a rigid body model, Ref. [11,12]. The Newton-Euler equations for classical mechanics can be rewritten as a system of four first order ordinary differential equations. The resultant force and moment are computed from aerodynamics and supplemented with contributions from ERU (Ejector Release Unit), propulsion and gravity. The governing system of equations is integrated in time applying a fifth order accurate Runge-Kutta scheme.

The flight mechanics module computes the next position and the grid deformation module adapts the grid to the new position. If the grid quality is accepted, the pseudo-steady-state (PSS) equations are solved and flight mechanics and grid deformation are updated within the innermost iteration loop.

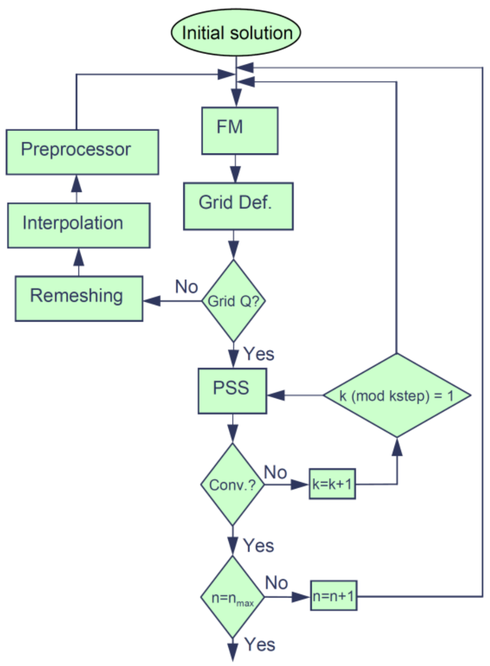

Figure 2. Scheme for coupling CFD and flight mechanics (FM).

Since time scales for flight mechanics in this context usually are much larger than for aerodynamics, it is not necessary to update the position of the moving object each sub-iteration. For time accurate computations in this paper a sub-iteration increment $k_{step} = 20$ is used.

If the grid quality check fails, a new grid for the time step is computed and the flow computations are restarted. This recurrent process continues until the grid quality check fails. In that case the grid is remeshed, the solution from the previous grid is interpolated to the new grid and new grid connectivity's and metrics are computed by the preprocessor. The computations proceed until the specified number of iterations is reached.

2 Computational Results

The system for store separation is first validated against an almost quasi-steady test case. The capability to also predict store separation from weapons bays is demonstrated for a generic rectangular cavity.

2.1 Store Separation from a Generic Wing-Sting-Pylon Configuration

The EDGE-system for trajectory computations is validated against a test case carried out at Arnold Engineering Development Center (AEDC) 4T Transonic Aerodynamic Wind Tunnel, described in Ref. [13]. This case concerns the release of a finned-store from a pylon attached to a clipped delta wing. The wind tunnel experiments were carried out using the AEDC Captive Trajectory Support (CTS). Apart from the release trajectories and the store attitudes, surface pressure data on the wing, on the pylon and on the store at several positions during the release are available for validation. The computed test case is transonic at Mach number 0.95, Reynolds number of 3 million based on the root chord of the wing and angle-of-attack of zero degrees.

The full-scale store model length of the store is 3.018 m. The store is mounted on the right side of the wing. Since the flow case is asymmetric a full model is used for the computations.

In Fig. 3, the ERU device is depicted. The physical appearance is not modeled in the computational domain i.e., its effect on the flow in the cavity is neglected. The ERU consists of two pistons with the ejector stroke length 0.10 m which are released simultaneously. The forward ejection location is 1.24 m and the aft ejector location is positioned 1.75 m aft of the store nose. The forward ejector force is 10675.7 N and the aft ejector force is 42702.9 N, both constant in time. This implies an initial pitch up maneuver.

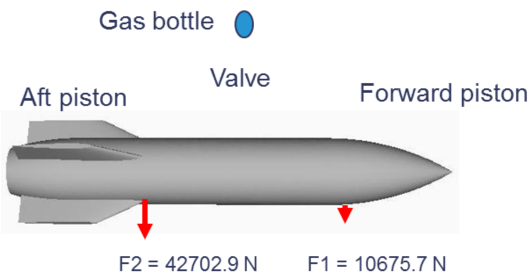

Fig. 3 ERU device

Approximately 55 milliseconds after it has left the original position, the pistons and the store cease to have contact with each other. The computations are started at the subsequent temporal measurement station, 60 milliseconds after the store has left the original position, see Fig. 4b. The effect of the ERU is taken into account through the initial values of the flight mechanics state variables.

Quasi-steady computations mimic the experimental CTS-technique; both rely on the assumption of quasi-steady flow, omitting unsteady effects. Both also adjust for dynamic effects using the same aerodynamic damping coefficients. For the quasi-steady computations, the following roll, yaw and pitch damping coefficients are used:

C_{lp} = -4.0/rad, C_{mq} = -40.0/rad, C_{nr}= -40.0/rad.

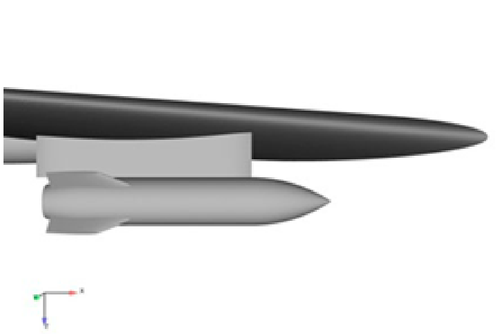

a. Mounted position

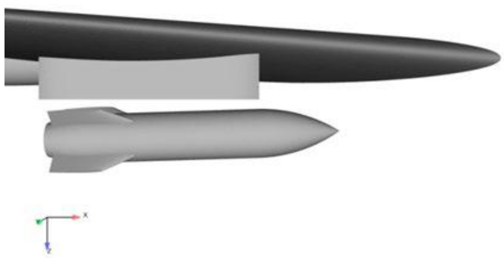

b. Initial position for computations

Fig.4 The store in different positions.

The computational grids are generated by a merge of the grid around the wing-sting-pylon configuration and the store grid using the local remeshing routine.

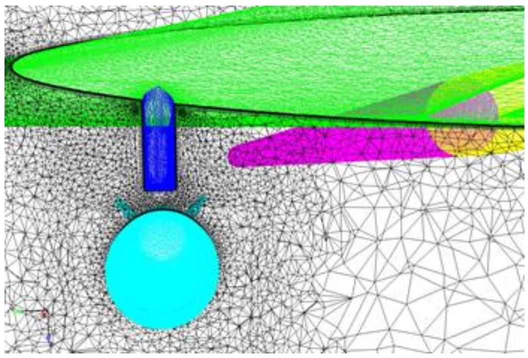

Fig. 5 Cross sectional cut through the Navier-Stokes grid containing 5.8 million nodes.

The Navier-Stokes grid contains 36 layers of prismatic elements, with roughly $6.8 \cdot 10^6$ nodes in total, depicted in Fig. 5.

Figure 6 shows cross comparison of trajectory and attitude angles for quasi-steady and time accurate Navier-Stokes computations versus experiments for the wing-pylon-sting store separation.

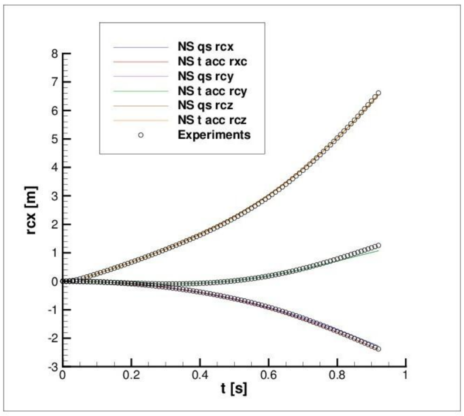

a. Trajectory coordinates

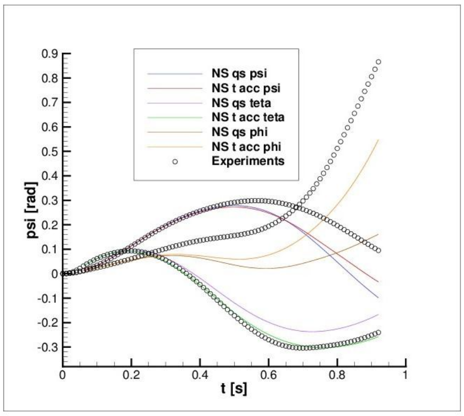

b. Euler angles

Fig. 6 Computational results for quasi-steady computations versus time accurate Navier-Stokes computations and experiments.

Comparisons between quasi-steady and time accurate computations show small differences for the trajectories but significant differences for the attitude angles. The computed trajectories for the wing-pylon-sting store separation agree reasonably well among the participants and they also agree well with experiments, especially for the first 0.4 sec. For the latter part of the simulation, the values of the attitude angles differ, especially for the pitch and roll angle.

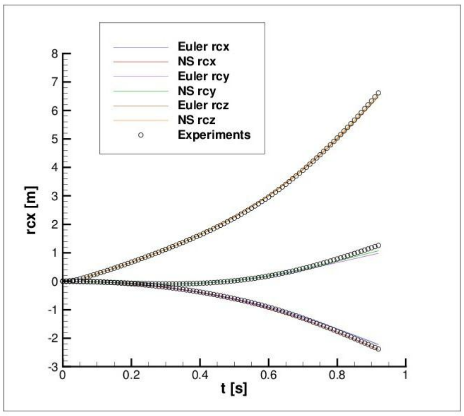

a. Trajectory coordinates

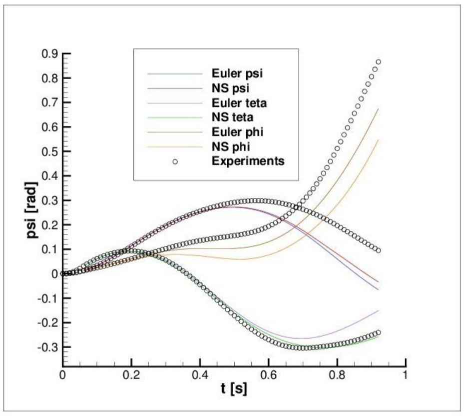

b. Euler angles

Fig. 7 Computational results for time accurate Euler and Navier-Stokes computations versus experiments.

Figure 7 show comparison between time accurate Euler and Navier-Stokes computations. The computed trajectory coordinates show small deviations from experiments. The attitude angles deviate to some extent from the experimental ones after t=0.4 sec, especially the roll angle. The Navier-Stokes results show consistently better agreement than the Euler results. The agreement of the computational results with experiments is comparable or better than results in previous publications for this test case.

3 Conclusion

The long term goal for this work is to develop a tool for analysis of aerodynamics around an internal weapons bay. This has however been beyond the scope of this paper.

Weapons bay flow is unsteady by nature, due to the mixing layer that impacts on the aft wall of the bay cavity and entailing extensive pressure oscillations inside the weapons bay. The aerodynamic forces and moments acting on the store can be unsteady depending on the strength of the mixing layer versus the inertial and gravity forces. This implies that the store movement will depend on at which moment the store is released. If the flow field is truly unsteady, then the standard tool for flight clearance, the wind tunnel CTS technique will be of limited use. The lack of repeatability is an obstacle for certification for flight clearance. It also complicates comparisons between various computational results.

Acknowledgements

The development of the store separation system has been carried out with the support of the Swedish Defense Materiel Administration, FMV. The authors also wish to acknowledge colleagues at FOI, Peter Eliasson for parallelizing routines for trajectory computations and for reviewing the implementation plan, and Henrik Edefur for generating the initial grid files.

References

[1] Lee, J. and Cenko, A.,"Evaluation of the GBU-38 Store Separation from B-1 Aft Bay", AIAA-2008-0185.

[2] Sickles, W. L., Hand, T. L., Morgret, C. H., Masters, J.S.,and Denny, A.G., ,"High-Fidelity, Time Accurate CFD Store Separation Simulations from a B-1B Bay with Comparisons to Quasi-Steady Engineering Methods",AIAA-2008-0186.

[3] Baum J. D., Lou H. and Löhner R.,"A New ALE Adaptive Unstructured Methology for the Simulation of Moving Bodies", AIAA-94-0414(1994).

[4] Baum J. D., Lou H., Löhner R., Goldberg E. and Feldhun A., "Application of Unstructured Adaptive Moving Body Methology to the Simulation of Fuel Tank Separation From an F-16C/D Fighter", AIAA-97-0166 (1997).

[5] Murman S.M., Aftomis, M.J., and Berger, M.J.., "Simulations of Store Separation from a F/A-18 with a Chartesian Method", Journal of Aircraft, Vol.41(2004), pp.870.

[6] Eliasson P., "Edge, a Navier-Stokes Solver for Unstructured Grids", Proceedings of Finite Volumes applications III, ISBN 1-9039-9634-1, pp. 527-534, 2002.

[7] Peng, S.-H., "Hybrid RANS-LES modelling based on zero- and one-equation models for turbulent flow simulation", Proceedings of 4th Int. Symp. Turb. And Shear Flow Phenomena, Vol. 3, pp. 1159-1164, 2005.

[8] Tang L., Yang J. and Lee, J., "Hybrid Cartesian Grid/Gridless Algorithm for Store Separation Prediction", AIAA-2010-508.

[9] Lars Tysell, "An Advancing Front Grid Generation System for 3D Unstructured Grids", ICAS-94-2.5.1, pp 1552-1564. Proceedings of the 19th ICAS Congress, Anaheim, California, USA, 1994.

[10] Tysell L., "Implementation of Local Remeshing Routines in Edge", FOI-R-2550-SE.

[11] Berglind, T. and Tysell, L., "Numerical Investigation of the Impact of Maneuver on Store Separation Trajectories", AIAA-2010-4241, 2010.

[12] Berglind, T. and Tysell, L., "Time-Accurate CFD Approach to Numerical Simulation of Store Separation Trajectory Prediction", AIAA 2011-3958, 2011.

[13] Fox J.H., "Generic wing pylon, and moving finned store", Arnold Engineering Development Center (AEDC), Arnold AFB, TN 37389-6001, USA.

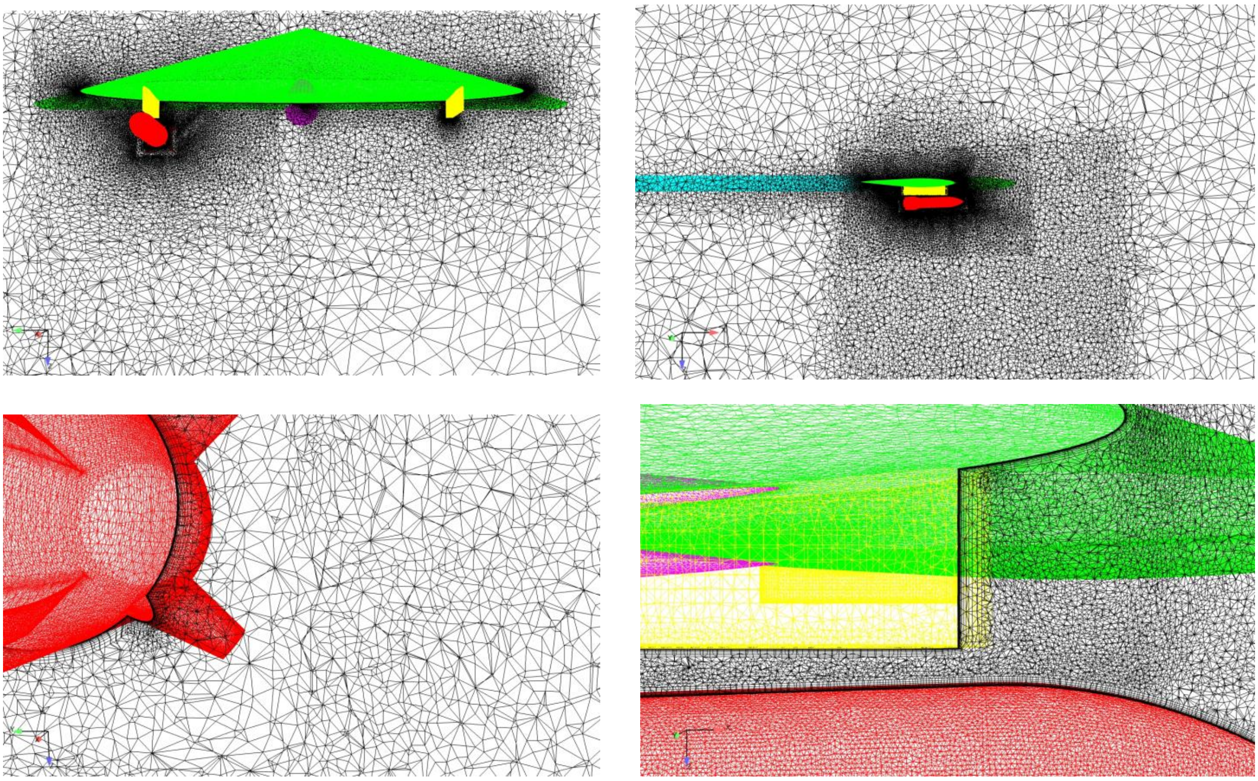

Figure 8. Views of the computational grid

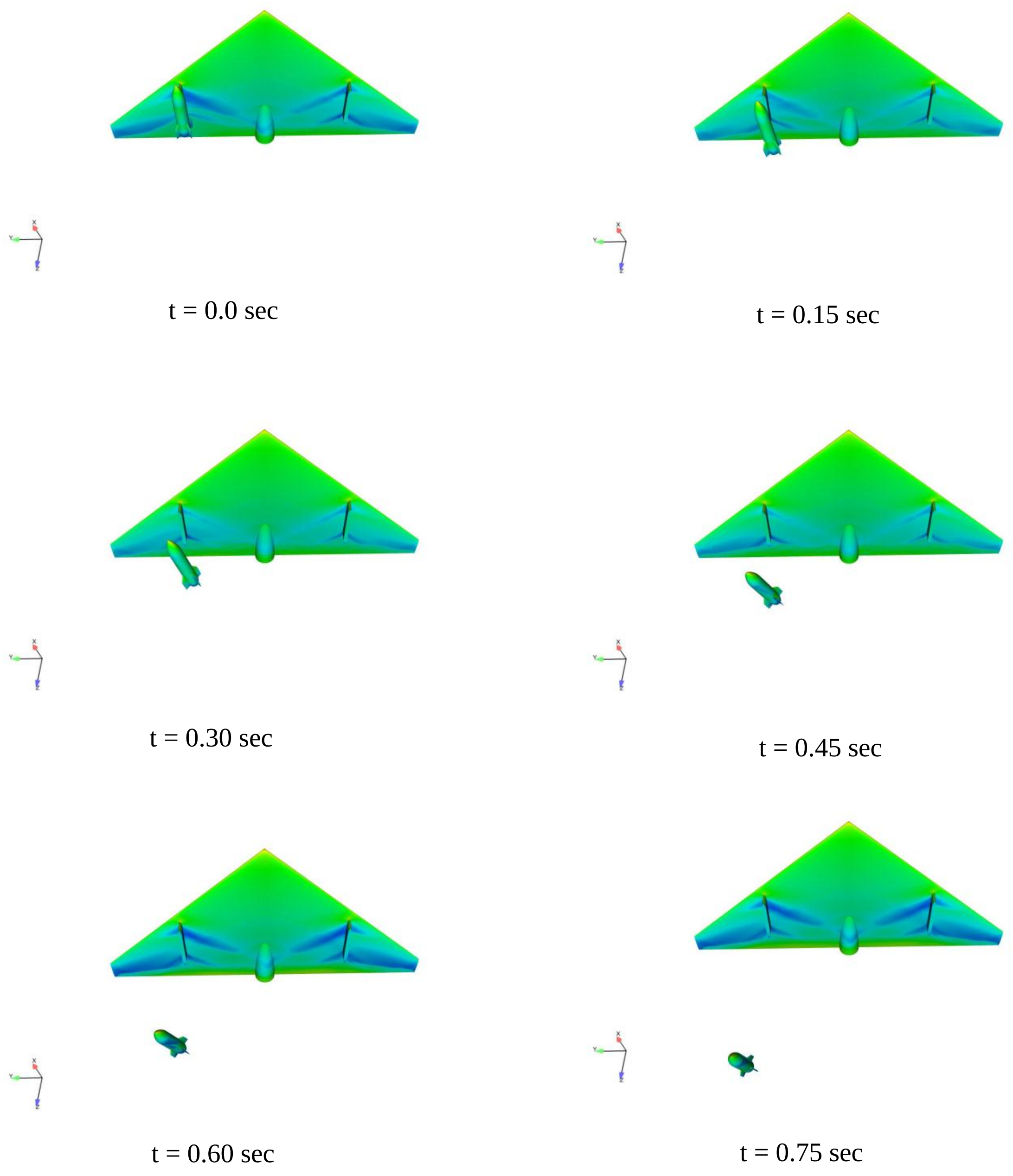

Figure 9. Pressure distribution on the Wing-Sting-Pylon configuration after 0.00, 0.15 , 0.30, 0.45, 0.60 and 0.75 sec

Numerical Investigation of Aerodynamic Interaction for a Quad-Rotor UAV Configuration

Min Kyu Jung and Oh Joon Kwon
Korea Advanced Institute of Science and Technology(KAIST), Daejeon, Korea

Keywords: *Quad-rotor, UAV Configuration, Aerodynamic Interaction, CFD, Unstructured Mesh*

Abstract

In the present study, numerical investigation about the mutual aerodynamic interaction of the rotors of a multi-rotor UAV (Unmanned Aerial Vehicle) configuration was conducted. For this purpose, time-accurate unsteady flow calculations were performed using a three-dimensional unstructured mesh CFD flow solver. The fluid motion was assumed to be governed by the three-dimensional, incompressible, inviscid, Euler equations. To handle the relative motion of the rotors, an overset mesh technique was adopted. To reduce the large computational time, the flow solver was parallelized based on a domain decomposition technique. As an application of the present method, simulations were made for a quad-rotor UAV in hover and in forward flight. It was observed that in the case of hovering flight, the mutual aerodynamic interaction of the rotors induces slightly higher inflow than an isolated rotor, and invokes unsteady fluctuating thrust variation. In forward flight, the tip vortices from the upstream rotors affect those at further downstream by reducing the effective angle of attack at the rotor blades and form a complex interactional wake structure. It was found that the mutual aerodynamic interaction leads to a deterioration of the attitude stability of the UAV in forward flight, and this aerodynamic interaction should be considered seriously in designing accurate attitude control algorithms for multi-rotor UAV configurations.

1 Introduction

For the past few decades, active researches have been conducted for Unmanned Aerial Vehicles (UAVs) as demanded by the practical usefulness for both civilian and military application purposes. Among the several UAV configurations, rotary-wing type vehicles have received quite an attention due to the unique capability of vertical take-off and landing (VTOL) [1]. The research and development have been performed particularly for multi-rotor UAVs, because of the simplicity of the flight mechanism which does not require any anti-torque system and swash plate for flight control [2-5].

Recently, quad-rotor UAVs became one of the standard platforms in the development and also in the practical field application of multi-rotor UAVs. With the four rotors, the two pairs are designed to rotate clockwise and counter-clockwise, respectively, to negate the production of torque on the vehicle. Because the rotors are set at a fixed pitch, the attitude of the vehicle is controlled by the difference of the individual rotor thrust attained by the rotational speed control [1].

In addition to the VTOL capability, quad-rotor-type UAVs have several other advantages. These vehicles are safer than conventional single rotor helicopters, because the rotor is generally in smaller size and is enclosed. Also, as the four thrust forces act at the same distance away from the vehicle center of gravity, more stationary hovering flight can be achieved. The four-rotor design helps simplifying the vehicle dynamics, and enables to reduce the cost of production and repair. However, in typical forward flights, highly coupled dynamics appear due to the mutual aerodynamic interaction of the rotors. In general, since multi-rotor UAVs are small in size and are light-weighted, typically less than 1 meter in size and 1 kilogram in weight, the vehicle attitude is very sensitive to external influences, such as the wind disturbance [1, 6].

To achieve an autonomous attitude control of the quad-rotor UAV vehicles during the mission flight, the aerodynamic characteristics of the rotors should be known accurately. Furthermore, the aerodynamic interaction between the front and rear rotors causes unsteady fluctuating behaviors of the rotor aerodynamic loads, and as a result brings in aerodynamic performance deterioration. It may also affect the flight characteristics and the stability and control behaviors of the vehicles. Therefore, precise understanding of the mutual aerodynamic interaction phenomena of the rotors is important.

In the present study, a numerical investigation has been conducted for simulating inviscid unsteady flows around a quad-rotor UAV configuration based on unstructured meshes. To describe the relative motion of the rotor blades, an overset mesh technique was adopted. The calculations were made for the UAV in hover and in forward flight, and the mutual aerodynamic interaction of the rotors and the performance characteristics were studied.

2 Numerical Method

2.1 Spatial Discretization and Time Integration

The fluid motion is governed by the three-dimensional, incompressible, inviscid, Euler equations, coupled with an artificial compressibility method. The equations can be recast in an integral form for arbitrary computational domain V with boundary ∂V:

$$\frac{\partial}{\partial t}\iiint_V Q\, dV + \iint_{\partial V} F(Q)\cdot\vec{n}\, dS = 0 \qquad (1)$$

where $Q=[\rho,\rho u,\rho v,\rho w,e_0]$ is the solution vector of the conservative variables for the mass, momentum and energy equations. The governing equations were discretized by using a vertex-centered finite-volume method. The flow domain was divided into a finite number of control volumes surrounding each vertex, which are made of a non-overlapping median-dual cell whose boundary surfaces are defined by the cell centroid, and the mid-point of the edge. The inviscid flux term, $F(Q)$, was computed using Roe's flux-difference splitting scheme [7]. The flow variables at each dual face were computed by adopting a linear reconstruction technique to achieve second-order spatial accuracy. In this approach, the face value of the primitive variables was calculated from those at the dual face using the averaged solution gradient of each control volume obtained from the least-square method. An implicit time integration algorithm based on a linearized second-order Euler backward differencing was employed to advance the solution in time. The linear system of equations was solved at each time step using a point Gauss-Seidel method.

2.2 Boundary Condition

On the solid surface of the rotor blades, the flow tangency condition was imposed. The density and pressure on the solid surface were obtained by extrapolating from the interior domain. At the far-field boundary, the characteristic boundary condition with Riemann invariants was applied.

2.3 Unstructured Overset Mesh Technique

To handle multiple bodies in relative motion effectively, an overset mesh scheme was adopted [8]. For the overset mesh method, a search procedure is needed for the identification of the donor cells that contain the vertices from the other overlapping mesh block. For unstructured meshes, the search should be performed for all nodes of all mesh blocks, because the nodes and the cells are randomly distributed. To overcome the large computational overhead involved in this search procedure, a fast and robust neighbor-to-neighbor search technique was implemented by utilizing the property of linear shape functions.

Once the search process is completed, the information is used for clarifying the node types and for determining the weighting factors necessary for the interpolation. In the present overset mesh method, a distance-to-wall technique was implemented for grouping active and non-active nodes. Hole-cutting for determining cell types as either active, interpolation, or non-active was performed based on the number of active nodes assigned to each tetrahedral cell. Then interpolation and transfer of the flow variables between adjacent mesh blocks are made. To reduce the error, the information from both the cell containing the interpolation receiver and also the neighboring cells enclosing that cell are used in the interpolation.

2.4 Parallel Computation

To reduce the large computational time required in handling a large number of cells, a parallel computational algorithm based on a domain decomposition strategy was adopted. The load balancing between the processors was achieved by partitioning the global computational domain into local subdomains using the MeTiS libraries. The Message Passing Interface was used to transfer the flow variables across the subdomain boundary. The load balancing was made for each sub-block mesh, and thus was not strictly enforced for the global computational domain.

3 Results and Discussion

3.1 Configuration and Computational Mesh

The quad-rotor UAV configuration adopted in the present study is shown in Fig. 1. The vehicle has four identical fixed-pitch rotors mounted at the end of four equally-space arms attached to the flat form. Out of the four rotors, two pairs are spinning in the opposite direction to maintain the vehicle in balance. The length from one rotor tip to the other rotor tip in the opposite side is 0.48 meters. The rotor adopted in the present study is the EPP1045 rotor produced by the Maxx Products International Inc. Each rotor is consisted of two blades that have an aspect ratio of 5.508. The diameter of the rotor is 10 inches, and the pitch length is 4.5 inches per revolution. The rotor is driven by Robbe ROXXY 2827-35 motor and BL-Ctrl V1.2 speed controller. The rotor rotates at 300rad/sec. The total weights of the UAV configuration with and without the battery are 8.5064N and 6.2132N, respectively.

In Fig. 2, the computational mesh is presented. The overset mesh is constructed with five mesh blocks; four sub-blocks covering each of the four rotors, and a main block representing the overall computational domain. To simulate the aerodynamic interactions between the rotors more accurately, fine cells are distributed around the rotor blades. The mesh consists of 961,034 vertices for the main block, and 286,792 vertices for each sub-block. The total number of vertices is 2,108,202, and the total number of cells is 11,596,480. For the simplicity of the numerical study, the airframe and the connecting arms are not modeled in the present study.

Fig. 1 Quad-rotor UAV configuration.

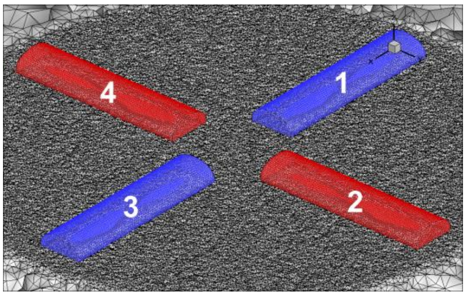

(a) Overset mesh blocks for four rotors

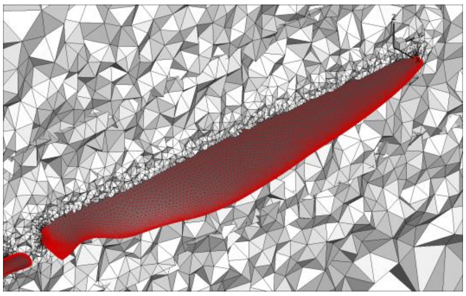
(b) Computational mesh around each blade

Fig. 2 Computational mesh for quad-rotor UAV.

3.2 Hovering Flight

At first, the aerodynamic interaction in the hovering flight condition was analyzed. In Fig. 3, the wake structure of the quad-rotor is presented by the λ_2-criterion when the blades are located at the azimuth angle of zero degree. It is observed that helically shaped vortex structures are formed under each rotor. It is shown that in this hovering flight there is not much interaction, at least a direct intersection between the wakes from each rotor, even though the wakes still influence the other rotors in close proximity.

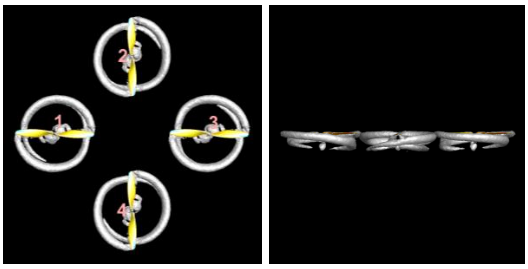
(a) Top and side views

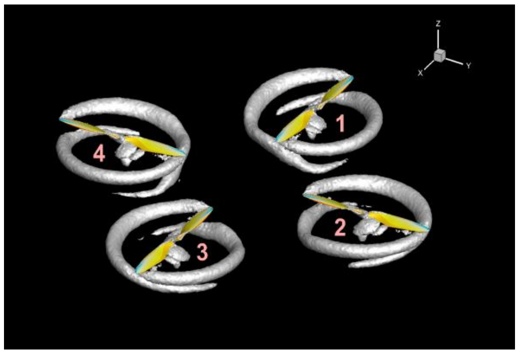

(b) Perspective View

Fig. 3 Rotor wake structure represented by iso-surface of λ_2-criterion for hovering flight.

In Fig. 4, the vertical downward velocity contours are presented at a plane half chord length below the rotor disk and at the vertical plane along the center of the first and third rotors for the hovering flight condition. It is observed that the velocity contours are almost symmetric along the diagonal lines between the rotors. There exist slight differences in the velocity contours as marked by the dotted and dash-dot lines. This is because each pair of the rotors is rotating in the opposite direction from the other one. At the vertical plane, the velocity contours appear almost symmetric. It is also observed that a slight upwash flow region exists at the center between the rotors as induced by the tip vortices from the rotor blades.

In Fig. 5, the blade sectional thrust distribution along the span is presented for a typical rotor for one rotor revolution. All four rotors exhibit a similar sectional thrust variation in this hovering flight. It is shown that even for the hovering flight condition, a significant fluctuation of the blade loading exists along the rotor azimuth angle, particularly near the blade tip around 45°, 135°, 225°, and 315°. This is because the rotor interacts with the other rotors, and the blade effective angle of attack is locally influenced by their wakes.

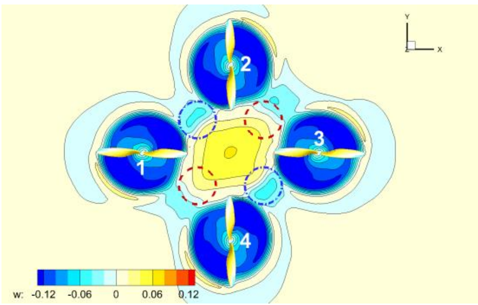

(a) Plane at half chord length below rotor disk

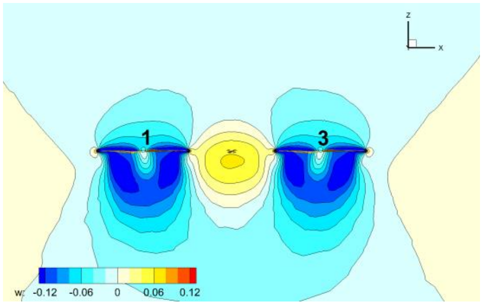

(b) Vertical center plane

Fig. 4 Vertical downward velocity contours for hovering flight.

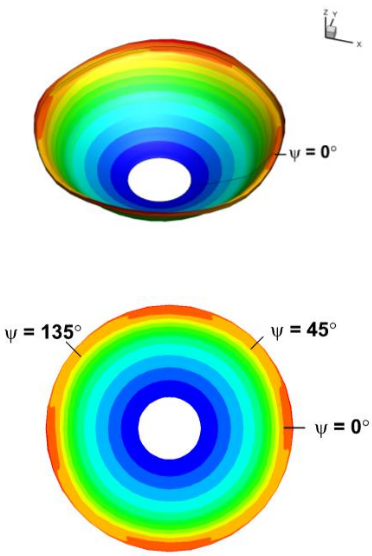

Fig. 5 Sectional thrust contour along blade span for one rotor revolution for hovering flight.

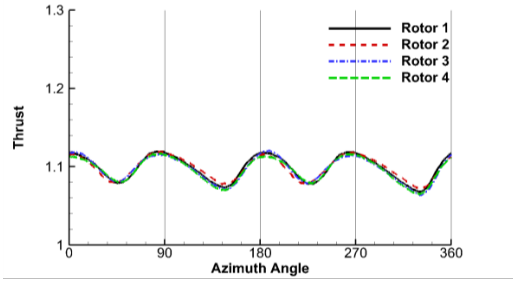

Fig. 6 Unsteady thrust variations of rotors for hovering flight.

Table 1. Time-averaged thrust of rotors and total moments on the vehicle for hovering flight.

		Time-averaged value
Thrust	Rotor 1	1.09817 N
	Rotor 2	1.09843 N
	Rotor 3	1.09675 N
	Rotor 4	1.09583 N
Moment	Pitch	0.00064 Nm
	Roll	-0.00071 Nm

In Fig. 6, the unsteady thrust variations of the four rotors are presented for one rotor revolution. It is shown that all rotors are in almost identical thrust variations, exhibiting a periodic change due to the aerodynamic interaction as described in Figs. 4 and 5, even though the magnitude of variation is small.

In Table 1, the time-averaged thrust of each rotor and the total moments on the vehicle by the four rotors are represented. It is again confirms that the time-averaged thrusts of all rotors are almost same. As a result, the time-averaged pitch and roll moments of the vehicle are near zero. For comparison, the calculation for an isolated rotor was also made. It showed that the thrust of an isolated rotor is 1.12489N, approximately 2.5% higher than the present rotors, again confirming the effects of the mutual aerodynamic interaction between the rotors.

3.3 Forward Flight

To investigate the mutual aerodynamic interaction of the rotors in forward flight, calculation was performed for the rotors when the vehicle flies at a freestream velocity of 5m/s. In the present calculation, the vehicle was assumed to be at an angle of attack of negative five degrees to the incoming freestream. The operating blade tip speed is 38.31m/s, and the tip advancing ratio is 0.174.

Figure 7 shows the wake structure behind the rotors as represented by the λ_2-criterion when the blades are located at the azimuth angle of zero degree. In the figure, the rotors 1 & 3 rotate clockwise, and the rotors 2 & 4 rotate counter-clockwise. The rotor 1 is the upmost one against the incoming freestream. It is shown that the rotors at the downstream are strongly influenced by the tip vortices trailed from the upstream rotors. It is also evident that the rotor disk vortices are formed at the sides of the rotor disk plane, and these disk vortices from upstream rotors strongly interact with those and also with the individual tip vortices of the downstream rotors. For example, the disk vortices from rotor 1 induce upwash to rotors 2 and 4 by increasing the effective angle of attack of the blades of those rotors, but increase the downwash on rotor 3. On the contrary, the wake from rotors 2 and 4 works in the direction of reducing the downwash for rotor 3.

In Fig. 8, the vertical downward velocity distributions at half chord length below and above the rotor disk plane are presented. It shows that relatively high downward velocity exists behind the rotor blades as induced by the wake of the individual rotor itself. In contrast, fairly high upwash is observed between the rotors as marked by the dash-dot region and the dotted region. This upwash is induced by the rotor disk vortices, and the magnitude is slightly higher between rotor 1 and rotor 4 as both rotor disk vortices are from the advancing sides. In contrast, the upwash with a less strength exists for a wider region between the rotor disk vortices from the retreating sides of rotors 1 and 2. The downstream rotor 3 is affected by all three upstream rotors. However, the influence by the three downstream rotors on upstream rotor 1 is relatively small.

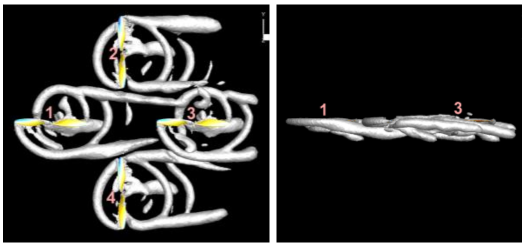

(a) Top and side views

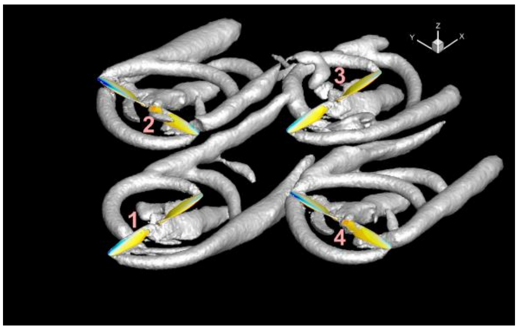

(b) Perspective view

Fig. 7 Rotor wake structure represented by iso-surface of λ_2-criterion in forward flight.

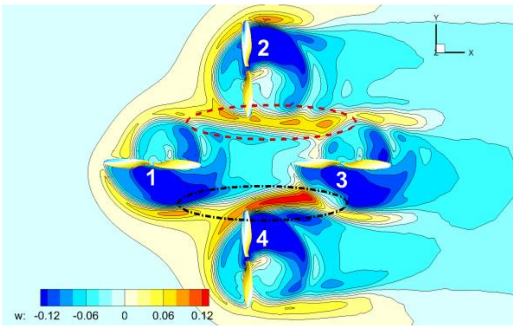

(a) Plane at half chord length below rotor disk

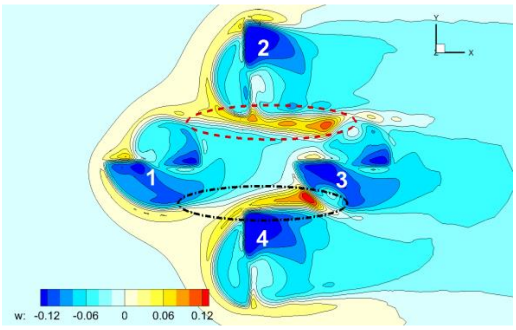

(b) Plane at half chord length above rotor disk

Fig. 8 Vertical downward velocity contours at half chord length below and above rotor disk plane in forward flight.

In Fig. 9, the sectional thrust contours over the rotor disk plane are presented for one blade. It is observed that rotor 3 has relatively smaller thrust loading than rotor 1 due to the higher induced downwash induced from the upstream rotors. It is also observed that the maximum thrust loading is obtained at the azimuth angles near 110 and 20 degrees for rotors 1 and 2, respectively. In contrast, in the case of rotors 3 and 4, the maximum thrust loading, slightly higher than that of rotors 1 and 2, is observed near the azimuth angles of 120 and 30 degrees as they interact with the wakes from the upstream rotors at the advancing side. It is also shown that higher thrust loading is distributed over a wider area for rotors 2 and 3 than rotors 4 and 1, particularly around the azimuth angles of 135 and 225 degrees.

In Fig. 10, the unsteady thrust variations of each rotor are presented for one rotor revolution. The phase difference of 90 degrees between the rotors in the figure is because the setting of the reference azimuth angle is different for each rotor. In general, the thrust obtained from rotor 3 is lower than that of rotor 1, although locally higher value exists. This again confirms that higher downwash flow is induced on rotor 3 as it is affected by the wake from the upstream rotors. It is also shown that higher thrust values are obtained for rotors 2 and 4, which is due to the upwash flow induced by the wake of rotor 1. Rotor 2 exhibits higher thrust loading than rotor 4 at two regions from 135° azimuth angle to 180° and from 315° azimuth angle to 360°. This is again due to the higher upwash induced by the tip vortex from the retreating side of rotor 1.

In Table 2, the time-averaged thrust of each rotor for one rotor revolution and the moments acting on the vehicle are presented. As discussed in Fig. 10, the time-averaged thrusts of rotors 2 and 4 are higher than that of rotor 1, and rotor 3 produces the smallest time-averaged thrust. As each rotor exhibits different time-averaged thrust behavior, a finite value of pitch and roll moments about the center of the four rotors is generated. This demonstrates that the attitude stability of the quad-rotor UAV can be deteriorated in forward flight due to the aerodynamic interaction between the rotors, which should be considered seriously in designing the autonomous flight control system of the vehicle.

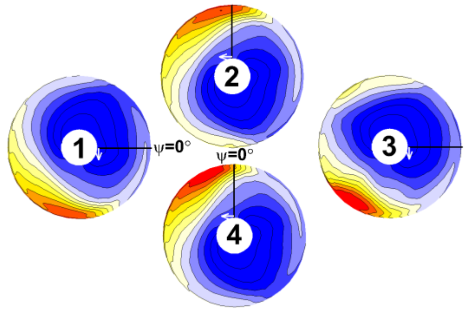

Fig. 9 Sectional thrust contours for one rotor revolution in forward flight.

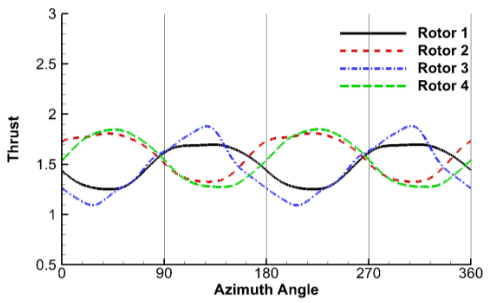

Fig. 10 Unsteady thrust variations of rotors in forward flight.

Table 2 Time-averaged rotor thrust and total moments on the vehicle in forward flight.

		Time-averaged value
Thrust	Rotor 1	1.49772 N
	Rotor 2	1.59025 N
	Rotor 3	1.46264 N
	Rotor 4	1.55175 N
Moment	Pitch	0.00963 Nm
	Roll	-0.0106 Nm

4 Concluding Remarks

In the present study, unsteady flow simulations of a quad-rotor UAV configuration were conducted, and the flow fields and the aerodynamic interaction phenomena of the rotors were investigated. For this purpose, an unstructured mesh flow solver was adopted, coupled with an overset mesh technique to handle the relative motion of the rotors.

The calculations were performed for the UAV in hover and in forward flight. It was observed that the aerodynamic interaction occurs even for hovering flight by reducing the overall thrust level of the rotors, and also by inducing periodic variation of thrust. However, the difference of the thrust between the rotors is quite small, and the overall moment on the vehicle is also negligible. The thrust reduction due to the mutual interaction is approximately 2.5%, compared to that produced by an isolated rotor.

In the case of the forward flight, the rearmost rotor shows reduction in thrust caused by the increased downwash induced by upstream rotors. In contrast, the level of thrust of the side rotors is slight increased as the effective angle of attack on the rotor blades is slightly increased from the upwash induced by the disk vortices of the upstream rotor. Unlike the hovering flight case, because of the strong interaction between the rotors, finite pitch and roll moments are produced on the vehicle. It is concluded that the mutual aerodynamic interaction should be seriously considered for accurately predicting the aerodynamic performance and the attitude control and stability for multi-rotor UAV configurations

Acknowledgments

This work was supported by the National Research Foundation of Korea (NRF) Grant funded by the Korean Government (2011-0029094). The authors also would like to acknowledge the support by the National Research Foundation (NRF) of Korea (Grant No. 201331019.01) through the Multi-phenomena Computational Fluid Dynamics (CFD) Engineering Research Center.

References

[1] G. M. Hoffmann, H. Huang, S. L. Waslander, and C. J. Tomlin, “Quadrotor Helicopter Flight Dynamics and Control: Theory and Experiment,” Proc. of the AIAA Guidance, Navigation, and Control Conference, AIAA 2007-6300, 2007.

[2] D. W. You, M. K. Jung, D. W. Won, M. J. Tahk, and O. J. Kwon, “Experimental and Numerical Studies on the Aerodynamic Analysis of the small-sized Multi-Rotor UAVs,” Proc. Of Spring Conference of the Korean Society for Aeronautical & Space Sciences, pp. 511-515, 2011.

[3] S. Bouabdallah, P. Murrieri, and R. Siegwart, “Toward Autonomous Indoor Micro VTOL,” Autonomous Robots, Vol. 18, pp. 171-183, 2005.

[4] P-J Bristeau, P. Martin, E. Salaun, and N. Petit, “The Role of Propeller Aerodynamics in the Model of a Quadrotor UAV,” Proc. Of the European Control Conference, pp. 683-688, 2009.

[5] S. Waslander, STARMAC Vehicle Dynamics, 2004.

[6] P. McKerrow, “Modelling the Dragonflyer Four-rotor Helicopter,” Proc. of the IEEE International Conference on Robotics and Automation, pp. 3596-3601, 2004.

[7] P. L. Roe, “Approximate Riemann Solver, Parameter Vectors and Difference,” Journal of Computational Physics, Vol. 43, No. 2, pp. 357-372, 1981.

[8] M. S. Jung, and O. J. Kwon, “A Parallel Unstructured Hybrid Overset Mesh Technique for Unsteady Viscous Flow Simulations,” Proc. of International Conference on Parallel Computational Fluid Dynamics, parCFD 2007-024, 2007.

Development of an unsteady wind tunnel experiment for vortex dominated flow at a Lambda – wing

S. Wiggen and G. Voß
Inst. of Aeroelasticity, Goettingen, DLR – German Aerospace Center, Germany

Keywords: *vortex, lambda wing, round leading edge, high sweep angle, unsteady experiment*

Abstract

A half wing model, a test rig and new wind tunnel walls were designed to study the vortex development at a lambda wing. It has a sweep angle of 53° and round leading edges. It is designed for pitching oscillations around a mean angle of attack of up to 20°, up to a Mach number of 0.7. Unsteady aerodynamic load data shall be delivered for aeroelastic calculations of Unmanned Combat Aerial Vehicles (UCAV).

Due to the highly nonlinear aerodynamic character, the design of the model had to take into account load cases with beginning and fully developed vortices. Furthermore, the different character at subsonic and transonic speeds had to be included. Coupled simulations with a finite element model including the mounting and the connection to the actuation system were performed to assess the dynamic stability. An optimized peniche reduces wing–wall interferences. The test concept and the process of the design will be described.

1 Introduction

Vortex development is a major steady and unsteady aerodynamic phenomenon for wings with medium to high sweep angles [1], [2], [3]. This results in high local loads which change significantly with the flight conditions of the aircraft. Furthermore, unsteady problems like wing rock or even buffet at various parts of the aircraft can occur. Depending mainly on the sweep angle, the airfoil nose radius and the Mach number, the vortices usually occur at higher angles of attack α. This is connected to high loads [3] and hereby high complexities for the model and test rig design. Dynamic wind tunnel experiments were mainly conducted at very low Mach and Reynolds numbers [4], [5].

In the DLR (German Aerospace Center) project FaUSST (German for: Advanced aerodynamic UCAV stability and control technologies) a generic lambda wing configuration of an UCAV is used to study the stability of that kind of aircraft [6]. Many modern UCAVs have a similar geometry and therefore similar problems. In contrast to the F17/ SACCON [7] configuration, which is also part of this project, the main focus for the IWEX (German for: Unsteady Vortex Experiment) model is the vortex development at a purely round leading edge. Therefore, the geometry was designed especially eliminating the apex vortex and the influence of the tip vortex. The steady and unsteady tests shall deliver validation data for aeroelastic computations.

The test concept will be described including the model geometry, the peniche and the new test rig in combination with new wind tunnel walls. The main focus is on the procedure of the structural design concerning different relevant load cases and the analysis of coupled fluid and structure computations to check the stability of the model.

2 Test concept

The model is designed for experiments in the Transonic Wind Tunnel Goettingen (DNW-TWG), performing pitching oscillations with up to 30Hz at a mean α of up to 20° and up to a free stream Mach number of 0.7. A half-wing model is attached to a hydraulic actuation system outside of the test section. The opening in the wall is sealed by a turnable disk (**Fig. 1** and **Fig. 2**). Hereby, a closed wind tunnel section and a continuous intersection of the wall and the model are achieved. This also facilitates the simulation and reduces the influence of gaps that otherwise exist. Furthermore, a peniche was designed to reduce the interferences between the wing and the wall.

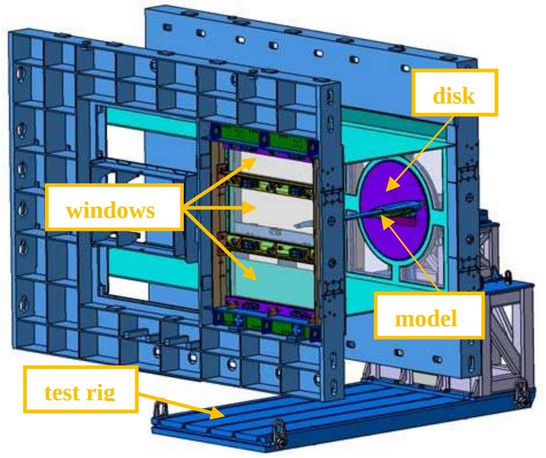

Fig. 1 Test section, test rig and model

2.1 Model geometry

The leading edge sweep angle is 53°. At the inner part, the trailing edge has a sweep angle of -26.5° (**Fig. 3**). The half span of the model is 0.51m. The twist varies linearly from 0° at the inner kink to -7.4° at the tip to reduce a strong tip vortex and shift the development of the main vortex inboard. There is a symmetric airfoil at the root and an asymmetric one for the main wing that blends into a symmetric one at the tip. The ratio of the leading edge radius to the chord is kept constant for nearly the complete span.

2.2 Peniche

The peniche was especially designed for angles of attack between 12° - 18° by the results of computational fluid dynamic (CFD) calculations. The shape and width were varied to minimize the differences compared to the geometry without wind tunnel walls. The effects on the flow originate from a horseshoe vortex at the leading and a corner separation at the trailing edge near the junction of the wall and the wing [8]. Without a peniche, this results mainly in a displacement of the main vortex in the direction of the tip which can lead to a change of the vortex topology by a merging of the tip and the main vortex [9].

The peniche has a span of 0.03m, is divided in two parts and can be replaced. Thus there is the possibility to use the model in other wind tunnels or with a peniche that is optimized for other measurement conditions e.g. moderate angles of attack.

2.3 Test section, walls and disk

The cross section of the test section of the TWG is 1x1m². For the iPSP (unsteady pressure sensitive paint) and the planed PIV (particle image velocimetry) measurements, the optical access is improved by new wind tunnel walls with larger glass windows. On the side opposite to the model, there are two identical windows with a larger and one with a smaller height (**Fig. 1**). Their sequence in vertical direction can be changed to improve the flexibility for the setup of the optical measurement systems. The concept was designed by the help of CAD software including possible camera view angles. Especially the high angles of attack, the sweep angle and the curvature of the airfoils had to be taken into account.

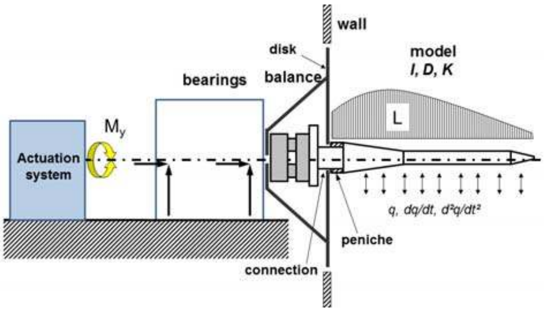

Fig. 2 Actuation system

The turnable disk is connected to the actuation system at the back of a piezoelectric balance, which is located between the model and the actuation shaft. This makes the measurement of all 3 forces and 3 moments without the influence from the disk, possible (**Fig. 2**). The distance between the disk and the wall was defined by the expected deformation of the mounting and the bearings.

3 Structural design and load calculations

The structure was designed using FE-models that were computed with MSC.NASTRAN and CATIA V5. The loads for the design were generated by a superposition of inertial and aerodynamic loads. Subsonic and transonic cases had to be selected because they differ in their behavior regarding the vortex development and therefore the load distribution. Initially, Mach numbers were selected that clearly show either the one or the other character to study this effect (**Fig. 3**), even though they are not part of the planned measurement envelope.

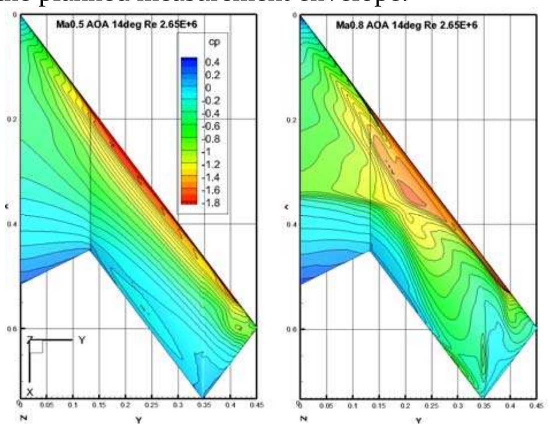

Fig. 3: Subsonic and transonic pressure distribution, α 14 deg

The goal of the design was a model which is as rigid as possible. So, no structural response was desired. The dynamic stability was checked by coupled fluid/structure computations to ensure that vibrations are always damped. Thus, the structural deformation contains mainly the frequency of the excitation. Otherwise, there exist inertia loads due to deformations, which differ significantly from those of the approximation of the superposition of static forces that were used for the design.

Flutter calculations were made with ZAERO, to generally assess the aeroelastic stability of the model for linear flow conditions occurring at small angles of attack. They showed almost no change of the eigenfrequencies with increasing dynamic pressure. On the one hand, the frequencies are well separated. On the other, with increasing order of the modes, they become very high due to the stiffness of the model. Hence, only the first 10 modes can be expected to be critical at all. Only the 3rd bending mode showed a tendency to become unstable, but for dynamic pressures far above that of the test. The reason might be that for highly swept wings or plates, this mode looks like a combination of a torsional and a bending mode.

3.1 Structural design

The structure was basically designed in two stages. First, the feasibility of a model with eigenfrequencies, well be above the test frequencies, was checked. After defining the dimensions for the connection to the balance and the actuation system, a FE-model with shell elements (**Fig. 4**) was created with ModGen, a parametric generator for FE - models with wing like structures [10], invented at the DLR Institute of Aeroelasticity. The advantage of the parametric model description was the capability to quickly vary geometrical, thickness and material parameters. Hereby, the influence of the constraints and the connection to the actuation system, especially on the dynamic structural behavior, was studied. Furthermore, approximations of the necessary material thickness and suitable positions of ribs and spars were checked, first with simple load distributions then with loads from the CFD computations. It was found that there would be no benefit from using fiber composite materials, also regarding the achievable eigenfrequencies. Complex stress distributions occur due to the geometry of the model. This results in a design where the advantages of the high strength and stiffness in the fiber direction would not be exploited sufficiently. Especially at the rear part of the kink, this is easy to understand. Therefore, aluminum was selected.

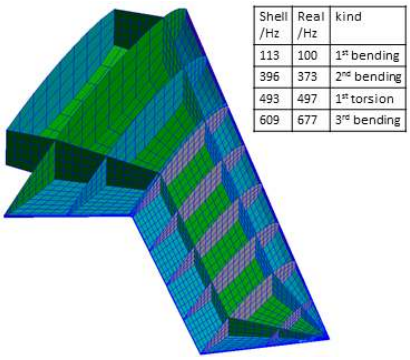

Fig. 4: Initial shell model, inner structure, not adapted to the final design

The disadvantages of the shell model compared to a model with solid elements can be regarded as only important for higher modes. The experimental analysis of the real structure showed that the shell model, especially after the spars and ribs were adapted to the final design, predicted slightly higher eigenfrequencies for the bending modes. Nevertheless, the modes are in good agreement regarding their shape and sequence. Taking into account that neither the screws nor their threads were included, this is a good result. The additional material at the leading and trailing edge for the connection of the upper and lower part (**Fig. 6**) was modeled by additional mass.

At the wing, the "natural" shear center of the airfoil section with two spars and a constant material thickness was expected to be at 40-45%. The thickness of the rear spar was increased to minimize the wing torsion, originating from torsional moment and wash-out, by shifting the elastic axis towards the trailing edge. This was also this reason for the design of the ribs and their position. Together with the spars, they create boxes which increase the torsional stiffness and also the rigidity of the thin rear part of the outer kink. This part can be critical regarding stronger deformations. Additionally, here are the highest inertia forces due to the pitch oscillations.

For the detailed design, FE-models with solid elements were created (**Fig. 5**). The screws were represented by Multi- Point Constraint (MPC) elements. In a later version, also the actuation system, the bellow coupling, the shaft with the two bearing pairs and the balance were included as solid elements, spring elements and MPCs. Initially, they were only represented as beam elements. During the design process, the stiffness of the mounting and actuation was tuned to experimental results. Especially the bearings and the connection between the shaft and the coupling are not ideally stiff in reality. Therefore, static and dynamic tests of the actuation system and mounting were performed. This part of the FE-model had the biggest uncertainties, especially since the inertia moment of the model was higher than that of the models that were usually tested with the actuation system. That is the consequence, as the model itself was designed as rigid as possible and for high loads and an effect of the high sweep angle. Therefore, the lowest eigenfrequencies and also the static deformations are very much affected by the deformation of the shaft. Small variations in its stiffness can have a huge impact on the eigenfrequencies and the dynamic behavior of the model.

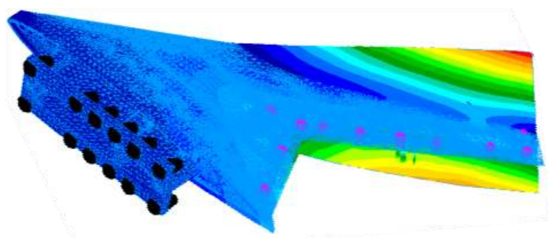

Fig. 5: Solid elements model, torsional mode

During the detailed design process only a small additional spar had to be added near the rear part of the kink and the spars at the tip were removed (**Fig. 6**). Otherwise, the basic structural setup stayed as before.

The detailed sizing of the structure was mainly done in the CATIA environment with a superposition of the quasi static inertia and aerodynamic forces. The aerodynamic loads were interpolated from the CFD results to a set of points for the force transmission. Essentially the same methods, which are based on radial basis functions [6], [12], were used as for the coupled calculations that will be discussed in the next section. Different sets of loads were selected to take the changing aerodynamic character into account. For the final sizing, they were deduced of computations at the free stream Mach numbers 0.5 and 0.7. Furthermore, they were all scaled to a maximum global normal force (section 0). Finally, different load distributions, but with the same overall normal force were checked in the sizing process. Hereby, the global lift or normal force can be used as the main monitoring value for the wind tunnel test.

Fig. 6: Upper (left) and lower half of the model

As the coupled dynamic simulations only deliver deformation, but no stress results, there were three approaches for this problem. On the one hand the displacement results of the coupled computations were interpolated to the surface of the FE model. However, this straight forward way leads to unrealistic stress peaks at some points where the deformation constraints were imposed. This is caused by the interpolation between the two different grids. If it is not smooth e.g. at corners it results in small errors. As the stress is the derivative of the deformation over space, differences are augmented. Nevertheless, those results could still be used for the analysis of the inner structure.

On the other hand, the aerodynamic loads f_{aero} at times t_i with maximal deformations were interpolated to the FE model and the maximal inertia loads due to the rotational acceleration were added. They are the amplitude of the pitch oscillation times its squared angular frequency ω (Eq. (1)).

$$f = f_{aero}(t_i) \pm rot.acc_{\max}(\hat{\alpha} \cdot \omega^2) \qquad (1)$$

If the elastic motion is small compared to the rigid rotation and mainly contains the excitation frequency, the error of neglecting the inertia forces due to the elastic displacement can be expected to be small. This is of course only valid for stable conditions. The analysis of the dynamic deformations will be explained in the next section. Their results were compared to the described superposition.
For special cases, e.g. where the bending mode was excited, the local acceleration was derived from the deformation results. It was analyzed and the values at relevant instants of time used to generate NASTRAN load - cards for the FE model. Then, the aerodynamic forces and the rotational acceleration were added to compute the stress results of the FE model.

3.2 Aerodynamic loads and coupled calculations

In the following section mainly those results of the CFD computations will be discussed, that were used to generate the design loads and check the steady and unsteady behavior of the model i.e. the coupled calculations. Especially the spanwise distributed coefficients are good indicators for the change of the load distribution. Furthermore, surface plots of the pressure difference between the upper and lower surface were used to illustrate the local loads. For this purpose, the results were interpolated with a barycentric approach to a structured grid, equal on upper and lower side, to facilitate the analysis and the computation of sectional values.

Steady results

The typical vortex at round leading edges [11] is a thickness caused vortex (**Fig. 7**) which is strongly affected by an interaction with the boundary layer. During the design process, static and coupled dynamic simulations were performed using the Navier - Stokes solver TAU [12] and a modal representation of the FE-models [6], [13]. For the final design loads, the wind tunnel walls were included. For the basic studies and the initial sizing, the geometry without wind tunnel walls was used. In the following this will be called *reference geometry*.

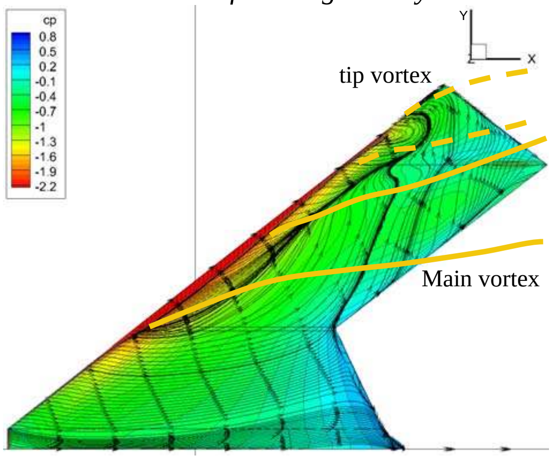

Fig. 7 Pressure distribution with beginning vortex development, α 15 deg, upper side

The steady behavior is mainly influenced by the heavily changing load and moment distributions. With increasing α, the main vortex moves inboard and detaches from the surface. At the outer part of the wing, the slope of the normal force is already decreasing, whereas at the inner part it is still positive (**Fig. 8**). This results in a more triangular distribution. The force maintains almost constant at the outer part where the vortex has detached from the leading edge.

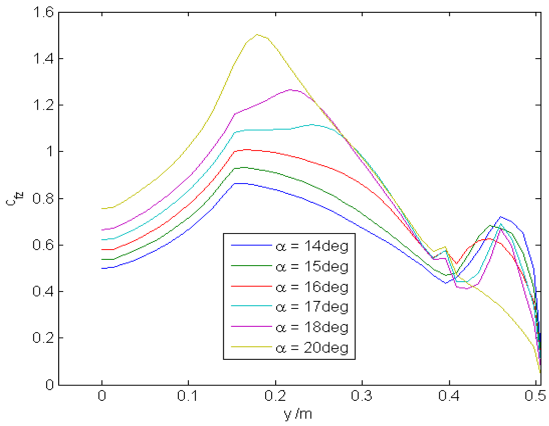

Fig. 8 Normal force coefficient distribution, α 14-20 deg, Mach 0.5, Re 2.65 Mil, reference geo.

The moment distribution (**Fig. 9**) is also affected by the inboard moving vortex extending from the leading edge of the inner part over the trailing edge of the outer part (**Fig. 7**). Hereby, the moment distribution, especially at the outer part, changes significantly. For lower α, the slope of the distributed moment is positive which then turns into negative. The effect of the decreasing lift at the leading edge is augmented by the increased suction at the trailing edge.

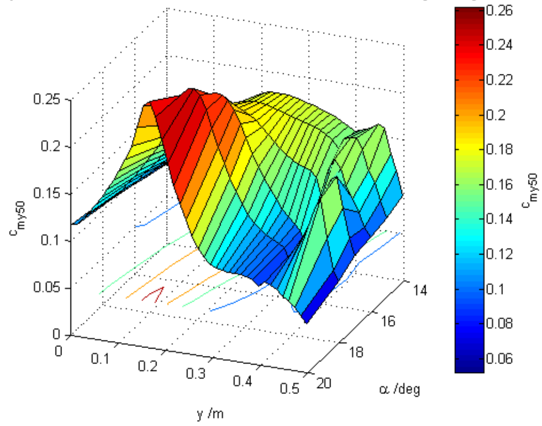

Fig. 9 Moment coeff. (at 50% chord) distribution, α 14-20 deg, Ma 0.5, Re 2.65 Mil, reference geo.

Combining both effects, the center of pressure x_{cp} moves further to the trailing edge (**Fig. 10**). On the one hand, this amplifies the strong washout effect (**Fig. 11**) caused by the high sweep angle. On the other hand, it will shift the vortex outboard again as the local α is reduced. Under coupled dynamic conditions this could cause very non- linear behavior.

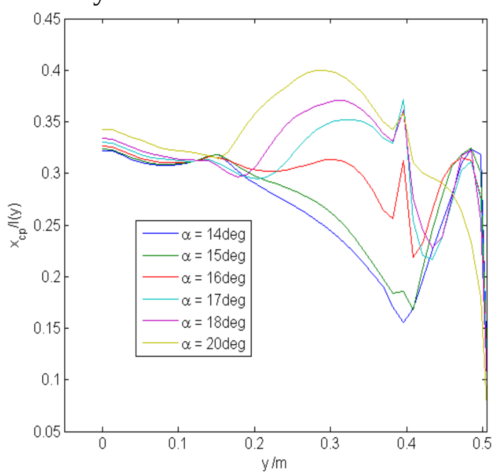

Fig. 10 Center of pressure over local chord *l*, α 14-20 deg, Ma 0.5, Re 2.65 Mil, reference geo.

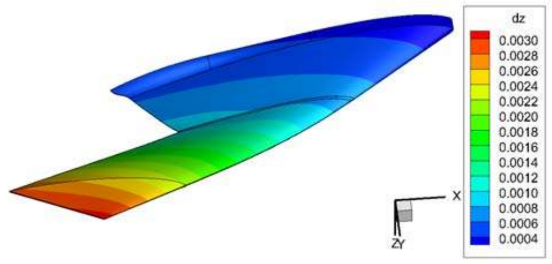

Fig. 11: Steady deformation only of the wing /m

Further computations at the Mach number 0.5, but a higher Reynolds number, showed that the effect on the center of pressure is reduced by an increase of the suction peak at the leading edge. This postpones the detachment of the vortex and minimizes the effect of the suction of the vortex at the rear part of the outer wing on the spanwise distributed values. But the local effects still exist in the same manner. These computations were already performed including the wind tunnel walls and the peniche. The correct flow conditions were adapted iteratively by a variation of the mass flow and checked at a monitoring point. The dynamic pressure was the same as for the computations at Mach 0.7 to obtain similar deformations.

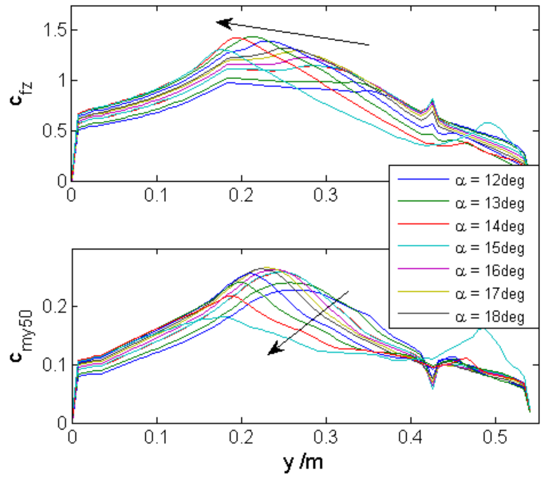

Fig. 12 Normal force and moment coefficient distrib., α 12-18 deg, Ma 0.7, Re 2.65 Mil, model geo.

With increasing transonic effects the vortex development changes. Shocks trigger the vortex to detach from the surface and change the direction due to the smaller velocity perpendicular to the shock front. Furthermore, the vortex - shock interaction shifts the development of the vortex to smaller angles of attack, compared to the subsonic cases (**Fig. 3**). This results in a decreasing normal force slope and hereby aerodynamic load (**Fig. 12**). Beyond an α of 16° at the Mach number 0.7, the strong vortex lift is reduced and the lift slope becomes negative.

This effect is very sensitive and strongly affected by the position of the shock. Depending e.g. on the turbulence model that can easily vary by some percent of the chord length already for the flow without vortices at a smaller α. To exclude the uncertainty of the computations regarding the extent of the transonic behavior and at which α the vortex moves inboard, all loads for the sizing process were scaled to a maximum lift force as reached for the subsonic cases, which was described before. This maximum global normal force $F_{z,max}$ is:

$$F_{z,\max}(Ma = 0.7, \alpha = 20°) = Fz(0.7,16°) \cdot \frac{Fz(0.5,20°)}{Fz(0.5,16°)} \qquad (2)$$

The steady coupled calculations generally showed a good and fast convergence behavior. So, no steady stability problem exists. From the polar plots and the pressure distributions, it was determined that the relevant cases for the stability examinations are at the angles of attack of 14.5° and 16.5°. The first one is slightly before the development and detachment of the vortex and the second one is thereafter.

Unsteady calculations

The coupled unsteady calculations, that will be discussed, consisted of the following combinations:

Unsteady aerodynamic calculations can be started based on the jig- shape or on the flight - shape of the coupled computations with steady aerodynamics. This yields for steady or oscillating angle of attack. To increase the convergence speed, coupled unsteady simulations usually are started based on coupled steady results. Theoretically:

If the aerodynamic loads have a damping character, calculations starting from the jig - or the flight - shape should yield the same results after some time. If the calculations with constant α and unsteady aerodynamics do not converge or

result in a limit cycle oscillation, a dynamic stability problem exists.
Vice versa, the non-equilibrium state of the jig - shape can be used to trigger and/or check if dynamic stability problems can occur. Furthermore, the modes mainly responsible for the static deformation are inherently excited by this. This was especially important due to the high impact on the lower eigenfrequencies and the difficulties in modeling the stiffness of the mounting of the model. The tests also included pitch amplitudes of 1°, starting from jig- and flight – shape, to examine the non-linear aerodynamic behavior and produce higher inertial effects. Amplitudes of 0.2° with frequencies from 5 - 30 Hz were used to study the general unsteady behavior of the vortex system.

The wavy characteristics of the lift and moment coefficient of the first 3 periods in **Fig. 13** and **Fig. 14** are caused by the strong influence of the small bending motion. This was excited by starting the computation based on the jig - shape. Consequently, even small dynamic deformations can have a huge effect on the global results. This yields for both, numeric and experimental tests. Vice versa, the aerodynamic response can be significantly different for coupled than for uncoupled computations if special modes are triggered. Additionally, it can be noticed that the bending mode is damped over time.

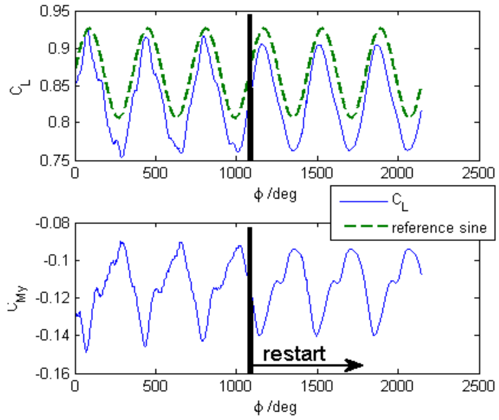

Fig. 13: CL, CMy over phase angle of motion, Ma 0.5, α = 14.5 ± 1deg, 20Hz, Period 1 – 6

A restart was done after the 3rd period, based on the flight - shape geometry. Even though the rotational motion is about 10 times higher than the bending motion, a significant discrepancy exists between the case with an active bending motion and where the deformations are small and mainly with the frequency of the excitation.

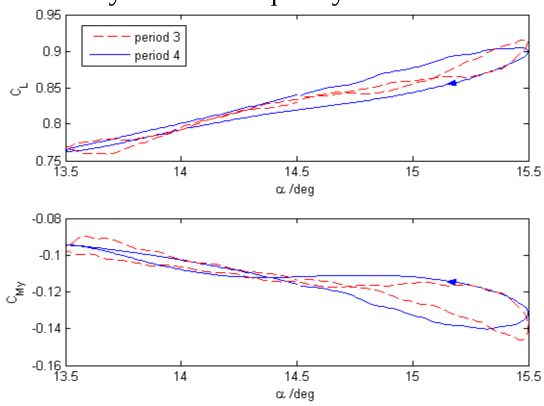

Fig. 14: CL, CMy over α, Ma 0.5, α 14.5 ± 1deg, 20Hz

The frequency variations at a mean α of 14.5°, where the vortex development begins, show that the influence of the high sweep angle and hereby the strong plunge - like movement of the outer part of the wing affects the vortex at the tip differently than the main one (**Fig. 15**). The normal force slope of the "quasi-steady" load becomes negative. Hence, at the outer part it decreases in phase with the angle of attack but increases in phase with the plunge velocity.

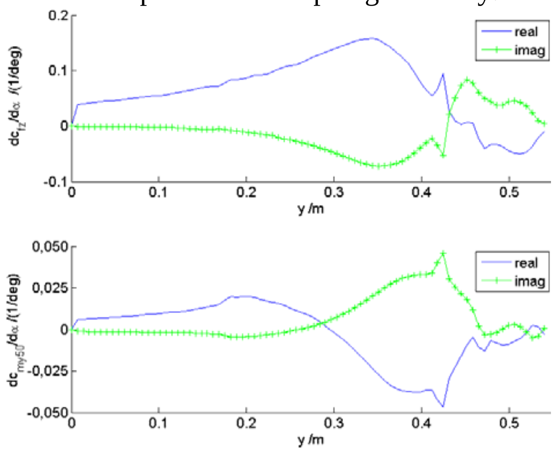

Fig. 15: 1st harmonic freq. response to α 14.5 ± 0.2deg, 25Hz, of normal force and moment, Ma 0.5

A phase shift exists (**Fig. 16**) between the main vortex and the tip vortex developing at the outer triangle of the wing (**Fig. 7**). Additionally, it is fed by a narrow co-rotating vortex along the leading edge. A phase angle ϕ of -180° of the transfer function, representing the harmonic part of $dc_p/d\alpha$, means increasing suction with α. So, the main vortex is in phase with the angle of attack. This means that both vortices could induce vibrations similar to a seesaw. However, the eigenfrequencies, that can be excited hereby, are much higher. In the simulations, this system of vortices seemed to be stable and the behavior was not changing significantly after the second or third simulated period of motion.

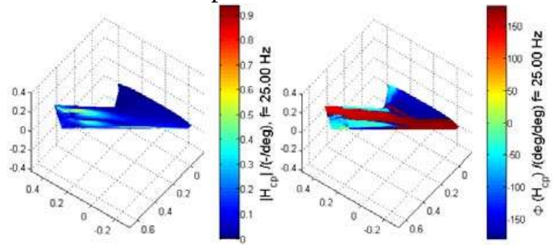

Fig. 16: 1st harmonic frequency response to pitching motion, 25Hz, of pressure, α 14.5 ± 0.2deg, Ma 0.5

The coupled dynamic simulations showed a damping of the structural vibration after an initial excitation, arising from the start, based on the jig-shape geometry. In **Fig. 17**, the heave and twist deformation of the first three periods is plotted over the wing span. This is the same case as shown in **Fig. 13** and **Fig. 14**.

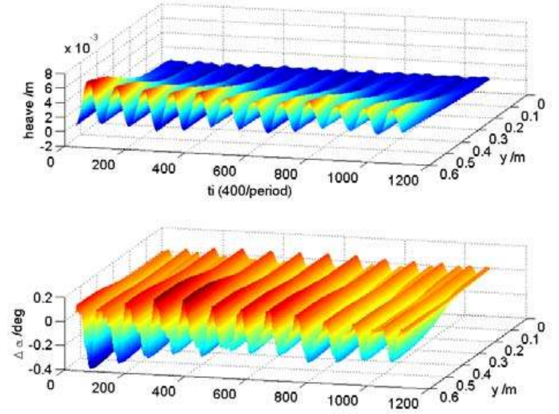

Fig. 17: spanwise heave and twist over time, Ma 0.5 , α 14.5 ± 1deg, 20 Hz period 1-3

In the last step it had to be ensured that the dominant part of the deformation is caused by the pitch excitation. It can be analyzed by a Fast Fourier Transformations (FFT) (**Fig. 18)** and if deemed necessary, again over time, of the spanwise heave and twist distribution. This is essential for the quasi - steady simplification of design loads as a superposition of aerodynamic loads and the rotational acceleration. The FFTs of the spanwise force and moment coefficients give an indication how the deformation affects the aerodynamic loads or vice versa - similar to **Fig. 18**. For these stability tests it was decided not to display the forces as generalized forces as the actual value is lost. For the future analysis of the aerodynamic data, the comparison with the wind tunnel data and sensitivity tests this representation will be more appropriate.

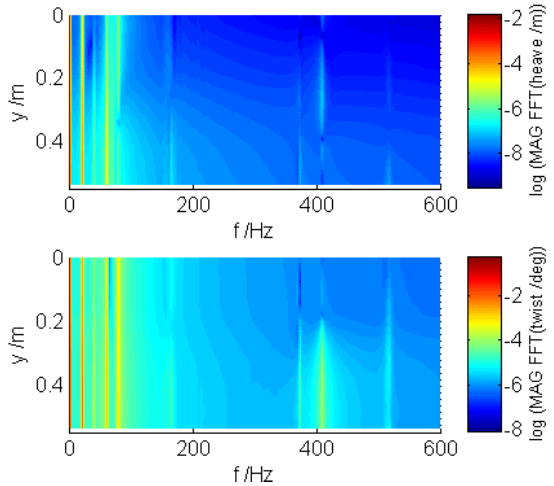

Fig. 18: FFT of heave and twist, along the wing span, α 14.5 ± 0.2deg, 20 Hz, Ma 0.5

As the deformations were small, their behavior damped and the dominant part with the frequency of the pitch excitation, the superposition was a fair simplification for the design loads.

Conclusion

For the design of the experiment and the wind tunnel model, the following criteria were important:

A good optical access to the measurement section should be achieved by the new wind tunnel walls. Wall interference effects had to be reduced.

The model had to be designed for high loads with small deformations. Important load cases had to be selected based on the analysis of CFD calculations and scaled as design loads.

Shocks triggered the vortex to develop at smaller angles of attack for transonic than for subsonic cases. Steady and unsteady coupled fluid/ structure computations were performed for the stability analysis of the model. They were compared to the superposition of the inertial and steady aerodynamic loads used for the design and sizing.

Especially the CFD computations including the wind tunnel walls and in a later phase also the deformation of the model were important to find a concept for a new test rig, wind tunnel walls and plan the experiment. The comparison to the reference geometry without the wind tunnel was used to verify influences. The scaling of the loads reduced the uncertainties of the sensitivity to transonic effects and ensured that the global normal force can be used as a safe monitoring parameter.

In the future, computations will be compared to the results of the experiments. The signals of the piezoelectric balance as well as the unsteady pressure and acceleration sensors can be used therefor. Additionally, the optical measurements deliver surface and flow field information (PIV, iPSP and optical deformation measurement system). Hereby, an increased understanding of the vortex development at round leading edges is achieved. Furthermore, the current simulation capabilities can be evaluated. The hereby gained experiences will be used for the design and analysis of real scale configurations.

References

[1] Livne E., “Future of Airplane Aeroelasticity”, Journal of aircraft, Vol. 40, No. 6, Nov. – Dec. 2003, pp. 1066-1092

[2] Hartwich P. M., Dobbs S. K., Arslan A. E. and Kim S. C., “Navier–Stokes Computations of Limit-Cycle Oscillations for a B-1 like Configuration”, Journal of Aircraft, Vol. 38, No. 2, 2001, pp. 239–247

[3] Gursul I., Gordnier R., Visbal M., “Unsteady aerodynamics of nonslender delta wings”, Progress in Aerospace Sciences 41, 2005, pp. 515–557

[4] Hummel D., Loeser T., “Low speed wind tunnel experiments on a delta wing oscillating in pitch”, 21st Congress of the International Council of the Aeronautical Sciences, 98-3.9.3. 21. ICAS Congress, Melbourne, 1998

[5] Voss G., Cumnuantip S., Neumann J., “A Steady Aeroelastic Analysis of an Unmanned Combat Aircraft”, Vehicle Conceptual Design, 29th AIAA Applied Aerodynamics Conference, AIAA 2011-3020, 2011

[6] Khrabrov A., Greenwell D., “Chapter 9 - TSAGI 70° AND 65° DELTA WINGS TEST CASES”, NATO RTO-TR-AVT-080

[7] Vicroy D. D., Loeser T. D., Schütte A., “SACCON Forced Oscillation Tests at DNW-NWB and NASA Langley 14x22-foot Tunnel”, AIAA Paper 2010-4394, 2010

[8] Gand F., Deck S., Brunet V. and Sagaut P., „Flow dynamics past a simplified wing body junction“, Physics of Fluids, Vol. 22, 115111, 2010

[9] Wiggen S., Voß G., ”Computations of the vortex development for a steady and unsteady Lambda-wing wind tunnel experiment”, accepted for DGLR Jahrestagung in Stuttgart, 2013

[10] Klimmek T., „Parameterization of topology and geometry for the multidisciplinary optimization of wing structures“, in Proceedings European Air and Space Conference, Manchester, 2009.

[11] Konrath R., Roosenboom E., Schröder A., Pallek D. and Otter D., “Static and Dynamic SACCON PIV Tests - Part II: Aft Flow Field”, AIAA Paper 2010-4396, June 2010

[12] Gerhold T., Friedrich O., Evans J., Calculations of Complex Three-dimensional Configurations Employing the DLR-TAU-Code, AIAA 97-0167, Reno, 1997

[13] Neumann J., “PyCSM – Python Computational Fluid Dynamics and Computational Structure Mechanics Coupling System”, Software Documentation and Technical Report, Institute of Aeroelasticity, Goettingen, November, 2010

Experimental Analysis on Dynamic Characteristics of an Ornithopter

Mitsuhiro Kamii[1], Hironori A. Fujii[1] and Ichiro Nakane[1]

1) Kanagawa Institute of Technology, Japan

Keywords: *Ornithopter, dynamic behavior, flapping, feathering, lead-lag*

Abstract

Ornithopter is an aircraft that moves its wings to fly like a bird. A flight model of an ornithopter is constructed and analyzed its flight characteristics experimentally in the present study. Size of the model for the experimental demonstration is wingspan 3.3m and, length 1.4m. The present flight model is constructed to enable the following three movements in the main wing: 1) flapping motion to move the wing into the vertical direction, 2) feathering motion to change the angle of attack in the flapping motion, and 3) lead-lag motion to move the wing into the horizontal direction.The flapping mechanism is implemented in the model employed with the ornithopter concept and feathering and lead-lag motions are realized in order to let the model produce both lift and thrust. Results of the experiment show sufficient lift to suspend the body with about 4kg and thrust with controllability.

1 Introduction

A model of the ornithopter has flown but not completely by Prof. Delawrier at the Institute of Aeronautics Study of University of Toronto in 2006 employed with jet engine as an auxiliary propulsion device.[1]

Aerodynamics of the ornithopter is studied by many researchers [2]-[12] and the importance of the three kinds of motion is understood in order to produce lift and thrust by the wing. These three kinds of motion includes, 1) flapping motion to move the wing into the vertical direction, 2) feathering motion to change the angle of attack in the flapping motion, and 3) lead-lag motion to move the wing into the horizontal direction. Wing motion is also studied rather than bird including insects, butterfly, mosquito, cicada, and some mechanisms are reported in their performance in order to simulate the motion of small air vehicles.

A model of bird flight is constructed by Nakazato and the model has flown successfully in 2007 [13]. The model has its wing span 3.3m with an engine 31,000rpm to flapping the wing and flew in average flight velocity 6m/s and ascending velocity 1m/s. The model is able to realize three movement, flapping, feathering, and lead-lag motion, and furthermore the flapping motion is synchronized to change its frequency increasing in the upward motion and decreasing in the downward motion, in other words, asymmetric flapping motion. The change of frequency in the flapping motion is a key idea to increase the efficiency in producing lift and thrust also increasing the performance of maneuverability in the flight of ornithopter and is designed in the model of Nakazato.

A flapping-of-wings wings machine differs in the flight method from the conventional airplane definitely. Therefore, there are merits and demerits in a flapping-of-wings wings machine. In this experiment, an experimental model is constructed and its flight characteristic is studied experimentally and improved in its design to obtain better flight performance.

Fig.1 Flight of Cygnus

2 Wing section and definition

2.1 Model

The dimensions of the model in the present study are as follows:

Wing area: S = 1.0 [m^2], Span: b = 3.3 [m], Mean aerodynamic cord: =0.30, Mass of the main wing: M = 2.6 [kg].

2.2 Wing section and definition

The wing section is selected as NACA65(2)415 which has moderate aerodynamic lift/drag performance. Some definitions of the aerodynamic characteristics are shown in which denotes the angle of attack, *V* velocity with *u* forwards velocity and *w* upwards velocity, and *L* and *D* denote lift and drag, respectively. The wing is assumed to move in the vertical plane of the flight direction and is examined in the flapping, feathering, and lead-lag motion.

1) Flapping motion means to move the wing up and down changing the magnitude and positive/negative of vertical velocity *w*.

2) Feathering motion means to rotate the wing changing the angle of attack positive and negative while flying, and

3) Lead-lag motion means to move the wing forwards and backwards while flying

These motions of wing induce lift and drag acting on the wing by the aerodynamic force and then produce vertical force *Fv* (upward positive) and horizontal force *Fh* (forwards positive). A bird will be able to fly successfully to forwards and upwards if the wing could produce positive *Fv* and *Fh* as the result of these three motions. The aerodynamic characteristics of the wing model are then examined in their resulting vertical force and horizontal force.

2.3 Model

Fig.2 The model

The model constructed for the present study is shown in Fig. 2. The gear system is employed to slowdown the motor rotation speed into the slow flapping speed and is shown in Fig.3.

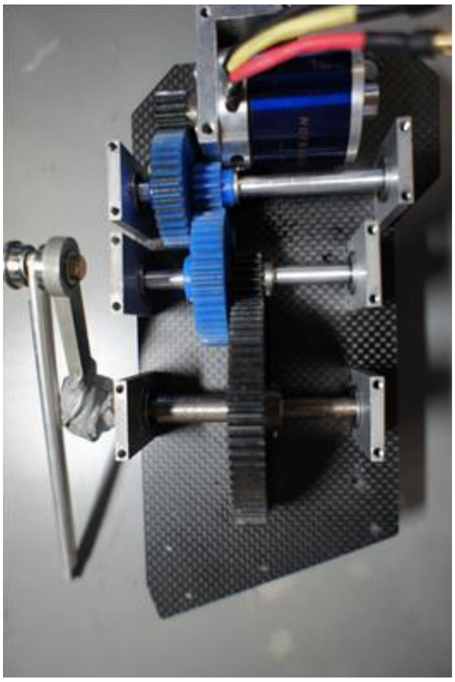

Fig.3 Gear box

The crank chain is the 7075 duralumin and the slowdown gear is made of plastic which is usually employed for radio control model. The rotation of the motor with 288 rpm is slowed down by the slowdown gear of a gear box. The body frame is shown in Fig.4 where the up-and-down main pipe of the body employs the fishing rod made from a carbon fiber. The truss frame structure is composed by a pipe made from stainless steel as a reinforcement frame.

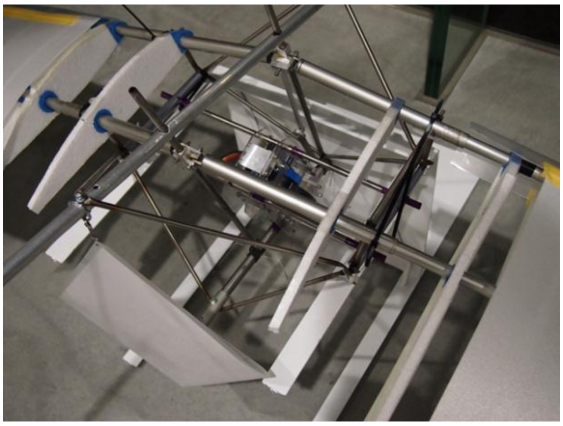

Fig.4 Frame

Figure 5 shows the features of the wing where the taper carbon pipe employed with the fishing rod is used at the front tip and the center of the wing. Nineteen of ribs made from styrene foam are installed in the wing and the styrene board in 1-mm thickness is stretched resulting in the surface.

Fig.4 Arrangement of the rib of a wing

2.4 Flapping-of-wings mechanism

The present movement of the wing is three motions as the flapping movement, feathering movement, lead lug movement. Wing of the birds is not necessarily merely exercising up and down only. A complicated frame and muscles are controlling the wings motion of the birds. Flapping movement is the movement to moves wings up and down. It launches strikes up and down corresponding to this movement. Wings are twisted and the feathering movement obtains lift in the case of twisting down wards.

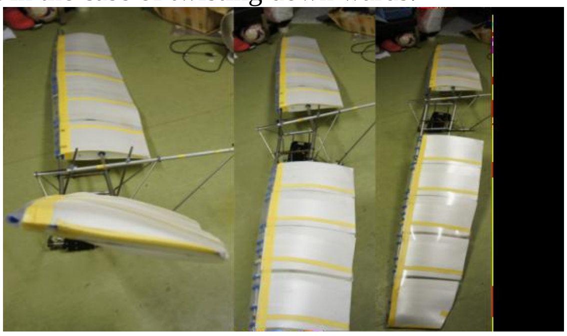

Fig.5 A motion and lead lug of wings

The leadlag maneuver is a maneuver which moves the aerofoil horizontally to forwards and backwards in order to obtains thrust. The flapping flight of a bird wing is reproduced by simulating these three maneuvers carried out simultaneously.

In order to add the lead-lag motion a slider is attached to the root of the main-wing. The slider is designed by passing a straight line pipe into the airframe frame and the straight pipe of the frame is attached in an inclined manner. The red line in Fig.6 shows the movement of the crank.

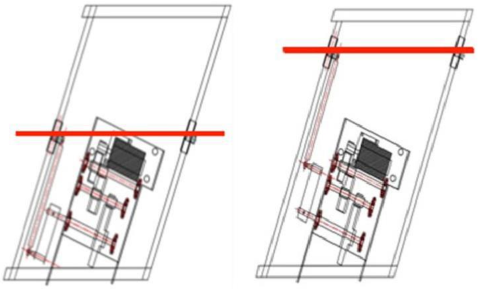

Fig.6 leadlag motion by the crank

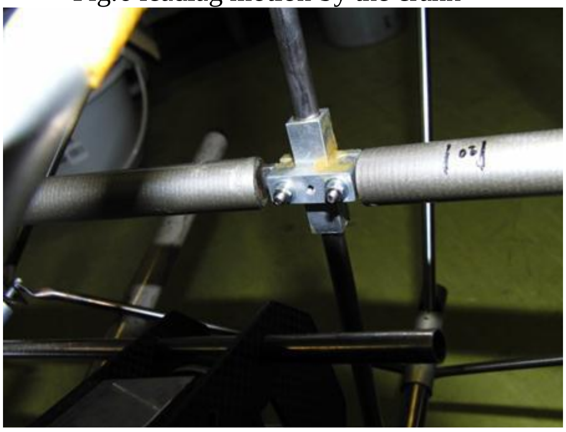

Fig.7 Structure of a slider

3 Experiment

3.1 The purpose of an experiment

It turned out that Ornithopter which we manufactured from old research has realized 3 movements of lead lug flapping feathering. So, in this experiment, before resulting in a flight experiment, we decided to confirm whether a lift and a thrust can be generated, so that this Ornithopter could fly. And I would like to use this experimental result for a future improvement.

3.2 Experiment outline

We conduct two experiments this time. First, like Fig.13-15, the experiment of a thrust attaches a string to the rear of the body, hangs down the string perpendicularly by a pulley, and attaches weight to the point. If The Ornithopter which this weight is placed on the electronic balance and placed on the rail has generated the thrust, weight will be pulled upwards and will become light. It can be checked out of which the value of the electronic balance was recorded on the personal computer, and the thrust has come. The data obtained from the experiment is appropriate, or analyzes with numerical-analysis software "Matlab2012", and compares data. The contents of numerical analysis are shown below.

Formulas

$$A=\frac{b2}{S}$$

$$w=\frac{1}{2}h\omega sin\omega t[m/s] \quad \cdots\cdot \quad (1)$$

$$\alpha = tan^{-1}\left(\frac{W}{s}\right)[rad] \quad \cdots\cdots \quad (2)$$

$$V = \sqrt{(u^2+w^2)}[m/s]$$

$$CL\alpha=\frac{\partial CL}{\partial \alpha}$$

$$K=\frac{1}{e\pi A}$$

$$CL = CL0 + CL\alpha\alpha$$

$$CD = CD0 + K\,CL2$$

$$L = \frac{1}{2}\rho V2SCL$$

$$D = \frac{1}{2}\rho V2SCD$$

$$Fv = L\sin\left(\frac{\pi}{2}-\alpha\right) + D\sin\alpha = L\cos\alpha + D\sin\alpha$$

$$Fh = L\cos\left(\frac{\pi}{2}-\alpha\right) - D\cos\alpha = L\sin\alpha - D\cos\alpha$$

$$ur = -\frac{1}{2}hr\,\omega sin\omega t\ [m/s]$$

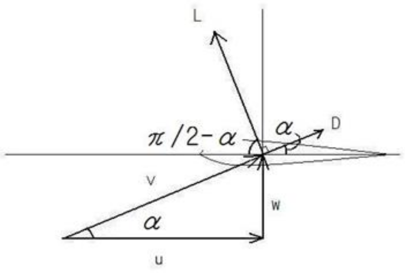

Fig.8 Wind velocities and forces

Numerical-analysis specifications
Assumption

In this analysis, the numerical values are employed those of the experimental model. The wings section is set to NACA652-415 and it is assumed that they consist semi- two-dimensional wings. As, and a wing area are shown below, suppose that it divides into five. The wing area is divided into five section and are supposed to move in lead-lag and flapping movements as shown in Fig.9 and Fig.10, respectively.

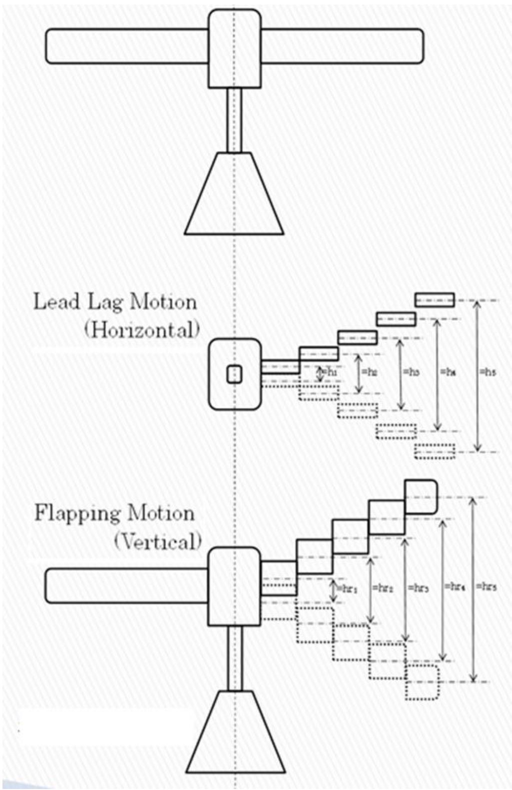

Fig.9 Division of wing elements

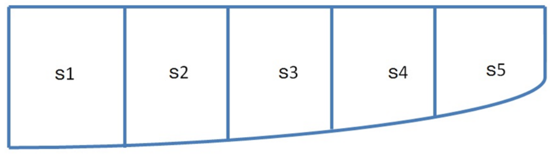

Fig.10 The five elements of the wings

$M = 2.6$ [kg]

$\rho = 1.177$ [kg/m3]

$S = 1.0$ [m2]

$b = 3.3$ [m]

$u = 6.5$ [m/s]

$h = 0.92$ [m]

$\omega = 4.8\pi$ [rad/s]

The induced drag is assumed to be not generated for simplification of analysis. The characteristic figure of the wings section of NACA652-415 is shown in Fig .11-12.

$CL\alpha = 6.09$

$CL0 = 0.3$

$CD0 = 0.04$

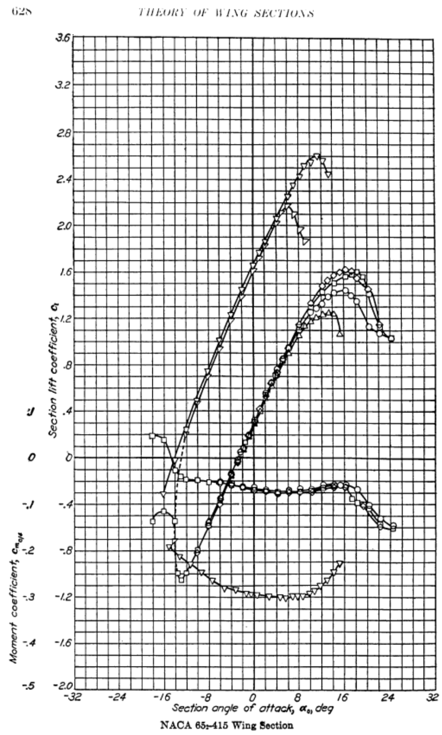

Fig.11 Lift-Drug Characteristics I

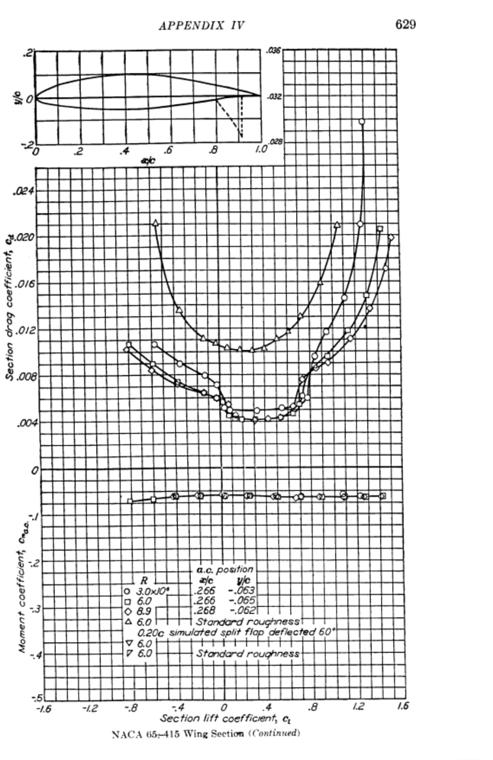

Fig.12 Lift-Drag Characteristics II

Flapping motion

Since the flapping motion is a only movement which makes wings only go up and down perpendicularly, flapping movement is descried as shown in the following equations from the formula (1) and (2), respectively.

$$w = 2.21\pi \, sin\,(4.8\pi t)\ [m/s] \quad \cdot\cdot\cdot\cdot (3)$$

$$\alpha = tan^{-1}[\frac{\{2.21\pi \, sin(4.8\pi t)\}}{6.5}]\ [rad] \quad \cdot\cdot\cdot\cdot (4)$$

Feathering motion

Feathering movement also changes the angle of attack α by changing the pitch angle of wings at the time of flapping movement. In order to make α small, β is changed with the value close to that of the angle of attack α.

$$\beta = \frac{-\pi}{4} sin\,(4.8\pi t)\ [rad] \quad \cdot\cdot\cdot\cdot (5)$$

The combination of the angle of attack, α and β, is set to the angle, $\alpha 2$.

$$\alpha 2 = \alpha + \beta = tan^{-1}[\frac{\{2.21\pi \, sin(4.8\pi t)\}}{6.5}] - \frac{1}{4} sin\,(4.8\pi t)\ [rad]$$

Each value is processed using these $\alpha 2$.

Lead lug motion

Lead-lag movement is the movement which makes wings get mixed up in a direction of movement, and *u* changes.

$hr = 0.28[m]$

$ur = -0.67\pi \, sin(4.8\pi t)\ [m/s]$

Let us note the velocity *u2*, as follows:

$u2 = u - ur = 6.5 + 1.2\pi \, sin(4.8\pi t)\ [m/s]$

Since *u* changes, α also changes. Setting α in that case to $\alpha 3$, we can obtain

$$\alpha 3 = tan^{-1}[\frac{\{2.21\pi \, sin(4.8\pi t)\}}{\{6.5 + 1.2\pi \, sin(4.8\pi t)\}}] - \frac{\pi}{4} sin\,(4.8\pi t)\ [rad]$$

Each numerical value is estimated using these $\alpha 3$.

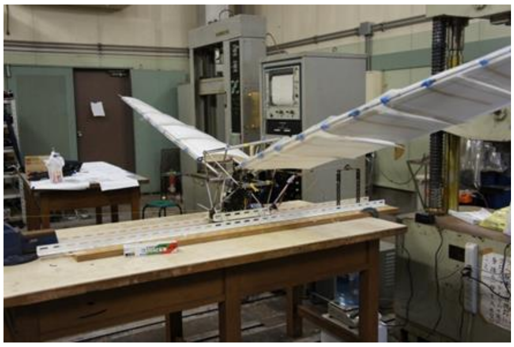

Fig.13 The thrust experiment I

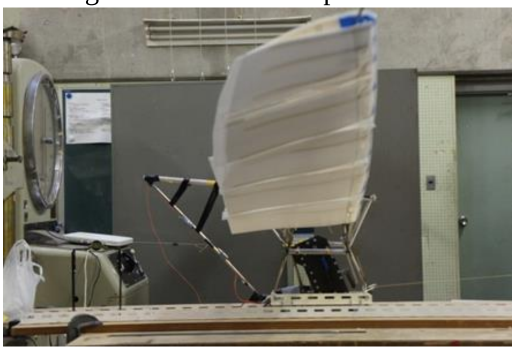

Fig.14 The thrust experiment II

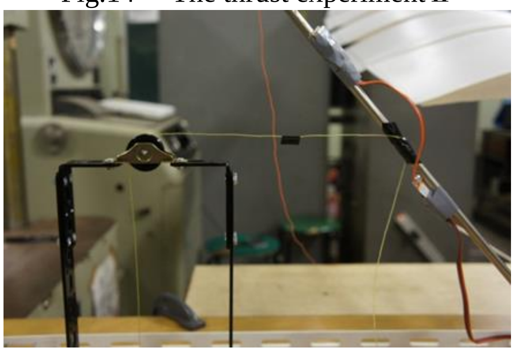

Fig.15 Pulley portion

Next, the lift is studied experimentally by hanging the body with a crane. The string is tied under the body being attached to the weight placed just under. The weight is placed on the electronic balance as in the case of the thrust experiment, the weight of the weight decrease lighter and the lift production is confirmed from this value if a lift occurs when the Ornithopter flutters.

Fig.16 The lift experiment

3.3 Experimental result

Thrust experiment

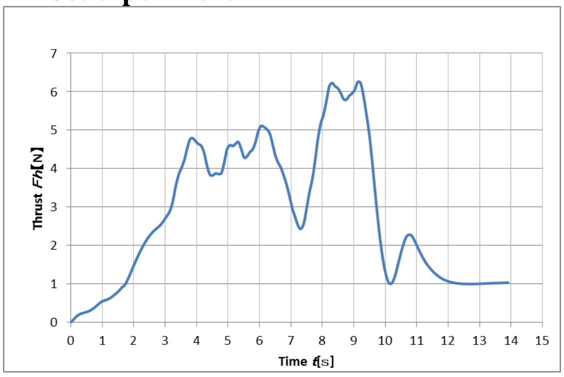

Fig.17 The time response of the thrust *Fh*

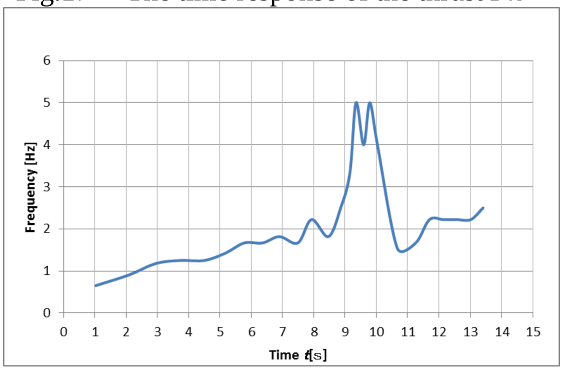

Fig.18 The time responce of the flapping frequency in the thrust experiment

Maximum thrust: 6.1N

Flapping frequency at the time of maximum thrust is as follows: When the flapping frequency exceeds 2.5Hz from 2.5Hz as shown in Figs.17-18, it turns out that the thrust has decreased. Analyzing the movie of the experiment, it turned out that flapping decrease smaller and the angle of attack increases larger (Figs. 19-20) where the flapping frequency is compared even with 2.5 Hz and was set to 5 Hz from 4 Hz.

Fig.19 The flapping amplitudes at the time of the flapping frequency of 2.5 Hz

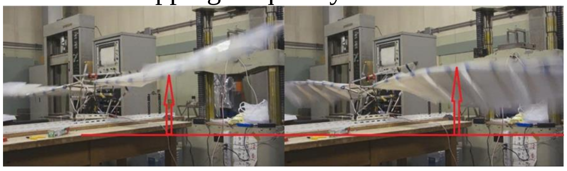

Fig.20 The flapping amplitudes at the time of the flapping frequency of 4 Hz

Numerical analysis is studied in order to verify whether the thrust obtained by the present experiment is appropriate. (Fig. 21)

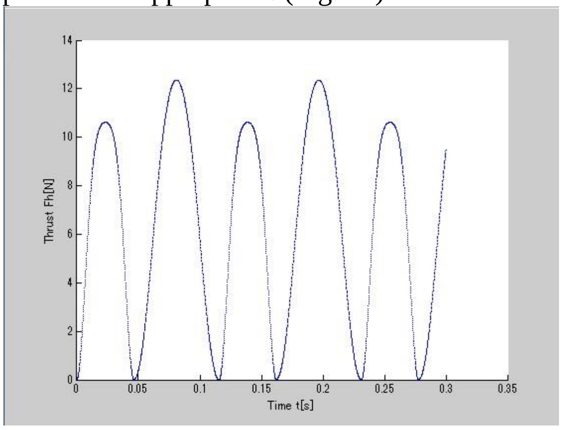

Fig.21 The numerical-analysis result of a thrust

The result of numerical analysis is shown in Fig. 13. In this analysis, flapping frequency is 2.4 Hz. As a result of numerical analysis, the thrust of about 12N is obtained.

Fig.22 Wing with the angle of attack in 2.5 Hz

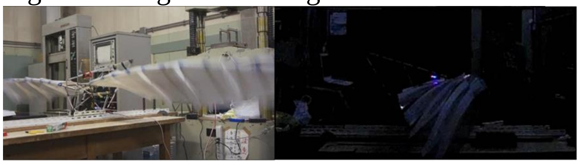

Fig.23 Wing with the angle of attack in 2.5 Hz

It is observed that there is a time period to strikes at least about 2.5 Hz with the wings type used as shown in Fig. 15, and the tip of the aerofoil stall in the angle of attack at the time of taking down. Moreover, when it comes to 5 Hz, most wings experience beyond the angle attack in stall.

Experiment for lift production

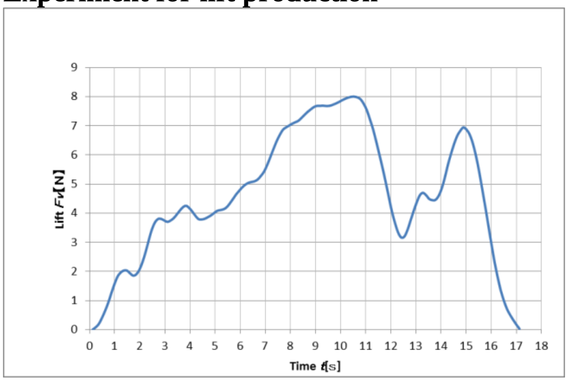

Fig.24 The time response of the lift *Fv*

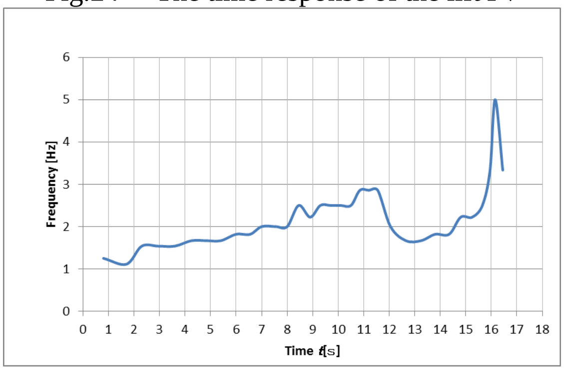

Fig.25 The time response of the frequency in a lift experiment

Maximum lifting capacity 8N

Also a result from which a lift falls is observed concerning to the lift if flapping frequency exceeds 2.5 Hz like a thrust experiment, Moreover, the result that the lift of 10N produced is assured in the numerical analysis. (Figs.26)

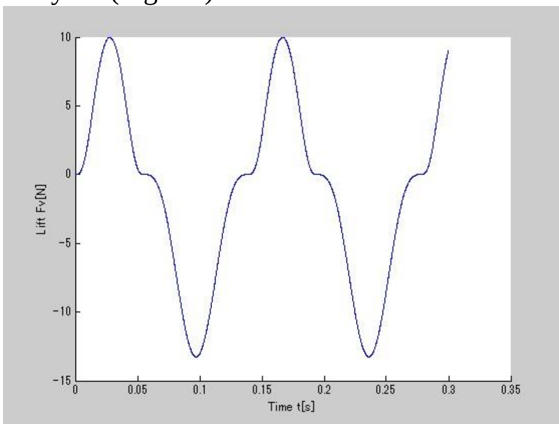

Fig.26 The numerical-analysis result of a lift

4. Conclusions

Result that lift and thrust decrease suddenly was observed when flapping frequency became larger than near 2.5 Hz in this experiment. This is considered to be the reason that the motion of a crank is not followed since the crank is too fragile in flapping of 2.5 Hz or more, but the flapping to decrease in the hardness of the present of wings. The experimental model's wing is too weak, because the angle of attack may approach to the stall angle of attack, when this wing becomes large flapping frequency. This is the reason to the experimental model is less than the numerical analysis results.

5. Recommendation

The rigidity of wings is necessary to be changed so that suitable flapping feathering can be performed also in still bigger flapping frequency. However, flapping and feathering motion decrease conversely in the case of low frequency when the rigidity is decrease and it is necessary to consider the structure with controllable rigidity of wings according to frequency. The generated thrust and lift in a present stage are not sufficient to fly the present body specification, the rigidity and flapping frequency of the optimal wings should be studied with the weight saving of the body.

References

[1] UTIAS Ornithopter No.1 – Wikipedia. http://ja.wikipedia.org/

[2] A. Azuma, Science of Model Airplane and Kite, pp.149-155, Denpa-Jikken-sya, (in Japanese.)

[3] J. Maglasang, N. Goto and K. Isogai, ”Development of Bird-like Micro Aerial Vehicle with Flapping and Feathering Wing Motions,” 'Trans. Japan Soc. Aero. Space Sci Vol. 51, No. 171, pp. 8-15, 2008.

[4] Dickinson, M. H. Lehmann, F. O. and Sane, S. P., “Wing Rotation and the Basis of Insect Flight,” Science, 284 (1999), pp. 1954-1960.

[5] Fujikawa, T., Sato,Y., Makata, Y., Yamashita, T., and Kikuchi, K., “Development of a Butterfly-Style Flapping Robot with Slider-Crank Mechanism Using Flexible Links (Mechanical Systems),” JSME Journal, C, 76(761), 151-157, 2010-01-25(in Japanese.).

[6] I. Inuzuka, T. Yamada, S. Yoshimura, “Multi-Objective Design of Flapping Wing Motion for Micro Air Vehicle (Fluids Engineering),” JSME Journal, B,75(754), 1215-1222, 2009-06-25. (In Japanese)

[7] R. Arita, and K. Ohba, “Experiment on the mechanism of mosquito's flapping flight using a realistic enlarged model of its wing : Effect of flapping motion on the lift and thrust characteristics,” JSME annual meeting 2007(6), 99-100, 2007-09-07 (in Japanese.).

[8] H. Nakai, M. Watanabe, and H. Tanaka, “Self-Excited Flapping Mechanism of Flexible Wings”, Proceedings of Movic Symposium, 2007(10), 27-32, 2007-08-08 (in Japanese.).

[9] K. Tsuyuki, and S. Sudo, “The Wing Structure and Flapping Behavior of Cicada,” JSME annual meeting 2003(5), 85-86, 2003-08-05 (in Japanese.).

[10] Jones. K. D. and Platzer, M. F., “An Experimental and
7
Numerical Investigation of Flapping-wing Propulsion,” AIAA Paper 99-0995, 1999.

[11] Smith, M. J. C., “Simulating Moth Wing Aerodynamics: Towards the Development of Flapping-wing Technology,” AIAA J., 34 (1996), pp. 1348-1355.

[12] Isogai, K., Shinmoto, Y. and Watanabe, Y. “Effects of Dynamic Stall on Propulsive Efficiency and Thrust of Flapping Wing,” AIAA J., 34 (1999), pp. 1145-1151.

[13] Nakazato, K., “Development of a Large Ornithopter with Span 3.3m,” The 23rd Aero-Aqua biomechanism Seminar, Keio University, Tokyo, 2009 March 23 (In Japanese),

[14] Nakazato, K., “Development of a Large Ornithopter with Span 3.3m,” The 23rd Aero-Aqua biomechanism Seminar, Keio University, Tokyo, 2009 March 23 (In Japanese)

[15] M. Takashi, H. Fujii, and K. Nakazato, “Aerodynamic Performance of Small Model of Ornithopter -Numerical Study for Experimental Model, AIAA 2011-6391, AIAA Guidance, Navigation, and Control Conference, 08 - 11 August 2011, Portland, Oregon.

Computational Design and Investigations of Closed-Loop, Active Flow Control Systems Based on Fluidic Devices, Improving a Performance of Wing High-Lift Systems

Wieńczysław Stalewski
Institute of Aviation
Al. Krakowska 110/114,
02-256 Warsaw, Poland
email: stal@ilot.edu.pl

Keywords: *CLC, active flow control, blowing-suction devices, wing high-lift system*

Abstract

The overall concept of Closed-Loop Control (CLC) system utilising fluidic devices for an active control of air flow on an aircraft wing has been presented. The main purpose of the system is to control autonomously the flow on the wing flap so as to protect it against strong separation and to improve this way the wing high-lift-system performance.

The developed concept of CLC-system is based on the row of nozzles located at the main-wing trailing edge. Air jets blown through the nozzles amplify stability of boundary layer on the flap protecting this way the flow against strong separation. The system works fully autonomously. This means that the air jets are activated automatically and only in such situations when there is the threat of strong flow separation on the flap.

When designing the CLC-system, several problems were solved, including design of the wing high-lift system, design of high-efficiency system of blowing mini-nozzles and development of the CLC-algorithm, which controls a fully autonomous work of the system.

The whole study was conducted using computational technique, and the results of the research were the base for development of the technology demonstrator tested in wind tunnel. Examples of CFD simulations using developed CLC algorithms have been presented.

1 Introduction

Advanced aeronautical-engineering design is increasingly based on the technology of smart structures, i.e. structures which are able to sense their environment, self-diagnose their condition and adapt in such a way so as to make the design more useful and efficient. One of the important directions of development of smart structures in the aeronautical engineering is their application to control the flow on the lifting surfaces of an aircraft. The research presented in this paper concerns this subject.

Considerable part of the presented study was conducted within the EU 7th FWP Project ESTERA, titled: Multi-level Embedded Closed-Loop Control System for Fluidic Active Flow Control Actuation Applied in High-Lift and High-Speed Aircraft Operations. Generally, the research aimed at development of the overall concept of Closed-Loop Control (CLC) system utilising fluidic devices for active control of the flow on the aircraft wing, so as to improve the wing-high-lift-system performance, especially to delay the flow separation on the wing flap and to increase the lift coefficient. The whole study was conducted using computational technique. The commercial U/RANS solver ANSYS FLUENT was applied as the computational-research tool.

The results of the research were the base for a development of the technology demonstrator, which was subsequently tested in a wind tunnel.

2 General Concept the CLC-System, Controlling the Flow on the High-Lift System of Aircraft Wing

The concept of the CLC-system controlling the flow around the wing high-lift system was developed based on series of CFD simulations. The general idea of the finally chosen concept is presented in Fig. 1. The CLC-system is designed to control the flow of air on the wing flap and to protect this flow against strong separation, which usually leads to a significant reduction of the lift force. The system should operate autonomously utilising the feedback between the flow actuators and sensors. The activity of the system is governed by the control unit, which receives and analyses signals from sensors and controls the activity of actuators. The sensors are placed on the upper surface of the flap. Generally they are the static pressure and wall shear sensors. Additional signals are received from environmental sensors that measure free-stream parameters, e.g. static and total pressure. Based on the signals received from sensors, the control unit controls the activity of actuators, which are the variable-mass-flow-rate valves and connected to them row of mini-nozzles located at a trailing edge of the main wing.

From a practical point of view, such a system would be applicable and useful, if air blown from the nozzles were able to prevent or eliminate a separation of flow on the flap. Such situation is shown in Figure 2, where the left drawing shows a flow separation on the flap (non-active blowing from the nozzles), while the right drawing shows the fully attached flow, which is the result of activation of blowing from the trailing-edge mini-nozzles.

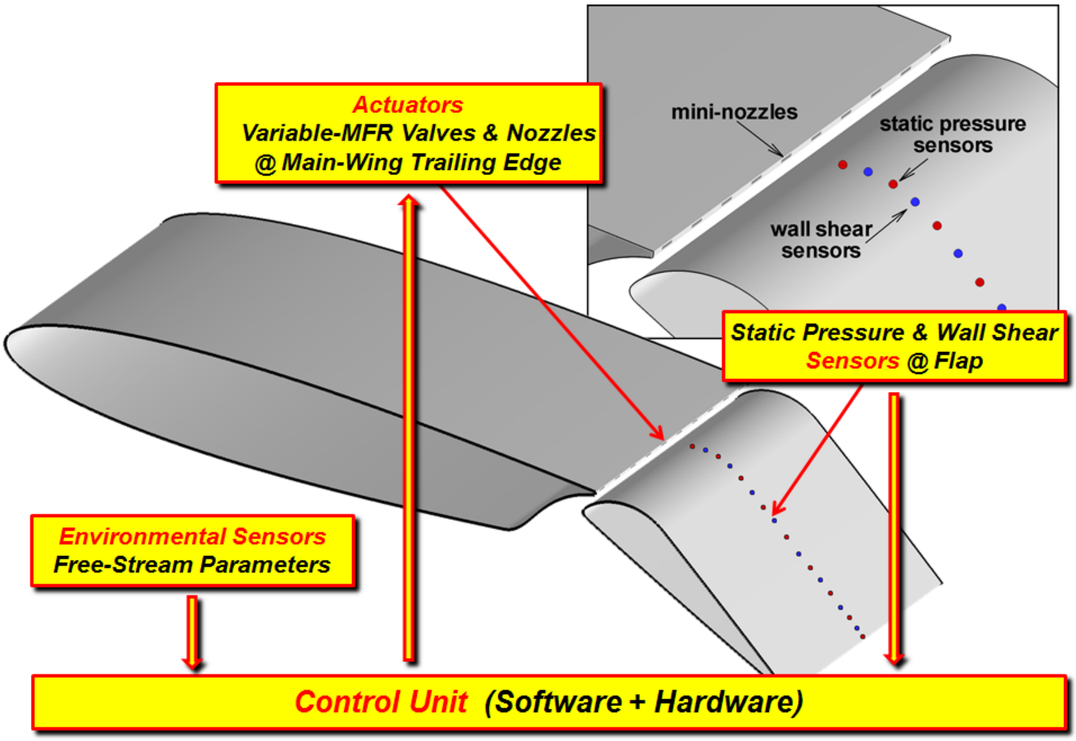

Fig. 1 General concept of developed CLC-system controlling the flow on the wing high-lift system.

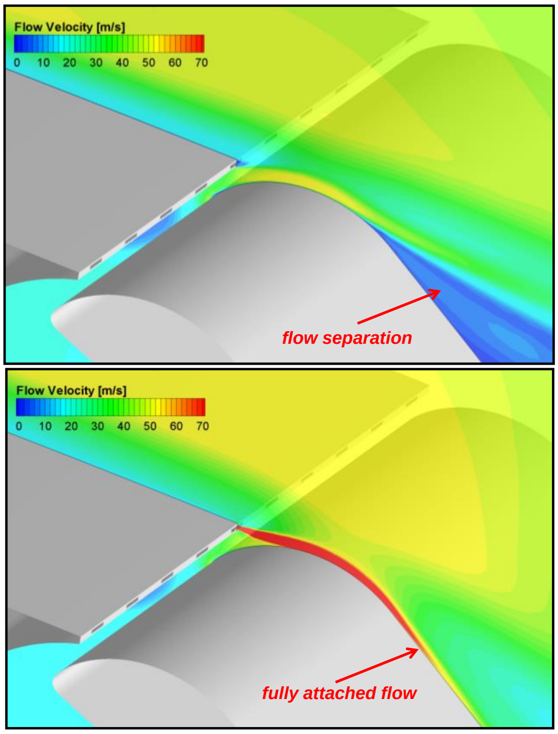

Fig. 2 System of mini-nozzles located at the trailing edge of main wing, controlling the flow on the flap. On the top: nozzles non-active, the flow separation on the flap. On the bottom: air-jets blown from the nozzles cause reattachment of flow on the flap.

A practical implementation of the presented CLC-system needed solving several problems, including:

- development of the wing high-lift system, supported by the system of mini-nozzles located at the trailing edge of the main wing
- optimal design of high-efficiency, feasible and reliable system of blowing mini-nozzles
- development of reliable and efficient algorithm controlling the autonomous work of the CLC-system

3 Aerodynamic Concept of the Wing High Lift System and Fluidic Devices Controlling the Flow on the Flap

Aerodynamic design and optimisation of the CLC-system was conducted for several airfoils equipped with typical high-lift devices. In the design process, aerodynamic properties of given high-lift system were evaluated using U/RANS solver ANSYS FLUENT, assuming steady or unsteady, compressible, viscous model of the flow with turbulence model k-ω, SST, Transitional Flows and fine computational grid ($y+ \approx 1$). In the design process, mainly 2D flow was analysed. However, for the most promising solutions, the 2.5D analyses were conducted, taking into account periodic slices of wing segment, with discrete spanwise distribution of nozzles. Such 2.5D configuration is presented in Fig. 2.

Examples of the designed high-lift systems supported by systems of mini-nozzles placed at the main-wing trailing edge are presented in Fig. 3 and Fig. 4.

Fig. 3 refers to the airfoil NACA0012 equipped with a single slotted flap. At the trailing edge of the main airfoil there is a mini-nozzle directed possibly optimally from the point of view of controlling the flow on the flap. At high deflections of the flap a strong flow separation appears on its upper surface, which is shown in upper-left drawing, in Fig. 3. After activation of sufficient-intensity air blowing from the nozzle, the flow reattached to the flap upper surface, which is shown in lower-left drawing. The flow reattachment caused considerable changes in pressure distribution on the airfoil (presented in right drawing in Fig. 3), which finally led to the increase of a lift coefficient from 1.98 (for separated flow) to 3.14 (for completely attached flow).

Similar phenomenon is presented in Fig. 4 which refers to the airfoil ILL115 (designed for high-speed small aircraft within EU Project CESAR) equipped with a Fowler flap. In this case the nozzle at the main-airfoil trailing edge was also directed possibly optimally from point of view of controlling the flow on the Fowler flap. Additionally special shaping of main-airfoil trailing edge was applied to utilise the Coanda effect, amplifying this way the increase of a lift coefficient after activating the blowing from the nozzle. In this case the lift coefficient rose from 2.72 for separated flow to 4.01 for fully attached flow.

Both presented examples of the design of high-lift-devices supported by fluidic devices show considerable increase of the lift coefficient after activating the blowing from the nozzles.

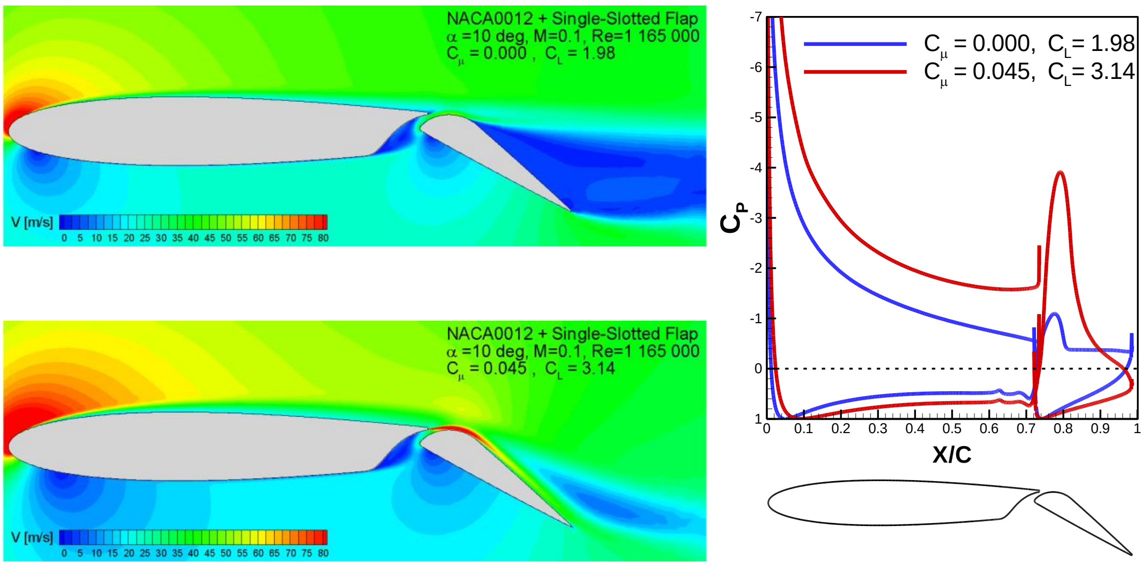

Fig. 3 Comparison of velocity-magnitude contours and pressure coefficient distribution for the airfoil NACA0012 with a single-slotted flap, for non-active (C_μ=0) and active (C_μ=0.045) jets blowing from mini-nozzles.

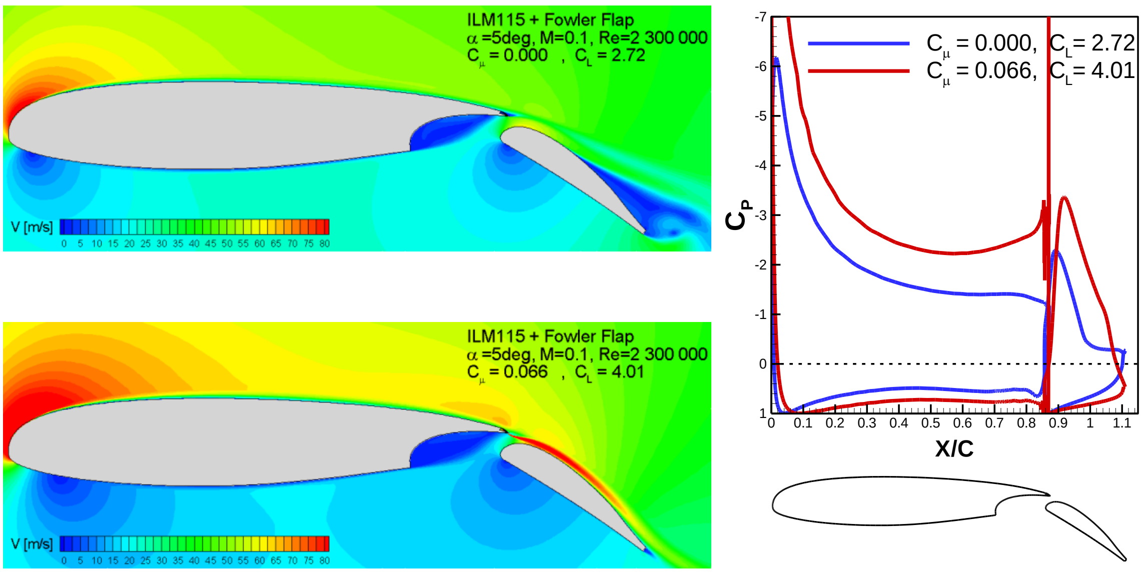

Fig. 4 Comparison of velocity-magnitude contours and pressure-coefficient distribution for the airfoil ILL115 with a Fowler flap, for non-active (C_μ=0) and active (C_μ=0.066) jets blowing from mini-nozzles.

Both solutions shown in Fig. 3 and Fig. 4 together with dedicated for them designed rows of main-wing-trailing-edge nozzles and CLC algorithms are the subject of pending patent claims.

Analysing carefully the pressure coefficient distributions presented in Fig. 3 and Fig. 4 one can formulate the general principle, telling that for separated flow on the flap, the pressure coefficient at the point located on the flap upper surface near the trailing edge is negative, while for fully attached flow on the flap this coefficient becomes positive. This applies, in principle, to all lifting surfaces where there is or there is no flow separation.

Based on this phenomenon a simple criterion of separation detection was formulated and implemented, which will be discussed in next sections.

4 Design and Optimisation of System of Mini-Nozzles Placed at the Trailing Edge of Main Wing

The development of a real CLC demonstrator designated for wind tunnel tests needed solving the design problem concerning 3D, feasible and reliable structure of mini-nozzles. The problem was solved using formerly developed methodology of parametric design and optimisation [1], [2].

It was assumed that the row of nozzles located at the trailing edge would consist of a system of triple mini-nozzles. Parametric model of such a structure was developed using the PARADES software [1], as it is shown in Fig. 5. The optimisation of this structure was conducted taking into account two objectives:

- minimisation of total pressure losses in the nozzle ducts
- uniform distribution of mass flow rate through all three ducts of the triple-nozzle

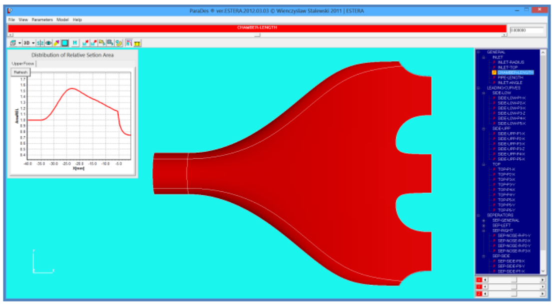

Fig. 5 The parametric 3D-model of the triple mini-nozzle.

5 CLC algorithm

The principal requirement concerning the CLC-system described in the Section 2 is that it should operate fully autonomously based on information received only from sensors monitoring the state of the flow on the wing surface and environmental sensors measuring free-stream static and total pressure. The blowing through the nozzles should be automatically activated when a threat of flow separation appears and deactivated when the flow can be fully attached naturally, without any support. The CLC algorithms discussed in this paper are based on simplified monitoring of the flow state on the flap. As it was mentioned in Section 2, one of the simplest criteria of flow separation on the flap is based on analysis of a sign of pressure coefficient C_{Pte} measured at the flap upper surface near the trailing edge. If $C_{Pte} \leq 0$ then it is likely that flow separation appears on the flap, otherwise the flow probably remains fully attached to the flap surface.

The general idea of the CLC algorithm based on the above separation criterion is presented in Figure 6. At the given moment of time t_0, the input data consist of: $\dot{m}(t_0), V_J(t_0)$ - current mass flow rate and jet-velocity of air blown through the nozzles, $P_{Ste}(t_0)$ - current static pressure measured by the sensor at the flap trailing edge, $P_{S\infty}(t_0)$, $P_{T\infty}(t_0)$ - free-stream static and total pressure. In the first step of the algorithm, the following dimensionless coefficients are calculated: $C_{Pte}(t_0)$ - pressure coefficient at the flap trailing edge, $C_\mu(t_0)$ - blowing momentum coefficient of air-jets blown from the nozzles. In the next step, a new value of blowing momentum coefficient is evaluated, generally based on the history of mutual dependencies between coefficients C_{Pte} and C_μ memorised until the time t_0. Evaluation of the new value of C_μ is realised by the function ***F***, definition of which is the fundamental problem needed solving to establish properly working CLC algorithm. In the final step, based on the new value of coefficient C_μ, the new value of required mass flow rate through the nozzles is evaluated.

The described CLC algorithm should be realised permanently during the aircraft flight. The crucial difficulty to properly define the function ***F*** is the detection of the moment when the blowing through the nozzles in unnecessary and should be stopped. This is because it is difficult to judge whether the fully attached flow on the flap is natural or is the result of supported it blowing air-jets.

The algorithms presented in this study cope with this problem based on the strategy of gradual reducing of the mass flow rate through the nozzles and continuous monitoring of the static pressure at the flap trailing edge. If the pressure is too low or when the pressure drop

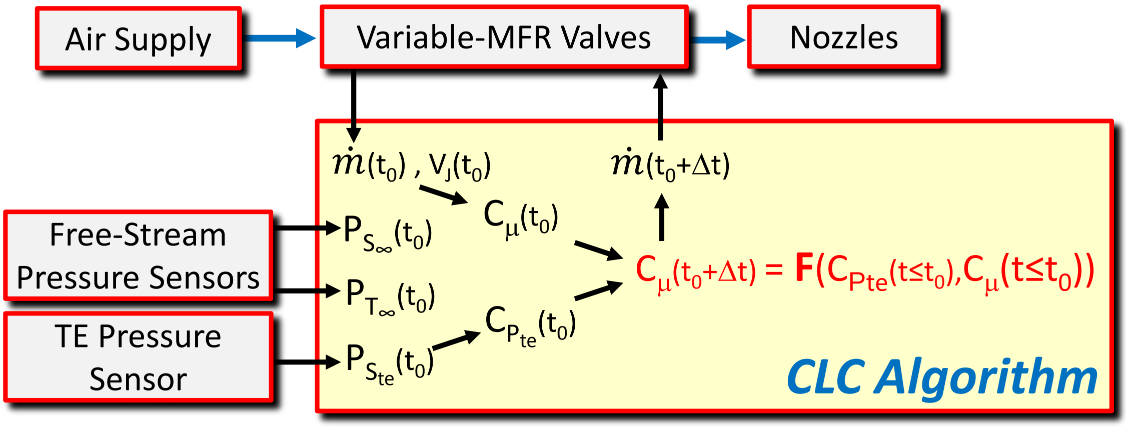

Fig. 6 The CLC algorithm investigated in presented study.

reaches too high speed, the reduction of mass flow rate is stopped, passing to the phase of fast increase of the mass flow rate of air blown through the nozzles.

6 CLC simulations

This section presents the examples of CFD simulations of simple CLC algorithms. The first of them was developed based on the function F defined as follows:

$$C_\mu(t_0+\Delta t) = \boldsymbol{F} = \begin{cases} \max(0\;, \; C_\mu(t_0) - D_m) \; if\colon \; C_{Pte}(t_0) > C_{P0} \\ \min(C_{\mu MAX}\;, \; C_\mu(t_0) + D_p) \; if\colon \; C_{Pte}(t_0) \le C_{P0} \end{cases} \quad (1)$$

where D_m and D_p are rates of blowing momentum coefficient, $C_{\mu MAX}$ is its upper limit and C_{P0} is a threshold of pressure coefficient indicating the flow separation. Fig. 7 shows the results of CFD simulation of flow around the airfoil NACA0012 with single-slotted flap. The deflection of flap was during first 5 seconds gradually increased from 0 to 35 degrees, during next 2 seconds was kept at level 35 degree and during next 5 seconds was decreased back to 0 degrees. The simulation of flow around the airfoil with a moving flap was conducted using unsteady model of flow and the *Dynamic Mesh* technique (deformable computational mesh) implemented in the FLUENT code. In Fig. 7 changes of the lift coefficient (C_L) as a function of time were compared for active and non-active CLC-system. Additionally, Fig. 7 presents time-variable: the flap-deflection angle (δ_{FL}) and blowing momentum coefficient (C_μ) of air blown through the nozzle when the CLC-system is active and it works according to the function ***F*** defined in Eq. (1). Fig. 7 shows, that for non-active CLC-system, when the deflection of flap reached 35 degrees, a flow separation appeared on the flap, leading to a decrease of the lift coefficient. The flow separation sustained until the deflection of flap was decreased to approximately 22.5 degrees, when the flow reattached itself to the flap upper surface. When the autonomous CLC-system was active, the same flow simulation had a different course.

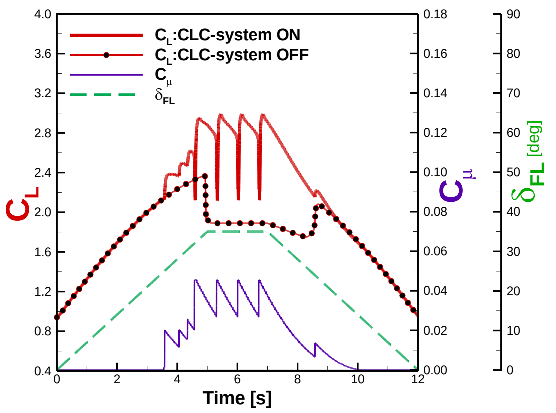

Fig. 7 Results of CFD simulation of work of the CLC-system controlling the flow on the single-slotted flap according to Eq.(1).

When the angle of a flap deflection was approaching to the critical 35 degrees, the blowing through the nozzle was automatically activated ($C_\mu > 0$), protecting the flow against strong separation and additionally leading to a significant increase of the lift coefficient. Such a state of the flow remained nearly all the time, when the threat of strong separation existed. However, the algorithm controlling the CLC-system according to the function ***F*** defined in Eq.(1), was testing cyclically the flow and was trying to judge whether the blowing through the nozzle was necessary, to keep the flow fully attached to the flap surface. During these tests, a momentary flow separation cyclically appeared which is shown in Figure 7 as momentary losses of the lift coefficient. In such situations the CLC-system rapidly enhanced the blowing through the nozzle, causing immediate reattachment of flow and increase of the lift coefficient. In the end, when the deflection of the flap was sufficiently small, the blowing through the nozzle was completely stopped by the CLC-system.

It must be underlined that the described above momentary losses of lift coefficient in real 3D realization of the CLC-system will not affect strongly the total lift coefficient of the whole wing or aircraft. It is assumed, that the presented above CLC algorithm, in real 3D case will be conducted only in a relatively thin test-section of the wing. In the rest of the flap-zone of the wing, the blowing from the nozzles will not be decreased, till in the test-section the flow on the flap is stable and completely attached. This way the fluctuations of the total lift coefficient of the whole wing or aircraft should not be significant.

To mitigate the presented in Fig. 7 momentary losses of the lift coefficient, the CLC algorithm should be sensitive not only with regard of current values of C_{Pte} but also with regard of speed of decrease of C_{Pte} when decreasing gradually the blowing momentum coefficient C_μ of air-jet blown from the nozzle. Therefore the additional criterion of the assessment, whether the blowing momentum coefficient should be increased or decreased could be based on a value of derivative dC_{Pte}/dC_μ evaluated only when the C_μ drops down. High value of the derivative would indicate a necessity of fast increase of C_μ, to avoid strong flow separation on the flap. This additional criterion, supplementing the algorithm defined by Eq. (1) may be formulated as follows:

$$C_\mu(t_0+\Delta t) = \boldsymbol{F} = \min(\,C_{\mu MAX}\,, C_\mu(t_0) + D_p) \\ if:\ \frac{dC_{Pte}}{dC_\mu}(t_0) > \Delta_{Pte} \quad for\ \ C_\mu \downarrow \qquad (2)$$

where Δ_{Pte} is the assumed constraint of the derivative dC_{Pte}/dC_μ. When assessing this derivative it is important to take into consideration possible high-frequency fluctuations of C_{Pte} and C_μ. Therefore the dC_{Pte}/dC_μ should be evaluated rather based on smooth approximation of functions C_{Pte}=$C_{Pte}(t)$ and C_μ=$C_\mu(t)$ than based on raw measured data.

Results of the CLC simulation based on the algorithm defined by Eq. (1) and (2) are presented in Fig. 8. Comparing Fig. 7 and Fig.8 one may conclude, that in fact, taking into account the additional criterion defined by Eq.(2) some mitigation of unfavourable momentary losses of the lift coefficient may be achieved.

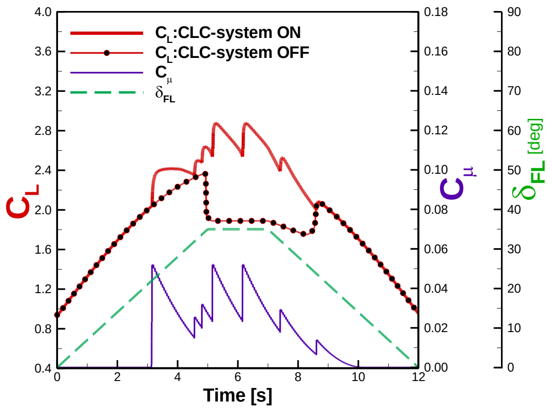

Fig. 8 Results of the CFD simulation of work of the CLC-system controlling the flow on the single-slotted flap according to Eq. (1) and (2).

7 Conclusions

The presented study aimed at answering the question whether the fluidic devices could be useful in fully-autonomous smart systems controlling the flow on aircraft lifting surfaces and wing high-lift devices. After giving an affirmative answer to this question, the main purpose of the research was to develop the overall concept of Closed-Loop Control system utilising fluidic devices for an active control of the flow on the aircraft wing, so as to improve its high-lift-system performance. The whole study was conducted using computational technique, and the results of the research were the base for development of the technology demonstrator which was investigated in a wind tunnel.

The developed concept of the CLC-system is based on the row of nozzles located at the main-wing trailing edge. Air jets blown through the nozzles are directed so as to amplify stability of boundary layer on the flap and this way to prevent a strong separation of the flow. The CLC-system works fully autonomously. This means that the air-jets are activated automatically and only in such situations when there is the threat of strong flow separation on the flap.

When designing the CLC-system, the several problems were solved, including design of the wing high-lift system, design of high-efficiency system of blowing mini-nozzles and development of the CLC-algorithm, which controls a fully autonomous work of the system.

Presented examples of 2D CFD simulations of simple CLC fluidic systems define direction for the development of this technology and offer hope for its practical use in future aircrafts.

Symbols and Abbreviations

CLC - closed loop control
C - wing/airfoil chord
C_L - lift coefficient
C_P - pressure coefficient
C_{Pte} - pressure coefficient measured at the flap trailing edge
C_{P0} - threshold of pressure coefficient C_{Pte} indicating the flow separation on the flap
C_μ - blowing momentum coefficient of air-jets blown from the nozzle(s)

$$C_\mu = \frac{\dot{m} \cdot V_J}{C \cdot q_\infty}$$

D_m, D_p - rates of blowing momentum coefficient
F - function defining CLC algorithm (see Fig. 6)
M - Mach number
q_∞ - free-stream dynamic pressure
$\dot{m}$ - mass flow rate of jet blown from the nozzle
$P_{S\infty}$ - free-stream static pressure
$P_{T\infty}$ - free-stream total pressure
Re - Reynolds number
t - time
V_J - velocity of jet blown from the nozzle
α - angle of attack
δ_{FL} - deflection angle of the wing flap
Δ_{Pte} - constraint of derivative dC_{Pte}/dC_μ

References

[1] Stalewski W., "Parametric Modelling of Aerodynamic Objects - The Key to Successful Design and Optimisation", *Aerotecnica Missili e Spazio. Italian Association of Aeronautics and Astronautics (AIDAA).* No.1/2,March-June 2012,pp.23-31.

[2] Stalewski W., Żółtak J., "Optimisation of the Helicopter Fuselage with Simulation of Main and Tail Rotor Influence", *Proceedings of the 28th ICAS Congress of the International Council of the Aeronautical Sciences*, Brisbane, Australia, 2012.

Acknowledgement

The research leading to these results has received funding from the European Union's Seventh Framework Programme (FP7/2007-2013) for the Clean Sky Joint Technology Initiative under grant agreement no. CSJU-GAM-SFWA-2008-001.

Experimental aircraft system identification from flight data: Procedures and Results

A. Fedele, N. Genito, A. Vitale and L. Garbarino
Italian Aerospace Research Centre (CIRA), Italy

Keywords: *Identification, aerodynamic derivatives, flight data.*

Abstract

This paper presents the results obtained by system identification from flight data of an experimental ultra-light aircraft called FLARE (Flying Laboratory for Aeronautical Research).

After a brief introduction, the description of the experimental ultra-light aircraft subjected to the identification process is provided. Then the simulation model, identified during the present activity, is introduced and the identification procedure and methodology adopted are explained. Finally the results obtained are presented followed by discussions and conclusions.

The identified vehicle model, obtained at the end of the activity here presented, was used to design a flight control system that successfully performed many autonomous take-off and landings.

The present work was carried out in the framework of the Italian funded project TECVOL, executed by the Italian Aerospace Research Centre (CIRA), with the aim of developing innovative technologies for flight autonomy and collision avoidance.

1 Introduction

Automatic take-off and landing system design requires high level of fidelity of simulation model. In fact to properly design a flight control system an accurate aircraft model is necessary.

Fidelity of vehicle simulation models depends to a large extent on the accuracy of the aero-dynamic database representing the aircraft.

In the majority of the cases an aerodynamic database derived from analytical predictions, wind tunnel measurements on a scaled model or extrapolation of existing data from similar configurations is incorporated.

Such a priori aerodynamic databases, although valid over the entire flight envelope, are often associated with certain limitations of validity arising from, for example, model scaling, Reynolds number, dynamic derivative, and cross coupling effects.

System identification methodology, evolved over the past decades, provides a powerful and sophisticated tool to identify from flight data aerodynamic characteristics valid over the entire operational flight envelope.

For conventionally stable flight vehicles, the most commonly and widely applied parameter estimation methods are regression analysis and output error method [1].

Regression analysis is based on linear models for the aerodynamic phenomena and requires error-free and compatible measurements.

The output error method is applicable to general nonlinear systems and accounts for measurement noise.

Parameter estimation needs to be followed by a step called model validation to asses model fidelity.

This paper presents an application of the output error method to an experimental ultra-light aircraft followed by a validation of the identified model.

2 Vehicle description

The technologies developed in the CIRA TECVOL project are deployed by means of a flying test bed consisting of a piloted aircraft equipped with On-Board Avionics System and On-Ground Control Station designed and integrated by CIRA. It is able to allow experimentation about autonomous take-off and landing, mission automation and detect, sense & avoid. The flying platform, called FLARE (Flying Laboratory for Aeronautical Research) and shown in Fig. 1, is an experimental ultra-light aircraft with designed empty weight of 281 Kg, max take-off weight of 450 Kg, max speed s/l about 218 km/h, cruising speed about 190 km/h, wing area of 13.2 m^2, wing span of 9.6 m and maximum engine power of 100 hp.

The vehicle's aerodynamic effectors are elevator, ailerons and rudder, for longitudinal, lateral and directional control, respectively. Moreover a plain flap is used to increase lift during take-off and landing. Wind tunnel tests and semi-empirical methods were used to compute a pre-flight aerodynamic model, which was the most reliable information on the vehicle aerodynamics before performing system identification from flight data. It is worthy to note that the pre-flight aerodynamic model and the one estimated from flight data have the same structure.

On board Avionics System includes all devices needed to perform the in-flight experimental validation of advanced guidance, navigation and control functionalities. The devices were selected among the Commercial-Off-The-Shelf (COTS) ones, and they include: the Flight Control Computer (FCC), the navigation sensor suite, a radar device, the digital electromechanical servos, and a digital bidirectional data link.

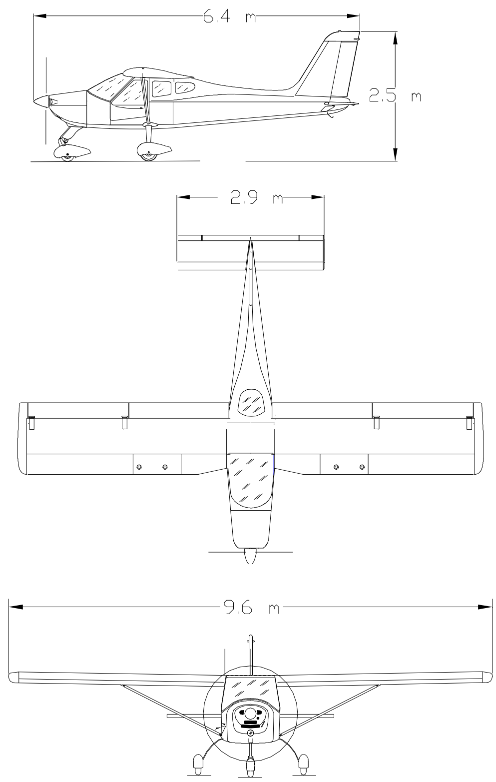

Fig. 1 Aircraft 3-view.

The FCC is an embedded real-time computer based on a PowerPC processor, provided by the supplier with a tool based on the most advanced control system rapid prototyping methodologies. This software environment enables the automatic coding of the real-time software directly from MATLAB/SIMULINK™ diagrams, thus being extremely efficient from data acquisition and algorithm in-flight testing point of view.

The Navigation sensor suite includes:

- Two differential GPS, one in code differential mode and one in RTK (Real-Time Kinematic) L1/L2 mode, capable to provide position measurements with an accuracy of few centimeters

- Solid state Attitude Heading Reference System (AHRS), used to measure body axis accelerations, Euler angles and angular rates
- Two dedicated sensors for height above ground level measurements, respectively using radar and laser technology (only one altimeter sensor can be mounted because of weight limitations)
- Air Data Computer (ADC) with a dedicated air data probe capable to provide Indicated Air Speed (IAS), True Air Speed (TAS), barometric pressure, aerodynamic angles.

A radar device is installed on the top of the plane, in order to detect other planes presence.

The digital electromechanical servos are used to command both aerodynamic surfaces and throttle, driven by the FCC.

Finally the digital bidirectional data link system allows exchanging data between on board FCC and the Ground Control Station (GCS) with a maximum bit-rate of 9.600 bit/sec in uplink and 115.200 bit/sec in downlink up to about 6 Km of operative range.

The GCS is installed in a big shelter fixed on the ground near the runway. It is designed to show telemetry data and to present it to the flight test engineers through dedicated Human Machine Interfaces (HMI). It can be used also for remote reconfiguration of the on board avionics system. Its main features are:

- Bidirectional data link with a range of about 6 Km
- GPS Base Station used to send the differential correction to the on board GPS
- Meteorological station
- Virtual Cockpit HMI
- Engineering HMI
- Automatic Collision Avoidance HMI.

3 Vehicle model

The vehicle model is a six degree of freedom non-linear model. This model is composed of the aircraft dynamic equations, the aerodynamic model and the thrust model.

The aircraft dynamic equations in body axes, assuming that the thrust T is aligned to the vehicle longitudinal X-axis and that the inertia products I_{xy}, I_{yz} are equal to zero because x-z plane is a plane of symmetry for the aircraft, are described in the following equations [2]:

$$\begin{cases} m\left(\dot{V}_x + qV_z - rV_y\right) = W_x - D\cos\alpha + L sen\alpha + T \\ m\left(\dot{V}_y + rV_x - pV_z\right) = W_y + Y \\ m\left(\dot{V}_z + pV_y - qV_x\right) = W_z - D sen\alpha - L\cos\alpha \\ \dot{p} I_x + qr\left(I_z - I_y\right) - \left(\dot{r} + pq\right) I_{xz} = l \\ \dot{q} I_y + pr\left(I_x - I_z\right) - \left(r^2 - p^2\right) I_{xz} = m \\ \dot{r} I_z + qp\left(I_y - I_x\right) - \left(\dot{p} - rq\right) I_{xz} = n \end{cases} \tag{1}$$

Where *L*, *D*, *Y* are lift, drag and lateral force; *l*, *m*, *n* are rolling, pitching and yawing moment in the body reference system; *p*, *q*, *r* are Euler angular rates; I_x, I_y, I_z, I_{xz} are inertia moments and products; *m* is vehicle's mass, *V* is vehicle's inertial velocity, *W* is weight force, *T* is thrust and α is angle of attack.

These equations contain the aerodynamic coefficients, that are evaluated in the aerodynamic model using the following equations:

$$\begin{aligned} C_L = {} & C_{L0} + C_{L0F}\delta_F + \left(C_{L\alpha} + C_{L\alpha F}\delta_F\right)\alpha + \\ & + \left(C_{L\dot{\alpha}} + C_{L\dot{\alpha}F}\delta_F\right)\frac{\dot{\alpha} c}{2V_{TAS}} + \left(C_{Lq} + C_{LqF}\delta_F\right)\frac{q c}{2V_{TAS}} + \\ & + \left(C_{L\delta s} + C_{L\delta s F}\delta_F\right)\delta_s \end{aligned} \tag{2}$$

$$\begin{aligned} C_D = {} & C_{D0} + C_{D0F}\delta_F + (K_D + K_{DF}\delta_F)\left[C_{L0} + \right. \\ & \left. + C_{L0F}\delta_F + \left(C_{L\alpha} + C_{L\alpha F}\delta_F\right)\alpha\right]^2 \end{aligned} \tag{3}$$

$$\begin{aligned} C_Y = {} & \left(C_{Y\beta} + C_{Y\beta F}\delta_F - C_D\right)\beta + \\ & + \left(C_{Yp} + C_{YpF}\delta_F\right)\frac{pb}{2V_{TAS}} + \left(C_{Yr} + C_{Y_r F}\delta_F\right)\frac{rb}{2V_{TAS}} + \\ & + \left(C_{Y\delta_R} + C_{Y\delta_R F}\delta_F\right)\delta_R \end{aligned} \tag{4}$$

$$C_l = C_{l0} + \left(C_{l\beta} + C_{l\beta F}\delta_F\right)\beta + \left(C_{lp} + C_{lpF}\delta_F\right)\frac{pb}{2V_{TAS}} + \\ +\left(C_{lr} + C_{lrF}\delta_F\right)\frac{rb}{2V_{TAS}} + \left(C_{l\delta_A} + C_{l\delta_A F}\delta_F\right)\delta_A + \\ +\left(C_{l\delta_R} + C_{l\delta_R F}\delta_F\right)\delta_R \tag{5}$$

$$C_m = C_{m0} + C_{m0F}\delta_F + \left(C_{m\alpha} + C_{m\alpha F}\delta_F\right)\alpha + \\ +\left(C_{m\dot{\alpha}} + C_{m\dot{\alpha}F}\delta_F\right)\frac{\dot{\alpha}c}{2V_{TAS}} + \left(C_{mq} + C_{mqF}\delta_F\right)\frac{qc}{2V_{TAS}} + \\ +\left(C_{m\delta_E} + C_{m\delta_E F}\delta_F\right)\delta_E \tag{6}$$

$$C_n = C_{n0} + \left(C_{n\beta} + C_{n\beta F}\delta_F\right)\beta + \left(C_{np} + C_{npF}\delta_F\right)\frac{pb}{2V_{TAS}} + \\ +\left(C_{nr} + C_{nrF}\delta_F\right)\frac{rb}{2V_{TAS}} + \left(C_{n\delta_A} + C_{n\delta_A F}\delta_F\right)\delta_A + \\ +\left(C_{n\delta_R} + C_{n\delta_R F}\delta_F\right)\delta_R \tag{7}$$

Where C_L, C_D, C_Y are non-dimensional lift, drag and lateral force coefficients, respectively; C_l, C_m, C_n are rolling, pitching and yawing non-dimensional moment coefficients; β is angle of sideslip, V_{TAS} is true air speed velocity, c is the mean aerodynamic chord, b is the wing span, δ_E is elevator deflection, δ_A is ailerons deflection and δ_R is rudder deflection. All the other symbols on the right side of equations above represent classical aerodynamic derivatives, which are the unknowns parts of the coefficients that we want to identify.

The aerodynamic coefficients depend also on flap position. This dependence is linearly modelled through the non-dimensional coefficient δ_F which varies between 0 (no flap deflection) and 1 (maximum flap deflection, 36 degrees). Each aerodynamic derivative is composed of the contribution without flap and the flap contribution (denoted by subscript $_F$). Both configurations, with and without flap deflection, are identified from flight data.

The model of the thrust is based on the Renard's formula:

$$T = C_T(\gamma)\rho D_p^4\left(\frac{\omega_p}{2\pi}\right)^2 \tag{8}$$

Where T is thrust, γ is advance ratio, ρ is density, D_p is propeller's diameter, ω_p is propeller's angular velocity and C_T is trust coefficient that is a parameter we want to estimate.

4 Aircraft model identification procedure

Purpose of this activity was the estimation of the six degree of freedom non-linear model of an experimental ultra-light aircraft called FLARE. The unknowns parameters of this model were the aerodynamic and thrust coefficients. The estimation of these parameters was divided in the following steps.

Before performing the identification, the navigation suite was calibrated in order to reduce measurements errors. Particular attention has been paid to Air Data System, which needs to be calibrated using GPS and AHRS data, to correct errors caused by the influence of vehicle's aerodynamic on the data collected in the proximity of the vehicle by the probe [3]. In particular flight test were carried out to correct the following measures:

- Angle of Attack
- Angle of Sideslip
- Indicated Air Speed.

Then a first estimation of the vehicle aerodynamic static parameters were evaluated performing different flight tests to collect equilibrium data during a steady descent flight with zero thrust. In fact in this conditions it is possible to evaluate lift and drag coefficients for different values of angle of attack and flap configurations. With these information a more accurate estimation of lift and drag coefficients using linear regression were obtained and updated in the aerodynamic database.

Next step was the estimation of the thrust coefficient with a series of steady state level flight tests. The estimated curve was obtained preserving the $C_T(\gamma)$ nominal shape, while fitting (in the least square sense) the experimental data.

At that point it was possible to identify the aerodynamic coefficients using an identification methodology with specified designed flight tests. At that purpose a linear decoupled model was used and the results obtained were validated using the non-linear model. The following section provides more details on this last estimation step.

5 Aerodynamic Model Identification methodology

Purpose of system identification is to estimate the vector of unknown parameters (in this case the aerodynamic derivatives), denoted with Θ, starting from the measurements of system output *z* and input *u,* knowing the structure of system's model. The measured system output *z* is affected by additive measurement noise *v*:

$$z(t_k)=y(t_k)+Gv(t_k) \qquad with\ k=1,\dots,N \tag{9}$$

where t_k is the discrete time index and G is the measurement noise distribution matrix.

An output error method [4] was used to perform system identification, in which model parameters are adjusted iteratively to minimize the error between the measured variables z (system output) and the estimated $\hat{y}$ (model predicted) responses.

The method is based on the Maximum Likelihood estimation principle, which permits to obtain the stability and control derivatives estimation by minimization of a cost function, called likelihood function. In the hypotheses of Gaussian measurement noise and known measurement error covariance matrix R, the likelihood function has the following form:

$$L(\Theta)=\left[(2\pi)^m|R(k)|\right]^{\frac{N}{2}} * \exp\left\{-\frac{1}{2}\sum_{k=1}^{N}[z(k)-\hat{y}(k)]^T R^{-1}(k)[z(k)-\hat{y}(k)]\right\} \tag{10}$$

The maximization of the likelihood function is equivalent to minimize its negative logarithm. Therefore the following cost function is introduced

$$J(\Theta)=\frac{1}{2}\sum_{k=1}^{N}[z(t_k)-\hat{y}(t_k)]^T R^{-1}[z(t_k)-\hat{y}(t_k)] \tag{11}$$

Since there isn't closed form analytical solution for the above optimization problem, numerical methods for minimization of the cost function are used. The Levenberg-Marquard optimization procedure is applied in this paper, using for initial values the aerodynamic derivatives taken from the pre-flight aerodynamic database. The Flow-chart of identification process is shown in Fig. 2.

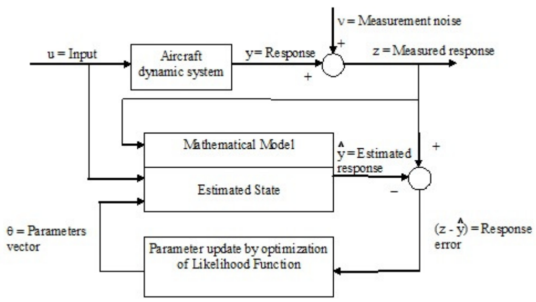

Fig. 2 Flow-chart of identification process.

The mathematical model used to predict the estimated responses is a six degree of freedom decoupled linear model.

In fact, in the hypothesis of symmetric aircraft about its longitudinal plane and assuming to fly at small sideslip angle, we can use the simplification of uncoupled and linearized longitudinal and lateral-directional dynamic equations. Then, the longitudinal dynamic behavior of the vehicle is described by the following equations:

$$\begin{aligned}\dot{X}_{lon} &= A_{lon}X_{lon} + B_{lon}U_{lon}\\ Y_{lon} &= X_{lon}\end{aligned} \tag{12}$$

where:

- A_{lon} and B_{lon} are the dynamic matrix of longitudinal linear model which contains the unknown parameters
- X_{lon} is the longitudinal state vector composed by true air speed velocity, angle of attack, pitch angle and pitch rate
- U_{lon} is the longitudinal input vector composed by elevator deflection and throttle command.

The lateral-directional dynamic behavior of the vehicle is described by the following equations:

$$\begin{aligned} \dot{X}_{lat} &= A_{lat} X_{lat} + B_{lat} U_{lat} \\ Y_{lat} &= X_{lat} \end{aligned} \tag{13}$$

where:

- A_{lat} and B_{lat} are the dynamic matrix of lateral-directional linear model which contains the unknown parameters
- X_{lat} is the lateral-directional state vector composed by angle of sideslip, roll rate, yaw rate and roll angle
- U_{lat} is the lateral-directional input vector composed by ailerons and rudder deflections.

In order to reduce unknown parameters' number and to get a better estimation, the following relations between lift and pitching moment derivatives were introduced:

$$C_{L\delta s} = -C_{m\delta s} \frac{c}{l_t} \tag{14}$$

$$C_{Lq} = -C_{mq} \frac{c}{l_t} \tag{15}$$

$$C_{L\dot{\alpha}} = -C_{m\dot{\alpha}} \frac{c}{l_t} \tag{16}$$

where l_t is the distance between vehicle gravity centre and horizontal tail aerodynamic centre.

The linear model was used because this representation is useful for the design of the flight control system and because the results obtained with this model could be extended to the non-linear model if correctly validated.

6 Results and discussion

At the beginning of system identification activity the vehicle static parameters were evaluated to improve the aerodynamic database accuracy. The results are presented in Table 1.

Table 1 Estimated aerodynamic static parameters.

Parameter	Flap = 0°	Variation with flap = 36°
K_D	0.068	0.012
$C_{L\alpha}$	4.35	0
C_{D0}	0.073	0.030
C_{L0}	0.30	0.35

Then the nominal thrust coefficient curve $C_T(\gamma)$, provided by the producer of the propeller, was validated using experimental data gathered in dedicated flight tests. Since the nominal curve was shifted with respect to experimental C_T values, it was corrected performing estimation from flight data.

Nominal and estimated thrust coefficients are presented in Fig. 3, together with the experimental data.

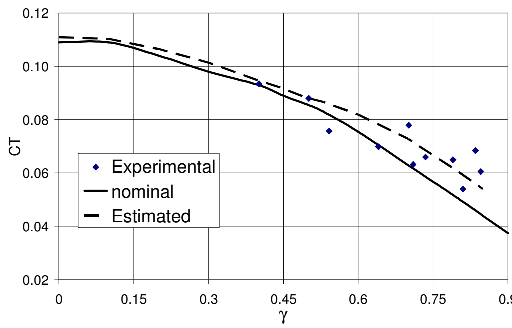

Fig. 3 Nominal and identified thrust coefficient.

The difference between nominal and estimated curves is always lower than 20% and increases with respect to the advance ratio. It is worthy to note that error on thrust coefficient estimation could have relevant effect only on the aerodynamic drag coefficient estimation, because the thrust is aligned to the vehicle longitudinal axis and the angle of attack experimented in flight is always small.

At that point the estimation of the aerodynamic derivatives, using the output error method based on the Maximum Likelihood estimation principle, was carried out.

Flight test manoeuvres were designed and performed in order to excite separately the aircraft longitudinal and lateral-directional modes. At that purpose two series of flight test were held. In the first series an elevator manoeuvre was selected as input to excite only the longitudinal mode. In the second series ailerons and rudder manoeuvres were used instead to excite only the lateral-directional mode. In both cases, the manoeuvres were performed with and without flap deflection. The types of manoeuvres that have been selected in both cases were the doublet and the 3-2-1-1. The intensity and step period of these manoeuvres were optimized through numerical simulations using the model based on a priori aircraft derivative data set.

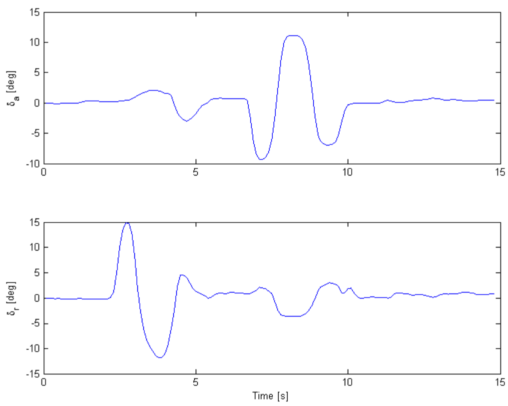

Fig. 4 Ailerons and rudder doublet manoeuvres held in flight in manual mode.

In Fig. 4 an example of ailerons and rudder doublet manoeuvres held in flight in manual mode is shown.

In order to perform system identification flight measurements of acceleration, velocity, height above ground level, angular rates, attitude, aerodynamic effectors and aerodynamic angles were collected at the sampling rate of 10 Hz.

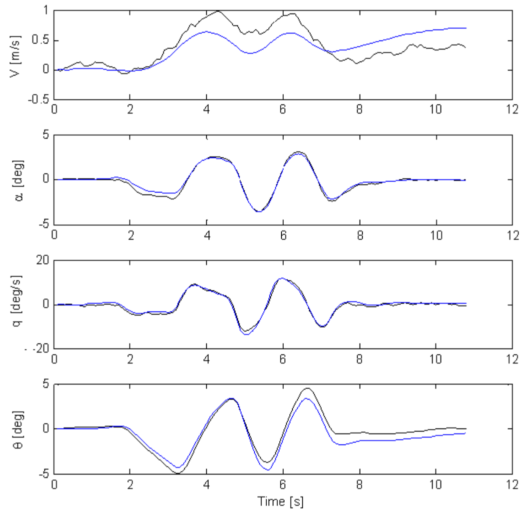

Fig. 5 Measured output and identified model output time histories match with a 3-2-1-1 stabilator manoeuvre as input.

In Fig. 5 the comparison between flight measurements and estimated response provided by the linearized model for the longitudinal mode is shown, where θ is pitch angle. All the values presented in the figures are normalized with respect to trim conditions.

The matching between the flight measured response and the model estimated response is good.

Estimated longitudinal aerodynamic derivatives results are presented in Table 2.

Table 2 Estimated longitudinal aerodynamic derivatives.

Parameter	Flap = 0°	Variation with flap = 36°
K_D	0.07	0
$C_{L\alpha}$	4.0	0.4
$C_{L\alpha dot}$	0.87	0
C_{Lq}	2.50	0
$C_{L\delta e}$	0.52	-0.018
$C_{M\alpha}$	-1.0	0.015

$C_{M\dot{\alpha}dot}$	-2.36	0
C_{Mq}	-6.75	0
$C_{M\delta e}$	-1.4	0.05
C_{D0}	0.07	0.023
C_{L0}	0.36	0.32
C_{M0}	-0.06	0.076

The lateral-directional results instead are presented in Fig. 6, where ϕ is roll angle. All the values presented in the figures are normalized with respect to trim conditions.

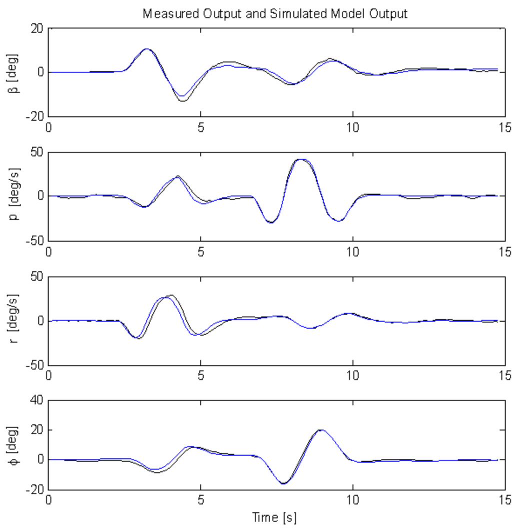

Fig. 6 Measured output and identified model output time histories match with an ailerons and rudder doublet manoeuvres as input.

In this case the matching between the flight measured response and the model estimated response is very good for all the state parameters.

Estimated lateral-directional aerodynamic derivatives results are presented in Table 3.

The validation of the estimated parameters was carried out through a six degree of freedom non-linear model. The estimated aerodynamics derivatives and thrust coefficient were included in the non-linear simulation model, where the longitudinal and lateral-directional dynamics are coupled together. New series of flight tests were executed to collect flight measurements of system input and output. The measurements of input were provided as input to the identified simulation model and the outputs of the simulation were compared with the correspondent flight measurements. All the simulations used for validation were open loop, that is, without the flight control system. In Fig.7-11 the comparison between flight measurements and identified model response provided by the non-linear model is shown. The input used is a 3-2-1-1 rudder manoeuvre and the output shown are angle of attack, angle of sideslip, roll rate, pitch rate and yaw rate.

Table 3 Estimated lateral-directional aerodynamic derivatives.

Parameter	Flap = 0°	Variation with flap = 36°
$C_{D\beta}$	0.2	0
$C_{Y\beta}$	-0.145	-0.103
C_{Yp}	-0.008	0
C_{Yr}	0.341	0.286
$C_{Y\delta r}$	0.13	0.08
$C_{l\beta}$	-0.04	-0.02
C_{lp}	-0.28	-0.07
C_{lr}	0.09	0
$C_{l\delta a}$	0.13	0.03
$C_{l\delta r}$	0	0.0066
$C_{n\beta}$	0.055	0.011
C_{np}	-0.003	-0.025
C_{nr}	-0.13	-0.04
$C_{n\delta a}$	-0.02	-0.002
$C_{n\delta r}$	-0.05	-0.008

The matching between measured and simulated data is good confirming that the identification technique was successfully applied to flight data.

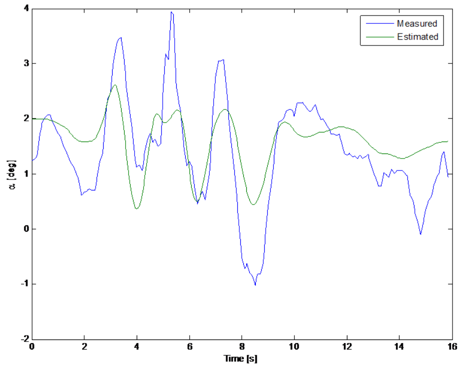

Fig. 7 Measured and estimated angle of attack time histories match with a 3-2-1-1 rudder manoeuvre as input.

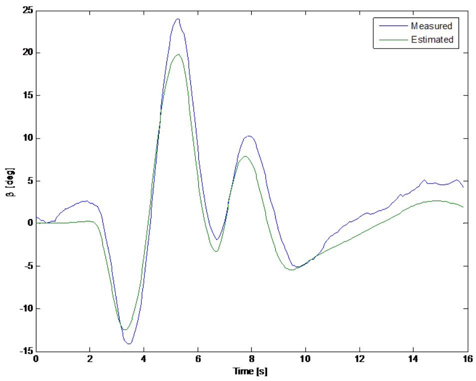

Fig. 8 Measured and estimated angle of sideslip time histories match with a 3-2-1-1 rudder manoeuvre as input.

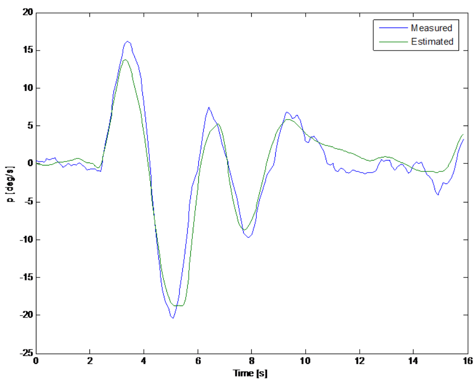

Fig. 9 Measured and estimated roll rate time histories match with a 3-2-1-1 rudder manoeuvre as input.

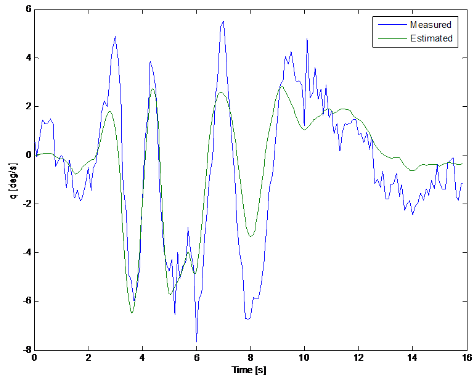

Fig. 10 Measured and estimated pitch rate time histories match with a 3-2-1-1 rudder manoeuvre as input.

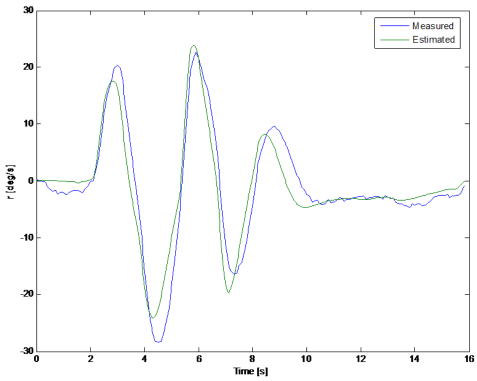

Fig. 11 Measured and estimated yaw rate time histories match with a 3-2-1-1 rudder manoeuvre as input.

7 Conclusion

In this paper an output error method for aerodynamic model identification was applied to actual flight data of an experimental ultra-light aircraft.

The method chosen is based on the Maximum Likelihood estimation principle, which permits to obtain the stability and control derivatives estimation by minimizing a cost function through suitable numerical procedure.

To perform aerodynamic derivatives estimation, two decoupled linearized model (for longitudinal dynamics and lateral-directional dynamics, respectively) were introduced. The estimation of the two models was performed independently by choosing suitable manoeuvres which in each test only excite the dynamic of interest. The identified parameters were finally included, together with the thrust coefficient also estimated from experimental data, in a nonlinear 6 degrees of freedom simulation model of the vehicle.

The validation of the identified model on data set not used in the identification process enhanced good capability of the model to reproduce the dynamics of interest and to match actual flight data, confirming that the identification technique was successfully applied to flight data.

Finally it is worthy to remark that the identified aerodynamic model was used to design a flight control system that successfully performed many autonomous take-off and landings [5][6][7].

References

[1] Jategaonkar R.V. and Thielecke F., "Aircraft parameter estimation - A tool for development of aerodynamic databases", *Sādhanā*, Vol. 25, No. 2, 2000, pp. 119-135.

[2] Roskam J., *Airplane Flight Dynamics and Automatic Flight Controls*, 1st ed., DARcorporation, Lawrence KS, 2001, Chap. 1.

[3] Lewis G., "Using GPS to Determine Pitot Static Errors", National Test Pilot School, 2003.

[4] Jategaonkar R.V., *Flight Vehicle System Identification: A Time Domain Methodology*, 1st ed., AIAA Progress in Aeronautics and Astronautics, Vol. 216, AIAA, Reston VA, 2006, Chap. 4.

[5] Di Vito V., De Lellis E., Marrone C., Ciniglio U., Corraro F., "UAV Free Path Safe DGPS/AHRS Approach and Landing System with Dynamic and Performance Constraints", *UAV Systems 2007 International Conference & Exhibition*, Paris, France, 2007.

[6] Di Vito V., De Lellis E., Marrone C., Genito N., Ciniglio U., Corraro F., "UAV Free Path Safe DGPS/AHRS Autolanding: algorithms and flight tests", *UAS 2008 International Conference & Exhibition*, Paris, France, 2008.

[7] Genito N., De Lellis E., Di Vito V., Garbarino L., Marrone C., "Autonomous Take Off System: Development and Experimental Validation", *3rd CEAS Air & Space Conference, 21st AIDAA Congress*, Venezia, Italy, 2011.

Experimental Study on Aerodynamic Characteristics of Ornithopter

Hiroki T Endo and Hironori A. Fujii
Kanagawa Institute of Technology, Atsugi, Kanagawa, Japan.

Keywords: *Ornithopter ,UAV flapping, feathering, lead-lag*

Abstract

Fundamental aerodynamic characteristics are studied for the ornithopter model as shown in this paper. Three types of movement of a wing are examined including 1) flapping motion to move the wing into the vertical direction, 2) feathering motion to change the angle of attack in the flapping motion, and 3) lead-lag motion to move the wing into the horizontal direction. The wing model in two dimensional motion in vertical plane is analyzed numerically in these motions. These numerical results show the importance of the method of combination between the Tri-motion. Result of the numerical analysis shows the possibility of producing the thrust and lift for a wing moving with an appropriate combination of tri-motion. An experimental device representing these motions is constructed in order to compare with results of numerical simulation. In summary, lift and thrust is proven numerically and experimentally to be able to be produced for a two-dimensional wing moving with appropriate motion.

1. Introduction

This Ornithopter is aircraft that imitate the flapping-wing flight of birds, bats, and ,insects, from Greek *ornithos* "bird" and *pteron* "wing", that is a "flap target," "flapping wing" as an alias.

While there have been from time immemorial challenge to manned flight, but the person who has not yet succeeded. Icarus in Greek mythology in Fig.1[14)], Emperor Shun of China has challenged, in medieval Europe Leonardo da Vinci has been a challenge in Fig.2 .

Recently, an ornithopter is tested by the University of Toronto Institute for Aerospace Studies (UTIAS) of Canada which flew about 300 m in 2006, but that of the auxiliary jet engine was used at the time of takeoff, the flight by ornithopter was not proven. [3]

Today, the mainstream of ornithopter research is a small machine about 5 ~ 50cm in Fig.3.

A model of bird flight is constructed by Nakazato and the model has flown successfully in 2006 in Fig.4. The model has its wingspan 3.3m with an engine 31,000rpm to flapping the wing and flew in average flight velocity 6m/s and ascending velocity 1m/s. The model is able to realize three movement, flapping, feathering, and lead-lag motion, and furthermore the flapping motion is synchronized to change its frequency increasing in the upward motion and decreasing in the downward motion, in other words, asymmetric flapping motion. The change of frequency in the flapping motion is a key idea to increase the efficiency in producing lift and thrust also increasing the performance of maneuverability in the flight of ornithopter and is designed in the model of Nakazato. The present paper is devoted to study the effect on the production of lift and thrust of such motion characteristics as flapping, feathering, and lead-lag. The present paper, based on this fact, to weigh the results of bygone numerical analysis and new experimental study employed with a two-dimensional wing model.

Fig.1 Icarus in Greek mythology [1]

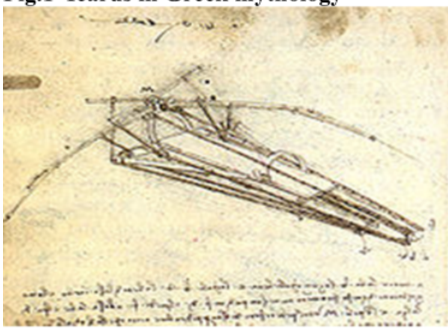

Fig. 2 Da Vinci 's ornithopter

Fig.3 Hammingbard ornithopter [2]

Fig.4 Wing span 3.3m Nakazato type rnithopter

Design and construction of an experimental model

2. Design and construction of an experimental model

Last year, we designed experimental apparatus to cause the Tri-motion and measure the force of the horizontal and vertical direction.

But , this model is measurement precision was low, and flapping mechanism did not assume that to put it on the real ornithopter.

This time, I carry out experiments using the mechanism to be installed in the actual ornithopter.

The body supposing a flight experiment is larger than the opening of a wind tunnel , therefore, produced a model that was scaled down to fit in wind tunnel, investigate at the aerodynamic characteristics using the "six component force balance".

Fig. 5 Six component force balance

Flapping mechanism was using the "crank mechanism" in the past, but I use the "swing drive mechanism" from this time.

Fig. 6 Crank mechanism ornithopter

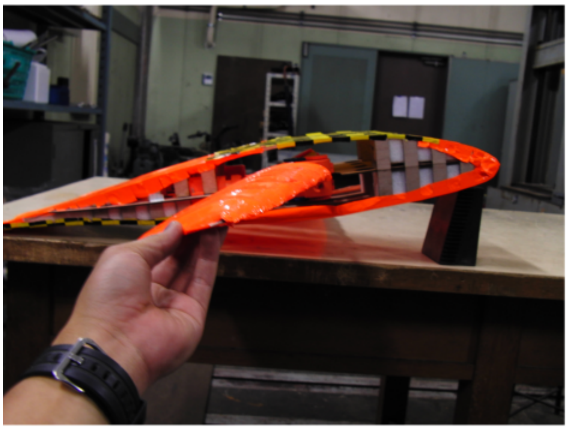

Fig. 7 Swing drive mechanism ornithopter

Swing drive mechanism was invented as a driving mechanism of the fish robot.

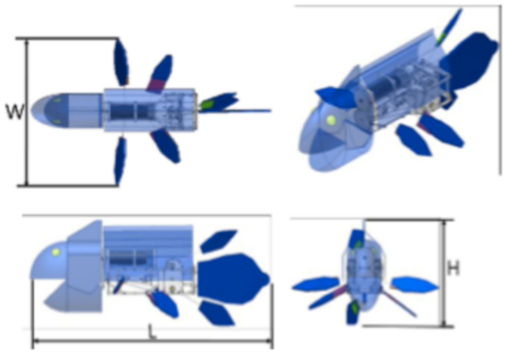

Fig. 8 Swing drive propulsion fish robot

The characteristic of this mechanism can perform "feathering motion" and "flapping motion" by one mechanism. Also, it has produced " feathering motion" by flexible material conventionally, but adjustment is difficult.

Fig. 9 Feathering angle adjustment during

However,it can adjust the feathering angle ,the case of this mechanism is easy.

Mechanism was designed that assumes the mounting of the aircraft in this case. Therefore, "Disk swing drive"adopted as the fish robot is not used . "Core swing drive" newly devised is adopted.

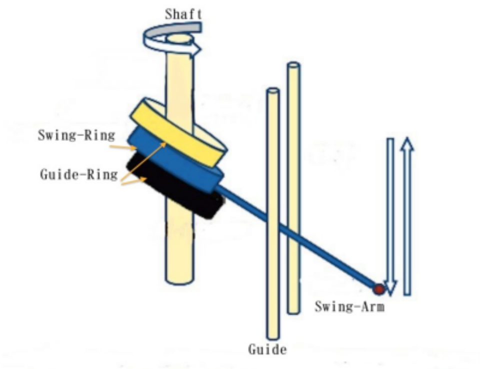

Fig. 10 Image of the swing drive

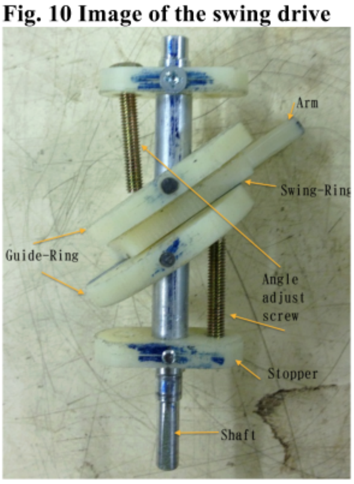

Fig.11 Disk swing drive

By adopting this mechanism, the control of the wing tip part has become possible.

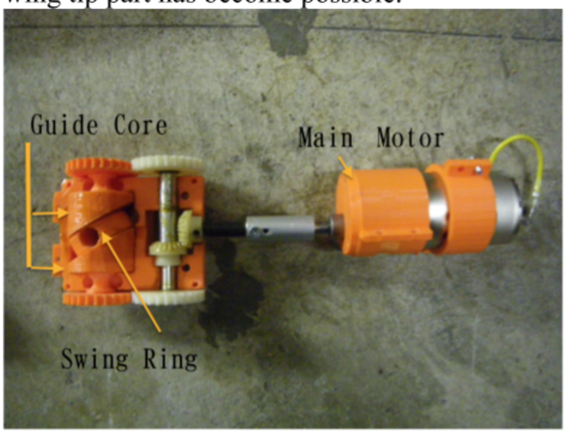

Fig.12 Core swing drive

In addition, it allowed to connect a link-mechanism to a tie rod of a swing drive and to operate the lead rag angle of the main wing.

Current problems of the swing drive, can not experiment of only flapping motion for simultaneous feathering motion and flapping motion. So we do not perform experiments only flapping motion this time.

3. Dimensions in Analysis and experiment

Dimensions employed in analysis are as follows,

Airfoil：S1223

Mass：M= 2.6 [kg]

Air density：$\rho = 1.165$ [kg/m^3]

Wing Area：S =0.150 [m^2]

Wing Span：b = 0.86[m]

Flow velocity：u = 5.0 [m/s]

Overall length：h = 0.92 [m]

Angular velocity：$\omega = 4.8\pi$ [rad/s]

Induced drag K=0(the induced drag does not occur for a two-dimensional airfoil)

I have already understood flight properties of the Canadian goose, so I made the wing that refer to this[]

Aerodynamic characteristics of S1223 are shown on Figs.14 and 15

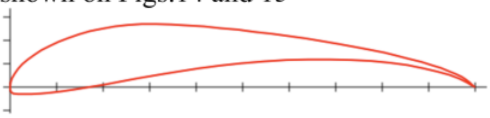

Fig.13 Airfoil **S1223**

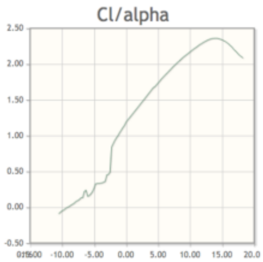

Fig.14 Lift coefficient corresponding with angle of attack

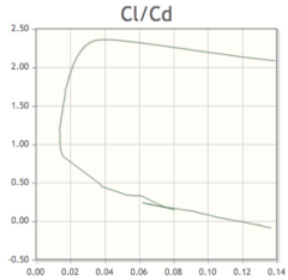

Fig.15 The relation between a lift coefficient and a drag coefficient

From Figs.13 and 14, it is seen that

$C_{L\alpha}$ =-3

C_{D0} = 0.04

In order to estimate the manufacture error of the wings, the relation between a lift coefficient and a drag coefficient, and the relation between an angle of attack and a lift coefficient is measured in

advance.

Moreover, in order to unite Reynolds number with Fig.13, the flow velocity u is adjusted.

Moreover, in order to unite Reynolds number with Fig.13, the flow velocity u is changed.

$$Re = \frac{\rho u L}{\mu} \quad \therefore \quad u = \frac{Re \cdot \mu}{\rho L}$$

L：Chord length

μ：Viscous

ρ：Air density

Respectively of air density and viscosity at the time of experiment,

$\mu = 1.869\ (10^{-5}\text{Pa}\cdot\text{s})$

$\rho = 1.165\ (\text{kg/m}^3)$

from this ,The flow velocity which should be measured

$Re_1 = 3.0\times10^6 \quad \therefore \quad u_1 = 30(\text{m/s})$

experimental result is shown on Fig.16 and Fig.17.

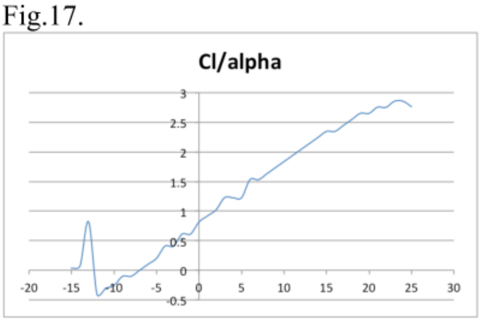

Fig.16 The experimental result of the relation lift coefficient and drag coefficient angle of attack

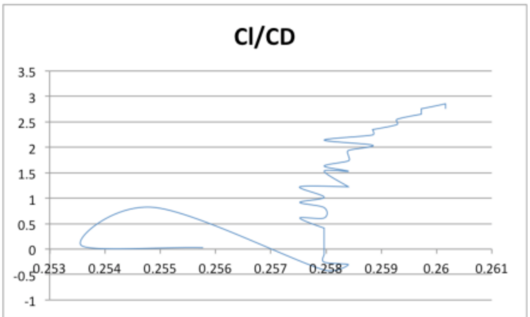

Fig.17 The experimental result of the relation between a lift coefficient and a drag coefficient

The present experimental conditions are as follow:

Airfoil：S1223

Air temperature：Temp=27.6(℃)

Air humidity：Rh=65(%)

Atmospheric pressure：P_0=997(hPa)

Air density：ρ’ =1.165[kg/m^3]

viscosity: μ’＝ ＝1.869 (10-5Pa・s)

Wing Area：S ‘= 1.5× 10^{-1} [m^2]

Wing Span：b’ = 0.86 [m]

Flow velocity：u’ = 5[m/s]

Flapping frequencies：f = 2 [Hz]

Angular velocity : ω ‘= 4.8π [rad/s]

In order to adjust the Reynolds number with Re=3.0×10^6, air density ρ’ =1.17[kg/m^3]and viscosity μ’＝1.869 (10-5Pa・s)at the time of experiment, it is considered as u'= h[m/s].

By the intensity convenience of an experimental device, flapping frequency is adjusted to be f = 2 [Hz].

4. Defining equation for each study

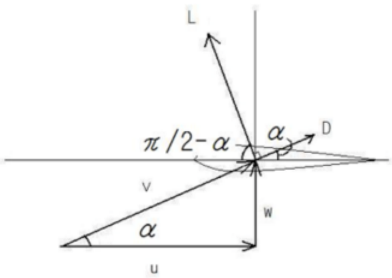

Fig.18 Definitions of the angle of attack

$$w = \tfrac{1}{2}\, h\, \omega \sin \omega t \quad [m/s] \tag{1}$$

$$\alpha = \tan^{-1}(w/u) \quad [rad] \tag{2}$$

$$A = b^2 / S \tag{3}$$

$$V = \sqrt{u^2 + w^2} \quad [m/s] \tag{4}$$

$$C_{L\alpha} = \partial C_L / \partial \alpha \tag{5}$$

$$K = 1 / e\pi A \tag{6}$$

$$C_L = C_{L0} + C_{L\alpha}\alpha \tag{7}$$

$$C_D = C_{D0} + K\, C_L^{\,2} \tag{8}$$

$$L = \tfrac{1}{2}\, \rho V^2 S C_L \tag{9}$$

$$D = \tfrac{1}{2}\, \rho V^2 S C_D \tag{10}$$

$$F_v = L \sin(\pi/2-\alpha) + D \sin\alpha = L \cos\alpha + D\sin\alpha \tag{11}$$

$$F_H = L \cos(\pi/2-\alpha) - D \cos\alpha = L \sin\alpha - D\cos\alpha \tag{12}$$

Flapping motion is the movement of the wings up and down in a vertical direction only , from Eqs. *(11)* and *(12)*,

$$\alpha = \arctan\left(\frac{h\omega \sin \omega t}{2u}\right) \tag{13}$$

Feathering motion varies the angle of attack α by changing the pitch angle of the wing flapping motion . Changing a value close to α and β in order to reduce the α.

$$\beta = -\frac{\pi}{4}\sin(2\pi t) \tag{14}$$

The value of α_2 is the addition of α and β

$$\alpha_2 = \alpha + \beta = \arctan\left(\frac{h\omega \sin \omega t}{2u}\right) - \frac{\pi}{4}\sin(2\pi t) \tag{15}$$

The analysis employs the value of α2.

Lead-lag motion is a movement back and forth in the direction of travel along the wing section, with changing u.

h_r: To-and-fro movement amplitude

h_r = 0.1[m]

$$u_r = -\frac{1}{2} h_r \omega \sin \omega t \tag{16}$$

If u after change is set to u2,

$$u_2 = u - u_r = u + \frac{1}{2} h_r \omega \sin \omega t \tag{17}$$

Since u changes, α also changes. The angle of attack combined with the flapping, feathering and lead-lag is set to be α_3,

$$\alpha_3 = \arctan\left(\frac{\frac{1}{2} h\omega \sin \omega t}{u + \frac{1}{2} h_r \omega \sin \omega t}\right) - \frac{\pi}{4}\sin(2\pi t) \tag{18}$$

Each numerical value is processed by using these α_3.

5. Experimental and analytical results

5.1

Result of combination flapping and feathering

Combination with flapping and feathering motion will call Duo-motion .This section introduces the analytical results by the Duo-motion. Fig 23 and 24 show the result numerical simulation of time response of Fv and F_H, respectively. Experimental results are shown for these cases in Figs.25 and 26 where Fig.25 and Fig.26 show the results of experiment for time responses of Fv and F_H, respectively.

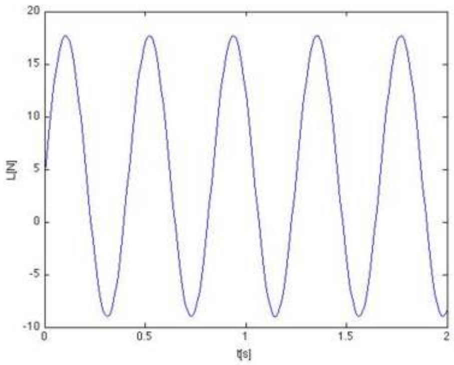

Fig.23 Analytical result of time response of F_V (Duo-motion)

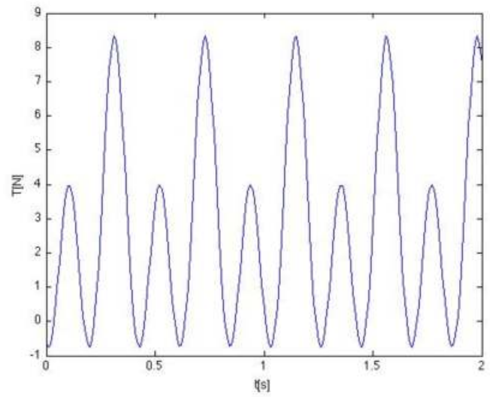

Fig.24 Analysis result of time response of F_H (Duo-motion)

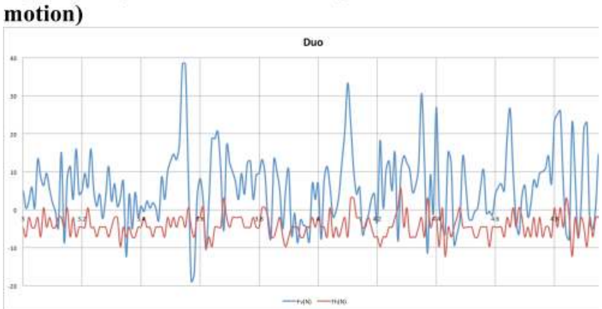

Fig.25 Experimental results for time response of F_H and F_V (Duo-motion)

5.2 Addition of lead-lag to the combination of flapping and feathering motion

Combination with flapping ,feathering and lead-lag motion will call Tri-motion .

This section introduces the analytical results by the Tri-motion. Fig.27 and 28 show the result numerical simulation of time response of F_V and F_H, respectively.

Experimental results are shown for these cases in Fig.29.

Blue line and red line on Fig.29 show the results of experiment for time responses of Fv and FH, respectively.

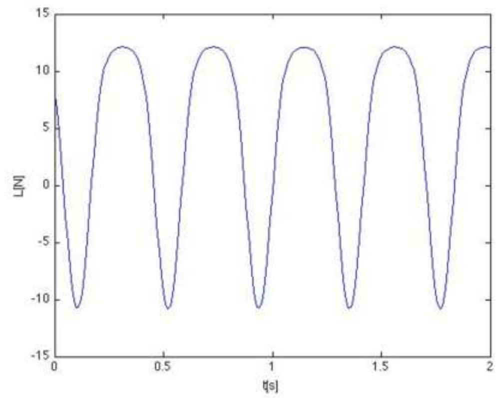

Fig.26 Analytical result of time response of F_V (Tri-motion)

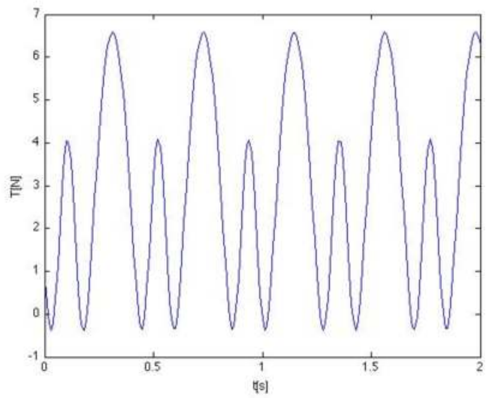

Fig.27 Analytical result of time response of F_H (Tri-motion)

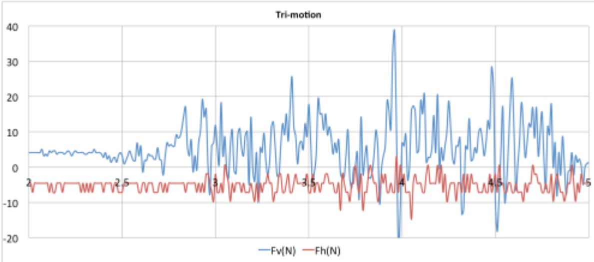

Fig.28 Experimental result of time response of F_H and F_V(Tri-motion)

6. Conclusion

Experimental lift and thrust value was approached to analysis value best ever.

This result to the upper equation is effective as a design method.

However, if it looks at from the side of energy efficiency, consumption power will be 3 times the required minimum power, and will be hard to be referred to as efficient.

It is surmised that a cause is either an electric system or a mechanism system. But,it cannot yet be specified.

Next phase performs kaizen on an actuator. Then will make out a flight test prototype.

References

[1] *Heaven's Lost Property* ,Studio AIC 2009

[2] Nano-hummingbird, Aero-vironment Inc

[3] UTIAS Ornithopter No.1 – Wikipedia.

[4] A. Azuma, *Science of Model Airplane and Kite*, pp.149-155, Denpa-Jikken-sya, (in Japanese.)

[5] J. Maglasang, N. Goto and K. Isogai, "Development of Bird-like Micro Aerial Vehicle with Flapping and Feathering Wing Motions," 'Trans. Japan Soc. Aero. Space Sci Vol. 51, No. 171, pp. 8-15, 2008.

[6] Dickinson, M. H. Lehmann, F. O. and Sane, S. P., "Wing Rotation and the Basis of Insect Flight," Science, 284 (1999), pp. 1954-1960.

[7] Fujikawa, T., Sato,Y., Makata, Y., Yamashita, T., and Kikuchi, K., "Development of a Butterfly-Style Flapping Robot with Slider-Crank Mechanism Using Flexible Links (Mechanical Systems)," JSME Journal, C, 76(761), 151-157, 2010-01-25(in Japanese.).

[8] I. Inuzuka, T. Yamada, S. Yoshimura, "Multi-Objective Design of Flapping Wing Motion for Micro Air Vehicle (Fluids Engineering)," JSME Journal, B,75(754), 1215-1222, 2009-06-25. (In Japanese)

[9] R. Arita, and K. Ohba, "Experiment on the mechanism of mosquito's flapping flight using a realistic enlarged model of its wing : Effect of flapping motion on the lift and thrust characteristics," JSME annual meeting 2007(6), 99-100, 2007-09-07 (in Japanese.).

[10] H. Nakai, M. Watanabe, and H. Tanaka, "Self-Excited Flapping Mechanism of Flexible Wings", Proceedings of Movic Symposium, 2007(10), 27-32, 2007-08-08 (in Japanese.).

[11] K. Tsuyuki, and S. Sudo, "The Wing Structure and Flapping Behavior of Cicada," JSME annual meeting 2003(5), 85-86, 2003-08-05 (in Japanese.).

[12] Jones. K. D. and Platzer, M. F., "An Experimental and Numerical Investigation of Flapping-wing Propulsion," AIAA Paper 99-0995, 1999.

[13] Smith, M. J. C., "Simulating Moth Wing Aerodynamics: Towards the Development of Flapping-wing Technology," AIAA J., 34 (1996), pp. 1348-1355.

[14] Isogai, K., Shinmoto, Y. and Watanabe, Y. "Effects of Dynamic Stall on Propulsive Efficiency and Thrust of Flapping Wing," AIAA J., 34 (1999), pp. 1145-1151.

[15] Nakazato, K., "Development of a Large Ornithopter with Span 3.3m," The 23rd Aero-Aqua biomechanism Seminar, Keio University, Tokyo, 2009 March 23 (In Japanese),

[16]Department, University, Country, 2008.

[17] Fukushima.H and Kawasaki.T and Sakon.Y "Study on the propulsion method using the swing drive mechanism" Kanazawa Institute of Technology (In Japanese),

[18] Electric mill Co., Ltd. Robot using power transmission and this power transmission mechanism , Japan Patent 4,742,172 , 2011-8-13 (In Japanese)

[19] Airfoil date , http://www.airfoildb.com/.

4:th CEAS Air & Space Conference
FTF Congress: Flygteknik 2013

Transonic Wing Design for a Regional Jetliner

M. Zhang and A. Rizzi
Royal Insititute of Technology (KTH), Sweden

R. Nangia
Nangia Aero Research Associates, Bristol BS8 1QU, UK

Keywords: wing design, airfoils, transonic, wave drag, Euler

Abstract

Aerodynamic shape optimization on a 3D laminar wing at transonic speed is studied, with three redesigns come out. The inviscid drag is improved and its pressure distribution has been refined. The wing root bending moment is also reduced a bit. The desired pressure at one cross section is specified and one redesign is obtained by Direct Iterative Surface Curvature method.

1 Introduction

The design of aircraft involves multi-disciplinary approach. The optimization needs to include aerodynamics and structural properties. It helps therefore to be able to parametrize and reduce the order of optimization effort. Within the FP7 NOVEMOR project, a Regional airliner (based on Embraer reference) is being studied. The ideas is to incorporate a fully parameterized wing including morphing LE / TE. A timely specific goal is to compare with other aircraft (e.g. Boeing Business Jet based on 737 series). An important aspect for transonic aircraft concerns wave drag estimation and its reduction.

1.1 Goals/challenges for efficient wing design

The authors will establish a computational design framework for a fully parametric virtual aircraft of the reference design with morphing surfaces. Our specific goal here is to explore the conceptual design space of the reference model to see if equal or superior aerodynamic performance can be achieved with respect to a conventional regional airplane, e.g., the A-320. The reference design (RD0) is mounted with a preliminary designed wingtip device which is about 10% (or 1.5 m) of the main wing semi-span, by reducing the inviscid drag 5%. The reference aircraft is designed as a regional jetliner cruising at transonic speed, with the designed requirements raised by EMBRAER. The MTOW is 58034 kg, with fuselage length 36.86 m, and wing span 34.46 m. It cruises at 11 km, with Mach 0.78, and C_L 0.47.

However, the winglet on the reference wing has some unfavorable aerodynamics. Figure 1 shows that the pressure distribution C_p from Euler solution for the spanwise stations near the wingtip inboard and outboard. It can be seen that all of the C_p distributions have a "cross-over" behavior that we should try to avoid.

1.2 Design algorithms

The design is carried out in two-folded. The whole wing is re-designed using the traditional gradient-based optimization method with some reasonable constrains on pitching moment, wing loading and bending moment [7], with the inviscid drag as objective function that to be minimized. This is a straightforward method and we trust the numerically computed gradient is correct. To ensure that the gradient indicates the correct search direction which leads conver-

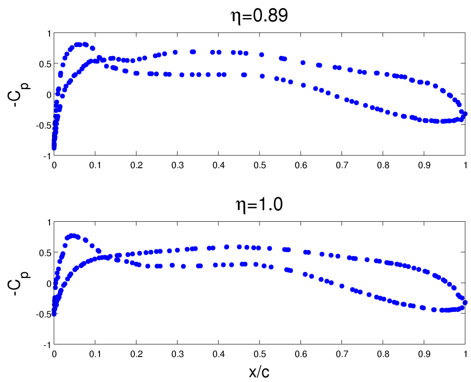

(a)

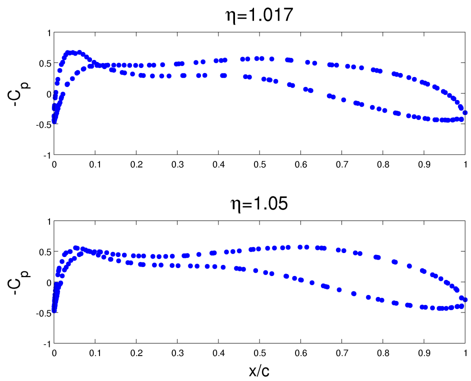

(b)

Figure 1: The pressure distribution C_p from Euler solution on the reference wing under cruise condition Mach $= 0.78$, $C_L = 0.47$, four spanwise stations near the end of the main wing ($\eta = 1$)

gence, we should either use the numbering-fixed mesh and virtually deform the nodes of the mesh according to geometry changes, or, as in this paper, re-mesh the model every time when the geometry changes to find the gradient, provided that the geometry change is big enough to effect the flow. Figure 3 shows the flow chart of solving the gradient-based optimal problem by re-meshing the model every time. The new geometry is found out by the optimizer in this design loop, while in case that the optimizer finds the local optimum, engineering action will be taken into account based on the solution from the optimizer, to ensure the global optimum is found. For example in this paper, RD1 is from the optimizer while RD1-1 and RD1-2 are from engineering method.

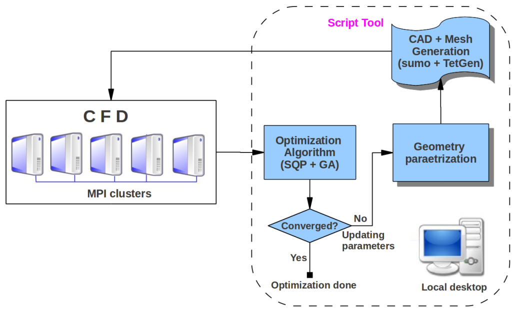

Figure 2: Flow chart of the gradient-based optimization procedure

The other approach leads to optimization is the Direct Iterative Surface Curvature (DISC) method, based on the relationship between change in geometry surface curvature $\Delta\kappa$ and the desired change in local pressure distribution ΔC_p:

$$\Delta\kappa = k\Delta C_p \tag{1}$$

where the gain k is modified depending on the local Mach-number and curvature. The relation is derived from the normal component of the momentum equation along the streamline [10].

1.3 Flow solver

The flow solver used in this paper is a Fortran code developed by Swedish Defence Research Agency (FOI) [6]. The code is called *Edge*, uses

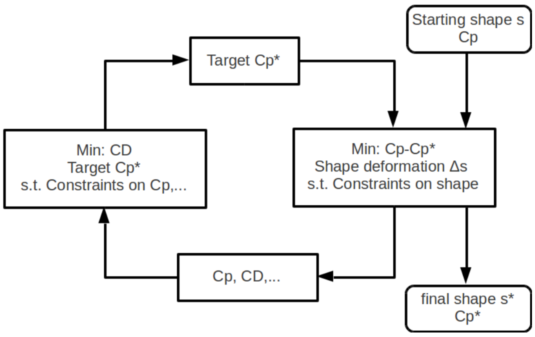

Figure 3: The design loop of CDISC approach

a n-stage Runge-Kutta time marching procedure to solve the 2D and 3D Euler and Navier-Stokes equations on an unstructured grid. It enables multi-grid method to accelerate convergence.

In this study 3D Euler equation is solved, the forces and moments are obtained by pressure integration. The drag directly from calculation is the inviscid drag.

2 Approach to Design Lifting Surfaces

Aircraft design mainly focuses on lifting surfaces design regarding to aerodynamic and structural issues. In this manner the objective turns to parametrize the *lifting surfaces* by a set of robust parameters which are suitable for optimization. There are several different parametrization schemes for lifting surfaces. In spite of the 3D planform parameters (wing area S_{ref}, wing span b, taper ratio λ, aspect ratio AR, sweep angle Λ, dihedral angle δ, etc.), the 2D airfoil shape for each wing section is the crucial issue in the process. It relates to the lift, drag, span load distribution, bending moment etc., which are important for aerodynamic and preliminary structural analysis.

The SUface MOdeler [1], sumo, developed by David Eller in KTH, is a tool aimed at rapid creation of aircraft geometries and automatic surface mesh generation. It stores the cross-sectional information (points) as skeletons for the components e.g., wings, fuselages, nacelles, and pylons. sumo together with the TetGen [16] automatic tetrahedral mesher can provide a high-quality unstructured volume mesh for Euler computation in few seconds. . The surface of the wing can be parametrized with sumo by patches of Bezier surfaces on airfoil stacks which are consisted of points. It allows rapid creation of aircraft geometries and automatic surface mesh generation. Figure 4 shows the mechanism that sumo representation for wing surface creation and how the control points (square) are applied to morph the airfoil leading and trailing edge (LE and TE). Details of how to parametrize the wing including the winglet device are shown in following sections.

[1] http://www.larosterna.com/sumo.html

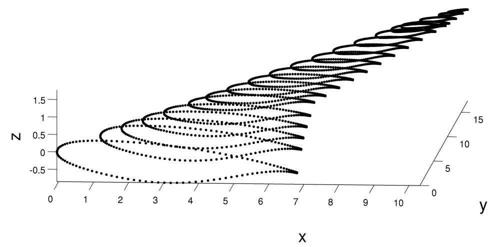

Figure 4: Wing surface creation with sumo: airfoil stacks

2.1 Airfoil parametrization

A more powerful parametrization for airfoils is the Class-Shape-Transformation (CST) method pioneered by Kulfan [4] and Sergio [5]. With a small number of design variables it enables a large variety of airfoils to be simulated.

The airfoil is modeled by 4th-order Bernstein polynomial (BPO) CST method, representing the airfoil by a symmetric component (thickness) and an asymmetric component (camber) respectively.

The thickness distribution(t) z_t is to define the shape function S_t with zero camber, while the camber shape(c) z_c is to define the shape function S_c with zero thickness.

$$S_t(x) = \sum_{i=0}^{4} A_{ti} \cdot S_i(x) \quad (2)$$

$$z_t = C(x) \cdot S_t(x) \quad (3)$$

$$S_c(x) = \sum_{i=0}^{4} A_{ci} \cdot S_i(x) \quad (4)$$

$$z_c = C(x) \cdot S_c(x) \quad (5)$$

Where the $S_i(x)$ is component of the 4th-order Bernstein polynomials $S_i(x) = \frac{n!}{i!(n-i)!}x^i(1-x)^{4-i}$, A_{ti} and A_{ci} are the coefficients added to the shape function that define the thickness and camber shape respectively, $i = 0, 1, 2, 3, 4$. $C(x)$ is the class function, that $C(x) = \sqrt{x}(1-x)$ for a shape with round nose and point aft-body. Note that the first term of A_t (or A_{t0}) defines the LE radius ($A_{t0} = \sqrt{2R_{LE}}$) [4], that we always want to fix or predefine. Similarly, the first term of A_c (or A_{c0}) is always 0 (zero LE radius) since the camber line has zero thickness. Both the number of A_t and A_c coefficients are reduced to 4 if we want to fix the LE radius of the airfoil. Thus the number of design variables for an untwisted airfoil is $4+4 = 8$, plus 1 for local twist, we have 9 design variables for one undeformed *section*.

The CST method is extended by PoliMI to morphing airfoils[5] . It applies to compliant leading and trailing edges. The Shape and Class Functions of CST are augmented by additional terms.

The approach used in this paper is similar, consistent with the two-stage thickness-camber design stated above. The deformed/morphing leading edge (LE) and trailing edge (TE) are defined by deforming the camber line, with thickness distribution remaining. Note that the central region of the wing (wing structural box) is undeformed. The continuity of the camber slope needs to be maintained, when deforming the LE/TE. The nose and tail displacements are notated by ZLE and ZTE. The quadratic Bezier curves are used to determine the deformed LE/TE camber line, see Figure **??**. Two more design variables ZLE and ZTE are added to each *section* if we include the morphing strategy.

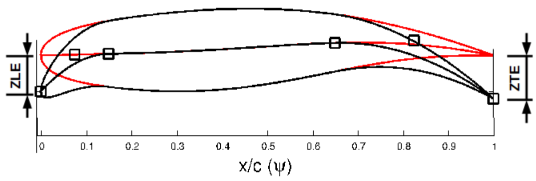

(a)

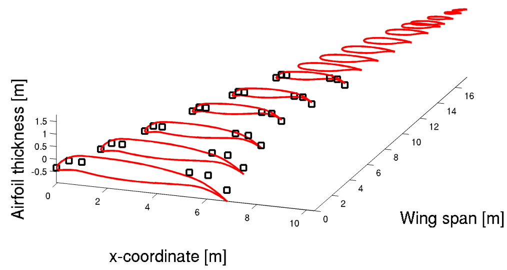

(b)

Figure 5: Wing surface creation with sumo: airfoil stacks and control points for morphing LE and TE

2.2 Geometry representation

The original reference design (RD0) is provided in IGES format. It is converted into *sumo* [2] geometry by importing the sectional information (points) from IGES, in order to proceed the automated mesh generation within the optimization process. The deviation from both models is really small, the main difference is that the wing from original IGES model has trailing edge gap ΔTE with maximum value less than $1\% \cdot c$, which c is the local chord along the span. *sumo* only considers the shape trailing edge, and it is closed by applying minimum change to the airfoil i.e., taking a wedge out of the whole chord by subtracting the $\frac{\Delta TE}{2}$ from both upper and lower surfaces at the trailing edge that preserving the shape of the airfoil mostly (Figure 6(a)).

The airfoil is parameterized by CST using 4th-order Bernstein polynomials (4th-BPO), which has sufficient accuracy to represent the RD0 geometry in *sumo*. Figure 6(b) shows the the maximum errors of the cross sections those parametrized by 4th-BPO CST method stated above, which splits the thickness and cambers into two design stages. We can see that the overall errors are quite small and less than 0.2%, it is safe to use this parametrization method to represent RD0 geometry.

The total number of variables N0 that parameterizing the whole wing with n sections will be

$$N0 = 11 \cdot n \tag{6}$$

In this paper, aerodynamic design and structural analysis are done sequentially. We only consider one point design, i.e., the cruise condition with LE and TE undeformed. Also the wing box capacity is preserved so the thickness for each cross section is fixed. Only cambers, twists and winglet cant angle are designed for optimized aerodynamics. So the number of variables N1 that parameterizing the whole wing with n sections in the aerodynamic design stage stated here is:

$$N1 = 5 \cdot n \tag{7}$$

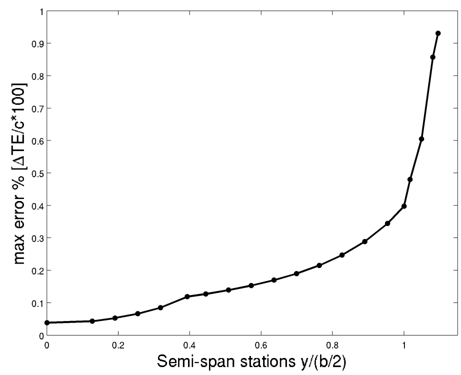

(a) Maximum error for RD0 geometry representation by *sumo* imported from CAD model

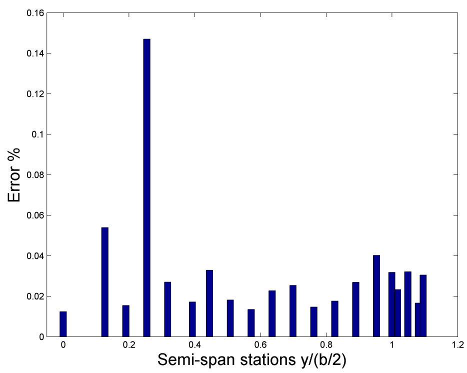

(b) Maximum error for RD0 geometry parametrization using 4th-BPO CST method in *sumo*

Figure 6: Errors in geometry representation along the span

3 Results and Discussion

3.1 Varying the twist and cambers

There are two designs RD1 and RD2 are represented in this paper, both of which show significant drag reduction. The inviscid drag is reduced from 14.9 *counts* (RD0) to around 10.5 *counts* (RD1, RD1-1 and RD1-2), around 30% reduction in numbers, while the pitching moment stays almost the same, adding a little nose-down pitch. Figure 7 shows the Euler solutions for a 2.7 M nodes mesh for RD0 and its three re-design configurations at transonic speed.

For lower C_L, the RD1 design has lower drag, however with the increasing C_L, the advantage in drag eliminates, while the RD1-1 and RD1-2 designs still hold a lower drag at higher C_L. This can be explained by the spanload shape in Figure **??**, RD1-1 and RD1-2 are more towards a triangular loading (as RD0), which has a benefit in lower wave drag when shock is strong, while RD1 has more elliptical loading at the outer board, that has a lower induced drag at lower C_L when wave drag is not dominated.

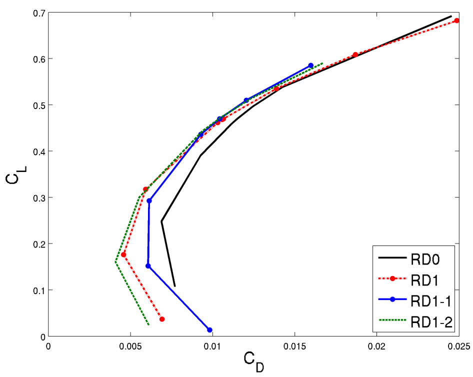

Figure 7: Euler solutions for RD0 and its three redesigns at Mach 0.78

Figure 8 shows the pressure distribution from Euler solution under cruise condition for the reference design RD0 and its three redesign cases by varying the twists can cambers on upper and lower surfaces. Figure 11 and 12 represents the pressure distribution and geometry comparisons for reference design (RD0) and its redesigns RD1 and RD1-1, RD1-2 in transonic inviscid flow.

The lambda shock at the root is much weakened in RD1 (around $\eta = 0.2$). At around kink $\eta = 0.4$ the mild double shock is replaced with a favorable pressure gradient up to 0.6 airfoil chord followed with a slightly stronger shock. RD1 design remedies the crossed pressure at the span-wise location after the wingtip (Figure 12 (b) and (c)), but a slightly shock appears at around $\eta = 1$, if one sees Figure 3.1 and Figure 12 (a) that the crossed pressure still exists while unfortunately a shock is raised. That is one of the sources where wave drag comes from.

To avoid the appearance of the shock around $\eta = 1$, the local airfoil is twisted up to reduce the local lift (Figure 12 (a), (d) and Figure 3.1), that is the way we get RD1-1. The adverse pressure gradient around $\eta = 1$ in RD1 has been refined in RD1-1, however, the "cross-over" pressure still exists, which is *inefficent* and the produced lift is much less than it is supposed to be.

From the two different designs RD1 and RD1-1 we see that the tip region is a problem, it either produces shock on the upper surface or on the lower side, where adds wave drag. The most efficient way is to not only vary the cambers and twists - making a slightly thiner local airfoil will probably cure the problem. This won't effect the fuel storage much since the location is around the wingtip and most of the fuel stored in the inboard wing. By reducing the thickness at wing tip section we get RD1-2.

RD1, RD1-1 and RD1-2 are better than the initial baseline RD0, which have more straight and fully-swept isobars along the wing. If we examine carefully their pressure isobars, we can see that on the the upper surface RD1-1 has quite nice looking straight isobars with reduced shock (Figure 3.1), while a tip shock on the lower surface is worsen, where in comparison it eliminates in RD1-2 design (Figure 8(b)).

The wing AR is around 10, and its bending moment shows that the root has the highest stress for the planar wing as we know from theory. The RBMs (at around 10% semi-span) for the design RD1, RD1-1 and RD1-2 are higher than the initial design RD0, that the wing needs to be designed to hold more loads. This situa-

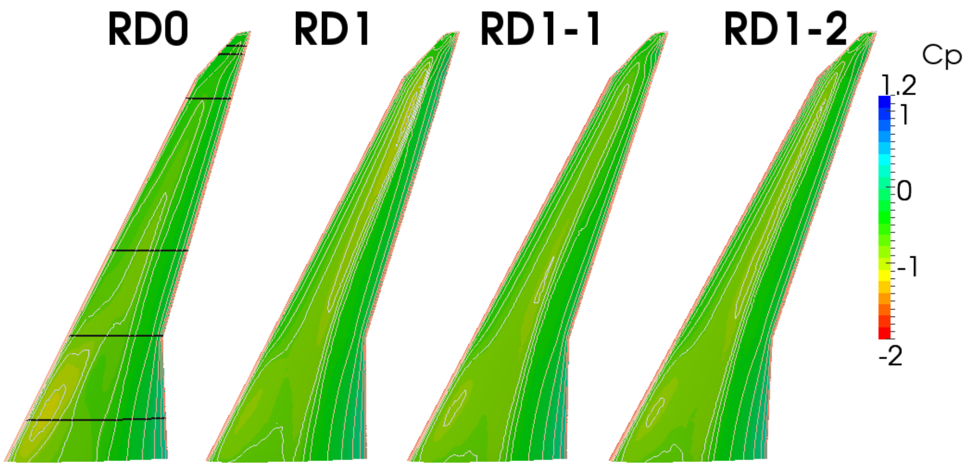

(a)

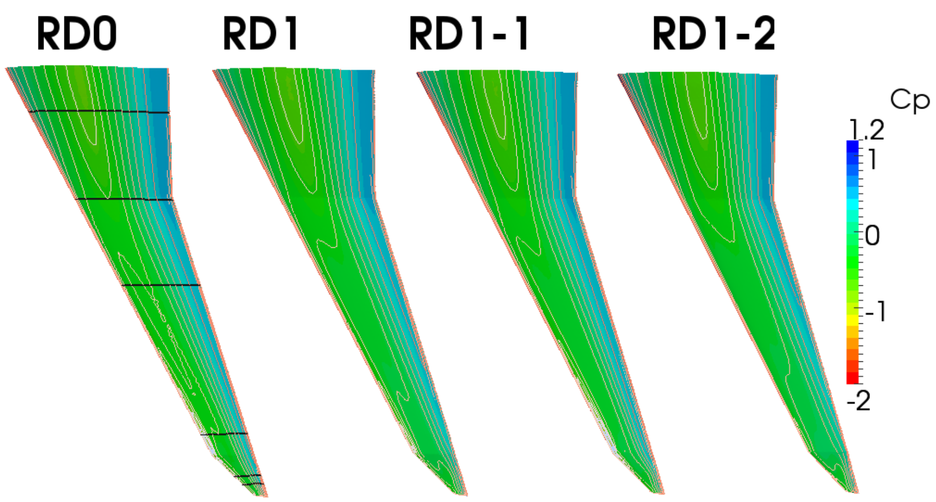

(b)

Figure 8: Pressure distribution from Euler solutions for RD0 and its three redesigns at Mach 0.78 and C_L 0.47 on a) upper, and b) lower surfaces. Marked span-wise stations are (from inboard) $\eta = 0.2$, $\eta = 0.4$, $\eta = 0.6$, $\eta = 0.95$, $\eta = 1.05$ and $\eta = 1.07$

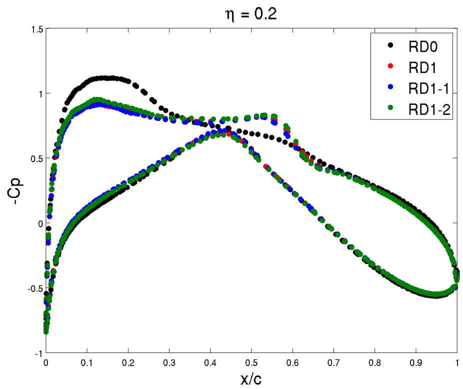

(a)

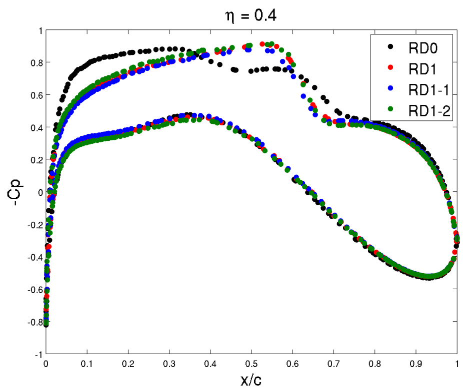

(b)

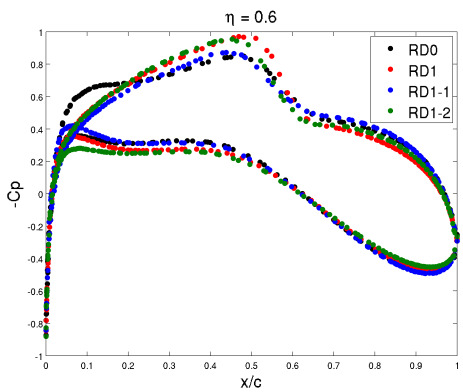

(c)

Figure 9: Pressure distribution in sections η =0.2,0.4,0.6, for RD0 and its three re-designs

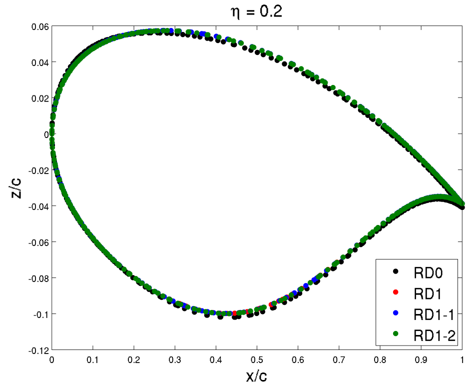

(a)

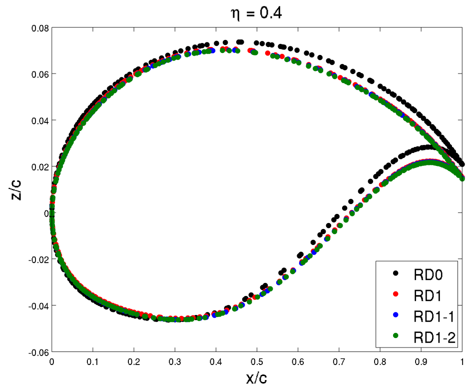

(b)

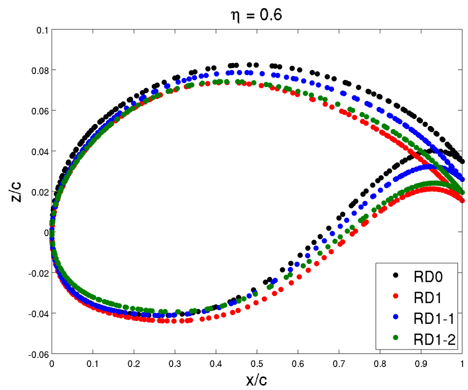

(c)

Figure 10: Airfoil geometry in sections η =0.2,0.4,0.6, for RD0 and its three re-designs

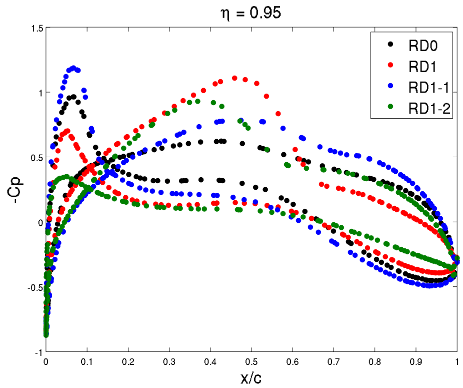

(a)

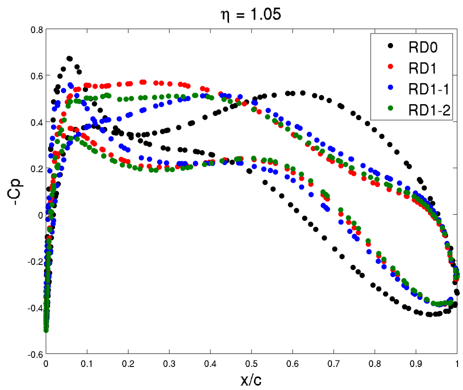

(b)

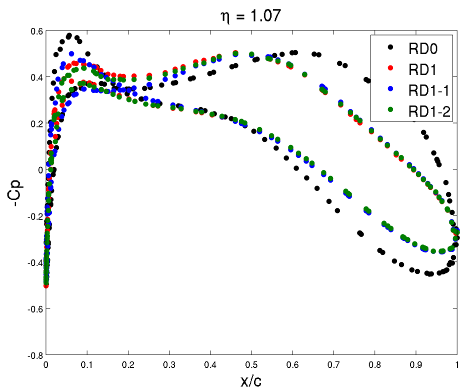

(c)

Figure 11: Pressure distribution in sections η =0.95,1.05,1.07, for RD0 and its three redesigns

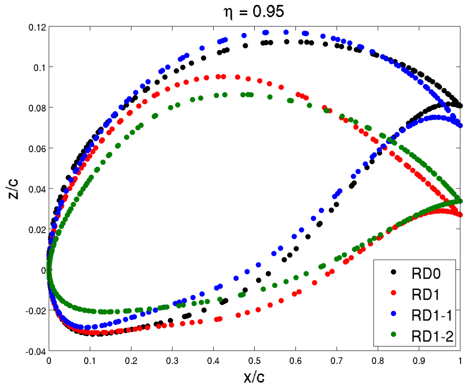

(a)

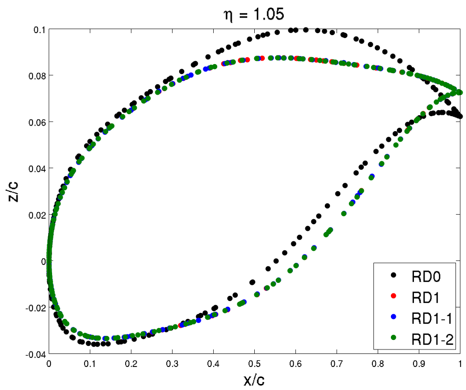

(b)

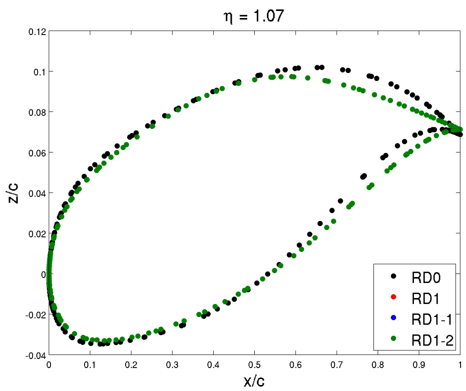

(c)

Figure 12: Airfoil geometry in sections η =0.95,1.05,1.07, for RD0 and its three redesigns

tion might be improved by carefully designing the folded angles on the wingtip.

3.2 On-going work for designing the folded angles

The initial design RD0 has a slightly folded angle 7 degrees. With carefully designing of the tip folded angles the lift force at the tip can be varied so that the bending moment w.r.t. the wing root is changed significantly. As the folded angle increasing it shows more triangular wing loadings that elliptical loadings progressively, i.e., the wing tip function decreases but wing root function increases, see Figure 14. Figure 15 shows the wing sections of those two wings with different folded angles, the sections are shown with wingtip shown as unfolded.

3.3 Preliminary results on target pressure

If we specify a target pressure on the wing, for example, the desired fully-swept isobar on the wing which gives minimum drag, then we can use the DISC method to design the wing by solving a inverse design problem. The pressure on the wing is presented by a number of sections, then the problem comes to design a series of airfoil stacks (as mentioned in 4). It is more complicated for a 3D wing design problem than the 2D airfoil design. Since the reference wing RD0 is tapered and swept (also twisted), we will design it in two steps:

1. consider the wing without sweep, the lift distribution and span load shape are constrains when design the airfoil stacks on the wing, the aspect ratio AR and taper ratio λ would effect them;

2. the cross section thickness t/c of a swept wing with sweeping angle Λ is equivalent to an unswept wing with cross section thickness $(t/c) \cdot cos(\Lambda)$;

Figure 16 shows the preliminary results using DICS approach to redesign the wing section $\eta = 0.4$, with its local lift coefficient preserved. The work is on-going. The flow inboard would influence the flow outboard.

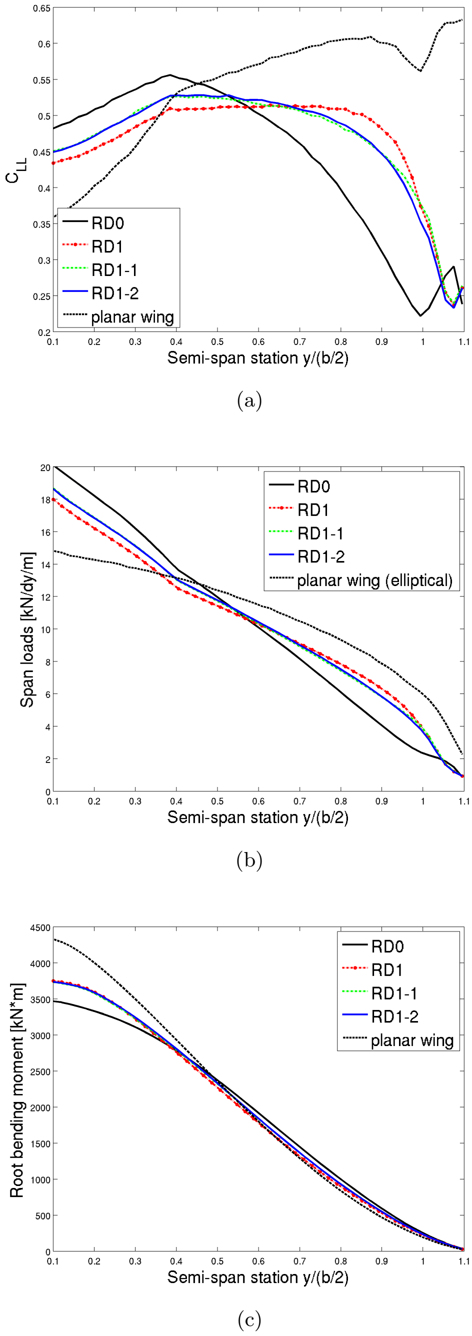

Figure 13: Euler solutions for RD0 and its three re-designs compared with the planar wing (only thickness) at Mach 0.78, $C_L = 0.47$, a), local lift coefficient C_{LL}, b) span load distribution, c) wing root bending moment at around 10% wing semi-span

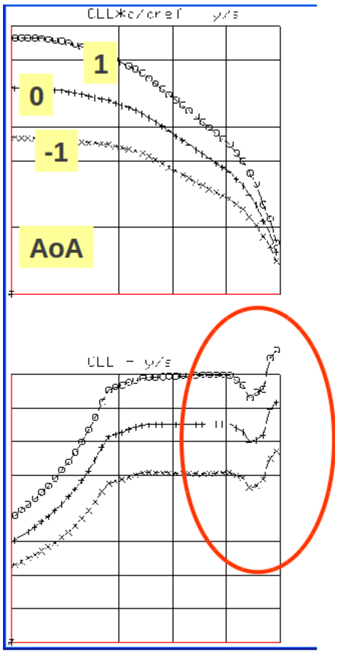

(a)

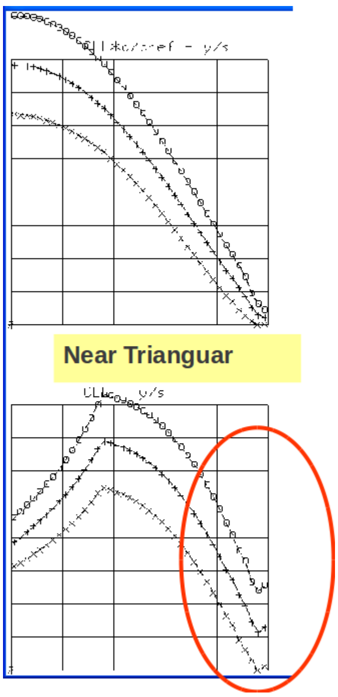

(b)

Figure 14: Span loads coefficient and local C_L from Nangia's panel code solution [15] on the RD0 geometry, at α = -1, 0, 1 deg , with folded angles (a) 60 degrees; (b) 63 degrees

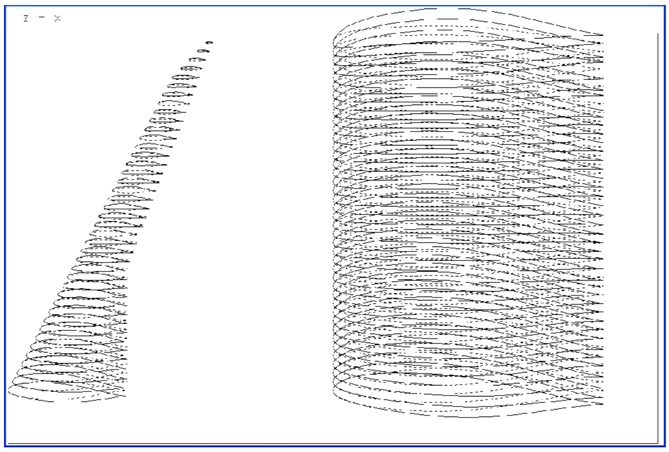

(a)

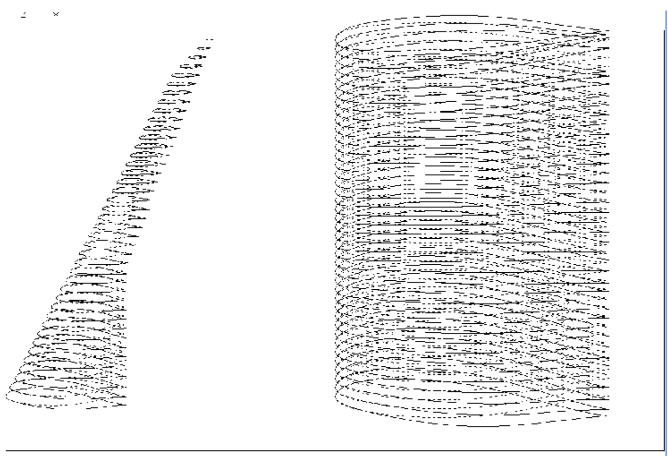

(b)

Figure 15: Designed wing sections with wingtip shown as unfolded according to Nangia's panel code solution [15] on the RD0 geometry with different folded angles: (a) folded angle 60 degrees; (b) folded angle 63 degrees

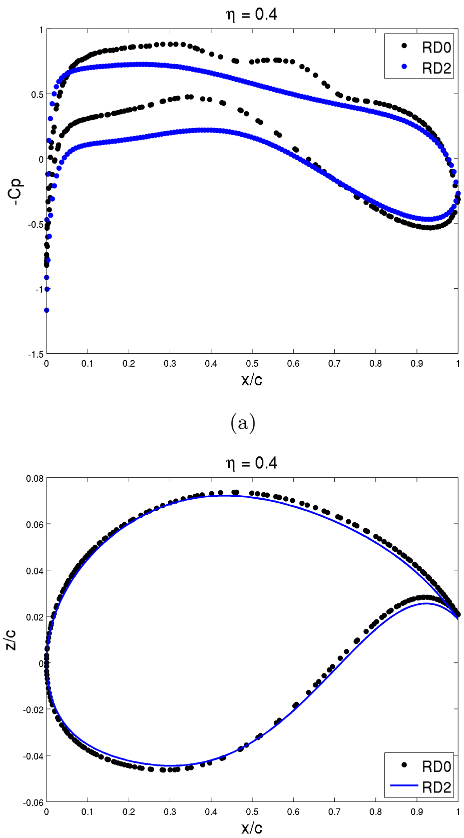

(a)

(b)

Figure 16: Pressure and geometry in section $\eta = 0.4$, for RD0 and its re-design RD2 using DISC approach

4 Future Work

This is a on-going work. The DISC approach will be carried out carefully to re-design from inboard to outboard.

5 Bibliography

References

[1] Ricci, S., Castellani, M., Romanelli, G., "Multi-Fidelity Design of Aeroelastic Wing Tip Devices", Proc IMechE Part G: Journal of Aerospace Engineering, 0(0) 1-13.

[2] Eller D., "Larosterna Engineering Dynamics Lab, Aircraft Modeling and Mesh Generation", available at: http://www.larosterna.com/sumo.html (accessed 01 June 2011).

[3] Eliasson, P., "Edge, a Navier-Stokes solver for unstructured grids", in Proc. Finite Volumes for Complex Applications III, ISBN 1 9039 9634 1, pp.527-534, 2002.

[4] Kulfan, B., "Universal Parametric Geometry Representation Method", Journal of Aircraft, Vol. 45, No. 1, January-February 2008.

[5] De Gaspari, A. and Ricci, S., "A Two-Level Approach for the Optimal Design of Morphing Wings Based on Compliant Structures", Journal of Intelligent Material Systems and Structures, Vol. 22, July 2011, pp. 1091-1111.

[6] Edge User Guide, FOI dnr 03-2870, ISSN-1650-1942, FOI, Swedish Defence Research Agency, Systems and Technology, Stockholm, Sweden, 2007

[7] Kuchemann, D. F.R.S., *The Aerodynamic Design of Aircraft*, 1st edition 1978. ISBN 0-08-020514-3.

[8] Nocedal, J. and Wright, S. J., *Numerical Optimization*, Springer, 2006. ISBN 0-387-30303-0. http://www.ece.northwestern.edu/ nocedal/book/num-opt.html.

[9] Qin, N., "Spanwise Lift Distribution for Blended Wing Body Aircraft", J. Aircraft, Vol.42, No.2, March-April 2005.

[10] Richard L. Campbell, "An Approach to Constrained Aerodynamic Design With Application to Airfoils", NASA-TP-3260.

[11] Grant, F., "The Proper Combination of Lift Loadings for Least Drag on a Supersonic Wing", NACA Rep. 1275, 1955.

[12] M. A. Potsdam, M. A. Page, and R. H. Liebeck, "Blended Wing Body Analysis and Design", AIAA-Paper 1997-2317, June 1997.

[13] Griva, I., Nash, S. G., Sofer, A., *Linear and Nonlinear Optimization*, 2nd edition 2008. ISBN 978-0-898716-61-0.

[14] Nangia, R.K., Boelens, O.J., Tormanlm, M. "A Tale of Two UCAV Wing Designs", AIAA 2010-4397, 2010.

[15] Nangia, R. K., Palmer, M. E., and Doe, R. H.,"Aerodynamic Design Studies of Conventional & Unconventional Wings with Winglets", AIAA 2000-3400, 2000.

[16] Si, H., "TetGen: A Quality Tetrahedral Mesh Generator and a 3D Delaunay Triangulator", available at: http://tetgen.berlios.de/ (accessed 28 June 2012).

[17] Richard, L. Campbell, "An Approach to Constrained Aerodynamic Design With Application to Airfoils", NASA Technical Paper 3260, November 1992.

4:th CEAS Air & Space Conference
FTF Congress: Flygteknik 2013

Steps Towards Automated Robust RANS Meshing

Maximilian Tomac and David Eller
Aeronautical and Vehicle Engineering - KTH, Stockholm, Sweden

Keywords: Hybrid mesh generation, Automatic mesh generation, Computational Fluid Dynamics

1 Introduction

The creation of high-quality discretizations for use in viscous flow simulations remains a challenging task [3, 8]. Even with modern software tools and substantial human effort, the application of state-of-the-art mesh generation algorithms in the presence of geometric features such as concave corners may still result in inadequate local mesh quality, which can severely affect the resolution of important flow features [15].

To address such issues, mesh generation tools for hybrid unstructured grids often expose a considerable number of algorithm configuration parameter [12, 1, 20]. The resulting flexibility does indeed enable the creation of sufficiently resolved hybrid meshes, although the process often requires a very considerable amount of time even for an experienced user. In a production environment where a large number of detailed simulations of a single aircraft configuration are performed, the cost in terms of man-hours may be acceptable. For other applications with requirements for short turn-around time, a more automated approach is desirable.

Since an automatic mesh generation procedure cannot rely on user intervention for the resolution of geometric complications or edge cases, a robust strategy for the handling of the surface geometry encountered in realistic aircraft configurations must be implemented. One possible solution is to accept a hybrid mesh with known regions of unacceptably low element quality, and then to augment the unstructured volume mesh with one or a number of structured overset blocks which can be manually adapted to better resolve critical geometric features [22, 15]. Obviously, this approach requires solver support for handling of overset grids, which is not necessarily available in state-of-the-art flow solvers for industrial use. Another approach to improve robustness is a transition to a combination of prismatic, tetrahedral and octtree-based mesh generation procedures, which has been shown to allow a surprising flexibility in the presence of difficult geometric features [10]. From the information available, it is however not clear how the resulting mixed mesh topology may affect the resolution of boundary layer flows.

The approach presented here is based on a segregated prismatic/tetrahedral mesh generation procedure, and aims to achieve robustness by means of local geometric modifications. Criteria chosen and algorithmic modifications make use of similar principles as in earlier work [2, 7, 9], but are adapted for the specific requirements of mesh generation for aircraft configurations. An existing set of open-source tools is exploited for mesh data structures, file format support, surface mesh generation and tetrahedral volume meshes.

Surface mesh generation capabilities of the current tool-chain have been presented earlier [19]; therefore, the present paper is focussed on the procedures employed in the volume mesh generation step. Such a decomposition is possible as the algorithms do not currently exploit any coupling with the surface mesh generation stage and can therefore also be utilized to create a hybrid prismatic-tetrahedral mesh around an existing triangular surface mesh.

2 Aim

In contrast to many other mesh generation procedures focussing on mesh quality, the aim of the present effort is to obtain the capability to robustly and with minimal user interference produce hybrid meshes suitable for engineering computations. The authors acknowledge that there are a multitude of challenging flow problems which will still require the application of different mesh generation tools and algorithms in order to create an acceptable computational mesh. Nevertheless, it is anticipated that a fast and comparatively robust tool will allow for significant savings in time and effort where meshes for many different routine flow simulations must be generated. An example of such applications may be the automated creation of a series of meshes for a full aircraft model in a windtunnel, which often requires a separate mesh for each run in order to correctly capture wall effects. Another use case which could possibly benefit substantially is the application to military aircraft with multiple external stores, where many different geometric configurations need to be handled.

With this in mind, the purpose of creating a hybrid prismatic mesh is to substantially increase mesh resolution in boundary layers, where the solution of high-Reynolds number flow cases exhibits large gradients. It is, however, important to note that the extent of the prismatic layer does not necessarily correspond to the size of the boundary layer; it is only the lower region of the layer which is intended to be sufficiently well resolved. The upper, outward part of the prismatic layer is sized to allow for a volumetrically smooth transition to the connected tetrahedral mesh. The distribution of prismatic layer extent normal to the wall need therefore not match the actual development of the boundary layer thickness.

3 Method

The mesh generation strategy is based on four phases, starting with the creation of a sufficiently resolved surface mesh. In a second step, the envelope mesh of the prismatic boundary layer mesh is determined; the robustness of this stage is the primary contribution of the present work. Thirdly, tetrahedral elements are generated to fill the volume between the envelope of the prismatic layer and the farfield boundaries, and finally, pentahedral elements are grown between adapted wall and envelope mesh.

3.1 Surface meshes

For the generation of unstructured surface meshes for full aircraft configurations, the open-source program `sumo`[1] can be used. The geometry is in this case represented by a moderate number of parametric surfaces, which can be linear-cubic or bicubic polynomial spline surfaces, analytically defined, or non-uniform rational b-spline (NURBS) surfaces.

Triangular surface meshes are then constructed by a method which accounts for a three-dimensional version of the Delaunay criterion [5]. Two mesh refinement passes are used in order to fulfil a set of triangle quality criteria which can either be determined based on heuristics or specified by the user. Heuristics exploit information which is available due to the fact the the geometry modelling component is specialized for aircraft configurations.

[1] Available from `http://www.larosterna.com/sumo.html`

If the use of `sumo` is not desired, a triangular surface mesh created with any other mesh generation tool can be used. Such meshes can be imported from files in CGNS [13], SU2, legacy VTK, the NetCDF-based format used by the TAU code, or STL format. Spherical farfield boundaries can in this case be generated automatically from a set of user-defined parameters.

3.2 Prismatic envelope

Once a surface mesh is available, the volume to be filled with prismatic elements is determined by constructing a second triangular surface with identical topology at a locally varying distance from the wall mesh. In the following text, this second triangulated surface is called the envelope, as it encloses the entire prismatic layer. In order to handle the multitude of geometric difficulties which can occur at this stage [8], the shell surface is not a simple extrusion of the surface mesh along local normals. Instead, a sequence of passes are applied as follows:

1. feature extraction and node classification;
2. selective smoothing of growth directions;
3. selective smoothing of layer height;
4. local untangling;
5. global collision avoidance;

with the aim of transforming the envelope surface into a suitable upper boundary of the prismatic mesh region.

Surface node classification The first step in creating the envelope surface is to detect and classify nodes with respect to geometric properties which necessitate special treatment of either local height or growth direction. Local criteria, such as the angle between the normals of adjacent triangles, are evaluated in order to assign a set of flags to each vertex of the wall mesh. Multiple flags may be combined; a vertex can, for instance, be classified as lying on a detected mesh feature line (ridge) and simultaneously carry either a *convex* or *concave* flag.

Some typical examples are vertices which are part of edges (which, again, may be blunt or sharp, convex or concave), or corner vertices. Figure 1 shows the wall surface of the F-16XL aircraft used in the cranked arrow wing project (CAWAPI,[11]), where blue regions mark vertices which carry any flag differing from the one used to indicate a locally flat surface.

One of the factors controlling the classification is a user-provided feature angle. This angle defines a limit for the dihedral angle between triangles, above which edges are considered to be part of feature lines.

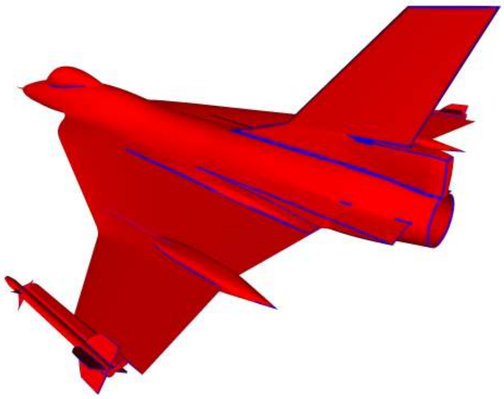

Figure 1: Detected geometric features.

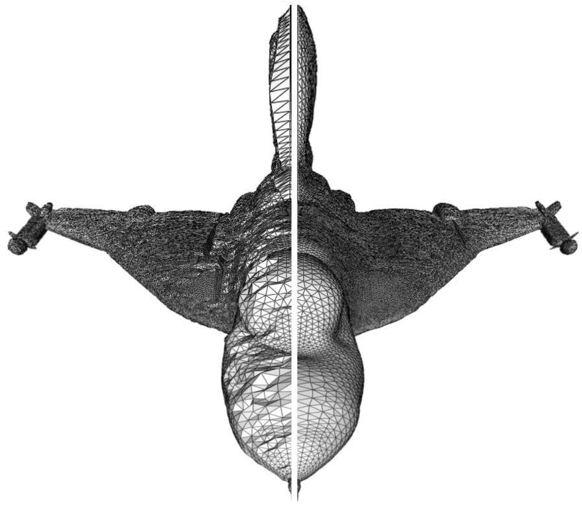

Figure 2: Effect of smoothing on envelope surface.

Therefore, the feature angle should be chosen larger than the maximum dihedral angle of adjacent wall triangles in smoothly curved regions.

Note that this feature detection phase only evaluates local geometry, and is not influenced by boundaries between components. This is seen at the junction between the canopy and fuselage or the vertical tail and root of the vertical tail in Figure 1.

Envelope smoothing. The envelope surface enclosing the prismatic layer is initialized using the vertex-based surface normal vectors obtained by averaging the normals of coincident triangles [18] and an initial height field. The local layer thickness at a vertex is at first chosen as the minimum of a maximum desired height and a constant factor multiplied with the length of the shortest edge connected to the vertex. Both the maximum height and the edge length factor (typically between 1.5 and 6.0) are provided by the user.

Due to triangle size variations and considerable local deviations between normal directions, the initial envelope surface tends to be very irregular in shape. The left side of Figure 2 shows an example for the F-16XL; no sound prismatic mesh can be generated between the wall and this boundary surface.

Therefore, three smoothing passes are performed either indirectly or directly to the envelope surface. During the first pass, a modified Laplacian smoothing operator is applied to the height field by means of a small number of Jacobi iterations, where the height modification operation is adapted depending on the value of the vertex flags identified earlier. Secondly, a similar procedure is utilized to smooth the growth directions (normals) with a different pattern of flag-dependent modifications. Modifications based on vertex flags aim at avoiding a deterioration of feature resolution which would result from isotropic smoothing; as an example, normal directions for vertices marked as being part of feature edges are smoothed exclusively with respect to other normals on the same edge.

On the right side of Figure 2, the resulting envelope surface after smoothing is displayed. This surface is sufficiently well-shaped to allow the generation of good-quality pentahedral cells.

Local untangling. The envelope surface generated in this way will often contain self-intersections which would result in entangled pentahedral elements. To remove such intersections, an algorithm using only local, edge-based geometry is run first, followed by a second, global procedure.

In the first phase, an edge-based limiter for the prismatic layer height is applied. For each edge $\boldsymbol{e}$ in the wall mesh, the angles β_1 and β_2 between the edge direction and the vertex normal vectors in the endpoints of the edge are computed. Using $\gamma = \pi - \beta_1 - \beta_2$, the maximum permitted height at the edge endpoint j is then obtained from

$$h_j < |\boldsymbol{e}| \frac{\sin \beta_j}{\sin \gamma} \quad \text{where} \quad \gamma > 0. \tag{1}$$

Once the local height is reduced accordingly, a simple smoothing of the height variable in the ring-2 neighborhood of all modified vertices is performed in order to soften the transition. Necessarily, this reduction of local layer thickness h in the vicinity of concave geometry will lead to some degree of irregularity in the prismatic region. Figure 3 shows a cross-section of the mesh around the Boeing/NASA common research model (CRM, [21]), colored by turbulent eddy

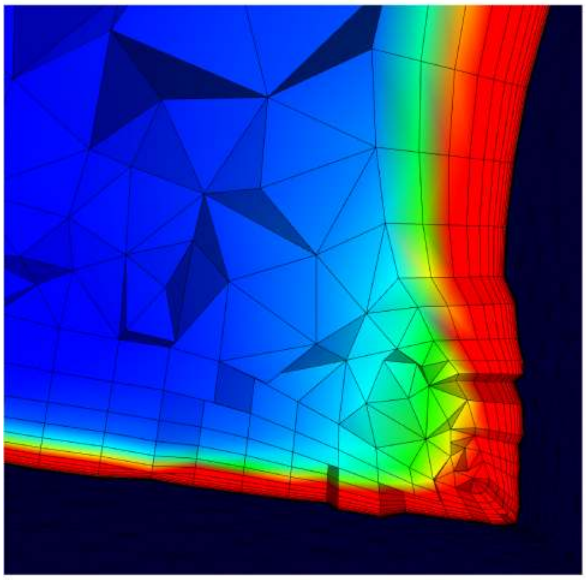

Figure 3: Contours of ν_t near fuselage-wing transition.

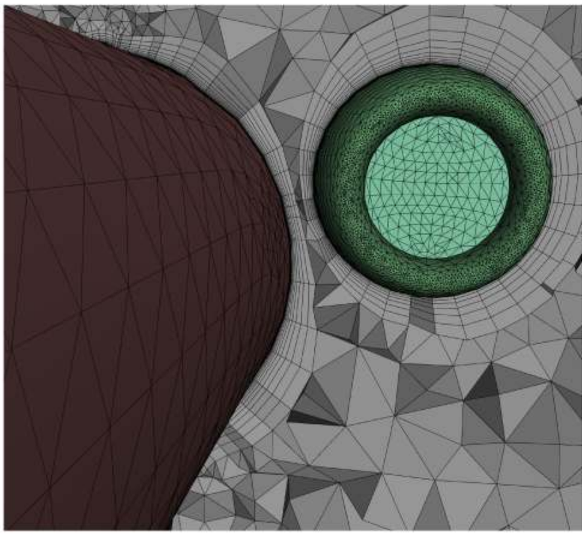

Figure 4: Envelope retraction to avoid intersection.

viscosity ν_t. It is apparent that the pentahedral layer thickness is reduced drastically near the wing-fuselage junction, but the transition from prismatic to relatively small tetrahedral elements does at least not cause an obvious distortion of the solution field.

Encroaching bodies. In some instances, the geometry of the envelope surface cannot be determined by purely local geometric considerations. An example is the region between a rear-mounted engine nacelle and the fuselage shown in Figure 4, where the unmodified prismatic region envelope enclosing the nacelle would intersect the layer around the fuselage.

As is visible in Figure 4, the potential collision was detected and the layers on both sides were retracted, i.e. their height reduced in order to alleviate the problem at the cost of a small number of moderately flat tetrahedral elements in the intervening space. Efficient detection of the risk of self-intersection is enabled by means of a search tree data structure, namely a balanced binary tree bounding volume hierarchy. This particular data structure is used to perform fast queries of the geometric neighbourhood of a point on the envelope to test for the presence of other points within a given critical radius. If any such point is then categorized as indicating collision by comparison of the corresponding local normal directions, the local envelope height is reduced accordingly. As the relation between height and intersection state can be rather irregular for complex geometries, the process of rebuilding the search tree and testing for self-intersection is repeated until no further collisions are detected. Often, just a two or three iterations are required; for very intricate geometries, as many of 20 repetitions can be needed which still does not account for a significant amount of computational effort (see Section 5.1).

Sharp edges. Surface meshes generated by `sumo` feature sharp trailing edges along all lifting surfaces. This restriction is carried over from the original purpose of the program, which is to generate meshes for potential-flow methods, and may be removed in a future update. Sharp trailing edges inevitably cause rather skewed prismatic cells and control volumes – in the sense of a vertex-centred finite-volume solver – which wrap around the edge. Although such a cell geometry may not be well suited for RANS-computations aimed at high accuracy, the capability to create meshes even in the presence of sharp trailing edges is considered an advantage. The lack of a separate, necessarily extremely narrow surface terminating a blunt or rounded edge allows to select the surface mesh resolution of the wing surface based on physical considerations, instead of gradually transitioning to the tiny triangles on the trailing edge closure surface patch.

3.3 Tetrahedral mesh

Before prismatic elements are generated in the region between wall and envelope layer, tetrahedral elements are created in the space between envelope and farfield boundaries. The efficient tetrahedral mesh generation program TetGen[2] developed by Han Si [17, 16] is employed for this purpose. A number of element quality parameter can be passed to TetGen in order to control the level of refinement. In many cases, these element quality criteria cannot be satisfied unless some of the bounding triangles are split to allow for smaller adjacent tetrahedra. As the method used to create prismatic elements builds upon the assumption that wall and envelope mesh have the exact same topology, such triangle splits need to be propagated to the wall mesh.

In order to relate vertices inserted by TetGen on the envelope mesh to the wall surface, each boundary triangle passed to TetGen is tagged with an integer identifying the corresponding wall triangle. Newly created envelope triangles inherit the same tag, so that it is possible to split the wall mesh by inserting a new wall vertex at the barycentric coordinates of the envelope vertex created by TetGen. The lookup procedure used to determine whether a vertex received back from TetGen corresponds to a previously defined envelope vertex or requires a wall triangle split makes use of the same bounding volume hierarchy also employed in resolving encroaching bodies as explained in Section 3.2.

Due to the ordering of the mesh generation phases, the splitting of the envelope performed by TetGen occurs after the local layer height field has been established. Therefore, some of the larger pentahedra may end up with a little larger height-to-width ratio than originally intended. This is not generally considered a substantial disadvantage since such disturbances usually only affect limited regions and are in some cases even beneficial from an element quality perspective.

The use of a Delaunay-procedure in TetGen entails certain restrictions on the type of surface mesh appropriate for the present approach. Triangle meshes dominated by large aspect ratio elements, such as, for example, surface meshes obtained by splitting a structured quadrilateral mesh, are not suitable. Although the envelope construction procedure of Section 3.2 is fully capable of handling such surfaces, the interface mesh seen by TetGen would still contain many triangles with large aspect ratio. Fulfilling a tetrahedral quality criterion based on the three-dimensional Delaunay property then leads to extremely many splits and entirely unacceptable node counts as the stretched interface mesh is transformed into a more isotropic refinement.

3.4 Extrusion of prismatic elements

Starting from the wall surface, prismatic elements are finally generated by filling the space between wall and envelope with a prescribed number of prismatic element layers. The height of the first prismatic cell is a user-defined value which is applied throughout the entire mesh. Starting from the second cell, a constant growth ratio is maintained such that the last cell reaches the local layer thickness. Hence, the growth ratio may differ substantially between regions of the mesh.

In some areas, the layer thickness may be so small that the above simple procedure would result in a growth rate below one, that is, the cell height would diminish away from the wall. An equally spaced distribution of cell heights across the layer is selected if such a situation arises. A typical geometrical feature exhibiting this limitation would be a detailed model of the narrow lateral gap between a control surface and the adjacent main wing structure.

3.5 Limitations

With the current implementation, all triangular boundaries are treated in the same manner, that is, prismatic layers are generated everywhere. For this reason, special boundaries such as symmetric planes (where no prismatic layers are desired) can not easily be integrated, since such boundaries would require remeshing to allow a connection of the coincident prismatic layer with matching quadrilateral elements on the symmetry plane.

Furthermore, some CAD models and derived surface meshes contain degenerate geometric details, which would not usually exist in an actual product but are caused by modelling simplifications. Such degeneracies can lead to the case where it is not possible to define a vertex normal which sustains an angle of less than 90° with the normals of all of the coincident triangles, which renders the construction of well-defined pentahedral elements impossible. In order to properly handle such geometric degenerate points, multiple vertex normals would need to be defined and the algorithm of Section 3.4 must be substantially modified.

An example for such degeneracies is shown in Figure 5, where the wing tip missile launcher rail is directly joined to the wing tip rib surface. The resulting two irregular corners are points where no well-defined pentahedral elements can be created. In this particular case, the critical corners were easily removed by adding a small ramp with a height of a single cell to the geometry definition.

4 Example applications

Two applications are presented in this study, a fairly simple wing-body-stabilizer configuration typical for a transonic transport aircraft (CRM) and a rather com-

[2] Available from http://www.tetgen.org

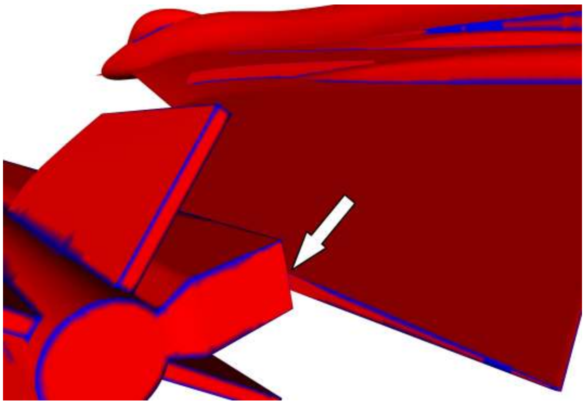

Figure 5: Corners between wing and launcher rail

plex, detailed geometry of a delta wing fighter prototype (F-16XL). This part of the study tries to answer or give an indication to the following questions:

- What are the main geometrical constraints prohibiting the present method from producing an acceptable hybrid mesh?
- Is the algorithm able to produce grids that are adequate in comparison to well-established advancing-front grid generators?
- Where possible discrepancies occurs, what is the source of error? Is it due to poorly resolved boundary layer, skewed prisms, or lack of resolution of the tetrahedral region?

4.1 Common Research Model

The Common Research Model is a geometrically fairly simple wing-body-stabilizer configuration developed for applied CFD validation studies [21]. In this study flow simulations for the CRM were performed for a set of Mach numbers between 0.7 and 0.87 and angles of attack from zero to six degrees at a chord Reynolds number of 5 million. The prismatic grids generated for this model follow the general grid guidelines from the fourth drag prediction workshop (DPW-4)[3]. In order to focus the evaluation on the quality of the volume mesh generation process, a surface mesh from the DPW-4 website was used, namely the medium-resolution grid generated by DLR, with 1.2 million surface triangles when mirrored.

4.2 F-16XL

The F-16XL aircraft on the other hand is a fairly complex configuration that presents many unique aerodynamic challenges across its aggregate flight envelope [11]. This vehicle incorporates cranked delta wings designed for efficient supersonic cruise. As a result, the wings are thin, highly swept, and feature relatively small leading-edge radii. The configuration investigated here also includes wing-tip missiles, air-dams, server pods, narrow gaps and other geometrical details that tend to be a challenge for many prismatic grid generators [4].

In this study the current prismatic grid generator was used to produce a hybrid grid of the F-16XL aircraft for a flow simulation of the very challenging transonic Flight Condition 70 (FC70, see [14]), at Mach 0.97 and a angle of attack at 4.3° and a chord Reynolds number of 89 million. At this angle of attack, significant interaction between the shock and a vortex emanating from the sharp inboard leading edge is expected to occur.

The surface grid used for evaluating mesh quality is the mirrored initial KTH/FOI surface grid [14] with 316 000 surface triangles. 35 prismatic layers were generated with an initial wall distance of 10^{-6} m ensuring $y^+ < 1$ everywhere.

5 Results

The flow solver Edge [6], developed at the Swedish defence research establishment (FOI), was used for the comparative simulations. Turbulence was modelled using the Spalart-Allmaras (SA) one equation model for the CRM cases and the Hellsten, Wallin and Johansson $k-\omega$ explicit algebraic Reynolds stress model (EARSM) for the F-16XL case. Since the purpose of the simulations was not to predict performance or gain new physical insights, but rather to evaluate the dependency of computed results on properties of the volume mesh generation scheme, only steady-state runs were performed. It is understood that this may well lead to inaccurate results for some of the cases investigated.

Edge is based on a finite-volume formulation where a median dual grid forms the control volumes with the unknowns allocated in the vertices of the primary grid. The governing equations are integrated to steady state, with a line-implicit approach in regions with highly stretched elements (e.g. the prismatic layer) and explicitly elsewhere with a three-stage Runge-Kutta time integration scheme. The steady state convergence is accelerated by FAS agglomeration multigrid. Solid surfaces were associated with weak adiabatic wall boundary conditions, while weak characteristic exterior conditions were used for the farfield boundary. For the F-16XL case the engine inlet and mixing plane conditions where set to the same values as presented in [4]. Details of the

[3] http://aaac.larc.nasa.gov/tsab/cfdlarc/aiaa-dpw/Workshop4/gridding_guidelines_4.html

mesh element and node counts can be found in Table 2.

CRM The initial mesh for the CRM geometry contained a comparatively coarse tetrahedral region with 7.7 million elements, generated with a tetrahedral quality criterion (for a definition, see [17]) of 1.2. For this mesh, some differences in pitch moment were observed when compared with the advancing-front mesh containing nearly twice as many elements in the tetrahedral domain. Therefore, the `sumo`-based mesh was re-generated with a tetrahedral quality criterion of 1.05, leading to a mesh with 17.6 million tetrahedral cells.

Figure 6 shows the drag polar for the CRM model for mach numbers 0.7, 0.85 and 0.87, where the more finely resolved farfield mesh was used. A comparison at lift coefficient $C_L = 0.5$ indicates that the drag

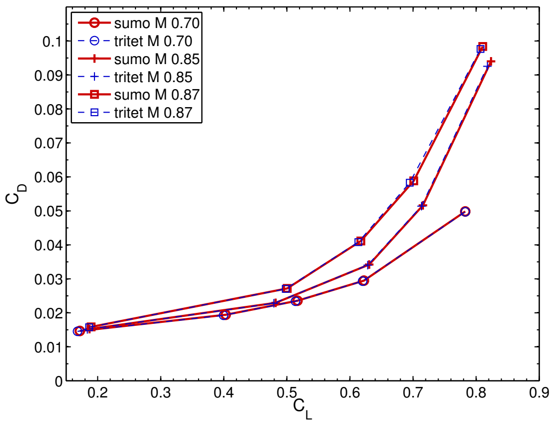

Figure 6: CRM drag polar comparison

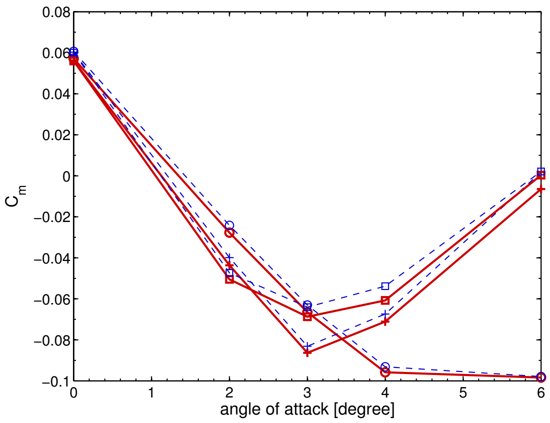

Figure 7: CRM pitch moment coefficient

only differs by 0.04% between the `sumo`-generated and reference grids. This difference is most likely significantly less than the overall accuracy of the simulation. In Figure 7 the pitch moment C_m as function of angle of attack is shown. Again good agreement between meshes is observed for moderate lift coefficients, while slightly larger differences occur at higher lift coefficients.

The effect of tetrahedral mesh resolution can be observed in the pressure distribution at the wing-kink station $y = 10.86$ m displayed in Figure 8. Although

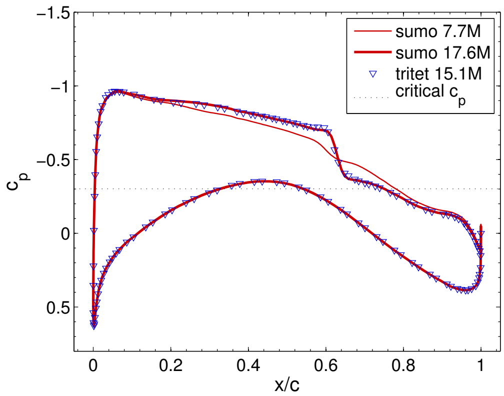

Figure 8: c_p at kink section for $\alpha = 2°$

the prismatic layer grids are very nearly identical between the two `sumo`-meshes, the shock is not resolved well with the coarser tetrahedral volume mesh. Refinement of the tetrahedral region results in a pressure distribution which is very close to the one obtained with the advancing-front mesh generator.

Figure 9 and Figure 10 show the surface pressure and skin friction distribution of the CRM at Mach 0.85 and angle of attack 2°. The upper side shows the solution based on the `TriTet`-generated grid while the lower side shows the solution based on the `sumo`-generated grid with 17.6 million tetrahedral elements. No significant discrepancies between the two solutions are found.

F-16XL Table 1 compares integrated forces and moments between the advancing-front mesh generated using `TriTet` and the hybrid prismatic/Delaunay grid produced using `sumo` and `TetGen`. While the discrepancies in lift force and pitching moment are relatively small, there is a considerable difference in total drag and especially frictional drag (more then 7%). The source of this mismatch becomes apparent when studying the surface pressure distribution in Figure 11, where the upper half shows the reference solution (`TriTet`-mesh) while the lower half presents

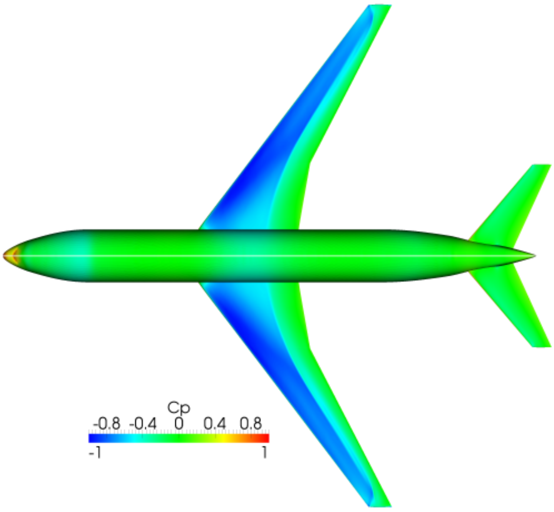

Figure 9: Pressure coefficient comparison

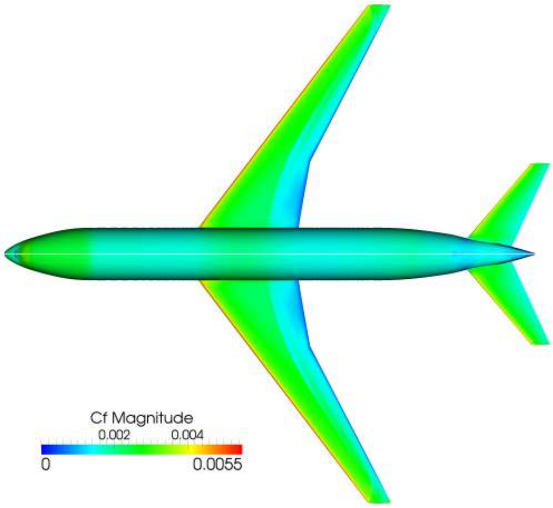

Figure 10: Friction coefficient comparison

Coefficient	`TriTet`	`sumo`	Difference
C_L	0.12010	0.12016	+0.05%
C_D	0.03760	0.03687	-1.94%
C_{D_f}	0.00508	0.00472	-7.09%
C_m	-0.12931	-0.12977	+0.36%

Table 1: Forces and moments coefficients, F-16XL

the results from the simulation on the `sumo` grid. The critical $c_p^\star = -0.052$ is indicated by the solid black line. The main observation is the forward shift of the

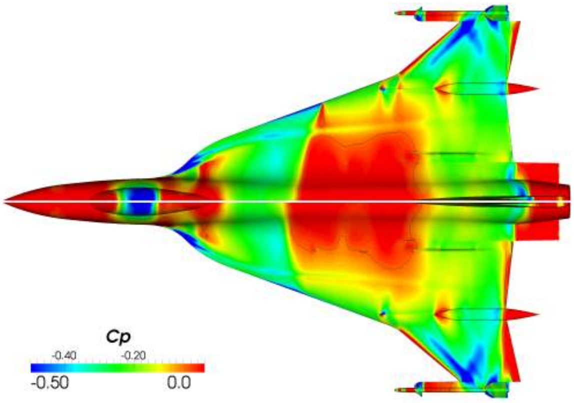

Figure 11: Surface pressure comparison for F-16XL

shock over the main wing, leading to a distortion in the entire flow topology of the `sumo` grid solution. Further studying the tetrahedral region (see Figure 12) in the near-field around the body, it is clear that the

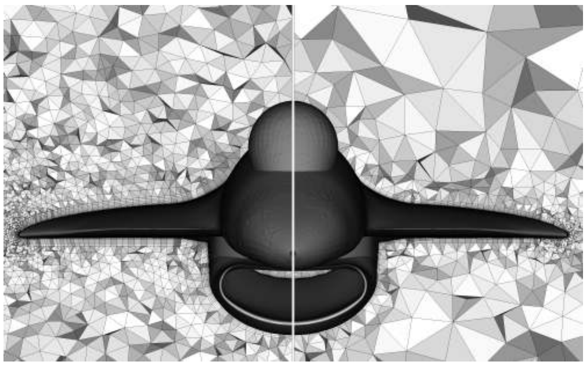

Figure 12: Grid comparison of near-field tetrahedral resolution for F-16XL case

`sumo` produced grid (right) has a significantly lower resolution in the tetrahedral domain compared to the `TriTet`-mesh (left).

At the time of writing, attempts to re-create the `sumo`-mesh with a more refined tetrahedral near-field region were unsuccessful. For this very intricate geometry, the rather complex envelope surface proved to be unsuitable for the generation of a high-quality tetrahedral mesh using the Delaunay-based algorithm implemented in `TetGen`.

5.1 Mesh generation performance

In Table 2, the size and computing time needed for the generation of the different hybrid grids used above

Grid	Generation time Prisms	[h:min:sec] Total	Surface triangles	Prism cells	Tet cells	Total cells	Total nodes
CRM TriTet	1:32:45	7:20:32	1212k	34.3M	15.1M	50.1M	20.3M
CRM ICEM-CFD	1:18:56	(1:51:23)	1212k	42.4M	14.2M	57.9M	23.7M
CRM sumo	0:02:01	0:10:17	1295k	45.4M	17.6M	62.9M	25.8M
F-16XL TriTet	0:17:30	4:50:21	316k	12.2M	14.8M	27.2M	8.8M
F-16XL sumo	0:00:56	0:04:11	593k	20.9M	3.4M	24.3M	11.1M

Table 2: Sizes and generation times of the computational grids.

are shown. Note that, depending on the specific geometry in question, the achievable degree of automation/scripting, and user experience, some of the tools listed may require non-negligible manual efforts, which is not considered here. Use of `sumo` entails only the setting of a small number of parameters, such as the desired height of the first cell and the number of layers.

While the method used in `sumo` has been outlined in Section 3, a short explanation is needed for the two other mesh generators mentioned in Table 2. The mesh generator `TriTet` [20] builds up the prismatic region layer by layer, whereupon the tetrahedral domain is gradually filled by means of a serial advancing front method. For the CRM case, which is typical in this respect, about 80% of the computing time expended by `TriTet` is used by the tetrahedral mesh generation phase.

The commercial software ICEM-CFD incorporates multiple algorithms for hybrid mesh generation. An advancing front method conceptually similar to the approach implemented in `TriTet` requires somewhat longer computing times than the latter. The mesh listed in Table 2, however, was generated with an algorithm resembling the procedure employed by `sumo`, where the prismatic region envelope is generated once and then split into pentahedral cells, while the surrounding volume is filled by means of a Delaunay tetrahedralization. This process is substantially faster at just below 2 hours, but does not immediately result in a mesh which passes the preprocessor of the Edge flow solver. Additional investigations into the controlling parameters are therefore needed before a fully representative comparison can be established.

For a resolution comparable to the `TriTet` mesh, i.e. 25.8 million nodes, `sumo` required a total computation time of slightly more than 10 minutes. A mesh for the F-16XL configuration with 11.1 million nodes was created in just over 4 minutes total time. It should be pointed out, however, that in this case the near-field resolution of the tetrahedral mesh turned out to be insufficient as explained above.

6 Conclusions

When comparing the mesh generation timings, an interesting observation can be made. For the common situation where parallel CFD solutions are performed on a compute cluster, the analyst may be evaluating post-processed results of a simulation based on a `sumo`-generated mesh before an advancing front mesh has been generated. This must be seen as a substantial advantage of the presented open-source method.

Obviously, this does not mean that there is no need for high-quality advancing-front mesh generation tools. A substantial proportion of relevant geometries and flight conditions likely require more detailed control over mesh generation parameters than what is available in a hybrid Delaunay method. However, for routine solutions where serial mesh generation time is a bottleneck, `sumo` or the underlying libraries can be used to accelerate the turnaround time considerably.

Unfortunately, the level of robustness originally aimed for has not yet been reached. There are still geometric configurations for which the envelope construction technique employed here fails to create a surface of sufficient quality, even when this should be geometrically possible. Additionally, a small number of degenerate, but relevant local geometric features can prevent the underlying approach from succeeding at all unless multiple vertex normals are allowed. Hence, this option will be evaluated for future inclusion in `sumo`.

Future developments should furthermore include the ability to re-mesh symmetry planes or other special boundary surfaces to match the adjacent pentahedral elements. A flexible solution of this particular problem does however, require that a representation of the surface geometry of the specific boundaries is available.

7 Bibliography

References

[1] ANSYS, Inc. *ANSYS ICEM CFD 12.1 USER MANUAL*, 2009. Available from: http://www.ansys.com.

[2] T. Baker. Mesh Generation for the Computation of Flowfields over Complex Aerodynamic Shapes. *Computers Math. Applic.*, 24(5/6):103–127, 1992.

[3] T. J. Baker. Mesh Generation: Art or Science? *Progress in Aerospace Sciences*, 41:29–63, 2005. doi:10.1016/0898-1221(92)90044-I.

[4] O. J. Boelens, K. J. Badcock, S. Gortz, S. Morton, W. Fritz, S. L. Jr. Karman, T. Michal, and J. E. Lamar. Description of the F-16XL Geometry and Computational Grids Used in CAWAP. *Journal of Aircraft*, 46(2):369–376, 2009.

[5] L. P. Chew. Guaranteed-Quality Mesh Generation for Curved Surfaces. In *Proceedings of the Ninth Annual Symposium on Computational Geometry*, San Diego, May 1993.

[6] P. Eliasson. Edge, a Navier-Stokes solver for unstructured grids. In *Finite Volumes for Complex Applications III*, pages 527–534, June 2002.

[7] R.V. Garimella and M.S. Shephard. Boundary layer mesh generation for viscous flow simulations. *International Journal for Numerical Methods in Engineering*, 49(1-2):193–218, 2000.

[8] Y. Ito. Challenges in unstructured mesh generation for practical and efficient computational fluid dynamics simulations. *Computers & Fluids*, 2012. Article in press. doi:10.1016/j.compfluid.2012.09.031.

[9] Y. Ito and K. Nakahashi. Improvements in the reliability and quality of unstructured hybrid mesh generation. *International Journal for Numerical Methods in Fluids*, 45(1):79–108, 2004.

[10] H. Luo, S. Spiegel, and R. Löhner. Hybrid Grid Generation Method for Complex Geometries. *AIAA Journal*, 48(11):2639–2647, 2010. doi:10.2514/1.J050491.

[11] C. J. Obara and J. E. Lamar. Overview of the Cranked-Arrow Wing Aerodynamics Project International. *Journal of Aircraft*, 46(2):355–368, 2009. doi:10.2514/1.34957.

[12] S. Z. Pirzadeh. Advanced Unstructured Grid Generation for Complex Aerodynamic Applications. *AIAA Journal*, 48(5):904–915, 2010. doi:10.2514/1.41355.

[13] D. Poirier, S. Allmaras, D. McCarthy, M. Smith, and F. Enomoto. The CGNS System. In *29th AIAA Fluid Dynamics Conference*. AIAA, June 1998. AIAA Paper 98-3007.

[14] A. Rizzi, A. Jirásek, J. E. Lamar, S. Crippa, K. J. Badcock, and O. J. Boelens. Lessons Learned from Numerical Simulations of the F-16XL Aircraft at Flight Conditions. *Journal of Aircraft*, 46(2):423–441, 2009. doi:10.2514/1.35698.

[15] S. Crippa. Improvement of Unstructured Computational Fluid Dynamics Simulations Through Novel Mesh Generation Methodologies. *Journal of Aircraft*, 48(3):1036–1044, 2011. doi:10.2514/1.C031219.

[16] H. Si. On Refinement of Constrained Delaunay Tetrahedralizations. In *Proceedings of the 15th International Meshing Roundtable*, September 2006.

[17] H. Si and K. Gaertner. Meshing Piecewise Linear Complexes by Constrained Delaunay Tetrahedralizations. In *Proceedings of the 14th International Meshing Roundtable*, pages 147–163, San Diego, September 2005.

[18] G. Thürmer and C. A. Wüthrich. Computing vertex normals from polygonal facets. *J. Graph. Tools*, 3(1):43–46, 1998.

[19] M. Tomac and D. Eller. From Geometry to CFD Grids – An Automated Approach for Conceptual Design. *Progress in Aerospace Sciences*, 47(8):589–596, 2011. doi:10.1016/j.paerosci.2011.08.005.

[20] L. Tysell, T. Berglind, and P. Eneroth. Adaptive Grid Generation for 3D Unstructured Grids. In *6th International Conference on Numerical Grid Generation in Computational Field Simulations*, June 1998.

[21] J. Vassberg, M. DeHaan, M. Rivers, and R. Wahls. Development of a Common Research Model for Applied CFD Validation Studies. In *26th AIAA Applied Aerodynamics Conference*, 2008. doi:10.2514/6.2008-6919.

[22] J. Vassberg, M. DeHaan, and T. Sclafani. Grid generation requirements for accurate drag predictions based on OVERFLOW calculations. In *16th AIAA Computational Fluid Dynamics Conference*, 2003. AIAA paper 2003-4124.

Improving the performance of the CFD code Edge using LU-SGS and line-implicit methods

E. Otero
Dept. Aeronautics, KTH, SWEDEN

P. Eliasson
FOI, SWEDEN

Keywords: convergence acceleration, LU-SGS, parallelization, ordering techniques, implicit time-stepping, line-implicit.

Abstract

The implicit LU-SGS solver has been implemented in the code Edge to accelerate the convergence to steady state. Edge is a flow solver for unstructured grids based on a dual grid and edge-based formulation. LU-SGS has been combined with the line-implicit technique to improve convergence on the very anisotropic grids necessary for the boundary layers. LU-SGS works in parallel and gives better linear scaling with respect to the number of processors, than the explicit scheme. The ordering techniques investigated have shown that node numbering does influence the convergence and that the native orderings from Delaunay and advancing front generation were among the best tested. LU-SGS for 2D Euler and line-implicit LU-SGS for 2D RANS are two to three times faster than the explicit and line-implicit Runge-Kutta respectively. 3D cases show less acceleration and need a deeper study.

1 Introduction

Computational fluid dynamics (CFD) has become a significant tool routinely used in the aerodynamic design and optimization of aircraft. CFD tools are used from the conception phase to the production as preliminary tests of a specific aircraft design. CFD simulations have largely replaced experiments to provide aerodynamic data. However, computing time can become very costly, thus convergence acceleration techniques are needed to speed up CFD solvers.

Edge [1] is a flow solver for unstructured grids based on a dual grid and edge-based formulation on node-centered finite-volume discretization. Edge uses an explicit multistage Runge-Kutta time integration solver [1] . Agglomeration multigrid (MG) acceleration speeds up the convergence rate based on the Full Approximation Scheme/Storage (FAS) [2] for nonlinear problems. This is combined with the line-implicit method [3] for RANS stretched meshes and integrates implicitly in time along lines in regions where the computational grid is highly stretched.

Implicit schemes which mitigate the CFL time-step limit of explicit schemes are becoming more and more spread in the CFD field, for reducing simulation time. The use of an explicit or implicit scheme is considered when dealing with problems solved by time- (or pseudo-time-)stepping. The time-step will have an influence either on the accuracy of the solution for time-dependent problems or on the convergence to steady-state for non-linear problems. This paper considers computation of steady states and focuses on the speed of convergence to steady-state.

An Implicit Lower-Upper Symmetric Gauss-Seidel (LU-SGS) [4, 5, 6] solver has been implemented in the code Edge. The LU-SGS approximate factorization method is attractive because of its good stability properties and limited memory requirement. The method considers a linearization which is inexactly solved by a few steps of a symmetric Gauss-Seidel method through a forward and backward sweep. A proper matrix dissipation type block matrix implicit operator has been defined [7] and controls, by parameters in the artificial dissipation model, contributions to the diagonal blocks of the system matrix [6] to make them "heavier".

In this paper acceleration techniques are investigated and applied. The parallelization of the code with the Message Passing Interface (MPI) [8] is presented, followed by the study of the effect of the node orderings [9] [10]. Then a line-implicit method [3] is combined with LU-SGS for stretched meshes.

2 Problem formulation

2.1 Governing Equations

The Reynolds-Averaged Navier-Stokes (RANS) equations are solved by Edge in conservation form for correct capturing of discontinuities such as shock waves. The conservation-law form of the Navier-Stokes equations concern the mass, momentum and energy and can be formulated as in Eq. (1).

$$\frac{\partial \boldsymbol{U}}{\partial t} + \nabla \cdot \boldsymbol{F} = Q \tag{1}$$

where $\boldsymbol{U}$ is the vector of the conserved variables $\begin{pmatrix} \rho \\ \rho u \\ \rho v \\ \rho w \\ \rho E \end{pmatrix}$ with E the total energy, ρ the density, and u, v, w the velocities. The pressure p is needed and computed from the conserved variables. Moreover $\boldsymbol{F} = \boldsymbol{F_I} + \boldsymbol{F_V}$, where $\boldsymbol{F_I}$ is the matrix of the inviscid fluxes and $\boldsymbol{F_V}$ is the matrix of the viscous flux,

$$\boldsymbol{F_I} = \begin{pmatrix} \rho u & \rho v & \rho w \\ \rho u^2 + p & \rho v u & \rho w u \\ \rho u v & \rho v^2 + p & \rho w v \\ \rho u w & \rho v w & \rho w^2 + p \\ u(\rho E + p) & v(\rho E + p) & w(\rho E + p) \end{pmatrix}$$

$$\boldsymbol{F_V} = \begin{pmatrix} 0 & 0 & 0 \\ \tau_{xx} & \tau_{yx} & \tau_{zx} \\ \tau_{xy} & \tau_{yy} & \tau_{zy} \\ \tau_{xz} & \tau_{yz} & \tau_{zz} \\ (\tau \boldsymbol{W})_x + \boldsymbol{q}_x & (\tau \boldsymbol{W})_y + \boldsymbol{q}_y & (\tau \boldsymbol{W})_z + \boldsymbol{q}_z \end{pmatrix}$$

with $\boldsymbol{W} = \begin{pmatrix} u \\ v \\ w \end{pmatrix}$ the primitive variables, $\boldsymbol{\tau}_{ij} = \mu \left(\frac{\partial W_i}{\partial x_j} + \frac{\partial W_j}{\partial x_i} \right) - \frac{2}{3} \mu \nabla \boldsymbol{W} \delta_{ij}$ the stress tensor, and $\boldsymbol{q}$ the conductive heat flux according to the Fourier's law.

The integral form of the Navier-Stokes equations (Eq. (1)) over a control volume Ω contained in the surface S reads as Eq. (2)

$$\int_\Omega \frac{\partial \boldsymbol{U}}{\partial t} d\Omega + \int_S (\boldsymbol{F_I} + \boldsymbol{F_V}) \boldsymbol{n} dS = \int_\Omega \boldsymbol{Q} d\Omega \tag{2}$$

where $\boldsymbol{n}$ is the outward normalized normal vector to S.

The control volume is defined by the so called dual grid and surrounds each node of the generated grid, connected by edges. A surface $\boldsymbol{n}S$ is given for each edge.

To the integral form (Eq. (2)) is applied a finite-volume discretization, Eq. (3), to the control volume V_0 surrounding the node v_0.

$$\begin{aligned} &\frac{d}{dt}(\boldsymbol{U}_0 V_0) + \sum_{k=1}^{m_0} \boldsymbol{F}_{I_{0k}} \boldsymbol{n}_{0k} S_{0k} \\ &+ \sum_{k=1}^{m_0} \boldsymbol{F}_{V_{0k}} \boldsymbol{n}_{0k} S_{0k} = \boldsymbol{Q}_0 V_0 \end{aligned} \tag{3}$$

with m_0, the number of neighbors to node v_0.

2.2 Implicit time-stepping

The resulting equations in Eq. (4) are discretized in time by the implicit (or Backward)

Euler ("BE") method to produce the final discretized system, Eq. (5).

$$V.\frac{d\boldsymbol{U}}{dt} + \boldsymbol{R}\left(\boldsymbol{U}\right) = 0 \tag{4}$$

$$V \cdot \frac{\boldsymbol{U}^{n+1} - \boldsymbol{U}^{n}}{\Delta t} + \boldsymbol{R}\left(\boldsymbol{U}^{n+1}\right) = 0 \tag{5}$$

The linearization of the residual $\boldsymbol{R}(\boldsymbol{U}^{n+1})$ by Eq. (6)

$$\boldsymbol{R}\left(\boldsymbol{U}^{n+1}\right) \approx \boldsymbol{R}\left(\boldsymbol{U}^{n}\right) + \frac{\partial \boldsymbol{R}\left(\boldsymbol{U}^{n}\right)}{\partial \boldsymbol{U}} \Delta \boldsymbol{U}^{n} \tag{6}$$

leads to a linear system of the form $\boldsymbol{M}\boldsymbol{x} = \boldsymbol{b}$, Eq. (7), to be solved approximately by an iterative linear solver.

$$\underbrace{\left(\frac{1}{\Delta t}V + \frac{\partial \boldsymbol{R}\left(\boldsymbol{U}^{n}\right)}{\partial \boldsymbol{U}}\right)}_{\boldsymbol{M}} \underbrace{\Delta \boldsymbol{U}^{n}}_{\boldsymbol{x}} = \underbrace{-\boldsymbol{R}\left(\boldsymbol{U}^{n}\right)}_{\boldsymbol{b}} \tag{7}$$

with

$$\Delta \boldsymbol{U}^{n} = \boldsymbol{U}^{n+1} - \boldsymbol{U}^{n} \tag{8}$$

and $\boldsymbol{M}$ and $\boldsymbol{b}$ are defined as the Left Hand Side (LHS) and Right Hand Side (RHS) respectively.

This implicit formulation approaches the Newton method as $\frac{1}{\Delta t} \to 0$. In this sense one can make assumptions about the convergence when approaching a zero value for the residual $\boldsymbol{R}$ where Newton's method has a quadratic convergence.

The implicit operator $\boldsymbol{M}$ can be constructed for an optimized convergence rate without affecting the solution limit $\boldsymbol{U}^n, n \to \infty$. If $\boldsymbol{A} = \frac{\partial \boldsymbol{R}(\boldsymbol{U})}{\partial \boldsymbol{U}}$ is the exact Jacobian, time-stepping becomes efficient because the spectrum of the linearized system will be significantly compressed compared to the original dynamic system. However this would require the storage and inversion of a big matrix. Since the steady solution is independent of $\boldsymbol{M}$, we try to find a compromise between computational cost of producing $\boldsymbol{M}$ and solving the system Eq. (7), and the loss of accuracy by approximation and inexact solution, [7].

Approximative methods for the construction of the Jacobian for different space discretizations are discussed in e.g. [11] and [12]. We have chosen the LU-SGS iterative method to solve the system. A special effort was previously made to define a proper LHS operator independently of the RHS for the best convergence [7]. A matrix dissipation operator shown to be the most optimized method offering parameters of freedom to increase the diagonal dominance of the system matrix and hence the linear convergence rate [7]. The following work is based on this first investigation.

3 LU-SGS solver

LU-SGS is an iterative solver developed by Jameson and Yoon [13], initially created for structured meshes and later on for unstructured meshes. It is almost matrix-free in the sense that one does not need to store the whole matrix but just access it by matrix-vector products and only a sequence of small $k \times k$ linear systems with k the number of unknowns per node needs to be solved by Gaussian elimination.

The LU-SGS scheme is related to the Symmetric Gauss-Seidel (SGS) relaxation method. First the block system matrix $\boldsymbol{M}$ is decomposed into a block lower triangular part $\boldsymbol{L}$, a block diagonal $\boldsymbol{D}$, and a block upper triangle $\boldsymbol{U}$ as Eq. (9). A block is the set of unknowns per node.

$$\boldsymbol{M}\boldsymbol{x} = (\boldsymbol{L} + \boldsymbol{D} + \boldsymbol{U})\boldsymbol{x} = \boldsymbol{b} \tag{9}$$

The SGS iteration is composed by sweeps, backward and forward,

$$\begin{aligned} \left(\boldsymbol{D} + \boldsymbol{L}\right)\boldsymbol{x}^{*} &= \boldsymbol{b} - \boldsymbol{U}\boldsymbol{x}^{\boldsymbol{n}} \\ \left(\boldsymbol{D} + \boldsymbol{U}\right)\boldsymbol{x}^{\boldsymbol{n}+\boldsymbol{1}} &= \boldsymbol{b} - \boldsymbol{L}\boldsymbol{x}^{*} \end{aligned} \tag{10}$$

If one restricts the number of forward and backward sweeps to one, the system simplifies to Eq. (11) with an initial solution $x^0 = 0$, giving then the present LU-SGS iteration.

$$\begin{aligned} \left(\boldsymbol{D} + \boldsymbol{L}\right)\boldsymbol{x}^{*} &= \boldsymbol{b}, \\ \left(\boldsymbol{D} + \boldsymbol{U}\right)\boldsymbol{x}^{1} &= \boldsymbol{b} - \boldsymbol{L}\boldsymbol{x}^{*} \end{aligned} \tag{11}$$

Since the SGS iterations are done inside each time-step, these are called inner or linear iterations. The number of linear iterations is retained as a tunable parameter. Moreover the implementation will focus on Eq. (10) with a minimal memory requirement of the order of $\mathcal{O}(N)$.

4 MPI parallelization

4.1 LU-SGS analysis

Before considering the parallelization using MPI we have to understand the data dependencies of the solution algorithms. The data dependencies are linked to the ordering of the unknowns and equations. For Edge, the ordering is associated with the graph of the grid so the ordering of unknowns and equations follows from the node numbering. Edge is parallelized by domain decomposition, so the Gauss-Seidel iteration only runs into trouble at inter-domain boundaries. Figure 1 illustrates the parallelization issue for a simple 1D case, with nodes numbered sequentially along the line, and two processors. Inside each subdomain, the algorithm runs without interruption, but as seen in Fig. 1, during the forward sweep, processor 2 cannot start to compute on domain i until processor 1 has finished updating domain i-1. In the backward sweep processor 1 would have to wait for processor 2.

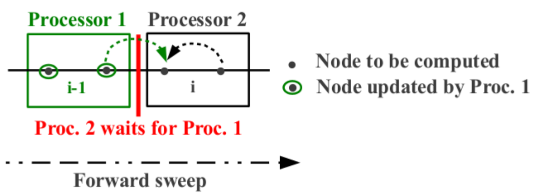

Figure 1: LU-SGS data dependency. 1D case

Analogous problems appear for any domain decomposition. We understand then, that the original LU-SGS algorithm does not parallelize in a straightforward way by domain decomposition.

4.2 Implementation

Clearly we wish to retain the LU-SGS convergence speed also after domain decomposition. Parallelization of LU-SGS proceeds by processors *not* waiting for updated values. Sharov, Luo, Baum and Löhner in [5] refer to this as a hybrid approach to exchange interprocessor data, and in the context of elliptic equations has been called chaotic updating.

This parallel LU-SGS version has been implemented as in Fig.2. The MPI data communication is executed after each forward sweep and for multiple iterations also at the end of each iteration after the backward sweep.

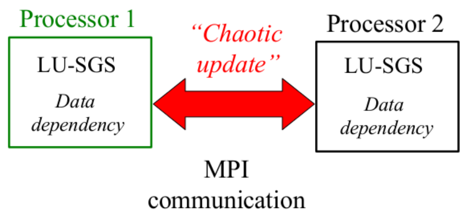

Figure 2: MPI LU-SGS parallelization

The degree of convergence deceleration suffered by the proposed scheme compared to a sequential LU-SGS will be looked into in the parallelization of LU-SGS.

5 Ordering techniques

From the strong data dependency of LU-SGS follows that the ordering of the nodes will influence the LU-SGS convergence. It is natural to look for the optimal ordering, but it is very hard to find for unstructured grids. The idea has been then to limit the search to *numberings which make geometric neighbor nodes have small number differences*. We start with variants of methods developed for low fill-in in Gaussian elimination on sparse matrices. In our setting, which never creates the "big" matrix for elimination, such orderings would provide spatial and temporal data locality which means to use data closely stored in the memory (spatial locality) or being reused as much as possible (temporal locality).

The Cuthill-McKee (CM) algorithm [9] groups by levels the nodes in the mesh. The nodes are ordered by increasing order of degree corresponding to the number of neighboring nodes. Reversing the final CM ordering produces the Reverse CM which may be the most used profile reduction ordering method [9]. The choice of starting node is a degree of freedom, and we add a physical approach to CM by first numbering the nodes along the boundaries, namely the airfoil wall and the outer boundary. The levels created will follow the desired starting boundary as shown in Fig. 3 to make numbering in layers.

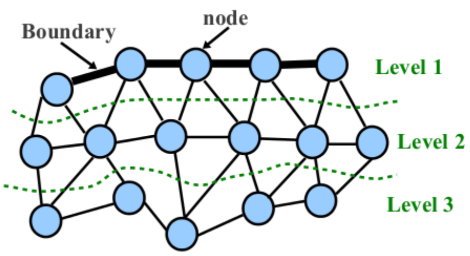

Figure 3: Level structure from strong boundary

6 Line-implicit LU-SGS

6.1 Definition

Another version of LU-SGS consists in combining the original LU-SGS implementation with a line-implicit method. By this combination we expect to improve the convergence in the prismatic stretched grids needed for resolution of boundary layers and wakes in RANS computations. The line-implicit method [3] consists in integrating the flow equations implicitly in time along structured lines in stretched regions of the grid, usually in the boundary layer. Figure 4 shows the implicit lines (emphasized) in the structured stretched area surrounded by an unstructured grid. The lines are the edges transversal to the prism layers.

The implementation of these combined schemes results in splitting the linear system of Eq. (7) into two parts. The first one corresponds to the anisotropic part where the lines are defined and the line-implicit method is applied. The remaining part computes the isotropic part by the original LU-SGS.

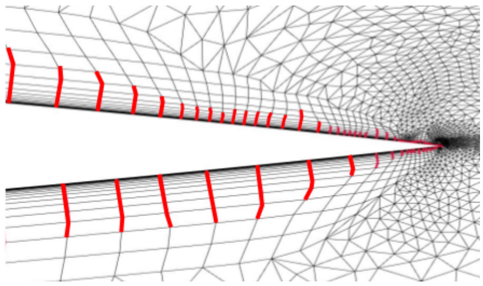

Figure 4: Implicit lines (emphasized) on stretched grid

6.2 Algorithm

The matrix $\boldsymbol{M}$ is split as $\boldsymbol{M} = \boldsymbol{L} + \boldsymbol{B} + \boldsymbol{T}$, with $\boldsymbol{T}$ corresponding to the block upper triangle $\boldsymbol{U}$ of the original LU-SGS, Eq. 9. The matrix $\boldsymbol{M}$ is ordered such that **B** contains the block diagonal and (possibly) blocksub- and blocksuper diagonals of the "implicit lines". Nodes are always strongly connected to nearest neighbors but also, depending on the spatial discretization scheme, to next nearest neighbors. This happens e.g. for the Jameson fourth order artificial dissipation terms or the Roe scheme extended to a High-Resolution scheme.

Figure 5 defines the block matrices $\boldsymbol{L}$, $\boldsymbol{B}$ and $\boldsymbol{T}$ whose dimensions vary with the size of the line to be solved.

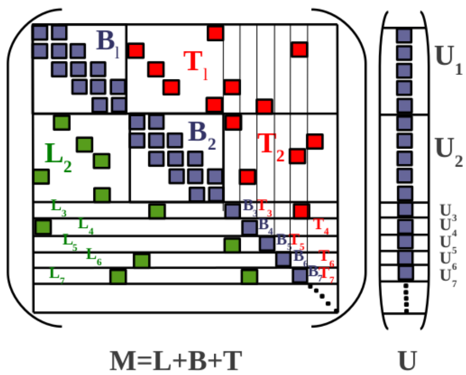

Figure 5: Linear system matrices definition

The line-implicit LU-SGS algorithm works such that when $\boldsymbol{B}$ is only the block-diagonal it solves by nodes with the original LU-SGS and when $\boldsymbol{B}$ includes the blocksub- and blocksuper-diagonals, LU-SGS is combined with the line-implicit method solving by lines.

The algorithm is line based in the sense that it works through lines computations. However inside each line it computes by nodes as the original LU-SGS, taking advantage of the sparsity of the matrices. A line l can have a size $nl > 1$ (line-implicit) or be a single node $nl = 1$ (LU-SGS). Initially a specific node ordering is created [14] and Section 5, which consists in storing all the lines followed by the remaining single nodes of the domain. For each line to be solved, the corresponding nl by z linear system block matrices are constructed, with $z \in [1 : N_{tot}]$ and N_{tot} the total number of nodes in the domain. Each kxk block in the matrix can be of size $k = 5$ for laminar 3D RANS problems or $k = 6$ for 3D RANS problems with Spalart-Allmaras one-equation model. This system can be expressed as a subset of the whole linear system (Eq. (7)) by the line indices l as shown in Eqs. (14) and (15) and the Fig. 5. This linear system is solved directly by LU decomposition.

In Eqs. (14) and (15) the line-implicit LU-SGS algorithm is presented using the following matrix annotations,

$$\boldsymbol{B}_{ii} = \frac{V_i}{\triangle t_i} + \sum_{j \in N(i)} \frac{\partial \boldsymbol{F}_{ij}}{\partial \boldsymbol{U}_i} \tag{12}$$

$$\{\boldsymbol{L}_{ij},\ \boldsymbol{T}_{ij}\}_{j \in N(i)} = \frac{\partial \boldsymbol{F}_{ij}}{\partial \boldsymbol{U}_j} \tag{13}$$

with $N(i)$, the set of neighboring nodes of node i.

The computations of Eqs. (14) and (15) apply to each line l of size nl or node if $nl = 1$. The total number of lines is defined by N_l. It can be noted that a computation by lines of one node each, implies N_l=N_{tot}. $\triangle \boldsymbol{U}^*$, $\triangle \boldsymbol{U}^n$ and $\triangle \boldsymbol{U}^{n+1}$ are initialized to zero. The algorithm is described inside an inner loop of N_{swp} sweeps.

For $iter = 1 : N_{swp}$

Forward sweep

For $l = 1, 2, \cdots, N_l$

$$\begin{aligned}\boldsymbol{B}_l \triangle \boldsymbol{U}_l^* = -\boldsymbol{R}_l - \boldsymbol{L}_l \triangle \boldsymbol{U}^* \\ -\boldsymbol{T}_l \triangle \boldsymbol{U}^n\end{aligned} \tag{14}$$

Backward sweep

For $l = N_l, N_l - 1, \cdots, 1$

$$\begin{aligned}\boldsymbol{B}_l \triangle \boldsymbol{U}_l^{n+1} = -\boldsymbol{R}_l - \boldsymbol{T}_l \triangle \boldsymbol{U}^{n+1} \\ -\boldsymbol{L}_l \triangle \boldsymbol{U}^*\end{aligned} \tag{15}$$

$n = n + 1;$

End $iter$;

7 Numerical Results

The convergence rate (residual decrease per time-step) and residual decrease vs. wall clock time are used for comparison with the Edge standard scheme, the explicit Runge-Kutta method. Multigrid acceleration and local time-steps are used in both LU-SGS and Runge-Kutta methods. The iteration number is the number of time-steps, each including a MG-cycle usually through three grid levels.

7.1 Ordering techniques

Structured meshes

The ordering from the generation of the structured single block 2D C-type mesh is lexicographic. Figure 6, where the z-axis counts node number, shows the ordering resulting from starting along the wake and boundary airfoil wall and ending at the outer layer of the C-type mesh.

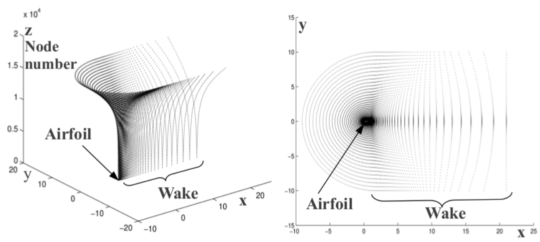

Figure 6: C-type mesh

Figure 7 shows the convergence of the different ordering techniques implemented based on the CM algorithm compared to the lexicographic ordering. The CM methods differ by the initial vectors which contain different sequences of node numbers and can have some sections reversed. These initial vectors preserve the pattern from the lexicographic ordering method, following the airfoil and wake. These similar patterns give however slower convergences than the lexicographic ordering (Fig. 7). It turns out that many variations on this theme give non-convergent iterations which are sensitive to the starting vector of the CM algorithm.

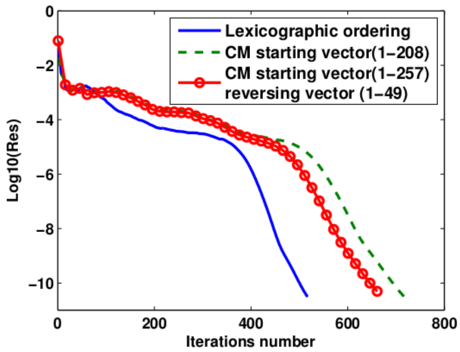

Figure 7: Ordering techniques. C-type mesh

Unstructured meshes

Unstructured grids are usually generated by advancing front (AF) or Delaunay methods, and we compare such orderings with the CM variants. The original ordering comes from an advancing front technique, Fig. 8, with the airfoil in the center. The fronts start at airfoil and outer boundary and advance, numbering the points in the process, until collision as can be observed by the free nodes remaining.

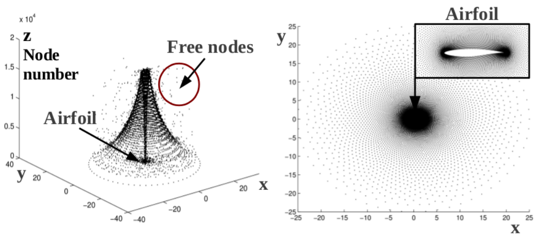

Figure 8: Advancing front ordering shape

Figure 9 illustrates the CM ordering path starting at the airfoil (cf. zoom) and at the outer boundary. As we can observe, CM follows exactly the pattern creating level structures (Fig. 3)

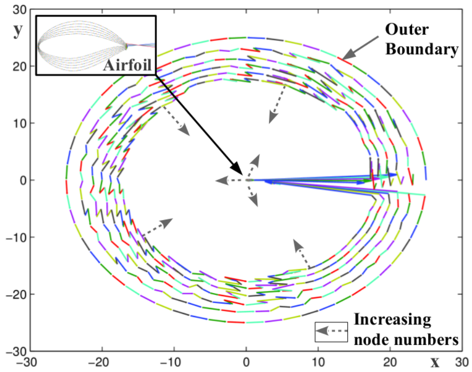

Figure 9: CM ordering starting at the strong boundaries

We can notice in Fig. 10 a), that the shapes from CM and advancing front (Fig. 8) look almost identical. The difference is that the nodes which are created when the advancing fronts collide and seem "randomly" numbered in AF have been brought into the pattern by CM. This cleaner technique, *CM outer-wall*, leads to similar convergence acceleration than AF as shown in Fig. 10 d). Other patterns as *increasing x* coordinate have given slower convergence.

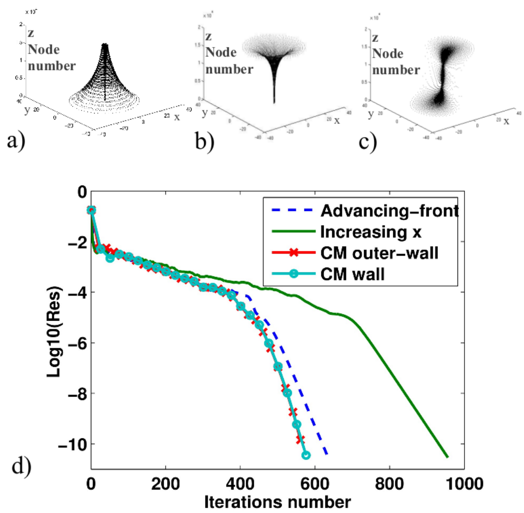

Figure 10: Ordering techniques. Shapes: CM outer-wall (a), CM wall (b), increasing x (c). Residual convergences (d)

7.2 MPI parallelization

The results shown in Figs. 11 and 12 are for inviscid transonic Mach 0.8 flow at 1.25° angle of attack on 2D viscous mesh.

The extremely low degree of convergence deceleration suffered by the proposed scheme compared to a sequential LU-SGS is shown in Fig. 11. This means that LU-SGS solver can be parallelized with little ill effects on convergence rate.

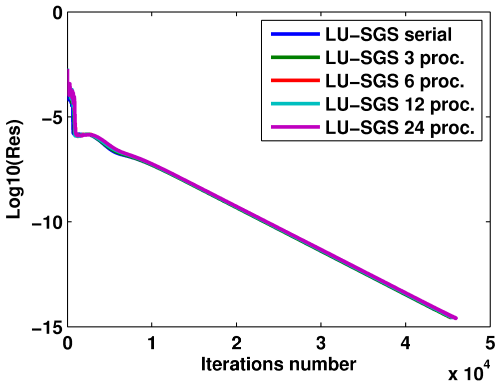

Figure 11: Residual convergence in iterations for different number of processors. NACA airfoil stretched mesh, 54K nodes.

Moreover Fig. 12 shows that LU-SGS scales linearly with number of processors.

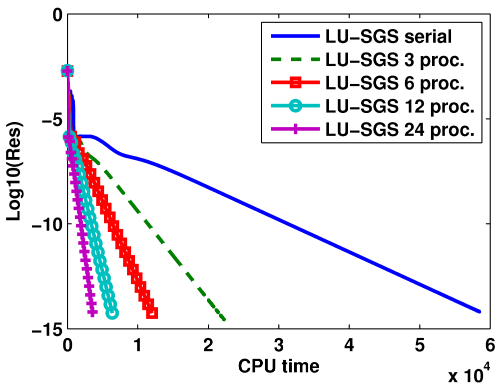

Figure 12: Residual convergence in time for different number of processors. NACA airfoil stretched mesh, 54K nodes.

The speed-ups obtained can be found in Fig. 13. The computations have been run for 3D case with 1.7M grid points in RANS simulations. Linear speed up is observed up to 32 processors. LU-SGS shows better scalability than Runge-Kutta because of the increased processor-local work required by the linear algebra work.

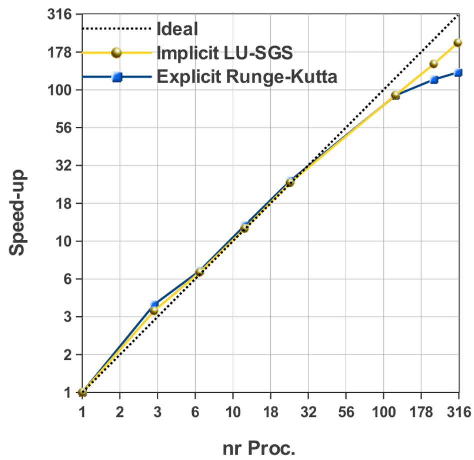

Figure 13: Speed-up for RANS computations in a 3D case (LANN wing), 1.7M points. 1-312 processors.

7.3 Line-implicit LU-SGS

The combined line-implicit LU-SGS has been run for 2D RANS turbulence model computations with 4 processors. The lines were computed on the prismatic layer defined on Fig. 14. Other line definitions by extending the stretched lines outside the boundary layer or by creating new lines outside the prismatic layer did not improve the convergence. The creation of lines in an isotropic mesh does not seem to make sense.

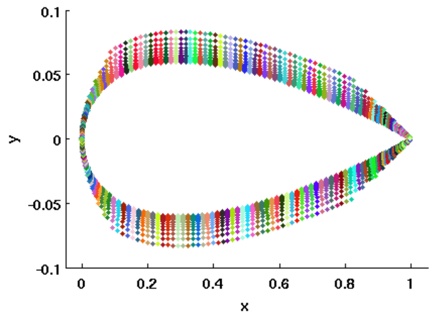

Figure 14: Stretched lines in the prismatic layer.

The efficiency of the combined solver is illustrated in Figs. 15 and 16. The convergence in iterations is 10 times faster than the line-implicit Runge-Kutta solver (Fig. 15) and 3 times faster in time (Fig. 16). By increasing the number of inner iterations or sweeps *Nswp* to 3, the convergence rate increases by a factor almost of 2 compared to one sweep indicating the convergence of the linear solution scheme in line-implicit LU-SGS.

The improvement with respect to the original LU-SGS is relevant being 9 times faster in iterations (Fig. 15) and almost 7 times faster in time (Fig. 16). As expected for RANS meshes, explicit Runge-Kutta is clearly the most inefficiant solver.

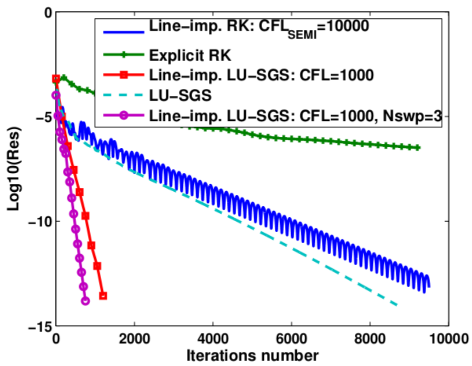

Figure 15: Line-implicit methods, convergence in iterations. 2D RANS turbulence model, 4 processors.

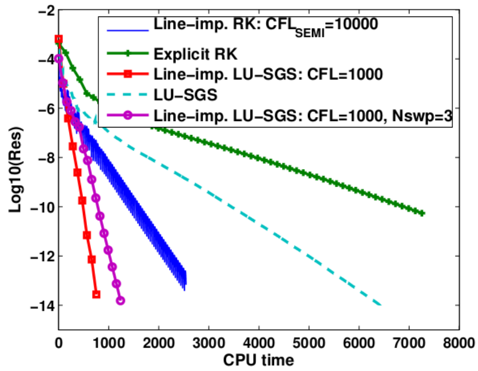

Figure 16: Line-implicit methods, convergence in time. 2D RANS turbulence model, 4 processors.

7.4 Euler and RANS computations

2D and 3D Euler, RANS and turbulence model computations have been run with unstretched (Euler) and stretched (RANS) meshes. The RANS mesh has a cell aspect ratio of 15,000 and a normal distance from the solid surface to the first interior node of 10^{-6} chord length. The number of grid points was of 16K and 54K in 2D and of 226K and 1.3M in 3D, for unstretched and stretched mesh respectively.

The results are shown in Figs. 17 and 18 below. For 2D simulations Figs. 17 a) and 18 a), LU-SGS has accelerated the convergence rate by a factor of 4 or 8 respectively and the computing time by a factor of 2 . 3D Euler cases Fig. 17 b) show no improvement; the increased convergence rate is slower than for 2D and is compensated by the increased computing time per step. However for 3D RANS computations Fig. 18 b), line-implicit LU-SGS is almost twice faster in time than line-implicit Runge-Kutta.

Computing times per step for inviscid, RANS laminar viscous, and RANS with Spalart-Allmaras turbulence model are shown in Table 1. The floating point work for LU-SGS as well as the Runge-Kutta scheme is proportional to the number of edges in the mesh graph and one would expect these ratios to be independent of spatial dimension, grid size, etc. But they do depend on the hardware since the compute/memory traffic ratio is different for the linear algebra of LU-SGS and the flux computations that dominate the RK scheme.

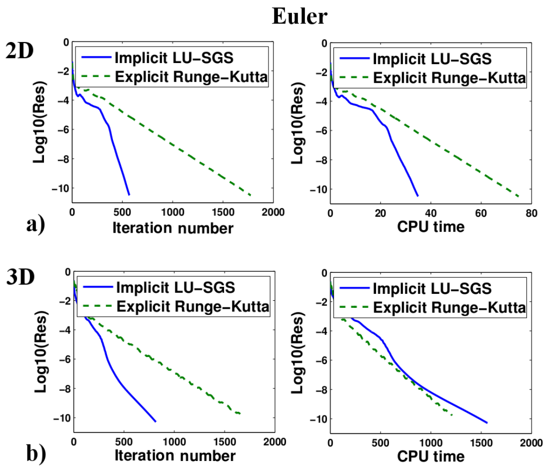

Figure 17: Euler parallel computations on unstretched grid for NACA airfoil with 8 processors (a) and M6 wing with 4 processors (b). Residual convergences in iterations (left) and time (right).

Table 1: Time in seconds (s) per iteration (It.); RANS on M6 wing 3D stretched mesh

	Euler	Laminar	RANS
LU-SGS [time(s)/It.]	29.9	68.6	90
RK [time(s)/It.]	9.2	13.1	15.7
RATIO LU-SGS/RK	3.3	5.2	5.7

Table 2 summarizes the LU-SGS convergence rates in decades of residual reduction per 1000 iterations. Different cases are considered, namely Euler and RANS simulations for 2D and 3D problems. LU-SGS solver shows to be most efficient for Euler computations. For RANS turbulence model cases, the best performance has been obtained with the combined line-implicit LU-SGS method.

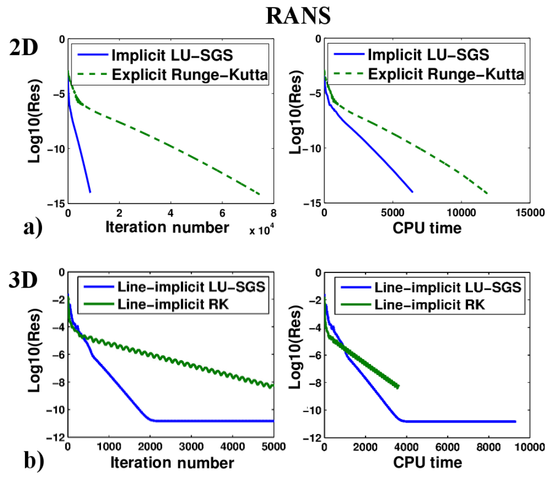

Figure 18: RANS turbulence model parallel computations on stretched grid for NACA airfoil with 4 processors (a) and CRM wing-body with 72 processors (b). Residual convergences in iterations (left) and time (right).

Table 2: Residual reduction in decades per 1000 iterations

Simulation	Decades /1000 It.	
	2D	**3D**
Euler (unstretched mesh)	23	8
RANS (stretched mesh) *Line-implicit LU-SGS*	10	5

8 Conclusion

The overall conclusion is that LU-SGS does provide faster computation and scales better on distributed memory machines than the original. The LU-SGS iteration as multigrid smoother does increase the convergence rate to steady state for all the flow models tested: transonic Euler, laminar Navier-Stokes, and RANS with turbulence model. The runtime scales linearly with number of processors and the chaotic update scheme used to approximate the Gauss-Seidel update seems to have no ill effects. There are many parameters to tune but numerical experiments have led to default settings which seem robust. For 2D cases the wall clock time is about halved to reach residual reduction by ten decades compared to the explicit Runge-Kutta smoother. 3D cases give less acceleration and the gain is essentially outweighed by the computational effort spent on linear algebra. For RANS computations with very thin cells on solid boundaries, further acceleration can be obtained by accurately solving the strongest couplings in the linear system, i.e., in the prismatic mesh layers along the edges transversal to solid boundaries and wake mean surfaces. A combination of the line-implicit technique with LU-SGS was implemented. For 2D cases, this accelerated the convergence by a factor of 10 in iterations and 3 in time compared to line-implicit Runge-Kutta. 3D cases were improved by reducing the computing time by almost half. Node numbering does influence the convergence. The native orderings from structured as well as unstructured 2D meshes generated by advancing fronts or Delaunay methods were, fortunately, among the best tested. Further work is needed to improve performance for 3D grids.

References

[1] Edge, theoretical formulation. Technical Report 03-2870, FOI, 2010.

[2] A. Borzì. Introduction to multigrid methods. Technical report, Institut für Mathematik und Wissenschaftliches Rechnen, Karl-Franzens-Universität Graz, Austria.

[3] P. Eliasson, P. Weinerfelt and J. Nordström. Application of a line-implicit scheme on stretched unstructured grids. *47th AIAA Aerospace Sciences Meeting*, January 2009. Paper 2009-163.

[4] J.S. Kim and O.J. Kwon. An efficient implementation of implicit operator for block lu-sgs method. *Computational Fluid Dynamics*, pages 154–159, July 2005.

[5] D. Sharov, H. Luo, J. D. Baum and R. Löhner. Implementation of unstructured grid gmres+lu-sgs method on shared-memory,cache-based parallel computers. *AIAA*, 2000. Paper 2000-0927.

[6] R. P. Dwight. *Efficiency improvements of RANS-based analysis and optimization using implicit and adjoint methods on unstructured grids*. PhD thesis, Faculty of Engineering and Physical Sciences, University of Manchester, 2006.

[7] E. Otero, P. Eliasson. Convergence acceleration of the cfd code edge by lu-sgs. Venice, Italy, 24-28 October 2011. CEAS conference.

[8] B. Barney. Message passing interface (mpi). `https://computing.llnl.gov/tutorials/mpi/`.

[9] A. George and J. W-H Liu. *Computer Solution of Large Sparse Positive Definite Systems*. Prentice-Hall, Englewood Cliffs, New Jersey 07632, 1981.

[10] S. Le Borne. Ordering techniques for two- and three-dimensional convection-dominated elliptic boundary value problems. Technical report, Lehrstuhl Praktische Mathematik, Universität Kiel, Germany, 2000.

[11] S. Langer and D. Li. Application of point implicit runge-kutta methods to inviscid and laminar flow problems using ausm and ausm+ upwinding. *International Journal of Computational Fluid Dynamics*, July 2011. Vol. 25, No. 5, June 2011, 255-269.

[12] S. Langer. Application of a line implicit method to fully coupled system of equations for turbulent flow problems. *International Journal of Computational Fluid Dynamics*, June 2013. Vol. 27, No. 3, 131-150.

[13] A. Jameson and S. Yoon. Lower-upper implicit schemes with multiple grids for the euler equations. *AIAA*, pages 929–935, 1987. Vol. 25, No. 7.

[14] E. Otero. Acceleration of compressible flow simulations with edge using implicit time stepping, June 2012. Licentiate thesis, University of KTH, Stockholm.

4:th CEAS Air & Space Conference
FTF Congress: Flygteknik 2013

Acoustic Probes for Pressure Pulsation Measurement In Gas Turbine Flow Duct and Combustor

Vladimir P. Shorin, Asgat G. Gimadiev, Nickolay D. Bystrov and Victor Y. Sverbilov
Samara State Aerospace University, Russian Federation

Keywords: gas turbine, dynamic pressure probe, frequency response, compensator

Abstract

Instabilities in flow duct of aircraft and industrial gas turbines can produce intolerably large pressure waves, which lead to fatigue, detachment of components, and costly outages and repair. The measurement of dynamic pressure amplitudes within the combustion chamber and characteristic points of compressor and turbine may be used in condition monitoring analyses to detect and correct instabilities before they cause serious damage. However, the technical challenge in physically measuring dynamic pressure placing the sensor directly at the pick-up point is a significant one, especially within the high temperature environment of the gas turbine combustion chamber. The article considers indirect measurement that involves fitting small bleed tubes (or conduits) from the pick-up point to a pressure sensor placed at a less extreme temperature location. This permits the use of freely available industrial pressure transducers instead of expensive piezoelectric crystal devices. Proposed measurement techniques provide minimal distortion of the signal over a wide frequency range at small dimension of the probe and high reliability. The transmission line method is used for sizing the correcting device of the probe. The developed probes were implemented for dynamic pressure monitoring in aircraft engines.

1 Introduction

Pressure pulsations in a flow duct of the gas turbine engine provide key information on dynamic behavior and stability of the compressor and the combustor. Therefore measurements of pressure pulsations in characteristic points of low and high pressure are usually carrying out at the engine development (Fig. 1).

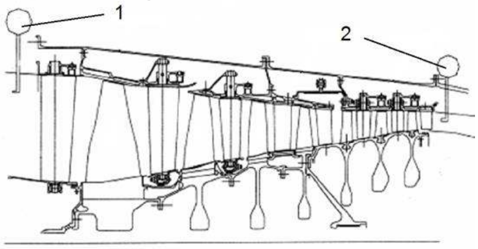

Fig.1 Pressure gauges at the input (1) and output (2) of the compressor

Two approaches are available today:

• Indirect Measurement,
• Direct Measurement.

The most effective solution for dynamic pressure is the Direct Measurement. A piezoelectric crystal device is proven to withstand the high temperatures of the combustion process and provide a reliable measurement system [1].

However, high temperature and a lack of space make it difficult to place the pressure sensor directly at the point of measurement in many cases. Indirect Measurements involve fitting small bleed tubes (or conduits) from the pick-up point to a pressure sensor located at a less extreme temperature location (Figure 2). This permits the use of freely available industrial pressure transducers.

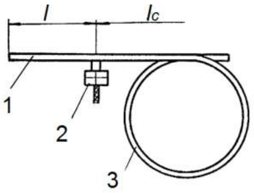

Fig.2 Acoustic probe: 1 – inlet channel, 2 – pressure gauge, 3 – correcting element (compensator)

2 Correcting elements

The inlet pipe brings distortions in transferring information especially at resonant frequencies. Some schemes and structures of acoustic probes were developed to decrease a dynamic error over a wide frequency range [2]. Figure 3 represents the probe with lumped compensator (acoustic resistor at the inlet) and Figure 4 - the device having distributed parameters. Their advantages are high accuracy and small dimensions.

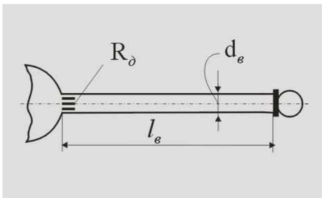

a

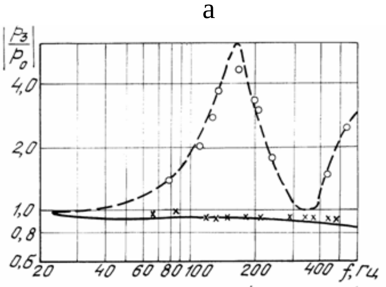

b

Fig. 3 Acoustic probe with resistive correcting element at the inlet (a) and its impact on the frequency response (b)

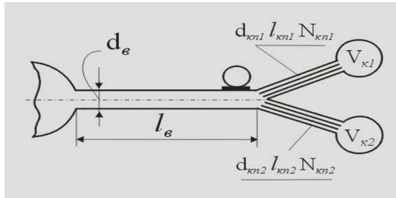

a

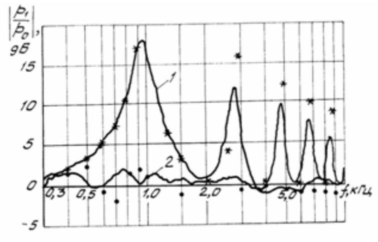

b

Fig. 4 Acoustic probe having elements with distributed parameters (a) and its impact on the frequency response (b)

The design example of the pressure probe is presented in Fig. 5. The corrective element is made in a form of a tube section filled with porous material.

Fig. 5 Pressure probe with porous compensator

3 Software

On the basis of the theory of acoustic circuits the mathematical model and the software (Fig. 6) for calculation of frequency characteristics of acoustic probes with uniform and non-uniform wave conduit (Fig. 7) regarding to gas temperature and the sectional area of the channel are developed.

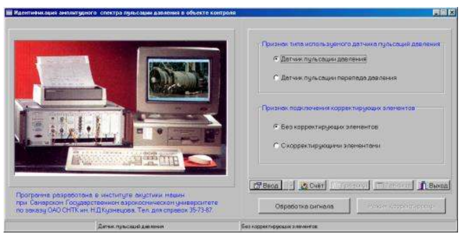

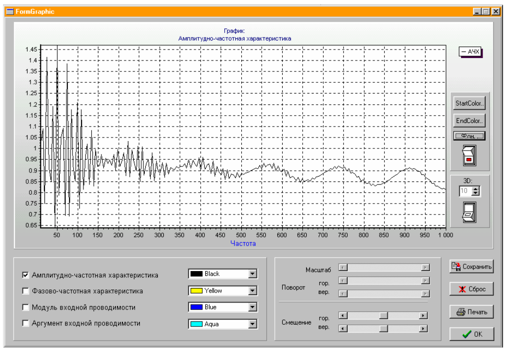

Fig. 6 Windows of the design program for parametric optimization of the acoustic probes

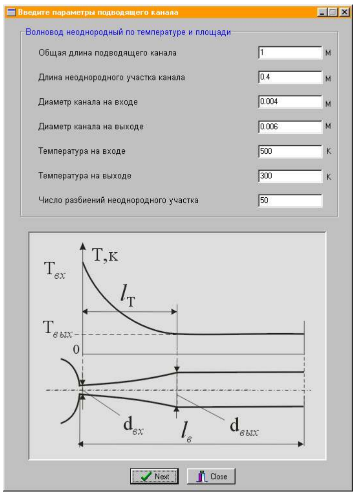

Fig. 7 Non-uniform wave conduit

The user can calculate optimal parameters of the probe for given temperature distribution on the length of the non-uniform channel within acceptable dynamic error. The instruments and the software developed provide high accuracy of a signal transfer from the pick-up point to the sensor.

After that the special software can perform additional reconstruction of the signal (if required) from the sensor deformed by the acoustic probe (Fig. 8).

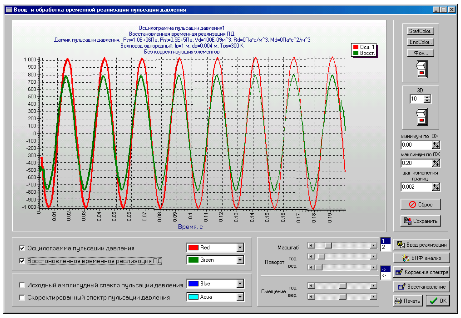

Fig. 8 Measured (green) and reconstructed (red) pressure oscillations

4 Conclusion

Indirect Measurement of pressure pulsations in gas turbine flow duct and combustor is presented. The general drawbacks of the indirect method - attenuation of the signal caused by the conduit length and distortions from acoustic resonance – are overcome using the acoustic probe of special design.

The acoustic probes and software presented are used for development tests of gas turbine engines demonstrating high accuracy and reliability at small dimensions.

References

[1] James C., Verhage A., "Dynamic Pressure Monitoring in Gas Turbines", SKF, November 2002. Available at the @ptitudeXchange site.

[2] Shorin V., Shakhmatov E., Gimadiev A. and Bystrov N., Acoustical methods and means for measuring of pressure pulsations, Samara State Aerospace University Publ., Samara, 2007, 132 pp. (in Russian)

Wind Tunnel Tests of a New Commuter Aircraft

S. Corcione and F. Nicolosi
Department of Industrial Engineering, Aerospace Engineering Division, University of Naples "Federico II", Via Claudio, 21 80125-Naples, Italy

P. Della Vecchia
Department of Industrial Engineering, Aerospace Engineering Division, University of Naples "Federico II", Via Claudio, 21 80125-Naples, Italy

Keywords: *wind tunnel tests, commuter aircraft, longitudinal and lateral-directional stability*

Abstract

Tecnam Aircraft Industries and the Department of Industrial Engineering (DII) of the University of Naples "Federico II" are deeply involved in the design of a new commuter aircraft. The wind tunnel tests campaign of the so called "P2012 Traveller" aircraft has been performed in the wind tunnel facility of the DII. Tests of a 1:8.75 scaled model have been performed on different configurations through a 3-component longitudinal and lateral directional internal strain gage balance, in order to estimate both longitudinal and lateral directional stability and control derivatives of the aircraft under investigation. Reynolds number during tests was about 0.55 million. Tests have been performed with transition strip placed on the all lifting surfaces(wing and tail-planes) at about 5% of the local chord. Many tests have been performed for different aircraft configurations with the aim to estimate the effects of the different components on the aerodynamic characteristics of the aircraft, (i.e. flaps rudder deflection, fuselage, nacelles, landing gear and winglets). Have been tested also 3 different positions of the horizontal plane, in order to evaluate its right positioning respect to the wing and ensure a good value of longitudinal static margin. Finally the complete aircraft lateral-directional stability and control derivatives have been evaluated, and the winglets effect on aircraft lateral stability has been highlighted.

1 Introduction

Commuter aircraft market is today related to old model. The major airlines in this segment have been demanding a replacement for many hundreds of "heritage" airplanes in the FAR23/CS23 category currently in service around the world - as many are now coming to the end of their useful commercial life. GAMA (General Aviation Manufacturer Association) 2011 Statistical Databook & Industry Outlook [1], which is usually a very useful and impressive source of data and statistics for general aviation, reports that the average age of general aviation registered aircraft is 46 years for single-engine piston powered aircraft and 15 years for single-engine turboprop aircraft. The average age for twin-engine 8-12 seats aircraft is 42 years for piston powered models and about 29 years for twin-engine turboprop commuter aircraft. These impressive data dramatically show the need of new aircraft model which will be characterized also by the application of new technologies like composite, light structures, new engines (with lower weight and lower fuel consumption) and new avionics and flight control systems. The main idea behind the introduction of the P2012 Traveller is ensuring that not only passenger demands for comfort and safety are met but that potential operators of the P2012 Traveller are now able to afford an airplane with significantly improved direct operating costs, more efficient maintenance procedures and appreciation for ensuring that the industry takes into account global environmental considerations such as the need for lower fuel burn and less noise emissions. The sizing of the P2012 has been accomplished through the use of classical methodologies and approach, like these ones suggested by Roskam [2], under the guidance of Prof. L. Pascale, designer of all Tecnam aircraft and known all over the world as one of the main expert in the design of general aviation aircraft.

Table 1 P2012 Traveller main external geometric data

Symbol	Description	Value
S_W	Wing area	25.4 m^2 (268.2 fts^2)
b_W	Wing span	14.0 m (45.9 fts)
AR_W	Wing Aspect Ratio	7.72
MAC_W	Wing mean aerodynamic chord	1.87 m (6.14 fts)
λ	Wing taper ratio	0.73
S_H	Horizontal tail plane area	6.10 m^2 (65.7 fts^2)
b_H	Horizontal tail plane span	5.70 m (18.7 fts)
AR_H	Horizontal tail plane Aspect Ratio	5.33
MAC_H	Horizontal mean aerodynamic chord	1.08 m (3.54 fts)
S_V	Vertical tail plane area (including the vertical fin)	3.52 m^2 (37.9 fts^2)
b_V	Vertical tail plane span	2.53 m (8.3 fts)
AR_V	Vertical tail plane Aspect Ratio	1.82
MAC_V	Vertical mean aerodynamic chord	1.40 m (4.59 fts)
l_F	Fuselage length	11.59 m (38.0 fts)
h_F	Fuselage maximum height	1.60 m (5.25 fts)
w_F	Fuselage maximum width	1.60 m (5.25 fts)

Table 2 : P2012 estimated flight performance

Rate of Climb (AEO)	8.1 m/s (1600 fts/min)
Max. Speed	99 m/s @s.l., 106 m/s @1800 m, 108 m/s @2400 m (192 kts @s.l., 205 kts @6000 fts, 209 kts @8000 fts)
Stall Speed (T.O. Configuration)	33 m/s (65 kts)
Stall Speed (Full Flap)	31 m/s (60 kts)
Minimum Control Speed (VMC)	38 m/s (74 kts)
Take Off Distance (15 m)	1840 fts
Landing Distance (15 m)	1660 fts

The design phase was supported by an extended phase of numerical investigation through a fast and very reliable panel code solver available at the DII, in order to provide a general aerodynamic analysis and a deep investigation on some particular effects(such as the wing-fuselage interference or the nacelle lift contribution), see [3], where a more detailed design phase description has been presented. The aerodynamic analysis was also essential to have an accurate estimation of aircraft stability and control derivatives (both longitudinal and lateral-directional) and to lead to a correct sizing of tail surfaces. At the end of this preliminary design phase the final configuration of the aircraft was carried out. The full scale aircraft has a wing area of 25.4 square meters, a wing span of about 14 meters, others main geometrical data are summarized in Table 1.

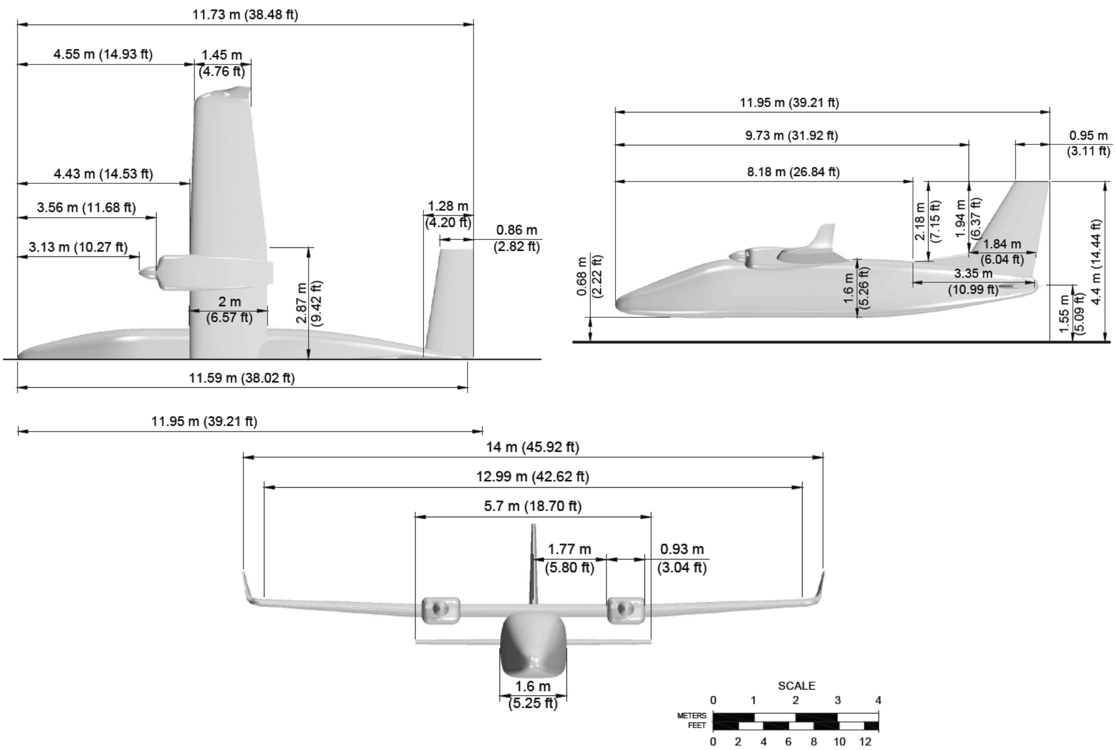

Fig. 1 P2012 Traveller three views (Courtesy of Tecnam)

The wing area has been estimated considering a maximum take-off weight calculation of about 3300 kg, the easy cabin access and a better aircraft clearance has leaded to the necessity of high-wing configuration. The design of the aircraft has been accomplished also considering the necessity to a fixed landing gear to achieve the goal of a low cost aircraft (both in terms of operative and maintenance costs). The concept of commonality of a family of aircraft could also lead in the future to different versions from 10 up to 19 passengers. The P2012, as design specifications, is characterized by a cruise speed of 209 kts at 8000 ft altitude, see Table 2. One of the main features for commuter aircraft is the take-off field length and the capability to operate on very short runways. The P2012 has been designed to have a very small minimum control speed and this leads to a take-off distance lower than 600 m, see Table 2, where the most significant estimated flight performance are shown. With the aim of verifying the aerodynamic characteristics and derivatives(both longitudinal and lateral directional), to which the flight performance of the aircraft depend on, an extensive campaign of experimental tests has been conducted in the wind tunnel facility of the DII. The experimental campaign is made of more than 300 tests. Complete aircraft and several partial configuration, such as isolated body and wing, body-tail, tail off configuration, etc., have been tested, in order to estimate the effects of the different components on the aerodynamic characteristics of the aircraft. In the present paper, the scaled model tested in the wind tunnel and the wind tunnel set-up will be illustrated. In 3.1 the complete aircraft longitudinal characteristics and derivatives will be presented, will be also highlighted the effect of flap deflection. An experimental investigation on the effect on longitudinal stability of vertical positioning of the horizontal tail will be discussed in 3.2. In 3.3 the effect of the aircraft components will be analyzed to better understand how they affect the longitudinal stability derivatives. Finally in 4 a summary of the complete aircraft lateral-directional and control derivatives experimental investigation will be presented, will be also highlighted the strong effect of winglet on the dihedral effect of the aircraft.

2 The scaled model and the wind tunnel set-up

A 1:8.75 scaled model of the P2012 Traveller has been tested in the main wind tunnel of the DII, whose main features are summarized in Table 3. Some external dimensions of the aircraft scaled model are illustrated in Table 4. The implementation of the model has been carried out in Tecnam, while changes and adjustments, such as the realization of the mechanisms for handling, to allow the deflection of the movable parts (flaps, rudder and elevator) and to allow the measurements of their deflections, have been made within the laboratory of the department. The model is made up of several disjoint components(wing, fuselage, nacelles, horizontal and vertical tail planes and landing gear) to allow the analysis of partial configurations, the model is also equipped with multiple hinged movable surfaces such as flaps, elevator and rudder. The measurements of the aerodynamic forces and moments acting on the model have been made possible through the use of internal strain-gage balances.

The strain gage balances used for the wind tunnel tests have been subjected to a calibration procedure for the correct estimation of the forces and moments, and to identify the right positioning of their centre. The model is placed in the test chamber through the assembly of the fuselage on the balance plate, fixed to a special sting, which carries the pattern to be located at about half of the test chamber, see Fig. 2. Since the wind tunnel of the DII is a subsonic wind tunnel(the maximum achievable Reynolds number is $6*10^5$), it has been impossible to reproduce the same Reynolds number of free flight for the full scale aircraft. So to avoid the onset of aerodynamic phenomena linked to the low Reynolds numbers, such as the formation of laminar separation bubbles and / or possible stalls for explosions of the laminar bubble, transitional strips have been applied on all components of the model in order to promote the transition of the flow. The right thickness and the right position of the transitional strips has been determined by tests of flow visualization through the use of fluorescent oil (transitional strips have been placed at 5% of local chord of all components, and have a thickness of about 0.5mm), see Fig. 3.

Table 3 Main characteristics of the main subsonic wind tunnel of the DII

Test section main dimensions	2.0 m x 1.4 m
Maximum speed	180 km/h
Turbulence level	0.10%

Fig. 2 P2012 Traveller scaled model in the DII's wind tunnel facility, complete aircraft and landing gear details

Table 4 P2012 Traveller, scaled model (1:8.75) main external dimensions

Symbol	Description	
b_W	Wing span	1.60 m
S_W	Wing area	0.33 m^2
l_B	Fuselage length	1.34 m
w_B	Fuselage max. width	0.18 m
MAC	Wing mean aerodynamic chord	0.214 m

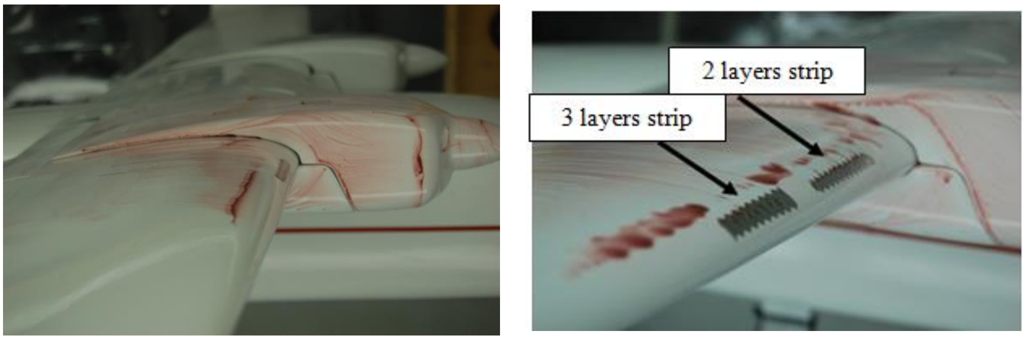

Fig. 3 Example of flow visualization of laminar separation bubble on the wing upper surface and the effects of the transitional strips with different thickness, Re=5.5*10^5 and α=4°

As a pole of reduction of the forces and moments(the hypothetical centre of gravity of the aircraft) has been set a fixed point located at 25% of the wing mean aerodynamic chord, in the longitudinal direction, and 25% of the wing mean aerodynamic chord in the vertical direction, lower than the wing mean aerodynamic chord position. The data relating to the forces measured were reported in terms of dimensionless coefficients.

It must be specified that the coefficients reported have been corrected in order to take into account the effects of wind tunnel walls, the correction procedure is the classical procedure, as that suggested by the POPE in "Low-Speed Wind Tunnel Testing" [4]. Fig. 4 shows an example of comparison between the uncorrected and the corrected pitching moment coefficient, which proved to be the coefficient most influenced by the applied wind tunnel corrections.

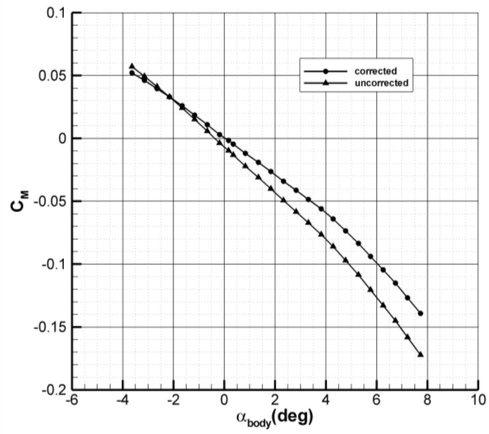

Fig. 4 Effect of the wind tunnel correction on the pitching moment coefficient, complete aircraft

3 Longitudinal Results

In this section will be presented some of the most significant longitudinal results. Results, related to the complete aircraft configuration, at three conditions of flap(clean condition 0°, take off condition 15° and landing condition 40°) will be presented in 3.1. Three different vertical positions of the horizontal tail have been tested, with the aim of identifying, among them, the position that would guarantee the highest longitudinal stability, results of this analysis will be presented in 3.2. In 3.3 will be shown the results of tests on different partial configurations of the aircraft, with the aim to highlight how each aircraft component contributes to the aerodynamic characteristics, and to estimate the effects of the fuselage, nacelles, winglets and landing gear on longitudinal stability derivative.

3.1 Complete Aircraft at Several Flap Deflection

The complete aircraft configuration(pods and landing gear off) has been tested at three different flap deflections, related to the clean condition(cruise flap 0°), take off condition (flap 15°) and landing condition(full flap 40°). Results are illustrated in Fig. 5 to Fig. 8, where are presented the curves of the lift, drag and pitching moment coefficient, while in Table 5 are summarized the lift curve slope, the slope of pitching moment both respect to the angle of attack and to the lift coefficient in order to estimate the position of the neutral point(shown in Table 5 as percentage of the wing mean aerodynamic chord). It must be highlighted that all curve slopes have been extracted in the linear range illustrated in the graphs with the solid line. As it can be seen from Table 5 the lift curve slope in clean condition is of about 0.0921/deg and the deflection of flaps produces an increase of about 11%, this is due to an increase of the wing area related to the flap deflection that causes an increase in the local chord. The neutral point moves forward of about 3% respect to the clean condition, moving from the 42% of MAC to the 39% of MAC, in the landing condition. This is due to the interaction of the wing wake with the horizontal tail plane, that causes a reduction of the dynamic pressure and a significant increase of the downwash on the tail surface. In Table 5 is also shown the minimum drag coefficient, and it can be seen how a flap deflection of 15° causes an increase of about 19% respect to the clean configuration, while the full flap condition leads to an increase of the minimum drag coefficient of about 160%. It must be underlined that the data reported in Table 5 are related to the wind tunnel condition ($Re=5.5*10^5$ and $M\approx0.1$), thus the value of the drag coefficient should be corrected to take into account the effect of the Reynolds number to carry out a more reliable prediction of the drag coefficient in the free flight condition of the full scale aircraft.

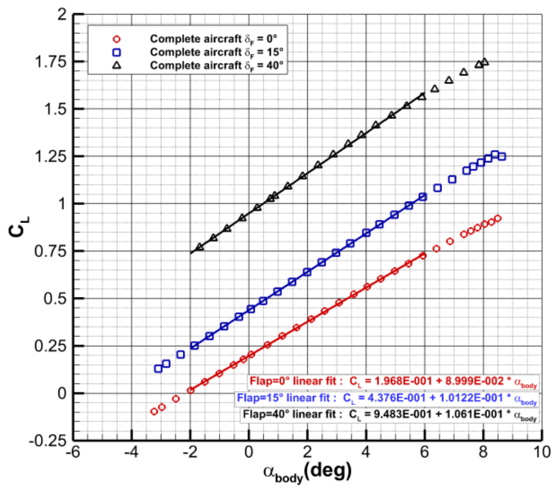

Fig. 5 Complete aircraft at several flap deflections, $Re=5.5*10^5$, C_L vs α

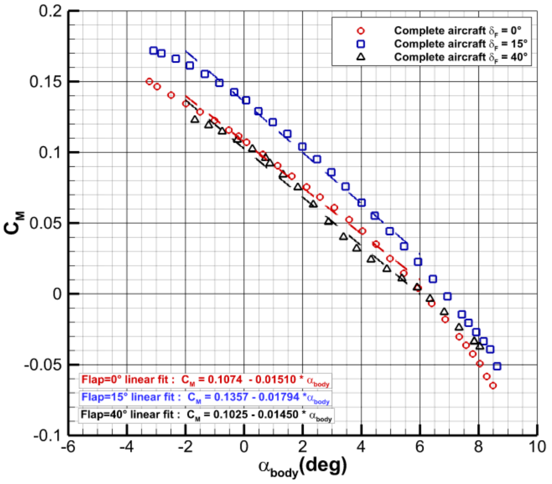

Fig. 6 Complete aircraft at several flap deflections, $Re=5.5*10^5$, C_M vs α

Table 5 : Complete aircraft at several flap deflections, Re=5.5*10^5, longitudinal aerodynamics coefficients and derivatives

CONFIGURATION	C_{L_α} (1/°)	C_{L_0}	C_{M_α} (1/°)	C_{M_0}	$C_{D_{min}}$	$\frac{dC_M}{dC_L}$	X_N (%MAC)
Complete δ_F=0°	0.0917	0.1968	-0.01510	0.0242	0.0406	-0.1631	41.31
Complete δ_F=15°	0.1015	0.4376	-0.01794	0.1465	0.0482	-0.1768	42.68
Complete δ_F=40°	0.1015	0.9483	-0.01450	0.1718	0.1059	-0.1427	39.27

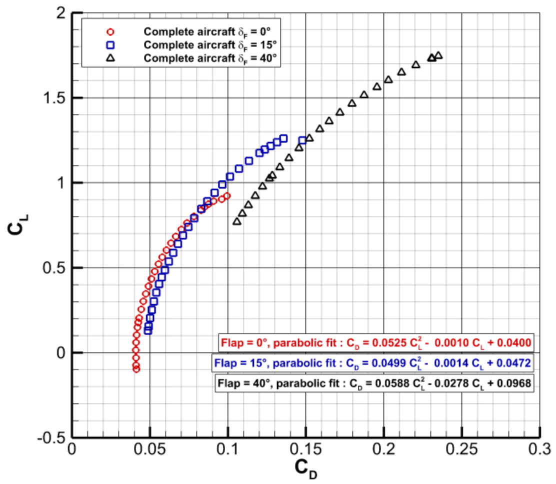

Fig. 7 Complete aircraft at several flap deflections, Re=5.5*10^5, C_L vs C_D

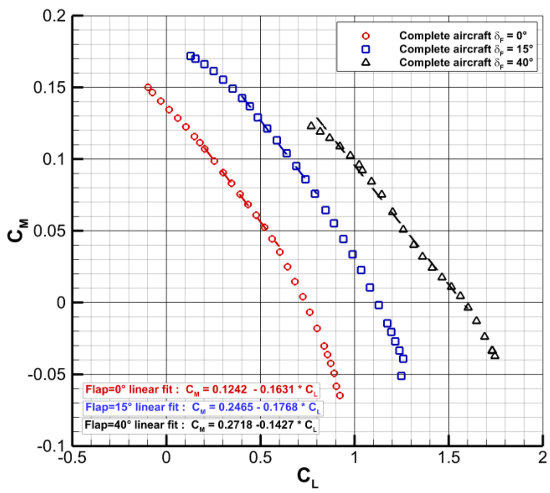

Fig. 8 Complete aircraft at several flap deflections, Re=5.5*10^5, C_M vs C_L

3.2 Effect of Vertical Position of the Horizontal Tail Plane

Since the tests of the complete aircraft configuration with different flap deflection have shown areas of a reduction of the longitudinal stability, and especially in landing condition (full flap deflection, 40°) tests have shown a reduction of 3% in the longitudinal stability, three different vertical position of the horizontal tail has been investigated, in order to evaluate if there are any better alternative positions of the horizontal tail. The original position has been named POS. A, while the two alternative position have been named POS. B and POS. C, progressively closer to the wing, as illustrated in Fig. 9. The vertical distances between the wing root trailing edge and the horizontal tail plane leading edge are illustrated in Table 6. The tested configuration is the complete aircraft with vertical tail off, because the POS. C has made it impossible to mount the vertical surface since the fuselage line has not been modified. Results of this investigation are shown in Fig. 10, where the pitching moment coefficient is illustrated. As it can be expected the effect on the lift curve has been quite negligible, thus the curves of the lift coefficient are not illustrated, while in terms of longitudinal stability it can be observed, and as it is clearly underlined by the derivatives illustrated in

Table 7, that in clean condition(cruise, flap 0°) the POS.C and POS. B are crucial because the tail is be invested by the wing wake, POS. C is found to be the most critical since the neutral point moves from 42.3% MAC of POS. A to 37.5% MAC. In take-off condition (flap 15°) POS. B is found to be the most critical, as matter of fact the neutral point moves from 42.7% MAC to 38.3% MAC. In landing condition (full flap 40°) the POS. A seem to be the most critical position, as already discussed in 3.1. At the end of this investigation, clearly appears how, in term of longitudinal stability, POS. A is the best compromise among all the tested flap conditions. Higher positions of the horizontal plane, which would provide its the mounting in the vertical plane, in cruciform or T configuration, have not been investigated, since they constitute configurations of greater constructive complication, and require heavier structure with consequent increase in aircraft structural weight. Instead lower positions have not been tested in order to not reduce the upsweep angle required for take-off and landing phase.

.

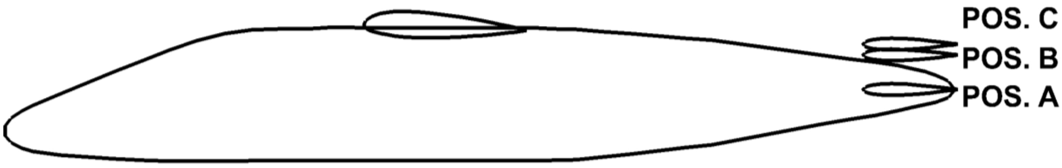

Fig. 9 Layout of the three different vertical position of the horizontal plane experimentally investigated

Table 6 : Tested vertical position of the horizontal tail plane

Vertical Distance between Wing Root T.E. and Horizontal tail L.E.		
	Scale 1:1	Scaled model (1:8.75)
POS.A	0.72 m	0.082 m
POS.B	0.30 m	0.034 m
POS.C	0.17 m	0.019 m

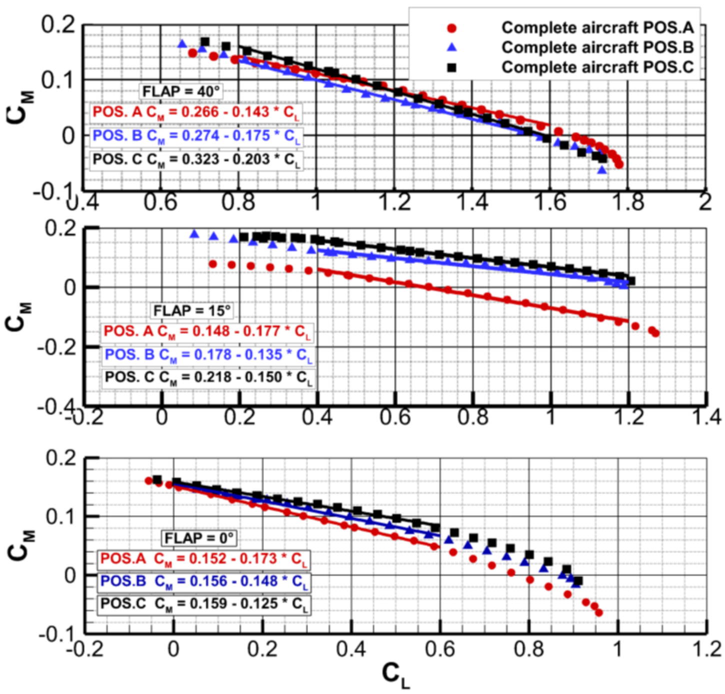

Fig. 10 : Effect of vertical position of the horizontal tail, lift and pitching moment coefficient

Table 7 : Effect of vertical position of the horizontal plane, results

CONFIGURATION	C_{L_α} (1/°)	$\frac{dC_M}{dC_L}$	X_N (%MAC)
FLAP = 0°			
POS. A	0.092	-0.173	41.3
POS. B	0.092	-0.148	39.8
POS. C	0.090	-0.125	37.5
FLAP = 15°			
POS. A	0.101	-0.177	42.7
POS. B	0.098	-0.135	38.5
POS. C	0.097	-0.150	40.0
FLAP = 40°			
POS. A	0.101	-0.143	39.3
POS. B	0.103	-0.175	42.5
POS. C	0.105	-0.203	45.3

3.3 Effects of aircraft components on the longitudinal characteristics and derivatives

In this section the most significant effects of the aircraft components on the longitudinal characteristics and derivatives will be discussed. Results of the configurations investigated are shown in Fig. 11, while in Table 8 the main longitudinal coefficient and derivatives are summarized. Fuselage and nacelles lead to a reduction of the longitudinal stability of about 10.5% and 5%, respectively. Winglet instead leads to an increase of stability of about 3%, while the landing gear seems to not affect stability in a sensible way(it can be observed a reduction of stability less than 1%). Winglets has also shown a sensible increase in the induced drag factor (indicated as e in Table 8), this means that the configuration with winglet on the induced drag should be reduced by about 9% respect to the configuration with winglet off, this should grant a better flight performance especially in the climb phase. From Table 8 it can be also obtained the complete aircraft basic drag coefficient, 0.0536. However this drag coefficient must be corrected to take into account the Reynolds number effect.

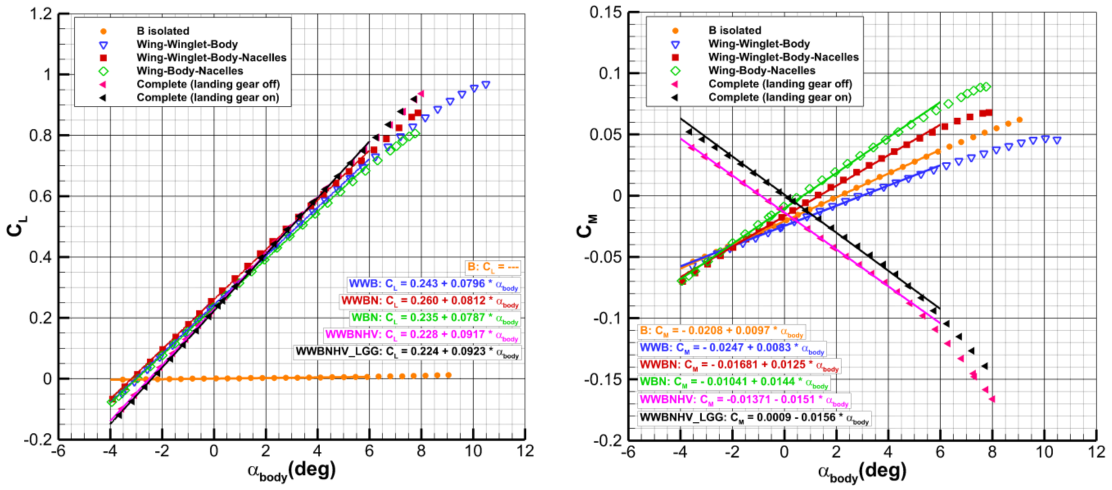

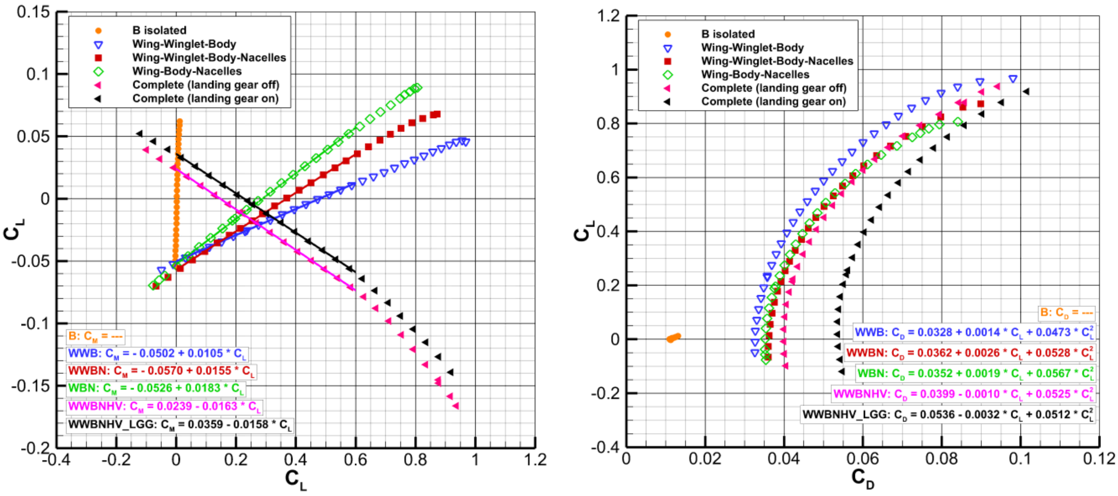

Fig. 11 : Effect of aircraft components, lift, pitching moment and drag coefficient

Table 8 : Effects of aircraft components, Re=5.5*10^5, longitudinal aerodynamics coefficients and derivatives

CONFIGURATION	C_{L_α} $(1/°)$	C_{M_α} $(1/°)$	C_{M_0}	C_{D_0}	$\frac{dC_M}{dC_L}$	X_N (%MAC)	e
Body Isolated	---	0.0097	-0.0255	0.0110	---	---	---
Wing-Winglet-Body	0.0796	0.0083	-0.0502	0.0328	0.105	14.5%	0.81
Wing-Winglet-Body-Nacelles	0.0812	0.0125	-0.0570	0.0362	0.155	9.5%	0.73
Wing-Body-Nacelles	0.0787	0.0144	-0.0526	0.0352	0.183	6.7%	0.67
Complete (landing gear off)	0.0917	-0.0151	0.0239	0.0399	-0.163	41.3%	0.78
Complete (landing gear on)	0.0923	-0.0156	0.0359	0.0536	-0.158	40.8%	0.80

4 Lateral-Directional Results

In this section a summary of the lateral-directional investigation will be presented. Results for the complete aircraft configuration (pods on and landing gear off) at several rudder deflection are presented in terms of yawing and rolling moment coefficient, see Fig. 12 and Fig. 13. The summary of lateral-stability and control derivates are presented in Table 9. In Fig. 15 is also presented the strong effect of the winglets on the aircraft dihedral effect. As it can be seen in Table 9 the winglets are almost neutral in terms of yawing moment while increase of about 40% the lateral stability derivative. These results are in accordance with experimental and numerical analysis of the winglets effect on the lateral stability, ref. [5]-[6]-[7]-[8]. The complete aircraft has shown a lateral stability of about 0.0014/° and a control derivative of about 0.0018/°, sufficient to guarantee a minimum control speed lower than 40 m/s in One Engine Inoperative condition. Fig. **12** shows a change in the yawing moment coefficient slope starting from a side slip angle of about 15°. At this angle the flow on the vertical tail plane tip separates, while the flow on the remaining portion of the vertical surface results to be strongly attached thanks to the vortex introduced by dorsal fin, avoiding the stall of this surface until 20° of sideslip angle.

Table 9 : Complete aircraft (pods on landing gear off), Re=5.5*10^5, lateral directional stability and control derivatives

CONFIGURATION	C_{N_β} $(1/°)$	C_{roll_β} $(1/°)$	$C_{N_{\delta_r}}$ $(1/°)$
Complete(pods on, landing gear off) δ_r = 0°	-0.0014	-0.0028	-0.0018
Complete(pods on, landing gear off) δ_r = 5°	-0.0017	-0.0028	-0.0018
Complete(pods on, landing gear off) δ_r = 10°	-0.0018	-0.0029	-0.0018
Complete(pods on, landing gear off) δ_r = 20°	-0.0015	-0.0031	-0.0018
Wing-Body	0.0011	-0.0015	---
Wing-Winglet-Body	0.0011	-0.0025	---

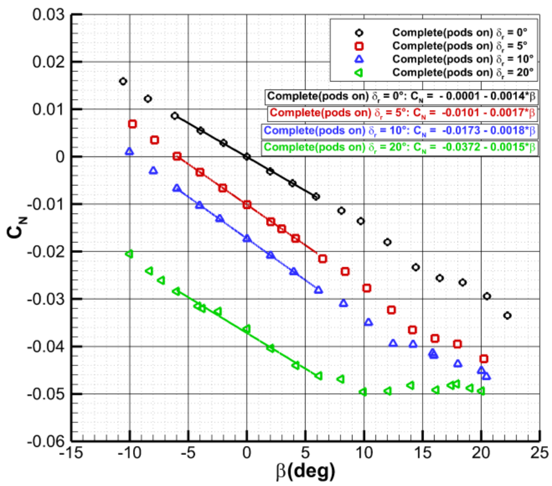

Fig. 12 Complete aircraft at several rudder deflection, C_N vs β, Re=5.5*10^5

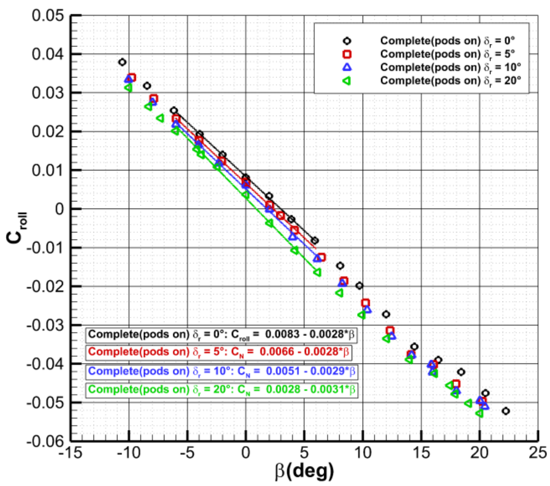

Fig. 13 Complete aircraft at several rudder deflection, C_{roll} vs β, Re=5.5*10^5

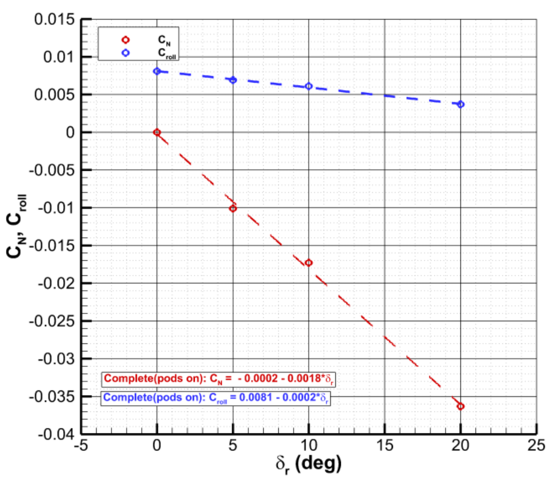

Fig. 14 Complete aircraft at several rudder deflection, C_N vs δ_r, Re=5.5*10^5

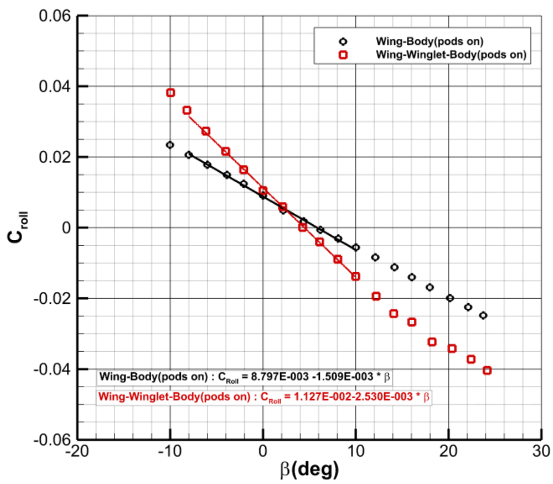

Fig. 15 Winglet effect on C_{roll}, wing-body configuration, Re=5.5*10^5

5 Conclusion

The experimental wind tunnel test campaign has confirmed the effectiveness of the preliminary design of the aircraft. The experimental results have revealed a good agreement with the numerical prevision carried out by the use of semi-empirical approaches, like that proposed in [2], and with the CFD analysis performed with a panel code solver, see [3]. Effects of flap deflection and of the vertical positioning of the horizontal surface have been deeply analyzed and have confirmed that the aircraft shows a good longitudinal stability in all flap condition, see 3.2. Effect of winglets have been evaluated, and it has been proved how the introduction of this device has a positive effect not only in terms of a reduction in the induced drag, with a positive effect on the aircraft flight performance, but also in terms of longitudinal stability, see 3.3. It has been also possible to evaluate the reduction in longitudinal stability introduced by the nacelles and the fuselage. The complete aircraft lateral stability and control derivatives have been estimated, confirming how the aircraft stability and control characteristics are sufficient to grant a minimum control speed lower than the desired one of about 38 m/s, and therefore the estimated take-off and landing distances, which are two main design features for commuter aircraft, have been met.

References

[1] GAMA (General Aviation Manufacturer Association) General Aviation Statistical Databook & Industry Outlook 2011, (2011).

[2] Roskam, J., "*Airplane Design, Part VI: Preliminary Calculation of Aerodynamic, Thrust and Power Characteristics*", 2nd ed., DARcoporation Lawrence Kansas, 2000, Chap 4.

[3] Nicolosi F., P. Della Vecchia, S. Corcione, "Aerodynamic analysis and design of a twin-engine commuter aircraft", *28th Congress of the International Council of the Aeronautical Sciences,* 23-28 September 2012, Brisbane, Australia, PAPER ICAS 2012-1.6.2, ISBN 978-0-9565333-1-9.

[4] Barlow, J.B., Rae, W.H., Pope, A., *Low-speed Wind Tunnel Testing*, 4th ed., John Wiley & Sons Canada, Limited, 2013.

[5] Jacobs, P.,F., Effect of Winglet on a First-Generation Jet Transport Wing V, Stability Characteristics of a Full-Span Wing With a Generalized Fuselage at High Subsonic Speeds, NASA, 1978.

[6] Jacobs,P.,F., Flechner, S.,G., The effect of winglets on the static aerodynamic stability characteristics of a representative second generation jet transport model, NASA, 1976.

[7] Nicolosi, P. Della Vecchia, Aerodynamic guidelines in the design and optimization of a new regional turboprop aircraft, *3rd CEAS Air and 21th AIDAA Congress*, Venice (Italy) 24-28 October 2011, pp. 577-587. ISBN 97888964271787.

[8] Nickel, K. and Wohlfahrt, M., *Tailles Aicraft in Theory and Practice*, American Institute of Aeronautics and Astronautics, Washington D.C., 1994.

[9] ESDU 82010, *Contribution of Fin to Sideforce, Yawing Moment and Rolling Moment Derivatives Due to Sideslip,(Y Sub V) Sub F,(N Sub V) Sub F,(L Sub V) Sub F,in the Presence of Body,Wing and Tailplane. 82010*, ISBN-13: 978-0856793882.

Wingtip Vortices in the Near-field – A Numerical and Experimental Investigation

Micheál S. O'Regan, Philip C. Griffin and Trevor M. Young
University of Limerick, Castletroy, Limerick, Ireland

Keywords: *vortex, wingtip, near-field, turbulent, vorticity confinement*

Abstract

The near-field (up to 3 chord lengths) development of a wing-tip vortex was investigated numerically and experimentally. The research was conducted on a NACA 0012 square tip half-wing at a Reynolds number of 3.2×10^5 at two angles of attack (10° and 5°). A Reynolds stress turbulence model using vorticity confinement was used to compute the vortex in the near-field and experimental measurements were taken with a five-hole probe and x-wire anemometer. The trajectory and mean flow of the computed vortex was in very good agreement with experiment as the circulation parameter and peak crossflow velocity were within 3% and 1% at the trailing edge (10°) and one chord length downstream (5°) respectively. The axial velocity excess and deficit was slightly under predicted for both angles of attack while the numerical Reynolds stress component ‹u'v'› was in very good agreement at the trailing edge for α = 5° but an order of magnitude smaller further downstream.

1 Introduction

The development, behaviour and structure of wingtip vortices are of great importance for both fixed and rotary wing aircraft. These high energy rotational structures pose a significant hazard as they can induce a rolling moment on following aircraft. It is because of this hazard that the Federal Aviation Administration (FAA) and the International Civil Aviation Organization (ICAO) require that aircraft following instrument flight rules have a minimum separation distance on take-off and landing ranging from four to six miles [1]. Furthermore, tip vortices shed from helicopter rotor blades interact with following blades, introducing pressure fluctuations which in turn cause significant vibration and noise [2-4]. Therefore, in order to reduce commercial airport congestion and flight separation times, as well as to reduce rotor blade vibration and noise, the turbulent and mean flow characteristics of wingtip vortices need to be measured or modelled accurately. A limited number of turbulent and experimental studies have been conducted in the near-field of a tip vortex [5-11].

The study by Ramaprian and Zheng [5] found that vortex rollup occurs quite rapidly and that the three-dimensional vortex is seen to become axisymmetric by about two chord lengths downstream. An axial velocity deficit of $0.68U_\infty$ was observed at a distance of x/c = 0.33 for α = 10°, where U_∞ is the free-stream velocity, x is the downstream distance, c is the chord length of the wing and α is the wing angle of attack. The deficit slowly increased towards free-stream conditions with downstream distance. The maximum cross flow velocity of $0.5U_\infty$ was measured at x/c = 0.67 for α = 10°.

Chow et al. [6] conducted mean flow and turbulence measurements on a tip vortex shed from a NACA 0012 wing profile. They recorded a core axial velocity excess of $1.77U_\infty$ and a maximum cross-flow velocity of $1.072U_\infty$ just behind the trailing edge of the wing. They also noted that the point of maximum turbulence intensity occurred near the point of maximum tangential velocity just behind the wing but further downstream the maximum turbulence intensity occurred in the centre of the vortex.

Chigier and Corsiglia [7] investigated the effect of the variation of angle of attack and streamwise distance behind a rectangular NACA 0015 wing. They found that for α ≤ 9° an axial velocity deficit occurred while at α ≥ 9° an axial velocity excess occurred. Core radius was also found to increase with the decay of tangential velocity as the vortex progressed downstream. Turbulence intensity in the core of the vortex was also found to be 12% at x/c =4 and 12°.

McAlister and Takahashi [8] recorded the mean velocity characteristics of a NACA 0015 tip vortex for Reynolds numbers between 1×10^6 and 3×10^6. They observed a core axial velocity excess of $1.5U_\infty$ and a maximum tangential velocity of $0.84U_\infty$ just behind the wing. Other notable features were: (a) An increase in chord size increased tangential and axial velocities; and (b) the use of a boundary layer trip changed the streamwise velocity component from an excess to deficit condition.

Gerontakos and Lee [9] investigated the near-field tip vortex behind a swept NACA 0015 wing section using a miniature seven-hole pressure probe. The study was focused on the effect of angle of attack and downstream distance on the axial velocity, cross flow velocity and vorticity distributions. The core axial velocity was wake-like for α ≤ 8° varying between $0.64U_\infty$ and $0.86U_\infty$. The tangential velocity was found to increase with increasing angle of attack and decrease with increasing downstream distance.

Anderson and Lawton [10] attempted to identify the conditions where an axial velocity in excess of the free-stream value will occur by making a correlation between vortex strength and axial velocity. They conducted research in the near field of a NACA 0015 wing section at Reynolds numbers varying between 0.25×10^6 and 1.25×10^6. They found that an increase in circulation strength resulted in a progressive increase in axial velocity which can exceed the free-stream value by up to 70% and low circulation values resulted in velocity deficit.

Birch et al. [11] conducted an investigation on a NACA 0015 airfoil and a high lift cambered airfoil using a seven-hole pressure probe at a Reynolds number of 2.01×10^5. The vortex strength reached a maximum behind the trailing edge and remained nearly constant up to two chords downstream. The vortex core radius was found to be independent of the vortex strength and the core axial velocity was found to be wake-like or jet-like depending on wing angle of attack.

Devenport et al. [12] conducted mean and turbulence measurements from 5-30 chord lengths downstream of a trailing vortex shed from a NACA 0012 half-wing. The core of the vortex was found to be laminar, and turbulent fluctuations in the core were believed to be produced from buffeting of the core by the surrounding wake turbulence.

In terms of computational modelling, the work of Churchfield and Blaisdell [13] investigated the current state of the art Reynolds-averaged Navier-Stokes (RANS) turbulence models in computing the formation of a wingtip vortex in the near-field. Four turbulence models were evaluated and the effect on solution accuracy of higher order numerical schemes, as opposed to more grid points, were also investigated. A Spalart Allmaras model with corrections for streamline curvature and rotation was found to predict the mean flow most accurately. Higher order numerical schemes were found to be less efficient than the addition of more grid points. All turbulence models were found to under predict the magnitudes of turbulence quantities.

Dacles-Mariani et al. [14] conducted a numerical and experimental study, which focused on the immediate near-field (less than 1 chord) of a NACA 0012 tip vortex. Mean velocity measurements were recorded using a seven-hole pressure probe and the computational model consisted of modified Baldwin-Barth turbulence model and fifth order finite differencing. The vortex core velocity distribution was found to correlate well with experiment but the turbulence quantities were not accurate. They concluded that eddy viscosity based models have no way of reproducing the stabilising effect of solid body rotation of the vortex.

The computational study by Craft et al [15] investigated the near-field generation and decay of wingtip vortices. Two eddy viscosity models and a Reynolds stress model were investigated. The eddy viscosity based models were found to have a very fast dispersal rate and deemed unsuitable for rotational flows such as that of a wingtip vortex. The Reynolds stress model was found to have a good correlation with experiment for mean flow but had a much faster decay of turbulent stress than experiment.

Given the large computational cost of running Large Eddy Simulation (LES) or Direct Numerical Simulation (DNS), the need to develop an advanced Reynolds Averaged Navier Stokes (RANS) model capable of predicting mean and turbulent characteristics of a wingtip vortex accurately stems from the obvious advantages in terms of both the complexity time associated with RANS modelling.

Furthermore, there have been relatively few experimental studies on turbulent flow characteristics of a wingtip vortex in the near-field [6,7] and even fewer numerical/experimental studies with the use of a Reynolds stress turbulence model [15].

Therefore, the objective of this research is to evaluate the capability of a Reynolds stress turbulence model coupled with a vorticity confinement model developed by Steinhoff et al [16] and refined by Loehmer [17] in computing mean flow and turbulent characteristics of a wingtip vortex in the near-field by comparing it to experimental data. A Reynolds stress model with vorticity confinement has previously been shown to give comparable results to LES [18].

2 Experimental setup and procedure

The experiments were conducted in a non-return medium speed wind tunnel. The tunnel test section has a cross section of 0.3 × 0.3m and a free-stream turbulence intensity of 0.5% as measured by hot-wire anemometer prior to experiment. The maximum tunnel velocity used in this study was 34m/s which yielded a chord based Reynolds number of 3.25×10^5. The NACA 0012 half wing model had 0.15m semi-span and a 0.14m chord. The model was mounted on a circular plate on the tunnel floor and could be rotated in increments of 5°. Mean velocity measurements were taken with an Aeroprobe five-hole probe and five Honeywell DUXL05D pressure sensors connected to a National Instruments 6210 data acquisition unit. A Labview virtual instrument simultaneously logged the pressure data. Measurements were recorded in Y and Z at four downstream locations (x/c = 0, 1, 2, 3) at two angles of attack (α = 5°, 10°).

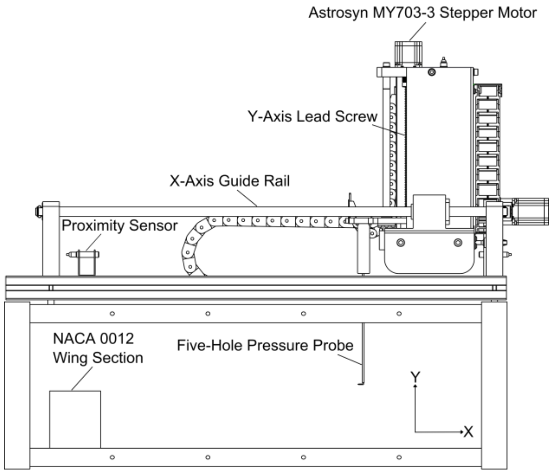

Fig. 1 Schematic of wind tunnel test section and traverse.

Initial square measurement grids of 121 points with spacing set to Δz = Δy = 5mm were surveyed to deduce the exact location of the vortex. More dense measurement grids of 324 points with spacing of Δz = Δy = 2mm were subsequently measured around the vortex core region to yield more detailed flow-field information. Turbulence measurements were recorded using a TSI 1240 x-wire probe in conjunction with a TSI IFA 300 anemometry system. The x-wire probe was calibrated for flow angles of +/- 30° rotating the probe in steps of 6°. The x-wire measurements were taken at 15 locations through the vortex core in steps of 1mm. The vortex core centre being determined from the point of minimum crossflow velocity magnitude (resultant of *v* and *w* vectors) deduced from the five-hole probe measurements. The x-wire measurements were recorded at a rate of 20 kHz for 13 seconds, yielding over 2.6×10^5 samples. A custom-built four-degree-of-freedom traversing system, shown in Fig. 1, was used to position the probes in the tunnel test section.

2.1 Experimental uncertainty

The mean velocity measurements are based on an average of 2000 pressure measurements sampled at a rate of 1 kHz at each grid point. The averaged pressure measurements are reduced to velocity components using Multi-probe data reduction software. The five-hole probe when used in conjunction with the Multi-probe software has an accuracy of 0.4° for flow angles and 0.8% for velocity magnitude within the angle range of +/- 55°. The calibration of the x-wire probe involved taking 17 points covering a velocity range of 0 – 50 m/s. The maximum velocity measured with the five-hole probe was approximately 40 m/s. The mean errors associated with the x-wire calibration are: less than 4% for velocities between 0 and 3 m/s, less than 2% for velocities between 3 and 17m/s, and less than 1% for velocities greater than 17m/s. The probes were positioned using a custom-built traverse with an accuracy of +/- 10µm in X, Y and Z and 1.2° for probe rotation. The vortex circulation strength was calculated by integration of velocity components tangent to a square path surrounding the vortex. The length of the square path used to calculate the circulation was 0.136m and the measurement increment was 0.002m. The length of the integration path was reduced by 0.04m, which resulted in a change of just 2% in the circulation value. The integral was therefore deemed converged and path independent. The free-stream velocity was recorded with a Furness Controls FC012 manometer and a pitot-static probe. The manometer was calibrated prior to experiment by Furness Controls Limited according to UKAS calibration standards and had a measurement range of 0 – 199.9 mmH_2O (0 – 56.6 m/s) with a manufacturer specified accuracy of +/- 1% of the range (+/- 0.4 m/s).

3 Numerical Method

Numerical modelling was carried out using finite volume CFD software Star-CCM+ version 7.04, (a commercially available CFD meshing and flow solver supplied by CD-adapco).

3.1 Mesh Generation

The computational mesh consisted of an unstructured mesh of polyhedral mesh elements. A polyhedral mesh is known for achieving a balanced solution to complex problems and is less computationally demanding than a tetrahedral mesh. Initial computations with a coarse grid of 1.5×10^6 cells were carried out to determine the vortex trajectory. A volumetric control was then created, which captured the trajectory of the wingtip vortex. The mesh density in the volumetric control accounted for over 70% of the overall cell count.

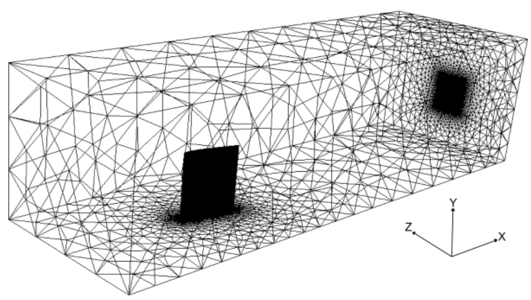

Fig. 2 Numerical mesh comprised of 5.7×10^6 cells.

The mesh density or grid spacing in the volumetric control was specified using the work of Churchfield and Blaisdell [13] and Dacles-Mariani [14] as a guideline to the grid spacing needed across the vortex core. This criterion was deemed suitable as a grid independence analysis. The vortex core radius $r_c = 8 \times 10^{-3}$m was estimated by calculating the distance between the points of maximum and minimum crossflow velocity. The grid spacing was 1.1×10^{-3} m which resulted in 15 grid points across the estimated core of the vortex in both cross stream directions (Y and Z). A screenshot of the computational mesh is shown in Fig. 2.

3.2 Turbulence Modelling

The inherent weaknesses of eddy viscosity based models at modelling complex rotational and swirling flows is well documented [14, 15, 19]. Attempts have been made to escape from these weaknesses by adding correction terms for rotation and streamline curvature [19, 20] but any widely valid approach needs to use a more advanced turbulence model capable of predicting the stress strain connection correctly such as Reynolds stress model or an explicit algebraic stress model [15]. The turbulence model chosen for this study was a full Reynolds stress model with the pressure-strain term modelled using the linear approach of Gibson and Launder [21] coupled with a vorticity confinement model developed by Steinhoff et al [16] and refined by Loehmer [17]. By solving for all the components of the Reynolds stress tensor, this model naturally accounts for effects such as anisotropy due to swirling motion, streamline curvature and rapid changes in strain rate. The model solves equations for the six unique Reynolds stress components and one for the isotropic turbulent dissipation ε. The vorticity confinement model adds a force term to the momentum equations to help confine the vorticity and keep it from spreading. The derivation and exact implementation of the force term to the Navier-Stokes equations can be found in Ref. [16].

4 Results and Discussion

4.1 Circulation

The circulation of the tip vortex at each of the four downstream locations was calculated using the following equation:

$$\Gamma = \sum_i \overline{v_i} \cdot \Delta \overline{l_i} \qquad (1)$$

where $\overline{v_i}$ and $\Delta\overline{l_i}$ are the velocity vector and segment length along the square path surrounding the vortex, respectively. The vortex circulation shown in Fig. 4 is given in terms of non-dimensional circulation parameter for α = 5° and 10° for the numerical and experimental cases. In general, the experimental and numerical circulation parameters are in good agreement with both remaining relatively constant with downstream distance. Prandtl's lifting line theory equates the circulation strength of a trailing vortex to the strength produced by the bound vorticity of the wing. Therefore, the bound root circulation will increase in direct proportion to the lift produced, which can be seen in Fig. 3 as the circulation parameter increases by more than 50% when the angle of attack increases from 5° to 10°. For α = 5° at x/c = 0 the numerical vortex strength is significantly greater than experimental. This would indicate that the experimental vortex was not fully rolled up at this location and that the vorticity shed from the wing was still being entrained into the vortex. It would also seem that the numerical model predicted the rollup of the vortex a little too early. At x/c = 1 the experimental vortex reaches its maximum strength and remains relatively constant until x/c = 3 as shown in Fig. 3. At x/c = 1 the numerical vortex circulation decays slightly from its peak at x/c = 0, and also remains relatively constant up to x/c = 3. For α = 5° the experimental vortex strength from x/c = 1 – 3 is an average of 18% less than the numerical vortex strength. In contrast, for α = 10° the experimental vortex strength is in close agreement at x/c = 0, where it is 3% greater than the numerical vortex strength. The experimental vortex strength increases up to x/c = 2, where it reaches its maximum strength and decays slightly at x/c = 3. The numerical vortex decays slightly at x/c = 1 and remains constant up to x/c = 3. This would indicate that the wing boundary layer vorticity is still feeding into the experimental vortex until x/c = 2 even though the vortex may appear to be fully rolled up. A promising result is the fact that the numerical vortex does not significantly decay with downstream distance and that the experimental vortex strength is only 8% greater than the numerical vortex strength at the last measurement location of x/c =3.

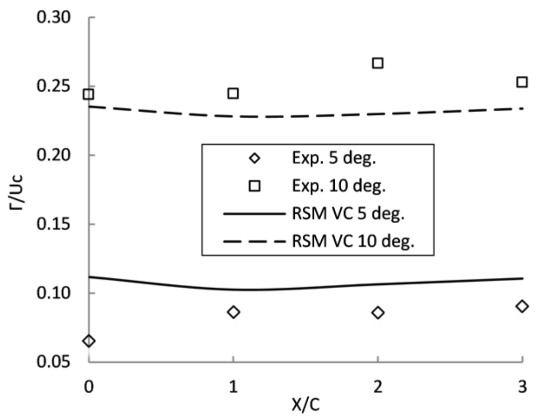

Fig. 3 Variation of normalised vortex strength with downstream distance.

4.2 Axial Velocity

There are two primary mechanisms that affect the axial velocity in the core of a tip vortex [6, 22]: (1) momentum deficit caused by the boundary layer on the wing and (2) axial development of crossflow velocities (*v* and *w*). The former has the effect of increasing vortex core pressure leading to a reduction in core velocity whereas the latter introduces a favourable pressure gradient and accelerates the inner core flow. Therefore, the boundary layer on the wing and the vortex rollup have opposite effects on the axial velocity [22]. The axial velocity was recorded for two angles of attack (5° and 10°) using a five-hole probe and computed numerically. For α = 10° at x/c = 0, five-hole probe measurements revealed regions of velocity excess and deficit. An axial velocity excess of $1.05U_\infty$ was recorded in the core centre (point of minimum crossflow velocity), while an excess of $1.13U_\infty$ was measured just outboard of the core centre. Velocity deficits of $0.73U_\infty$ and $0.8U_\infty$ were measured at the edge of the vortex core diameter. The numerically predicted axial velocity at x/c = 0 was $0.98U_\infty$ without vorticity confinement and was $1.0U_\infty$ with the vorticity confinement model applied as can be seen in Fig. 4. This slight under prediction of the vortex core axial velocity can be can be linked with the fact that numerical circulation is slightly less than experiment as seen in Fig. 3. The work of Anderson and Lawton highlights a linear proportionality between the circulation parameter of a vortex and its axial velocity.

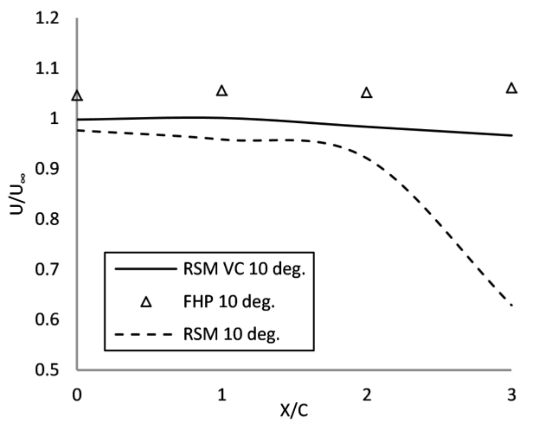

Fig. 4 Development of axial velocity with downstream distance for α = 10°.

The experimental core centre axial velocity remained constant with downstream distance with a value of $1.06U_\infty$ being recorded at x/c = 3. In contrast, the numerical core centre axial velocity decayed to $0.62U_\infty$ without the vorticity confinement model activated but only decayed slightly to $0.96U_\infty$ with the vorticity confinement model applied. For α = 5°, the core centre exhibited a deficit axial velocity condition at all four downstream locations. At x/c = 0 the core centre axial velocity predicted by the numerical model with and without vorticity confinement was $0.8U_\infty$ and $0.76U_\infty$ respectively. Interestingly, the experimental core centre axial velocity at x/c = 0 was $0.67U_\infty$ which showed that the numerical model without vorticity confinement was in better agreement. The core centre axial velocity predicted by the numerical model with vorticity confinement increased to $0.93U_\infty$ at x/c = 1 and it remained constant up to x/c = 3. The experimental core centre axial velocity increased up to x/c = 2, where it reached its maximum value of $0.83U_\infty$ and remained constant until x/c = 3. The core centre axial velocity predicted by the numerical model without vorticity confinement increased to $0.88U_\infty$ at x/c = 2 but dropped significantly at x/c = 3 to $0.82U_\infty$. The discrepancies in axial velocity results can be linked to section 4.1 as the numerically predicted vortex is weaker than the experimental vortex for α = 10° but stronger for α = 5°.

4.3 Crossflow Velocity

As seen in Fig. 5 a line along y = 8 was taken through the vortex centre at x/c = 1 for α = 5° and very good agreement is achieved between numerical and experimental values. The vortex core diameter for α = 10° was 0.018m and 0.02m at x/c = 0 for the experimental and numerical cases respectively.

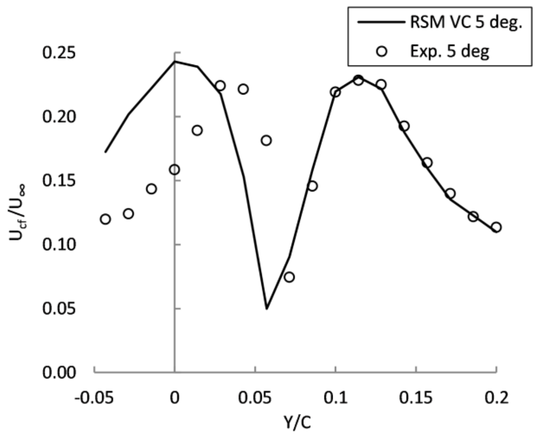

Fig. 5 Normalised crossflow velocity magnitude taken on a line y = 8 across the vortex core at x/c = 1 for α = 5°.

The numerical core diameter remained unchanged with downstream distance while the experimental vortex decreased to 0.014m at x/c = 3, which would indicate the vortex became more tightly wound. The vortex core diameter for α = 5° was slightly smaller being 0.012m for both numerical and experimental cases at x/c = 0. The experimental core diameter again remained constant up to x/c = 3, while the numerical core diameter increased to 0.016m at x/c = 3. The increase in core diameter is attributed to the decaying crossflow velocity with increasing downstream distance which would lead to a less tightly wound vortex core.

The crossflow velocity vectors *(jv + kw)* for both the numerical and experimental cases for α = 10° are shown in Fig. 6. The vectors clearly show the clockwise rotation of the tip vortex as it moves slightly upward and inward at the first measurement location of x/c = 0. The vectors for both the numerical and experimental cases appear unsymmetrical at x/c = 0 as rollup is still taking place. The magnitudes of the vectors are seen to be larger at the outer boundary of the vortex core and approach zero in the centre of the vortex (a characteristic which allows the identification of the vortex core location). As the vortex progresses downstream the vectors become axisymmetric as can be seen in Figs. 6 (c) and (d) at a location of x/c = 3. Unlike free-to-air vortices, the vortex has moved inboard and upward which is said to be an inviscid effect caused by the proximity of the wind tunnel walls [14]. The numerical and experimental vortices shifted inboard by the same amount of 0.1c or 10% of the chord by the last measurement location of x/c = 3 for both angles of attack (5° and 10°). It is clear from Fig. 6 that the experimental vectors have a larger magnitude than the numerical vectors which is probably the reason why the numerical axial velocity is slightly under predicted for α = 10°. A maximum experimental crossflow velocity of $0.74U_\infty$ was recorded at x/c = 0 for α = 10°. The maximum numerical crossflow velocity of $0.5U_\infty$ was also recorded at x/c = 0 for α = 10°. The maximum experimental crossflow velocity for α = 10° decreased by 22% at x/c = 1 to $0.58U_\infty$ and remained constant up to x/c = 3. The maximum crossflow velocity for the numerical case followed a similar trend for α = 10°, decreasing by 12% to 0.44 U_∞ at x/c = 1 and to $0.41U_\infty$ at x/c = 3. As expected, the maximum crossflow velocities decreased significantly with decreasing angle of attack. For α = 5°, a maximum experimental crossflow velocity of $0.34U_\infty$ was recorded at x/c = 0, a 50% decrease in the peak crossflow velocity from α = 10°. The maximum numerical

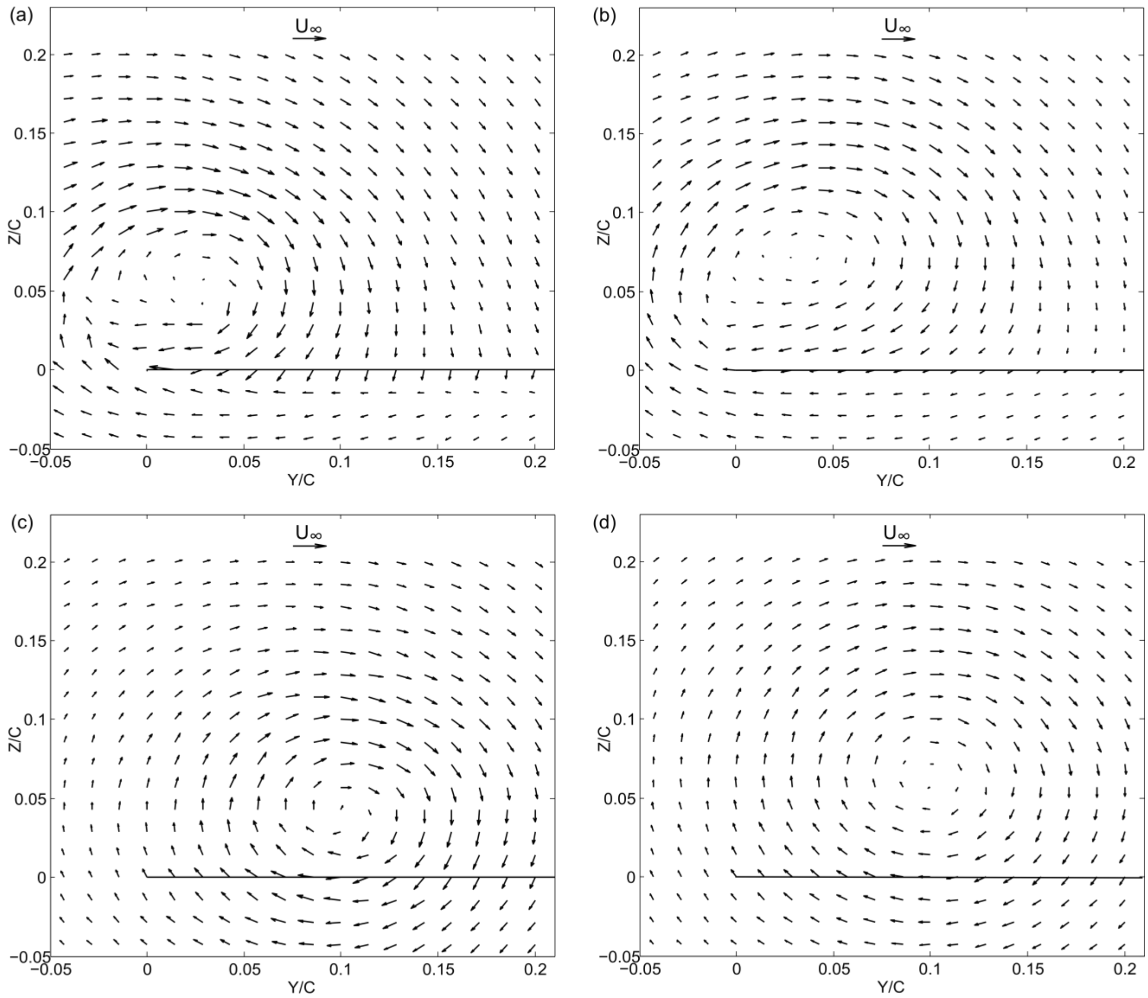

Fig. 6 Normalised cross-flow velocity vectors (*jv* + *kw*)/U∞ for α = 10°: (a) x/c = 0, Experimental (b) x/c = 0, Numerical (c) x/c = 3, Experimental (d) x/c = 3, Numerical. Scale vector U∞ indicates velocity magnitude.

crossflow velocity for α = 5° was $0.29U_\infty$ at x/c = 0, a 42% decrease from α = 10°. Both the numerical and experimental vortices had a maximum crossflow velocity of $0.25\ U_\infty$ at x/c = 1 for α = 5°, which remained constant for the experimental vortex but decreased slightly to $0.22U_\infty$ for the numerical vortex. The vortex core diameter was estimated by calculating the distance between the peaks of crossflow velocity taken on a line through the vortex centre.

4.4 Reynolds Stress

The ‹*u'v'*› Reynolds shear stress component was obtained from x-wire measurements and predicted from the Reynolds stress numerical model coupled with the vorticity confinement model. The ‹*u'v'*› component was normalised by the square of the free-stream velocity and is shown in Fig. 7 at a location of x/c = 0 for α = 5°. Both the numerical and experimental ‹*u'v'*› component exhibited positive and negative values across the core of the vortex similar to the work of Chow et al [6]. Peak experimental stress levels of 0.0007 and -0.0007 were measured at x/d_c = 0.25 and 0.5 respectively, where d_c is the vortex core diameter. Peak numerical stresses of -0.0003 and 0.0002 were measured at x/d_c = -0.16 and 0.33. The stresses were found to decrease with increasing downstream distance and the maximum experimental stress by x/c = 1 had decayed to -0.0002, while the numerical stress was an order of magnitude smaller. The numerical values of ‹$u'v'$› for α = 10° were an order of magnitude smaller than experiment at all downstream locations (x/c = 0-3).

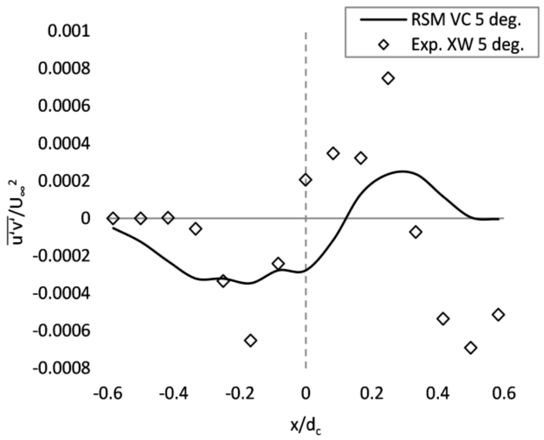

Fig. 7 Normalised Reynolds shear stress ‹*u'v'*› across vortex core diameter for α = 5° at x/c = 0.

5 Conclusions

The near-field of a wingtip vortex has been investigated both numerically using a Reynolds stress turbulence model coupled with a vorticity confinement model and experimentally using a five-hole probe and x-wire anemometer. The vortex trajectory, shape and size of the vortex correlate extremely well with experiment. An upward and inboard movement was characteristic to both vortices. The same inboard shift was noted for the numerical and experimental vortices. The circulation parameters agreed with Prandtl's lifting line theory and the numerical vortex strength was in close agreement for both angles of attack. The numerical vortex attained its maximum strength quicker than the experimental vortex which indicates that the numerical model predicts the vortex rollup too quickly. It also shows that the experimental vortex is continually trapping the wing boundary layer vorticity further downstream. A linear trend between the circulation and angle of attack was noted and the magnitude of crossflow velocities was also thought to be linked to the discrepancy in axial velocities. The maximum crossflow velocities were obtained at a location of x/c = 0 for all cases and angles of attack. The crossflow velocities were found to decrease at x/c = 1 but stabilised thereafter up to the last measurement location of x/c = 3. The experimental vortex core diameter became slightly smaller with downstream distance for α = 5° but remained unchanged for α = 10°. The numerical vortex core diameter remained unchanged with downstream distance for α = 10° but increased slightly for α = 5°. The slight increase in vortex core diameter could be the result of decaying crossflow velocities, which ultimately would lead to the vortex becoming less tightly wound. The numerical model was found to slightly under predict the axial velocity excess and deficit for α = 5 and 10°. The lower crossflow velocities predicted by the numerical model were thought to have had a direct effect on the discrepancy between axial velocities. The magnitude of the Reynolds stress component ‹$u'v'$› was in relatively good agreement at x/c = 0 for α = 5°. The Reynolds stress displayed both positive and negative values across the vortex core. This result is promising, showing that the Reynolds stress and turbulent fluctuations in the vortex core can be reasonably accurately predicted just aft of the trailing edge for α = 5°. The numerical Reynolds stresses were found to dissipate extremely quickly further downstream and to be an order of magnitude smaller than the experimental values from x/c = 1-3 for α = 5° and at all locations for α = 10°.

References

[1] Gerz, T., Holzäpfel, F., and Darracq, D., "Commercial aircraft wake vortices" *Prog. Aero. Sci.*, Vol. 38, 2002, pp. 181-208
[2] Yu, Y.H., "Rotor blade-vortex interaction noise", *Prog. Aero. Sci.*, Vol. 36, 2000, pp. 97-115
[3] Yu, Y.H., Gmelin, B., Splettstoesser, W., Philippe, J.J., Prieur, J., and Brooks, T.F., "Reduction of helicopter blade-vortex interaction noise by active rotor control technology", *Prog. Aero. Sci.*, Vol. 33, 1997, pp. 647-687

[4] Beaumier, P., and Delrieux, Y., "Description and validation of the ONERA computational method for the prediction of blade-vortex interaction noise", *Aero. Sci. Tech.* Vol. 9, 2005, pp. 31-43
[5] Ramaprian, B.R., and Zheng, Y., "Measurements in Rollup Region of the Tip Vortex from a Rectangular Wing", *AIAA Journal*, Vol. 35, No.12, 1997, pp. 1837-1843.
[6] Chow, J.S., Zilliac, G.G., and Bradshaw, P., "Mean and Turbulence Measurements in the Near Field of a Wingtip Vortex", *AIAA Journal*, Vol. 35, No.10, 1997, pp. 1561-1567
[7] Chigier, N.A., and Corsiglia, V.R., "Wind-Tunnel Studies of Wing Wake Turbulence", *J. Aircraft*, Vol. 9, No. 12, 1972, pp. 820-825.
[8] McAlister, K.W., and Takahashi, R.K., "NACA 0015 Wing Pressure and Trailing Vortex Measurements", NASA TP-3151, Nov. 1991.
[9] Gerontakos, P., and Lee, T., "Near-field Tip Vortex behind a swept wing model", *Experiments in Fluids*, Vol. 40, 2006, pp. 141-155.
[10] Anderson, E.G., and Lawton, T.A., "Correlation between Vortex Strength and Axial Velocity in a Trailing Vortex", *AIAA Journal*, Vol. 40, No.4, 2003, pp. 699-704.
[11] Birch, D., Lee, T., Mokhtarian, F., and Kafyke, F., "Structure and Induced Drag of a Tip Vortex", *AIAA Journal*, Vol. 41, No. 5, 2004, pp. 1138-1145.
[12] Devenport, W.J., Rife, M.C., Liapis, S.I., and Follin, G.J., "The Structure and development of a Wingtip Vortex", *J. Fluid Mech.*, Vol. 312, 1996, pp. 67-106.
[13].Churchfield, M. J., and Blaisdell, G.A., "Numerical simulations of a wingtip vortex in the near field", *J. Aircraft*, Vol. 46, No. 1, pp. 230-243.
[14] Dacles-Mariani, J., Zilliac, G.G., Chow, J., and Bradshaw, P., "Numerical/Experimental Study of a Wingtip Vortex in the Near Field", *AIAA Journal*, Vol. 33, No.9, 1995, pp. 1561-1568.
[15] Craft, T.J., Gerasimov, A.V., Launder, B.E., and Robinson, C.M.E., "A computational study of the near-field generation and decay of wingtip vortices", *Inter. J. Heat Fluid Flow*, Vol. 27, 2006, pp. 684-695.
[16] Steinhoff, J., Lynn, N., and Wang, L. "Computation of high Reynolds number flows using vorticity confinement", *UTSI Preprint*, 2005.
[17] Loehmer, R. "On limiter for minimal vorticity dissipation", *Proceedings of the 47th AIAA Aerospace Sciences Meeting*, Orlando, 2009, pp. 1-7.
[18] Kimbrell, A.B., "Development and verification of a Navier-Stokes solver with vorticity confinement using OpenFOAM" Master's Thesis, University of Tennessee, USA, 2012.
[19] Czech, M., Miller, G., Crouch, J., and Strelets, M., "Predicting the near-field evolution of airplane trailing vortices", *Com. Rend. Phys.*, Vol. 6, 2005, pp. 451-466.
[20] Spalart, P.R., and Shur, M., "On the sensitization of turbulence models to rotations and curvature", *Aero. Sci. Tech.* Vol. 5, 1997, pp. 297-302.
[21] Gibson, M.M., and Launder, B.E., "Ground effects on pressure fluctuations in the atmospheric boundary layer", *J. Fluid Mech.* Vol. 86, No. 3, 1978, pp. 491-511.
[22] Shekarriz, A., Fu, T.C., Katz, J., and Huang, T., "Near-field behavior of a tip vortex", *AIAA Journal*, Vol. 31, No. 1, 1993, pp. 112-118.

4:th CEAS Air & Space Conference
FTF Congress: Flygteknik 2013

A Simple Laboratory Approach to Investigate Boundary Layer Transition due to Free Stream Particles

Conny Schmidt and Trevor M. Young
MABE Department, University of Limerick, Ireland

Emmanuel P. Benard and Lei Zhao
Department of Aerospace Engineering, University of Glasgow, Scotland, UK

Keywords: *laminar flow technology, ice crystals, particle wake, turbulent contamination*

Abstract

Application of drag reduction technology based on laminar flow in a commercial environment is still being hindered by unanswered questions regarding its operational reliability. A malfunction of a laminar flow system, even if temporary, could have a considerable effect (depending on the extent of its application) on the overall fuel planning; and, for more ambitious designs, possibly even on the handling characteristics of a correspondingly equipped aircraft. Nevertheless, a first small scale application has recently been introduced into routine commercial airline service. The encounter of ice crystals, as occurring in cirrus cloud, is known to result in performance degradations or even a temporary complete loss of laminar flow. Actually occurring mechanisms are not well understood and previously proposed critical parameters have not yet been verified experimentally. Difficulties encountered while attempting to recreate conditions in the laboratory that are representative of the real occurrences have led to several alternative experimental methods. This study presents results from a relatively simple method, in terms of its complexity, providing for further insight into the phenomenon that a small particle is capable of producing a turbulent event while travelling through an initially laminar boundary layer. Using this method, for a smooth spherical particle, a critical Reynolds number in the order of 300 has been determined above which the generation of a turbulent-spot-like disturbance will occur.

1 Introduction

The depletion of cheap fossil fuel reserves has focused research attention on improving aircraft efficiencies within a short time frame, and this has revived the interest in laminar flow technology due to its great potential to reduce fuel consumption. If applied to all aircraft components that are currently rated as being practical, namely the wings' upper surfaces, the empennage and the engine nacelles, overall drag reductions of approximately 16% [1] are thought to be realistic. This would translate into a reduction of fuel consumption in the order of 10% [2].

The principles to achieve such benefits are Natural Laminar Flow (NLF), a passive technique based on extended regions of accelerated flow over specifically designed contours, and the active method of Laminar Flow Control (LFC) based on suction through a perforated or slotted surface, which prevents the boundary layer over that surface growing in thickness above critical values. Each technique has both its advantages and drawbacks; however, their combination to the so-called Hybrid Laminar Flow Control (HLFC) seems to be capable of overcoming most of the issues.

In this respect, it is worth noting that the principle of NLF has recently found its first introduction into commercial airline service with the current design of the engine nacelle's leading edge in Boeing's new 787 Dreamliner [3]. As this innovative development can only contribute a fuel reduction in the order of 1.5 % [4] – and hence does not exploit the full potential of Laminar Flow Technology – operational factors that result in temporary loss of laminar flow are not of great concern. However, future models could be designed for laminar flow runs of 50 % chord or more [5] over the wings' surfaces, and, in such circumstances, the operational factors need to be thoroughly understood [6].

Due to environmental effects, such as insect contamination and constraints associated with the design of the suction system, the application is limited to altitudes above 20000 feet that is the last portion of climb, the cruise and the initial decent.

At these altitudes, encountering ice crystals, as occurring in cirrus cloud, has been identified to partially deteriorate laminar boundary layers up to the point of complete loss of the anticipated benefits depending on the prevailing ice crystal size and flux [7-9]. The effect has been entirely attributed to an ice crystal's ability to produce turbulence within its wake while travelling through the initially laminar boundary layer [7]; however, the actual mechanisms are not well understood and the critical parameters not accurately defined [10].

From the Hall criteria [7] (representing the first and to date most comprehensive study of the phenomenon) a critical Reynolds number of 150 can be derived for a spherical cylinder of a length-to-diameter ratio, L/D, of 2.5. This had been chosen by Hall as an approximation that is quite representative of actual ice crystals as occurring in cirrus cloud.

Other previously published studies considered related to this phenomenon were mainly concerned with spherical particles; however the scatter of proposed critical Reynolds numbers for the latter was seen to be quite large with values ranging from 450 to 1000 [11].

2 Background

From several attempts to investigate the problem, both in the laboratory and numerically, it has been identified that the physical phenomenon is composed of a number of distinguishable mechanisms, as listed below:

(1) The particle is in or nearly in equilibrium within the free stream outside of the boundary layer.
(2) The particle's transverse velocity component is small when compared to its stream-wise component for the majority of trajectories [12].
(3) The ratio of the particle density to that of the surrounding flow medium is in the order of 10^3, thus the particle cannot adapt to the rapid velocity changes within the boundary layer.
(4) The critical (high velocity) region is the particle's side which is closest to the affected surface (see Figure 1).
(5) The orientation of the wake originating from the particle is in opposite direction to that of the boundary layer development.

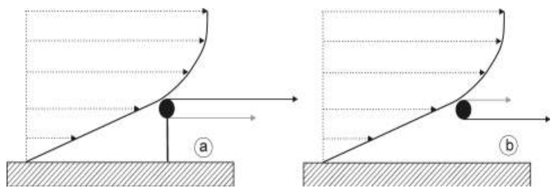

Fig 1. The critical side of a particle for the fixed case (a) and the suspended case (b), reproduced from Schmidt & Young [10].

The combination of all these mechanisms simultaneously in a laboratory experiment can only be achieved with great difficulty [10]. In fact, the only laboratory method known to the authors of being capable to recreate the full set of parameters requires a complex experimental setup [13]. Furthermore, the results obtained so far from this approach still involve some degree of ambiguity due to encountered technical difficulties in terms of the applied measurement procedures and also due to the novelty of the approach making benchmarking a complicated task.

3 Experimental Work

3.1 An Alternative Approach

This work focuses on an alternative laboratory approach developed by the authors [14], which greatly reduces the experiment's complexity, while enabling the simultaneous simulation of at least four of the above-mentioned mechanisms.
It is based on the concept of swinging a particle through the laminar boundary layer over a flat plate by making it the oscillating weight of a pendulum, subsequently called the Pendulum Approach (PA). While overcoming many issues that were connected to more conventional experimental methods, due to the nature of the pendulum, only one particle impact at a time could be captured making measurements very time consuming. Thus, more detailed results could not be obtained in this way.

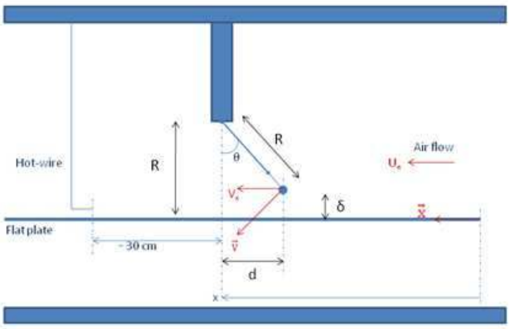

Fig. 2 The experimental setup of the Rotating Arm Approach, reproduced from Dabadie & Coisnon [15].

As illustrated in Figure 2, these difficulties have been overcome by replacing the pendulum by a rotating arm, which allows for a sequence of particle impacts to be measured without the requirement to manually interfere with the experimental setup. This methodology is subsequently called the Rotating Arm Approach (RAA).

3.2 The Experimental Setup

The experiments have been carried out in the low speed wind tunnel facility at the University of Glasgow. It has a 4 m long test section with a square cross sectional area of 0.91 m side length. The maximum achievable velocity, *U*, produced by a fan located downstream of the test section, was 2.4 m/s; the turbulence intensity, *Tu*, has been determined to amount to 0.5 %.
The flat plate, approximately 3.7 m in length, consisted of several sections of carefully aligned plywood boards (along the vertical centre plane); the most upstream one being equipped with an elliptical leading edge. By partially blocking the test section outlet above the plate using grids, thus introducing a slight pressure gradient, the stagnation point was forced onto the upper surface. This was verified by smoke flow visualization.
For the PA, a spherical particle of 6 mm diameter was fixed by a thread of adjustable length to the test section ceiling. Devices for launching and capturing the particle, subsequent to a single swing through the plate's boundary layer, have been installed.
For the enhanced experimental setup, namely the RAA, the pendulum has been replaced by a thin metal rod that could be rotated by an electric motor around its pivot point (see Fig. 2). To the outer end, a small needle (designed for acupuncture) of a very small diameter has been attached, to which the particle was fastened. This has been done in order to avoid the rotating arm to be supercritical within the boundary layer regions. Since the RAA had to allow for a full rotation within the test section, the flat plate had been lowered vertically, in order to keep the rotating arm as long as possible. A short arm would reduce the ratio of the stream-wise and the transverse velocity components of the particle within the proximity of the boundary layer, which should ideally be kept as large as possible. It would be unacceptable when both

components were of the same order of magnitude.

3.3 Measurement Procedures

At the anticipated measurement location (2.1 m downstream of the leading edge) a boundary layer thickness, δ, of approximately 23 mm was achieved at a free stream velocity, U, of 1.5 m/s, assuring local Reynolds number regions above the infinite stability limit [16]. Hot wire boundary layer traverses resulted in mean velocity profiles that were in close agreement to the Blasius solution (see Fig. 3).

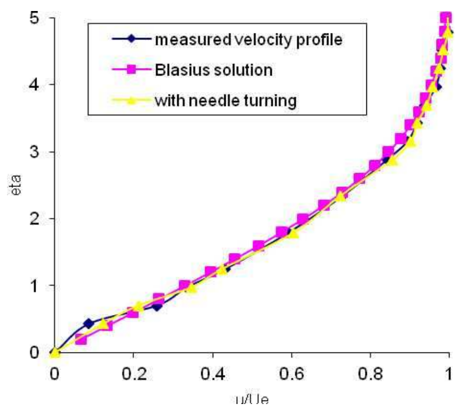

Fig. 3 Measured boundary layer velocity profiles in comparison to the Blasius solution.

During both the PA and the RAA tests, hot wire measurements were taken at a sampling rate of 20 kHz. These measurements occurred 300 mm downstream of the point of maximum deflection location in each case at several transverse positions above the plate throughout the boundary layer.
While for the PA, the drag force acting on the particle has proven to be sufficient to accelerate it to free-stream speed before entering the boundary layer, for the RAA the rotational speed of the motor needed to be set appropriately. As pointed out earlier, the PA allowed for a single measurement only at a time, before the system had to be manually "reloaded". During the RAA, a minimum sequence of 30 particle impacts has been recorded for each measurement position.

The RAA also involved the requirement to examine whether or not the current experimental setup (as being quite intrusive) would have an adverse effect onto the boundary layer. For this purpose the rotational arm was set into motion at a speed comparable to that of the free stream with no particle attached to it and the boundary layer traverse repeated. As is apparent from Figure 3 the effect was found to be negligible. This could be further substantited by subsequent smoke flow visualisation (see Fig. 9).

3.4 Measurement Results

Figure 4 shows example illustrations of the voltage signals as obtained from a hot wire boundary layer traverse when being affected by a 6 mm diameter particle during an RAA experiment. The single impacts are clearly distinguishable.

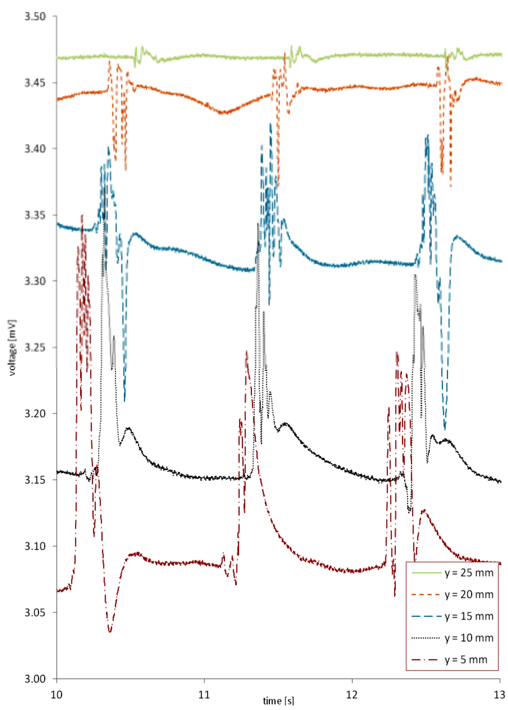

Fig. 4 Example hot wire signals at several transverse locations throughout the boundary layer, impacted by a 6 mm diameter particle at a speed of 1.5 m/s.

Again, as also found during the PA experiments [14], the traces taken close to the plate's surface show the distinct features of a turbulent spot as one would expect from surface mounted hot film measurements. Further away, the signals change to having accelerated and decelerated portions of similar magnitude. Towards the boundary layer edge, the decelerated amplitudes become more prominent. Near the edge of the boundary layer the signals reduce in strength thus indicating that the effect produced by the particle is limited to regions within the shear layer as anticipated. This, as with the PA experiments, compares well to measurements taken on artificially generated turbulent spots by Cantwell et al. (1978) [17].

Whereas the laminar state of the boundary layer could be fully recovered inbetween two subsequent impacts for weaker signal disruptions (towards the boundary layer edge), this was not always the case when stronger disturbances of the measurement signals were observed (e.g. close to the plate's surface).

Nevertheless, the information obtained from the RAA experiments appears to be adequate for future ensemble-averaged representation, which is of particular importance when conducting statistical analysis.

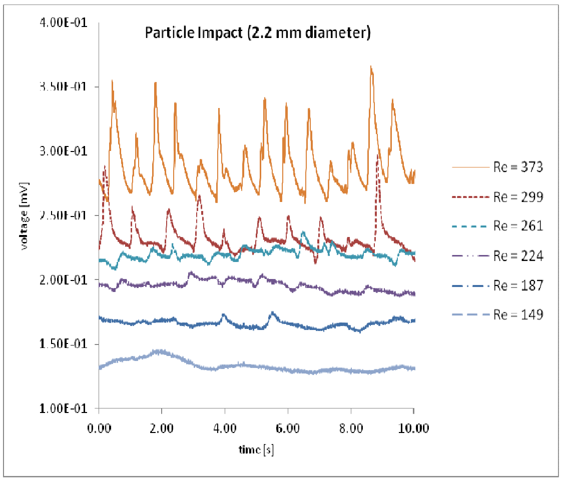

Fig. 5 The impact of a 2.2 mm diameter particle at several free stream velocities.

In a further experiment, work was undertaken to determine whether or not a critical particle Reynolds number exists for the generation of the previously-described turbulent-spot-like structures. For that reason, particles of different diameters, namely 2.2 mm and 4.0 mm, were driven through the flat plate's laminar boundary layer at several free stream velocities by making use of the RAA. In each case, the speed of the rotational arm was set to match the stream-wise velocity component of the particle at the edge of the boundary layer (before entering it) to that of the free stream. The corresponding particle Reynolds numbers were based on the particle's diameter and the current free stream velocity. This was believed to be valid, since close to the plate's surface the velocity of the air approaches zero due to the no-slip condition, while the particle is still moving at full speed.

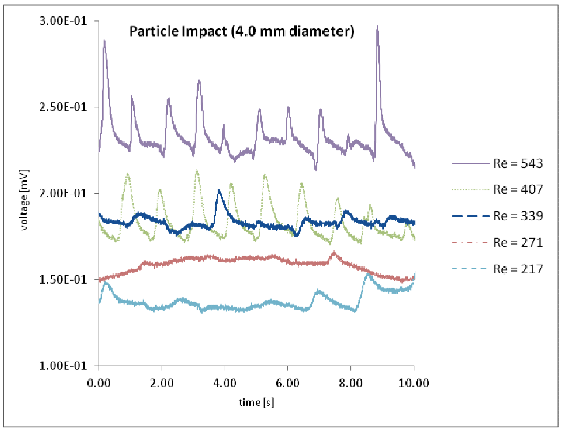

Fig. 6 The impact of a 4.0 mm diameter particle at several free stream velocities.

The density and the dynamic viscosity were both adjusted in accordance to the measured temperature and the pressure prevailing in the laboratory.

Consequently, for the same sized particle the experiment with the lowest free stream speed corresponds to the smallest particle Reynolds number.

The boundary layer state has been determined from a surface mounted hot film located approximately 300 mm downstream of the particle impact position. As is apparent from Figures 5 and 6, the experiments run at the lowest velocities resulted in readings where the upstream passage of the particle could hardly be identified for both chosen diameters. With increasing speed, thus increasing particle

Reynolds number, the single impacts become mor and more pronounced in the measurement signals; however, initially they rather appear as small amplitude disturbances which may grow or decay when travelling downstream depending on the stability of the affected boundary layer.

In fact, the structures that are typical of a turbulent spot do not develop below particle Reynolds numbers close to 300 in either case. However, the determination of an exact value is connected to some amount of ambiguity.

In order to obtain a clearer picture, the ensemble averaged RMS values of the signals have been determined in each case. These have been achieved by deriving the exact frequency of the single impacts from the rotational speed of the rotating arm and subsequent superposition of the corresponding signals over the calculated time frames. Figures 7 and 8 show the results for the 2.2 mm diameter and the 4.0 mm diameter case, respectively, in dependence of the resultant particle Reynolds number. In both cases, while remaining low at smaller Reynolds numbers, the curves are seen to sharply rise towards greater values.

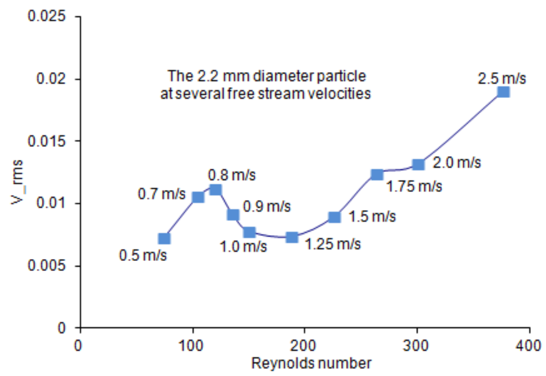

Fig. 7 Ensemble averaged RMS values of hot film measurements subjected by a 2.2 mm diameter particle at several free stream velocities.

Surprisingly, the critical Reynolds number seems to be somewhat greater for the particle with the larger diameter; however, more data is required to fully substantiate such a statement.

Furthermore, it is currently not known if addtional parameters, like for instance the ratio of boundary layer thickness to particle diameter, the local Reynolds number based on the distance from the plate's leading edge or the curvature of the particle's surface, will also play a role. All of these parameters were subject to considerable changes during this experiement.

It should be noted that in neither of the experiments a particle impingement on the plate's surface occurred.

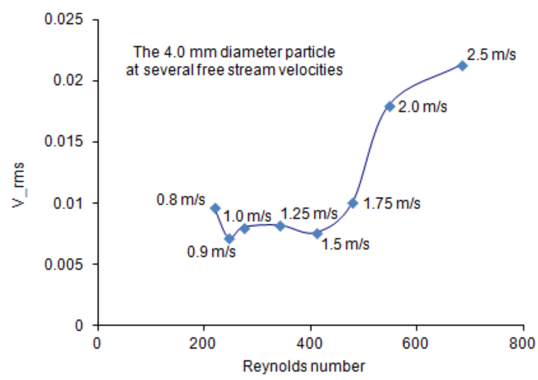

Fig. 8 Ensemble averaged RMS values of hot film measurements subjected by a 4.0 mm diameter particle at several free stream velocities.

Figure 9 shows illustrations from preliminary smoke flow visualizations at different stages during a RAA experiment (the flow direction is from right to left in each case). The impact of the device holding (and rotating) the arm is strong within the upper regions of the wind tunnel test section; however, the flow field in the vicinity of the flat plate (near the bottom of each illustration) appears not to be influenced much. Within the upper image the arm swings down towards the plate with some vortices emerging from the rotational arm. These probably originate from its relative velocity component in the transverse direction. The picture in the middle shows the particle after entering the flat plate's shear layer. Even though being entirely immersed in it, the effect of the particle onto the laminar boundary layer seems to be minor at that stage. This can be expected, since the outer regions of the boundary layer are still moving sufficiently fast to provide for a very low particle Reynolds number based on its relative velocity.

When examining the illustration at the bottom of Figure 9, however, the particle has passed the point of maximum deflection (and thus of maximum stream-wise relative velocity) and is already guided away from the surface. In this case, the turbulent event generated by the particle within the boundary layer is clearly visible.

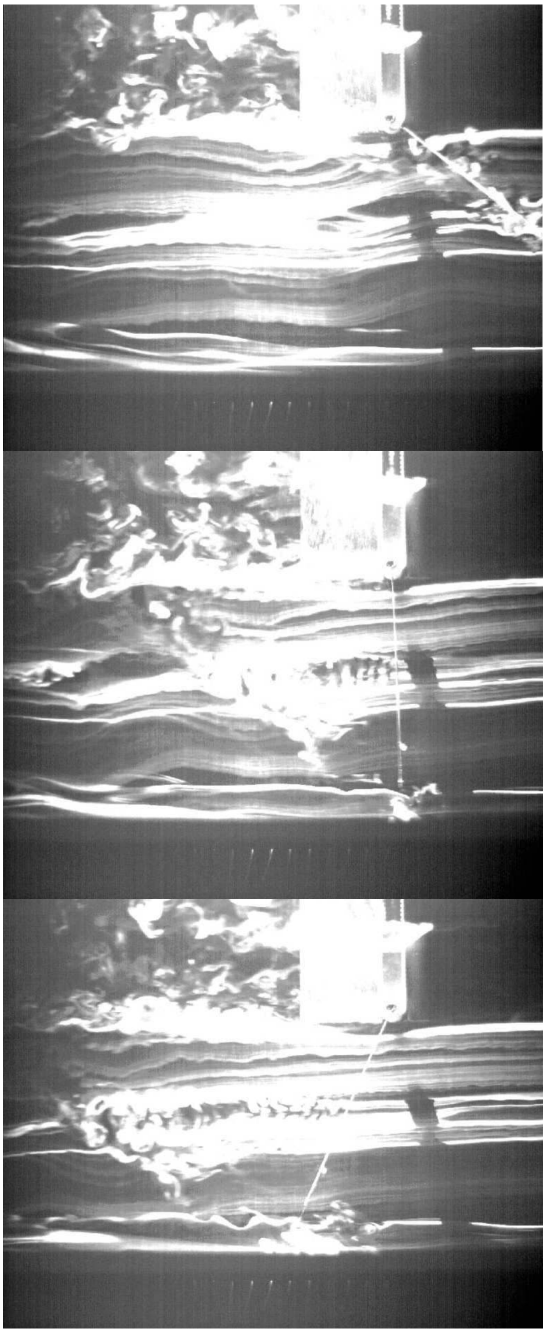

Fig. 9 Smoke flow visualization of a particle impact during the RAA, reproduced from Zhao [18].

It should be noted that neither of the illustrations show a development of vortices from the acupuncture needle representing the connection between the particle and the rotational arm. Thus, this component is assumed to be subcritical at all times.

4 Discussion

First results from the PA were shown to be promising. The main outcome obtained so far may be summarized as follows [14]:

(1) Hot wire traverses of the laminar boundary layer over a flat plate under the upstream influence of a passing particle closely resembled the occurrence of a turbulent spot when compared to previously published information [17].
(2) Only slight differences were found when comparing the data from a particle with surface impingement to that of a particle making no contact to the plate.
(3) The critical particle Reynolds number, Re_p, at which a turbulent event could be generated by a spherical particle was found to be substantially lower than previously published values (for the scenario this work is concerned with).
(4) The measurement data did not show any particle effect within the free stream regions.

While point (1) is generally in line with the original assumptions [7, 19-20], point (2) is in clear contradiction to the suggestion of Petrie et al. [21] that there must be a surface impact of the particle in order to produce a turbulent event.

Point (3) may be a result of the non-uniform flow field encountered by the particle which is characterized by strong shear, especially in regions close to the plate's surface. Thus, the shear parameter, K, as proposed by Sakamoto & Haniu [22], may have to be taken into consideration here.

Point (4), besides showing that the chosen experimental setup has succeeded in providing for near equilibrium conditions of the particle to the surrounding flow field within the free stream regions, substantiates the findings of Ladd & Hendricks [23]. In failing to detect any impact of a particle when suspending it from within the laminar boundary layer over an ellipsoid in water, they concluded that there must be a relative velocity component between the particle and the flow medium, in order to be effective.

Nevertheless, it must be stressed, that the above results are based on single particle impacts. The subsequently-employed RAA was capable of capturing a sequence of occurrences, thus allowing for an ensemble averaged representation of the data, which will increase confidence in the established conclusions.

Additionally, the temporary alteration of the affected velocity profile incurred by a passing particle (when considering that the no slip condition must also apply to the particle's surface) could have an impact on the stability of the laminar boundary layer [12]. In other words, very small (hence otherwise subcritical) particles could have an effect if occurring with sufficient frequency, an observation that has found only little consideration until now (this was not considered by Hall [7] for example). However, the results of this study may provide further insights into this phenomenon.

5 Proposal for Future Work

The information obtained in this work does not give an indication of whether or not the turbulent event produced by a particle's impact would eventually result in a fully turbulent boundary layer. Due to the nature of the experiment, namely determining whether or not a turbulent-spot-like flow structure is generated by a particle passing through an otherwise laminar shear layer, the measurement location was chosen as close as possible to the particle's impact. The gathered data shows that this is insufficient to detect in what way the particle, when travelling through the laminar boundary layer, influences its "natural" transition to a turbulent state.

Thus, it is recommended to also monitor the changes in the transition region during future experiments. However, care should be taken that these results are not affected by the intrusiveness of potential measurement equipment located further upstream.

Furthermore, two modifications are proposed as an upgrade to the current setup:

(1) A means should be provided to relate all particle impact measurements to a common time scale as this could alleviate the post-processing procedures considerably.

(2) In addition, a means should be provided to temporarily hold the rotation of the particle in order to allow for the flow field to recover its original state before a subsequent particle impact occurs.

On the other hand, it should be noted that the proposed method is quite suitable to investigate the influence of particle flux.

Having established a critical particle Reynolds number of a smooth spherical particle for a turbulent event to be generated, subsequent experiments should also include investigations on cylindrical particles of the dimensions as proposed by Hall [7], namely a length-to-diameter ratio, *L/D*, of 2.5, as this would provide for useful correlation of laboratory results to those partially derived from flight tests. In a final step, particle geometries that are more representative of actually occurring ice crystal shapes should be explored. It is worth noting this regarding that such experiments have already begun. Dabadie & Coisnon (2011) [15] investigated the effect of both a cylinder (L/D ~ 3.3) and a sphere of the same diameter (6.0 mm) at otherwise identical experimental conditions on the shape factor of the local boundary layer profile. While both values were affected, the influence of the cylinder was considerably larger approaching values that are commonly considered turbulent.

This is expected, since also in a uniform flow filed, the critical value of a cylinder is considerably smaller, especially, when not being of infinite length.

It should be noted that the RAA may have the potential for a water channel experiment. This would allow for an additional increase of the experiment's dimensions at further reduced speeds, and thus for considerable alleviations with regard to applied measurement techniques and optional flow visualisation.

6 Conclusions

(1) The information on the mechanisms leading to the transition of a laminar boundary layer due to a small particle travelling through it is incomplete.

(2) The previously proposed critical particle parameters above which transition is triggered within the affected boundary layer have not been experimentally verified until today.

(3) Conventional laboratory methods are not likely to capture all facets of the naturally occurring mechanisms without appreciable efforts.

(4) An alternative method, which was developed by the authors specifically for this purpose and which is quite simple in terms of its complexity, has been successfully employed in this study.

(5) A particle travelling through an initially laminar boundary layer is capable of producing a turbulent event, which closely resembles the characteristics of a turbulent spot when compared to previously published information.

(6) An impingement of the particle onto the plate's surface is not required for such a turbulent event to be generated; it is assumed to be a result of turbulent contamination originating from the particle's wake above certain critical conditions.

(7) The critical Reynolds number of a smooth spherical particle for a turbulent event to be produced within the affected laminar boundary layer has been determined to be approximately in the order of 300.

Acknowledgments

This study has only been possible by cooperation with the University of Glasgow, who kindly provided their wind tunnel facility. It owes thanks to both academic and technical staff for their scientific input, and technical support, respectively.

References

[1] Schrauf G & Kühn, W., "Future needs and laminar flow technology". Air Space Eur 2001, 3(3–4): 98–100.

[2] Young TM. "*Investigations into the operational effectiveness of hybrid laminar flow control aircraft*", PhD Thesis, Cranfield University, UK, 2002.

[3] Boeing, "Boeing 787 Dreamliner Livery Change Enhances Airplane Performance", press release, Seattle, 10th Jul 2006, accessed 28th Feb 2013: http://www.boeing.com/news/releases/2006/q3/060710d_nr.html.

[4] Young, T.M., "An investigation into potential fuel savings for 110–130 seat passenger transport aircraft due to the incorporation of natural laminar flow or hybrid laminar flow control on the engine nacelles", J. Aero. Eng., Vol. 227(8), 2013.

[5] Joslin, R.D., "Aircraft laminar Flow Control", Annu. Rev. Fluid Mech., Vol. 30, 1998, pp. 1-29.

[6] Young, T.M., Brown, P.R.A., Fielding, J.P. The Impact of Cloud Encounter on Hybrid Laminar Flow Control Aircraft Operations, CEAS Aerospace Aerodynamics Research Conference, Cambridge, Paper 58, 10-12 June 2002.

[7] Hall, G.R., "On the Mechanics of Transition Produced by Particles Passing Through an Initially Laminar Boundary Layer and Estimated Effect on the Performance of X-21 Aircraft", Northrop Corp., Contract-No.: N79-70656, 1964.

[8] Davis, R.E., Maddalon, D.V., Wagner, R.D., "Performance of Laminar Flow Leading Edge Test Articles in Cloud Encounter", NASA CP-1987-2487, Langley Research Center, USA, 1987.

[9] Fowell, L.R. & Antonatos, P.P., "Some Results from the X-21A Program", AGARDograph, Part I, Recent Developments in Boundary Layer Research, May 1965.

[10] Schmidt C., Young M.T., "Turbulent Contamination of Laminar Flow due to free Stream Particles," 12th AIAA ATIO Conference, 17th-19th Sep, Indianapolis, USA, 2012.

[11] Schmidt, C. & Young, T.M. The Impact of Cirrus Cloud on Laminar Flow Technology, 7th AIAA Aviation Technology, Integration and Operations Conference (ATIO), 18-20 Sep, Belfast, Northern Ireland, 2007.

[12] Schmidt, C. & Young, T.M., "The impact of freely suspended particles on laminar boundary layers", 47th AIAA Aerospace Sciences Meeting (ASM), 5-8 Jan, Orlando, Florida, USA, 2009.

[13] Schmidt C., "Laminar Flow Breakdown due to Particle Interaction", AFRL-AFOSKR-UK-TR-2012-0035, Final Report, Contract-No.: EOARD 11-3044, 2012.

[14] Schmidt, C., Young, T.M., Benard, E.P., Atalay, S., “The influence of cirrus cloud on drag reduction technologies based on laminar flow”, CEAS/KAT net II Conference on Key Aerodynamic Technologies, 12th-14th May, Bremen, Germany, 2009.

[15] Dabadie, C., Coisnon, R., “Etude de la transition par particule”, Institut Supérieur de l'Aéronautique et de l'Espace, Dép. Aérodynamique, Energétique et Propulsion, Toulouse, France, 2011.

[16] Schlichting, H. “Boundary Layer Theory”, 7th Edition, McGraw-Hill Book Company, 1979.

[17] Cantwell, B., Donald, C., Dimotakis, P., “Structure and entrainment in the plane of symmetry of a turbulent spot”, , J. Fluid Mech., Vol. 87, 1978, part 4, pp. 641-672.

[18] Zhao, L., “Experimental study of laminar to turbulent transition effect by flying particles”, MSc thesis, Dep. Aerospace Engineering, University of Glasgow, Glasgow, UK, 2010.

[19] Hall, G.R., “Interaction of the wake from bluff bodies with an initially laminar boundary layer”, AIAA Journal, Vol. 5, No. 8, pp. 1386-1392, 1965.

[20] Hall, G.R., “Interaction of the wake from bluff bodies with an initially laminar boundary layer”, AIAA-1966-126, Aerospace Sciences Meeting, 3rd, New York, N.Y., Jan 24-26, Paper 66-126, 1966.

[21] Petrie, H.L., Morris, P.J., Bajwa, A.R., Vincent, D.C., “Transition induced by Fixed and Freely Convecting Particles in Laminar Boundary Layers”, The Pennsylvania State University, Appl. Res. Lab., PA, USA, 1993.

[22] Sakamoto, H. & Haniu, H., “The formation mechanism and shedding frequency of vortices from a sphere in uniform shear flow”, J. Fluid Mech., Vol. 287, 1995, pp. 151-171.

[23] Ladd, D.M., Hendricks, E.W., “The effect of background particulates on the delayed transition of a heated 9:1 ellipsoid”, Exp. in Fluids, Vol. 3, 1985, pp. 113-119.

Computational Investigation of the Influence of Ground Proximity on the Aerodynamics of an Isolated Wheel

T. D. Kothalawala, A. Gatto, L. Wrobel
Brunel University, UK

Keywords: *Aerodynamics, CFD, Ground Proximity, Landing Gear, Wheel*

Abstract

Landing gear is known to be one of the main contributors to the noise generated from an aircraft on approach. The scope of this work is to carry out an initial exploratory investigation using an isolated wheel to aid in the understanding of the aerodynamics around a landing gear. The isolated wheel considered in this paper was modelled in free air initially to provide a baseline and thereafter with decreasing ground proximity. The effect of Yaw and Turbulence Intensity (Tu) with decreasing ground proximity were also modelled to understand how these variables affect the aerodynamic flow field around the wheel.

1 Introduction

The effect of ground proximity on the aerodynamics of an aircraft's landing gear is a complex problem which has received little attention in the aircraft industry. Landing gear is a major contributor to the noise levels generated from aircraft on approach and results from unsteady variations in the flow field as the air interacts with the exposed components of the gear. The resultant affect of this noise produces significant disruption and discomfort to the many millions of people who live in the vicinity of airports.

One of the first studies to consider wheel aerodynamics was conducted by Fackrell [1] who performed an experimental investigation using an isolated wheel in contact with the ground. This study which used a moving floor on a range of wheel profiles, showed that less drag is produced from an isolated rotating wheel than from a stationary wheel in contact with the ground. Local areas of separation over the top of the wheel were also found. The rotating wheel configuration in contact with the ground was also found to produce a much higher pressure at the upstream area of contact patch beneath the wheel. Based on [1], McManus and Zhang [2] also carried out a computational study for a wheel in contact with the ground. This study was focused on the same wheel geometry in [1] with lift and drag force coefficients of C_D=0.48 and C_L=0.35 being obtained from a stationary wheel in contact with the ground. Areas of separation were also identified on the top rear shoulders of the wheel as well as counter-rotating vortices on the lower half of the wheel. These vortices were thought to be caused by the interaction between the flow over the top of the wheel and the main flow emerging from the sides. For the case of the rotating wheel, the flow also separated near the top of the wheel subsequently forming an arch shaped vortex. Additionally for this configuration, the flow travelling from under the front of the wheel in contact with the ground formed another separated region, but this region was found to be smaller for the rotating wheel than the stationary wheel. More recently an experimental study was carried out by Zhang et al[3] on a single wheel in free air. This study also showed lines of separation around the top of the wheel as the air from the hub area interacts with the air around the sides of wheel. The flow was also found to pass around the edges of the wheel and meet at the rear causing four streamwise trailing vortices to appear.

2 Methodology

2.1 Wheel Geometry

The wheel geometry modeled in this study was the 'A2' configuration detailed in [1] and used in the computational results detailed in [2]. The diameter and breadth of the wheel are 0.416m and 0.191m respectively.

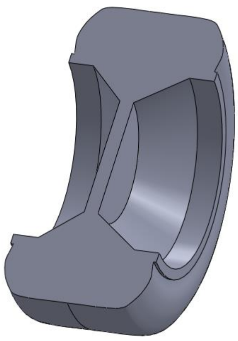

Fig. 1 Cross-sectional view of wheel in CAD.

2.2 Computational Approach

Pointwise© mesh generation software was used to create all grids. Initially, the wheel was placed in the center of the computational domain to consider the free air configuration with the main structured grid containing over 2 million cells. Criteria to be met included; keeping the Equiangle Skewness below 0.9, keeping the Jacobians (volume of the blocks) positive and ensuring a wall spacing around the surfaces of the wheel corresponds to a y+ value

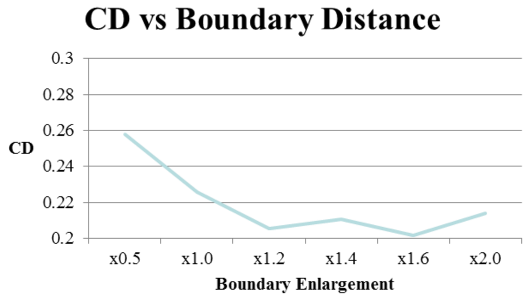

Fig. 2 Graph showing C_D vs. Boundary Distance.

of near 1. The inlet free stream velocity ($U\infty$) was kept at 70m/s giving a Reynolds number of 1.9×10^6.

2.2.1 Boundary & Mesh Refinement Study

A boundary and mesh refinement study was carried out to find the most appropriate sized grid which provides a good accuracy whilst keeping the computational time to a minimum. For the boundary refinement study, the far field boundary distance was changed by 0.5, 1.2, 1.4, 1.6 & 2 times the original grid size. From these simulation results, the values of C_L & C_D were obtained and plotted on a graph (Fig. 2), against the boundary enlargement. The final boundary size chosen for the study was where C_D was within 99% of the final value of C_D. Similarly for the mesh refinement study, a mesh density study was also conducted using grids of 1, 4 and 6 million cells. Using the same approach used for the boundary study, a final mesh of over 3 million cells was chosen.

2.3 Computational Grid

According to the boundary and mesh refinement study, the most appropriate sized grid consisted of over 3 million cells and a far field boundary distance 1.2 times the original grid size. The final configuration is shown in Fig.3.

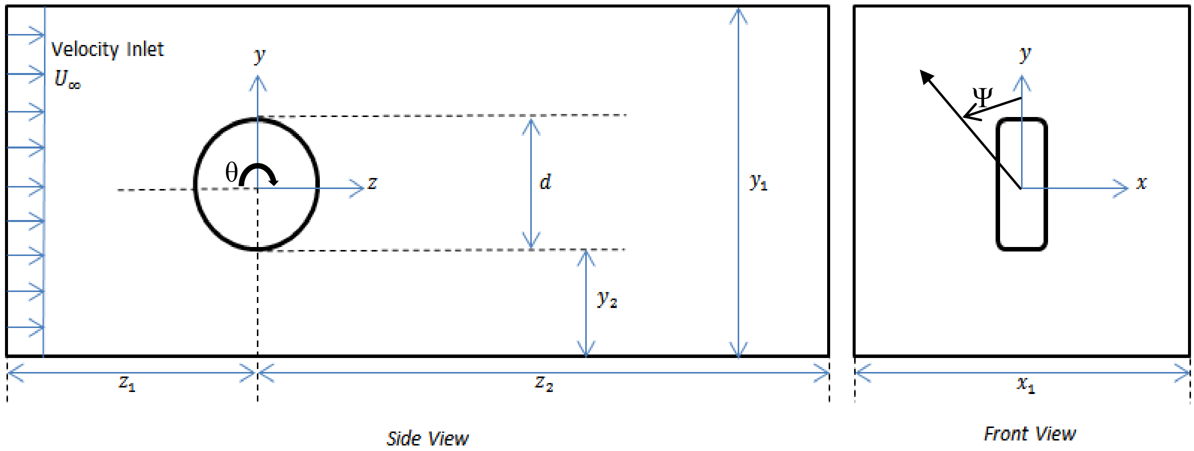

Fig. 3 Computational Geometry.

Overall, the inlet domain had a width $x_1/d=$ 2.19 and a height of $y_1/d=$ 6.04. The inflow boundary was placed at a distance of $z_1/d=$ 6 upstream of the wheel and the outflow boundary placed at a distance of $z_2/d=$ 18 downstream of the wheel. To understand the effect of decreasing ground proximity, the wheel was modeled closer to the ground by halving the distance from the bottom of the wheel to the ground by half in two instances, i.e. $y_2/d=2.52$ (free air), $y_2/d=1.26$ and $y_2/d=0.63$.

2.3.1 Simulation Parameters

Both RANS & URANS methods were used for simulation in the present work. The flow around a wheel of an aircraft's Landing gear is highly unsteady due to the large amounts of flow interactions. Therefore the unsteady URANS solver is expected to provide results to a better level of accuracy compared to the steady RANS solver. Comparisons between RANS & URANS can therefore be made directly.

2.3.2 Turbulence Modeling

The turbulence model used for this study is the two equation Realizable k-ε model, due to its simplicity and accuracy [6]. This model is known for working with boundary layers, strong and adverse pressure gradients, separation, rotation and recirculation; all of which are involved in the flow around a landing gear in turbulent flow conditions. This model has also been used in similar studies with reasonably good accuracy [2]. The turbulence settings within the boundary conditions for the inlet were set to have turbulence intensity (Tu) of 0.2%, 1.0% and 5.0% respectively.

2.3.3 Boundary Conditions

The inlet boundary condition was set as a velocity inlet and the outlet boundary condition was set as a pressure outlet with a gauge pressure of zero. The walls of the computational domain and the wheel were kept as a stationary wall with a symmetry condition.

2.3.4 Solution Settings

During the steady state solution in the RANS condition, the simulations were run until it the residuals converged by up to five orders of magnitude. In some simulations, the flow did not converge for a few thousand iterations but had become steady. In this case, the simulation was terminated. For the unsteady solver, a time step of 0.01s was used with 20 iterations per time step. For these cases the model was also simulated until the residuals converged by up to three orders of magnitude.

3 Results

For the wheel in free air, the path of the flow around the wheel, Fig.4, shows the air coming on to the wheel and colliding with the front face, representing a stagnation region. The flow accelerates from 70m/s to 98m/s as it travels around the sides of the wheel as the air approaches the hub section. The air was found to flow into the hub and is thereafter circulated inside. At the back of the wheel, wakes of significant breadth and depth are formed.

The coefficient of pressure (Cp) along the centerline of the wheel from the RANS & URANS cases, Fig. 5, were found to have a very similar shape to the pressure distribution observed in Lazos's study [4]. The graph in Fig. 5 shows the stagnation pressure at 0° where Cp≈1. When looking at the side view cross section of the wheel (as shown in Fig. 3 denoted 'side view'), the pressure is at a maximum where the flow hits the wheel and then reduces to a minimum as the air travels around the top and bottom of the wheel. At this angular position from URANS, velocity increases to 91m/s as the air accelerates around the top & bottom of the wheel due to the curvature. The velocity reduces thereafter by 50% at the back of the wheel where θ=180°. The RANS curve also shows low pressure on top of the wheel at θ≈90-130°, indicating that separation is caused near the top rear of the wheel. The area on the curve where $C_{p\approx}0$, shows the area of the wake formed behind the wheel. Comparing the RANS

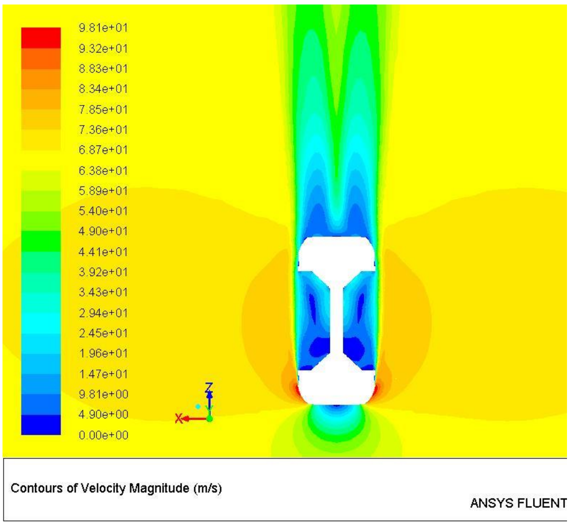

Fig. 4 Top view Velocity Magnitude Contour Plot across cross-section on wheel in free air

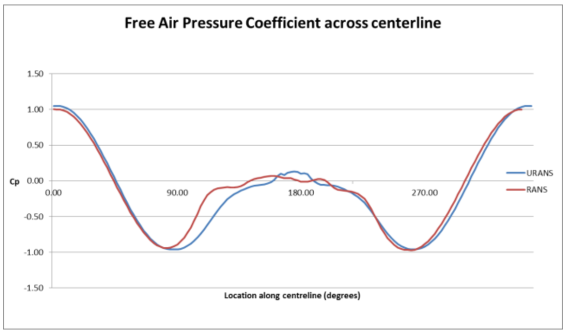

Fig. 5 Graph of URANS Cp across Centerline.

to the URANS results, lift and drag forces were found to be C_D=0.41 and C_L =0 respectively and C_D=0.21 and C_L =0.04 using the RANS method. This difference of 51% in the value of C_D between the URANS & RANS shows that there is a significant difference between the unsteady flow being modeled in a steady environment.

3.1.1 Ground Effect

The wheel was lowered closer to the ground twice from its position in the center of the computational domain. As the wheel gets closer to the ground, there is a trend for the drag to increase in both RANS & URANS simulations as shown in Table 1. This was expected as there is increased activity between the bottom of the wheel and the ground. Using the steady solver the velocity of the flow beneath the wheel varies between 83m/s to 90m/s in free air and at y_2/d=0.63. This shows that as the wheel gets closer to the ground, the velocity between the ground plane and the wheel increases.

	RANS		URANS	
Distance	Cd	Cl	Cd	Cl
y_2/d=2.52	0.21	0.04	0.41	0.00
y_2/d=1.26	0.22	0.00	0.46	0.00
y_2/d=0.63	0.26	-0.01	0.41	0.00

Table 1 Coefficient of Drag & Lift in RANS & URANS as wheel gets closer to the ground

In McManus and Zhang's study [2], a value of C_D =0.48 was obtained using URANS for the for a wheel in contact with the ground. The value of C_D obtained here in transient conditions at y2/d=0.63 was C_D =0.41. This is only a 15%

difference compared to the value obtained in [2] giving some confidence in the results.
Similarly, [2] states a value of C_L = 0.35 for the wheel in contact with the ground. In this study a value of zero was achieved when simulated in URANS, indicating possibly that close proximity to the ground was needed for a change in lift to develop.
Velocity contour plots across the centerline of the wheel for both RANS & URANS modeled in free air, and at y_2/d=0.63, are shown in Fig. 6.

In the RANS simulation in free air (a), circulation occurs on the rear lower side of the wheel at 200°, and on the upper half there is a reduced area of circulation at θ=125°. The speed in which the flow travels over and under the wheel at 90° & 270° is also greater by 5-10% when compared to the URANS simulation. As the wheel gets closer to the ground, the RANS simulation shows the areas of circulation at θ=105° & θ=240° and a stronger wake formed behind the wheel.

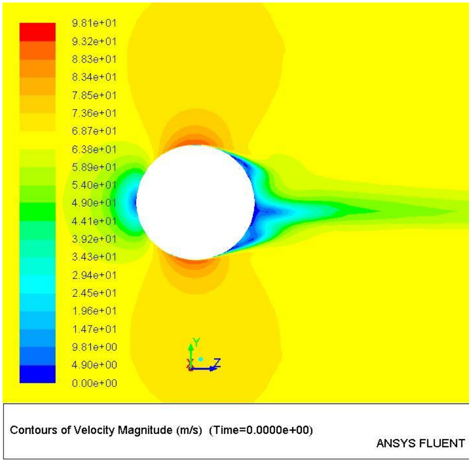

(a) RANS – Free Air

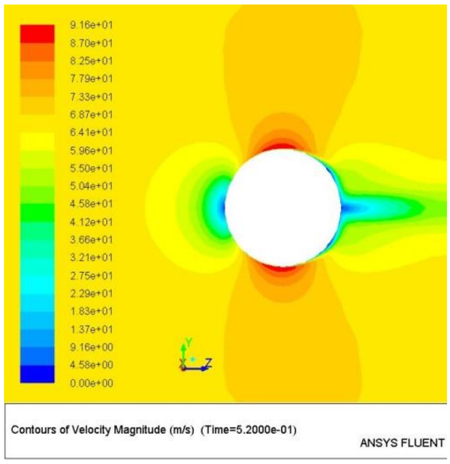

(d) URANS – Free Air

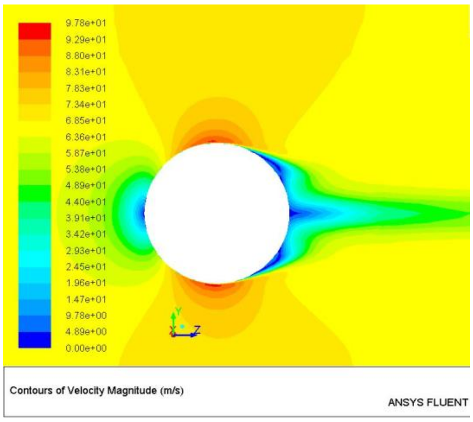

(b) RANS – y_2/d = 0.63

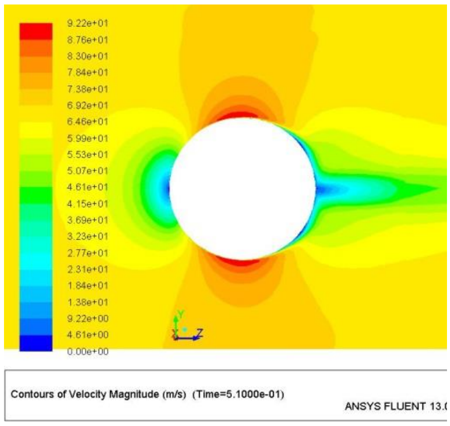

(c) URANS – y_2/d = 0.63

Fig. 6 Velocity Magnitude Contour plots x=0 plane

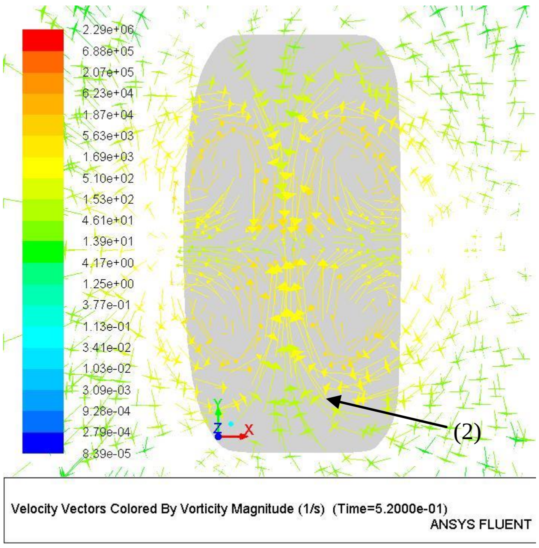

(a) y_2/d = 2.52 - Free air

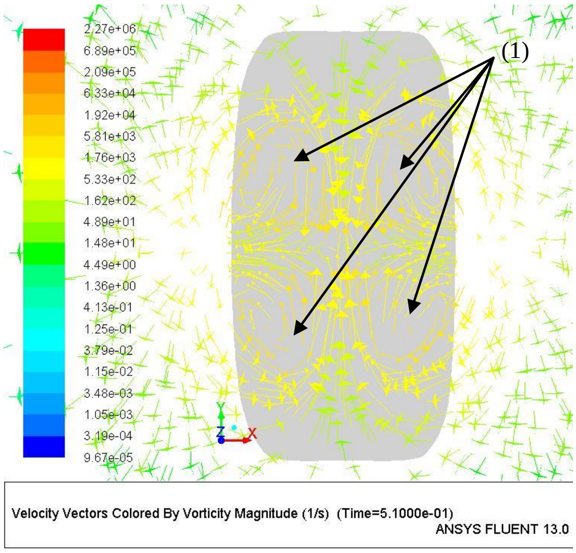

(b) y_2/d = 0.63

Fig. 7 Velocity Vectors showing vorticity behind the wheel in z/d=0.504 in URANS solver

As the air travels to the rear of the wheel, the flow tries to accommodate the wheels curvature but as it interacts with the flow coming upwards from underneath the wheel, the air is circulated, Fig. 7 – (a) (2). Plots showing the vorticity behind the wheel in the plane z/d= 0.504 in free air and at the closest point to the ground modeled, is shown in Fig. 7. Areas of circulation are experienced in both simulations. As the wheel is lowered closer to the ground, the strength of the vorticity increases by 3%, Fig. 7-(b), compared to the wheel in free air. The vortices found in Fig. 7, compare well with the study conducted by Zhang, Smith & Sanderson [3]. They found four vortices at the rear of the wheel caused by the air passing around the edges of the wheel meeting at the rear. A comparable general flow structure is found in this study for the wheel in free air and is shown in Fig. 8.

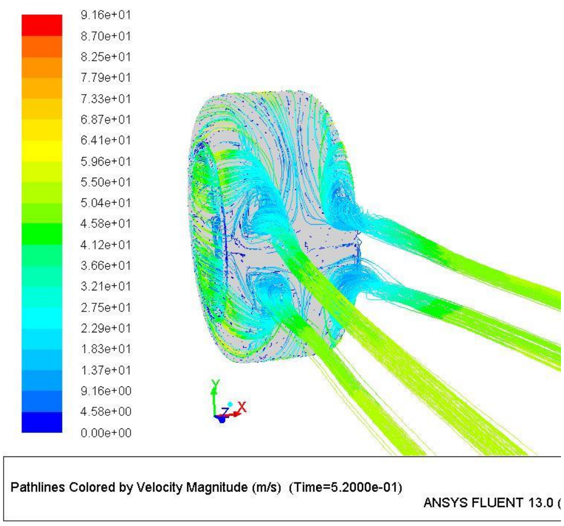

Fig. 8 Pathlines of Velocity Magnitude at y_2/d=2.52, URANS

3.1.2 Effect of Yaw (ψ)

The effect of yaw was modeled by rotating the wheel at 5, 10 & 20 degrees anticlockwise about its vertical y-axis. The simulations with varying yaw angle were also modeled with decreasing ground proximity. As an angle of yaw is applied and increased on the wheel in free air (Fig. 9), the wake created off the shoulder on the right becomes larger due to the decelerated flow in the hub on the right. As the angle of yaw increases, the area of circulation inside the hub increases. With 5° of yaw, the mean velocity of the flow in the right hub is 43m/s, but as the angle increases to 10° and 20°, the velocity decreases to 41m/s and 35m/s respectively. The main reason behind this reduction in velocity is thought to be due to more obstruction on the flow caused by the

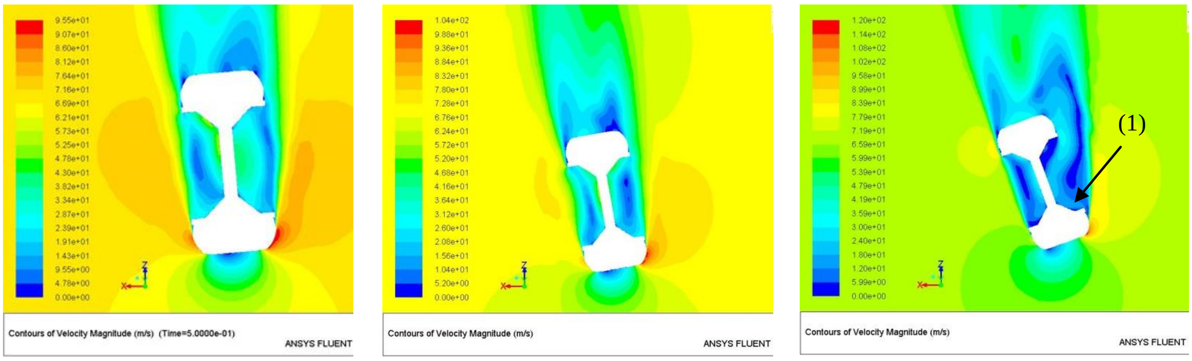

(g) RANS – Free Air 5° (f) RANS – Free Air 10° (e) RANS – Free Air 20°

Fig. 9 Top view Contour Plots of Velocity Magnitude across centerline of wheel with varying yaw angle

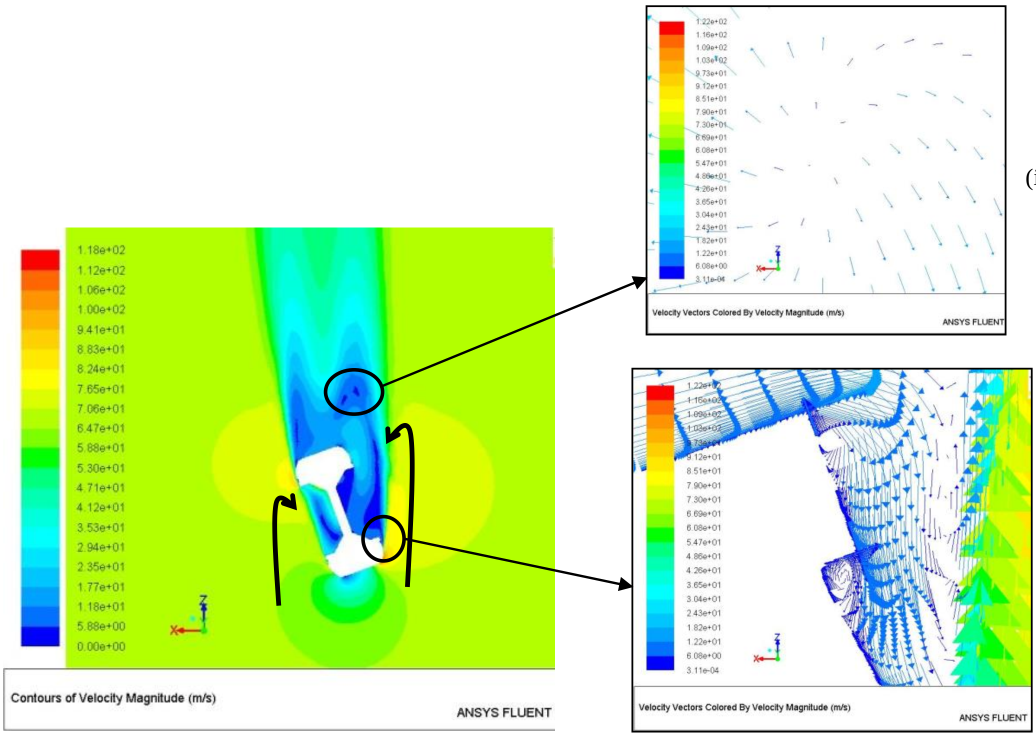

(i)

(h)

Fig. 10 Top view Velocity contour plot of flow around wheel at y_2/d=0.63

front face of the wheel, Fig. 9 – (e) (1). With only 5° of yaw applied on the wheel, Fig 9. (e), there is minimal change to the path of the flow compared to the wheel with 20° of yaw, Fig. 9 – (g), applied. Therefore the speed of the flow is reduced in and around the hub area of the wheel as the angle increases. On all three angles of yaw, separation of the flow is seen on both of the shoulders at the back of the wheel.

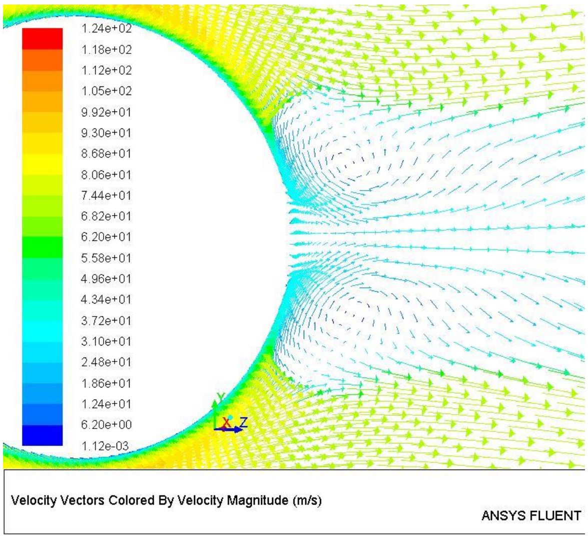

Fig. 11 Velocity Vector plot on cross section of wheel in free air

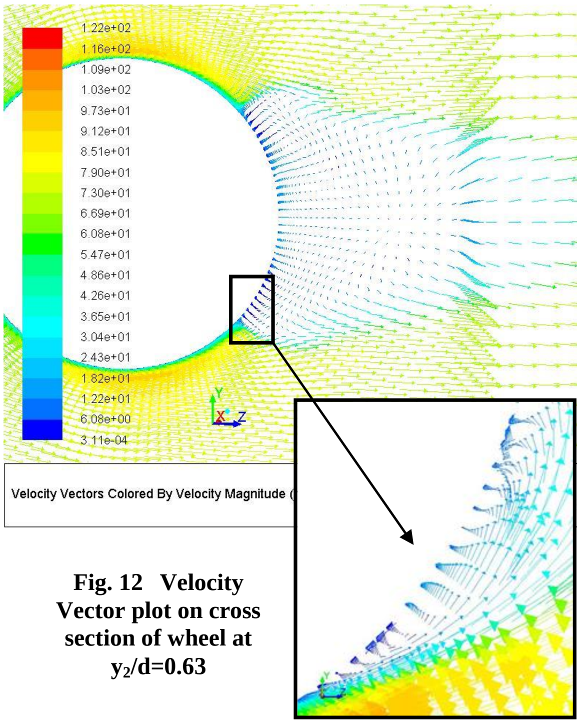

Fig. 12 Velocity Vector plot on cross section of wheel at y_2/d=0.63

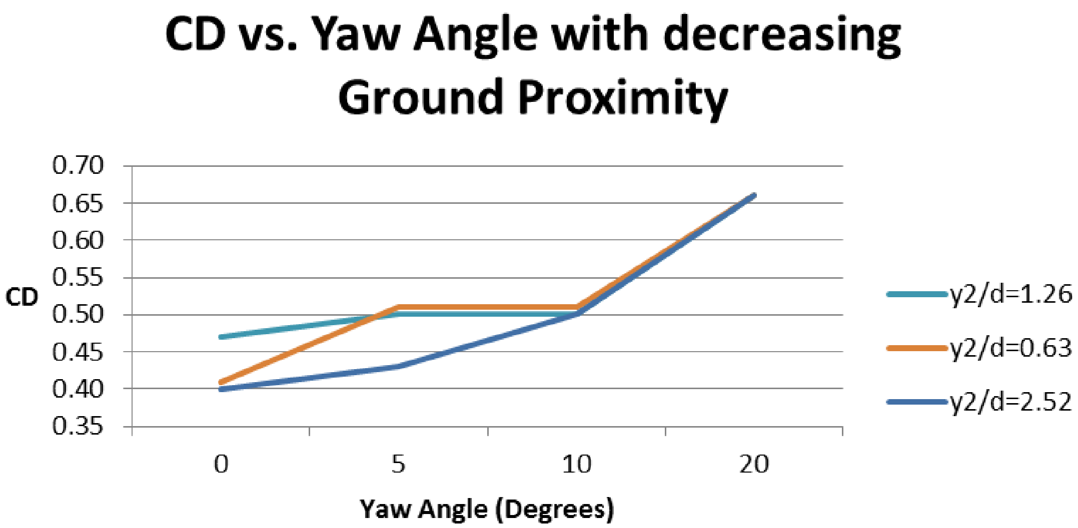

Fig. 13 Graph of C_D vs. Yaw angle with decreasing ground proximity

With the wheel at a distance of 0.26m from the ground shown in Fig. 10, the flow takes the path of the arrows as illustrated. The angle that the wheel is yawed causes the flow into the right hub to be obstructed by the front of the wheel. Alternatively, the flow in the left hub is circulated as it flows into the hub hitting the back edge. The enlarged section of the rim in Fig 10. – (h), shows the area of circulation caused by the oncoming flow interacting with the sharp corner edges of the rim. The wake behind the wheel also has areas where the air takes a more vortical characteristic Fig. 10 – (i). caused by the air travelling upwards from beneath the wheel at the back interacting with the wake.

The wake behind the wheel in free air with 20° of yaw (Fig. 11), shows a uniform and symmetrical wake about the wheel's centerline on the x=0 plane. However as the wheel is at a distance of 0.26m from the ground (Fig. 12), the air behind the wheel is pushed into one large wake covering most of the back edge of the wheel. Areas of circulation occur at θ≈240° near the ground side of the wheel (Fig. 12 enlargement) caused by the accelerated flow travelling from underneath the wheel, colliding with the air flowing from over the top.

Overall, the value of the coefficient of drag increases as the yaw angle increases with decreasing ground proximity, Fig. 13. As the yaw angle increases and the wheel is at its closest to the ground, the size of the wake is larger and pushed together, as seen when comparing Fig. 11 & Fig. 12. For these cases, C_D increased by 55%.

3.1.3 Effect of Turbulence Intensity (Tu)

The previous grids simulated and discussed in the present study all had turbulence intensity set to 0.2%. To analyze the effect of turbulence intensity, the Tu was changed to 1.0% & 5.0%. These grids were simulated in both RANS & URANS along with decreasing ground proximity.

The drag coefficient for these simulations (Fig. 14) shows that the drag increases as the turbulence intensity increases and as the wheel gets closer to the ground. As the distance from the wheel in free air to the ground is halved once, the drag coefficient is 6-12% higher for all intensities compared to when the wheel is at its lowest point to the ground at $y_2/d=0.63$. There is also an increase in velocity around the wheel as the turbulence intensity increases. In free air with a turbulence intensity of 0.2%, the velocity on the sides of the wheel is 70m/s but as the wheel was lowered by 0.786m, and turbulence

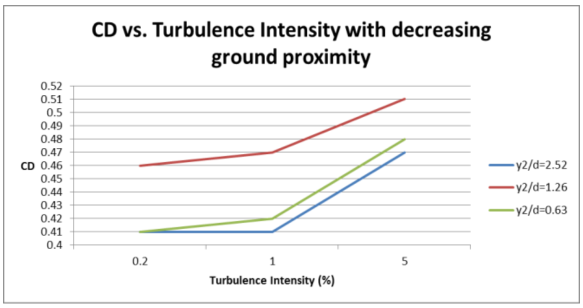

Fig. 14 Graph of C_D vs. Turbulence intensity with decreasing ground proximity

intensity increased to 5.0%, the velocity around

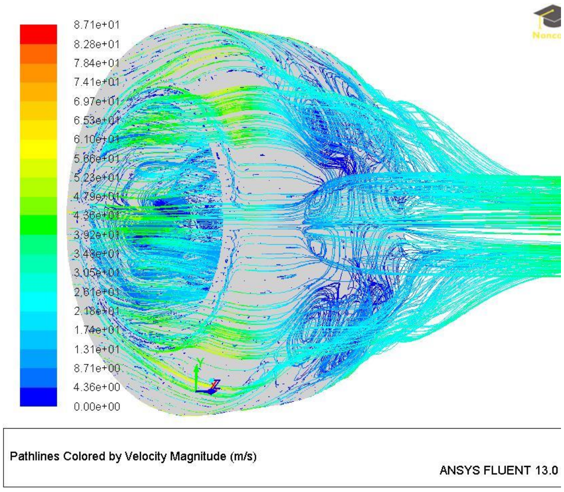

Fig. 15 Pathlines of Velocity Magnitude at $y_2/d=0.63$, with Tu=5.0%, RANS

the sides of the wheel increases to 79m/s. Additionally, at 0.625m from the ground with turbulence intensity of 5.0% (Fig. 15) four vortices are shown at the back of the wheel emanating from each shoulder as the flow separates. Comparing Fig. 15 to Fig. 16 which is simulated in the unsteady environment (URANS), the vortices created off the surface of the wheel are more prominent. In transient conditions, the four vortices can be seen to extend off the rear shoulders of the wheel, Fig. 16 – (a), but the vortices created in the RANS are more compact and pushed together forming a larger single wake. As can be seen from the contour scale, the velocity of the vortices and the flow in Fig. 15 is larger compared to the wheel in free air.

4 Conclusion

In this study both RANS & URANS methods was used to simulate and analyze the aerodynamics around a single landing gear wheel with decreasing ground proximity. The analysis also involved investigating the effect of varying yaw angle and turbulence. The results indicate that as the yaw angle & Tu increased with decreasing ground proximity, the value of C_D increased. Circulation is also experienced around the rims and inside the hub due to the

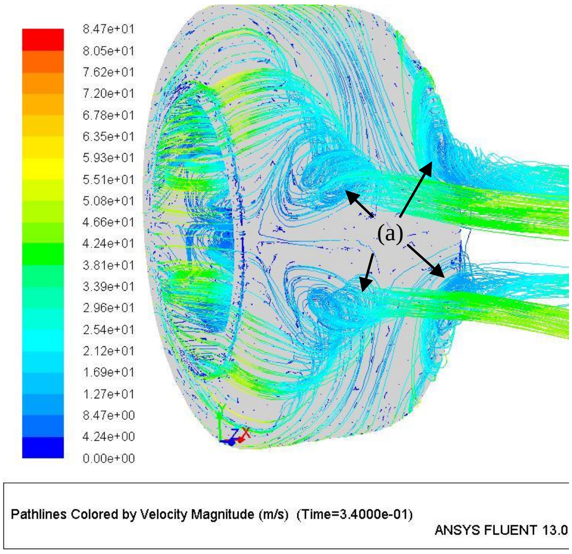

Fig. 16 Pathlines of Velocity Magnitude at y2/d=0.63, with Tu=5.0%, URANS

sharp edges on the wheel. As the yaw angle increases, a larger wake is created behind the wheel towards the right hand side (when looking in the +z direction). This indicates a region of low velocity being circulated in the hub on the sheltered side to the front of the wheel, not allowing air to travel directly past the wheel.

Substantial vorticity was also found behind the wheel, both in free air and with decreasing ground proximity. As the ground is approached the strength of the vorticity behind the wheel also increased. This increase was found in conjunction with four vortices trailing downstream.

References

[1] Fackrell J.E., “The Aerodynamics of an Isolated Wheel Rotating in Contact with the Ground,” Ph.D. thesis, University of London, U.K.., 1974.

[2] McManus J. and Zhang X., “A Computational Study of the Flow Around an Isolated Wheel in Contact With The Ground”, ASME, Vol. 128, May 2006, pp. 520-530.

[3] Zhang X., Ma Z., Smith M. and Sanderson M., “Aerodynamic and Acoustic Measurements of a Single Landing Gear Wheel”, AIAA, 19th AIAA/CEAS Aeroacoustics Conference, May 2013.

[4] Lazos B. S., “Mean Flow Features Around the Inline Wheels of Four-Wheel Landing Gear”, AIAA, Vol. 40, No. 2, February 2002, pp. 193-198.

[6] Ansys Fluent User Guide, Ansys Inc, Release 13.0, November 2010, pp. 645-646

Effects of Roll Maneuver on Unrestrained Aircraft Wing/stores Flutter

S. A. Fazelzadeh
Shiraz University, School of Mechanical Engineering, Shiraz, Iran

A. Mazidi
Yazd University, Department of Mechanical Engineering Yazd, Iran

A. H. Ghasemi
Islamic Azad University, Shahr Babak Branch, Shahr Babak

Keywords: flutter, unrestrained aircraft, external stores, roll maneuver

Abstract

The flutter of an aircraft wing carrying a fuselage at its semispan and arbitrary placed external stores under roll maneuver is studied. Maneuver terms are combined in the governing equations which are obtained using the *Hamilton's principle. The wing is represented* by a classical beam and incorporates bending-torsion flexibility. Theodorsen unsteady aerodynamic pressure loadings are considered to simulate the aeroelastic loads. The Galerkin method is subsequently applied to convert the partial differential equations into a set of ordinary differential equations. Numerical simulations are validated against several previous published results and good agreement is observed. In addition, simulation results are presented to show the effects of the roll angular velocity, fuselage mass, external stores mass and their locations on the wing flutter of an aircraft in free-flight condition. Parametric studies show that the predicted stability boundaries are very sensitive to the aircraft rigid body roll angular velocity, fuselage mass and external stores mass and locations.

1 Introduction

The flutter prediction of an unrestrained aircraft wing with stores as shown in Fig. 1 is of paramount importance for the analysis and design of an aircraft. Clearly, estimating the aeroelastic instabilities of such wing configurations is critical to establish the flight envelope of newly design aircrafts. One of the first works devoted to the aeroelasticity of aircraft wings with external store is the paper by Goland and Luke on the determination of the flutter speed of a uniform cantilever wing with tip mass[1]. Lottati considered the aeroelastic stability of a swept wing with tip weights for an unrestrained vehicle [2]. In his work a composite wing has been studied and it was observed that flutter occurs at a lower speed as compared with a clean wing configuration. Also, Edwards and Wieseman [3] studied the flutter and divergence of three check cases includes unrestrained airfoils and wing models.

Although these works and several others addressed the problem of the wing-store aeroelasticity, the effect of the aircraft maneuvers on the unrestrained aircraft wing instability has not received much attention in the literature and only few works about the maneuver effects on the aeroelastic behavior of wing-stores configuration have been conducted. The maneuver has a significant influence on the dynamic response and instability of the wing-store configuration. Since rigid body rotations due to maneuver angular velocities, such as the one produced by a roll maneuver, can adversely affect the aircraft aeroelastic stability region, it is critical to include maneuvering angular velocities in aeroelastic analysis.

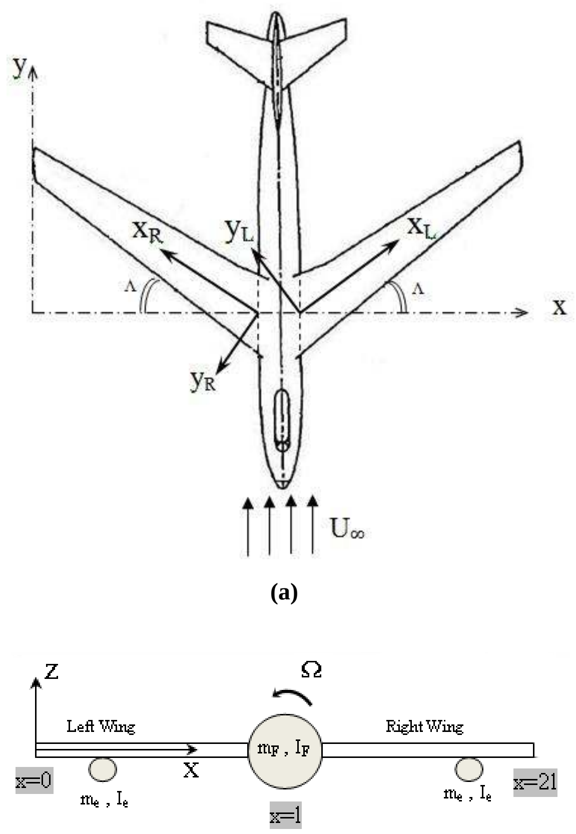

(a)

(b)

Fig. 1 Schematic of an unrestrained aircraft wing under roll maneuver, (a) Top view and (b) Front view

Meirovitch and Tuzcu [4, 5] have presented different works on simulating the motion of flexible aircrafts and derived some integrated approaches to control the complex maneuvering of an airplane. Two flight dynamics problems including the steady level cruise and a steady level turn maneuver were considered. The aeroelastic modeling and flutter characteristics of wing-stores configuration under different maneuvers was investigated by Fazelzadeh et al. [6, 7]. They have showed that the combination of flexible structural motion and maneuver parameters affects the flutter speed of the wing-stores configuration. Also, Mazidi et al. [8] studied the flutter of a swept aircraft wing-store configuration subjected to follower force and undergoing a roll maneuver.

To add to the aforementioned bulk of literature in this field, the aeroelastic modeling and flutter study of the unrestrained aircraft wings containing arbitrarily placed masses under roll maneuver is considered in this study.

2 Governing Equations

The equations of motion and boundary conditions are derived using Hamilton's variational principle that may be expressed as [9]:

$$\int_{t_1}^{t_2}[\delta U_T - \delta T_T - \delta W_T]dt = 0 \qquad (1)$$
$$\delta w = \delta\theta = 0 \quad \text{at} \quad t = t_1 = t_2$$

where U and T are strain energy and kinetic energy, and W is the work done by non-conservative forces. Also, the subscript 'T' means total system. The use of Hamilton's principle is especially convenient in cases of unusual boundary conditions, because the equation(s) of motion and boundary conditions are determined in a unified procedure. Therefore The Hamilton's principle yields the equations of motion in the form of partial differential equations with accompanying boundary conditions.

The kinetic energy can be divided into three parts; wing, fuselage and store, i.e. $T_T = T_W + T_e + T_F$. The subscripts w, e and F identify the wing, externally mounted mass and aircraft fuselage, respectively. The first variation of the wing kinetic energy is:

$$\delta T_W = \delta T_{W_1} + \delta T_{W_2} \qquad (2)$$

where δT_{w_1} and δT_{w_2} are the first variation of the right and left wing kinetic energy, respectively.

$$\begin{aligned}\delta T_{w_1} &= \int_0^1\iint_A \rho\dot{\mathbf{R}}_{w_R}.\delta\dot{\mathbf{R}}_{w_R}\,dxdA\\ \delta T_{w_2} &= \int_0^1\iint_A \rho\dot{\mathbf{R}}_{w_L}.\delta\dot{\mathbf{R}}_{w_L}\,dxdA\end{aligned}\tag{3}$$

$\mathbf{R}_w$'s are displacement vectors of arbitrary points of the right and left wings that are given by:

$$\begin{aligned}\mathbf{R}_{w_R} &= \mathbf{R}_{O_R} + \mathbf{r}_{w_R}\\ &= (R_X\cos\Lambda - R_Y\sin\Lambda)\mathbf{i}_R\\ &+ (R_X\sin\Lambda + R_Y\cos\Lambda)\mathbf{j}_R\\ &+ [w_1 + (y_1 - ab)\theta_1 - R_Z]\mathbf{k}_R\\ \mathbf{R}_{w_L} &= \mathbf{R}_{O_L} + \mathbf{r}_{w_L}\\ &= (R_X\cos\Lambda - R_Y\sin\Lambda)\mathbf{i}_L\\ &+ (-R_X\sin\Lambda - R_Y\cos\Lambda)\mathbf{j}_L\\ &+ [w_2 + (y_2 + ab)\theta_2 - R_Z]\mathbf{k}_L\end{aligned}\tag{4}$$

where $\mathbf{R}_O$'s are the wings root position vector with respect to airplane center of gravity, shown in Fig. 1 and $\mathbf{r}_w$'s are the position vector of arbitrary points of the wings with respect to the wings root. The velocity vector of any points on the wing can be obtained through transport theorem as below:

$$\dot{\mathbf{R}}_{w_i} = \frac{\partial \mathbf{R}_{w_i}}{\partial t} + (\mathbf{\Omega}\times\mathbf{R}_{w_i}) + \mathbf{V}_{airplane}\tag{5}$$

In this equation, two first terms represent the velocity of the point refers to coordinate system located on the airplane center of gravity. The third term represent the velocity of airplane refers to inertial coordinate system located on the earth as:

$$\mathbf{V}_{airplane} = v_{xa}\hat{\mathbf{I}} + v_{ya}\hat{\mathbf{J}} + v_{za}\hat{\mathbf{K}}\tag{6}$$

Here it is assumed that the airplane has roll maneuver. So the angular velocity of the airplane refers to right and left wing coordinate systems are:

$$\begin{aligned}\mathbf{\Omega}_R &= -\Omega\sin\Lambda\mathbf{i}_1 + \Omega\cos\Lambda\mathbf{j}_1\\ \mathbf{\Omega}_L &= -\Omega\sin\Lambda\mathbf{i}_2 + \Omega\cos\Lambda\mathbf{j}_2\end{aligned}\tag{7}$$

By substitution of Eqs. (3-7) in Eq. (2) the first variation of the wing kinetic energy can be represented. Using the same kinematical procedure, the first variation of the store and fuselage kinetic energy can be derived. It should be noted that the velocity vector of any point on the store and fuselage, as before, is obtained through transport theorem.

The strain energy is considered next. The total strain energy, normally, consists of wing, fuselage and store strain energy. Here, it is assumed that the fuselage and stores are rigid bodies. Consequently, the total strain energy is equal to the wing strain energy. The first variation of the strain energy is:

$$\begin{aligned}\delta U = \int_V [&\sigma_{xx}\delta\varepsilon_{xx} + \sigma_{x\eta}\delta\varepsilon_{x\eta} +\\ &\sigma_{x\xi}\delta\varepsilon_{x\xi}]dxdA\end{aligned}\tag{8}$$

where σ_{ij} and ε_{ij} are stress and strain components, respectively. η and ξ are the principal axes of the wing cross section that defines a local coordinate system on the shear center of the cross section.

The use of strain-displacement relations, together with the generalized Hooke's law, permits the strain energy to be expressed in terms of deformation quantities. Using these expressions and integrating by parts, Eq. (8) recasts as:

$$\begin{aligned}\delta V_{R.w} &= \int_0^1 \{[EI\,w_1'''' + abEI\,\theta_1'''']\delta w_1 +\\ &\qquad [abEI\,w_1'''' + S\theta_1'''' - GJ\theta_1'']\delta\theta_1\}\,dx\\ \delta V_{L.w} &= \int_1^{21} \{[EI\,w_2'''' + abEI\,\theta_2'''']\delta w_2 +\\ &\qquad [abEI\,w_2'''' + S\theta_2'''' - GJ\theta_2'']\delta\theta_2\}\,dx\end{aligned}\tag{9}$$

where $\delta V_{R.w}$ and $\delta V_{L.w}$ are the right and left wing strain energy, respectively.

The virtual work of the aerodynamic forces acting on the wing may be expressed as:

$$\delta W_{n.c} = \int_0^l (L_1 \delta w_1 + M_1 \delta\theta_1)\,dx + \int_l^{2l} (L_2 \delta w_2 + M_2 \delta\theta_2)\,dx \tag{10}$$

where L and M are aerodynamic lift and moment, respectively.

Substituting Eqs. (2-10) into Eq. (1), and noticing that for every admissible variation ($\delta w_1, \delta\theta_1, \delta w_2, \delta\theta_2$) the coefficient of these variations must be zero, the aeroelastic governing equations are obtained as:

$$EIw''''_1 + m\ddot{w}_1 + mx_\theta\ddot{\theta}_1 + m\ddot{H} - mR_X\alpha - 2mR_Y\alpha\sin\Lambda\cos\Lambda - m\Omega^2 w_1 - mx_\theta\Omega^2\theta_1 + m\Omega^2 R_Z + m_F(\ddot{w}_1 + e_F\ddot{\theta}_1 + \ddot{H} - \Omega^2 w_1 - \Omega^2 e_F\theta_1)\big|_{x=l} + \sum_{i=1}^N m_e\delta_D(x_1 - x_{ei})(\ddot{w}_1 + e_p\cos\Lambda\ddot{\theta}_1 + \ddot{H} - R_X\alpha - 2R_Y\alpha\sin\Lambda\cos\Lambda - \Omega^2 w_1 - \Omega^2 e_p\cos\Lambda\theta_1 + \Omega^2 R_Z) - L_1 = 0 \tag{11}$$

$$-GJ\theta''_1 + mx_\theta\ddot{w}_1 + I_\theta\ddot{\theta}_1 + mx_\theta\ddot{H} - mx_\theta R_X\alpha - 2mx_\theta R_Y\alpha\sin\Lambda\cos\Lambda - mx_\theta\Omega^2 w_1 - I_\theta\Omega^2\theta_1 + mx_\theta\Omega^2 R_Z + \sum_{i=1}^N m_e\delta_D(x_1 - x_{ei})(e_p\cos\Lambda\ddot{w}_1 + k_e{}^2\cos^2\Lambda\ddot{\theta}_1 + e_p\cos\Lambda\ddot{H} - e_p\cos\Lambda R_X\alpha - 2e_pR_Y\alpha\sin\Lambda\cos^2\Lambda - e_p\cos\Lambda\Omega^2 w_1 - k_e{}^2\cos^2\Lambda\Omega^2\theta_1 + e_p\cos\Lambda\Omega^2 R_Z) - M_1 = 0 \tag{12}$$

$$EIw''''_2 + m\ddot{w}_2 + mx_\theta\ddot{\theta}_2 + m\ddot{H} - mR_X\alpha - m\Omega^2 w_2 - mx_\theta\Omega^2\theta_2 + m\Omega^2 R_Z + \sum_{i=1}^N m_e\delta_D(x_2 - x_{ei})(\ddot{w}_2 + e_p\cos\Lambda\ddot{\theta}_2 + \ddot{H} + R_X\alpha - \Omega^2 w_2 - \Omega^2 e_p\cos\Lambda\theta_2 + \Omega^2 R_Z) - L_2 = 0 \tag{13}$$

$$-GJ\theta''_2 + mx_\theta\ddot{w}_2 + I_\theta\ddot{\theta}_2 + mx_\theta\ddot{H} - mx_\theta R_X\alpha - mx_\theta\Omega^2 w_2 - I_\theta\Omega^2\theta_2 + mx_\theta\Omega^2 R_Z + \sum_{i=1}^N m_e\delta_D(x_2 - x_{ei})(e_p\cos\Lambda\ddot{w}_2 + k_e{}^2\cos^2\Lambda\ddot{\theta}_2 + e_p\cos\Lambda\ddot{H} + e_p\cos\Lambda R_X\alpha - e_p\cos\Lambda\Omega^2 w_2 - k_e{}^2\cos^2\Lambda\Omega^2\theta_2 + e_p\cos\Lambda\Omega^2 R_Z) - M_2 = 0 \tag{14}$$

In these equations x_e denotes the store distance from the wing root and e_p is the distance between the store center of gravity and the wing elastic axis. Also, m_e and k_e are the store mass and radius of gyration, respectively. In addition, m_F and k_F are the fuselage mass and radius of gyration, respectively and e_F is the distance between the fuselage center of gravity and the wing elastic axis.

3 Solution Methodology

Due to intricacy of aeroelastic governing equations, it is difficult to get the exact solution. Therefore, in order to solve the aeroelastic governing equations in a general way, the Galerkin's method is used [10]. To this end, w, θ (bending and torsion generalized coordinates) are represented by means of series of trial functions, φ_i that should satisfy the boundary conditions, multiplied by time dependent generalized coordinates, $\mathbf{q_i}$.

$$w = \varphi_1{}^{\mathbf{T}}\mathbf{q_1} \qquad , \theta = \varphi_2{}^{\mathbf{T}}\mathbf{q_2} \tag{15}$$

By applying the Galerkin procedure on these governing equations and use of orthogonal properties in the required integrations the following set of ordinary differential equations are obtained.

$$\mathbf{M}\ddot{\mathbf{q}} + \mathbf{C}\dot{\mathbf{q}} + \mathbf{K}\mathbf{q} = 0 \tag{16}$$

Herein, **M**, **C** and **K** denote the mass matrix, the damping matrix and the stiffness matrix, respectively, while **q** is the overall vector of generalized coordinates. Finally, Eq. (16) converts to:

$$\dot{\mathbf{Z}} = [\mathbf{A}]\,\mathbf{Z} \tag{17}$$

where the state vector $\mathbf{Z}$ is defined as:

$$\mathbf{Z} = \{\mathbf{q}^T \;\dot{\mathbf{q}}^T\}^T \tag{18}$$

and the system matrix [A] has the form:

$$[\mathbf{A}] = \begin{bmatrix} [\mathbf{0}] & [\mathbf{I}] \\ -[\mathbf{M}]^{-1}[\mathbf{K}] & -[\mathbf{M}]^{-1}[\mathbf{C}] \end{bmatrix} \tag{19}$$

The problem is now reduced to that of finding out the eigen-values of matrix $[\mathbf{A}]$ for a given values of the air speed parameter U_∞. The eigen-value ω is a continuous function of the air speed. For $U_\infty \neq 0$, ω is in general complex, $\omega = \mathrm{Re}(\omega) + i\,\mathrm{Im}(\omega)$. When $\mathrm{Re}(\omega) = 0$ and $\mathrm{Im}(\omega) \neq 0$ the wing is said to be in critical flutter condition. At some point, as U_∞ increases, $\mathrm{Re}(\omega)$ turns from negative to positive so that the motion turns from asymptotically stable to unstable.

Table. 1 Validation of the flutter speed and frequency for a wing in free flight condition.

Method	Flutter Speed (m/s)	Error (%)	Flutter Frequency (rad/s)	Error (%)
Exact (Goland & Luke [1])	**292.72**	**---**	**19.17**	**---**
Lottati [2]	**289.68**	**-1.04**	**19.42**	**1.3**
Gern & Librescu [11]	**293.61**	**0.31**	**21.68**	**13.09**
Present	**308.72**	**5.46**	**18.30**	**- 4.53**

4 Results

As stated in the previous section, the solution to this aeroelastic problem through the extended Galerkin method is sought by using a numerical integration scheme. Six bending modes and six torsion modes are considered in the solution procedure to this end. The effects of the external mass value and location and the roll angular velocity on the flutter speed of unrestrained wings are simulated. Relevant data for the particular wing-weight combination used here are the same as those utilized in Ref. [1].

In Table 1, for the purpose of validating the results in the absence of the roll angular velocity, is compared with previous published papers and good agreement is observed.

The effect of the store mass on the flutter boundary and corresponding flutter frequency of the unrestrained wing is illustrated in Fig.2 for different values of the roll angular velocity. The store is assumed to be placed at the middle of the wing span and the nondimensional fuselage mass is $\eta_F = 1$.

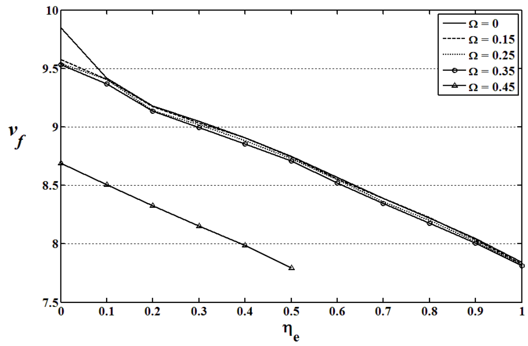

(a)

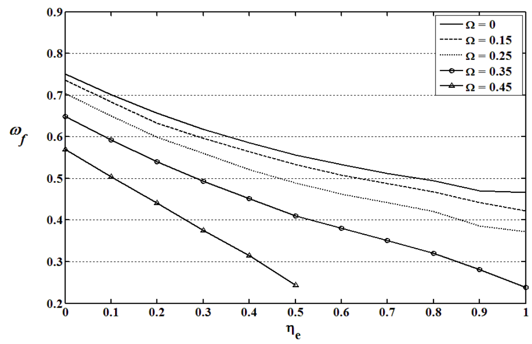

(b)

Fig. 2 Effects of the store mass ratio on the wing flutter boundary for $\eta_F = 1$ (a) Flutter speed, (b) Flutter frequencies.

Fig. 2(a) shows that the stability region of the wing is limited when the larger external mass is attached to it. This is almost independent of the roll angular velocity. Also, effects of the roll maneuver angular velocity on postponing the wing flutter are clear in this figure. Figure 2(b) illustrates that increasing the store mass value will decrease the flutter frequency, noticeably, for all values of the roll maneuver angular velocity.

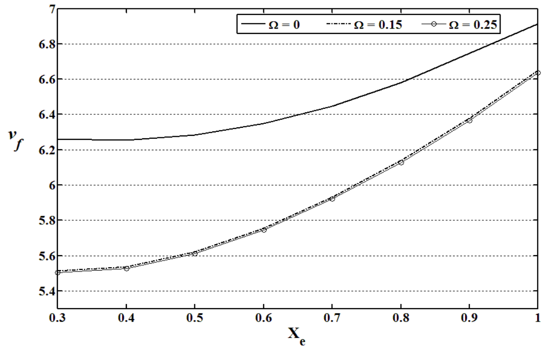

(a)

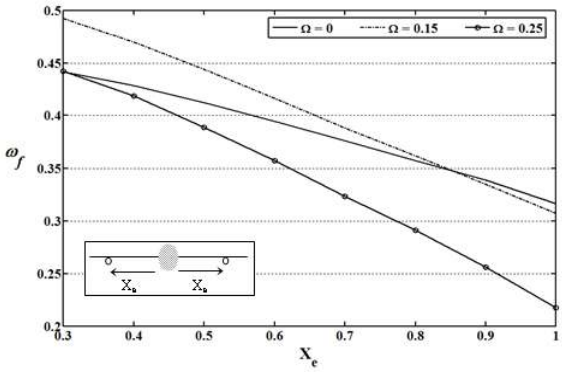

(b)

Fig. 3 Effects of the spanwise position of the store on the wing flutter boundary for $\eta_e = \eta_F = 1$:(a) Flutter speed, (b) Flutter frequencies.

The influence of the spanwise location of the store on the flutter speed and frequency of the unrestrained wing for selected values of the roll angular velocity is shown in Fig. 3. In this case the store and fuselage mass ratio is $\eta_e = \eta_F = 1$ and the store is assumed to be located at the wing elastic axis. It can be seen in Fig. 3(a) that increasing the distance of the store from the wing root, in this case, will increase the flutter speed. Also, it can be seen that increasing the roll angular velocity will decrease the flutter speed, noticeably. Figure 3(b) also reveals that the flutter frequency drops in the usual way by moving the store towards the wing tip. Moreover, the magnitude of the roll angular velocity has noticeable influence on the flutter frequency.

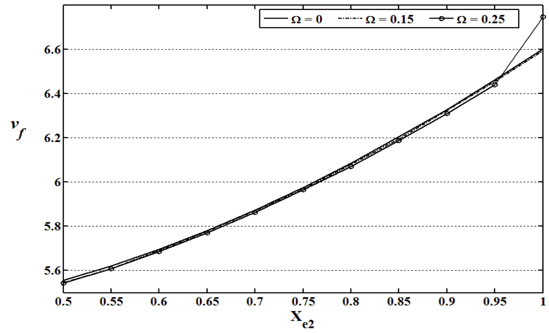

(a)

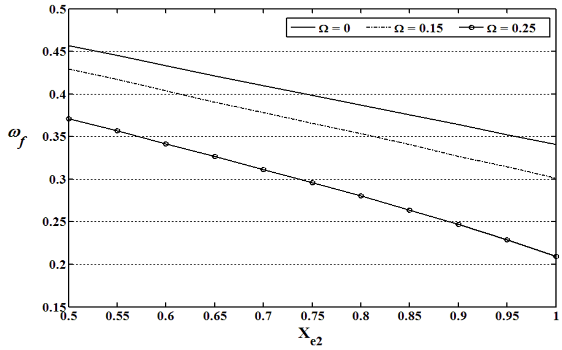

(b)

Fig. 4 Effects of the spanwise position of the second store on: (a) the flutter speed and (b) the flutter frequency for $X_{e_1} = 0.3$ and $\eta_{e_1} = \eta_{e_2} = \eta_F = 1$.

Figure 4 demonstrates the effect of the spanwise location of the stores on the wing flutter speed and frequency of the unrestrained wing with four stores for the selected values of the roll angular velocities. For every half of the wing, the first store is assumed to be placed at the $X_{e_1} = 0.3$ and only the second store slides from the middle of the wing half to the wing tip. Both stores and fuselage have equal mass ratio of $\eta_{e_1} = \eta_{e_2} = \eta_F = 1$. It is clear from the Fig. 4(a) that increasing the distance of the second store from the wing root, in this case, will increase the flutter speed. Influence of the second store spanwise location on the flutter frequency is shown in Fig. 4(b). It can be seen that sliding the store toward the wing tip will decrease the flutter frequency for all values of the roll angular velocity.

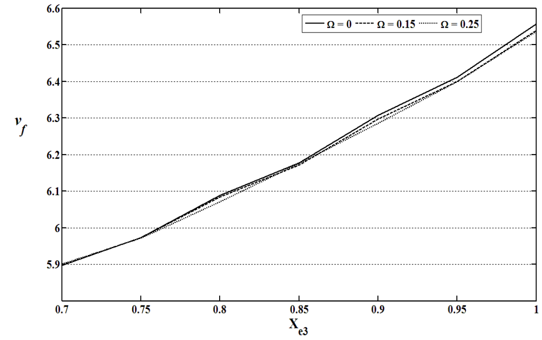

(a)

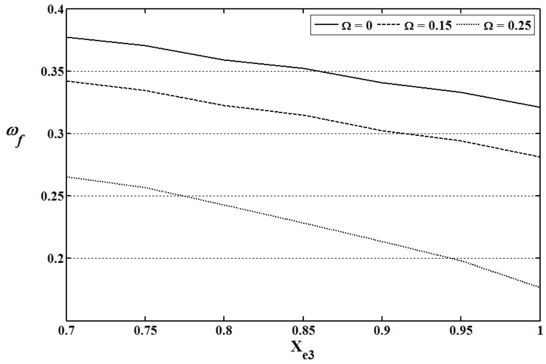

(b)

Fig. 5 Effects of the spanwise position of the third store on: (a) the flutter speed and (b) the flutter frequency for $X_{e_1} = 0.3$, $X_{e_2} = 0.5$ and $\eta_{e_1} = \eta_{e_2} = \eta_{e_3} = \eta_F = 1$.

Figure 5, also, demonstrates the effect of the spanwise location of the third store on the wing flutter speed and frequency of the unrestrained wing with six stores for the selected values of the roll angular velocities. For every half of the wing, the first and second stores are assumed to be placed at the $X_{e_1} = 0.3$ and $X_{e_2} = 0.5$, respectively and the third store slides from the $X_{e_3} = 0.7$ to the wing tip. stores and fuselage have equal mass ratio of $\eta_{e_1} = \eta_{e_2} = \eta_{e_3} = \eta_F = 1$. As before, it can be seen that sliding the third store toward the wing tip, increases the flutter speed and decreases the flutter frequency.

The influence of the chordwise location of the external masses on flutter speed and the frequency of the maneuvering and non-maneuvering unrestrained swept wing carrying four stores is shown in Fig.6. The external masses are located at $X_{e_1} = 0.25$, $X_{e_2} = 0.5$, $X_{e_3} = 0.75$, $X_{e_4} = 1$ and the dimensionless mass ratios are $\eta_{e_1} = 0.2$ and $\eta_{e_2} = \eta_{e_3} = \eta_{e_4} = 0.1$. It is observed that sliding the external masses toward the front of the wing will increase the flutter speed in both cases of the wing with and without roll maneuver. As it can be seen in this figure, for maneuvering unrestrained wing, the flutter frequency increases while the external masses slide toward the wing leading edge.

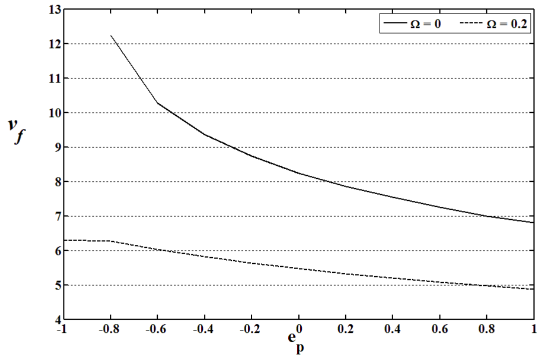

(a)

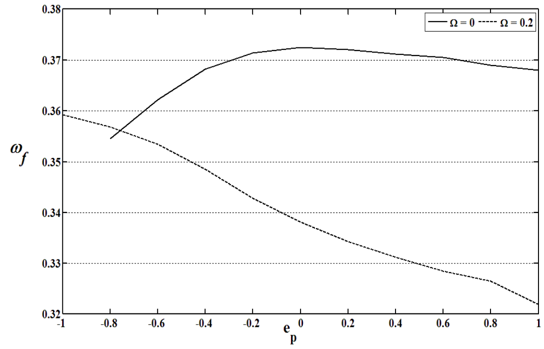

(b)

Fig. 6 Effects of the distance between the stores center of gravity and the wing elastic axis on: (a) the flutter speed and (b) the flutter frequency for $\Lambda = 15$ and $X_{e_1} = 0.25$, $X_{e_2} = 0.5$, $X_{e_3} = 0.75$, $X_{e_4} = 1$, and $\eta_{e_1} = 0.2$, $\eta_{e_2} = \eta_{e_3} = \eta_{e_4} = 0.1$.

References

[1] Goland, M. and Luke, Y.L., The flutter of a uniform wing with tip weights, Journal of Applied Mechanics, Vol. 15, 1948, pp. 13-20.

[2] Lottati, T. A., Aeroelastic stability characteristics of a composite swept wing with tip weight for an unrestrained vehicle, Journal of Aircraft, Vol. 24, No. 11, 1987, pp. 793-802.

[3] Edwards, J.W. and Wieseman, C.D., Flutter and divergence analysis using the generalized aeroelastic analysis method, Journal of Aircraft, Vol. 45, No. 3, 2008, pp. 906-915.

[4] Meirovitch, L. and Tuzcu, I., Multidisciplinary approach to the modeling of flexible aircraft, International Forum on Aeroelasticity and Structural Dynamics, Madrid/Spain, 2001, pp. 435-448.

[5] Meirovitch, L. and Tuzcu, I., Integrated approach to the dynamics and control of maneuvering flexible aircraft, NASA, CR-2003-211748, 2003.

[6] Fazelzadeh, S.A., Marzocca, P. A., Rashidi, E. and Mazidi, A., Effects of rolling maneuver on divergence and flutter of aircraft wing store, Journal of Aircraft, Vol. 47, No. 1, 2010, pp. 64-70.

[7] Fazelzadeh, S. A., Mazidi, A., Rahmati, A. R. and Marzocca, P., The effect of multiple stores arrangement on flutter speed of a shear deformable wing subjected to pull-up angular velocity, Aeronautical Journal, Vol. 113, 2009, pp. 661-668.

[8] Mazidi, A., Fazelzadeh, S.A., and Marzocca, P. A., Flutter of aircraft wings carrying a powered engine under roll maneuver, Journal of Aircraft, Vol. 48, 2011, pp. 874-884.

[9] Dowell, E H., Crawley, E.F., Curtiss, H.C., Peters, D.A., Scanlan, R.H., and Sisto, F. A Modern Course in Aeroelasticity, Kluwer Academic, Dordrecht, 1995.

[10] Fletcher, C.A.J., Computational Galerkin methods. Springer-Verlag, New York. 1984

[11] Gern, F. H., Librescu, L., Static and dynamic aeroelasticity of advanced aircraft wings carrying external stores, AIAA Journal, Vol. 36, 1998, pp.1121-1129.

Aircraft Hydraulic Fluid On-Line Condition Monitoring System for Maintenance and Troubleshooting Purposes

Vänni Alarotu, Jussi Aaltonen & Kari T. Koskinen
Department of Intelligent Hydraulics and Automation, Tampere University of Technology
PL 589, FI-33101 Tampere, Finland

Capt. Mika Siitonen
Finnish Air Force Materiel Command, Finland

Keywords: *Aircraft, Hydraulic Fluid, Condition Monitoring*

Abstract

Perfect overall condition of the aircraft's hydraulic system is essential to ensure the airworthiness of the aircraft. Usually indications of upcoming faults in hydraulic systems are visible as increased amount of particles in the hydraulic fluid. During the recent years the real-time on-line particle counters have developed to be reliable and accurate measuring instruments for particle quantity. The benefits in comparison to conventional off-line measurement methods have been thoroughly studied and proven in recent researches. However, free air, which is usually present in the hydraulic systems of the aircraft due to their complex structure, is known to cause measurement errors when using on-line particle counters.

This paper presents an on-line condition monitoring system which can reliably measure fluid quality and monitor the condition of the aircraft hydraulic system. Method to remove the measurement disturbances caused by free air are discussed and their implementation to the condition monitoring unit is presented. The functionality of the condition monitoring unit is verified with measurements made in real working conditions while unit was connected to an aircraft. The results of the measurements are studied and the further study and development of the on-line condition monitoring unit is handled shortly.

1 Introduction

Recent development of on-line capable hydraulic fluid condition monitoring sensors and applicable data analysis methods have made fluid on-line condition monitoring to become more relevant option in condition monitoring of hydraulic systems. Particle quantity and fluid chemical quality can be measured by online sensors which can directly be installed in the system to continuously monitor the parameters describing the condition of the fluid and the system itself. Online sensors give possibility to monitor hydraulic systems in real-time and thereby to react faster in upcoming maintenance needs and failures.

During recent years there has been increasing number of online condition monitoring applications in aircraft hydraulic systems [1][2]. However these applications have mostly relied on prognosis based on indirect measurements rather than direct measurement of particle quantity or fluid quality. Direct online measurement of fluid quality involves many challenges in aircraft hydraulic systems because of flight safety issues, complex structure of hydraulic systems, harsh environmental and operating conditions. This makes obtaining of reliable direct on-line condition monitoring measurement data difficult.

In aircraft applications fluid quality and particle quantity are typically monitored by either bottle samples or by sampling with portable on-line particle counter. Even though benefits of portable on-line particle counters in comparison to bottle samples are well reported and undeniable, bottle samples are still most widely used method. Continuously measuring on-line sensors are likely to give even more reliable results than sample based on-line measurement. They can also give other benefits such as means for troubleshooting, which is known to be very difficult and time consuming task in complex hydraulic systems.[3][4]

The use of on-line sensors involves many challenges especially in continuous operation. In aircraft hydraulic systems retrofitting sensors directly to the system is typically very difficult and expensive due to flight safety issues. Thus integrating sensors to ground support equipment used with aircrafts very frequently is a viable alternative. Sensors integrated directly to system would also be prone to disturbances always present in the system such as undissolved air, extensive vibrations and extreme environmental conditions.

2 On-line Condition Monitoring Unit

Optical particle counting sensors usually cannot differentiate air bubbles from solid particles and thus air bubbles cause measurement error. Free air is typically always present in aircraft hydraulic systems in some extent due to system structure. Earlier studies have however shown that the disturbance caused by free air can be overcome by pressurizing the fluid and dissolving air into fluid by pressure and then measuring particle count from the pressurized fluid. [5][6][7][8]

An on-line aircraft hydraulic system condition monitoring system which is insensitive to disturbances caused by the free air in hydraulic fluid was developed to give possibility to reliably measure the fluid quality and monitor the condition of aircraft hydraulic systems. Condition monitor system measures both the particle quantity and fluid chemical quality characteristics. The sensors used for these measurements are Argo Hytos OPCom II for particle quantity and Argo Hytos LubCos H2O+ for fluid chemical quality characteristics. On-line condition monitoring unit utilizing these sensors can be used to monitor the condition of hydraulic fluid itself and also the condition of hydraulic system and its components. In addition to the general condition monitoring important applications are also troubleshooting and prognostics of the hydraulic system.

The system is connected in between the aircraft and the portable hydraulic test stand and it measures always when aircraft hydraulic system is powered by the hydraulic test stand.

The condition monitoring system consists of two parts: Hydraulic part and user interface (Fig. 1).

Fig. 1 Condition monitoring system: Hydraulic part (left) and user interface (right)

These two parts of the system are connected with each other with a single electric cable carrying control and measurement signals and also power supply for the user interface. The condition monitoring system is operated with the user interface which also processes and stores the measurement data.

One of the main emphasis areas while developing the condition monitoring system was its ability to remove the error and disturbances caused by free air in hydraulic fluid. Methodology to do this and verifications of the method has been studied in earlier research in detail and the experiences of those were utilized

[6]. The hydraulic diagram of the system is presented in Fig. 2.

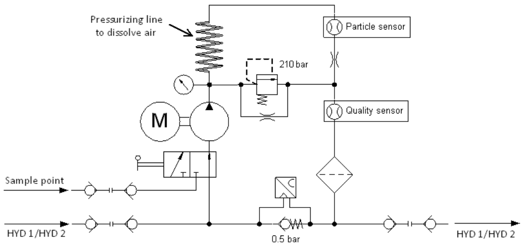

Fig. 2 Hydraulic system of the condition monitoring system.

Hydraulic fluid taken from the main return line between the aircraft and the portable hydraulic test stand is pressurized by the hydraulic pump and then directed through a long pressurized line to the sensors. Free air in the hydraulic fluid is dissolved during its passage through the long pressurized line to sensors and disturbances caused by it are minimized [6].

3 Tests

During the development project several prototypes of the condition monitoring system were tested in real working environment as well as in laboratory conditions. Laboratory tests mainly focused on validating and verifying accuracy and repeatability of measurements and also systems capability to handle free air in the fluid.

In the field tests the system was connected between the aircraft and standard portable hydraulic test stand as shown in Fig. 3. Field tests consisted of two different kinds of test sets.

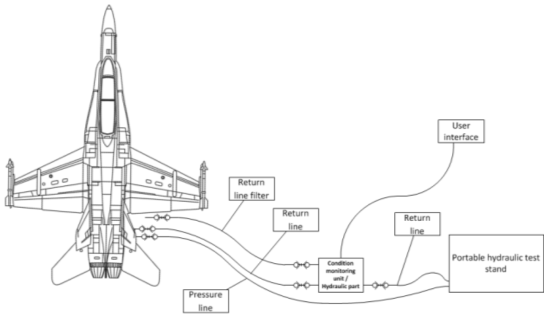

Fig. 3 Test assembly for first set of tests.

In first test set the condition monitoring system was used to measure the fluid quality while stabilator, leading edge flaps (hydraulic motor), air brake, ailerons and trailing edge flaps were actuated separately. The purpose was to measure the fluid quality variations of different actuators. Measurements were also done while running built-in-tests (for example so called “exerciser”) the purpose being to identify signatures of different actuators from flow and fluid condition data measured.

The second set of tests was conducted to define the baseline for fluid quality. In these tests condition monitoring system was connected only to the portable hydraulic test stand in loop or between aircraft and test stand in idle which made it possible to get baseline quality measurements nominative to the individual aircraft and the test stand.

4 Results of the test sets

Different characteristics of the hydraulic fluid were measured during the test sets. These characteristics were the ISO code of the hydraulic fluid, volumetric flow, temperature, relative humidity, permittivity and conductivity of the hydraulic fluid.

The measurements of the first test set where different systems of the aircraft were used are shown in Fig. 1-5. The measurements of the second test set where the condition monitoring unit was installed only to the portable hydraulic test stand are shown in Fig. 6-10.

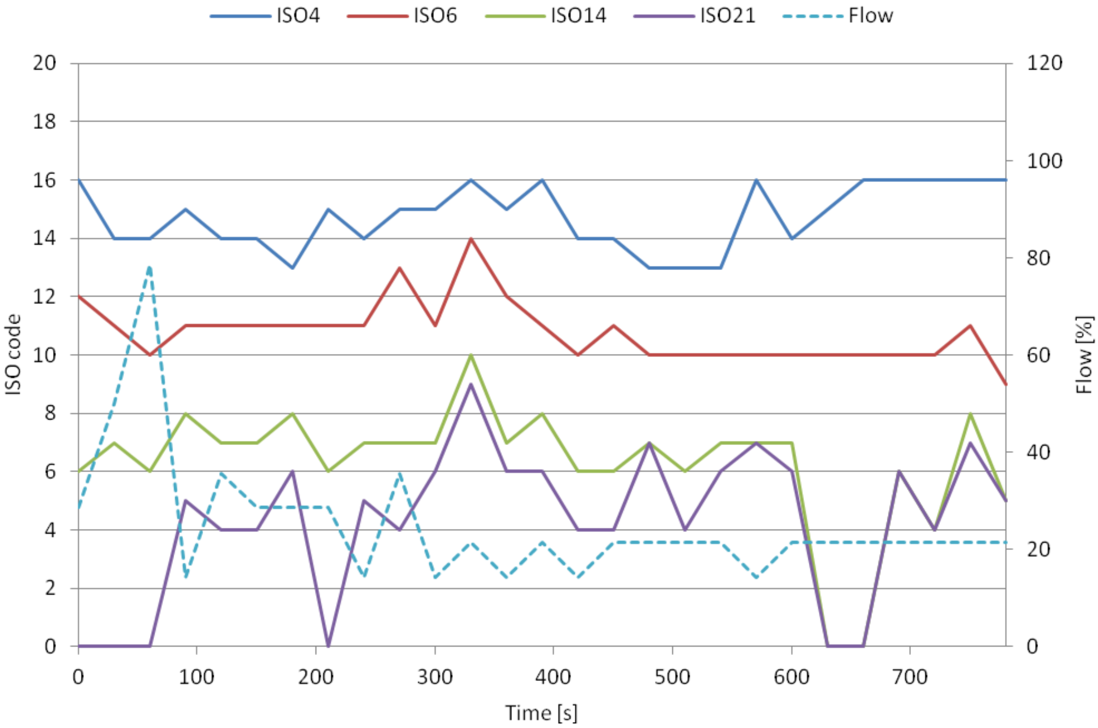

Fig. 1 Particle quantity and flow volume measurements of the first test set.

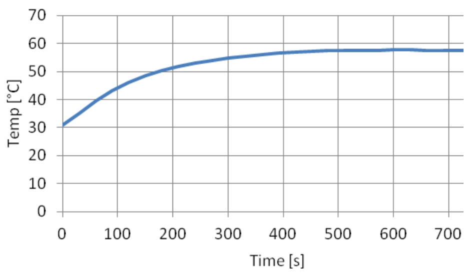

Fig. 2 Temperature of the hydraulic fluid during first test set.

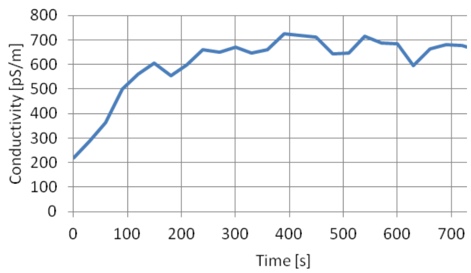

Fig. 4 Conductivity of the hydraulic fluid during first test set.

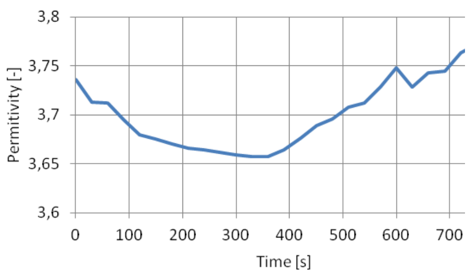

Fig. 3 Permitivity of the hydraulic fluid during first test set.

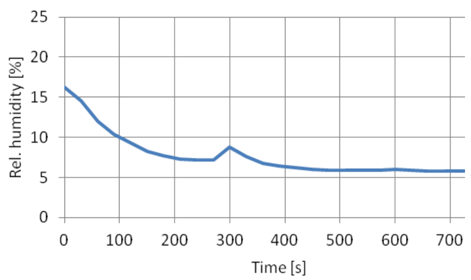

Fig. 5 Relative humidity of the hydraulic fluid during first test set.

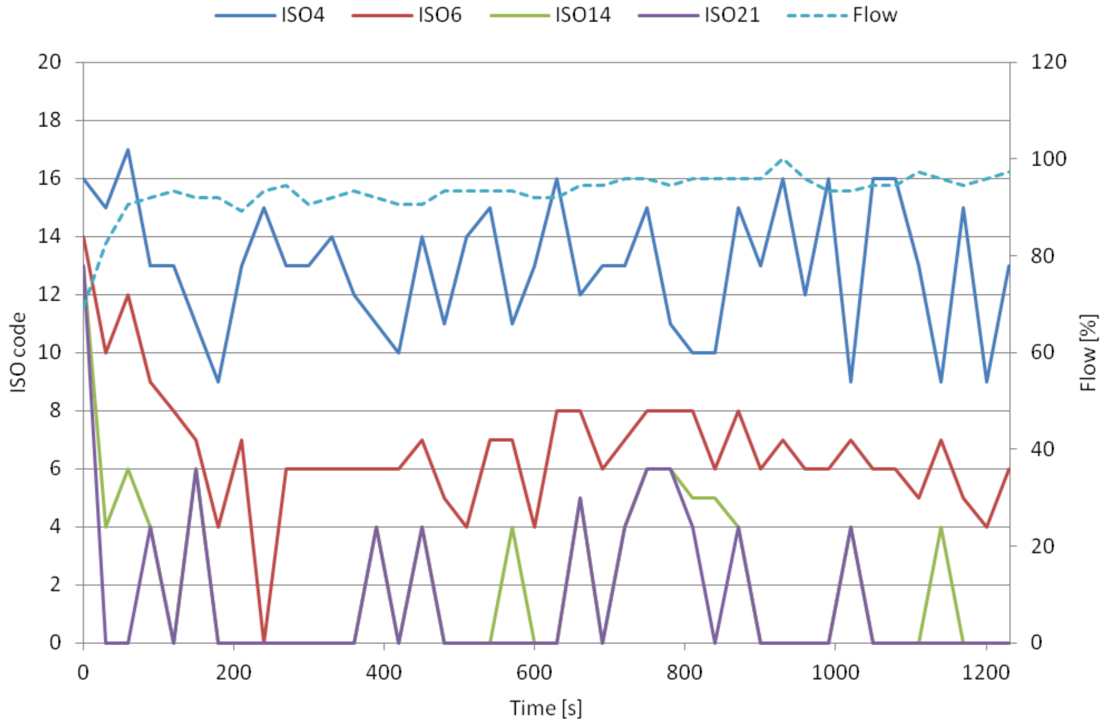

Fig. 6 Particle quantity and flow volume measurements of the second test set.

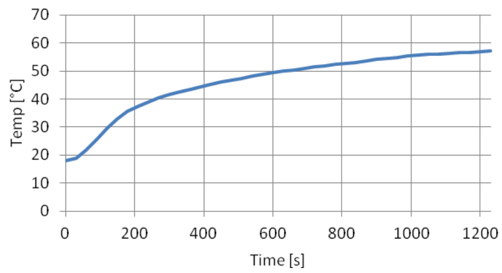

Fig. 7 Temperature of the hydraulic fluid during second test set.

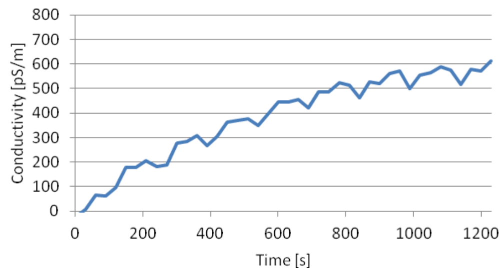

Fig. 9 Conductivity of the hydraulic fluid during second test set.

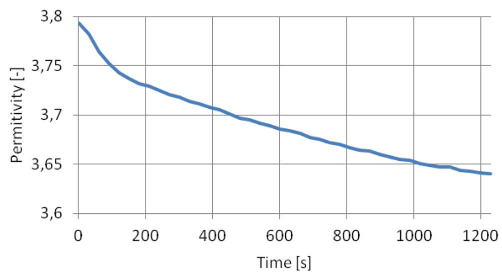

Fig. 8 Permitivity of the hydraulic fluid during second test set.

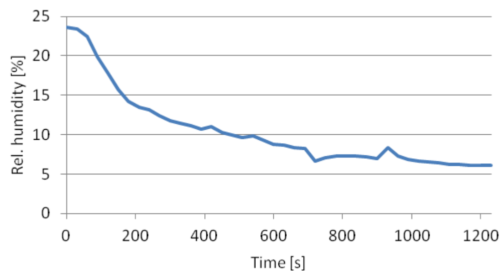

Fig. 10 Relative humidity of the hydraulic fluid during second test set.

4.1 Results of the first test set

As it can be seen from the Fig. 1 the flow through the condition monitoring system is quite eratic especially in the start. This is caused by the different systems which were run during the test. During the highest peak in the flow the built-in test sequence called "exerciser" was executed which actuates all control surfaces of the aircraft at the same time. This test sequence propably loosened some larger particles from the hydraulic system as the numbers of the ISO codes indicating the amount of larger than 14µm and 20µm particles rise slightly after the sequence was executed.

In general during the first test set when the control surfaces of the aircraft were actuated the ISO code of the hyrdraulic fluid rose after a short period of time. By studying these time intervals and with more profound knowledge of the hydraulic system it is possible to use the condition monitoring system for troubleshooting and prognostic purposes.

The measurements of hydraulic fluid quality characteristics shown in the Fig. 2-5 are highly dependent on the temperature of the hydraulic fluid. At the start of the test set the temperature of the fluid was approximately 30°C and at the end of the test set the temperature was about 58°C. Because of this dependancy to the fluid temperature only the measurements made after approximately 400 seconds have passed can be used to evaluate the quality of the hydraulic fluid. The fluid quality sensor itself has been calibrated in 25°C by the factory so the measurements have to be scaled to this temperature or methods to better control the oil temperature in the condition monitoring system has to be studied in the future.

4.2 Results of the second test set and problems found during both test sets

The measurements where the on-line condition monitoring unit was connected only to the portable hydraulic test stand are presented as the results of the second test set. The measurements done with this test stand provided a good base to validate the information obtained from the measurements made from the aircraft with the particle counter and flow sensor. The temperature of the fluid rose to approximately 58°C only when the last two measurement points were saved. This unfortunately prevented the more consistent comparison of the two test sets when it comes to fluid quality characteristics.

When observing the measurement data obtained from the flow sensor it can be seen that it only shows flow variation and not the actual flow through the condition monitoring unit. This is due to measurement principle which is based on pressure difference over the unit. Because the unit should not disturb the operation of the aircraft system it has very low flow resistance and therefore pressure difference is hard to measure with high accuracy in the operating conditions in question. This level of information is however enough to indicate certain operating points and states of the system.

It can also be observed while comparing the ISO codes of the first and second test sets presented in Fig. 1 and Fig. 6 that the hydraulic fluid in the portable test stand has much less particles in it. This difference in particle numbers is however very small which is caused by the fact that in both test sets the hydraulic fluid coming to the monitoring system has already passed through filters and most of the larger than 10 µm particles have been filtered. This however is a problem related only to these particular tests because in practical operation the return line of the aircraft will be replaced by a special filter cup. In these tests it was not used for safety reasons only.

The characteristics of the fluid quality, although more measurements would have been needed in constant temperature, were in line with what was expected. The quality characteristics of the hydraulic fluid in hydraulic test stand were the same or slightly better than the characteristics of the hydraulic fluid in aircraft. These values were also in line with the measurements made in earlier tests [7].

5 Discussion

The tests presented in this paper were the first tests in real working conditions performed with the on-line condition monitoring system.

Flow measurement with the pressure differential sensor was found to be problematic very early in the testing and it was found not to be capable to give exact flow measurements but only indication of flow variations. This information can be used to identify operating points and states but is not completely satisfactory for prognosis and fault finding purposes planned.

As mentioned in chapter 4.2 because of the return filter of the aircraft hydraulic system, the hydraulic fluid coming to the condition monitoring system is quite clean already and bigger particles were not present anymore when the hydraulic fluid entered the condition monitoring unit. An adaptor which can be used to get non-filtrated hydraulic fluid from the aircraft to the condition monitoring system has already been manufactured but the use of this adaptor was not yet approved when the presented tests were made. The testing of this adaptor is also one of the main interests in the future.

Last concern risen during the tests was the temperature of the hydraulic fluid. As the measurements of the fluid quality characteristics are highly dependable on the temperature it is essential that methods to keep the temperature of the fluid constant should be studied. During the tests it was noticed that the fluid temperature stabilized to approximately 58°C. This was however only dependant of the system characteristics. Either methods to regulate the temperature of the hydraulic fluid or scaling the measurements according to the temperature should be studied.

6 Future research

After the aforementioned improvements to the condition monitoring system have been made and the operation of the system has been verified, future studies of the condition monitoring unit will concentrate on methods to reliably make necessary measurements for troubleshooting and prognostic purposes. For these studies the on-line condition monitoring units will be issued to the daily maintenance of the fleet.

In addition to better track and observe the condition of the aircrafts the accumulated measurement data can also be used to further develop the maintenance procedures used with the aircrafts. One of these procedures will be measurement based maintenance where the actual needs for component changes during standard maintenances are predicted from the measurement data. Other application studied will be finding faulty components by executing different test sequences with the aircraft and detecting patterns in particle analysis to identify components which need to be changed. The contents of the standard maintenances could also be improved with these methods. These studies need the extensive amount of long term measurement data from wide selection of aircrafts per aircraft model which is possible to gather with the condition monitoring unit when it is issued to the fleet.

Conclusions

Field tests where the operation of on-line condition monitoring system was tested gave consistent and reasonable results. Also the overall functionality of the system was deemed good although some parts to improve were found. Only really notable problem found was that the differential pressure sensor used to indicate flow through the system did not perform satisfactorily.

As an expected result it was also found that the return line filters of the aircraft filter out most of the larger than 10µm particles from the hydraulic fluid. To overcome this problem the condition monitoring system has a feature which makes it possible to measure hydraulic fluid properties and particles before aircrafts return line filters. This however requires connecting an additional hose to the aircraft and is therefore used only in trouble shooting, periodical analyses and if dramatic changes in quality of filtered fluid are found. Upcoming major faults in the hydraulic system can be found from the filtered fluid with adequate reliability to initiate measurements from sample line.

References

[1] Byington, C.S., Watson, M., Edwards, D. and Dunkin, B., "In-line health monitoring system for hydraulic pumps and motors," *Aerospace Conference, 2003 Proceedings. 2003 IEEE*, vol.7, pp.3279-3287.

[2] Sanket, A., Byington, C. and Watson, M., "Fuzzy inference and fusion for health state diagnosis of hydraulic pumps and motors," *Fuzzy Information Processing Society, 2005. NAFIPS 2005. Annual Meeting of the North American*, 26-28 June 2005, pp.13-18

[3] Rinkinen, J., "Condition monitoring and in-line maintenance of oil in circulating lubrication system. In: Lahdelma, S. & Palokangas, K. (eds.)," *Proceedings of the 3rd International Seminar Maintenance, Condition Monitoring and Diagnostics*, Oulu, Finland, 2010, pp.136-151.

[4] Multanen, P., "Bottle sampling analysis and on-line particle counting - methods, sampling, handling, results, analysis, problems & errors," *3th Pamas Benelux Meeting*, Mechelen, Belgium, 2001, p. 11.

[5] Aaltonen J., Alarotu V. and Koskinen K.T., "Aircraft Hydraulic System Fault finding and Troubleshooting Using On-Line Particle Counters," *The Eight International Conference on Condition Monitoring and Machinery Failure Prevention Technologies*, Cardiff, Wales, 2011, pp. 1275-1282.

[6] Aaltonen J. and Koskinen K.T., "Detecting and eliminating the measurement error caused by free air in aircraft hydraulic system on-line particle counting," *The Twelfth Scandinavian International Conference on Fluid Power*, Tampere, Finland, 2011, pp. 229-240.

[7] Virta P., Aaltonen J., Koskinen K.T. and Vilenius M. "Experiences of monitoring the condition of military aircraft hydraulic systems," *Condition Monitor, An International Newsletter*, No. 280, 2010, pp. 9-14.

[8] Virta P., Aaltonen J., Koskinen K.T. and Vilenius M., "Experiences on the condition monitoring of military aircraft hydraulic systems," *The Sixth International Conference on Condition Monitoring and Machinery Failure Prevention Technologies*, Dublin, Ireland, 2009, pp. 753-764.

4:th CEAS Air & Space Conference
FTF Congress: Flygteknik 2013

Combined Virtual Iron Bird and Hardware-in-the-Loop Simulation Research Environment for Jet Fighter Hydraulic Systems

Vänni Alarotu, Jussi Aaltonen, Kari T. Koskinen
Department of Intelligent Hydraulics and Automation, Tampere University of Technology
PL 589, FI-33101 Tampere, Finland

Capt. Mika Siitonen
Finnish Air Force Materiel Command, Finland

Keywords: Virtual Iron Bird, Hardware-in-the-loop, Hydraulic system, Hydraulic Pump, Fighter

Abstract

Ability to study complete aircraft systems in practice even in laboratory environment is very important and valuable asset in various R&D activities during the life cycle of an aircraft. Conventionally complete aircraft systems have been studied with functional simulators, i.e. iron birds, and flight testing with measurement system equipped aircraft. These both methods are however extremely expensive and time consuming to realize and are thus usually used only in large scale projects, typically only by manufacturer during initial development of an aircraft type and its later versions. Continuous developments in computing power available at reasonable price as well as in modelling and simulation methodology have made iron bird virtualization an applicable alternative. Development in commercially available software and specialized generic computer data acquisition hardware have in the other hand made it possible to build hardware-in-the-loop simulation environments on very reasonable budget and time frame. This paper presents combined virtual iron bird and hardware-in-the-loop simulation research environment for F-18C/D hydraulic systems. Basic principles behind the research environment are introduced and the structure of the environment is discussed in detail. A HIL-simulation scenario including hydraulic pump of the system 1 of F-18 as a hardware pump is presented and discussed. HIL-simulation research environment is also validated and verified on the basis of the scenario.

1 Introduction

Ability to study operation and interactions of aircraft's systems is very valuable and even crucial in various R&D activities. However studying them by flight tests or field measurements is usually very expensive and time consuming. One way to study the complete systems is to use the functional simulator, i.e. iron bird. However, building a functional simulator requires large facilities and huge resources and is thus usually only done by the manufacturer for the initial design purposes of a certain aircraft type.

Modern simulation tools and methodology offer a cost-effective alternative for traditional physical iron birds. Dynamic multi-domain simulation and modelling tools allow the simulation of flight, aircraft structures and systems including all of their interactions with each other and also with flight environment. This makes it possible to create a virtual iron bird which can be used to study most of the same things as a physical iron birds without large facilities and substantial capital investments. Virtual Iron Birds can also be used at the very early stages of aircraft development since the system can exist only as simulation models and there is no need to have any physical components available.

Even though computer simulations can give us plentiful information on systems they usually do not adequately proof component's or system's airworthiness. Thus it is also necessary to examine the operation of the real component before entering the flight testing phase. These tests have traditionally been made in specialized test rigs only remotely resembling the actual operating environment and load conditions. Hardware-in-the-Loop (HIL) simulation combined with the virtual iron bird enables studying components and systems in more realistic environment without taking any flight safety risks and using only minimal resources in comparison to traditional methods.[1][2][3]

2 Combined Virtual Iron Bird and Hardware-in-the-Loop Simulation Research Environment

The combined virtual iron bird and hardware-in-the-loop simulation research environment for F-18C/D systems consists of a software environment, a flight simulator with necessary detailed system models, and hardware environment, which enables using real hydraulic components in connection with the simulation models.

Simulation models of the software environment are coded with Matlab/Simulink which provides readily made toolboxes with necessary functions for the Simulink code to control physical components alongside the simulation.

Software environment is based on Hutfly 2 flight simulator which is a six degree of freedom flight simulation model of F-18 C/D [4]. In addition to the aircraft flight model the Hutfly 2 also includes graphical user interface, flight control system model with control laws, atmosphere model, aerodynamic force definition based on aerodynamic coefficients and movement equations. Hutfly 2 is coded with Matlab/Simulink.

Hutfly 2 has later been upgraded with complete and detailed semi-empirical hydraulic system models which makes it possible to use it to study the F-18's hydraulic systems and also gives greater accuracy to flight control system modelling. [5][6]

Besides of studying hydraulic system behavior during simulated flight the upgraded Hutfly 2 has also other uses. One of these applications is the ability to study the behavior of different hydraulic systems during real flight events and maneuvers. This can be done by feeding real pilot commands extracted from logged real-life mission data to simulation model. This approach has been successfully applied, for example, in generating load spectrum for hydraulic pump endurance tests.

Data Acquisition Toolbox of the Matlab/Simulink library provides input and output blocks which can be included directly to the Simulink code. This enables the possibility to seamlessly merge real-life components and the simulation model.

Hardware Environment of the combined virtual iron bird and hardware-in-the-loop simulator research environment is shown in Fig. 1.

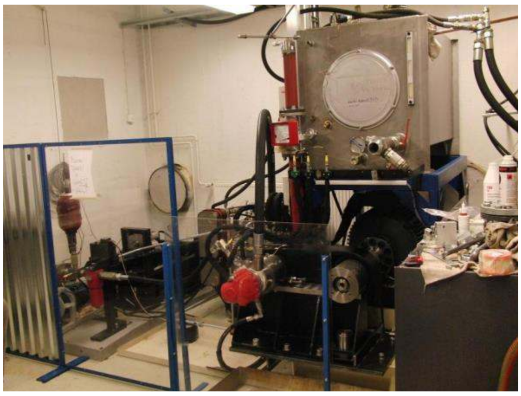

Fig. 1 Hardware environment

Hardware environment's main power is provided by 110kW electric motor driven by frequency converter drive. The motor usually drives a variable delivery constant pressure hydraulic pump used in an aircraft. The rig can also be used to drive other rotating devices, which in aircraft are driven by airframe mounted auxiliary drive, such as fuel pump or

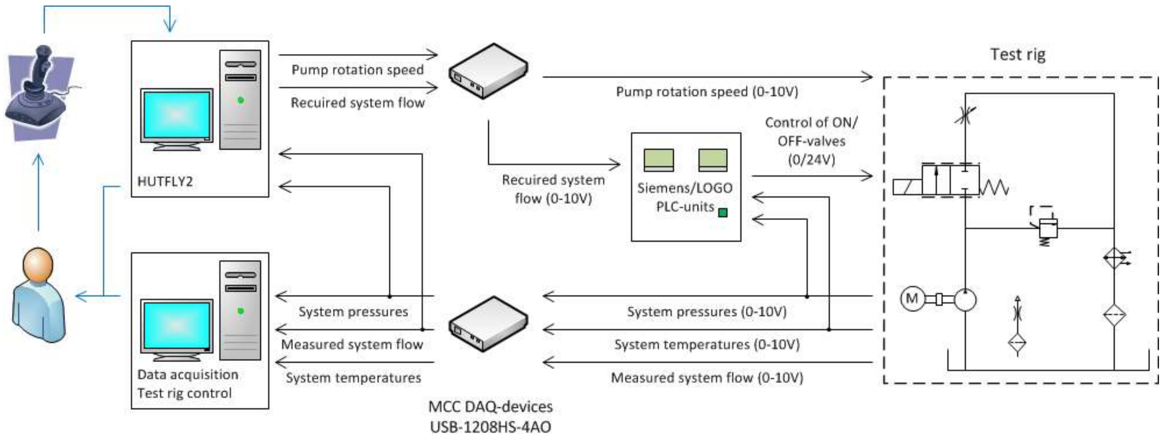

Fig. 2 Schematic diagram of the test environment

generators. Other hydraulic components, such as actuators, can also be connected to the hardware environment.

The hydraulic system is water cooled and facilities are protected by an automatic water mist fire suppression system. The room where the hardware environment is located can be monitored remotely through web camera and the control software of the hardware system can also be operated remotely. These features enable continous and monitored operation of the system for prolonged periods of time.

Schematic diagram of the test environment is presented in **Error! Reference source not found.**. It consists of the modifiable hardware environment, two computers where the Hutfly 2 and data acquisition software are running, DAQ-devices connecting computers and the test rig with each other and two programmable logic controller devices.

Used data acquisition devices are low-cost generic DAQ-cards. They both include eight analog inputs, four analog outputs and 16 Digital I/O connections. Two programmable logic controller units are used parallel to computer control. These units are used in digital hydraulic flow control and also in secondary control functions such as for example safety functions.

3 Hardware-in-the-Loop Simulation Arrangement for the Hydraulic Pump

HIL-simulations of the hydraulic pump were chosen to be the test scenario because of the relative simplicity and also because of the amount of previous research done on the hydraulic pump makes the validation of results possible [7].

The operating point of hydraulic pump is defined by rotational speed and flow requirement. All of these variables are solved in the upgraded Hutfly 2. Thus the HIL-interface for pump HIL-simulations can be realized by simply adding necessary I/O-functions to virtual iron bird. These I/O-functions include the real pump as a part of the simulation model by transferring operating point variables to hardware part of the system and measured system variables from the hardware back to the simulation model.

Pump of the System 1 was selected to be the hardware pump whilst pump of the System 2 is completely simulated because most of the power of the system 1 is consumed by flight control actuators but system 2 also powers many auxiliary systems.

The flow requirement from the hydraulic pump is controlled with a digital flow control unit (DFCU). The DFCU in this case consisted of four ON/OFF- valves. This flow control unit provides ten different modes with different flow levels passing through the DFCU. These flow levels are presented in Fig. 3.

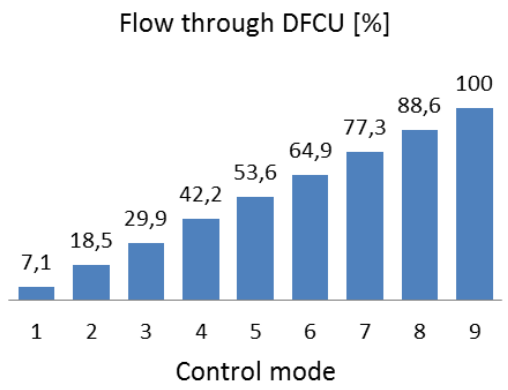

Fig. 3 The control mode scheme for DFCU.

The control mode of the DFCU is decided simply by the flow requirement of the system. The DFCU was chosen to control flow of the test rig because this valve type is quite robust and also easy to fix if something in it breaks. This feature is important when long lasting endurance tests are made nad DFCU also has a sufficient accuracy in flow control.

4 Simulations and results

HIL-simulations of the hydraulic pump were done to prove the research environment concept and to validate its reliability by verifying that same kind of phenomena that has earlier been found in simulation studies and field and laboratory measurements can also be found from combined virtual iron bird and HIL-simulator.

The simulations did not try to reproduce any specific flight manoeuvres or flight events but the aim was only to introduce as high power variation in the hydraulic system as possible to cause high frequency and amplitude flow demand changes to the hydraulic pump. These high frequency and amplitude flow variations are known to cause distinctive phenomena which have also been found from real aircraft and computer simulations.

The simulated flow requirement produced by the simulation model as a result of rapid direction and orientation changes of the aircraft is shown in Fig. 4.

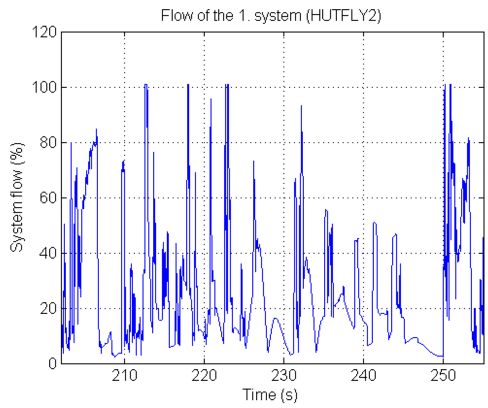

Fig. 4 Flow requirement of the 1. system of the aircraft.

As it can be seen from Fig. 4 fast movements of the aircraft during the simulation were able to create extensive flow requirement from the hydraulic pump which also changed very rapidly and these changes were sometimes very extreme. This behavior reflects accurately the flow requirements of the aircraft hydraulic system during aerobatic manoeuvring.

The hydraulic test rig was monitored to be able to follow the simulation results in real-time quite well. This can be seen from Fig. 5 where the flow output of the hydraulic test rig is presented.

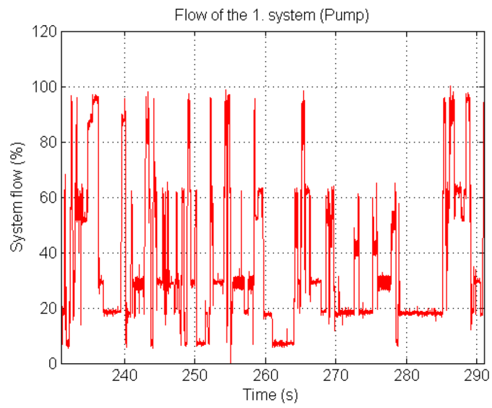

Fig. 5 Flow output of the hydraulic pump controlled by DFCU.

The test rig produced similar flow patterns as the simulation model although some smaller flow changes were not visible because of the resolution of the digital flow control unit. The changes in flow requirement from the pump can also be more sudden and greater in volume in the test rig as the flow is controlled with ON/OFF –valves.

The rotation speed of the hydraulic pump follows the throttle which was controlled by a slider of a joystick which was used to control the aircraft in Hutfly 2. The control output range was 0-10V which is scaled to match input range of the drive. This can be seen when comparing the control output in Fig. 6 and the test rig pump rotation speed in Fig. 7.

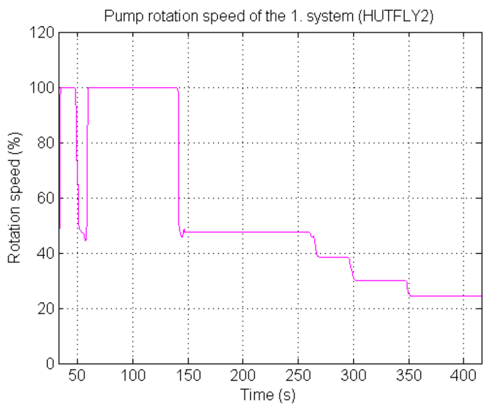

Fig. 6 Control output of pump rotation speed generated by simulation model.

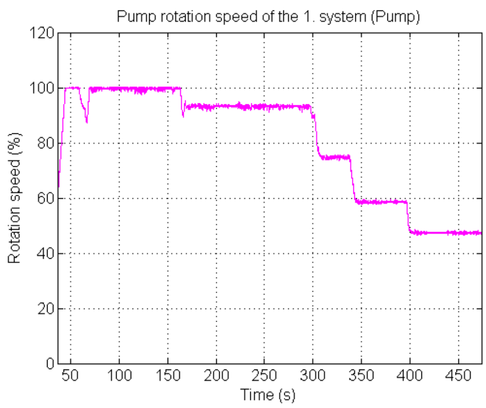

Fig. 7 Rotation speed of the test rig hydraulic pump.

It was monitored during the simulation that the pump rotation speed followed the control output in real time. This can also be seen from Fig. 6 and Fig. 7. The electric motor generated small delay in the change of the rotation speed and there was also a built in ramp function in frequency converter drive control but feature was also desired as the hydraulic pumps in aircraft are driven by the aircraft engines which have their own dynamics in responding to the control because of inertia and fuel control system.

System pressure measured from the test rig was fed back and used in the simulation model instead of the system pressure solved by the simulation model. The system pressure measured in the test rig during the HIL-simulation is shown in Fig. 8. The maximum pressure in Fig. 8 and also in Fig. 9 represents the maximum pressure of the pressure sensor measuring the system pressure. The normal operation pressure of the 1.system is approximately 80% from the maximum pressure range of the sensor as can be seen from Fig. 8.

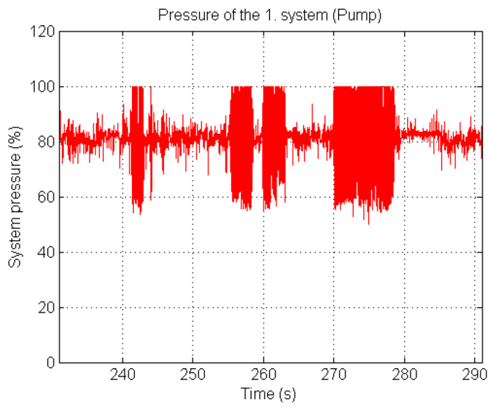

Fig. 8 Pressure level of the test rig hydraulic system.

Two of the phenomena usually occurring in the hydraulic pump which were the target of interest during the measurements are visible in Fig. 8. Most specific and regular phenomenon is the low frequency and low amplitude fluctuation of the system pressure level. These fluctuations can be quite drastic during flight and they are usually caused by the large changes in flow requirement from the hydraulic pump. The high frequency and high amplitude pressure ripple occurring four times in Fig. 8 is also a typical phenomenon found in real aircraft related to pump regulator operation in fast high amplitude flow changes.

The hydraulic system of the aircraft is of a semi-closed-loop type with the self- pressurized hydraulic reservoir. However, reservoir dynamic cause the supply pressure of the hydraulic pump to fluctuate and also sometimes drastically drop to zero in certain operating points and flight manoeuvers [7]. This fluctuation was replicated during the simulation measurements. These fluctuations are visible in Fig. 9.

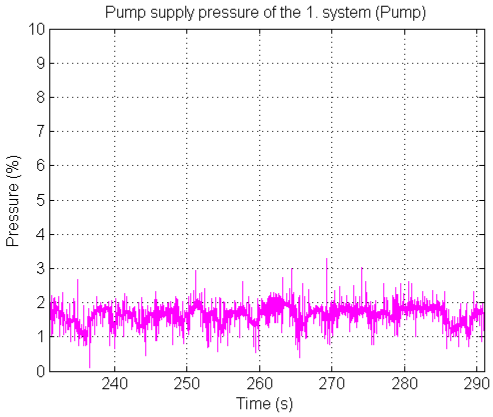

Fig. 9 Supply pressure of the test rig hydraulic pump.

Phenomenon which unfortunately did not occur during tests was the drastic drop in pump supply pressure. The reason for this is that the hydraulic system of the test rig is open-loop system with quite large fluid reservoir. The pressure drop feature is constructed to the HIL-software but the conditions for this phenomenon to happen were not fulfilled during this test run.

The presented measurements in this paper were done during a short testing of the HIL-system. Because of the short duration of the test the temperature of the hydraulic oil was relatively low during the test. Oil temperature is presented in Fig. 10.

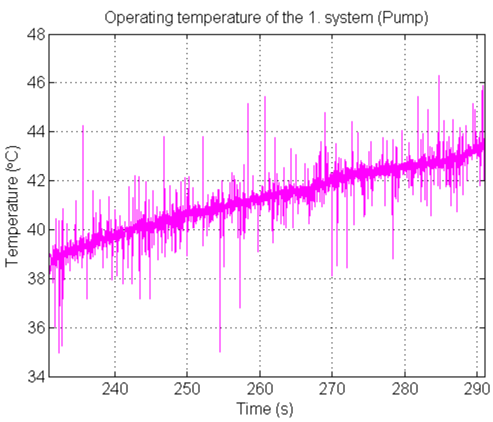

Fig. 10 Oil temperature of the test rig hydraulic system.

The low fluid temperature may also be a reason for some of the phenomena occurring in measurements. Especially it may cause the high frequency and high amplitude pressure ripple presented in Fig. 8. The temperature of the hydraulic fluid in the aircraft can rise to over 100°C during flight which changes the properties of the fluid when compared to the properties of the fluid when the simulation measurements were made. Thus the results obtained from the measurements with the HIL-system may differ to some extent from the real operation of the hydraulic pump.

In general the simulation results and observations made during the testing of the HIL-system were as expected. HIL -simulation results showed that hardware pump operated as a part of the simulation and when compared to a completely simulated scenario there was only minor differences in measured values of the HIL -simulation. Differences were caused mostly by the digital flow control unit used to control the flow rate in the test rig. The flow control unit simply did not control the flow at accuracy needed in this application. However the response of the flow control unit in terms of speed was quite adequate and frequency of the load spectrum is thus replicated very closely. HIL-simulation also replicated most of the phenomena observed in earlier tests and simulations.

5 Future improvements

There were some parts for improvements found in the HIL-system during the testing. It can be seen in the presented measurement data that there is difference in time axis of the simulation data and measurement data even though the events were observed to happen simultaneously in simulation and real-life. The reason for this is most likely that simulations and measurements were done with different computers and DAQ-devices which were not hardware synchronized with each other. This will be fixed simply by synchronizing the DAQ-devises which was not done during the first tests presented in this paper.

There are also disturbances especially in presented pressure and temperature measurements. The facilities where the test rig is located are known to be prone for disturbances for measurement signals. Also the sensors are located in places where sometimes heavy vibrations may occur. These may cause extra disturbances to the measurement signals and although improvements to negate these disturbances have already been made some other ways to minimize them should still be studied. The pump that was used in these tests should also undergo a complete overhaul to minimize additional disturbances.

It is also recognized that the current software environment is only good for concept testing and validation purposes because it cannot guarantee real-time operation in more complicated simulation cases but the system must be converted to actual real-time software environment such as xPC-Target.

6 Conclusions

The concept of combined virtual iron bird and hardware-in-the-loop-simulator was successfully tested in a simple and limited scenario. The tested system was observed to be able to replicate different key phenomena which have already been found from the system during earlier studies. Although some parts to be improved were found during the tests the obtained results prove the low-cost concept used in this study to combine virtual iron bird and HIL-simulator to be viable and technically sound. The combination of virtual iron bird and HIL-simulator may improve the cost efficiency of future component testing and also make possible to study aircraft components more closely in their operational working environment.

7 References

[1] Karpenko, M. and Sepehri, N., "Hardware-in-the-loop simulator for research on fault tolerant control of electrohydraulic actuators in a flight control application," Mechatronics, Vol. 19, No 7, October 2009, pp. 1067-1077.

[2] Montazeri-Gh, M., Nasiri, M., Rajabi, M. and Jamshidfard, M., "Actuator-based hardware-in-the-loop testing of a jet engine fuel control unit in flight conditions", Simulation Modelling Practice and Theory, Vol. 21, No 1, February 2012, Pages 65-77.

[3] Yao, J., Jiao, Z. and Yao, B., "Robust Control for Static Loading of Electro-hydraulic Load Simulator with Friction Compensation," Chinese Journal of Aeronautics, Vol. 25, No 6, December 2012, Pages 954-962.

[4] Öström J. Hutfly2, "Matlab/Simulink –pohjainen lennonsimulointiohjelmisto," report B-86. Helsinki University of Technology, Laboratory of Aerodynamics. **85**. Available at: http://www.aero.hut.fi/pubs/reports/B-56.pdf

[5] Hietala, J-P; Aaltonen, J; Koskinen, K.T.; Vilenius, M. Aircraft hydraulic system model integration to flight simulation model. The Twelfth Scandinavian International Conference on Fluid Power, SICFP'11, May 18-20, 2011, Tampere, Finland. 271-280.

[6] Hietala, J-P; Aaltonen, J; Koskinen, K.T.; Vilenius, M. Comparison between an aircraft speed brake actuator high order linear model and a semi-empirical non-linear model in real time simulation . AST 2011, 3rd International Workshop on Aircraft System Technologies, March 31 - April 1, 2011, Hamburg, Germany. 65-71

[7] Aaltonen, J., Koskinen, K.T. & Vilenius, M. Pump supply pressure fluctuations in the semi-closed hydraulic circuit with bootstrap type reservoir. In: Vilenius, J. & Koskinen, K.T. (eds.) Tenth Scandinavian International Conference on Fluid Power, May 21-23, 2007, pp. 117-133.

4:th CEAS Air & Space Conference
FTF Congress: Flygteknik 2013

Modeling of backlash in drivetrains

Akoto, L. C., Spangenberg, H.
German Aerospace Center e.V.

Keywords: *drivetrain, backlash, inertia, elasticity, damping*

Abstract

The presence of backlash in drivetrains is a major source of limitations as it introduces nonlinearities that reduce their efficiency in speed and position control. Existing models in backlash assume massless shaft, and use only elasticity and damping properties to describe the transmitted torque. This assumption makes them inaccurate since it does not account for the contribution of the body's inertia. Thus, a new and simple model that takes into account the rotational inertia, elasticity and damping properties is proposed. The importance and validity of this approach is shown analytically, graphically and with an example of a simple failure case of shaft rupture. Preliminary analysis shows that real system behavior is predicted more closely than in previous model. Thus, the new model can be used for better prediction of system behavior for definition and optimization.

Abbreviations and terms

θ: Angular displacement
α: Half of backlash angle
k: Elasticity
c: Internal damping
j: Inertia
T: Torque
SDOF: Single Degree of Freedom
PPM: Phase plane model
JCK: Inertia Damping Elasticity
Backlash: Clearance between mating gear teeth

1 Introduction

The presence of backlash in drivetrains is a major source of limitations that introduces nonlinearities in system behavior, a consequence of which might be problems with safety and/or reliability, which are crucial in the design of aerospace systems. This paper focuses on the analysis of existing backlash models followed by the proposal of a new modeling approach. In this study, some commonly used backlash models are examined. As an example a shaft model with backlash is considered. Many alternatives for estimating the effect of backlash in drivetrains exist. Some of these include the dead-zone model and the modified dead-zone model [1, 2]. On the other hand, there are limitations of the accuracy level of these models. Since existing backlash models differ in their results and do not predict system behavior perfectly, a critical examination of the modeling approaches must be carried out to find an optimal approach for highly complex drivetrains.

For clarity, the highly complex drivetrain is replaced by a shaft with backlash which greatly reduces the complexity. Thus, a shaft with backlash is considered which is usually modeled as a massless shaft [1, 2]. This is a strong simplification since every shaft has a mass which is a measure of its inertia or its tendency to resist a motion induced by an external force. In [3] it is equally shown that the mass of a system is crucial in the study of noise and vibrations. An example where this importance is reflected is the undamped natural frequency of a translational system approximated as an SDOF. Given the mass (m) and the spring elasticity (k) the undamped natural frequency of the system is given by $\sqrt{k/m}$. This is an important aspect in system condition monitoring which is not reflected in the massless approximation of the shaft.

2 Modeling approaches

Previously used approaches in modeling of backlash are shown in Equations (1) to (4) [1, 2, 4, 5, 6 and 7].

Equation (1): is the dead zone approach [1, 2]. The approach approximates the shaft as a pure spring with no damping.

Equation (2): A commonly used modification of (1) known as the modified dead zone model [1, 2, 4], where damping has been introduced in the transmitted torque while maintaining the intervals.

Equation (3): This expression is obtained from the analysis of a massless beam [1, 2]. It keeps the same expression of the transmitted torque in (2), but introduces the elasticity and damping influences in the intervals

Equation (4): Represents the phase plane model, which was developed using the physical system represented by Equation (3). Its main difference from (3) is its new interval resulting from the phase plane analysis [1, 2].

Equation (5): Represents the physical system of the new modeling approach, enhancing (3) with inertia.

The simple approach described by Equation (1) will not be considered in the following analysis. Henceforth analysis will be mostly done on the modeling approaches of Equations (2) to (5).

An example of a shaft with backlash considered in this analysis is shown in Fig 1.

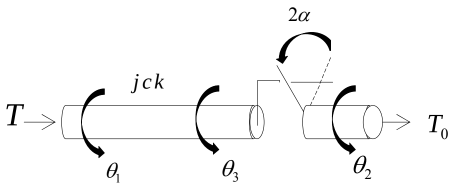

Fig. 1 Physical system: a shaft with backlash

The formulation of the new approach, supplements the approaches according to [1, 2] with the consideration of the inertia (j), elasticity (k), and inner damping (c) of the shaft. It is modeled such that the system is driven by a torque (T) on one end and outputs a torque (T_0) on the other end. The driving torque is expressed as a function of *displacement*, defined as $\theta_d(t)=\theta_1(t)-\theta_2(t)$, its time derivative $\dot{\theta}_d(t)=\dot{\theta}_1(t)-\dot{\theta}_2(t)$, and its second derivative $\ddot{\theta}_d(t)=\ddot{\theta}_1(t)-\ddot{\theta}_2(t)$ without using the state $\theta_3(t)$ [3]. The backlash angle is defined symmetrically as $\theta_3(t)-\theta_2(t)$ within the backlash gap 2α such that $|\theta_3(t)-\theta_2(t)|\le\alpha$.

$$T=\begin{cases} k(\theta_d-\alpha) & \theta_d>\alpha \\ 0 & |\theta_d|\le\alpha \\ k(\theta_d+\alpha) & \theta_d<-\alpha \end{cases} \tag{1}$$

$$T=\begin{cases} k(\theta_d-\alpha)+c\dot{\theta}_d & \theta_d>\alpha \\ 0 & |\theta_d|<\alpha \\ k(\theta_d+\alpha)+c\dot{\theta}_d & \theta_d<-\alpha \end{cases} \tag{2}$$

$$T=\begin{cases} 0 \quad or \quad k(\theta_d-\alpha)+c\dot{\theta}_d & \theta_d+(c/k)\dot{\theta}_d>\alpha \\ 0 & |\theta_d+(c/k)\dot{\theta}_d|\le\alpha \\ 0 \quad or \quad k(\theta_d+\alpha)+c\dot{\theta}_d & \theta_d+(c/k)\dot{\theta}_d<-\alpha \end{cases} \tag{3}$$

$$T=\begin{cases} k(\theta_d-\alpha)+c\dot{\theta}_d & (\theta_d,\dot{\theta}_d)\in A^+ \\ 0 & (\theta_d,\dot{\theta}_d)\in A^0 \\ k(\theta_d+\alpha)+c\dot{\theta}_d & (\theta_d,\dot{\theta}_d)\in A^- \end{cases} \qquad (4)$$

Where:

$$A^+=\left\{(\theta_d,\dot{\theta}_d):\begin{cases} f(\theta_d+\alpha,\dot{\theta}_d)\ge 2\alpha, & \dot{\theta}_d>0 \\ k(\theta_d-\alpha)+c\dot{\theta}_d\ge 0, & \forall\dot{\theta}_d \end{cases}\right\}$$

$$A^-=\left\{(\theta_d,\dot{\theta}_d):\begin{cases} f(\theta_d-\alpha,\dot{\theta}_d)\le -2\alpha, & \dot{\theta}_d<0 \\ k(\theta_d+\alpha)+c\dot{\theta}_d\le 0, & \forall\dot{\theta}_d \end{cases}\right\}$$

$$A^0=\{(\theta_d,\dot{\theta}_d)\}\setminus(A^+\cup A^-)$$

$$f(\theta_d+\alpha,\dot{\theta}_d)\approx(\theta_d+\alpha)+(c\dot{\theta}_d/k)e^{-k(\theta_d+\alpha)/c\dot{\theta}_d-1}=2\alpha$$

$$T=\begin{cases} 0 \;\; or \;\; k(\theta_d-\alpha)+c\dot{\theta}_d+j\ddot{\theta}_d & \theta_d+(c/k)\dot{\theta}_d+(j/k)\ddot{\theta}_d>\alpha \\ 0 & \left|\theta_d+(c/k)\dot{\theta}_d+(j/k)\ddot{\theta}_d\right|\le\alpha \\ 0 \;\; or \;\; k(\theta_d+\alpha)+c\dot{\theta}_d+j\ddot{\theta}_d & \theta_d+(c/k)\dot{\theta}_d+(j/k)\ddot{\theta}_d<-\alpha \end{cases} \qquad (5)$$

The fifth equation represents the new approach being analyzed in this paper, and will be compared to the approaches 2 to 4.

2.1 Magnitude of Transmitted Torque

The expression of the torques from Equations (2) to (5) are such that starting from (2) each next expression is an enhancement of the previous. While in Equations (2) to (4) only the damping and elasticity effect are included in the approximation, Equation (5) takes additionally into account the inertia and should be closer to real physical systems [3]. One can see that, either only the intervals are enhanced as in the case from (2) to (4) or the magnitude of the torque is also enhanced as in (5). Considering only the torque expressions (without the backlash boundaries), these logical enhancements lead to the following limiting expressions:

$$\lim_{j\to 0} \; Equation\ (5) = Equations\ (4)\ \&\ (3) \qquad (6)$$

$$\lim_{c\to 0} \; Equations(4)\ \&\ (3) = Equation\ (2) \qquad (7)$$

$$\lim_{(j,c)\to(0,0)} \; Equation(4) = Equation(2) \qquad (8)$$

Thus it can be seen that there is convergence in the models according to the above limiting expressions. The fact that the expression of the transmitted torques are different, leads to the suggestion that, the magnitude of the transmitted torques of equations (2) to (4) are different from (5). This can be demonstrated by setting $\alpha=0$ in equations (2) to (5). In that case, there is no backlash and the system can be considered as continuous. Observe that only equation (5) reduces to the torque expression of a rotating system approximated as a Single-Degree-of-Freedom (SDOF where $T=k(\theta)+c\dot{\theta}+j\ddot{\theta}$). Thus equation (5) is more likely to approximate the system behavior closer. To show that (5) approximates better than the others, it suffices to choose a single combination of j, c and k for which it predicts real system behavior closer than the others. Using the system properties $j=[10Kgm^2]$, $c=5[Nm/rad/s]$ $k=10[Nm/rad]$ and $\alpha=0[rad]$ with an arbitrary sinusoidal input the following graphs in Fig 2 (a) depict the behavior of the different models.

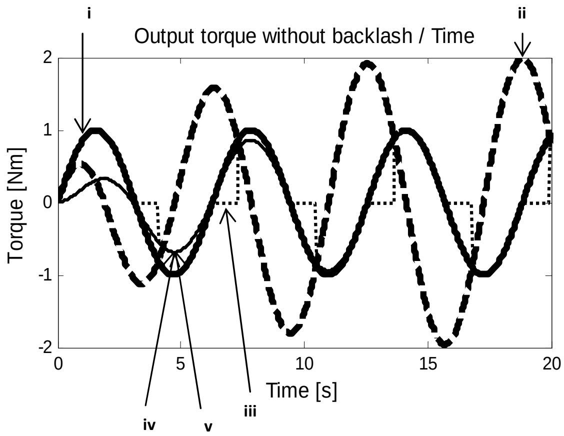

Fig 2 (a) Torque versus time

Where:

i. Input torque
ii. Output torque of the continous shaft
iii. Output torque of phase plane model (Eq 4)
iv. Output torque of physical system used in developing the phase plane model (Eq.3)
v. Modified dead zone model (Eq. 2)

In Fig 2 (a), it can be seen that the curve depicting the behaviour of the continous shaft at resonance is different from all the others in magnitude and phase. It can also be seen that though the phase plane model (iii) has a step, in general the phase and magnitude are similar to those of the iv. And v. due to their convergence. This is contrary to expectation since the backlash was set to zero and should therefore approximate to the continuous system. On the other hand, Fig 2 (b) shows a perfect match between the new model (JCK-model) and the continous shaft.

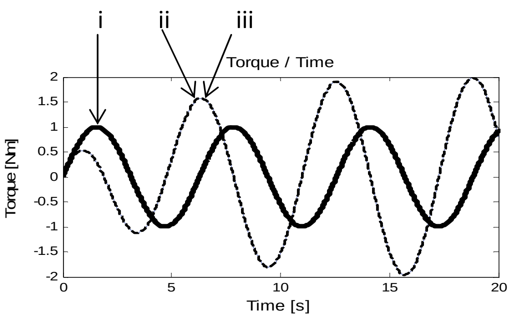

Fig. 2(b) Torque vs time

Where:

i. Input torque
ii. Output torque of continous shaft
iii. Output torque of proposed backlash model (JCK-model)

As was shown earlier, the transmitted torques are given by different expressions. Consequently their curves are different as observed from the graphs above. The JCK model reflects reality more which can be seen from its convergence with the continuous system when its backlash is set to zero.

2.2 Intervals of Transmitted Torque

In order to illustrate further discrepancies, the backlash boundaries expressions of Equations (2), (3) and (5) are examined. Equation (4) is not considered in this section because it is simply a derivative of (3) and also does not consider the inertia. The solutions to the interval expressions are obtained assuming the following initial conditions: at $t = 0$, $\dot{\theta} = \ddot{\theta} = 0$ i.e. the shaft starts from rest. We also assume that the system has a backlash angle such that $\alpha = 1rad$. Let the shaft also be arbitrary with the following properties: $j = 10[Kgm^2]$, $c = 10[Nm/rad/s]$ and $k = 5[Nm/rad]$.

These graphs show the intervals where the torques act, with the X-axis as a symmetric axis as illustrated in the Fig. 3 below.

In order to understand the graphs let us consider the plot (Fig. 3) of the backlash boundary expressions from the massless beam used in developing the phase plane model [1, 2] Equation (3), noted as massless beam for the phase plane model (PPM). It can be observed that this graph is symmetric relative to the X-axis. The upper half plot represents the right contact above which the torque is non-zero (region A). The lower half plot represents the left contact below which the torque is non-zero (region C). The area between the upper and lower halves is the free play region with a torque of zero (region B).

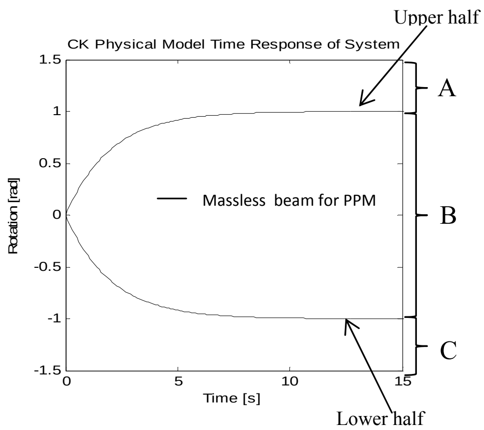

Fig. 3 Interval plot: phase plane model's physical system (Equation 3)

The different regions are governed by the following expressions:

$$\text{A:} \quad T=0 \quad or \quad k(\theta_d-\alpha)+c\dot{\theta}_d; \quad \theta_d+(c/k)\dot{\theta}_d>\alpha$$

$$\text{B:} \quad T=0; \quad \left|\theta_d+(c/k)\dot{\theta}_d\right|\leq\alpha$$

$$\text{C:} \quad T=0 \quad or \quad k(\theta_d+\alpha)+c\dot{\theta}_d; \quad \theta_d+(c/k)\dot{\theta}_d<-\alpha$$

If we now superimpose the discussed plot with the interval plot of the modified dead zone model we get the following (Fig. 4):

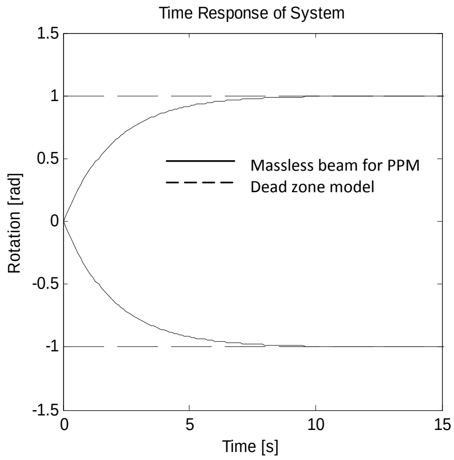

Fig. 4 Superimposed intervals

We can observe that both graphs; the modified dead zone model in dash lines and the physical system of the phase plane massless beam model in continuous line converge over time. During the first few seconds, the modified dead zone model predicts the interval differently and less accurately. It can be observed that even when the phase plane massless beam physical model predicts a non-zero torque, the modified dead zone model predicts a zero torque, thus making the modified dead zone model less accurate. Introduce mass into the beam with $j=10\left[Kgm^2\right]$, results in the graphs shown Fig. 5 below. It can be observe that though all three modeling approaches converge over time. The massless beam for PPM and the mass beam models predict the physical system behavior better than the modified dead zone model. This is because in addition to the elasticity of the shaft they also take into account the damping effects. It can also be observed that the mass beam model is quite similar in profile to the massless beam for PPM model.

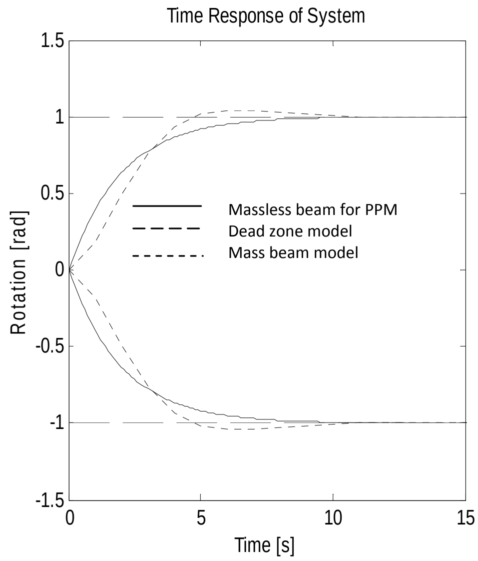

Fig. 5 Superimposed intervals of all three models

Though similar, they are not matching perfectly. The reason is that the mass beam model takes into the inertia which is not considered in the massless beam model. We can see that within the first 3 seconds, the mass beam predicts a zero output torque within a smaller region while at the same time the other two models predict larger regions, with the modified dead-zone model predicting an even larger and more erroneous region. After 3 seconds, the massless beam for PPM predicts a smaller response region compared to the mass beam (JCK) model until their convergence at about 10 seconds. The same observation can be noticed for the modified dead zone model after 5 seconds. It can also be seen that the lines cross each other which indicates that the regions where there is a positive, zero or negative torque equally varies and depends on the approximation of the beam. From theory, Equation (5) actually reflects more the physical behavior of the real system. Since the massless approach does not predict the system behavior exactly, it is therefore worth considering the JCK model for backlash modeling because it takes into account the contribution of the inertia and should lead to more accurate system behavior and sizing.

A further difference can be seen when plotting the rotation velocity regions of the Massless beam for PPM (continuous curve) and the proposed model (dash curve) as shown in Fig. 6 below:

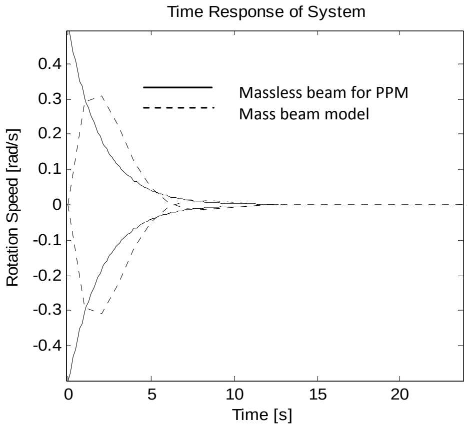

Fig. 6 Superimposed velocity intervals

Fig. 6 shows convergence of the plots over time but a mismatch of the approximations at the beginning, even with a reversal of the regions with non-zero torques for the mass model. It can be observed that though the motion of the system starts from rest according to the initial conditions above, the continuous curve does not reflect these conditions, giving a direct observation on the limitation of the massless beam assumption. This difference is as a result of the orders of the differential equations used in modeling the system, where the Mass beam model is a second other approximation unlike the massless beam which is a first order approximation.

3 Failure mode simulation analysis

A simple failure case was simulated and the behavior of the output rotation observed and compared. Here a linear input (i) shown in Fig 8 (a) was used. The failure mode simulated was a pseudo-shaft rupture where the input torque was abruptly set to zero during simulation. The block diagram representation of the Simulink models of Equations (2) to (5) is shown in Fig. 7 below.

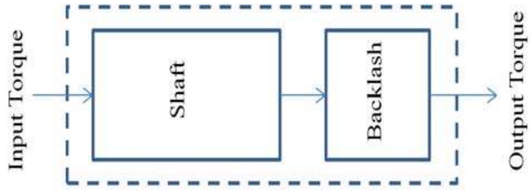

Fig 7 Modeling method

For this simulation, the following system parameters were used: $j = 50[Kgm^2]$; $c = 10[Nm/rad/s]$; $k = 0.01[Nm/rad]$, and a backlash angle such that α = 0.01 $[rad]$. The backlash zones of the models are shown in Fig. 8 below:

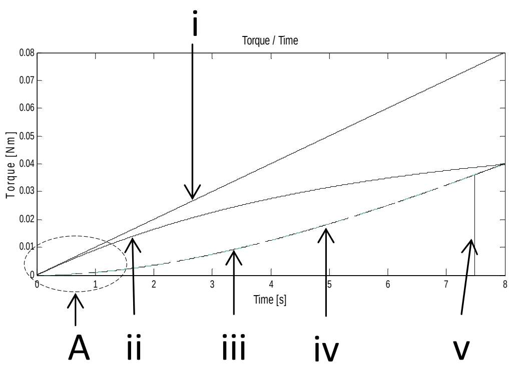

Fig 8 (a) Free-play regions of the different backlash models

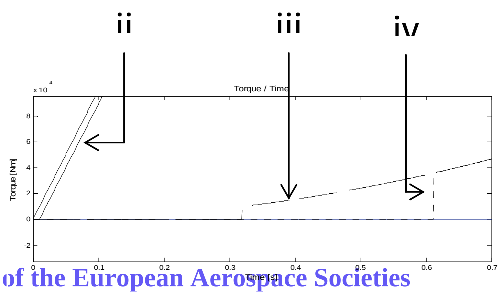

Fig 8 (b) Zoomed plot of Region A

Where the torques are according to Table 1 below:

ID	Torque
i	Input torque
ii	Output torque of proposed model (Eq. 5)
iii	Output torque of physicakl system used in developing the phase plane model (Eq. 3)
iv	Phase plane model (Eq. 4)
v	Modified dead zone model (Eq. 2)

Table 1 Torques and IDs

All models show different response times for which the output torque becomes non-zero. In this case, the response time is considered as the time needed by the system to get out of the backlash zone. This difference is a result of the different approximations of the models which account for different times need for torque to be transmitted from one end of the shaft to the other. The response time of the modified dead zone model is the largest while that of the proposed model is the smallest. After 10 seconds of simulation time the failure was simulated and the various profiles from the different models are plotted in Figure 9 below:

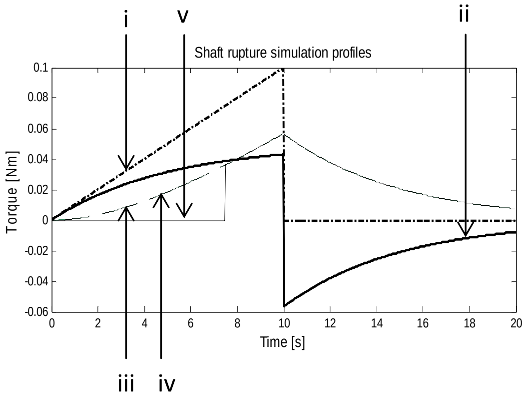

Fig 9 Shaft's rupture failure simulation profiles

Where the torques (i) to (v) are according to table 1 above.

In Fig 9, after around $t = 7s$, a convergence can be seen in all other models (iii, iv, v) except the proposed model (ii). At $t = 10s$ the input torque (i) is abruptly set to zero. While all models except the proposed model have a slope that approaches zero with a negative gradient from the time of rupture, the proposed model shows a sudden flip in the torque as a result of the rupture and further reduces to $T = 0$ with a positive gradient. The behavior of the proposed model is closer to that of an SDOF because of this reversal of torque, which normally occurs in any situation where the action force abruptly goes to zero in a situation of opposing action and reaction forces. A consequence of this unexpected behavior in the old models is that, vibration studies of systems may not be very accurate because if the mass of the system is not considered then the models may portray inaccurate system behavior, different from system with mass as shown in the case in Fig. 9. This may lead to wrong natural frequency calculations, wrong damping values, etc. On the other hand the new model reflects real system behavior better because it captures certain system behaviors not seen in the other models such as the case of shaft rupture in Fig 9 and the resonance behavior of Fig 2.

4 Analytic proof of proposed backlash model (JCK)

To validate this model, an analytic proof of concept is presented at the Appendix (**Section 6**). As a summary in this section, the analytic proof comprise of the approach and theorems taken from [1] and [2] used in the development of the phase plane analysis. From Fig. 1, the torque on the left hand side (T) acts upon a system with the following properties: inertia (j), torsional spring elasticity (k), and internal damping constant (c). T_0 is the output torque. As represented in Fig. 1, let θ_1 be the angle of the input side of the shaft, θ_3 the angle of the driving axis at the backlash, and θ_2 the angle of the driven member. Examining the model shown in Fig. 1, one can easily deduce an exact expression of the torque using Newton's law of motion to obtain its corresponding equation of motion as:

$$T(t) = j\ddot{\theta}_s + c\dot{\theta}_s + k\theta_s = j(\ddot{\theta}_d - \ddot{\theta}_b) + c(\dot{\theta}_d - \dot{\theta}_b) + k(\theta_d - \theta_b) \quad (9)$$

Where $\theta_s = \theta_d - \theta_b$ and $\theta_b = \theta_3 - \theta_2$

Here the torque (T) is formulated as a function of angular displacement, velocity and acceleration using of θ_1 and θ_2 without the use of θ_3. It is equally shown that there is contact when system surpasses the backlash zone and no contact within it. For a complete proof please refer to the Appendix, section 6.

5 Conclusion

It was demonstrated that the new model with mass consideration converges to the phase plane model and the massless beam model as the mass of the beam approaches zero. If in addition, the damping of the shaft is reduced to approach zero, then, all three models can be approximated by the modified dead zone model. From the differences observed in the magnitude, regions and failure analysis, physical system behavior can be better approximated using the new model (equation (5)) with mass consideration for estimating the backlash effect in drivetrains. Worthy to note is that the phase plane model was developed using a massless beam, thus inertia is not considered. On the other hand the new model takes into account the mass of the beam; hence it contains extra system behaviors that are not observed in either the phase plane model or the other models mentioned above. The results of this investigation predict new conditions (different from the other models) for determining when there is right or left contact within the backlash region. Using appropriate expressions for the torques, their formulation and validation is shown in the Appendix, section 6. The state space derivative from equation (5) as shown in the appendix, yields the following expression:

$$\boxed{\ddot{\theta}_b + \frac{c}{j}\dot{\theta}_b = \begin{cases} \max\left(0, \ddot{\theta}_d + \frac{c}{j}\dot{\theta}_d + \frac{k}{j}(\theta_d - \theta_b)\right), & \theta_b = -\alpha \quad (T \le 0) \\ \ddot{\theta}_d + \frac{c}{j}\dot{\theta}_d + \frac{k}{j}(\theta_d - \theta_b), & |\theta_b| < \alpha \quad eq\ 20 \\ \min\left(0, \ddot{\theta}_d + \frac{c}{j}\dot{\theta}_d + \frac{k}{j}(\theta_d - \theta_b)\right), & \theta_b = \alpha \quad (T \ge 0) \end{cases}}$$

…(*)

(*) is henceforth presented as a new method in estimating backlash.

The advantage of the proposed model is that, one gets not only a better backlash region, but also the right magnitude of transmitted torque. The next step is to validate the approach with measured data.

References

[1] M. Nordin., J. Galic and P. Gutman., "New Models for Backlash and Gear Play", *International Journal of Adaptive Control and Signal Processing*, Vol. 11, 1997, pp. 49-63.

[2] G. Tao., F. L. Lewis. (Eds.): *Adaptive Control of Nonsmooth Dynamic System*, Springer-Verlag London Limited, Great Britain, 2001, Chap. 1.

[3] A. Brandt.: *Introduction to Noise and Vibration Analysis*, Saven EduTech AB, Täby, Sweden, 2001.

[4] A. Lagerberg.: "Control and Estimation of Automotive Powertrains with Backlash," Ph.D. Dissertation, Department of Signals and Systems, Chalmers University of Technolgy, Göteborg, Sweden 2004.

[5] M. Tallfors., "Parameter Estimation and Model Based Control Design of Drive Train Systems," Licentiate Thesis, Kungliga Tekniska Högskolan, Stockholm, Sweden, 2005.

[6] A. Lagerberg., Bo S. Egardt.: "Backlash Gap Positioning Estimation in Automotive Powertrains," European Control Conference, Cambridge, UK, 2003.

[7] J. H. Baek., Y. K. Kwak and S. H. Kim: "Analysis on the influence of Backlash and Motor Input Voltage in Geared Servo System" The 11th Mediterranean Conference on Control and Automation, Rhodes, Greece, 2003.

APPENDIX

6 Complete analytic proof of proposed backlash model (JCK)

To validate this model, a complete analytic proof of concept is presented here. As was stated under section 4 above, the goal is to formulate the torque (T) shown in equation (9) above as a function of angular displacement, velocity and acceleration using of θ_1 and θ_2 without the use of θ_3.

6.1 Assumptions

The following assumptions are made:

- The impact when the backlash gap is closed is inelastic
- Contact can occur between the driving and driven members on either side of the backlash

6.2 Definitions

The following definitions are used:

- **Right contact:** $\theta_b = \alpha$, $\dot{\theta}_b = \ddot{\theta}_b = 0$
- **Left contact:** $\theta_b = -\alpha$, $\dot{\theta}_b = \ddot{\theta}_b = 0$
- **Contact:** 'Contact' if there is either left or right contact

T > 0 implies right contact, because otherwise no positive torque could be transmitted. Combining this condition with equation (9) yields:

$$T(t)>0 \Rightarrow T(t)= j(\ddot{\theta}_d - 0)+c(\dot{\theta}_d - 0)+k(\theta_d - \alpha)= \ldots$$

$$j\ddot{\theta}_d + c\dot{\theta}_d + k(\theta_d - \alpha) > 0 \qquad (10)$$

Similarly, T < 0 implies left contact. This condition in combination with Equation (9) yields:

$$T(t)<0 \Rightarrow T(t)= j(\ddot{\theta}_d - 0)+c(\dot{\theta}_d - 0)+k(\theta_d + \alpha)= \ldots$$

$$j\ddot{\theta}_d + c\dot{\theta}_d + k(\theta_d + \alpha) < 0 \qquad (11)$$

Logical negation of (10) and (11) yields:

$$\begin{cases} k(\theta_d - \alpha) + c\dot{\theta}_d + j\ddot{\theta}_d & \Rightarrow \quad T \geq 0 \\ k(\theta_d + \alpha) + c\dot{\theta}_d + j\ddot{\theta}_d & \Rightarrow \quad T \leq 0 \end{cases} \qquad (12)$$

Respectively, equations (9) to (12) lead to equation (5). From the expression of the torque in Equation (12) we can define the following areas:

$$A^{+} = \{(\theta_d, \dot{\theta}_d, \ddot{\theta}_d): j\ddot{\theta}_d + c\dot{\theta}_d + k\theta_d \geq k\alpha \qquad (13)$$
$$A^{r} = \{(\theta_d, \dot{\theta}_d, \ddot{\theta}_d): \left| j\ddot{\theta}_d + c\dot{\theta}_d + k\theta_d \right| < k\alpha \qquad (14)$$
$$A^{-} = \{(\theta_d, \dot{\theta}_d, \ddot{\theta}_d): j\ddot{\theta}_d + c\dot{\theta}_d + k\theta_d \leq -k\alpha \qquad (15)$$

Where A^{r} represents the interior free play gap of the backlash.

6.3 Lemma 1

During a non-zero interval, persistent right contact is only possible in A^{+} and persistent left contact only in A^{-}.

Proof by contradiction:

a) **Persistent right contact only in** A^{+}:

We assume right contact outside A^{+}. From (9) and (13), it follows that: $T = j\ddot{\theta}_d + c\dot{\theta}_d + k\theta_d - k\alpha < 0$

Hence a persistent negative torque with right contact implies a pull force which is physically impossible. Hence we can only have a persistent right contact in A^{+}.

a) **Persistent left contact only in** A^{-}**:**

We assume right contact outside A^{-}. From (9) and (15), it follows that: $T = j\ddot{\theta}_d + c\dot{\theta}_d + k\theta_d + k\alpha > 0$

Hence a persistent positive torque with left contact implies a push force which is physically impossible. Hence we can only have a persistent left contact in A^-.

6.4 Lemma 2:

If the system state $(\theta_d, \dot{\theta}_d, \ddot{\theta}_d)$ at the initial time $t = t_0$ lies in A^+ with $\theta_b(t_0) = \alpha$ (right contact), with $\theta_b(t_0) = \alpha$, $\forall t_1 > t_0$: $(\theta_d, \dot{\theta}_d, \ddot{\theta}_d) \in A^+$ for all $t \in [t_0 \quad t_1]$.

If $(\theta_d(t_0), \dot{\theta}_d(t_0), \ddot{\theta}_d(t_0)) \in A^-$ with $\theta_b(t_0) = -\alpha$ (left contact), then $\theta_b(t_1) = -\alpha$ for all times $t_1 = t_0$ such that $(\theta_d(t \ ), \dot{\theta}_d(t \ ), \ddot{\theta}_d(t \ )) \in [t_0 \quad t]$

a) Proof of right contact:

Right contact in the interior of A^+ together with (9) implies that $T > 0$. Right contact is maintained as long as there is positive torque. At the boundary of A^+, i.e. with $j\ddot{\theta}_d + c\dot{\theta}_d + k\theta_d = k\alpha$, it holds from (5) that $T = 0$ and together with (9) this yields to:

$$T(t) = j(\ddot{\theta}_d - \ddot{\theta}_b) + c(\dot{\theta}_d - \dot{\theta}_b) + k(\theta_d - \theta_b) = 0$$

$$\Rightarrow \quad T = j\ddot{\theta}_d + c\dot{\theta}_d + k\theta_d - (j\ddot{\theta}_b + c\dot{\theta}_b + k\theta_b) = 0$$

But $j\ddot{\theta}_d + c\dot{\theta}_d + k\theta_d = k\alpha$

$$\Rightarrow \quad j\ddot{\theta}_b + c\dot{\theta}_b + k\theta_b = k\alpha \tag{16}$$

To solve (16) we use the following conditions: Steady state condition: $\theta_b = \alpha$, $\dot{\theta}_b = \ddot{\theta}_b = 0$ and the initial condition with $t = t_0$. With consideration of these conditions,

$$\theta_b(t) = Ae^{\lambda_1 t_0} + Be^{\lambda_2 t} + \alpha \tag{17}$$

With:

$$A = \frac{\dot{\theta}_b(t_0)}{\lambda_1} e^{-\lambda_1 t_0} - \left[\frac{\lambda_1\theta_b(t_0) - \dot{\theta}_b(t_0) - \lambda_1\alpha}{\lambda_1 - \lambda_2}\right] \frac{\lambda_2}{\lambda_1} e^{-\lambda_1 t_0}$$

and

$$B = \frac{\lambda_1\theta_b(t_0) - \dot{\theta}_b(t_0) - \lambda_1\alpha}{e^{\lambda_2 t_0}(\lambda_1 - \lambda_2)}$$

Starting with right contact ($\theta_b = \alpha$), equation (17) becomes a constant $\theta_b = \alpha$, thus right contact is preserved.

The symmetric proof applied to the left contact and the trajectory in A^- is as follows:

b) Proof of left contact

Left contact in the interior of A^- together with (9) implies that $T < 0$. As long as there is negative torque, left contact is maintained. At the boundary of A^-, i.e. with $j\ddot{\theta}_d + c\dot{\theta}_d + k\theta = -k\alpha$, it holds from equation (5) that $T = 0$ and together with (9) this yields to:

$$T(t) = j(\ddot{\theta}_d - \ddot{\theta}_b) + c(\dot{\theta}_d - \dot{\theta}_s) + k(\theta_d - \theta_b) = 0$$

$$\Rightarrow \quad T = j\ddot{\theta}_d + c\dot{\theta}_d + k\theta_d - (j\ddot{\theta}_b + c\dot{\theta}_b + k\theta_b) = 0$$

But $j\ddot{\theta}_d + c\dot{\theta}_d + k\theta_d = -k\alpha$

$$\Rightarrow \quad j\ddot{\theta}_b + c\dot{\theta}_b + k\theta_b = -k\alpha \tag{18}$$

To solve (18) we use the following conditions: When $\theta_b = -\alpha$, $\dot{\theta}_b = \ddot{\theta}_b = 0$ (steady state condition) and let the initial time $t = t_0$ (initial condition), then we have that:

$$\theta_b(t) = Ae^{\lambda_1 t_0} + Be^{\lambda_2 t} - \alpha \tag{19}$$

With:

$$A = \frac{\dot{\theta}_b(t_0)}{\lambda_1} e^{-\lambda_1 t_0} - \left[\frac{\lambda_1\theta_b(t_0) - \dot{\theta}_b(t_0) - \lambda_1\alpha}{\lambda_1 - \lambda_2}\right] \frac{\lambda_2}{\lambda_1} e^{-\lambda_1 t_0}$$

and

$$B = \frac{\lambda_1\theta_b(t_0) - \dot{\theta}_b(t_0) + \lambda_1\alpha}{e^{\lambda_2 t_0}(\lambda_1 - \lambda_2)}$$

Starting with left contact ($\theta_b = -\alpha$), equation (19) becomes a constant $\theta_b = -\alpha$ thus, left contact is preserved.

6.5 Theorem (Release condition):

We assume that $\theta_b(t_0)=\alpha$ or $\theta_b(t_0)=-\alpha$, thus we have contact at time t_0. Contact is lost at the first time $t_1 > t_0$ such that the trajectory $(\theta_d, \dot{\theta}_d, \ddot{\theta}_d)$ reaches the release set A^r.

Proof

This follows from the fact that right respectively left contact cannot be lost in A^+ respectively A^-, and that in A^r, which lies between A^+ and A^-, contact is not possible. When contact is lost we know that $T=0$ and equation (9) leads to:

$$\ddot{\theta}_d - \ddot{\theta}_b + \frac{c}{j}(\dot{\theta}_d - \dot{\theta}_b) + \frac{k}{j}(\theta_d - \theta_b) = 0 \qquad (20)$$

Letting $x = \theta_d - \theta_b$ and solving the above equation, we get:

$$\theta_b(t) - \theta_d(t) = Ae^{\lambda_1 t_0} + Be^{\lambda_2 t} \qquad (21)$$

With:

$$A = \left[\frac{\lambda_1 x(t_0) - \dot{x}(t_0)}{\lambda_1 - \lambda_2}\right]\frac{\lambda_2}{\lambda_1}e^{-\lambda_1 t_0} - \frac{\dot{x}(t_0)}{\lambda_1}e^{-\lambda_1 t_0}$$

and $B = \dfrac{\dot{x}(t_0) - \lambda_1 x(t_0)}{e^{\lambda_2 t_0}(\lambda_1 - \lambda_2)}$

With: $x(t_0) = \theta_d(t_0) - \theta_b(t_0)$ and $\dot{x}(t_0) = \dot{\theta}_d(t_0) - \dot{\theta}_b(t_0)$

Since θ_d, $\dot{\theta}_d$ and $\ddot{\theta}_d$ are given and equation (21) gives θ_b, equation (22) gives $\dot{\theta}_b$ and $\ddot{\theta}_b$ Furthermore, when $|\theta_b| = \alpha$, contact is achieved. Solving for θ_b as a state space model, an exact solution is obtained.

Using equation (19), $|\theta_b| \le \alpha$ and the release condition we get:

$$\ddot{\theta}_b + \frac{c}{j}\dot{\theta}_b = \begin{cases} \max\left(0, \ddot{\theta}_d + \frac{c}{j}\dot{\theta}_d + \frac{k}{j}(\theta_d - \theta_b)\right), & \theta_b = -\alpha \quad (T \le 0) \\ \ddot{\theta}_d + \frac{c}{j}\dot{\theta}_d + \frac{k}{j}(\theta_d - \theta_b), & |\theta_b| < \alpha \quad eq\ 20 \\ \min\left(0, \ddot{\theta}_d + \frac{c}{j}\dot{\theta}_d + \frac{k}{j}(\theta_d - \theta_b)\right), & \theta_b = \alpha \quad (T \ge 0) \end{cases}$$

… (22)

An interpretation of this state equation would be a limited integrator with the time derivative $\ddot{\theta}_d + \frac{c}{j}(\dot{\theta}_d - \dot{\theta}_b) + \frac{k}{j}(\theta_d - \theta_b)$ and limiter α.

From equation (22), θ_b, $\dot{\theta}_b$ and $\ddot{\theta}_b$ are known and given θ_d, $\dot{\theta}_d$ and $\ddot{\theta}_d$, the torque T is found by equation (9). The expression above describes a non-linear dynamical system, not a function, that gives the torque T with given θ_d, $\dot{\theta}_d$ and $\ddot{\theta}_d$.

The derivation demonstrates that this new formula for modeling backlash incorporates contact and persistent contact depending of the direction of the applied torque at the boundaries of the free play region as well as no contact within the free play region.

4:th CEAS Air & Space Conference
FTF Congress: Flygteknik 2013

Aeroelastic Tailoring Through Combined Sizing and Shape Optimization Considering Induced Drag

S. Deinert and Ö. Petersson and F. Daoud
Cassidian Air Vehicle Engineering, Germany

H. Baier
Technische Universität München, Germany

Keywords: Shape Optimization, Aeroelastic Tailoring, Induced Drag

Abstract

Multidisciplinary design optimization (MDO) is more and more being applied during the entire aircraft development process solving strongly interrelated problems. In this context a multidisciplinary design optimization framework is being developed at Cassidian that enables combined shape and sizing optimization to improve aircraft performance taking into account aeroelastic effects. The framework allows fully coupled aeroelastic shape optimization based on the vortex lattice method together with linear finite element analysis using gradient based optimization methods. Three components form the shape optimization framework: A parametric geometry kernel, a multidisciplinary optimization program and an aerodynamic solver. The architecture of this framework is described shortly before demonstrating its capabilities using the example of a full generic transport aircraft configuration. Two different approaches of addressing structural and aerodynamic requirements during the optimization are examined and discussed. First, a sequential treatment of the aerodynamic aspects and the structural criteria is performed minimizing induced drag through shape with a subsequent structural sizing optimization. The second approach combines the shape and sizing optimization while simultaneously considering structural as well as aerodynamic requirements.

1 Introduction

In modern aircraft development multidisciplinary design optimization (MDO) is gaining importance. It helps covering the great design space in a directed search for good aircraft design solutions using numerical analysis methods. Here, the optimizer is used to find a feasible solution considering many design driving requirements simultaneously. Traditionally, MDO is used with sizing or fibre angle design variables. However, since the outer shape of the aircraft has a great influence on all major disciplines, it should also be included in the multidisciplinary design optimization process, especially in earlier design phases. This increases the design freedom for the optimization, yet, on the other hand modifying the shape of an aircraft while performing several different types of numerical analyses requires new ways of modelling and parametrization in MDO that sustain the consistency between all analysis models of the design driving disciplines.

As stated before, one of the main advantages of using multidisciplinary design optimization is the simultaneous consideration of a great number of requirements originating from several different disciplines. This helps managing the strong interdependencies between some of the key design disciplines balancing the aircraft design. One example of such interdependency is aeroelasticity, which is formed by the two strongly interrelated disciplines of structures and aerodynamics. The elastic deformation of the structure influences the air flow around the aircraft altering the aerodynamic forces which, in turn, deform the structure. In the context of aeroelastic tailoring, MDO is often used to exploit these aeroelastic effects to gain benefits for the aircraft design. This is also one example where varying the shape, additionally to the common sizing or fibre angle design variables, offers more design freedom. The main application of aeroelastic tailoring is passive load alleviation to lower the load on the structure in certain flight states. Apart from structural aspects, aerodynamic properties such as induced drag are affected by aeroelastic effects as well. Structural deformations may change the lift distribution from which the induced drag is directly dependent. Since induced drag represents a major component of the overall drag of an aircraft, applying MDO to conduct aeroelastic tailoring with induced drag consideration already in early development phases shows great potential for performance improvements.

For these reasons, a multidisciplinary shape optimization framework is being developed at Cassidian. Its first application is intended to support shape finding during the conceptual design stage. The decisions made here, have great impact on the performance of the aircraft, which makes any improvements at this stage very desirable. Usually, the general plan-form of the aerodynamic surfaces are determined at this stage. Here, shape optimization can be used to enhance the plan-form definition process. The analysis tools included in the framework have to take into account the amount of available data at the respective design stage. Therefore, the aerodynamic and structural analysis methods applied for this first task are adapted to the conceptual design stage in terms of modelling effort, reliability and fidelity of results. This means that the linear finite element method is applied to perform the structural analysis and the aerodynamic analysis uses the vortex lattice method to calculate lift, induced drag and the pressure distribution. Yet, the framework is designed in such a way that higher fidelity analysis methods for evaluation in later design phases can also be included. Using this framework, the effects of different approaches to the problem of aeroelastic tailoring regarding induced drag are examined.

2 Multidisciplinary Shape Optimization Framework

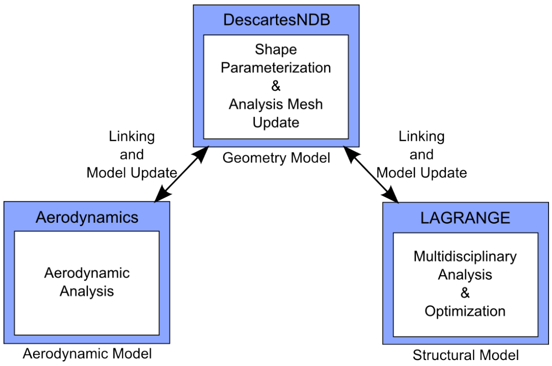

Figure 1: Framework overview

The multidisciplinary shape optimization framework consists of three main components (see Fig. 1), which will be described briefly in the following. In order to perform shape optimization in such a framework, not only the mentioned consistency of analysis models is important, but also sensitivities have to be calculated when applying gradient based optimization algorithms. Therefore, the mesh sensitivities of each analysis model have to be calculated with respect to every defined shape design variable. More detailed information on the framework itself and the approach for gradient calculation can be found in [1]. Apart from the description of the framework, the functionality of this approach was also established there using the example of a standard rectangular wing.

2.1 Shape Parametrization

As discussed before, shape optimization with more than one analysis discipline requires creation and update of reliable and consistent analysis models (e.g. aerodynamic mesh or structural finite element model). At any point during the optimization, all considered analysis models must reflect the same design, yet, each one has to be adapted to the specific needs of its respective analysis discipline.

The applied solution to this problem is the creation of a central parametric geometry model that serves as basis for all derived analysis models (similar to [2]). Thus, shape changes are first performed on the parametric geometry model and then reproduced by all linked analysis models. This significantly reduces the number of required shape parameters even for extensive shape changes compared to individual analysis mesh parametrization. It also guarantees consistency due to the same origin of each analysis model and reduces the number of required interfaces between the analysis components. To eliminate the need for re-meshing analysis models following a shape change, the models are mapped onto the parametric geometry using relative coordinates. Hence, mesh nodes stay at the same relative position on the parametric geometry and move conformally.

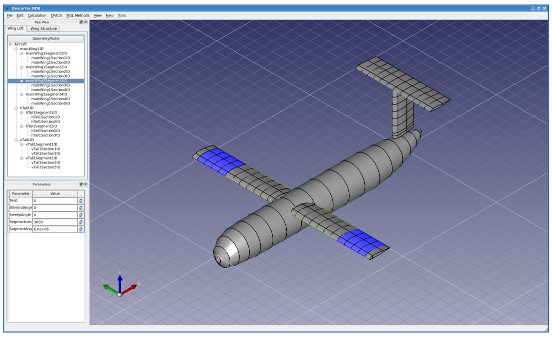

Figure 2: *DescartesNDB* graphical user interface

To parametrize the geometric model, the data format CPACS (Common Parametric Aircraft Configuration Scheme) developed open-source by the DLR (German Aerospace Centre) [3] is applied. This data format allows the parametric description of a complete aircraft model stored in XML. To generate a geometric model based on the CPACS parameters, a software tool named *DescartesNDB* (Descartes Numerical Design Board) is being developed at Cassidian. It is based on another open-source program from DLR called *TIGLViewer* [3] and utilizes the OpenCascade CAD kernel [4]. *DescartesNDB* (see Fig. 2) offers the capabilities to generate, map and update aerodynamic and structural analysis models [5]. During shape optimization, it handles the shape parametrization making the CPACS parameters together with some additional properties available as potential shape design variables.

2.2 Aerodynamic Solver

The first aerodynamic solver to be implemented into the shape optimization framework is the open-source vortex lattice solver *AVL* (Athena Vortex Lattice [6]). It was chosen due to its high robustness and computational efficiency while providing good quality results for early design phase problems. *AVL* allows computation of aerodynamic influence coefficient (AIC) matrices, which can be applied for coupled aeroelastic analysis. These AIC matrices allow calculation of aerodynamic loads by a simple matrix vector product significantly speeding up the convergence iterations during aeroelastic analysis compared to repeated aerodynamic analyses. *AVL* was modified so that it enables the export of AIC matrices for usage in an external program. Also, the export of an induced drag AIC matrix calculated through Trefftz Plane analysis was added. This induced drag AIC matrix can be included in the aeroelastic analysis to determine the lift induced drag of an aeroelastic flight state.

2.3 Multidisciplinary Design Optimizer

The in-house MDO program *LAGRANGE* serves as optimizer and multidisciplinary solver in this framework. *LAGRANGE* features its own finite element structural solver and has been developed at Cassidian since the early 1980s. It allows fully coupled aeroelastic optimization with sizing and composite fibre angles. An extensive design criteria model (e.g. strength, stability, aeroelastic effectiveness, flutter, trimming etc.) has been added. Since aeroelastic analysis is applied to generate the loads on the structure, all constraints are evaluated with realistic flight state loads. *LAGRANGE* includes a number of gradient based optimization algorithms. Combined with analytical sensitivity calculation this allows large scale optimizations.

Coupling *LAGRANGE* and *DescartesNDB* in this framework enables simultaneous sizing and shape optimization of aircraft configurations with realistic aeroelastic flight state loads.

3 Optimization of a Full Aircraft Configuration

The multidisciplinary shape optimization framework presented shortly in section 2 has been applied to the configuration of a generic transport aircraft. For this, the aircraft configuration is defined in a CPACS dataset through which the parametric model is determined. Based on this geometric model, the structural as well as the aerodynamic analysis mesh is generated.

3.1 Optimization Problem

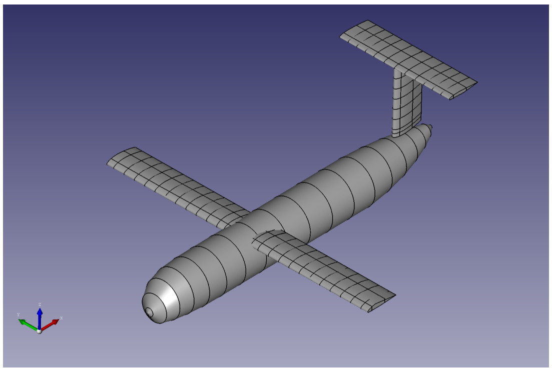

Figure 3: *DescartesNDB model of the generic transport aircraft*

3.1.1 Model Definition

The basic configuration of this generic transport aircraft is a high wing with a T-tail (see Fig. 3). The fuselage is modelled as a rounded-off tube. Since it is not considered as an objective for the shape optimization, it is represented only in a basic form to connect main wing and tail of the aircraft. A maximum take-off mass (MTOM) of 15 tons is assumed for this aircraft concept. The overall dimensions of the aircraft are $19m$ wing span and $22m$ length. Chord length of the main wing as well as the stabilizers is assumed as $2.2m$. The initial plan-form shapes of wing and tail surfaces are rectangular to provide a neutral starting point for the shape optimization. Four segments in the CPACS data set are defined to construct the right half of the main wing. Each of these segments has two bounding sections which yields a total of 5 sections in the right half wing. Every section is assigned a standard 4-digit NACA airfoil to define the wing profile. The root section in the symmetry plane lying inside the fuselage is allocated a symmetric NACA 0015 profile to account for the lower lift generation due to the fuselage. The remaining sections of the main wing have NACA 4415 profiles. Using a symmetry condition, the left half of the wing is built up accordingly.

Horizontal and vertical tail are both defined with symmetric profiles (NACA 0012 and NACA 0021 respectively). Two segments and three sections specify the symmetric horizontal stabilizer with a wing span of $8m$. The vertical stabilizer also consists of two segments and three sections with a span of $4.5m$.

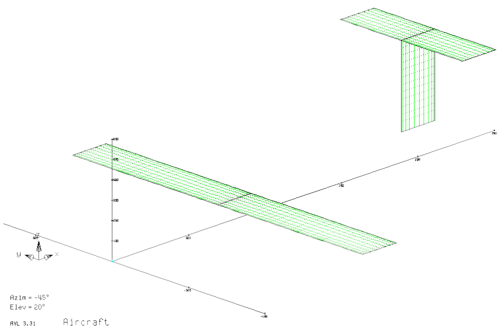

Figure 4: Aerodynamic analysis model in *AVL*

Fig. 4 depicts the aerodynamic *AVL* model of this configuration. Since only the wings of the configuration are regarded in this shape optimization, the fuselage is not modelled. Main wing and horizontal stabilizer show a cosine panel distribution in chord and span direction. An overall number of 1120 vortex elements is used to construct the aircraft.

The structural *LAGRANGE* model can be

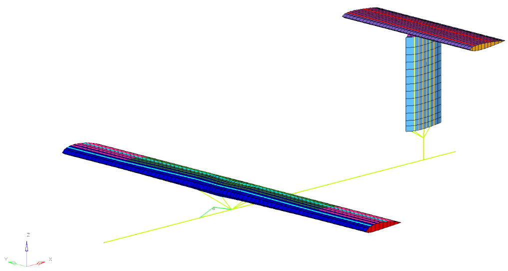

Figure 5: Structural finite element analysis model

seen in Fig. 5. To build up the structure, triangle and quadrilateral shell elements are used for skin, spars and ribs, whereas rods and bars represent the spar caps and stringers. The fuselage is only modelled as a stick with bar elements and concentrated masses for payload and fuselage structural weight to provide an elastic connection between main wing and tail of the aircraft. All components of the aircraft are made of aluminium. The inner structure of the main wing consists of 2 spars and 29 ribs for the full wing. Horizontal tail and vertical tail both have also 2 spars with 15 and 9 ribs respectively. Stringers are generally placed between the two spars of each aerodynamic surface. The aircraft model is mounted at its centre of gravity. Counting all finite elements and the concentrated masses of the fuselage and payload, the finite element model mass sums up to $13446kg$.

Coupling of aerodynamic forces and structural displacements for the aeroelastic analysis is realized with infinite plate splines [7].

3.1.2 Load Case Definition

Three aeroelastic load cases are specified for the following optimization. The first one is a $1g$ level cruise flight at Mach 0.3, which will be used for the induced drag evaluation. The two remaining load cases are $-1g$ and $+2.5g$ ultimate load flight states (i.e. with a safety factor of 1.5 on the loads), which are considered as design driving for the structural integrity. All of the presented analysis load cases include inertia loads based on the structural mass of the aircraft model. This means that aerodynamic lift forces from the *AVL* analysis are superposed with the structural inertia loads during aeroelastic analysis to provide a realistic interaction between weight distribution and lift.

3.1.3 Design Variable Definition

As already mentioned, a combination of sizing and shape design variables will be used to optimize the aircraft configuration. The sizing design variables are specified in the structural model. Here, the skin thickness of wing, horizontal and vertical tail can be varied. Skin thickness design variables are sectioned by spars and ribs and linked symmetrically between the right and left half of the aircraft. Also the cross section of the 1D spar cap elements is declared as design variables. These variables are divided by ribs and linked symmetrically between the left and right half of the airplane. All skin thickness variables may be varied between $0.8m$ and $8mm$, whereas the 1D spar cap cross sections are limited between $50mm^2$ and $200mm^2$ for the main wing and $25mm^2$ and $100mm^2$ for the tail section. Thus, a total number of 240 structural sizing design variables are defined.

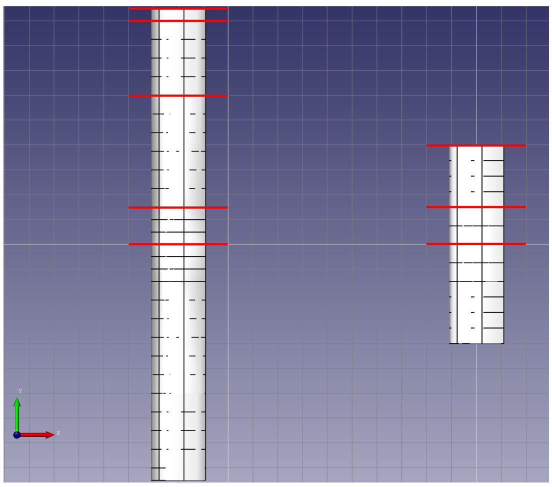

Figure 6: Positions of shape design variables (twist and chord length)

To modify the shape of the aerodynamic surfaces, the optimizer is given a set of parameters influencing twist and chord lengths. On the one hand, the installation angles of the main wing and the horizontal tail are variable, which cause a rotation of the whole aerodynamic surface around its span direction. On the other hand, the twist and the chord length can be modified section wise for main wing and horizontal tail (see Fig. 6). Since the thickness-to-chord ratio is kept constant, an increase in chord length of a section also amplifies the wing height at this position. Hence, the optimizer can influence twist, taper ratio and height of those two surfaces. The modifications are limited between $-5°$ and $5°$ for the angles and $1200mm$ to $2500mm$ for the chord lengths. Thus, in addition to the structural sizing design variables, 16 shape design variables are defined.

Since the aircraft shape is modified to improve the aerodynamic properties of the cruise flight state, the two remaining analysis load cases ($-1g$ and $2.5g$) are also influenced by this and have to be trimmed to equilibrium of forces individually. For this task, two trimming design variables are defined for each of the two load cases (over all angle of attack of the main wing and trim angle of the horizontal tail plane). Hence, aeroelastic trimming to reach equilibrium of forces is included into the optimization problem in the form of trimming design variables and constraints. Trim constraints are formulated for the overall lift using the MTOM of 15 tons as well as the overall pitching moment of all three aeroelastic load cases. These constraints are formulated as inequality constraints giving an allowable range around the desired target value. Thus, 4 trimming design variables included during the optimizations as well; in case of pure sizing optimization with fixed shape 6 trimming variables are defined to trim all 3 load cases.

3.1.4 Structural Constraints

To represent the structural requirements, a set of constraints is defined based on the finite element model (see Fig.5). Stability constraints for 2D skin buckling are defined for all skin patches in the three aerodynamic surfaces bounded by spars, ribs and stringers not considering the leading and trailing edge regions. This accounts for a total of number of 552 buckling constraints per load case. Also the von Mises stresses in the finite elements affected by the sizing design variables are defined as constraints (i.e. 3220 stress constraints per load case). Therefore, 3772 structural constraints are considered per aeroelastic load case.

3.2 Optimization Approach

To examine the effects of different approaches to the described optimization problem, several optimization runs were conducted with the models and load cases defined in section 3.1.

The first step was to conduct a sizing optimization using all three load cases with the objective of weight minimization. As described in section 3.1.3, the sizing design variables for this consisted of the skin thickness and spar cap cross sections of all three lifting surfaces. This created realistic skin thickness distributions and satisfied all structural constraints defined in section 3.1.4. The skin thickness distribution resulting from this optimization can be seen in Fig. 7. The overall structural mass of the finite element model (including the fixed concentrated masses for fuselage and payload) decreased to $13033kg$. The total mass of all variable elements initially amounted to $1455kg$ and decreased by roughly 28%. All subsequent shape optimizations used this result as a starting point. Thus, these shape optimization started with a realistic and feasible structural model.

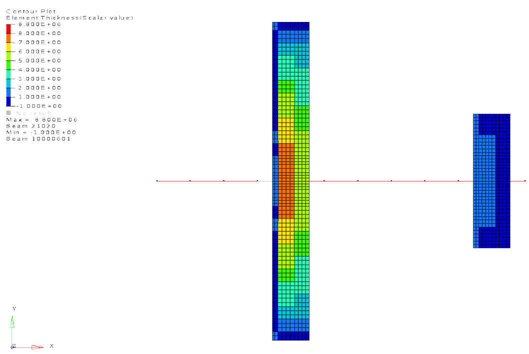

Figure 7: FE skin thickness distribution after preliminary sizing optimization

Regarding the following shape optimizations two fundamental approaches were examined:

- Two sequential optimizations with an initial shape optimization focusing on aerodynamic induced drag minimization and a subsequent sizing optimization in order to satisfy the structural requirements
- A combined structural/aerodynamic shape and sizing optimization to minimize induced drag and account for the structural requirements simultaneously

Both approaches applied realistic aeroelastic flight loads and considered the elastic behaviour of the structure. Due to the same initial design, the loads on the structure were equivalent at the starting point of both optimization approaches.

3.3 Sequential Aerodynamic and Structural Shape Optimization

3.3.1 Aerodynamic Shape Optimization

The objective of the aerodynamic shape optimization was to minimize the induced drag for the $1g$ level cruise flight load case. Only the shape design variables (installation angle, twist and chord length of wing and HTP) described in 3.1.3 were available to the optimizer. To provide an initial thickness distribution for the skin, the result of the preliminary sizing optimization was set as initial design. Loads on the structure were calculated by aeroelastic analysis. Representing the structural weight at $1g$, a set of forces was superposed with the aerodynamic loads during this optimization. Changes to the structural mass during the optimization were not considered in order to conduct a purely aerodynamic optimization with elastic behaviour. To fix the lift and pitching moment, trimming constraints described in section 3.1.3 were included to assure that the lift force stayed equal to the equivalent of $15t$ MTOM at $1g$ and the pitching moment around the centre of gravity remained close to zero. No trimming variables were defined, since the twist shape variables could be used to adjust lift and pitching moment.

Fig. 8 shows the resulting shape of the structural model including the elastic deflection due to the aeroelastic load of the $1g$ cruise load case. Together with the span wise lift distribution of Fig. 10 one can see that the optimizer increased the chord length in the area of the main wing root to its maximum gage in order to compensate for the lower lift generation there due to the symmetrical airfoil simulating the fuselage influence. This high root wing chord combined with the increased main wing installation angle diminishes the dent in the lift distribution. Since all other twist variables in the wing were defined relative to the installation angle, the twist angles show a decreasing behaviour going from root to tip (Fig.11) in order to move the lift distribution towards the ideal elliptic distribution (Fig. 10). At the tip of the wing, the twist variable assumed the lower gage value ($-5°$) and to lower the lift at this position even further the optimizer increased the chord length of the negatively oriented airfoil to heighten its effect. This explains the general tendency of the negative taper ratio and the high chord length at the wing tips (Fig. 8). Because no structural criteria were included in this optimization run, the disadvantages of a negative taper ratio were not considered by the optimizer. All in all, one can see that the optimizer managed to fit the lift distribution quite closely to the aerodynamically ideal elliptic lift distribution (dashed black line) with the exception of the lift loss in the fuselage region. The shape of the horizontal tail changed only slightly due to its initial lift distribution being close to elliptic. It was mainly modified to trim the pitching moment for forward flight. The induced drag objective could be decreased by 11.8% compared to the initial configuration at a constant lift coefficient of 0.54.

An analysis of this design using the structural criteria of section 3.1.4 examining all three defined aeroelastic load cases showed that the structural integrity for the aerodynamically optimized design could not be guaranteed. Therefore, a subsequent sizing optimization was conducted in order to satisfy these constraints as well.

3.3.2 Structural Sizing Optimization

The objective for this optimization remained the induced drag, so that the optimizer would keep the induced drag as low as possible while adjust-

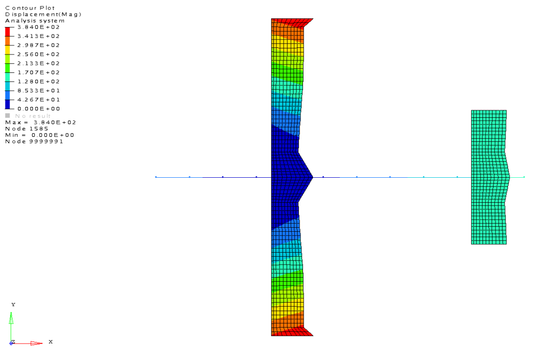

Figure 8: Aerodynamically optimized structural model with displacements during $1g$ cruise flight

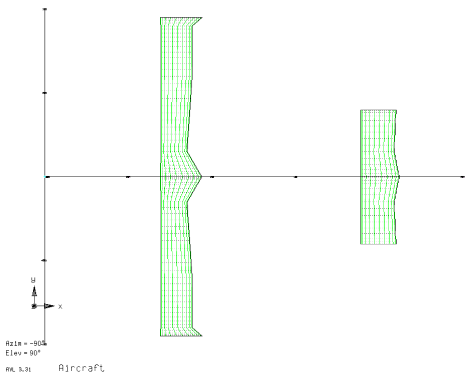

Figure 9: Resulting AVL model after aerodynamic optimization

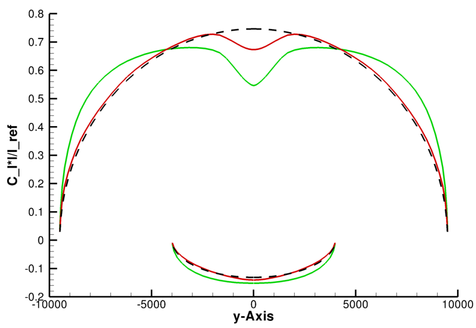

Figure 10: Elastic lift distribution after aerodynamic shape optimization (Green: Initial; Red: Optimized; Dashed Black: Ideal)

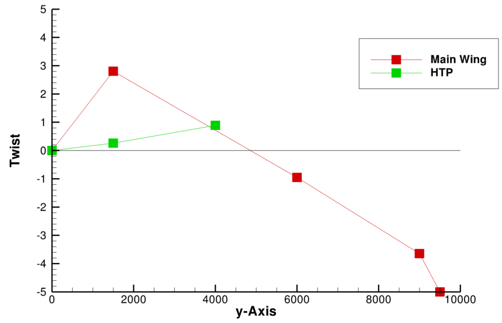

Figure 11: Twist distribution of the right hand half aircraft after aerodynamic shape optimization

ing the structural variables to find a feasible configuration. The shape design variables were fixed to conserve the previously found shape and the same set of sizing variables already used in the preliminary sizing optimization were activated. Now all three load cases from section 3.1.2 were considered. For these load cases the structural constraints (section 3.1.4) were defined and evaluated. Since the twist shape design variables were fixed for this optimization, trimming design variables (angle of attack of main wing and trim angle of HTP) were defined for all three load cases (section 3.1.3). To incorporate the effect of mass changes, variable inertia loads instead of a fixed set of forces as in the previous optimization were included for the inertial forces. The trim constraints remained the same as in the previous optimization (MTOM at $1g$, $-1g$ and $2.5g$ respectively and pitching moment around the centre of gravity close to zero).

Fig. 12 shows the resulting thickness distribution of this optimization. One can see that most of the skin patches were increased to their maximum thickness of $8mm$. Therefore, all structural requirements were satisfied. This also explains the weight increase of $1745kg$ to an overall structural mass (including concentrated masses) of $14602kg$ during this sizing optimization. In Fig. 13 a reduction in lift of the main wing can be noticed. Using the structural mass distribution between main wing and tail of the aircraft, the optimizer minimized the trim drag by shifting the centre of gravity significantly towards the aft of the plane. Therefore the overall lift stayed constant but the negative lift of the horizontal tail used for trimming the pitching moment could be reduced. Due to this considerable increase in skin thickness, all structural constraints were satisfied by a wide margin. This shows that the added structural constraints are not dominating the optimization problem, instead, the objective function is improved using the new set of design variables.

Shifting the weight distribution and, therefore, minimizing the trim drag reduced the overall induced drag even further so that a total of 19.9% of induced drag could be saved compared to the initial base configuration after the two sequential optimization steps at constant $C_L = 0.54$.

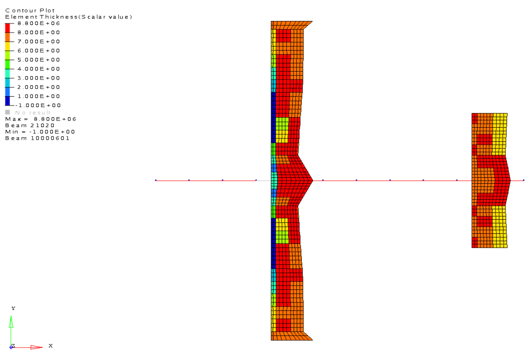

Figure 12: Skin thickness distribution after subsequent sizing optimization

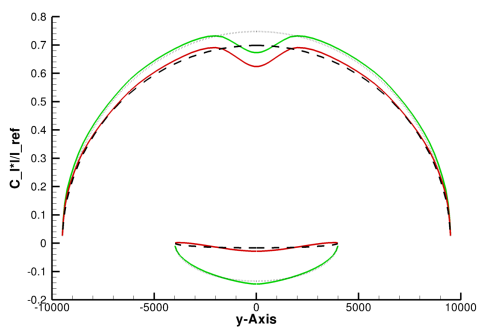

Figure 13: Elastic lift distribution after subsequent sizing optimization (Green: Initial; Red: Optimized; Dashed black: Ideal)

3.4 Combined Aerodynamic and Structural Shape/Sizing Optimization

The second approach to this optimization task was to combine the optimization runs from the previous sections 3.3.1 and 3.3.2 into one shape and sizing optimization, minimizing aeroelastic induced drag while considering all the mentioned structural criteria. To start from the same configuration as the first approach, the result of the preliminary sizing optimization was used for the initial skin thickness distributions and the spar cap cross sections. Apart from that, the same set of shape design variables as before was extended by the previously used sizing design variables. All three aeroelastic load cases were considered for evaluation of the structural constraints of section 3.1.4. Since the twist and installation angle shape design variables could be used to trim the $1g$ cruise load case and to minimize the induced drag simultaneously, trimming design variables for main wing and horizontal tail were only defined for the two structurally design driving load cases of $-1g$ and $2.5g$. During the aeroelastic analysis of all three flight states, variable structural inertia loads dependent on the current values of the design variables were superposed.

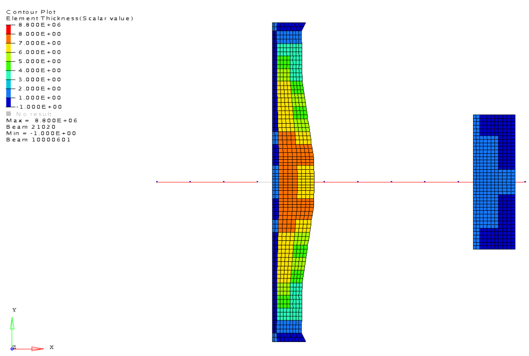

Figure 14: Resulting structural model of the second approach including skin thickness distribution

The resulting shape of the finite element structural model including the skin thickness distribution and the aeroelastic deformation of the $2.5g$ flight state can be seen in Fig. 14 and Fig. 15 respectively. It is shown that the chord length in the root section of the main wing

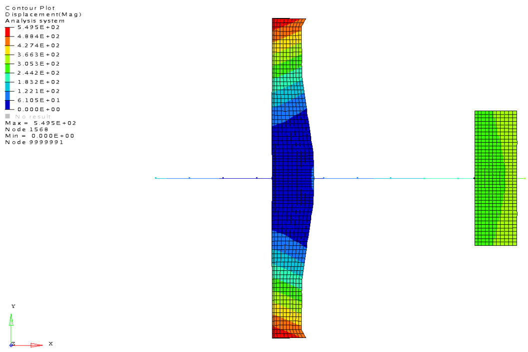

Figure 15: Displacements of the 2.5g pull-up manoeuvre

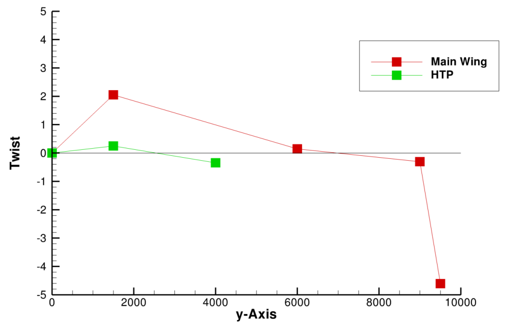

Figure 16: Twist distribution of the right hand half aircraft after combined shape/sizing optimization

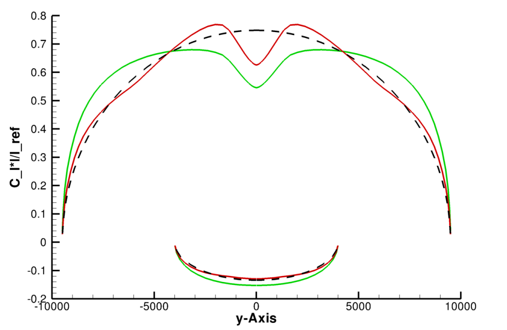

Figure 17: Elastic lift distribution after combined optimization (Green: Initial; Red: Optimized; Dashed Black: Ideal)

was increased to the maximum allowed value of 2500mm, which then decreases towards the wing tip. At the wing tip, the chord slightly gained in length similar to the result of the aerodynamic shape optimization. The final twist distribution for main wing and horizontal tail plane of this optimization is shown in Fig. 16, which also exhibits the general tendency of decreasing twist angles towards the wing tip after an initial rise near the wing root. The increase of the chord length at the wing tips occurred for the same reasons as in the first approach. In order to increase the effect of the negative twist angle at the wing tip the chord length was increased to lower the local lift generation at the wing tip even further. The effects of these shape changes on the span wise lift distribution can be seen in Fig. 17. The local lift generation at the root section of the main wing was increased, whereas the lift was lowered in the outer two thirds of the wing span near the wing tip. This has two positive effects for the design, the first one was to match the ideal elliptic distribution more closely for a lower induced drag and the second was to reduce the root bending moment of the main wing by shifting the aerodynamic loads inward. The decrease of the bending moment together with the increased wing height at the wing root (thickness-to-chord ratio constant) allowed satisfaction of the structural constraints using a combination of shape and sizing design variables. The shape of the horizontal tail plane was increased almost to the maximum allowed chord length, while installation angle and twist assumed only very small values. This enabled lowering the skin thickness almost to the minimal gage in this component. One can notice that the overall negative lift of the tail plane was reduced slightly compared to the initial state, decreasing trim drag, however, not as distinctively as in the sizing optimization of the first approach. After this optimization run, the induced drag objective function decreased by 8.9% compared to the initial state while keeping the lift coefficient constant at 0.54. During the optimization the weight of the structural model increased by 220kg to a total weight of 13253kg.

3.5 Comparison of Results

Comparing the final results of both optimization approaches one can say that both times the optimizer managed to influence the lift distribution with the given shape design variables and the elastic behaviour of the structure in order to improve the induced drag. The remarkably high induced drag savings of the sequential approach (-19.9%) compared to the combined approach (-8.9%) have to be put into perspective with the structural weight increase of $+1745kg$ for the sequential approach as against $+220kg$ for the combined procedure. However, the final lift distribution of the first approach was closer to the aerodynamic ideal than the result of the combined procedure. In terms of the structural requirements, both cases managed to satisfy all constraints. Yet, the significant increase in skin thickness during the sizing stage of first approach makes it difficult to assess the quality of the design regarding the structural constraints. In this case, any of the usually expected disadvantages due to the negative taper ratio in the main wing were covered up by the global increase in skin thickness through which the optimizer shifted the centre of gravity to save trim drag. Therefore, a fair comparison could only be attempted without the effects of mass trimming. This could be reached with either constraining the position of the centre of gravity during the optimization or using mass as an objective for the sizing stage of the sequential approach to keep the optimizer from adding more weight than necessary to satisfy the structural constraints. In case of the mass objective function a constraint on the induced drag might become necessary to prevent unwanted increase in induced drag. Overall the result of the combined approach appears more balanced and offers more weight capacity for payload and fuel.

4 Conclusions

The shape optimization framework has been successfully applied to the example of a generic transport aircraft using two different approaches to minimize induced drag while satisfying structural requirements. Both of these approaches managed to reduce the aeroelastic induced drag objective function using a combination of shape and sizing design variables. Even though the combined shape and sizing optimization did not produce the high induced drag savings of the sequential one, the overall design of the combined procedure shows more potential for further development when regarding structural weight and manufacturing aspects as well. The reference area for the aerodynamic coefficients used in these optimizations was kept constant to allow direct comparison of these values, yet, the actual wing area did change due to the chord length modifications altering the wing loading of the design. For the future, a constraint should be included limiting the change in wing area or wing loading to uphold comparability between initial and end designs regarding flight performance aspects. Also the significant increase in structural weight for trimming purposes should be prevented during the sizing optimization either by a constraint on the position of the centre of gravity or by using weight as an objective function for this step.

References

[1] S. Deinert, Ö. Petersson, F. Daoud, and H. Baier. "Aircraft Loft Optimization With Respect To Aeroelastic Lift And Induced Drag Loads". In: *10th World Congress on Structural and Multidisciplinary Optimization*. 2013.

[2] J. A. Samareh and K. G. Bhatia. "A Unified Approach to Modeling Multidisciplinary Interactions". In: *8th AIAA/USAF/NASA/ISSMO Symposium on Multidisciplinary Analysis and Optimization*. 2000.

[3] C. M. Liersch and M. Hepperle. "A Distributed Toolbox For Multidisciplinary Preliminary Aircraft Design". In: *CEAS Aeronautical Journal* 2 (2011), pp. 57–68.

[4] Open CASCADE S.A.S. *Open CASCADE Technology - 3D modeling & numerical simulation*. www.opencascade.org. Apr. 2013.

[5] R. Maierl, Ö. Petersson, and F. Daoud. "Automated Creation Of Aeroelastic Optimization Models From A Parameterized Geometry". In: *International Forum on Aeroelasticity & Structural Dynamics*. 2013.

[6] M. Drela and H. Youngren. *AVL 3.30 User Primer*. 2010.

[7] R. L. Harder and R. N. Desmarais. "Interpolation Using Surface Splines". In: *Journal of Aircraft* 9 (1972), pp. 189–191.

About Feasibility of a 5th generation Light Fighter Aircraft

S. Chiesa and M. Fioriti
Dept. of Mechanical and AeroSpace Engineering –Politecnico di Torino, Italy

Keywords; *Light Fighter, 5th Generation Fighter, Fighter Conceptual Design, Fighter Layout*

Abstract

The paper is aimed to illustrate an idea about the feasibility of a peculiar aircraft, i.e. a 5th Generation Light Fighter. At first a short description of previous "generations" of Jet Fighter is given, introducing the interest that has always been originated by the concept of "Light Fighter" for every of the first four Fighter Generations. The derivation of the first idea of a new 5th Generation Light Fighter is then described. Then to further investigate the feasibility of idea, a Conceptual Design Study has been driven up by utilizing peculiar tools, both for quantitative and qualitative (i.e. the aircraft layout definition) evaluations. The results, with the further support of preliminary studies about Subsystems, shows the feasibility of the concept.

1 General Introduction

Fighters conceptual design is a very challenging research theme, and many papers and books deal with such a topic [1], [2], [3], [4], [5]. It is particularly interesting to consider dimensional boundaries for future fighter aircraft in relation to the technological generation.

It is well known that fighter aircraft (only considering Jet engine fighters) evolution is very well described by several technological generations occurred along the time since the WWII; in the following Table 1 the five Fighter generations are synthetically defined.

In Figg 1 - 4 the first four Technological Generations are simply characterized by statistical plot showing Engine Thrust (T) and Empty Weight (W_e) related to Maximum Take-Off Weight (W). The same is made in Fig 5 for the 5th Generation; please note that even if not shown in the figures for first four generations, a lot of data are available, but this is not true for the 5th Generation that comprises very few Aircraft, with data known only for a part of them.

It can be noticed that for first four Generations we have always aircraft with size significantly reduced; we are speaking, for example, about Aircraft represented in Fig.6, that are interesting as, even with performances and capabilities reduced in comparison with other fighters of the same generation, but generally still appreciable, the reduced size means reduced costs. So the Light Fighters can have a good Efficacy to Cost ratio and they can be the only solution for Operators with limited financial resources.

2 5th Generation Light Fighter pre-design

In order to give answers to the question proposed in Fig. 5, i.e. "is it possible a 5th Generation Light Fighter and how large its size could be ?", please consider Fig.7; the plot, line "1", presents again the relation We= K_1 W, already seen in Fig. 5 and the line 2 represents W (equation: W=W).

Table 1 Jet Fighter Generations

GENERAT.	PERIOD	TECHNICAL CHARACTERISTICS	REFERENCE AIRCRAFT
1^	1943 - 1950	-Subsonic -Straight wing -Turbojet engines	Messerschmidt Me 262 Lockheed P80 DeHaviland Vampire
2^	1950 - 1960	-Transonic – Low supersonic -Wing swept back -Turbojet with or without A.B.)	North America F 86 Dassault Mystère MIG 15/17/19 SAAB J29 Tunnan
3^	1955 - 1980	-Mach 2 and more -SuperSonic shape -Turbojet with A.B.	Lockheed F104 SAAB J35 Draken McDonnell F 4 Phantom II Dassault MirageIII / F1
4^	1975 - 2010	-Mach 2 and more -SuperSonic shape / moderate W/S -Low by pass ratio Turbojet with A.B. -Relaxed Stability / advanced FCS	Boeing F 15 Eagle Lockheed Martin F 16 Eurofighter Typhoon SAAB J39 Gripen
5^	2000 -	-Like 4^ Generation -Stealth / Internal Weapons bays -Advanced Avionics	Lockheed Martin F 22 . Lockheed Martin F 35 . Sukhoi PAK 50

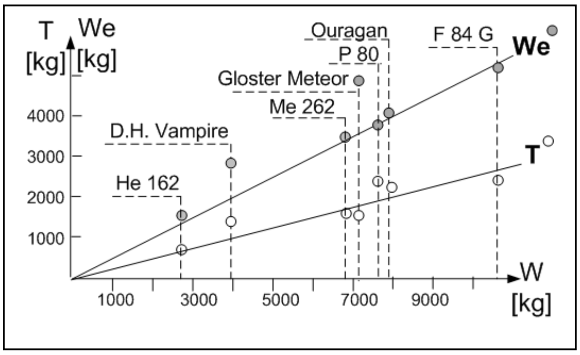

Fig. 1 First Fighters Generation

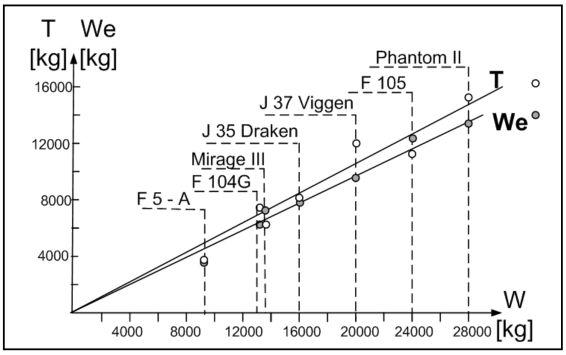

Fig. 3 Third Fighters Generation

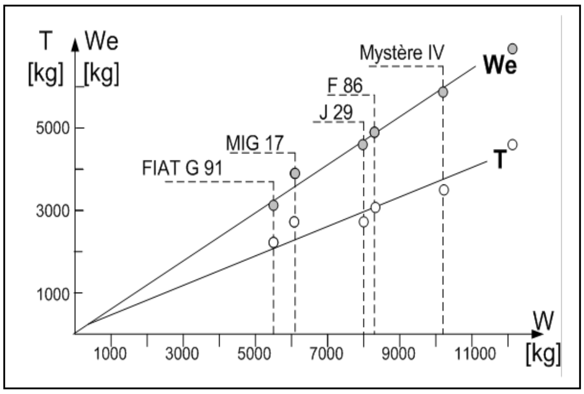

Fig.2 Second Fighters Generation

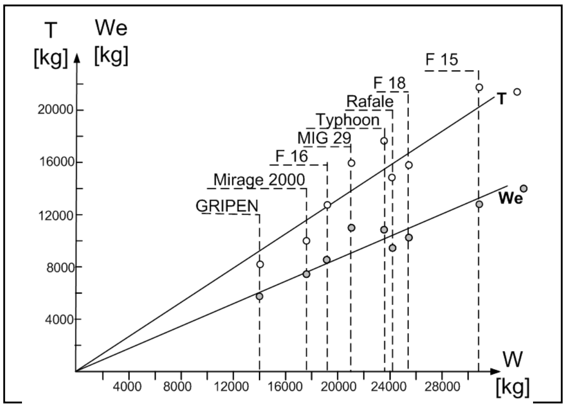

Fig. 4 Fourth Fighters Generation

Weight", to be proportional to W; by the way that it is not true for elements with weight not related to total weight W, for example the Pilot and the elements connected to the Pilot (furnishing and life Support Systems), the Mission Avionics (almost in part), and, partially, on board gun. So we can defined a

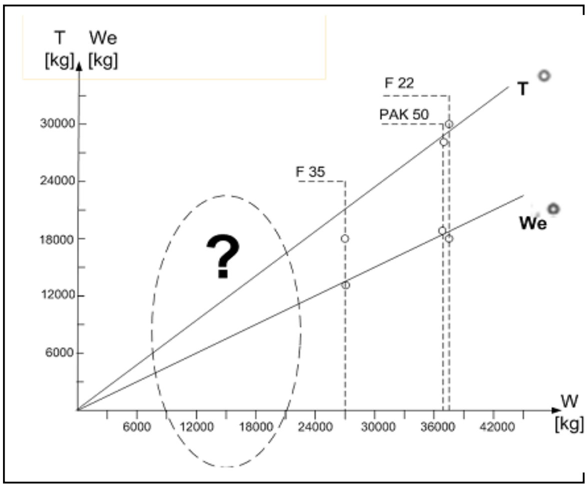

Fig. 5 Fifth Fighters Generation

W_{FIX}, that, by considering one Pilot and related elements, avionics, and a gun (Mauser 27 mm can be a reasonable choice), can be assumed = 1500 kg; the line 3, in Fig. 7, represents We + W_{FIX}. So the "gap line 2 –line 3" represents the sum of fuel and Pay Load weights. By considering W_{FUEL} for F 22, Pak 50 and F35 and reporting them starting from Line 3, the line 4 (representing the sum We + W_{FIX} + W_{FUEL}) is obtained, (by considering W_{FUEL} =K_2 W).

Reminding that the "gap line 2 – line 3" represents the possible weight of Pay Load and Fuel, it is clear that this weight is function of W. So from the Figure it is clear that W_{pl} + W_{Fuel} decreases when W decreases and if it becomes the minimum acceptable a plane with such weight represents a minimum size for the kind of plane.

By the way, if a minimum value for W_{pl} + W_{Fuel} is mandatory, it is possible to indify the corresponding value of W. In the Fig. 7 it is shown how W_{pl} + W_{Fuel} = 6000 kg is related to about W= 15000 kg, so we will have We=7500 kg. It is to be noticed that, with the values considered, we will have:

$$W=We+ W_{FIX} + W_{FUEL} + W_{pl}$$

By substituting numerical values we will obtain:

$$W= 7500 + 1500 + 6000 =15000 \text{ kg}$$

It is to be noticed how the decision of assuming W_{pl} + W_{Fuel} =6000 kg has been conceived; the first step of the process is the choice of W_{pl} =1500 kg, with the assumption that this is only payload carried in internal weapon bays. Such a choice has been based on consideration of two possible internal pay load configurations, illustrated in Fig.8. Two typical missions are considered: a "Ground attack" and an "Air to air". As to the first one, a three guided bomb GBU 16 Paveway II, plus two Air to Air self defence missiles AIM 9X Sidewinder weapons suite and as to the second one three Air to Air Missiles

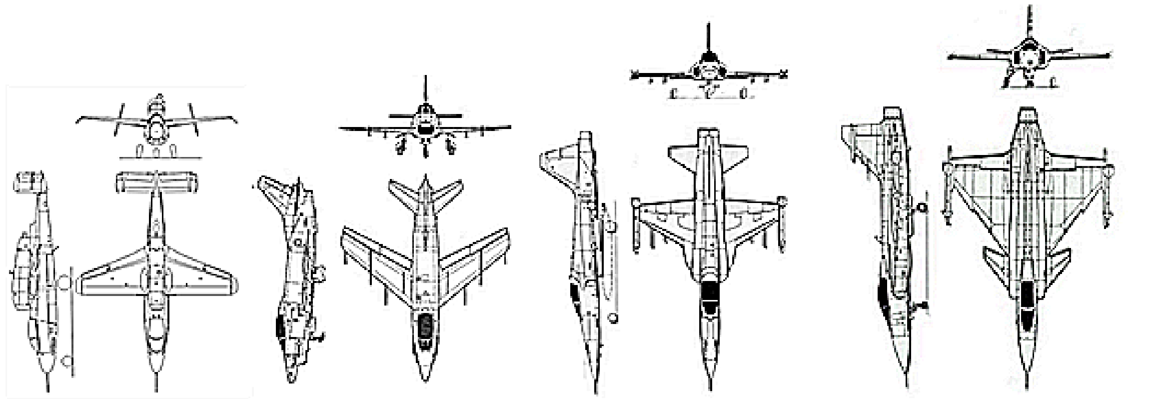

He 162 (1st Gen.) FIAT G 91-R (2nd Gen.) Northrop F 5 - A (3th Gen) Saab JAS 39 GRIPEN (4th Gen.)

Fig. 6 Light Fighter (of 1th to 4th Generation)

AIM 120 AAMRAM plus two Air to Air self defence missiles AIM 9X Sidewinder weapons suites are considered. As shown in Fig. 8, since

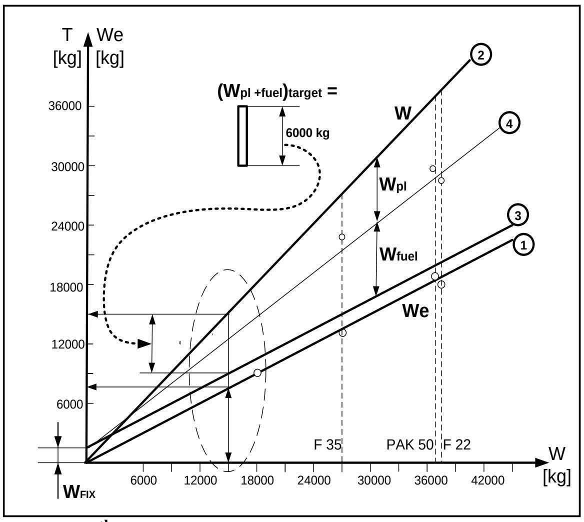

Fig.7: 5th Generation Light Fighter size definition

Name	Size (L x φ_{max}) [m]	Weight [kg]	Range [km]
AIM-9X Sidewinder	2.85 x 0.63	86	30
AIM-120 AAMRAAM	3,66 x 52,58	151	75
GBU-16 Paveway II	3,7 x 0.36	447	-

Fig.8: Weapon's suites

the dimension of GBU 16 Paveway II and AIM 120 AAMRAM both weapons suites can be considered sizing the volumes of internal weapons bays. From weight point of view, the ground attack weapons suite will determine a weight of 1513 kg, well corresponding to the previous assumption of W_{pl} =1500 kg that has led to the first definition of the aircraft as shown in Fig.7. It is important to observe that the aircraft will consequently be sized in "Ground Attack" configuration with Wpl=1513 kg (only internal and with the exception of gun ammunitions, accounted in W_{FIX}), whereas in Air to Air mission the same clean configuration will present a Take-off weight 900 kg lower due to different weight of the considered internal weapons suites, with advantage in combat agility. Assuming, as power plant, two EJ 200 (the same of Eurofighter "Typhoon"), with a total thrust of about 18000 kg, this brings to a considerable Thrust to Weight ratio. Looking at Fig.5 this kind of Thrust to Weight ratio is more than adequate for the 5th Generation standard (in particular better than the one of F 35). For both missions an internal fuel weight of 4500 kg (as suggested in Fig.7) seems, at first, adequate also considering the just hypothesized Propulsion System; in particular please note that 4500 kg of internal fuel is similar to the value of Eurofighter Typhoon, for which any pay load is necessarily dropped. Anyway the Take-off weight of 15000 kg could be exceeded considering dropped payload and/or external fuel tanks, in the case that "heavy/long range ground attack missions" are requested.

The aforesaid data seem to define a concept of a 5th Generation Fighter with appealing characteristics, even if with a size equal 2 / 3 of the Lockheed F 35 one.

In order to verify the feasibility of such a Plane concept, a Conceptual Design Process has been driven up about.

3 5th Generation Light Fighter conceptual design

As to validate the hypothesis of a 5th Generation Light Fighter, a typical procedure of Conceptual Design has been applied. Such a procedure based on a methodology set up and tested by the Authors [3], consists in two main parts; the first is the application a computerized tool for requirements synthesis [4]. Then, on the basis of consequent results, in good accordance with "pre-design" hypothesis, a configuration study, aimed to aircraft architectural layout definition, has been performed. A very first definition of structural layout and of main On Board Subsystems have been added; the

SubSystems possible installation, considering structural layout, has been verified. Having obtained positive results also in these cases, a preliminary dynamic Flying model has been set up and it has confirmed acceptability of performances and flight qualities even if at very preliminary level.

3.1 Requirement Synthesis

The tool utilized for the quantitative definition of future aircraft main characteristics, widely described in [4], as well as classical, popular calculation tools (see for example [5] and [6]), is founded on an organized series of Performances, Empirical Aerodynamic, Weight estimation, Statistical Relationships. In comparison with other methodologies, also previously proposed by the Authors [7], the simplicity of use (the tool is based on a Spreadsheet MS EXCEL) and adaptabiliyty to kind of aircraft have been pursued; moreover, on the contrary of other conceptual design methodologies that do not take into consideration the aircraft layout topics, such a tool estimates values like fuselage length, the wing longitudinal position, the wing platform with Mean Aerodynamic Chord and Aerodynamic Pressure Center (Subsonic and, if it the case, Supersonic) location and the longitudinal abscissa of aircraft Center of Gravity. This last value is evacuated on the basis of Weights estimated for the various elements of the aircraft and of values of abscissas of relative CoG of various elements, either estimated by the Program or supplied as Inputs by the Operator. The Program correlates the positions of Aerodynamic Pressure Center and of Center of Gravity, also indicating the position of the Main Landing Gear (giving the opportunity of evaluating the height and sutability of sitting angle) and also offering basic indications for the structural layout. In the case of Supersonic aircraft, the Wing-Mach Cone interaction is considered. These features of the Program are exemplified in Figure 9.

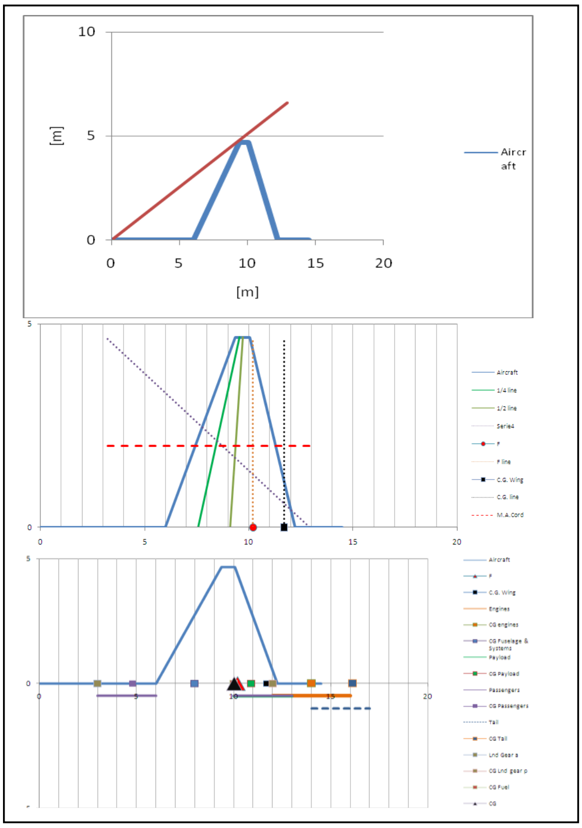

Fig. 9 Layout indications

As to the more usual aspect of the Conceptual Design methodologies, i.e. the definition, on the basis of the requirements, of the numerical values of the main characteristics that define the Aircraft Concept, the inputs numerical values and the values of the parameters hypothesized in the present case study are respectively summarized in Table 2 and Table 3. On the basis of aforesaid values, collection of data that globally define the

Table 2 Inputs of Conceptual Design Program

INPUT	VALUE	INPUT	VALUE
Pay load	1500 kg	L_{TO}	700 m
N° of Crew	1	L_{land}	700 m
Range	2000 km	Airfield altitude	sea level
Cruise speed	1100km/h	N° of Engines	2
Cruise altitude	7500 m	Engine Thrust dry	60000kN
S.S. cruise speed	Mach 1.4	SFC_{dry}	0.8kg/kg/h
S.S. cruise altitude	7200 m	Engine Thrust AB	90000kN
Comb. turn radius	5000m	SFC_{AB}	1.8 kg/kg/h
Mach max	2.2	Engine weight	989 kg
		W_{FIX}	1500 kg

Table 3 Hypothesized values (parameters)

PARAMETERS	VALUES	PARAMETERS	VALUES
C_{Lmax}	1.5	% Composite Wing	0.85
$C_{Lmax\ TO}$	1.7	% Composite Fuselage	0.85
$C_{Lmax\ LAND}$	2.3	K_i Weight Coefficient for several elements	
Aspect Ratio	2.7		
Taper Ratio	0.11		

aimed Concept have been obtained. Among these data the most significant are reported in Table 4. The graphical representation, usually defined "Matching Chart", is a further output of the tool; for the specific application of 5th Generation Light Fighter, it is reported in Fig.10. It shows how the "Design Point" is defined by the values W/S = 400 kg/mq e T/W = 1.2; such a point satisfy, at minimum value of T/W (i.e. at minimum W if engines have been already choosen), all performances requirements, graphically expressed, at the basis of the project. The Take-off Weight W=15022 kg obtained from the tool practically is the same of W=15000 kg defined in pre-design phase. The values obtained from the Matching Chart bring to a wing surface S= 37.5 mq (see Table 4) and confirm the Propulsion System based on two EJ 200.

First of all the results of Conceptual Design Programme perfectly agree with the hypotheses elaborated in pre-design phase, and so balanced to lead towards a further activity of the studied aircraft layout definition.

3.2 Aircraft Layout definition

The next activity of 5th Generation Light Fighter layout definition has been helped by the specific Conceptual Design methodology utilized that, as seen, has already given many information about aircraft architecture. Moreover it has been the occasion of setting up and testing a new procedure of "Fighter Layout Definition", in phase of elaboration by the Authors. Fig 11 shows how this procedure is aimed to operate either immediately after the calculation tool of Conceptual Design, or even contemporarily to it, exchanging data step by step. In this way the results of Conceptual design are a mix of

Table 4 Outputs of Conceptual Design Programme

OUTPUT	VALUE	OUTPUT	VALUE
Sw	37.5 mq	Weight wing	1014 kg
Sweep angle	23°	Weight fuselage	1375 kg
Wing span	10.1 m	Weight tail	304 kg
Root Chord	6.7 m	Weight Land.Gear	330 kg
Tip Chord	0.74m	Weight AIRFRAME	3023 kg
Fuselage Length	14.5 m	Weight ENGINES	1978 kg
Nose-TopRootChord	6 m		
X CoG	10.11m	Weight FCS	465 kg
X MLNDG	12 m	WeightHYDRAULIC	75 kg
		Weight ELECTRIC	525 kg
Weight empty	7461 kg	Weight ECS	240 kg
WFIX	1500 kg	Weight FUEL-SYST	255 kg
Weight FUEL	4547 kg	Weight ENG.SYST.	225 kg
Wpay load	1513 kg	Weight AVIONICS	675 kg
W (MTOGW)	15022 kg	WeightSYSTEMS	2460 kg
		Weight empty	**7461 kg**

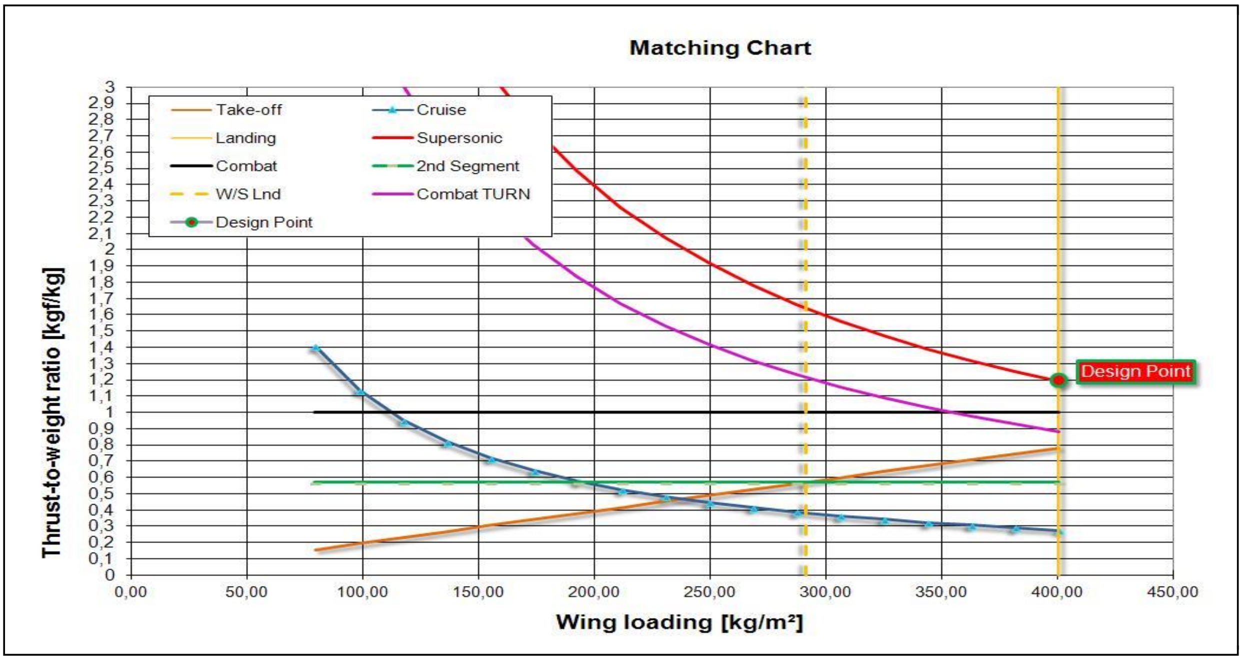

Fig. 10 "Matching chart" plot

numerical values and architectural characteristics, i.e. a graphical visualization, even if simplified, of the aircraft. It is also relevant that the layout definition activity tends to operate as feed-back of the numerical definition activity. The possibility of obtaining practically at the same time and in a coordinate way numerical and graphical results increases the value added by the conceptual design methodology, improving the definition level and the precision of elaborated concepts.

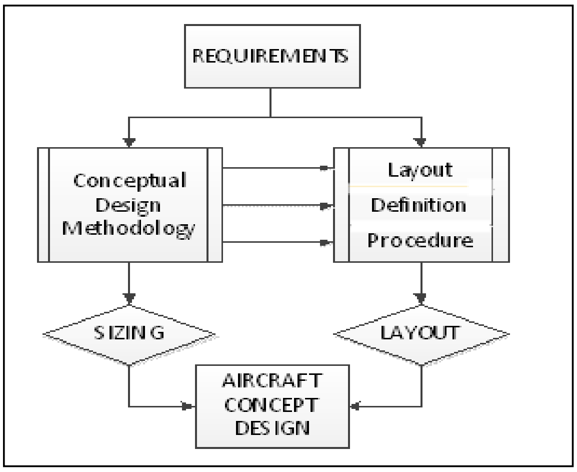

Fig. 11 Layout definition in Conceptual Design

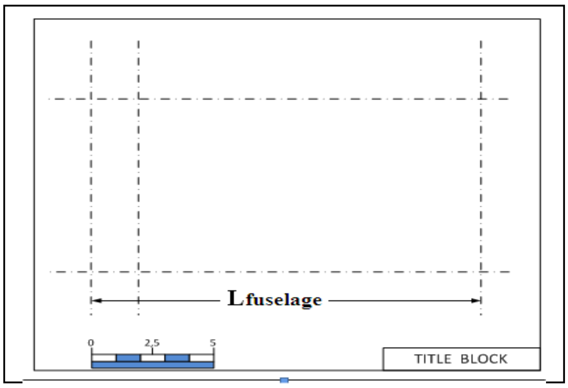

Fig. 12 Base of Layout definition procedure

Fig.12 shows as the basis of the procedure of layout definition for aircraft Concept can be a simple sheet of paper on which the definition of the two views, top and side, is set up.

As shown in Fig. 13 the layout definition can be carried on manually drawing, or by conducting the same operations, in sequence as the Procedure says, but performed on CAD-3D.

As already said the Procedure must be applied precisely, in order to obtain standardization and enough repetitive results and also because the defined sequence of operations appears to be the most useful.

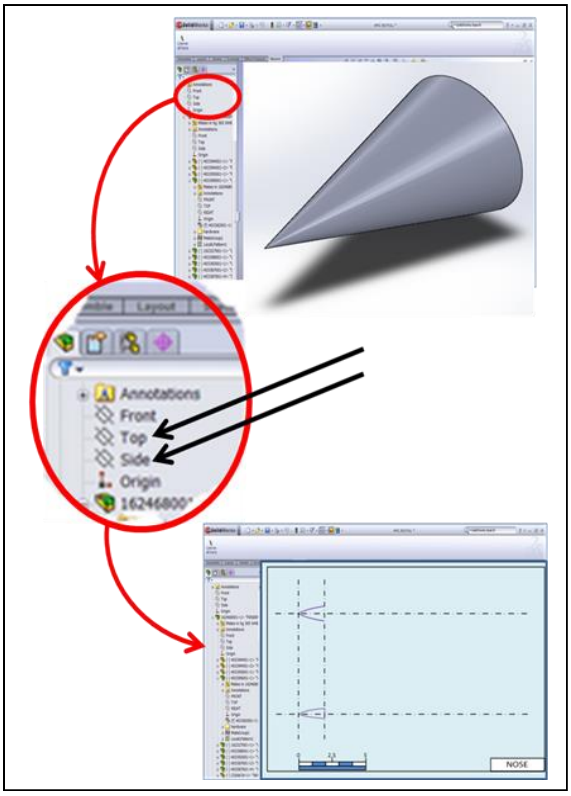

Fig. 13 Layout definition and CAD-3D

Fig. 14 shows results obtained for 5th Generation Light Fighter, by applying the layout definition Procedure in close link with Conceptual Design tool application; in fact some iterations of the tool have been suggested by some evidence appeared during architectural layout definition. In the same Fig.14 the logical steps that bring to the layout definition are listed; for any of them the solution chosen, in the studied case is indicated, so allowing to recreate the logical path that has brought to define the 5th Generation Light Fighter layout. Such a layout has appeared so satisfactory to be adopted becoming essential part of the 5th Generation Light Fighter Concept. A direct consequence is the possibility of defining the classical “Three view drawing” representation (see Fig. 15) that integrates numerical values and architectural concepts.

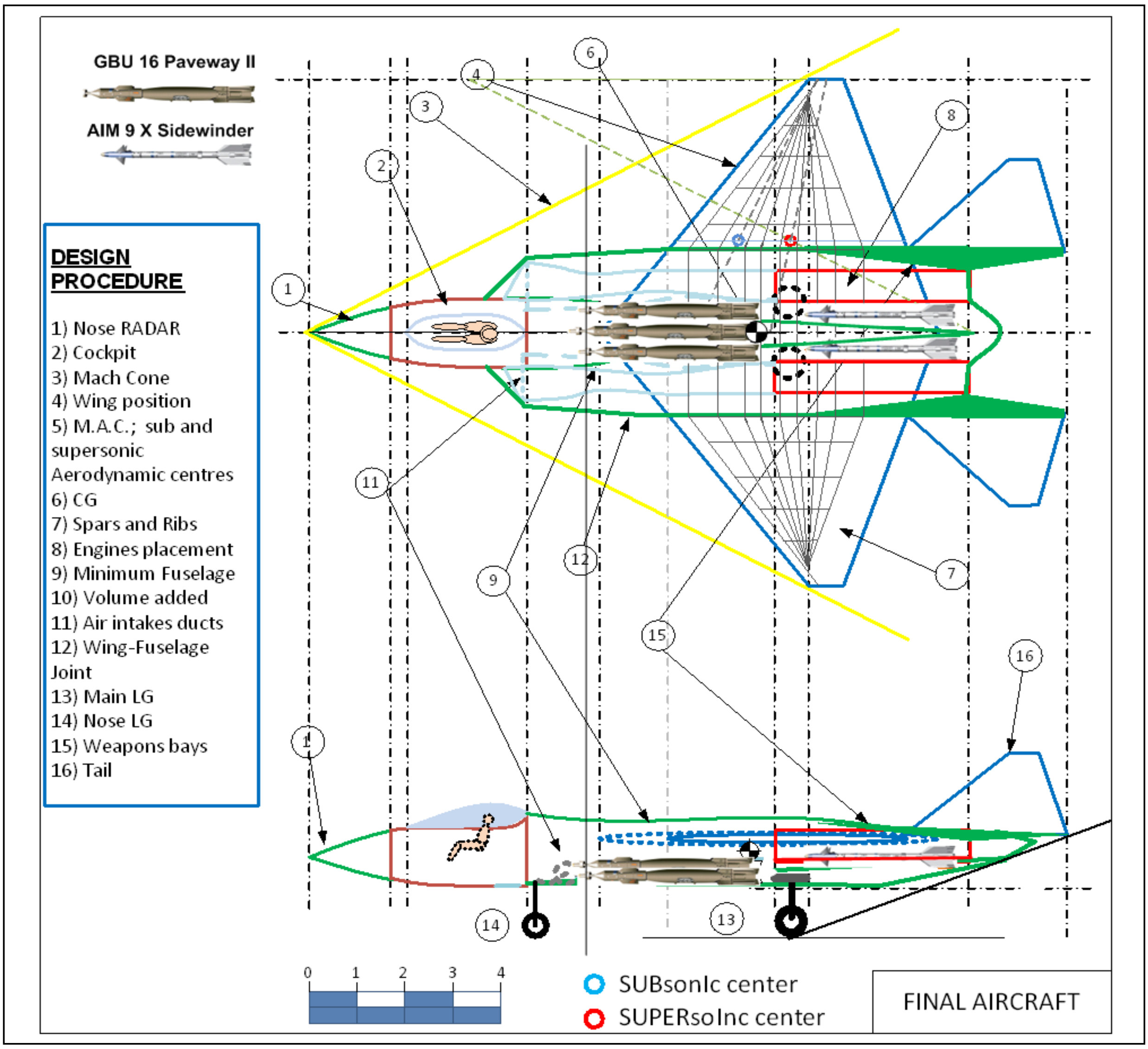

Fig.14 Fighter Layout definition procedure

Moreover by utilizing the aircraft graphic definition in CAD-3D context, we obtained the aircraft 3D model, with possibility of defining, on such a base, a preliminary Structures Layout (shown in Fig. 16). It is to be noticed that such activity has been well addressed by several choices provided by the Layout Definition Procedure (see Fig 14 again).
Please note that the availability of such aircraft 3D-CAD model with preliminary structural layout offers possibility of studying subsystems and equipments integration in the airframe and so obtaining a useful Digital Mock Up, even if at Conceptual Level [8].

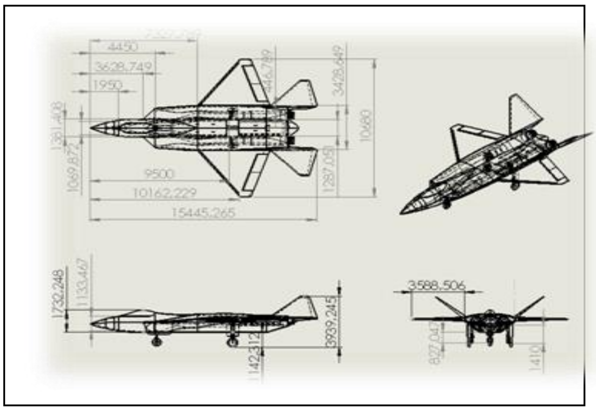

Fig. 15 5^{th} Generation Light Fighter Concept

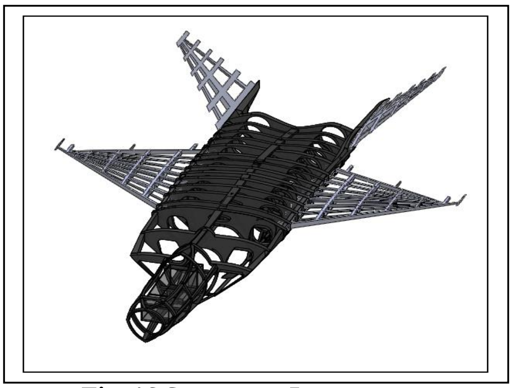

Fig. 16 Structures Layout

3.3 Further definitions activities

The good results of Conceptual Design bring to consider also a preliminary definition of the Sub-Systems of the plane. Sub-Systems preliminary definition is very useful for a better conceptual design of a plane if it is driven up in synergic way, exactly as we discussed about Conceptual Design and Architectural definition [9]. Obviously, it is not possible to describe here the solutions elaborated for all the On Board

Table 5 Global values for Avionics

ΣWeight: 994 [kg]	ΣVolumes: 1470[liters]	ΣPower required: 19.49 [kW]

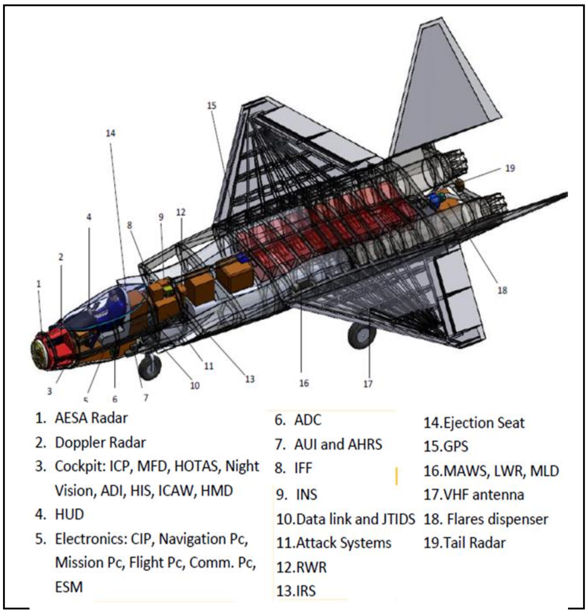

Fig. 17 Avionic installation

Systems, even if a preliminary sizing has been performed for all of them [10] by utilizing a specific tool developed by the Authors [11]. Result of these activities was that the several On Board Systems have been demonstrated feasible maintaining each wheight estimated by the Conceptual Design Tool (see Table 4).

As peculiar aspects of the On Board Systems Configuration elaborated, particularly interesting are:

-The definition of an advanced Avionic System. Globally it appears characterized by the values shown in Table 5. With such values the possibility of installing Avionics into the airframe has been verified (Fig. 17).

-An “All Electric” configuration that has led to the adoption of “bleedless ECS (Environmental Control System)” and of electric actuators for Flight Control System and Landing Gear (Hydraulic System has been maintained only for wheels brakes, as confirmed by its reduced weight as shown in Table 4).

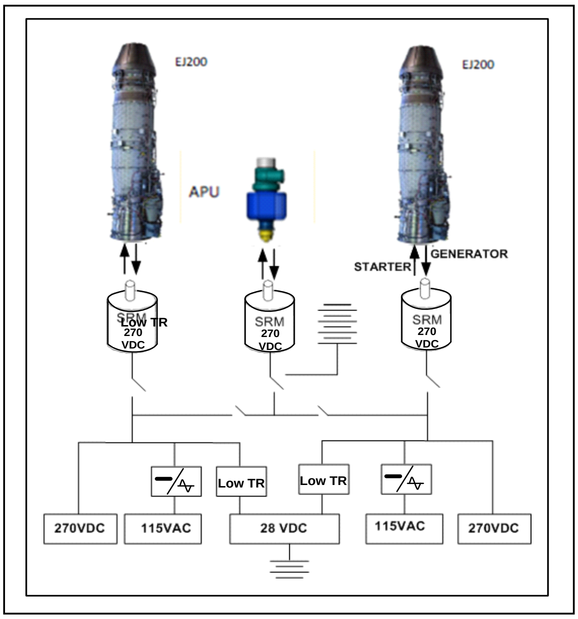

Fig. 18 Electric Generation System

The scheme of Electric Generation System (that allows the starting of engines and APU too) is reported in Fig.18. It reveals a certain similarity with the one of F 35 (in particular the adoption of Generation voltage of 270 VDC and of three 90 kW “Switched Reluctance Machine-SRM” as Starter/Generators), but with the advantage of the greater flexibility offered by twin engines configuration.

As further activity aimed to confirm the feasibility of considered Concept, we remind the realisation of a dynamic model of the Aircraft to play in X-PLANE context; it is well known that X-PLANE is FAA approved as Flight Simulator, so the model and the positive results obtained from its tests will represent a good, even if preliminary, verification of Aircraft Flight qualities and performances [12]. To offer example of application to the 5th Generation Light Fighter study in Fig. 19 a sequence of a Take-Off and the sequence of Landing Gear retraction are shown.

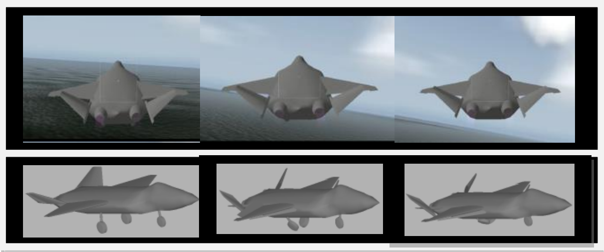

Fig. 19 X_PLANE dynamic model of the Concept

4 Conclusions

The elaborated Concept, also for the fact that the study has been extended to a preliminary definition of On Board Systems and to the development of a dynamic model for Flight Simulation seems to be complete enough and impressive. From the results obtained the feasibility of the 5th Generation Light Fighter seems confirmed. Even if the activity has been carried on in Academic context and with relevant educational follow up, we think that the first confirmation to the hypothesis expressed in "pre-design" ambitious about 5th Generation Light Fighter is realistic. This hypothesis consequently seems worth of further future deeper analysis, even in Industrial context, taking into account the possible advantages, in particular in a reduced financial resources situation.

References

[1] Antona E., Chiesa S., Corpino S. and Viola N., "L'avamprogetto dei Velivoli", *Memorie dell'Accademia delle Scienze di Torino. Classe di Scienze Fisiche Matematiche e Naturali*, vol. 144 - 2009, pp. 81-90

[2] Saha, U. K., Mitra, M., Menon, S. J., John, N. T., Gajapathi, S. S., and Behera P. , "Preliminary design analysis of a lightweight combat aircraft", *Proceedings of the Institution of Mechanical Engineers, Part G: Journal of Aerospace Engineering*, Vol. 222, 2008.

[3] Chiesa S., Borello L., Maggiore P., "An academic experience about aircraft design: affordable advanced jet trainer", *22nd ICAS Congress*, Harrogate, UK, August-September 2000

[4] Fioriti M., "Adaptable Conceptual Aircraft Design Model" *presented to* Advances in Aircraft & Spacecraft Science, Technopress Journal, 2013

[5]Raymer D. P., "Aircraft Design: A Conceptual Approach" Fourth Edition, AIAA Education,1992

[6]Roskam J., *Airplane Design – Part1: Preliminary sizing of Airplanes* ed., Design Analysis & Research Co., Ottawa, 1989.

[7] Chiesa S., Guerra G., "Progetto concettuale di velivoli da trasporto", *Ingegneria* n°7-8, 1983.

[8] Camatti D., Corpino S., Pasquino M., "Digital Mock-Up: a useful tool in aircraft design", *22nd ICAS Congress*, Harrogate, UK, August-September 2000.

[9] Chiesa S., Fioriti M., Viola N."Methodology for an integrated definition of a system and its subsystems: the case-study of an airplane and its subsystems". In: *Systems Engineering - Practice and Theory* / Prof. Dr. Boris Cogan. InTech, Rijeka, pp. 1-26. ISBN 9789535103226

[10]Saez Aviles L."Jet Fighter Aircraft Design*" Degree Thesis at Politecnico di Torino*, 2012

[11]Chiesa S., Di Meo G., Fioriti M., Medici G., Viola N. "ASTRID-Aircraft on board Systems Sizing and Trade-Off Analysis in Initial Design". *Research and Education in Aircraft Design – READ"*, Brno, Czech Republic, (2012)

[12] Chiesa S., Chiesa A., Chille' V., Rougier A., Viola N. "Supporto alla definizione di Sistemi, a livello concettuale, mediante strumenti di modellazione e simulazione" *Convegno AFCEA-MIMOS Difesa 2010*, Roma, 2010, http://www.mimos.it/difesa2010

Propulsion integration and flight performance estimation for a low observable flying wing demonstrator

Lykourgos Bougas, Mirko Hornung
Technical University of Munich – Institute of Aircraft Design, Boltzmannstr.15, D – 85748 Garching b. München, Germany

Keywords: *propulsion integration, flight performance, UAV, flying wing*

Abstract

Within the consortium of the Sagitta project, aiming to develop technologies for Unmanned Aerial Vehicles (UAVs), the Institute of Aircraft Design is contributing with the areas of propulsion integration, novel control concepts and overall configuration integration. Major in-house research topics are the development of novel flight control effectors as well as reliable propulsion integration solutions, including thrust vectoring. In order to complement the research activities a scaled flying demonstrator has been selected as an airborne test bed. The overall project, joining multiple universities and research organizations, has been initiated and supported by Cassidian. The configuration of the flying demonstrator is a low observable, low aspect ratio diamond shaped flying wing system. In this paper the primary characteristics of the configuration will be summarized as well as the principal driving requirements for the design and integration of the propulsion system and the major aspects of his initial layout will be presented. Furthermore a performance estimation will conclude the present work, which is considering also data from other Sagitta partners.

Nomenclature

Symbol	Unit	Description
$A_{capture}$	[m²]	Inlet capture area
AoA	[°]	Angle of attack
AoS	[°]	Angle of sideslip
b	[m]	Wing span
CD_0	[-]	Zero lift drag
c_r	[m]	Root chord
$D_{pre-entry}$	[N]	Inlet pre entry drag
$\dot{m}_{total}$	[kg/s]	Air mass flow
MTOW	[kg]	Max take off weight
P_∞	[N/m²]	Ambient pressure
$P_{capture}$	[N/m²]	Static pressure at the inlet´s face
S_{ref}	[m²]	Reference area
T/W	[-]	Thrust to weight ratio
V_∞	[m/s]	Free stream velocity
$V_{capture}$	[m/s]	Velocity at the inlet´s face
Λ	[-]	Aspect ratio
ϕ_{LE}	[°]	Leading edge sweep angle
ϕ_{TE}	[°]	Trailing edge sweep angle

Introduction

Understanding the related physical effects is the basis for the development of any novel systems for any engineering application. Simulations or ground tests are key means to describe and quantify the principal effects accurately. These studies and/or tests are tailored along specific design cases, which often under predict or even neglect the side effects of the integration of those systems in to an operational aircraft. In order to capture all integration effects flight trials become necessary to develop the aircraft gradually into an operative system.

Within the Sagitta project and besides principal research activities, a scaled demonstrator prototype is under development, proceeding from initial simulations, through ground tests, to flight trials, with the ambition to integrate and test novel technologies in-flight and finally provide operationally proven technologies.

The current publication will summarize the major considerations leading to the initial design of the propulsion system and focus on its principal characteristics. Furthermore considering results from other partners of this project, as for example aerodynamic data from wind tunnel tests, a performance estimation will be presented, intending to identify the current operational status and highlight issues raising potential design improvements.

1 Overall system characteristics

Identification of performance potentials of the flying wing configurations is one major goal of the scaled demonstrator. Therefore no customized configuration, optimized to fit the needs of individual research topics has been chosen. The configuration rather represents a design with a full scale development potential. This fact premises from each subsystem to be developed with respect to the requirements of other subsystems and the overall design. Therefore severe emphasis has been given on the integration aspects of the designed components.

The chosen configuration is a low observable (LO) diamond shaped flying wing with an aspect ratio of 2.1. The total length and wingspan of the demonstrator measures approximately 3 meters, without the nose boom. The chosen airfoil for the outboard wing area is a symmetric NACA64A012, hence the airplane shall be able to fly in both orientations, i.e. with all loft openings (ex. engine inlets, landing gear panels concentrated on the one side of the aircraft´s loft) facing the ground or upside down. The inboard profile has been modified to accommodate space for components and payload. The major characteristics of the demonstrator aircraft are summarized in table 1.

b	[m]	3.088	Λ	[-]	2.010
c_r	[m]	3.000	S_{ref}	[m²]	4.748
ϕ_{LE}	[°]	55	MTOW	[kg]	125
ϕ_{TE}	[°]	-25	T/W	[-]	0.38

Table 1-1: Major characteristics of the scaled demonstrator

Flight control of a flying wing configuration featuring novel control surfaces and thrust vectoring without vertical stabilizers is one aspect of investigation. To enable a stepped approach in expanding the control capabilities and although the demonstrator´s control surfaces are sized to offer sufficient yaw control, additional vertical fins will be mounted during the first flights for enhanced directional stability.

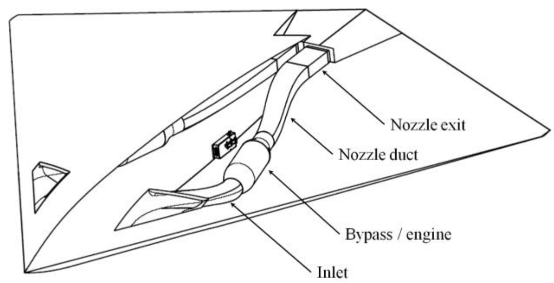

Fig. 1-1: Isometric cutaway view of the aircraft´s loft and propulsion ducts.

Regarding the propulsion system a twin buried jet configuration has been chosen. The inlets represent a typical low observable design for the lower subsonic regime. The nozzle exits are placed well before the trailing edge.

2 Propulsion system design and data deck

As previously described the driving requirement for the propulsion integration is the LO design of the aircraft. In order to deny a direct view to the engine´s first compressor and last turbine stages the propulsion duct features S – shaped ducts for the inlet and nozzle duct respectively. Placing the nozzle exits ahead of the trailing edge enhances the heat dissipation of the hot jet plume obscuring and reducing the infrared signature.

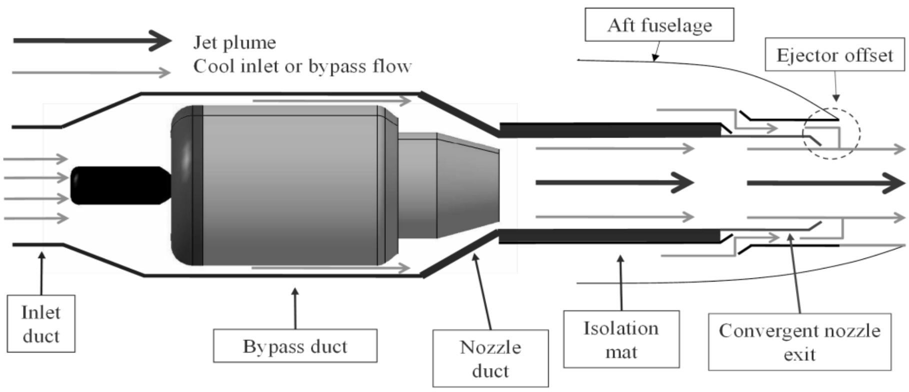

Fig. 2-1: Concept of the propulsion duct.

As illustrated in figure 2-1 the propulsion duct consists of the engine encased by the bypass duct. The bypass duct is installed after the inlet duct and prior to the nozzle duct. The nozzle duct shall be manufactured of composite ceramic materials and covered with a appropriate isolation mat. The heaviest component by far is the engine, followed by the heat resistant and thermal insulated nozzle duct. The actual longitudinal and lateral position of the engine has to be conformal to the requirement for the UAV to have a static stability margin of 5% or better. At the current design point the engine is placed slightly behind the 50% line. This requirement and other considerations, as the internal packaging, manufacturing and mounting and accessing the components of the propulsion duct, have a significant impact on the design of the propulsion system.

2.1 Engine data deck

In order to enable full performance simulation an engine data deck had to be modeled. That includes the installed thrust slope over the engine's throttle setting for the entire flight envelope. Also the corresponding fuel flow has to be calculated at these points.

In an iterative process a turbojet model gas turbine with 300N nominal thrust has been selected for the propulsion system. Based on manufacturer's specifications and experimental data from ground tests such a numerical engine deck has been developed in the propulsion simulation software Gasturb. In this engine model there are several uncertainties regarding the actual performance of the individual engine stages, hence these have not been measured. For these points empirical values from equivalent engines have been taken into account.

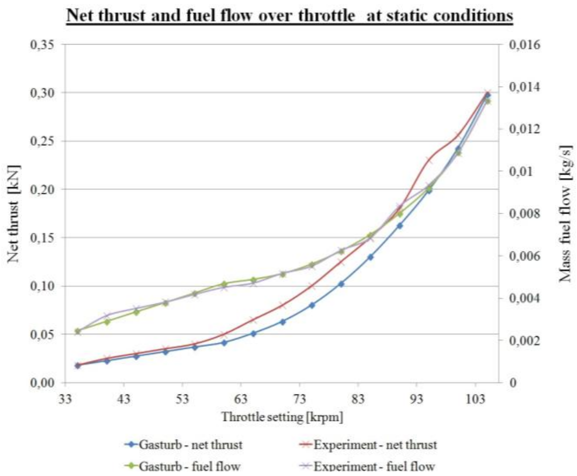

Fig. 2-2: Analytically calculated and experimentally measured net thrust

The flight envelope for the demonstrator has been defined for a Mach range up to 0.25 and an altitude of 2500m above sea level. The engine model off-design point calculations have been performed for the envisaged flight envelope.

The uninstalled engine data deck has been corrected by accounting thrust losses due to installation effects, pre - entry inlet and base drag of the aft body fuselage. Hence no accurate data regarding the pressure losses in the inlet duct were available an initial empirical value for S – ducts of 93.5% of pressure recovery has been considered in the analysis with Gasturb. In the reality this value will vary over the flight envelope and the complete range of throttle settings.

Hence the inlet is highly integrated to the aircraft's loft the traditional term of capture area can't be applied here. Therefore an equivalent dimension is necessary, which in this case is the projection of the inlet opening to a plane normal to the flight direction. This projection of the inlet opening is sized to match the mass flow requirements, estimated for the engine and the cooling duct at flight conditions of mach 0,2 at 2500m. This Mach conditions correspond to 15% less than the aimed cruise Mach speed. This is due to a compromise between slightly higher pre entry drag at the design cruise point but also having a greater inlet opening for safe operation at low speeds. Also due to the absence of secondary inlet openings for operation at very low speed and / or high incidence, the upper inlet lip is well rounded. Furthermore a slightly greater opening accommodates greater mass flow, if needed. One of the high end goals of the demonstrator is to test fluidic flight controls. That might be in terms of circulation control effectors or fluidic thrust vectoring. Ongoing feasibility studies tend to address the conceptual and integration issues of such systems, in the present configuration of UAV. The extra air mass needed therefore, might be able to be extracted as bleed from the inlet, with respect to the actual air flow need for the propulsion system and the interaction with the engine's cycle. The resulted advantage might be less aerodynamic drag, compared to having a dedicated scoop inlet.

The pre entry drag has been estimated according to Eq. (1).

$$D_{pre-entry} = \dot{m}_{total} \cdot \left(V_{capture} - V_{\infty}\right) + A_{capture} \cdot \left(P_{capture} - P_{\infty}\right) \quad (1)$$

Equation 1: Pre entry drag

Additional effects like base drag have also been considered to complete the engine deck for the installed thrust and fuel consumption estimation.

$$C_{P_B} = \frac{P_B - P_{\infty}}{0{,}5 \cdot \rho V_{\infty}^2} = -C_{D_B} \quad (2)$$

Equation 2: Base drag of blunt surfaces [1]

The maximum installed thrust at sea level per duct is exemplary illustrated below.

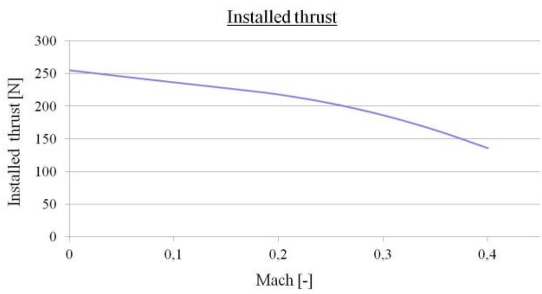

Fig. 2-3: Installed thrust per duct at sea level.

Due to the complex effects of such highly integrated inlets and aft body fuselage it is considered that these considerations provide approximate values for the initial studies. Numerical analysis and experimental data from ongoing and planed activities will help to mature these estimations.

3 Control surfaces concept and aerodynamic data deck

For the calculation of the mission and performance data it is necessary to take into consideration the trimmed aerodynamic data, i.e. the penalties on lift and drag that result from flap deflections.

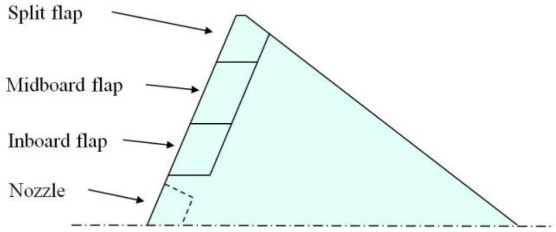

Fig. 3-1: Control surfaces layout.

As mentioned in chapter 2 the target value for the longitudinal stability margin is 5%. The demonstrator is laterally unstable for some AoAs and AoSs combinations. Control concepts that combine the functions of the individual flaps may be possible and result to a higher aerodynamic performance. Nevertheless for this study the flaps do have separated control functions. For trimming the aircraft only the inboard flaps may be used. Furthermore the split flaps are sized to ensure lateral control. In order to have enhanced lateral stability two detachable vertical stabilizers will be mounted.

This configuration of a clean loft with the two vertical stabilizers is defined as the clean configuration for the studies in the present paper. Other configurations are with extended landing gear and with an a additional optical sensor, the Gimbal. These configurations have been tested in a wind tunnel campaign and the results are the input for the aerodynamic data deck used for the performance analysis.

3.1 Aerodynamic data deck

For the performance analysis an aerodynamic data set (ADS) has been created. Input therefore are experimental data from a wind tunnel campaign [2]. Next to the pure zero lift drag of the clean configuration some corrections were necessary in order to account for penalties due to several antennas, interference and turbulence effects. These drag increments are based on Hoerner S.F. [3]. The zero lift drag of the clean configuration with corrections has been estimated $CD_0 = 0.0076$ and regarded constant for the current flight envelope. The drag increment for the extended landing gear is $\Delta CD_0 = 0.0186$, which is significant in proportion to the aircraft itself. Generally the aircraft's loft is very smooth and every aerodynamic distortion induces major penalties with respect to the clean configuration.

Further input for the ADS is the trimmed lift slope. With respect to the aircraft's configuration and it's longitudinally stability, trimming the aircraft results a reduced effective lift.

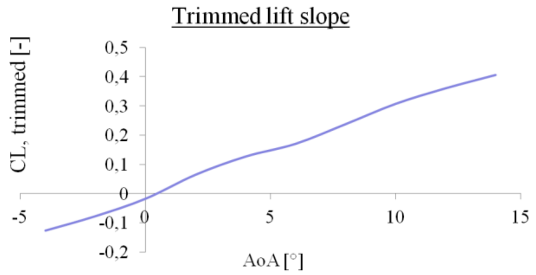

Fig. 3-2: Trimmed lift slope

The trimmed polar is also an input for the performance analysis. Hence the deflection of the inboard flap influences the lift distribution and is AoA dependent, the drag increments due to trimming are considered in the trimmed polar.

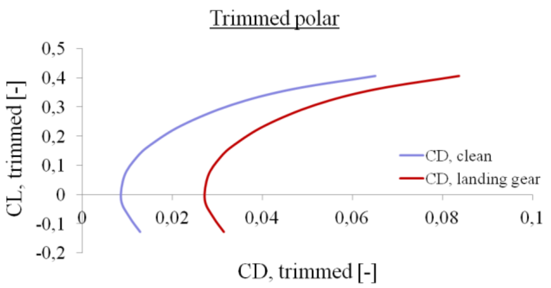

Fig.3-3: Trimmed polar

The values correspond to the reference area of $S_{ref} = 4.748m^2$.

4 Performance estimation

Integrating all performance characteristics (e.g. aerodynamics, weights, thrust and SFC) of all disciplines and partners of the Sagitta project in an overall performance model enables a global demonstrator performance assessment. The performance estimation shall serve as an initial statement of the performance of the aircraft with respect to the requirements for a reasonable operation. The mission and performance have been calculated with the aircraft performance program (APP).

4.1 Assumptions and requirements

Before summarizing the results of the performance analysis, the global assumptions have to be defined.

The demonstrator's design MTOW for this study case is 125kg. The payload in this case can be the optical sensor or other experimental equipment. For the mission up to 32kg fuel can be taken onboard

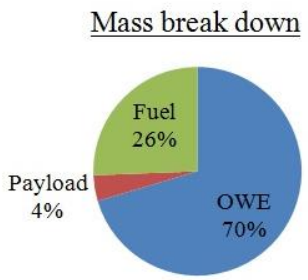

Fig. 4-1: Mass break down of the demonstrator

Derived from the requirement of a maximum +/- 5g for the structure and a gust load of 7.5m/s the cruise speed has been limited at mach 0.25. Furthermore a limit for the AoA of 14° and a ceiling of 2500m are set. The elevation of the airfield is assumed at 500m above sea level.

4.2 Mission performance

For comparison reasons throughout the evolution of the aircraft a design mission has been defined, which profile is illustrated in Fig. 4-2. The major segments are listed below:

Segment	Comment - conditions
Ground operation	For app. 12 minutes
Take off	Full power
Climb	2500m at Mach 0.23
Cruise	2500m at Mach 0.23
Descent	At 750m
Loiter	For app. 5 minutes
Descent	To 500m
Climb	To 750m - Missed approach
Loiter	For app. 10min
Descent	To 500m - landing.
Ground operation	For app. 3 minutes

Table 4-1: Design mission segment list.

The design mission starts with app. 12 minutes of ground operation, in order to allow pre flight systems check with running engines. Take off with full thrust follows and climb at 2500m with simultaneous acceleration at Mach 0.23. Cruise conditions can be optimized either for range or endurance. The descent to a loiter altitude at 750m follows. For safety reasons at least one missed approach has to be considered in the calculations as well as some reserve time for loitering in case of systems needing pre landing check. This is taken into account by the final segments of the mission. At the end of the flight mission app. 3 minutes of ground operation have also been considered.

Without any mission optimization, i.e. optimization of the climb and cruise segment, the pure cruise endurance is 15 minutes. Then the decent has to be initiated in order to conduct the safety segments as described above. The time and fuel reserve for the latter is considered as fix and with an estimated endurance of 17 minutes.

The actual endurance will vary from the presented estimation for several reasons. It shall be mentioned that a scaled UAV of this weight class can only be operated in a closed range, hence the straight flight path segments may be limited. Furthermore testing of the flight and mission control systems will require to fly the aircraft in many and different points of the flight envelope. Therefore it can be assumed that a significant part of the actual mission will consist out of maneuvering segments. These aspects will be considered in the following performance analysis, where specific points of the flight envelope will be studied carefully.

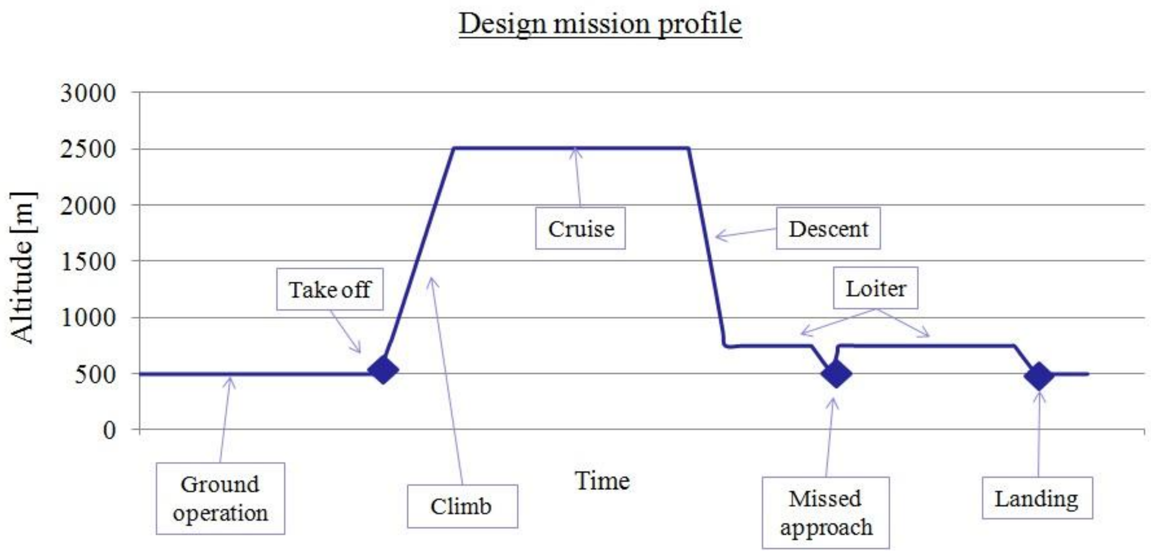

Fig. 4-2: Profile of the design mission over time.

4.3 Point performance

The assumptions mentioned in chapter 4.1 are still valid for the point performance analysis. For the point performance analysis following results are important: the sustained load factor envelope, the specific excess power (SEP) and the turning rate.

Some of the requirements for the flight performance are crucial for the operation of the demonstrator and represent minimum safety reserves. These have to be fulfilled with one engine inoperative (OEI). Other have to be met only with all or both engines operative (AEO).

Following requirements are defined:

1. A sustained load factor of 3g at 2500m for the clean configuration, with a total weight of 125kg and AEO.
2. A climb gradient of 10% at 650m above sea level, for the take off configuration, i.e. extended landing gear, with a total weight of 125kg and AEO.
3. An instantaneous load factor of 5g at 2500m, with approximately 50% fuel and AEO.

The feasibility of these requirements with respect to the given conditions is summarized in Table 4-2.

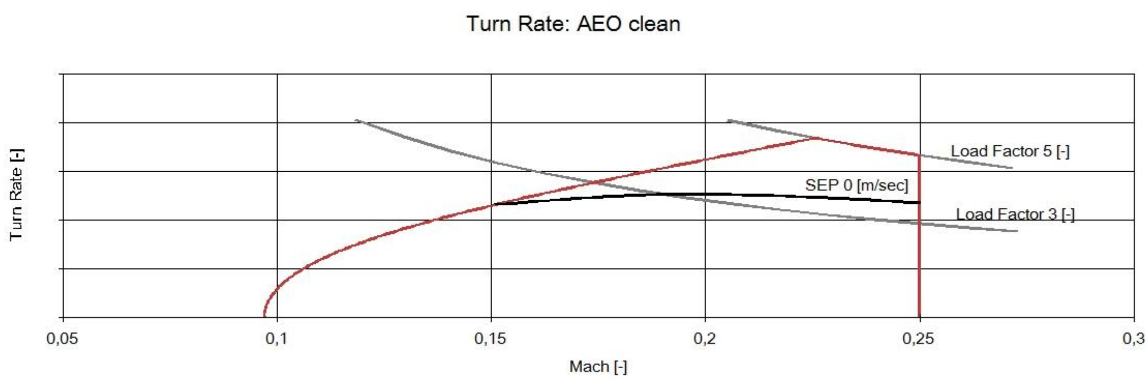

Fig. 4-3: Turn rate and instantaneous load factor for the clean configuration, with 50% fuel at 2500m.

Requirement	Comment - conditions
Sustained 3g	Between mach 0.24 - 0.25
Climb rate: 10%	Beyond mach 0.095
Instantaneous 5g	Beyond mach 0.225
Max speed	Mach 0.25 at 2500m

Table 4-2: Feasibility of performance requirements.

In the crucial case of OEI with MTOW the available SEP allows slight climb conditions beyond the take off velocity.

4.4 Take off and landing performance

The take off and landing performance has been calculated by analytical means. The used methods are described detailed in [4]. The configuration specific assumptions are listed in Table 4-3. The demonstrator does not have any high lift devices and the necessary lift for this study is assumed to be provided at trimmed conditions by the wing only. No tail wind has been considered.

Parameter	Units	Comment - conditions
Runway elevation	[m]	500 - above sea level
MTOW	[kg]	125
T/W	[-]	0.38
AoA_{max}	[°]	14
$CD_{0, landing\ gear}$	[-]	0.0272
$V_{take\ off}$	[m/s]	1.1 V_{stall}
$V_{over\ obstacle}$	[m/s]	1.3 V_{stall}
Obstacle height	[m]	10
Roll friction coefficient	[-]	0.025

Table 4-3: Take off analysis assumptions

The take off profile consists typically out of the acceleration level ground roll, the rotation, the airborne transition segment and the climb over the obstacle height. In the present study the obstacle height is overflown during the transition segment.

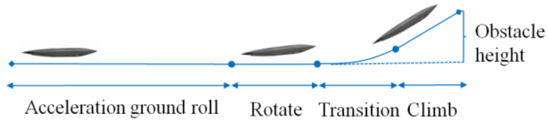

Fig. 4-4: Segment profile for the take off analysis.

The total take off distance is S_{to} = 362m long, consisting of a 235m ground and a 127m airborne segments respectively. Two uncertainties at the present moment are the actual rotation time and the impact of the ground effect on the actual available lift.

The segments of the approach on the other hand are equivalent, with an approach at 7% sink rate (over the obstacle) or a constant sink speed of 3m/s. For the case of an emergency landing direct after taking off, the maximum landing weight would be approximately equal to the MTOW. With an approach speed of 1,3 V_{stall} over the obstacle and a touch down speed of 1,1 V_{stall} the approximate landing distance is S_{land} = 442m without tail wind, considering the airborne approach segment of S_{app} = 162m and the ground segment of $S_{gr.roll}$ = 280m.

For this study the transition from the approach to touch down is realized by a flare segment. The demonstrator on the other hand shall land on an automatic mode and with a direct path or carrier landing approach without a flare. This kind of approach may allow a more precise and feasible automatic lading. In this case the airborne segment may be reduced further.

5 Conclusion

This paper described the principal assumptions for the flight performance studies with the means of analytical preliminary design methods. The presented results allow both a first estimation on the status of the performance of the demonstrator and to focus on the critical points of the operational envelope, particular the performance at low speeds and at OEI conditions. Ongoing numerical and experimental activities aim to deliver more realistic data about the available thrust for more accurate performance analysis.

Literature:

[1] Nicolai L., Carichner G., *Fundamentals of aircraft and airship design. Vol I—aircraft design.* AIAA Education Series (2010), p.66.
[2] Hövelmann A., Breitsamter C., "Aerodynamic Characterisitcs of the Sagitta Diamond Wing Demonstrator Configuration ", Berlin, 2012, DGLR Kongress 2012.
[3] Hoerner S.F., *Fluid Dynamic Drag: Practical Information on Aerodynamic Drag and Hydrodynamic Resistance*.
[4] Raymer D.P., *"Aircraft Design: A Conceptual Approach"*, AIAA Education Series (2006), p.546-552.

The Concept of the Joined Wing Scaled Demonstrator Programme

Cezary Galiński
Institute of Aviation, Poland

Jarosław Hajduk
Air Force Institute of Technology, Poland

Miłosz Kalinowski, Katarzyna Seneńko
Warsaw University of Technology, Poland

Keywords: *joined-wing, UAV, optimization, flight testing*

Abstract

Joined wing is an unconventional aeroplane configuration considered as a candidate for future airplanes. It consists of two lifting surfaces similar in terms of area and span. One of them is located at the top or above the fuselage, whereas the second is located at the bottom. Moreover one of lifting surfaces is attached in front of an aeroplane Centre of Gravity, whereas the second is attached significantly behind it. Both lifting surfaces join each other either directly or with application of wing tip plates (box wing). Application of this concept was proposed for the first time by Prandtl in 1924. It has many possible advantages like induced drag reduction and weight reduction due to the closed wing concept. Unfortunately it is much more complicated to design than conventional aeroplane due to the strong aerodynamic coupling and static indeterminacy. Therefore it was not possible to build successful aeroplane in this configuration before computer aided design systems became available and even its early versions were not powerful enough.

This paper presents the concept of the project dedicated to design and build scaled demonstrator in joined wing configuration. Particular attention is put on various approaches to the aeroplane optimisation. Also flight characteristics of the small flying model are discussed. It was designed and built as a part of preparatory phase of the project. It is currently flight tested to investigate various control concepts predicted for large UAV demonstrator which will be built later in the project.

1 Introduction

Application of the joined wing airplane configuration was proposed for the first time by Prandtl in 1924 [1]. According to his paper it is optimal in terms of induced drag generation, thus promising smaller fuel consumption. Unfortunately it is much more complicated to design than conventional airplane. As a result attempts do build practical airplane with application of conventional analytical and experimental methods could not be successful [2, 3]. Initial attempts to apply computer aided design software [4-11] gave promising results, but revealed also difficulties arising from the concept complexity. These difficulties are caused by aerodynamic, structural and manufacturing reasons. Joined wing is aerodynamically closely coupled which means strong interaction between wings. As a result detailed aerodynamic analysis was not possible without CFD software but its early versions were not powerful enough. Large meshes are necessary to describe joined wing accurately enough, so very capable computers were required and unfortunately unavailable. On the other hand, potential weight reduction comes from the static indeterminacy of the configuration. Once again powerful computers were necessary to analyse it with FEM method with satisfactory accuracy. Moreover, static indeterminacy causes significant manufacturing problems due to tight tolerances required to assembly the joined wing with no random internal stresses. Tight tolerances are achievable only now with application of modern CAM systems. All these tools are currently available, so attempts to design a joined wing airplane are more frequent [12-19]. However in most cases researchers concentrate on configuration where front wing is attached at the bottom of fuselage and aft wing is installed either at the top of the fuselage or at the top of the vertical stabilizer. According to our experience this configuration cannot provide expected advantages.

First attempts to design a joined wing in Poland were undertaken in late eighties [20]. A few flying models were also built, exhibiting excellent handling qualities (Fig.3). All these efforts were focused on the most popular joined wing configuration with front wing at the bottom of the fuselage. However results of investigation lead to the conclusion that joined wing airplane could fly much better in upside down position. The most probable reason of this fact comes from the interaction between wings. Front wing wake is very close to the aft wing if gap between wings is too small. It becomes even smaller at high angles of attack if front wing is located below aft wing. As a result aerodynamic advantages are diminished. They may be recovered if aft wing is installed high at the top of the vertical stabilizer, however this requires strong stabilizer, which decreases potential weight reduction. Configuration, with front wing above aft wing should work in the opposite way, thus delivering expected advantages, providing that fuselage is reasonably high.

Fig. 1. Wind tunnel joined wing models applied by Warsaw University of Technology in early nineties.

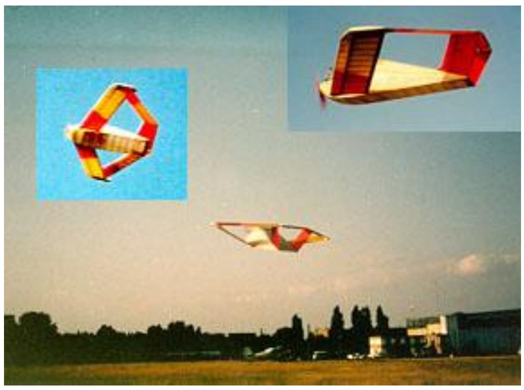

Fig. 2. First flying model of joined wing airplane build and tested by authors.

Topic was recently refreshed. Series of simple CFD analyses were carried out to check if previous conclusions were correct [15]. Current results confirm, that joined wing airplane L/D grows together with increasing gap between wings. Moreover, assuming the same gap, configuration with front wing above aft wing provides not only greater maximum L/D, but also greater L/D in wider range of angles of attack. In particular L/D at high angles of attack is greater in this configuration, which suggests advantageous flight endurance. Configuration with front wing below aft wing is advantageous only at low angles of attack assuming that aft wing is installed at the top of the vertical stabilizer. However, weight advantage should be reduced in this case due to the increased loads of vertical stabilizer.

Configuration with negative stagger (lower wing in front) is quite popular between researchers, so its characteristics are quite well known. On the other hand only a few attempts to design join-wing with positive stagger (higher wing in front) were undertaken [21]. Therefore the project was undertaken to acquire detailed knowledge and experience related to the last configuration. The project consists of the multidisciplinary optimisation software development, numerical analysis, wind tunnel tests and flight tests campaign. UAVs are used for flight testing to save resources, however manned research vehicle is also envisaged in the future. Software development is run simultaneously with other tasks, assuming that it will be used in future projects, whereas other tasks will be performed with already existing data and software. Analyses presented in [15] were used as a starting point for this project and to build the small flying model with wing span of 1.2m and takeoff weight of 1.1kg. The purpose of this model was to evaluate general airworthiness of applied airplane configuration and for qualitative testing of the control system consisting of 11 control surfaces. Moreover area of vertical surfaces were adjusted basing on pilot's observations concerning airplane dynamic stability. Result of this experiment should shorten and verify detailed CFD calculation time, necessary to build larger UAV later in this project. It will have wing span of 3m and takeoff weight of 25kg. It will be used for wind tunnel investigation and for detailed flight testing. Aerodynamic optimisation software described in [22-24] is used to define details of the large model. Multidysciplinary optimisation software developed in this project should allow converting this model into "commercial" UAV in the future project, since it will provide possibility of optimising not only aerodynamics, but also strength and weight of the airframe.

2 Small join wing model flight test results

The model with wing span of 1.2m and takeoff weight of 1.1kg was built according to simplified optimisation procedure presented in [15]. It has total wings area equal to 0.216m^2. This gives wing loading of 5kg/m^2, which is quite large for the model in this size. However with motor powerful enough it gives airspeed range large enough to achieve safe range of Reynolds numbers. Still Reynolds numbers are small, so only qualitative characteristics can be investigated with this model. Anyway possibility to receive valuable results has to be considered as a significant achievement of microelectronics, since miniature systems like servos with weight of just 4.5 gram or micro Flight Data Recorder with 3-axial accelerometer and GPS receiver weighting together 62g, became available just a few years ago. This allows obtaining complex information from flight testing at the very beginning of the project, because labour-consumptions necessary to build a model is much smaller than previously. For a comparison, model described in [25] required more than 4000 man-hours to be built, whereas model described here required only about 600 man-hours.

Configuration and conditions for the first flight:

Takeoff mass	1030 g
Stability margin	~15%

(neutral point calculated according to [15])

Propulsion system

Motor	AXI 2217/12 (69.5g)
Batteries	Dualsky 3S1750 mAh (146 g)

Propeller APC 6x4E

Control system configuration:
RC receiver Jeti Duplex R12 (20g)
Batteries NiMH Eneloop AAA 4S (54 g)
Servos 11 x HS-35 (4.5g each)
4 flaps along whole span of the front wing used as flaperons
4 flaps along whole span of the rear wing used as elevons
Rudders on both wing tip plates performed only external deflections
Central rudder performed symmetrical deflections.
Aileron action equal to 55% of full flaps deflection.

Conditions:
Ambient temperature -4^0C
Wind speed 1 – 2.5 m/s

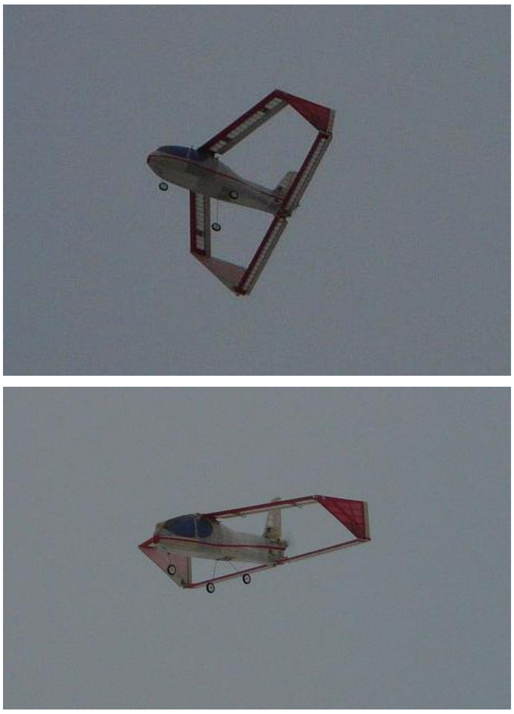

Fig. 3. First flight of the small join wing model.

2.1 Pilot's observations from the first flight

Hand launch against the wind, easy, symmetrical with small tendency to descend. Steady climb after takeoff at full power with elevons set in neutral position. The same elevons setting can be used at reduced power for horizontal flight. Small tendency to turn right required ailerons to be deflected slightly to the left. First impression was positive. Model properly reacted to the ailerons control, with very fast reaction for full deflection but also with precise control with small deflection. Correct damping of rolling motion after ailerons return to the neutral. Longitudinal control correct and providing an impression of very good control. Damping of pitching motions strong. Directional control relatively small, but observable and undoubtful. It is possible to perform flat turns with rudders deflection only Small tendency to roll is observable in this manoeuvre. It is possible to perform sideslip with small ailerons deflection.
Large range of airspeeds can be achieved with elevator trimmer only. Model performs correct turns with bank angle of 45^0 at reduced power with no tendency to airspeed loss. Correct steady turn with no need to adjust with controls. Correct rolling in opposite directions with no tendency of residual yaw, even without directional control.
Perception of airspeed loss in deep windup turns at reduced power, with some rocking and stalling but without spinning – model is still controllable and can be recovered from the turn, accelerate etc.
Climbing is correct and steady at full power. Airspeed can be easily controlled with trimmer. Obvious airspeed reduction and large positive pitch angle with elevator fully up but climb rate reduction is not obvious. Climb rate and climb angle are large. Transition from climbing to horizontal flight or descend after power reduction is smooth and easy. Airspeed can be also easily controlled with trimmer in gliding, but effect on sink rate is quite small. Propulsion disengagement is accompanied by observable tendency to turn left but it is easy to balance with ailerons trimmer. Correct stability and control in gliding. Turns can be performed easily without tendency to airspeed loss or instability. Recovery from the dive with pitch angle of -45^0 is acceptable and requires no

controls deflection from neutral position. However, model is similar rather to aerobatic airplanes with similar size than to high wing trainers.
Approach to stall with slowly increasing elevator deflection was successful. Model behaved properly up to the full deflection of elevator. However model behaves like flying wing rather than conventional airplane, i.e. pitching up is not visible but rather increased sink rate in slow flight. Tendency to yaw to the left was observable during glide with high elevator deflection.
Attempt to use front flaps appeared successful. Their deflection has significant effect on longitudinal balance but is steady and easy to predict. It is similar to reaction of conventional model airplane with aft centre of gravity. Front flap deflection down raises the fuselage nose slightly up and airspeed falls down but without tendency to the continuous pitch angle increase or stalling. Deflection of the elevator down recovers previous fuselage orientation, but airspeed remains reduced. Tendency of pitching down and acceleration is observable after front flaps are returned back to neutral. Front flap deflection up results with obvious tendency to pitch down. Sink rate is still observable after fuselage orientation is recovered with elevator.
Approach to landing was correct but sink rate and angle were quite large after propulsion was disengaged. Quick loss of energy after elevator deflection up is visible. Therefore elevator deflection up cannot be used to reduce the sink rate. Propulsion should be rather used to achieve this goal, which is typical for flying wings. Touchdown was performed with relatively large airspeed in comparison to models with the similar size.

3 The concept of multidisciplinary optimization

Simple optimization procedure described in [15] allowed designing and building successful small model of the joined wing airplane. Advanced aerodynamic software presented in [22-24] is used to design large scaled demonstrator. But it is not enough to design successful commercial UAV or manned airplane in joined wing configuration because weight and strength properties are still not optimal. Therefore software for multidisciplinary optimization is developed to handle this complex challenge. One of attempts to do it is described below.

3.1 Optimization process

Two different procedures are considered because of the problem complexity and coupling of disciplines in multidisciplinary optimization. In both cases optimization is based on gradient methods. These methods have to calculate objective function only a few times, which is advantageous because objective function calculation takes a lot of time in this case. First procedure is called “independent”. It assumes adding structural optimization into aerodynamic optimization loop. An independent full structural optimization is made for each step of geometry optimization. There are two independent objective functions here. Function of structural optimization is based on penalty function, which is maximizing stresses in structure to the predefined limit (minimizes mass). Geometry optimization is based on an objective function determining an airplane’s range.
This connection does not guarantee finding global maximum of range with regard to outside geometry and structure simultaneously. It can only allow finding optimal structure for optimal geometry. That is why second procedure was created to compare solutions. It seems to be simpler but it needs much more calculations.
In the second procedure there is one function consisting of objective function with penalty function. In each step both parameters of geometry and structure are optimized. Because of that much more aerodynamic analyzes are needed to find aerodynamic derivatives. Cost of calculation is compensated by possibility of finding global minimum with regard to all parameters of optimization.

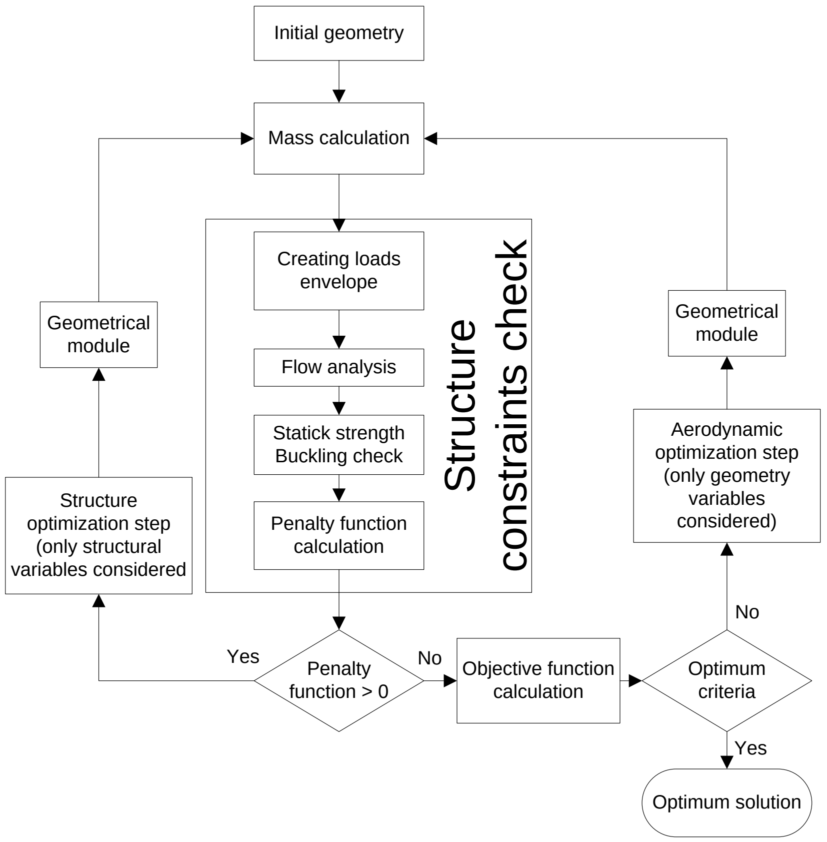

Fig 4. Independent optimization

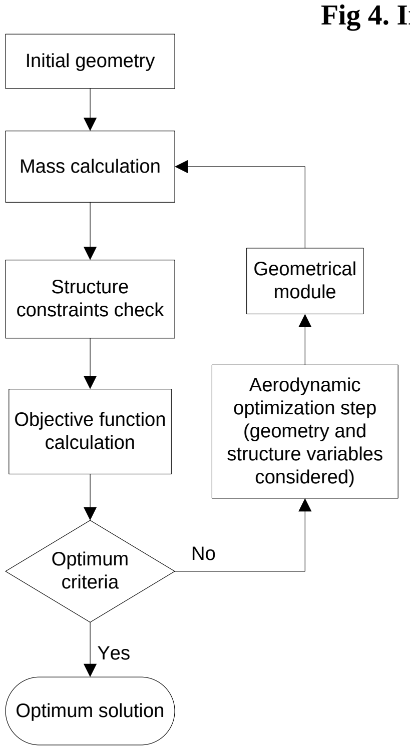

Fig 5. Conjugate optimization

3.2 Definition of optimization criterion

The most important questions which must be answered before starting optimization are the following: what should be optimized, in what range and what is an optimization criterion. First and second question are not hard to answer but the third one can make some problems. For high performance airplanes we try to make one value extreme (e.g. velocity or mass). In this case optimization criterion is direct function of structural and aerodynamic analyzes results. The problem appears when we want to optimize an airplane in the type of general aviation. Usually in this type of design the most important parameter is the longest range.

Electrical propulsion is desired in the current programme to enable propulsion testing in the wind tunnel. We are also considering it for the future airplane. Unfortunately electric airplane has only small reserve of electric energy Q and because that takeoff and landing consumes significant amount of this reserve during typical mission. That is why optimization criterion was created considering the whole mission profile. The range should achieve maximum value with constant value of payload M_{pay}.

$$L = L_{climb} + L_{cruise} + L_{desc} \quad (1)$$

Total mass of an airplane M_{TO} is a sum:

$$M_{TO} = M_{pay} + M_0 \quad (2)$$

Total mass of electric airplane is constant during flight. It is different than in airplanes with internal combustion engine. Mass M_0 is a mass of empty airplane and depends directly on structure and geometry of airplane, which will be optimized. We can take an assumption that airplane will be using energy only during climbing and cruise. Descent and landing will be performed with a motor turned off.

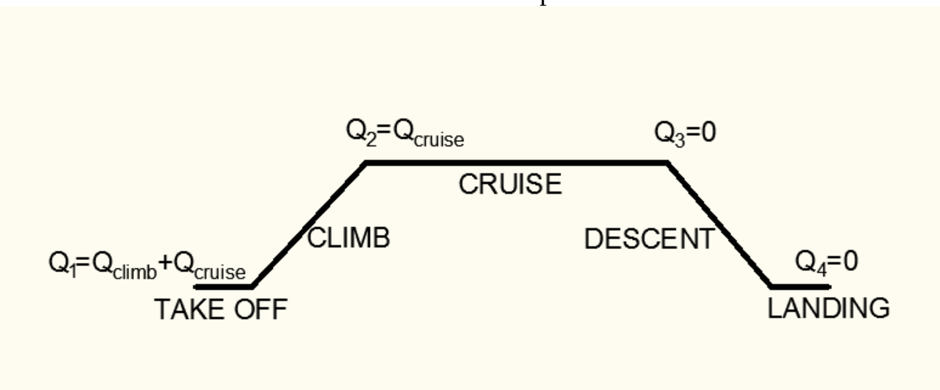

Fig.6. Mission profile of joined wing in type of *general aviation*

This assumption allows manipulating with optimal and economy airspeeds in different flight phases. During climbing we want airplane to have the highest rate of climb w_{climb} with maximum thrust of the motor. Rate of climb can be calculated with an assumption that whole available energy is used for work against resistance and for climbing.

$$w_{climb} = \frac{N_e \eta_p - N_{Cd}}{mg} \quad (3)$$

,where $N_{Cd} = mg\sqrt{\frac{2mg}{\rho S} \cdot \frac{C_x^2}{C_z^3}}$. (4)

Following these equations we see that w_{climb} depends on altitude and velocity of flight. To calculate the time of climb, we take an assumption that velocity of climb changes in linear way with altitude. Therefore the distance traveled during climbing can be calculated as:

$$L_{climb} = h_{cruise} \cdot \frac{V_{climb\,1} - V_{climb\,2}}{w_{climb\,1} - w_{climb\,2}} \quad (5)$$

Cruise should be performed with an optimal energy consumption. Range of cruise can be calculated as:

$$L_{cruise} = V_{cruise} \int_{Q_{cruise}} \frac{dQ}{I} = \frac{C_z}{C_x} \cdot \frac{\eta_p}{mg} \cdot Q_{cruise} \cdot U \quad (6)$$

Descent should be performed with descent angle γ corresponding to optimal airspeed, which means also with maximum lift-to-drag ratio. This value can be estimated approximating $C_x(C_z)$ characteristic with quadratic function and calculating maximum of $\frac{C_z}{C_x}$ using this function. Distance traveled during descent can be calculated as:

$$L_{desc} = h_{cruise} \cdot \left(\frac{C_z}{C_x}\right)_{max} \quad (7)$$

Phase of flight	Climb	Cruise	Descent
Power taken	N_e	$P_d \cdot V_{cruise}$	0
Vertical velocity	$w_{climb} = w_{max}$	$w_{cruise} = 0$	$w_{descent} = w\left(\gamma_{opt}\right)$

Table 1. Assumptions for the following phases of flight.

All values of aerodynamic coefficients existing in equations are calculated with aerodynamic simulation. Finally, value of whole range is taken as objective function which is maximized.

3.3 Module of a load envelope

This is the simplest module, which we use to define critical points of the load envelope created with airworthiness regulations CS-23. Additionally maximal pitching angular accelerations are calculated with this module. It will be used to calculate structure load due to inertia.

3.4 Geometry module

This part of the program generates geometry, modifies it and creates a mesh. Module makes three-dimensional surface parametric model. Geometry of the fuselage includes frames and stringers, geometry of the wing has ribs, distributed spar flanges and shear webs. Frames of the fuselage are not optimized and are used to put loads from instruments. Stringers are simulated as beams with variable cross-section. Ribs are modelled as shell elements. Airplane's structure is assumed to be metallic. However, testing this software for composite structures is also planned.

The model is parametric and parameters characterize global geometry and also thickness of structure elements. Aerodynamic Adjoint analysis is planned to minimize number of parameters because too many parameters makes time of computing longer. Only these parameters which have the greatest effect on the flow will be optimized. Optimization of the structure will be made with dividing it into areas of the same thickness. These thicknesses will be changed during optimization.

Finally model created by the program will be divided into finite elements. The same mesh will be used to aerodynamic and structural computations to economize time.

3.5 Aerodynamic module

Aerodynamic simulation is performed many times in the course of optimization so limit of accuracy is imposed by time of computing. Advanced CFD methods are too time-consuming thus impossible to apply in large optimization problems. Too simple models like model of vortex line can give wrong results. Panel methods seem to be optimal solution. Time of one analysis is no longer than a few minutes so aerodynamic module can be used several times during one step. It will not make computing much longer.

PanAir program is used as an aerodynamic solver [26-28]. It is a simple open source code which was used in similar purposes many times [29, 30]. It will be used to calculate aerodynamic characteristics and maximum lift-to-drag coefficient during flight on cruise altitude (balance analysis).

Aerodynamic module will also calculate pressure distribution for critical conditions of the load envelope. These distributions will be used as loading for structural module. Balance analyses performed iteratively are also necessary in these calculations.

3.6 Structural module

Only symmetric loadings are taken into optimization process in purpose to simplify the process. A few additional analyzes, calculating internal forces in the structure, should be introduced if asymmetric loadings are also necessary. Structure loading consists of aerodynamic pressure, inertial forces of the structure and instruments and also forces and moments imposed by the motor.

Structure analyses will be performed by FEM program CalculiX [31], which is also an open source code. Internal forces calculation in the structure requires applying different FEM models for wings and fuselage. Support conditions are the most important difference between models. They are shown in Fig.7.

Internal forces calculated for different types of loading are correlated to obtain all possible combinations of loading during flight. Finally load envelope of all correlated loadings is generated and strength of the structure is verified. Moreover buckling calculations for most critical loadings are also done.

Finally module produces a map of reserve factor (RF) values, which is used for penalty function calculation.

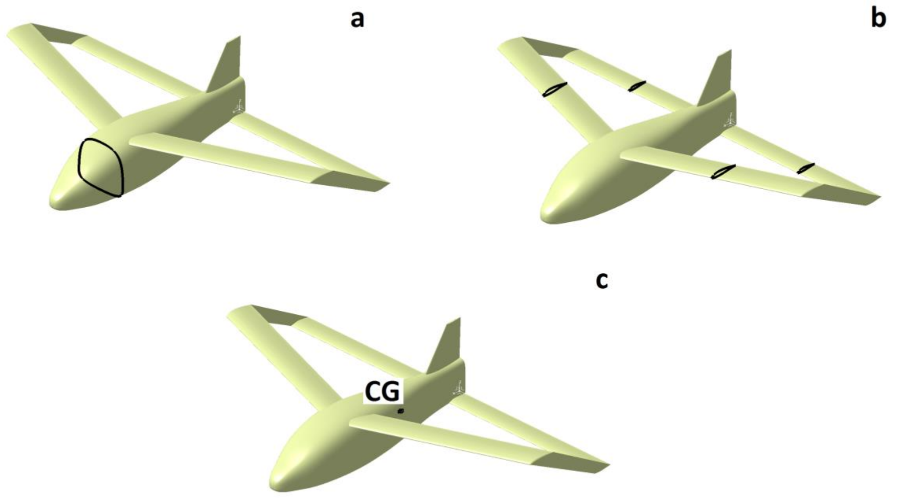

Fig.7. Support conditions of FEM models (a – for wing calculations, b – for fuselage and tail-plane calculation, c – for load from inertia calculation)

4 Conclusion

Research programme was undertaken to explore characteristics of the join wing airplane with positive stagger (upper wing in front). The programme will consist of optimization software development, numerical analyses, wind tunnel tests and UAVs flight tests. So far small model was built to investigate basic airworthiness. An airplane performed well, exhibiting correct stability and control characteristics. Larger model will be built and tested later in the project. It will be designed with application of existing aerodynamic optimization software. Multidysciplinary optimization tool is developed to convert scaled demonstrator into practical UAV or manned experimental airplane.

5 Acknowledgements

This work was supported by The National Centre for Research and Development under grant No. PBS1/A6/14 (179787).

References

[1] Prandtl, L. “Induced drag of multiplanes”, NACA TN 182, 1924

[2] Makarov, I. W. “Lietalnyie apparaty MAI”, Izdatielstwo MAI, Moscow, 1994, pp. 64-65

[3] Sopher, R. “Design of a fairing for the junction of two wings”, Journal of Aircraft 1967 0021-8669 vol.4 no.4 (379-382)

[4] Fairchild Samuels M., “Structural Weight Comparison of a Joined Wing and a Conventional Wing”, Journal of Aircraft 1982 0021-8669 vol.19 no.6 (485-491)

[5] Wolkovitch, J. „The joined wing - An overview”, Journal of Aircraft, Vol.23 No.3, March 1986, pp. 161-178

[6] Miura H., Shyu A., Wolkovitch, J. “Parametric weight evaluation of joined wings by structural optimization”, Journal of Aircraft 1988 0021-8669 vol.25 no.12 (1142-1149)

[7] Hajela P., Chen J. L. “Preliminary weight estimation of conventional and joined wings usingequivalent beam models”, Journal of Aircraft 1988 0021-8669 vol.25 no.6 (574-576)

[8] Kroo, I., Gallman, J. “Aerodynamic and Structural Studies of Joined Wing Aircraft”, Journal of Aircraft, Vol. 28, No. 1, January 1991, pp. 74-81

[9] Burkhalter J. E., Spring D. J., Key M. K., “Downwash for joined-wing airframe with control surface deflections” Journal of Aircraft 1992 0021-8669 vol.29 no.3 (458-464)

[10] Gallman J. W., Smith S. C., Kroo I. M., “Optimization of joined-wing aircraft” Journal of Aircraft 1993 0021-8669 vol.30 no.6 (897-

905)

[11] Gallman, J. W. „Structural optimization for joined-wing synthesis**",** Journal of Aircraft, Vol.33 No.1, January 1996, pp. 214-223

[12] Blair M., Canfield R., Roberts R., "Joined-Wing Aeroelastic Design with Geometric Nonlinearity", Journal of Aircraft 2005 0021-8669 vol.42 no.4 (832-848)

[13] Rasmussen C., Canfield R., Blair M., „Joined-Wing Sensor-Craft Configuration Design" Journal of Aircraft 2006 0021-8669 vol.43 no.5 (1470-1478)

[14] Kim Y. I., Park G. J., Kolonay R. M., Blair M., Canfield R. A. "Nonlinear Response Structural Optimization of a Joined Wing Using Equivalent Loads", AIAA Journal 2008 0001-1452 vol.46 no.11 (2703-2713)

[15] Mamla P., Galinski C. "Basic Induced Drag Study of the Joined-Wing Aircraft", Journal of Aircraft 2009 0021-8669 vol.46 no.4 (1438-1440)

[16] Bond V., Canfield R., da Luz Madruga Santos Matos M., Suleman A., Blair M., "Joined-Wing Wind-Tunnel Test for Longitudinal Control via Aftwing Twist", Journal of Aircraft 2010 0021-8669 vol.47 no.5 (1481-1489)

[17] Jansen P., Perez R., Martins J., "Aerostructural Optimization of Nonplanar Lifting Surfaces", Journal of Aircraft 2010 0021-8669 vol.47 no.5 (1490-1503)

[18] Paletta N., Belardo M., Pecora M., "Load Alleviation on a Joined-Wing Unmanned Aircraft", Journal of Aircraft 2010 0021-8669 vol.47 no.6 (2005-2016)

[19] Bindolino G., Ghiringhelli G., Ricci S., Terraneo M., "Multilevel Structural Optimization for Preliminary Wing-Box Weight Estimation", Journal of Aircraft 2010 0021-8669 vol.47 no.2 (475-489)

[20] Galinski, C. "Results of Testing of Models of Joined-Wing Utility Class Aircraft", SAE paper No. 921013, SAE Aerospace Atlantic Conference, Dayton OH, 7-10 April 1992

[21] http://en.wikipedia.org/wiki/Dewald_Sunny

[22] Stalewski W., Zoltak J. "Optimisation of the Helicopter Fuselage with simulation of Main and Tail Rotor Influence", paper 1.4.1 in proceedings of the ICAS'2012 conference, Brisbane, 23-28 September 2012

[23] Stalewski W., Zoltak J. "Multi-objective and multidisciplinary optimization of wing for small aircraft", proceedings of the CEAS'2011 conference, Venice, 24-28 October 2011

[24] Stalewski W., "Parametric modelling of aerodynamic objects – the key to successful design and optimisation", Aerotecnica of Missili & Spazio, journal of Aerospace Sciences, Technologies and Systems, vol. 91, n. 1-2 March-June 2012

[25] Galinski C., Goraj Z. „Experimental and numerical results obtained for a scaled RPV and a full size aircraft", Aircraft Engineering and Aerospace Technology, vol. 76, Issue 3, pp. 305-313

[26] Derbyshire T., Sidwell K.W.: PAN AIR Summary Document, (Version 1.0).NASA Contractor Report 3250, 1982.

[27] Magnus A.E., Epton M.A.: PAN AIR - A Computer Program for Predicting Subsonic or Supersonic Linear Potential Flows About Arbitrary Configurations Using A Higher Order Panel Method, Vol. I. Theory Document (Version 1.0).NASA Contractor Report 3251, 1980.

[28] Sidwell K.W., Baruah P.K., Bussoletti J.E.: PAN AIR - A Computer Program for Predicting Subsonic or Supersonic Linear Potential Flows About Arbitrary Configurations Using A Higher Order Panel Method, Vol. II. User's Manual (Version 1.0).NASA Contractor Report 3252, 1980.

[29] Blair M., Moorhouse D., Weisshaar T.: System design innovation using multidisciplinary optimization and simulation, 8th Symposium on Multidisciplinary Analysis and Optimization, September 2000

[30] Amadori K., Jouannet C., Krus P.: Use of Panel Code Modeling in a Framework for Aircraft Concept Optimization, 11th AIAA/ISSMO Multidisciplinary Analysis and Optimization Conference, Portsmouth, USA, 2006.

[31] http://www.calculix.de/

RAPID – Robust Aircraft Parametric Interactive Design
(A Knowledge Based Aircraft Conceptual Design Tool)

Raghu Chaitanya.M.V*, Patrick Berry¤, Petter Krus*
**Linköping University, SE-58183, Linköping, Sweden*
¤Saab Aeronautics, SE-581 88, Linköping, Sweden
raghu.chaitanya@liu.se

Keywords: *Aircraft Conceptual Design, Knowledge Based, XML Data*

Abstract

Conceptual design is the early stage of the aircraft design process where results are needed faster both analytically and visually so that the design can be modified or changed at the earliest stages. Although there is no necessity for a CAD model from the very beginning of the design process it can be an added advantage to have the model, to get the impression and appearance.

Tango and RAPID are knowledge based aircraft conceptual design applications being developed in Matlab and CATIA respectively. The user can work in parallel with both programs and exchange the data between them via XML. This paper describes the knowledge based design automated methodology of RAPID and its application in the courses "Aircraft conceptual design" and "Aircraft project course" at Linköping University. A multifaceted user interface is developed to assist in the whole design processes.

1 Introduction

Conceptual design tools always need to be refined and improved. There is no end to it and this is how it should be. One such much needed refinement is to be able to communicate between the analytical design tool and the 3D environment, i.e. CATIA. Data communication between conceptual design programs has always been a major obstacle which now has found a solution through this work, presently being done at Linköping University. A seamless connection appeals to the designer, but it has to work both ways. There are a handful of existing software tools in the industry, at universities and research centers. Some have connections to CAD programs, but the connection is usually not seamless and even more rarely they work both ways [11].

Existing aircraft conceptual design tools:

- RDS [1]
- ADS [8]
- Desktop Aero [10]
- J2 Universal Tool Kit [7]
- Piano [9]
- CEASIOM [3]
- PADLab [4]
- VSP [4]
- Bauhaus Luftfahrt: Conceptual Design Tool (CDT) [6]

2 Knowledge Based Engineering Design

Knowledge Based Engineering can be explained as reusable information that exists in the specific method or form; this knowledge is reused either manually or automatically and the whole process of using existing knowledge such that it adapts to the new environment can be termed as *Knowledge Based System* (KBS) [12] and [13]. The automation is performed in CATIA [22] using Power Copy and User Defined Feature (UDF) wherever necessary. *Visual Basic* (VB) scripts use the power copies and Knowledge Pattern use UDFs to save the knowledge that is created for automation. Power Copy or UDF is a set of features stacked together that can be reused at a later stage. A Catalog is needed to store the location of the UDF. The Knowledge Pattern Algorithm script is written using the *Engineering Knowledge Language* (EKL) to control the UDF. UDF is used repeatedly to obtain a desired configuration. Further the UDF can be updated depending on the necessity and used accordingly. Creating a KBS is time consuming and the user needs to have some knowledge of the system in case of modifying it; once it is built there are numerous uses of it and could help the user build the necessary system quicker faster and in less time.

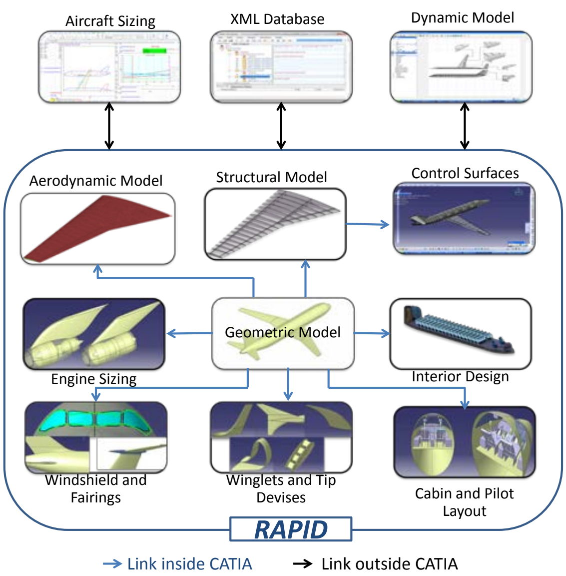

Fig. 1 RAPID Tool

3 Data management

Data created in RAPID s saved as an XML document. XML stands for "eXtensible Markup Language". XML contains both the information and is self-explanatory format. XSL Transformation (XLST) is used to change one XML Document to another XML Document [21]. For more information on XML database and XML data handling in RAPID refer *"Integrated Aircraft Design Network"* [20].

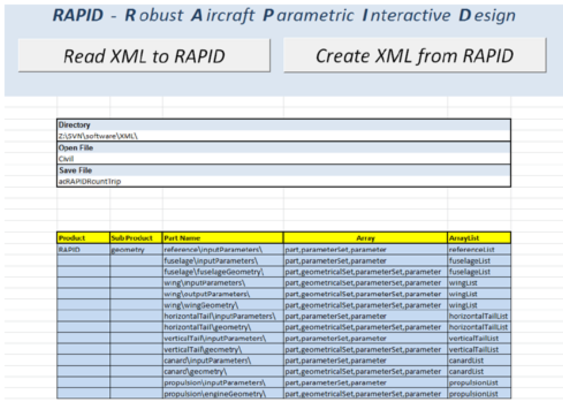

Fig. 2 RAPID-XML Interface

3.1 Create an XML file for CATIA parameter sets

Creating the XML is done in the following way:

- Parameter Sets that need to be represented in XML are written in the excel sheet as rows.
- These Rows from excel are read into VBA and compared with the whole list of parameter sets from CATIA.
- The matched Parameters and Parameter Set are formed into XML strings using DOM Object.
- The Final XML DOM object is written and saved as an XML document.

3.2 Read XML file

- The Required XML Document is loaded into VBA.
- Each XML node in the document is parsed, the Data in the last nodes is extracted and updated into the corresponding CATIA Parameters.
- CATIA is updated using CATIA – VB Scripts for the changes to reflect.

4 RAPID

RAPID is a geometry oriented design tool used in the framework of aircraft conceptual design. The core incentive to use CATIA is to allow the geometry propagation from conceptual design to preliminary design. *Knowledge Pattern* (KP) and *Visual Basic* (VB) embedded in CATIA are used for automation at necessary stages. There are three ways the user can design the aircraft in RAPID.

- By modifying the existing model after loading from XML data library.
- By updating the model from the Sizing Excel.
- By bottom-up design approach.

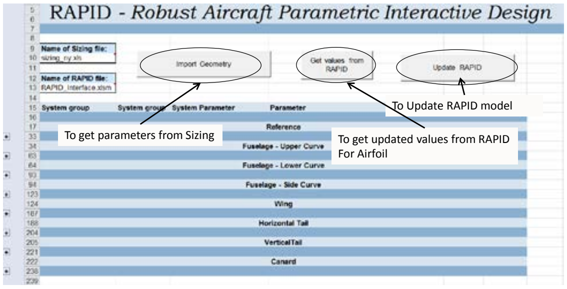

Fig. 3 User interface for Geometry

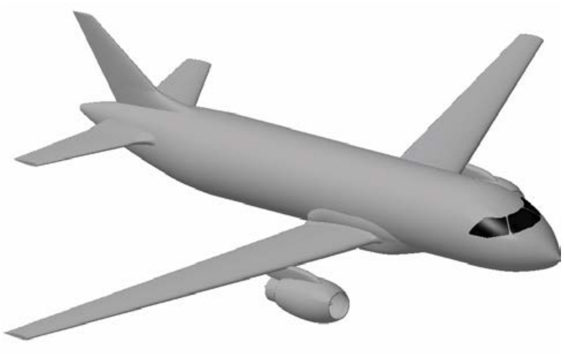

Fig. 4 Example of Civil transport aircraft geometry loaded from database

The bottom-up design approach can be employed in RAPID to design from scratch or the user can load the existing aircraft model from the XML data library. The user begins by modifying the fuselage curves according to design requirements and later adapting the wing. The empennage is automatically sized depending on the given fuselage parameters and wing parameters. The adaptability of the model helps to obtain different aircraft configurations.

4.1 Geometry Model

After the initial setup of the wireframe model of the aircraft, a more detailed geometry can be developed (Fig. 6). The user chooses the number of frustums needed for the fuselage and the number of partitions needed for wing, empennage and canard depending on the requirement.

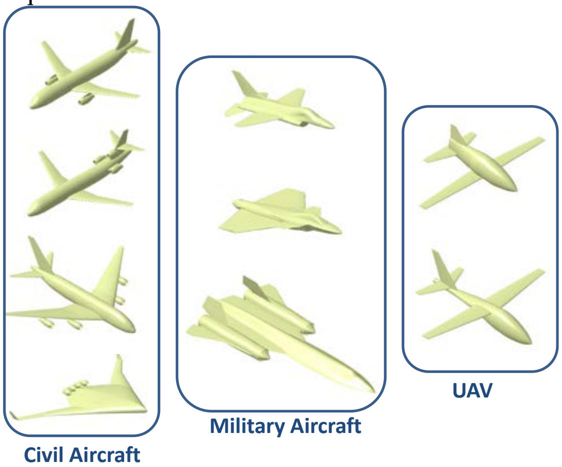

Fig. 5 Different aircraft configurations of geometry model RAPID

4.1.1 Fuselage Geometry Description

Fuselage wireframe is composed of four supporting splines; they are upper curve, bottom curve, side curve and center curve (Fig. 6). The splines are created in desired manner which are then taken as reference for the instantiation of frustums. A frustum is formed by two Bézier curves joined by a surface. Bézier curves are parametric and can be modified to get desired cross-section at each frustum (Fig. 7).

A quarter of the fuselage cross-segment is portrayed by third-order Bézier curve. The angle is measured from the horizontal line for “upper line” and “lower line” and angle is measured from the vertical line for “side upper line” and “side lower line”. The Points 1, 4 and 7 shown in Fig. 7 are the intersection points with the fuselage curves while points 2, 3, 5 and 6 are positioned along the respective lines as a fraction.

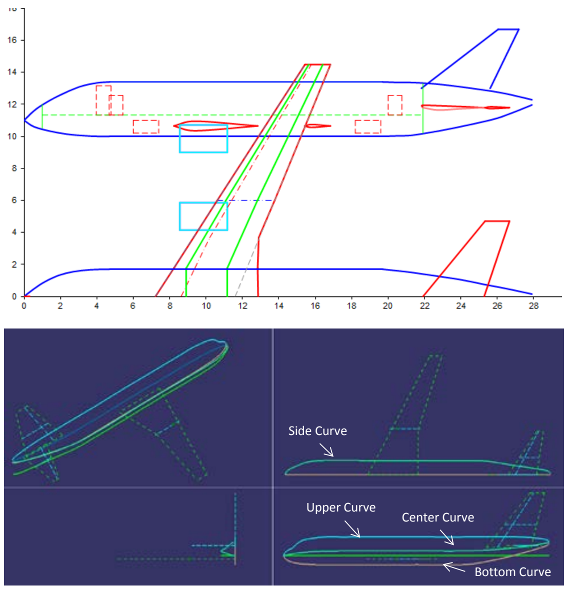

Fig. 6 Fuselage curves in Sizing Excel (Top); Fuselage curves in RAPID (Bottom)

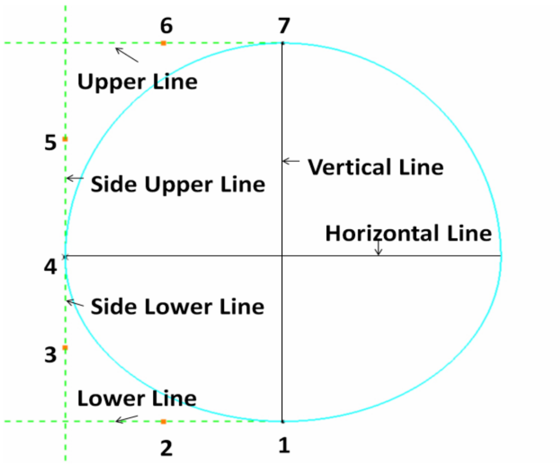

Fig. 7 Description of RAPID fuselage Cross-section [11]

4.1.2 Wing Geometry Definition

Wing wireframe is generated by taking the reference area, taper ratio and aspect ratio as reference. The user has an option to choose the angle either from leading edge or 25% root chord to obtain trapezoidal wing area (shown in dotted line in Fig. 8). There also exists another reference area method to choose from such as Double delta, Gross Method and Wimpress Method. The RAPID area method uses the trapezoid area as a reference, after instantiating required number of partitions the chord at each airfoil can be modified to obtain different wing shape as shown in Fig. 8.

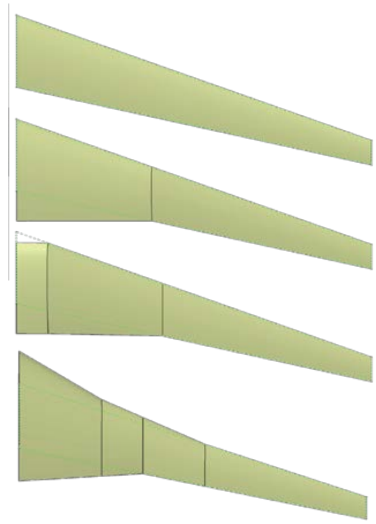

Fig. 8 Different wing shapes modified after instantiation of partitions

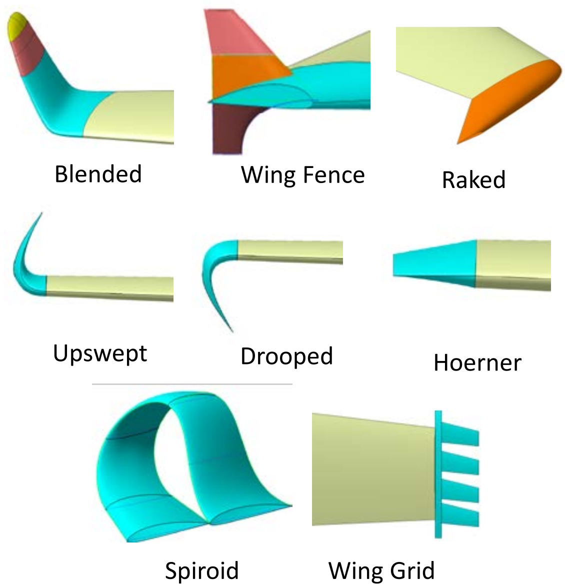

Fig. 9 Different types of Winglets [15]

Each partition is made up of two airfoils joined by a surface. The airfoils are generated using third-order Bézier curves. The same partition template is used for horizontal tail, vertical tail and canard. Since the airfoil is parametrically defined, it can be used to obtain "n" number of airfoil shapes [14]. Different types of winglets and wing tip devices can be chosen. The wireframe is first instantiated and later number of wing partitions are instantiated. The projected areas of each partition are summed up automatically to give the final area of the wing and winglets.

4.1.3 Engine Sizing

Two types of engines turbofan and turbojet can be sized in RAPID. Thrust, Specific fuel consumptions (SFC), Weight, Length, Diameter and By-pass ratio are the key parameters that size the engine. Turbofan engine is sized to suit commercial aircrafts engine dimensions with a bypass ratio from 3 to 20; turbojet engine to suit the dimensions of business jets and military engines with no after burner engines from 0.1 to 15.

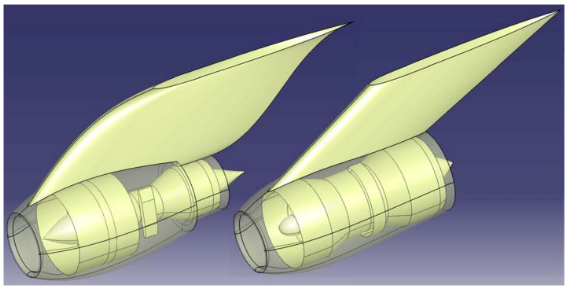

Fig. 10 Turbofan (left) and turbojet engine (right) [11]

Mixed-flow and separate-jet are two kinds of nacelles available; straight and smooth pylon types can be chosen. Nacelle design depends on the type of engine and various parameters can be changed to obtain the desired contour. Pylon is designed in contest with nacelle, start and end values are changed accordingly. Air inlet and duct for military application is a work in progress.

4.2 Interior Design

Comfort is the privilege that a passenger craves for while travelling. Aircraft Interiors is a major part of the Aircraft Design process. Cabin space has to be utilized in a intelligent fashion using most of the space, identifying the comfort factors for passenger, able to accommodate the maximum number of passengers according to the requirement. FAR 25 rules have been implemented in cabin design.

4.2.1 Cockpit Design

The cockpit design consists of windshield design, cockpit layout and ergonomic study. Flat panels and blended windshield can be generated. The wing shield uses the visibility pattern as the wireframe and later number of panels can be instantiated shown in Fig. 11.

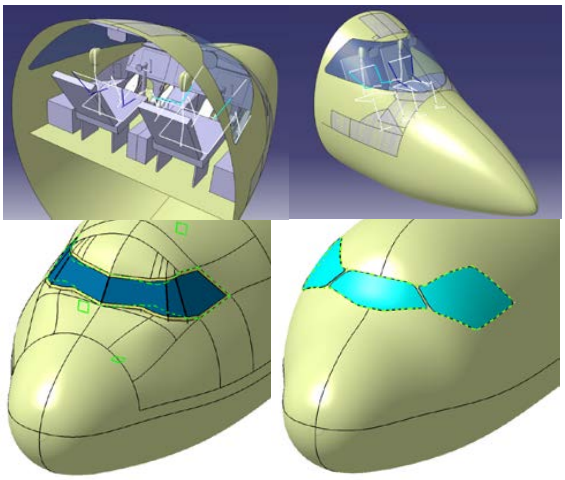

Fig. 11 Cockpit and Windshield model [16] [17]

4.2.2 Cabin Layout

Seating layout, Doors, windows, galley, lavatory, and containers can be configured from the cabin interior layout. FAR rules have been applied to all the entities listed above. The overall length of the cabin needed is computed and the user will know the cabin length available at all times. Depending on the number of passengers; type of galley, number of galleys, and number trolley in each galley and number of food trays needed are computed. The weights of first class, business class and economy seats are computed after instantiation.

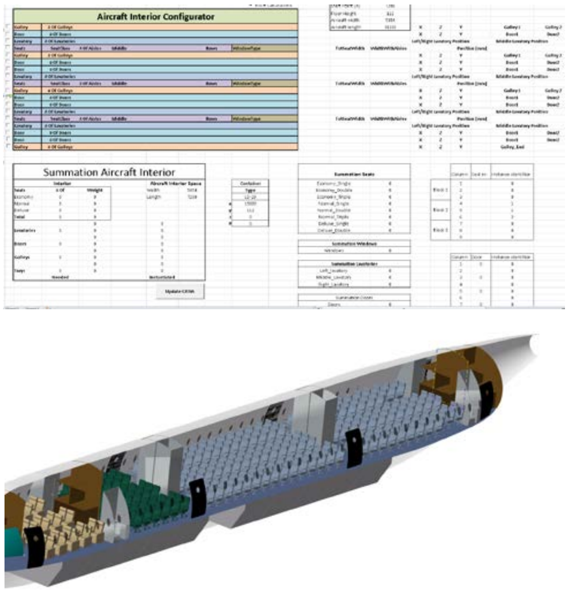

Fig. 12 Cabin Layout Interface and Cabin Interior

5 Applications

5.1 The Jet Family Project

In the course “Aircraft Conceptual Design” assignment was to design a family of turbofan powered aircraft according to FAR 25. The aircraft family includes three family members. The number of seats range from 75 to 110 (design payload), at 32 inch pitch, but high density versions had to allow two more rows of seats and seat pitch of 28 inches. In addition to this a two class internal layout had to be studied. The two classes were business and economy. 15% of the passengers in each version had to be seated in business class and the rest in economical class. The seat pitch in business class was 34 inches and in economy class, 30 inches. The family of aircraft had to be equipped with one and the same wing. The assignment also includes a study on how an optimal aircraft should be designed (for each family member) and how much you lose in weight and efficiency by keeping the wing unchanged. Interior design for this assignment was very important (as for all designs) as it leads to the length of the cabin. It includes a study on the number of doors and sizes required for different family members.

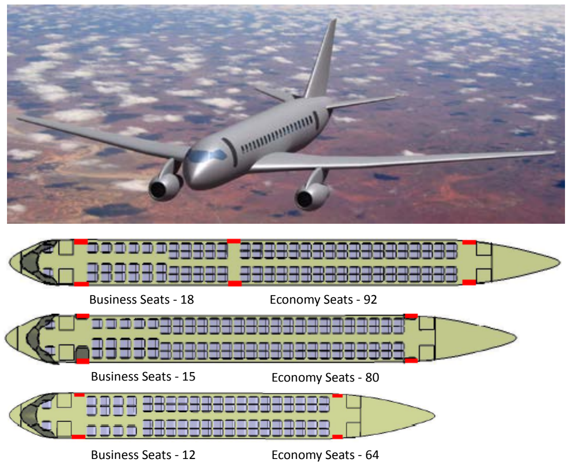

Fig. 13 One of the student aircraft and interiors with two class seating configurations and an artistic view of the aircraft.

It is also important to provide the required spacing at the emergency exits for evacuation. Number of toilets, galleys and the number of cabin crew required for the different family members also needs to be figured out. Where to put and access passenger luggage and cargo on the aircraft needs to be addressed. Also to consider all kinds of ground handling while on the ground, i.e. the possibility to service the aircraft by means of different vehicles during ground stop.

- M_{des} : 0.82 at 35000 ft for all family members
- Range : 2500 NM at design payload for in-between member of the family
- Reserves : 200nm + 30 min holding
- T-off field length (SL, ISA +20) max : 1900 m for all members
- Landing field length (SL, ISA +15) max: 1500m for all members
- Individual passenger weight (including luggage) : 110 kg
- Pilots including personal luggage : 104 kg each
- Attendants (including personal luggage) : 100 kg each

5.2 The Mid-Jet aircraft Project

The Mid-Jet project was to build a aerobatic, aesthetic, striking and overwhelming single seat sport jet. To test and demonstrate the flight performance and characteristics a scaled model was built. As a first part of the project, a study was conducted on the existing single seat sport jets and later came up with different concepts. Many different concepts were studied from each team in the group, finally one concept was chosen for further studies. A conceptual design had been performed for full scale version. The initial model was built in RAPID. Later on many different features had been added during the detail design process. A demonstrator was built and tested with a scaled down version.

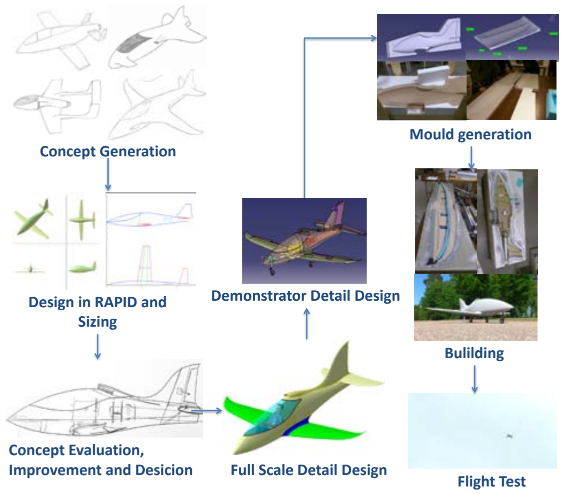

Fig. 14 Mid-Jet aircraft project process

6 Conclusion and Future work

This paper shows it is possible to communicate between the analytical tool and the CATIA environment and doing it both ways. Knowledge based automated design of RAPID is presented along with its applications. Different types of aircraft configurations can be obtained with less effort. As RAPID is developed based on relational design, any changes made to the geometric model will update the entire design. Different cross-sections and airfoils can be obtained for fuselage and wing like features respectively. An initial size of the engine is obtained from the engine sizing, nacelle and pylon can be shaped accordingly. The geometry model is well defined to carry over to the preliminary design. Details such as cockpit model, windshield, fairings, winglets, interior layout can be observed at early stages of design. An XML database is used to save the design data and also communicate with Tango.

Future work includes weight estimation, drag calculation, structural design, optimization. An improvement in the existing structural model and aerodynamic model is needed to update the mesh automatically so that it can be used in optimization framework.

Acknowledgement

NFFP, The Swedish National Aviation Engineering Programme [1], has provided funding for this project. The authors thank the NFFP founders for this support.

The authors would also like to thank the students of Aircraft Conceptual Design and Aircraft Project courses of the Linköping University for their excellent work during the courses.

References

[1] VINNOVA, Swedish National Aviation Engineering Research Programme, http://www.vinnova.se/en/Our-activities/Cooperation-Programmes/National-Aviation-Engineering-Research-Programme/

[2] Raymer D. RDS-student: software for aircraft design, sizing, and performance, Volume 10, AIAA education series, Washington DC, 2006

[3] CEASIOM. Computerised Environment for Aircraft Synthesis and Integrated Optimisation Methods software, http://www.ceasiom.com

[4] PADLab software, http://www.luftbau.tu-berlin.de/menue/forschung/padlab/

[5] Hahn A. Vehicle Sketch Pad: Parametric geometry for conceptual aircraft design, *Proc 48th AIAA Aerospace Sciences Meeting*, Orlando, Florida, 2010

[6] Ziemer S. A conceptual design tool for multi-disciplinary aircraft design, *Proc Aerospace Conference*, IEEE, Big Sky, *Montana*, USA, 2011

[7] j2 Universal Framework, http://www.j2aircraft.com/

[8] ADS – Aircraft Design Software, http://www.pca2000.com

[9] Piano , Aircraft design and Competitor Analysis http://www.piano.aero/

[10] Desktop Aeronautics, http://www.desktop.aero

[11] Staack, I., Raghu Chaitanya, M. V., et al., "Parametric Aircraft Conceptual Design Space," *Proc 28th Congress of the International Council of the Aeronautical Sciences*, Brisbane, Australia, 2012.
[12] Amadori K., *"Geometry Based Design Automation: Applied to Aircraft Modelling and Optimization"*, Ph.D. Dissertation, Department of Management and Engineering, Linkoping Univ., Linkoping, No. 1418, 2012
[13] Tarkian, M., *"Design Automation for Multidisciplinary Optimization"*, Ph.D. Dissertation, Department of Management and Engineering, Linkoping Univ., Linkoping, No. 1479, 2012
[14] Melin. T, Parametric Airfoil Catalog, Part I, Linköping University, ISBN: 978-91-7519-656-5, 2013
[15] Rajendran. S, Design of Parametric Winglets and Wing tip devices : A Conceptual Design Approach, M.Sc Thesis, Linköping University, 2012
[16] Tassel. W, Development of a Complete Parametric CAD Model of a Cockpit Layout for Civil Airplane Under CATIA CAD Software, M.Sc. Thesis, Linköping University, 2010.
[17] Singh A N., and Govindarajan V K., Raghu Chaitanya M V., Petter Kurs, "Knowledge Based Design Methodology for Generic Aircraft Windshield and Fairing - A Conceptual Approach", *51st AIAA Aerospace Sciences Meeting including the New Horizons Forum and Aerospace*, Grapevine, Texas, USA, 2013
[18] Roskam. D., *Airplane Design Volume 2*. Kansas: Roskam Aviation and Engineering Corporation, 1985
[19] FAR Rules: http://www.faa.gov/
[20] Raghu Chaitanya, M. V., Staack, I Krus P., "Integrated Aircraft Design Network", *Proc CEAS European Air and Space Conference*, Linköping, Sweden, 2013.
[21] XML: http://www.w3.org/
[22] CATIA V5 R21: http://www.3ds.com/
[23] Microsoft Excel : http://www.Microsoft.com/

4:th CEAS Air & Space Conference
FTF Congress: Flygteknik 2013

Integrated Aircraft Design Network

Raghu Chaitanya. M. V, Ingo Staack, Petter Krus
Linköping University, SE-58183, Linköping, Sweden
raghu.chaitanya@liu.se

Keywords: *aircraft conceptual design, parametric modeling, Knowledge based, sizing, XML database*

Abstract

This paper describes the XML based multidisciplinary tool integration in a conceptual aircraft design framework, developed by the Division of Fluid and Mechatronic Systems (FluMeS), Linköping University. Based on a parametric data definition in XML, this approach allows for a full 3D CAD integration. The one-database approach, also conducted by many research organizations, enables the flexible and efficient integration of the different multidisciplinary processes during the whole conceptual design phase. This central database approach with a detailed explanation of the developed geometry description and the data processing, focusing on the CAD integration is presented. Application examples of the framework are presented showing the data build up and data handling.

1 Introduction

Information is generated by tools, normally coupled towards intern or proprietary data structures. In a multidisciplinary design process information has to be propagated among tools and has to be fully accessible to any tool at any time. This dilemma leads either to a central “one-tool” or a “one-database” approach.

The one-tool approach cannot solve the problem since it is not a practical and justifiable solution as different applications need different tools for different needs. Hence the best and optimal solution would be the one-database approach. RAPID and Tango are tools are being developed in CATIA and Matlab respectively, to address one-database approach. In order to maintain flexibility and allow the developer to choose the preferred work method, both programs are implemented in parallel. Switching between the two is possible at any time [1]. Within this framework traditional handbook methods [2] till [4] are employed in the design. Similar aircraft conceptual design programs, [5] till [9] are developed by research institutions, universities and companies.

2 Data Management

Data created in RAPID or Tango can be delivered in the “*eXtensible Markup Language*”, (XML) format [15]. XML allows applications to represent electronic documents or text data in an easy to understand and transferable format between programs.

XML is made up of markup tags and data to represent the information. An XML forms a tree structure, this makes it easy to retrieve data and find relationship between different information represented in the XML.

Transformation of XML Document is favorable performed by XSL Transformations (XLST). XSLT uses XPath language to navigate in XML documents. It can serve for complex translations such as element and attribute editing (add, remove, replace), rearrangement, sorting, perform tests and make decisions [15].

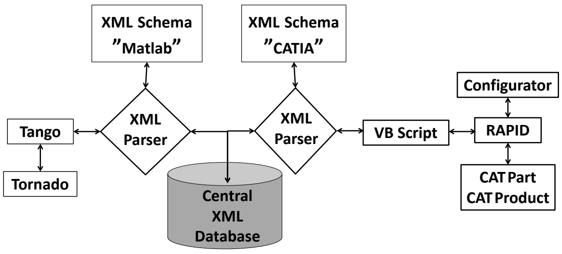

Fig. 1 XML data flow the two main applications RAPID and TANGO with the help of XSLT.

2.1 XML Integration

2.1.1 RAPID XML Export

Excel Visual Basic Application (VBA) is used to configure the CATIA [16] parameter or geometrical sets and generates into an XML. The following steps are implemented in creating XML from RAPID

- **Configuration of Parameter and Geometric sets through Excel:**
  Configuring the parameters through Excel will reduce the effort of adding changes to the code whenever a new parameter/geometrical set need to be added to the XML. The configuration contains three main parts in Excel:
  Parameter String: represents the parameter set/geometrical set from CATIA. All the parameters within the parameter set will be made as XML. Example: `reference\inputparameters`
  Parameter Array: used for making XML tags to the parameter sets or geometrical sets and parameters. Depending on the depth of the XML tree, number of values in the Array String is needed. Example: `XML node- <part name= "reference">`.
  Array List: Needed to put together parameter sets from the same part into one list. Each part will have one corresponding Array List. Example: `fuselage\inputParameters\&` `"fuselage\instantiatedGeometry\"` should come under the same part fuselage in XML. So they have same array list Name `fuselageList`.

- List "Hash", is a dictionary object [18] (key, value) that is used in the code because of the Array List column that comes from Excel. The Array List column gives only Array List Names but does not create them. This handles the grouping of the parameter sets with the same Array List into one list instead of separate ones. For the first time an array list for a given name is created, thereafter it does not create a new array list if the name already exists.

- **Value Parsing:**
  To parse the CATIA parameters and translate them to XML, two loops are used: The outer loop runs through all the parameter lists from CATIA and inner loop, runs through the parameter list of the Excel sheet. Strings from CATIA are compared with strings from Excel and the matching strings from CATIA are created as XML.

- **Writing into XML using DOM Object:**
  For efficient XML editing, Microsoft. XMLDOM object is used in the VBA section to translate the parameter/geometric sets into XML. The DOM object creates the XML file and takes care of the formatting and structure. This data set tree related access method also helps in modifying the XML without any hassles or cumbersome coding.

- **Spline from CATIA to XML:**
  The spline in CATIA cannot be handled similar to that of the rest of the parameter/geometrical sets, as the coordinates of the points in the splines are not available directly in CATIA tree. The geometrical set in CATIA is taken

as a parameter string from Excel, where the sketches are added. One array each is used to store the x, y, z coordinates of the spline control points from the `exchange Curves`. Example: `“fuselage\exchangeCurves”`.

- Finally the XML DOM object is written to file and saved as XML.

2.1.2 XML to RAPID Import

The following steps are performed to read XML to RAPID:

- **Parsing the XML using DOM object:** The XML file is loaded into a DOM Object. This DOM object is parsed for the required information and tags.

- **Recursive Function to get child nodes:** The values of parameters that need to be updated into CATIA are stored in the child nodes with a `value tag`. A recursive function is used to get all the child nodes with a `value tag` from the XML and the corresponding text in these nodes. These texts are the new values to be updated.
- **Constructing the Parameter Strings to be updated:** The parameter string that needs to be updated in CATIA needs to be constructed; a recursive function is used to get the parent nodes for the child nodes with the `value` tag. These parent node tags are appended along with “\” to form the string.

- **Spline from XML to CATIA:** The existing spline is deleted first. The spline values in XML are stored as Control Points with x- and y-value Nodes `(xvalue, yvalue)`. These Nodes are recursively read using DOM object. Using these x/y points, new Control Points are formed and then a new spline is created in CATIA

- **Updating CATIA:** The parameter Strings along with the corresponding values are updated in the CATIA using VBA – CATIA Functions.

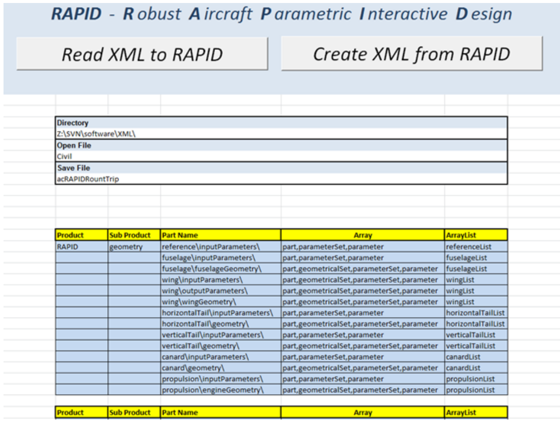

Fig. 2 The RAPID-XML Interface

2.2 Tango XML

Tango makes usage of the underlying Java DOM application classes in Matlab that serves for the XML data handling. This data is handled object oriented within geometrical or functional classes, so that every class includes the class-related XML parsing functionalities. This method allows for greater flexibility and fast replacement or appending of new classes.

The basic classes are product–geometry related arranged (e.g., wing and underlying wing partition class), whereas the higher level classes are product-functional (system) related (e.g., fuel system, primary flight control system). This class reference transition within the dataset makes it necessary to work with part pointers in order to link the functional classes with its related geometrical properties in the geometry related classes; Examples are the control surfaces (geo. def.) that are part of the PFCS (sys. def.) and the wing fuel tanks (geo. def.) that are part of the fuel/propulsion system (sys. def.). By these links, the strict hierarchal XML (tree) data structure becomes extended by cross-branch couplings, described by the part pointers.

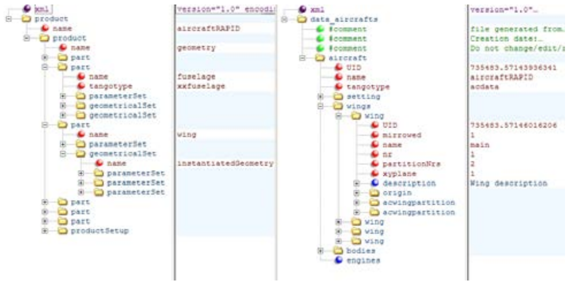

Fig. 3 Data Structure adapted towards the tools needs (Right side: Tango XML, Left Side: RAPID XML

3 Aircraft Geometry Data Description

Aircraft geometry is one of the most import features as it holds the entire information that is needed for the whole aircraft analysis. The aircraft data stored in XML format can be exchanged between different software, thereby decreasing the need and time to redo the aircraft.

3.1 Fuselage geometry description

The geometry is generated with the help of four splines namely `upper curve`, `bottom curve`, `side curve` and `center curve`. These splines form the base for the generation of the fuselage; later the number of frustums for the cross-sections definitions can be instantiated automatically depending on the necessity. Frustums are formed by joining two Bézier cubic curves at each end by means of a surface. The instantiated frustums can be modified to form a wide range of fuselage cross section geometries.

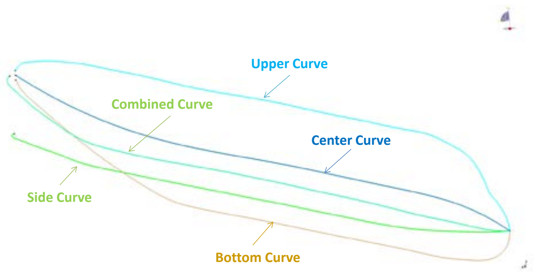

Fig. 4 The spline line fuselage curves

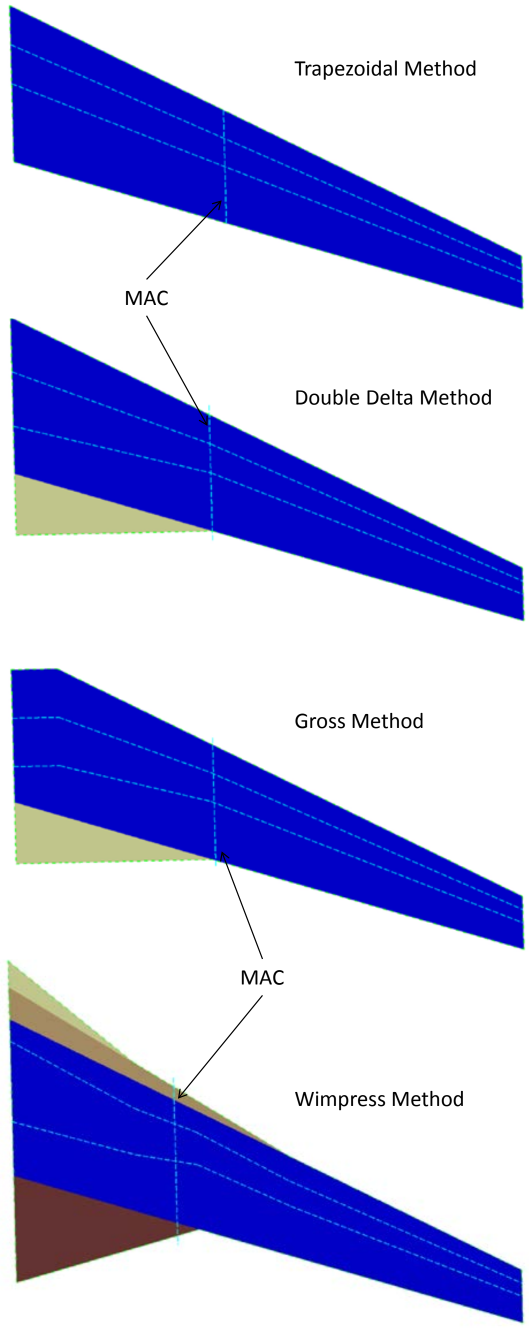

Fig. 5 The four different wing reference area methods used in RAPID

3.2 Wing geometry description

The reference area is the foundation to create a wing. Four different reference area methods are implemented [12]:

- Trapezoidal Method
- Double delta Method
- Gross Method
- Wimpress Method

During instantiation first the trapezoidal area is created, thereafter this area is used as a building block and the rest of the area methods are implemented as in Fig. 5. The wing boundary modifies itself depending on the specified reference area method. The number of wing partitions chosen by the user can be instantiated automatically. Each wing partition is formed by joining two airfoils by a surface. The airfoil is completely parametric and can be modified to obtain a wide variety of airfoils [10].

4 Framework approach

The flow of data between each discipline in a multidisciplinary design environment is coupled and saved in XML format [13] [14], and is accessible by all the required tools. The database definition (including several component libraries like functional assemblies) is parametrically defined in such a manner that a data refinement over time alongside the project is possible. In this way, a transition-less process from low or medium fidelity (in e.g. Tango) up to high fidelity (e.g., in RAPID) is realized as shown in Fig. 8

5 Application examples

This section shows the application examples of the framework, showing the data build up and data translation between RAPID and Tango and vice versa. Two examples have been tested to investigate the data flow processed in the correct approach. In RAPID, as the user has different options of reference area, this might be difficult to pick the correct method. A number of parameters are accessible for the user in order to obtain various configurations. This might lead to a geometry that is over-defined or has a lot of parameters to play with.

5.1 Example 1

In this example the double delta reference method is used. The cross-sections of the fuselage range from a circle to an ellipse. The data was successfully exchanged in both ways.

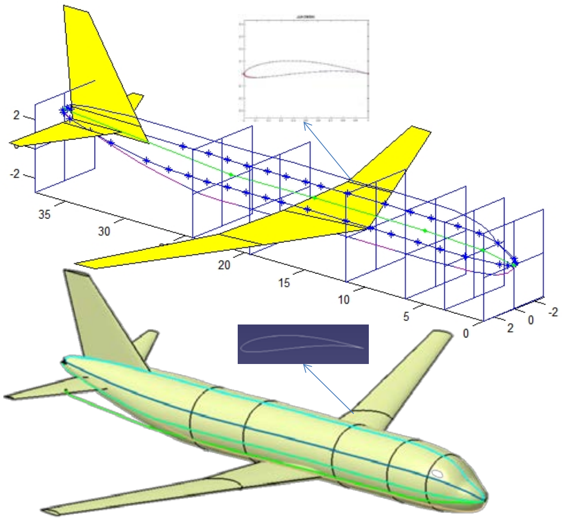

Fig. 6 Civil Aircraft in Tango (top) and RAPID (bottom)

5.2 Example 2

A much complicated fighter aircraft was selected to test as shown in Fig. 7. Data exchange showed promising results. It is to notice that the data structure in the background of both examples is similar with modified parameters with added lifting surface “canard” in the fighter example.

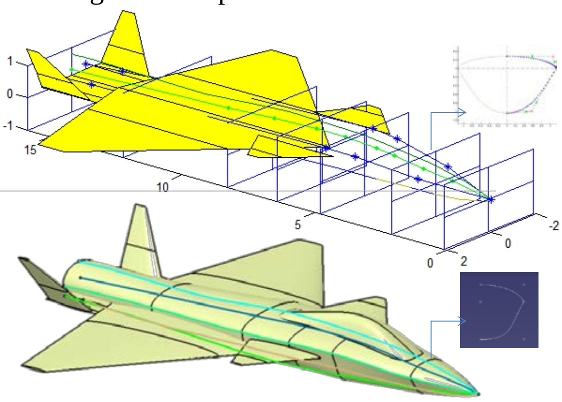

Fig. 7 Military Aircraft in Tango (top) and RAPID (bottom)

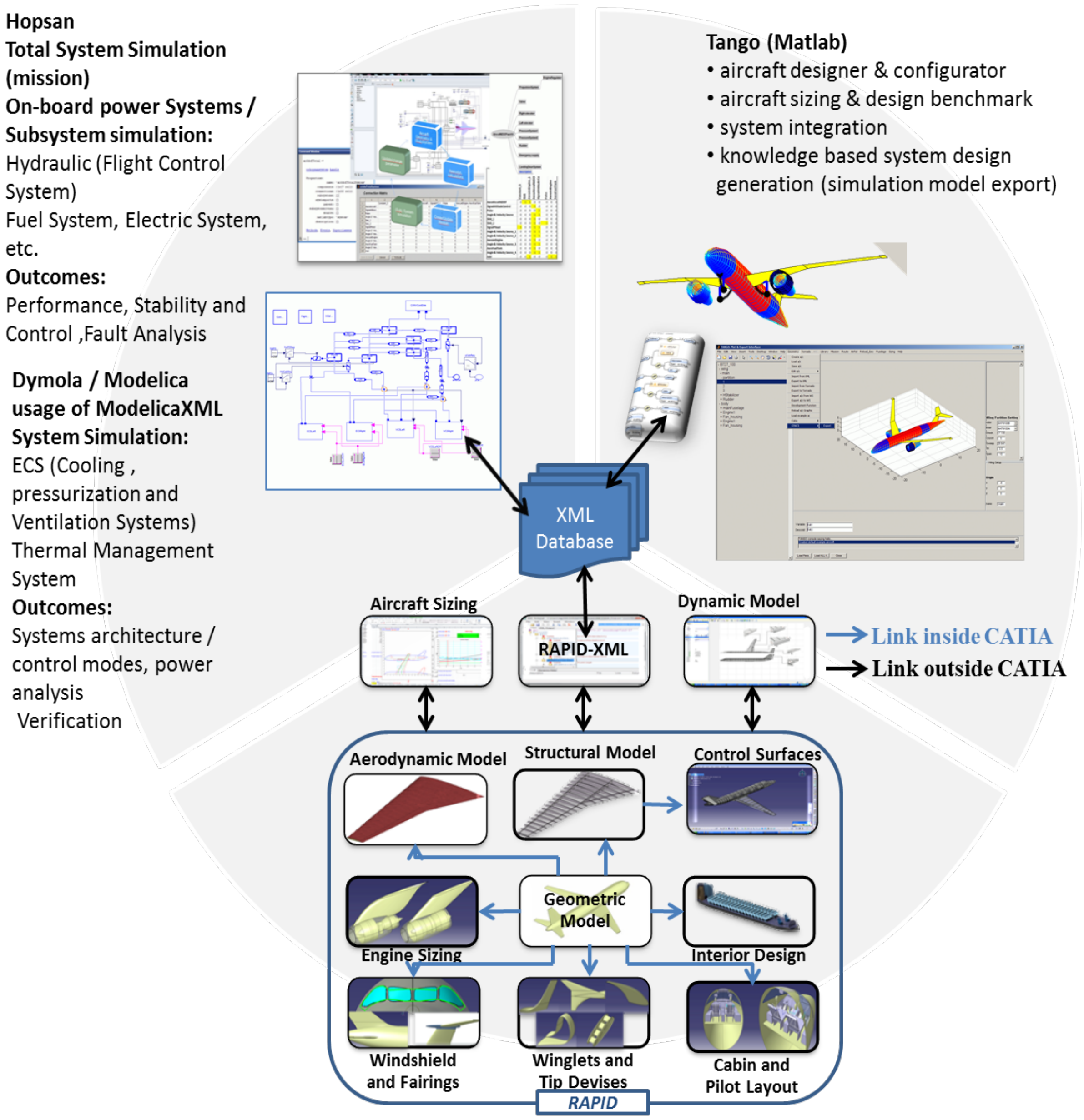

Fig. 8 Integrated Aircraft Design Network

6 Conclusion

The paper shows the multidisciplinary conceptual aircraft design analysis based on a central parametric XML database. This database -containing all project related data- is intended to grow simultaneously with the refined specification of the airplane.

Main advantage using XML is the easy and smart access from literally any programming language which makes it, together with the fact that it is human readable ASCII code, predestinated to be used in multidisciplinary and therewith multi-tool frameworks. These features serve for an easy adaptation and integration of new tools, scripts, etc. Due to the XML data tree structure, the developer has to arrange the data in a certain position, however the strict tree structure fit not totally towards the needs of a complex product as an aircraft; here, because of the transition of the class alignment from geometrical placement (low level) towards system description (high level), these trees have to be extended by cross-nodes pointers.

The 3D CAD description of this data setup is a small fraction of the original data needed in the CATIA environment to establish the geometry; here, extensive usage of knowledge base descriptions, namely *knowledge pattern* and *power copy* concepts are used. This method limits the design space in favor of a slim dataset consisting of rather significant parameters. This allows for a direct access of the geometry for other tools, like a geometrical optimization outside the CAD environment. The unified geometry makes meshing easier and serves for no aperture for high fidelity CFD analysis.

As proposed in Fig. 6 even simulation models can be generated out of the (mainly geometry) XML aircraft description.

Acknowledgement

Funding of this work was provided by NFFP, the Swedish National Aviation Engineering Program [11]. The contributing authors wish to thank the NFFP founders for this support. The First author would like to thank Krishnaveni Chitrapu for the helpful suggestion for XML creation from CATIA.

References

[1] Staack, I., Raghu Chaitanya, M. V., et al., “Parametric Aircraft Conceptual Design Space,” *Proc 28th Congress of the International Council of the Aeronautical Sciences*, Brisbane, Australia, 2012.

[2] Raymer D. Aircraft design - a conceptual approach, 5th edition, AIAA education series, Washington DC, U.S.A, 2012

[3] Roskam J. Airplane design- part1: Preliminary Sizing of Airplane, DARcoporation, Lawrence, 1985

[4] Torenbeek E. *Synthesis of subsonic airplane design*, Delft University Press, Delft, Netherlands, 1995

[5] Raymer D. RDS-student: software for aircraft design, sizing, and performance, Volume 10, AIAA education series, Washington DC, 2006

[6] CEASIOM. Computerized Environment for Aircraft Synthesis and Integrated Optimization Methods software, http://www.ceasiom.com

[7] PADLab Software, http://www.luftbau.tu-berlin.de/menue/forschung/padlab

[8] Hahn A. Vehicle Sketch Pad: Parametric geometry for conceptual aircraft design, *Proc 48th AIAA Aerospace Sciences Meeting*, Orlando, Florida, 2010

[9] Ziemer S. A conceptual design tool for multi-disciplinary aircraft design, *Proc Aerospace Conference*, IEEE, Big Sky, *Montana*, USA, 2011

[10] Melin. T, Parametric Airfoil Catalog, Part I, Linköping University, ISBN: 978-91-7519-656-5, 2013

[11] VINNOVA. Swedish national aviation engineering research programme, http://www.vinnova.se/en/Our-activities/Cooperation-Programmes/National-Aviation-Engineering-Research-Programme/

[12] Isikveren. A. T., Quasi-Analytical Modeling And Optimization Techniquiques For Transport Aircraft Design, Ph.D. Dissertation, Royal Institute of Technology (KTH), Stockholm, 2002

[13] Risheng Lin and Abdollah A. Afjeh, An XML-Based Integrated Database Model for Multidisciplinary Aircraft Design, Journal of Aerospace Computing, Information, and Communication 2004 1:3, 154-172

[14] Ho-Jun Lee, Jae-Woo Lee, Jeong-Oog Lee, Development of Web services-based Multidisciplinary Design Optimization framework, Advances in Engineering Software, Volume 40, Issue 3, March 2009, Pages 176-183, ISSN 0965-9978,

[15] http://www.w3.org/

[16] CATIA V5 Release 21, http://www.3ds.com/

[17] Microsoft Excel, http://www.Microsoft.com/

[18] http://msdn.microsoft.com

4:th CEAS Air & Space Conference
FTF Congress: Flygteknik 2013

Preliminary Design for Flexible Aircraft in a Collaborative Environment

Pier Davide Ciampa, Björn Nagel
German Aerospace Center (DLR), Germany

Darwin Rajpal, Gianfranco La Rocca
Delft University of Technology, The Netherlands

Keywords: *CPACS, Collaborative Design, DEE Initiator, Aeroelastic Engine, OAD*

Abstract

The work presents a collaborative design approach, developed to account for the structure flexibility effects in the pre-design stages of generic aircraft configurations. A streamlined design process is developed between DLR and TU Delft, to support the transition from an initial aircraft conceptual solution, to physics based simulations. The TU Delft DEE initiator is the conceptual tool providing the initial design, which is used to instantiate further analysis tool. An Aeroelastic Engine module is responsible for the abstraction of the aircraft structural properties, and the generation of the fluid-structure disciplinary couplings, necessary to account for the flexibility effects. Multiple distributed disciplinary solvers are available, and accessible via a decentralized architecture. All the analysis modules are integrated in the design workflow by means of the open source distributed framework RCE, and the DLR's central data model CPACS. The approach is tested for the pre-design of a conventional aircraft and a box-wing configuration, designed for a set of top level aircraft requirements. Hence, the flexibility effects for both cases are presented. The results demonstrate the importance of accounting for the flexibility effects already in the pre-design phase, especially in case of box-wing configurations, where difference in design performance can occur when ignoring such effects.

1 Introduction

The current visions and technology roadmaps on the future of the air transportation systems pose ambitious challenges for the design of the next generations' air vehicles [1, 2]. However, the assessment of game-changing technologies cannot rely on the conventional pre-design methodologies, which are primarily based on statistical data, and on the application of technology factors to account for potential benefits. Thus, in order to correctly assess the vehicles' behavior and performance, and to minimize the risks associated with the development of unconventional aircraft configurations, physics based simulations have to be included in the early stages of the design process.

Nevertheless, the sophisticated physics based analysis codes currently available in every aeronautical discipline, can be effectively used at the early stages, only if highly automated in the model pre-processing, analysis execution and post-processing of the results.

As identified in Ref.3, automated analysis capabilities relief the designer from allocating significant part of the development cycle to repetitive and non-creative tasks, and enable the large design space exploration required by unconventional designs.

However, state of the art aircraft pre-design systems are often based on automated, but monolithic design codes which cannot easily be managed, or adapted to cope with new configurations, or as new analysis modules become available [4]. The challenge is even higher if analysis modules developed by different parties are planned to be integrated within the same design process.

Further, as soon as the interdisciplinary dependencies are accounted into the design process, the application of MDAO (Multidisciplinary Design Analysis and Optimization) techniques can support the designers to correctly capture the overall aircraft's behavior. However, the introduction of physics based models into MDAO applications demands for disciplinary expertise within the aircraft design process, and for the cross-disciplinary consistency of the analysis models.

In order to cope with the mentioned challenges, DLR is developing a design environment to enable collaborative MDAO applications, within multiple internal projects [5], and with external institutions as well [6, 7].

This paper presents the implementation of a streamlined collaborative OAD (Overall Aircraft Design) process, which makes use of the design and analysis capabilities distributed between DLR and TU Delft, in order to support physics based simulations of conventional and unconventional configurations, already in the pre-design phase.

Among the many tools and disciplines involved in the process, the proposed design system includes a dedicated tool account for the flexibility effects due to the aero-structural interactions, already at the conceptual and preliminary design stages. In fact, although well-established methods are available for linear aeroelastic analyses of modern airplanes, there is still a limited capacity to bring them into the early stages of the design process [8]. Typically the postponed assessment of these effects to the later design stages, adds an "aeroelastic penalty" to the final designed structure [9, 10], and it may even lead to a complete redesign process for novel aircraft. One of the goals of this work is to assess the effect of accounting the flexibility effects in the early design phase, which, as discussed in Section 4, are particularly significant in case of unconventional aircraft such as box-wing configurations.

The integration of the disciplinary modules, such as the aerodynamic and the structural solvers, and the coordination of the workflow governing the fluid structure interactions, is implemented by making use of a centralized data model CPACS (Common Parametric Aircraft Configuration Schema), and the DLR open source framework RCE (Remote Computer Environment).

A brief introduction to the collaborative design environment architecture and to the central data model CPACS is provided in Section 2. The design and analysis components are presented in Section 3. Section 4 describes the application of the process for two test cases, a conventional and a box-wing aircraft configuration and discusses the results. Conclusions and outlook are provided in Section 5.

2 Collaborative Design Environment Architecture

Distributed design approaches [13] offer the flexibility to adapt the design workflow, when new design modules become available, and to tailor the scope of the design investigation. The German Aerospace Center (DLR) has been developing a decentralized design environment to foster the collaboration among disciplinary specialists and the integration of disciplinary expertise into a collaborative overall aircraft design process. The design environment is built on the central data model CPACS (Common Parametric Aircraft Configuration Schema) [11, 12], an arbitrary number of analysis modules, and on the open source design framework RCE (Remote Component Environment) [13], enabling the orchestration of the design workflows.

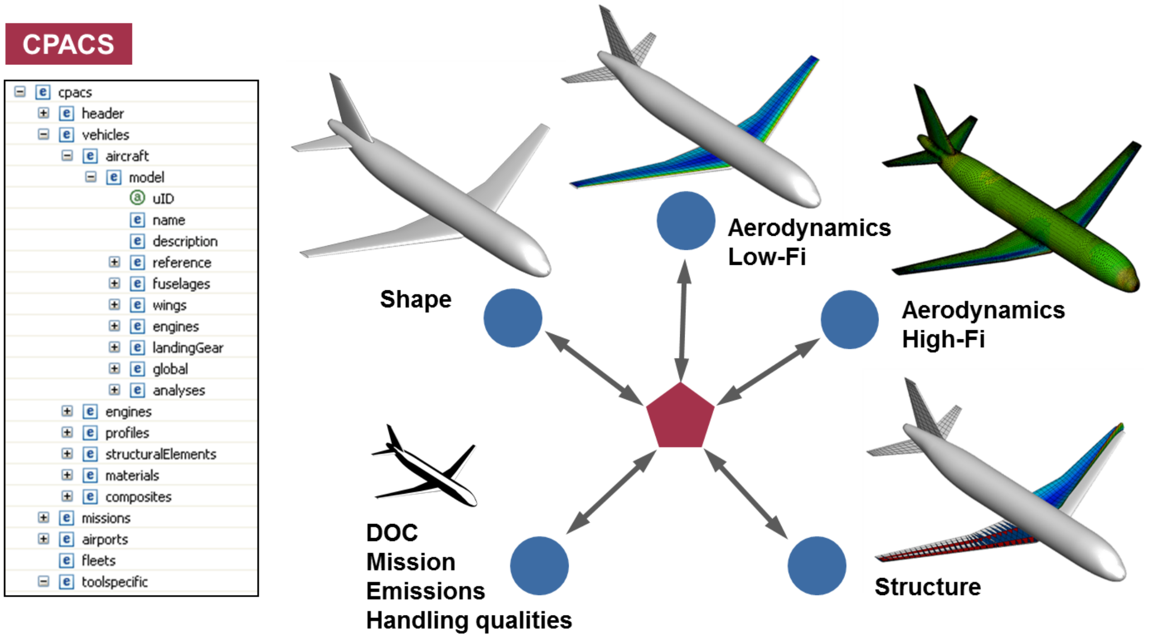

Fig. 1 CPACS (Common Parametric Aircraft Configuration Schema) concept.

CPACS is a data format based on XML technologies, and used for the interdisciplinary exchange of product and process data between heterogeneous analysis codes and name spaces. CPACS contains data such as the geometry of the aircraft model, but also all the parameters needed to initialize and to drive the disciplinary analysis modules, for instance the aerodynamic and the structural solvers. Figure 1 depicts the CPACS concept as a unique data structure, instantiating the disciplinary analysis modules.

The framework RCE enables the orchestration of the design process, and integration of the analysis modules in a workflow. The RCE architecture is based on a decentralized computing system, in which the analysis competences are hosted and run on dedicated servers. Thus, in the design workflow only input and output data are made accessible to the integrator designer, and exchanged during the process, whereas the source codes are controlled by the tools' developers and the disciplinary experts. The system is in operational use in all the DLR aeronautical branches [14, 15], and with external research and academic institutions [6, 31].

3 Overall Aircraft Design (OAD) of flexible aircraft

Typically, during the conceptual aircraft development, many design details are not available, and the overall aircraft synthesis relies on the definition of TLAR (Top Level Aircraft Requirements), such as transportation mission and operational constraints, and on the output of overall aircraft parameters, such as MTOW (Maximum Take Off Weight), aerodynamics efficiency, etc. [16, 17]. Nevertheless, the actual blending of the pre-design activities into the conceptual phases is pushing the development of more sophisticated conceptual design engines, which are capable to instantiate models with number of details beyond the typical conceptual stages [18,19]. Nevertheless, including physics based aeroelastic analyses in these early stages, has to cope with the challenge to generate the appropriate analysis models in a time efficient manner, and guarantee the automated couplings among the heterogeneous disciplinary abstractions.

Further, the shift to physics based analysis at the beginning of the design cycle is associated with the increase of the "aircraft modeling complexities” [20], typically leading to an increased number of the design variables, and a higher domain expertise required to set up the analysis parameters.

Hence, in an OAD application the designers’ team faces the following challenges:

- Generation of an initial design, with a sufficient quality, and details, to serve the instantiation of further physics based analysis modules
- Automate the setup of an increased number of parameters, and design variables, associated to execution of the physics based analysis modules;
- Handle and setup consistent disciplinary couplings in MDAO applications, for a multitude of heterogeneous analysis tools.

The aforementioned challenges depend on the complexity of the modeling, and on the physics phenomena representation supported by the disciplinary analysis. Hence the following disciplinary levels can be identified:

- level 0: consisting of typical conceptual OAD approaches, based on empirical relations, and existing databases [16, 17];
- level 1: refers to disciplinary analysis based on simplification on the modeling, and on the representation of the physics phenomena, mainly accounting for linear effects;
- level 2: refers to an accurate modeling of the aircraft components, accounting for a higher level of details, and physics representation accounting for non-linear phenomena;
- level 3: refers to the state of the art of physics simulations, mainly dedicated to non-linear local effects, and whose disciplinary models cannot be fully automated, as required for extensive MDAO applications.

The introduced levels classification is indicated in Table 1, with focus on the aero-structural applications.

Table 1 Disciplinary Levels Classification

Level	Aerodynamics	Structures
L0	Empirical performance estimation	Handbook masses estimation
L1	Subsonic analysis (VLM, Panel method)	Simplified models (FEM beam)
L2	Transonic nonlinear analysis (Euler)	Detailed models (FEM shells), non-linear analysis
L3	Nonlinear non automated (RANS)	Nonlinear local analysis (buckling, crash)

The current study focuses on the integration of L0 and L1, in OAD as a blended conceptual and preliminary design stage. The TU Delft DEE Initiator module is used to generate an initial design synthesis, providing a limited number of top level aircraft requirements. Hence the initial design is coupled via the CPACS format to the physics based modules, such as the aerodynamics and the structural solvers, whose results are integrated into the aircraft synthesis process, till convergence.

The next sections introduce the main aforementioned design modules.

3.1 DEE Initiator

The DEE Initiator [18] is a MATLAB based conceptual design tool able to generate a baseline aircraft configuration, starting from a limited set of top level requirements, such as payload size and arrangement, range, cruise speed, takeoff and landing field length. Apart from conventional turboprop and turbofan aircraft, the Initiator can deal with some non-conventional aircraft configurations, such as box-wing aircraft and blended wing bodies. This is a clear distinctive feature, which makes the Initiator different than any other commercial conceptual design tool currently available on the market.

The Initiator implements some of the classical aircraft synthesis methods available in literature, but integrates and supports them by means of simple geometry models generated on the fly, a vortex lattice aerodynamic simulation tool and an optimization toolbox. These “extra ingredients" make the design process much less dependent on statistics and allow addressing other concepts than conventional aircraft. As shown in Fig.2, the Initiator mainly consists of an initialization module, a geometry model generator, some analysis modules and an optimizer. The "Initiator's initiator", called Initializer, has the task of deriving a first aircraft guesstimate, based on pure statistical data. To this purpose the Initiator can automatically access a large and extensible aircraft data base, which includes also data of non-conventional aircraft configurations extracted from design studies available in literature.

Before proceeding with any further analysis, wing loading and thrust weight ratio are automatically adjusted using an optimization routine, to make sure the aircraft design point satisfies typical top level requirements, such as takeoff and landing field length, climb rate and gradients at OEI conditions, etc.

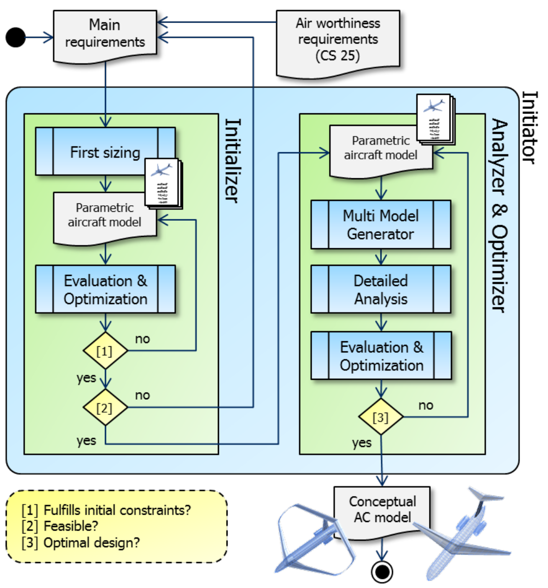

Fig. 2 DEE Initiator structure.

The Initiator geometry modeler is able to create simple aircraft models, where volumes, areas, distances, etc., can be extracted and used as input for the implemented semi-empirical analysis and sizing methods.

In particular, these geometry models are used to feed TORNADO, an open source vortex lattice method (VLM) suitable for conceptual design purpose. Although TORNADO is a low fidelity analysis tool, it allows the Initiator to account on more physics based aerodynamic results than those otherwise assumed based on statistics and generally only valid for conventional aircraft configurations.

A genetic algorithm optimizer has been developed on purpose to endow the Initiator with robust optimization capabilities. The Optimizer allows the designers to assess the impact of various objectives and constraints on the final design of the aircraft and its performances. The optimizer and the VLM tool are particularly useful for the initial sizing of joined-wing systems, where the relative positioning of the front and rear wing and their relative lift distributions need to be properly set to achieve proper stall behaviour and exploit the Prandtl's best wing system concept for minimum induced drag [21].

Some other of the Initiator analysis modules include a class I and class II weight estimation tool, a module for parasite drag estimation and a module for stability & control.

The Initiator can be operated both interactively, via an advanced GUI, and in batch mode. The latter functionality enables the Initiator to be integrated and operated via any workflow management system, such as RCE. Functionalities are in place to export all the generated values (geometry, weights, performance parameters, etc.) in form of Excel tables, or other formats, such as the CPACS described in the previous section.

In this study, the Initiator has been used to generate, starting from a set of top level requirements, two aircraft configurations: one conventional and the other featuring a box-wing system. The generated geometrical models for these types of configurations are shown in Fig.3. The models are thus exported into CPACS format, and can be used to initiate the higher fidelity design and analysis process which is described in details in the next sections.

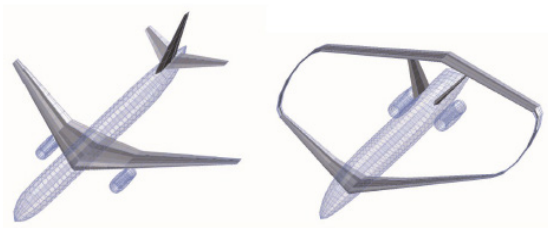

Fig. 3 Geometry models generated by the Initiator for a conventional and a joined-wing aircraft.

3.2 Physics based aeroelastic analysis

As soon as an initial design point is available, the model is advanced to the Aeroelastic Engine, a module developed to support the modeling and the analysis of the complete flexible aircraft for preliminary MDAO applications in a collaborative environment [22, 23]. The module provides hierarchy of physics based disciplinary models for the aeroelastic analysis, and supports the generation of the disciplinary couplings. Although complex analytical methods [24] exist for the structural analysis in the pre-design phases, the proposed investigation is based on the use of Finite Element (FE) representations to cope with unconventional designs. First function of the Aeroelastic Engine is to extract the structural properties that are needed for the aeroelastic modeling of the aircraft. This process, identified as *aeroelastic abstraction*, is dependent on the level of details of the disciplinary analysis involved in the modeling and analysis step. As a Level-1 model, the Aeroelastic Engine initializes the structural layout of the primary structures, extracts the structural properties of the complete aircraft, and finally assembles a multibody FE representation, based on a beam formulation. The primary structures of the lifting surfaces and of the fuselage components are identified, and beam's cross sectional properties (e.g., flexural and torsional stiffness) are derived from the geometry and from the explicit definition of the wingbox layout and fuselage's frames. Substructures, such as stiffeners, are taken into account by a smeared stiffness approach [25]. Figure 4 shows the assembled FE level-1 model produced by the module, for a conventional aircraft.

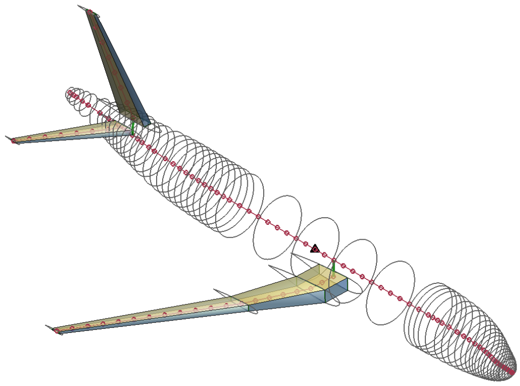

Fig. 4 Aeroelastic Engine FE level-1 Model Abstraction.

The level-1 formulation is part of a hierarchical set of models available for pre-design activities, which can be extracted from a unique centralized model definition [20, 26]. The Aeroelastic Engine provides an internal solver for the FE analysis and post-processing of the assembled models, in order to determine the displacements and the stress fields of the aircraft under multiple load cases. A number of sizing strategies, such fully stress design, and flexural buckling criteria, are implemented for the dimensioning of the selected primary structures.

3.3 Flexibility effects

In order to account for the aircraft flexibility effects, the fluid-structure interactions (FSI) need to be considered in the aero-structural analysis and sizing process. The aero-structural coupling is implemented by first mapping the aerodynamics forces on to the structural model, and then transferring the computed displacements on the structural nodes to the aerodynamic geometry. In a collaborative environment, loosely coupled analysis tools, such as the ones for the aerodynamics and for the structural analysis, are generally employed, with the consequent challenge of automating the generation of the necessary coupling links. The Aeroelastic Engine employed in this research is designed to accelerate the integration of the aero-structural discipline models by automating the required coupling operations on the base of the fidelity of the aerodynamic and structural solvers involved, and the setup of few parameters from the designer side. In the current study an available level-1 VLM aerodynamics tool, interfaced with CPACS [26], is used to estimate the aerodynamics efficiency at various conditions of the flight envelope, and to provide the aerodynamics loading distribution on the lifting surfaces, as resulting from the critical design maneuvers.

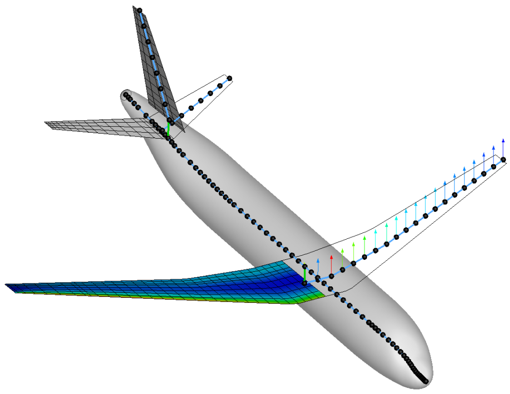

Fig. 5 FSI coupling provided by the Aeroelastic Engine. VLM lattice and pressure distribution (starboard), FE nodes, and nodal forces (port)

Figure 5 shows the results of overlaying the disciplinary models. The aerodynamics mesh and the calculated pressure distribution are shown on the starboard side of the aircraft; whereas the structural FE model is shown for port side. Further on the FE nodes of the main wing are shown the aerodynamics loads, as resulting from the mapping schema from the VLM lattice to the structural grid. Figure 6 shows the structural nodal displacements of the FE model due a test wing-fuselage loading case, and the propagation of the displacements on the geometry, via mesh deformation techniques available in the module, applied directly on the initial geometry, or on the disciplinary grid.

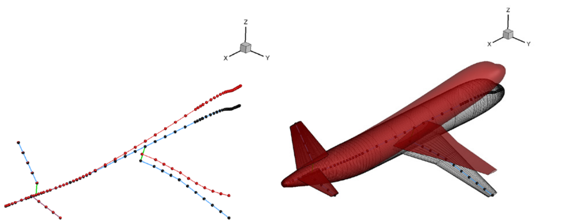

Fig. 6 a) FEA nodal displacements b) Aero-structural deformation propagated to the initial geometry.

The level of automation provided by the Aeroelastic Engine offers the possibility to iterate between the aero and the structural model, hence enabling designers to account for the flexibility effect in the early aircraft design phase.

4 Study cases

The next sections describe the implemented workflow, and two design cases. A tube and wings configuration, and a box-wing design have been selected to demonstrate the ability to address both conventional and unconventional configurations, when using physics based analysis tools.

4.1 Design Workflow

Starting with a minimum set of inputs, such as the transport mission requirements, the DEE Initiator module determines the initial estimation of the aircraft performance for the given design mission, such as the required fuel mass, and the aircraft dimensioning. Hence the initial design is forwarded to the physics based analysis modules, for the aero-structural sizing loop provided by the Aeroelastic Engine.

A 2.5 g pull-up maneuver is selected as critical loading condition, and the aero-structural sizing of the primary structures is performed under fully stressed design constraints, as typical of preliminary aircraft design. The use of the Aeroelastic Engines to size the wing allows to account for a physics based mass estimation.

The aerodynamic performance of the initial design is then calculated, accounting for the structure flexibility effect by means of the Aeroelastic Engine. The FSI coupling is taken into account to determine the lift and drag coefficients of the aircraft, for relevant combinations of angle of attack, Mach and Reynolds number. Hence, the updated aircraft aerodynamic performance, corrected by the flexibility effects, is used to update the overall aircraft design process, and the new aircraft synthesis computes new values of MTOW, and fuel weight. Hence, the design is reanalyzed through the physics based segment of the design process. The multifidelity synthesis loop will continue till the convergence of the design masses [28]. A schematic of the implemented workflow is shown in Fig.7.

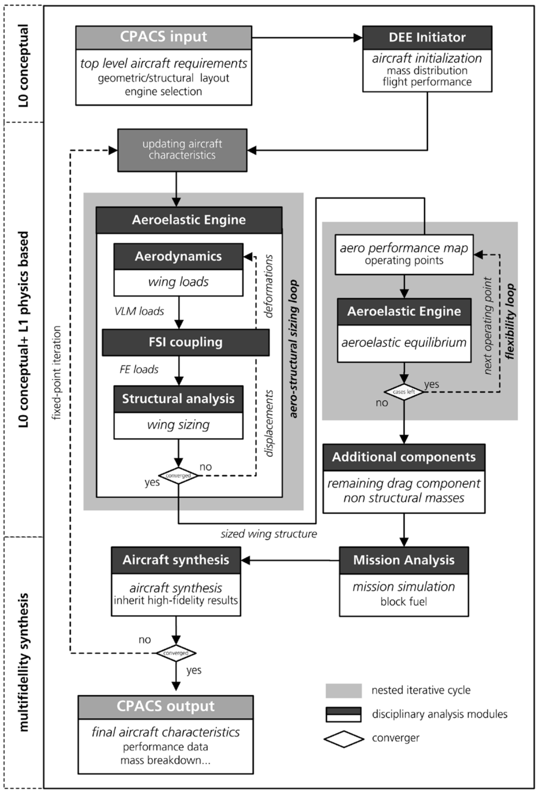

Fig. 7 Design process workflow.

The developed OAD workflow provides a significant level of flexibility, and can be executed with the following modalities:

- Only conceptual design, and excluding the physics based modules in the OAD synthesis: labeled as *L0 design process*;
- Conceptual and physics based design modules, whose analysis results are used to update the OAD synthesis. Although the aero-structural L1 solvers are employed for the structural sizing, the flexibility correction on the aerodynamic performance is excluded: labeled as *L0 + L1 Rigid design process*.
- Conceptual and physics based models, including the flexibility loop in the OAD synthesis: labeled as *L0 + L1 Flexible design process*.

In this, way the designer can tailor the process according to required level of accuracy and/or computational speed.

4.2 Conventional configuration

The conventional configuration is designed to satisfy the TLAR established for the collaborative design challenge, launched during the 2nd symposium on Collaborative Aircraft Design, held in December 2012 at DLR, Hamburg [29].

Among the others, the main mission's requirements are a design range of 2000 nm, at Mach 0.79, with 190 passengers. Although the set of TLAR is sufficient for the conceptual synthesis, additional tools' specific inputs are required for the other disciplinary modules, e.g. materials allocation, selection of the propulsion system technologies. Table 2 provides an excerpt of the design requirements, and other properties used for the aero-structural sizing.

Table 2 TLAR design challenge.

Parameter	Value
Design range (nm)	2000
PAX	190
Mach cruise	0.79
Initial climb	FL 350
Pull-up maneuver n	2.5
σ (MPa)	326
τ (MPa)	242

The overall aircraft synthesis is repeated three times: only conceptual design process (L0 level), conceptual and physics based (L0 + L1 level) with and without flexibility effects. Figures 8 shows the design solution as synthesized by the DEE Initiator, exported as CPACS format, and visualized by the CPACS geometry interpreter TIGLViewer [30]. Figure 9 shows the disciplinary models generated by the analysis tools, namely the aerodynamics VLM lattice for the lifting surfaces, and the FE beam model of the aircraft. The nodal deflections are also shown for the main wing, under the critical sizing load case. The results of the OAD process, such as the take-off mass (mTOM), and fuel mass (mFM), for each of the three synthesis cases, are reported in Table 3.

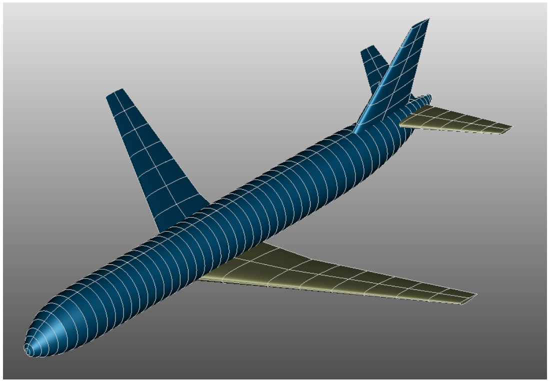

Fig. 8 CPACS Conventional aircraft generated by the DEE Initiator, as visualized in TIGLViewer.

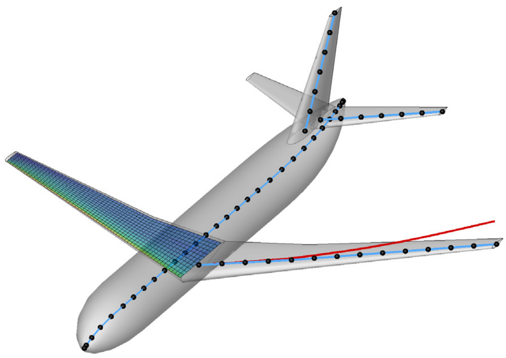

Fig. 9 Aeroelastic Engine VLM lattice (with pressure distribution) and structural model (with nodal displacements shape) of the initial conventional.

Table 3 OAD results Conventional configuration.

OAD	Conceptual L0	Conceptual L0 + Physics based L1	
	Initial	Δ^1 Rigid %	Δ^2 Flexible %
mTOM [kg]	83145.7	-13%	+1.5%
mFM [kg]	18947	-9%	+3%
OEM [kg]	45198	-17%	+1%

1: Δ% respect to initial OAD values
2: Δ% respect to rigid OAD values

The converged aircraft design masses show a difference between the L0 conceptual case, and the one including the physics based analysis. The main difference is in the operating empty mass (OEM) values, resulting by an under estimation of the computed structural masses. For a conventional configuration, conceptual design tools (L0) can provide very accurate results, since extensive database are available, and the synthesis process is calibrated on real aircraft data. On the other hand, physics based analysis would need to account for the simulation of a multitude of critical flight conditions and phenomena, to produce accurate results, without calibration factors. In the current chain a limited set of critical flight conditions, and failure criteria are taken into account, resulting in an under estimation of the sized structures. Nevertheless, the physics based chain enables the simulation of the aircraft physics behavior, by accounting for the deflected flying shape during the various mission segments. For an aircraft featuring a conventional swept-back wing system with moderate aspect ratio, the structural flexibility is known to result into a degradation of the aerodynamics performance respect to the rigid analysis [9], as shown as well by the results in Table 3. In fact the flexibility effect, when propagated through the OAD loop, generates an increase in fuel mass, and OEM in order to satisfy the defined TLAR.

4.3 Unconventional configuration

Additionally the described approach is applied for the analysis of a box-wing configuration. In order to have a reference model to evaluate the resulting designs, the set of TLAR is taken from an existing design from Ref. 30.

As for the previous design case, the aircraft is redesigned three times, using the different modalities offered by the implemented design systems.

Figure 10 shows the model generated by the by the DEE Initiator, and exported as CPACS.

Figure 11 shows the physics based analysis models, i.e. the aerodynamics lattice, and the FE model, and the wing system displacements produced by the critical loading condition.

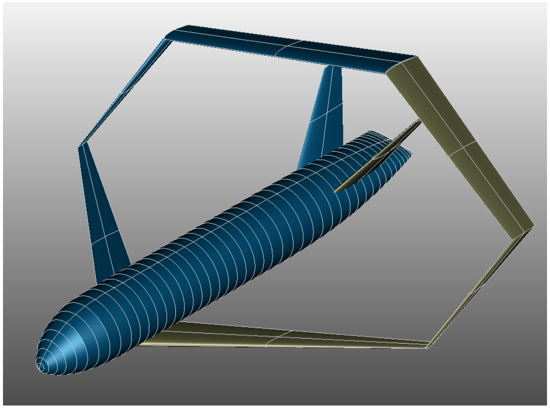

Fig. 10 CPACS box-wing aircraft generated by the DEE Initiator, as visualized in TIGLViewer.

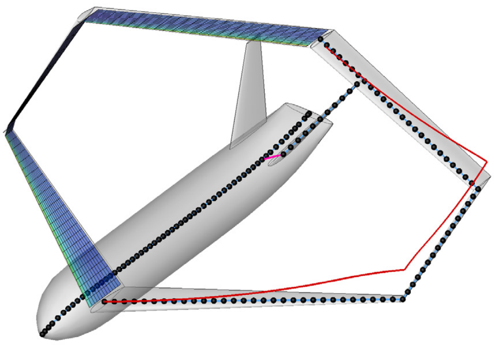

Fig. 11 Aeroelastic Engine VLM lattice (with pressure distribution) and structural model (with nodal displacements shape) of the initial box-wing design.

The results of the aircraft performance and converged design masses are shown in Table 4.

For this case the differences on the final design masses are very limited between only conceptual (L0 level), and the physics based case without flexibility (L0 + L1 rigid). The conceptual module includes in its database box-wing designs, whose data are the results of simulations as well, and it makes use of simplified physics calculation methods for the synthesis. Hence, the conceptual results are much closer to the results synthesis of the physics based approach. On the other hand, for this test case are more interesting the results when the flexibility effects are accounted in the OAD process (L0 + L1 flexible), which were not accounted for in the reference design. In contrast with the conventional case, the OAD synthesis of this specific box-wing design, results in lower design masses and fuel consumption when including the flexibility effects respect to the rigid analysis. It is necessary to point that the behavior of such a configuration is less predictable a priori by the designer, contrary to a cantilever wing type. Therefore, the aero-structural response could be design specific, and an extensive design space exploration using physics based analysis is required to generalize the exhibited trends.

Table 4 OAD results box-wing configuration.

OAD	Conceptual L0	Conceptual L0 + Physics based L1	
	Initial	Δ^1 Rigid %	Δ^2 Flexible %
mTOM [kg]	245551	+1.5%	-2%
mFM [kg]	77474	+1.3%	-2.8%
OEM [kg]	126327	+1.2%	-1.9%

1: Δ% respect to initial OAD values
2: Δ% respect to rigid OAD values

5 Conclusions and Outlook

The presented collaborative approach and the described design modules, aims at improving the conceptual/preliminary design process, for conventional and unconventional aircraft configurations. A physics based OAD process is developed by DLR and TU Delft, making use of distributed design modules, sharing the centralized parametrization CPACS, and connected by RCE framework. The proposed approach aims at enhancing the design process by accounting for the structure flexibility effects on the estimation of the aircraft performance and on the overall synthesis process. The proposed design approach is based on the use of the DEE Initiator, a conceptual aircraft design module capable to initialize also unconventional aircraft, and of the Aeroelastic Engine, a module developed to support loosely coupled aeroelastic analysis in collaborative MDAO applications. The assembled design system was tested for two design studies. The first study case, presents the OAD results of a conventional aircraft, designed to satisfy the TLAR specified in the collaborative design challenge.

Here the flexible effects have a marginal impact, and the degradation of the performance is expected by the designer. Further, the study highlights the complexities faced by the designer when introducing physics based analysis in the predesign stage.

The second case consists in the OAD of a box-wing configuration. For this design a purely conceptual approach is not sufficient to understand the aircraft physics behavior, and flexibility effects exhibit a large impact on the aircraft performance. Nevertheless, the shown response could be design dependent, and an extended exploration of the design space is necessary to capture and to generalize the trends. Further, only static aero-structural effects are accounted for in this study, and dynamic instabilities are expected to have a critical impact on the design results.

The proposed design process has shown to provide further insight into physics based modeling of aircraft at the early stages, and will be extended in future studies.

Additionally, the distributed approach contributes to the development of improved aircraft design methodologies, but also to the generation of a common, and understanding, between heterogeneous parties, on potential future aircraft configurations. A complementary study, making use of the developed design process, is presented in Ref. 33.

The synergy between the presented design competences is expected to increase in the next studies, encompassing additional design modules, and larger design space explorations, and optimization design cases.

Contact Details

Pier Davide Ciampa
German Aerospace Center (DLR)
Blohmstraße 18, 21079 Hamburg, Germany
Email: pier-davide.ciampa@dlr.de
Telephone: +49-40-42878-2727

References

[1] Report of the High Level Group on Aviation and Aeronautical Research "Flightpath 2050 Europe's Vision for Aviation", 2011.

[2] Strategic Research and Innovation Agenda (SRIA), Advisory Council for Aviation Reseacrh and Innovation in Europe (ACARE), 2012

[3] La Rocca, G., "Knowledge Based Engineering Techniques to Support Aircraft Design and Optimization", doctoral dissertation, Faculty of Aerospace Engineering, TU Delft, Delft 2011.

[4] Kroo, I., Manning, V., "Collaborative Optimization: Status and Directions", *8th AIAA Symposium on Multidisciplinary Analysis and Optimization*, Long Beach, 2000.

[5] Zill, T., Böhnke, D., Nagel, B., "Preliminary Aircraft Design in a Collaborative Multidisciplinary Design Environment", *AIAA Aviation Technology, Integration, and Operations (ATIO)*, Virginia Beach, 2011.

[6] Nagel, B., Böhnke, D., Gollnick, V., Schmollgruber, P., Rizzi, A., La Rocca, G., Alonso, J.J., "Communication in Aircraft Design: can we establish a common language?", *28th International Congress of the Aeronautical Sciences*, Brisbane, 2012.

[7] Pfeiffer, T., Nagel, B., Böhnke, D., Rizzi, A., Voskuijl, M., "Implementation of a Heterogeneous, Variable-Fidelity Framework for Flight Mechanics Analysis in Preliminary Aircraft Design", *German Aeronautics and Space Congress*, DLRK, 2011, Bremen, Germany.

[8] Livne, E., "Future of Airplane Aeroelasticity", *Journal of Aircraft*, Vol. 40, No. 6, 2003, pp. 1066-1092.

[9] Wright J. R., and Cooper, J.E, *Introduction to Aircraft Aeroelasticity and Loads*, AIAA Education Series, 2007.

[10] Howe, D., *Aircraft Loading and Structural Layout*, AIAA Education Series, 2004.

[11] Liersch, C.M., Hepperle, M., *"A Distributed Toolbox for Multidisciplinary Preliminary Aircraft Design", CEAS Aeronautical Journal*, Vol. 2, p. 57 – 68, Springer, 2011.

[12] http://code.google.com/p/cpacs.

[13] http://code.google.com/a/eclipselabs.org/p/rce/

[14] Nagel B., Zill, T., Moerland, E., Boehnke, D., "Virtual Aircraft Multidisciplinary Analysis and Design Processes – Lessons Learned from the Collaborative Design Project VAMP", *4th CEAS Air & Space Conference*, Linköping, Sweden, 2013.

[15] Moerland, E., Becker, R.-G., Nagel, B., "Collaborative understanding of disciplinary correlations using a low-fidelity physics based aerospace toolkit", *4th CEAS Air & Space Conference*, Linköping, Sweden, 2013.

[16] Torenbeek, E., Synthesis of Subsonic Airplane Design, Delft Univ Press, 1982.

[17] Raymer, D., Aircraft Design: A Conceptual Approach, 4th ed., AIAA Education Series (2006).

[18] La Rocca, G., Langen, T., Brouwers, Y., "The Design and Engineering Engine. Towards a

modular System for collaborative Aircraft Design", 28th International Congress of the Aeronautical Sciences, Brisbane, 2012.
[19] Rizzi, A., "Modeling and simulating aircraft stability and control The SimSAC project", Prog Aerospace Sci, Vol 47, 2011, pp.573-588.
[20] Ciampa, P.D., Zill, T., Nagel, B., "A Hierarchical Aeroelastic Engine for the Preliminary Design and Optimization of the Flexible Aircraft", *54th AIAA/ASME/ASCE/AHS/ASC Structures, Structural Dynamics, and Materials Conference,* Boston, 2013
[21] Frediani A. "The Prandtlplane", *ICCES04, Tech Science Press*, Madeira, Portugal, 2004, pp. 19-31.
[22] Ciampa, P.D., Zill, T., Nagel, B., "Aeroelastic Design and Optimization of Unconventional Aircraft Configurations in a Distributed Design Environment", *53rd AIAA Structures, Structural Dynamics, and Materials Conference*, Honolulu, 2012.
[23] Zill, T., Ciampa, P.D., Nagel, B., "A Collaborative MDO Approach for the Flexible Aircraft", *54th AIAA/ASME/ASCE/AHS/ASC Structures, Structural Dynamics, and Materials Conference,* Boston, 2013
[24] Ardema, M., Chambers, A., Hahn, A., Miura, H., and Moore, M., "Analytical Fuselage and Wing Weight Estimation of Transport Aircraft", NASA TR 110392, May 1996.
[25] Ciampa, P. D., Nagel B., and van Tooren, M. J. L., "Global Local Structural Optimization of Transportation Aircraft Wings", *51st AIAA Structures, Structural Dynamics, and Materials Conference 18th AIAA/ASME/AHS Adaptive Structures Conference*, Orlando, 12-15 April 2010.
[26] Nagel, B., Rose M., Monner H.P. and Heinrich, R., "An Alternative Procedure for FE-Wing Modelling", *Deutscher Luft- und Raumfahrtkongress*, Braunschweig, 2006.
[27] Rajpal, D., "Developement of Distributed MDO System for Non Planar Aircraft Studies", M.Sc. thesis, TU Delft, 2013.
[28] Böhnke, D., Nagel, B., Gollnick, V., "An Approach to Multi-Fidelity in Conceptual Aircraft Design in Distributed Design Environments", *32nd IEEE Aerospace Conference, Big Sky*, 2011.
[29] http://code.google.com/p/cpacs/downloads/detail?name=DesignChallenge.pdf
[30] http://code.google.com/p/tigl/
[31] Bottoni, C., Scanu, J., "Preliminary design of a 250 passenger PrantlPlane aircraft", M.Sc. thesis, University of Pisa, 2004.
[32] Boehnke, D., Nagel, B., Zhang, M., Rizzi, A., "Towards a Collaborative and Integrated Set of Open Tools for Aircraft Design", *51st AIAA Aerospace Sciences Meeting*, 07-10 January 2013, Grapevine, Texas.
[33] Ciampa P.D., Nagel B., Meng, P., Zhang, M., Rizzi A., "Modeling for Physics Based Aircraft Predesign in a Collaborative Environment", *4th CEAS Air & Space Conference*, Linkoping, Sweden, 2013.

4:th CEAS Air & Space Conference
FTF Congress: Flygteknik 2013

Modeling for Physics Based Aircraft Predesign in a Collaborative Environment

Pier Davide Ciampa, Björn Nagel
German Aerospace Center (DLR), 21089 Hamburg, Germany

Pengfei Meng, Mengmeng Zhang, Prof. Arthur Rizzi
Royal Institute of Technology (KTH), 10044 Stockholm, Sweden

Keywords: *CPACS, Collaborative Design, CPACScreator, CEASIOM, RCE*

Abstract

The work presents a collaborative design environment, developed to account high fidelity analysis in the aircraft pre-design stage for conventional and unconventional configurations. The approach build up on centralized model architecture, based on the DLR developed namespace CPACS, and on available CPACS compatible aircraft design competences, distributed among DLR and KTH, communicating each other via a distributed architecture. In the presented approach, the centralized model is generated by the CPACScreator, a management system under development at KTH, capable to instantiate in a time efficient manner CPACS models, which are suitable for high fidelity analysis. A design process is setup between DLR and KTH, to support the designer towards an all-physics based design, already at the early stages of the development. The multiple disciplinary solvers available are accessible via a decentralized architecture, and integrated in a collaborative workflow by means of the open source framework RCE. The approach is tested for the pre-design analysis of conventional and unconventional configurations. Results for both cases are presented.

1 Introduction

The current visions on the future of the air transportation systems pose ambitious challenges for the design of the next generations' air vehicles [1, 2]. Therefore unconventional aircraft configurations are currently investigated by the research and the industry communities. However, the assessment of novel aircraft technologies cannot exclusively rely on the conventional pre-design methodologies, which are primarily based on statistical data, and on the simple application of technology factors to account for the potential benefits. Thus, in order to minimize the development risks associated with unconventional aircraft designs, physics based simulations have to be included in the early stages of the design process.

The recent advancement in computational performance and simulation capabilities provide accessibility to sophisticated, and at the same time efficient analysis module, in all the aeronautical disciplines. Nevertheless, these codes are often not included in the aircraft pre-design activities, due to the complexity, and the time demand, faced by the designer's team to pre-process and to instantiate the multiple disciplinary specific models required during the Overall Aircraft Design (OAD) activities.

Further, as soon as interactions are accounted in the design process, the use of physics based analysis in MDAO (Multidisciplinary Analysis and Optimization) applications requires not only the disciplinary expertise, but also the management of the cross-disciplinary models consistency.

The need for a unified model triggering multiple analysis modules has been widely recognized in the aircraft design community.

Many successful integrated design systems have been developed, to automate the execution of the design process from top level aircraft requirement (TLAR), to a design solution [3, 4].

Nevertheless, state of the art of aircraft pre-design environmentss are often still based on automated, but monolithic design codes which cannot easily be replaces, or adapted to cope with new configurations, or when improved disciplinary analysis modules become available [5]. The challenge is even higher if analysis modules developed by different parties are planned to be integrated within the same design process. On the other hand distributed design approaches offer the desired flexibility, but need to guarantee consistency among the disciplinary abstractions generated within the design process.

In order to address the mentioned challenges, the DLR is developing a collaborative design environment, enabling the setup of distributed aircraft design process, based on heterogeneous physics based analysis modules. The core of the environment is the definition of the centralized model CPACS (Common Parametric Aircraft Configuration Schema), which is developed to foster the synergy between distributed design competences, simulation tools and experts [6]. Furthermore a number of analysis modules developed by different parties, are already CPACS compatible, and can be employed in developing distributed overall aircraft design workflows [7, 8].

This paper focuses on the challenges faced by the designer at the early stages of the development, in the setup of a physics based collaborative aircraft design process.

A centralized management system under development at KTH, named CPACScreator, is included in the process, and allows the efficient generation of CPACS models oriented to high fidelity analysis. Hence a collaborative process is developed between DLR and KTH, to support the physics based pre-design of conventional, and unconventional configurations.

The integration of the disciplinary modules, such as the aerodynamic and the structural solvers, and the coordination of the design process are implemented in a workflow by making use of the DLR open source framework RCE (Remote Computer Environment).

A brief introduction to the collaborative design environment architecture and to the central data model CPACS is provided in Section 2. The challenges for physics based modeling, and the CPACScreator management system is presented in Section 3. Section 4 describes the collaborative workflow and the distributed analysis competences. Two aircraft configurations, a conventional and an unconventional design, serve as study cases for described approach, and the analysis results are presented in section 5.

2 Collaborative Design Environment

The German Aerospace Center (DLR) has been developing a decentralized collaborative design environment to foster the collaboration among disciplinary specialists, and the integration of disciplinary expertise into a collaborative overall aircraft design process [10, 11]. The design environment is built on the central data model CPACS (Common Parametric Aircraft Configuration Schema) [12], an arbitrary number of analysis modules, and on the open source design framework RCE (Remote Component Environment) [13], enabling the orchestration of the design workflows. CPACS is a data format based on XML technologies, and used for the interdisciplinary exchange of product and process data between heterogeneous analysis codes and name spaces. Figure 1 depicts the CPACS concept as a unique data structure, instantiating heterogeneous disciplinary analysis modules.

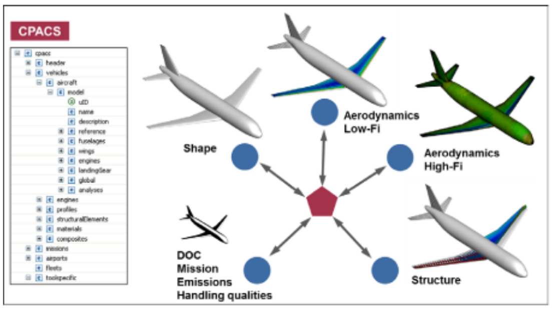

Fig. 1 CPACS concept.

The framework RCE enables the integration and the coordination of the analysis modules in the design environment. The system is implemented with a decentralized computing architecture, in which the analysis competences are hosted and run on dedicated servers, which are distributed among the disciplinary tools' developers. The system is in operational use in all the DLR aeronautical branches [9], and with external research and academic institutions [7, 14].

3 Modeling for physics based analysis

The collaborative design environment described extends the capabilities to assemble flexible design workflows, making use of heterogeneous disciplinary analysis modules.

Furthermore, the physics phenomena can be represented with a variable level of simplification, and of modeling details.

Hence the following classification is adopted to identify the disciplinary levels:

- level 0: consisting of typical conceptual OAD approaches, based on empirical relations, and existing databases [3, 4];
- level 1: refers to disciplinary analysis based on simplification on the modeling, and on the representation of the physics phenomena, mainly accounting for linear effects;
- level 2: refers to an accurate modeling of the aircraft components, accounting for a higher level of details, and physics representation accounting for non-linear phenomena;
- level 3: refers to the state of the art of physics simulations, mainly dedicated to non-linear local effects, and whose disciplinary models cannot be fully automated, as required for extensive MDAO applications.

The introduced levels classification is indicated in Table 1, with focus on the aero-structural applications.

Table 1 Disciplinary Levels Classification.

Level	Aerodynamics	Structures
L0	Empirical performance estimation	Handbook masses estimation
L1	Subsonic analysis (VLM, Panel method)	Simplified models (FEM beam)
L2	Transonic nonlinear analysis (Euler)	Detailed models (FEM shells), non-linear analysis
L3	Nonlinear non automated (RANS)	Nonlinear local analysis (buckling, crash)

The current study focuses on the design complexities which need to be tackled when physics based L1 and L2 analysis modules are introduced at the at the early design stages. A complementary study focuses on the L0 and L1 integration [27].

3.1 Modeling complexities in Aircraft Design

A main challenge when including high fidelity analyses in conceptual and preliminary OAD, is the capability to initialize, and to generate the dedicated disciplinary models in a time efficient manner. The robust automation of the modeling is the key to enable the large exploration of the design space, required by the design of unconventional configurations.

However, the shift to higher fidelity analysis at the beginning of the design cycle is also associated with the increase of the "aircraft modeling complexities" [15]. Respect to the traditional conceptual approach, these can be translated into several challenges faced by the designers at the beginning of the design process:

- Generate a “high quality” representation of the aircraft geometries, supporting the abstraction of appropriate disciplinary models;
- An increased number of parameters, and design variables, associated to the set up and execution of the physics based analysis;
- The initialization of a higher number of details to be provided, and leading to an increased number of effects to be included in the design process;
- Ensuring the robustness of the centralized model, through the variations driven by parametric and optimization processes;
- Ensuring the disciplinary expertise support, to setup consistent disciplinary couplings in MDAO applications.

The generation of geometries for unconventional aircraft configurations, such as for the Blended Wing Body, and boxwing, is an example of increased complexity the designer has to face, due to the high number of interconnected and integrated parts. Hence a conventional parametrization may not be sufficient to describe the configuration at the early stages, or may not be mapped to the input data set required by a conceptual aircraft design tools.

A second aspect to consider when introducing high fidelity analysis in OAD applications is the adequacy of the initialized aircraft model to be further processed by the physics based solvers. For instance from an aerodynamics perspective, the centralized model should contain enough information on the shape, to enable a seamless transfer to automated grid generators. Or enough details, to cope with the modeling of the control surfaces.

From a structural perspective, enough details could be translated into the explicit definition of the inner wings’ structural layout, such as spars and ribs, or even skin panels’ stiffeners.

Additionally, depending of the level of details modeled, different analysis solvers should be employed. For instance in the computation of the aerodynamics derivatives, the control surfaces’ deflections could be actually modeled by deforming the wing geometry around the hinge points, or they could be accounted as modified boundary conditions, depending on the solver capabilities.

Further, from a designer perspective, the details modeled, and the design criteria applied should be consistent in order to account for the right phenomena as design drivers. As example modeling explicit stiffeners would add additional benefits mainly if local buckling considerations are included during the sizing process.

From the aforementioned considerations it raises the need for a model management system, ensuring freedom and consistency when transferring the data included into a centralized model, to the distributed high fidelity analysis modules. A main effort to provide such a system within the CPACS community is under development at KTH, named as CPACScreator.

3.2 CPACScreator

The CPACScreator, derived from the SimSAC ACBuilder tool [16], is the management system, under development at KTH, supporting the aircraft designer in the generation of a centralized CPACS data models.

The CPACScreator works as a visual renderer and editor of the CPACS XML files, and it provides gateways into multi-fidelity aerodynamic and multi-disciplinary analysis for the CPACS models. CPACS and CPACScreator system can generate models with multiple levels of details, suitable for multidisciplinary and multifidelity analysis. All the functionalities in CPACScreator are implemented in MATLAB, including the 3D model rendering part. This feature promises easier real collaboration from distributed analysis modules.

The CPACScreator supports all the CPACS hierarchical structure, and it can fully display CPACS’s rich aircraft definitions, e.g. major aircraft components such as fuselages, wings, nacelles, and sub-components such as trailing edge devices, spoilers, spars, ribs, wing panels’ stiffeners, fuel tanks, and fuselage subcomponents, and it is continuously updated to be compatible with the new CPACS releases.

CPACScreator enables users to generate, and to modify all the geometry parameters in an interactive and graphical way. In CPACScreator, all the geometry parameters are represented on CPACScreator's panel, which can be modified by the users and the 3-D model will be updated instantaneously for each action.

CPACScreator main graphical panel is shown in Fig. 2.

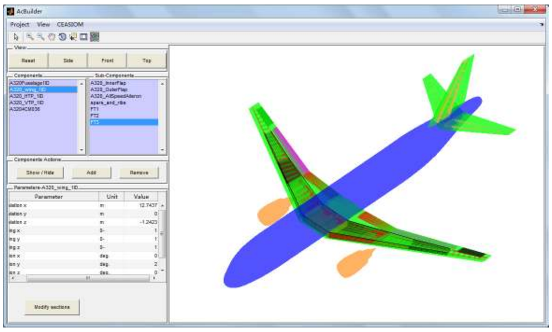

Fig. 2 CPACScreator interface.

3.3 Object Oriented Modeling

The CPACS schema definition contains an object oriented description of all the aircraft components, with a hierarchical structure adopting parent/child relations. As example a wing component may have as children the segments defining its external geometry, but also its internal structural components.

Figure 3 shows the detailed model of a wing component according to the CPACS definition, as assembly generated by the CPACScreator, and it appears clear the aforementioned challenge for the designer to instantiate such a detailed model.

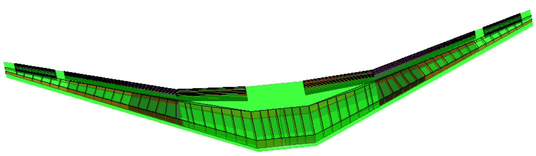

Fig. 3 CPACScreator detailed wing's components instantiation and modeling.

Further several relations are allowed between components, such as the spatial positioning in relative or absolute coordinates. These have to be properly handled in an optimization study, since they may determine the width of the design space under investigation. Under this perspective, the CPACScreator is also the assembling factory for aircraft components.

An aircraft can be built from scratch, element by element, by loading predefined templates for each element from the library. The user can start a new project by loading an aircraft template, an already existing aircraft, or just an element.

Only the elements really used to build a model will be loaded. The restriction on the order of assembly is inherited from the model hierarchy. Components on the same level of the hierarchy can be assembled and sized in any order, but child components only after their parents. Hence, the CPACS components can be assembled to describe arbitrary vehicles, and the CPACScreator plays a key role in facilitating the process for the analysis of the unconventional aircraft configurations.

4 Distributed Analysis Competences

In this paper multiple design competences available at DLR and KTH, are integrated in a collaborative design process. The focus is on the high fidelity aerodynamics and structural analysis. All the modules available are connected via CPACS. Starting from an initial low fidelity CPACS aircraft description, the CPACScreator is used to enrich the initial model with all the necessary details required for the generation of high fidelity analysis models (L1, L2). A short description of the analysis competences integrated in the workflow follows.

4.1 CEASIOM analysis suite

CEASIOM, the Computerised Environment for Aircraft Synthesis and Integrated Optimisation Methods, developed within the European 6th Framework Programme SimSAC (Simulating Aircraft Stability And Control Characteristics for Use in Conceptual Design) [16], is a framework tool for conceptual aircraft design that integrates discipline-specific tools like: CAD & mesh generation, CFD, stability & control analysis, etc., all for the purpose of early preliminary design. CEASIOM is an ad-hoc design framework. The CEASIOM framework offers possible ways to increase the concurrency and agility of the classical conceptual-preliminary process.

Figure 4 presents an illustration of the CEASIOM software, showing aspects of its four core functions: geometry & meshing [17], CFD [18], aeroelasticity [19], and flight dynamics [20].

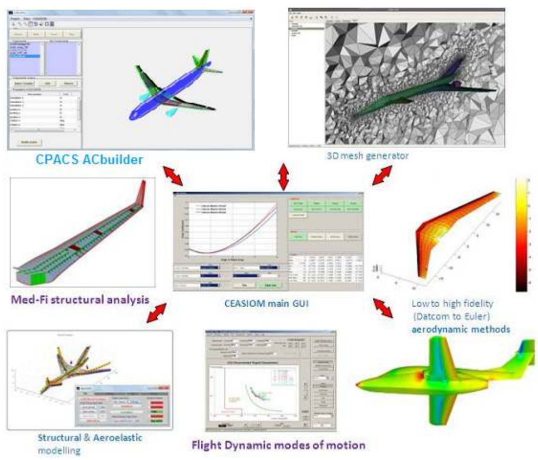

Fig. 4 CEASIOM suite models.

Although CEASIOM can be used as a standalone design framework, its analysis modules can be accessed by the described collaborative environment via CPACS, and the CPACScreator. For instance in the present work the CEASIOM aerodynamic module is responsible for the generation of the aerodynamics models, and analysis, with the following capabilities:

- Steady and unsteady TORNADO vortex-lattice code (VLM) for low-speed aerodynamics and aeroelasticity;
- Euler EDGE CFD code for the high-speed aerodynamics and aeroelasticity.

4.2 Aero-structural Analysis

The Aeroelastic Engine, is a module under development at DLR to support the modeling and the analysis of the complete flexible aircraft for preliminary MDAO applications in loosely coupled, and collaborative environment [21, 22]. The module provides a hierarchical set of physics based structural models, based on Finite Element (FE) representations [15].

As a level-1 model, the Aeroelastic Engine provides the structural properties of the complete aircraft, and assembles a multibody FE representation, based on a beam formulation. The primary structures of the lifting surfaces and of the fuselage components are identified, and beam's cross sectional properties (e.g., flexural and torsional stiffness) are derived from the geometry and from the explicit definition of the wingbox layout (e.g. ribs and spars components), and the fuselage's frames. Substructures, such as stiffeners, are taken into account by an equivalent approach [23]. As level-2, the extracted structural properties are used to initialize a 3D FE shell model for the analysis of wing structures. Hybrid formulation can be adopted as well. Figure 5 overlays the generated full stick FE aircraft model, with the FE shell wingbox one. Both the representations are abstracted from the same CPACS model. The Aeroelastic Engine module also provides the capability for automated fluid structure interaction coupling, with several levels of aerodynamics solvers, in order to provide the aero-structural sizing loop of the primary structures.

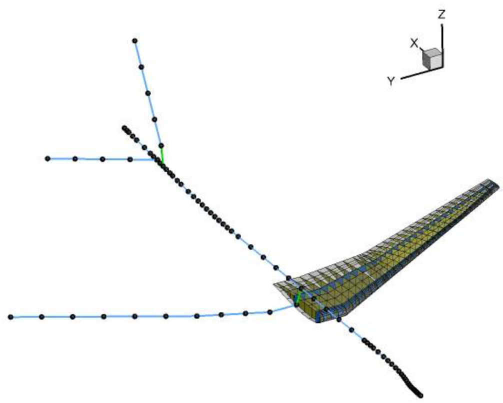

Fig. 5 Aeroelastic Engine FE hierarchical models (beam, and 3D shell) extracted by the CPACS file.

4.3 Overall Aircraft Design synthesis

Once the physics based analysis solutions are available, it is necessary to feed back the results in the overall aircraft synthesis loop. For this task the conceptual design level VAMPzero is selected [24]. Based on a multifidelity architecture, the program dynamically selects the appropriate calculation routines for a given input dataset. If values of some aircraft characteristics are already provided in the input dataset, they are directly inherited and not recalculated in VAMPzero's internal sizing process. This enables the program to import higher fidelity results and override its own calculation routines, a unique feature that is exploited in the presented workflow.

5 Study Cases

The described collaborative approach is demonstrated in this section for the analysis of two different aircraft configurations. The selected design cases highlight two main capabilities achieved within the described collaborative approach in automated modeling for physics based analysis:

- Automated generation of geometries for automated CFD meshing and analysis;
- Automated allocation of structural details for FEM analysis.

5.1 Towards high fidelity aerodynamics

The first capability of the CPACScreator, targets the generation of a geometry suitable for high fidelity aerodynamics, and is shown with a conventional aircraft configuration B777-200ER. As representative flight condition, the aircraft is analyzed at the transonic speed of Mach 0.84. The aircraft is available as CPACS format [25], and the resulting external geometry is shown in Fig. 6.

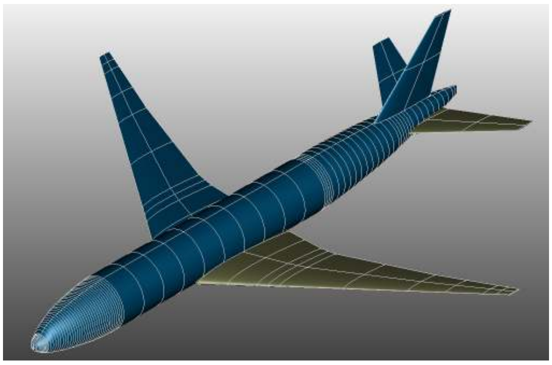

Fig. 6 CPACS geometry B777-200 ER visualized in TIGLViewer.

Hence the configuration is transferred via CPACS to the CPACScreator, which enables the connection to the aerodynamics solvers available in the CEASIOM framework.

Figure 7 overlays the multi-level generated aerodynamics models: the lattice used by the VLM code (level 1), and the unstructured surface mesh used by the Euler solver (level 2).

The computational grids are both extracted from the same CPACS representation model. The generation of the disciplinary models from CPACS, typically requires the interpretation and geometrical operations from the CPACS objects. Nevertheless the automated generation of the unstructured volumetric mesh requires the enrichment of some geometrical features, such as the smoothing of sharp edges, and of wing surface intersection, in order to produce a well posed spatial discretization for the flow solution.

This automatic feature is provided by the CPACScreator-CEASIOM coupling, and represents a key enabler for automated MDAO applications.

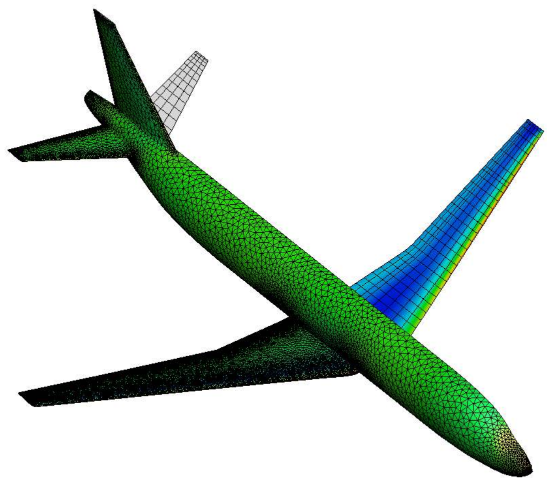

Fig. 7 VLM and Euler aerodynamics models extracted by the CPACS file.

The generated models are used to compute the aerodynamics properties for the defined flow condition, and compare the differences in the results.

Figure 8, shows the drag polar at Mach 0.84 obtained by both Euler and VLM codes. In the

VLM solution the Prandtl-Glauert correction is applied to account for the compressibility effect. However the speed is in the high-subsonic regime, in which linearised theory does not hold. It can be observed that the drag predicted by VLM is much smaller than the one predicted by Euler, due to the absence of the wave drag.

Figure 9 shows the pressure coefficient distribution (Cp) obtained from the Euler solution at cruise condition.

The significant shock formed at the wing upper surface around 75% of the chord line, is the main responsible for the discrepancy between the models in the computed aerodynamics performance.

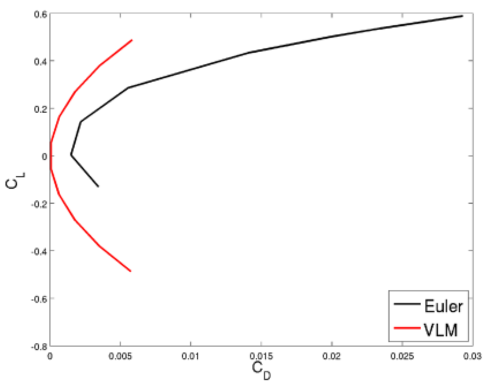

Fig. 8 Euler and VLM drag polars for B777 at Mach 0.84.

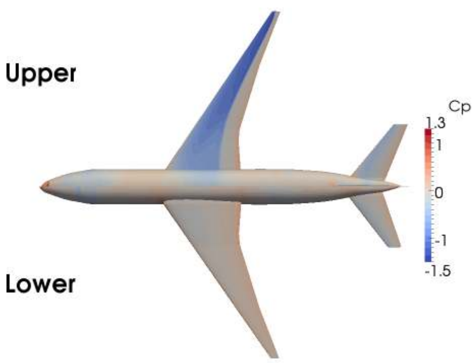

Fig. 9 Cp from Euler solution for B777 at M=0.84, CL=0.528

5.2 Towards high fidelity structures

The second capability enables the detailed structural analysis of the lifting surfaces, and it is tested with a PrandtlPlane configuration. The initial aircraft is available as CPACS file, which was generated by an external conceptual design tool [26, 27], and whose TLAR are taken by a reference design featuring 250 passengers [28]. The initial CPACS file external geometry is shown in Fig.10.

In this case the CPACScreator is employed to enrich the existing CPACS model, by adding the explicit definition of the primary structural components to the wing objects, such as ribs and spars. Figure 11 shows the CPACScreator generated model, with the complete wings' structural components.

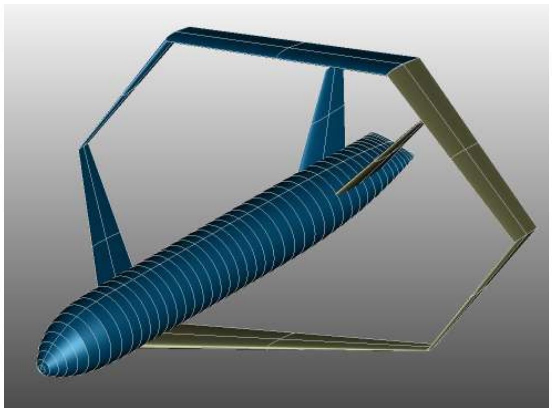

Fig. 10 CPACS PradtlPlane.

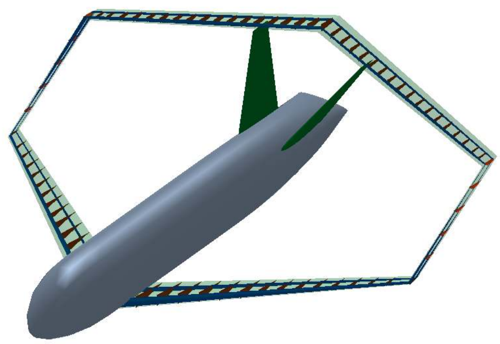

Fig. 11 CPACScreator PrantdlPlane featuring detailed wing primary structural components.

Hence the enriched CPACS model contains sufficient details to be forward to the Aeroelastic Engine, and a FE model is generated. The structural FE model is coupled with the aerodynamics loading provided by the VLM code, and the primary structures are sized for a 2.5g pull-up maneuver, which is selected to be representative of the critical sizing condition for the wing system.

Figure 12 shows the disciplinary models employed by the Aeroelastic Engine for the aero-structural sizing of the wing masses.

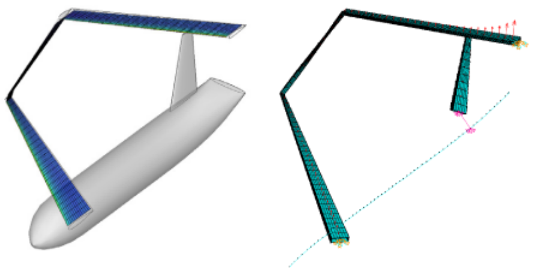

Fig. 12 VLM aerodynamics solution, and FE model used for the aero-structural sizing.

Thereafter, the results from the structural and aerodynamics analysis are forwarded to VAMPzero, which uses the high fidelity results for the overall aircraft synthesis. The results of the aero-structural wing mass sizing, and the calculated aircraft operating empty mass (OEM), and required fuel mass are reported in Table 2, and compared with the reference [28].

Table 2 PrantlPlane design study results.

OAD	Reference [28]	Current
Wing Mass [kg]	31321	+4.7%
Fuel Mass [kg]	85353	+3.5%
OEM [kg]	103300	+2.4%

The results differences of the current approach with the reference values, are within an acceptable range. In the current approach a limited amount of constraints, and critical design points have been used for the structural sizing. Nevertheless, it is also important to highlight the differences in the calculation methods between the two works. Although both make use of physics based analysis for the aerodynamics performance, the wing structural behavior is analyzed by physics based method, only in the current study, whereas calibrated estimation methods are used in the reference work. Due to the object oriented architecture, the CPACScreator enables the automated generation of detailed wings' structural layout, for any type of aircraft configuration. This feature provides an enabler to close the gap between the initialized aircraft, and the structural FEM analysis models.

6 Conclusions and Outlook

The presented paper highlights the challenges of modeling for physics based analysis in aircraft pre-design. A collaborative approach is developed by KTH and DLR, making use of distributed disciplinary competences, linked by a centralized data model (CPACS). Apart from the automation of the design process, which is an essential element to perform large design exploration, additional capabilities are required when dealing with high fidelity analysis, and the increasing modeling complexity. In this paper the CPACScreator, a management system developed to generate and to enhance CPACS objects, is serving two main functions. The first is the generation of aircraft geometries suitable for automated CFD analysis, as demonstrated with the Boeing 777-200ER design case. The second is the instantiation of complex structural components, such as the wing's primary structural layout for FEM analysis, as demonstrated with the PrandtlPlane configuration case. The major benefits of the presented approach are the understanding of the aircraft physics behaviors, and the minimization of the risks associated with the performance prediction of unconventional configurations at the pre-design stages. Furthermore it is demonstrated the flexible generation of physics based collaborative design process. This synergy is expected to be exploited in future studies, for extensive MDAO applications of unconventional designs.

Contact Details

Pier Davide Ciampa
German Aerospace Center (DLR)
Blohmstraße 18, 21079 Hamburg, Germany
Email: pier-davide.ciampa@dlr.de
Telephone: +49-40-42878-2727

References

[1] Report of the High Level Group on Aviation and Aeronautical Research "Flightpath 2050 Europe's Vision for Aviation", 2011.

[2] Strategic Research and Innovation Agenda (SRIA), Advisory Council for Aviation Reseacrh and Innovation in Europe (ACARE), 2012.

[3] Torenbeek, E., Synthesis of Subsonic Airplane Design, Delft Univ Press, 1982.

[4] Raymer, D., Aircraft Design: A Conceptual Approach, 4th ed., AIAA Education Series (2006).

[5] Kroo, I., Manning, V., "Collaborative Optimization: Status and Directions", *8th AIAA Symposium on Multidisciplinary Analysis and Optimization*, Long Beach, 2000.

[6] Liersch, C.M., Hepperle, M., "A Distributed Toolbox for Multidisciplinary Preliminary Aircraft Design", CEAS Aeronautical Journal, Vol. 2, p. 57 – 68, Springer, 2011.

[7] Nagel, B., Böhnke, D., Gollnick, V., Schmollgruber, P., Rizzi, A., La Rocca, G., Alonso, J.J., "Communication in Aircraft Design: can we establish a common language?", *28th International Congress of the Aeronautical Sciences*, Brisbane, 2012.

[8] Pfeiffer, T., Nagel, B., Böhnke, D., Rizzi, A., Voskuijl, M., "Implementation of a Heterogeneous, Variable-Fidelity Framework for Flight Mechanics Analysis in Preliminary Aircraft Design", *German Aeronautics and Space Congress*, Bremen, Germany, 2011.

[9] Nagel B., Zill, T., Moerland, E., Boehnke, D., "Virtual Aircraft Multidisciplinary Analysis and Design Processes – Lessons Learned from the Collaborative Design Project VAMP", *4th CEAS Air & Space Conference*, Linköping, Sweden, 2013.

[10] Zill, T., Böhnke, D., Nagel, B., "Preliminary Aircraft Design in a Collaborative Multidisciplinary Design Environment", *AIAA Aviation Technology, Integration, and Operations (ATIO)*, Virginia Beach, 2011.

[11] Zill, T., Ciampa, P.D., Nagel, B., "Multidisciplinary Design Optimization in a Collaborative Distributed Aircraft Design System", *AIAA Aerospace Sciences Meeting, Nashville*, Tennessee, 2012.

[12] http://code.google.com/p/cpacs

[13] http://code.google.com/a/eclipselabs.org/p/rce/

[14] Rizzi, A., Zhang, M., Nagel, B., Boehnke, D., Saquet, P., "Towards a Unified Framework using CPACS for Geometry Management in Aircraft Design", *50th AIAA Aerospace Sciences Meeting*, Nashville, Tennessee, 2012.

[15] Ciampa, P.D., Zill, T., Nagel, B., "A Hierarchical Aeroelastic Engine for the Preliminary Design and Optimization of the Flexible Aircraft", *54th AIAA Structures, Structural Dynamics, and Materials Conference*, Boston, 2013.

[16] Rizzi, A., "Modeling and simulating aircraft stability and control The SimSAC project", Prog Aerospace Sci, Vol 47, 2011, pp.573-588.

[17] Tomac, M. and Eller, D., "From geometry to CFD grids An automated approach for conceptual design", Prog Aerospace Sci, Vol 47, 2011, pp.589596.

[18] Da Ronch, A., Ghoreyshi, M and Badcock, K.J., "On the generation of flight dynamics aerodynamic tables by computational fluid dynamics", Prog Aerospace Sci, Vol 47, 2011, pp.597620.

[19] Cavagna, L., Ricci., and Travaglini, L., "NeoCASS: An integrated tool for structural sizing, aeroelastic analysis and MDO at conceptual design level", Prog Aerospace Sci, Vol 47, 2011, pp.621635.

[20] Goetzendorf-Grabowski, T., Mieszalski, D. and Marcinkiewicz, E., "Stability analysis using SDSA tool", Prog AerospaceSci, Vol 47, 2011, pp.636646.

[21] Ciampa, P.D., Zill, T., Nagel, B., "Aeroelastic Design and Optimization of Unconventional Aircraft Configurations in a Distributed Design Environment",*53rd AIAA Structures, Structural Dynamics, and Materials Conference*, Honolulu, 2012.

[22] Zill, T., Ciampa, P.D., Nagel, B., "A Collaborative MDO Approach for the Flexible Aircraft", *54th AIAA Structures, Structural Dynamics, and Materials Conference,* Boston, 2013

[23] Ciampa, P. D., Nagel B., and van Tooren, M. J. L., "Global Local Structural Optimization of Transportation Aircraft Wings", *51st AIAA Structures, Structural Dynamics, and Materials Conference*, Orlando, 12-15 April 2010.

[24] Böhnke, D., Nagel, B., Gollnick, V., "An Approach to Multi-Fidelity in Conceptual Aircraft Design in Distributed Design Environments", *32nd IEEE Aerospace Conference, Big Sky*, 2011.

[25] Boehnke, D., Nagel, B., Zhang, M., Rizzi, A., "Towards a Collaborative and Integrated Set of Open Tools for Aircraft Design", *51st AIAA Aerospace Sciences Meeting*, 07-10 January 2013, Grapevine, Texas.

[26] La Rocca, G., Langen, T., Brouwers, Y., "The Design and Engineering Engine. Towards a modular System for collaborative Aircraft Design", *28th International Congress of the Aeronautical Sciences*, Brisbane, 2012.

[27] Ciampa P.D., Nagel B., La Rocca, G., "Preliminary Design for Flexible Aircraft in a Collaborative Environment", *4th CEAS Air & Space Conference*, Linköping, Sweden, 2013.

[28] Bottoni, C., Scanu, J., "Preliminary design of a 250 passenger PrantlPlane aircraft", M.Sc. thesis, University of Pisa, 2004.

An Application of AHP, TOPSIS-Fuzzy and Genetic Algorithm in Conceptual Aircraft Design

Moreira, E.E. T., Schwening, G. S. and Abdalla, A. M.

Escola de Engenharia de São Carlos – University of São Paulo, Brazil

Keywords: *conceptual design, AHP, TOPSIS, genetic algorithm, aircraft design*

Abstract

This work approaches the conceptual design of an aircraft using a combination of three innovative tools. Genetic Algorithm is used in order to find the optimum solution inside the search space. Generated conceptual aircrafts are evaluated by AHP and TOPSIS in fuzzy environment. These tools allowed the creation of a complete system for multidisciplinary optimization that was tested in an aircraft conceptual design and achieved good performance. The main limitation of the method is the need of creating a good model to determine operational performance from general characteristics.

1 Introduction

One of the most challenging parts in the design of an airplane is determining the optimal balance of general characteristics. Although being one of the fastest phases in the whole aircraft design, the conceptual design plays an important role in achieving the best operational performance and fulfillment of the market's requirements.

One of the difficulties in this job is to estimate several interdependent characteristics that will only be known when the whole design phase is completed. Generally, previous knowledge based on experience is used in order to predetermine these values, but when new technologies are applied this information and statistics are rare or nonexistent.

Several works in this area have successfully found solutions for this problem using Orthogonal Steepest Descent, Monte Carlo and Evolutionary Algorithms in order to achieve good solutions but evaluated the conceptual aircraft with simple mathematical functions of performance values and characteristics which may not lead to the best desired balance.

Another complication is caused by the difficulty in evaluating the airplanes qualities and how they are important to the market acceptance. This is an imperative factor that can lead the whole project to failure, since the design may begin from the clients' specifications and requirements. The solution for this problem is the evaluation supplied by the combination of Analytic Hierarchy Process (AHP) and Technique for Order of Preference by Similarity to Ideal Solution in fuzzy environment (TOPSIS-fuzzy).

The usage of AHP among TOPSIS-fuzzy has already been proved as a good solution for multi-criteria decision processes [1]. Considering this, it is a good tool to be used in optimization processes that requires ordering individual by performance.

This work proposes a new method to determine the general characteristics of an airplane and can be extrapolated to any kind of project. It mainly depends on the quality of the assumptions made in the model that determines operational performance from design.

Using AHP and TOPSIS-fuzzy to evaluate possibilities and Genetic Algorithms (GA) to find the best solution in the search space, it was created a complete system for conceptual project of general aircrafts, allowing better operational performance and bigger market acceptance.

2 Theory

This work proposes the combination of three different methods in order to create an optimization tool where establishing the importance of each performance characteristics and estimating parameters are difficult processes. AHP is used among TOPSIS-fuzzy in order to give a rational and efficient way to evaluate the different choices while GA allows creating different combinations of project characteristics without having the direct estimation of unknown parameters.

2.1 Genetic Algorithm

GA is a method created in the 50's and 60's to optimize complex problems including those with function discontinuities and unknown mathematical representation [2]. It is based on natural selection theory and uses the concept of individual as each possible solution for the optimization problem. It also employs the concepts of crossing-over and mutation. The implementation of this method is of relative simplicity but requires a good perception of how the choices of each detail affect the convergence time and success.

This optimization approach is an iterative process where iteration is analogous to a generation, also called population, which has a group of individuals, each one with its specifics characteristics coded in a sequence of values called chromosome. The first generation is randomly created by a uniform distribution between 0 and 1. To evolve to the next populations, the individuals pass by three other phases that are the selection, the crossing-over and the mutation.

2.1.1 Encoding

The encoding is a very important part of the genetic algorithm operation. It is responsible to cover the desired search universe without creating impossible or inexistent individuals.

There are several ways to represent the characteristics. For this paper, the chosen method was the real number encoding, where the individual is represented by a sequence of numbers between zero and one. Each value is related to a characteristic as can be seen in Eq. 1.

$$V = V_l + n\,(V_h - V_l) \qquad (1)$$

Where V is the final value, V_l and V_h are the lower and higher limits of the search space for that variable and n is the respective value in the sequence.

2.1.2 Selection Phase

The selection phase consists of randomly choosing individuals that will be crossed and will originate a new chromosome giving best chances to better individuals. The main purpose of this phase is simulating the natural law where a more adapted member of a population is more likely to mate and generate descendants.

In order to qualify the individual for the selection phase, it is necessary to define a fitness function. This function is defined as function of the parameters optimized, and gives the higher values for the best individuals in the competition. This way, the definition of this fitness function has fundamental importance in the performance of the optimization.

The chosen mechanism for the selection phase consists of a biased roulette wheel, where the individuals are selected with a probability directly proportional to its fitness function. The algorithm consists of the following steps:

- Sum all the individuals' fitness;
- Randomly generate a number between *0* and *1*;
- Multiply this number by the sum of fitness, this is the cut point;
- Sequentially sum the individual's fitness until the accumulated value is greater than the cut point;
- The last individual to be summed is the selected individual.

2.1.3 Crossing-Over

There are many ways of crossing the selected individuals but the main goal is generating a new chromosome that merges the characteristics of both selected parents.

Using this logic, the crossing-over operator was defined as the following steps:

- Randomly generate an integer between one and the size of the sequence, this is the cut point;
- Randomly generate a real number between zero and one, this is the weight W;
- Go through the sequence defining the child's numbers as $WV_1 + (1 - W)\, V_2$ until the cut point;
- Go through the rest of the sequence defining the child's numbers as $WV_2 + (1 - W)V_1$.

Using this technique, it is possible to guarantee that most of the time the child's are not going to be too similar to one of its parents.

2.1.4 Mutation

The third step has the goal of preventing the premature convergence of the population; it biases the characteristics' values from the blended value of the parents. It is also used to create variations in the population and to make the algorithm reach unexplored places inside the search space.

The mechanism responsible for the mutation was defined as:

- Go through the sequence of a chromosome;
- For each value in the sequence, generate a normally distributed deviation with mean equal to zero and standard deviation arbitrarily chosen;
- Add this deviation to the value.

It is important to note that a too big standard deviation would make the search look like a random search and a too low standard deviation would make the population converge prematurely.

2.1.5 Convergence

After a big number of iterations, this process tends to converge to the global maximum of the fitness function, respecting all the constraints given by the problem. The test to stop iterating is done comparing the difference between susceptive populations or simply the observation by the operator if the fitness function is close to the estimated evaluation of the global maximum.

2.2 AHP

The Analytical Hierarchy Process (AHP) is an effective method to obtain the weight of each relevant criterion optimized. The method consists in establishing a hierarchy with the elements of the decision according to the evaluation problem proposed.

The relevant criteria chosen are compared in pairs by the operator taking into account its relative relevance following the standard shown in Table 1.

Table 1 Intensity Scale of Comparison

Intensity of Importance	Definition
1	Same importance
3	Moderately more important
5	Strongly more important
7	Very strongly more important
9	Absolutely more important
2,4,6,8	Intermediate values

The results of the criteria comparison is then summarized in a matrix A. The element a_{ij} of the matrix is the result of the comparison of the *i-th* and *j-th* terms.

After normalizing the matrix A, the weight of the criteria is founded by calculating the eigenvector relative to the maximum eigenvalue of it.

It is also necessary to calculate a final consistency ratio (*CR*). It is an index that demonstrate if the pairwise comparisons were sufficient consistent. If $CR < 0.1$, the evaluation was satisfactory. The calculation of *CR* is demonstrated in Eq. 2.

$$CR = (\lambda_{max} - n) \,/\, [RI\,(n - 1)] \qquad (2)$$

Where λ_{max} is the maximum eigenvalue of the matrix A and *RI* is the random index.

2.3 TOPSIS - Fuzzy

The TOPSIS consists in establishing a positive-ideal solution and a negative-ideal solution which gather, respectively, the bests and worsts characteristics in each criterion. Calculating and evaluating the distance between the competing solutions and the ideal solutions it is possible to determine the best solution.

When TOPSIS is used with crisp numbers it presents limitations for selection problems where the criteria are evaluated generally with linguistic values that bring imprecision. The TOPSIS technique, parameterized linguistically by fuzzy numbers, allows dealing with linguistic variables and its uncertainty.

The first step of TOPSIS consists on evaluating each competing solution according to each criterion. The evaluation is done based in fuzzy membership functions that represent linguistic values. Each linguistic value is associated with a fuzzy triangular number, as shown in Table 2.

Table 2 Linguistic Values and Fuzzy Numbers

Linguistic Values	Fuzzy Numbers
Very Low (VL)	(0, 0, 0.2)
Low(L)	(0, 0.2, 0.4)
Medium(M)	(0.2, 0.4, 0.6)
High(H)	(0.4, 0.6, 0.8)
Very High (VH)	(0.6, 0.8, 1)
Excellent(E)	(0.8, 1, 1)

The next step is to introduce the respective criteria weight calculated by the AHP method. This step is made simply multiplying the evaluation relative to a criterion by the respective criterion weight.

Finally it is possible to calculate the distance between the competing solutions and the ideal solutions. The distance between a competitor and one ideal solution is demonstrated in Eq. 3.

$$D = \sum \sqrt{\frac{(n_1 - a_1)^2 + (n_2 - a_2)^2 + (n_3 - a_3)^2}{3}} \qquad (3)$$

Using these distances it is possible to rank the alternatives giving them score values. The final score of a competitor is calculated by Eq. 4.

$$CC = D^-/(D^- + D^+) \qquad (4)$$

Where CC is the score, D^- is the distance between the competitor and the ideal negative competitor and D^+ is the distance between the competitor and the ideal positive competitor.

2.4 Performance Estimation

The criteria used in the AHP and TOPSIS-fuzzy evaluation are values of performance and operation of the aircrafts. These values were calculated based on the parameters passed by the GA.

It was intended to apply the algorithm in a general aircraft design optimization. This way, the following parameters were considered in the model:

- Takeoff distance;
- Stall speed;
- Maximum rate of climb;
- Service ceiling;
- Endurance;
- Range.

The parameters were chosen by being the typical performance requirements of the general aircraft market. In other word, these are the common performance data analyzed by the buyer. It is important to note that the landing distance was not considered in the evaluation because it is expected that this distance will be less than the takeoff distance for light aircrafts [3].

2.4.1 Takeoff Distance

Takeoff distance estimation was done using a numerical integration model. Traction of the propulsive system was estimated considering the engine power constant and establishing a linear model for the variation of the propeller efficiency with the velocity. In opposition, it was estimated considering a fixed friction coefficient and a fixed drag coefficient C_D.

2.4.2 Stall Speed

Stall speed was estimated using the maximum value of the lift coefficient of the wing, C_{Lmax} and the maximum takeoff weight, MTOW, in the sea level density.

2.4.3 Maximum Rate of Climb

Maximum rate of climb was estimated dividing the difference between the available power and the minimum required power by the weight force [4]. The calculation of the rate of climb was done considering the sea level elevation.

2.4.4 Service Ceiling

The service ceiling is the height where the maximum rate of climb reaches the value of 100 ft/min. It was used an iterative method to estimate the service ceiling.

2.4.5 Endurance

Endurance and range were calculated using a simple numerical integrative method. For the endurance, it was used the velocity of minimum required power, while for the range it was used the velocity of minimum drag. It was discounted *20%* of the fuel because of the takeoff and climb flight regime and others *20%* for descendant flight, loitering and landing procedures. The time step using in the integration was *30* seconds.

2.4.6 Weight Estimation

It is very important to estimate the weight of the components and the aircraft in order to determine its performance. However, estimating the weight of an aircraft is not a simple task. There are several methods of general aircraft weight estimation, e. g. the Cessna Method [5]. In this work it was used a more recent method presented by Kundu [6].

In order to simplify the calculation, the aircraft weight was considered as in Eq. 5.

$$W_{Total} = W_{fus} + W_{lg} + W_t + W_w + W_{pp} \quad (5)$$

Where W_{Total} is the total aircraft weight, W_{fus} is the fuselage weight; W_{lg} is the landing gear weight; W_t is the tail weight; W_w is the wing weight and W_{pp} is the power plant weight.

2.5 Proposed Algorithm

The proposed algorithm consists in merging the methods previously detailed in order to create an optimizing design tool.

The steps of the algorithm are:

1) Determine criteria weights – The evaluation is done by pair comparisons of each criteria using AHP.
2) Generate the first population – The first population is generated randomly considering a range of typical values.
3) Evaluate first population's performance – The evaluation of the first population is made for each individual using the weights provided by AHP and TOPSIS-fuzzy method. The final scores calculated are used as fitness function to the next iteration of the GA.
4) Iterations of GA and TOPSIS-fuzzy evaluation – The genetic algorithm runs other iterations using the previous population's TOPSIS-fuzzy evaluations; always adopting AHP weights calculated in Step 1.
5) Reaching the best aircraft concept – Step 4 is repeated until convergence is reached; the optimal aircraft concept is found.

The diagram of the method can be seen in Fig. 1.

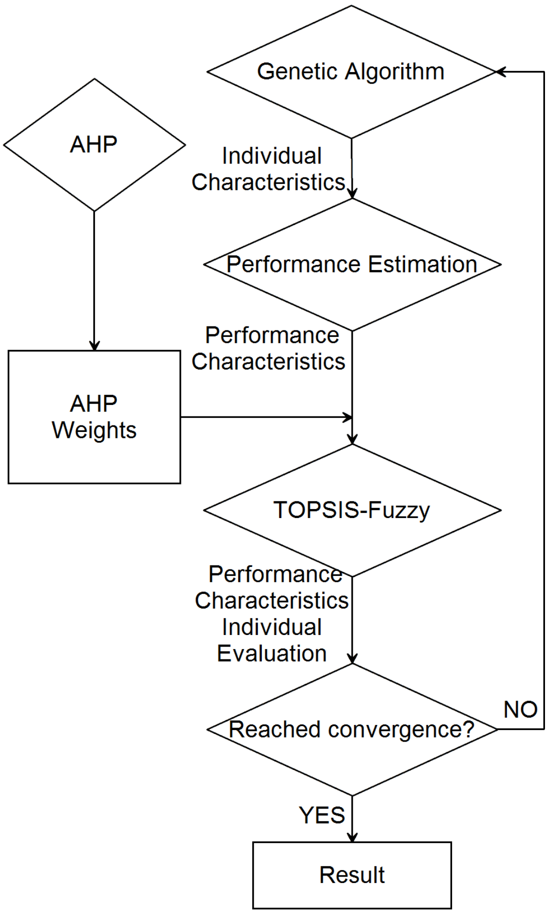

Fig. 1 Complete Method Diagram

3 Method Application

The model was applied in a general aircraft design optimization problem. It was intended to evaluate the performance of the tool in determining project parameters in an aircraft design.

3.1 Determining Criteria Weights

The criteria weights were determined after comparison of the criteria. The pairwise comparison matrix is show in Table 3.

Table 3 Pairwise Comparison Matrix

	C1	C2	C3	C4	C5	C6
C1-Takeoff distance	1.000	2.000	1.000	3.000	2.000	1.000
C2-Stall Speed	0.500	1.000	0.500	1.000	1.000	0.333
C3-Rate of Climb	1.000	2.000	1.000	4.000	3.000	0.500
C4-Serviçe Ceiling	0.333	1.000	0.250	1.000	1.000	0.500
C5-Endurance	0.500	1.000	0.333	1.000	1.000	0.500
C6-Range	1.000	3.000	2.000	2.000	2.000	1.000

After establishing the normalized matrix, it was calculated its eigenvector referent to its maximum eigenvalue. The values of the weight are shown in Table 4 among the value of *CR*.

Table 4 Criteria Weigh and CR

Criteria	Weight	CR
C1-Takeoff distance	0.22	0.03
C2-Stall Speed	0.10	
C3-Rate of Climb	0.23	
C4-Serviçe Ceiling	0.09	
C5-Endurance	0.10	
C6-Range	0.26	

3.2 TOPSIS-fuzzy

With the weights already determined by AHP, it was necessary to establish the TOPSIS-fuzzy evaluation of the competitors. The result of the TOPSIS-fuzzy evaluation will be considered as the fitness function in the GA routine. This way, the best evaluated aircrafts will have preferences in the selection phase.

The determination of the ideal competitors in respect with each criterion was done and is show in Table 5.

Table 5 Ideal Competitors

Criteria	Ideal Positive Competitor	Ideal Negative Competitor
C1-Takeoff distance	(0, 0, 0)	(1, 1, 1)
C2-Stall Speed	(0, 0, 0)	(1, 1, 1)
C3-Rate of Climb	(1, 1, 1)	(0, 0, 0)
C4-Service Ceiling	(1, 1, 1)	(0, 0, 0)
C5-Endurance	(1, 1, 1)	(0, 0, 0)
C6-Range	(1, 1, 1)	(0, 0, 0)

Takeoff distance and stall speed had their ideal positive competitor as (*0, 0, 0*) and the ideal negative competitor as (*1, 1, 1*) because lowers takeoff distances and stall speeds are better in this analysis. The others criteria were established oppositely as it is desirable to have higher rates of climb, service ceilings, endurances and ranges.

Considering that the evaluation of the competitor is commonly made by an operator, it was necessary to create an automatic method of evaluation of the competitors to be used in the algorithm, otherwise, the algorithm would became impracticable.

The solution was to discretize the values of the performance parameter based on typical general aircraft values. The diagram in Fig. 2 shows the classification ranges for takeoff distance.

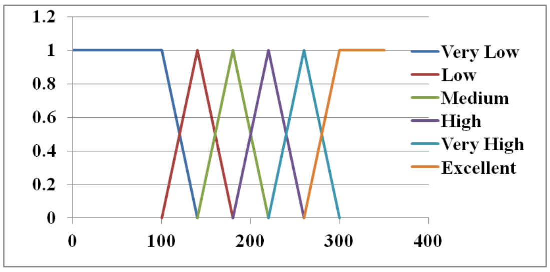

Fig. 2 Takeoff Distance Ranges

The calculation of the fuzzy number that represents an aircraft characteristic is done based on each criterion range classification. The final fuzzy number was weighted by the respective fuzzy linguistic values of its characteristic. Then the linguistic values were converted to a fuzzy triangular number and weighted according to the criterion respective weight provided by AHP.

To illustrate the process, it is calculated the fuzzy number in respect to the takeoff distance criterion for an aircraft that has a takeoff distance of *150* meters.

According to Fig. 2, this takeoff distance is *0.75* low and *0.25* medium. The fuzzy number that represents low and medium are (*0, 0.2, 0.4*) and (*0.2, 0.4, 0.6*), respectively. This way, the fuzzy number that represent the takeoff distance of *150* meters is determined in Eq. 6.

$$0.75 \,.\, (0, 0.2, 0.4) + 0.25 \,.\, (0.2, 0.4, 0.6) = (0.05, 0.25, 0.45) \quad (6)$$

To reach the final fuzzy number, it is necessary to multiply the number above by the weight calculated by AHP for the takeoff distance, which values *0.22* as can be seen in Table 3. This way, the final fuzzy number is (*0.011, 0.055, 0.099*).

Following this step to the six criteria established it was calculated the fuzzy numbers in respect to the criteria for all aircraft in each iteration of the GA.

In order to determine the score of each competitor they were calculated the distances to the ideal competitors, as the sum of the distances of each criterion to the respective value of the ideal competitor, defined in Table 5. The scores of the aircraft were determined based on the values of the two distances to the ideal competitors using Eq. 4. These scores were used as fitness in GA.

3.3 Genetic Algorithm Optimization

Considering the TOPSIS-fuzzy evaluation model established, the genetic algorithm was intended to search the aircraft which would lead to the best fitness value.

The characteristics that were optimized are shown in Table 6.

Table 6 Ranges of Characteristics Optimized

Limits	Lower	Higher
Wing Area (m^2)	8.0	15.0
Wing Aspect Ratio	4.0	8.5
Horizontal Tail Area Ratio	0.2	0.4
Horizontal Tail Aspect Ratio	2.5	5.0
Fuel Capacity (kg/m^2)	2.6	6.0

Using the values encoded it was possible to determine the general geometry and weights, which would be used to determine the performance parameters later.

The possible power plants were two motors which are listed in Table 7.

Table 7 Power plants

Engine N°	1	2
Number of Cylinders	4	6
Power (hp)	80	120
Specific Consumption (kg/J)	6.67E-08	7.65E-08
Dry Weight (kg)	61.0	80.7

The first engine was used when the value was less than *0.5* and the second was used for values higher than *0.5*.

The Horizontal Tail Area Ratio is the ratio between Horizontal Tail Surface and Wing Surface. This was done in order to make more difficult the creation of disproportional individuals (e. g. big wings and small horizontal tail). Using this definition and fixed tail volume coefficients it was possible to define the whole tail and the fuselage length.

The fuel capacity was defined as Mass of Fuel/Wing's Area.

3.4 Final Results

After in 417 iterations, the algorithm reached the convergence. The characteristics of the optimized aircraft are presented in Table 8.

Table 8 Parameters of the Aircraft

Parameter	Value
Maximum Takeoff Mass (kg)	604.26
Wing Area (m^2)	15.00
Wing Aspect Ratio	6.62
Horizontal Tail Area (m^2)	5.53
Horizontal Tail Aspect Ratio	4.54
Engine	2

The performance values of the optimized aircraft are shown in Table 8.

Table 9 Performance of the Aircraft

Parameter	Value
Takeoff Distance (m)	91.0
Stall Speed (km/h)	66.6
Rate of Climb (ft/min)	1943.0
Service Ceiling (m)	10957.0
Range (km)	921.00
Fitness (CC)	0.497

The optimization was made three times and led to the same solution in all of them.

The convergence curves of the first optimization are shown in Fig. 3.

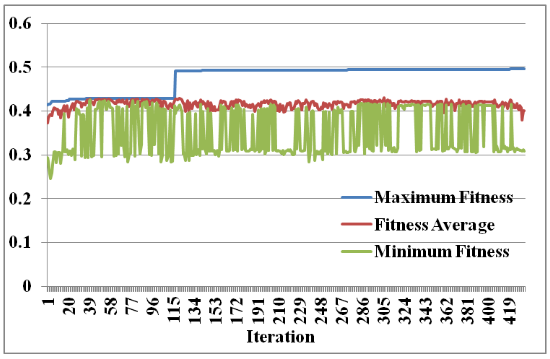

Fig. 3 Convergence

4 Discussion

The results obtained by the method were satisfactory as the optimized aircraft presented good performance parameters. The method has proven to be effective for the optimization of complex problems with multiple goals such as the conceptual design of a general aviation bi-place aircraft.

Besides, this method presents an alternative for dealing with the problem of establishing the appropriated fitness function for the GA.

However, the method does not include all parameters relevant to a conceptual design optimization or to an efficient selecting process. The calculations of the performance values of the aircraft were simplified in this work and a refinement can be done in order to introduce other characteristics to be optimized and to add new criteria to be considered.

Future works will be made in order to refine performance calculations and implement cost analysis in the system. Moreover, the AHP TOPSIS-fuzzy method can be tested with other optimization techniques.

Despite all limitations and approximations of the method, it represents a very powerful tool to aid the design process of any kind of aircraft or other products.

References

[1] Dagdeviren M., Yavuz S. and Kilinc N., "Weapon selection using the AHP and TOPSIS methods under fuzzy environment", *Expert Systems with Application*, Vol. 36, No. 4, 2009, pp. 8143-8151.

[2] Goldberg D. E., "Real-Coded Genetic Algorithms, Virtual Alphabets and Blocking", *Complex Systems*, Vol. 5, 1991, pp. 139-167.

[3] Mair W. A. and Birdsall D. L., *Aircraft Performance*, 1st ed., Cambrige University Press, United States of America, 2003, Chaps. 4, 5, 6, 7.

[4] Smetana F. O., *Flight Vehicle Performance and Aerodynamic Control*, 1st ed., American Institute of Aeronautics and Astronautics, United States of America, 2001, Chaps. 3, 7.

[5] Roskam J., *Airplane Design*, 1st ed., Roskam Aviation and Engineering Corporation, United States of America, 1985, Part V, Chaps. 5, 6, 7.

[6] Kundu A. K., *Aircraft Design*, 1st ed., Cambridge University Press, United States of America, 2010, Chap. 8.

4:th CEAS Air & Space Conference
FTF Congress: Flygteknik 2013

Parametric Design Studies for Propulsive Fuselage Aircraft Concepts

Arne Seitz and Corin Gologan
Bauhaus Luftfahrt e.V., 80807 Munich, Germany

Keywords: *Distributed propulsion, propulsive fuselage, wake filling, boundary layer ingestion*

Abstract

Breaking with the classical separation of airframe and powerplant system, new synergy effects may be rooted in close design coupling and the approach of distributing the production of thrust along the main components of the airframe. Beside greater configurational flexibility, airframe structural relief, improved noise shielding, and, the potential for control power augmentation, distributed propulsion is particularly interesting due to the reduced propulsive power demands expected from the notion of aircraft wake filling. In previous work, the concept of a propulsor encircling the aft-fuselage with intent to entrain the fuselage boundary layer was identified to be one of the most promising concepts for aircraft wake filling. In this paper, the analytical basis for the quantification of efficiency benefits connected to the propulsive fuselage concept is discussed. Appropriate control volume and consistent efficiency chain definitions are introduced. A simplified boundary layer model is derived from axisymmetric fuselage CFD simulation and used to determine the momentum deficit ingested by the fuselage propulsor. Based on a novel figure-of-merit for vehicular efficiency, the Energy Specific Air Range, ESAR, the dependency of aircraft cruise efficiency on basic propulsion system and aircraft design changes is parametrically investigated. Specifically, the sensitivities of vehicular efficiency w.r.t. wing aspect ratio and flow transition characteristics, propulsor size, and aircraft design cruise Mach number are studied.

1 Nomenclature

1.1 Abbreviations

BLI	Boundary Layer Ingestion
CFD	Computational Fluid Dynamics
CFRP	Carbon Fiber Reinforced Polymers
EIS	Entry Intro Service
ESAR	Energy Specific Air Range
FPR	Fan Pressure Ratio
GTF	Geared Turbo Fan
HPT	High Pressure Turbine
LPT	Low Pressure Turbine
LTH	Luftfahrttechnisches Handbuch
MAC	Mean Aerodynamic Chord
MTOW	Maximum Take-Off Weight
OEW	Operating Empty Weight
OPR	Overall Pressure Ratio
PSC	Power Saving Coefficient
SAR	Specific Air Range
TSFC	Thrust Specific Fuel Consumption
TSPC	Thrust Specific Power Consumption

1.2 Symbols

D	[N]	Drag
F	[N]	Thrust

h	[m]	Duct height
L	[N]	Lift
m	[kg]	Mass
M	[-]	Mach number
p	[N/m²]	Pressure
P	[W]	Power
Re	[-]	Reynolds number
S	[m²]	Wing area
V	[m/s]	Velocity
x	[m]	Fuselage axial coordinate
β	[-]	Ingested drag ratio
γ	[-]	Isentropic exponent
δ	[-]	Boundary layer thickness
η	[-]	Efficiency
φ	[rad]	Sweep angle

1.3 Subscripts

*	Boundary layer ingestion case
0	Ambient conditions, free stream
1	Propulsion system intake
2	Fan inlet
A/C	Aircraft
D0	Zero-lift drag
ec	Energy conversion
ing	Ingested
LE	Leading edge
m	Area averaged mean
N	Net
ov	Overall
pd	Propulsive device
pr	Propulsive
ref	Reference
rel	Relative
t	Total
T	Transition
tr	Transmission

2 Introduction

In view of the ambitious long-term environmental targets recently set by the European Commission [1] and the Advisory Council for Aeronautics Research in Europe (ACARE) [2] a serious consideration of revolutionary technology concepts and novel aircraft morphologies is warranted. In particular, new propulsion system technologies have been subject to an ongoing series of large European research projects, aiming at innovative core engine architectures [3], improved thermal efficiency through increased overall pressure ratios [4], new sub-system technologies [5], as well as improved propulsive efficiency through advanced low-pressure spool systems, both ducted propulsive devices [6] and Open Rotor systems [7]. However, retaining conventional propulsion system integration, still a noticeable gap is expected between the achievable system efficiency gains and the dramatic emission reductions targeted [8].

Breaking with the classical separation of airframe and power plant system, the idea of distributing the production of thrust along the main components of the airframe may facilitate new synergy effects covering aerodynamics such as the reduction of wetted areas and the reduction of flow dissipation through wake filling, propulsion system aspects such as the feasibility of very low specific thrust configurations, airframe structural relief, improved noise shielding, as well as potential control power augmentation.

A classification of distributed propulsion types was given by Kim [9] covering jet flaps, the cross-flow fan, multiple discrete engines, and, distributed multi-fans driven by a small number of engines. As an additional approach to distributed propulsion integration the concept of a single or counter-rotating propulsor encircling the fuselage with intent to entrain the fuselage boundary layer and distribute the thrust along the viscous wake generated by the fuselage was initially evaluated by Steiner et al. [10]. Distributed propulsion, and, specifically this so-called "propulsive fuselage" concept are currently under investigation in EU-funded Level 0 research [11]. According to the results presented in [10], the propulsive fuselage is considered to be one of the more promising concepts for aircraft wake filling, and hence the reduction of propulsive power required. A number of conceptual implementations of the propulsive fuselage idea such as the VoltAir platform [12] can be found in the literature [10-13]. Typical challenges associated with a propulsive fuselage configuration include the radial distortion of the propulsor in-flow field due to local fuselage downwash, angle-of-attack and side-slip operation, centre of gravity and connected loadability issues, fuselage fatigue, as well as ice and foreign object ingestion. An exemplary configuration is shown in Figure 1.

In the present paper, a synopsis of the analytical basis for the quantification of vehicular efficiency benefits connected to the propulsive fuselage concepts will be given. As part of this, appropriate control volume and efficiency chain definitions will be introduced. The analytical formulation will capture the propagation of effects due to basic aircraft design changes up to the integrated vehicular level.

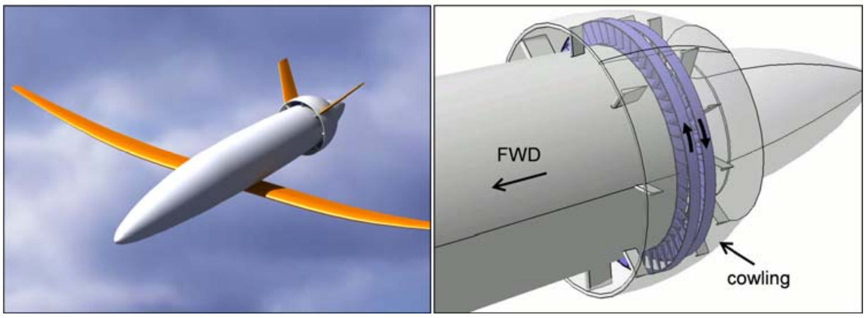

Fig. 1: Visualisation of propulsive fuselage concept developed at Bauhaus Luftfahrt

3 Theoretical Basis and System Definition

Starting from today's highly optimised transport aircraft, the propulsion system and its synergistic airframe integration is expected to be a key factor for further significant gains in vehicular efficiency. Taking classical propulsion system paradigms, however, improvements in the propulsion system efficiency, e.g. through larger propulsor sizes facilitating lower specific thrust, and thus, improved propulsive efficiency, normally creates a complex array of integration issues. These may include geometric challenges as well as airframe structural weight penalties, depending on the propulsion system type and installation position. Moreover, the increased wetted areas of nacelles resulting from large propulsive devices may yield significant penalties in aircraft parasite drag, thereby, impairing vehicular efficiency. While under-wing engine installation promotes structural relief to the wing, it however, detrimentally impacts on its localised drag and lift characteristics. As a result of this, optimum ByPass Ratios (BPRs) for state-of-the-art turbofan engines have not yet exceeded values of 10 to 12 [14]. Synergistic propulsion / airframe integration, however, should aim at alleviating the aircraft-level drawbacks of highly efficient power plant solutions.

3.1 The Principle of Wake Filling

Particularly addressing the reduction of aircraft effective drag the concept of boundary layer ingesting propulsion systems has been known for a long time. Viscous and form drag ranges between 55 to 65% of the total drag of transport category aircraft. Different from the vortex-induced drag, these drag components, in particular the low-momentum boundary layer flow caused by skin-friction on wetted surfaces, are manifested as a momentum deficit in the aircraft wake. Applying momentum and energy conservation laws, it can be easily shown that filling this momentum deficit through a momentum delta produced by the propulsion system yields a reduction in propulsive power required for aircraft operation. Key is the reduction of jet overvelocities, here, as the gain of net thrust is only linearly correlated to excess jet velocity, in contrast, expended kinetic energy is quadratically dependent. Due to its large share of the total wetted area of an aircraft, the fuselage is most attractive for the application of wake filling. In Figure 2, different configurational cases for a boundary layer ingesting propulsion system encircling the aft-fuselage, referred to as fuselage propulsors, in the following are schematically shown (B through D) and contrasted to the conventional case of podded power plants (A).

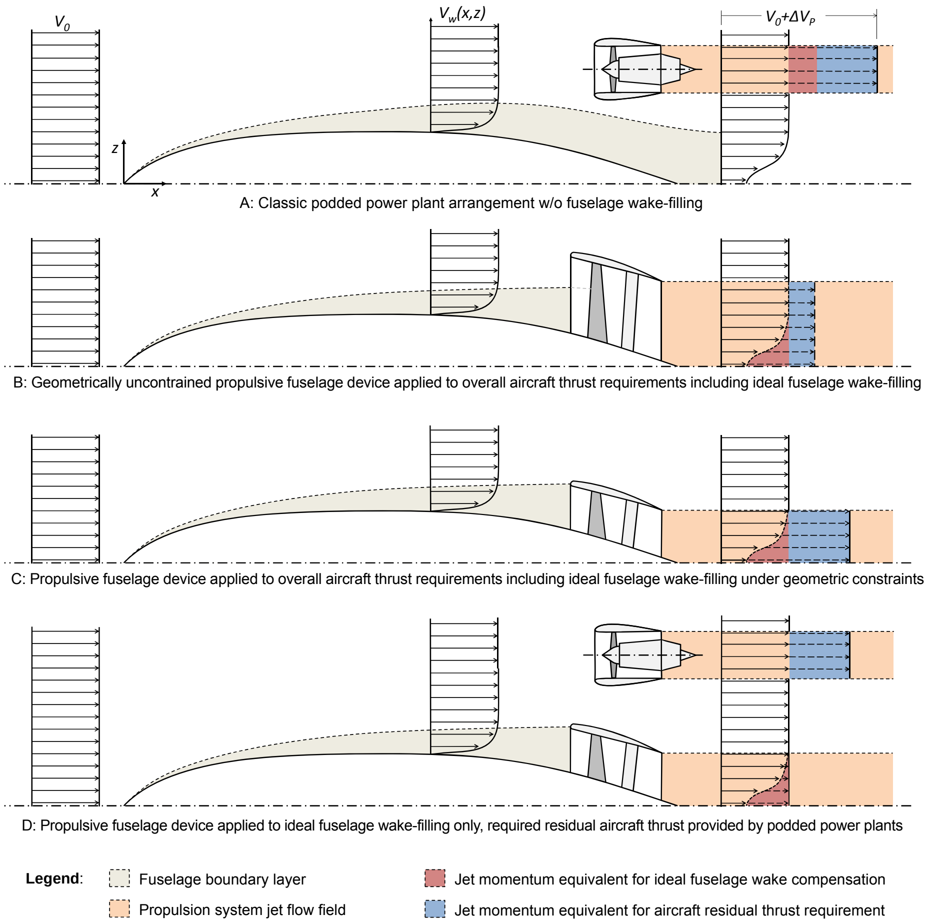

Fig. 2: Considerations for optimum wake-filling based on the propulsive fuselage concept

Figure 2 illustrates the differences in mean excess velocities in the propulsive jet, ΔV_P, that are necessary over the free-stream velocity, V_0, in order to produce the thrust required by the aircraft. The jet equivalent momentum shares for fuselage wake compensation and the residual aircraft thrust requirement are indicated in blue and red, respectively. As can be seen, the benefit of the wake filling effect on the overall energy balance of the aircraft improves as more viscous drag, i.e. momentum deficit, is recovered through boundary layer ingestion. A singularity is encountered as ΔV_P approaches zero. For the determination of optimum ΔV_P as a design consideration, furthermore, propulsion system internal losses, as well as system weight implications need to be taken into account. In practice, even, the reduction of ΔV_P may by constrained by geometric limitations, such as the required ground clearances during take-off rotation (compare cases B and C). As a an interesting approach one may consider a FP device solely designed to recover the fuselage wake momentum deficit, while all residual thrust required is delivered by conventionally podded power plants.

3.2 Definition of Control Volumes and Efficiency Figures

The consistent treatment of conventionally installed, i.e. podded, and highly integrated propulsion systems such as the propulsive fuselage concept requires unified standards for the definition of the efficiency chain through the entire power plant system, as well as appropriate interfacing to the airframe. This particularly includes the consistent definition of the control volumes and the corresponding system-level efficiency figures. For reasons of practicality it is convenient to adhere to common definitions used in propulsion system performance simulation software [15]. In Figure 3, a unified scheme of control volume definitions is proposed for podded and BLI ducted propulsion systems.

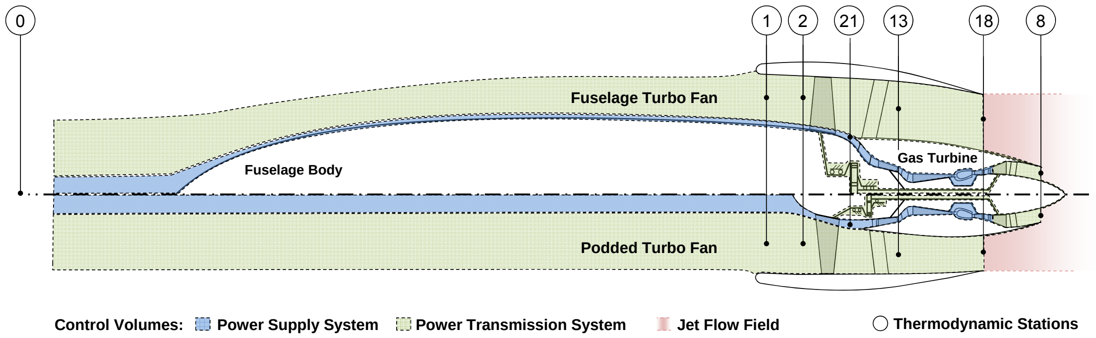

Fig. 3: Control volume definition for podded and propulsive fuselage power plant system installation

The visualization in Figure 3, reflects the classic distinction of the power supply system, the power transmission system, and, the jet flow field. On the lower half-sectional view, a podded turbofan engine is shown, while upper half-section correspondingly depicts an exemplary propulsive fuselage configuration, here, an aft-fuselage mounted BLI turbofan. The control volumes for the definition of the efficiencies of the power supply system, η_{ec}, the power transmission system, η_{tr}, and, the jet flow field, η_{pr}, are highlighted in colour. The product of these three propulsion system efficiency figures defines the overall efficiency of the EPS, η_{ov}, which describes the ratio of effective propulsive power, P_{thrust}, and the power extracted from the energy source, P_{supply} [16,17]:

$$\eta_{ov} = \frac{P_{thrust}}{P_{supply}} = \frac{F_N \cdot V_0}{P_{supply}} = \eta_{ec} \cdot \eta_{tr} \cdot \eta_{pr} \qquad (1)$$

$$\eta_{ec} = \frac{P_{useful}}{P_{supply}}; \quad \eta_{tr} = \frac{P_{jet}}{P_{useful}}; \quad \eta_{pr} = \frac{P_{thrust}}{P_{jet}} \qquad (2)$$

where F_N denotes the net thrust of the installed power plant and V_0 represents the free stream velocity. In the usual case of heat engines P_{supply} equals the product of fuel mass flow, W_F, and the fuel heating value, *FHV*. The interface for thrust / drag book keeping between the propulsion system and the airframe is geared to the stream tube of air flow entering the propulsion system. That means, aerodynamic effects in the stream tube ahead of the inlet frontal face are incorporated in the power plant sizing and performance analysis. Nacelle external aerodynamics are considered to contribute to the overall aircraft characteristics, thereby, feeding back to the net thrust required to operate the aircraft, $F_{N,t}$. Knowing $F_{N,t}$, F_N requirements for the installed individual power plants can be derived.

It can be seen from Figure 3, that viscous wake and boundary layer effects developing from fuselage skin-friction inside the stream tube volume belong to the propulsion system internal efficiency bookkeeping. As a result of this, the fuselage viscous drag forming inside the stream tube is removed from the aircraft drag balance.

The energy conversion efficiency, η_{ec}, incorporates the chain of energetic conversion between the energy source aboard the vehicle and the useful power for the considered application, P_{useful}. In case of classical turbo engines, η_{ec} equals the core efficiency, η_{core}. As can be seen in Figure 3, η_{core} accounts for the High Pressure (HP) system including upstream effects of the core mass flow, such as the inner stream tube, intake and ducting losses, as well as, the polytropic compression in the fan and the low pressure compressor. Therefore, the useful power represents the ideal core excess power, available for the Low Pressure Turbine (LPT) to drive the outer fan, i.e. the part of the fan working on the bypass mass flow.

The transmission efficiency, η_{tr}, relates the power in the propulsive jet, P_{jet}, to the useful power provided by the power supply system, P_{useful}. In case of turbofan engines, η_{tr}, comprises the LPT, the core nozzle, the Low Pressure (LP) shaft, an optional fan drive gear system, the fan, as well as all internal losses associated with the propulsive device, i.e. outer stream tube, intake, bypass ducting and nozzle losses. In a propulsive fuselage configuration, shear friction losses between the propulsive jet and the aft-fuselage body need to be considered as part of the nozzle losses. In turbofan engine, core efficiency, η_{ec}, and the transmission efficiency, η_{tr}, are often combined to the thermal efficiency, $\eta_{th}= \eta_{ec} \cdot \eta_{tr}$. The propulsive efficiency, η_{pr}, captures the ratio of effective propulsive power, P_{thrust}, and the power in the the jet, P_{jet}, for ducted propulsive devices. The propulsive and transmission efficiencies may also be combined to the propulsive device efficiency, η_{pd}, which will be of importance later in this paper:

$$\eta_{pd} = \frac{P_{thrust}}{P_{useful}} = \frac{F_N \cdot V_0}{P_{useful}} = \eta_{pr} \cdot \eta_{tr} \tag{3}$$

3.3 Metrics for Performance Evaluation

System performance evaluation and optimisation requires the mapping of the unified definition of the propulsion system efficiency chain to system operating conditions. At the isolated propulsion system level, the classic Thrust Specific Fuel Consumption, *TSFC*, is usually employed. In case, different types of energies are used in the propulsion systems, e.g. a combination of fuel and electrical energy the recently proposed, Thrust Specific Power Consumption, *TSPC*, may be used [16]. For the highly integrated propulsive fuselage concept, efficiency and performance assessment at a vehicular level are even more important. A useful metric for the evaluation of the efficiency potentials connected to boundary layer ingesting propulsion systems is the Power Saving Coefficient, *PSC*, introduced by Smith [18]:

$$PSC = \frac{P - P^*}{P} \tag{4}$$

where P^* and P represent the propulsive powers required to operate the aircraft at a given flight condition with and without BLI. Depending on the scope of investigation, either Eq. (1) of Eq. (3) may be used to express the *PSC* in terms of the aircraft overall net thrust requirements, and, propulsion system efficiency:

$$PSC = 1 - \frac{\eta}{\eta^*} \cdot \frac{F^*_{N,t}}{F_{N,t}} \tag{5}$$

where η^* and $F^*_{N,t}$ refer to the vehicular configuration including BLI, while η and $F_{N,t}$ denote the corresponding properties for conventional, podded propulsion installation, i.e. the baseline or reference case. If only BLI effects on the propulsive device need to be assessed, e.g. in case η_{ec} is independent from whether the boundary layer is ingested into the propulsor or not, the efficiencies used in Eq. (5) are based on the definition of η_{pd} given in Eq. (3). If η_{ec} cannot be considered as independent from BLI effects, here, Eq. (1) should be employed instead.

Recall, in Section 3.2, $F_{N,t}$ was generally defined as the total net thrust required to operate the aircraft, effects in the propulsion stream tube excluded. Now, assuming a certain amount of aircraft drag captured inside the propulsion stream tube (and ingested into the propulsive device), the actual net thrust requirement of the aircraft is reduced, accordingly:

$$F^*_{N,t} = F_{N,t} - D_{ing} \tag{6}$$

For stationary level flight, the ratio of ingested viscous drag, D_{ing}, and aircraft total net thrust requirement in the reference case, $F_{N,t}$, can be expressed in terms of drag coefficients (cf. [10]):

$$\beta = \frac{D_{ing}}{F_{N,t}} = \frac{C_{D0,ing}}{C_D} = \frac{C_{D0,ing}}{C_{D0}} \cdot \frac{C_{D0}}{C_D} \tag{7}$$

where $C_{D0,ing}$ is the coefficient of the ingested zero-lift drag, C_{D0} represents the overall zero-lift drag coefficient, and C_D the total drag coefficient including the lift-dependent drag share. The PSC then becomes:

$$PSC = 1 - \frac{\eta}{\eta^*} \cdot (1 - \beta) \tag{8}$$

Figure 4 shows a parametric study of Eq. (8). The improving power savings with increasing ingested drag ratio can be seen. As the losses in the propulsion stream tube connected to the ingestion of viscous wake flow with reduced momentum and strong non-uniformities in the flow will yield a degradation of propulsion system efficiency, the relative change of propulsion system efficiency due to BLI, $\Delta\eta_{rel}$, is used as an array parameter in the plot.

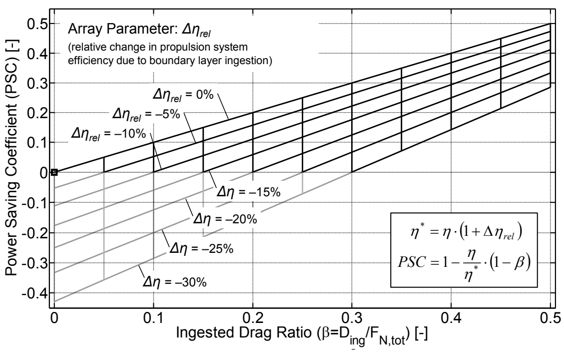

Fig. 4: Theoretical power saving potentials as function of ingested drag ratio and relative change in propulsion system efficiency

The reducing impact of $\Delta\eta_{rel}$ with increasing β is apparent, negative $\Delta\eta_{rel}$ values, however, are expected to increase as β improves. The undesirable region of the carpet, i.e. negative PSC, is shaded in grey. The diagram offers a direct means of evaluating the quality of a given BLI propulsion system configuration.

Finally, for an integrated aircraft-level efficiency assessment, a generalization of the well-known Specific Air Range (SAR) metric, is used in the present context [16]:

$$ESAR = \frac{dR}{dE} = \frac{V_0 \cdot L/D}{TSPC \cdot m_{A/C} \cdot g} = \frac{\eta_{ov} \cdot L/D}{m_{A/C} \cdot g} \tag{9}$$

The Energy Specific Air Range, *ESAR* indicates the change of aircraft range (*R*) per change of energy (*E*) in the system, *dR/dE*. It, thereby, allows for the convenient evaluation of aircraft performance, again, independent from the type of energy source. The aircraft properties required for ESAR evaluation include the lift-to-drag ratio, *L/D*, aircraft mass, $m_{A/C}$, and, the propulsion system overall efficiency, η_{ov}.

4 Setup of Study

For the design investigations in the present work an air transport task of 4800nm distance at 300 passengers design payload was chosen, which, today, is typically fulfilled by twin-engine wide-body aircraft, such as an Airbus A330-300 type. In this section, an overview of the employed models and the captured design sensitivities is given, founding the basis of the studies presented later in this paper. This includes the propulsion system as well as the airframe. One part of the section is especially dedicated to the modeling of the propulsion stream tube losses associated with the propulsive fuselage concept.

4.1 Description of Aircraft Model

The baseline aircraft for the studies presented later in this paper was derived from a parametric model produced for an Airbus A330-300 aircraft. In order to facilitate the fuselage fan propulsion system, the aft fuselage section of the conventional reference model was adjusted. Tab. 1 shows a predicted mass breakdown of the baseline aircraft model. Structural component weights, equipment and operational items weights are calculated according to handbook methods of Torenbeek [19]. Propulsion system weight estimation is discussed in the next section.

Tab. 1 Mass breakdown of baseline aircraft model

Weight Items	Baseline Aircraft Model
Airframe Structure	78915 kg
Propulsion Group	17009 kg
Equipments	18899 kg
Operational Items	6477 kg
OEW	121300 kg
Payload	28025 kg
Trip Fuel	59088 kg
Reserve Fuel	8587 kg
MTOW	217000 kg

Component zero-lift and vortex induced drag shares were calculated according to Torenbeek [19] methods, while wave drag prediction refers to the method of Korn [20]. The drag breakdown of the baseline aircraft at a typical cruise condition is given in Tab. 2.

Tab. 2 Drag breakdown of baseline aircraft model

Drag Items	Drag Coefficient	Drag Share
Wing	0.0064	24.6%
Winlet	0.0001	0.4%
Fuselage	0.0058	22.2%
Stabilizer	0.0011	4.0%
Fin	0.0007	2.6%
Nacelles	0.0009	3.4%
Pylons	0.0002	0.7%
Leaks & Protuberances	0.0006	2.1%
C_D Zero-lift	0.0157	60.2%
C_D Induced	0.0094	36.1%
C_D Wave	0.0010	3.7%
C_D Total	0.0261	100.0%

C_L=0.55, FL350, M0.82, S_{ref}=361.63m²

The design studies are conducted at constant Maximum Take-Off Weight, MTOW, wing reference area and taper ratio. Changes in weights, drag and propulsion system efficiency, hence, result in an impact on design mission stage length. The parametric model incorporates the sensitivities of important aircraft design variables on aircraft weights, dimensions and drag as documented in the following.

The impact of Design Mach Number on wing sweep was captured through a linearised correlation derived for the baseline aircraft model:

$$\varphi_{LE} = 3.88 \cdot (M_0 - 0.686) \quad [rad] \qquad (10)$$

The equation represents wing sweeps that result in the same wave drag as for the reference case. The impact of aspect ratio and wing sweep on vortex-induced drag is modeled according to Torenbeek [19, Eq. F-9], while the impact on wing weight is modeled according to LTH [21]. The LTH formula is corrected for high aspect ratios based on results from numerical aeroelastic simulations conducted with the methods documented in [22] and [23]. The reduced vortex-induced drag with increased aspect ratio increases the ratio of the fuselage drag to total drag, and, hence, β and the impact of a propulsive fuselage.

Also captured in the model is the impact of the wing chord dimensions on Reynolds Numbers and the resulting impact on the laminar and turbulent skin friction coefficients according to Raymer [24, Eqs. 12.25 to 12.29]. The transition point from laminar to turbulent flow on the wing is determined for the wing root, the kink and tip, based on the local Reynolds number using the following linearized correlation for the transition Reynolds number, Re_T, derived for the baseline aircraft model:

$$\mathrm{Re}_T = 10^6 \cdot (19.32 - 30.47 \cdot \varphi_{LE}) + \Delta \mathrm{Re}_T \qquad (11)$$

Between root, kink and tip, the transition point is linearly interpolated. A maximum transition point of 60 % based on the local chord is defined in order to account for gaps of the trailing edge flap system. The model is derived from different experimental results for natural laminar flow and hybrid laminar flow control taken from [25] and captures the effect of increased Re_T with reduced leading edge sweep. For the reference aircraft (φ_{LE}=32.5°, ΔRe_T=0, M_0=0.82), Re_T is $2.03 \cdot 10^6$ resulting in an area-averaged transition point based at the Mean Aerodynamic Chord (MAC) of approximately 5%. ΔRe_T is introduced in order to allow for the consideration of skin friction drag reduction due to laminar flow technologies, which may have a significant impact on the ingested drag ratio, β, for propulsive fuselage configurations. A synopsis of important β sensitivities captured by the aircraft model is presented in Figure 5.

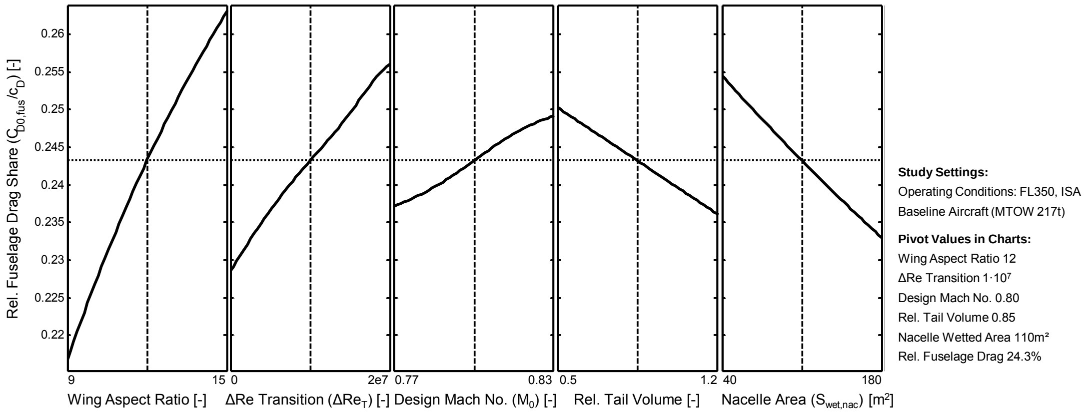

Fig. 5: Matrix of partial dependencies showing selected sensitivities of fuselage relative drag share based on model of typical twin-engine wide-body aircraft

4.2 Description of Propulsion System Model

For the intended studies, the baseline aircraft model was equipped with advanced power plants. Propulsion system sizing and performance simulation was conducted using the gas turbine performance program GasTurb®11 [26]. A two-spool geared unmixed flow turbofan architecture was chosen for the studies performed. Typical design laws were applied for cycle and flow path sizing, including iterations for design net thrust, Overall Pressure Ratio (OPR), outer and inner Fan Pressure Ratios (FPRs), fan tip speed, as well as the nozzle thrust and discharge coefficients based on References [14] and [27]. Turbo component efficiency and cycle temperature levels, as well as ducting pressure losses were adjusted to reflect technology status corresponding to Entry-Into-Service, EIS, year 2035. Technology settings retained constant throughout the performed studies. Consistent High Pressure Turbine (HPT) cooling settings were adopted for all gas turbine designs investigated, based on the approach presented in Reference 14. A best and balanced OPR was determined w.r.t. turbine entry temperature and corresponding cooling air demand. Compressor work split was chosen to allow for uncooled LPTs considering twin-engine aircraft application. Core size effects on the efficiency of turbo components were neglected, in the first instance. Gearbox losses intrinsic to Geared TurboFan (GTF) architecture were incorporated mechanical losses of the low pressure spool, however, independent from reduction gear ratios resulting from the asynchronism of fan rotational speed and the rotational speed of the LPT. Nacelle dimensions, i.e. the length to diameter ratios of fan cowlings, were determined based on a correlation given in [14].

Power plant system weight estimation was based on a component build-up approach. The estimation of turbo component masses is based on the method presented in Reference 14. Accordingly, the mass of rotating parts in turbo components, such as disks, blade and hub structures, are calculated in a stage-wise correlation to the An^2 metric, i.e. local annulus cross-sectional area (A) multiplied with the rotational spool speed (n) squared, and, the specific strength of the material used [14]. For the prediction of fan component masses in this paper, the method was extended through a geometry-oriented approach for the estimation of the stationary masses, i.e. shrouds and casings, stator vanes and structures. Therefore, the stationary parts were approximated through geometric primitives. Shroud and casing were assumed to be bodies of revolution featuring rectangular cross sections. Stators / struts were represented through cuboid bodies. The masses of the individual parts, subsequently, resulted from the product of displaced material volume and corresponding density. Considering technology standards, the design of fan stationary parts was assumed to be based on Carbon Fiber Reinforces Polymers (CFRP). For fan rotor mass estimation, a material specific strength, i.e. material density per yield strength, was chosen to reflect a mix of 20% titanium and 80% CFRP. The estimation of propulsor drive gearbox masses is based on a correlation given in Reference 28 exhibiting sensitivity to gear ratio and output torque, which was calibrated to reflect the advanced technology status considered in the present paper. The estimation of nacelle component and equipment masses refers to the methods described in Reference 14. A representative component mass breakdown calculated for an advanced GTF based on the set of methods described above can be found in Reference [16].

For the weight estimation of the fan module of the propulsive fuselage PPS which in the present arrangement features a very high hub to tip ratio compared to podded fans designs, the method described in Reference [10] was employed using identical material properties as for advanced GTF fan type. The power transmission to the fuselage fan is a key element of the propulsive fuselage concept. In the present context, mechanical transmission via gearbox system was assumed. As a first approach, gear system weights were linearly extrapolated from gearbox weights calculated for podded GTF power plants acc. to [28] using the ratio of fan inlet hub diameters as a scaling parameter. Fuselage fan cowling weight was scaled using its external wetted area based on an empirically derived area specific weight. The weights of nacelle geometry adapting devices, i.e. morphing systems, potentially required in order to cater for varying boundary layer shaping at different aircraft operating conditions were neglected, in the first instance.

4.3 Modelling of Stream Tube Losses

The momentum deficit formed by fuselage skin friction in front of the power plant intake of a propulsive fuselage arrangement manifests as a total pressure loss relative to the total pressure of the undisturbed free stream at flight velocity V_0. Hence, the total pressure ratio in the propulsion stream tube expressed as an equivalent isentropic ram pressure recovery factor yields:

$$\frac{p^*_{t,1}}{p_{t,1}} = \frac{\left(1+\frac{\gamma^*-1}{2}\cdot M^{*\,2}_{1,m}\right)^{\gamma^*/\gamma^*-1}}{\left(1+\frac{\gamma-1}{2}\cdot M_0^{\,2}\right)^{\gamma/\gamma-1}} \approx \frac{\left(1+0.2\cdot M^{*\,2}_{1,m}\right)}{\left(1+0.2\cdot M_0^{\,2}\right)} \quad (12)$$

where $p^*_{t,1}$ represents the total pressures at the propulsion intake including boundary layer effects and $p_{t,1}$.denotes the corresponding total pressure obtained from ideal ram pressure recovery. As a convenient simplification, the isentropic exponents, γ and γ^*, may be assumed identical. While the free stream Mach number, M_0, is directly correlated to V_0, the equivalent mean intake Mach number in the BLI case, $M^*_{1,m}$, requires special consideration.

For the determination of $M^*_{1,m}$, here, CFD simulated velocity profiles at different longitudinal positions of an axisymmetric fuselage geometry with typical wide-body dimensions [10, 29] were employed. In order to allow for parametric investigation of fuselage length, flight Mach number and altitude, the velocity profiles were normalized, boundary layer thicknesses, δ, were determined and extrapolated based on a classic correlation for turbulent boundary layer thickness ($\delta = c_\delta \cdot x_{Fus} \cdot Re_x^{-0.2}$) given in [30]. Different relative longitudinal intake positions along the fuselage surface were covered through interpolation of the scaled velocity profiles. The representative mean intake velocities of fuselage propulsors, $V^*_{1,m}$, and thus $M^*_{1,m}$, were computed from annular integration of the scaled and interpolated velocity profiles.

5 Parametric Design Results

In this section, initial results based on the previously discussed methodological setup are presented including an isolated sizing study of a BLI fuselage fan propulsion system, as well as an aircraft integrated sizing study comprising sensitivities of the vehicular efficiency of propulsive fuselage configurations w.r.t. to selected sizing and technology parameters. For both studies, the control volume and corresponding efficiency definitions elaborated in Section 3 were applied. The *PSC* interpretation adopted referred to the control volume of the propulsive device, i.e. assuming zero additional ram pressure losses in the core engine stream tube in excess of the area averaged stream tube losses at the complete power plant intake. For the studies presented, ideal wake filling is assumed, i.e. the nozzle thrust coefficients used during power plant performance simulation referred to widely uniform jet velocities, in the first instance.

5.1 Fuselage Fan Sizing Study

As a first study, an isolated sizing study for the BLI fuselage fan system was performed. Therefore, the duct height of the aft-fuselage mounted propulsive device, h^*_1, was varied at invariant thrust requirements and a prescribed ingested drag ratio $\beta = 20\%$ which is in good correspondence to the drag breakdown of the baseline aircraft model previously given in Table 2, assuming all fuselage zero-lift drag to be utilized for wake filling purposes. In Figure 6, basic properties of the BLI propulsive fuselage configuration are displayed for the initial parametric power plant sizing study. The plotted characteristics illustrate the growing air intake area, A_1, as well as the improving stream tube total pressure recovery ratio, $p^*_{t,1}/p_{t,1}$, as h^*_1 is increased. Here, the trend of $p^*_{t,1}/p_{t,1}$ directly results from the model discussed in Section 4.3.

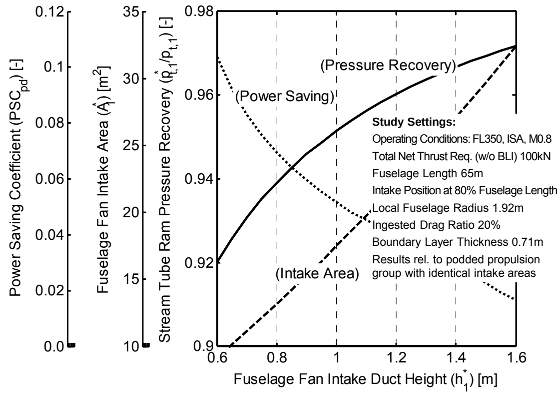

Fig. 6: Basic propulsion system characteristics obtained from initial BLI fuselage fan sizing study

The obtained $p^*_{t,1}/p_{t,1}$ values decline to approximately 92% at the lower end of the h^*_1 range shown in the figure. It should be noted, however, that duct heights h^*_1 of the propulsive fuselage configuration smaller than the boundary layer thickness, $\delta = 0.71$m in the case presented in Figure 6, do not appear meaningful, as the wake-filling potential is not fully exploited. In practice, a lower limit of h^*_1 for complete fuselage BLI is expected to be greater than δ, in order to cater for various operating conditions including e. g. different fuselage angles of attack.

Also shown in Figure 6 is the *PSC* of the propulsive fuselage configuration relative to conventional podded propulsion group at identical air intake areas. The power saving potential of the propulsive fuselage configuration is significant, featuring a maximum value of 10% for the given study conditions. Interestingly, the *PSC* reduces as intake area is increased – irrespective of the simultaneously improving stream tube pressure recovery. In order to understand this initially counterintuitive behaviour, a deeper analysis of the underlying trends in propulsion system characteristics is necessary. Therefore, Figure 7 shows the direct comparison of the BLI propulsive fuselage configuration and the corresponding conventional podded propulsion group, plotted versus fan face area.

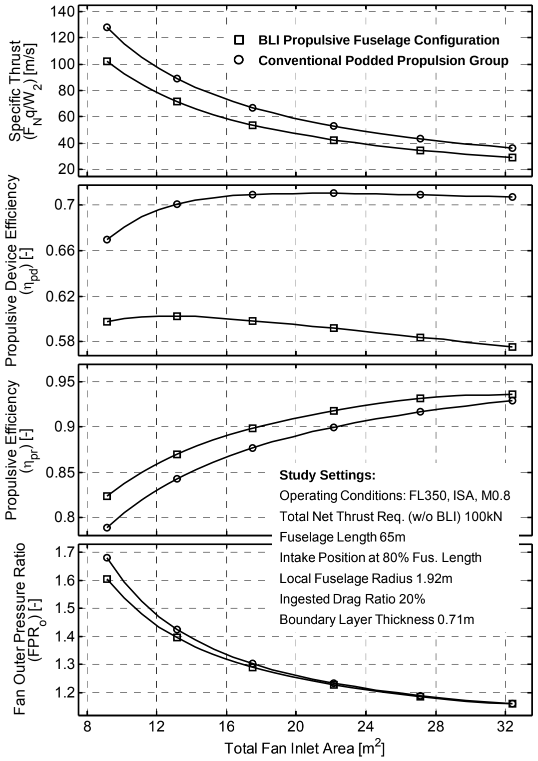

Fig. 7: Direct comparison of BLI fuselage fan and conventional podded fan

The figure illustrates the reduced net specific thrust levels, F_N/W_2, for the propulsive fuselage compared to the podded propulsion arrangement for a given fan face area, which directly reflects the reduced net thrust requirement due to the ingested fuselage zero-lift drag. Hence, the offset in F_N/W_2 is 20%, throughout the study shown. Considering this, one might expect a similar trending behaviour in fan pressure ratios. The relative trending in FPR, however, is superimposed by the non-constant stream tube pressure recovery ratio in the fuselage fan case, leading to convergence in FPR trends for both configurations as fan face area grows.

As expected, η_{pr} improves with reducing F_N/W_2. The reduction of F_N/W_2, however, as an inverse effect on the efficiency of the transmission system, η_{tr}, (cf. Figure 3): As an intrinsic characteristic of ducted propulsive devices, the impact of pressure losses in the transmission system scales inversely proportional to F_N/W_2. As a plausibility check, consider the limit of F_N/W_2 approaching zero, in which case all useful power, P_{useful}, cf. Eq. (2), would be required to compensate for transmission system losses, thereby yielding $\eta_{tr} = 0$.

For the BLI propulsive device, irrespective of the improving $p^*_{t,1}/p_{t,1}$ trend with increasing intake area, the stream tube losses still exceed the losses occurring in the free incidence case, i.e. podded power plants. Due to this fact, η_{tr} of the fuselage propulsor is penalised more significantly through reducing F_N/W_2 than the podded reference, and, transmission system efficiencies, therefore, diverge. This effect can be seen in the plot of η_{pd} shown in Figure 7, and, is the reason for the opposing trends of PSC and $p^*_{t,1}/p_{t,1}$ in Figure 6. Examining Figure 7, again, the individual intensities of the previously characterised opposing trends of η_{pr} and η_{tr} form the shape of the individual η_{pd} curves for both propulsion options, and thus, influence the locus of the corresponding η_{pd} optima.

5.2 Aircraft Integrated Design Sensitivities

As a second step, the potentials of the propulsive fuselage concepts were evaluated at the integrated aircraft level. Therefore, the isolated propulsion system performance model was supplemented by the methods for weight estimation outlined in Section 4.2, and, connected to the aircraft model discussed in Section 4.1. Based on this setup, net thrust requirements and fuselage drag shares, i.e. ingested drag ratios, were obtained from the aircraft model and propulsion system characteristics including TSFC, nacelle wetted area and propulsion system weights were iteratively fed back to aircraft performance simulation. As the relevant figure of merit for the vehicular efficiency, block *ESAR*, i.e. the total energy consumed per block distance traveled, was used in the study. A synopsis of trends of important aircraft characteristics obtained from a variation of fuselage fan intake duct height, h^*_1, is presented in Figure 8 (overleaf). In the study, the complete fuselage share of aircraft total drag was assumed to be ingested in the propulsive fuselage power plant system. The results displayed for block *ESAR*, *PSC* and propulsion group mass are characterised as relative changes compared to a reference aircraft configuration featuring identical technology settings, but under-wing podded propulsion systems. In a preceding trade study, an *ESAR* optimal BPR of 18 – which corresponds to of approximately F_N/W_2 of 83m/s – had been identified for the reference GTF power plants.

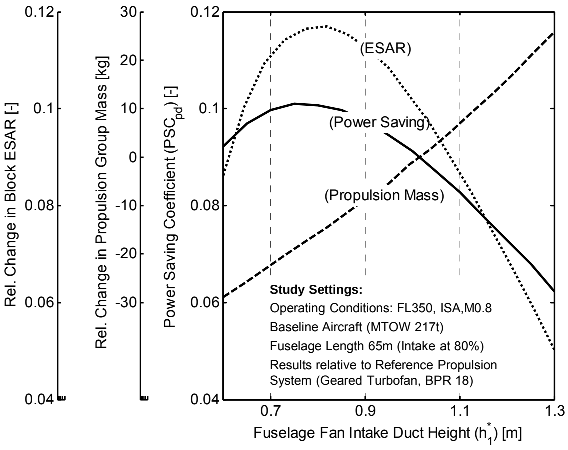

Fig. 8: Basic aircraft characteristics obtained from initial BLI fuselage fan sizing study

It can be seen that both figures of merit, the *PSC* and block *ESAR*, exhibit stationary points w.r.t. h^*_1. The *PSC* optimum of 10.0% improvement over the conventional reference case results from two important counteracting effects: Firstly, the PSC benefit, in general, declines as F_N/W_2 reduces. Note that the concave *PSC* trending versus F_N/W_2 seen in Figure 6, has changed to a convex curve shaping as the reference for *PSC* evaluation was retained constant in the present context. And secondly, towards the lower end of the h^*_1 range, power saving potential is strongly penalised relative to the fixed podded reference due to the decreasing $p^*_{t,1}/p_{t,1}$. Moreover, if h^*_1 underruns the value of δ, the theoretical potential for fuselage drag ingestion cannot be fully utilised.

The obtained *PSC* benefit is propagated to block *ESAR* including vehicular cascade effects yielding an optimum *ESAR* gain over the reference configuration of 11.7%. The *ESAR* and *PSC* stationary points almost coincide w.r.t. h^*_1. The slight dislocation of the maximum block *ESAR* to the right, relative to the *PSC* optimum, is rooted in the reduced dependency on the ingested drag ratio, β, compared to the *PSC* metric. Recall, as the wetted area of the fuselage propulsion group grows with size, β reduces against increasing h^*_1. The value improvements found for both, power saving and vehicular efficiency, appear comparable to results published in the past [10]. Also captured in the *ESAR* figure-of-merit, is the fuselage propulsion group weight trend versus system size, which breaks even with the reference at h^*_1 value slightly above 1m (cf. Figure 8).

Finally, starting from the identified *ESAR* optimum, a preliminary investigation the *ESAR* sensitivities was performed with regard to selected technology parameters, and, design cruise Mach number as a classic operational variable. The obtained partial dependencies can be seen in Figure 9.

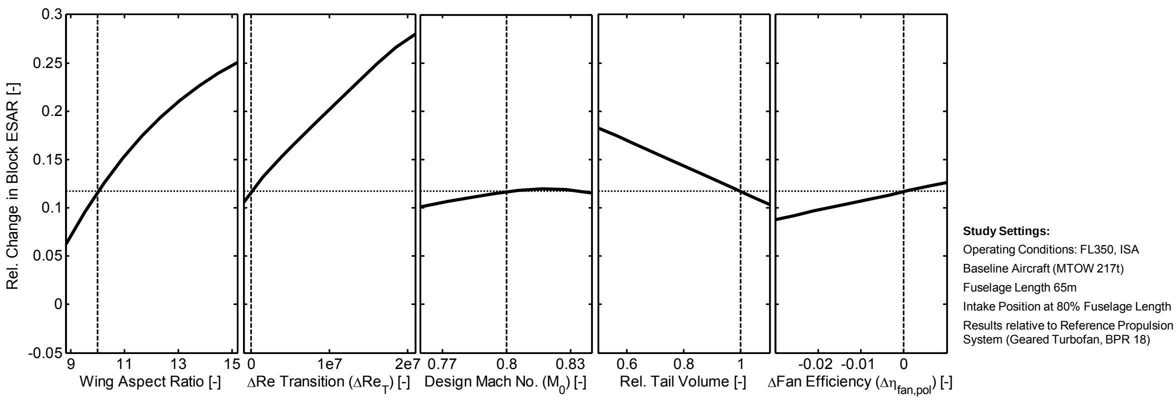

Fig. 9: Matrix of partial dependencies showing sensitivities of aircraft energy specific air range for propulsive fuselage concept

Extrapolating from the previously identified 11.7% *ESAR* improvement over the reference case, the impacts of wing aspect ratio and the defined delta in wing flow transition Reynolds number are dominant, both individually triggering changes in *ESAR* of the order to 20% within the investigated range of parametric variation. Also, the relative reduction of tail volume would suggest a significant improvement in *ESAR*. It should be noted, that all of these three *ESAR* sensitivities are rooted in the corresponding impact on relative fuselage drag, and thus, the ingested drag ratio (cf. Figure 5). In contrast to this, *ESAR* exhibits only a minor penalty due to degradations in fan polytropic efficiency which would be an expected result of the inevitable inflow distortion in a propulsive fuselage configuration. The block *ESAR* sensitivity obtained for design cruise Mach number suggests the propulsive fuselage configuration to be robust against speed variation. This would be significant difference from well-known ducted and unducted propulsion options in podded configuration which typically benefit from reduced operational speeds [14].

6 Conclusion and Future Work

In this paper, the analytical basis for the quantification of efficiency benefits connected to the propulsive fuselage concept were discussed. Appropriate control volume and consistent efficiency chain definitions were introduced. The concept of a Power Saving Coefficient, PSC, formerly introduced by Smith, was translated to be directly applicable to state-of-the-art propulsion system performance simulation software. A parametric model for typical wide-body aircraft application was developed, thereby, sensitivities in mass and drag breakdown w.r.t. important design and technology parameters were captured. A multidisciplinary set of methods for propulsion system design and performance was compiled and connected to the gas turbine performance program GasTurb®11. A simplified boundary layer model was derived from axisymmetric fuselage CFD simulation and used to determine the momentum deficit ingested by the fuselage propulsor.

In a first parametric sizing study of the propulsive fuselage power plant system, up to 10% power saving potential was identified relative conventional podded power plants sized for identical fan inlet areas. In a succeeding study, the power saving and efficiency potentials of the propulsive fuselage configuration were evaluated at the vehicular level. Here, dedicated optima were found for both, the PSC as well as a recently introduced figure-of-merit for vehicular efficiency, the Energy Specific Air Range, ESAR. At optimum conditions, the previously found maximum values of the PSC were echoed. Capturing the aircraft-level cascade effects of reduced propulsive power demand, peak ESAR improvement yielded 11.7% relative to a technologically similar reference aircraft equipped with under-wing podded geared turbofans featuring a bypass ratio of 18. In a preliminary sensitivity study, finally, the individual impacts of decisive aircraft design and technology parameters on ESAR were investigated. A most interesting result from this preliminary analysis was the relatively small speed sensitivity of propulsive fuselage vehicular efficiency which, if confirmed by more detailed studies in the future, would represent a clear distinction from well-known principles of advanced podded propulsion system options.

The presented studies highlighted the significant power savings, and thus, the vehicular efficiency potentials of propulsive fuselage aircraft concepts. Important aspects in quantifying these potentials even more precisely are associated with the mapping of the aerodynamics in the propulsion stream tube. Future work should focus on an extension of the presented set of methods in order to improve boundary layer flow representation and its interaction with the propulsive device. An appropriate resolution of the velocity profiles through the propulsor also in the radial dimension could lead to a more precise estimation of the wake filling quality, and, basic design requirements for wake ingesting fuselage propulsors could be back-derived. Moreover, preliminary observations during the present work substantiated the intuitive expectation of significant performance penalties if the core engine ingests the inner portion of the fuselage boundary layer flow. Future work should, therefore, explore suitable solutions for the integration of fuselage fan power supply. This should also include novel ways of power transmission to the large fuselage propulsor, e.g. through (hybrid-) electric power train options.

7 Acknowledgements

The authors would like to thank Julian Bijewitz and Clément Pornet for their support in reference engine and aircraft modeling, respectively, as well as, Askin Isikveren and Sascha Kaiser for fruitful technical discussions. In particular, the authors would like to thank Hans-Jörg Steiner for his preceding research on distributed propulsion at Bauhaus Luftfahrt and valuable advice during the preparation of this paper. This research was conducted within the FP7-L0 project DisPURSAL (Grant Agreement No. FP7-323013), co-funded by the European Commission.

References

[1] European Commission, “Flightpath 2050: Europe’s Vision for Aviation,” 2011.

[2] Advisory Council for Aviation Research and Innovation in Europe, “Strategic Research & Innovation Agenda,” 2012.

[3] G. Wilfert, “NEW Aero engine Core concepts (NEWAC).” FP6-2005-Aero-1, Contract No. AIP5-CT-2006-030876, European Commission Directorate General for Research and Innovation, 2006.

[4] R. von der Bank, “Low EMissions COre-Engine TEChnologies (LEMCOTEC).” FP7-AAT-2011-RTD-1, Proposal No. 283216, European Commission Directorate General for Research and Innovation, 2010.

[5] H. Sendrane, “Engine BREAK-through components and sub-systems (E-BREAK).” FP7-AAT-2012-RTD-1, Proposal No. 314366, European Commission Directorate General for Research and Innovation, 2011.

[6] J.-J. Korsia, “Environmentally Friendly Aero-Engine (VITAL).” Contract No. AIP4-CT-2004-012271, European Commission Directorate General for Research and Innovation, 2005.

[7] D. Bone, “valiDation of Radical Engine Architecture systeMs (DREAM).” FP7-AAT-2007-RTD-1, Proposal No. 211861, European Commission Directorate General for Research and Innovation, 2008.

[8] A. T. Isikveren, A. Sizmann, and M. Hornung, “Realising Flightpath 2050: Initial Investigation of Potential Technological Solutions.” SAE 2011 AeroTech Congress and Exhibition, Toulouse, France, 11ATC-0562, 2011.

[9] H. D. Kim, “Distributed propulsion vehicles,” in 27th International Congress of the Aeronautical Sciences (ICAS), 2010.

[10] H. Steiner, A. Seitz, K. Wieczorek, K. Plötner, A. T. Isikveren, and M. Hornung, “Multi-Disciplinary Design and Feasibilty Study of Distributed Propulsion Systems,” in 28th International Congress of the Aeronautical Sciences (ICAS), 2012.

[11] A. T. Isikveren (coordinator), “Distributed Propulsion and Ultra-high By-pass Rotor Study at Aircraft Level (DisPURSAL).” FP7-AAT-2012-RTD-L0, Proposal No. 323013, European Commission Directorate General for Research and Innovation, 2012.

[12] S. Stückl, J. van Toor, and H. Lobentanzer, “VoltAir – The All Electric Propulsion Concept Platform – A Vision for Atmospheric Friendly Flight,” in 28th International Congress of the Aeronautical Sciences (ICAS), 2012.

[13] A. Bolonkin, “A high efficiency fuselage propeller (‘Fusefan’) for subsonic aircraft,” in World Aviation Conference, San Francisco, 1999.

[14] A. Seitz, “Advanced Methods for Propulsion System Integration in Aircraft Conceptual Design”, PhD Dissertation, Institut für Luft- und Raumfahrt, Technische Universität München, 2012

[15] "Performance prediction and simulation of gas turbine engine operation for aircraft, marine, vehicular, and power generation". Final Report of the RTO Applied Vehicle Technology Panel (AVT) Task Group AVT-

036, North Atlantic Treaty Organisation (NATO), February 2007. TR-AVT-036.

[16] A. Seitz, O. Schmitz, A.T. Isikveren, M. Hornung, “Electrically Powered Propulsion: Comparison and Contrast to Gas Turbines”, Paper No. 1358, Deutscher Luft- und Raumfahrtkongress 2012, Berlin, September 2012

[17] A. Seitz, A.T. Isikveren, M. Hornung, "Pre-Concept Performance Investigation of Electrically Powered Aero-Propulsion Systems", AIAA-2013-3608, presented at 49th AIAA/ASME/SAE/ASEE Joint Propulsion Conference and Exhibit, San José, CA, USA, 14-17 July, 2013

[18] L. H. Smith Jr., "Wake ingestion propulsion benefit". Journal of Propulsion and Power, Vol. 9, pp 74-82, 1993.

[19] E. Torenbeek. "Synthesis of Subsonic Airplane Design". Kluver Academic Publishers, Dordrecht / Boston / London, 1982.

[20] O. Gur, W. Mason, and J. Schetz. "Full configuration drag estimation". AIAA 2009-4109, In 27th AIAA Applied Aerodynamics Conference, San Antonio, Texas, 22 - 25 June. American Institute of Aeronautics and Astronautics, Inc., 2009.

[21] Luftfahrttechnisches Handbuch. www.lth-online.de, 2006.

[22] K. Seywald, "Wingbox Mass Prediction considering Quasi-Static Nonlinear Aeroelasticity", Diploma Thesis, Technische Universität München, 2011.

[23] D. Eisenbarth, "Elastic Instability Analysis and Integration for a Non-Linear Structural Design Tool", Term Paper, Technische Universität München, 2013.

[24] D. Raymer, "Aircraft Design: A Conceptual Approach". AIAA Education Series. American Institute of Aeronautics and Astronautics, Inc., New York, NY, 4 edition, 2006.

[25] M. Hepperle, "MDO of Forward Swept Wings", KATnet II Workshop, 28-29 January 2008, Braunschweig.

[26] Kurzke, J., Gasturb11, Compiled with Delphi 2007 on 27 January, 2010.

[27] Grieb, H., Schubert, H. (Ed.), “Projektierung von Turboflugtriebwerken“ Birkhäuser Verlag, Basel-Boston-Berlin, 2004.

[28] C. Reynolds, "Advanced Propfan Engine Technology (APET) Single- and Counterrotation Gearbox / Pitch Change Mechanism, Final Report", Pratt & Whitney United Technologies Corporation, NASA-CR-168114, Vol. 1 & 2, 1985

[29] L. Van Dyck, "Design study of a boundary layer ingesting Propulsive Fuselage concept". Master's Thesis, Delft University of Technology, 2012.

[30] H. Schlichting and K. Gersten, Grenzschicht-Theorie, Berlin Heidelberg: Springer-Verlag, 2006.

4:th CEAS Air & Space Conference
FTF Congress: Flygteknik 2013

On inspection systems for repairs of composite structures in aircrafts

Marie Jonsson, Örjan Festin and Bengt Wälivaara
Compraser Ekonomisk Förening, Westmansgatan 47, 58216 Linköping, Sweden;
marie.jonsson@compraser.se; orjan.festin@compraser.se; bengt.walivaara@compraser.se

Lars Wistfors
Exova Materials Technology, Box 1340, 581 13, Linköping, SE-58113, Sweden
lars.wistfors@exova.com

Keywords: *vision system,cleaning, repair, composites, documentation, CFRP*

Abstract

In repairs of fiber reinforced products, contaminants like oil or dust and the position and fiber orientation of the plies used, are crucial for success. On-site quality control is usually performed manually and documentation consists of signed procedures. One reason for this manual approach has been the difficulty to apply reliable portable procedures and technology for automatic inspection of both the pre-preg tapes and weaves used to build a carbon fiber reinforced product and of the material to be repaired. Since these materials are black, and/or glossy, display poor contrast and have low form-stability; commercially available inspection systems that can be used during repairs have been scarce. Also strict standards and regulations within the aerospace industry inhibit the introduction of new technologies in the manufacturing chain. In order to reduce the connection between operator/technician skill and resulting quality automated inspection systems can be introduced.

Vision technology based systems are commonly used in many industrial sectors for quality inspection. One well established field of use is found in the electronic industry when verifying the position of electronic components on circuit boards. Another is the automotive industry, for example, in adaptive weld seam tracking.

New and interesting systems for contaminant inspection of fiber reinforced materials are also surfacing, which can be used in repairs to check cleanliness and ensure bondability.

The paper looks at these different technologies, and relates them to the challenges posed by inspection and documentation during repair of aircrafts structures. Thus this paper is a "state of the art" survey of potential vision and contaminant inspection technologies applicable for manufacturing and repair of fiber reinforced products. Technical challenges that must be addressed by a quality assurance system used for repairs are also described.

1 Introduction

Components made of Fiber Reinforced Plastics (FRP) have been used in aircrafts since the 1950's due to their light and strong properties which makes the material suitable for high performance structural components. The reduced weight (compared to metallic products) also means reduced fuel consumption which is an important competitive trait in today's industry and a strong commercial driver for increased use of FRP for civil passenger aircrafts and other industrial sectors.

FRP is also common in marine applications, for example in hulls, where the material adds the benefit of corrosion resistance. It is also becoming more common in the automotive industry, where for example the BMW i3 has a passenger cell built (almost) completely in Carbon Fiber Reinforced Plastics (CFRP). In the high-volume automotive industry however, short cycle times together with low scrap rates are key issues that has to be handled by the manufacturing system.

1.1 Some repair basics

As with any material, FRP products may be damaged from impact or for other reasons like wear, misuse etc. In many cases, especially regarding aircrafts, it is not economically feasible to replace a damaged part, for instance an entire wing section; instead the part must be repaired or at least partially replaced. The decision to repair or replace depends on many factors like economy, damage type and size, product interface and location etc. For the aircraft industry, guidelines on when and how to repair are well established. A comprehensive description of repairs and procedures is given in [1] which is part of the summary below.

Any damage must first be properly assessed before a decision can be made on how the damage should be repaired. Damage in metal structures can often be determined with ocular inspection since dents or scratches are visible on the surface. For FRP structures however, even serious damage can be hidden. Delamination where fiber layers have separated causing reduction in strength may occur below a (seemingly) undisturbed surface. The same goes for fiber fractures. Methods for damage assessment in FRP materials ranges from tap testing (tapping the material and listening to the response sound) to NDT methods using C-scans and thermography. These are very important technologies for repair of FRP structures but will not be covered in this paper.

After the damage has been assessed, material is removed from the damaged areas. The extent of the area to be removed depends on damage size, repair method and type of FRP structure and other geometrical properties (for example the thickness). In the aircraft industry there are also guidelines on the removed volume and geometry. Material removal is mostly done through routing, using hand machines together with precut patterns or by abrasive grinding. In this stage it is important to detect and avoid any contamination of the part, from for example dust or oil. This will be further discussed under 2.1.

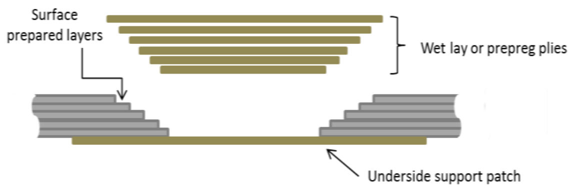

Fig. 1 - Stepped scarf repair (adapted from ref [1]) also known as stepped joint.

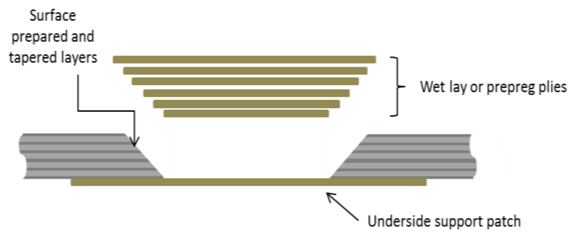

Fig. 2 - Tapered scarf repair (adapted from ref [1]) also known as scarfed joint.

The choice of repair method is often, as described above, guided by rules set by different industry organizations. One common repair method is the "scarfed repair technique", with stepped or tapered interfaces between the repair and the product (see Fig. 1 and Fig. 2). In stepped scarfed repair, routing is used to create a stepped void. The removed volume is then rebuilt using wet lay or pre-preg plies, where each ply has the same fiber direction as the corresponding layer of the removed material. The direction of the fiber is chosen according to repair manuals and drawings of the part, and correct information on the structure is crucial. For a tapered interface, the void is created using abrasive grinding, and the volume is then rebuilt as previously described. To create the tapered hole with correct taper angle and placing the plies in the correct position and orientation requires skill and training.

These two repair methods result in very strong joints with strength close to the original strength of the material. The repairs must however, as implied earlier, be conducted by trained staff and in a suitable environment. Also, to achieve optimum results the area needs to be vacuum bagged and heat cured.

The two methods described rely on the removed material to be rebuilt on-site. Another method is to remove damaged material using routing and grinding (consistent with scarfed repair), and then make a mold of the created cavity used later as a template for a repair patch. The mold is done by applying gelcoat and plaster. The mold is removed when cured and transported to another facility where used as a male tool to recreate the (removed) void in a female tool. The female tool is also created using plaster, and used as a base for pre-preg lay-up and curing of the repair patch. Using this method, the repair patch can be created in a controlled environment. The repair patch is then brought to the sight and applied together with an adhesive (for example an epoxy) to the cavity.

1.2 Documentation and verification of repairs

Verification during the repair process is today mainly done through ocular inspection by the technician performing the repair. Documentation is many times done through a checklist, subsequently signed off as each step is conducted. This method relies on the skill of the technician and very little information on the repair is documented, as most often only a pass/fail or checkbox is recorded. To improve quality assurance an objective verification and documentation method is required which does not solely rely on human skill. With an increased use of FRP products, the demands for proper documentation will increase not only in aircraft industry but also in other sectors. Thus it is important to investigate suitable technologies and methods.

2 Surface inspection systems

More objective inspection can be obtained by using surface inspection systems, such as visions systems, contamination detection systems etc. A wide range of such systems are today commercially available, few are however designed for usage in FRP manufacturing or repairs.

2.1 Systems for surface contamination inspection

Contamination, depending on structure, can be more or less invasive. Honeycomb structures for example must be kept secure from contaminations, since any contaminant may penetrate far into the structure. Contaminants also affect bonding between the pre-preg plies/repair patch and the part that is repaired, and may thus affect the resulting quality of the repair.

A clean surface has a higher surface energy and has better adhesion properties than a contaminated surface. The most common way to check the surface energy and contaminants is to use the water break test, where water is sprayed on the surface to check for droplets. If drops are formed the area has to be re-cleaned and checked again. This method has several drawbacks; one is that water itself may be a contaminant, leaving traces of for example salts, carbonaceous species and/or a thin layer of water hydroxyl (-OH) groups strongly bound to the outermost polymer chains resulting in bad adhesion properties.

Others are that the method is slightly arbitrary and leaves room for subjective interpretation and is thereby hard to document properly.

Other more advanced methods are increasing in use. Optically Stimulated Electron Emission (OSEE) for example, utilizes the photo electric effect. The physical principle this method rely on is that many surfaces (metallic in particular) emit electrons when illuminated with ultraviolet light at the proper frequency (energy). The emitted electrons are then collected with a sensor and the current (electron flow) can be measured [Fig.3].

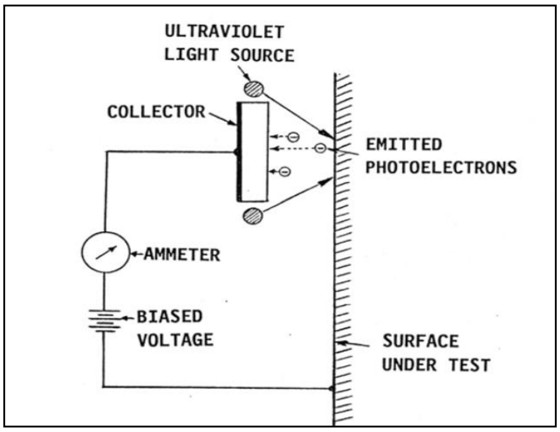

Fig. 3 - The physical principle of the OSEE technique (adapted from ref [2]).

Any contaminant on the surface either inhibits or increases the electron emission, depending on the contaminant properties. Most contaminants are non-photo emitting, thus decreasing the measured current. This method is simple and fast, and relatively inexpensive and has been used on epoxy resin and carbon fiber composites to determine bondability for (subsequent) adhesive joining [3]. However, calibration is required for each combination of substrate material and contaminant. Measurements are performed at discrete points, meaning several readings must be made to cover a large surface.

Fig. 5 - The 4100 ExoScan Series FTIR Scanner (courtesy of Agilent Techchnologies, www. chem.agilent.com)

Infrared spectroscopy is a method where a surface is subjected to infrared light and the absorbed wavelengths are analyzed and used to draw conclusions of the material. One example of infrared spectroscopy applied is the Fourier transform infrared (FTIR) spectrometer used in many laboratories to establish the chemical composition of an un-known substrate. FTIR equipment has traditionally been bulky and unsuitable for on-site applications. However, Agilent Technologies have developed a hand-held FTIR scanner, see Fig. 5. The scanner, along with FTIR technology in general, is currently evaluated as a potential technique for monitoring surface preparation of composite (fiber) material prior to bonding with promising result [4]. The project is conducted in collaboration with Boeing and indicates that FTIR can detect siloxane contaminants from removed peel-ply (a protectant film). Agilent Technologies have done tests showing that the ExoScan can be used to detect the presence of hydraulic fluids and distinguish between surface preparation/cleaning methods [5]. The scanner however will only cover small parts of the surface and several measurements has to be taken on different areas to get a full coverage.

Fig. 4- Example of a surface (left), clean to the naked eye, displaying large amounts of contaminants when illuminated with UV-light (right) (courtesy of UV Light Technology Ltd, http://www.uv-light.co.uk/)

A more direct method is to use UV-light to detect surface contamination. Here the surface is illuminated with UV-light to look for any fluorescent objects [6]. Most organic and some inorganic compounds display this effect. If desired, image processing may be used to check the degree of cleanliness of the surface, i.e. the area fraction of the total area displaying a fluorescent behavior. One advantage of this type of method is that a large area can be examined in a short time.

2.2 Vision repair-aid systems

As previously mentioned (see 1.1) it is important to know the fiber directions of the material to be repaired and to keep track of the orientation of the applied plies in order to achieve a high quality repair. Empiric experience shows that the deviation should preferably not be larger than ±5°. One way to identify fiber directions is to use 2D vision systems together with one or several contrast enhancing light sources. Preliminary investigations show that it is possible to deduce fiber directions in, for instance, uncured pre-preg tapes and weaves using this technique [7]. Another advantage of 2D vision systems is that other kinds of unwanted objects, such as pieces of ply protection films, are more easily detected and documented.

A repair patch can consist of up to 50 different plies (and sometimes even more) in different orientations. Using a 2D vision system enables the position and orientation of each ply to be documented when building up the repair patch. The system can also be used to verify the correct ply fiber orientation and give a pass/fail signal to the technician, thus not only be used as a documentation tool, but as a quality assurance resource.

One disadvantage using 2D vision is that only little or no information on the topography is obtained. If the geometry is of a more complex nature, a portable laser scanning device may be preferable. Especially if the area to be repaired is large requiring a large repair path, bubbles may appear in the laminate. Bubbles are hard to detect by a 2D system, since they display poor contrast. They are however easily detected with laser scanning systems as the height difference from the (nominal) surface can be identified.

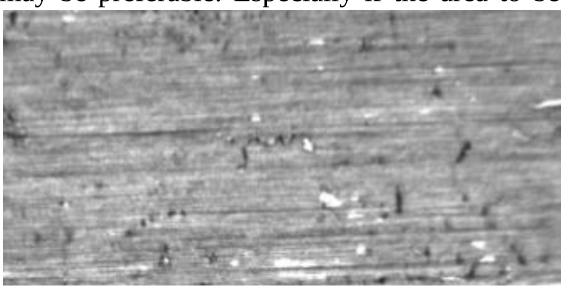

Fig. 6 - Photo of a uni-directional pre-preg tape using an industrial camera together with a contrast enhancing a light source.

2.3 Equipment guidelines and future possibilities

When repairing damaged aircraft parts, the replacement material is preferably of the same FRP type as for the original structure. Any vision or quality control system (i.e., surface inspection system) used has, due to economic and practical reasons, to be as generic and portable as possible. Thus the system must handle different materials with different (optical) properties. Also, repairs may have to be carried out "in the field", and any equipment used needs to be easily transported and have to handle a variety of climate and ambient conditions. For a surface inspection system using vision this means that either the technology has to be able to handle variance in ambient lighting, or create good ambient light conditions itself (like external lamps, or with the ability to close off areas to control glare). Also, since one of the goals should be to minimize the connection between operator/technician skill and quality and documentation, the system has to be user friendly. Herein lies the crux as the system has to be technically advanced in order to manage different site conditions, but tailored with packaged functions and settings so that any readings does not have to rely on setup skill or fine-tuning on behalf of the operator. The latter will hold especially true if FRP materials become more and more common in automotive, where repairs may be done by persons with little knowledge of FRP materials.

Another important issues not discussed in this paper are the issues that will arise when the possibility to measure certain features, like cleanliness, presents itself. Questions like what should be measured, how it should be documented and what are the limits will have to be addressed. With today's "pass or fail" documentation this will require a lot of testing

and may result in a snowball of questions that need to be answered.
Another is the link between documentation and chosen technology. The need for certain measurements in order to document properly will probably impact which technology is chosen for the task.

2.4 Conclusions and future work

FRP materials are increasing in use, both in the aerospace industry and in other sectors. Repair however, is still often performed manually by experts using manual inspection and documentation methods. User friendly and robust vision systems and surface contamination inspection systems would very much increase quality assurance for repairs. Vision systems and technology have proven ability to manage the special requirements of FRP material. Simple 2D systems can with proper lighting be used to detect fiber/pre-preg orientation. Handheld FTIR scanner may be used for surface contamination inspection. The systems must, however, be further developed to fit the repair case (used in ambient light) and to balance high versatility with user friendliness and ruggedness in order to deliver the required benefits.

References

[1] Halliwell S., *Repair of fibre reinforced plastics (FRP) structures,* NCN Best practice guide ,2012

[2] Date R.P., “Bond surface evaluation by OSEE instrument Titan IV payload fairing”, Power Point Presentation, THE AEROSPACE CORPORATION, 1991

[3] Parker, B. & Waghorne, R., “Testing Epoxy Composite Surfaces for Bondability”, *Surface and Interface analysis,* Vol 17, pp.471-476

[4] Flinn, A., (2012) “Infrared Spectroscopy; a potential quality assurance method for composite bonding”, FAA JAMS 2012 Technical Review Meeting, Baltimore MD, USA.

[5] Seelenbinder, J., “Measurement of Composite surface contamination using Agilent 4100 ExoScan FTIR with diffuse reflectance sampling interface”, Application note Agilent Technologies

[6] Kohli R. & Mittal K.L., *Developments in surface contamination and cleaning*, vol. 4. 1st ed., Elsevier Inc. 2012, chap. 3.

[7] Festin Ö., “Vision system based quality assurance for Carbon Fiber Composite manufacturing.”; 24th SICOMP Conference Linköping, 2013

Modeling and Numerical Simulation of an Open-Loop Miniature Capacitive Accelerometer for Inertial Navigation Applications

Petre Negrea, Teodor Lucian Grigorie, Liviu Dinca, Jenica Ileana Corcau
University of Craiova, Faculty of Electrical Engineering, Romania

Keywords: MEMS, accelerometer, capacitive sensing, modeling, simulation. inertial navigation

Abstract

The paper deals with an analogue capacitive micro-accelerometer both from the point of view of mathematical modeling and through the achievement of certain numerical simulations which must confirm the mathematical models and in the same time help to establish the optimal architecture of the system. The capacitive transducer is one of differential type, with two fixed plates and one moving, which play the role of proof mass.

1 Introduction

New technology tendencies in systems miniaturization led to the development of an important segment among modern applications - Micro-Electro-Mechanical Systems (MEMS) technology. A short definition of the MEMS is that they are small devices that can integrate both mechanical and electrical components on the same substrate. The process through which they are provided lies in laborious techniques, difficult to implement called generally micro-fabrication. One of the major advantages of such devices is that they sense, control and actuate on micro scale. The MEMS future is the integration and development of a higher complexity and a larger number of such devices as parts of certain equipment as complex and precise as possible [1]-[4].

The interdisciplinary nature of the MEMS is reflected in their widespread use in various fields, such as mobile phone, automotive, medical, aircraft, etc. [5].

One of the most important MEMS sensors, representing the basis of the INS (Inertial Navigation Systems) is the accelerometer. It is an instrument that senses external accelerations and converts them into electrical signals. The physical principle underlying the accelerometer consists in the measurement of the displacement of a proof mass elastic attached on a fixed substrate. The detection of this displacement can be performed in different ways, but one of the most common is the capacitive one. The architecture of the detection circuit can be conceived with a simple structure or a differential structure [6]-[8].

This paper deals with such a detection method, with differential structure, and is related to a research project that wishes the development of High-precision micro and nano smart sensors for space inertial navigation applications, project financed by Romanian Space Agency (ROSA) at Department of Electric, Energetic and Aerospace Engineering, Faculty of Electrical Engineering, University of Craiova, Romania.

Here presented work exposes an analogue capacitive micro-accelerometer both from the point of view of mathematical modeling and through the achievement of certain numerical simulations to confirm the mathematical models, and in the same time helps to establish the optimal architecture of the system.

2 Mathematical Model of the Detection Unit

The differential capacitive transducer resides in two fixed plates and one moving, which plays the role of the proof mass.

The accelerometer operation principle relies on the action of the input acceleration of a proof mass that has a parallelipipedic shape and is placed on a substrate using four silicon flexible bars (Fig. 1 [9]). On the same substrate there are two electrodes, placed on opposed sides of the mobile plaque. The couple of fixed electrodes and the mobile plaque form two capacitors whose capacities vary with the application of an acceleration that has the ability to change the proof mass position.

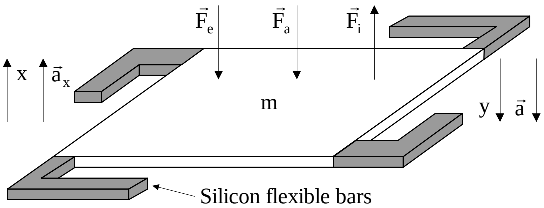

Fig. 1 Mechanical model of the accelerometer.

When the fixed electrodes are not supplied by electric energy, according to Fig. 1 the motion equation of the proof mass is [9]-[12]

$$m\frac{d^2y}{dt^2} = m\frac{d^2x}{dt^2} + b\frac{dx}{dt} + kx, \qquad (1)$$

with

$$F_e = kx, F_a = b\frac{dx}{dt}, F_i = ma = m\frac{d^2y}{dt^2}, \qquad (2)$$

and m - proof mass, $\vec{a}$, y acceleration and position of the carrying vehicle, $\vec{a}_x$, x acceleration and proof mass position with respect to the carrying vehicle, $\vec{F}_e$, $\vec{F}_a$, $\vec{F}_i$ - the elastic, the damping and respectively the inertial forces, k - total elasticity constant. The viscous damping coefficient b is given by [9], [14]

$$b(x) = \frac{1}{2}\mu A^2\left[\frac{1}{(d_0 - x)^3} + \frac{1}{(d_0 + x)^3}\right], \qquad (3)$$

where μ is the air viscosity, A is the mobile plaque area and $2d_0$ is the distance between the fixed electrodes.

If the fixed electrodes are supplied by a high frequency square wave phase-opposite voltages, then Eq. (1) becomes [9]-[12]

$$m\frac{d^2y}{dt^2} = m\frac{d^2x}{dt^2} + b(x)\frac{dx}{dt} + kx - F_{el}; \qquad (4)$$

F_{el} - electrostatic resultant force.

To determine the proof mass displacement x and, implicit the applied acceleration a, the capacitive detection device should be coupled with a charge amplifier whose output voltage reflects the acceleration change (Fig. 2 [9], [13]).

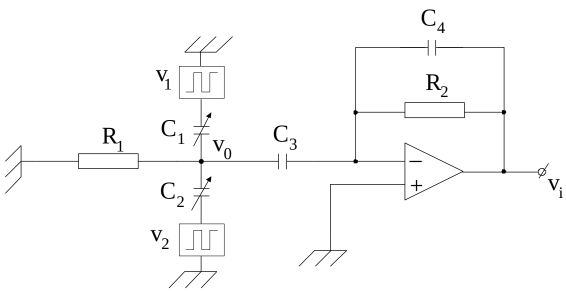

Fig. 2 Detection device with charge amplifier.

Considering only a limited number of harmonics in the square waves v_1 and v_2 voltages developments [15]

$$v_1 = \frac{2V_1}{\pi}\left(\cos\omega t - \frac{\cos 3\omega t}{3} + \frac{\cos 5\omega t}{5} - \right.$$
$$\left. - \frac{\cos 7\omega t}{7}\right), \qquad (5)$$
$$v_2 = -v_1,$$

the resultant electrostatic force results with the next equation

$$F_{el} = F_{el1} - F_{el2} = = \frac{1.1715\varepsilon_0 A V_1^2}{\pi}\left[\frac{1}{(d_0-x)^2} - \frac{1}{(d_0+x)^2}\right]. \quad (6)$$

F_{el1}, F_{el2} – the electrostatic forces acting on the mobile plate; $\omega = 2\pi f$ with $f = 10^5\,\text{Hz}$; V_1 – amplitude of the v_1 and v_2 voltages.

As a consequence, the dynamic equation of the system becomes

$$\frac{d^2x}{dt^2} = a - \frac{k}{m}x - \frac{\mu A^2}{2m}\left[\frac{1}{(d_0-x)^3} + \frac{1}{(d_0+x)^3}\right]\frac{dx}{dt} - + \frac{1.1715\varepsilon_0 A V_1^2}{\pi m}\left[\frac{1}{(d_0-x)^2} - \frac{1}{(d_0+x)^2}\right]. \quad (7)$$

3 Numerical Simulation of the Model

Numerical simulation of the model, for positive and negative acceleration inputs, suggests that the acceleration detection can be performed through the determination of $v_i(t)$ magnitude (see, for example, Fig. 3). Still a very serious problem occurs here. If the signal $v_i(t)$ is demodulated through the extraction of its magnitude, one cannot precisely know if the determined acceleration is positive or negative. As one could see, the acceleration sign is influenced by the $v_i(t)$ phase. As a consequence, during the detection stage one should use a phase-sensitive demodulator as the one depicted by Fig. 4 ([13], [16]).

The demodulator Matlab/Simulink model, depicted by Fig. 5, leads to the characteristics in Fig. 6 for the voltage waveforms up to the input in the low-pass filter (LPF), for positive and negative values of acceleration. The input is a square wave function with the magnitude V_i=1V and the frequency f=10^5Hz. In Fig. 6 were considered the influences of the acceleration sign over the signal phase of the input $v_i(t)$. One can notice that the demodulator operates as a rectifier: in the case a>0 it rectifies along a negative alternation of $v_i(t)$ and in the case a<0 it rectifies along a positive alternation of $v_i(t)$.

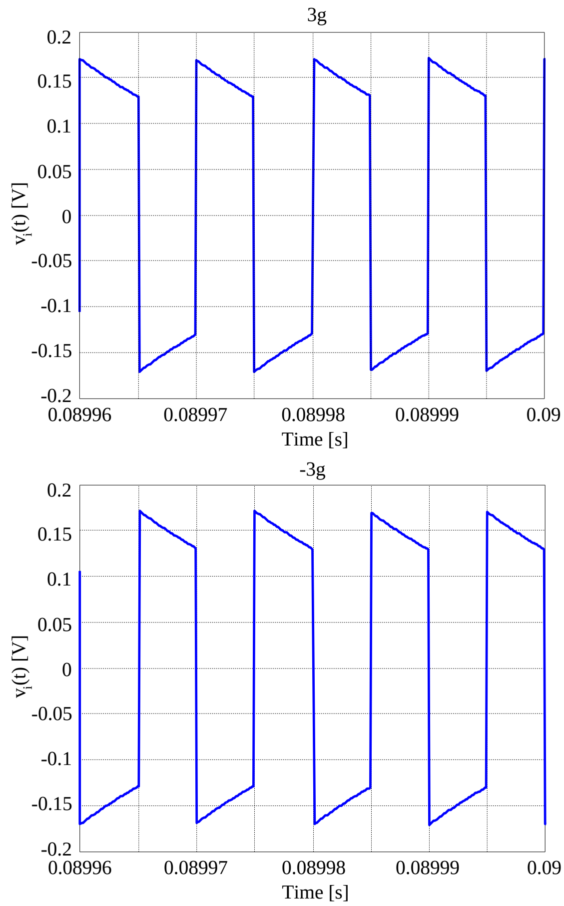

Fig. 3 Zoom of $v_i(t)$ characteristic for 3g and -3g acceleration step signals.

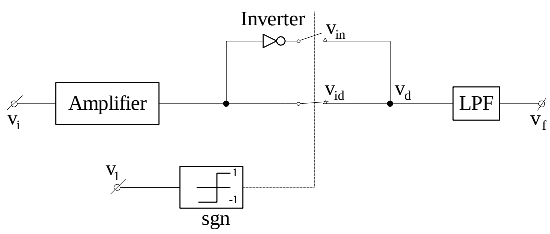

Fig. 4 Phase-sensitive demodulator.

The phase-sensitive demodulator output can be calculated with

$$v_f = k_A \bar{v}_d(t) = k_A \frac{1}{T}\int_0^T v_d(t) = = \frac{k_a k_A}{T}\left[\int_0^{T/2}(-1)v_i(t)dt + \int_0^T v_i(t)dt\right] \quad (8)$$

where T represents the period of the signal $v_i(t)$ that generates $v_d(t)$.

Therefore, we get

$$v_f = \frac{-2k_a k_A}{T}\frac{\varepsilon_0\varepsilon_r A}{C_4 d_0^2} v_1 x \cdot \left[\int_0^{T/2} -v_1(t)dt + \int_{T/2}^{T} v_1(t)dt\right] = \frac{-2k_a k_A}{T}\frac{\varepsilon_0\varepsilon_r A}{C_4 d_0^2} v_1 x(-TV_1) = \frac{2k_a k_A \varepsilon_0\varepsilon_r AV_1}{C_4 d_0^2} x = k_f x, \quad (9)$$

where

$$k_f = \frac{2k_a k_A \varepsilon_0\varepsilon_r AV_1}{C_4 d_0^2}. \quad (10)$$

The first graphical characteristics in both columns of Fig. 6 show the voltage v_{ia} at the output of the amplifier (signal amplified by the gain k_a=-10). From the second characteristic (v_{in}) can be observed how the signals, inversed initially (amplified with -1), evaluate only in the negative, respectively in the positive half-plane due to the switch and to the sign function. The same thing is observed from the third graphic (v_{id}), but for the negative alternation of the original v_{ia} signal at input. By adding the v_{in} and v_{id} signals, a rectified v_d signal is obtained. This signal is stabilized on -10 V (a<0) or on 10 V (a>0) output voltage despite spikes, occurring at every crossing through zero of the summed rectangular signals. These spikes are due to the sine wave signal v_1 which controls the switches.

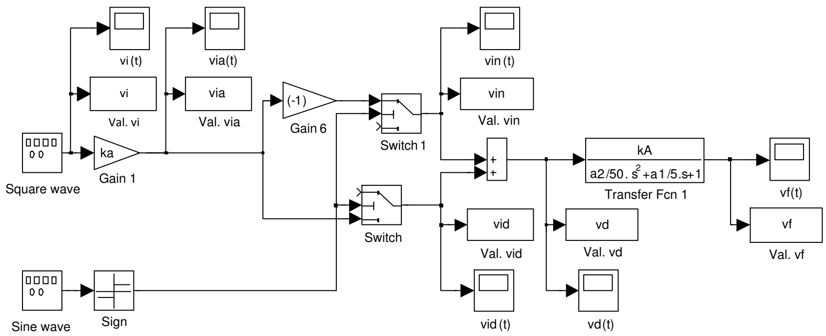

Fig. 5 Matlab/Simulink model of the demodulator.

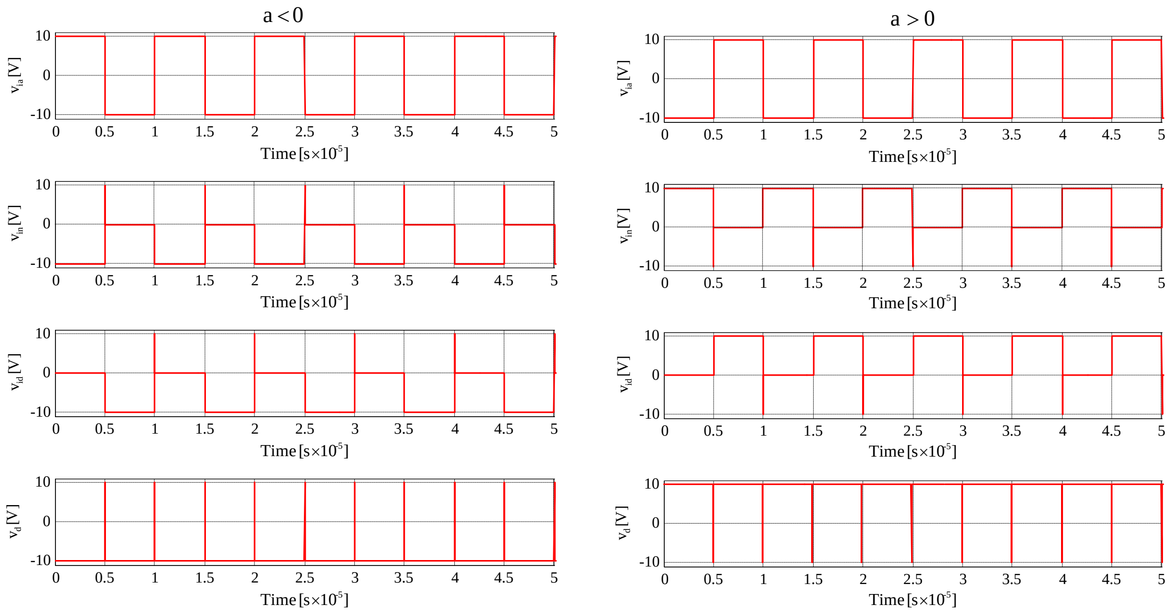

Fig. 6 Voltage waveforms up to the input in the low-pass filter.

The Matlab/Simulink model of the entire accelerometer is presented in Fig. 7. To simulate the accelerometer some step-like inputs acceleration signals were used. In order to emphasize all the possible aspects of the problem, theirs values were chosen as follows: positive and negative values, lower and higher magnitudes and respectively a combination between step inputs that should outline the accelerator ability to follow be means of its output the input quantity. For example, for simple step-like inputs with the values a=-5g and a=5g, the characteristics in Fig. 8 and Fig. 9 were obtained.

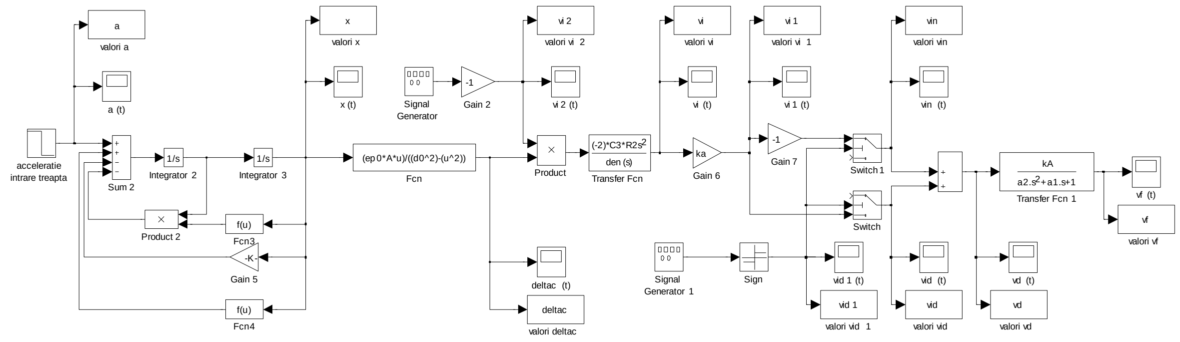

Fig. 7 Matlab/Simulink model of the accelerometer.

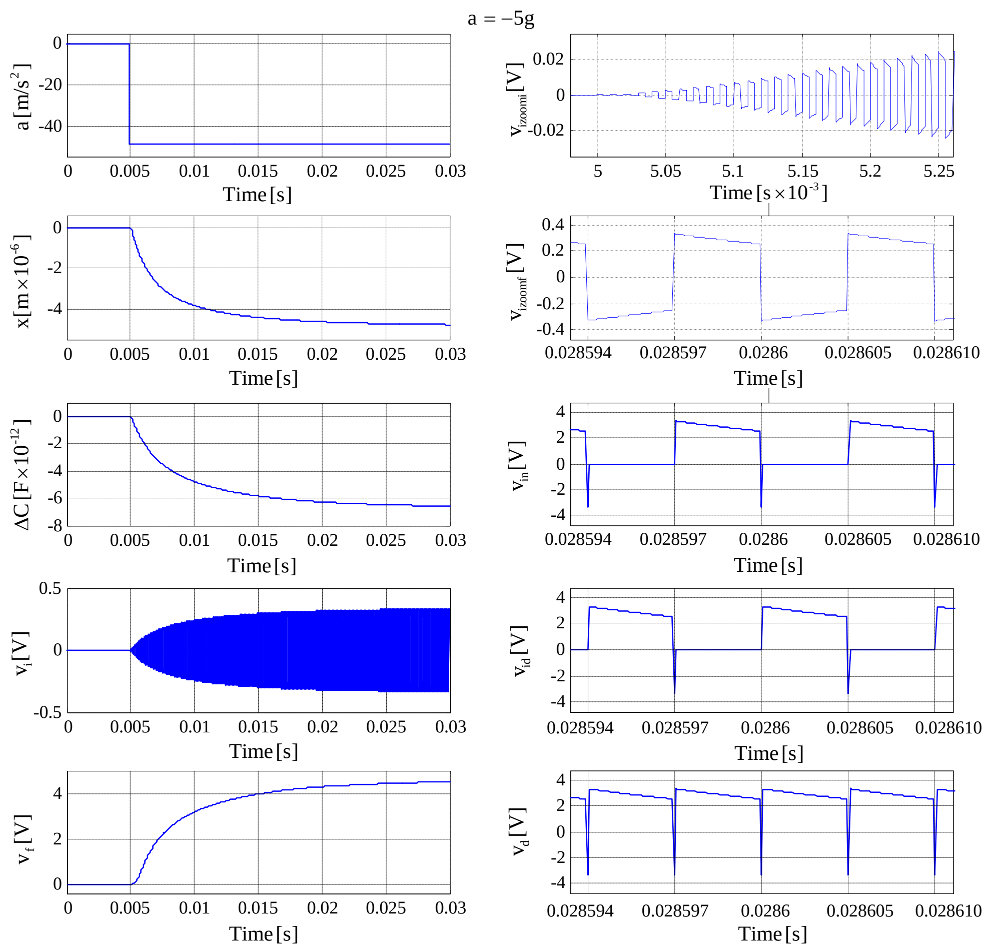

Fig. 8 The time-evolution of all quantities from the block-scheme for a=-5g.

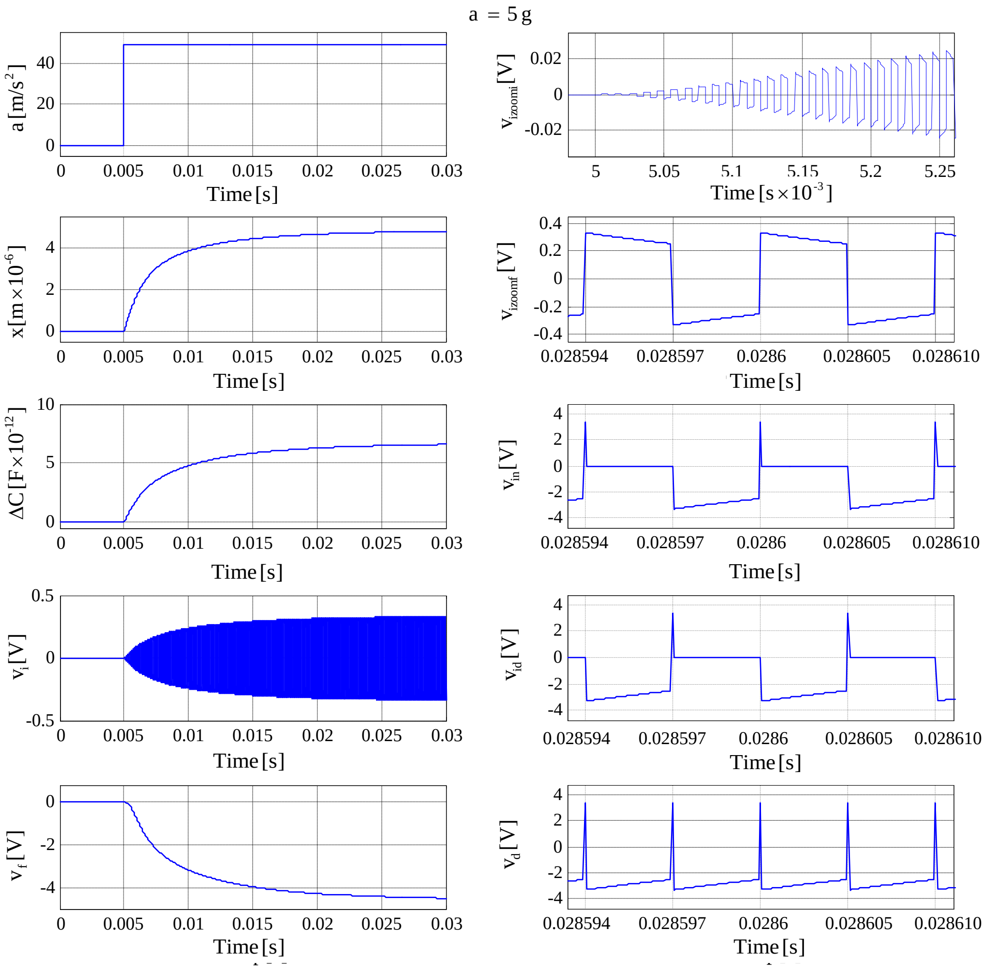

Fig. 9 The time-evolution of all quantities from the block-scheme for a=5g.

The graphical representation of the steady values of the voltage v_f (Fig. 10) obtained for various values of the acceleration revealed a linear zone only in the $-4g \div 4g$ acceleration range. Also, the shape of this characteristic comes to certify its symmetry with respect to the positive and negative accelerations.

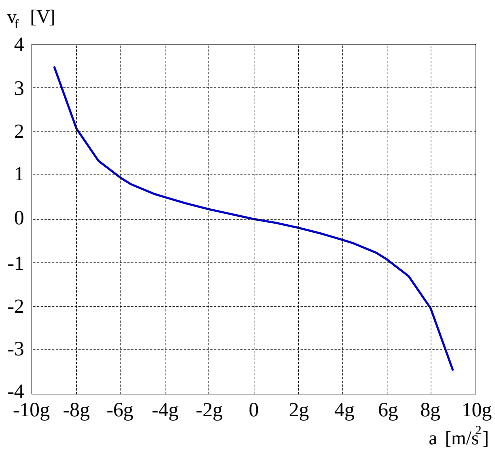

Fig. 10 Static characteristic of the accelerometer.

4 Conclusions

Modeling and numerical simulation of an open-loop miniature capacitive accelerometer were performed. As application software, the Matlab/Simulink package was used. Sensor architecture includes a capacitive detection device coupled with a charge amplifier and a phase-sensitive demodulator. The numerical simulations showed that the accelerometer can operates in open loop within $-4g \div 4g$ range, where the nonlinearities of its static characteristic are relatively small. If one intends to measure accelerations higher than $4g$, it is strictly necessary to close its loop, in order to avoid the overlapping of the two characteristics that present strong nonlinear features ($V_i = f(a)$ and $v_f = f(V_i)$) for $a > 4g$.

Acknowledgment

This work was supported by Romanian Space Agency (ROSA), project STAR, No. 27/19.11.2012, "High-precision micro and nano smart sensors for space inertial navigation applications", code 168/2012.

References

[1] Chollet, F. and Liu, H.B. "A (not so) short Introduction to Micro Electromechanical Systems", version 5.0, 2012, <<http://mems cyclopedia.org/introMEMS.html>>.
[2] PRIME Faraday Partnership, "An Introduction to MEMS". Loughborough University, Leics LE11 3TU, 2002.
[3] Timmer, W. (Editor), Micromechanics and MEMS: Classic and seminal Papers to 1990. IEEE Press, New York, 1997.
[4] Marinis, T., "The Future of MEMS". Draper Laboratory, 555 Technology Square, Cambridge, MA 02139, 2007.
[5] Allen, J., Micro Electro Mechanical Systems design, CRC Press, Boca Raton, 2005.
[6] Stovall, S., "Basic Inertial Navigation". Naval air warfare center weapons division, California, 1997.
[7] Andrejasic, M. "MEMS accelerometer: seminar" University of Ljubljana, Faculty for mathematics and physics, Department of physics, 2008.
[8] Baxter, K., Capacitive sensors: Design and applications. IEEE Press, New York, 1997.
[9] Lungu, R. and Grigorie, T.L., Traductoare accelerometrice si girometrice, Sitech Publisher, Craiova, 2005.
[10] Grigorie, T.L., "The Matlab/Simulink modeling and numerical simulation of an analogue capacitive micro-accelerometer. Part 1: Open loop". The IEEE 4nd International Conference on Perspective Technologies and Methods in MEMS Design, Polyana, Ukraine, 21 - 24 may, 2008.
[11] Aron, I. and Grigorie, T.L., "Regimurile dinamice ale unui microaccelerometru". Revista Electrotehnica, Electronica, Automatica (EEA). Bucuresti, No. 4, 2004.
[12] Aron, I. and Grigorie, T.L., "Simularea unui circuit de detectie din accelerometrele capacitive". Revista Electrotehnica, Electronica, Automatica (EEA). Bucuresti, No. 3, 2004.
[13] Kraft, M. "Closed-loop accelerometer employing oversampling conversion", Coventry University PhD Thesis, 1997.
[14] Negrea, P. and Grigorie, T.L. "Mathematical modeling and numerical simulation of the detection unit in a miniaturized capacitive accelerometer". 11th International Conference on Applied and Theoretical Electricity – ICATE 2012, Craiova, October 25-27, 2012.
[15] Web page: <<http://cnyack.homestead.com/ files/afourse/fssq1.htm>>.
[16] Van Paemel, M. "Interface circuit for capacitive accelerometer". Sensors and Actuators, vol.17, 1989.

Deorbiting of spacecraft at the end of life with electrodynamic tethers stabilized by passive oscillation dampers

R. Mantellato, M. Pertile, G. Colombatti, A. Valmorbida
University of Padova – CISAS "G. Colombo", Padova 35131, Italy

E. C. Lorenzini
University of Padova – Department of Industrial Engineering, Padova 35131, Italy

Keywords: *Electrodynamic tethers, satellites deorbiting, passive damping*

Abstract

Since the beginning of human space era the number of debris orbiting the Earth produced accidentally or intentionally by artificial satellites has been continuously growing. Nevertheless, only in the last years the alarming growth of space debris induced many space agencies all over the world to adopt debris mitigation strategies. Present guidelines indicate the need to deorbit new satellites launched into low Earth orbit (LEO) within 25 years from their end of life. Our task, which is part of an international EU-funded project, is to develop a new technology suitable to deorbit a satellite at the end of life with as small an impact as possible on the mass budget of the mission. In fact, a deorbit maneuver with chemical rockets can strongly affect the satellite propulsion budget, thus limiting the operational life of the satellite. An alternative to the traditional chemical rockets consists in using an electrodynamic tether that, through its interaction with the Earth ionosphere and magnetic field, can take advantage of Lorentz forces for deorbiting purposes. This is a particularly promising technique because it is passive, light and effective. However, Lorentz forces produce a low and yet continuous injection of energy into the system that, in the long run, can bring the tether to instability. This paper addresses this issue through the analysis of the benefits provided by a viscous damping device installed at the attachment point of the tether to the spacecraft. The analysis carried out by means of linearization of dynamics equations and numerical simulations show that a well-tuned damper can efficiently absorb the kinetic energy from the tether thus greatly increasing the system stability.

1 Introduction

Due to recent guidelines on the deorbiting of LEO satellites at their end of life provided by the Inter-Agency Space Debris Coordination Committee (IADC) [1] the attention of governments, space agencies and researchers on this issue has grown worldwide in the last years [2]-[5]. Several concepts are under study to provide new alternatives to carry out deorbiting maneuvers in a low-cost, safe and reliable way (Ref. [6] provides a good overview for microsatellites). One of these options involves the use of an electrodynamic tether to produce a Lorentz drag that can rather quickly deorbit small and large satellites [7]. The present work is part of a EU-funded research framework [8] whose aim is to develop the technology of electrodynamic tethers suitable for deorbiting satellites from generic Earth orbits (LEO). One of the issues that must be tackled within this project is the stability of the tether dynamics throughout the deorbit maneuver. The interaction between tether and plasmasphere, in fact, produces a continuous injection of energy into the system that increases the amplitude of the tether oscillations over time. This effect can involve a reduction of the system efficiency and, in the worst case, cause dynamic instability [9]. The task of the present work is to investigate how to dissipate part or the whole of the energy introduced by Lorentz forces by means of a damper installed at the attachment point between tether and spacecraft. The issue is to study how to maximize the energy transfer from the electrodynamic tether into the damper and thus its dissipation. An analysis was carried out by means of the linearization of the dynamic equations through which the natural frequencies and the stability of the system were evaluated. Previous studies [10] have shown that the main instabilities associated with the tether libration arise through a coupling between the in-plane and the out-of-plane tether motions with the system going eventually unstable in the orbit plane. For this reason the tether dynamic has been studied by first analyzing the in-plane motion and later the 3D dynamics. It is worth pointing out that the damping device works on both in the in-plane and out-of-plane oscillations and thus it can also take energy out of coupled oscillations like a tether “skip-rope” motion. Peláez *et al.* [11] derived the dynamics equations for a two-bar model taking into account the gravitational forces together with a simplified model of the Lorentz forces. In order to investigate a more general case, we removed the electrodynamics forces to study the free-vibration dynamics of a tether-damper system modeled as two rigid bars (see later on). Simulations show that the in-plane linearized model provides information with general validity on the response of this system.

2 Equations of motion

2.1 Description of model

The damped tether system is modeled with a two-bar model to represent the dynamics of the tether and damping device. Fig. 1 shows the orbital reference frame for a generic tether modeled with two rigid bars. The spacecraft centered in *O* is orbiting the Earth (point *E*) in a circular orbit which is characterized by a semi-major axis *a* and an orbital angular velocity:

$$\omega = \sqrt{\frac{\mu}{a^3}} \tag{1}$$

The *x* axis is along the local vertical toward the outer space, *z* is toward the orbital velocity and *y* completes the right-handed frame. According to this definition, the unit vectors of the two bars are given by Eq. (2) and (3) in which the notations sin*x* = *sx* and cos*x* = *cx* has been adopted and it will be kept throughout the paper.

$$\underline{u}_1 = \left(c\vartheta_1 c\varphi_1, -s\varphi_1, c\varphi_1 s\vartheta_1\right) \tag{2}$$

$$\underline{u}_2 = \left(c\vartheta_2 c\varphi_2, -s\varphi_2, c\varphi_2 s\vartheta_2\right) \tag{3}$$

A damper of mass m_1, a tether of mass m_2 and an end mass m_B are attached to the spacecraft. In-plane angles ϑ_1 and ϑ_2 define the attitude of the bars in the orbit plane and the out-of-plane angles φ_1 and φ_2 orthogonally the orbit plane. We assumed that the bars are individually rigid and that their masses are negligible with respect to that of the spacecraft. The system orbit is assumed unperturbed and the center of mass of the system is in *O*. In this paper the first bar represents the damper device and the second bar the conductive tether. The system total length is $L = L_1 + L_2$ and the end mass is modeled as a point mass placed in *B*. With reference to the orbital frame the tether system is subjected to the forces generated by the Earth spherical gravitational potential and to the apparent forces due to the constant angular rate of the orbital frame around the Earth.

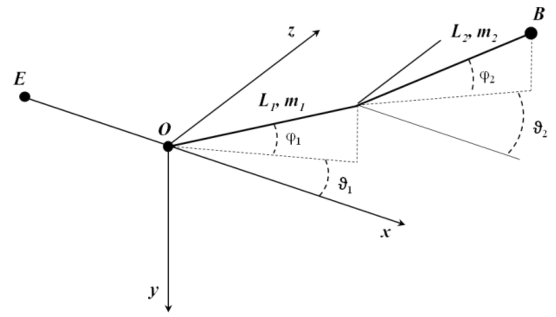

Fig. 1 Synodic reference system

2.2 Generalized forces

We utilized the Lagrangian function to derive the equations of motion of the two-bar model as in Refs. [10] and [11], taking ϑ_1, ϑ_2, φ_1 and φ_2 as generalized coordinates and $\tau = \omega t$ as the independent variable. Unlike Pelaez *et al.* (see [11]) we did not take into account the electrodynamics effect on the conductive tether in this study because we are interested in understanding how the introduction of a damping system in a two-bar model affects the dynamics of the tether system. For this reason, we first studied the free vibration of the system when the initial conditions of the second bar (i.e., the tether) are perturbed off equilibrium. The damper, modeled as a spring-dashpot system, contributes to the tether dynamics derivative and proportional terms that produce the dissipative torque and elastic restoring torque, respectively. Furthermore, generalized forces acting on the first bar were computed by following the procedure outlined in Ref. [10].

As stated above the damper's torque has both derivative and proportional terms that are given in Eqs. (4) and (5) where b and k are the damping and elastic coefficients, respectively. Equation (6) gives the first bar angular velocity $\underline{\Omega}_1$ expressed in the orbital frame. Considering the very low torsional stiffness of long tethers, the motion about the longitudinal axis was neglected.

$$\underline{M}_b = -b\underline{\Omega}_1 \tag{4}$$

$$\underline{M}_k = -k(0, \vartheta_1, \varphi_1) \tag{5}$$

$$\underline{\Omega}_1 = \omega \underline{u}_1 \times \dot{\underline{u}}_1 \tag{6}$$

The generalized forces due to the two terms of the damping system are computed by means of Eqs. (8) and (9) that are added to the right-hand side of the equations of motion (see Par. 2.3). Equation (7) defines the virtual work done by the generalized forces expressed in terms of the generalized coordinates.

$$dW = \underline{M} \cdot \underline{\Omega}_1 \frac{d\tau}{\omega} = Q_{\vartheta_1} d\vartheta_1 + Q_{\varphi_1} d\varphi_1 \tag{7}$$

$$Q_b = \underline{M}_b \cdot \underline{\Omega}_1 = -b\omega^2 \left(c^2\varphi_1 \dot{\vartheta}_1^2 + \dot{\varphi}_1^2\right) \tag{8}$$

$$Q_k = \underline{M}_k \cdot \underline{\Omega}_1 = -k\omega\left(c^2\varphi_1\vartheta_1\dot{\vartheta}_1 + \varphi_1\left(c\varphi_1 s\vartheta_1 s\varphi_1 \dot{\vartheta}_1 + c\vartheta_1\dot{\varphi}_1\right)\right) \tag{9}$$

The in-plane and out-of-plane components of the viscous terms are:

$$Q_{b\vartheta_1} = \frac{1}{\omega}\frac{\partial Q_b}{\partial \dot{\vartheta}_1} = -2b\omega c^2\varphi_1\dot{\vartheta}_1 \qquad Q_{b\varphi_1} = \frac{1}{\omega}\frac{\partial Q_b}{\partial \dot{\varphi}_1} = -2b\omega\dot{\varphi}_1 \tag{10}$$

The components of the elastic terms are as follows:

$$Q_{k\vartheta_1} = \frac{1}{\omega}\frac{\partial Q_k}{\partial \dot{\vartheta}_1} = -kc\vartheta_1\varphi_1 \qquad Q_{k\varphi_1} = \frac{1}{\omega}\frac{\partial Q_k}{\partial \dot{\varphi}_1} = -kc\varphi_1\left(c\varphi_1\vartheta_1 + s\vartheta_1 s\varphi_1\varphi_1\right) \tag{11}$$

2.3 Two-bar equations of motion with spring-dashpot device

The Lagrangian equations describing the dynamic of the damped two-bar model are reported in Eqs. (14) – (17). They were obtained starting from the undamped two-bar Lagrangian function as in Ref. [11] adding the terms listed in Eqs. (10) and (11) to the right hand side of the equations. The following non-dimensional coefficients were adopted:

$$\Lambda = \frac{L_1}{L} \quad \delta_1 = \frac{m_1}{m_B} \quad \delta_2 = \frac{m_2}{m_B} \tag{12}$$

Four additional coefficients, in the equations of motion, are functions of the mass and geometry parameters as follows:

$$\begin{gathered} A = \Lambda(3+\delta_1+\delta_2) \quad B = (1-\Lambda)(2+\delta_2) \\ D = -\Lambda(2+\delta_2) \quad E = (1-\Lambda)(3+\delta_2) \end{gathered} \tag{13}$$

In conclusion, the four equations governing the three-dimensional motion of the damped two-bar model are as follows:

$$\begin{aligned} & Ac\varphi_1\ddot{\vartheta}_1 + \tfrac{3}{2}Bc(\vartheta_2-\vartheta_1)c\varphi_2\ddot{\vartheta}_2 \\ & -\tfrac{3}{2}Bs(\vartheta_2-\vartheta_1)s\varphi_2\ddot{\varphi}_2 - 2As\varphi_1\dot{\varphi}_1(1+\dot{\vartheta}_1) \\ & +3bWc^2\varphi_1\dot{\vartheta}_1 - 3Bs\varphi_2c(\vartheta_2-\vartheta_1)\dot{\varphi}_2(1+\dot{\vartheta}_2) \\ & -\tfrac{3}{2}Bs(\vartheta_2-\vartheta_1)c\varphi_2(\dot{\vartheta}_2^2+2\dot{\vartheta}_2+\dot{\varphi}_2^2) \\ & +s\vartheta_1(3Ac\vartheta_1c\varphi_1+\tfrac{9}{2}Bc\vartheta_2c\varphi_2) \\ & +3kVc\varphi_1(c\varphi_1\vartheta_1+s\vartheta_1s\varphi_1\varphi_1)=0 \end{aligned} \tag{14}$$

$$\begin{aligned} & A\ddot{\varphi}_1 + \tfrac{3}{2}Bs(\vartheta_2-\vartheta_1)s\varphi_1c\varphi_2\ddot{\vartheta}_2 \\ & +\tfrac{3}{2}B[c\varphi_1c\varphi_2+s\varphi_1s\varphi_2c(\vartheta_2-\vartheta_1)]\ddot{\varphi}_2 \\ & +\tfrac{3}{2}Bc(\vartheta_2-\vartheta_1)s\varphi_1c\varphi_2(\dot{\vartheta}_2^2+2\dot{\vartheta}_2+\dot{\varphi}_2^2) \\ & +As\varphi_1c\varphi_1\dot{\vartheta}_1(2+\dot{\vartheta}_1)+3bW\dot{\varphi}_1 \\ & -3Bs(\vartheta_2-\vartheta_1)s\varphi_1s\varphi_2\dot{\varphi}_2(1+\dot{\vartheta}_2) \\ & -\tfrac{3}{2}Bs\varphi_2c\varphi_1\dot{\varphi}_2^2+c\varphi_1(\tfrac{3}{2}Bs\varphi_2+As\varphi_1) \\ & +s\varphi_1c\vartheta_1(3Ac\vartheta_1c\varphi_1+\tfrac{9}{2}Bc\vartheta_2c\varphi_2) \\ & +3kVc\vartheta_1\varphi_1=0 \end{aligned} \tag{15}$$

$$\begin{aligned} & Ec\varphi_2\ddot{\vartheta}_2 - \tfrac{3}{2}Dc\varphi_1c(\vartheta_2-\vartheta_1)\ddot{\vartheta}_1 \\ & -\tfrac{3}{2}Ds\varphi_1s(\vartheta_2-\vartheta_1)\ddot{\varphi}_1 \\ & -\tfrac{3}{2}Dc\varphi_1s(\vartheta_2-\vartheta_1)(\dot{\vartheta}_1^2+2\dot{\vartheta}_1+\dot{\varphi}_1^2) \\ & +3Ds\varphi_1c(\vartheta_2-\vartheta_1)\dot{\varphi}_1(1+\dot{\vartheta}_1) \\ & -2Es\varphi_2\dot{\varphi}_2(1+\dot{\vartheta}_2)+3Es\vartheta_2c\vartheta_2c\varphi_2 \\ & -\tfrac{9}{2}Dc\vartheta_1s\vartheta_2c\varphi_1=0 \end{aligned} \tag{16}$$

$$\begin{aligned} & E\ddot{\varphi}_2 + \tfrac{3}{2}Dc\varphi_1s\varphi_2s(\vartheta_2-\vartheta_1)\ddot{\vartheta}_1 \\ & -\tfrac{3}{2}D[c\varphi_1c\varphi_2+s\varphi_1s\varphi_2c(\vartheta_2-\vartheta_1)]\ddot{\varphi}_1 \\ & -\tfrac{3}{2}Dc\varphi_1s\varphi_2c(\vartheta_2-\vartheta_1)(\dot{\vartheta}_1^2+2\dot{\vartheta}_1+\dot{\varphi}_1^2) \\ & -3Ds\varphi_1s\varphi_2s(\vartheta_2-\vartheta_1)\dot{\varphi}_1(1+\dot{\vartheta}_1) \\ & +\tfrac{3}{2}Ds\varphi_1c\varphi_2\dot{\varphi}_1^2-\tfrac{9}{2}Dc\vartheta_1c\varphi_1c\vartheta_2s\varphi_2 \\ & +Es\varphi_2c\varphi_2\left[3c^2\vartheta_2+(1+\dot{\vartheta}_2)^2\right] \\ & -\tfrac{3}{2}Ds\varphi_1c\varphi_2=0 \end{aligned} \tag{17}$$

As k and b are dimensional terms, respectively expressed in $[kg{\cdot}m^2/s^2]$ and $[kg{\cdot}m^2/s]$, two additional coefficients V and W are needed to the equations non-dimensional. The coefficients are defined as:

$$V = \frac{1}{\omega^2 m_B \Lambda L^2} \quad W = \frac{2}{\omega m_B \Lambda L^2} \tag{18}$$

2.4 In-plane equations

Previous studies [10] have highlighted that dynamics instabilities due to Lorentz forces eventually occur in the orbital plane. For this reason it is worth studying the in-plane dynamics of the damped two-bar model decoupled from the out-of-plane motion first, thus simplifying the equations of motion and allowing for a better understanding of the problem. Setting the out-of-plane angles φ_1 and φ_2 to zero Eqs. (14) and (16) yield:

$$\begin{aligned}&\ddot{\vartheta}_1+\tfrac{3B}{2A}c(\vartheta_1-\vartheta_2)\ddot{\vartheta}_2+\tfrac{3W}{A}b\dot{\vartheta}_1\\&+\tfrac{3B}{2A}s(\vartheta_1-\vartheta_2)\dot{\vartheta}_2\left(2+\dot{\vartheta}_2\right)\\&+3c\vartheta_1 s\vartheta_1+\tfrac{9B}{2A}c\vartheta_2 s\vartheta_1+\tfrac{3V}{A}k\vartheta_1=0\end{aligned}\tag{19}$$

$$\begin{aligned}&\ddot{\vartheta}_2-\tfrac{3D}{2E}c(\vartheta_1-\vartheta_2)\ddot{\vartheta}_1\\&+\tfrac{3D}{2E}s(\vartheta_1-\vartheta_2)\dot{\vartheta}_1\left(2+\dot{\vartheta}_1\right)\\&+3c\vartheta_2 s\vartheta_2+\tfrac{9D}{2E}c\vartheta_1 s\vartheta_2=0\end{aligned}\tag{20}$$

The numerical integration of the set of equations (19) and (20) is faster than those for the 3D-case, thus allowing for a more detailed study of the problem. Once the behavior of the system is well understood in the orbital plane, the results can be easily applied to the out-of-plane case and eventually to the 3D case.

2.5 Linearized in-plane equations

In order to gain insights into the dynamics of the coupled system we linearized Eqs. (19) and (20) to obtain a set of two linear second-order differential equations given in Eq. (21) which can be solved with traditional mathematical methods (e.g. the Laplace transform):

$$\begin{cases}\ddot{\vartheta}_1+\eta E\left[bW\dot{\vartheta}_1+\left(A+\tfrac{3}{2}B+Vk\right)\vartheta_1\right.\\\qquad\left.-\tfrac{3B}{4E}\left(2E-3D\right)\vartheta_2\right]=0\\\ddot{\vartheta}_2+\eta A\left[\tfrac{3D}{2A}bW\dot{\vartheta}_1+\tfrac{3D}{4A}\left(A+\tfrac{3}{2}B+Vk\right)\vartheta_1\right.\\\qquad\left.-\left(E-\tfrac{3}{2}D\right)\vartheta_2\right]=0\end{cases}\tag{21}$$

where $\eta=\frac{12}{4AE-9BD}$. As it can be seen by inspection of Eq. (21) there is a coupling between the dynamics of the two bars. This coupling accounts for a continuous exchange of energy between the two bars. The introduction of the damping device makes this coupling partially controllable. We can search for the pair of values (b^*,k^*) that maximize the transfer of kinetic energy from the tether to the damper where the energy can be dissipated.

2.6 Optimal damping as a function of elastic coefficient: analytical solution

We can solve the set of differential equations (21) by means of Laplace transform. After several algebraic manipulations we find the free-dynamics solution in the time domain. For cases of interest the solution can be written in the compact form:

$$\begin{cases}\vartheta_1(t)=A_{11}e^{\alpha_1 t}\sin(\omega_1 t+\xi_{11})\\\vartheta_2(t)=A_{21}e^{\alpha_1 t}\sin(\omega_1 t+\xi_{21})\end{cases}\tag{22}$$

where the coefficients A_{11}, A_{21}, α_1, ζ_{11} and ζ_{21} are functions of the system mass and geometry parameters defined in Eq. (12) as well as the initial conditions. Note that Eq. (22) takes into account only the first mode of vibration associated with the first natural frequency ω_1. We would need to add the second mode of vibration associated with the higher frequency ω_2 to complete the solution. Nevertheless, the second mode of vibration (and note that $\omega_2 >> \omega_1$) can be neglected without significant loss of accuracy because it has a very fast relaxation time compared to the first.

By inspection of Eq. (21) and with the aid of numerical analysis it is possible to demonstrate that all coefficients appearing in Eq. (22), with the only exception of α_1, are essentially independent of the damping and elastic coefficients b and k. Moreover, the natural frequency ω_1, in accordance with what Pelaèz *et al.* found in [11], is practically constant,

$$\omega_1\cong\sqrt{3}\quad\forall(b,k)\in I\subset\Re^2\tag{23}$$

for any pair of (b, k) in I with $b > 0$ and $k > k_{cr}$ (see later on for the definition of k_{cr}). In Eq. (22) α_1 is the first mode of vibration decay constant that determines the relaxation time of the damped oscillation $\tau^*=1/\alpha_1$. In other words, the more negative α_1 is the quicker the oscillation damps out. The decay constant is strongly dependent on the damping and elastic coefficients:

$$\alpha_1 = f_1(\delta_1, \delta_2, \Lambda, b, k) \qquad (24)$$

This fact gives us the chance to control its value through the values of b and k. Specifically, given a certain value of the elastic coefficient k, we can analyze the partial derivative of Eq. (24) with respect to the damping coefficient and look for a global minimum of the function (see the Appendix for the explicit formulation):

$$\frac{\partial \alpha_1}{\partial b} = f_2(\delta_1, \delta_2, \Lambda, b^*, k) = 0 \qquad (25)$$

We studied Eq. (25) and found that a value b^* does exist and is unique in $\Re^+$. Fig. 2 shows the trend of the decay constant as function of b and k obtained by solving Eq. (25) for several values of k. The black dashed line fits the points defined by the pairs of (b^*,k) values. As it is clearly sketched in Fig. 2, higher (in absolute value) decay constant values are obtained for negative elastic coefficients: hence the more negative the value of k the higher α_1. However, the negative value of k cannot be decreased at will because the damper dynamics becomes unstable for a specific value of $k < 0$. This value, named critical elastic coefficient k_{cr}, is a function of the parameters defined in Eq. (12). Thus, it is true that the optimal k is as follows:

$$k^* = \lim_{k \to k_{cr}^+} k \qquad (26)$$

but for k very close or equal to k_{cr} the system becomes unstable independently of the value of b. This means that the best dissipation is indeed attained for negative values of k but for a value of k slightly higher (less negative) than k_{cr}. Consequently, the best (b^*,k) pair is a tradeoff between dissipation efficiency and dynamics stability requirements.

It is worth to point out here that the value of k_{cr} is negative unlike in a classical spring-dashpot system for which negative values of the elastic coefficient imply instability. The difference is due to the fact that the term Vk in Eq. (21) is not the only restoring force acting on the two-bar system. The total restoring force is indeed a sum of terms associated with the gravitational gradient (i.e., the tether tension) and the spring elastic coefficient of the damper. The analysis of the linear system reported in Eq. (21) yields:

$$k_{cr} \cong -\frac{A + \frac{3}{2}B}{V} \qquad (27)$$

where A and B, defined in Eq. (13), represent the gravitational contribution of the restoring force. After inspection of A, B and V it is possible to state that the absolute value of k_{cr} increases when the system mass parameters as well as the overall tether length L increase.

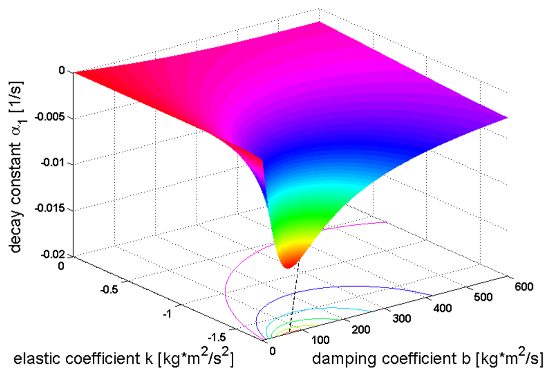

Fig. 2 Decay constant as a function of damping and elastic coefficients. Mass and geometry parameters are defined in Par. 3.1.

3 Numerical simulations results

In this section we compare the results obtained from the three mathematical models governed by equations given in Par. 2.3, 2.4 and 2.5. More precisely we will compare the b Vs. k curves obtained from the different models. To do this we need to integrate numerically Eqs. 14-17 and Eqs. 19-20 and look for the optimal damping coefficient which minimize the decay time τ*. For this purpose we introduce two parameters:

$$MKE = \frac{\int_0^{T_{sim}} E_k \, d\tau}{T_{sim}} \tag{28}$$

$$TDE = \frac{\int_0^{T_{sim}} E_d \, d\tau}{n_{sim}} \tag{29}$$

Equation (28) defines the Mean Kinetic Energy (*MKE*) that is the kinetic energy of the second bar (i.e. the tether) averaged over a given number of orbits n_{sim} that corresponds to a simulation non-dimensional time equal to $T_{sim} = 2\pi n_{sim}$. Equation (29) defines the Total Dissipated Energy (*TDE*) that is the amount of energy dissipated by the damping device per orbit. Theoretically, the minimum value of relaxation time should corresponds to a minimum of the *MKE* and a maximum of the *TDE*. In fact, a faster decay time means that in the time span considered the oscillations of the tether are smaller and, consequently, that the damper is working in the most efficient way. In the next Par. 3.1 we will show how these hypothesis were validated with the aid of numerical simulations.

3.1 Linearized model: energy and relaxation time

By means of the analytical solution of Eq. (25) we can preliminarily study and characterize the behavior of the damped two-bar system for different values of the (*b*,*k*) pair. We assigned to the mass and geometry parameters typical values, that is, L_1 = 10 m, L_2 = 3000 m, a damper mass equal to 1 kg and tether width and thickness equal to 1 cm and 50 µm, respectively. Using these values into Eq. (25) and calculating *MKE* and *TDE* by means of Eqs. (28) and (29) we constructed Fig. 3 that depicts the energy levels as a function of the damping coefficient *b* when an initial in-plane angular velocity of the tether equal to 0.02 °/s is considered.

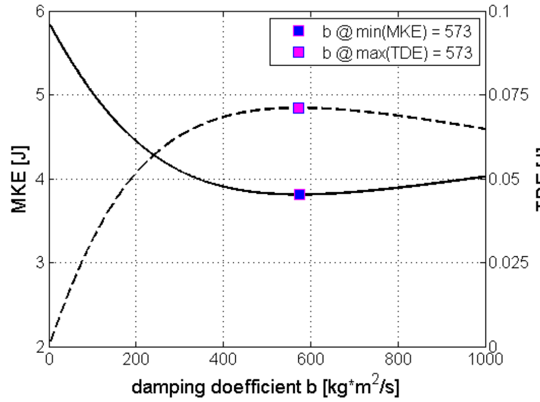

Fig. 3 Typical energy trends as functions of the damping coefficient (for *k = 0*).

As it can be seen from Fig. 3, the *MKE* and *TDE* graphs exhibit global minimum and maximum, respectively, in correspondence of the same value of the damping coefficient (573 $kg{\cdot}m^2/s$ for the system under study assuming $k = 0$) as it was mentioned in Sec. 3. Furthermore, Fig. 4 shows that the adoption of an optimal damping coefficient brings about the best value of the relaxation time. In fact, the solid black line in the figure is associated with $b = b$* and, being the steepest curve, it implies that the system is damped in the quickest time.

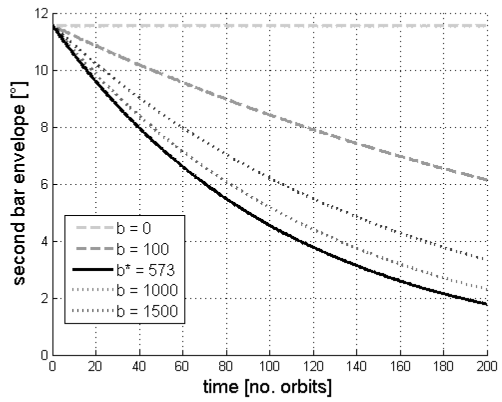

Fig. 4 Tether oscillation decay envelopes for different values of the damping coefficient (for *k = 0*).

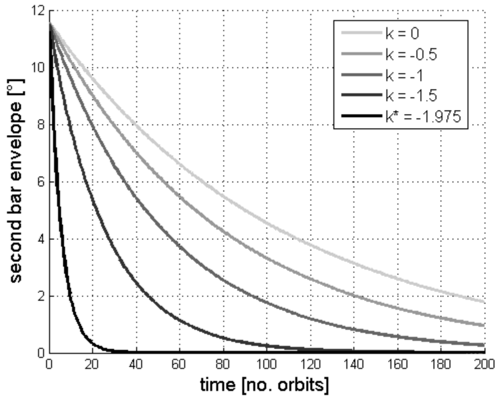

Fig. 5 Tether oscillation decay envelopes for different values of the elastic coefficient (for $b = b^*$).

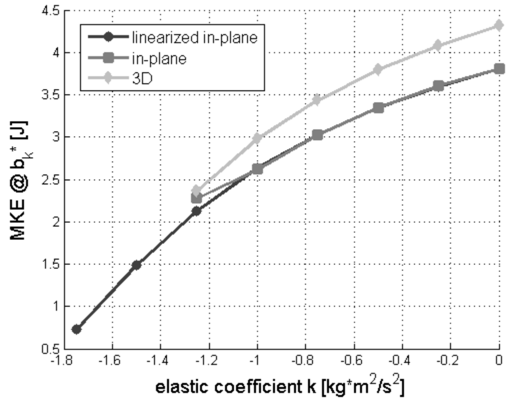

Fig. 6 Mean kinetic energy level as a function of the damper's elastic coefficient (for $b = b_k^*$).

Fig. 5 depicts how the elastic coefficient affects the damping mechanism. As it was anticipated in Par. 2.6 the more negative k the faster the oscillation damping. The fastest damping occurs for $k = k^* = -1.975\ kg{\cdot}m^2/s^2$ (actually for a value slightly higher than k^* to avoid damper instability). Note that the curves in Fig. 5 refer to the optimized cases where the optimal values of b were found by solving the implicit Eq. (25).

3.2 Comparison between models

In this last paragraph the results obtained from numerical simulation employing the mathematical models described in Pars. 2.3 - 2.5 are shown. To this end, we carried out several simulations adopting different values of k, each one providing the curves for *MKE* and *TDE* as in Fig. 3. For all simulations we recorded four parameters:

1) the damping coefficient in correspondence of the *MKE* global minimum (b_k^*);
2) the minimum value of *MKE*;
3) the damping coefficient in correspondence of the *TDE* global maximum (b_d^*);
4) the maximum value of *TDE*.

Combining these parameters in different ways it was possible to build Figures Fig. 6 - Fig. 9.

Figures Fig. 6 and Fig. 7 show the trends of the minimum values of *MKE* and the maximum values of *TDE*, respectively, for different values of the elastic coefficient.

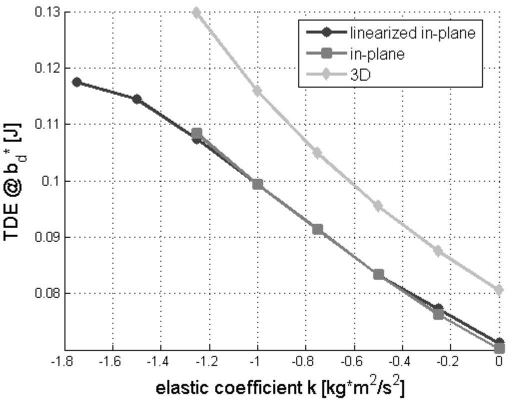

Fig. 7 Dissipated energy level as a function of the damper's elastic coefficient (for $b = b_d^*$).

It is possible to observe that negative values of the elastic coefficient lead to lower levels of kinetic energy (down to 45-50%) and higher levels of dissipated energy (up to 60%). Therefore, we can infer that assuming negative values of k improves simultaneously the kinetic energy transfer from the tether to the damper and its dissipation due to viscous damping. Note that for the 3D case the out-of-plane energy contributions were discarded and only the in-plane component was taken into account to allow for a correct comparison with the (in-plane only) 2D models.

At last, Figures Fig. 8 and Fig. 9 show the pairs of values (b^*, k) considering the b_k^* and b_d^* values respectively [points (1) and (3) in the previous list]. The analytical curve refers to the values obtained by solving the implicit Eq. (25).

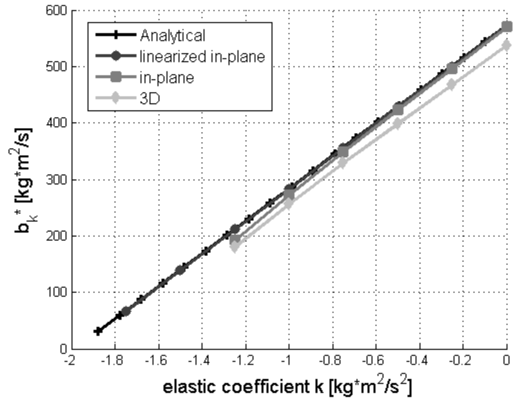

Fig. 8 Optimal damping coefficient (b_k*) Vs. elastic coefficient

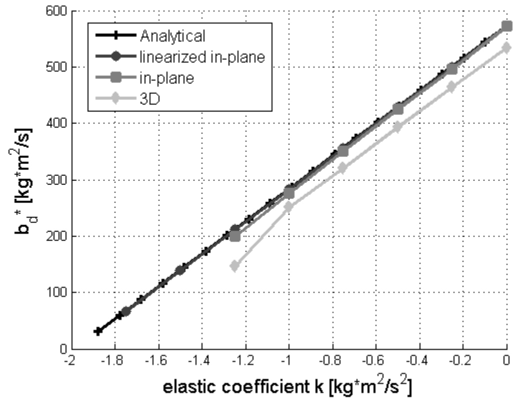

Fig. 9 Optimal damping coefficient (b_d*) Vs. elastic coefficient

All results reported in this paragraph clearly show how the information on the damped two-bar system derived from the linearized model through analytical computation are consistent with those obtained from the non-linear models by means of numerical simulations. The 3D case exhibits some differences with respect to the 2D models. For example, the energy levels are somehow higher (15-20%), most likely due to the fact that the system initial energy is higher for the 3D case (both in-plane and out-of-plane initial angular velocities were set to 0.02 °/s). Moreover, the optimal values of damping coefficients b_k* and b_d* are, with the elastic coefficient being equal, always slightly smaller (about 5%) than for the 2D cases. Also note that for all non-linear models the value of the critical elastic coefficient k_{cr} has shown to be higher (less negative) than in the linearized model. However, the trends of all functions are very similar. Consequently we can conclude that the linearized model provides reliable information on the dynamic response of the damped two-bar model and the model was instrumental in optimizing the pair (b,k) that gives an efficient energy dissipation.

4 Conclusion

The free-vibration response of a system consisting of a long electrodynamic tether and a damper has been investigated by means of different mathematical models with the goal of finding an optimal configuration of the damper device aimed at minimizing the tether oscillations. The damped model is a natural evolution of the undamped two-bar model used by several authors to study the lateral dynamics of an electrodynamic tether driven by Lorentz forces. The analytical solution of the linearized equations of motion in the orbit plane has highlighted the existence of an optimal combination of damping and elastic coefficients that minimize the tether kinetic energy and simultaneously maximize its dissipation through the viscous damper. Results obtained through numerical simulations have shown a good match between the analytical model and the non-linear models (both in 2D and 3D). Moreover, the transfer of the energy from the tether to the damper device has proven to be effective when the appropriate values of the elastic and damping coefficients are adopted.

Acknowledgements

This work was supported by project 262972 (BETs) funded by the European Commission FP7 Space Program.

Appendix

The explicit formulation of Eq. (25) is:

$$U+\sqrt{T+S}+\frac{\dot{S}}{2\dot{U}}=0$$

where:

$$U=-\frac{b^{*}W_m}{2(1-\alpha\beta)}$$

$$T=U^2-\frac{2(kV_m+3(2+\alpha+\beta))}{3(1-\alpha\beta)}$$

$$S=\frac{\sqrt[3]{4}X+Z^2}{3\cdot\sqrt[3]{2}(1-\alpha\beta)Z}$$

$$\dot{U}=\frac{\partial U}{\partial b^{*}}\qquad \dot{S}=\frac{\partial S}{\partial b^{*}}$$

with:

$$\alpha=\frac{3B}{2A}\qquad \beta=-\frac{3D}{2E}\qquad V_m=\frac{3V}{A}\qquad W_m=\frac{3W}{A}$$

$$\begin{aligned}X&=(3+kV_m+3\beta)^2-9b^{*2}W_m^2(1+\alpha)\\&+6(1+\alpha)(3+kV_m+3\beta)(1+6(1-\alpha\beta))+9(1+\alpha)^2\end{aligned}$$

$$\begin{aligned}Y&=27b^{*2}W_m^2(1+\alpha)[3(3+kV_m+3\beta)\\&+9(1+\alpha)(1-\alpha\beta)-(1+\alpha)(kV_m+3(2+\alpha+\beta))]\\&+216(3+kV_m+3\beta)(1+\alpha)(1-\alpha\beta)[kV_m\\&+3(2+\alpha+\beta)]+2(kV_m+3(2+\alpha+\beta))^3\end{aligned}$$

$$Z=\left[Y+\sqrt{Z^2-4X^3}\right]^{1/3}$$

References

[1] Inter-Agency Debris Coordination Committee (IADC), *IADC Space Debris Mitigation Guidelines*, October 2002.

[2] Somenzi L., Iess L and Peláez J., “Linear stability analysis of electrodynamic tethers”, *Journal of Guidance, Control and Dynamics*, Vol. 28, No. 5, 843-849, 2005.

[3] Kojima H. and Sugimoto T., “Stability analysis on in-plane and out-of-plane periodic motions of electrodynamic tether system in inclined elliptic orbit”, *Acta Astronautica*, Vol. 65, 477-488, 2009.

[4] Iess L., Bruno C., Ulivieri C., *et al.*,"Satellite De-orbiting by means of electrodynamic tethers Part I: General Concepts and Requirements", *Acta Astronautica*, Vol. 50, No. 7, 399-406, 2002.

[5] Iess L., Bruno C., Ulivieri C., and Vannaroni G.,"Satellite De-orbiting by means of electrodynamic tethers Part II: System Configuration and Performance", *Acta Astronautica*, Vol. 50, No. 7, 407-416, 2002.

[6] Jablonski, A.M., “Deorbiting of microsatellites in Low earth Orbit (LEO); An Introduction”. Technical Memorandum DRDC Ottawa TM2008-097, June 2008.

[7] Sanmartin J.R., Charro M., Chen X., Lorenzini E.C., Colombatti G., Zanutto D., Roussel J-F, Sarrailh P., Williams J.D., Xie K., Metz, G.E. Carrasco J.A., Garcia-de-Quiros F., Olaf Kroemer O., Rosta R., van Zoest T., Lasa J., Marcos J. “A Universal System to Deorbit Satellites at End of Life” *Journal of Space Technology and Science*, Vol. 26, No. 1, 21-32, 2012.

[8] European Commision FP7 Space Program, “Propellantless deorbiting of space debris by bare electrodynamic tethers”, www.thebetsproject.com.

[9] Zanutto D., Colombatti G. and Lorenzini E. C., “Electrodynamic Tethers For Deorbiting Maneuvers”, *3rd CEAS Air&Space Conference*, Venice, Italy, 2011.

[10] Peláez J., Lorenzini E. C., López-Rebollal O. and Ruiz M., “A new kind of dynamic instability in electrodynamic tethers”, *Journal of the Astronautical Sciences*, Vol. 48, No. 4, 449-476, 2000.

[11] Peláez J., Ruiz M., López-Rebollal O. and Lorenzini E. C., “Two-bar model for the dynamics and stability of electrodynamic tethers”, *Journal of Guidance, Control and Dynamics*, Vol. 25, No. 6, 1125-1135, 2002.

4:th CEAS Air & Space Conference
FTF Congress: Flygteknik 2013

Multidisciplinary approach for assessing the atmospheric impact of launchers

A. D. Koch, C. Bauer, E. Dumont, F. Minutolo and M. Sippel
German Aerospace Center (DLR), Bremen, Germany

P. Grenard and G. Ordonneau
ONERA - the French Aerospace Lab, Palaiseau, France

H. Winkler
Institute of Environmental Physics (IUP), University of Bremen, Bremen, Germany

L. Guénot and C. Linck
Safran Herakles, Saint-Médard-en-Jalles, France

C. R. Wood, J. Vira, M. Sofiev and V. Tarvainen
Finnish Meteorological Institute (FMI), Helsinki, Finland

Keywords: *rocket exhaust plume, European launchers, atmosphere, CFD, diffusion model*

Abstract

Exhausts from rockets influence the atmospheric chemistry and the atmospheric radiative transfer. Assessing these effects requires a multidisciplinary approach. It ranges from combustion calculations in the rocket engines to plume simulations on different scales. The plume is first analysed with computational fluid dynamic models and engineering methods. Then a diffusion model is applied and lastly a chemical transport model is used for simulations on a global scale. This approach is currently being implemented in the Atmospheric Impact of Launchers project, which is funded by ESA as part of its CleanSpace Initiative. Therefore, the focus of this study lies on rockets launching from Kourou, which are Ariane 5, Vega and Soyuz.

1 Introduction

During ascent a launcher flies through all layers of the atmosphere. Throughout its flight, the rocket's propulsion systems emit chemical products, which can influence the atmospheric chemistry. In addition, the particles coming from the solid rocket motors can affect the atmospheric radiative transfer processes. Especially the potential impact on stratospheric ozone is important. Research in this field serves as a basis for ecologically sensitive design of launch vehicles. This research falls into three main categories: measurement campaigns, computer simulations, and laboratory experiments.

Early studies on the atmospheric impact of launchers were conducted by NASA as part of the Space Shuttle program. Recently, Stevens et al. [21] observed the Space Shuttle's water vapour plume during the Shuttle's last flight.

Two important measurement campaigns were conducted in the US, the Rocket Impacts on Stratospheric Ozone (RISO) campaign and the Atmospheric Chemistry of Combustion Emissions Near the Tropopause (ACCENT) campaign. A WB-57F aircraft was flown through the exhaust plumes of rockets shortly after launch and in-situ measurements were taken. The RISO campaign ran from 1996–1998. Plumes from the Space Shuttle as well as Titan, Delta, Atlas and Athena rockets were investigated [2], [12], [13], [16], [17], [20]. For the ACCENT campaign measurements were made during the years 1999–2000. Plumes from Atlas IIAS, Athena II, Delta II and the Space Shuttle were studied [1], [3], [5], [11], [15], [18].

Simulations have allowed the study of further launch vehicles and scenarios. Denison et al. [4] studied the relevance of NO_x in comparison to Cl_x emissions. Brady, Martin and Lang [1] compared the effects of different propellant combinations including solid rocket propellant, NTO/Aerozine-50, LOX/RP-1 and LOX/LH2. Karol, Ozolin and Rozanov [7] studied the Russian Energia rocket, which utilises both LOX/kerosene and LOX/LH2. Lately, two modelling studies were conducted on the role of NTO/UDMH by investigating the Proton rocket [14], [26]. The impact of Ariane 5 was studied by Jones, Bekki and Pyle [6].

Laboratory experiments have played an important role in studying isolated reactions under controlled circumstances. Especially heterogeneous reactions were studied in the laboratory. Molina et al. [9] determined the reaction rate of the chlorine activation reaction on alumina particles. These particles make up a significant part of the exhaust products of solid rocket motors. Thus, heterogeneous reactions on such particles need to be taken into account.

The objective of this paper is to present a multidisciplinary approach for assessing the atmospheric impact of launchers. This work is part of the Atmospheric Impact of Launchers (ATILA) project, which belongs to the ESA CleanSpace Initiative. The project started in May 2012 for a duration of 18 months. Its aims are twofold. The first objective is to increase the knowledge about the European launchers. The second objective is to conduct a joint study with experts from all relevant disciplines and use higher-order numerical methods where reasonably possible. Engineering models are used to assess the phenomena between the computational points calculated with the higher-order methods. To our knowledge such an approach has not been applied in the past. Murray et al. provide an overview of the uncertainties that need to be addressed [10]. This paper presents a multidisciplinary approach that includes

- the formation of hot gas and the nozzle-exit conditions,
- the early and intermediate evolution of the rocket plume,
- and the impact on the Earth's atmosphere.

2 Launchers under study

The ATILA project investigates two types of scenarios. First, a flight from the ACCENT measurement campaign was selected to validate the applied methods. It corresponds to the measurement performed on 24 September 1999 when the WB-57F aircraft flew six times through the exhaust plume of an Athena II rocket at an altitude of 18.7 km. Second, launchers operating from Kourou in French Guiana are studied. These launchers are Ariane 5, Soyuz and Vega. In addition to 18.7 km, the altitudes 30 km, 42 km and 50 km were selected as reference altitudes where higher-order methods are used.

3 Methods

Studying the impact of launchers on the atmosphere requires several disciplines. Therefore, the study is conducted in a number of steps, which are shown in Fig. 1. The overall approach is to use higher-order methods where it is reasonably possible and lower-order methods and tailored engineering models in all other cases. The higher-order methods applied are computational fluid dynamics (CFD) and a chemical transport model (CTM). Lower-order methods are used for calculating the nozzle-exit

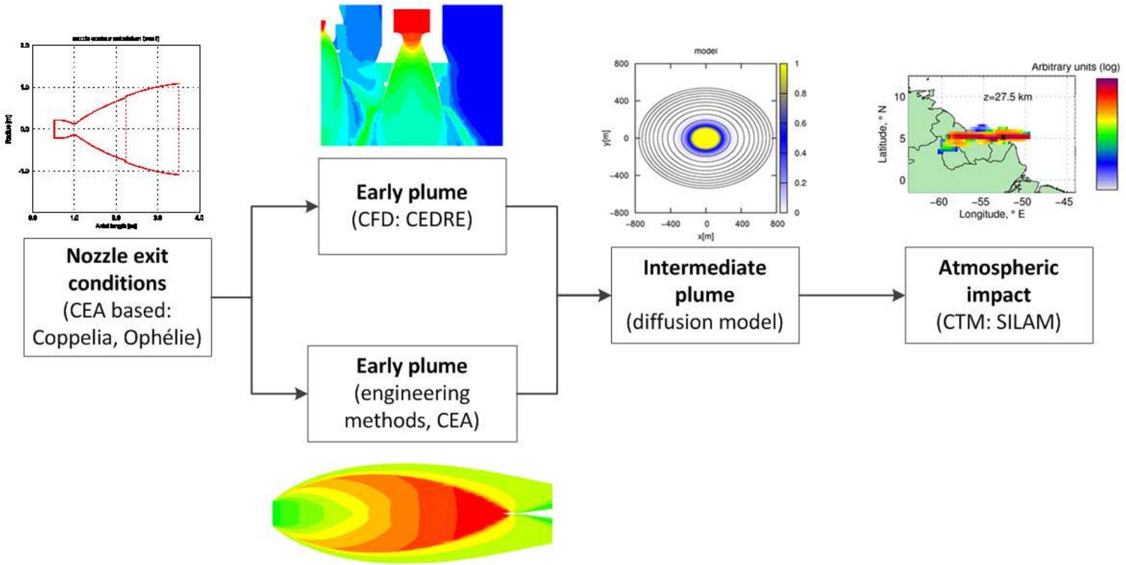

Fig. 1 Simulation tool chain

conditions and partly the evolution of the plume behind the nozzle. Nose-to-tail CFD computations are computationally expensive. Therefore, this method was only used for a few selected cases. The results of these computations serve as reference points for the engineering methods.

3.1 Nozzle-exit conditions

The first step is to calculate the thermodynamic conditions and chemical products in the nozzle exhaust plane. The launchers under study have liquid and solid propulsion systems. For both systems tools were used that are based on NASA's CEA code (Chemical Equilibrium with Applications). The results at the nozzle-exit are then fed into the early plume model. Nose-to-tail CFD computations were performed for selected points using ONERA's CEDRE code. These computations included the gas expansion in the nozzle. The conditions in the chamber were used as input to the CFD computations. The chemical reactions in the nozzle and the afterburning reactions in the rocket plume were considered as part of the CFD computations. The CFD meshes were generated on the basis of CATIA V5 models.

Calculations for the liquid propulsion engines were performed by ONERA. Their in-house code Coppelia (Calcul et Optimisation des Performances Energétiques des Systèmes Liés à l'Autopropulsion), which is derived from CEA, was used. The engines under study are Vulcain 2 for Ariane 5 and the RD-107/108 engines with their main and steering chambers for Soyuz.

In the case of the solid rocket motors Herakles used their thermodynamic code Ophélie, which is based on CEA. Nozzle-exit conditions for the motors Castor 120 for Athena II, P80 for Vega and EAP for Ariane 5 were calculated.

3.2 Early plume

In the frame of the ATILA project the early plume describes the region of the plume that is still affected by shocks and afterburning reactions. The CFD computations performed at chosen altitudes include that entire area. For all other points an engineering model is being developed at the DLR. Afterburning reactions are foreseen to be calculated with CEA.

3.2.1 CFD

3D models are used for Ariane 5 and Soyuz while Athena II and Vega are represented with a 2D axisymmetric mesh each. Meshes are about 200,000 cells for the Vega cases, generated with the GMSH open source mesh generator, and about 3 million cells for the 3D cases of Soyuz and Ariane 5, created with the CENTAUR™ mesh generator. The models include refinements near the nozzle exit and in the mixing layer between plume and outer flow. The model domains extend 700 m (Vega, Soyuz), 750 m (Athena II) and 1500 m (Ariane 5) downstream from the nozzle exit. The outer radius of the meshes varies between 40 and 300 m. A single mesh was used for the Vega calculations at 18.7 km, 30 km and 42 km. In case of Ariane 5 the outer radius had to be increased for the 50 km case when compared to the 30 km case. Soyuz was computed at 30 km only.

Turbulence is modelled through a k-ω shear-stress transport model. However, these Reynolds-averaged Navier-Stokes models are not fully adapted to axisymmetric flows. Therefore, some constants of the original model by Menter [8] were modified following a strategy already used for a k-ε model by Turpin and Troyes [23]. The modified values of these constants are $\sigma_{\omega 2}$=0.714, β_2=0.0783 and γ_2=0.47.

The chemistry is modelled using a semi-detailed kinetic scheme shown in Table 1. More details and reaction rates are provided in [22]. The chemical scheme consists of three main paths of reactions: H_2 and O_2 reactions 1 to 8, CO and CO_2 reactions 9 to 11 and chlorine species reactions 12 to 17. In the Soyuz case only the first 11 reactions of the chemical kinetic scheme are used as no chlorine species are present in the exhaust gas.

Alumina particles are modelled in two ways depending on their size. The smallest particles, estimated to represent about 5% of the total particle mass, are treated as an equivalent gas phase within the gas solver. The large particles, estimated to have a diameter of 8 µm and representing 95% of the total mass, are treated by a dedicated Eulerian dispersed phase solver.

Table 1 Chemical reactions taken into account in the CFD simulations

Number	Reaction
1	$H + O_2 \Leftrightarrow OH + O$
2	$O + H_2 \Leftrightarrow H + OH$
3	$OH + H_2 \Leftrightarrow H + H_2O$
4	$OH + OH \Leftrightarrow O + H_2O$
5	$H + H + M \Leftrightarrow H_2 + M$
6	$H + OH + M \Leftrightarrow H_2O + M$
7	$H + O + M \Leftrightarrow OH + M$
8	$O + O + M \Leftrightarrow O_2 + M$
9	$CO + OH \Leftrightarrow CO_2 + H$
10	$CO + O2 \Leftrightarrow CO_2 + O$
11	$CO + O + M \Leftrightarrow CO_2 + M$
12	$H + HCl \Leftrightarrow H_2 + Cl$
13	$H + Cl_2 \Leftrightarrow HCl + Cl$
14	$HCl + OH \Leftrightarrow H_2O + Cl$
15	$HCl + O \Leftrightarrow OH + Cl$
16	$Cl + Cl + M \Leftrightarrow Cl_2 + M$
17	$H + Cl + M \Leftrightarrow HCl + M$

A comparison of the Mach number distribution at different altitudes is shown in Fig. 2. The general plume structure is also visible in this plot. In addition, the boundaries of the mixing layers were extracted, s. Fig. 3. The plots show that the plume structure is similar across all three altitudes but that with increasing altitude and thus decreasing atmospheric pressure the plume becomes wider and more elongated.

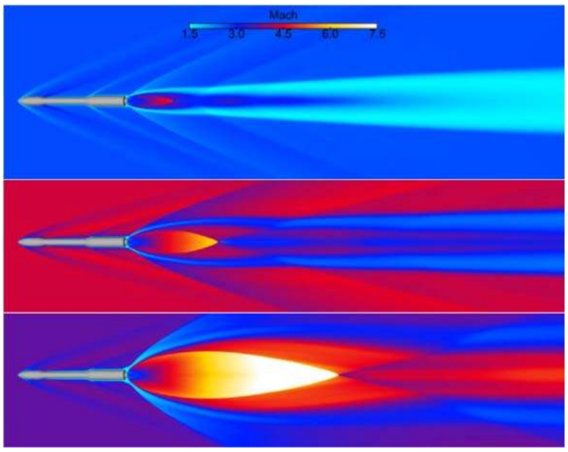

Fig. 2 Mach number evolution with altitude for the Vega rocket: 18.7 km (top), 30 km (middle) and 42 km (bottom).

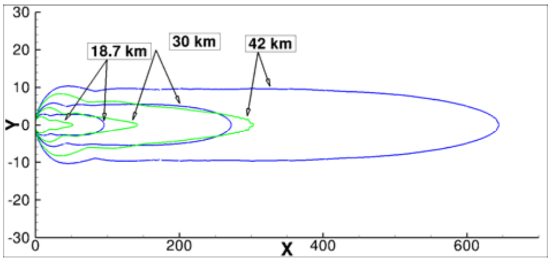

Fig. 3 Self-similar behaviour of the plume of Vega at different altitudes: internal (green) and external (blue) boundaries of the mixing layer.

3.2.2 Engineering methods

The CFD simulations are computationally intensive. Therefore, alternative approaches need to be implemented for calculating approximate solutions for the early plume at altitudes which are not considered by the CFD. Rocket exhaust plumes exhibit a characteristic structure [19] that can be divided into a near- and a far-field. In the near-field directly behind the nozzle exit the plume consists of an approximately inviscid core that is surrounded by a viscous mantle. In the viscous mantle surrounding air mixes with the exhaust gases and afterburning reactions occur. The inviscid core is separated from the viscous region by a shock wave. The pressure from the external flow turns this shock wave towards the centreline where it is ultimately reflected. This process repeats and so a periodic structure forms. Further downstream in the far-field this structure erodes due to dissipative effects.

The geometrical structure and thermodynamic properties of the exhaust flow in the near-field can be modelled with the method of characteristics [24]. The main input parameter to this model is the static pressure ratio, which is the pressure at the nozzle exit divided by the external pressure.

Woodroffe [25] developed a one-dimensional model for the far-field. It targets low-altitudes up to about 50 km and also takes chemical reactions into account.

3.3 Intermediate plume

The intermediate plume region begins when shocks and afterburning reactions have subsided. During this phase the strong concentration gradients in the radial direction are the main driver in the evolution of the plume. Fast chemical reactions and mixing with ambient air occur. These effects are described by a tailored plume model, which was developed at the IUP. The simulated domain is the cross section of the plume; a typical timescale is about an hour. The model consists of a chemical module and a short-range transport module. The chemistry module simulates gas phase and heterogeneous reactions in the plume. The transport module calculates the mixing with ambient air by solving the axisymmetric diffusion equation

$$\frac{\partial C}{\partial t} = \frac{1}{r}\frac{\partial}{\partial r}\left(rD\frac{\partial C}{\partial r}\right) \qquad (1)$$

where r is the radial coordinate, C is the concentration of a chemical species, and D is the diffusion coefficient.

Denison et al. [4] have related diffusion coefficients to observed plume expansion rates. They have introduced a radius dependent diffusion coefficient *D(r)* with an empirical parameter *b*.

$$D(r) = br \qquad (2)$$

As the mean radius of the plume increases with time, also the mean *D(r)* acting on the plume increases. Therefore, *D(r)* qualitatively resembles the effect of a diffusion coefficient increasing with time as predicted by Taylor's turbulent diffusion theory. For *D(r)* as defined in Eq. (2) an analytic solution of the axisymmetric diffusion equation exists. It can be fitted to the experimental data, and the parameter *b* can be determined.

For Athena II a comparison between model runs and measurement data was performed. Fig. 4 shows the observed plume diameter as a function of time in comparison with the modelled plume size. Four model runs were performed with different radius dependent diffusion coefficients *D(r)*.

The diameter of the plume was measured by Danilin et al. [3] at six aircraft intercepts between 3.7 min and 36.2 min after launch. Additionally, from the data of Popp et al. [11] the plume size at five of these intercepts can be calculated. Popp et al. use the full-width at half-maximum (FWHM) volume mixing ratio of ClO to determine the plume size. In order to convert the FWHM to diameter it has been assumed here that the distribution of species in the plume is a Gaussian, and that the diameter is given by four standard deviations. Note, however, that in particular the ClO measurements of Popp et al. show scatter and the distributions deviate from a Gaussian.

The diffusion model was initialised with data from the Athena II CFD simulations 700 m behind the launcher. At this distance from the rocket, the gas temperature has decreased below 400 K, and the chemical scheme of the model can be used without missing any high-temperature reactions.

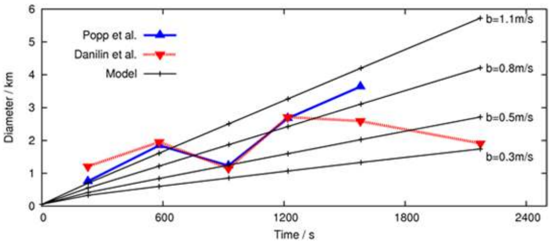

Fig. 4 Observed Athena II plume diameter [3], [11] as a function of time in comparison with model results.

3.4 Atmospheric impact

Finally, the output of the intermediate plume model is inserted into a CTM as point sources along the vertical dimension. The data is linearly interpolated to give a smooth vertical profile as a source term. At the FMI the in-house code SILAM (System for Integrated Modeling of Atmospheric Composition) is used. With SILAM it will be possible to calculate the effect of the exhaust gases on the atmosphere and the spread of the particles in the stratosphere over many years. SILAM has been adapted to the special case of simulating rocket plumes. In particular, (i) the model transport modules were extended to handle dispersion in both the free troposphere and the stratosphere, (ii) the chemistry transformation scheme was adjusted and extended, and (iii) an interface to the intermediate plume model, s. section 3.3, was created. Extension (i) is necessary because SILAM has been developed for the troposphere, but here we wish to also consider stratospheric impacts, e.g. in the ozone layer. This poses the challenge to configure optimal grid and numerical procedures for the horizontal and the vertical dimensions at such great altitudes. In case of (ii) one important family of reactions is chlorine chemistry. It plays a significant role for solid rocket motors.

4 Conclusion and outlook

Assessing the effect that rocket exhausts have on the atmosphere requires a multidisciplinary effort. The simulations within the ATILA project span several time and size scales ranging from combustion in rocket engines to simulations on a global scale. By bringing together partners from several European institutions ATILA will allow to assess the global effects and in particular increase the current knowledge about European launchers. Especially by applying higher-order methods, in this case CFD and CTM simulations, we intend to deepen the knowledge about the effects of rocket exhausts. In addition, we learn more about the modelling aspects of this integrated effort, which can then benefit other research teams.

The work described herein is funded by ESA through the General Studies Programme under contract no. 4000105828/12/F/MOS. The project Atmospheric Impact of Launchers is part of the ESA CleanSpace Initiative.

References

[1] Brady B. B., Martin L. R., Lang V. I., “Effects of launch vehicle emissions in the stratosphere”, *J. Spacecr. Rockets*, Vol. 34, No. 6, 1997, pp. 774-779.

[2] Cziczo D. J., Murphy D. M., Thomson D. S., “Composition of individual particles in the wakes of an Athena II rocket and the Space

Shuttle", *Geophys. Res. Lett.*, Vol. 29, No. 21, 2002.

[3] Danilin M. Y., Popp P. J., Herman R. L., Ko M. K. W., Ross M. N., Kolb C. E. et al., "Quantifying uptake of HNO3 and H2O by alumina particles in Athena-2 rocket plume", *J. Geophys. Res.*, Vol. 108, No. D4, 4141, 2003.

[4] Denison M. R., Lamb J. J., Bjorndahl E. Y., Lohn P. D., "Solid rocket exhaust in the stratosphere: plume diffusion and chemical reactions", *J. Spacecr. Rockets*, Vol. 31, No. 3, 1994, pp. 435-442.

[5] Gates A. M., Avallone L. M., Toohey D. W., Rutter, A. P., Whitefield, P. D., Hagen, D. E. et al., "In situ measurements of carbon dioxide, 0.37–4.0 µm particles, and water vapor in the stratospheric plumes of small rockets", *J. Geophys. Res.*, Vol. 107, No. D22, 4649, 2002.

[6] Jones A. E., Bekki S., Pyle, J. A., "On the atmospheric impact of launching the Ariane 5 rocket", *J. Geophys. Res.*, Vol. 100, No. D8, 1995, pp. 16,651-16,660.

[7] Karol I. L., Ozolin Y. E., Rozanov E. V., "Effect of space rocket launches on ozone", *Ann. Geophysicae*, Vol. 10, 1992, pp. 810–814.

[8] Menter F. R., "Two-equation eddy-viscosity turbulence models for engineering applications", *AIAA Journal*, Vol. 32, No. 8, 1994, pp. 1598-1605.

[9] Molina M. J., Molina L., Zhang R., Meads R., Spencer D., "The reaction of $ClONO_2$ with HCl on aluminum oxide", *Geophys. Res. Lett.*, Vol. 24, No. 13, 1997, pp. 1619–1622.

[10] Murray, N., Bekki, S., Toumi, R., Soares, T., "On the uncertainties in assessing the atmospheric effects of launchers", *Progress in Propulsion Physics*, Vol. 4, 2003, pp. 671-668.

[11] Popp P. J., Ridley B. A., Neuman J. A., Avallone L. M., Toohey D. W., Zittel P. F. et al., "The emission and chemistry of reactive nitrogen species in the plume of an Athena II solid-fuel rocket motor", *Geophys. Res. Lett.*, Vol. 29, No. 18, 2002, pp. 1887–1890.

[12] Ross M. N., Ballenthin J. O, Gosselin R. B., Meads R. F, Zittel P. F., Benbrook J. R., Sheldon W. R., "In-situ measurement of Cl_2 and O_3 in a stratospheric solid rocket motor exhaust plume", *Geophys. Res. Lett.*, Vol. 24, No. 14, 1997, pp. 1755-1758.

[13] Ross M. N., Benbrook J. R., Sheldon W. R., Zittel P. F., McKenzie D. L., "Observation of stratospheric ozone depletion in rocket exhaust plumes", *Nature*, Vol. 390, 1997, pp. 62–64.

[14] Ross M. N., Danilin M. Y., Weisenstein D. K., Ko M. K. W., "Ozone depletion caused by NO and H_2O emissions from hydrazine-fueled rockets", *J. Geophys. Res.*, Vol. 109, D21305, 2004.

[15] Ross M. N., Friedl R. R., Anderson D. E., Ash G., Berman M.R, Gandrud B. et al., "Study blazing new trails into effects of aviation and rocket exhaust in the atmosphere", *Eos, Transactions, American Geophysical Union*, Vol. 80, No. 38, 1999, pp. 437, 442-443.

[16] Ross M. N., Toohey D. W., Rawlins W. T., Richard E. C., Kelly K. K., Tuck A. F. et al., "Observation of stratospheric ozone depletion associated with Delta II rocket emissions", *Geophys. Res. Lett.*, Vol. 27, No. 15, pp. 2209–2212, 2000.

[17] Ross M. N., Whitefield P. D., Hagen D. E., Hopkins A. R., "In situ measurements of the aerosol size distribution in stratospheric solid rocket motors exhaust plumes", *Geophys. Res. Lett.*, Vol. 29, No. 7, pp. 819–822, 1999.

[18] Schmid O., Reeves J. M., Wilson J. C., Wiedinmyer C., Brock C. A, Toohey D. W. et al., "Size-resolved particle emission indices in the stratospheric plume of an Athena II rocket", *J. Geophys. Res.*, Vol. 108, No. D8, 4250, 2003.

[19] Simmons F. S., *Rocket exhaust plume phenomenology*, The Aerospace Press, El Segundo, CA, 2000, Chap. 2.

[20] Smith T. W. Jr., Edwards J. R., Pilson D., "Summary of the impact of launch vehicle exhaust and deorbiting space and meteorite debris on stratospheric ozone", TRW Space & Electronics Group, 1999.

[21] Stevens M. H., Lossow S., Fiedler J., Baumgarten G., Lübken F.-J., Hallgren K. et al., "Bright polar mesospheric clouds formed by main engine exhaust", *J. Geophys. Res.*, Vol. 117, D19206, 2012.

[22] Troyes J., Dubois I., Borie V., Boischot A., "Multi-phase reactive numerical simulations of a model solid rocket exhaust jet", *42nd AIAA/ASME/SAE/ASEE Joint Propulsion Conference & Exhibit*, Sacramento, CA, 2006, paper 4414.

[23] Turpin G., Troyes J., "Validation of a two-equation turbulence model for axisymmetric reacting and non-reacting flows", *36th AIAA/ASME/SAE/ASEE Joint Propulsion Conference & Exhibit*, Huntsville, AL, 2000, paper 3463.

[24] Vick A. R., Andrews E. H. Jr., Dennard J. S., Craidon C. B., "Comparisons of experimental free-jet boundaries with theoretical results obtained with the method of characteristics", NASA TN D-2327, 1964.

[25] Woodroffe J., "One-dimensional model for low-altitude rocket exhaust plumes", *AIAA 13th Aerospace Sciences Meeting*, Pasadena, CA, 1975, paper 244.

[26] Yatsenko O. V., "Refined estimates of the effect of jet discharges from launch vehicles on the kinetics of the stratospheric ozone", *Russ. J. Appl. Chem.*, Vol. 79, No. 9, pp. 1479–1488, 2006.

High Performance Green Propellants

Niklas Wingborg
Swedish Defence Research Agency, FOI

SE-147 25 Tumba, Sweden

niklas.wingborg@foi.se

Keywords: green propellant, ADN, dinitramide, hydrazine, performance, REACH

Abstract

The interest in green propellants has emerged during the last decades. To stay competitive on a global market, green propellants need to have equal or higher performance compared to current toxic propellants. Possible green high performance mono, bi, hybrid and solid propellants have been identified and some future key development activities are presented.

1 Introduction

Current propellants, such as hydrazine and its derivatives, nitrogen tetroxide and ammonium perchlorate are associated with health and environmental concerns. This is due to their toxic, volatile, carcinogenic or other harmful properties. In response to this the interest for less toxic or "green" propellants has emerged during the last decades. The last years this has further been emphasized by the REACH regulation which might result in the banning of hydrazine in Europe. If so, other hazardous propellants might be next to follow. It is thus of importance for the European space propulsion community to be proactive and prepare for what might come.

The European space propulsion industries compete on a global market and must be competitive to not lose market shares to countries with more reluctant chemical health regulations. It is thus important not to introduce harsher demands on the propulsion industry than on the chemical industry in general and to not use green propellants with inferior performance. However, high performance green propellants enable increased competitiveness due to easier handling, lower life cycle cost and higher specific impulse.

This paper presents different green propellant alternatives with higher performance than current storable propellants.

2 Liquid monopropellants

A number of different less toxic propellant options have been considered to replace monopropellant hydrazine. They who have received most attention the last years are;

- Hydrogen peroxide
- Nitrous oxide fuel blends
- Ionic liquids

2.1 Hydrogen peroxide

Apart from hydrazine, hydrogen peroxide (H_2O_2) is the most thoroughly studied monopropellant worldwide. Due to its high oxygen balance it can also be used as liquid oxidizer and it has been studied for propulsion applications at least since 1934 [1]. Its use for propulsion has been reviewed [2] and its properties are well documented [3-5]. The limited specific impulse of monopropellant hydrogen peroxide, 165 to 185 s depending on the concentration, and concerns of its storability has in the past displaced it from use in space crafts. However, during the last decade it has received renewed attention.

Hydrogen peroxide is very reactive and thermodynamically unstable and decomposes slowly even in its most stabilized form [5]. The concerns for the storability and the safe use of hydrogen peroxide have been debated during the years. It is reported that these concerns might be exaggerated and that hydrogen peroxide can be handled safely [6, 7]. The stability and compatibility of hydrogen peroxide should thus be studied thoroughly to determine its future potential.

2.2 Nitrous oxide fuel blends

Nitrous oxide has been considered as a green oxidizer for hybrid rockets and as a monopropellant by its own for many years. Recently, monopropellant blends of nitrous oxide and fuel have been studied, so called nitrous oxide fuel blends, NOFB [8]. This type of propellant seems very appealing due to its high performance, ease of ignition, low toxicity and low cost. However, little is known about its explosive properties. Since the fuel/oxidizer blend will exist both in the liquid and in the gaseous state, the risk of explosion due to adiabatic compression must be considered. Little data on the sensitivity of NOFB propellants have been published and thus it is hard to determine if it is safe to handle.

2.3 Ionic liquids

By definition an ionic liquid is a salt with a melting point below 100°C used in the liquid state. Ionic liquid monopropellants are usually mixtures of an oxidizer salt, fuel and water. The most studied oxidizer salts for this application are;

- HNF (hydrazinium nitroformate) [9, 10]
- HAN (hydroxylammonium nitrates) [11, 12]
- ADN (ammonium dinitramide) [13, 14]

Some of their properties are shown in Table 1.

Table 1. Properties of some oxidizer salts considered for ionic liquid monopropellants.

Salt	Formula	Mw	Solubility[a] (%)	Ω (%)
HNF	$N_2H_5C(NO_2)_3$	183.1	53 [15]	+13
HAN	NH_3OHNO_3	96.0	95 [16]	+33
ADN	$NH_4N(NO2)_2$	124.1	78 [17]	+26

a) Solubility in water at 20°C.
b) Oxygen balance; excess oxygen when forming CO_2 and H_2O.

The most important property to obtain a monopropellant with high I_{sp} is high solubility. For this reason ADN and HAN are most promising. Apart from having lower solubility, HNF is synthesized using hydrazine [18] which may not be acceptable in Europe in the future due to REACH.

HAN has been studied since the 1960s and was extensively studied in the 1980s for liquid gun propellants applications [19]. In the 1990s the interest for HAN based liquid monopropellants for space craft propulsion increased due to the toxic concerns of hydrazine [11, 12, 20, 21].

The HAN based monopropellant AF-M315E, developed by the US Air Force Research Laboratory, has been selected for NASA’s space technology demonstration program. The goal of the so called Green Propellant Infusion Mission is to demonstrate AF-M315E in space in 2015 [22].

ADN is mainly intended as oxidizer in solid rocket propellants. In the beginning of the 1990s, the Swedish Defence Research Agency, FOI, supported by the Swedish Armed Forces, started its research on ADN in order to develop minimum smoke solid propellants for tactical missile applications [23].

In the mid-1990s, FOI in cooperation with the Swedish Space Corporation, SSC, started to study ADN based liquid monopropellants. The first ADN-based liquid monopropellants developed, LMP-101 and LMP-103, had poor thermal stability, but this was solved by adding ammonia. In this way LMP-103S was developed which is used on the Prisma satellite launched in 2010.

While SSC/ECAPS have focused on thruster development, FOI have continued improving the propellants and developed the high performance, low volatile propellant FLP-106, seen in Fig. 1.

Fig. 1 Monopropellant FLP-106.

So far no thorough comparison has been made between the different green monopropellant alternatives and thus it is currently not possible to say which monopropellant will be preferred in the future. To overcome this, a comparative study is recommended.

3 Bi-propellants

With the inclusion of hydrazine on the REACH list there is a perceived risk other hydrazines, such as monomethylhydrazine, MMH, and unsymmetrical dimethylhydrazine, UDMH, will also be subjects for harsher regulations. Less toxic hypergolic fuels are thus of interest. MMH and UDMH are usually used in combination with the storable oxidizer nitrogen tetroxide, NTO (N_2O_4). Due to its volatility and toxicity green substitutes to NTO is also considered [24].

In the USA work is currently ongoing in the development of ionic hypergolic fuels to replace MMH [25]. Silanes [26] and DMAZ [27] have also been studied. The calculated I_{sp} for some fuels, in combination with NTO, are shown in Table 2. While DMAZ/NTO and Si_2H_6/NTO have lower performance than MMH/NTO it appears that the fuels FF1 and FF2 can exceed the performance of MMH. However, the hypergolic nature of these fuels needs to be studied.

Table 2. Optimum I_{sp} for different fuels.

Fuel	**I_{sp} (s) [a]**
MMH	342
Disilane, Si_2H_6	324
FF1	353
FF2	343
DMAZ	337

a) Oxidizer NTO, $\varepsilon = 50$, vacuum, $p_c = 10$ bar.

Very few storable oxidizers exist and finding substitutes to NTO is a very challenging endeavor. In Table 3 the calculated I_{sp} for the most common storable oxidizers are presented with MMH as fuel. The result shows that NTO is superior from a performance point of view. The second best is hydrogen peroxide of 98% concentration. However, as previously mentioned, the storability and safe use of hydrogen peroxide are still debated.

Table 3. Optimum I_{sp} for different storable oxidizers.

Oxidizer	I_{sp} (s) [a]
NTO, N_2O_4	342
H_2O_2 (98%)	336
IRFNA	326
N_2O $_{(L,\ 298\ K)}$	317

a) Fuel MMH, $\varepsilon = 50$, vacuum, $p_c = 10$ bar.

Due to inferior performance and debated safe use of hydrogen peroxide, it is not obvious NTO can be replaced without substantial loss in performance.

While there are substantial benefits replacing MMH with a greener alternative, this may not be the case for NTO. Worthwhile benefits could be gained just by replacing MMH, as this propellant is the significantly more dangerous component. The safety and environmental issues concerning NTO are much less severe than those arising with MMH since [27];

- NTO is not suspected of causing cancer.
- NTO occur naturally in the environment and are also used by other industrial activities.
- The safe-working exposure limits permitted for NTO are orders of magnitude higher than hydrazine [27].

However, if the use of hydrogen peroxide can be accepted it seems possible, from a performance point of view, to replace MMH/NTO with 98% hydrogen peroxide in combination with the fuel FF1 as seen in Table 4.

Table 4. Optimum I_{sp} for different fuels with H_2O_2.

Fuel	I_{sp} (s) [a]
MMH	336
Disilane, Si_2H_6	320
FF1	345
FF2	339
DMAZ	333

a) Oxidizer H_2O_2 98%, $\varepsilon = 50$, vacuum, $p_c = 10$ bar.

4 Hybrid propellants

Hybrid rocket motors have seen a renewed interest the last decades. In theory they show high performance and safety but in reality high performance is hard to obtain due to insufficient regression rate of the solid fuel and poor combustion efficiency.

To improve the regression rate fuels as paraffin and GAP are studied. However, both materials have poor mechanical properties. At FOI a method to improve the mechanical properties of GAP has been developed.

Curing GAP with the isocyanate Desmodure N3300 results in a low strength material, see curve no 1 in Fig. 2. By using other isocyanate curing systems, the elasticity can be improved substantially, see curve no. 2 and 3 in Fig. 2. By modifying the curing systems it was possible to further improve the elasticity to 700% and at the same time increase the strength to more than 2 MPa, see curve no. 2b and 3b in Fig. 2.

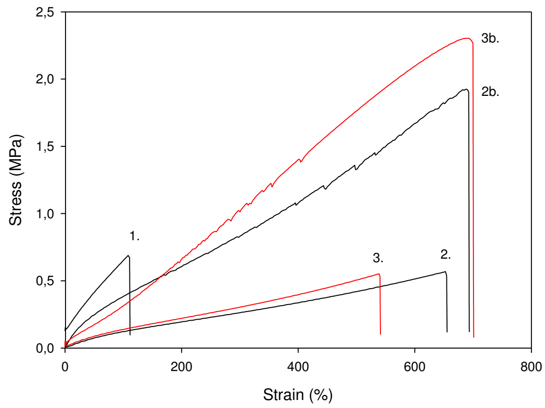

Fig. 2 Tensile test curves for GAP-based binders with different curing systems.

Aluminum powder is often considered as fuel in hybrid motors to improve performance. At FOI a way to improve the combustion rate of aluminum powder has been developed. This is referred to as activated aluminum. By using activated aluminum, both increased combustion efficiency and regression rate can be obtained. In cooperation with Nammo Raufoss, activated aluminum were tested in a H_2O_2 fed hybrid rocket motor showing an increased regression rate in the range of 25-30% [28]. The test firing is shown in Fig. 3.

Fig. 3. Testing of activated aluminum in a H_2O_2 hybrid rocket motor. Credit Nammo Raufoss.

However, the use of hydrogen peroxide for hybrid rockets must, as in the previous examples, be assessed. Other possible high performance liquid oxidizers are NTO (storable) and LOX (cryogenic).

5 Solid propellants

State-of-the-art solid propellants are based on the oxidizer ammonium perchlorate (AP), NH_4ClO_4. AP is in many ways an excellent oxidizer due to its relative low explosive hazardness and the possibility to tailor its ballistic properties. However, AP has negative impacts on the environment and on personal health.

Perchlorate anions is a widespread, environmentally persistent contaminant discovered in the U.S. groundwater and drinking water supplies that affect tens of millions of people [29, 30]. At high enough concentrations, perchlorate can affect thyroid gland functions, where it is mistakenly taken up in place of iodide. Apart from impacting the thyroid activity in humans, AP forms vast amount of hydrochloric acid on combustion.

One material that has the potential to replace AP, without performance penalty, is ADN. ADN is today manufactured by EURENCO Bofors on license from FOI. The quality of the ADN produced is very good but the particle shape is needle shaped and thus not suitable for solid propellant formulation. At FOI a method to produce spherical ADN particles, prills, has been developed [31, 32]. The prills are produced by spraying molten ADN through a nozzle. In the nozzle the molten ADN form droplets which then solidify to the desired prills. To meet the increased international demand of prilled ADN, the prilling method has been up-scaled to produce 20 kg of prills per day. Jet milling has also shown to be a promising low cost method to produce small ADN particles.

An ADN propellant with a GAP-based binder has been formulated containing 70% bimodal prilled ADN. The propellant had a low viscosity, excellent thermal stability, high burning rate and a pressure exponent below 0.5. 3 kg case bonded grains were cast and test fired in 2010, see Fig. 4 [23].

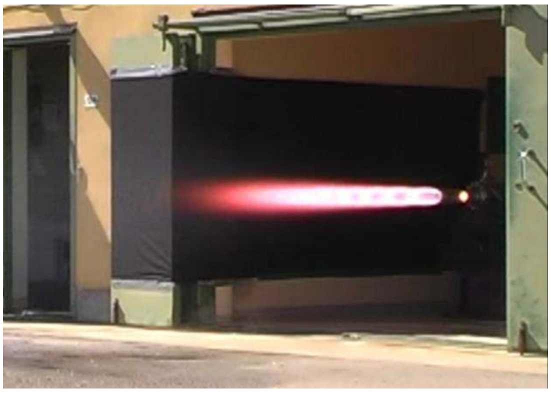

Fig. 4 Test firing of a 3 kg ADN/GAP rocket motor.

Current development of high performance solid ADN propellants for space applications is ongoing in the FP7 project HISP [33].

A new ADN synthesis method has been invented. The new method has the potential to substantially decrease the cost of ADN, increase the purity and decrease the amount of by-products formed.

By using 200 μm prills and jet milled ADN good castability was obtained with a current maximum solid loading of 74% ADN in GAP. Promising tensile testing results show that ADN/GAP propellants with mechanical properties corresponding to many current composite propellants can be developed by using bonding agents and plasticizers as seen in Fig. 5.

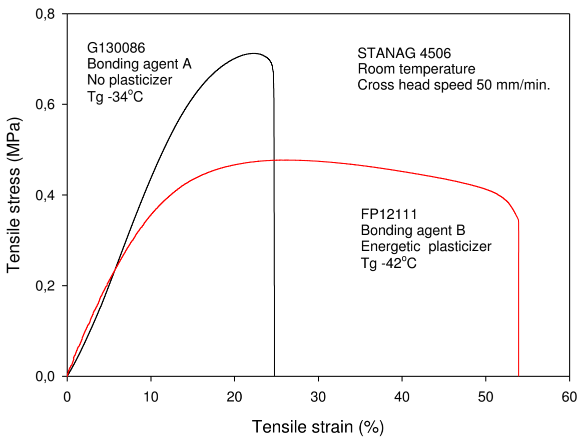

Fig. 5 Typical tensile test curves for ADN/GAP (70/30) propellants with different binder systems.

All the substantial progress achieved shows promise for ADN propellants in future solid rocket motors. However, the burning rate of ADN/GAP propellants may be too high for some applications. ADN based propellants with lower burning rate should thus be developed by using non-energetic binders, such as HTPB.

6 Discussion and conclusions

Many possible green propellants have been identified and substantial development is ongoing worldwide. However, the development of green propellants in Europe is divergent and not harmonized and hence there is a risk that the resources available will not accomplish any major breakthrough. ESA and the European Commission should pave the way to focus the resources to safe guard the competitiveness of the European space propulsion industry.

The author suggests the following activities to be performed, possibly in the framework of Horizon 2020;

- The thermal stability and compatibility of hydrogen peroxide should be studied thoroughly to determine its future potential.
- A comparison between the different green monopropellant alternatives developed should be performed.
- Green hypergolic fuels to replace MMH should be developed.
- Solid ADN propellants with lower burning rate should be developed.

7 References

1. Walter, H., Report on rocket power plants based on T-substance. 1947, NACA.
2. Wernimont, E., et al., Past and present uses of rocket grade hydrogen peroxide, in 2nd International Hydrogen Peroxide Propulsion Conference. 1999: Purdue University, IN, USA.
3. Dadieu, A., R. Damm, and E.W. Schmidt, Raketentreibstoffe. 1968, Wien: Springer-Verlag.
4. Schumb, W.C., C.N. Satterfield, and R.L. Wentworth, Hydrogen peroxide. 1955: Reinhold Publishing Corporation.
5. Davis, D.D., et al., Fire, Explosion, Compatibility and Safety Hazards of Hydrogen Peroxide. 2005, NASA.
6. Musker, A.J., et al., Hydrogen peroxide - From bridesmaid to bride, in 3rd ESA International Conference on Green Propellants for Space Propulsion. 2006: Poitiers, France.
7. Ventura, M., et al., Rocket Grade Hydrogen Peroxide (RGHP) for use in Propulsion and Power Devices - Historical Discussion of Hazards, in 43rd AIAA/ASME/SAE/ASEE Joint Propulsion Conference & Exhibit, AIAA, Editor. 2007, AIAA: Cincinnati, OH, USA.
8. Mungas, G., et al., NOFBX Monopropulsion Overview, in 14th Annual FAA Commercial Space Transportation Conference. 2011.
9. Schöyer, H.F.R., et al., Overview of the Development of Hydrazinium Nitroformate-Based Propellants. J. Propulsion Power, 2002. **18**(1): p. 138-145.
10. Marée, A.G.M., et al., Technology Status of HNF-Based Monopropellants for Satellite Propulsion, in 2nd International Conference on Green Propellants for Space Propulsion. 2004: Chia Laguna, Sardinia, Italy.
11. Jankovsky, R.S., HAN-Based Monopropellant Assessment for Spacecraft, in 32nd AIAA/ASME/SAE/ASEE Joint Propulsion Conference. 1996: Lake Buena Vista, FL, USA.
12. Meinhardt, D., et al., Development and Testing of New, HAN-based Monopropellants in Small Rocket Thrusters, in 34th AIAA/ASME/SAE/ASEE Joint Propulsion Conference. 1998: Cleveland, OH, USA.
13. Anflo, K., T.A. Grönland , and N. Wingborg, Development and Testing of ADN-Based Monopropellants in Small Rocket Engines, in 36th AIAA/ASME/SAE/ASEE Joint Propulsion Conference. 2000: Huntsville, AL, USA.
14. Wingborg, N., C. Eldsäter, and H. Skifs, Formulation and Characterization of ADN-Based Liquid Monopropellants, in 2nd International Conference on Green Propellants for Space Propulsion. 2004: Chia Laguna, Sardinia, Italy.
15. Hatano, H., et al., eds. Characteristics of HNF. 20th International Pyrotecnic Seminar. 1994: Colorado Springs, CO, USA.
16. Kappenstein, C., N. Pillet, and A. Melchior, New Nitrogen-Based Monopropellants (HAN, ADN, HNF). Physical Chemistry of Concentrated Ionic Aqueous Solutions, in Propulsion for Space Transportation of the XXIst Century. 2002: Versailles, France.
17. Wingborg, N., Ammonium Dinitramide-Water: Interaction and Properties. J. Chem. Eng. Data, 2006. **51**(5): p. 1582-1586.
18. Schöyer, H.F.R., et al., Overview of the Development of Hydrazinium Nitroformate. J. Propulsion Power, 2002. **18**(1): p. 131-137.
19. Klingenberg, G., et al., Liquid Propellant Gun Technology. Vol. 175. 1997: AIAA.
20. Meinhardt, D., S. Christofferson, and E. Wucherer, Performance and Life Testing of Small HAN Thrusters, in 35th AIAA/ASME/SAE/ASEE Joint

Propulsion Conference. 1999: Los Angeles, CA, USA.
21. Mittendorf, D., W. Facinelli, and S. R. Experimental Development of a Monopropellant for Space Propulsion Systems. in 33rd AIAA/ASME/SAE/ASEE Joint Propulsion Conference. 1997. Seattle, WA, USA.
22. Aerojet Grows Missile Defense Propulsion Business. http://www.aerojet.com/news2.php?action=fullnews&id=341.
23. Wingborg, N., et al., Development of ADN-based Minimum Smoke Propellants, in 46th AIAA/ASME/SAE/ASEE Joint Propulsion Conference. 2010: Nashville, TN, USA.
24. Valencia-Bel, F. and M. Smith, Replacement of Conventional Spacecraft Propellants with Green Propellants, in Space Propulsion 2012. 2012, 3AF: Bordeaux, France.
25. Zhang, Y., et al., Ionic Liquids as Hypergolic Fuels. Angew. Chem. Int. Ed., 2011. **50**: p. 9554-9562.
26. Hidding, B., et al., Silanes/H2O2: A High-Performance Synthetic Bipropellant for Chemical Space Propulsion. J. Propulsion Power, 2008. **24**(1): p. 144-147.
27. Mellor, B. and M. Ford, Investigation of Ignition Delay with DMAZ Fuel and MON Oxidiser, in 42nd AIAA/ASME/SAE/ASEE Joint Propulsion Conference. 2006, AIAA: Sacramento, CA, USA.
28. Rönningen, J.-E. and J. Husdal, Test Results From Small-Scale Hybrid Rocket Testing, in Space Propulsion 2012. 2012: Bordeaux, France.
29. Urbansky, E.T., Perchlorate as an Environmental Contaminant. Environ Sci & Pollut Res, 2002. **9**(3): p. 187-192.
30. Gu, B. and J.D. Coates, Perchlorate; Environmental Occurrence, Interactions and Treatment. 2006: Springer.
31. Eldsäter, C., et al., ADN Prills: Production, Characterisation and Formulation, in 40th International Annual Conference of the Fraunhofer ICT. 2009: Karlsruhe, Germany. p. 24.
32. Johansson, M., et al., Spray Prilling of ADN, and Testing of ADN-Based Solid Propellants, in 3rd International Conference on Green Propellants for Space Propulsion. 2006, ESA: Poitiers, France.
33. HISP-project. http://www.hisp-fp7.eu/.

4:th CEAS Air & Space Conference
FTF Congress: Flygteknik 2013

Criteria for the Selection of Targets for Active Debris Removal

Benjamin Bastida Virgili and Holger Krag
ESA Space Debris Office, ESOC/ESA, Robert-Bosch-Str. 5, 64293 Darmstadt, Germany

Keywords: *active debris removal (ADR), risk on orbit, ranking of objects, mitigation guidelines*

Abstract

There is consensus that the future evolution of the space debris environment in the LEO (Low Earth Orbit) regime is not stable and that active debris removal (ADR) needs to be considered to control the growth rate. First ADR mission designs are being intensively discussed and significant effort is put into the identification of suitable removal candidate objects.

In this paper we analyze the effect of ADR on the long term evolution of the space debris environment in LEO in different scenarios using the European Space Agency's (ESA) Debris Environment Long Term Analysis (DELTA) model (with variations on the implementation of the mitigation measures, on the traffic models and evolution, on the removal selection criteria and on the solar flux). For each of the scenarios we derive a list of candidates based on the objects involved in catastrophic collisions. A combined list is then created with the objects which appear repeatedly in the different scenarios. Finally, this list is used as input for ADR simulations and the effectiveness of the removal is evaluated in terms of number of objects reduced and number of collisions avoided, as well as the risk reduction for other missions in orbit, after 50 years, 100 years and 200 years.

1 Introduction

The number of human made objects in space has undergone a steady increase since the beginning of spaceflight. The concern that the future environment growth might be dominated by collisions, rather than by launches and explosions, was expressed already decades ago. In response to this, the IADC (Inter-Agency Space Debris Coordination Committee) formulated a set of mitigation requirements that were issued in 2002 [1]. These requirements aimed at a limitation of the growth rate rather than at a reduction of the object population below the current numbers. These IADC guidelines recommend the spacecraft to perform collision avoidance maneuvers while operational, and to be passivated and perform a re-orbit or de-orbit maneuver in order to be outside from the LEO protected regions in less than 25 years at the end of their operational life.

As shown in recent studies undertaken with different environment prediction tools from various agencies [2, 3, 4, 11], the current environment will continue to grow, even in the case of no further mission deployments (i.e. a "no further release scenario"), as can be seen in Fig. 1.

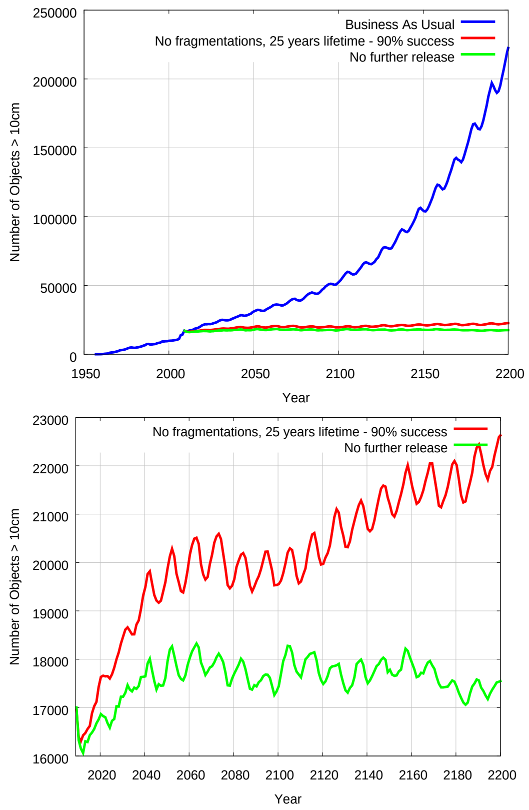

Figure 1. (top) DELTA results on the future evolution of the number of objects in LEO in a Business as Usual (BAU) scenario, in a no-further-release scenario and in a Partial Mitigation (PM) scenario with 90% accomplishment of mitigation measures. (bottom) Focus on the two last scenarios.

In Fig. 1 we also observe the environmental evolution in a scenario where 90% of the new objects launched in space follow the IADC mitigation guidelines, which confirms that even in an optimistic level of adoption of the mitigation guidelines a linear growth is to be expected. However, the comparison with the Business as Usual (BAU) scenario, where the growth is exponential, shows the necessity and urgency of fully applying the mitigation guidelines for all future launches. The growth in all scenarios is mainly due to collisions caused by fragments generated by other collisions (so-called feedback collisions). This observed instability indicates that the existing and currently proposed mitigation measures are not sufficient to stop the increase of the collision rate, even when they are strictly implemented. It has to be noted that all the models use assumptions on the future launch activities and solar flux, which have significant associated uncertainties.

To stabilize the environment, the idea of actively removing objects from space has been raised. Active debris removal (ADR) implies missions with the capability to interact with passive spacecraft or rocket bodies in order to reduce their remaining orbital lifetime. Obviously, such efforts are only acceptable if all mitigation measures proposed by IADC are followed strictly [5]. Various ADR mission design proposals are currently under discussion. The analysis of optimal environment remediation strategies has just begun, but in parallel, mitigation measures might have to be intensified as well for a balance of activities that lead to effective results. Furthermore, the selection and ranking of targets by their deployment orbit and their physical properties needs to be optimized.

Although the IADC formulated the mitigation requirements in 2002, the evolution of the population during the last 10 years and the relatively low number of attempts to significantly shorten the orbital lifetime of LEO objects that operated above 600km altitude [6] has brought the situation to a point where ADR needs to be considered as an additional measure to stabilize the growth of the population, as different studies have shown in the last years [2, 3, 4].

Previous studies have looked into optimal target orbital regions for ADR or for other criteria to select the possible removal targets, while others have looked at the effect of varying the start epoch for ADR activities, and at the effect of the number of objects to be removed per year [2, 5].

1.1 DELTA (Debris Environment Long-Term Analysis)

ESA's Debris Environment Long Term Analysis (DELTA) model is one of the models that contribute to the IADC studies on long term evolution, which have already been used to derive the mitigation guidelines and have also proven the need for ADR. The original DELTA has been modified by ESA to implement the required aspects to perform active debris removal scenarios. DELTA is a three-dimensional, semi-deterministic model, which in its entirety allows a user to investigate the evolution of the space debris environment and the associated mission collision risks in the low, medium and geosynchronous Earth orbit regions over the years. DELTA is able to examine the long-term effects of different future traffic profiles and debris mitigation measures, such as passivation and disposal at end-of-life.

DELTA uses an initial space object population as input and forecasts the evolution of all objects larger than 10cm in size for our studies. The population is described by representative objects, evolved with a fast analytical orbit propagator which takes into account the main perturbations. The initial population has been extracted from ESA's MASTER-2009 (Meteoroid and Space Debris Terrestrial Environment Reference) model [13]. DELTA uses a set of detailed future traffic models for launch, explosion and solid rocket motor firing activity. They are each based on the historical activity of the eight preceding years. This is one of the main causes for uncertainties in the results, as varying the future traffic models has a big impact, and there is no certainty on the actual evolution of the space activity in the future. The collision event prediction is done by using a target centered approach, developed to stochastically predict impacts between all objects within the DELTA population [7, 8, 9]. The fragmentation, or break-up, model used is based on the EVOLVE 4.0 (NASA) break-up model [10]. The future solar flux evolution has a strong effect on the results, as the atmospheric drag is the main factor for the natural decay of objects and is correlated to it. ESA has its own solar and geomagnetic activity prediction model (SOLMAG), which uses data from past solar cycles to predict the future ones. Different solar activity predictions have been used within DELTA in order to check their effect and to have valid and conclusive results with different future evolutions.

2 Generating a list of candidates for removal

During the last 4 years, many different simulation scenarios have been run in DELTA in the frame of various studies and publications, as well as for maintenance and improvement of the software. Initial populations extracted from MASTER (for 1st May 2005 and, once available, for 1st May 2009) were used, where an identifier allows to trace back the objects to the real ones in the catalog. In the MASTER population of 2009, as compared to the one of 2005, an increase of 250 objects can be assigned to the growth in the US catalog. Then, we have checked the results of each of the simulations (each having a large number of Monte-Carlo (MC) runs) and generated a list with the objects implied in catastrophic collisions. We have then counted the number of MC runs of each simulation leading to catastrophic collisions involving the listed objects. From this, statistics have been generated per simulation and a ranking has been derived. Afterwards, a combined list has been produced including the results of all of the simulations, following the same approach, so that we have global ranking. In this list we have filtered out objects that were not involved in collisions in simulations of at least 100 MC runs.

2.1 Simulation cases used as background

We have used the results of 84 different simulations to generate the list, all of them with a propagation time span of 200 years in the future. From these, 21 are based on a "no-further-release" scenario, a situation where the initial population is propagated and only the collisions are responsible for the increase of the population, as no explosions occur and no new objects are added in space. A total of 7 are based on a "Business-As-Usual" (BAU) scenario, where the launch traffic for the future is based on the traffic of the past 8 years, explosions continue to happen, also based on their occurrence the past, and no mitigation measure is applied. Another 21 are based on a "partial mitigation" (PM) scenario, where future launches are based on the past, no explosions occur, and the mitigation requirements from IADC guidelines are applied, and, finally, 17 are based on the propagation of new explosion or collision clouds through the initial population, in order to see the effect of a particular event in the global evolution. The remaining 18 simulations had as objective testing the improvements and upgrades of DELTA.

The differences between the simulations based on the same scenario are the possible initial population (2006 or 2009), the solar flux prediction used, the rate of success of the mitigation requirements, the variation of the launch rates, and the application of various ADR concepts.

In fact, there are 29 simulations where ADR has been tested in combination with different scenarios. The variations are on the number of objects removed per year, the year for the missions' start, and the criteria for the selection of the objects to be removed.

2.2 Statistics of the list

The global ranking contains 1850 objects, associated to real objects from the catalog, having a probability above 1% of being involved in a catastrophic collision. The vast majority of these objects are payloads (P/L) and rocket bodies (R/B), as stated in Tab. 1. The catalog has around 12000 objects in LEO at the current epoch (August 2013), from which almost 9000 are fragments.

In Fig. 2 we can observe the distribution, in 0.5% probability bins, of the objects according to the probability of being involved in a catastrophic collision. As could be expected, the growth in number of objects is almost exponential when reducing the probability.

Table 1. Type of objects in the ranking above a given probability of being involved in a catastrophic collision (P/L: payload; R/B: rocket body; MRO: mission-related object; Frag: fragment)

Collision prob	P/L	R/B	MRO	Frag.	**Total**
>1%	1045	660	135	10	1850
>5%	60	66	9	1	136
>7%	12	22	3	0	37
Top10 (>9.5%)	2	8	0	0	10

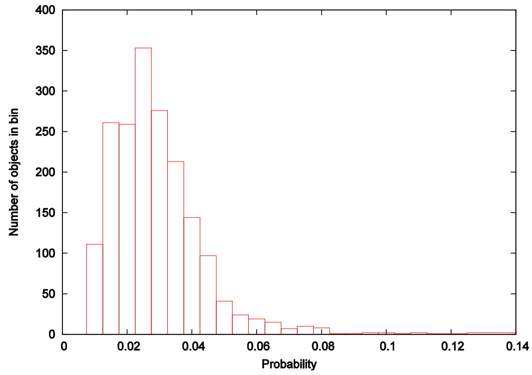

Figure 2. Histogram of distribution of objects in the ranking according to the probability of being involved in a catastrophic collision.

The top-10 objects have a probability of catastrophic collision above 9.5%. Moreover, the object on the top of the list has a collision probability of 13.8%. The eight R/B in this top-ten are from the same family, with masses between 8 and 9 tons. Six of them are in an altitude around 850 km and inclination around 71°, while the other two are in a Sun-synchronous inclination at 815 km and 1000 km, respectively. The two payloads are also in Sun-synchronous orbits and have masses of 8 and 4 tons, respectively. In total, these 10 objects represent a mass of almost 80 tons and an accumulated average cross-section of 370 m^2.

However, as can be seen in Fig. 3, there is no apparent relation between the probability of collision and the area or the mass of the object (except for the few objects in the top risk region). So it is clear that performing an ADR according to a ranking based solely on area or mass will not be the most effective way. The mass of all the objects in the list sums up to 1800 tons (from the total mass in LEO which is around 2500 tons).

The orbital distribution (mean altitude versus inclination) and the respective probability can be observed in Fig. 4. There are clearly regions (1000km-82°, 800km-99°, 850km-71°, …) with a higher concentration of objects having higher probabilities, where it could be possible to perform ADR missions which would remove more than one object per mission more efficiently, as was already discussed in [2].

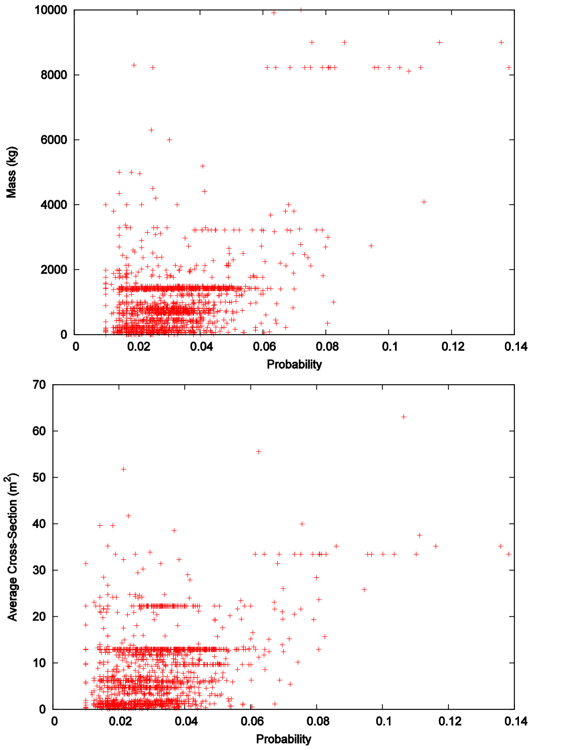

Figure 3. Mass (top) and average cross-section (bottom) vs. probability of being involved in a catastrophic collision for the objects in the ranking.

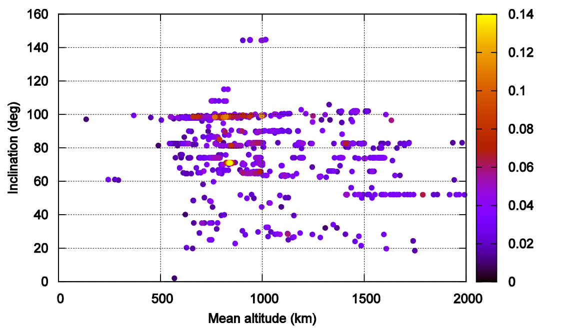

Figure 4. Orbital distribution (mean altitude vs. inclination) with the corresponding probability of being involved in a catastrophic collision (color code) of the objects in the ranking.

3 ADR according to a collision risk based ranking

The objective of generating a global ranking is to have a different criterion as the ones used in previous studies to select the candidates for ADR. The method of generation of this list, which combines many different scenarios and takes into account 200 years of propagation, provides an overview which is independent of the scenario itself.

To demonstrate the relevance of the list, we have simulated ADR scenarios by selecting the objects from the list according to their ranking. We have chosen four reference scenarios, defined by a simulation time span of 200 years, starting with the MASTER-2009 population of 1st May 2009 above 10 cm, a high solar flux prediction, the implementation of the lifetime limitation of 25 years with 0, 30, 60 or 90% of success, assuming no new explosions on orbit, a launch traffic based on that of 2001-2009, and an operational lifetime for new payloads of 8 years. The 0%-success scenario is almost a BAU case, with the difference that we consider that no more explosions occur on orbit, while the 90% scenario is the one used for the IADC study [11]. It must be taken into account that recent studies [14] show that for the past years the compliance rate with the mitigation guidelines is rather poor with about 30% success in meeting the lifetime reduction requirement in LEO. Also, still some explosions occur in orbit every year. The scenarios selected try to give a wide range in which we could expect to find the real evolution.

For the ADR scenarios, we consider starting the ADR missions 15 years after the epoch of the object population (i.e. in 2024), to take into account that the technology is not available today. We have simulated the removal of 5 objects per year, for all the duration of the simulation (ADR5) or only during the first 35 years (ADR5L). For each of the cases, we have performed 40 MC runs.

The evolution of the population for the four reference scenarios, which differ on the success rate of the mitigation measures (0% PM, 30% PM, 60% PM or 90% PM) and the ADR applied to each of them can be seen in Fig. 5, whereas the cumulative number of catastrophic collisions is shown in Fig. 6.

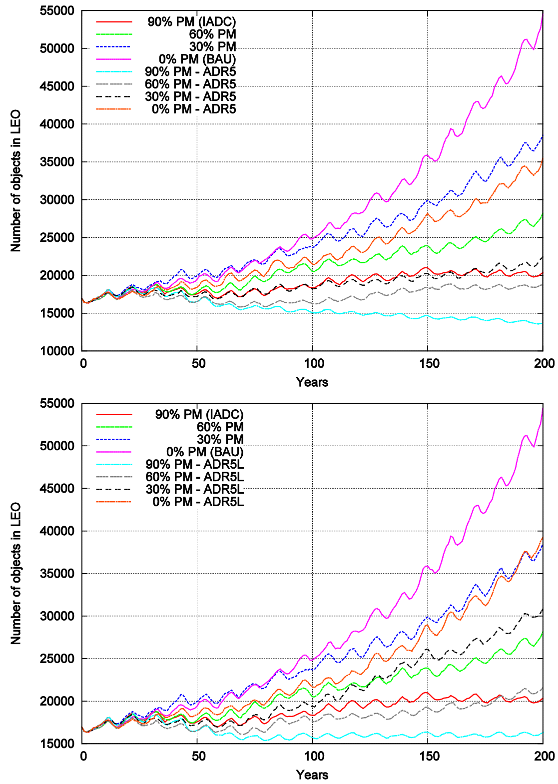

Figure 5. Evolution of population above 10 cm in LEO for the four reference scenarios (0, 30, 60 and 90% of success of the mitigation measures) and for the ADR of 5 objects per year with no end date (ADR5) (top) or with only 35 years of missions (ADR5L) (bottom).

From Figures 5 and 6 we point out some interesting observations. At the end of the simulation time, the ADR5L in a 0% PM (BAU) scenario provides similar results to an implementation of 30% PM, while the ADR5 is slightly better. However, if we compare the situation after 100 years, the two ADR scenarios for 0% PM are closer to the 60% PM than to the 30% PM scenario. Also the scenario ADR5 in 30% PM is similar to the 90% PM (IADC) during all the simulation time. Basically, in the current status where only 30% of objects deorbit in less than 25 years at the end of the operational lifetime, it would be required to remove 5 objects per year forever (with the associated economic cost) to keep a population in space similar to the one we would have if full compliance with the existing guidelines could be established and, in consequence, only failures during operations would leave uncontrolled objects in space. Hence, these findings are an important argument in order to convince spacefarers to improve the compliance to the IADC mitigation guidelines.

The number of objects and of collisions for the ADR5 and ADR5L scenarios with 60% PM and 90% PM are always below the 90% PM scenario without ADR (except at the end of the simulation time for the ADR5L 60PM%). This shows the expected positive effect of removing the objects using the ranking as criteria for the selection.

After 50 years where ADR5 and ADR5L have identical results (as the same objects are removed in both cases), their curves start slowly diverging, so that the first differences are only appreciated 30 year after the end of the ADR missions. However, the effect of these 35 years of removals is noticeable if compared to the reference scenarios with no ADR.

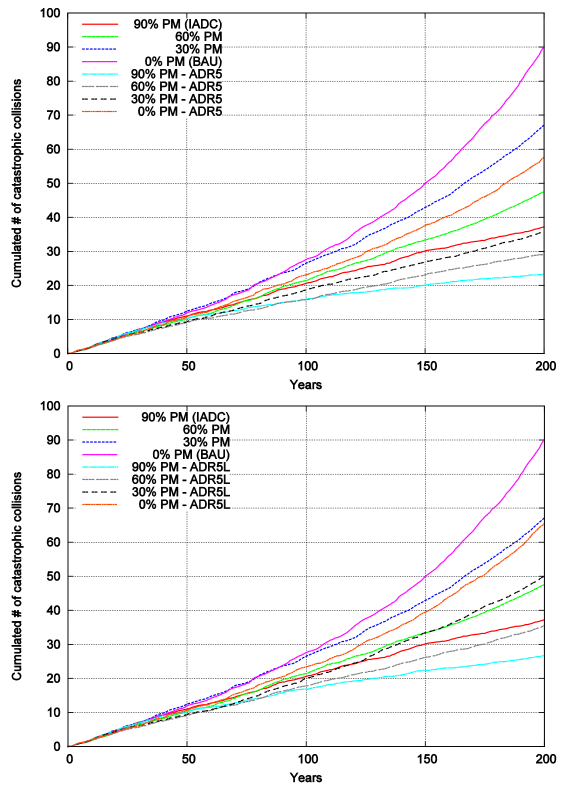

Figure 6. Cumulative number of catastrophic collisions for the four reference scenarios (0, 30, 60 and 90% of success of the mitigation measures) and for the ADR of 5 objects per year with no end date (ADR5) (top) or with only 35 years of missions (ADR5L) (bottom).

3.1 Effectiveness of the ADR missions

3.1.1 ORF and CRF

In order to quantify the effectiveness of the ADR missions, two metrics have been proposed [2, 12]. The first, which we call the Object Reduction Factor (ORF), indicates the relation between the number of objects removed and the reduction, due to the ADR, in the total number of objects compared to the reference scenario. The second, that we call the Collision Reduction Factor (CRF), gives the relation between the number of objects removed and the reduction in the number of catastrophic collisions. In Table 2 we see these factors for the tested ADR scenarios after 50 years of simulation, in which case the ADR5 and the ADR5L are still the same. We also provide the relative population growth, which is the variation of the population in relation to the initial one (composed of almost 17,000 objects). In Table 5, the population growth for the reference scenarios is shown for comparison, and to remark that in all the reference scenarios the population increases with respect to the initial conditions, stressing again the need for ADR.

As can be seen in Table 2, after 50 years the effect of ADR is still relatively imperceptible, with only 1 to 3 collisions avoided. However, the population decreases already by more than 1000 objects, which represents a decrease between 5 and 10% in relation to the reference scenarios, and we observe that the population growth is stable relative to the initial population.

In Tables 3 and 4, the ORF, CRF and population growth are provided after 100 years and at the end of the simulation respectively.

Table 2. Quantitative results for the ADR scenarios after 50 years, for the four different success rates of the mitigation measures and for the ADR of 5 objects per year.

	ADR5-90	ADR5-60	ADR5-30	ADR5-0
Reduction in # objects (a)	1002	1241	2725	1011
Reduction in # collisions (c)	0.8	1.1	3.2	1.2
# AR objects (b)	162	162	162	162
ORF (a/b)	6.19	7.66	16.82	6.24
CRF (b/c)	202.50	147.27	50.63	135.00
Population growth (%)	-2.23%	-2.48%	1.52%	8.62%

Table 3. Quantitative results for the ADR scenarios after 100 years, for the four different success rates of the mitigation measures and for the ADR of 5 objects per year with no end date (ADR5) or with only 35 years of missions (ADR5L).

	ADR5-90	ADR5L-90	ADR5-60	ADR5L-60
ORF (a/b)	8.24	16.31	10.60	17.93
CRF (b/c)	86.09	43.78	70.71	45.00
Pop growth (%)	-11.15%	-7.48%	-3.91%	3.72%
	ADR5-30	ADR5L-30	ADR5-0	ADR5L-0
ORF (a/b)	13.77	13.46	8.40	19.47
CRF (b/c)	50.77	24.55	88.00	38.57
Pop growth (%)	7.44%	14.41%	26.73%	27.75%

Table 4. Quantitative results for the ADR scenarios after 200 years, for the four different success rates of the mitigation measures and for the ADR of 5 objects per year with no end date (ADR5) or with only 35 years of missions (ADR5L).

	ADR5-90	ADR5L-90	ADR5-60	ADR5L-60
ORF (a/b)	8.35	25.04	11.79	40.59
CRF (b/c)	57.97	15.58	43.48	13.61
Pop growth (%)	-19.29%	-3.83%	10.51%	27.37%
	ADR5-30	ADR5L-30	ADR5-0	ADR5L-0
ORF (a/b)	20.12	47.38	23.83	94.32
CRF (b/c)	25.72	9.42	24.54	6.53
Pop growth (%)	32.35%	82.00%	109.26%	131.57%

In Table 3 we observe that after 100 years the ADR5 has approximately half the effect than the ADR5L (the ORF is about half and the CRF about double), for almost all the mitigation scenarios. This proves that the ranking made is correct and that the first objects on the list have a bigger impact on the evolution of the environment. However, we observe that there is a difference of around 5% on the population growth between ADR5 and ADR5L, implying that the extra 250 objects removed in the ADR5, although having a smaller effect than the first 160 objects removed in both ADR5 and ADR5L, have also an influence to the control of the environment.

In Table 4 we see that after 200 years the difference in effectiveness between ADR5 and ADR5L has increased even more, now being between 3 and 4 times better for ADR5L in relation to ADR5. But again, the overall population growth is between 15% and 50% higher for the ADR5L, prove that the extra 400 objects removed in the ADR5 have also a

Table 5. Population growth (%) of the reference scenarios after 50, 100 or 200 years.

	90% PM	60% PM	30% PM	0% PM
50 years	3.7%	4.8%	17.6%	14.6%
100 years	8.1%	20.9%	39.6%	46.3%
200 years	20.1%	66.1%	127.3%	221.7%

contribution to the environment control. In any case, both ADR5 and ADR5L have a population growth much smaller than the mitigation scenarios without ADR, around 20% in 100 years of simulation and around 50% after 200 years, as can be checked comparing Tables 3 and 4 versus Table 5.

3.1.2 Risk for other spacecraft

Satellite operators are primarily interested in the safety of their spacecraft and in how much propellant will be needed for collision avoidance maneuvers. To cope with this point of view, we have looked at the risk variation in some regions where many satellites are located. We have selected four representative orbits: ISS (400 km altitude and 51.6° inclination), and sun-synchronous orbits (SSO) at an altitude of 600, 700 and 800 km. All the cases assume a circular orbit and consider controlled objects (so with no decay). We are then interested in the risk variation after 50, 100 and 200 years of simulation.

The figure of the risk variation is calculated as shown in Eq. 1.

$$\Delta R = \frac{(f_{ADR} - f_{ref})}{f_{ref}} [\%] \qquad (1)$$

Where f_{ADR} is the flux above 10 cm encountered in one of the ADR scenario at a given time, and f_{ref} the flux of the reference scenario with the same PM success rate at the same epoch. This encountered flux can be described as the number of impacts that an object with a cross section of 1 m^2 would have during 1 year, which is equivalent to the risk of having a collision for any given satellite if we scale it with the correct cross section and the time in orbit.

In Tables 6, 7 and 8 the risk variation in these four representative orbits after 50, 100 and 200 years respectively.

Table 6. Risk variation in different orbital regimes for the ADR scenarios after 50 years of simulation, for the four different success rates of the mitigation measures and for the ADR of 5 objects per year.

	ADR5-90	ADR5-60	ADR5-30	ADR5-0
ISS	-2.2%	0.8%	-4.0%	-5.4%
SSO-600	-6.4%	-6.6%	-12.0%	-3.7%
SSO-700	-6.3%	-7.4%	-14.4%	-3.8%
SSO-800	-11.0%	-13.9%	-27.4%	-7.7%

Table 7. Risk variation in different orbital regimes for the ADR scenarios after 100 years of simulation, for the four different success rates of the mitigation measures and for the ADR of 5 objects per year with no end date (ADR5) or with only 35 years of missions (ADR5L).

	ADR5-90	ADR5L-90	ADR5-60	ADR5L-60
ISS	-6.8%	-6.3%	-4.6%	-5.2%
SSO-600	-11.3%	-13.7%	-16.9%	-10.4%
SSO-700	-23.8%	-22.2%	-33.2%	-21.2%
SSO-800	-28.7%	-25.6%	-35.8%	-22.7%
	ADR5-30	ADR5L-30	ADR5-0	ADR5L-0
ISS	-11.0%	-0.9%	-19.3%	-18.7%
SSO-600	-12.5%	-6.0%	-11.0%	-14.7%
SSO-700	-28.1%	-23.6%	-13.5%	-17.5%
SSO-800	-34.2%	-28.9%	-17.9%	-19.1%

Table 8. Risk variation in different orbital regimes for the ADR scenarios after 100 years of simulation, for the four different success rates of the mitigation measures and for the ADR of 5 objects per year with no end date (ADR5) or with only 35 years of missions (ADR5L).

	ADR5-90	ADR5L-90	ADR5-60	ADR5L-60
ISS	-14.7%	-7.2%	-11.6%	-12.8%
SSO-600	-29.3%	-19.8%	-34.3%	-21.1%
SSO-700	-46.1%	-31.1%	-51.5%	-33.3%
SSO-800	-50.8%	-33.1%	-49.3%	-30.2%
	ADR5-30	ADR5L-30	ADR5-0	ADR5L-0
ISS	-19.7%	-21.2%	-23.6%	-20.1%
SSO-600	-35.8%	-17.9%	-30.1%	-21.3%
SSO-700	-49.3%	-28.9%	-38.7%	-30.7%
SSO-800	-50.4%	-27.1%	-41.4%	-31.3%

We can observe that in all the cases the risk for the operational spacecraft decreases in the ADR scenarios compared with the no-ADR ones. The impact of the ADR depends on the operational orbit and is more noticeable on orbits where the objects have longer orbital lifetimes (increasing with altitude, of about 25 years at 600 km and around 200 years at 800 km for a typical spacecraft (A/M=0.005m^2/kg)). This decrease on the risk is due to the removal of objects that would have been involved in a catastrophic collision if they had not been removed in time and that would have created many new fragments in orbits with long lifetimes. This result demonstrates again the usefulness of the ranking for selecting the targets for removal.

It is also remarkable that in the SSO orbits tested, the risk reduction is of around 10% after 50 years, around 25% after 100 years and around 40% after 200 years. This shows that ADR would be an effective way to clean the environment and that it would permit the designers and operators of satellites to continue using the highly interesting orbits without compromising the missions due to too large number of collision avoidance maneuvers and force them to accept a higher unavoidable collision risk (from non-traceable objects).

We can also see that the risk reduction is similar for the different success rates of the mitigation measures, which shows that ADR reduces the risk independently of what the background population is. However, we want to remind that these figures are just relative to each of the references, and that the risk is higher in a 0% PM scenario than in a 90% PM. This means, for example, that the risk reduction of 50% in the 30% PM ADR5 scenario in SSO-800km has, however, a higher absolute risk than a 90% PM without ADR. To give the numerical justification, in Table 9 we provide the risk variation of the scenarios without ADR with respect to the initial flux for each of the orbits. We want to stress again that even if ADR is an effective way for cleaning up the environment, the correct implementation of the IADC mitigation guidelines is much more effective (see the 250% increase of the risk at SSO

Table 9. Risk variation in different orbital regimes for the four different success rates of the mitigation measures relative to the initial flux after 50, 100 and 200 years.

		90% PM	60% PM	30% PM	0% PM
50 years	ISS	-47.7%	-56.1%	-62.2%	-69.3%
	SSO-600	-5.9%	-4.4%	5.1%	8.6%
	SSO-700	22.0%	20.1%	40.7%	35.8%
	SSO-800	-10.1%	-9.5%	13.7%	-2.0%
100 years	ISS	-43.2%	-50.1%	-51.7%	-51.3%
	SSO-600	-29.4%	-15.8%	-4.2%	14.0%
	SSO-700	-2.9%	19.9%	39.8%	48.1%
	SSO-800	-13.4%	1.5%	20.5%	23.7%
200 years	ISS	-47.8%	-44.9%	-40.7%	-26.8%
	SSO-600	-26.4%	9.0%	46.9%	104.2%
	SSO-700	0.1%	60.7%	131.2%	250.8%
	SSO-800	-17.0%	19.5%	85.0%	169.5%

700km after 200 years for the 0% PM versus the 0% increase in the 90% PM scenario). ADR from selected objects from a ranking should be seen as a necessary, but complementary, measure that would help to even further decrease the risk.

4 Conclusion

We have developed a novel way of generating a ranking of the objects candidates for ADR, based on selecting the objects being involved in a catastrophic collision from previous environment simulations, and ranking them according to the number of MC runs where they lead to catastrophic collision events, yielding an estimate for the overall probability of collision. This list is similar to other lists independently obtained, with the main difference being that now the lifetime of the objects is implicitly considered in the computation of the probabilities. The resulting list has been used as input for the selection of ADR candidates in a few simulation scenarios and the results show the effectiveness of this removal strategy in order to reduce the increase of the population.

We have shown that removing only a small percentage of objects on the top of the list (less than 10%, corresponding to 160 objects) has a significant impact on the evolution of the environment and is more effective (in terms of ORF and CRF metrics) compared to a costly continuous removal. However, stopping the removal yields an increased population growth because collisions will occur that involve objects further down the considered list.

We have also seen that ADR is an effective complementary way to reduce the risk of collision for operational satellites in the current (and probably also future) most frequently used orbits. This is important for the satellites operators, as they can expect a reduction of collision avoidance maneuvers between 10% and 50%, with the implicit reduction of cost and extension of the operational lifetime.

However, and more important, is the fact that ADR is only beneficial when the mitigation guidelines are correctly and fully implemented by all space fairing nations and operators. In any other situation, ADR would be ineffective, as new debris would take the place of the ones removed. This issue was already addressed theoretically in [5] and has been assessed by simulations in the current study. We have shown that over 200 years a 90% success on the implementation of the mitigation guidelines is equivalent to 30% success and ADR of 5 objects per years, in terms of collisions and number of objects in LEO. This implies that, with the current level of compliance to the IADC mitigation guidelines, feasible ways of sharing the costs of the needed ADR missions have to be found just in order to reach the same environment situation that would result from just following mitigation guidelines, which in any case means lower cost and fewer technological complexity than for conducting ADR missions.

ADR missions are not yet a reality because many difficulties, both technically and politically, still have to be overcome. ESA, with its Clean Space initiative, is working to improve the situation and to be able to perform a demonstration mission of ADR in the years to come.

References

[1] IADC. “IADC Space Debris Mitigation Guidelines”. 2002.

[2] B. Bastida Virgili, H. Krag. “Strategies for Active Removal in LEO.” ESA SP-672, *Proc. of the 5th European Conference on Space Debris.* 2009

[3] J.-C. Liou. “An active debris removal parametric study for LEO environment remediation.” *Adv. Space Res*. 2011. doi:10.1016/ j.asr.2011.02.003

[4] H. Lewis et al. “The Space Debris Environment: Future Evolution”. *CEAS 2009 European Air and Space Conference*, Manchester, UK. 26 - 29 Oct 2009

[5] B. Bastida Virgili, H. Krag. “Analyzing the Criteria for a Stable Environment”. *AAS/AIAA Astrodynamics Specialist Conference*, Girdwood, AK, USA. AAS11-411. 2011

[6] H. Krag, T. Flohrer, S. Lemmens. “Consideration of Space Debris Mitigation Requirements in the Operation of LEO Missions”. *Space Operations: Experience, Mission Systems & Advanced Concepts, Progress in Aeronautics and Astronautics.* AIAA, Reston, VA, USA, 2013.

[7] R. Walker, C.E. Martin et al. “Analysis of the effectiveness of space debris mitigation measures using the Delta model”. Adv. Space Res. Vol. 28, No. 9, pp 1437-1445. 2001

[8] C.E. Martin, R. Walker, H. Klinkrad. “The sensitivity of the ESA DELTA model”. *Adv. Space Res*. Vol. 34, pp 969-974. 2004

[9] R. Walker, C.E. Martin. “Cost-effective and robust mitigation of space debris in Low Earth Orbit”. *Adv. Space Res*. Vol. 34, pp 1233-1240. 2004

[10] N.L. Johnson et al. “NASA's new breakup model of evolve 4.0”. *Adv. Space Res*. Vol. 28 No. 9, pp 1377-1384. 2001

[11] J.-C. Liou et al. “Stability of the Future LEO Environment – An IADC Comparison Study”. *6th European Conference on Space Debris*. 2013

[12] J.-C. Liou, N.L. Johnson. “A sensitivity study of the effectiveness of active debris removal in LEO”. *Acta Astronautica*. 64, 236-243. 2008.

[13] Institute of Aerospace Systems. Technische Universität Braunschweig. “Maintenance of the MASTER Model”. Final Report ESA contract 21705/08/D/HK. 2009.

[14] H. Krag, S. Lemmens, T. Flohrer, H. Klinkrad. “Analysing Global Achievements in Orbital Lifetime Reduction at the End of LEO Missions”. ESA SP-723 , Proc. of the *6th European Conference on Space Debris*. 2013

Environmental impact assessment of space sector: LCA results and applied methodology

Michele De Santis and Giorgio Urbano
D'Appolonia S.p.A., Italy

Gian Andrea Blengini
Politecnico di Torino, Italy

Rainer Zah and Simon Gmuender
EMPA, Switzerland

Andreas Ciroth
GreenDelta TC, Germany

Keywords: *Life Cycle Assessment, Space Mission, European Space Agency, Carbon footprint.*

Abstract

In the framework of the Clean Space Initiative, promoted by ESA for increasing attention to the environmental impacts of its space activities, the "LCA4Space project" (ESA Contract No. 4000105605/12/F/MOS) aimed at evaluating, through the LCA methodology, the environmental performances of two space missions (Astra 1N and MetOp-A) together with the elaboration of sector specific methodological LCA guidelines.

A cradle to grave approach was applied to the two missions and a common methodology for European space sector was elaborated. All spacecraft phases from Concept and Design to manufacturing up to End-of-Life, through launch and use, were evaluated.

The OpenLCA 3.1 software was used for the LCA model and more than 60 new datasets (import/export to Ecospold), specifically dedicated to space sectors, were created.

Include some results and conclusions.

1 Introduction

The space community, and ESA (European Space Agency) in particular, have been recognizing the importance of integrating environmental aspects since the earliest stages of space missions design, thus giving a significant contribution towards more environmentally friendly practices. This is also demonstrated by the ESA's Frame Policy for Sustainable Development (ESA/C(2010)29), in which the basic principles governing the framework policy for sustainability are outlined, referring to the contribution to the 20/20/20 target and to the achievement of a Green Competitive Space Technology.

The implementation of Life Cycle Assessment (LCA) methodology as a tool to better understand the environmental impact of space programmes is included in the above mentioned ESA Frame Policy. The main motivation is to explore the applicability of LCA to space system design and, where appropriate, re-design of on-going and new ESA missions, under the umbrella of eco-design.

Thereby all the phases involved in a space mission have to be considered: design, production and procurement of parts and components, assembly, testing, up to use, potential disposal phase, etc.

A consortium led by D'Appolonia, an Italian engineering consulting company part of the RINA Group, and constituted by Politecnico of Torino, EMPA, Swiss federal laboratories for materials testing and GreenDelta, a German company engaged in sustainability assessment, supports ESA within the "LCA4Space" project in applying LCA to two selected space missions, by means of the elaboration of a sector-specific methodology, which takes into account the complexity of the aerospace industry (ESA Contract No. 4000105605/12/F/MOS).

Main objective of the study is to support ESA to achieve a comprehensive understanding of a space mission's life-cycle impacts and to acquire the necessary methodological background.

2 The LCA Methodology

The LCA methodology is a holistic approach to estimate the environmental impact of a product or service throughout its life cycle (cradle-to-grave approach). LCA has been widely, and successfully applied to several industrial sectors in order to understand environmental trade-offs, optimize processes, support policy making and as an eco-design tool.

According to ISO standards 14040:2006 [1] and 14044:2006 [2], LCA comprises four major stages:

- Goal and scope definition - The goal phase defines the overall objectives of the study. The scoping phase sets the boundaries of the system under study, the sources of data and the functional unit to which the achieved results refer.
- Life cycle inventory (LCI) – A detailed compilation of all the inputs (material and energy) and outputs (air, water and solid emissions) at each stage of the life cycle is performed;
- Life cycle impact assessment (LCIA) – Aims at quantifying the relative importance of all environmental burdens obtained in the LCI by analyzing their influence on the selected environmental impact categories;
- Interpretation - where the results from the LCI and LCIA stages are interpreted in order to find hot spots and compare alternative scenarios.

3 The two analyzed missions

Two space missions have been investigated: Astra 1N, a telecommunication mission for broadcasting purposes and MetOp-A, an earth observation mission for meteorological purposes.

3.1 Astra 1N

Astra 1N is a satellite actually in use for digital and HD telecommunications, that is providing significant growth potential to key European markets [3].

Astra 1N is an Eurostar E3000 model with launch mass of 5400 kg and spacecraft power of more than 13kW. The satellite, launched (dual launch) by Ariane 5 in August 2011 is specified for a minimum service life of 15 years.

The spacecraft has three deployable antennas and one top-floor steerable antenna [4]. The satellite is designed and manufactured by Astrium and managed by SES, while ESA is not directly involved in this mission.

3.2 Met-Op A

MetOp-A is Europe's first polar-orbiting satellite dedicated to operational meteorology. It is a satellite actually in use for providing weather data services, in order to monitor our climate and improve weather forecasting.

In fact MetOp is a series of three satellites to be launched sequentially to provide data over the next 14 years, starting in 2006, and forms the space segment of EUMETSAT's Polar System (EPS) [5].

A new generation of European instruments that offer improved remote sensing capabilities to both meteorologists and climatologists is carried with a set of instruments provided by the United States. The new European instruments enhance the accuracy of:

- Temperature and humidity measurements;
- Wind speed and wind direction measurements, especially over the ocean;
- Profiles of ozone in the atmosphere.

MetOp-A has a mass of 4085 kg (only payload weights 931 kg) and spacecraft power of more than 1812 W. The satellite, launched by Soyuz ST Fregat in 17 October 2006 is specified for a minimum service life of 5 years, but it is still in use, although some instruments are out of order [6].

4 Approach of the “LCA4Space” project

The analysis has been conducted following ISO standards, ILCD Handbook, prepared by The Directorate General–Joint Research Centre (DG-JRC) of the European Commission (EC) - Institute for Environment and Sustainability (IES), with the support of a software for LCA modelling, openLCA. DG-JRC-IES acted as an advisor during the project [7].

In parallel the methodological framework of LCA applied to space projects has been created.

4.1 Goal of the study

ESA is certainly interested in using LCA results as a decision making support tool to improve its missions’ sustainability. Nevertheless, there is currently an exploring interest in assessing whether possible environmental improvements (e.g. related to changes in the technologies suppliers are using) are having any consequences in the background system or other parts of the technosphere (e.g. additionally required material need to be produced or new production facilities using distinct technologies need to be built).

For these reasons, according JRC guidelines, the decision context of the study is situation C – Accounting, i.e monitoring environmental impacts of a product. In particular it is situation C1, which includes benefits that the analysed system may have outside its system (e.g. benefits of recycling or co-products).

4.2 Scope of the study

4.2.1 Functional unit

The selected functional unit is the entire space mission from its conceptual design until its final disposal.

This choice enables a detailed analysis of mission’s environmental impacts and highlights the phases and single processes contributing substantially to the overall impacts (hot spots and contribution analysis). It is hence possible to understand which phases and subsystems bring the greater environmental impacts and plan future improvement activities whose impacts will be later tested in an iterative procedure.

4.2.2 System boundary and cut-off criteria

The life cycle stages of a satellite are typically split into 7 phases, according to ECSS (European Cooperation for Space Standardization) standards [8]:

1. Phase 0 - Mission analysis/needs identification (not included in LCAs),
2. Phase A – Feasibility,
3. Phase B - Preliminary Definition,
4. Phase C - Detailed Definition,
5. Phase D - Qualification and Production,
6. Phase E_1 –Utilization – Launch, Phase E_2 –Utilization – Ground Operations,
7. Phase F – Disposal.

According to the ESA approach, space projects have a life cycle, from concept definition to end-of-life (phases A to F). To run a Space project, heavy assets (e.g. infrastructures/plants/facilities) must be constructed/developed and they also hold a life cycle made of phases impacting the environment. Finally, a space project is aimed at producing, launching and operating a satellite, which can be regarded as the project’s “Product”. Also the satellite, as a product, holds its own life cycle, as part of a supply chain.

There is not therefore only one life cycle to be considered and studied, but rather three inter-dependent life cycles, which need to be integrated and jointly understood in terms of environmental and resource use implications:

1. Space Project Life Cycle (phases A - F),
2. Space Asset (Infrastructure) Life Cycle,
3. Space Product Life Cycle.

The co-existence of three life cycles can generate confusion and misunderstandings when LCA has to be applied. It is therefore important to clarify their inter-relation.

A proposed conceptual scheme for the integration of the three life cycles is presented in Fig. 1.

With emphasis on the Space Project Life Cycle, the following subdivision is proposed:

- Concept & Design (phases A, B),
- Manufacturing (phases C and D),
- Use / operation (phases E1 and E2),
- End of life (phase F).

As it can be seen in the Fig. 1, there are some overlaps and some discrepancies among the three life cycles.

ESA personnel are typically involved in activities that fall within the yellowed boxes, and they likely tend to associate the LCA to those activities. On the contrary, an LCA practitioner is more familiar to the product life cycle, i.e. the orange path. Thus, ESA personnel have to expand their view in order to incorporate the first phases of the satellite life cycle, i.e. manufacturing and transporting of basic materials and chemicals, up to sub-components that are typically purchased by ESA (or their suppliers). These activities are outside the yellow path, and ESA personnel hold a limited knowledge about the environmental life cycle impacts. On the other hand, the LCA practitioner has to pay an effort to include in the system boundaries the design phase and R&D activities that are typically excluded from an LCA (see ILCD guidelines), as they are outside the orange path.

Beyond helping the ESA personnel and the LCA experts to create a common understanding and a strategy to proceed with the application of LCA to space projects, the above scheme can be

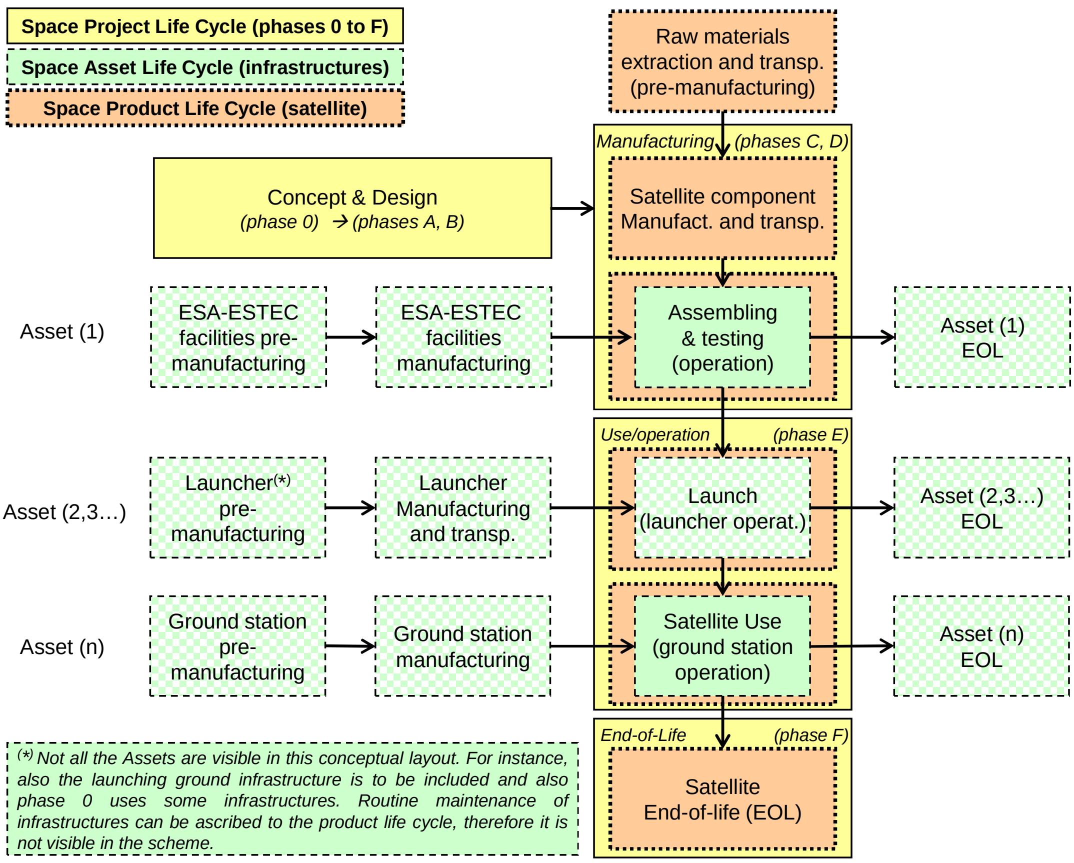

Fig. 1: Integration of three life cycle stages

helpful to:

- set up a strategy to organise data collection and elaboration;
- present the results of the LCA in a more understandable manner and outline future developments.

4.3 Life Cycle Inventory

Data gathering has been a critical activity of these two LCAs. For each phase (A to F) a critical analysis has been conducted in order to understand what kind of activities are performed in each phase and to assess their inputs (material, energy consumptions, etc.) and outputs (products, wastes, etc.).

ESA and its industrial partners have received a questionnaire for data collection concerning space missions, satellites and sub-systems. The data has been validated and if necessary completed with data from literature and background databases (Ecoinvent v2.2) [9]. Approaches adopted for data mining and data gaps management are explained in paragraph 4.4, in order to efficiently manage, assess, and improve the data quality in the LCA models.

The activities related to the **Concept and Design (C&D)** strongly depend on the type of the satellite and can show variations.

The consortium has adopted two approaches in parallel: bottom-up and top-down modelling, for all C&D phases.

In the bottom-up approach, LCI databases are based on data for specific unit processes, often aggregated or linked into larger processes finally modeling larger parts of product life cycles or entire product LCIs. In this study, inventory data related specifically to the research and development of a typical ESA mission is assumed based on expert interviews (i.e. amount of labours required for the mission, etc.).

A top-down approach is essentially the breaking down of a system to gain insight into its compositional sub-systems. In this study, the reported inventory data about the whole space industry is derived from environmental reports [10] and an allocation factor based on economic data for different space mission typologies [11] is used to derive the environmental impact related to an earth observation and telecommunication mission.

The top-down approach has finally been used in modelling activities, due to the uncertainties of bottom-up modelling.

As C&D activities are concerned, ESTEC man-year (and its associated consumptions, like energy, water, electronic equipment, waste produced, business travels, infrastructure) was selected as the parameter to allocate impacts related to C&D activities from phase A to phase E1.

An iterative approach has been also used for modelling the **Manufacturing** phases. All the components (plus fuels and consumables, such as hydrazine) constituting different satellite systems have been carefully modelled: over 60 new datasets were created by the consortium and they can be easily used in future LCAs of space missions, since they can be exported/imported in Ecospold v.1 format.

Each dataset was presented according the following scheme:

- Reference product;
- Functional unit;
- Description: Short description of the functions, properties and structure of the reference product (including pictures and references);
- Supplier;
- Production site: Relevant for the calculation of the transportation distances;
- Inventory: If no dataset is available in Ecoinvent, a proxy dataset is suggested;
- Dataset quality: the data quality and the assumed relevance of the dataset are provided.

The C&D and manufacturing phases have been integrated for completeness with datasets dedicated to AIT (Assembly – Integration – Test) activities. One kind of test, as the most representative has been analyzed, for the three typologies:

- Mechanical: Electrodynamic vibration shakers;
- Thermal: Thermal vacuum testing;
- Environmental: Anechoic test.

Moreover clean rooms (100 and 100.000 classes) uses have been modelled according LCA principles.

All the **Transport Systems** have been taken into account with corresponding distances:

- Different supplier of systems constituting payload and service modules;
- Final delivery of satellites for launch to Korou in French Guyana, by Ariane 5 (Astra 1N) and to Baikonur Cosmodrome, by Soyuz (MetOp-A).

For **Launch Campaign** data is based on information from previous studies.

Three different sub phases have been identified and modelled:

- Launch preparation with hydrazine filling and Ground Station man-year dataset [10];
- Launch itself (considered by launcher LCA) [12];
- LEOP (Launch and Early Operation Phase)/IOT (In-Orbit tests) with ESOC man year dataset [10].

For the phase E_2 (**Use Phase**) activities have been modelled with the same approach adopted for C&D, considering three main sub-activities:

- Ground station operations for TT & C (Telemetry, Tracking & Control);
- Flight operations for TT&C;
- Ground station activities for data exchange (broadcasting for Astra 1N, meteorological data for MetOp-A).

Finally two alternative **End-of-Life** solutions have been considered: satellite re-entry in atmosphere (MetOp-A) or insertion in a secondary orbit (Astra 1N). In Fig. 2 and Fig. 3 models elaborated with software openLCA are presented.

4.4 Data mining approach

The establishment of high quality inventory datasets is in general very resource demanding and, within this project, it was not always possible to close all inventory data gaps.

Nevertheless, the consortium has provided a stepwise procedure and a set of recommendations on how to identify the most relevant inventory data and on how to handle data gaps and data quality (Fig. 4).

Moreover as regards specific data collection a questionnaire has been set up. The questionnaires submitted to Astrium had the goal of speeding-up data collection and maximising the quantity and quality of primary data about the space missions life cycles.

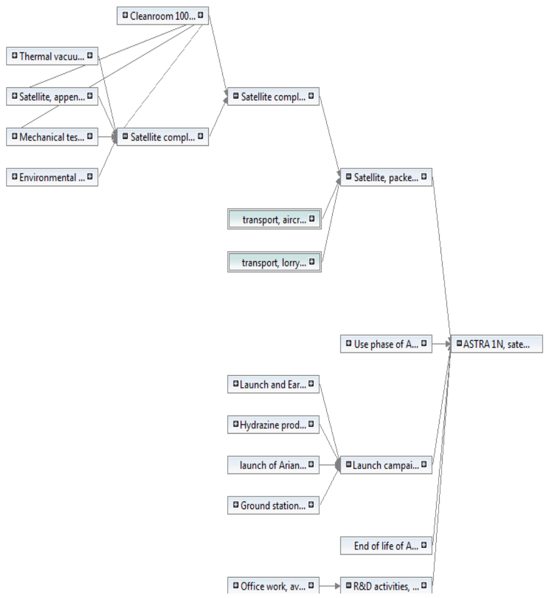

Fig. 2: Astra 1N LCA model [openLCA 1.3]

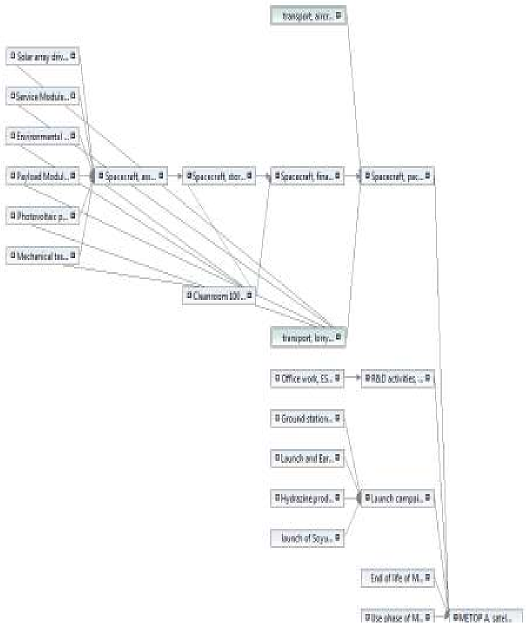

Fig. 3: MetOp-A LCA model [openLCA 1.3]

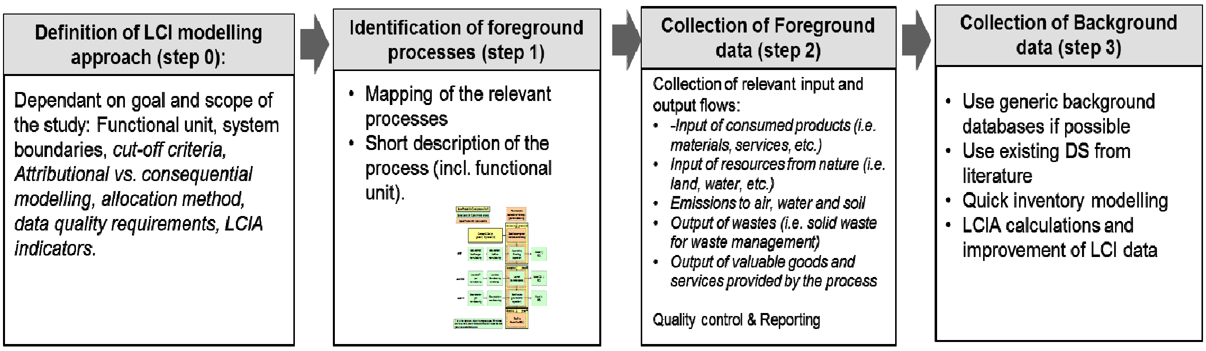

Fig. 4: Steps for modeling and Inventory Data Collection

The questionnaires are subdivided in two main parts:

- Part 1: presentation of data needs and identification of documents that could contain useful information; identification of involved organizations;
- Part 2: more detailed questionnaire, with quantitative data, that have to be filled in when the corresponding data cannot be retrieved from the documents identified in Part 1.

Instead for generic data collection, when specific data are not available, several sources of data have been used:

- ESA Sustainability report [10];
- CDF reports [13];
- LCA-studies (e.g., the ESA launcher LCA) and "ECSS standards" [12].

Table 1: Life Cycle Impact Categories [High (***) – Medium (**) – Low (*) importance]

Impact category	Relevance for Space App.	Chosen Indicator Mid-Point
Acidification (*)	Lower importance for space applications. However, the combustion of energy resources causes NOx and Sox emissions forming acid rains.	(ILCD 2011 midpoint, Acidification) Mole H+ eq.
Climate Change (***)	Politically the most important env. impact factor (reg. Kyoto protocol). Key environmental. indicator in aviation and transport sector.	Climate Change (IPCC 2007, GWP500a) - kg $CO_{2\ eq.}$
Ecotoxicity (**)	High awareness at ESA for potential toxic effects.	USEtox 2008, Ecotoxicity – PAF (Potentially Affected Fraction) CTUe
Eutrophication (*)	Lower importance for space applications	Recipe – Freshwater/ Marine eutrophication - kg $P/N_{\ eq.}$
Human Toxicity (**)	High awareness at ESA for potential toxic effects caused in the production and launch phases	Human Toxicity (USEtox, Human toxicity –) - CTUh
Ionizing radiation (*)	Lower importance for space applications	Ionizing Radiation (ILCD 2011 midpoint, Ionizing radiation - human health) kg U235 eq.
Land Use (*)	Lower importance for space applications	Recipe - Agricultural/Urban land occupation + natural land transformation– m^2
Metal depletion (**)	Probably of some importance for the space sector, as a variety of scarce resources are used.	Metal depletion (ReCiPe midpoint (H), Metal depletion) kg Fe-Eq
Non-renewable energy depletion (**)	Probably of some importance for the space sector. This indicator is closely linked with the GWP.	Non - renewable energy depletion (CML 2001, resources - depletion of abiotic resources) - kg antimony-Eq
Ozone depletion (***)	Highly relevant for space industry, as it could get in the future one of the largest emitters of ozone-depleting substances (Ross, Toohey et al. 2009)	Ozone depletion (ILCD 2011 midpoint, Ozone depletion) - kg $R_{11\ eq.}$
Particulate matter/Respiratory inorganics (*)	PM emission impacts seem to be of lower importance due to the temporal and spatial limits of space activities,	Particulate matter/respiratory inorganics (USEtox, Human toxicity - total) CTUh
Photochemical ozone formation (*)	Lower importance for space applications	Recipe – kg NMVOC
Water depletion (*)	Lower importance for space application.	Recipe – Water depletion – m^3

4.5 Life cycle impact assessment

Overall, it is recommended assessing the impacts of space missions on a mid-point level, since uncertainty is lower as compared to end-point indicators and ESA is well experienced in multi-criteria decision making.

Several impact categories mid-point indicators have been selected (according DG-JRC-IES recommendations) in order to evaluate (Table 1):

- Climate Change;
- Nature and Biodiversity;
- Environment, health and quality of life;
- Natural resources and wastes.

The consortium has also defined a space sector oriented range of indicators, from the most specific ones (***) till less ones (*).

In general, only emissions interacting with the terrestrial environment or human health are considered within the current LCA framework. Also within this study, only the impacts of substances which directly or indirectly interact with the terrestrial environment are considered.

5 Results and Discussion

A contribution analysis was carried out in order to identify the share of each main step: concept and design, satellite manufacturing (including AIT), launch campaign, ground operations and EoL.

The End-of-Life phase, both for Astra 1N and MetOp-A, is a zero impact phase, according to selected indicators. Only for MetOp it is foreseen a re-entry in atmosphere with a mass of around 500 kilograms, falling in the ocean.

Due to the huge amount of results provided across the entire project, only the main indicators (for space sector), have been presented, considering the contribution analysis:

- Climate change (Fig.5);
- Ecotoxicity (Fig.6);
- Metal Depletion (Fig.7);
- Non renewable energy depletion (Fig.8);
- Ozone Depletion (Fig.9);
- Human toxicity (Fig. 10).

A comparison based on these selected mid-point indicators, between the two missions is presented in the following Figures.

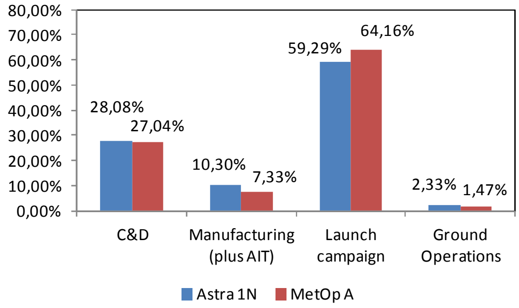

Fig. 5: Climate Change

The launch phase is the most impacting phase as regards carbon footprint and green house gases emission, for both missions (almost two third of total values). It is followed by Concept and Design (less than one third for Astra 1N and MetOp). Low values are instead referred to manufacturing phases (around 10%) and ground operation management (around 2%).

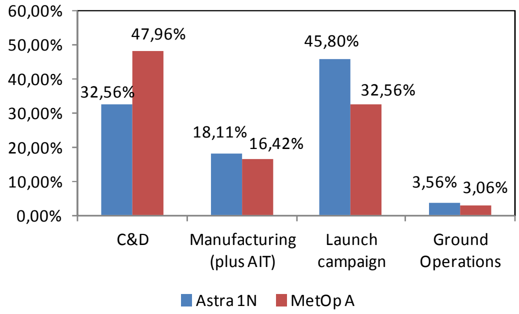

Fig. 6: Ecotoxicity

About Ecotoxicity C&D phase and Launch campaign concur together for over the 75% of total impact values; in Astra 1N outnumbers Launch, in MetOp-A the C&D. This is due to high amount of energy and fuels required for performing the activity.

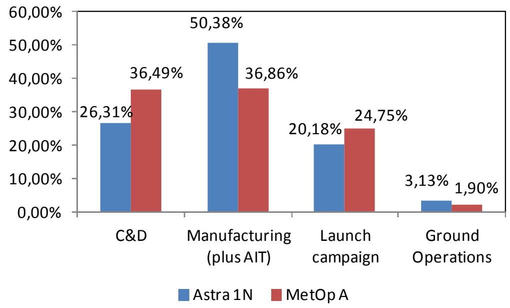

Fig. 7: Metal Depletion

Due to the large amount of materials used, the manufacturing phase is the most important for metal depletion indicator, followed by C&D and others.

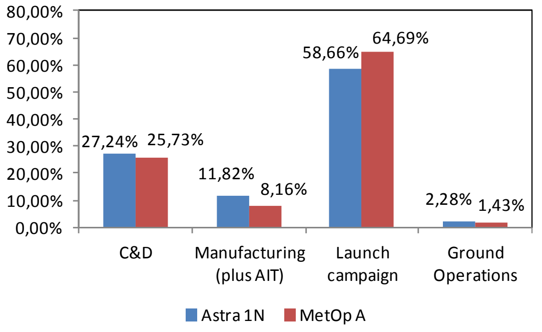

Fig. 8: Non-renewable Energy Depletion

High amount of energy used for launch is responsible for the value of Launch campaign, followed by C&D where energy for building is needed.

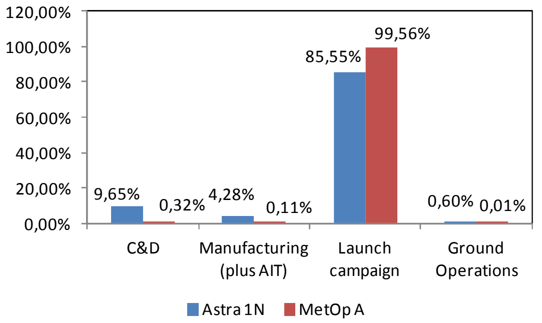

Fig. 9: Ozone Depletion

As regards Ozone Depletion the launch campaign accounts for almost the global values of this indicator, both for MetOp-A and Astra 1N.

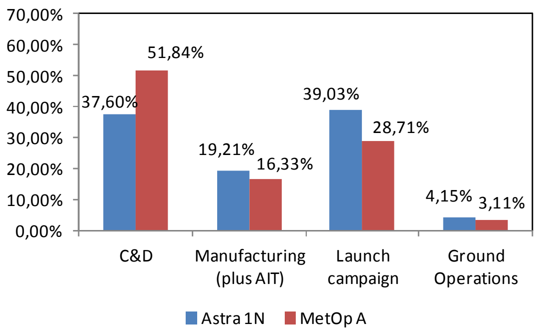

Fig. 10: Human Toxicity

Finally Human Toxicity has the same trend of ecotoxicity: the sum of C&D and Launch is around the 75% of total value.

5.1 Hot spots and sensitivity analysis

Several hot spots have been identified, using as reference four main indicators (climate change, metal and water depletion, non-renewable energy depletion); the launches, the building construction for performing various operations and some heavy metals (platinum, rhodium) plus gold use are the heaviest contributors to impacts.

A sensitivity analysis was performed in order to highlight the variation of the results by changing some parameters.

In particular the following parameters have been taken into account:

- Wastefactor in order to evaluate the value of rejected pieces across manufacturing phases (values of 1,1 and 2 have been evaluated compared to standard value equal to 1). In practice 1,1 or 2 times the amount of materials, components and subcomponents has to be produced to manufacture one satellite;
- C&D contribution in order to assess the uncertainties linked to consortium assumptions (the C&D contribution has been doubled);
- Allocation of a third of protoflight model (only for MetOp-A).

The different impact indicators are affected by these variations in a measure that does not overcome the 30% of their values.

Finally two normalization options have been provided:

- the European citizen living one year, based on characterization factors of the various assessment method cited in table methods;
- plane cargo with a payload of 65 tons.

6 Conclusions

The article reported about one specific purpose of the "LCA4Space" project that has been the contribution to overcome some of the barriers that have so far limited the use of LCA in the space sector. Among the others, based on the experience matured across the project, the followings are the main barriers one has to face:

- Specificity of space projects, which have peculiar characteristics often totally different from other sectors that, however, share technologies and know-how with aerospace (automotive, aeronautics);
- Heavy difficulties in input data collection, due to system complexity but also to high confidentiality of industrial partner data (e.g. manufacturing might be underestimated since not all subcomponents might be reflected appropriately);
- Use of non-standard materials and industrial processes;
- Difficulties in qualifying new environmental friendly materials and processes.

The aforementioned barriers can be, at least partially, overcome by setting up a sector specific LCA methodology and related tools, based on a careful analysis of the different types of space missions and projects as well as on the critical evaluation of the different phases of a space mission. This is what has been pursued across the "LCA4Space" project and this has been so far the main contribution of the project to the application of LCA as a methodological approach to evaluate space missions.

References

[1] ISO 14040:2006, *Environmental management - Life cycle assessment - Principles and framework*, 2006.

[2] ISO 14044:2006, *Environmental management - Life cycle assessment - Requirements and guidelines*, 2006.

[3] Astrium, *Communications Satellites Programme*, May 2012.

[4] Astrium, Eurostar 3000 - *Input for life cycle analysis*, 26th October 2012

[5] Astrium, Service Module & Satellite Integration test plan, 2002

[6] Astrium, *Satellite flight acceptance review*, 2011

[7] DG JRC/IES, *ILCD Handbook*, 2011

[8] The European Cooperation for Space Standardization, *ECSS documents* (Standards, Handbooks and Technical Memoranda), 2013

[9] The Swiss centre for Life Cycle Inventories, *Ecoinvent Converted ecoinvent 2.2 Data as Unit Processes with Links to other Processes, including uncertainty Data*, 2010.

[10] ESA, *Sustainable development, 2009-2010 report*, 2011

[11] ASD Eurospace, The *European space industry in 2011*, 2012

[12] BIO Intelligence Services, *Environmental Impact Of Launchers*, 2011

[13] ESA, *Concurrent Design Facility reports on several space missions*.

4:th CEAS Air & Space Conference
FTF Congress: Flygteknik 2013

Risk Assessment and Analysis of Disposal and Re-entry of Space Debris

Chiranjeev Jain[1, a] and Prashant Ganesh[2, b]
[1] Research Scholar, Department of Mechanical Engineering, Sri Sairam Engineering College, West Tambaram, Chennai, India.

[2] Research Scholar, Department of Electrical and Electronic Engineering, Sri Sairam Engineering College, West Tambaram, Chennai, India

[a] chiranjeev.jain@gmail.com, [b] prashantganesh92@gmail.com

Abstract

At this very moment there are hundreds and thousands of "dead satellites" orbiting the Earth. Along with them, varying size of space debris are also lingering around the Earth. A recent study has found data indicating that the risk of debris colliding with healthy satellites is significant even if we stop future launches. Most of the Dead Satellites deviate from their Original path of motion due to mis functioning and pose a big threat in space. In the coming years any new launch can result into cascading collisions with exponential increase in space debris. In an effort to pervert such buildup of collisions, this paper suggests methods to remove nonfunctional satellites from orbits by two major methods. In both the methods we will be sending a satellite which will help achieve the operation. The first method focuses on utilising the working parts of the satellite which can be accomplished by using a Radioisotope thermoelectric generator powered satellite having a mechanical arm which will tether with the Nonfunctional Satellite and store it in PICA or AVCOT made compartment. The compartment will shield the satellite during reentry. The second method focuses on getting rid of the satellite by either launching it into deep space or by destroying it during reentry. This is achieved either by gravitational catapulting or by manual catapulting. Apart from suggesting methods we had also analysed the risks of orbital collision and analyse the operational hazard faced by satellites.

1 Introduction

As of 2009, NASA estimated that there are about 19,000 particles that are bigger than 10 cm and approximately about 10 million objects that are smaller than 1 cm. Debris is classified into two categories, large debris (of size greater than 10 cm) and Small debris (of size less than 1 cm). Objects that lie between 1 cm and 10 cm are also considered as large object but we cannot track these objects. So they are ignored. Fig. 1 shows an representation of the current scenario in space.

Whenever a satellite, space mission or a manned mission is launched, they tend to leave behind debris of varying sizes in various orbits. Collision between any two objects can be disastrous and can produce shrapnel from the impact. Each piece of shrapnel has the potential to collide with other objects and can cause further damage. Thus causing a cascade of collisions. When this happens, it can render a whole orbit unusable.

Our paper basically focuses on removing the dead satellites, rocket boosters and equipment lost during space missions. By removing these objects we can reduce the number of collisions and the amount of debris formed. Our selection criterion is based on the size of the object. We will mostly be focusing on larger objects which are a lot easier to tether when compared to smaller ones.

Table 1: Objects present in space (Functioning and Non-functioning) as of 01 August 2013[1]

Object Type	In Orbit	Decayed
Payload	3752	3493
Rocket Body	1969	3658
Debris	11079	15280
Total	16800	22421

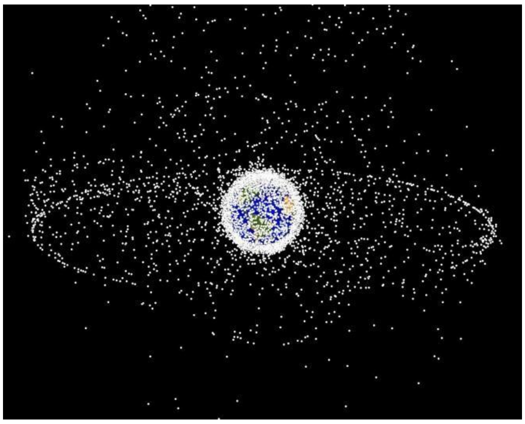

Fig 1. Artist's rendering of the current scenario in space.

In order to perform the above mentioned manoeuvres, we would like to state a few formulae that would be applicable.

Escape Velocity:

$$v_e = \sqrt{\frac{2GM}{r}}, \qquad (1)$$

V_e- Escape Velocity
M- Mass of both the satellite
r- Altitude of the satellite

Gravitational Sling:

The velocity obtained during the gravitational slinging on Earth is derived from simple equations of motion:

$$\acute{v} = \sqrt{4u^2 + v + 4uv\cos\emptyset} \qquad (2)$$

Where,
v'= Final Velocity gained by satellite
u= Velocity of Satellite
v=Velocity of Planet
φ=Angle of Attack

2 Risk Assessment

The unprecedented growth of debris population in the LEO regime and even in higher orbits has resulted in an increased emphasis on Risk Assessment during design, mission and non-operative phase. The Objective of Risk Assessment for non-functional satellite is to Predict, Protect and Reduce the orbital exposure to the functioning satellite.

The Risk at satellite level is characterized by:

1. Probability of collision
2. Probability of Penetration
3. Probability of Failure

The first two methods can be assessed using traditional tools such as BUMPER-II and ESABASE2. The third method can be assessed by a complicated and recently developed tool-

PIRAT(Particle Impact Risk and Vulnerability Assessment Tool).

The Objects in space are similar to that of gas molecules considered in Kinetic theory of gases where the molecules are randomly distributed and can collide with each other. The Probability of collision is given by:

$$C = 1\text{-}e^{(S \times V \times C \times T)} \qquad (2)$$

C- Collision Risk
S- Spatial Density, #/Km^3
V- Relative Collision Velocity, Km/s
A- Cross-Section of Satellite at Collision Risk, Km^2
T- Time at risk, s

3 Disposal Methods

In the following methods of disposal of satellites, a single satellite would be sent to space which is capable of performing all the manoeuvres required. The satellite will have a cylindrical cargo bay which is large enough to hold satellites and its solar panels. The bay has doors that can be opened and closed using a mechanical linkage.

The satellite will also have a robotic arm along with a tether. The Momentum exchange tether will be used in all the methods.

The momentum exchange tether is a rotation tether that can grab any spacecraft and then release it at a later time. This tether is usually used in orbital manoeuvring. The tether would have a hinge in the middle which will make it flexible. The tether will be stored in the satellite when not in use.

The satellite is assumed to be power with Radioisotope thermoelectric generator. This will facilitate all the functions of the satellite including propulsion.

3.1 Method 1: Retaining the Satellite:

In this method we would focus on bringing the satellite back to Earth. The satellite launched will fly parallel to the Non-functional satellite. Once it attains the necessary velocity, the tether will extend out of the satellite and tether with the debris. The robotic arm will extend and will grab the solar panel. It would then dismantle the panel and store it in bay.

The solar panels need to be removed so the size of the satellite can be reduces and also the panels can be reused later.

Once the panels are removed, the tether would slowly contract bringing the
The satellite is launched and will attain a velocity so that it orbits in synchronism with the Non-functional satellite. The orbit can be higher or lower. Once synchronism is attained, the arm will extend and grab the satellite into its cargo bay.

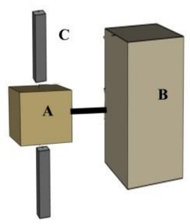

Fig. 2 Tethering of two satellites. A. The non-functional Satellite B. Satellite sent from earth.

Once it's secured, the satellite along with the non-functional satellite will make a re-entry and land in the designated area from where it can be picked up.

The major advantage of this method is that we can reuse the parts from the satellite. Components, solar panels, fuel can be used. Some satellites will have nuclear fuels. We can use this method to safely bring it back to Earth.

3.2 Method 2: Destroying the Satellite:

The second method mainly focuses on destroying the satellite. This is achieved in three ways.

3.2.1 Destroy through re-entry

The first method focuses on the destroying the satellite through reentry. The reentry process can be used to get rid of small satellites. Small satellites are chosen because they can be burnt during re-entry.

Satellite that is sent from Earth will “throw” the satellite into Earth’s atmosphere. To do this, the satellite will have to fly at the same velocity as the non-functional satellite at an orbit above or below it. Once it attains such a position, it will tether with the non-functional satellite. Using its propulsion unit, the satellite along with its tether will rotate along its axis. Once enough momentum is achieved, the tether will release the non-functional satellite. This will launch the non-functional satellite back to Earth, where it will burn during re-entry.

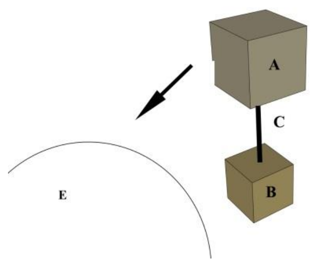

Fig. 3: A. Satellite sent from earth B. The non-functional Satellite. E. Earth The arrow shows the direction in which the non-functional satellite will be thrown.

3.2.2 Launch it into deep space:

The second method to destroy satellites is by catapulting them into deep space. This method is very similar to the first methods mentioned. After tethering, the satellite will rotate along with the non-functional satellite. Once the centrifugal velocity is greater than the escape velocity, the tether would release it in such a way, it would be launched into deep space.

3.2.3 Gravitational Sling:

The third method to destroy the satellite is based on the principle of gravitational sling. Gravitational sling is usually used in deep space missions where a satellite uses the gravitational field of a planet to either gain velocity of change momentum. We can obtain the velocity of the satellite from Eq. 2. If this velocity is greater than the escape velocity, Eq. 1 the satellite will escape from the gravitational field.

This is a similar approach here, but it will not be using the exact principle of gravitational sling. The engine will fire at regular intervals and hence would slowly move out of earth’s gravitational field and into deep space.

Seen in India’s first moon mission, Chandrayaan, where a similar maneuver was employed to go into lunar orbit (Seen in fig. 4).

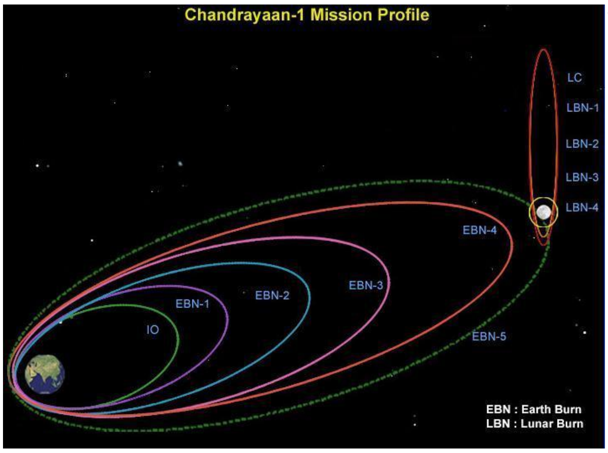

Fig. 4 The varying orbits of Chandrayaan-1due to gravitational sling.

4 Conclusion and Directions For Future Work:

The countless amount of space debris has emerged as a serious threat to future of space programs.Various modernistic methods have been discussed in this paper for disposal and removal of non functioning satellite or space debris from outer space to pave way for future launches without any risk of cascading collisions. In the present work it was observed that these tasks can be performed by sending a rendezvous satellite which can store the non-functioning satellite or debris and dispose it or destroy. These methods has advantages it does not need to consider the shape and size of the debris or non-functioning satellite as a robotic arm with mechanism is involved in tethering. Future work includes the analysis of tethering considering angular rate of debris and the rendezvous satellite. Also a feasibility study could be performed on which method be suitable for particular situation considering by prioritising the disposal based on the risk of collision or to minimize the distance travelled by the satellite. The rendezvous satellite can also be sent to International Space Station(ISS) which can be included in future work.

References

[1] Space Surveillance Data Available From Joint Space Operations Center, 01 August 2013, <http://www.space-track.org>.

[2] McKnight D.S., and Di Pentino F.R., "New insights on the orbital debris collision hazard at GEO", Acta Astronautica, Vol No. 85, 2013, pp. 73–82

[3] Kessler D.J. and Cour-Palais B.G., "Collision Frequency of Artificial Satellites: The Creation of a Debris Belt", Journal of Geophysical Research, Vol.83 A6, 1978, pp. 2637-2646.

[4] Welty N., Rudolph M., Schafer F., Apeldoorn J. and R. Janovsky"Computational methodology to predict satellite system-level effects from impacts of untrackable space debris", Acta Astronautica, Vol. 83, 2013, Pages 35–43.

[5] Krag H., Flegel S., Gelhaus J., Moeckel M., Wiedermann C. and Kempf D., "Final report—Maintenance of the ESA MASTER Model", European Space Agency, 2011.

[6] Agapov V., Molotov I., Khutorovsky Z. and Titenko V., "Analysis of the Results of the 3 Years Observations of the GEO Belt and the HEO Objects" ISON Network, IAC-08-A 6.1.02, 2008.

[7] N.L. Johnson, "Orbital Debris: The Growing Threat to Space Operations", AAS 10-011, February 2010.

[8] Putzar R., Schäfer F. and Lambert M., "Vulnerability of spacecraft harnesses to hypervelocity impacts," International Journal of Impact Engineering, Vol. 35, no. 12, pp. 1728-1734, 2008.

[9] Ziniu W., Ruifeng H., Xi Q., Xiang W. and Zhe W., "Space Debris Re entry Analysis Methods and Tools", Chinese Journal of Aeronautics, Vol. 24, 2011, 387-395.

[10] Klinkrad H., "Space debris: models and risk analysis", Chichester: Praxis Publishing Ltd, 2006, pp. 241-287.

[11] Ailor W., Bonaparte L. and Shelton A.F., "A strategy for reducing hazards from reentry debris" AIAA, 2006.

[12] Baker R.L., Weaver M.A. and Moody D.M., "Orbital spacecraft reentry breakup", 50th

International Astronautical Congress, IAA-99-IAA.6.7.04, 1999.

[13] Reyhanoglu M. and Alvarado J., "Estimation of debris dispersion due to a space vehicle breakup during reentry", Acta Astronautica, Vol. 86, May–June 2013, pp. 211-218

[14] Shoemaker M.A., van der Ha J.C., Fujita K., "Trajectory reconstruction of Hayabusa's atmospheric reentry", Acta Astronautica, Vol. 71, February–March 2012, pp. 151-162.

[15] Levin E., Pearson J. and Carroll J., "Wholesale debris removal from LEO", Acta Astronautica, Vol. 73, April–May 2012, pp. 100-108.

[16] Moskwa P. and Alby F., "Overview on space debris activities in France", Advances in Space Research, Volume 23, Issue 1, 1999, Pages 261-270.

[17] Adimurthy V. and Ganeshan A.S., "Space debris mitigation measures in India", Acta Astronautica, Vol. 58, Issue 3, February 2006, pp. 168-174.

[18] Flury W. and McKnight D., "Space debris: An international policy issue", Advances in Space Research, Vol. 13, Issue 8, August 1993, pp. 299-309

[19] Christiansen E.L., Hyde J.L. and Bernhard R.P., "Space Shuttle debris and meteoroid impacts", Advances in Space Research, Volume 34, Issue 5, 2004, Pages 1097-1103.

[20] Reynolds R.C., Loftus J.P. and Kessler D.J., "Issues arising from the NASA safety standard to control orbital debris", Advances in Space Research, Volume 19, Issue 2, 1997, Pages 381-389.

[21] Anilkumar A.K., Ananthasayanam M.R. and Subba Rao P.V., "A constant gain Kalman filter approach for the prediction of re-entry of risk objects", Acta Astronautica, Volume 61, Issue 10, November 2007, Pages 831-839

[22] Hu R.F., Wu Z.N. and Qu X., "Debris reentry and ablation prediction and ground risk assessment system", Acta Aeronautica et Astronautica Sinica, Vol.32, Issue 3, 2011,390-399.

[23] Tewari A., "Entry trajectory model with thermomechanical breakup", Journal of Spacecraft and Rockets, Vol. 46, Issue 2, 2009, 299-306.

[24] Bonnal Ch. and Naumann W., "Debris mitigation: Technical challenges of the ariane 5 passivation" Advances in Space Research, Vol. 23, Issue 1, 1999, pp. 249-252.

[25] Ganeshan A.S., Rathnakara S.C., Gopinath N.S. and Padmanabhan P., "Collision probability of spacecraft with man-made debris", IAA, 88-552 (1988), pp. 143–154.

[26] D.J. Kessler, "Orbital debris issues", Advances in Space Research, Vol. 5, Issue 2, 1985, pp. 3-10

Life Cycle Assessment – Solid Rocket Motor Case CEAS 2013

M. Saint-Amand, L. Dariol
EADS Astrium ST, France

J.Ouziel,
EADS Astrium ST, France

Keywords*: Life Cycle Assessment, Clean Space, Ariane 6, Solid Rocket Motor Case*

Abstract

Environmental impacts, including global warming, are now a major political and economic issue.

Life Cycle Assessment (LCA) is a driver for decision making which allows quantifying products' environmental impact from raw materials phase until end of life.
This methodology is based on the analysis of every aspect and phase of a product or program through its overall life cycle, from design or acquisition to disposal or recycling.

LCA is a structured and standardized method and management tool through ISO 14040 & ISO 14044.

Efficient resources and technologies contribute also to reduce costs by decreasing material inputs, energy consumption and waste.
This approach meets two of the major objectives of all futures Space Programme: costs control and environmental impacts.
Solid Rocket Motor Case study was made through an internationally recognised tool named SimaPro.

Results enable to specify the significant impacts and life cycle phases with a major contribution on the environment.
For the Ariane 6 Solid Rocket Motor Case, raw materials seem to have the biggest impact on abiotic depletion and global warming potential while production phase shows significant impact on aquatic and terrestrial eco-toxicity.

Furthermore the results interpretation allows carrying out improvement on materials and processes with proposal of sustainable solutions.

The oral presentation would depict the methodology implemented within Astrium-ST for the environmental impact assessment and the Ariane 6 Solid Rocket Motor Case study.

1 General Introduction

The application of Eco-Design can benefit business, users and society at the same time because it meets the common interest of obtaining more efficient products in an economic as well as an environmental dimension.

There is a consensus that the most suitable approach to evaluate environmental impact of products and services is the Life Cycle Thinking (LCT) and the Life Cycle Assessment (LCA).

Life Cycle Thinking and Life Cycle Assessment are scientific approaches behind a growing number of modern environmental policies and business decisions.

There are many advantages of carrying out LCA:

- Improve product design as eco-design tool,
- Provision of environmental information,
- Marketing,
- Financial benefits,
- LCA links to Environmental Management System (ISO 14001).

This paper will describe the simplified Life Cycle Assessment ran in 2012 on Solid Rocket Motor Case at Astrium Space Transportation.

This study takes place at preliminary stage; which allows identifying at early stage life-cycle phases, materials and processes which will have the biggest environmental impact.

The product, considered for this study is a large scale Solid Rocket Motor Case demonstrator which is dedicated to materials and technologies maturation dedicated to the future Ariane 6 launcher. The first flight of this launcher is planned in 2021 with 20 years Program duration at least, and its main driver is the Life Cycle Cost. Thus, environmental impact has to be a driver of these materials and technologies choices in eco-conception process to ensure competitiveness robustness regarding existing and future environmental policy and associated cost impact limitation.

2 Life Cycle Assessment

Life Cycle Assessment is a driver for decision making.
The most important applications are:

• Analysis of the contribution of life cycle stages to the overall environmental load, usually with the aim to prioritise improvements on products or processes,

• Comparison between products for internal communications.

LCA findings are multi-criteria (e.g. global warming potential, ozone layer depletion, human toxicity, metal depletion, etc.) and provide environmental impacts quantification at different levels, (system, subsystem, equipment, process, etc.) and at different life cycle phases. This approach is called "cradle to grave" or even "cradle to cradle".

Assessment of environmental impacts is made through commercial software including calculation methods, environmental indicators and standard data.
Astrium ST is using SimaPro, the worlds most widely used LCA software.

LCA is a structured and standardized method and management tool through ISO 14040 & ISO 14044.
International Standard Organization 14040 states the framework, the principles and the general requirements for an LCA.
ISO 14044 specify the different steps leading to an LCA.

The four main steps are:

- Definition of goal and scope of the study,
- Inventory of inputs and outputs,
- Environmental Impact assessment,
- Interpretation and use of results.

3 Simplified LCA on Solid Rocket Motor Case (SRMC)

As the whole SRMC lifecycle has not been fully taking into account for this study, the approach behind this study is called "Simplified Life Cycle Assessment" (SLCA).
Simplified LCA follows the main requirements from the ISO 14040 and ISO 14044.

The purpose of this analysis run in 2012 was to identify the main environmental impact of the SRMC at an early stage.

Simplified LCA run on the SRMC enables to:

- identify improvements areas on the product at different life cycle phases,

- choose relevant environmental performances indicators,

- determine the significant environmental indicators of the product and reveal the main components that could be impacted by future obsolescence (caused by REACH regulation, RoHs,…)

In the following paragraph, each stage of the SRMC assessment is presented. Further explanation and detailed descriptions will be related during the presentation.

3.1 Perimeter & Scope

3.1.1 Functional unit

The Simplified LCA which was run on the SRMC involve in quantifying environmental impacts of each life cycle phase: raw materials extraction, raw materials transports, production of the motor case, transport of the motor case to the solid rocket motor factory, launch, , end of life…

In order to facilitate the results interpretation and assure the repeatability of LCA comparison on this same type of products (solid motor case), it is mandatory to introduce a reference called "functional unit" (ISO 14041 requirements).

For the SRMC the functional unit is:

"Enable the propulsion of the SRMC of the future Ariane 6 from Kourou"

This reference value unit will allow bringing back the environmental impacts to a one and single use taking into account the life length.

3.1.2 Perimeter

In a second approach, it is essential to accurately establish the perimeter of the study.

The purpose of this step is to identify the main life-cycle phases which will be included in the scope of the SRMC study.

For this assessment two different perimeters were established. The first perimeter was analyzed in priority because there are included in the Astrium scope of action.

Indeed, when deciding the perimeter it is important to keep in mind that the life cycle phases which are included within the perimeter should be the life cycle phases in which the manufacturer could bring some improvements.

The scope of this study is showed on the graph below :

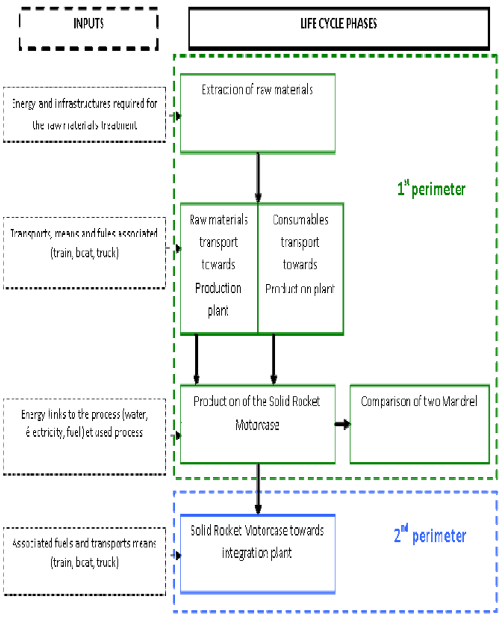

Fig. 2 Perimeter of the SRMC assessment,

The second perimeter involves integrating the environmental impact of the conveyance of the rocket to the launch pad. This study should be performed when the industrials scenarii are established.

4 Life Cycle Inventory

This SLCA has been set-up at early stage of the SRMC definition. This is why a specific range of motor case has been selected in order to run the analysis.

In order to facilitate the collect for each life cycle phase, the SRMC has been divided in 8 distinct sub-assemblies:

1 – Metal (***yellow***)
2 – Thermal protection (***grey***)
3 – Composite A (***dark blue***)
4 – Composite B (***red***)
5 – Composite C (***orange***)
6 – Assembly A (***pink***)
7 – Assembly B (***green***)
8 – Assembly C (***light blue***)

The data collection is a determinant phase during LCA. This tedious phase must be conducted with minutia in order to be as exhaustive as possible. It is mandatory to obtain a large amount of information and to define the most accurate hypotheses.

It is necessary to set some hypotheses regarding the data inventory, such as, eliminate materials and consumables which are estimated as insignificant (materials and processes which represent less than 0.1 % weight by weight)

In order to build the model in the software, it is useful to rely on different databases. All the software databases list a wide range of environmental properties (more than 13 000 data).

For the SRMC study, 23 materials records, 20 consumables records, 2 transports records and 25 process records were directly created within the software thanks to preexisting data.

It is important to notice that for the data collection within the commercial database, it is needed to make assumptions. Because of SRMC specificities and high level of technology, every materials and processes are not available in the commercial database.
Therefore the results of this Simplified LCA are marred by uncertainties due to a large number of hypotheses and assumptions made on specific process, materials and consumables during the model phase in the software.

Some uncertainties studies were conducted downstream in order to check and validate these hypotheses.

In the future, it would be interesting to work on a specific database for space sector, as it is proposed in the Clean Space program in order to avoid this kind of uncertainties.

5 Environmental Impact Indicators

A choice has been made regarding environmental impacts indicators linked to the data of the SRMC lifecycle.

This indicators choice should take into account the actual environmental trends and environmental aspects having some interactions with the SRMC.

- Abiotic depletion :

This environmental impact indicator treats about the natural energetic resources ‘depletion (fuel, hard coal, crude oil, natural gas …)

With each raw material is associated an ADP coefficient (Abiotic Depletion Potential) which is linked to the renewable or depleted criteria.
The reference unit for this indicator is the Kg equivalent Sb.

- Acidification :

Acidification refers literally to processes that increase the acidity of water and soil systems by hydrogen ion concentration.
Therefore this indicator takes into account gas emission (SO2, NOx, NH3…)

The reference unit for this indicator is Kg equivalent SO2.

- Global Warming Potential :

Global-warming potential (GWP) is a relative measure of how much heat a greenhouse gas traps in the atmosphere. A GWP is calculated over a specific time interval, commonly 20, 100 or 500 years.
A wide range of components participate to the global warming such as CO2, CO, CH4, COVs, SF6…
The reference unit for this indicator is Kg equivalent CO2.

- Ozone Layer Depletion :

The major contributors on these impacts are the chlorofluorocarbons (CFC or HCFC) or bromine atoms in halons. They are able to reach the stratosphere when degrading ozone around the globe. The reference unit for this indicator is Kg equivalent CFC-11.

- Human Toxicity, Fresh Water Aquatic Ecotoxicity, Terrestrial Ecotoxicity :

These three environmental impacts cover the effects of hazardous substances on human health, terrestrials and aquatic medium. These substances could be present within a natural habitat or at plant.

The wide diversity of molecules and improvements areas, caused damages, which are depending of the "cocktail" effect, brings such a complexity that this category is one of the most difficult to be modeled within the Software. Therefore the results should be considered with precautions.

6 Results

6.1 Characterized results

Characterized results are results which are presented as bar chart. Each bar is equivalent to an environmental impact indicator. Each environmental impact is expressed on a 100 % basis.

The purpose of this type of results is not to compare the environmental indicators between each other but to identify which are the most contributors for one impact (life cycle phase or one specific raw material or one specific processes…).

This type of results is mandatory by the standard ISO 14040/14044.

Below is represented the characterised results for the perimeter 1 of the SRMC life cycle:

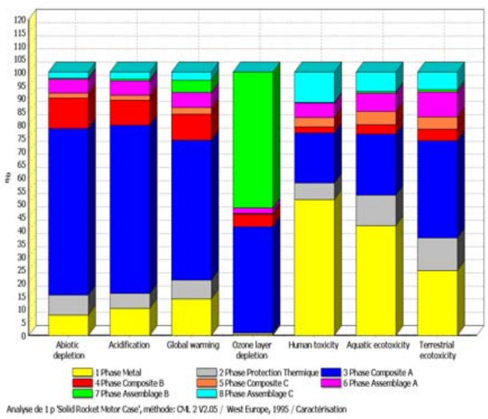

Fig 3: Characterized results of SRMC per sub-assemblies

Composite phases (A, B, C) have a major impact on the abiotic depletion, acidification and global warming.
Contrary to metal phase and assembly C which have a major impact on toxicities indicators.

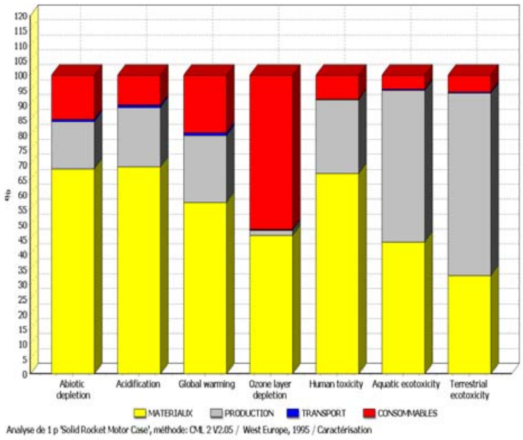

Fig.4: Characterized results of SRMC per life-cycle phase

Raw materials seem to have the biggest impact on abiotic depletion and global warming potential while production phase shows significant impact on aquatic and terrestrial eco-toxicity.
Interpretation and detailed explanation will be depicted during the presentation.

6.2 Normalized results

Normalized findings are presented as a “score” for each environmental impact indicator to an inhabitant’s equivalent. This approach is possible when the results of the SRMC are divided by the global emissions of certain population.

See below the emissions listed for the West Europe on one year (for each environmental impact indicator per reference unit).

Impact indicator	Unit	West Europe, 1995	Kg eq by West Europe Population per Year
Abiotic Depletion	kg Sb eq	6,74E-11	14 836 795 252
Acidification	kg SO2 eq	3,66E-11	27 322 404 372
Global Warming	kg CO2 eq	2,08E-13	4 807 692 307 692
Ozone Layer Depletion	kg CFC-11 eq	1,20E-08	83 333 333
Human Toxicity	kg 1,4-DB eq	1,32E-13	7 575 757 575 758
Fresh Water Aquatic Ecotoxicity	kg 1,4-DB eq	1,98E-12	505 050 505 051
Terrestrial Ecotoxicity	kg 1,4-DB eq	2,21E-11	45 248 868 778

Fig.5: Emissions listed for West Europe on 1995 (SimaPro)

Once the normalisation has been run with the results of the SRMC life cycle assessment and the tables above we obtain:

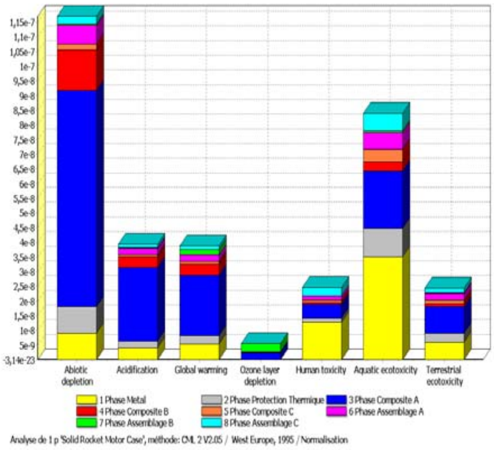

Fig.6: Normalized results of SRMC per sub-assemblies

The major environmental impacts of SRMC are abiotic depletion and aquatic eco-toxicity compared to the west Europe emission.

Interpretation and detailed explanation will be depicted during the presentation.

Others results and uncertainties analysis will be presented as well.

Conclusion

Simplified assessment of the SRMC enables to highlight the major environmental impact and the main contributors.

This approach came from the will of Astrium ST to limit and reduce the global environmental impact of its own activity.

A main Astrium’s objective is to improve our LCA skills regarding methodology and tools in order o to propose full LCA in the coming years.

This study reveals the complexity of the LCA methodology for product like SRMC.

Space sector has to be at the forefront on this topic in order to be able to turn today's constraints into tomorrow's opportunities.

Astrium thanks the CNES for its financial participation within the framework of the « Projet d'Investissements d'Avenir » (PIA).

Being a pioneer in adopting eco-friendly approach, the European industry takes the opportunity to foster innovation and develop new technologies.

References

[1] ILCD Handbook "Analysis of existing Environmental Impact Assessment methodologies for use in Life Cycle Assessment", European Union, 2010.

De-orbit motor for nanosatellites based on solid propulsion

Willianne Welland
Aerospace Propulsion Products BV, Westelijke Randweg 25, 4791 RT Klundert, The Netherlands
w.welland@appbv.nl, +3l (0)168 388 182

Daniel Faber and Arthur Overlack
Innovative Solutions In Space BV, Molengraaffsingel 12-14, 2629 JD Delft, The Netherlands
d.faber@isispace.nl, +31 (0)15 256 9018

Laurens van Vliet, Wolter Wieling and Flavia Tata Nardini
Netherlands Organisation for Applied Scientific Research (TNO), Lange Kleiweg 137, 2288 GJ Rijswijk, The Netherlands, laurens.vanvliet@tno.nl, +31 (0)88 866 1236

Keywords: Space debris mitigation, de-orbit motor, solid propulsion

Abstract

Analyses performed by ESA and NASA indicate that the only means of sustaining the orbital environment at a safe level for space operations will be by carrying out both active debris removal and end-of-life de-orbiting or re-orbiting of future space assets.

Existing and expected debris mitigation regulations require LEO spacecraft to de-orbit within 25 years. Given typical spacecraft ballistic coefficients, this places an upper limit of perigee of around 600 km altitude for nanosatellites such as CubeSats. Also with operational nanosatellite constellations being deployed in the coming years there is an increased need to remove small spacecraft from LEO much faster to ensure that defunct satellites can be replaced within the constellation with new satellites.

Practical deployable drag systems being developed as products can lower the ballistic coefficient sufficiently to allow perigee up to 800 km altitude, however this still rules out many launches above that altitude for CubeSats and MicroSats that ride as secondary payloads. There is also the problem that a drag system does not reduce the total intersected time-area product, thus debris impact probability is not reduced even if the lifetime requirement is met.

This paper provides an overview of a recently developed de-orbit system using a CubeSat sized solid rocket motor, that was successfully demonstrated in February 2013 by test firings at ambient and -40 °C.

The system has sufficient propulsive capability to lower the perigee of a 3U CubeSat from a 1000 km altitude circular orbit to an elliptical orbit that complies with the 25 year maximum orbit lifetime. Test results are presented for the de-orbit system, generating around 180 N thrust and 600 Ns total impulse at atmospheric pressure. Furthermore the challenges and solutions of implementing such a system inside a nanosatellite mission (both technical, programmatic and legal) will be addressed.

All thrusters have an off-axis thrust component that causes the spacecraft attitude to be unstable when thrust is applied. Analysis will be

presented showing that sufficient gyroscopic stiffness can be achieved at reasonable spin rates to maintain stability of a 3U CubeSat in a long-axis spin. Attitude control algorithms were tested in simulation to demonstrate that the spin rate and pointing accuracy can be achieved using only traditional CubeSat magnetic sensors and actuators.

With the successful execution of the demonstrator tests the de-orbit motor has reached TRL 4. Further development of the de-orbit module towards in-flight demonstration *would comply with ESA's Clean Space* Initiative.

1 Background

In response to concerns about orbital debris, international guidelines have been created recommending that satellites be removed from orbit within 25 years of launch [1], which have been adopted as law in a number of countries [2]. For example recently updated regulations such as ESA's "Requirements on Space Debris Mitigation for Agency Projects" and France's "Space Operations Act" impose regulations on environmental impact of space activities. This presents a challenge for the CubeSat community, which has been enabled by the availability of cost-effective and opportunistic launches as secondary payloads. As most nanosatellites are only removed from orbit by the effect of drag, which reduces rapidly with altitude, the regulations effectively prohibit the use of certain classes of orbits. Unless mitigation methods can be found to comply with the orbit lifetime requirements, there will be fewer CubeSat launches available and costs will rise.

The risk of impacts between spacecraft and debris in a crowded constellation orbit has the potential to significantly undermine the reliability and thus the feasibility of the constellation. This is especially true if the planned spacecraft density is high due to the use of large numbers of relatively cheap nanosatellites. Removing old or defunct satellites from a constellation allows replacement and renewal of the constellation without escalating the impact risk due to crowding.

1.1 Expected CubeSat orbit decay

Achieving de-orbit by passive means requires launching to an altitude from which the satellite orbit will decay and re-enter in a timely manner. The de-orbit time is thus dependent on the spacecraft ballistic coefficient and the state of the Earth's atmosphere. CubeSats have a mass of 1 to 1.5 kg per 1-Unit volume, and a typical drag coefficient [3] of 2.0 results in approximate ballistic coefficients for a 1-unit CubeSat of between 50 and 75 kg/m^2 and for a 3-unit CubeSat of between 50 and 225 kg/m^2. Applying standard methods for calculating orbital lifetime [4], for this range of ballistic coefficients the 25 year orbital lifetime is not met for orbits with perigee above about 600 km altitude.

1.2 De-orbit by increase of cross-sectional area

Passive solutions to reduce the orbit lifetime include deployable sails, balloons and tethers that increase the cross-sectional area and hence reduce the ballistic coefficient. In order to meet the 25 year lifetime requirement at 1000 km altitude, a ballistic coefficient of around 0.5 kg/m^2 is required.

The effective area of a sail is half the total area, as the satellite is not expected to hold the large sail oriented in the velocity direction. A 3-unit Cubesat weighing 3.9 kg thus requires an area of 15.6 m^2 in order to achieve timely de-orbit from 1000 km. Proposed commercial drag sails for nanosatellites that are suitable for up to 6-unit CubeSats currently only provide a drag area between 0.5 and 4.0 m^2 [5,6,7].

Larger sails are under development for CubeSat flights, up to 25 m^2 in area [8]. These are flown as primary payloads on technology demonstration missions and take up a volume of two CubeSat units (10 x 10 x 20 cm^3), therefore they are less suitable for most nanosatellites smaller than a 6-unit CubeSat.

1.3 Drag sails impact probability

The expected number of collisions over the spacecraft's lifetime (P_i) is defined as the number of particles encountered by the spacecraft within the volume swept by the object over its lifetime. Therefore the expected number of collisions is equal to the volume swept by the object over its lifetime (V), multiplied by the particle density of debris (p_d), see Eq. 1.

$$P_i = V.p_d \tag{1}$$

If we assume the orbital velocity (v) to be constant, then the volume (V) can be expressed as in Eq. 2.

$$V = v.At \tag{2}$$

Where A = cross sectional area; and t = orbital lifetime. The orbital lifetime (t) is inversely proportional to deceleration of the spacecraft due to drag (a_d), see Eq. 3.

$$t = \frac{K}{a_d} = \frac{K}{\frac{1}{m}\left(\frac{1}{2}\rho v^2 C_d A\right)} \tag{3}$$

Where K = a constant that depends on initial orbital parameters; m = mass of the spacecraft; ρ = gas density; and C_d = drag coefficient. Combining Eq. 1, 2 and 3 gives an expression for the expected number of collisions over the spacecraft's lifetime, see Eq. 4.

$$P_i = \frac{2mKp_d}{\rho v C_d} \tag{4}$$

The derivation of these equations assumes C_d, m, ρ, and p_d to be constant for the purpose of comparison, which is considered a reasonable approximation for comparison of a CubeSat with and without a drag sail. This shows that the impact probability is not reduced by increasing the cross sectional area through use of a drag sail, and thus brings into question the validity of the 25 year lifetime requirement and the use of drag sails to reduce impact hazards.

1.4 De-orbit by chemical propulsion

In addition to lowering the impact probability due to lower lifetime swept volume, a chemical propulsion de-orbit system has the advantage of immediate confirmation of removal of spacecraft and/or debris from orbit or into an orbit that will quickly decay. It also provides the operational flexibility to lower the orbital altitude at either the beginning or the end of the mission.

In order to achieve the 25 year de-orbit requirement, a nanosatellite in a 1000 km circular orbit must have its perigee lowered to 400 km, requiring a delta-V of around 155 m/s. For a 3.9 kg CubeSat, this requires around 600 N.s total impulse to be exerted along the anti-velocity vector. Ideally such a system would be fit within the volume and mass envelope of one CubeSat unit (volume 10 x 10 x 10 cm^3 and mass 1300 grams).

2 System design

The Nanosatellite Kick Stage (NKS) is a suitably sized solid rocket motor developed by ISIS, APP and TNO. Adopted from technology applied for European launch vehicle igniters, the NKS uses an Ammonium Perchlorate /Fuel/ Hydroxy Terminated PolyButadiene based propellant leading to a specific impulse of around 240 seconds. Several performance characteristics were identified as desirable for a nanosatellite thruster: maximum acceleration of 11 g; low heat transfer to the satellite structure; operation over a temperature range of -40 to +85 degrees Celsius; and low mass.

A small and safe igniter has been developed that does not need a safe and arm device. To prevent an undesired ignition, i.e. caused by EMC or by switching on the electronics, a significant power input is required to the igniter. Normally 0.1 J is sufficient to ignite a standard igniter (like for the ESA standard initiator and the NASA standard initiator). In this design around 50 J is needed, which gives a significant safety margin and is no problem to be supplied by a small battery.

The NKS is mounted to a CubeSat by a single bracket at the top of the motor. Finite element analysis was used to verify the bracket can survive launch vehicle loads for a range of launchers and loading from the thruster itself. The single bracket allows easy assembly and disassembly after the rest of the satellite has been assembled. It also serves to minimize (conductive) heat transfer to the nanosatellite structure from the hotter regions of the motor such as around the rocket nozzle and lower portion of the combustion chamber.

Figure 1 shows the NKS in a CubeSat structure. The mounting bracket is shown side-on across the top of the motor and connects to the CubeSat rails. Above that bracket (grey) are the igniter (brown) and control electronics (light green), and below the bracket is the body of the NKS (green). The lower rib between the CubeSat rails does not make contact with the thruster.

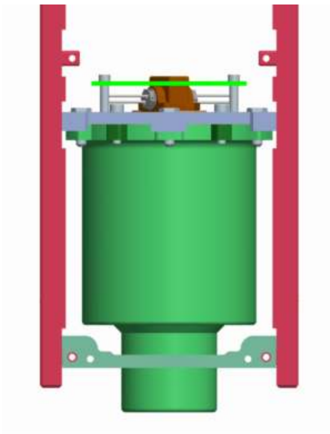

Fig. 1 CAD model of the Nanosatellite Kick Stage shown mounted in a CubeSat structure

3 Attitude control

All thrusters have an off-axis thrust component that causes the spacecraft attitude to be unstable when thrust is applied. Spin stabilization was investigated for a 3-unit CubeSat thrusting along the long-axis in the presence of significant thrust misalignment. The total on-axis impulse fraction for a range of thruster misalignment angles and satellite spin rates was simulated, yielding results as shown in Fig. 2. For expected misalignment up to 0.2 radians, sufficient gyroscopic stiffness is achieved at a spin rate of 20 rad/sec for all operating temperatures.

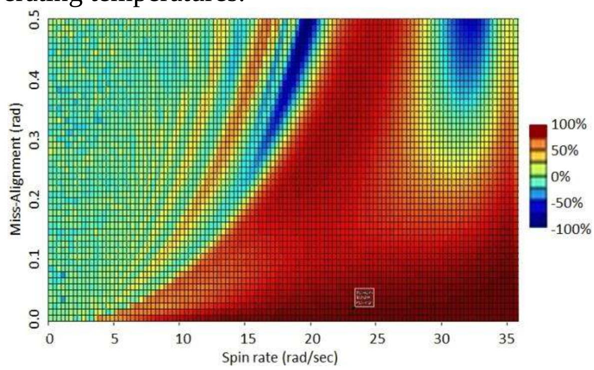

Fig. 2 On-axis thrust percentage at +85°C

To limit the impact on CubeSat requirements, it is desirable to point and spin up the 3-unit CubeSat used in this example by using standard off-the-shelf CubeSat magnetic sensors and actuators. Building on existing attitude control algorithms [9], a successful control strategy was implemented in two steps; first aligning the spacecraft and then slowly increasing the spin rate.

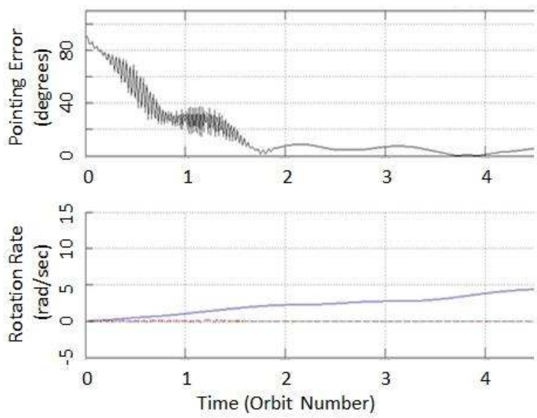

Fig. 3 Scenario 3

It can be seen in Fig. 3 that a pointing error of less than 5 degrees can be achieved. Only the first four orbits are plotted here in order to show details of the initial pointing maneuver.

4 Test results

4.1 Test Setup

Three firing tests were conducted of the NKS in an almost flight representative configuration, mounted in a vertical thrust stand as shown in Fig. 4. The thrust stand and test motor were instrumented with several sensors that will not be present on flight units.

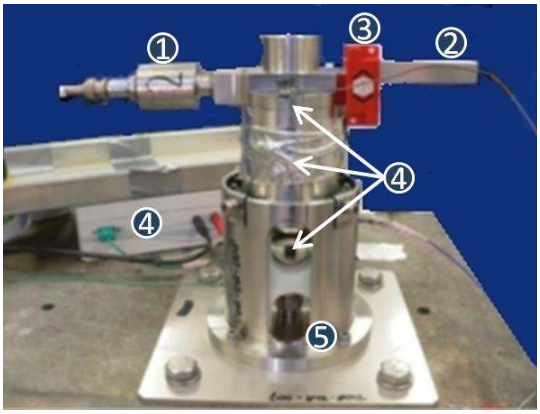

Fig. 4 NKS demonstrator on the thrust stand

A pressure sensor (1) measures chamber pressure inside the rocket motor. The pressure sensor causes the mass to be asymmetric on the thrust stand, so a counterweight (2) is installed on the opposite side of the motor from the pressure sensor to balance the system.

A shock sensor (3) was set to trigger at 10 g in the vertical direction.

Temperature sensors (4) were placed at 5 positions: next to the nozzle, two locations on the cylinder wall, on the base and in the electronics box.

A load cell (5) measured the downwards force produced by the motor. The influence of gravity and bias drift on the sensor readout was removed through calibration immediately before and after the firing.

Video recordings were also taken with three different cameras from different angles. A screen shot of one of the videos is shown in Fig. 5.

Fig. 5 NKS firing on thrust frame

4.2 Results

Three tests were performed, with the results shown in Table 1. The first two tests were performed on the same day, at ambient temperatures. Inside the preparation facility the temperature remained around 15 degrees all day.

Table 1 Test Results

Test #	Parameter	Value
1	Temperature	Ambient (15 °C)
	Total Impulse	608 N.s
	Max Thrust	199 N
	Burn Time	4.2 s
2	Temperature	Ambient (15 °C)
	Total Impulse	604 N.s
	Max Thrust	186 N
	Burn Time	4.2 s
3	Temperature	Cold (-40 °C)
	Total Impulse	607 N.s
	Max Thrust	178 N
	Burn Time	4.7 s

The third test was performed two weeks later, after conditioning the assembled motor at low temperature (-40 °C) for 21 hours. The time between removing the demonstrator from the conditioning cabinet and the actual firing was between 6 and 7 minutes and the thermal properties of the casing provide sufficient certainty that the propellant grain was still very close to the conditioning temperature at the time of firing.

The thrust profiles for each test are shown overlaid in Fig. 6, in blue, red and green for the first, second and third tests respectively. These have been aligned on the time axis.

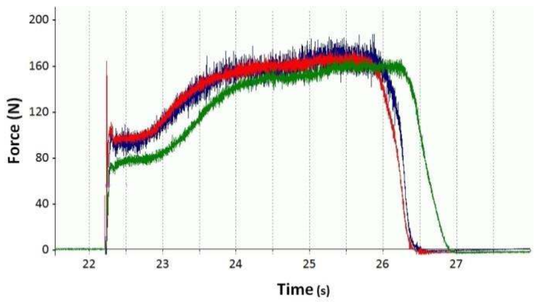

Fig. 6 Thrust profile for all three tests

Motor surface temperatures during and after the first demonstration test are shown in Fig. 7. The maximum temperature of 149 °C occurred next to the nozzle, approximately 120 seconds after ignition. The temperature of the control electronics is not shown on the table and had little change from the ambient temperature in the test area.

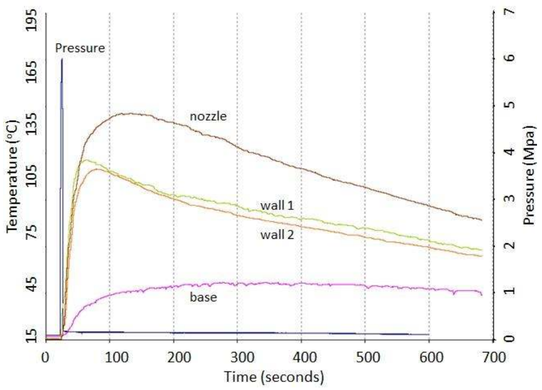

Fig. 7 Temperature at various points on the motor surface

Shock sensors did not trigger in any of the tests.

5 Discussion

5.1 Discussion of results

The test results showed remarkably consistent performance, with <1% variation in total impulse. The maximum acceleration for a 3-unit CubeSat of mass 3.9 kg would be 5.2 g, well below the limit of 11 g. Additionally, no shocks greater than 10g were present.

The (reproducible) pressure and thrust increase after ~0.5 s of burning is caused by partial nozzle obstruction due to the deposition of not fully combusted metal and metal oxide particles onto the nozzle.

The heat transfer to the satellite structure appears to be quite manageable as the vast majority of the heat released from burning the propellant leaves the system in the exhaust. Maximum temperatures at the base, where the bracket would mount the motor to the CubeSat structure, were below 50 °C in all tests. Radiative transfer from the wall or nozzle areas is expected not to raise the temperature of the CubeSat structure by more than a few tens of degrees, and multi-layer insulation can be added if this is considered problematic.

Successful operation has been demonstrated at temperatures of ambient (+15) and -40 °C. Additional tests are planned at the maximum operating temperature of +85 °C.

The mass of the flight system is expected to be 1.18 kg, slightly below the requirement.

5.2 Technical challenges

Formation of debris particles is a particular problem for solid rocket motor exhaust, especially when metal powder is used to increase the burn temperature and thus specific impulse. During combustion metal oxide is formed that can precipitate forming liquid or solid particles. The propellant formulation used in the firing tests was an available formulation and contained metal fuel. One goal for optimizing the concept design of the de-orbit module will be to reduce the risk of particles in the exhaust while maintaining sufficient specific impulse. The reduction or deletion of metal fuel will also reduce the observed metal deposition onto the nozzle and corresponding pressure increase in the motor.

Proving the reliability of a solid rocket motor requires a certain number of tests to arrive at a sufficient statistical confidence. This is particularly important for ignition and thrust performance in space conditions.

Safety must be considered paramount in all solid rocket motor development and operation as the potential for damage to equipment and personnel is significant for any unproven design. The associated procedures and equipment have both financial and schedule costs. Developing a solid rocket motor is not to be taken lightly, however once the safety and reliability have been proven the motor can be handled, installed and operated with confidence inside the envelope design.

5.3 Programmatic challenges

Following reliability testing, it is necessary to satisfy launch providers that there is no risk to the launch vehicle. This process can be time-consuming, and must be commenced early in the spacecraft development program. It is expected that the NKS will achieve a type-acceptance from various launch providers, making it easier for each spacecraft developer to gain launch approval.

Using a solid rocket motor of this size exceeds the CubeSat specification [10] requirement 2.1.5 for total stored chemical energy. This may cause further programmatic challenges if working with launch providers that wish to see strict adherence to this standard.

5.4 Legal challenges

The foreseen solid propellant is a UN class 1 material (explosive according to the United Nations hazard classification system). In order to be able to transport and store the NKS loaded with the solid propellant, the NKS has to be approved for transport by a competent authority. APP (and TNO) have experience with the application for transport approval of solid rocket motors. Based on suitable propellant data and the motor design the competent authority will issue a transport classification. An Ammonium Perchlorate based propellant as foreseen to be used in the NKS will probably result in a UN class 1.3 transport classification.

Solid propellants and solid rocket motors furthermore need to comply with the specific import and export regulations for military or dual use goods.

6 Conclusions

Solid rocket motors have been shown to be an effective means for meeting existing and expected debris mitigation regulations as well as reducing the impact probability. A motor has been developed that is suitable for de-orbiting a 3-unit CubeSat from a 1000 km orbit. Spin-stabilization has been shown as a viable control scheme, and can be implemented using the most common type of CubeSat magnetic attitude sensors and actuators.

With the successful execution of the demonstrator tests the de-orbit motor has reached TRL 4. Further development of the de-orbit module towards in-flight demonstration would comply with ESA's Clean Space Initiative.

7 Acknowledgments

This work was performed under a Prequalification ESA Programme and would not have been possible without the support of the Netherlands Space Office.

8 References

[1] "UN Space Debris Mitigation Guidelines", UN Office for Outer Space Affairs, Vienna, 2010.

[2] Blount, P.J. and Gabrynowicz J.I. (editors), "Space Law: Selected Documents 2008", Journal of Space Law (supplement), The National Center for Remote Sensing, Air, and Space Law, University of Mississippi School of Law, 2009.

[3] Larson, W.J. and Wertz, J.R. (editors), Space Mission Analysis and Design, 3rd ed., Microcosm Press and Kluwer Academic Publishers, ISBN 1-881883-10-8, E1 Segundo, California and Dordrecht/Boston/London, 2005.

[4] "Process for Limiting Orbital Debris", NASA-STD-8719.14, 2009.
[5] Harris, S., "CubeSat sail system is able to pull small satellites out of orbit", The Engineer, Centaur Communications, 23 November 2012.
[6] Shmuel, B., Hiemstra, J., Tarantini, V., Singarayar, F., Bonin, G., and Zee, R.E., "The Canadian Advanced Nanospace eXperiment 7 (CanX-7) Demonstration Mission: De-Orbiting Nano- and Microspacecraft", The 26th Annual AIAA/USU Conference on Small Satellites, paper SSC12-I-9, Logan, Utah, USA, August 2012.
[7] "CUBESAT DISPOSAL, AEOLDOS: Aerodynamic End-Of-Life DeOrbit System", Clyde Space Ltd., Fact Sheet, 2012, http://www.clyde-space.com/documents/2765 (retrieved 10 June 2013).
[8] Lappas, V., Adeli, N., Visagie, L., Fernandez, J., Theodorou, T., Steyn, W., Perren, M., "CubeSail: A low cost CubeSat based solar sail demonstration mission", Advances in Space Research, Vol. 48, No. 11, 2001, pp. 1890–1901.
[9] Ilyin, A.A., Ovchinnikov, M.Yu., Penkov, V.I., "Algorithms of the Magnetic Attitude Control System for the Small Spin-Stabilized Satellite", Keldysh Institute of Applied Mathematics of Russian Academy of Sciences, Preprint No. 19, Moscow, 2005.
[10] Munakata, R., Lan, W., Toorian, A., Hutputanasin, A., Lee, S., "CubeSat Design Specification", Rev. 12, The CubeSat Program, Cal Poly SLO, 2009.

4:th CEAS Air & Space Conference
FTF Congress: Flygteknik 2013

Collaborative understanding of disciplinary correlations using a low-fidelity physics based aerospace toolkit

Erwin Moerland[1], Richard-Gregor Becker[2] and Björn Nagel[1]
German Aerospace Center (DLR)
[1]Institute of Air Transportation Systems, Hamburg, Germany
[2]Institute of Propulsion Technology, Cologne, Germany

Keywords: *Collaborative Design, Multidisciplinary Design and Analysis, Knowledge Management, CPACS, RCE*

Nomenclature

CPACS	Common Parametric Aircraft Configuration Scheme
RCE	Remote Component Environment

Abstract

Covering all relevant physical effects and mutual influences during aircraft preliminary design at a sufficient level of fidelity necessitates simultaneous consideration of a large number of disciplines. This requires an approach in which teams of engineers apply their analysis tools and knowledge to collaboratively approach design challenges.

In the current work, recent technical advancements of the German Aerospace Center (DLR) in data and workflow management are utilized for establishing a toolbox containing elementary disciplinary analysis modules. This toolbox is focussed on providing fast overall aircraft design capabilities. The incorporated empirical and physics based tools of low fidelity level can be used for setting up modular design workflows, tailored for the design cases under consideration. This allows the involved engineers to identify initial design trends at a low computational effort. Furthermore, areas of common physical affinity are identified, serving as a basis for communication and for incorporating tools of higher fidelity in later phases of the design process. Clear visualisation methods aid in efficiently translating knowledge between the involved engineers within the identified areas of common affinity.

A system-of-systems approach is established by applying the elementary aircraft design toolbox for the establishment of requirement catalogues for engine preliminary design. The engine designers at their turn deliver initial performance correlations for application in the aircraft design toolbox. In this way, a clear synergy is established between the design of both the airframe and power plant. Using this approach, engineers of different technical backgrounds share their knowledge in a collaborative design approach.

The use case guiding the present work involves a conventional short to medium range aircraft sent at half the design range. The wing area and aspect ratio are varied to investigate the influence on the engine requirements catalogue for this particular mission.

1 Introduction

Aircraft design is a complex procedure, which involves an increasing amount of disciplines considered simultaneously. During recent years, Multidisciplinary Design & Optimization (MDO) techniques have become state-of-the-art and are evolving continuously. Applications to design of novel aircraft are however only occasionally seen and wide exploitation of modular MDO processes at industry level is not yet clearly observed [1], [2]. Due to the large complexity of analysing the multitude of relations between involved design disciplines, the analysis of novel configurations cannot be handled by a single person anymore. Collaborative approaches in teams of specialists and integrators are required to master the challenge of understanding the relevant physical effects involved in the design of aircraft [3].

A lot of effort has been put in generating technical solutions to aid design teams in connecting their disciplinary analysis capabilities. The virtual extended enterprise as developed during projects VIVACE [4] and CRESCENDO [5] forms a tangible example of this development. Within these and similar projects, focus has been placed on exchanging explicit[1] knowledge by using common data exchange formats and setting up technical design frameworks for interconnecting analysis codes. Aside this development, methods for collaboration in teams of engineers have also been investigated.

The Common Parametric Aircraft Configuration Scheme (CPACS) is an xml-based data model developed at the German Aerospace Centre (DLR), representing an explicit description of the aircraft in a structured manner. Aside a geometrical description of the vehicle, other relevant conceptual design data such as missions, fleets and airports are exchanged using CPACS [6]. With the parallel development of the Remote Component Environment (RCE) at DLR, a framework for connecting analysis tools on distributed servers has been created [7], using CPACS as interface.

The technical achievement of using frameworks for interconnecting analysis tools applying the aforementioned data exchange methods is showing large benefits. Experience gained during the DLR collaborative design projects "TIVA" and "VAMP" [8] however shows that operating a numerical analysis system in a team of specialists presents a large challenge of its own. Therefore, as also introduced by Kroo [9], a larger part of the research should focus on addressing challenges at the organizational level of MDO. The collaborative way of working, indicated as third generation in Fig. 1, is required to share implicit[1] knowledge within the design team. The indicated shift in focus toward organizing effective collaboration among all involved engineers is however still in its early stages.

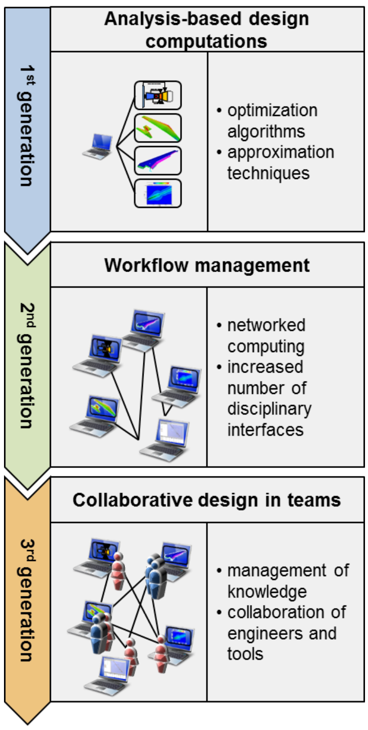

Fig. 1 Evolving generations in MDO

[1] 'Explicit' (or formal) knowledge: knowledge that can be captured in design rules, implicit (or tacit) knowledge: knowledge possessed by an individual, mostly based on experience, which is difficult to communicate via words and symbols [17].

The main question guiding the collaborative design effort is:

How to enable communication among engineers having different specialisms?

In the present study, it is investigated how multidisciplinary interactions and affinity for common disciplines can be identified and used as a basis for communication (see Fig. 2). Using a practical design problem, experience is gained on the needs to ensure effective collaborative approach in aerospace design teams. As indicatively shown in Fig. 2, common disciplinary affinity between knowledge bearers serves as starting point for comprehensible communication within the team. This area of common affinity can be defined by shared explicit knowledge, e.g.: design parameters exchanged between disciplines, but also by the less straightforwardly identifiable implicit knowledge, e.g.: common theoretical methods applied within the analysis codes.

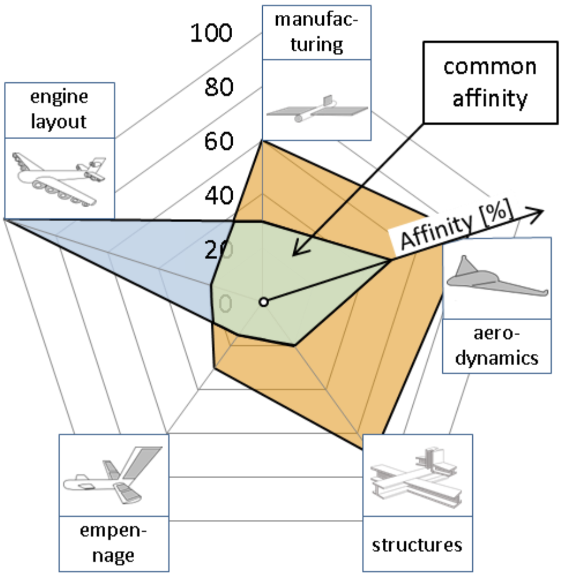

Fig. 2 Common affinity of two knowledge bearers serving as basis for communication.
- blue: pre-engine designer,
- orange: aircraft pre-designer,
- green: area of common affinity

2 Low-fidelity toolkit for mutual understanding and knowledge transfer

In a previous study, the authors investigated the possibility to perform a system-of-systems approach in aircraft design [3]. Defining the area of common affinity (see Fig. 2) between the involved engineers proved not to be straightforward. On the implicit level, this was mainly caused by the difference in engineering backgrounds of the involved parties. On the explicit level this was due to the difference in applied design methods and – practically – due to differences in applied data exchange formats.
For serving the assessment of the overall system under analysis, large commonality among the involved analysis tools is required. Furthermore, the incorporated tools (and maybe even engineers) should be modular in a sense that a change of analysis methods within the process requires only little effort. For the current investigation, a basic pool of low-fidelity physical analysis tools is created using the technical capabilities provided by the CPACS data exchange format and the integration framework RCE as a basis. The main goal of the modular system of analysis tools is to create the possibility to quickly identify physical effects and cross-disciplinary influences.

The studies at low fidelity level are used for identifying common knowledge affinity between the involved disciplines. After identifying these correlations, higher-level analysis modules can be incorporated in the design system to increase the certainty of the identified correlations. Since expert knowledge is required to interpret results of the overall system, this process tends to go beyond plainly connecting analysis tools and observing the results. Instead, a system of distributed low and high-level competencies is created.

The fidelity level of analysis modules used in aircraft design can be subdivided in four levels:

Level-0 tools are based on statistical or empirical design rules and allow exploration of the conventional design space only.

Level-1 tools are based on a simplification of the physics of the design problem. These tools are applicable to simple extensions of the conventional design space and mostly involve physical behaviour of a linear nature.

Level-2 tools are based on accurate physical representations of the disciplines involved in the design problem: the geometrical representation is much more detailed; the physics underlying the analysis code is of high detail or a combination of the both. Tools of this level may be used for analysing unconventional designs.

Level-3 tools represent the most accurate simulation capabilities. These are used to capture detailed local effects and mostly do not allow for automation.

Tab. 1 Main properties of analysis modules, per fidelity level

	Assumed accurateness	Computational speed per analysis	Design space exploration	Application to unconventional Designs	Automation easiness
Level-0	-	++	+	no	++
Level-1	-	+	++	+/-	+
Level-2	+	-	-	++	-
Level-3	++	- -	- -	+	- -

The main properties of the analysis modules of different fidelity level are summarised in Tab. 1. The current work focuses on the interconnection of tools of level-1 fidelity in order to efficiently scan the design space at low calculation effort. The level-0 tool VAMPzero is used for initiating the aircraft as well as for closing the iterative design loop [10]. It calculates the aircraft properties for which level-1 analysis modules are currently still under development.

After analysing physical properties of the aircraft concept model, its ‘goodness’ is evaluated according to the requirements set in the initiation phase of the concept assessment. As can be seen in Fig. 3, within such an evaluation again multiple disciplines are represented. In the current study the aircraft costs are analysed using a low-level DOC calculation module. Climate impact, as well as noise and capacity assessment is part of future work.

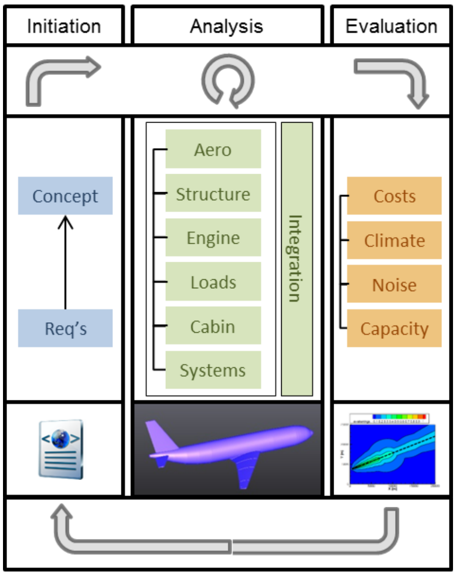

Fig. 3 Phases in aircraft concept assessment

All tools within the toolkit under development, both in the analysis as in the evaluation category, include a connection to the central data exchange format CPACS. The tools are therefore modularly applicable; the user can for example choose to exchange individual analysis modules using different approaches or of different fidelity level. The modules making up the analysis toolkit are hosted on multiple dedicated servers and analyses can be triggered using the RCE framework.

To provide the workflow integrator[2] clear and concise information on the analysis modules

---

[2] As elaborated in [3], design teams within multidisciplinary design approaches ideally consist of one or more *workflow integrators* connecting all involved analysis modules to logical design workflows, supported by the *specialists* individually interpreting the results of their disciplinary modules. An *operator* takes care of the overall course of action within the design process.

within the toolkit, a standard has been developed for connecting the tools to the RCE framework. This tool wrapping plainly consists of a standard folder structure to be used for input and output data, as well as scripts for encapsulating the tool. These scripts trigger the actual calculation and control tool execution behaviour. Furthermore, the end user is provided a well-balanced amount of status information through filtering the often excessive output information for main output messages. The excessive calculation logbooks can be used by the specialist for debugging purposes on the dedicated server when a tool does not provide the intended results.

The main purpose of having a standard for tool wrapping is generating the possibility for flexible application to a multitude of design questions and aircraft configurations. From experience it is found that this collaborative approach requires a change in mind-set of the developing engineer: (s)he needs to be constantly aware of how external users without the experience of a disciplinary specialist will try to approach the tool at hand and clearly define its application boundaries. In this *design for collaboration* approach, putting large effort in writing a proper wrapping code generally saves lot of time during the application period of the module. This wrapping code has to provide the end user with clear information on assumptions, warnings and errors encountered during tool execution. Assumptions and warnings need to be built up to flexibly react on the contents of the provided input.

3 Simultaneous aircraft and engine design

As can be seen from Fig. 2, the area of common affinity between aircraft and engine designers is relatively small. This is also seen in the industry, in which the airframe and engines are often designed by separate parties. At the DLR, two parallel projects for aircraft and engine preliminary design are currently executed. The design cycles are synchronised in such a way, that the aircraft design workflow provides design points for the design of the corresponding engine. The generated engine performance data is at its turn used to determine the performance of the complete integrated airframe.

In light of these projects, the current study encompasses the generation of an aircraft analysis workflow aimed at generating request for proposal (RFP) documents for the layout of a corresponding engine concept. Fig. 4 shows an N2-chart of the connections between the low-level tools as used within the analysis, as well as the purpose and name of each tool. This chart has been established through communication with all specialists that programmed the individual analysis modules. Since within the actual tool connections data of an explicit nature is exchanged, this step in the setup of the analysis workflow will be aided by automatic identification of required input data in future work. This will allow for more time to be spent on exchanging implicit knowledge, e.g.: on the appropriateness of a tool to generate required input data.
After identifying the required input and available output of each analysis module, the N2-chart aids in logically ordering the workflow in an initiation, iterative and evaluation phase.
The application of CPACS as central data exchange format considerably reduces the required amount of actual connections between the modules within the RCE framework, since information of consecutively executed modules is appended to this single data file.

To reduce complexity in the analysis workflow, the engine is represented by a database containing pre-calculated performance data. The database tables are created by performing thermodynamic analyses of the engine cycle at a multitude of operating points. Therein, the underlying engine deck is fixed in terms of principle cycle parameters such as turbine entry temperature (TET), overall pressure ratio (OPR) and fan pressure ratio (FPR). However, using ‘rubber engine’ scaling principles, the available engines can be scaled in mass flow by +/- 20%.

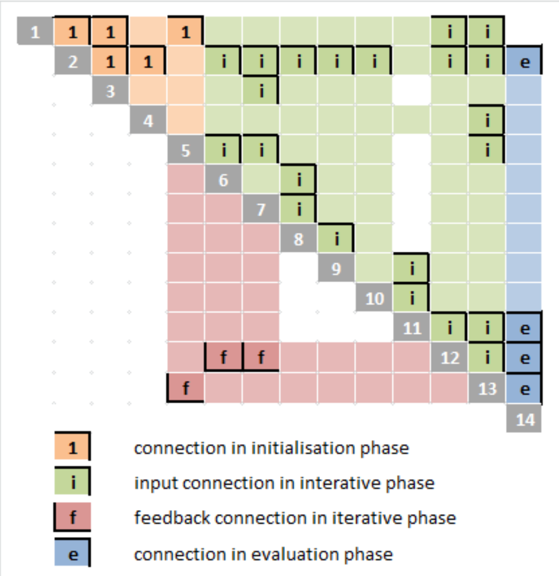

#	purpose	tool
1	TLAR & basic aircraft geometry	user input
2	geometry variation	GPP
3	mass initialisation	VAMPzero
4	aerodynamic performance map	Tornado
5	engine mass & performance map	TWDat
6	loadCase determination	LCG
7	weight and balance	WandB
8	spanwise loading	TRIM_VL
9	wing primary mass	PESTwing
10	wing secondary mass	PESTsewi
11	mass tree update	CMU
12	aircraft mass synthesis	VAMPzero
13	fuel mass and engine scaling	FSMS
14	direct operating costs	DOC

Fig. 4 N2-Chart providing the connections between analysis modules in the aircraft analysis workflow

The more the engine differs from its validated unscaled basic thermodynamic cycle, the more care has to be taken in interpreting the corresponding performance data. In Fig. 5, an engine performance map as read out from TWDat and interpreted by the mission simulation module FSMS is shown. As concluded during the design studies, the current simplified representation however has its limitations: no engine ratings are included, allowing the aircraft engineer to theoretically let the aircraft fly at full thrust throughout the entire design mission. In setting up a workflow involving engine data, the aircraft engineer needs to provide the engine designer the intended mission data of the airframe in order to attain proper performance data coverage.

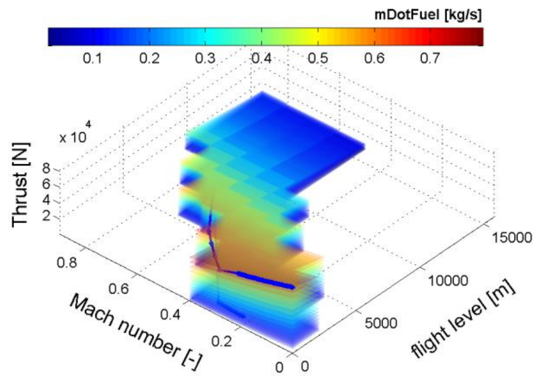

Fig. 5 Interpolation within the performance map of the CFM56 engine. Blue line: interpolation trajectory throughout the simulated mission

A resulting engine requirements catalogue for the short- to medium range A320-like reference aircraft ‘D150’ is shown in Tab. 2. The mission simulation tool FSMS is adjusted to specifically calculate the following design points for the catalogue:

One Engine Inoperative (OEI) condition determines the required engine scaling factor according to Certification Specifications chapter 25.121 [11]. For a fly out manoeuvre with engine failure exactly occurring at decision speed V1, the engine is scaled such that the minimum fly out gradient and velocity are attained by the aircraft.

End of Field (EOF) is the condition with the largest fly out climb angle, reached shortly after the ground run. This is generally the point with the highest shaft speed and turbine inlet temperature requirements.

Mid Cruise (MCR) is used as the aerodynamic design point providing the highest component efficiencies for minimizing engine specific fuel consumption.

Top of Climb (TOC) is the point just before the aircraft starts its cruise phase, used to determine the maximum non-dimensional engine performance parameters, such as corrected component mass flows and speeds.

Once the engine performance data is calculated, an additional database entry in TWDat can be added to verify its correspondence to the established requirements. This at its turn might lead to an update of the requirements catalogue.

Tab. 2 Engine design point data for the requirements catalogue [a/c: D150, engine: CFM56-5A5, des. range: 1800 nm]

		one engine inoperative (OEI) [JAR 25.121]	end of field (EOF)	mid cruise (MCR)	top of climb (TOC)
$T_{required}$	[N]	82383	78327	19936	26973
$T_{delivered}$	[N]	80880	78327	19936	26973
time	[m':s'']	0'50''	0'45''	139'	29.6'
altitude	[m]	64	45	10376	10000
Mach	[-]	0.23	0.26	0.78	0.78
α	[deg]	9.4	8.0	4.1	3.6
γ	[deg]	2.4	8.0	0.0	1.1
θ	[deg]	11.8	16.0	4.1	4.7
dT_{ISA}	[deg]	0	0	0	0
rating	[-]	OEI	MTO	MCR	MCL
ECS	[-]	on	on	on	on
WAI	[-]	on	off	off	off
HPX	[-]	tbd	tbd	tbd	tbd

nPax	[-]	150	H_{OEImax}	[m]	tbd
nEng	[-]	2	$H_{airport}$	[m]	0
t_{climb}	[m']	28'	MTOM	[t]	73500
TOFL	[m]	2120	MLM	[t]	64500
Vappr	[m/s]	tbd	ESF	[-]	1.019

ECS: env. control system, WAI: wing anti-icing, HPX: eng. power off take, ESF: eng. scaling factor

Using the N2 Chart (Fig. 4), the required modules are connected using the CPACS data format within the integration framework RCE. Fig. 9 shows the resulting workflow, specifically aimed at generating requirement catalogues for engine predesign. After initializing the aircraft geometry according to the design of experiments study at hand (see section 4), an iterative loop is started in which the engine scaling factor is brought to convergence. In the current setup, the wing and engine mass is determined using level-1 tools, whereas the other aircraft masses are determined using VAMPzero. Modules having no direct input connection as identified in the N2-chart (Fig. 4) are executed in parallel to save calculation time. After reaching convergence, the engine requirements catalogue is obtained for the configuration under investigation.

As already stated in section 2, in setting up such an analysis workflow, the need for a balanced combination of workflow integrators with general knowledge in connecting the specialists' tools on the one hand and disciplinary specialists on the other hand is clearly observed. The specialists need to ensure the connected tool is used properly and results are interpreted in a proper way, whereas the workflow integrator should provide general knowledge for the integration in analysis workflows and question the generated overall results at hand.

4 Design Study: influence of wing planform on engine scaling requirement

In the present work, it is chosen to keep the fidelity level of the applied tools low enough to provide relatively quick calculation results, although modelling the effects to be studied with physical relations. The workflow for the design study, depicted in Fig. 9 can be divided in six main parts.

The **initiator** part will use a geometric pre-processor to adjust the baseline aircraft geometry in CPACS. For the current study, a predefined geometrical description of the D150 aircraft is applied. As indicated in Fig. 6, the wing area and aspect ratio are varied around the baseline values of the D150 aircraft. VAMPzero is used to obtain a first mass estimation and in parallel, the aerodynamic performance map is generated using Mach, Reynolds and angle of attack sweeps in the vortex-lattice programme Tornado [12].

After the initiation, an engine performance map and weight is loaded from TWDat (see section 3) and in two parallel branches, the wing primary and secondary masses are estimated. Within the tools PESTwing and PESTsewi, a beam model representation for main wing structure sizing and empirical relations for secondary structure mass estimation are applied. The required wing loading is determined using a trimming routine incorporating a connection the vortex-lattice code AVL [13]. To complete the aircraft mass determination, VAMPzero is again used to **estimate the aircraft masses** not belonging to the wing group.

Knowing the aircrafts aerodynamic, engine and mass properties, the design mission is flown using the mission simulator FSMS to obtain the fuel requirements and the required **engine scaling factor**. Aside required fuel mass, payload-range diagrams as well as emission values are calculated, and the requirements catalogue for the new engine is provided (see section 3).

The determination of aircraft masses and engine scaling factor is iteratively performed, until the scaling factor **converges** and the engine required for the investigated configuration is obtained.

Within the **concept evaluation**, the direct operating costs are determined, after which the **DOE** is continued.

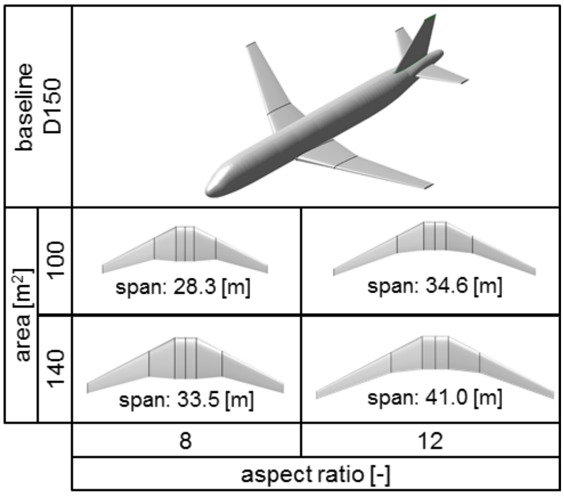

Fig. 6 Geometry changes within the performed design of experiments. Wing area: 100-140 [m^2], aspect ratio: 8-12 [-].

Applying proper visualization methods aids considerably in establishing clear interdisciplinary communication among involved engineers. In [14], the usage of “level transfer functions” to assist in communicating physical relationships among the parties involved in a design exercise is suggested. Transfer functions are used for communicating metrics on one design level to understandable research objectives for another level. Such plots provide a “feel” for the involved engineers on how known geometrical parameters influence higher-level objectives.

Fig. 7 shows the required engine scaling factor and aircraft operating empty mass (OEM) for the studied geometric parameters. For the D150 reference aircraft, a scaling factor close to 1.0 is obtained. The difference is caused by the low-level physics being used in the workflow. A technology factor of 1.069 is used to correct the determined wing mass within the workflow to its known baseline value for the reference aircraft. It can be concluded that the aircraft with a slender wing and low wing area has the least stringent requirement on engine performance. The classical opposing aeroelastic correlation is seen when combining parts (a) and (b) of the figure: a slender wing leads to better aerodynamic efficiency (and thereby a low engine scaling factor), however the aircraft mass increases due to the large structural loads imposed by such a configuration.

Fig. 8 shows a resulting performance correlation for the aircraft. Within this level transfer function, the influence of the performance measures wing loading (W/S) and thrust-to-weight ratio (T/W) on fuel requirements is shown for the geometries with correspondingly scaled engine. The boundaries of the T/W-W/S area a consequence of the parameter variation chosen within the current study.

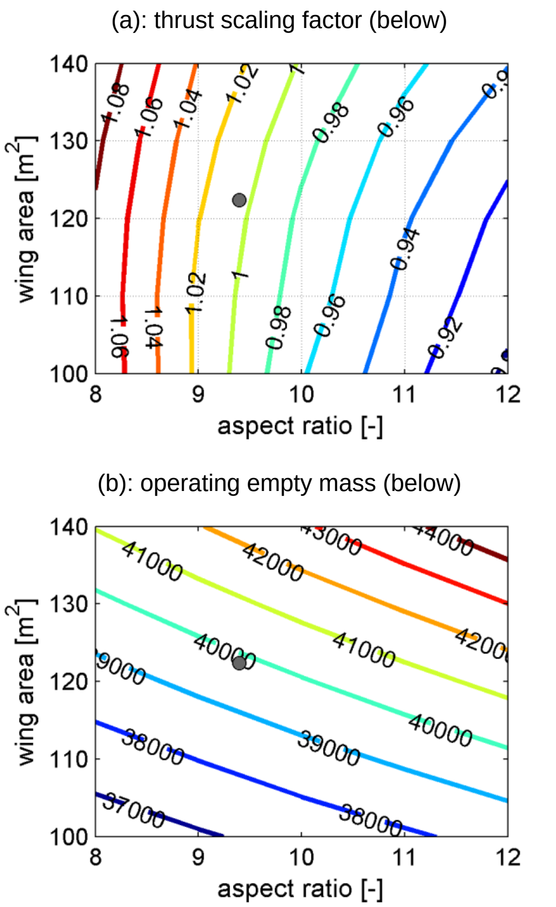

Fig. 7 Disciplinary parameter transfer plot: the influence of wing area and aspect ratio on engine scaling requirements (a) and aircraft empty mass (b) [D150 reference aircraft indicated by grey dot]

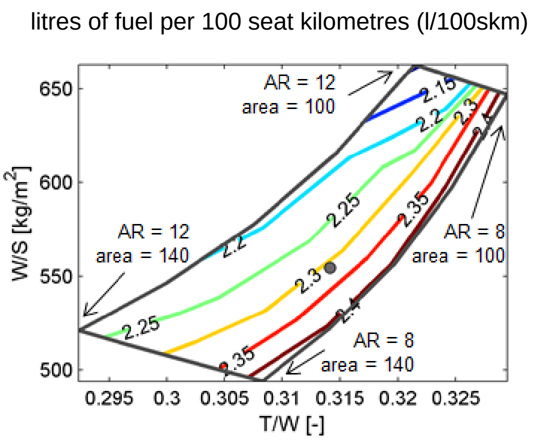

Fig. 8 Level transfer function showing relative effect on litres of fuel per 100 seat-kilometres for changing wing loading and thrust-to-weight ratio [D150 reference aircraft indicated by grey dot]

The data represented within the figures above are obtained using a scalable database entry in the engine performance database TWDat. When a team of engineers chooses to further investigate a specific design point, a new data deck should be generated for the scaled engine at hand, in order to improve the accuracy of the results. For this the requirements catalogue as in Tab. 2 can be used.

In future work, correlations like the ones shown in Fig. 7 and Fig. 8 will be used as a basis for communication within teams of engineers. Disciplinary dependencies can be identified and the decision making process is supported by clarifying visualisations. After extending the toolkit with physical analysis modules for disciplines not yet covered, the design space is extended by considering less conventional aircraft configurations. Instead of using a predefined geometrical description of the reference aircraft in CPACS, an aircraft initiator based on knowledge-based engineering principles can be applied to attain a starting configuration [15].

When needed, connections to modules of higher fidelity level can be established using RCE, to cover the parts of the underlying physics that cannot be handled by level-1 tools.

5 Conclusion

Although the technical means to connect aircraft analysis modules are available, large potential for improvement is still found in the application of these modules within multidisciplinary analysis workflows. Methods aimed at efficiently translating knowledge between researchers of various backgrounds involved within aircraft predesign are currently under development. The current work investigated how multidisciplinary interactions and areas of common affinity might serve as initial basis for communication among engineers.

The generation of modularly applicable analysis components requires a change in attitude of the design engineer. It proves to be a large effort to program these components such that a wide variety of aircraft configurations can be analysed without the need for problem-specific tool adjustments. Furthermore, providing disciplinary specific output using visualisations and messages understandable for a widely oriented public, such as workflow integrators, requires major thoughts. Identifying areas of common affinity between the engineers involved forms a starting point for the latter issue.

An initial application of a low level toolkit for combining aircraft and engine predesign has been shown. In the future, the toolkit will be extended with more low-level physics based analysis tools and applied to generate visualisations of cross-disciplinary correlations. When operators, workflow integrators and specialists gather in design teams, these kind of visualisations aid in understanding each other’s considerations and interests. The flexibility of arbitrarily connecting analysis modules facilitated by RCE allows the design team to investigate physical trends at a level of detail appropriate to the question at hand.

Once mutual understanding of physical correlations is created, initial design space extensions can be studied using the combined explicit and implicit knowledge of the involved design team members. Extending the design space requires careful analysis of tool results and applicability considerations, since results cannot directly be validated by comparison to familiar aircraft designs. Especially at this stage, clear and streamlined communication among engineers is of utmost importance.

Outlook

In future work, more level-1 modules will be incorporated within the toolkit. When developing these new modules, the modularity of its application in workflows specifically aimed at providing a quick answer to the design question at hand should always be kept in mind. Furthermore, the level-1 toolkit will serve as basis for incorporation of uncertainty considerations within the analysis modules. By adding uncertainty values to the results, the possibility to not only determine the ‘goodness’ of an aircraft concept or requirements catalogue, but also with which certainty such a statement can be made is established.

A continuation of simultaneous aircraft and engine design is foreseen. The workflow and toolkit will be used to investigate combined unconventional aircraft and engine concepts, among which a strut-braced wing configuration with counter-rotating open rotor (CROR) engine is anticipated. A semi-automated aircraft and engine concept analysis workflow is to be established by incorporating the thermodynamic performance analysis and preliminary engine design environment GTlab [16]. In contrast to the pre-calculated and scaled performance decks used in the present study, airframe and engine conceptual design processes will be directly coupled in order to find the optimum engine cycle parameters for a given set of airframe and mission requirements. This will bring collaboration among aircraft and engine specialists and integrators in predesign phases to a higher level.

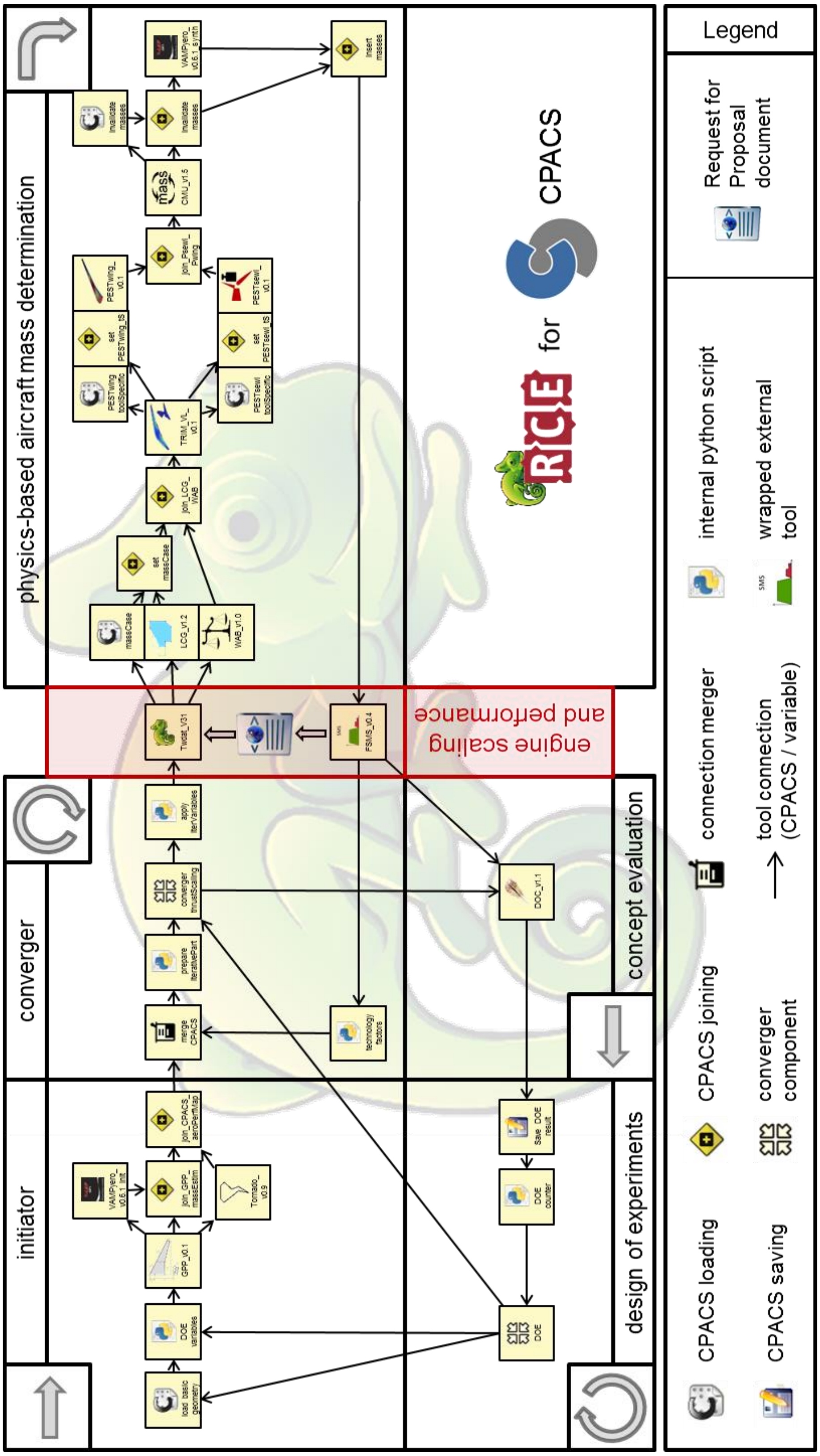

Fig. 9 Workflow of level-1 fidelity in RCE for CPACS

Acknowledgement

The authors wish to thank Daniel Böhnke, Till Pfeiffer and Felix Dorbath for providing their tool contributions, bugs and help in resolving these in the aircraft analysis workflow.

Contact details

Erwin Moerland
German Aerospace Center (DLR)
Blohmstraße 18, 21079 Hamburg, Germany
Email: erwin.moerland@dlr.de
Telephone: +49-40-42878-4141

References

[1] G. La Rocca, "Knowledge based engineering techniques to support aircraft design and optimization," Doctoral Thesis, Delft University of Technology, Delft, The Netherlands, 2011.

[2] J. Agte, O. Weck, J. Sobieszczanski-Sobieski, P. Arendsen, A. Morris, and M. Spieck, "MDO: assessment and direction for advancement—an opinion of one international group," *Structural and Multidisciplinary Optimization*, vol. 40, no. 1–6, pp. 17–33, Apr. 2009.

[3] E. Moerland, T. Zill, B. Nagel, H. Spangenberg, H. Schumann, and P. Zamov, "Application of a distributed MDAO framework to the design of a short- to medium-range aircraft," *61th German Aerospace Congress (DLRK), Berlin, Germany*, 2012.

[4] VIVACE Consortium, "VIVACE - Final Technical Leaflet," 2007.

[5] CRESCENDO Consortium, "CRESCENDO - Forum participants handbook," 2012.

[6] C. Liersch and M. Hepperle, "A distributed toolbox for multidisciplinary preliminary aircraft design," *CEAS Aeronautical Journal*, vol. 2, no. 1, pp. 57–68, 2011.

[7] D. Seider, M. Litz, M. Kunde, R. Mischke, and P. Kroll, "RCE: Distributed, Collaborative Problem Solving Environment." 2012.

[8] B. Nagel, T. Zill, E. Moerland, and D. Böhnke, "Virtual Aircraft Multidisciplinary Analysis and Design Processes - Lessons Learned from the Collaborative Design Project VAMP," *The International Conference of the European Aerospace Societies (CEAS), Linköping, Sweden*, 2013.

[9] I. Kroo, "Multidisciplinary Design Architectures : History and Status Optimization and Design," no. June. Stanford University, Palo Alto, CA, USA, 2006.

[10] D. Böhnke, B. Nagel, and V. Gollnick, "An Approach to Multi-Fidelity in Conceptual Airplane Design in Distributed Design Environments," *IEEE Aerospace Conference, Big Sky, USA*, 2011.

[11] European Aviation Safety Agency, "Certification Specifications and acceptable means of compliance for large aeroplanes CS-25, Amendment 13," 2013.

[12] T. Melin, "Tornado." [Online]. Available: http://www.redhammer.se/tornado/. [Accessed: 03-Jun-2013].

[13] M. Drela and H. Youngren, "AVL." [Online]. Available: http://web.mit.edu/drela/Public/web/avl/. [Accessed: 24-Jul-2012].

[14] A. Hahn, "Providing Quantifiable Governance." NASA Technology Frontiers-ASH, 2010.

[15] P.-D. Ciampa, B. Nagel, and G. La Rocca, "Preliminary Design for Flexible Aircraft in a Collaborative Environment," *The International Conference of the European Aerospace Societies (CEAS), Linköping, Sweden*, 2013.

[16] R.-G. Becker, F. Wolters, M. Nauroz, and T. Otten, "Development of a gas turbine performance code and its application to preliminary engine design," *60th German Aerospace Congress (DLRK), Bremen, Germany*, 2011.

[17] L. Prusak, "The Knowledge Notebook: What do we mean wen we say 'knowledge'?," Washington, pp. 44–45, 2006.

Ad hoc Collaborative Design with Focus on Iterative Multidisciplinary Process Chain Development applied to Thermal Management of Spacecraft

Doreen Seider, Achim Basermann, Robert Mischke, Martin Siggel, Anke Tröltzsch and Sascha Zur
Simulation and Software Technology
German Aerospace Center (DLR)
51147 Cologne, Germany

Keywords: Collaborative Design, Integration Framework, MDAO, RCE

Abstract

In multidisciplinary design optimization, different experts from different disciplines located often at different sites solve a problem in common. Efficient and effective collaboration is essential. This paper describes an approach how software technologies enable ad hoc collaboration during the development of process chains used in multidisciplinary design optimization. The German Aerospace Center develops a framework that supports this kind of ad hoc collaboration. It is used for optimizing the thermal management of spacecraft. As a result, the development phase of the process chain gets more efficient, because the technical effort of collaboration is reduced.

1 Introduction

The design study of complex objects such as aircraft or spacecraft often involves many different disciplines. The involved experts work in different organisations, which are often spread across multiple sites. Collaborative work requires lots of communication via e-mail or phone and data and tools have to be shared and exchanged. Multidisciplinary collaboration can be cumbersome due to the communication overhead.

In the initial design phase, the tools of the different disciplines are developed and an automated design process chain to couple them is set up. Tools include simulation codes, analysis applications, or optimization algorithms. At this stage, the tools are still evolving and subject to frequent changes because of bug fixes and new features. Keeping the tools of all disciplines at all sites always up to date is a challenge. The conventional approach in multidisciplinary design is collecting all required tools and running them on one dedicated compute machine. This approach can be a limitation due to

- Software licensing issues, as research tools are often based on commercial software for numerical computation and simulation, whose licenses are too expensive for an additional installation on the compute machine.
- Platform specific tools, which require specific operating systems or "exotic" hardware platforms such as compute clusters, graphic cards, accelerators etc.
- Impractical centralized installation of frequent software updates.

This paper describes an approach to support collaboration in initial design phases within distributed environments, where tools can remain at each developer's machine. The approach ensures that every involved discipline can always

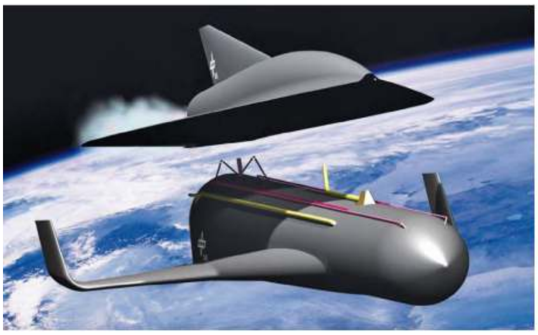

Figure 1: The SpaceLiner while separating from its main tank.

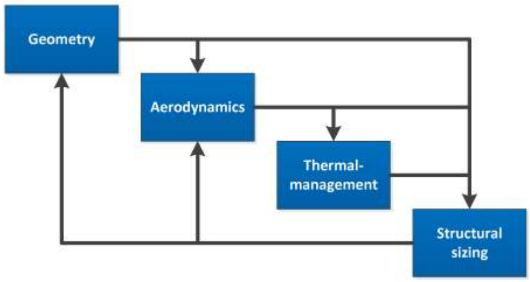

Figure 2: Involved disciplines in the MDO problem.

use the latest version of tools from all other disciplines. It reduces the mentioned coordination overhead between project members and allows an efficient and iterative process chain development.

In Section 2 the design optimization of the SpaceLiner [1] is introduced – a revolutionary concept between aviation travel and space travel for ultra fast passenger transport (see Fig. 1). Requirements for ad hoc collaboration are elaborated in Section 3. In Section 4 the implementation of the introduced ad hoc collaboration approach is presented.

2 Multidisciplinary Design Optimization in Thermal Management of Spacecraft

When designing spacecraft, one of the major issues is to devise its thermal management. This is particularly true for thermal protection systems (TPS) during atmospheric re-entry. One part of current DLR research focuses on the development of new hybrid structures with integrated thermal control units for future space transportation systems and hypersonic planes like the SpaceLiner [1] (see Fig. 1).

Beside passive thermal management techniques through heat sink elements consisting of materials with extremely high heat conductivity and forced radiation cooling, magnetohydrodynamic (MHD) effects with cooled magnets for heat reduction [2] are in the focus of DLR research.

The goal of the overall project is to find the optimal preliminary SpaceLiner design which considers all disciplines together (see Fig. 2). The involved disciplines are:

- Geometry (e.g., maximum length or nose radius of the spacecraft),
- Aerodynamics (e.g., a solution in compliance with minimum lift and maximum drag requirements),
- Thermal management (e.g., the choice or combination of the cooling system and its parameters),
- Structural sizing (e.g., the computation of structural masses).

The objective of the optimization problem is to locate the design with the maximum glide ratio subject to an upper mass constraint and to several geometry constraints for a fixed trajectory. As the considered disciplines together build a highly coupled system and a change of input in one simulation tool affects also the output of several other ones, multidisciplinary design optimization (MDO) techniques have to be applied [3, 4]. The application of the appropriate MDO technique for the addressed optimization problem is a research topic of its own and out of the scope of this paper.

The design optimization of the SpaceLiner requires the close collaboration between experts of all disciplines, especially in the initial design phase. As most of the involved physical phenomena cannot be computed exactly but rather have to be approximated by numerical simulation tools, tools of the mentioned disciplines are integrated in an appropriate design process chain. Especially in the initial design phase, the tools are subject to constant development and improvements, which results in challenges during the development of the process chain. Another problem arises from the fact that the involved experts do not only belong to different disciplines, but also work in different institutes located on different sites in Germany.

3 Ad hoc Collaboration in Multidisciplinary Process Chain Development

As in the thermal management of spacecraft, multidisciplinary design is often performed using automated process chains. Process chains consist of multiple tools. The tools belong to different disciplines, and therefore have dependencies between each other that must be considered during execution. To set up those process chains, integration frameworks are widely used [5]. As described in Section 2, process chains with multidisciplinary character have specific requirements regarding collaboration. Especially, this affects the phase when involved tools are being developed, and the process chain is being set up. To allow collaboration in this phase, the used framework must enable the user to use tools of other disciplines easily, in the latest version, from remote, and ad hoc. Based on these demands, requirements are derived that an integration framework must fulfill.

A user should be always able to use the latest version of a certain tool. On the other hand, the tool developer wants to provide frequent updates of his tool during the development phase. Thus, the tool developer must be able to integrate and provide his tool to others in an effective and efficient way. This can be ensured, if the integration process itself is simple and robust and if the distribution of the tool is as transparent as possible for the developer.

A user must be allowed to use tools on demand which can run remotely on different sites. This implies different requirements to the integration framework: first, a local installation of the framework must be able to connect on demand to the rest of the distributed process chain. Second, the framework must be able to execute the tools. Third, the local configuration of the framework to e.g. setup the network should be easy and transparent for the user.

In summary, a tool developer must be able to easily integrate his tool in a single local integration framework. He must be enabled to configure his framework in a way that it can connect on demand to an overall network of frameworks from experts of other involved disciplines. It must be possible for a tool user to access and execute tools as long as the associated integration framework is part of the network.

The benefits of collaboration in multidisciplinary design with the approach outlined above are:

- Control over tool under development: The tool stays all the time on the machine controlled by the developer and will not be distributed in an unmanageable way.
- Frequently centralized updates of tool: Newer versions of the tool can be provided by the developer by updating it on his local machine without additional overhead.
- Tool users can directly make use of new versions and can give feedback instantly (e.g., if dependencies to tools of other disciplines are violated or not considered properly).

For the multidisciplinary optimization of thermal management the integration framework RCE (Remote Component Environment) [6] is used from the beginning of the project. As the demand for collaboration during the iterative multidisciplinary process chain development increases, RCE was extended with the support for collaboration in that phase by considering the requirements from above.

Other integration frameworks were evaluated concerning support for multidisciplinary optimization and collaboration. is an open-source integration framework developed at NASA Glenn Research Center (GRC). It focuses on the support for multidisciplinary design analysis and optimization (MDAO) [7]. Compared to RCE it provides more powerful and more multi-purpose optimization methods. OpenMDAO allows for execution of tools on remote machines like compute clusters. Centralized tool distribution is not addressed.

PHX ModelCenter® is an commercial integration framework developed and purchased by Phoenix® Integration. It supports distributed computing. Specific server can be set up where tools can be integrated and distributed to ModelCenter instances. This approach supports centralized tool distribution, but it is limited to distribution from server-side. From a user's machine tools can only be consumed from remote and not distributed to others.

4 Ad hoc Collaboration using RCE

Multidisciplinary design and optimization is a complex task. From a specialist's perspective, dependencies between disciplines must be understood. Based on these dependencies, the interfaces of tools must be defined and tools must be coupled correctly.

From a technical perspective, the tools, which are often located at different sites, must be executed and data must be transferred. Both the tools and the data are heterogeneous: Tools are written in different languages, or run on different operating systems. Data is represented in different formats, or values may use different measurement units.

Tools and data are continuously changing during the development phase of a multidisciplinary process chain. That leads to a demand for ad hoc collaboration (see Section 3).

In multidisciplinary optimization of thermal management, engineers prefer to focus on the specialist side of the optimization task. To reduce the technical effort to a minimum, the integration framework RCE (Remote Component Environment) is used. The following subsections introduce RCE and explain how it enables ad hoc collaboration from a technical point of view.

4.1 Distributed Multidisciplinary Process Chains

In multidisciplinary process chains, each involved discipline is represented by at least one tool. RCE allows the integration of tools, the composition of tools to process chains, and their distributed execution from one single site. RCE is a distributed system. Instances run of different machines. Each running instance is called a node in the RCE network.

RCE instances can be started with a graphical user interface (GUI), which also provides a graphical editor for defining process chains. All available tools are listed in the editor, an can be simply dragged into the process chain editor. A tool is called available if it is integrated on at least one node. When a process chain is executed, RCE executes each tool on the node where it is integrated. Tool execution ordering and data transfer are handled automatically.

4.2 Networking and Communication

A typical approach to networked computing is the client-server model, in which a central instance (the "server") controls all interactions within the network. While this approach is easy to implement, the resulting network layouts are quite static, which is not ideally suited for ad hoc collaboration. To provide more flexibility, the structure of a RCE network is based on the peer-to-peer approach. In this concept, any RCE node can choose to accept network connections from other nodes. All nodes that are directly or indirectly connected are combined into a virtual network which is independent of the underlying physical network. As communication requests between nodes without a direct connection are forwarded ("routed") by intermediate nodes, each pair of nodes can transparently communicate with each other. With the flexibility that this approach offers, both ad hoc and long-term networks can be set up easily.

One important design criterion of the current RCE network system was that as long as a physical network connection can be established in either direction, communication within the virtual network can flow in both directions. This property allows simple solutions to common networking problems. For example, a typical scenario is where members of a working group are located in different networks, each of which is protected by a firewall that allows no incoming connections. This situation can be easily handled by setting up an RCE node (called a "relay") in a public network that is reachable from each protected network. As working group members only need to make connections from their protected network to a public one, problems associated with network management are greatly reduced or even completely eliminated.

While this simple solution would be possible with a client-server approach as well, the peer-to-peer approach allows to extend this setup in many ways. For example, multiple relays can be connected to each other, which is often useful to link users or resources located at different institutes into the same virtual network.

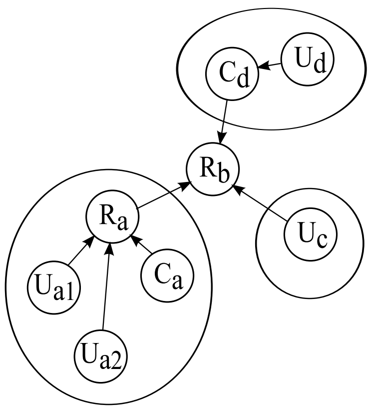

Figure 3: Network of RCE nodes configured as relays (R), compute nodes (C) and user frontend machines (U).

Fig. 3 shows such a setup, where a relay node R_a is located within the local network of an institution, and another relay R_b is set up on a publicly available machine (for example, in a DMZ).

U_{a1} and U_{a2} represent RCE installations on team member's machines in the same network as R_a. These installations only need to be configured with the information how to connect to R_a to access the whole virtual network with all connected resources, which greatly simplifies the handling of ad hoc network changes.

U_c represents a user at a different institute who chooses to connect to R_b directly, without an intermediate relay.

C_a represents a compute node located in the same network as relay R_a. By simply connecting to R_a, it can make its resources available to all members in the virtual network, including U_c. This kind of resource sharing would be difficult without RCE, as the network containing C_a does not allow incoming connections from other institutes.

C_d represents a compute node that is directly connected to the central relay as well, making its resources available in a similar way as C_a.

While this example has used the typical roles of relay, compute node and user machine so far, any combination of these can be configured as well. For example, the compute node C_d has been set up to allow incoming connections from user machines like U_d, which combines the roles of compute node and relay into one. In the same manner, user machines can act as compute nodes or as relays for colleagues as well.

Adding new remote sites or compute resources to the virtual network (for example, by connecting them to R_b as well) requires no action on part of the working group members. From their perspective, the new resources simply appear and are immediately ready to use. Similarly, new members connecting to any part of the virtual network are immediately able to consume all published resources of other members, and publish their own resources (including tools) as well.

4.3 Ad hoc Distribution of Tools

As described in Section 3, from a technical point of view a prerequisite of ad hoc collaboration in multidisciplinary process chains is a framework which allows the integration of tools. To integrate a tool into RCE following requirements must be fulfilled:

- The tool must be executable via a single command line call, and without any user interaction during execution,
- the tool's input must only be command line parameters and files,
- all input files must be located in a specific folder, and
- all output files generated by the tool must be written in a specific folder as well.

In the integration concept of RCE, an integrated tool is treated as a black box. I.e., it is seen in terms of its inputs and outputs without any knowledge of its internal working. Fig. 4 summarizes RCE's tool integration concept.

RCE executes a tool as it would be executed to run standalone. It invokes a pre-defined command line call, which usually includes the executable and optional parameters. RCE waits asynchronously for the tool's termination. During execution, it continuously fetches the standard console output generated by the tool. It provides it immediately to the user (GUI and log file) even if the tool execution is done on a remote RCE node.

Tools are developed to run standalone. If they become a part of an automated process chain extra tasks must be usually performed to fit into the chain. This includes e.g. the conversion of input files into a different file format or writing output data calculated by the tool into a shared database. As these tasks are only needed if the tool is executed within a process chain, they must not be part of the tool's logic. Therefore, RCE supports pre and post processing steps: It provides the possibility to execute two given scripts in conjunction with the tool execution itself. One script is executed right before the execution of the tool, and the other one right after the tool is finished.

An integrated tool is configured via RCE's graphical user interface (GUI). Tool-specific configuration GUIs can be defined by tool developers in specified configuration description files. Out of these files, the GUIs for the tool configuration are automatically generated during RCE's runtime.

For each tool integrated into RCE, a description file must be provided by the tool developer. All relevant information like paths to the tool's executable or to the pre/post processing scripts, the icon a tool shall be shown within the GUI, etc. must be defined there. At startup time, RCE is processing these files and then integrates the tool. If the integration of a tool was successful, a new item is added to the list of tools that are available for building process chains.

Once a tool has been integrated into one RCE instance, e.g., the tool developer's instance, it

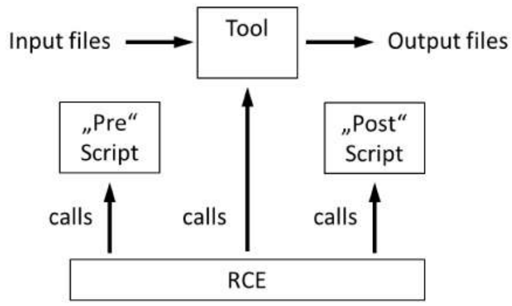

Figure 4: Tool integration concept of RCE.

is instantly being distributed in the RCE network the correspondent node is part of. As only a descriptive information about the tool is distributed, the distribution step is fast and not expensive in terms of communication. As soon as another node has received the information, this node's user can immediately start using the tool in its process chains as if it is installed on its local machine. The actual execution of the tool is performed on the node's machine that it is integrated on. This distinction ensures that the actual tool does not need to be transferred to other machines, and that no conflicts with outdated versions of the tool can occur.

The tool's executable and related files are referenced locally on the executing node's machine. If a new version of the tool is available, only updates to local files are required. From then on, only the new version of the tool will be distributed and can be used by others.

Once a tool has reached a stable state, it is usually desirable that it is available even if the tool developer's node is not connected to the RCE network. In that case the tool can be moved to a compute node, which are designed to be connected permanently (see Section 4.2).

4.4 Ad hoc Distribution of Optimization Methods

Multidisciplinary process chains are often utilized for optimization purposes. To improve the performance of the optimization, it might be required to design and implement a custom optimization method first that fits well to the specific optimization problem.

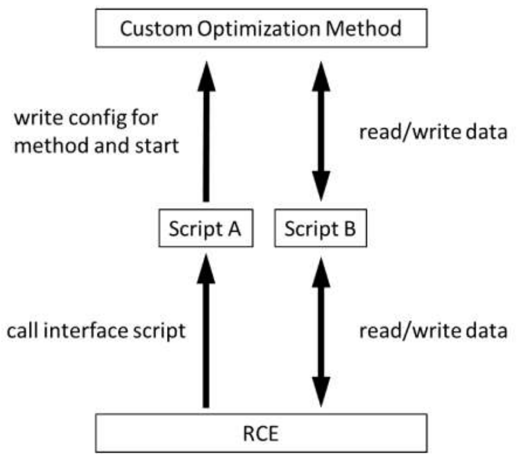

Figure 5: Optimizer integration concept of RCE.

The development of a custom optimization method is more efficient if the developer can test its method with tools the method is designed to optimize. If the developer can share the current state of the method to others, involved in the process chain, he can get feedback from them. This leads to a more effective development as well.

It is possible to integrate custom optimization methods into RCE without having to wait for a new release of RCE. The optimizer component defines a script interface which allows any user to integrate his optimization method in RCE and to distribute it to others. For doing so, there is a template folder containing two predefined scripts. The first script will be called by RCE to start the optimization method. The other script is responsible for handling the communication work, e.g. exchanging new design and response variables between RCE and the optimization method (see Fig. 5).

Using these scripts (written in Python), the user can define his own methods in any programming language that can be triggered using Python. It is also possible to define method configurations in further template files. With those, RCE will automatically generate a graphical user interface and deliver the information the user enters to the optimization method. While designing the new method, the user will be able to use it within RCE, without having to configure anything outside of the framework.

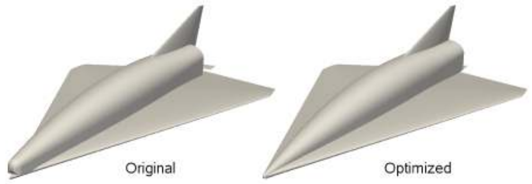

Figure 6: First results of the optimization of the SpaceLiner geometry.

The execution of the method is performed on the node's machine providing the method. Again, version conflicts are avoided. If the optimization method is available in a newer version, only files on the node's machine must be updated.

5 Multidisciplinary Design Optimization in Thermal Management of Spacecraft using RCE

In DLR, for the optimization of thermal management of the SpaceLiner RCE is used from the beginning of the project. One current setup consists of experts for the structural sizing discipline in Bremen, Germany, sharing their tools with experts from aerodynamics in Cologne, Germany, via RCE. Both groups are able to develop their tools and test them immediately within a process chain using real world data. Problems in the tools or even mistakes in the design of the process chain can be tracked down much easier and sooner than without the ad hoc collaboration support provided by RCE.

Fig. 7 illustrates the process chain we established in RCE so far. Three of the four involved disciplines mentioned in Section 2 are already integrated. First results of the optimization are available and are visualized in Fig. 6.

6 Conclusions

Using the example of optimizing the thermal management of spacecraft we demonstrated the demand of collaboration when developing tools and setting up multidisciplinary process chains. We pointed out how collaboration in that phase can be supported by integration frameworks.

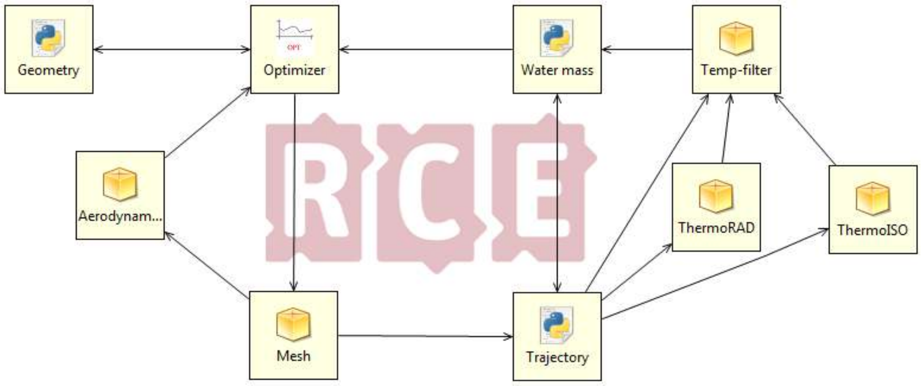

Figure 7: Current version of the process chain for optimizing the SpaceLiner's thermal management implemented in RCE.

We introduced a process chain, where we utilized the collaboration support provided by the integration framework RCE.

In the presented use case of thermal management in spacecraft design, the ad hoc collaboration approach enables efficient collaboration between experts working at different sites. The tool specialists use newly implemented optimization methods immediately. The optimization specialists develop new methods always against the latest version of the involved tools. From an end user's point of view, the introduced approach allows time savings and simplifies collaborative work.

Collaboration is always about humans. Software technologies can support collaboration but can not guarantee efficient and effective collaboration. To address the human aspect collaboration needs to be considered from a psychological point of view as well. Questions should be answered such as: Which kind of people collaborate best? Which circumstances prevent people from collaboration? What motivates people to collaborate? In the end, software technologies can be used as an enabler for collaboration again, if the answers are used to derive the right ideas for new supportive software.

Based on experiences made in multidisciplinary optimization RCE will be extended continuously. Currently, tools can be distributed from one expert to another. This does not ensure that an expert from another discipline knows how to use the tool correctly. RCE will address this issue in the future. Information about the person, who is responsible for the tool, will be distributed next to the tool itself. Documentation of the tool will be directly integrated in RCE as well as an opportunity for instant messaging.

References

[1] Sippel M. Introducing the spaceliner vision. In *7th International Symposium on Launcher Technologies, Barcelona, Spain*, 2007.

[2] Böttcher C. and Longo J. M. Simulation and analysis of magnetohydrodynamic flows using the dlr tau code – mediums air and argon. In *International ARA Days, Arcachon, France*, 2008.

[3] Martins J. R. R. and Lambe A. B. Multidisciplinary design optimization: Survey of architectures. *AIAA Journal, in press*, 2013.

[4] Tedford N. P. and Martins J. R. R. Benchmarking multidisciplinary design optimization algorithms. *Optimization and Engineering*, 11:159–83, February 2010.

[5] Bachmann A., Litz M., Kunde M., and Schreiber A. Advances in generalization and decoupling of software parts in a scientific

simulation workflow system. In *Fourth International Conference on Advanced Engineering Computing and Applications in Sciences*, 2010.

[6] Seider D., Fischer P. M., Litz M., Schreiber A., and Gerndt A. Open source software framework for applications in aeronautics and space. In *IEEE Aerospace Conference, Mountain View, MT, USA*, pages 1–11. IEEE, 2012.

[7] Justin S. Gray, Kenneth T. Moore, and Bret A. Naylor. OPENMDAO: An Open Source Framework for Multidisciplinary Analysis and Optimization. In *13th AIAA/ISSMO Multidisciplinary Analysis and Optimization Conference*, Fort Worth, Texas, August 2010. AIAA.

Application of CAD/CAM/CAE Systems to the Process of Aircraft Structures Analysis by Means of Reverse Engineering Methods

Aleksander Olejnik, Stanisław Kachel, Adam Kozakiewicz
Military University of Technology, Poland

Keywords: reverse engineering, identification of the aircraft structure.

Abstract

The paper deals with application of the reverse engineering approach to the research studies on thin-walled structures. Attention is paid to the methodology dedicated to reverse the design process of aircraft structures and to enable studies intended to evaluate design and strength properties of aircrafts, both newly designed and being in service. The reversing methodology outlined by the authors was used to reproduce bodies and internal structures of selected aircrafts already operated by Polish Air Forces and those that shall be introduced in nearest future. The study reveals a universal algorithm suitable for identification of external loads and aircraft properties related to their static stability as well as for needs of numerical analysis defining dynamic deterioration of structures.

1 Introduction

Strength assessment of aircrafts that have been in service for long years still remains a sophisticated problem since no information is available both on the manufacturer's assumptions with regard to design and calculated lifetime as well as historical information of load spectra the equipment was exposed to in the past. In such a case reasonable decisions related to operation lifetime of aircrafts can be taken only after preliminary investigation of all factors that may affect durability of the structure. Since the operation lifetime depends on many factors and contribution of each factor can be expressed in appropriate figures and calculations, each decision related to the operation history of the equipment should be preceded by a thorough strength analysis. The computation models for assessment of condition demonstrated by thin-walled structures are developed with use of reverse engineering methods.

1.1 Purposes of the study

The analysis of service regimes how aircrafts are operated by Polish Air Forces as well as similar issues to be resolved worldwide involved the need to carry out the following:

1) develop algorithms for reproduction of aircraft structures on the basis of accurate coordinate measurements;
2) develop methods for integration of the CAD/CAM/CAE systems with the systems for accurate measurements of coordinates,
3) carry out strength computations on selected aircrafts to prove the outcome of these computations;

In order to accomplish the foregoing objectives it was necessary to drawn up the following:

1) a method for integration of CAD/CAM/CAE systems with the available systems of measurements;
2) a method for development of computation models for aircrafts;
3) a method for analysis of external loads applied to aircrafts, for which only historical information about the operation is available;

The way of how the foregoing objectives were achieved is outlined in subsequent sections of this study.

2 Integration of CAD/CAM/CAE systems with systems of measurements

2.1 The method for extraction of information from a database containing measurement results

Reproduction of geometry for existing objects needs application of the reverse engineering methods. Modern measuring equipment "Fig. 1" offer the possibility to carry out really accurate measurements of coordinates that serve then as the basis to create of a virtual model.

Fig. 1. The TRITOP system for measurements of coordinates.

Most of modern measuring instruments stores information about the object as a set of point, where the number of points ranges from 10^5 to 10^{10} or even more [1] "Fig. 2". The accurate reproduction of geometry for an aircraft that exists in a real world substantially depends on quality of the method for precise measurements of coordinates, accuracy of measuring instruments as well as on the CAD system that is to be used for development of a virtual object.

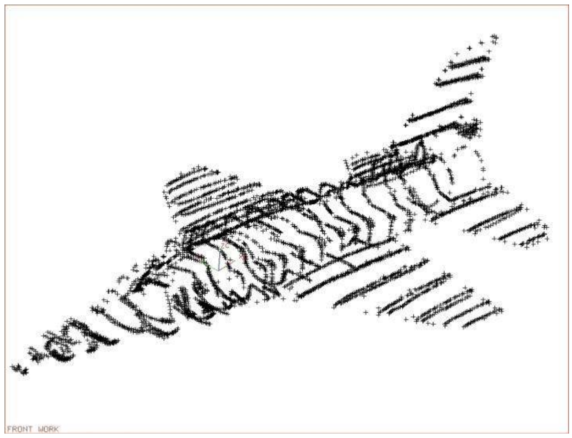

Fig. 2. The set of points obtained from accurate measurements of coordinates.

Even though the number of measuring points is large [2], reaching as many as 10^6 points on the object surface and across various sections of the aircraft components and subassemblies "Fig. 2", "Fig. 3", it is indifferent to accuracy of the structure reproduction.

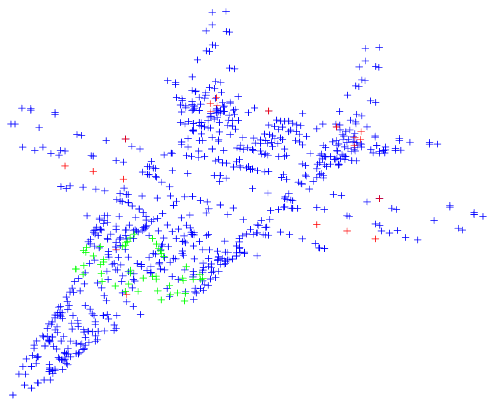

Fig. 3. A lattice of points obtained from accurate measurements of coordinates for the MiG-29 aircraft.

On the contrary, it may be one of the reasons for corrugation of surface when a virtual model of an aircraft is being developed, which means that measurements were taken with insufficient accuracy. Information about the object stored in the form of a set of points " Fig. 2", "Fig. 3" is poorly legible, therefore it is necessary to develop a method capable of extracting the necessary information from the database with selection of points that are really useful so that the points that meet the filtration criteria can be used for plotting of defining curves for objects to be reproduced " Fig. 4".

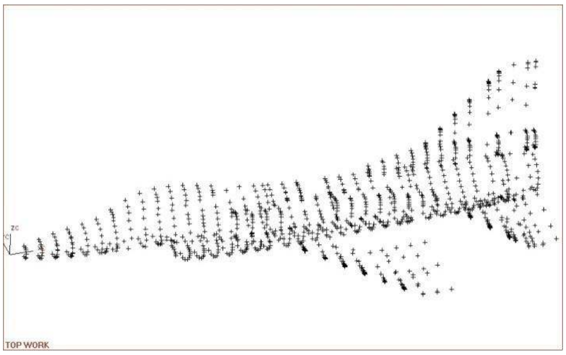

Fig. 4. The points obtained from filtration of the database with accurate measurements of coordinates.

However, such a process intended to reproduce the aircraft structure is very sophisticated and time-consuming. In case of large structures the process must be limited to consideration of natural structuring of the aircraft into such components as a fuselage, a wing and a tail unit " Fig.5".

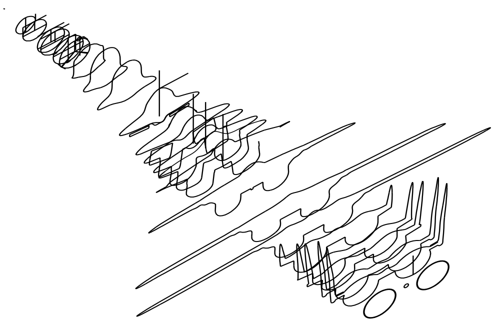

Fig. 5. Defining curves plotted on the basis of measurement points for the MiG-29 aircraft.

For such subassemblies their structure is reproduced with consideration to relevant distances between load-bearing components with simultaneous parameterization of the structure. Development of a digital model for an aircraft with more sophisticated dynamic arrangement, e.g. MiG-29 needs knowledge about auxiliary parameters of curves that define geometry of subassemblies within the lifting structure (e.g. air advection – wing) of the object to be reproduced.

The method of interactive optimization is frequently used in many fields of research and scientific studies. The extraction of the necessary set of points from the space of measurements is based on the criterion of standard deviation Eq. (1) that defines the discrepancy between the curve plotted on the basis of measurements and the theoretical one obtained by means of software tools incorporated into CAD systems "Fig. 6".

$$\sigma = \sqrt{\frac{\sum_{i=1}^{n}[d(i)]}{n}} \tag{1}$$

where σ - standard deviation; $n = n_g + n_d$

$$e_g = \frac{\sum_{i=1}^{n_g} +d(i)}{n_g}; \qquad e_d = \frac{\sum_{i=1}^{n_d} -d(i)}{n_d}$$

where:

e_g, e_d – average upper and lower values of deviations, $+d(i)$ – upper deviation from the theoretical curve, $-d(i)$ – lower deviation from the theoretical curve, n_g, n_d - number of measurement points.

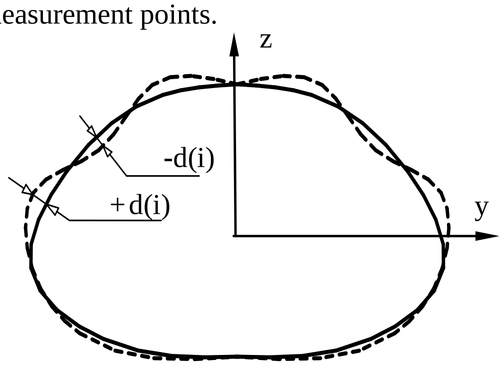

Fig. 6. Parameters for selection of a theoretical curve on the basis of the curve plotted on the basis of measurement results.

The development of a CAD model on the basis of measurement points is a certain compromise between accurate measurements and the curves plotted with the predefined tolerance. Generally, any 3D curve can be reproduced as a form of the spline representation "Fig. 7".

On the other hand, curves that are necessary for development of the object geometry are expressed in a form of a following sum Eq. (2):

$$p(t) = v_0 f_0(t) + \cdots + v_k f_k(t) \qquad (2)$$

where v_i - vectors depends on the assumed location for the origin of the adopted coordinates.

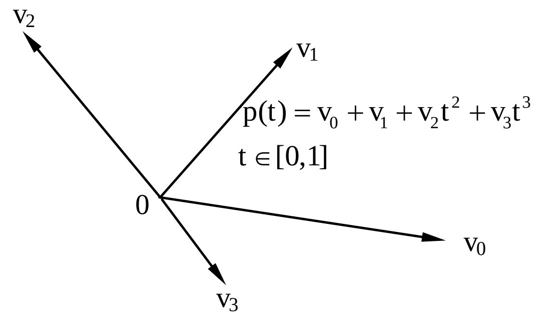

Fig. 7. Representation of a spline curve.

In practice, the general form for representation of curves Eq. (2) as shown in Fig. 7 is insufficient for reproduction of aircraft geometry. In order to overcome that drawback it is necessary to use the general equation for representation of curves Eq. (3):

$$p(t) = p_0 f_0(t) + \cdots + p_k f_k(t) + v_0 g_0(t) + \cdots + v_i g_i(t) \quad (3)$$

where:

$p_0, \dots, p_k$ - basic points, $v_0, \dots, v_i$- free vectors,

$g_0, \dots, g_i$ - any functions that determine shape of the reproduced curve

The f_i and g_i functions determine properties of curves reproduced on the basis of the defined points [3] (a cloud of points).

2.2 The approach of geometrical structures

The approach that consists in plotting of geometrical curves based on sets of points can be explained on the interpolation problem. One can assume a set of points (a cloud of points) "Fig. 2" to "Fig. 4" $u_0, \dots, u_n$ together with the corresponding values of $u_0, \dots, u_n$. For the set of points defined in the foregoing way it is possible to plot a spline curve $p(t)$ with the maximum degree of n that meets the condition $p(u_i) = p_i$. The problem has exactly one solution Eq. (4)

$$p(t) = \sum_{i=0}^{n} p_i \left(\prod_{j=0}^{n} \frac{t-u_j}{u_i-u_j} \right) \qquad (4)$$

For the problem formulated in the foregoing way it is possible to select the curves that match the shape of the reproduced object with sufficient accuracy "Fig. 8".

The relationships Eq. (3) and Eq. (4) enabled to develop a computation procedure set down in GRIP [4] language (Graphics Interactive Programming) for the Unigraphics system.

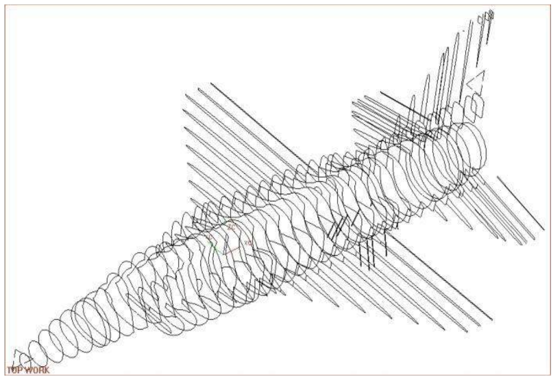

Fig. 8. Base curves plotted for further reproducing of the aircraft geometry.

Plotting of a 3D curve takes into consideration the fact of basic geometric transformations applied to components and subassemblies in GRIP language.

Major benefits from the above algorithm for the appropriate selection of curves and surfaces to match the objects to be reproduced include:

1) elimination of redundant geometrical measurements that are useless for description of models within CAD systems,
2) reduced number of variables that are then used for the process when major parameters are defined,
3) possibility to define inference rules with regard to maintaining of intermediate values.

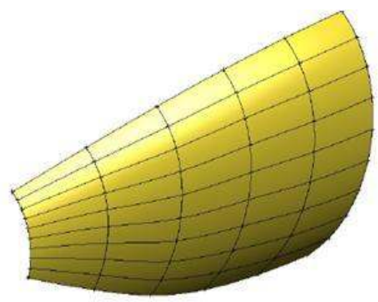

Fig. 9. Surface of the fuselage shell obtained for boundaries of the measurement interval.

Elimination of measurements errors on the basis of the algorithm that makes it possible to optimize selection of points for plotting of curves [1, 4] leads to reduction of time necessary to develop a virtual model “Fig. 9”).

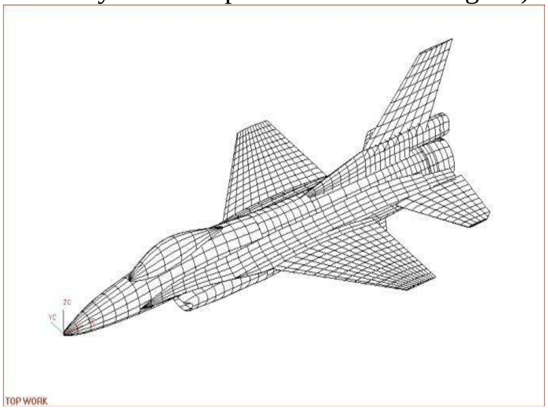

Fig. 10. Distribution of defining curves plotted for the F-16 aircraft with use of the cyclic optimization method.

Definition of reproduction and modification rules makes it possible to modify the object geometry, whilst the parameters imposed by the designer remain unaltered. Components of a CAD model “Fig. 10” serve as the basic structure for a preliminary object.

3 Simulation of aerodynamic conditions for aircraft models

3.1 Aerodynamic models of flows

The analysis of modern aircraft structures needs a broader view to the process of aerodynamic numerical computations that are indispensable for simulation of external loads that affect such structures. Some models assume that the trail is a flat surface, other ones take into consideration the trail curvature (e.g. the Non-Linear Vortex Lattice Method – NVLM). More information about various field-based methods can be found in [5, 6, 7]. Nowadays the analyses of 3D flows employ such approaches as Mimetic Finite Differences (MFD), Finite Element Method (FEM) and the Boundary Element Method (BEM) [8, 9]. Both the methods of Mimetic Finite Differences and the Finite Element Method enable direct resolving of the Navier and Stokes equation.

Table 1. Classification of mathematical models

No.	Model	Assumptions
1	Navier & Stokes	viscous, compressible and heat conducting fluid, unsteady and compressive turbulent flow
2	Euler	non-viscous fluid
3	Garrick	laminar flow
4	Small transonic turbulences	slight turbulences
5	Prandtl & Glauert	laminar flow
6	Laplace	non-compressive fluid

There is a custom to classify mathematical models of flow round with regard to major constraints imposed during development of a physical model [10, 8]. These constraints lead to the situation that some properties of real fluids are disregarded but simpler mathematical models are obtained in return, however these simplified models also reflect the real flow round with sufficient accuracy. Table 1 summarizes classification of mathematical models with specification of the most popular models and with the major assumptions for the most complex Navier & Stokes model and with some auxiliary constraints for the remaining models.

3.2 Viscous model

The Navier & Stokes model is formulated for heat conducting fluids with unsteady (turbulent) and compressive flow. The assumption of an adequate model of turbulences, e.g. the Baldwin & Lomax one Eq. (5) leads to development of the most general model in terms of fluid mechanics. Models of that type are dealt with in [8, 9, 10, 11]

$$\frac{\partial F}{\partial t} + \frac{\partial G}{\partial x_j} = 0 \qquad (5)$$

where:

$$F = [\rho, \rho u_i, \rho e]^T$$

$$G = \begin{bmatrix} \rho u_j \\ \rho u_i u_j + p\delta_{ij} - \left(\frac{1}{Re}\right)\tau_{ij} \\ \rho u_i\left(e + 0.5 u_i u_j\right) - p u_j + \frac{1}{Re}\left(\frac{1}{Pr\ q_j} - u_i \tau_{ij}\right) \end{bmatrix}$$

where: ρ - fluid density, V – velocity with u_i coordinates (i = 1,2,3), p - pressure, δ_{ij} - Kronecker delta, Re – Reynolds number, Pr – Prandtl number, e – specific internal energy, q_j - (j = 1,2,3) coordinates of the heat flux, τ_{ij} – coordinates of the stress tensor.

Transformation of the model Eq. (5) makes it possible to achieve both the Reynolds and the Prandtl models that are successfully applied to numerical computations.

3.3 Euler model

When flow round in non-viscous fluid is considered and Re→ ∞, the equation Eq. (5) can adopt the form of Eq.(6):

$$\begin{gathered}\rho_t + div\,\rho V = 0\\ (\rho V)_t + div(\rho V)V + grad\,p = 0\\ (\rho e)_t + div[(p+\rho e)V] = 0\end{gathered} \quad (6)$$

with the following status Eq. (7):

$$e = \frac{p}{\rho(k-1)} + 0.5\rho V^2 \quad (7)$$

3.4 Potential-based model

For the potential-based model the assumption about non-turbulent (laminar) flow is adopted Eq. (8).

$$rot\,V = 0 \quad (8)$$

For the foregoing condition there exists such a parameter $\Phi(x, y, z, t)$ that Eq. (9):

$$\nabla\Phi \equiv grad\,\Phi = V \quad (9)$$

that in fluid mechanics is referred to as the velocity potential. When no additional assumptions related to the Φ potential, the Garrick model is achieved Eq. (10).

$$\frac{\partial^2\Phi}{\partial t^2} + \frac{\partial}{\partial t}V^2 + V\,\nabla(0.5V^2) = a^2\nabla^2\Phi \quad (10)$$

where:

$$a^2 = a_\infty^2 - (k-1)\left[\frac{\partial\Phi}{\partial t} + 0.5(\nabla\Phi)^2 - 0.5U_\infty^2\right]$$

The formula Eq. (10) serves as the basis to develop equations that describe flow at various velocity ranges. With the additional assumption Eq.(11):

$$\Phi = \Phi_\infty + \varphi \quad (11)$$

and Eq. (12)

$$mod\,\nabla\varphi \ll U_\infty; \quad mod\,\nabla\varphi \ll mod\,a_\infty \quad (12)$$

where φ stands for the velocity potential of turbulences. With the following assumption Eq. (13) for the φ potential

$$mod\,\nabla\varphi \ll mod\,[U_\infty - a_\infty] \quad (13)$$

and in consideration to (12), the equation (10) leads to the formula Eq. (14):

$$\frac{\partial^2\varphi}{\partial x^2} + \frac{\partial^2\varphi}{\partial y^2} + \frac{\partial^2\varphi}{\partial z^2} = \frac{1}{a_\infty^2}\left[U_\infty\frac{\partial}{\partial x} + \frac{\partial}{\partial t}\right]^2\varphi \quad (14)$$

It is the equation that is valid for flow round at both subsonic and supersonic velocities. Under the assumption that the flow is steady (laminar) Eq. (14) can be converted to the form Eq. (15):

$$(1 - Ma_\infty^2)\frac{\partial^2\varphi}{\partial x^2} + \frac{\partial^2\varphi}{\partial y^2} + \frac{\partial^2\varphi}{\partial z^2} = 0 \quad (15)$$

which is referred to as the Prandtl & Glauert equation. Under the assumption that the flow is non-compressible $(Ma_\infty = 0)$ the formula Eq. (15) leads to the Laplace equation Eq. (16)

$$\frac{\partial^2\varphi}{\partial x^2} + \frac{\partial^2\varphi}{\partial y^2} + \frac{\partial^2\varphi}{\partial z^2} = 0 \quad (16)$$

which can be written with use of the del operator in the form of Eq. (17)

$$\nabla^2\varphi = 0 \quad (17)$$

The form of Eq. (16) and Eq. (17) equations can be achieved after substitution of variables: $\tilde{x} = (1 - Ma_\infty^2)x;\ \tilde{y} = y;\ \tilde{z} = z.$

The application scopes for these models are shown in Fig. 11. The methods of that type include the Vortex Lattice Method [10] that can be applied to both subsonic and ultrasonic ranges of velocities.

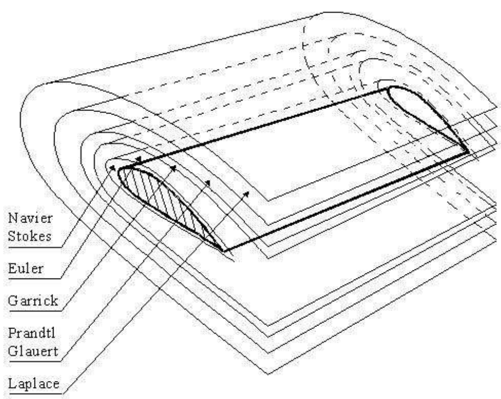

Fig. 11. Application ranges for the flow round models.

Use of the foregoing deliberations made it possible to carry out numerical computations for pressure distribution on the surfaces of Su-22 and MiG-29 aircrafts and to draw up aerodynamic characteristic curves for these structures. The computations were performed with use of VORLAX and PANAIR software packages.

3.5 Computation example

The VORLAX [10] and PANAIR [7] software packages were applied to compute distribution of pressures on the surfaces of Su-22 and MiG-29 aircrafts, pressure distribution is imaged in "Fig. 12" and "Fig. 13". The computations were carried out under the assumption that the Mach number Ma=0.4. Results of computations were compared against the result of experimental studies carried out in the aerodynamic tunnel owned by the Military University of Technology in Warsaw [12].

There is a number of field-based methods [13] and they can be classified under various criteria. From the viewpoint of their applicability to needs of aircraft flight mechanics the most attention is paid to the methods that enable distribution of air pressures on lifting surfaces that perform unsteady motions. In the papers [14, 15, 16 , 17, 18] there are some possible approaches to developed a numerical characteristics.

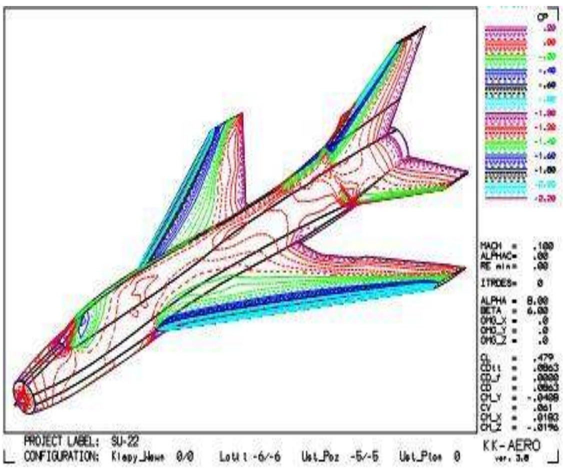

Fig. 12. Distribution of air pressures on the surface of the Su-22 aircraft.

The essence of that method consists in continuous generation of vortex trail. In contrary to iterative methods, where the initial geometry of the trail is assumed with expansion to infinity and its final shape is found out after a series of subsequent iterations, the UVLM (Unstady Vortex Lattice Method) method uses on-line determination of the trail geometry whilst time (or computation increment) exists as an explicit variable. It is assumed that the airfoil moves against steady or flowing air.

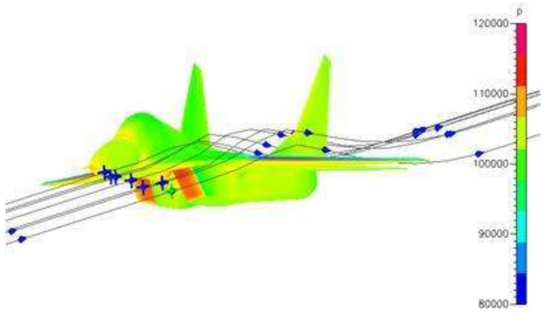

Fig. 13. Air pressure distribution and lines of airstreams on the surface of the Mig-29 aircraft.

The UVLM method is particularly suitable for analysis of loads that arise during execution of various manoeuvres (e.g. a roll or a fixed turn) as well as for determination of aerodynamic loads after sudden swiveling of tailpiece surfaces (or at other similar moments of flights). The example how the Finite Volume Method [19, 20, 21, 22] can be applied to determination of air pressure distribution on the aircraft surfaces is shown in "Fig. 13" [23].

The differential pressure can be determined directly, upon resolving an integral equation (for the DLM method) or indirectly, by application of the Kutta-Żukowski formula, similarly to the conventional VLM (Vortex Lattice Method) method [24], or from the Bernoulli equation [6].

3.6 Investigation in a wind tunnel

The Institute of Aviation Technologies within the Military University of Technology (WAT) operates a wind tunnel for low velocities of air and with the clearance diameter of ∅ 1.1m. The tunnel was used to investigate behaviour of an F-16 aircraft model "Fig. 14" for both symmetric and asymmetric round flow of air. The aircraft model was designed in the scale of 1:19 "Fig. 14".

Fig. 14. The F-16 aircraft model inside a wind tunnel.

The methodology for computation of aerodynamic characteristics was developed on the basis of [12]. Investigation results are shown in the tables and graphs that depict curves for the major aerodynamic parameters such as [12]:
$C_D= f(\alpha)$; $C_L = f(\alpha)$; $Cm = f(\alpha)$;
$E = f(\alpha)$; $C_L = f(C_D)$; $Cm =f(C_L)$.

4 Numerical analysis of the structure strength and free vibrations of MiG-29 and F-16 aircrafts

4.1 Numerical model of the MiG-29 aircraft

Panel methods and algorithms developed for reproduction of aircraft structures served as the basis for development of computation models "Fig. 15" to "Fig. 16" for examples of model visualization) for combat aircrafts in service of Polish Army.

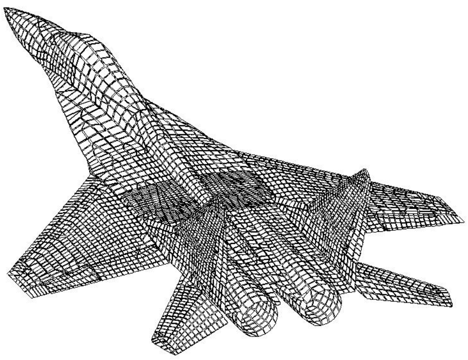

Fig. 15. Computation model for the Mig-29 aircraft.

Dynamic investigations of the MiG-29 aircraft as well as other airplanes being in service were carried out for the structure and strength properties of the aircrafts.

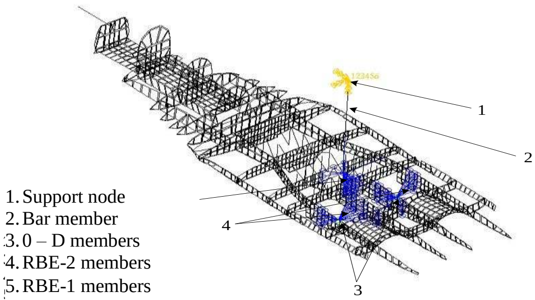

Fig. 16. Model of the internal structure for the Mig-29 aircraft.

The analysis was performed with use of the MSC Patran / Nastran software.

4.2 Results of analysis of free vibrations for the MiG-29 aircraft

The adopted numerical models were subjected to computations within the MSC Nastran software package. Frequencies of free vibrations are summarized in Table 2.

Table 2. Frequencies and forms of free vibrations.

Form			f [Hz]
Sym.	Asym.	Type	
+	-	aileron tilt	5.83
+	-	1^{st} flexural of a wing + 1^{st} flexural of a vertical tail unit	10.1
-	+	1^{st} flexural of the vertical tail unit + 1^{st} flexural of a wing	13.4
-	+	1^{st} flexural of a wing + 1^{st} flexural of a vertical tail unit	15.9
-	+	tail plane tilt	20.5

As compared to the methods of 1D or 2D digitalization [25, 26, 27, 28, 29, 30] it is the universal approach and can be applied to computation of dynamic properties for whichever structured, nearly in the natural way with no additional simplifications.

4.3 Modeling and strength analysis of damages structure of aircraft frame

The strength analysis of the vertical tail unit for the MiG-29 aircraft was imposed by the need to remedy that aircraft component "Fig.17". The completed analysis with appropriately construed results should provide the answer to the question whether the considered design of the vertical tail after having the subassembly repaired after former damage [23]. The plating for the vertical tail unit as well as the longerons are made of the carbon composite KMU-4L (КМУ-4Л).

Fig. 17. The damaged vertical tail unit of the MiG-29 aircraft after an emergency landing.

The major metallic component is the cantilever for the front spar made of the D19czAT (Д19чАТ n) aluminium alloy.

4.4 Description of the computation model

The numerical analysis for the aircraft tailpiece assumes loads from the load envelope “Fig. 18”. The computation model for the vertical tail unit has been developed within the PARTAN package on the basis of the tailpiece geometry. The example of result from the stress analysis is depicted in “Fig. 19”

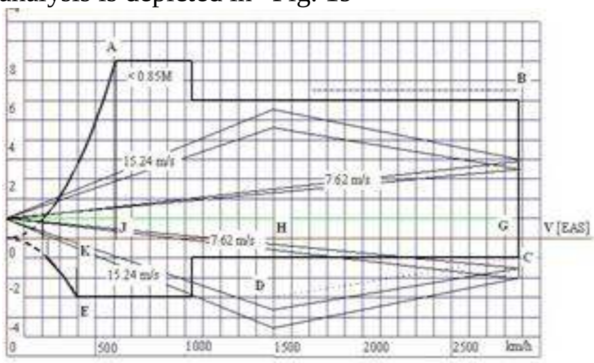

Fig. 18. envelope for the MiG-29 aircraft according to the MIL-A-8861 B (AS) regulations.

The FEM model for the cantilever of the head spar suitable for further numerical analyses has been developed on the basis of a CAD model.

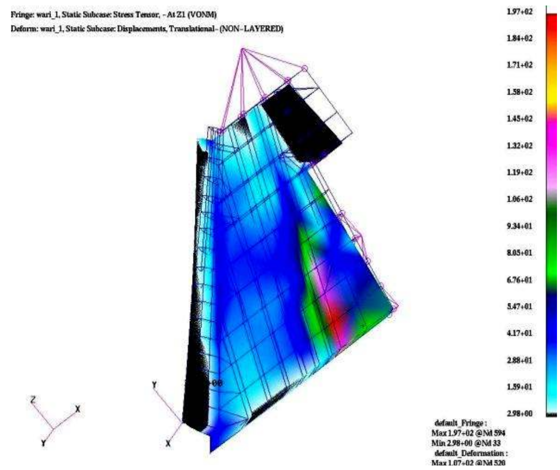

Fig. 19. Stress within the plating structure for the vertical tail unit of the Mig-29 aircraft

Results from the numerical analysis of the cantilever under the prescribed load (for the conditions and in “Fig. 18”) for both damage-free and damaged structure of the vertical tail unit are summarized in Table 3.

Table 3. Results from the analysis of the head cantilever

Damage-free plating of the fin	
Maximum displacement [mm]	Reduced stress σ_{zred} [MPa]
1.91	10.5÷20.5
Damaged plating of the fin	
Maximum displacement [mm]	Reduced stress σ_{zred} [MPa]
9.41	229÷343

5 Conclusions

The disclose methodologies have been developed with the aim to apply them for assessment of technical condition demonstrated by aircrafts that have been in service for the Polish Air Forces for more than twenty five years as well as F-16 aircrafts that are currently introduced to regular operation. The disclosed methodology for examination of thin-walled aircraft structures can be easily applied to development of adequate computation models suitable for the analyze status of flights and advance of dynamic deterioration of other airplane structures, including Tu-154M.

References

[1] Ziętarski S., "AI-based optimization method for the analysis of co-ordinate measurements within integrated CAD/CAM/CAE systems", ImechE 2003.

[2] Olejnik A., (Development of a computer-aided system for analysis of maintainability and repair technologies for aircrafts and helicopters operated by Polish Air Forces, Warsaw, 1994-1997, in Polish

[3] Kiciak P., Fundamentals for modeling of curves and surfaces, WNT Publishing House, Warsaw, 2000, in Polish

[4] Electronic Data Systems Corporation, UNIGRAPHICS, Modelling, GRIP, Maryland 2000.

[5] Kandil O.A., Mook D.T., Nayfeh A.: Non-linear prediction of aerodynamic load on lifting surfaces. Journal of Aircraft, Vol. 13, No 1, 1976.

[6] Katz J., Plotkin A., Low - speed aerodynamics. Second edition, Cambridge University Press, 2001.

[7] Rom J.: High angle of attack aerodynamics, subsonic, transonic and supersonic. Springer - Verlag, 1992.

[8] Rohatyński E.: The Boundary Element Method (BEM) for fluid mechanics, Bulletin of the Institute of Aviation) Nr 145, pp. 136-144, 1996, in Polish.

[9] Wu J.C., Wahbach M.M.: Numerical solutions of viscous flow equations using integral representations. Lecture Notes in Physics, vol. 59, Springer, 1976.

[10] Miranda L.R., Elliot R.D., Baker W.M.: A generalized vortex lattice method for subsonic and supersonic flow applications. NASA CR 2865, 1977.

[11] Goraj Z., Molicki W., Paturski Z., Modelling of pressure distribution on lifting surfaces with use of the superpanel method, The 27th Symposium 'Modelling in Mechanics, 1988, in Polish.

[12] Olejnik Olejnik A. at al., Experimental characteristics of the F-16 aircraft model in symmetric flow round, Report of the Military University of Technology (WAT), Warsaw 2005 (not published), in Polish.

[13] Goraj Z., Molicki W., Paturski Z., Modelling of pressure distribution on lifting surfaces with use of the superpanel method, Proceedings from the 27th Symposium 'Modelling in Mechanics', 1988, in Polish.

[14] Electronic Data Systems Corporation, UNIGRAPHICS, Modelling, GRIP, Maryland 2000.

[15] Goetzendorf-Grabowski T., Application of the panel-based method to compute supersonic aerodynamic characteristics of aircrafts with use of flight simulators,Warsaw Universityof Technology, in Polish

[16] Goraj Z., Pietrucha J., Modifications of the flow round model for improvement of the panel-based method, Bulletin of the Institute of Aviation), vol. 4/1993 (135), in Polish.

[17] Dowell E.H., Ueda T.: Doublet point method for supersonic unsteady lifting surfaces. AIAA Journal, Vol. 22, No. 2, pp. 179-186, 1984.

[18] Konstadinopoulos P.A. et al.: A vortex - lattice method for general unsteady aerodynamics. Journal of Aircraft, Vol. 22, No 1, 1985.

[19] Fluent User's Guide, www.fluent.com

[20] Chung T.J.: Computational Fluid Dynamics. Cambrige University Press, Cambrige, 2002.

[21] Versteeg H.K., Malalasekera W.: An introduction to Computational Fluid Dynamics. The Finite Volume Method. Longman Scientific Technical, Essex, England, 1995.

[22] Eymard R., Gallouet T., Herbin R.: Finite Volume Methods , LATP, Marseille, 1997.

[23] Olejnik A., Application of digital models developed for aircrafts to analysis of loads, strength issues and vibrations of aircrafts with sophisticated aerodynamic and structural properties, PBG nr 0T00A 038 18, Warsaw, 2002, in Polish.

[24] Hedman S.G.: Vortex lattice method for calculation of quasi steady state loadings on thin elastic wings. Rep. 105, Aeronautical Research Institute of Sweden. Rep. No. 105, 1965.

[25] Błaszczyk J., Dynamic model of an aircraft with variable geometry of wings suitable for examination of free vibrations by means of the Finite Element Method, Bulletin of the Military University of Technology (WAT), No. 36, vol. 3, 1987, in Polish.

[26] Dżygadło Z., Błaszczyk J.,- Dynamic model of a deformable aircraft for suitable to analysis of free vibrations by means of the finite element method. Biul.WAT XXVI, 4, 1977. J.Tech.Phys. 18,2,1977, in Polish.

[27] Dżygadło Z., Błaszczyk J., Nowotarski I., Olejnik A., Sobieraj W., Studies within the nodal problem No. *02.01 entitled: 'Fundamentals for mechanic* properties of materials, machinery, structures and technological processes, IPPT PAN, Warsaw, 1986 in Polish.

[28] Dżygadło Z., Nowotarski I., Olejnik A., A discrete model for aircraft deformation applicable to investigation of free vibrations. Bulletin of the Military University of Technology (WAT), No. 33, vol. 11, 1984, in Polish.

[29] Dżygadło Z., Nowotarski I., Olejnik A., Analysis of free vibrations for a deformable aircrafts with constrained steering surfaces, Bulletin of the Military University of Technology (WAT), No. 33, vol. 11, 1984, in Polish

[30] Dżygadło Z., Olejnik A., Numerical strength-oriented modeling of axially-symmetric panel and sheath arrangements, Bulletin of the Military University of Technology (WAT), No. 29, vol. 12, 1980)., in Polish.

Collaborative multi-partner modelling & simulation processes to improve aeronautical product design

E.H. Baalbergen, J. Kos and W.F. Lammen
National Aerospace Laboratory NLR, Amsterdam, the Netherlands

Keywords: secure cross-organisational collaborative engineering, collaborative modelling and simulation, surrogate modelling, Behavioural Digital Aircraft, Crescendo

Abstract

Designing a modern aircraft, including all its systems and components, is a tremendous collaborative engineering activity involving teams of engineers from various disciplines working concurrently across organisational and geographical boundaries. To achieve the challenging objectives of contemporary and future aeronautics, and to maintain global industrial leadership, a high level of integrated system design of the aircraft is needed. This requires a higher level of collaborative engineering through modelling and simulation along the supply chain to improve cost and time efficiency.

To achieve a step change in the way multi-disciplinary teams working collaboratively in an extended enterprise carry out modelling and simulation processes, the 'Behavioural Digital Aircraft' (BDA) concept has been developed. This paper presents this concept and the emerging needs for innovative collaboration technologies as well as advanced modelling and simulation technologies. This paper next discusses the security constraints that teams of collaborating engineers face in practice and that may hamper multi-partner collaborative engineering efforts, and introduces a practical interoperability solution to deal with the security constraints. This paper finally describes the application of surrogate modelling as an effective method to enable collaborative modelling and simulation activities in the extended enterprise, while allowing partners to protect their intellectual properties. The effectiveness of the surrogate modelling and the interoperability solution are demonstrated in a realistic design case following the BDA concept.

1 Introduction

During the past century, aircraft have evolved into complex systems comprising multiple even more complex subsystems. Building aircraft evolved from pioneering by a single man in a barn, into tightly orchestrated multi-disciplinary, multi-engineer, and multi-partner concurrent and collaborative engineering activities that cross organisational and national boundaries. Key steps in the concurrent and collaborative engineering process are the transfer of requirements and the sharing of the digital mock-up along the aircraft development life-cycle.

To meet society's needs with respect to safety, comfort and environmental impact, such as formulated in European Aeronautics: a vision for 2020[7] and Flightpath 2050 *Europe's Vision for Aviation*[6], and to maintain global industrial leadership, a higher level of cost and time efficient integrated system design of the aircraft is needed.

Modelling and simulation by multi-disciplinary teams in the collaborative multi-partner enterprise enables to achieve cost and time-efficient development of new aeronautical products. However, collaborative modelling and simulation activities are often hampered by the protection of intellectual property rights (IPR) and the variety of practices and constraints of different companies in aeronautical industry. The Behavioural Digital Aircraft (BDA) concept proposes using essentially distributed dataset and platforms to collaboratively mature the definition of aircraft behavioural characteristics, while respecting the company practices and constraints in aeronautical industry [5].

Mastering the aircraft's behaviour collaboratively considerably impacts the way of working of many engineers from different organisations and disciplines involved in the design of a new aircraft type and its systems and components. It impacts both the frequency and the contents of the exchange of information. For example, joint behaviour analysis of the aircraft manufacturer's overall design and the suppliers' detailed designs is a step change in the exchange of information compared to current practices. Such simultaneous analysis allows maturing the requirements earlier in the design process, thereby reducing the risk of potential rework later. Specific BDA supporting technologies addressing the increased frequency and type of information exchange are needed to respect the security constraints in aeronautical industry as well as the protection of the intellectual property contained in detailed behaviour models.

This paper explains the notion of the BDA, discusses the security constraints that teams of collaborating engineers are involved with, and presents two complimentary solutions that enable engineering teams to collaborate in the context of the BDA.

2 The Behavioural Digital Aircraft

New possibilities of collaborative engineering and modelling and simulation technologies have been investigated and demonstrated in the EU FP7 CRESCENDO project [3][5]. The CRESCENDO project initiated a step change in the way multi-disciplinary teams working collaboratively in an extended enterprise carry out modelling and simulation activities by developing the notion of the BDA [12]. The BDA consists of three key concepts, namely BDA data set, platforms, and users, as illustrated in Fig. 1.

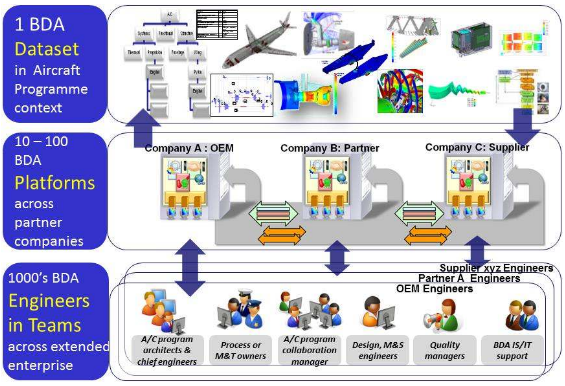

Fig. 1 Illustration of the Behavioural Digital Aircraft concept as developed in CRESCENDO [5].

The BDA data set is a multi-partner, multi-level, multi-disciplinary, multi-quality behavioural digital representation of the evolving aircraft and its constituent systems and sub-systems. A single, but distributed and federated BDA data set would typically exist and evolve for a given major aircraft development program.

BDA platforms implement collaborative services and behavioural multi-physics simulation capabilities to manage, manipulate, preserve, reuse and enrich the models and associative data needed to create, evolve and mature the BDA data set. CRESCENDO defined a generic BDA architecture specification that any given BDA platform implementation should comply with. Different aircraft and engine manufacturers, partners and suppliers need to use only part of the complete functional specification, and may choose different vendor solutions to implement the BDA platform for their organisations. Typically, multiple interoperable BDA platforms will exist across the extended enterprise.

Finally, there could typically be thousands of BDA users, collaborating in teams across the extended enterprise, creating and sharing their information more efficiently through the BDA platforms, to create and evolve the BDA data set.

Tens of realistic multi-partner collaborative scenarios from the various stages of the lifecycle of aircraft development have been demonstrating the BDA concept at the CRESCENDO Forum [4][11][18]. In addition, Industrial Deployment labs were set up, providing Information and Communication Technology (ICT) infrastructures that facilitate the implementation of the demonstrators in true industrial settings.

3 Security constraints

The implementations of the BDA platforms are largely enabled by state-of-the-art digital analysis and modelling and simulation tools and technologies. ICT not only supports the ever more complex design activities in terms of ever increasing computing power and data storage capacity, but also provides ever increasing capabilities for collaboration among teams of aeronautical engineers. Over the past decades, the collaboration capabilities have evolved from e-mail, simple file exchange, and dedicated network connections into integrated multi-user facilities such as web conferencing, extended enterprises, and collaborative product life-cycle support and workflow systems.

Despite the available collaboration support, security constraints often hamper the seamless execution of collaborative engineering activities across organisational boundaries, and hence threaten the interoperability among BDA platforms. For example, multi-partner workflows ideally span the networks of the partners involved and run smoothly across their organisations. In practice, however, security measures impose restrictions that prohibit seamless communication among engineers and their workflows. The ideal situation and the less ideal actual situation are depicted with the help of a realistic collaborative scenario in Fig. 2. A solution to deal with the actual situation is presented in section 4.

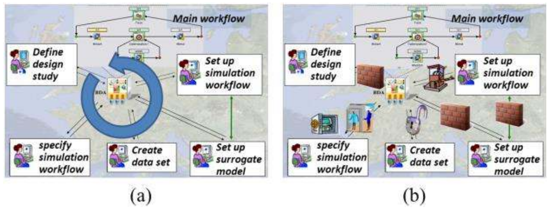

Fig. 2 Example collaborative scenario. Ideally, the activity and data flow runs smoothly across the organisations (a), but in practice security measures such as firewalls hamper a seamless flow (b).

Security constraints are of paramount importance to protect an organisation's assets, and hence may not, and generally cannot, be bypassed. The constraints serve to ensure IPR, to protect ownership, to safeguard the ICT infrastructure against viruses and illegal access, to comply with regulations such as export controls, to maintain security policies, trust, and non-disclosure agreements that apply for particular customers and in specific secure collaboration contexts, and to maintain licensing policies (e.g., commercial software licenses generally prohibit third parties to use the licensed software). Simply requesting or even requiring a collaborating partner to loosen its security constraints and corresponding protection measures to enable engineers to cross organisational boundaries is not an option.

Engineers already have to deal with the security constraints in their daily work, such as badges and passwords, security rules included in employment contracts, the impossibility to quickly install non-standard software on the workplace PCs, and ICT security measures such as firewalls and proxy servers. In practice, security constraints, and in particular the network access restrictions that support those constraints, throw up barriers for smooth cross-organisational collaborative engineering.

Solutions for collaboration over organisational boundaries have been developed and applied throughout the years in collaboration projects. These solutions typically require extensive tailoring to the collaborative situation, such as special contracts and agreements for accessing an organisation's resources through, for example, a combination of virtual private networking, web services, special fire-wall settings, and dedicated protocols and software. Such solutions, however, are valid for specific situations only and generally are costly and require the involvement of security officers, juridical experts and ICT network specialists.

In the CRESCENDO project, the experiences with respect to collaboration barriers posed an urgent need for a rapidly available solution that enables engineers to collaborate across organisational boundaries, thereby dealing with the network access restrictions while still obeying the security constraints. A practical technical solution to support seamless execution of collaborative cross-organisational workflows while respecting the most common security constraints has been developed in the BDA context. This solution is described in the next section. In addition, a complementary solution for protecting a company's IPR, namely taking detailed modelling and simulation capabilities into a distributable black-box surrogate model, is described in section 5.

4 Interoperability solution respecting security constraints

As indicated in the previous section, situation-specific solutions that support the execution of cross-organisational workflows involving network restricted partners have been developed, in particular in projects that involved collaborative engineering, such as the EU projects CESAR[2] and VIVACE[9]. In the context of CRESCENDO, promising solutions have been further combined, generalised and matured into the so-called 'Building blocks for mastering network Restrictions involved in Inter-organisational Collaborative engineering Solutions', or BRICS for short. BRICS facilitates smooth execution of collaborative engineering workflows across organisations and BDA platforms [1].

BRICS comprises a protocol and supporting software that may be used in combination with existing workflow management systems and secure data sharing repositories to transform local workflows into cross-organisational collaborative workflows. Such workflows define and orchestrate multi-user collaborative engineering activities in terms of the chain of tools and processes to be executed by various engineers from various disciplines working at various organisations. BRICS supports the coordinated, efficient and secure execution of collaborative workflows by enabling the execution of tools or parts of the chain to be assigned to engineers working in other organisations.

One of the key features of BRICS is that it enables remote engineers, including those who "suffer" from network access restrictions, to fully participate in collaborative workflows. Here, BRICS deals with and obeys the security constraints, policies, rules, and measures of the participating organisations. To allow an organisation to have full control over their own resources, BRICS supports a man-in-the-loop to decide upon whether or not to allow a workflow that runs elsewhere to trigger tools, to access information and to use computing resources within the organisation. To achieve this, BRICS notifies a remote engineer when applicable, and enables the notified engineer to either initiate the execution of a single-task job or to arrange for automated repeated execution of similar tasks in a multi-task job under his or her own control. BRICS keeps the extra burden placed on the engineers involved to a minimum by automating actions such as sending and handling notifications and transferring data as much as possible, yet within the security constraints of the organisations involved.

BRICS is based on a simple protocol that arranges the execution and data flow between the orchestrating workflow in one organisation and a remote engineer in another organisation who is assigned to execute a tool from or part of the workflow. A sequence diagram for this protocol is depicted in Fig. 3. An 'end user' application is illustrated in Fig. 5.

The diagram shows two actors Workflow and Remote engineer, with a Shared data repository in between. The cross-organisational collaborative Workflow acts as 'master' that issues a command to the Remote engineer acting as 'slave'.

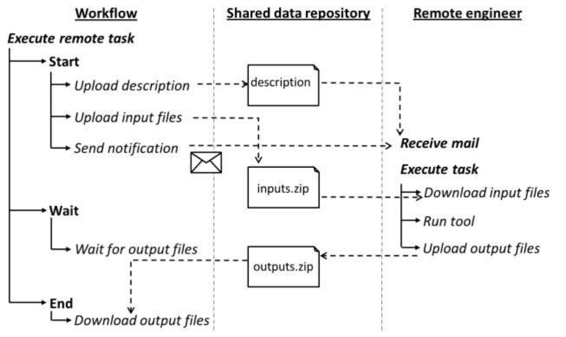

Fig. 3 Simplified sequence diagram of the BRICS protocol for single-task jobs

BRICS provides the master with three commands for outsourcing the execution of a tool or part of the workflow to the slave and to handle the notification and data transfers involved: Start, Wait, and End. The Shared data repository serves to exchange the data files involved among the master and the slave.

The Start command uploads the specified input data for the remote task to the Shared data repository. Next, it sends a notification (e.g., an e-mail message) to the Remote engineer. Upon receipt of the notification, the Remote engineer may decide upon whether or not to execute the task. The engineer typically decides to participate based on earlier agreements and on knowledge of the remotely orchestrated job. The engineer next fetches the input data, and performs the job using the local BDA platform. Finally, the results are uploaded to the Shared data repository. The slave's part of the protocol can be handled manually as well as automatically, under the Remote engineer's control.

The Wait command polls for the expected results of the remote task to be present on the Shared data repository. The master uses the Wait command to synchronise the Workflow execution with the remote task.

The End command retrieves the outputs from the Shared data repository. The master uses the End command to fetch the outputs of the remote task, and next proceeds with the execution of the workflow using the outputs as if the task was executed locally.

The protocol described thus far is suitable for the execution of single-task jobs. If the same protocol were applied for a loop, the Remote engineer would repeatedly be notified to execute the same task again with slightly different input data. Since the handling of a consecutive series of similar notifications is cumbersome, time consuming and error prone, BRICS has an extended protocol for gracefully dealing with multi-task jobs (cf. Fig. 4).

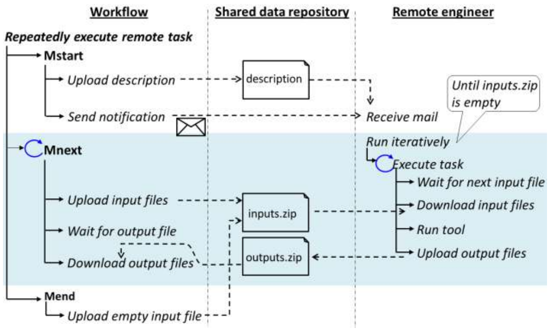

Fig. 4 Simplified sequence diagram of the BRICS protocol for multi-task jobs

This protocol is based on the three commands Mstart, Mnext and Mend. The master used the Mstart command to notify the Remote Engineer once, who is expected to repeatedly (and possibly automatically) execute the same task with different successive inputs. The master next iteratively uses the Mnext command to upload the inputs for an iteration, to wait for the results of the iteration to be present, and to finally fetch the results. The sequence of iterations is terminated using the Mend command.

The BRICS commands support the application of the protocols for single-task and multi-task jobs in workflows, tools and scripts that orchestrate the execution of (engineering) tools across multiple organisations. Workflows may be equipped with the Start, Wait, and End (and Mstart, Mnext, and Mend) commands to outsource the execution of particular tools or parts of the workflow, and as such may be transformed from local into cross-organisational collaborative workflows. An example transformation is illustrated in Fig. 5.

BRICS makes use of existing data repositories and notification mechanisms. Example data storage and exchange solutions that may play the role of Shared data repository are shared file systems, File Transfer Protocol

(FTP) servers, products such as Microsoft SharePoint, and the CRESCENDO BDA server based on Eurostep Share-A-space [12]. These servers typically provide the means for settings up a secure shared data repository. The basic notification mechanism used by BRICS is e-mail. BRICS can directly link to Simple Mail Transfer Protocol (SMTP) servers in several configurations. BRICS also provides means for relaying notifications if e-mail traffic is restricted.

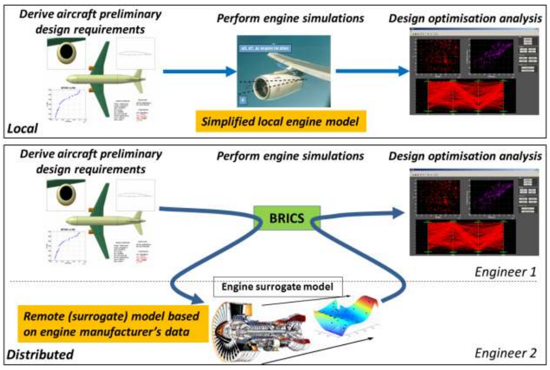

Fig. 5 BRICS supports the transformation of a local tool chain (upper) into a distributed tool chain (lower), where a local simplified model is replaced by a remotely available surrogate model

In the CRESCENDO project, BRICS has been successfully applied during the development of collaborative scenarios and solutions as well as in the final results of these efforts. Although most of the engineers involved in the development had to deal with network access restrictions, BRICS enabled them to quickly and readily use and test their in-house solutions with other partners' solutions in an interoperable way. As such, the engineers were enabled to work collaboratively early in the development phase. The final results have been demonstrated in several cross-organisational collaborative aeronautical design workflows that were realised as BDA implementations and that involved an aircraft manufacturer and its suppliers, including:

- A coupled modelling and simulation process among Airbus and NLR as part of the aircraft-engine preliminary design workflow[11]. This process is used as example in the next section. Cranfield University and Dassault Systèmes provided the simulation tooling on aircraft level running at Airbus. During the test phase, these partners used BRICS to test their solutions.
- In coupled modelling and simulation processes as part of demonstrators for the 'Collaborative approach to manage Pylon Trade-Off Studies and Aerostructural Optimization monitoring', among Airbus and the Onera premises in Lille and Paris[17][18]. SAMTECH provided the optimisation tooling on aircraft level running at Airbus. During the test phase, SAMTECH used BRICS to test its tooling.
- Virtual testing & virtual certification, enabling Airbus to link with shared BDA data models[13].

BRICS has been used within, and integrated with commercial as well as proprietary tools to transform optimisation loops and other 'low and medium frequency' workflows [14][15] into cross-organisational collaborative workflows. BRICS has been applied from within (shell) scripts, Visual Basic (VBA) scripts, MATLAB code, and the workflow and optimisation products Isight/SEE, BOSS Quattro, AirCADia, and SPINEware. BRICS has been installed and used in industry (Airbus and SAAB), at research institutes (NLR, DLR, ONERA in Paris as well as Lille, and Cranfield University), at software providers (SAMTECH and Dassault Systèmes), and a Small to Medium enterprise (PARAGON).

5 Surrogate modelling to facilitate industrial collaboration

As explained in section 2, the BDA concept gives rise to application of innovative collaborative modelling and simulation processes, enabling cost and time efficient aircraft development. Present models and simulation processes have been advanced to take full advantage of the BDA concept. Some of these advancements have been illustrated and achieved on a preliminary design case that was developed in the CRESCENDO project[11], in which the aircraft-engine requirements are matured collaboratively.

During the aircraft preliminary design phase the aircraft manufacturer needs to provide the engine manufacturer with a set of engine requirements for driving the development of consequential engine configurations. In the meantime, the engine manufacturer is required to develop future engine design concepts aligned with requests from the aircraft manufacturer. The product design process can be improved if the behaviours of the aircraft and engine designs are analysed simultaneously and in an integrated way: optimising the aircraft design using a flexible engine model, referred to as a ‘rubber engine’[16]. The application of a rubber engine is a common step during the preliminary design phase but usually does not involve detailed engine behaviour as predicted by the engine manufacturer.

Aero-engines are complex systems and their behaviour can be predicted sufficiently accurately only after the particular engine design has been reviewed and evaluated by engine experts. Therefore it is cumbersome to integrate this process into the aircraft design process directly. Furthermore, the engine is developed by a company other than the aircraft manufacturer. Protection of intellectual property prevents the engine manufacturer from sharing the complete engine design analysis process with the aircraft manufacturer.

A solution to this problem is the use of surrogate modelling to support the collaboration[11]. In this context, a surrogate model is considered a black-box abstraction of a database of detailed (rubber) engine simulation inputs and results representing the engine design and behaviour. The Surrogate model is ready for use with very low computation time. With a surrogate model, the aircraft manufacturer has the flexibility to evaluate various engine designs, while the intellectual property of the engine manufacturer is respected and kept in-house. The engine surrogate model is specifically useful for extensive trade-off studies at aircraft level as it requires low computational effort.

In the context of the aircraft-engine preliminary design case, the engine surrogate model is defined as an analytical expression of the behaviour of an engine. The behaviour of the engine itself can be predicted by conducting real-world experiments with the engine or by means of simulation using detailed system simulation models. Since the real-world experiments are too expensive, simulation is used as source for the surrogate model. Several engine system simulations are performed for various input settings, resulting in a data set of listed input-output combinations, called data points. One data point represents, for example, one design configuration with the corresponding engine behaviour represented in the output values. The sampling of the data points is based on a so-called Design-of-Experiment (DoE), which should provide sufficient variability in the input values to cover the desired input range of the surrogate model. Once the data set has been produced, a surrogate model can be derived that matches the input-output combinations using data fitting techniques, such as polynomial regression. The surrogate model predicts the system output in the available data points but is also able to predict output values in between these data points. This is useful to evaluate (theoretical) designs that have not been simulated yet using the detailed engine models.

The development of the engine surrogate model for use in the aircraft-engine preliminary design workflow involved three steps performed by the three partners involved (cf. Fig. 6):

(1) Creating a data set of detailed engine simulations, by Rolls-Royce Deutschland;
(2) Creating the surrogate model, by NLR; and
(3) Integrating the surrogate model with the aircraft preliminary sizing tool used by the aircraft manufacturer, by Airbus France.

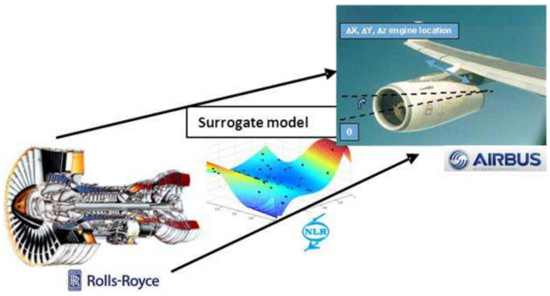

Fig. 6 Integration of the engine surrogate model into the aircraft sizing tool as applied by the aircraft manufacturer.

For the engine surrogate model, Rolls-Royce performed simulations of 400 engine configurations using their own automated preliminary design process (Computational Preliminary Power Plant Optimisation, C3PO[10]). Six input parameters (Maximum take-off thrust, Maximum climb thrust, Maximum cruise thrust, Fan diameter, Stator outlet temperature, and High pressure compressor exit temperature) have been varied within predefined ranges using a Latin hypercube sampling DoE method. After the automated calculation of the 400 engine configurations, the results were reviewed and filtered by an engine performance specialist. Finally, a data set, including the seven output parameters Engine weight, and both Specific fuel consumption and By-pass ratio at take-off, climb and cruise, was produced.

NLR created the engine surrogate model. Based on the produced data set, a 6-dimensional input space and a 7-dimensional output space have been identified. The NLR data fitting tool MultiFit [19] was used for analysing the application of various data fitting methods, in order to produce the best fit for the engine surrogate model. The surrogate model was next validated and improved iteratively in collaboration with Rolls-Royce, by evaluating additional engine configurations 'outside' the original data set.

Airbus used the preliminary sizing tool SIMCAD for preliminary design optimisation of a conceptual aircraft configuration. The engine surrogate model has been integrated in the SIMCAD tool using the AirCADia model-based design and optimisation tool from Cranfield University [8], to account for robust optimisation and variability of engine performance requirements respectively. The engine surrogate model, which predicts important design parameters such as engine weight, enables the aircraft sizing model to take advantage of the inclusion of a more detailed engine model during the optimisation.

To prepare for deployment in industrial preliminary design processes, the engine surrogate modelling method has been integrated in a cross-organisational aircraft-engine preliminary design workflow between Airbus as aircraft manufacturer, Rolls-Royce as engine manufacturer, and NLR as simulation service provider; see Fig. 7.

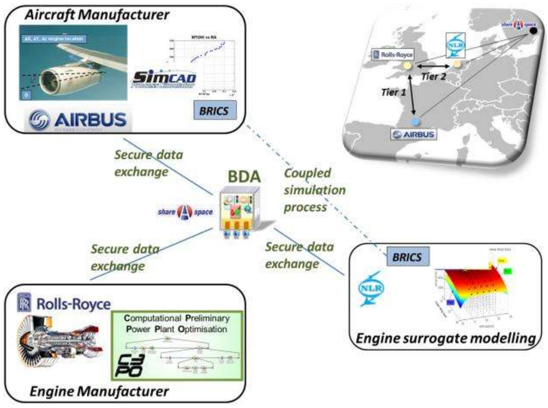

Fig. 7 Cross-organisation aircraft-engine preliminary design workflow containing engine surrogate modelling.

In the CRESCENDO project, the workflow has been set up according to the BDA paradigm, and has been demonstrated in an industrial setting. The cross-organisational workflow demonstrates collaboration on two different levels: the creation and the execution process of the engine surrogate model.

The creation process of the engine surrogate model as explained above has been performed by sharing several iterations of the engine data set between Rolls-Royce and NLR through the BDA. Furthermore the reviewing and approval process of the surrogate model by the engine manufacturer and publishing it finally to the aircraft manufacturer has been performed through the BDA.

The actual execution process of the engine surrogate model has been performed in a cross-organisational co-simulation. The interfaces of the surrogate model have been integrated into the SIMCAD/AirCADia program that runs the aircraft preliminary design optimisation loop at Airbus while the surrogate model resides at NLR. This cross-organisational optimisation loop is a practical example of a BRICS enabled collaborative workflow, in which the IPR protection of the simulation provider and that of the engine manufacturer are respected. The loop combines the two complementary methods (surrogate modeling and interoperability respecting security constraints) presented in this paper into one demonstration.

The workflow illustrated a new collaborative approach in which the aircraft and engine manufacturers and simulation service providers collaboratively mature the engine requirements during the preliminary design phase. This approach contributes to the removal of non-value added rework cycles in early and later design stages. Specifically the application of an engine surrogate model is advantageous as it allows for extensive trade-off studies at aircraft level because of the low computational effort while the intellectual property of the engine manufacturer is respected.

The engine surrogate modelling workflow has been developed as a demonstrator in the context of the CRESCENDO test case scenario: ‘A collaborative approach to manage the maturity indicator for design convergence between the Airframe- & Engine-Manufacturer’. A total of eleven partners were involved in the setup of this scenario.

6 Conclusion and future work

The overall Behavioural Digital Aircraft (BDA) concept provides innovative approaches to improve collaboration in simulation process orchestration and associated data management to help develop new aeronautical products in a cost and time efficient way.

This paper described BRICS solutions for secure collaborative multi-partner modelling and simulation processes in the BDA context. The results show how aeronautical engineers experience the benefits of seamless collaborative modelling and simulation across organisational boundaries for their daily work. One conclusion that can be drawn from the experiences is that BRICS successfully supports cross-organisational secure collaborative engineering, thereby catering for participation of partners with network restrictions while obeying the increasingly strong security constraints. The solutions realised with BRICS are suitable for collaboration among industry and its suppliers, including small to medium enterprises.

The aircraft-engine preliminary design case involving engine surrogate modelling illustrated that surrogate modelling is a key technology to enable collaborative modelling and simulation activities in the extended enterprise. It caters for extensive trade-off studies at aircraft level and it reduces non-value added rework cycles in early and later design stages, while respecting intellectual property rights of the partners involved.

Further exploration and application of the BDA concept in aircraft preliminary design will radically improve the way in which modelling and simulation is performed within aircraft design processes. The European Framework Project TOICA (‘Thermal Overall Integrated Conception of Aircrafts’), which is envisaged to start in September 2013, has gathered 32 partners to work on this radical improvement in the thermal domain by simultaneously modelling and simulating in a collaborative environment the thermal behaviour of aircraft airframe systems, equipment and components. TOICA’s ambition is to:

- Develop the means to improve and optimise the whole aircraft thermal behaviour and deduce the relevant change to bring in the overall architecture of the systems.
- Transform the current thermal analysis to a complete transverse and collaborative thermal process impacting the overall aircraft design thanks to early collaborations of system and equipment providers.
- Improve the collaborations among all actors for a deeper integration of the thermal constraints in the architecture and preliminary design phases.
- Extend the Behavioural Digital Aircraft environment with new capabilities able to support architect decisions during the trade-off to hold at aircraft and component levels.

Benefitting from results from a range of previous European projects, such as the collaboration results presented in this paper, TOICA is a key part of the overall roadmap to create and manage the behavioural modelling of aircraft, thereby supporting the Vision 2020 and FlightPath 2050 Vision.

Acknowledgements

The research leading to these results has received funding from the European Union's Seventh Framework Programme FP7/2007-2013 under grant agreement no. 234344 (CRESCENDO). The authors would like to acknowledge all colleagues from the CRESCENDO project partners who contributed to the success of the collaborative design studies that provided valuable input for the research described in this paper. The authors also thank the TOICA Consortium for providing its information.

References

[1] Baalbergen E.H., Lammen W.F. and Kos J.: "Mastering Restricted Network Access in Aeronautic Collaborative Engineering across Organizational Boundaries", PDT Europe 2012, The Hague, the Netherlands, 25-26 September 2012.

[2] Baalbergen E.H., Vankan W.J. and Kanakis A.: "A practical approach for coordination of multi-partner engineering jobs in the design of small aircraft", CESAR Special Issue of Journal Czech Aerospace Proceedings / Letecký zpravodaj, Journal for Czech Aerospace Research, No. 3, November 2009, p.5-9.

[3] Coleman P.: "Innovations in collaborative modelling and simulation to deliver the Behavioural Digital Aircraft: A summary of results from the CRESCENDO project", PDT Europe 2012, The Hague, The Netherlands, 25-26 September 2012.

[4] Coleman P.: CRESCENDO consortium partners, Innovations in collaborative modelling and simulation to deliver the Behavioural Digital Aircraft, CRESCENDO Forum Participants Handbook, Toulouse, France, June 2012.

[5] Coleman P. and Tabaste O.: "The behavioural digital aircraft vision for simulation in collaborative product development", 2013 MSC Software Users Conference, Irvine, USA, 7-8 May 2013, and Gaydon, UK, 15-16 May 2013.

[6] EU High Level Group on Aviation Research: *Flightpath 2050. Europe's Vision for Aviation: Maintaining Global Leadership & Serving Society's* Needs, European Commission, 2011.

[7] EU Sherpa Working Group: European Aeronautics: European Aeronautics: Vision for 2020: Meeting Societies Needs and Winning Global Leadership, European Commission, 2001.

[8] Guenov M.D., Nunez M. and Gondhalekar A.C.: "Comparing Design Margins in Robust and Deterministic Design Optimisation", in, C. Poloni, D. Quagliarella, J. Périaux, N. Gauger and K. Giannakoglou (Eds.), EUROGEN 2011. Evolutionary and Deterministic Methods for Design, Optimisation and Control with Applications to Industrial and Societal Problems, Capua, Italy, 2011

[9] Kesseler E. and Guenov M. (eds.): Advances in Collaborative Civil Aeronautical Multidisciplinary Design Optimization, Progress in Astronautics and Aeronautics Series, 233, American Institute of Aeronautics and Astronautics, Reston, VA, 2010.

[10] Kupijai P., Bestle D., Flassig P. and Kickenweitz D.: "Automated multi-objective optimisation process for preliminary engine design", ASME 2012 turbine technical Conference & Exposition (TurboExpo 2012), GT2012-68612, 2012..

[11] Lammen W., Kickenweitz D., Laudan T. and Kupijai P.: "Integrate Engine Manufacturer's Knowledge into the Preliminary Aircraft Sizing Process", Airtec 7th International Conference *"Supply on the Wings" Aerospace* – a leading innovator, Frankfurt/Main, Germany, 6-8 November 2012.

[12] Murton A. and Shaw N.: "Developing an Architecture and Standard to Support Innovations in Collaborative Modelling and Simulation", PDT Europe 2012, The Hague, The Netherlands, 25-26 September 2012.

[13] Ölvander J. and Steinkellner S.: "Model Based Collaborative Engineering from Requirements to Verification and Validation", presented at 6th MODPROD Workshop on Model-Based Product Development, Linköping, Sweden, and 7-8 February 2012.

[14] Parchem R., Flassig P. and Wenzel H.: "Collaborative Robust Engine Design Optimization", presented at SIMULIA Community Conference 2013, Vienna, Austria, 21 May 2013.

[15] Parchem R. and Wenzel H.: "Executing Optimization Processes in the Extended Enterprise", NAFEMS World Congress 2013, 1st SPDM Conference, Salzburg, Austria, 9-12 June 2013.

[16] Raymer D.P., Aircraft Design: A Conceptual Approach, Fourth edition, AIAA, Reston, VA, USA, 2006.

[17] Tabaste O., Laudan T., Grihon S. and Arbez P.: "Being Prepared for the Future: Trade-off Management Technology for Architects within Designing the Robust Virtual Aircraft", presented at Global Product Data Interoperability Summit, Phoenix, 2012; also presented at NAFEMS North *America Conference '12*, Washington, DC, USA, 11-12 September 2012.

[18] Tabaste O., Arbez P, Grihon S., Laudan T., Thomas M.: "Illustration Of Comprehensive Behavioural Digital Aircraft Enablement through Use Cases", NAFEMS World Congress 2013, 1st SPDM Conference, Salzburg, Austria, 9-12 June 2013.

[19] Vankan W.J., Lammen W.F. and Maas R.: "Meta-modeling and multi-objective optimization in aircraft Design", in [9], chapter 6, 2010.

4:th CEAS Air & Space Conference
FTF Congress: Flygteknik 2013

Conceptual Aircraft Design including Hybrid Laminar Flow Control

Kristof Risse and Eike Stumpf
Institute of Aerospace Systems (ILR), RWTH Aachen University, Germany

Keywords: Hybrid Laminar Flow Control (HLFC), Conceptual Aircraft Design, MICADO

Abstract

A methodology for conceptual design and optimization of aircraft with hybrid laminar flow control (HLFC) systems integrated into wing and empennage is described. The conceptual aircraft design platform MICADO is enhanced by the necessary methods for sizing of HLFC system architecture as well as prediction of aerodynamic characteristics, including transition location. The integrated sizing methodology allows to assess the net benefit of HLFC system integration on overall aircraft level and to minimize aircraft fuel consumption by variation of aircraft design parameters, cruise conditions and HLFC system parameters. The applicability of the developed methodology in conceptual aircraft design is demonstrated for a conventional long range passenger aircraft.

Nomenclature

ALI	Attachment Line Instability
CFI	Cross Flow Instability
HLFC	Hybrid Laminar Flow Control
ISA	International Standard Atmosphere
MICADO	Multidisciplinary Integrated Conceptual Aircraft Design and Optimization
NLF	Natural Laminar Flow
OAD	Overall Aircraft Design
TSI	Tollmien-Schlichting Instability
C_D	Total aircraft drag coefficient
C_L	Total aircraft lift coefficient
C_l	Local lift coefficient
C_Q	Suction coefficient
$C_{d,profile}$	Local profile drag coefficient
$C_{d,visc}$	Local viscous drag coefficient
$C_{d,wave}$	Local wave drag coefficient
L/D	Lift-to-Drag ratio
$MTOW$	Maximum Take-Off Weight, kg
OWE	Operating Weight Empty, kg
$SLST$	Sea-Level Static Thrust, kN
T/W	Thrust-to-Weight ratio
W/S	Wing loading, kg/m^2
x/c_{trans}	Relative transition location

1 Introduction

Facing the ambitious goals to reduce fuel consumption and ecological impact of commercial aircraft, drag reduction through laminar flow is one of the most promising technologies [6]. Next to natural laminar flow (NLF), hybrid laminar flow control (HLFC) is the best proven concept [3, 12, 8]. The reduction of friction drag, which amounts about half of total aircraft drag, is achieved by an extension of laminar flow area over the surfaces by delaying flow transition. Transition from laminar to turbulent flow is mainly governed by three instability mechanisms: Tollmien-Schlichting instability (TSI), cross flow instability (CFI) and attachment line instability (ALI). The HLFC wing concept integrates NLF by shaping of wing and airfoil geometry with laminar flow control by active boundary layer suction at the wing leading edge. It is especially suited for large aircraft with high transonic cruise Mach numbers, mostly implying large wing sweep angles and high cruise Reynolds numbers. At these conditions, ALI and especially CFI become dominant and cannot be controlled anymore by natural or passive laminar flow concepts, which motivates the application of HLFC [26].

The net benefit on aircraft level due to the achieved drag reduction is lowered by an additional mass and the suction power requirements from the integrated HLFC system. Another impact can be an additional wing mass, e.g. due to thinner HLFC airfoils. It is thus the main task on conceptual and preliminary design level to find a well-balanced overall design of an HLFC aircraft with optimum key performance characteristics, e.g. minimum block fuel on a selected study mission. This requires an integrated overall aircraft design (OAD) methodology that incorporates methods for HLFC wing aerodynamics and system component sizing for the specified requirements and design conditions. The main difficulty herein lies in a reliable assessment of aerodynamic characteristics including transition behaviour for a given aircraft configuration and flight condition. Further, a sound HLFC system component sizing has to account for wing pressure distribution and suction velocity requirements. The methodology presented in this paper addresses these problems by incorporating the required methods into an existing OAD environment to allow for an integrated design and assessment of the HLFC technology on aircraft level. In the following section, the used OAD platform is introduced and its enhancements towards HLFC assessment are described. A case study for a conventional long range aircraft with integrated HLFC system is then discussed to show the applicability of the methodology in conceptual aircraft design.

2 Methodology for Aircraft Design including Hybrid Laminar Flow Control

The HLFC design methodology presented in this paper is based on the MICADO[1] software platform developed at the Institute of Aerospace Systems (ILR) of RWTH Aachen University. A detailed description is given in reference [23]. The MICADO design logic and underlying methods relevant for HLFC aircraft design are shortly discussed in the next paragraph, followed by a specific description of the integrated HLFC methods.

2.1 Aircraft Design Platform MICADO

The MICADO environment incorporates a white sheet, requirement driven design approach, i.e. an automated full design synthesis can be initiated with minimum user input in terms of a set of top-level aircraft requirements. The integrated sizing approach allows to capture the impact of particular design changes or the integration of innovative systems or technologies on overall aircraft level, including mass snowball effects and resizing of main aircraft components. MICADO has already been used for several applications in aircraft design and operational studies as well as systems and technology integration and assessment (see e.g. references [2, 14, 17, 18, 5]).

The design process of the MICADO environment is schematically illustrated in Fig. 1. First, the different aircraft components are sized with respect to the top-level requirements. The initial aircraft layout is assessed in the performance analysis block, comprising prediction of aerodynamic characteristics, estimation of aircraft component and system masses and a detailed mission analysis. The detailed mission simulation model [1] uses aircraft mass, flight condition dependent drag polars and engine per-

[1]Multidisciplinary Integrated Conceptual Aircraft Design and Optimization.

formance decks[2] to calculate block fuel on the aircraft design mission. All sizing and analysis programs are re-executed until convergence in key design parameters (e.g. maximum take-off weight ($MTOW$), block fuel) is achieved, where wing loading W/S and thrust-to-weight ratio T/W are kept constant during design iteration. The fully converged aircraft design can then be assessed and optimized towards selected evaluation parameters, e.g. block fuel on a study mission, costs, emissions or noise.

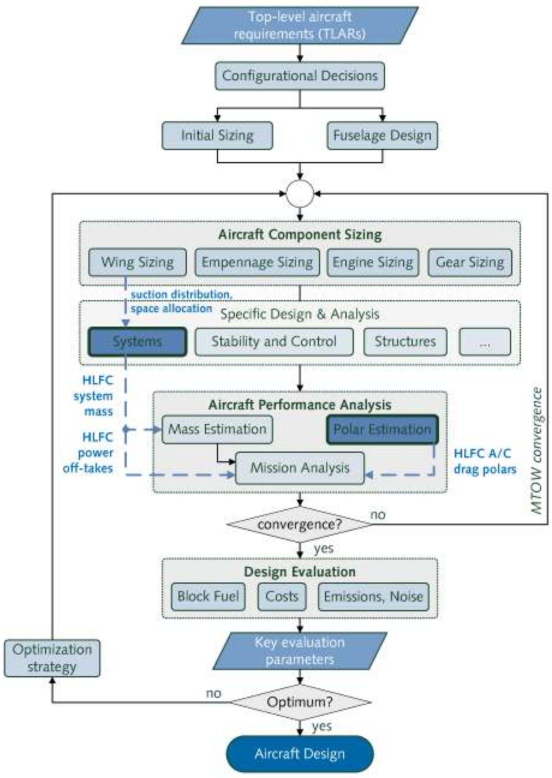

Figure 1: Process overview of ILR MICADO environment and integration of HLFC design methodology.

To capture the impact of HLFC systems integration into overall aircraft design, the MICADO environment has been enhanced by additional methods. The dark blue blocks and the dashed blue arrows in Fig. 1 schematically illustrate the affected program blocks within the MICADO design process. Changes have mainly been done to systems design and aerodynamic drag estimation methods; the mass estimation and mission analysis programs capture the relevant effects. The implemented aerodynamic and systems design methods are described in the following sections.

[2]The MICADO Engine decks contain performance parameters (e.g. thrust, fuel flow, cycle parameters) in dependence on Mach number, altitude, spool speed and system off-takes and are based on thermodynamic engine models built with the software GasTurb [13].

2.2 HLFC Aerodynamics Methodology

The MICADO program for turbulent aerodynamics estimates trimmed full aircraft configuration polars in subsonic and transonic flight regime. The DLR multi-lifting-line tool LIFTING_LINE [9, 11] is used to estimate lift, induced drag, as well as pitching moment. Total aircraft drag is accumulated from induced drag, viscous drag and wave drag, as illustrated in Fig. 2. Corrections for fuselage and nacelles are also taken into account. A detailed description of the implemented methods along with a validation for application to transport aircraft configurations can be found in reference [15].

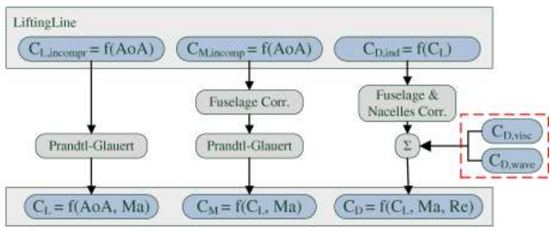

Figure 2: Overview of MICADO aerodynamic prediction program [15]. The highlighted viscous and wave drag components are affected by the HLFC drag estimation method.

Lift, moment and drag polars are determined in dependence on flight condition (Mach number, altitude) and aircraft configuration (take-off, climb, cruise, approach and landing). This array of polars is required for the detailed mission simulation.

Since the aerodynamic characteristics of an HLFC wing are highly governed by airfoil shape and transition instability mechanisms, the wing profile drag estimation has been enhanced by a quasi-three dimensional (3D) method, using airfoil characteristics at selected wing sections from an airfoil database. Every airfoil in the database is defined by its geometrical airfoil shape, its design lift coefficient, onflow conditions (Mach and Reynolds number), as well as leading and trailing edge sweep angle within a 3-D wing planform. HLFC airfoil drag polars are determined by applying the following process[3]:

1. 3D to 2D transformation of geometry and onflow conditions.
2. Determination of pressure distribution using program MSES developed by Drela [4].
3. 2D to 3D transformation of pressure distribution according to Lock [19], using local sweep angle (at shock location for transonic Mach numbers).
4. Laminar boundary-layer calculation using program Coco developed by Schrauf [25] (including specified suction distribution).
5. Local linear stability analysis for determination of TSI and CFI using program Lilo developed by Schrauf [24]; ALI is analysed via a modified version of the Pfenninger criterion [21].
6. Transition prediction by correlation of different instability analyses.
7. Calculation of airfoil profile (viscous plus wave) drag for determined transition location.

The drag polars are calculated for a wide range of lift coefficients and Mach numbers to cover the whole flight regime in the mission analysis. The calculated polar points are interpolated by a cubic splining method and written into an SQLite database. Within the MICADO aerodynamic program mentioned above, the 2D airfoil characteristics are applied for determination of 3D wing polars. For every Mach number and global lift coefficient C_L, the local lift coefficients C_l from the determined trimmed spanwise lift distribution at selected wing design sections are used to get the belonging viscous and wave drag coefficients from the database. The local C_d's are weighted by its related subareas to get the 3D wing profile drag. The wing drag polars are finally accumulated with the other components' polars to full aircraft configuration polars.

[3]The implemented wing and airfoil design methodology will be described in detail in another paper.

The described steps have been implemented into an automated robust process, which integrates a sophisticated transition prediction methodology into conceptual aircraft design. This allows for a more realistic and quantitative estimation of HLFC drag polar shape (at design and off-design conditions), instead of, for example, only assuming a constant drag count reduction relative to a turbulent drag polar.

To illustrate the level of detail of the implemented methodology, the determined drag polars of a selected midboard wing HLFC airfoil are shown in Fig. 3 ($Ma_{design} = 0.85$).

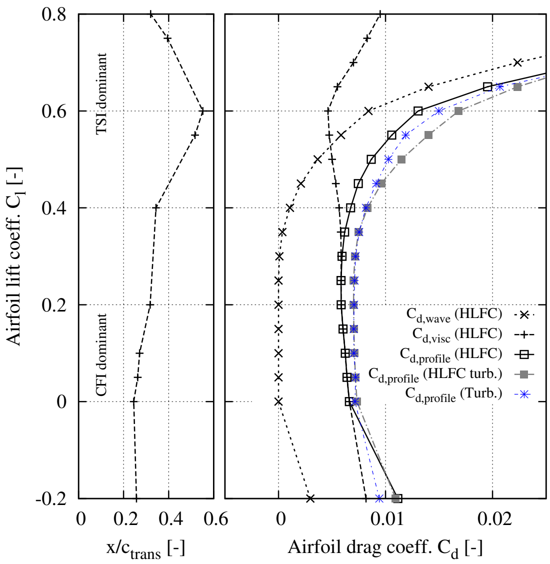

Figure 3: Transition location and drag polars as example for HLFC aerodynamics methodology.

The right part of the figure shows the profile drag polar $C_{d,profile}$, as well as its break-down into viscous $C_{d,visc}$ and wave drag $C_{d,wave}$. In the left part of the figure the predicted transition location x/c_{trans} on the airfoil upper side is shown as a function of lift coefficient C_l. Starting with early transition at low C_l's, where CFI is dominant over TSI, the extent of laminar flow grows with increasing C_l. The transition location reaches its maximum of more than half of the chord length at $C_l = 0.6$ and then decreases with higher C_l's due to dominant TSI. Note the influence of the transition location on the viscous drag polar.

Further shown in the right figure are the drag polar for the same HLFC airfoil with full turbulent flow ($C_{d,profile}$ (HLFC turb.)) due to transition at the leading edge, as well as that of an airfoil designed for turbulent flow ($C_{d,profile}$ (Turb.)) at the same design conditions[4]. The drag benefit of the HLFC airfoil versus the turbulent airfoil can be seen. For higher lift coefficients ($C_l > 0.65$), the high wave drag of the HLFC airfoil compensates its viscous drag benefits, motivating a careful balance between drag components as well as instability mechanisms. The relevant C_l region for cruise strongly depends on the global aircraft C_L, where the lift-to-drag ratio L/D reaches its maximum. The selected local airfoil C_l and C_d then result from the corresponding trimmed lift distribution over the wing. Note that the described specific effects of moving transition at different lift coefficients in combination with optimum cruise C_L are considered for flight altitude selection and fuel estimation during mission simulation.

Next to an improved representation of HLFC aerodynamics, the integration of the airfoil database method into MICADO ensures capturing of possible wing weight impacts, e.g. due to thinner HLFC compared to turbulent airfoils.

2.3 HLFC Systems Design Methodology

The MICADO program sizing the conventional system architecture has been described by Lammering [14, 16]. The implementation of the model is based on a modular net structure of energy sources, sinks, and conductors, using the ATA-100 chapter classification. It sizes all relevant aircraft systems in terms of mass, centre of gravity, and mission dependent energy consumption.

The MICADO systems design program has been enhanced by a module to size the HLFC system architecture. It applies the simplified suction system concept as developed in line with the ALTTA project for the Airbus A320 fin [10]. The implemented model and equations are based on the methodology described by Pe [20]. For a given aircraft configuration and design flight condition, the implemented method determines the overall HLFC system mass, centre of gravity and power requirements.

The pressure and suction distributions determined in the aerodynamic process for selected wing design sections are used as input to determine the mass flow through the porous wing surface. An analysis of the flow conditions in the double structure, the plenum chamber and the inlet and outlet of the compressor allows to estimate the electrical power required by the compressor to establish the necessary suction pressure. A selected number of compressors are distributed over the wing half span, where the available space inside the wing leading edge at the respective spanwise position is considered for the determination of compressor size. The compressor power requirement is used to determine the mass of compressors, motors and inverters. Further, wires and ducts are positioned inside the aircraft to connect the compressors with the electrical power source and with the outflow valves, respectively. Wire and duct masses are calculated according to its overall lengths and diameters, where ducting mass is a main contributor to overall HLFC system mass. The HLFC system architecture can be sized for application of HLFC to both wing and tails. Also, different architecture options for compressors (centralized or decentralized) and ducting (collective or separate) exist.

For HLFC systems integration into conceptual aircraft design, it is important that the model is sensitive towards relevant design parameters. In Fig. 4 the sensitivities of HLFC system power and mass towards flight Mach number (Ma) and altitude are shown (relative changes versus design point at $Ma = 0.85$, 33000 ft). The HLFC system power increases significantly with increasing Mach number and decreasing flight altitude. For a constant suction coefficient, high onflow velocities increase suction velocities and thus mass flow, leading to higher power requirements. Also, the increased volume flow accelerates the flow in the ducts, leading to addi-

[4] Airfoil geometries have been designed by the German Aerospace Center (DLR) in line with the LuFo projects HIGHER-LE and VER^{2}SUS.

tional pressure losses and thus power requirements. The negative influence of lower flight altitudes is due to higher air density that also increases mass flow. The underlying model of the International Standard Atmosphere (ISA) is represented by the slight bending of the curves for altitudes higher than 11 km ≈ FL 360.

The smaller relative change of overall HLFC system mass compared to relative change of power is due to the fact that the increasing power requirement mainly sizes compressor and motor masses. Still, these only amount less than half of total system mass, while ducting mass – as a main mass contributor – is sized by aircraft dimensions and keeps nearly unaffected by the cruise conditions

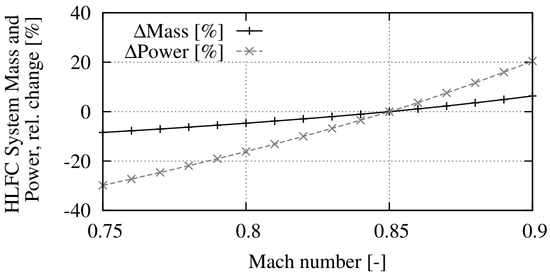

(a) Variation of Mach number

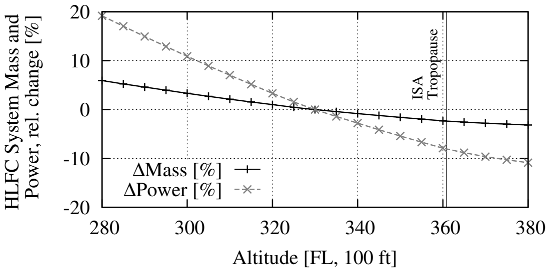

(b) Variation of flight altitude

Figure 4: Relative change of HLFC system power and mass as function of cruise flight conditions.

Figure 5 shows the behaviour of HLFC power and mass as function of varying suction requirements in terms of maximum suction coefficient $C_{Q,max}$. The suction distribution is exemplified in Fig. 5(b) by three sample distributions, shown together with the upper surface pressure distribution, which has been kept constant for this sensitivity study. An increase of $C_{Q,max}$ by 50% leads to a power increase by around 75%, which underlines the motivation to realize low suction rates.

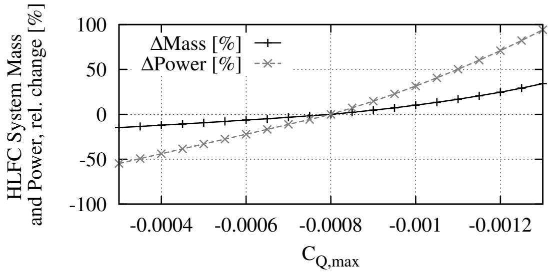

(a) Variation of maximum suction coefficient $C_{Q,max}$

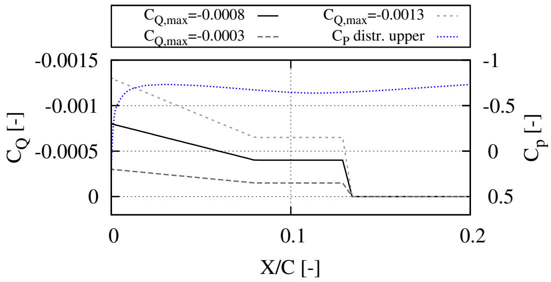

(b) Sample suction distributions C_Q over relative chord length X/C (pressure distribution C_p kept constant)

Figure 5: Relative change of HLFC system power and mass as function of suction distribution.

The integration of the HLFC sizing method into the overall aircraft system architecture also accounts for relevant system interdependencies, e.g. increased maximum shaft power offtakes can lead to higher total electrical generator mass. HLFC system mass and centre of gravity are considered for accumulation of structural and system masses to the operating weight empty (OWE), and the determination of overall aircraft centre of gravity. The influence of shaft power offtakes on the engine fuel flow – and thus specific fuel consumption – is automatically captured by the engine performance model and the mission analysis program (cf. Fig. 1).

2.4 Resizing of Aircraft Components

As mentioned above, W/S and T/W are kept constant during MICADO design iteration, since they are the main drivers for fulfilling top-level aircraft requirements. With varying $MTOW$, wing (and thus empennage areas) as well as the propulsion system in terms of sea-level static thrust ($SLST$) are re-scaled. This leads to a combined component resizing and mass snowball effect, i.e. smaller lifting areas and propulsion system become lighter, the lower OWE reduces consumed fuel and $MTOW$, which in turn leads to smaller components, and so on. Keeping the component geometries constant can lead to suboptimal designs, e.g. in terms of an over-powered, too heavy propulsion system; this especially holds for technologies such as HLFC, which lead to significant reduction of $MTOW$. In the HLFC design studies in the following section, the additional block fuel saving potential due to component resizing will be discussed and quantified.

3 HLFC Design Study: Application to Long Range Aircraft

To show the applicability of the presented HLFC design methodology it is applied to a conventional long range aircraft design[5]. The following paragraph presents the turbulent baseline aircraft designed with MICADO. HLFC designs are then discussed for the baseline and an optimized aircraft configuration.

3.1 Turbulent Baseline Design

The turbulent baseline aircraft has been designed with MICADO for a range of 8150 NM and a standard capacity of 470 passengers; further top-level requirements used for the design are summarized in the upper part of Table 1. After design convergence the baseline aircraft has been assessed on a 4000 NM study mission. Key aircraft characteristics of the converged design, including calculated block fuel (BF) on design and study mission, are given in the lower part of Table 1. The general arrangement of the MICADO long range aircraft design is shown in Fig. 6.

[5]Aircraft key characteristics have been specified by Airbus in line with the LuFo project HIGHER-LE [7].

Table 1: Top-level requirements and key aircraft characteristics of the MICADO long range baseline design.

Top-level requirements		
Design range	8150	NM
Std. passenger number	470	–
Design payload	44650	kg
Cruise Mach number	0.85	–
Initial cruise altitude	33000	ft
Take-off field length	3261	m
Landing field length	2073	m
Key aircraft characteristics		
Maximum take-off weight	405.0	t
Operating weight empty	212.2	t
Wing area	565	m^2
Wing span	80	m
Sea-level static thrust	511	kN
Block fuel (design mission)	134.3	t
Block fuel (4000 NM mission)	63.5	t

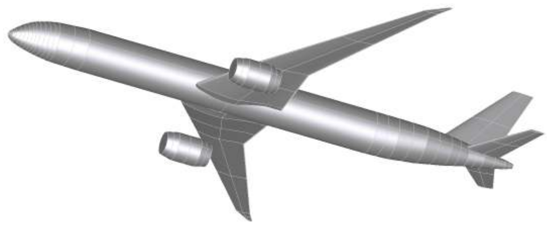

Figure 6: 3D view of MICADO baseline aircraft design.

3.2 HLFC Aircraft Designs

The HLFC design process as described above has first been applied to the baseline aircraft (first design called 'HLFC Ref.'). To enable a more efficient HLFC wing design, a parameter variation of the HLFC main design drivers Mach number and wing leading edge sweep has been conducted, resulting in a reduction of the Mach number to $Ma = 0.80$ and of the outboard wing leading edge sweep angle from 34° to 28° (second design called 'HLFC Opt.'). These two HLFC designs are discussed below.

The HLFC system layout has been designed for the whole aircraft, applying a decentralised compressor architecture with collective ducting, using three compressors per wing side, one per

Table 2: Comparison of HLFC systems design results for 'HLFC Ref.' and 'HLFC Opt.' design.

	HLFC Ref.	HLFC Opt.
Mach number [-]	0,85	0,8
LE Sweep [°]	34	28
Fixed Aircraft Geometry		
Total mass [kg]	753	759
Power Req. [kW]	243	226
Resized Aircraft Geometry		
Total mass [kg]	730	694
Power Req. [kW]	235	206

horizontal and one per vertical tail. The HLFC system has been sized for the respective design cruise Mach number, initial cruise flight level, and the suction distributions at the selected wing design sections. Table 2 compares the HLFC systems sizing results for the two HLFC designs, and each for fixed and resized aircraft geometry (cf. section 2.4). The resizing slightly reduces mass and power requirements due to smaller suction areas and ducting lengths. Between the two designs, there are no significant differences from the OAD point of view. The slightly reduced power requirement for the 'HLFC Opt.' design is due to reduced Mach number and lower suction rates. To analyse the impact on aircraft performance, an off-design sensitivity study has been conducted on the 4000 NM study mission. The additional power off-takes of $\sim$ 250 kW from the engines yield a block fuel increase of around $\sim$ 0.5%, and the additional mass of $\sim$ 800 kg (less than 0.5% of OWE) increased BF by $\sim$ 0.2%. This shows the small influence of the pure HLFC system integration on the overall aircraft design. Note that the large relative changes shown in Fig. 4-5 are also strongly attenuated in this OAD context.

For both HLFC aircraft designs, suction has been applied only to the upper wing surface, using a Krueger flap as leading edge device for shielding against contamination. Wing aerodynamics have been estimated by the described quasi 3-D methodology. HLFC has also been applied to the tails by assuming a constant net drag reduction of 6 drag counts. Since significant 3D effects can be expected on the inboard wing at the fuselage junction, the transition point has been set to the leading edge at the root, linearly increasing to the predicted transition location at the kink section. The wing tip segment has been assumed to be fully turbulent as well. This is illustrated in Figure 7, which shows the resized right wing planform of the 'HLFC Opt.' design with the predicted extend of laminar flow area. The spanwise positions of the three compressors determined by the HLFC systems program are also shown (compressor diameters not to scale, placement on front spar only schematically).

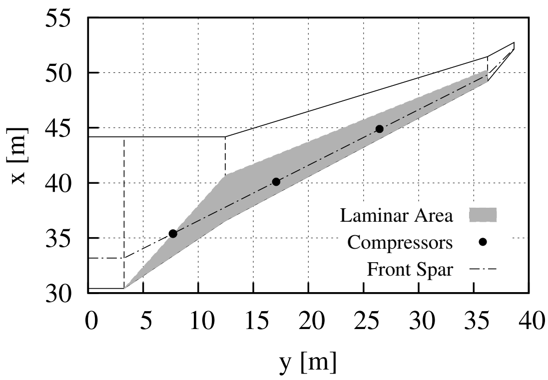

Figure 7: Wing planform of 'HLFC Opt.' design with predicted laminar flow area and compressor positions.

Figure 8 compares the determined full aircraft configuration drag and L/D polars of the two HLFC designs (without aircraft resizing effects) against the turbulent baseline aircraft (black solid curve). The grey curves represent the 'HLFC Ref.' design, where the dashed curve shows the polars when applying HLFC only to the wing, and the dotted curve refers to the application of HLFC to both wing and tails. The 'HLFC Opt.' design (blue dotted line) exhibits even more drag benefits due to improved HLFC design conditions at reduced Mach number and sweep angle. Also, note the peakier L/D curve and the more favourable transonic behaviour at high lift coefficients.

The mission analysis results for the converged aircraft designs are compared in Fig. 9. The

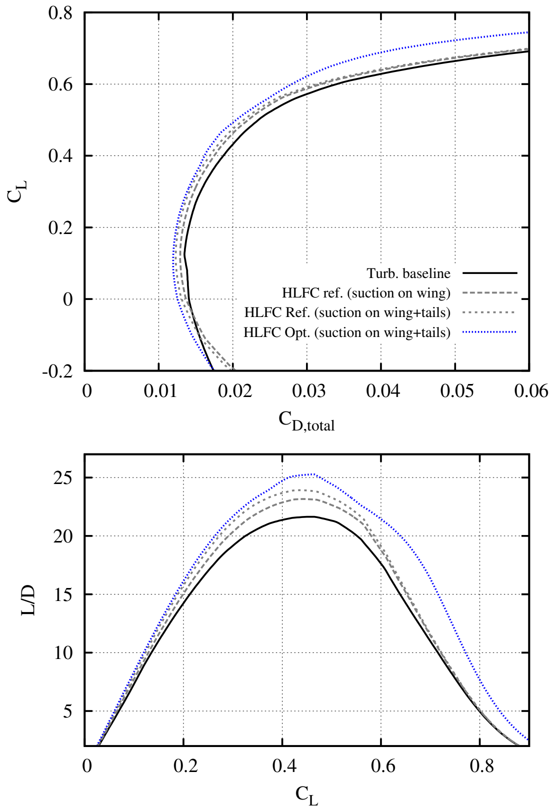

Figure 8: Comparison of HLFC full aircraft configuration polars against turbulent baseline.

optimized altitude profiles[6] and the corresponding lift coefficient (saw tooth like) profiles over the design range are shown in the upper figure. Note that altitudes are automatically adapted to the optimal cruise lift coefficients (point of maximum L/D) that are slightly lower for the HLFC designs (cf. Fig. 8). The initial cruise altitude requirement of 33000 ft is fulfilled for all designs; it is checked independently on the optimum initial flight level on the design mission. The lower figure shows the thrust curves and the consumed fuel over the design range. The thrust peaks in take-off and climb segments point out the realistic consideration of increased fuel consumption on segments with higher thrust ratings. The reduced slopes in the block fuel curves of the HLFC designs are mainly due to the high drag benefits.

[6]The altitude profile is optimized such that specific air range is maximized at all cruise mission increments.

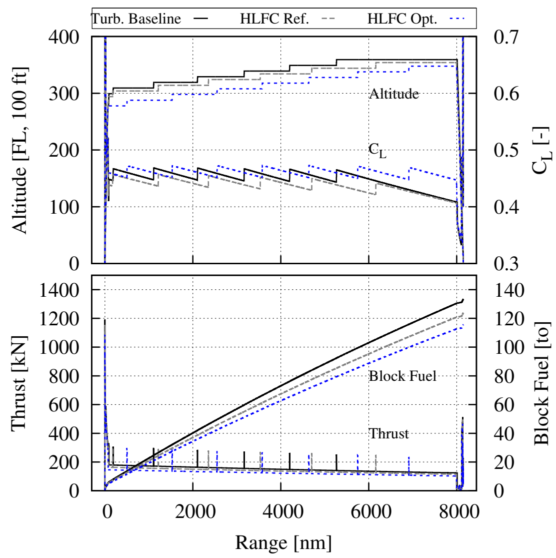

Figure 9: Comparison of mission analyses on 8150 NM **design mission: Altitude and C_L profiles, thrust and consumed fuel.**

In Fig. 10 the accumulated shaft power (solid) and bleed-air offtakes (dashed) over the design mission are compared between the 'HLFC opt' (blue curve) and the baseline design (black curves). The HLFC system is assumed to be active only during cruise above initial cruise flight level, leading to the difference in shaft power offtakes of about 235 kW.

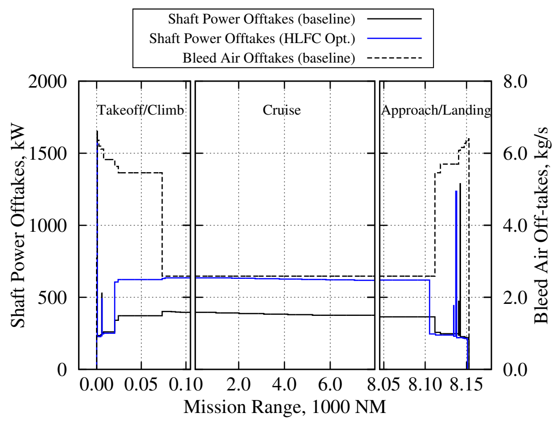

Figure 10: Shaft power and bleed air offtakes on design mission for 'HLFC Opt.' and baseline design.

The OAD assessment of the HLFC designs in terms of relative change of key design parameters compared to the turbulent baseline design are shown in Fig. 11. The two left bars represent the 'HLFC Ref.' design results, without and with component resizing (cf. section 2.4); likewise, the two right bars refer to the 'HLFC Opt.' design. For the designs without resizing, wing area S_{ref} and thrust $SLST$ keep constant, while these parameters scale with $MTOW$ when resizing aircraft components (cf. bars in Fig. 11).

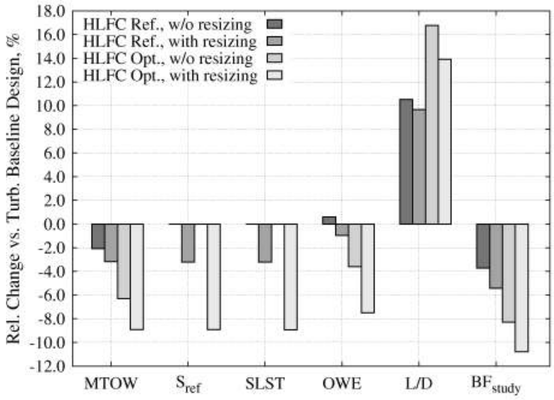

Figure 11: Relative change of key design parameters of HLFC designs vs. baseline.

For the 'HLFC ref.' design, the OWE increases not only due to additional HLFC system mass, but mainly due to thinner HLFC airfoils. Note that the small OWE increase (left bar) is already attenuated by a pure mass snowball effect (mainly systems) due to reduced $MTOW$. This effect is intensified for the design with component resizing, leading to a net OWE decrease. The L/D benefit is slightly reduced for the resized design due to the smaller wing. Net benefits in terms of block fuel on the 4000 NM study mission of $\sim 4\,\%$ (without resizing) and $\sim 5.5\,\%$ (with resizing) are obtained.

Further OAD improvements are achieved by the 'HLFC Opt.' design. The wing weight increase due to thinner HLFC airfoils is similar, but has been overcompensated by the wing weight decrease due to reduced outboard leading edge sweep angle. The second main driver is the additional L/D benefit resulting from the better HLFC airfoil design at reduced Mach number and sweep angle. The block fuel reduction increases to more than $8\,\%$ without resizing and to nearly $11\,\%$, when exploiting component resizing potential. The improved resized configuration of the 'HLFC Opt.' design is compared to the baseline geometry in the topview in Fig. 12, showing the rescaled smaller wing and the reduced sweep angle of wing and empennage.

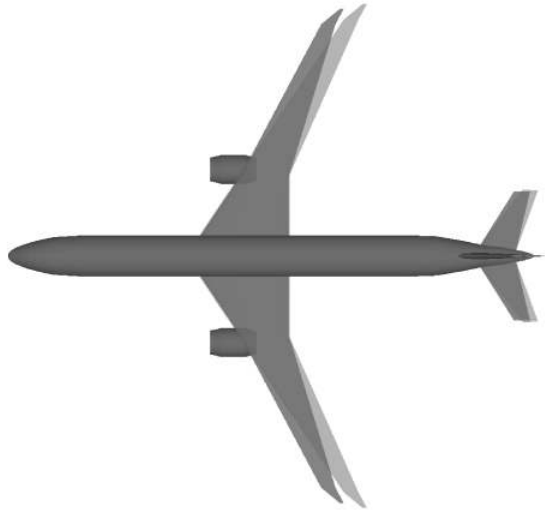

Figure 12: Comparison of resized 'HLFC opt.' design (smaller wing area and reduced outboard leading edge sweep) with baseline geometry.

The obtained block fuel reduction of $\sim 11\,\%$ underlines the fuel saving potential of the HLFC technology. Still, it has to be noted that the designs presented in this paper assumed full laminar flow during cruise. An outfall of the HLFC system or laminar flow in general and the sizing of the aircraft towards additional reserve fuel requirements will lower the achieved net benefit. A consistent framework for sizing towards operational requirements (called LAOPS) has already been presented and applied (cf. references [17, 5, 22]).

4 Conclusion and Outlook

In this paper a conceptual design methodology for aircraft with hybrid laminar flow control has been presented. The aircraft design platform MICADO has been enhanced by additional modules for HLFC aerodynamics and systems design. The underlying methodologies have been discussed and the relevant sensitivities to aircraft design parameters have been shown. The methodology has been applied to the design of an HLFC long range aircraft. The results showed the capability of the developed methodology to design and assess aircraft with integrated HLFC systems, and to capture relevant impacts into key aircraft design characteristics, e.g. block fuel net savings. Two HLFC designs with different cruise Mach number and wing sweep angle have been discussed, which yielded significant block fuel savings. The results also revealed the improved fuel saving potential due to aircraft component resizing. The resized 'HLFC Opt.' design showed a net block fuel benefit on the study mission of nearly 11 %, which underlines the strong fuel saving potential of the HLFC technology.

In further studies the airfoil database will be enhanced to exploit the MDO capabilities of MICADO in combination with the HLFC design methodology. Further design optimizations including HLFC system parameters as well as aircraft and wing design parameters will be conducted to further investigate the fuel saving potential of the HLFC technology on overall aircraft level.

Acknowledgments

The research presented in this paper has been originated from the German LuFo projects HIGHER-LE and VER^{2}SUS. The authors would like to thank all involved people from Airbus, the German Aerospace Center (DLR) and the Hamburg University of Technology (TUHH) for financing, leading or contributing to these projects. The authors also thank Geza Schrauf for kindly providing his transition prediction programs for integration into the ILR aerodynamic tool chain. Likewise thanks to Mark Drela for providing his MSES code. Further thanks go to Florian Schültke and all other involved colleagues at the ILR.

References

[1] Anton, E., Lammering, T., and Henke, R. A comparative analysis of operations towards fuel efficiency in civil aviation. In *Applied Aerodynamics: Capabilities and Future Requirements* (Bristol, BS8 1TR, UK, July 2010).

[2] Anton, E., Lammering, T., and Henke, R. Fast estimation of top-level requirement impact on conceptual aircraft designs. In *10th AIAA Aviation Technology, Integration, and Operations (ATIO)* (Fort Worth, Sept. 2010), AIAA.

[3] Braslow, A. L. A history of suction-type laminar-flow control with emphasis on flight research. Monographs in Aerospace History 13, NASA History Division, 1999.

[4] Drela, M. A users guide to MSES 3.05, 2007.

[5] Franz, K., Lammering, T., Risse, K., Anton, E., and Hoernschemeyer, R. Economics of laminar aircraft considering off-design performance. In *8th AIAA Multidisciplinary Design Optimization Specialist Conference* (Honolulu, HI, Apr. 2012), AIAA.

[6] Green, J. E. Laminar flow control - back to the future? In *38th Fluid Dynamics Conference and Exhibit* (Seattle, WA, June 2008), AIAA.

[7] Heidmann, P., and Schaeufele, S. Airbus document on HLFC research baseline, June 2010.

[8] Henke, R. A320 HLF fin flight tests completed. *Air & Space Europe 1*, 2 (1999), pp. 76–79.

[9] Horstmann, K. *Ein Mehrfach-Traglinienverfahren und seine Verwendung fuer Entwurf und Nachrechnung nichtplanarer Fluegelanordnungen.* DFVLR Forschungsbericht, German Aerospace Center (DLR), Dec. 1987.

[10] Horstmann, K., Schrauf, G., Sawyers, D., and Sturm, H. A simplified suction system for an HLFC leading edge box of an A320 fin. In *CEAS Aerospace Aerodynamics Research Conference* (Cambridge, UK, June 2002).

[11] Horstmann, K. H., Engelbrecht, T., and Liersch, C. A multi-lifting-line method for design and check of nonplanar wing-configurations. Online.

[12] Joslin, R. D. Overview of laminar flow control. Tech. Rep. TP-1998-208705, NASA, Langley Research Center, Hampton, Virginia, Oct. 1998.

[13] Kurzke, J. *Gas Turb 11 - Design and Off-Design Performance of Gas Turbines*, 2007.

[14] Lammering, T., Anton, E., and Henke, R. Technology assessment on aircraft-level: modeling of innovative aircraft systems in conceptual aircraft design. In *10th AIAA Aviation Technology, Integration, and Operations (ATIO)* (Fort Worth, Sept. 2010), AIAA.

[15] Lammering, T., Anton, E., and Henke, R. Validation of a method for fast estimation of transonic aircraft polars and its application in preliminary design. In *Applied Aerodynamics: Capabilities and Future Requirements* (Bristol, BS8 1TR, UK, July 2010).

[16] Lammering, T., Anton, E., Risse, K., and Franz, K. Impact of systems integration on fuel efficiency in preliminary aircraft design. In *3rd International Workshop on Aircraft System Technologies* (Hamburg, Mar. 2011), Shaker Verlag, pp. 171–180.

[17] Lammering, T., Anton, E., Risse, K., Franz, K., and Hoernschemeyer, R. Influence of off-design performance on design synthesis of laminar aircraft. *Journal of Aircraft, Vol. 49, No. 5* (2012), pp. 1324–1335.

[18] Lammering, T., Risse, K., Franz, K., Peter, F., and Stumpf, E. Assessment of innovative leading edge devices considering uncertainties in conceptual design. In *12th AIAA Aviation Technology, Integration, and Operations (ATIO)* (Indianapolis, Sept. 2012), AIAA.

[19] Lock, R. An equivalence law relating three-and two-dimensional pressure distributions. Tech. rep., Her Majesty's Stationery Office, 1964.

[20] Pe, T., and Thielecke, F. Synthesis and topology study of HLFC system architectures in preliminary aircraft design. In *Proceedings of the 3rd CEAS Air & Space Conference, Venice, Italy* (2011).

[21] Pfenninger, W. Some results from the X-21 program. Part I: Flow phenomena at the leading edge of swept wings. In *Recent developments in boundary layer research, Part IV, AGARDograph 97* (1965).

[22] Risse, K. Final report of ILR contribution to LuFo project VER2SUS. Tech. rep., Institute of Aerospace Systems (ILR), RWTH Aachen University, 2012.

[23] Risse, K., Lammering, T., Anton, E., Franz, K., and Hoernschemeyer, R. An integrated environment for preliminary aircraft design and optimization. In *8th AIAA Multidisciplinary Design Optimization Specialist Conference* (Honolulu, HI, Apr. 2012), AIAA.

[24] Schrauf, G. *LILO 2.1 Users Guide and Tutorial.* Bremen, Germany. GSSC Technical Report 6, originally issued Sep. 2004, modified for Version 2.1 July 2006.

[25] Schrauf, G. Coco - a program to compute velocity and temperature profiles for local and nonlocal stability analysis of compressible, conical boundary layers with suction. Zarm technik report, Airbus Bremen, Germany, 1998.

[26] Schrauf, G. Status and perspectives of laminar flow. *Aeronautical Journal 109*, 1102 (2005), pp. 639–644.

4:th CEAS Air & Space Conference
FTF Congress: Flygteknik 2013

Collaborative Aircraft Design using AAA and CEASIOM linked by CPACS Namespace

A. Rizzi, P. Meng
Royal Insititute of Technology, Sweden

B. Nagel, D. Boehnke
German Aerospace Center (DLR), Germany

W. A. J. Anemaat, J. Carroll
Design Analysis and Research Corporation, USA

key words: *Aircraft design, geometry representation, CPACS, AAA, CEASIOM*

Abstract

This paper represents a collaborative work between the preliminary design tool AAA and conceptual design tool CEASIOM linked by CPACS. Higher-fidelity analysis can be carried out by CEASIOM with inputs from AAA. The philosophy of the design loop is spelled out in this paper, with a test case Avanti P-180 for higher-fidelity CFD solutions and the pitch control analysis.

1 Introduction & Overview

Figure 1 spells out the details in the early steps of aircraft design for the definition of the configuration. It illustrates two design *loops* in the conceptual design phase that follow the first-guess sizing (usually done by a spread-sheet) to obtain the initial layout of the configuration. The first one, the pre-design loop, is aimed at establishing a very quick (time-scale can be from one to a few weeks) yet technically consistent sized configuration with a predicted performance. The second one, the concept-design loop, is a protracted and labour intensive effort involving more advanced first-order trade studies to produce a refinement in defining the minimum goals of a candidate project. At the end of the conceptual design phase all the design layouts will have been analyzed, and the "best" one, or possibly two, designs will be down-selected to the preliminary design phase. During the preliminary definition, project design is still undergoing a somewhat fluid process and indeed warrants some element of generalist-type thinking, but the minimum goals of the project have already been established during the conceptual definition phase and the aim is to meet these targets using methods with higher order than those used during the conceptual definition phase. Furthermore, the participants in this working group are mostly genuine specialists in each respective discipline. Figure 1 indicates the way in which data, or information, is passed between specialist groups during the design process. The specialist groups must consider the level of advanced technology to be adopted together with all of the other active constraints on the design. The data flow lines indicate how the technology areas influence the aircraft configuration though its performance. The specialist departments/offices provide the input data to the project designers who then coordinate a systematic search to find the "optimum" configuration and settle disputes between conflicting specialist opinions. There exists today a good deal of *inefficiencies* in interactions between all these various groups.

The thesis of this paper is that there are several and different tools in the tool-chain to carry out this design process, and that the overall efficiency of the process is enhanced by increasing the collaboration between the different tools. The two tools in question are the Advanced Aircraft Analysis (AAA) suite for conceptual design and CEASIOM for preliminary design and CPACS is the namespace for the means of data collaboration. An example of the Piaggio Avanti illustrates the collaboration that is possible and describes how the data is shared.

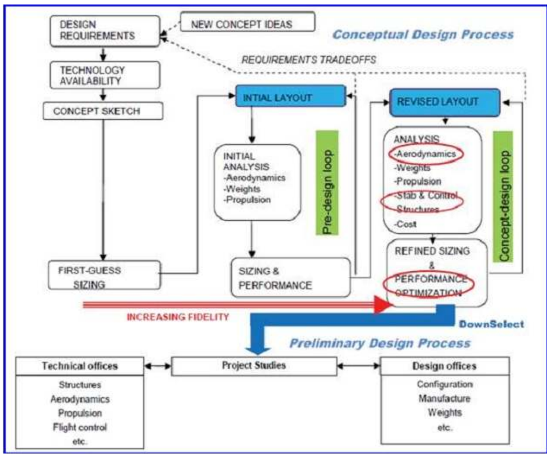

Fig. 1: The two design loops in the conceptual design phase process and the down-select to project study in preliminary design

2 Brief Description of the Tools

2.1 Advanced Aircraft Analysis (AAA)[1]

The current version of AAA is based on the methods of Airplane Design Parts I-VIIIby Jan Roskam, Airplane Flight Dynamics Parts I-II by Jan Roskam, Airplane Aerodynamics and Performance by Jan Roskam and Eddie Lan and methods developed for airplane design by DARcorporation engineers . Since 1991, when DARcorporation acquired the rights for AAA and continued development of AAA as a commercial venture, AAA has been improved and upgraded several times.

Advanced Aircraft Analysis provides a powerful framework to support the iterative and non-unique process of aircraft preliminary design. The AAA program allows design engineers and preliminary design engineers to take an aircraft configuration from early weight sizing through open loop and closed loop dynamic stability and sensitivity analysis, while working within regulatory and cost constraints.

AAA contains 10 independent application modules. Each module is designed to perform those tasks necessary to evaluate the characteristics of a given aircraft at each stage of the preliminary design: Weight, Aerodynamics, Performance, Geometry, Propulsion, Stability and Control, Dynamics, Loads, Structures, Cost Analysis. Figure 2 shows the geometry module in AAA with the 3-view option.

AAA contains AeroPack an interface to Shark/AP, a fully functioning three-dimensional aircraft drafting tool. Shark/AP supports multiple layering and import/export of common file formats of most commercially available drafting tools, contains a surface modeller, solid modeller and has all standard PC-CAD capabilities.

Shark/AP supports the generation of the following types of curves: Points, Straight single segment lines, Poly straight segment lines, Circles/Arcs, Ellipses, B-Splines and Conics. For the curves listed above, utilities such as Trim/Break/Extend, Corner/Fillet/Chamfer, and Project/Convert/Smooth/Join are available for modification. These curves and utilities listed above can be used to construct a three dimensional outline of any component or assembly and can then be used to construct surfaces and wireframe models.

Shark/AP contains a group of tools specifically designed for airplane design drafting. The group of tools is called AeroPack and includes: Polyconic surfaces, Tangent surfaces, Airfoil generation, Planform generation, Area curve, Obscuration Plots, Import Airplane.

Geometry between the analysis part (AAA) and the CAD program (two separate programs, the CAD program is called Shark/AP) is exchanged trough a text file. The methods for import and export are implemented in AeroPack which is still a part of AAA today.

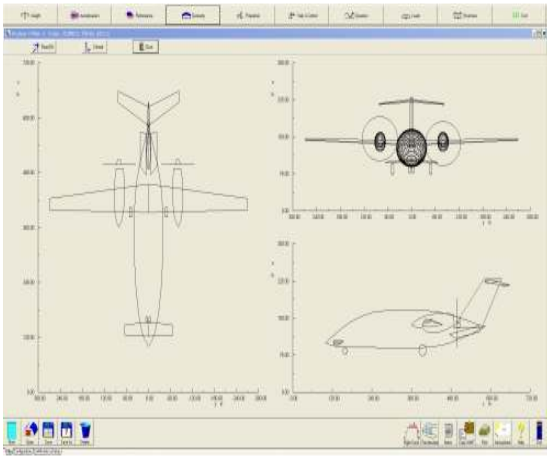

Fig. 2: Advanced Aircraft Analysis 3-View Module

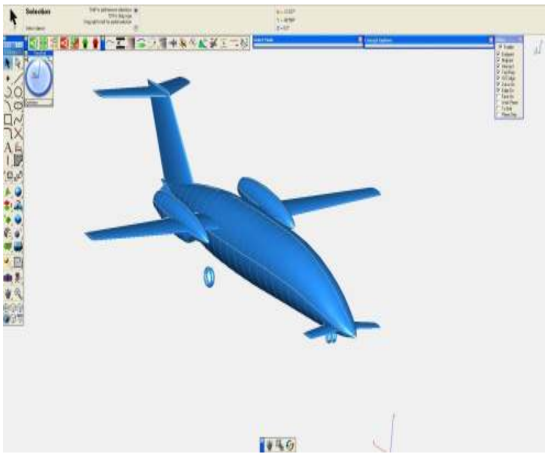

Fig. 3: Shark/AP

2.2 CEASIOM

CEASIOM, the Computerised Environment for Aircraft Synthesis and Integrated Optimisation Methods, developed within the European 6th Framework Programme SimSAC (Simulating Aircraft Stability And Control Characteristics for Use in Conceptual Design), is a framework tool for conceptual aircraft design that integrates discipline-specific tools like: CAD & mesh generation, CFD, stability & control analysis, etc., all for the purpose of early preliminary design[2]. CEASIOM is an ad hoc framework. The CEASIOM framework offers possible ways to increase the concurrency and agility of the classical conceptual-preliminary process. Figure 4 presents an illustration of the CEASIOM software, showing aspects of its four core functions: geometry & meshing, CFD, aeroelastics and S&C (flight dynamics).

Signicant features developed and integrated in CEASIOM as modules are:

- Geometry module ACbuild-sumo[3]

A customized geometry construction system coupled to surface and volume grid generators; Port to CAD via IGES

- Aerodynamic module AMB-CFD[4]

A replacement of current handbook aerodynamic methods with new adaptable-fidelity modules:

- ◦ Steady and unsteady TORNADO vortex-lattice code (VLM) for low-speed aerodynamic and aero-elasticity
- ◦ Inviscid EDGE CFD code for high-speed aerodynamics and aero-elasticity
- ◦ RANS (Reynolds Averaged Navier-Stokes) flow simulator for high-fidelity analysis of extreme flight conditions

- Stability and Control module S&C [5]

A simulation and dynamic stability and control analyzer and flying-quality assessor. Test flights with six Degrees of Freedom flight simulation, and performance prediction, also includes human pilot model, Stability Augmentation System (SAS) and a LQR based flight control system (FCS) package are among the major functionalities of this module.

- Aero-elastic module NeoCASS[6]

Quasi-analytical structural analysis methods that support aero-elastic problem formulation and solution.

- Flight Control System design module FCSDT[7]

A designer tookit for flight control-law formulation, simulation and technical decision support, permitting flight control system design philosophy and architecture to be coupled in early in the conceptual design phase

CEASIOM is meant to support engineers in the conceptual/preliminary design process of the aircraft, with emphasis on the improved prediction of stability and control properties achieved by higher-fidelity methods than found in contemporary aircraft design tools. Moreover CEASIOM integrates into one application the main design disciplines, aerodynamics, structures, and flight dynamics, impacting on the aircraft's performance. It is thus a tri-disciplinary analysis brought to bear on the design of the aero-servo-elastic aircraft [8,9] CEASIOM however does not carry out the initial sizing of a baseline configuration.

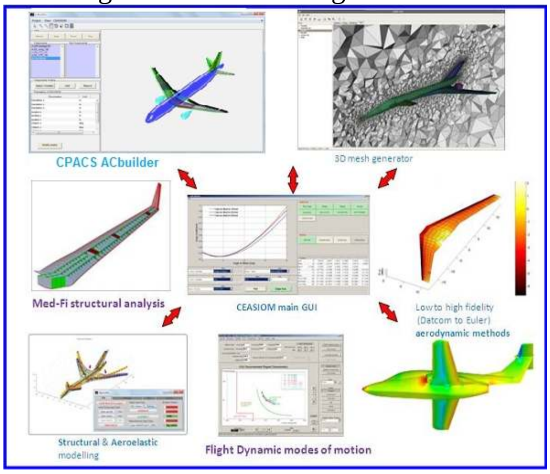

Fig. 4: Core modules ACbuilder-sumo, AMB-CFD, NeoCASS and S&C (SDSA, J2 and FCSDT) in the CEASIOM software

3 Brief Description of the Data

3.1 Description of CPACS[i]

CPACS, the Common Parametric Aircraft Configuration Schema, advocated by DLR, is a common language in air transportation system for different aircraft analysis modules. CPACS makes it easier to synchronize the work steps in different aviation research institutions, to enhance direct communications in between, thus facilitating the process of making innovative and efficient aircrafts. In particular, CPACS's ability to handle un-conventional aircraft models makes it an inevitable new standard for current aircraft analysis tools should they want to be upgraded to tools incorporating un-conventional and innovative aircraft models. In addition, CPACS is capable of describing characteristics of different aircraft analysis area, e.g. geometry, aerodynamics, structure, engine propulsion, climate impact, fleets and mission, which makes it a comprehensive, unified, and well-structured information carrier, promoting multi-disciplinary and multi-fidelity design analysis from distributed environments.

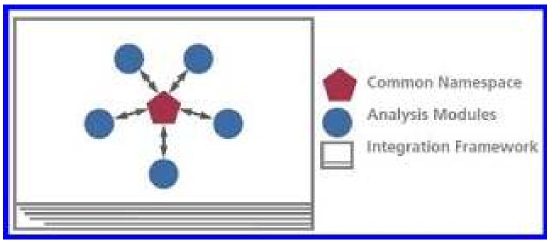

Fig. 6: CPACS common namespace

Since 2005 the Common Parametric Aircraft Configuration Schema (CPACS) is developed by DLR for the exchange of information on the level of preliminary design. The system is in operational use at all aeronautical institutes of DLR and has been extended for civil and military aircraft, rotor-craft, jet engines and entire air transportation systems.

The data-format is based on XML technology. An assessment of alternatives for modeling languages for preliminary aircraft design is reported in Böehnke et al[11] ongoing works include the documentation of the schema that described the syntactic definition on

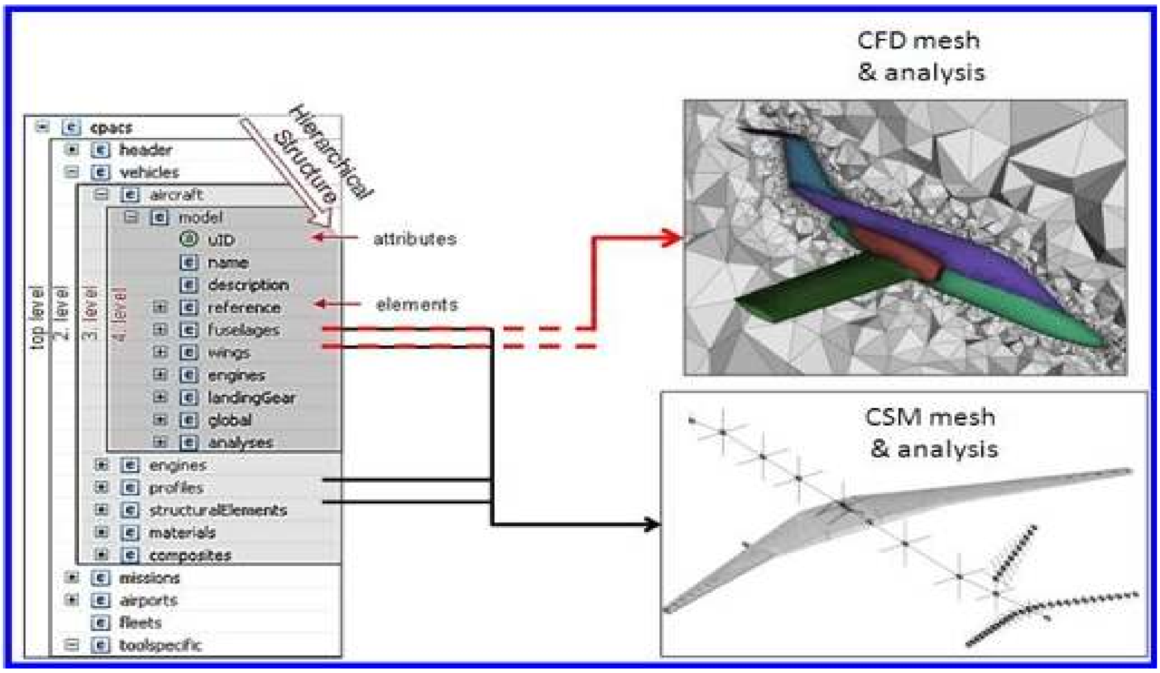

Fig. 5: Root structure of the CPACS data format

CPACS. Additionally, some getting started documents are being prepared. Some supportive libraries handling XML and geometric data are available and are described in more detail in the following section as they are included in the Chameleon@RCE framework.

Applications in aircraft design and optimization are shown by Liersch [12] and Zill [13,14]. An approach to multi-fidelity using CPACS is outlined by Böehnke [11, 15] implemented a chain of analysis modules that coupled works of TU Delft, KTH Stockholm and DLR.

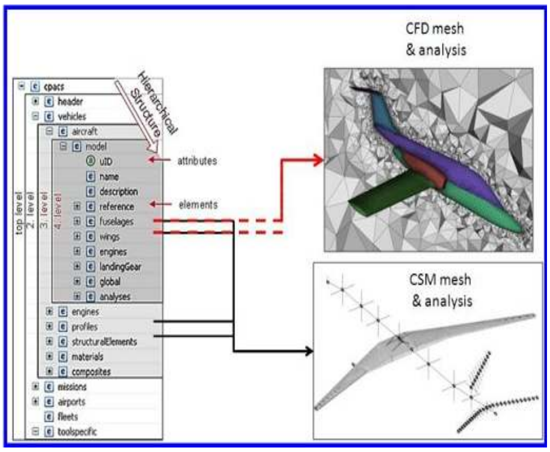

Fig. 7: Root structure of the CPACS data format

CPACS holds detailed interpretable type definitions for semantic entities from the air transportation system. Precise definitions for geometric elements like aircraft, wings, sections, elements, profiles, points, and transformations are given. Additional elements can be defined which are out of the scope of this paper. Figure 6 indicates the rich feature-tree hierarchy of the CPACS language. CPACS not only holds information on the objects but also data for the connected analysis modules. Such tool-specific data is transferred along with the dataset and carries further information, such as parameters for numerical methods, to the analysis modules. In this way, analyses involving sequences of modules can be defined.

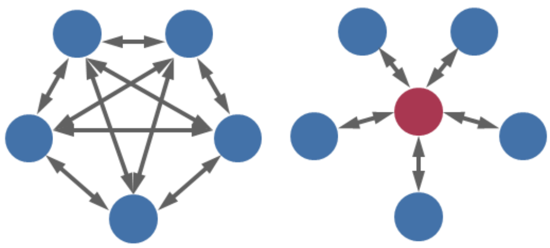

Fig. 8: CPACS advantage of unified data managment in a multi-code framework: left) without unified data N to N interface; right) with unified data (red pentagon) N to 1 interfaces

3.2 Conversion (with possible massaging) and wrappers

3.2.1 AAA-Geometry

The Geometry Module in AAA help the user determines the geometry of the fuselage, wing, horizontal tail, vertical tail, v-tail and canard and calculates related parameters. Lifting surfaces such as wing, horizontal tail, vertical tail, v-tail and canard are defined either using the straight tapered method or the cranked surface method. The cranked lifting surface module has more detailed user inputs such as panel twist, panel dihedral, panel root and tip chords, panel root and tip locations etc. Bodies such as the fuselage, nacelles, tailbooms, stores etc. are defined in the AeroPack section of AAA. All bodies are described by cross-sections along the body axis (stations). Each cross-section consists of four conic sections. Each conic is defined by three sets of coordinates and a rho-value. Especially, the main highlights of the Geometry Module in AAA include: straight and cranked lifting surfaces can be defined for two-dimensional geometry; detailed fuselage geometry information, such as fuselage camber, inclination angles of each segment and cross-sectional area distribution can be obtained in the fuselage module where all cross-sections of the fuselage are showed; the control surfaces on each lifting surface can be plotted; fuel volume can be calculated, and fuel in cranked wings is accounted for.

The Coordinate System Definition is defined as where the (0,0,0) reference point is located. For the Fuselage, Nacelles, Stores, Tailbooms Coordinate System, the reference point is located at the apex points of the component. AAA can then export the components into AeroPack to create 3D CAD models AAA describes components according to two types: Lifting Surface, and Section Body. Specifically, AAA uses the following parameters to represent aircraft geometries:

- Lifting Surface type of components

IsMirrored	Symmetry
PanelCnt	Number of Panel to describle this lifting surface
P<n>RAirfoil	Name of Root Airfoil for Nth panel
P<n>NormalRoot	Root Airfoil Normal Vector
P<n>TAirfoil	Name of the Tip Airfoil for Nth panel
P<n>NormalTip	Tip Airfol Normal Vector
P<n>LERoot	Nth Panel leading edge root corner point
P<n>TERoot	Nth panel trailing edge root corner point
P<n>LEtip	Nth panel leading edge tip corner point
P<n>TEtip	Nth panel trailing edge tip corner point

- Section Body type of component

IsMirrored Symmetry
MirrorPlane Plane of Symmetry (origin point; normal SectionCnt vector)

For each section

S<n>_CrvCnt	Number of curves in Nth section
SC<n.m>_Type	Type of N.M curve (Conic, Line or Point)

For Conics:

SC<n.m>_Pnt1	N.Mth Conic y-z data point 1
SC<n.m>_Pnt2	N.Mth Conic y-z data point 2
SC<n.m>_Ctrl	N.Mth Conic y-z control point
SC<n.m>_Rho	N.Mth Conic rho value

For Lines

SC<n.m>_Pnt1	N.Mth Line y-z end point 1
SC<n.m>_Pnt2	N.Mth Line y-z end point 2

For Points

SC<n.m>_Pnt1	N.Mth y-z point

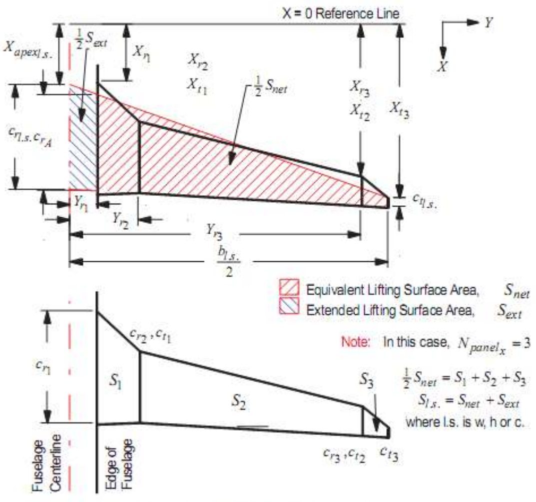

Figure 6. Cranked Surfaces Definition

Fig. 9: Cranked Surfaces Definition in AAA

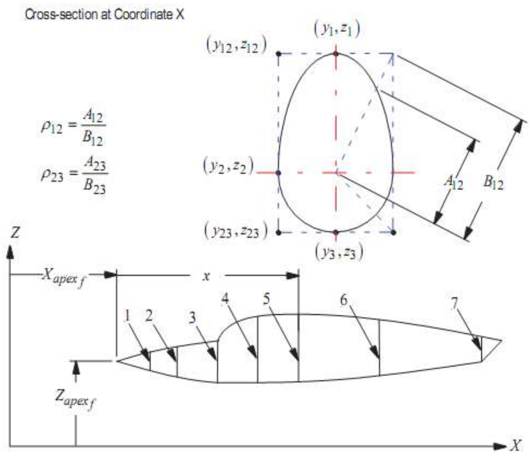

Figure 10. Cross Section Definition

Fig. 10: Cross Section Definition

3.2.2 AAA-CEASIOM/sumo interface

The data format stored in AAA's *.geo files and SUMO's *.smx files is quite different. They use different ways to describe aircraft geometry. For example, AAA lists all the components in the header part at the beginning, SUMO not; In terms of component definition, SUMO describes by defining the coordinates of each section for all the components and so contain essentially the same information, while AAA uses geometry parameters, thus more compactly.

The SUMO SMX file is an XML file defined standard XML technology. The converter from AAA to SUMO is a Matlab program which first read component geometry parameters into a hierarchical structure (Matlab structure). These geometric parameters is translated into component attributes such as component center, and for wingSkeleton type dihedral, twist, chord, section coordinates w.r.t local axis; for bodySkeleton body height, width, point coordinates in local frames.

3.2.3 CEASIOM Geometry[17]

The particular set of shape parameters adopted in SimSAC is referred to as the CEASIOM geometry. The parameters describe a model built from components such as fuselage, wing1, wing2, horizontal tail, etc., and the parameters have immediate interpretation for the aerodynamicist. The geometric model describes lifting surface planforms (with twist and dihedral) and cross-sections from a library of airfoil shapes, control surfaces, engine configurations, and a simple fuselage model. The geometry is created and edited by the ACBuilder interactive module, and saved in XML format. Further processing steps, such as payload and fuel positioning, estimations of weights and balance, etc., record their results by augmenting the XML file. The CEASIOM Piaggio geometry is shown in Figure 10, right.

CEASIOM geometry is easily interrogated for lifting surfaces such as wing, vertical tail, and stabilizer for VLM analysis. CEASIOM geometry may also be appropriate for Euler flow solutions. Thus, at the next higher level of detail, SUMO can be used to refine the CEASIOM model into a more detailed geometry based on a moderate number (often less than 30) spline surfaces, Figure 11, left. This description is used to generate a triangular mesh on the surface, for a 3D panel method and as surface mesh for CFD solutions based on the Euler equations, Figure 11, right. When viscous flow models are called for, the geometry can be exported to CAD systems and/or mesh generation software by means of IGES files. The CEASIOM system has taken steps in this direction, as described below in Figs 10, 11, and 12.

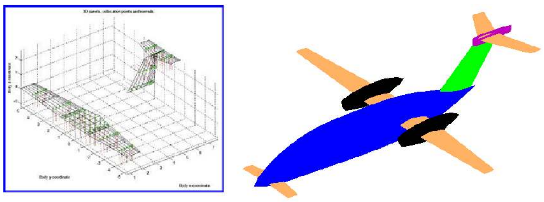

Fig. 11 Left) VLM Geomtry; Right) CPACSCreator

Fig. 12: Left) SUMO model; Right) Unstructured volume mesh

3.2.4 Data flows – export to AAA

The data flows described how data are sent to CPACS from AAA is represented in Fig. 12. The non-meshable AAA geometry is converted to a meshable grid that is available for higher fidelity CFD and stability analysis via CPACS.

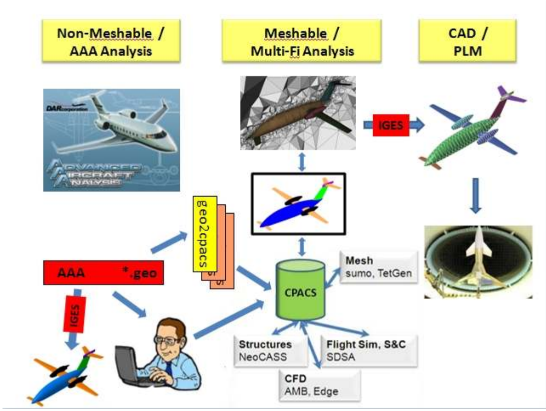

Fig. 13: Linking conceputal design code to preliminary design code via CPACS

3.2.5 Data flows – import to AAA

Once aerodata is obtained, the goal is to return it to AAA for further performance analysis. For example the VLM results described above can be used for stability and control analysis. Another advantage is for example the Euler results (higher-fidelity) can complement and enrich the aerodata for the Avanti with realistic transonic results. This part will be the future work that is working on.

4 Test Cases – Piaggio P-180

4.1 Transonic aerodata

Piaggio's aerodynamic performances at maximum cruise flight condition[18]: Mach number 0.7, Altitude 9450 m, with cruise lift coefficient CL = 0.28. Using the AAA - CEASIOM sumo Interface, the AAA geo model was translated into a Sumo model, where unstructured volume mesh was generated by Tetgen method, and then Edge Euler calculation was applied. We can see that the local Mach number begins to rise to above sonic at around a quarter of the chord, thus the shock wave forms. The inviscid drag at the cruise point is 16.9 counts calculated by Euler solver, see Figs, 13, 14 and 15.

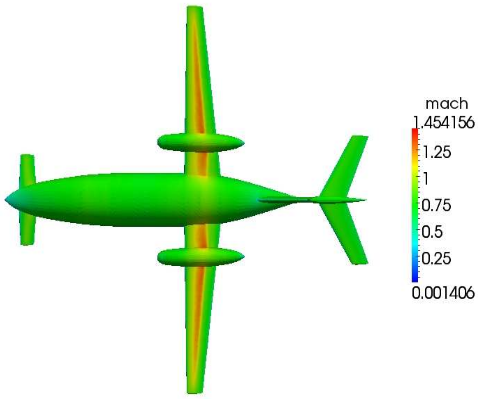

Fig. 14: Mach contour plot for M=0.7 and CL=0.28

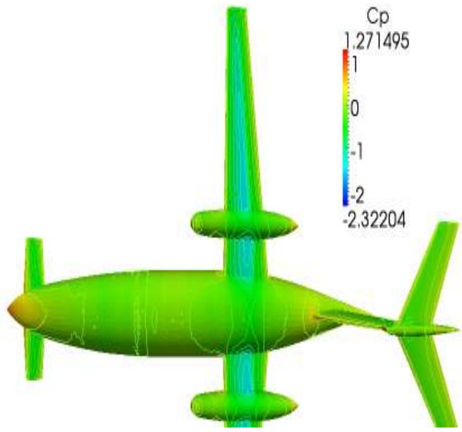

Fig. 15: Cp contour plot on upper surface

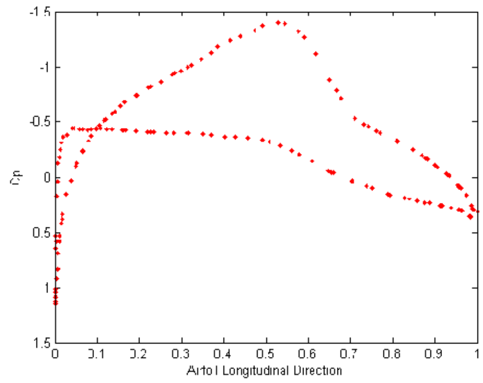

Fig. 16: Cross section pressure distribution at around half of the semi-span wise station

The inviscid drag is calculated from Euler solver, shown in Fig. 18. We can see that the drag begins to arise significantly between Mach 0.6 and 0.7, where the wave drag takes a large part. It is calculated that at cruise point the wave drag is 9.6 counts, or 56.7% of the inviscid drag. It should be able to be improved, due to the inefficiency of the wing, if we go back to Fig. 17, that the Cp is "cross-over" and the wing doesn't produce enough lift.

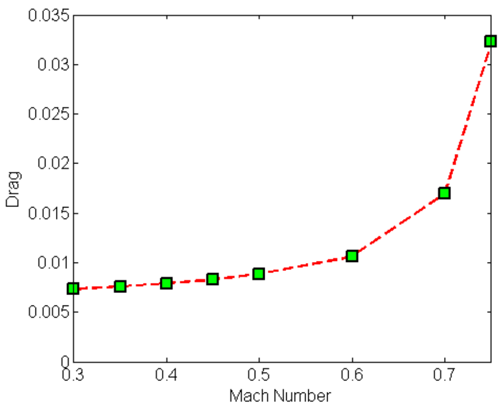

Fig. 17: Inviscid drag polar at CL=0.28

4.2 Stability and control analysis

Figs. 18 and 19 show the pitch trim predicted by VLM. By enabling the Euler solutions for transonic regime that we can analysis the longitudinal stability in a more realistic way.

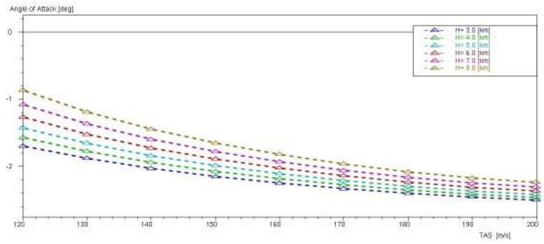

Fig. 18: Trimmed Angle of Attack of Aventi-P180 at different speeds and altitudes, predicted by VLM

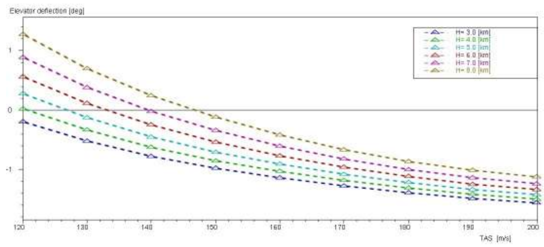

Fig. 19: Trimmed elevator deflection (mounted on the horizontal tail) of Aventi-P180 at different speeds and altitutes, predicted by VLM

References

[1] AAA_Geometry Design Assistant for Airplane Preliminary Design Willem A.J. Anemaat and Balaji Kaushik, 49th AIAA Aerospace Sciences Meeting including the New Horizons Forum and Aerospace Exposition4 - 7 January 2011, Orlando, Florida

[2] Rizzi, A.: Modeling and simulating aircraft stability and control The SimSAC project, Prog Aerospace Sci, Vol 47, 2011, pp.573-588. see also www.ceasiom.com (Date 15.12.2011)

[3] Tomac, M. and Eller, D.: From geometry to CFD grids An automated approach for conceptual design, Prog Aerospace Sci, Vol 47, 2011, pp.589596

[4] Da Ronch, A., Ghoreyshi, M and Badcock, K.J.: On the generation of ight dynamics aerodynamic tables by computational fluid dynamics, Prog Aerospace Sci, Vol 47, 2011, pp.597620

[5] Goetzendorf-Grabowski, T., Mieszalski, D. and Marcinkiewicz, E.: Stability analysis using SDSA tool, Prog AerospaceSci, Vol 47, 2011, pp.636646
[6] Cavagna, L., Ricci., and Travaglini, L.: NeoCASS: An integrated tool for structural sizing, aeroelastic analysis and MDO at conceptual design level, Prog Aerospace Sci, Vol 47, 2011, pp.621635
[7] Richardson, T.S, Beaverstock, C., Isikveren, A., Meheri, A., Badcock, K.J. and Da Ronch, A.: Analysis of the Boeing 747-100 using CEASIOM, Prog Aerospace Sci, Vol 47, 2011, pp.660673
[8] Rizzi, A., Eliasson, P., Goetzendorf-Grabowski, T., Vos, J.B., Zhang, M. and Richardson, T.S., Design of a canard configured TransCruiser using CEASIOM, Prog Aerospace Sci, Vol 47, 2011, pp.695705
[9] Richardson, T.S, McFarlane, C., Isikveren, A., Badcock, K.J. and Da Ronch, A.: Analysis of conventional and asymmetric aircraft configurations using CEASIOM Prog Aerospace Sci, Vol 47, 2011, pp.647659
[10] A. Rizzi, M. Zhang, B. Nagel, D. Boehnke, P. Saquet, Towards a Unified Framework using CPACS for Geometry Management in Aircraft Design, 50th AIAA Aerospace Sciences Meeting, 09-12 January 2012, Nashville, Tennesses
[11] Böhnke, D., Reichwein, A., and Rudolph, S., Design Language for Airplane Geometries using the Unified Modeling Language. ASME Int. Design Engineering Technical Conferences (IDETC) & Computers and Information in Engineering Conference (CIE), (2009)
[12] Liersch, C.M. and Hepperle, M.: A Distributed Toolbox for Multidisciplinary Preliminary Aircraft Design, CEAS Aeronautical Journal, Vol 2, No1-4, 2011, Pages 57-68
[13] Zill, T., Böhnke, D., Nagel, B., Gollnick, V.: Preliminary Aircraft Design in a Collaborative Multidisciplinary Design Environment, AIAA Aviation Technology, Integration and Operations Conference, (2011)
[14] Zill, T., Ciampa,P.D. , Nagel, B.: Multidisciplinary Design Optimization in a Collaborative Distributed Aircraft Design System, accepted for AIAA Aerospace Science Meeting, (2012)
[15] Böhnke, D., Jepsen, J., Pfeier, T., Nagel, B., Gollnick, V., Liersch, C.: An Integrated Method for Determiniation of theOswald Factor in a Multi-Fidelity Design Environment, 3rd CEAS Air & Space Conference , (2011)
[16] Pfeier, T., Nagel, T., Bhnke, D., Rizzi, A., Voskuijl, M.: Implementation of a Heterogeneous, Variable-Fidelity Framework for Flight Mechanics Analysis in Preliminary Aircraft Design, DGLR Congress, (2011)
[17] A. Rizzi, J. Oppelstrup, M. Zhang, M. Tomac, Coupling Parametric Aircraft Lofting to CFD & CSM Grid Generation for Conceptual Design, 49th AIAA Aerospace Sciences Meeting, 4-7 January 2011, Orlando, Florida
[18] http://www.piaggioaero.com/

4:th CEAS Air & Space Conference
FTF Congress: Flygteknik 2013

Virtual Aircraft Multidisciplinary Analysis and Design Processes – Lessons Learned from the Collaborative Design Project VAMP

Björn Nagel[1], Thomas Zill[1], Erwin Moerland[1] and Daniel Böhnke[1]
[1]*German Aerospace Center (DLR)*
Institute of Air Transportation Systems, Hamburg, Germany

Keywords: *Collaborative Design, Multidisciplinary Design Optimization, Knowledge Management, Overall Aircraft Design, Integration*

The assessment of unconventional aircraft configurations and novel technologies at high levels of confidence requires integrating all analysis tools at appropriate high levels of fidelity. With this ambition, a design system has been developed and implemented at DLR permitting the connection of tools of elevated fidelity in an overall aircraft design (OAD) process with significantly reduced effort. This paper gives an introduction into the distributed design system with its data-centric coupling approach. The application to the optimization of short range aircraft within the DLR project VAMP (Virtual Aircraft Multidisciplinary Analysis and Design Processes) is discussed. A main outcome of the project are the lessons learned which refer to the numeric optimization process as well as to the collaboration process within the team of heterogeneous specialists coming from eleven departments spread over Germany.

1 Introduction

Reliability of results is a key requirement if aircraft design studies aim at the assessment of technologies as basis for strategic forward planning. However, achieving quantified, high levels of confidence is very difficult in OAD: Due to the high number of disciplines involved, only fast tools can be used going in line with strongly simplifying models. While redesigns of conventional aircraft can be calculated satisfactorily by making use of empirical correlations, integration of novel technologies and design of unconventional configurations cannot reach high levels of confidence using these conventional OAD methods.

The integration of novel technologies in the design process can be realized following two approaches: One alternative is developing novel fast tools which are appropriate for conventional OAD processes and represent the novel technologies in a simplified way. Since by nature there is no reliable experience available, the development and validation of simplified models can cause excessive effort and still result in simplified analyses. The other alternative is building an OAD system based on higher fidelity models which resolve novel technologies explicitly. Like this, the effort for the implementation of the novel technologies into the disciplinary analysis models is minimized and the accurately modeled physics permit highly reliable results. Interdisciplinary interactions which initially might have not been expected can potentially be observed in the analysis whereas simplified models would only resolve expected couplings. However, significant effort for computing and the integration of the high number of analysis tools poses a serious challenge.

The German Aerospace Center has launched the project TIVA (Technology Integration for the Virtual Aircraft) in 2005, aiming at the identification of technologies for the efficient integration of analysis software into large workflows. The follow-on project TIVA 2 developed coupling technologies around the central data model CPACS (Common Parametric Aircraft Configuration Scheme) from 2007 till 2009. From 2010 till 2013 the project VAMP (Virtual Aircraft Multidisciplinary Analysis and Design Processes) developed the capability to realize multidisciplinary optimization of configurations in a large team of specialists and has been further developing the coupling technologies according to the requirements identified during the application.

Section 2 of this paper provides a short introduction to the current status of the coupling technologies. Section 3 shows the analysis tools and the implemented variable fidelity workflow. Section 4 discusses the validation strategy and shows exemplary results. Section 5 presents the optimization approach used. Sections 2-5 widely refer to specialized publications in course of the project. Section 6 presents the lessons learned from the practical application of the coupling techniques. Beyond technical issues on multidisciplinary optimization and computing, knowledge was built on the implementation of a collaborative design team with approximately 25 persons from 11 departments allocated in 6 DLR sites spread over Germany. The paper ends with a description of the way forward in collaborative MDO within the DLR in section 7.

2 Networked Design System

Software for interlinking tools on different servers is becoming state of the art. Prominent commercial examples are ModelCenter [7], iSIGHT [8] and OPTIMUS [9]. An open source alternative is the "Remote Component Environment" (RCE) [10], which is based on ECLIPSE technologies [11]. Implementing networked design workflows is widely assisted by these software systems. However, tools of elevated level of fidelity require explicit modeling and hence rely on extensive data sets for input and output. Since no software can know how the namespace of one tool needs to be mapped to the next tool in the workflow, a large workload for the operator is inevitable. This error prone step in the design process is responsible for the majority of the overall effort for advanced fidelity OAD using the latest software technologies. The technology considerably simplifying this problem is a central data model which is CPACS in the DLR environment.

This is a typical example of the well-known ability of standards to turn an N^2 problem (where N is the number of software packages and N^2 is the number of possible connections among them) into an order N problem. Software "wrappers" need to be created for the individual tools. Wrapper components around the analysis software contain both the translation from/to CPACS and the commands to launch the analysis application

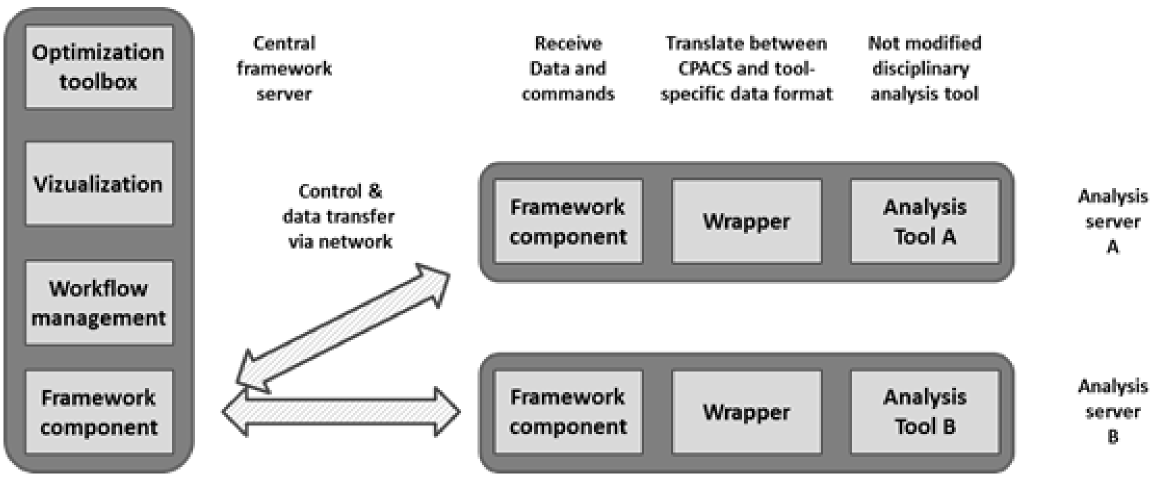

Figure 1: Distributed design system

in batch mode once the necessary data is provided. Therefore, from the outside, a wrapped program looks like a single application that includes a CPACS interface. Usually the tool developers are responsible for creating the wrapper for their own tool with support from integration experts providing an introduction to CPACS and sample implementations

CPACS is implemented as a Schema Definition (XSD) for the Extensible Markup Language (XML). In this manner, it defines the elements, attributes and structure of all the information that may be used within CPACS models. The explicit data models used for analyses are instantiated following all rules of the XSD and employ only the information that is required for the specific use case. The format is human readable and computer processable.

For convenient handling of CPACS files, the software library TIXI was developed [3]. TIXI provides an Application Programming Interface (API) for C, C++, Python, Java, MATLAB and FORTRAN. Based on the libxml2 library [4], TIXI permits to easily integrate XML-handling functionality into wrappers including the creation of documents, creation and deletion of nodes, addition and removal of element attributes and reading and writing multidimensional arrays or arrays of vectors.

Processing geometry information stored in CPACS can be performed using the TIGL library [5]. Analogue to TIXI, TIGL permits simple access to the open source CAD software OpenCASCADE [6], specifically tailored for the CPACS data model. Based on design parameters stored in CPACS, functions provided by TIGL range from computing arbitrary surface points via detecting intersections between components to exporting geometries e.g. in IGES/VTK format.

Aiming at applications in aircraft design, the root elements of the data model hierarchy represent the typical components used in the conceptual design of aircraft. Thus, for low levels of fidelity and small numbers of variables the format is relatively simple, easy to understand, and similar to parameterizations used in other aircraft conceptual design tools.

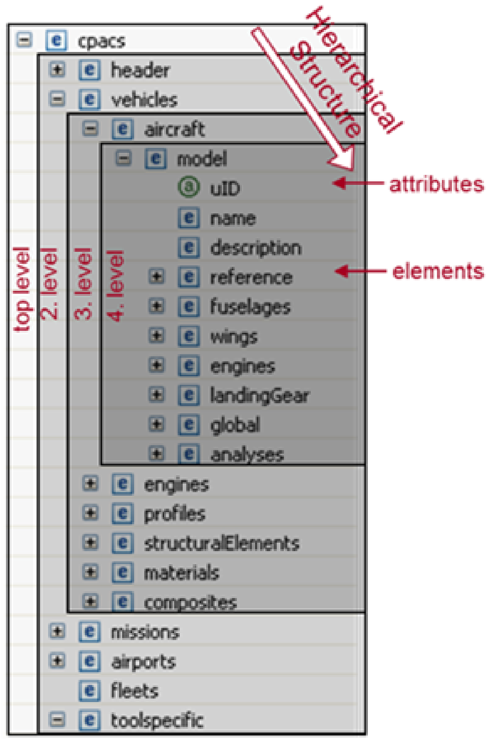

Figure 2: CPACS hierarchical data structure

Complex designs and unconventional configurations can, in principle, be realized by combining different kinds of components within CPACS. The definition of assemblies uses hierarchies between components permitting a functional description of the entire vehicle. Individual components and assemblies can be used multiple times in higher-order assemblies in an efficient way through the use of Unique Information Identifiers (UIDs). Each time a component is referred to, it can be geometrically transformed through scaling and rotation (relative to the global coordinate system or to the parent assembly) so as to define new components. Due to the hierarchical nature of the data model, transformations of assemblies act on all children elements.

When moving from the root of the data hierarchy to its branches, the level of detail increases. Thus, while performing a conceptual design with a CPACS model that only contains root information, more detailed analyses can be carried out by adding more branches to the original model. In this way, CPACS is capable of handling data for multiple levels of geometric and/or analysis fidelity. The schema definition is set up to support variable-fidelity applications and to avoid conflicts in the data model. However, challenges of variable fidelity such as linking models of different fidelity-level are not solved by the data model itself but must be realized in the design optimization process [24].

One important feature of CPACS is the handling of both product and process information, i.e. not only the aircraft is described but also tool-specific information to control parts of the analysis process. One example is found in the inclusion of control parameters to drive the meshing of geometries for structural analyses.

CPACS is a living format undergoing a structured development process. In principle, CPACS can be expanded to model arbitrary aircraft design problems. The format is published under open source license agreement together with a growing documentation database [1]. A more detailed description of the approach underlying CPACS and the data content is given in [1] and in [2].

3 VAMP Analysis Tool Set

The design tools used in VAMP can be categorized into three levels:

The first level is comprised by the conceptual design tool VAMPzero which was created during the project [12]. Based on empirical correlations it provides classical stand-alone OAD capabilities and returns basic aircraft characteristics and performance for given mission requirements and/or vehicle specifications. Due to the highly modular program architecture, VAMPzero can be adapted to different sets of input and output data. Furthermore, individual analysis components can be replaced by external tools.

A second level of tools is constituted by disciplinary analysis modules which physically resolve the necessary disciplines of OAD. These tools have their origin in the portfolio of the disciplinary research institutes of DLR. The level of fidelity is selected to be as low as possible while still being in active use by the specialists for investigating technologies of concern.

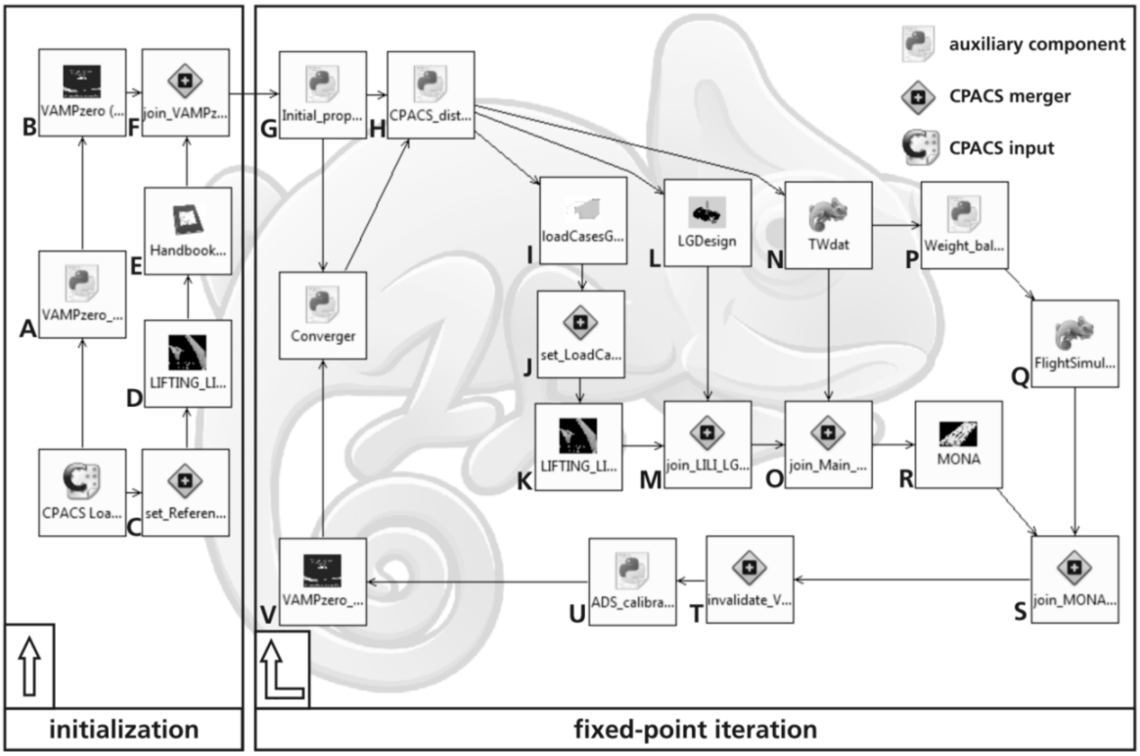

Figure 3: VAMP aircraft analysis workflow

The third level comprises tools of higher fidelity going in line with execution times which exceed the practical limits of optimization workflows. In addition, this level contains analysis tools modelling disciplines which do not drive the design in the specific studies and are executed only once during post processing.

Figure 3 shows the main OAD analysis workflow implemented in the RCE framework containing first and second level tools.

The process is initiated by VAMPzero (B) from an initial CPACS dataset (A), which specifies the outer geometry of the aircraft, its initial structural topology and the mission requirements. It determines the performance and mass properties of the aircraft on a conceptual design level, which are used to initialize the execution of the downstream analysis modules.

In parallel, aerodynamic performance maps for a multitude of combinations of Mach and Reynolds number as well as angles of yaw and attack are computed by the potential-theory code LIFTING_LINE (D).

HandbookAero (E) subsequently determines the missing drag components and corrects the performance maps accordingly.

Subsequently, the CPACS-mapping component join_VAMPzero_LILI (F) merges the results of the parallel branch into a single CPACS-object and the iterative synthesis process commences.

Depending on the mass properties of the aircraft in the current cycle, loadCaseGenerator (I) determines load case definitions for a maximum take-off mass layout.

Subsequently, a second instance of LIFTING_LINE (K) is run to calculate the spanwise load distributions for the set of defined load cases.

Concurrently, LGDesign (L) determines the mass of the nose and main gear by taking into account amongst others the current center of gravity as well as the corresponding aircraft mass and the geometric layout of the landing gear.

In parallel, TWdat (N) provides a scaled engine performance map for the required static thrust at sea-level. The individual results are subsequently consolidated into a single CPACS-object.

After these calculations the workflow splits up into another parallel branch. Reading amongst others the current weight and balance case for the aircraft, the aerodynamic performance map as well as the engine characteristic map, FlightSimulation (Q) determines the required trip fuel for the design transport mission.

Simultaneously, MONA (R) performs a FEM-based structural sizing of the main wing, taking into account the current engine mass, ground forces introduced by the landing gear as well as aerodynamic load distributions for the defined load cases.

Up to this point, the disciplinary analysis modules have enhanced the conceptual sizing results of the first VAMPzero instance. To allow for a new synthesis calculation by a second instance of VAMPzero, invalidate_VAMPzero (T) deletes all data that are not provided by the high-fidelity components in the iterative cycle from the current CPACS-object.

For system calibration purposes the component ADS_calibration (U) allows for the manipulation of any element in the CPACS-object. VAMPzero's aforementioned multifidelity capabilities enable to account for these enhanced results in a new synthesis calculation (V), preserving the high-fidelity results and determining updated global aircraft characteristics using its conceptual design methods.

The results are fed back to the converger, which repeats the iterative synthesis loop until the convergence criterion is satisfied by all global convergence parameters. When convergence is reached, the design data can be extracted from VAMPzero (V).

Attached to this overall aircraft analysis workflow additional tools are used which refine details of the aircraft model. One example is a tool for automated cabin layout, which uses knowledge patterns together with user input in order to generate realistic internal geometries and mass distributions (Figure 4). This permits to introduce design requirements for the cabin into the OAD process and to derive relevant mass data. In the same time, this model acts as an interface to more detailed research into the cabin which makes use of the resulting configuration: Based on the generated pre design geometry a full CAD model of the cabin can be generated automatically which permits subsequent meshing for internal CFD computations [23].

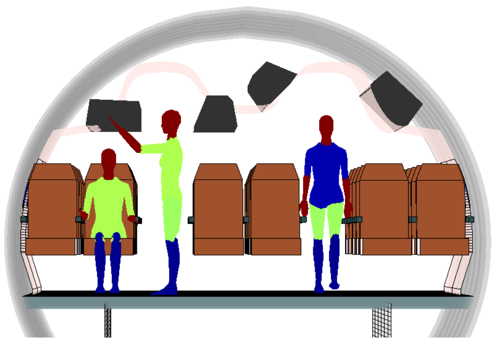

Figure 4: Automatically generated twin aisle cabin for a next generation short range study

All information of relevance to other analyses is stored in the central CPACS model. The inner geometry and mass entities for example are handed over to structural fuselage model generators such as TRAFUMO. In analogy, ELWIS is a different model generator which creates wing structures including explicit modelling of the movables. Figure 5 shows a global FEM model composed of TRAFUMO and ELWIS sub models, both based on the same CPACS data model. Details such as the explicit fuselage-wing interface and modelled movables inclusive support structure are contained [19]. These are examples of higher fidelity tools which are used for more detailed structural analyses which require explicit FEM shell and beam models.

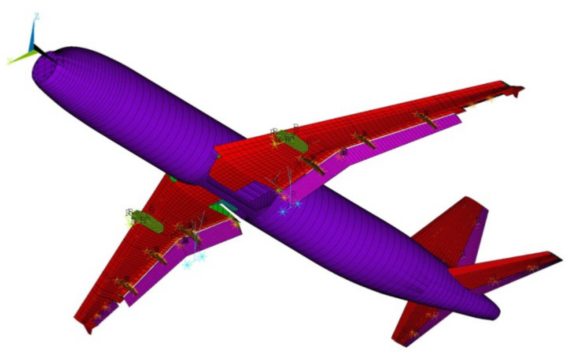

Figure 5: Global FEM model of reference short range configuration

Besides the tools which where exemplarily mentioned, further tools are available e.g. for the computation of flight performance and handling qualities, external noise, gaseous emissions and climate impact.

4 Validation

The validation of extensive MDO workflows for OAD principally poses a serious challenge. VAMP used two conventional aircraft configurations as use-case which can be compared with in-production short range (D150) and long range (D250) aircraft.

Validation was performed on two levels: On OAD level the global workflow was used to re-design the real configuration and to perform trade studies over some major design parameters such as aspect ratio and wing area.

The calculated main performance characteristics were compared with published data of the real aircraft. Figure 6 shows exemplary a payload-range range diagram for a reference configuration with overlaid CO2 emissions per seat km.

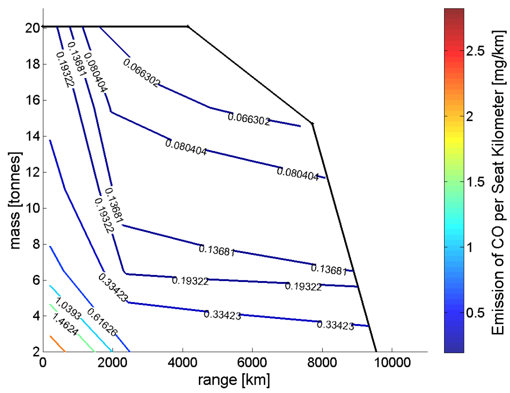

Figure 6: Calculated payload-range characteristic for reference short range configuration with CO2 emissions per seat km

In addition, results were compared with other OAD tools i.e. the Preliminary Aircraft Design and Optimization code PrADO of TU Braunschweig. The comparison of results within parameter studies permits to investigate differences in sensitivities resulting from different models employed. Furthermore, this comparison offered very valuable opportunities for the debugging of the systems [14].

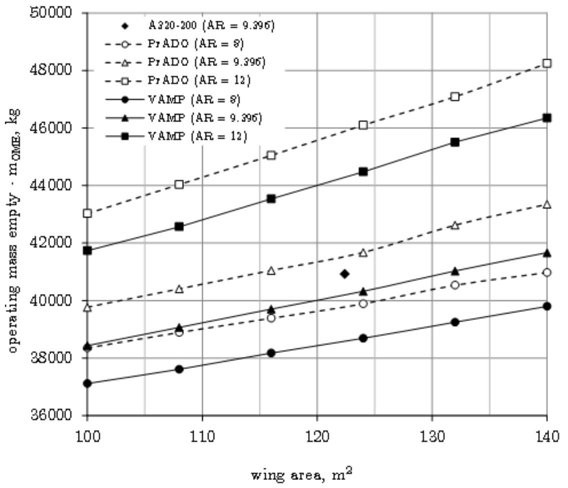

Figure 7: Comparison of OEW between DLR framework and PrADO tool for variation of wing area and aspect ratio

On top of the validation on OAD level, validation was performed on level of the individual disciplinary tools. Table 1 shows exemplary results from the validation of the structural mass estimation [20].

component	error D150 [%]	error D250 [%]
skins + stringer	0.1	-0.1
spars	-5.4	5.4
ribs	-12.4	12.4
flap bodies	20.6	-20.6
flap track carriages	30.6	-1.5
flap tracks (incl. att.)	7.2	-7.2
total	**0.1**	**1.2**

Table 1: Comparison of results from the ELWIS tool with reference short and long range aircraft data using same calibration factors

5 Optimization Concept

The cost for numerical design optimization scales well with the computational cost of the employed analysis system. In the VAMP workflow, the low-fidelity conceptual design module VAMPzero, which is used to initiate the process and later to perform the multifidelity synthesis, and the higher fidelity disciplinary modules are combined into an integrated aircraft design workflow. As performing direct design optimization with the workflow can be costly, the question in the VAMP project was, if these different levels of fidelity can be exploited efficiently in an optimization process.

In this context, a straightforward approach would be to perform the optimization solely with the low-fidelity module and only reanalyze this optimum design with the VAMP workflow in the notion that both will provide similar results, which only differ in the degree of detail of the analyses.

A key-issue of this approach will surface when doing so. Aircraft syntheses calculations performed with a low- and a high-fidelity code will not provide identical quantitative results. Due to even only minor differences in the analysis modules, dissimilar absolute values and sensitivities of the design objectives and constraints will be obtained from both methods, although identical inputs have been provided. Hence, aircraft optimized for the same targets may turn out completely different depending on the level of fidelity employed. To still benefit from the multifidelity foundation of the VAMP workflow, a multifidelity optimization framework, using a selective calibration approach, was implemented. The basic concept of this approach is depicted in Figure 8.

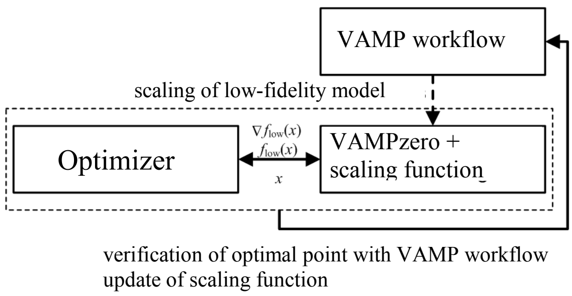

Figure 8: VAMP optimization concept

In this framework the computationally expensive VAMP workflow is run only to provide high-fidelity results to build and calibrate a correcting additive scaling function during the course of the optimization process, while all optimization calculations are performed solely with VAMPzero. Within this iterative MDO framework, convergence to an optimum design is achieved by employing a trust region optimization strategy. By successively recalibrating the low-fidelity model by means of the scaling function, the move limits of the trust region, i.e. its radius and center point, are then adapted after each low-fidelity optimization loop. This leads the optimizer to the optimum point of the high-fidelity model. As shown in [15], this multifidelity approach provides significant savings in high-fidelity analyses compared to established MDO methods, such as metamodeling or standard black-box optimization approaches.

6 Lessons Learned

The advanced software infrastructure which is available today might stimulate the impression that building comprehensive workflows has become a straightforward task. In fact, many computational challenges could be solved in the past, opening now the view to the next generation of challenges. The following paragraphs summarize the lessons learned during the VAMP project.

The computing system was set up as decentralized workflow with specialized software tools of experts being executed on their hardware. The reason for this decision is twofold: First, some software has specific hardware or licensing requirements. The linked structural crash simulation for example relies on a computer cluster. The effort for networked computing is smaller than the effort for implementation and maintenance of all codes on a centralized hardware. Second, in this setup the owners of software keep control over its utilization. The latter reason has shown to be decisive for collaborative design. One aspect in this sense is, of course, costs and revenue. However, even more critical it is seen that utilization of expert codes by non-experts bears the risk of unrealistic results which damage the reputation of the tool owner. The decentralized approach leaves the control explicitly at the owner.

The decentralized approach permits efficient workflow management and parallel executions of tasks. However, this advantage is alleviated by data transfer effort and irregularities caused by network interruptions or maintenance events of the heterogeneous hard and software. The inclusion of restart capabilities of complex workflows is an unsolved challenge.

The first challenge in building a workflow is interconnecting all tools in a way that input data and output data are interconnected in a correct way. While interconnecting non-matching data types leads to errors which can easily be detected, the debugging of a workflow where improper values are generated is far more difficult. The assessment if a specialist's code generates reasonable results requires expert's knowledge. Hence, the process integrator cannot solve this task alone but needs to communicate with the specialists.

However, in frameworks it can be hard to identify which of the included codes returns improper results, especially within iteration loops. Thus, debugging requires the capability to flexibly organize discussions and potentially physical meetings of different specialists. In the practical work this has been a bottleneck. Most involved persons did not work full time in the project hence were not permanently available. Organizing an ad-hoc meeting of multiple part-time involved specialists can cause significant delay in debugging.

Beyond organisation, knowledge constitutes a central challenge of collaborative design in heterogeneous teams of experts. The required expertise in the different disciplines is built in the team by persons who are specialized in individual disciplines. It is a matter of fact that specialization in one discipline goes in line with reduced activities and competences of that person in the other disciplines. In heterogeneous teams of experts, the overlap of knowledge can be small causing problems in understanding another. Therefore communication needs to be very depict and explicit. Different standards and conventions in the different disciplines amplify this effect.

Extensive reporting and data management can prevent some problems of interdisciplinary communication. However, beyond correctly handing over data sets, comprehension of the over-all process is a main challenge for the team which is mandatory already during the first debugging of the coupled system. Excessive information libraries might even be prejudicial for comprehension.

During the project it was experienced that gaining comprehension can be realized much better during physical meetings than in any kind of decentralized communication such as videoconferencing. The entire project team conducted full meetings every three months. The meetings usually had durations of two days or more also providing room for individual dialogues next to the official agenda during the evening events.

Physical meetings also tend to make a positive impact on motivation which is another important aspect of collaboration in heterogeneous teams: By nature, specialists have their main interest in their discipline. Usually there is also some interest for the over-all configuration since it provides input data for their field of specializations. The interest in most of the other disciplines is significantly lower. Thus, for OAD studies involving higher levels of fidelity, all specialists are required in order to comprehend the process but the individual specialists only have a natural interest in a small fraction of the entire process. In VAMP, the OAD task was complemented by five tasks focussing on disciplinary tool development or analysis of technologies. These tasks which investigated topics like the loads process, stability and control or external noise were coordinated by the dedicated specialists and used the OAD dataset. Like this, the interests of OAD experts and disciplinary specialists could be satisfied in the same time. This setup of the project also permitted to shift the workforce according to the hard-to-predict requirements of the networked approach. The deep insight into the configuration led to the question how to document results of large workflows since the merged analyses of all experts can lead to excessive reports.

In the course of the project the CPACS data model was successively updated. While additive extensions did not cause drawbacks, modifications of existing conventions went in line with severe effort for modifications of the tool wrappers. Thus, the initial definition of CPACS as aircraft dictionary on classical OAD-level was straightforward. The later integration of higher fidelity parameterizations together with the object oriented approach was a successive learning process which resulted from the involvement of disciplinary specialists. In the current version 2.1 of CPACS all disciplines relevant for OAD have been revised by dedicated specialists and further large relevant modifications are unlikely.

7 Way Forward

Beyond the successfully performed validation of the system for two existing aircraft, the quantification of confidence levels also for less conventional configurations is targeted. While the disciplinary tools are validated to a wide extent, the propagation of uncertainties through the workflow is in the focus of the follow-on project “Future Enhanced Aircraft Configurations” (FrEACs). Furthermore, the skills for collaborative MDO in heterogeneous teams will be further advanced in the extended project team which now comprises 18 departments of DLR.

One measure for reducing uncertainties is moving towards higher levels of fidelity. The DLR project DIGITAL-X aims at high fidelity analyses incorporating aero-structural interactions and the required application of high performance computing. AEROSTRUCT is a sister project in the German national research programme in cooperation with Airbus and CASSIDIAN. Interfaces between high fidelity modelling and the pre-design oriented CPACS design system permits seamless integration.

The CPACS data model is extended for the representation of military configurations within the DLR project FAUSST and its successor MEPHISTO in cooperation with CASSIDIAN.

iLOADS is a project which extends DLR’s capabilities in loads predictions as they are necessary for the certifications of modifications of DLR’s research aircraft. In this frame, the elementary loads process of VAMP will be extended by load case analyses for conventional and unconventional configurations.

A sister project to FrEACs is PEGASUS, which investigates design methods for turbo engines. The analysis is performed by coupling analysis models for each individual component.

The data interfacing makes use of CPACS, creating the basis for coupled design of airframe and engine. Basic OAD capabilities developed in VAMP are used in PEGASUS for determining design point data for engine layout. FrEACs and PEGASUS are coordinated and working on the same use cases [26].

The assessment of the climate impact of aviation was investigated in the project CATS. Based on the CPACS system, operational analyses on world fleet level were realized leading to the quantitative distribution of emissions. Through usage of climate models, the assessment of temperature rise caused by aircraft operations became quantifiable. The follow-on project WeCare extends this capability by introducing operational measures for mitigating climate impact. Due to the CPACS interface, operational measures can be combined with airframe technologies from the FrEACs project and engine technologies from the PEGASUS project.

Applications of the CPACS system in external projects are realised e.g. in the project AIRPORT2030 within the Excellence Initiative of the German government, which investigates the interface between airport and aircraft. Another example is the project FAIR which investigates novel energy sources and propulsion concepts for future aircraft. In both projects, the core OAD capability was used as basis. The project work then extended the system for the specific applications.

Operating complex information systems in teams of heterogeneous experts and the utilization of concurrent design facilities are in the focus of the iTALENT project within the frame of the Aeronautics Research Programme of the City of Hamburg [30], [31].

In order to foster interdisciplinary collaboration also with external partners, DLR has published all relevant technologies under open source licence. In consequence of this decision, joint development and research activities were launched. Examples are the utilization of Knowledge Based Engineering (KBE) techniques and integration of flexible effects together with TU Delft [27] and techniques for model build up and integration of high fidelity aerodynamic analyses also for unconventional configurations together with KTH Stockholm [28]. In result of these activities, tools from the CEASIOM “Computerised Environment for Aircraft Synthesis and Integrated Optimisation Methods” public domain tool suite were made available via the CPACS model and used within DLR’s framework [18]. A follow-on activity was linking CEASIOM tools with the commercial conceptual aircraft design tool AAA “Advanced Aircraft Analysis” of the DAR Corporation [29]. The CPACS system is also used by CASSIDIAN eg. together with TU Munich in [32] for aircraft loft optimization with respect to aeroelastic lift and induced drag loads

8 Conclusions

A distributed system for aircraft design was developed and implemented at DLR. The coupling of multidisciplinary analysis codes of different levels of fidelity is realised by the central data model CPACS. Within the VAMP project, an over-all design workflow spanning over tools from eleven departments was realized and optimization studies using adapted algorithms were performed. While coupling tools in a distributed environment can be realized with reasonable effort; the operation of complex, interdisciplinary IT systems in heterogeneous teams of experts constitutes the major challenge nowadays. VAMP established a first successful collaboration process.

The publication of all required coupling technologies under open source licence was premise to create an active user community which can now significantly reduce its effort for MDO by sharing tools and competences. This opens the way to practice research into the collaborative application of MDO systems aiming at the exploitation of both, the performance of advanced tools as well as expertise and creativity of the engineers.

9 Acknowledgement

The authors like to thank the VAMP project partners for the excellent collaboration:

- Institute of Aeroelastics (DLR-AE) Thomas Klimmek, Sunpeth Cumnuantip, Rene Liepelt, Gabriel Chiozzotto
- Institute of Aerodynamics (DLR-AS) Carsten Liersch, Lothar Bertsch
- Institute of Propulsion Technology (DLR-AT): Tom Otten, Richard Becker, Sebastien Guerin
- Institute of Structures and Design (DLR-BK): Dieter Kohlgrüber, Klaus Harbig, Julian Scherer
- Institute of Composite Structures and Adaptronics (DLR-FA): Sebastian Freund, Falk Heinecke
- Institute of Flight Systems (DLR-FT): Jana Ehlers, Christian Raab
- Institute of Simulation and Software Technologies (DLR-SC): Doreen Seider, Markus Kunde, Martin Siggel
- Institute of System Dynamics and Control (DLR-SR): Gertjan Looye, Thiemo Kier

Corresponding Author

Björn Nagel
German Aerospace Center (DLR)
Institute of Air Transportation Systems (LY)
Blohmstraße 18, 21079 Hamburg, Germany
Email: bjoern.nagel@dlr.de
Telephone: +49-40-42878-3804

Literature

[1] D. Böhnke "Common Parametric Aircraft Configuration Schema" http://software.dlr.de/p/cpacs/
[2] C. M. Liersch, M. Hepperle, A distributed toolbox for multidisciplinary preliminary aircraft design, *CEAS Aeronautical Journal (2011) 2:57–68*.
[3] M. Litz, A. Bachmann, M. Kunde, "TIVA XML Interface," http:// software.dlr.de/p/tixi/
[4] http://www.xmlsoft.org/
[5] M. Litz, A. Bachmann, M. Kunde, "TIVA Geometric Library," http:// software.dlr.de/p/tigl/
[6] http://www.opencascade.org/
[7] http://www.phoenix-int.com/software/phx-modelcenter.php
[8] http://www.3ds.com/products/simulia/
[9] http://www.noesissolutions.com/Noesis/optimus-details
[10] D. Seider, M. Litz, A. Schreiber, P. M. Fischer, A. Gerndt, Open Source Software Framework for Applications in Aeronautics and Space, *IEEE Aerospace Conference, 2012*.
[11] http://www.eclipse.org/
[12] D. Böhnke "VAMPzero Conceptual Aircraft Design and Synthesis Code" http:// software.dlr.de/p/vampzero/
[13] http://software.dlr.de/
[14] T. Zill, D. Böhnke and B. Nagel, Preliminary Aircraft Design in a Collaborative Multidisciplinary Design Environment, *11th AIAA Aviation Technology, Integration, and Operations (ATIO) Conference, including the AIAA, 2011, Virginia Beach, VA, USA*.
[15] T. Zill, P. D. Ciampa, B. Nagel, Multidisciplinary Design Optimization in a Collaborative Distributed Aircraft Design System, *50th AIAA Aerospace Sciences Meeting (ASM) 2012, Nashville, USA*
[16] http://www.openvsp.org/
[17] T. Pfeiffer, B. Nagel, D. Böhnke, A.Rizzi, M. Voskuijl, Implementation of a Heterogeneous, Variable-Fidelity Framework for Flight Mechanics Analysis in Preliminary Aircraft Design, *German Aeronautics and Space Congress, DLRK, 2011, Bremen, Germany*.
[18] A. Rizzi, M. Zhang, B. Nagel, D. Böhnke, Towards a Framework with Unified Geometry Management for Virtual Aircraft Design, *AIAA Aerospace Sciences Meeting, 2012*.
[19] F. Dorbath, B. Nagel, V. Gollnick, A knowledge Based Approach for Automated Modelling of Extended Wing Structures in Preliminary Aircraft Design, *German Aeronautics and Space Congress, DLRK, 2011, Bremen, Germany*.
[20] F. Dorbath, B. Nagel, V. Gollnick, A knowledge based approach for extended physics-based wing mass estimation in early design stages, *28th International Congress of the Aeronautical Sciences, Brisbane, AU, 2012.*

[21] P. D. Ciampa, T. Zill, B. Nagel, CST parameterization for unconventional aircraft design optimization, *International Council of the Aerospace Sciences (ICAS) 2010, Nice, France*
[22] P. D. Ciampa, T. Zill, B. Nagel, Aeroelastic Design and Optimization of Unconventional Aircraft Configurations in a Distributed Design Environment, *53rd AIAA Structures, Structural Dynamics, and Materials Conference,2012, Honolulu, USA*
[23] J. Fuchte, S. Rajkowski, A. Wick, Rapid Model Creation for Cabin CFD Simulations, *Aircraft Systems Technology, AST, Hamburg, Germany, 2011*
[24] D. Böhnke, B. Nagel, V. Gollnick, An Approach to Multi-Fidelity in Conceptual Aircraft Design in a Distributed Design Environment, *IEEE Aerospace Conference, 2011.*
[25] B. Nagel, D. Böhnke, V. Gollnick, P. Schmollgruber, A. Rizzi, G. La Rocca, J. J. Alonso, Communication in Aircraft Design: Can we establish a Common Language?, *International Council of the Aerospace Sciences (ICAS) 2012, Brisbane, Australia*
[26] E. Moerland1, R.-G. Becker, B. Nagel. Collaborative understanding of disciplinary correlations using a low-fidelity physics based aerospace toolkit, *4th CEAS Air & Space Conference, Linkoping, Sweden, 2013.*
[27] P.D. Ciampa, B. Nagel, G. La Rocca., Preliminary Design for Flexible Aircraft in a Collaborative Environment, *4th CEAS Air & Space Conference, Linkoping, Sweden, 2013.*
[28] P.D. Ciampa, B. Nagel, P. Meng, M. Zhang, A. Rizzi, Modeling for Physics Based Aircraft Predesign in a Collaborative Environment, *4th CEAS Air & Space Conference, Linkoping, Sweden, 2013.*
[29] A. Rizzi, P. Meng, B. Nagel, D. Boehnke, W. A. J. Anemaat, J. Carroll, Collaborative Aircraft Design using AAA and CEASIOM linked by CPACS Namespace, *4th CEAS Air & Space Conference, Linkoping, Sweden, 2013*
[30] A. Bachmann, J. Lakemeier, E. Moerland, An Integrated Laboratory for Collaborative Design in the Air Transportation System, *19th ISPE International Conference on Concurrent Engineering, Trier Germany, 2012*
[31] E. Dineva, A. Bachmann, E. Moerland, B. Nagel, V. Gollnick, Empirical Performance Evaluation in Collaborative Aircraft Design Tasks, *20th ISPE International Conference on Concurrent Engineering, Melbourne, Australia, 2013*l
[32] S. Deinert, Ö. Petersson, F. Daoud, H. Baier, Aircraft Loft Optimization With Respect to Aeroelastic Lift and Induced Drag Loads, *10th World Congress on Structural and Multidisciplinary Optimization, Orlando, Florida, 2013*

4:th CEAS Air & Space Conference
FTF Congress: Flygteknik 2013

Investigation of multi-fidelity and variable-fidelity optimization approaches for collaborative aircraft design

G. La Rocca and J. Jansen

TU Delft, The Netherlands

T. Zill
German Aerospace Center DLR, Hamburg, Germany

Keywords*:* *Multidisciplinary design optimization, collaborative aircraft design, multi-fidelity, variable-fidelity optimization*

Introduction

During the last decades the demands on safety and environmental performance of aircraft have steadily increased. In the near future, these challenging levels of performance will have to be reached by further improving the current aircraft configurations, whilst, on a longer term, novel configurations will need to be developed. To be able to make these improvements, different conceptual design methods and tools will be required, which are more flexible to support collaborative design, less dependent on statistics and able to exploit in a more efficient manner physics-based analysis tools and optimization approaches

In this paper a conceptual aircraft design workflow developed at the TU Delft, in collaboration with the German Aerospace Center DLR, is presented. A number of design and analysis modules, both off the shelf and in house developed, have been integrated by means of an open-source workflow integration environment. The data exchange is based on the central data model CPACS (Common Parametric Aircraft Configuration Schema) proposed by DLR. The outcome is a flexible design workflow, which enables the use and the interchange of tools that are developed and managed by different experts. The workflow consists of two levels of fidelity, one incorporating empirical and statistical models for initial aircraft sizing and one relying on more physics-based models for higher-fidelity analysis. The adopted multi-fidelity architecture allows the implementation of an efficient variable-fidelity MDO approach, where surrogate models generated using the low fidelity part of the workflow are corrected using a lower amount of more computationally expensive results from the higher-fidelity toolset. This approach is demonstrated for the redesign of single-aisle passenger aircraft wing and it is then compared to a standard MDO approach, based on the generation of a single set of surrogate models, and to a direct simulation-based approach with no use of any surrogate modeling. The results of this study indicate that the variable-fidelity approach converges faster to the same optimum as the single fidelity surrogate modeling approach and its efficiency grows with the number of design variables.

1 Introduction

A challenging roadmap has been devised both in Europe and US to the help the aerospace industry stepping into a new age of sustainable growth [1]. However, the ambitious performance and environmental impact targets set for the future aviation cannot be achieved without major improvements in the way aircraft are designed today. New tools and methods are required to support distributed and collaborative design, increase the level of automation in the design process and support the implementation of multidisciplinary design optimization (MDO). Such tools and methods must be able, in the short term, to improve the performance of current designs, and, in the long term, to support the development of novel aircraft configurations.

There are continuous attempts by industry and academia to develop complex integrated design tools to cover the whole aircraft design cycle, from drafting to high fidelity multidisciplinary analysis and optimization [2]. Eventually, these systems turn useful to address only one part of the design process, e.g., the conceptual design phase, where only low fidelity analysis tools or simple semi-empirical methods are generally employed. For this reason, many conventional design tools appear particularly inadequate to support the development of innovative aircraft configurations, for which more computationally expensive physics-based tools are required to deal with the lack of statistics and the integrated nature of novel configurations such as blended wing body and box-wing. Monolithic or too tightly integrated design tools are then difficult to scale up and maintain and, above all, they are unsuitable for collaborative design initiatives [3,4].

This paper demonstrates the possibility to develop flexible, extensible and scalable design frameworks, where tools of various levels of fidelity, developed and managed by different institutes, can be easily federated to support an affordable MDO strategy. A variable-fidelity optimization approach is proposed here, which is based on response surfaces generated using low fidelity but fast analysis tools and intermediate fidelity but more computationally expensive analysis tools.

The architecture of the main design and optimization framework is described first. Then the main functionalities of the various design and analysis tools are discussed. The application of the variable fidelity optimization strategy is elaborated and discussed in section 3-5. To this purpose, the wing of an A320-like aircraft has been optimized for minimum take off weight and for minimum fuel. Finally, a comparison in terms of accuracy and computational efficiency is provided, where the proposed variable-fidelity optimization strategy is compared with an optimization approach based on a single response surface and one that does not make use of any surrogate model.

2 The Aircraft Design Workflow

A simplified flowchart of the design workflow developed for this work is provided in Figure 1. It consists of various functional modules, integrated by means of a selected framework system called RCE and exchanging data using a standard data format called CPACS. Both RCE and CPACS are addressed in more details later in this section.

The main workflow components are the following:

1. Conceptual design
2. Aerodynamic analysis
3. Wing structural analysis
4. Mission analysis

Two different conceptual design tools have been used to demonstrate the flexibility of the framework, namely VAMPzero [3] from DLR and the Initiator from TU Delft [4]. These tools are used for the initial sizing of the aircraft geometry, and for a preliminary analysis of various disciplines which provides the necessary inputs for the higher-level modules.

The aerodynamic analysis module actually consists of two modules: the freeware commercial vortex-lattice code AVL, which is used to determine the lift and induced drag coefficients and a in house developed tool, based on handbook methods, for the determination of the profile and wave drag

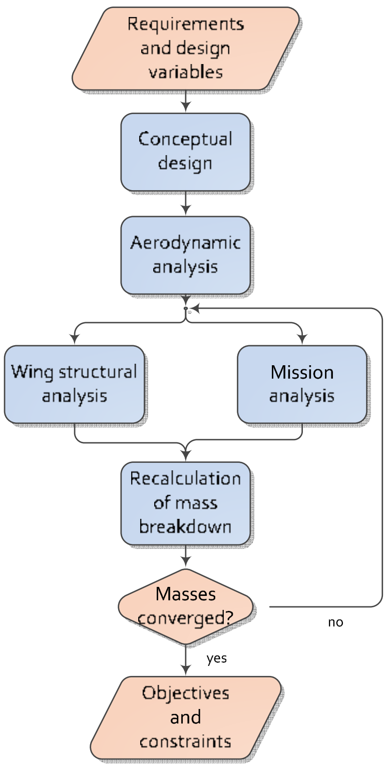

Figure 1: the assembled MDO workflow

coefficients of the full aircraft configuration.

The conceptual design and aerodynamic analysis are performed once in the process, while the subsequent modules for structural and fuel weight estimation are executed in a fixed point iteration, until the masses of the configuration are converged.

The wing structural analysis is performed by EMWET, a quasi-analytical wing weight estimation method developed at the TU Delft [5].

The fuel mass required for the given design mission is performed in parallel by a simple mission analysis tool developed at DLR. Although simple, the tool goes beyond the simple fuel fractions and Breguet equations approach implemented in VAMPzero and in the Initiator, because it is based on equations of motion, engine data and aerodynamic performance maps.

At the end of the iterative part of the workflow VAMPzero is used to recalculate the mass breakdown of the configuration since the wing mass and the fuel mass have been updated. If this iteration is converged the design process is finished.

An optimizer is finally included, which iteratively executes the above mentioned workflow according to the set objective. Otherwise a design of experiment (DOE) module runs the workflow (completely or only parts) to generate the required response surface(s). In this case the optimizer can make use of the response surfaces rather than the computationally expensive design and analysis modules. Details are provided from section 3 to 5.

2.1 Integration technologies for the collaborative workflow: RCE, CPACS.

The aircraft design workflow described in the previous section was integrated by means of a dedicated software framework called RCE (Remote Component Environment). Figure 2 shows an overview of the integrated system in the RCE environment. RCE is an open-source workflow integration environment developed by DLR, which provides means to easily connect various analysis tools [6]. As for many other commercial workflow automation tools, the scope is to reduce the amount of time designers have to deal with communication issues, due to the distributed nature of their tools. Furthermore it provides, off the shelf, several components that can be useful to the designer, such as optimizers and Design of Experiments components.

Several software systems for interlinking tools are available on the market, such as ModelCenter [7], iSIGHT [8] and OPTIMUS [9]. They all offer, next to the core functionality of control and data transfer, other features like advanced process management, optimization and visualization. In the context of this research, RCE was selected both because of its free availability and for its increased flexibility compared to the industry-standard products.

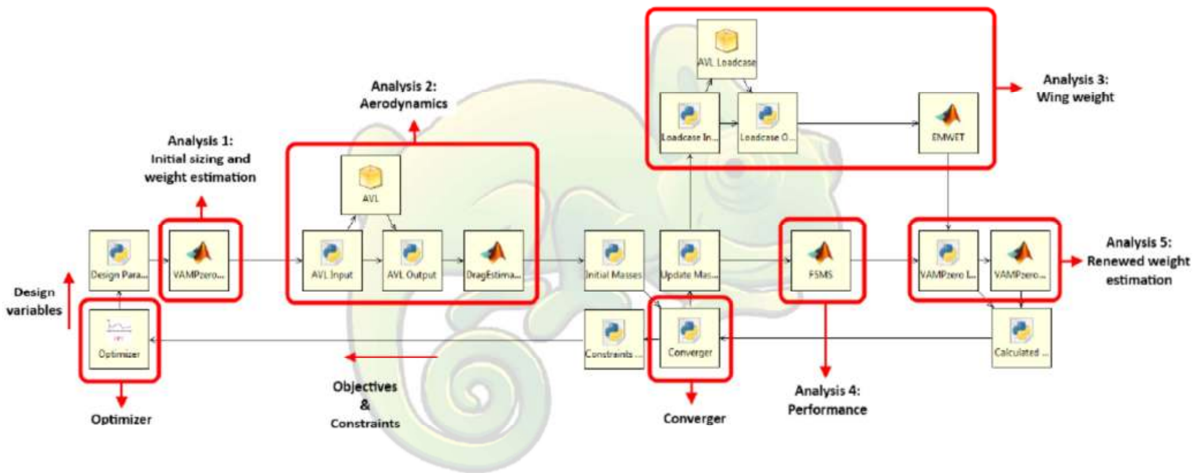

Figure 3: detailed analysis workflow as implemented in RCE. Main functional blocks are indicated with red frames

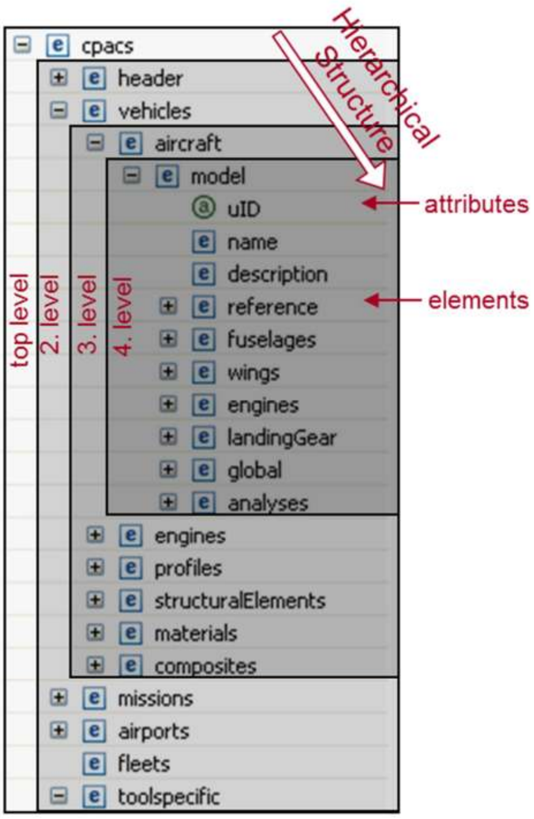

Figure 2: the multilevel CPACS schema [10]

The other enabling element to the modularity and flexibility of the design framework is represented by CPACS, the data exchange format used for the communication between the analysis tools. CPACS is a hierarchic XML-structure developed by DLR for use in multidisciplinary aircraft design processes. The format is published under open source license agreement together with a growing documentation database [10]. A general CPACS structure contains all information about the aircraft configuration to be designed, e.g. wing and fuselage geometry and aerodynamic performance maps. Furthermore it is able to store extra information regarding aircraft missions, airports and aircraft fleets (see figure 3). Moving from the root to the branches of the CPACS hierarchical structure, the level of detail increases. Thus, when performing a conceptual design with a CPACS model that only contains the root information, more detailed analyses can be carried out by adding more branches to the original model. In this way, CPACS is capable of handling data for multiple levels of geometric and/or analysis fidelity. The schema definition is set up to support variable-fidelity applications and to avoid conflicts in the data model. However, challenges of variable fidelity such as linking different fidelity-level models are not solved by the data model but must be realized in the design optimization process [3].

Most of the tools employed in the framework do not “speak CPACS” natively. Hence, to allow their communication and interoperability, dedicated software “wrappers” need to be created for each individual tool.

These wrappers contain both the translation from/to CPACS and the commands to launch the analysis application in batch mode once the necessary data is provided. Eventually, a wrapped program looks like a single application that includes a CPACS interface. It is responsibility of the tool developers to create wrappers for their tools. Documentation and support are available in [ref. 10].

2.2 The conceptual design tools

The conceptual design tool mainly used in this work is VAMPzero from DLR [11]. This tool has been specifically designed for multidisciplinary aircraft design processes. It is object-oriented, written in Python and its analysis and sizing methods are taken from known handbooks such as Raymer [12], Torenbeek [13] and Roskam [14]. It accepts dedicated XML-files as input, builds an aircraft design based on the given requirements, and gives this design as an output in CPACS-format. The strong point of VAMPzero is that it accepts whatever values the user has provided as input (of course there is a minimum amount of input), and designs an aircraft based on this. If the designers provide only top level parameters, a complete aircraft is generated. If the designers provide some requirements and some geometrical parameters, those are used to derive the remaining geometrical parameters and the aircraft performances.

Another version of the workflow was built replacing VAMPzero with the Initiator from TU Delft. The Initiator is a Matlab based conceptual design tool with similar analysis and sizing capabilities to VAMPzero, but with the extra ability to generate conceptual designs of non-conventional aircraft configurations, such as blended wing body and boxed wing configurations. Also to serve this purpose, the Initiator includes a Vortex Latex Method aerodynamic tool and an optimizer. It can link with an external KBE application for the generation of relatively detailed fuselage layouts and is able to output both CPACS files and complete PDF aircraft reports. Details can be found in [4]. In its current implementation, the

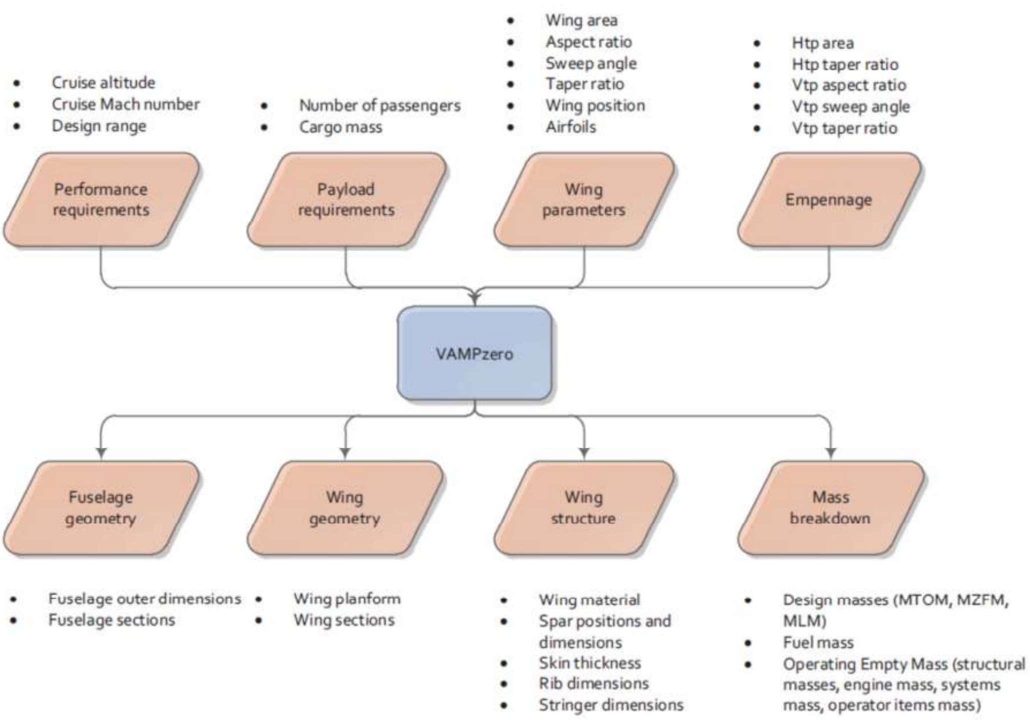

Figure 4: input/output architecture of VAMPzero

Initiator is geared toward interactive design, although it can operate in batch mode, generating complete aircraft design, starting from a limited set on top level requirements. However, when operated in batch mode, it does not offer the same flexibility of VAMPzero, because only few geometrical parameters can be defined as input. Hence, the Initiator could be used inside the optimization framework only to deliver once, an initial design (output via CPACS). Still, the possibility to plug in and out the Initiator and VAMPzero are a demonstration of the large flexibility offered by the workflow and the CPACS data exchange format.

2.3 The aerodynamic analysis tools

The aerodynamic analysis module shown in figure 1 is actually a suite of various tools, necessary to achieve the following goals (see figure 3):

- An accurate estimate of the lift over drag ratio during a typical cruise situation. This is a necessary figure to compute the two objectives defined in the optimization process.
- An aerodynamic performance map providing lift and drag coefficients as a function of altitude, angle of attack and Mach number. This performance map is used by the mission analysis module.

However, VAMPzero can only provide an estimate of the aerodynamic coefficients at cruise condition, derived on the basis of very simple empirical equations. Hence, to achieve the two goals mentioned above, it was necessary to make use of more elaborated and higher fidelity methods.

The freeware Athena Vortex Lattice code, known as AVL [15], was chosen as aerodynamic solver to obtain the lift and induced drag coefficients of the trimmed aircraft at various flight conditions. Since the Vortex-Lattice method is not able to determine any viscous and wave drag component, a drag estimation tool was developed on purpose, based on handbook methods and statistics [16]. The (various components of the) aerodynamic tool was validated with wind tunnel tests available from literature, for isolates airfoils, wings and complete aircraft configuration, up to transonic speed. The tool proved to offer adequate accuracy and sensitivity to the relevant design parameters.

2.4 The wing structural analysis tools

The TU Delft tool EMWET was used to achieve a more accurate wing weight estimation than possible using the simple class II prediction methods of VAMPzero and the Initiator. EMWET is a so called *class II &1/2* weight estimation method, which makes use of analytical methods to size the main structural components of the wing subjected to critical loads, and semi-empirical, statistics based relations to estimate the weight of the wing secondary structure. The theory implemented in EMWET is thoroughly described in reference [5]. Validation results have shown that outstanding wing weight predictions can be achieved for aircraft of different size and configuration, while the tool offers excellent sensitivity to many design parameters, ranging from airfoils and planform shape parameters, to structure configuration and material properties of the various components. AVL was used again to compute the critical aerodynamic loads required as input by EMWET.

2.5 The mission analysis tools

FSMS (Fairly Simple Mission Analysis) is the other Matlab tool developed on purpose for this research, to predict the fuel mass required to fly a given mission, with higher accuracy and detail than possible when using the simple fuel fraction method featured by VAMPzero or the Initiator. FSMS uses flight mechanics relations from handbooks with values determined by analytical simulations (e.g. lift over drag) to estimate the aircraft fuel consumption during each stage of the mission. Apart from providing a more accurate fuel mass value, FSMS can provide extra useful information, such as fuel consumption, velocities and aerodynamic efficiency during each interval of the mission.

3 Set up of the optimization problem

Twelve wing planform optimizations have been performed in this work, using three sets of increasing amount of design variables, two objective functions and two different optimization approaches. These two approaches were actually two different implementations of the MDF (Multidisciplinary Design Feasible) strategy, both based on the use of Response Surface Modes (surrogate models) to reduce the computation time.

The first optimization approach was based on the direct use of Response Surface Models obtained by running the whole workflow and it will be addressed here as *RSM approach*.

The second approach was based on the use of Variable-Fidelity Modeling, and was intended to exploit the multi fidelity nature of the given workflow to improve the computational efficiency of the optimization process. To this purpose, different sets of response surfaces were generated using separately the low fidelity branch of the workflow to generate a large number of computationally cheap experiments, and the higher fidelity branch to compute a low number of more accurate but computationally expensive experiments. The low fidelity and the high fidelity response surfaces where then combined into one set of so called Variable Fidelity Response Models, where, in practice, the coarse but higher fidelity model was used to improve the accuracy of the dense but lower fidelity one. This approach will be addressed here as *VFM approach*.

The results of both the optimization approaches are provided and compared in section 5.

3.1 The objective functions

The main goal was the optimization of the Airbus A320 wing for a certain mission. Two different objective functions were evaluated; Maximum Take Off Mass (MTOM) and block fuel (Mfuel). To evaluate these two objectives both aerodynamic, structural and performance properties of the design are required, hence the multidisciplinary nature of the workflow described in the previous sections.

3.2 The design variables

Three different sets of design variables were used. The first set consists just of the wing area and aspect ratio of the wing. These were interesting optimizations, because the resulting (three-dimensional) response surfaces could be visualized and offer visual insights to the designer. For the second set of design variables, the sweep angle and taper ratio of the wing were added. In this way the complete wing planform could be varied by the optimizer. Finally in the third set of design variables the wing twist at the root, kink and tip locations of the main wing were added. For the sake of simplicity, the shape of the wing sections was not varied, although their impact of the objectives is obviously acknowledged. The purpose of performing the optimization using a growing set of design variables was to understand the convenience of the two aforementioned optimization strategies according to the number of variables. In all the optimization cases, the real-life dimensions of the A320 were used as initial values.

3.3 The constraints

A number of constraints were implemented. First, the take off and landing field length were set to be not longer (<2300m and <1900m respectively) than for the reference A320 configuration. Since the aircraft was mainly optimized for cruise condition, a constraint was put on the wing loading (<600.5kgf/m^2), such that no unreasonably high values could occur, hence requiring larger or more complex high lift devices than the reference aircraft. Finally, a constraint was set on the initial climb angle, such that the resulting configuration would be able to take off with a climb angle of at least 2.4 degrees in case of one engine inoperative, as required by FAA, for 2 engine aircraft. To guarantee the static longitudinal stability of the aircraft, a constraint was put on the static margin (SM>5% of the mean aerodynamic chord).

4 The response surfaces generation strategy

In order to generate the experiments for the various response surfaces, the *maximin* Latin Hypercube Design approach was used. The actual response surface interpolations were performed using the Kriging technique, as implemented in the freeware DACE [17] Kriging toolbox.

The generated Kriging models, both for the RSM and VFM approach, were systematically updated during the optimization process, by computing the optimum on the response surface, comparing it with the result obtained by running the full workflow for that set of design variables and, in case of significant discrepancy, by including that new experiment into the (re)generation of the surrogate model.

4.1 Generation of the Variable Fidelity Model surface

While the generation of the response surfaces for the RSM approach is straightforward, the VFM approach makes use of a low-fidelity response surface and a bridge function to approximate the results of a high-fidelity surface model (figure 5). The bridge function is defined as an additive function and it is made by constructing a Kriging model based on the results of a few selected high-fidelity evaluations. The variable fidelity modeling approach can be summarized as follows:

1. Calculation of the experiments for the low fidelity response surface. A large number can be chosen because of the low computation cost (3 minutes in our case).
2. Calculation of the experiments for the high-fidelity model. A smaller number of points is required than during the direct Response Surface optimization. In this work, half as many experiments were used (each point required 25 minutes of computation time).
3. Generation of the Kriging models with the low and high fidelity experiments.
4. The high fidelity model is evaluated at a number of sample points and the difference in these points with the low fidelity model is computed. These deltas represent the actual bridge values.
5. Generation of a Kriging model using the bridge values computed at previous step, i.e. construct the bridge function model.
6. Add the Kriging bridge model to the Kriging low fidelity model to form the variable-fidelity model.
7. Perform an optimization on the obtained variable fidelity model.
8. Compute a new bridge value by evaluating the difference between the high fidelity and the low fidelity model at the location of the discovered global optimum.
9. Update the Kriging bridge model with this calculated value.
10. Re-perform the optimization with the updated variable fidelity model.
11. Check for convergence, if not converged go back to step 8. Two criteria for convergence were used: the relative difference between the objective value of two consecutive iterations should be lower than 0.001, and the relative difference between the objective value obtained from the Kriging model and the objective value determined from the analysis of the workflow should also be lower than 0.001.

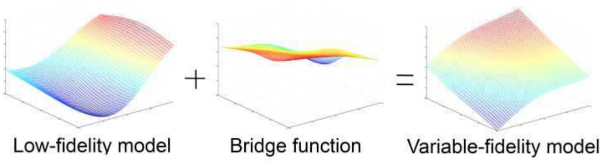

Figure 5: definition of the Variable fidelity response surface as sum of the low fidelity model and the bridge function

A similar implementation of this approach can be found in [Ref. 18].

5 Results & conclusions

Table 1 summarizes the optimization results using the direct RSM approach, while table 2 summarize the results obtained using the VFM approach. Figure 6 show the resulting wing planform, only for the optimization case with 7 design variables, respectively for minimization of MTOM and required fuel mass (i.e. optimization cases 3, 6, 9 and 12 in the tables).

It is interesting to note that the two optimization approaches converged to the same solutions, which in both cases seems very plausible: in case of fuel mass minimization the wing assumes a more slender shape with a higher aerodynamic efficiency, but yielding a higher MTOM. In case of MTOM minimization, the wing gets more compact and yields a total structural weight saving, although with a higher block fuel mass. The actual values of MTOM, fuel mass, L/D and wing mass for all the optimization cases can be found in figure 7.

Optimizing for MTOM

Case	S [m^2]	A [-]	Λ [deg]	λ [-]	ϵ_{root} [deg]	ϵ_{kink} [deg]	ϵ_{tip} [deg]	MTOM (opt.)	MTOM (workflow)	% error	Nr. of eval.	Nr. of updates
1	120.29	8.42	-	-	-	-	-	72235	72240	0.007	12	2
2	120.89	8.25	23.3	0.262	-	-	-	71781	71786	0.007	24	3
3	119.77	8.00	23.3	0.278	2	2	0	71725	71720	0.006	42	5

Optimizing for Mfuel

Case	S [m^2]	A [-]	Λ [deg]	λ [-]	ϵ_{root} [deg]	ϵ_{kink} [deg]	ϵ_{tip} [deg]	Mfuel (opt.)	Mfuel (workflow)	% error	Nr. of eval.	Nr. of updates
4	123.7	10	-	-	-	-	-	13784	13784	0.087	6	3
5	133.13	9.74	26.1	0.203	-	-	-	13578	13587	0.066	12	6
6	121.84	10	23.7	0.226	2	2	0	13525	13536	0.044	21	4

Table 1 results of the optimization processes based on the response surface modeling (RSM) approach.

Optimizing for MTOM

Case	S [m^2]	A [-]	Λ [deg]	λ [-]	ϵ_{root} [deg]	ϵ_{kink} [deg]	ϵ_{tip} [deg]	MTOM (opt.)	MTOM (workflow)	% error	Nr. of l-f eval.	Nr. of h-f eval.	Nr. of updates
7	120.29	8.36	-	-	-	-	-	72238	72189	0.066	50	6	4
8	120.36	8.34	23.3	0.259	-	-	-	71810	71793	0.024	50	12	4
9	119.27	8.42	23.4	0.247	3.4	2	0	71637	71591	0.064	50	21	6

Optimizing for Mfuel

Case	S [m^2]	A [-]	Λ [deg]	λ [-]	ϵ_{root} [deg]	ϵ_{kink} [deg]	ϵ_{tip} [deg]	Mfuel (opt.)	Mfuel (workflow)	% error	Nr. of l-f eval.	Nr. of h-f eval.	Nr. of updates
10	123.73	10.0	-	-	-	-	-	13778	13768	0.075	50	6	3
11	121.92	10.0	24.2	0.215	-	-	-	13713	13715	0.007	50	12	6
12	121.67	10.0	23.4	0.224	2	2	0	13530	13539	0.066	50	21	5

Table 2 results of the optimization processes based on the variable fidelity surface modeling (VFM) approach

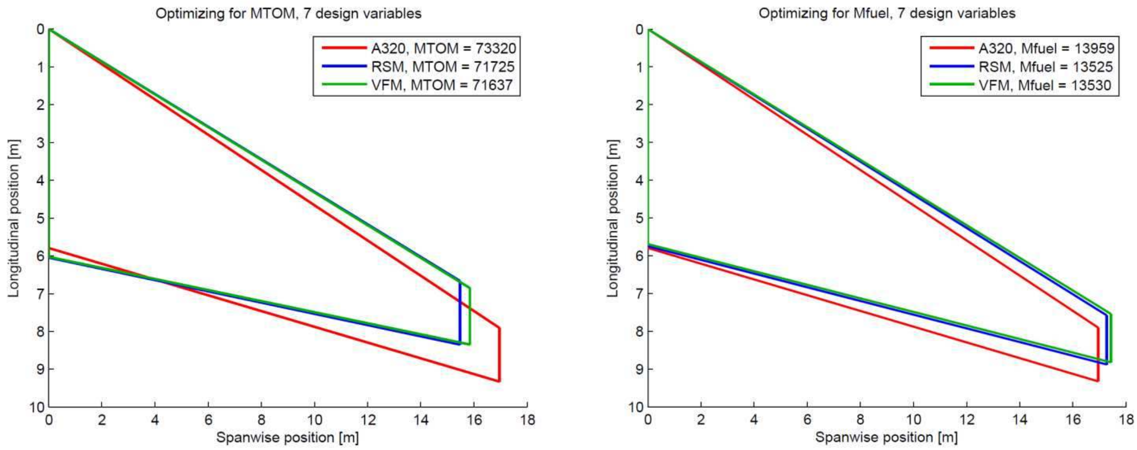

Figure 6: reference and optimized wing planforms for the two objective functions, using the RSM and VFM approaches

What is actually more interesting to observe is the comparison of the estimated computation time between direct optimization (no response surface modeling at al), the RFM approach and the VFM approach, as summarized in Table 3. In all cases, the use of response surfaces makes the optimization process faster. Then it can be observed that the more design variables are involved, the better the VFM performs also with respect to the RSM approach. In the case of 4 design variables, the VFM approach appears to be marginally better, while in the case of 7 design variables the process using VFM was on average 6 hours faster than using the RSM approach.

Something which does not immediately become apparent from the table is the fact that, once the designer has produced a response surface, he/she has a model from which all kinds of other objective values can be obtained (for the specific set of design variable). This makes the use of response surfaces even more advantageous than direct optimization using the workflow.

For what concerns the use of the VFM approach, the designer should always be sure that the low fidelity part of the model is able at least to describe a similar trend to the high fidelity results. If this is the case, as it was in this specific design case, then the VFM approach is not only usable, but it provides a very interesting optimization approach in conceptual aircraft design.

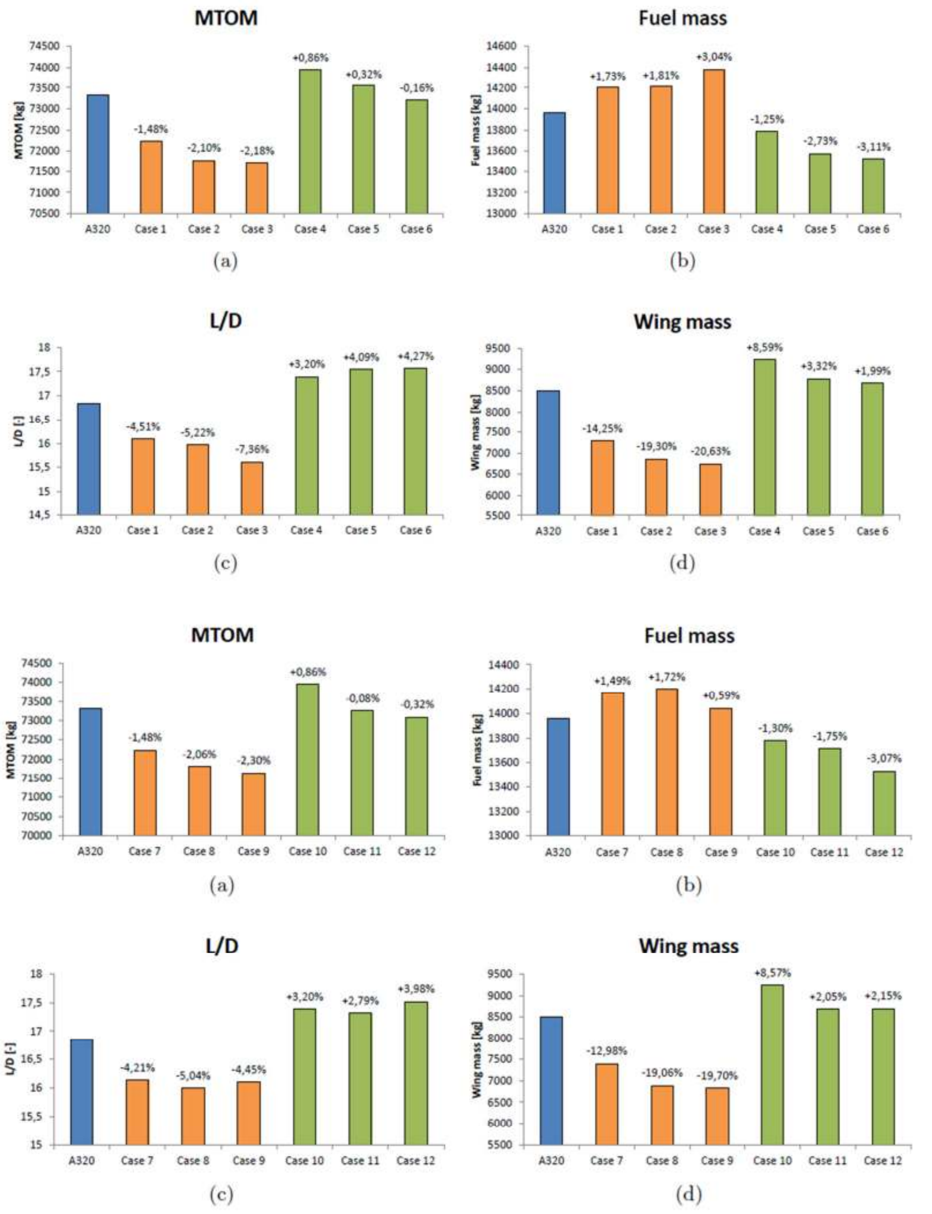

Figure 7: detailed results of the optimizations processes. Top four plots relative to the RSM approach, bottom 4 relative to the VFM approach

		Low-fidelity evaluations (3 min.)	High-fidelity evaluations (25 min.)	Nr. of updates (25 min.)	Percentage error	Estimated time [hr]
MTOM 2 DV	Regular	-	28	-	-	11.7
	RSM	-	12	1	0.011	5.4
	VFM	50	6	3	0.091	6.3
MTOM 4 DV	Regular	-	60	-	-	25
	RSM	-	24	2	0.042	10.9
	VFM	50	12	3	0.123	8.8
MTOM 7 DV	Regular	-	72	-	-	30
	RSM	-	42	4	0.278	19.2
	VFM	50	21	5	0.147	13.4
MFuel 2 DV	Regular	-	15	-	-	6.3
	RSM	-	12	2	0.186	5.9
	VFM	50	6	2	0.083	5.9
MFuel 4 DV	Regular	-	52	-	-	21.7
	RSM	-	24	5	0.366	12.1
	VFM	50	12	5	0.431	9.7
MFuel 7 DV	Regular	-	62	-	-	25.8
	RSM	-	42	3	0.278	18.8
	VFM	50	21	4	0.211	13.0

Table 3: computation time comparison between regular optimization, RSM and VFM

References

[1] ACARE. Aeronautics and air transport: Beyond vision 2020 (towards 2050) - background document. in, www.acare4europe.com, 2010

[2] La Rocca G. Knowledge based engineering techniques to support aircraft design and optimization, PhD thesis, Faculty of Aerospace Engineering, TU Delft, Delft, 2011

[3] Nagel B, Bohnke D, Gollnick V, Schmollgruber P, Alonso JJ, Rizzi A and La Rocca G." Communication in aircraft design: Can we establish a common language?", 28th International Conference of the Aeronautical Sciences

[4] La Rocca G. and Langen T. "Communication in aircraft design: Can we establish a common language?," 28th International Conference of the Aeronautical Sciences, Brisbane, AU, 2012.

[5] Elham, A, La Rocca, G. and van Tooren M.J.L. "Development and implementation of anadvanced, design-sensitive method for wing weight estimation," Aerospace Sciences and Technology, 2012.

[6] Seider D, Litz M, Schreiber A, Fischer P.M. and Gerndt A, "Open Source Software Framework for Applications in Aeronautics and Space," IEEE Aerospace Conference, 2012.

[7] http://www.phoenix-int.com/software/phx-modelcenter.php

[8] http://www.3ds.com/products/simulia/

[9] http://www.noesissolutions.com/Noesis/optimus-details

[10] Böhnke D. "Common Parametric Aircraft Configuration Schema" http://code.google.com/p/cpacs/

[11] Bohnke D., Nagel B., and Gollnick V., "An approach to multifidelity in conceptual aircraft design in distributed design environments," in Aerospace Conference, IEEE, 2011

[12] Raymer D., Aircraft Design: A Conceptual Approach. AIAA Education Series, 2006.

[13] Torenbeek E., Synthesis of Subsonic Airplane Design. Delft University Press, 1976.

[14] J. Roskam, Airplane Design. DARcorporation, 1997.

[15] Drela M. and Youngren H., Avl (athena vortex lattice)," May 2011.

[16] Jansen, J. "Investigation of multi fidelity and variable fidelity optimization approaches for collaborative aircraft design", MSc thesis, TU Delft, 2012.

[17] "Dace - a Matlab Kriging toolbox," Technical Report IMM-TR-2002-12, 2002.

[18] Zill T. and Ciampa P., "Multidisciplinary design optimization in a collaborative distributed aircraft design system," 50th AIAA Aerospace Sciences meeting, 2012

4:th CEAS Air & Space Conference
FTF Congress: Flygteknik 2013

Feasibility study of a nuclear powered blended wing body aircraft for the Cruiser/Feeder concept

G. La Rocca, M. Li
TU Delft, The Netherlands

M. Chiozzi
La Sapienza, University of Rome, Italy

Keywords: *Cruiser/Feeder, blended wing body, nuclear propulsion, in-flight passenger exchange*

Abstract

This paper describes the conceptual study of a nuclear powered blended wing body aircraft for the cruiser/feeder concept. According to this radically new aviation paradigm, large transport aircraft (cruisers) carry passengers over long distances, while remaining airborne for very long periods. Smaller aircraft (feeders) take off from local airports, intercept the cruiser, dock and enable in-flight exchange of passengers and supplies. Preliminary studies indicated that cruiser concepts based on engines burning kerosene would be too heavy and feeders would need to operate also as tankers. Propelling the cruiser with a nuclear power source would yield very high efficiency parameters, even if the weight of the system would result higher due to the required reactor shielding. The blended wing body configuration was selected both for its potential advantages in terms of aerodynamic and structural efficiency, as well as for the use flexibility of its internal volume, necessary to integrate power plants and shielding, accommodate 1000 passengers and host the loading/unloading station for in-flight payload exchange. The daring nature of the proposed solution is compatible to the foreseen entry into service date, which is set for the last part of this century. The peculiar nature of the aircraft under consideration has required a somehow different conceptual design approach, than generally used for conventional passenger transport aircraft. Apart from the inherent complexity related to the design of such a novel and integrated configuration as a blended wing body, the typical design approach based on the use of simple performance equations and statistics to achieve a first estimation of the main weight contributors was of little use in this case. From one side, the fuel mass used to perform the mission is just negligible; from the other, a method was necessary to account for the weight of the radiation shielding, which is a significant contribution to the overall aircraft weight. Rather than in the numerical results of the sizing process, the value of the design work described in this paper should be found in the very design approach and the preliminary ideas for integrating the passenger docking system and the nuclear power plant.

1 Cruiser/feeder Operations and Cruiser Top Level Requirements

The cruiser/feeder operational concept is currently investigated within the FP7 research project RECREATE (REsearch on a CRuiser Enabled Air Transport Environment) as a promising pioneering idea for the air transport of the future. One of the objectives of this project is to assess, on a conceptual design level, the feasibility of the cruiser/feeder operations as a potential solution to reduce fuel burn and CO_2 emission levels [1]. The operational concept is schematically illustrated in Figure 2. The cruisers take off from dedicated airfields specifically designed to account for the big dimensions of these aircraft, as well as for the safety requirements associated to the presence of the nuclear power plants. When flying at cruise altitude, the cruiser is supposed to follow a closed loop trajectory, mainly located upon oceans or un-inhabited regions. While cruising, the cruiser is intercepted at various locations by feeders, which dock and allow the exchange of passengers, crew members, goods and waste. Thanks to the nuclear power plant, the cruiser can achieve such high levels of endurance, that in

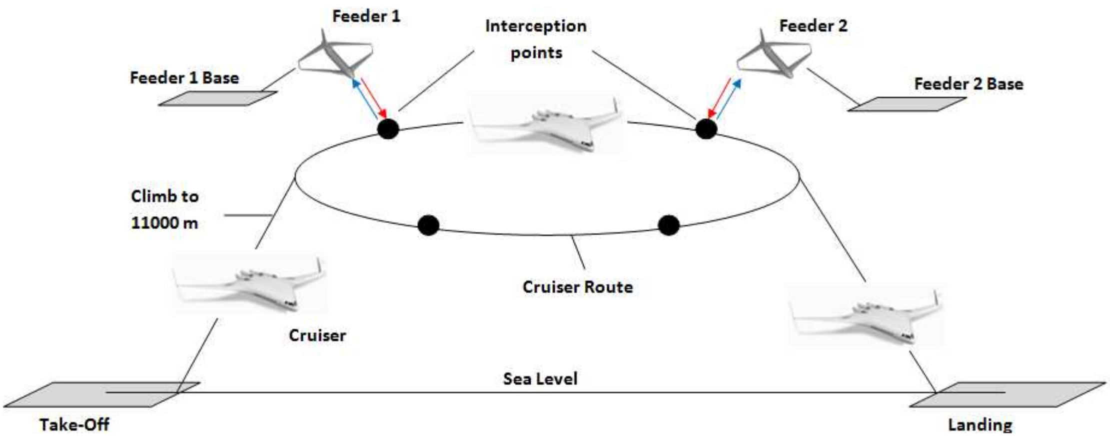

Figure 2: the cruiser/feeder operational concept

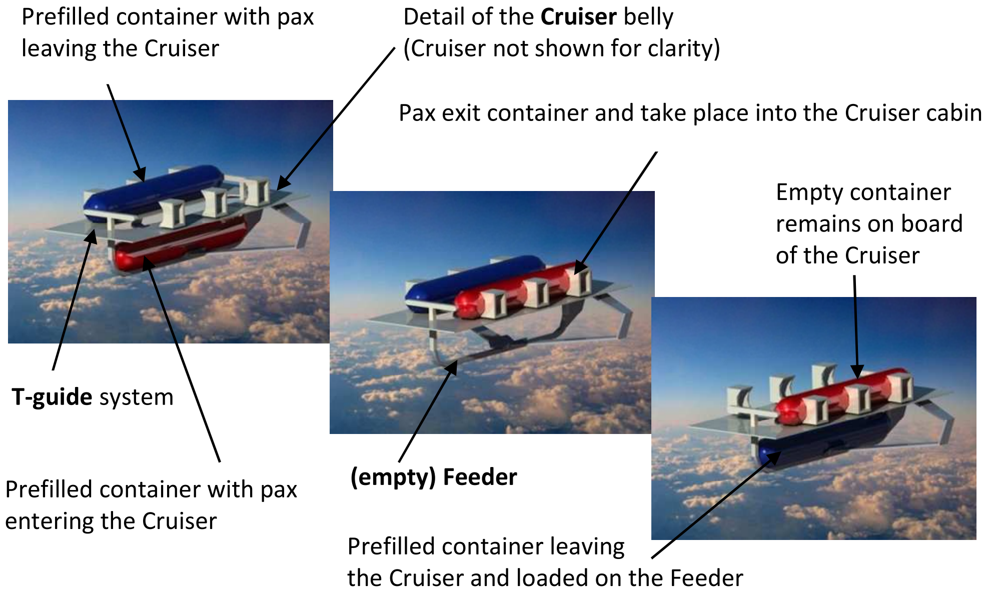

Figure 1: in flight docking and payload exchange concept

practice, the need to land is limited to the need of extraordinary maintenance, which cannot take place on board during flight, or in case of emergency.

At the moment of writing, a box wing type of configuration is considered for the role of feeder, due to its good take off and landing performance and the possibility to have direct lift control, thanks to movable surfaces that can be installed both on the front and back wings. Besides these features, the closed wing system appears a suitable structural solution to enable the detachment of the prefilled pressurized containers, which are the envisioned means to transfer payload to and from the cruiser.

The proposed docking and payload exchange approach is schematically illustrated in Figure 1. After the feeder has docked below the cruiser (a trapeze system is foreseen to facilitate the attachment of the feeder under the large cruiser belly and guarantee its stable positioning), the feeder detachable fuselage is lifted into the cruiser and, through a T-guide mechanism, shifted on one side to allow the passengers disembarking and accessing the cruiser main decks. A second detachable fuselage, prefilled with the passengers and goods that must leave the cruiser, will be loaded onto the empty feeder (using the same T-guide mechanism), in the place left vacant by the just delivered fuselage. Then the feeder will detach from the cruiser and reach the nearby landing destination. These exchange operations will be performed several times, as different feeders will intercept and dock on the cruiser, during its long range orbiting trajectory.

Parameter	***Value***	***Note***
nr of passengers	1000 PAX	100 kg each
MTOW	900000 kg	
Range	> 60,000 nm	1 week endurance
Cruise speed	M = 0.8	
Docking Speed	M= 0.7	
L/D	>20	
Cruise altitude	h_{cruise} > 11000 m	
Reactor Lifetime	Between 5000 and 10.000 hours	
Payload Transfer Concept	Single container exchange concept (100 pax each)	

Table 1: Cruiser Top Level Requirements

Table 1 collects the top level requirements established within the RECREATE project for the design of the cruiser. The high aerodynamic efficiency required for making this operational concept worthwhile, plus the demands set by the aforementioned docking and containers exchange approach, have led to the selection of a blended wing body configuration for the cruiser.

2 Preliminary Sizing Process of the Nuclear Propelled Blended Wing Body Cruiser

The peculiar nature of the aircraft under consideration has required a somehow different conceptual design approach, than generally used for conventional passenger transport aircraft. The fact that the considered configuration is a blended wing body, where the center section of the aircraft is required to perform more functions (e.g., lift generation, control, payload transfer and storage) has required an integrated and iterative approach to define the interiors layout, the aerodynamic shape and the masses distribution.

The typical aircraft conceptual design process starts with a preliminary weight estimation, where basic performance equations are used to estimate the necessary amount of fuel. From that, plus the aid of statistical data from reference aircraft, an initial estimation of the aircraft MTOW and OEW can be achieved. However, in the case of a nuclear propelled aircraft, where the amount of fuel mass used to perform the mission is negligible, a different approach was required to pursue the initial aircraft weight breakdown.

The design process implemented to achieve the preliminary sizing of the nuclear propelled blended wing body cruiser is summarized by means of the N2 chart provided in Table 4. The main phases of the design process are shown on the diagonal of the chart and all the input/output required/generated by each phase are listed on the upper and lower part of the matrix, respectively.

3 Definition of the Cruiser Planform

As a first step, the typical inside-out approach has been used to derive a suitable planform for the cruiser center body. The following assumptions have been made:

- Total deck area sufficiently large to accommodate a total of 1000 passengers in two classes.
- Cargo volume equal to 322.6 m^3. This amount was estimated on the basis of the passenger/freight ratio of existing wide body aircraft.
- Two nuclear reactors with an approximate cylindrical shape of 5 m diameter and 10 m length, including shielding (core cylinder 3m by 3 m). Two reactors were selected for pure redundancy purposes, although one would have been sufficient to deliver the required power. The initial size of the reactors was based on reference values provided by the nuclear energy experts in the consortium and will require verification, in a later stage of the project.
- Sufficient space to accommodate two fuselage-like containers (to be exchanged with the feeders), sufficiently large to transport 100 passengers and some freight. On the basis of the typical fuselage dimension of existing aircraft able to accommodate 100 passengers, it has been assumed the use of cylindrical containers with diameter of 3 m and length of 25 m.

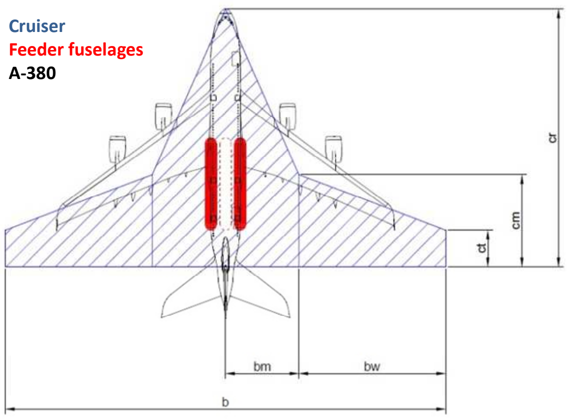

Figure 3: first iteration of the cruiser planform

The rest of the planform, i.e. the span and the shape of the actual wings of the Cruiser (in other words, the outer sections of the BWB lifting surface) was sized in view of achieving the required high aerodynamic efficiency value indicated in Table 1. To this purpose, different values of the total cruiser span have been investigated, by modifying solely the outer wing planform, until a design was found able to achieve an aerodynamic efficiency value larger than 20. A textbook method was used to estimate the parasite friction coefficient *f*, while the maximum aerodynamic efficiency was estimated using the following equation [2,3]:

$$\left(\frac{L}{D}\right)_{max} = \sqrt{\frac{\pi \cdot b^2 \cdot e}{4 \cdot f}}$$

The simple double trapezoidal planform shape (center body and outer wing) resulting from this very first iteration is shown in Figure 3. The two exchangeable fuselages (plus some space in between for the T-guide mechanism) are shown in red. The top view of an Airbus A-380 is superimposed on the picture to give a sense of the overall Cruiser dimensions. The data of this preliminary aircraft sizing are summarized in Table 2.

Description	*Symbol*	*Value*
Maximum root thickness	t_{root}	10m
Root chord length	c_r	60m
Inner part taper ratio	l_1 (c_m/c_r)	0.416
Main wing taper ratio	l_2 (c_t/c_m)	0.25
Inner part length	b_m	20m
Outer wing length	b_w	40m
Span length	**b**	120m
Wing Surface	**S**	2947m^2
Aspect ratio	**A**	4.89
Zero Lift Drag Coefficient	C_{D0}	0.006
Maximum aerodynamic efficiency	$(L/D)_{max}$	23.32

Table 2: Preliminary sizing and analysis of the cruiser planform

The simplified shape resulting from this preliminary sizing step was subsequently refined to account for the actual integration of payload, interiors and main systems. The external shape was refined as result of a more accurate, although simple, aerodynamic study performed with a commercial vortex lattice method tool. A limited number of airfoils was selected, scaled and twisted in order to achieve a quasi-elliptical lift distribution for minimum induced drag, while minimizing the aerodynamic pitching moment (in view of the controllability aspects) and maintaining the target value of aerodynamic efficiency. The main views of the aircraft with relevant sections are illustrated in Figure 8-Figure 10.

On the lower deck there is space for two passengers seating areas, a front and a back cargo hold, and two resting areas that can be used by passengers and the crew. In the middle, space is reserved for the pressurized containers for payload transfer (there will always be one on board of the cruiser) and the T-mechanism. The middle deck accommodates the majority of economy passengers (730 seats) and the cockpit. The top deck accommodates the business class. The two nuclear reactors are located in special bays, on the right and left side of the passenger area, well separated and isolated by protection walls. The two bays can be opened in flight to jettison one of reactors in case of emergency, without drastically affecting the longitudinal position of the aircraft center of mass.

4 Preliminary Weight Estimation

The Cruiser maximum takeoff weight WTO is the sum of the following three weight components:

- WPL (Payload Weight). It is the sum of passengers weight Wpax and cargo weight Wcargo.
- WOE (Operative Empty Weight). It includes the weight contributions of structures, engines, lubricants, and crew.
- WP (Power Plant Weight). It includes the weight of the nuclear reactors, the cooling system and the shielding. It does not include the weight of the engines, whose contribution is accounted in WOE).

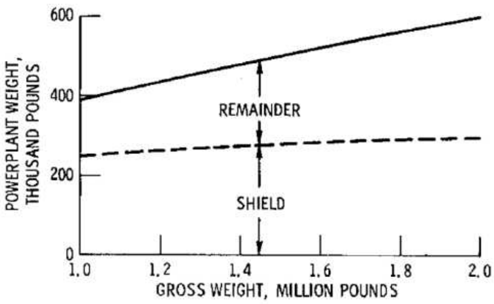

Figure 4: Nuclear power plant weight estimation

In order to estimate the Power Plant Weight WP, the key plot provided in Figure 4 is used [4,5]. Here WP is expressed as a function of WTO and is defined as the sum of two main contributions, namely the *shield* weight and the *remainder*, which includes the weight of the nuclear core and the cooling system. The following linear relation was derived based on the plot above (WTO is in 10^3 kg):

$$WP(WTO) = 0.143 \cdot WTO + 116.6$$

By expressing WOE as function of WTO, the following relation is derived:

$$WOE_I\,(WTO) = WTO - WP\,(WTO) - WPL$$

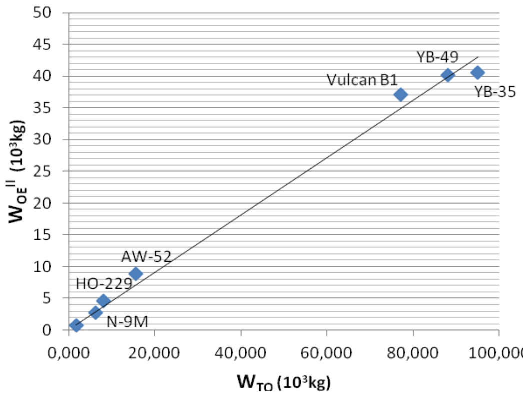

Figure 5: WOE vs WTO relation based on statistics (only blended wing body and flying wing considered)

A second equation is required to derive WOE and WTO. To this purpose, statistical analysis has been performed to derive a relation between WOE and WTO, where only flying wing type of

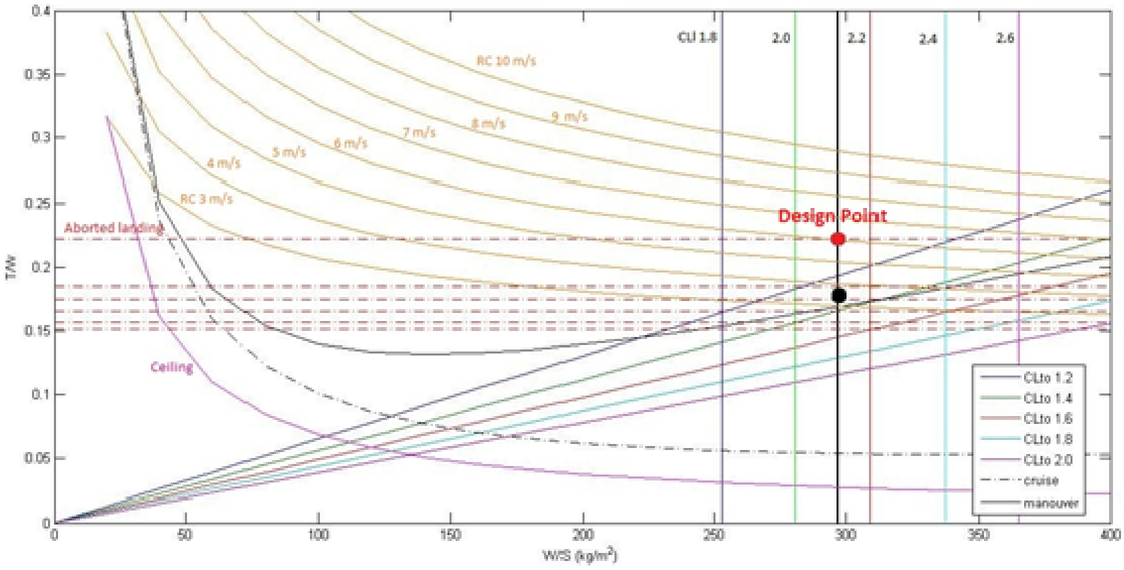

Figure 6: Wing loading vs thrust loading plot and cruiser design point

aircraft have been taken in consideration. The result is shown in Figure 5, from which the following equation was derived (WTO is in 10^3 kg).

$$WOE_{II}\,(WTO) = 0.46 \cdot W_{TO}$$

By imposing $WOE_I = WOE_{II}$ it is possible to derive a first estimation of WOE, WTO, and WP. The results are shown in Table 3 and compared to the values of the two largest wide body passenger aircraft now in operations, namely the Airbus A-380 and the Boeing B747-800 [6]. It can be noticed that WTO is lower than the value provided as top level requirements, while the estimated payload weight percentage is almost twice the value of the wide body aircraft considered in the comparison.

	Cruiser	*% W_{TO}*	*A-380*	*% W_{TO}*	*B-747*	*% W_{TO}*
W_{TO} (10^3kg)	**875**	-	560	-	343	-
W_{OE} (10^3kg)	**383.3**	**43.7**	277	49.5	212	61.8
W_{PL} (10^3kg)	**250**	**28.6**	85	15.2	60.5	17.6
W_P (10^3kg)	**241.7**	**27.6**	-	-	-	-
W/S (kg/m^2)	**297**	-	662.7	-	850	-

Table 3: Weight breakdown of the cruiser & comparison with A390 and B747

The particularly low wing loading of the cruiser is noteworthy. BWB have generally low wing loading (around 350 kg/m^2), although not as low as the cruiser. At this stage it was not possible to increase it by reducing the wing area, because this reduction could have been achieved only affecting the outer wing area (the planform area of center body being dictated by the interiors constraints discussed above). Reducing the outer wing area would have induced a negative effect on the maximum L/D and a reduction of the cooling system area, now assumed to be integrated in the wing.

5 Required Thrust Estimation

In order to estimate the required thrust and power plant power and then proceed with the selection of appropriate engines, the classical wing loading (W/S)–thrust loading diagram (T/W) plot was generated. To this purpose, a number of possible sizing conditions (take off, landing, stall, climbing, ceiling, maneuver) was selected, as detailed in Table 5. The final plot is shown in Figure 6. The design point (red dot) is set by choosing the minimum thrust required to meet all the operational requirements, at the maximum allowed wing loading computed in the previous section.

It can be noticed that for take-off and landing, the following value of maximum lift coefficient are sufficient: CL_{TO} = 1.4 and CL_L= 2.2. Both these values are relatively low, when compared to those of conventional wide body aircraft (up to CL_L = 3). This is mainly a consequence of the low wing loading of the cruiser.

The sizing requirement for T/W appears to be the one related to aborted landing with one engine inoperative (OEI). It follows that a total thrust of 1900 kN is required, which could be provided by four engines similar to the GE-115B. This is currently the most powerful jet engine and can provide a maximum thrust of 512 kN [7].

For what concerns the power, a maximum value of 344.5 MW is required during maneuvering. This value is the one to be used to size the nuclear reactors (see Table 5).

From the graph, it is possible to estimate the rate of climb RC achievable by the Cruiser, which is equal to 6 m/s and very close to that of other wide body aircraft such as the Airbus A-380 and the Boeing B-747 [6].

6 Refined Weight Estimation approach and balance of the aircraft

In case of conventional aircraft, so called Class II methods are usually applied to estimate the weight of the main structural component groups (Wing, fuselage, empennages, etc.). The sum of these components generally yields a different operative empty weight value (WOE) than obtained during the initial weight estimation phase, using Class I methods (statistics and Breguet formulas). Hence, Class I and II methods are generally iterated until a consistent set of weight estimates is obtained. Various Class II weight estimations are available in literature [2,3], but they are not generally applicable to aircraft such as the one under consideration here, given its unconventional design and the lack of statistical values to perform suitable regressions.

To this purpose a more physics based weight estimation approach, a so called Class II and half method, has been adopted to achieve a more reliable weight estimation, at least for the primary (load carrying) structural elements of the aircraft. The employed approach is based on a method specifically developed by Torenbeek for lifting surfaces [8], which makes use of the actual loads acting on the main structural components (spars, skins, ribs) to estimate their thicknesses and thus their weight.

This method has been applied to the outer wing of the BWB, first, and then to the center body of the BWB, which is also a lifting body. This latter weight contribution was then corrected by adding the weight contribution of the internal multi-bubble structural system used to accommodate the payload and carry the pressurization loads (see Figure 10). To this purpose, the sizing approach proposed in [Ref. 9] has been used. Finally, the weight contributions of engines, landing gears and other systems are added. In this case manufacturers' data and some semi-empirical rules (such as Class II weight estimation method for landing gear) have been used.

The total weight estimation for the cruiser is computed by adding the derived structural weight contributions to the payload and the power plant system weight contributions (as computed in Section 4).

$$WTO = Wwing + Wfus + WPL + WP = 924.7 \cdot 10^3 \text{ kg}$$

Since the obtained weight estimation does not differ significantly from the initial Class I estimation (which was 5.4% lower), no iterations were considered necessary.

A preliminary estimation of the center of gravity (c.g.) range of the aircraft was used to define a proper positioning of the landing gear. Aerodynamic simulations have been performed to estimate the position of the neutral point and assess the controllability of the aircraft, even in the most adverse (forward) position of the c.g, at approach speed and with deployed flaps. The aircraft appears to be slightly unstable when the c.g. is in its most aft position. However, the presence of one empty payload container on board is sufficient to move the c.g. in front of the neutral point and achieve stability. More details on all the weight calculations, and the stability and controllability analysis can be found in [ref. 10].

7 Considerations on the use of nuclear propulsion

The dream to achieve a nuclear powered aircraft has existed for a very long time. Extensive research took place during the cold war [4,5]. However, environmental concerns and depletion of fossil fuel resources have recently rekindled the interest in nuclear powered aircraft also for civil applications [11]. Indeed, a turbofan engine that utilizes heat energy from a nuclear reactor, does not require fossil fuel and does not emit carbon dioxide or nitrogen oxide, therefore it does not contribute to global warming. In addition, the range potential of a nuclear powered aircraft is substantially greater in comparison with a conventional aircraft. Because energy from nuclear fuel costs only a fraction of that for fossil fuel, nuclear powered cruisers also hold out significant promise to reduce the cost of air transportation.

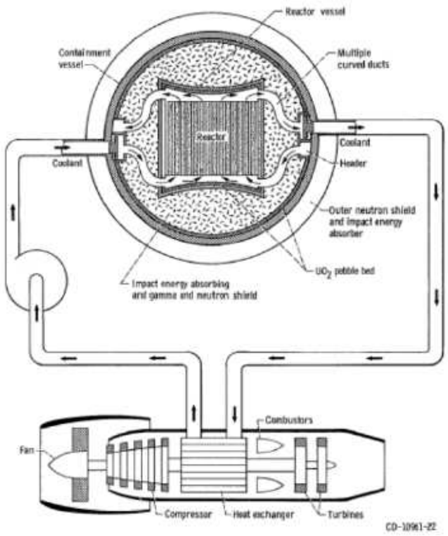

Figure 7:indirect Brayton cycle using a heat exchanger to extract the heat generated by a helium cooled reactor

The major disadvantages of nuclear propulsion are the obvious safety and security concerns. A practical nuclear cruiser design must have complete shielding to reduce the radiation doses to allowable levels in all directions, so that neither the crew and passengers onboard, nor the maintenance and servicing crew on the ground, receive radiation doses significantly greater than that normally received from natural sources. A nuclear cruiser must also have safety provisions that are designed to prevent the release of radioactive material in the worst aircraft accidents.

At the current state of work in the RECREATE project, the use of turbofan engines based on the indirect Brayton cycle and the use of compact helium cooled reactors are considered (see Figure 7), as described in [12]. Differently than a conventional gas turbine, the combustion chamber is replaced (or complemented, in case of hybrid configurations) by a heat exchanger, which transfers the heat generated by the nuclear reactor to the compressed air. Although this concept was selected because of its compactness, and the possibility to adopt a hybrid fuel system, preliminary studies reveal that, due to the poor heat transfer properties of the air, the use of helium as coolant might lead to very large heat exchanger, with severe consequences on the aircraft weight and the practical ability to place the heat exchanger between compressor and turbine. The use of another medium as reactor coolant (e.g. liquid metal or molten salt) may alleviate this problem, while retaining a compact core.

A parallel study has been performed to investigate the benefit of replacing the Brayton cycle with a Rankine cycle [13]. Indeed, this is a common solution for nuclear power stations and marine applications (large vessels and submarines). The adoption of the Rankin cycle would lead to the replacement of the turbofan engines with ducted fan engines, driven by the steam obtained from the nuclear reaction. The steam would need to be cooled down and the water sent back to the nuclear reactor in a closed loop cycle. However, this appears to be less convenient for cruiser, because of the very large condensers needed to reject the waste heat that cannot be converted into work. Although the wing surface is suited to facilitate condensation, it is not capable of rejecting all the waste heat to its surroundings (again because of air poor heat transfer properties). Extra complex and heavy air cooled condensers would be required, as well as the need to fly at lower altitude. As described in the next section, the design and integration of the nuclear propulsion system will be object of further research within the RECREATE project.

8 Conclusions and future work

The work presented in this paper represents the first step into the feasibility study of a nuclear propelled aircraft for the cruiser/feeder concept. Although the proposed concept has been supported by some preliminary calculations, significant developments are required to turn the nuclear cruiser design from an interesting exercise into a credible option for future aviation. The purpose of the RECREATE project, in this respect, is to perform only a basic exploration of this concept, to provide a preliminary assessment of the possible technical, safety and certifications related issues to be included in development roadmap. The very next steps concerning the conceptual design of the nuclear cruiser include a general review and consolidation of the results presented in the previous sections, plus the set-up of an aerodynamic analysis campaign to derive a proper combination of airfoils and planform parameters. Although a detailed aerodynamic analysis might appear premature for a concept that is still so fluid, the integrated nature of the BWB configuration requires a proper simultaneous choice of the aerodynamic shape and the rest of the parameters governing the interiors layout and the overall aircraft flight performance. Considering the absence of an actual tail, a thorough assessment of the stability and controllability performance of the aircraft, both longitudinal and lateral-directional, is necessary.

The design of the docking and loading mechanism of the detachable fuselages will require also careful attention. At the moment no sufficient information was available to propose even a simple relation to account for the weight penalty of this mechanism.

For obvious reasons, the most urgent research activities concern with the nuclear propulsion system and its integration. The number of reactors, their type (nuclear fuel and coolant), their size, the accurate sizing and weight estimation of the shielding, the layout of the energy conversion system, the choice of the Brayton or Rankine cycle to drive turbofan or turboprop engines are just some of most urgent topics to be addressed before the closure of RECREATE.

9 References

[1] REsearch on a CRuiser-Enabled Air Transport Environment. Project public website http://www.cruiser-feeder.eu

[2] E. Torenbeek, Synthesis of subsonic airplane design. Springer, Delft, 1982

[3] D.P. Raymer. Aircraft design: A conceptual approach. 4th ed., Washington D.C., 2006.

[4] F. E. Rom, C. C. Masser, “Large nuclear-powered subsonic aircraft for transoceanic commerce”, NASA, 1971

[5] J.L. Anderson, F.E Rom, "Assessment of lightweight mobile nuclear power systems" NASA, Lewis Research Center Cleveland, Ohio, NASA technical memorandum NASA TM X-71482, 1973.

[6] P. Jackson, “Jane’s all the world’s aircraft”, Jane’s information group, 2004

[7] www.geaviation.com/engines/commercial/en/ge90-115b.html

[8] E. Torenbeek, “Development and Application of a Comprehensive, Design-sensitive Weight Prediction Method for Wing Structures of Transport Category Aircraft”, Delft University of Technology, September 1992.

[9] V. Mukhopadhyay, J. Sobieszczanski-Sobieski, I. K. G. Q. C. C., “Analysis Design and Optimization of Non-cylindrical Fuselage for Blended-Wing-Body (BWB) Vehicle,” Proceedings of the 9th AIAA/ISSMO Symposium on Multidisciplinary Analysis and Optimization, Sept 2002.

[10] M. Chiozzi, “Conceptual Design of a Nuclear Powered Blended Wing Body Aircraft for the Cruiser/Feeder Concept”, MSc thesis, Delft University of Technology and University of Rome La Sapienza, 2013.

[11] B. Khandelwal, A. Prakash, G. Hegde, and T. Mahmood, "Study on Nuclear Energy Powered Novel Air Transport Model and its Feasibility study," AIAA, no. 2011-6038, 2011

[12] W.C. Strack and L.H. Fishbach, "Nuclear powered VTOL aircraft," NASA, Lewis Research Centre Cleveland, Ohio, NASA technical memorandum NASA TM X-52524, 1968.

[13] K.L. Hsia, “Nuclear Aircraft Propulsion System Conceptual Design”, MSc thesis, Delft University of Technology, 2013

Acknowledgement

The research leading to the results presented in this paper was carried out within the project RECREATE (REsearch on a CRuiser Enabled Air Transport Environment) and has received funding from the European Union Seventh Framework Programme under grant agreement no. 284741.

External Inputs	• PLW • PW = PW(TOW) • OEW = OEW(TOW) • Feeder fuselage lenght • Cruise velocity • Stall velocity • Cruise altitude • T.O. distance	• Passengers Surface • Cargo Volume • Reactor Volume • Coolers Volume • L.E. sweep angle • Airfoil type • Airfoil positon	• Number of reactors • Engines Weight • Fixed L.E. and T.E. surfaces • Slats and Flaps Surfaces • Ailerons Surface • Flap Type • Material density	
	Preliminary Sizing	• Root chord lenght • Fuselage span, Wing span • Taper ratio 1, Taper ratio 2 • C_{Ldes} , C_{D0} • Aspect Ratio • Wing Surface • TOW, OEW, PW • Root thickness • Tip chord, Center Line chord	• Number of engines • Reactors Weight • MZFW • MLW	
	• Aerodynamic Efficiency	**General Anrchitecture**	• t/c ratios • Coolers dimensions • Mean chord sweep angle • Volume Pressurized • Wing Surface	• 3D rendering • Mesh
	• TOW • OEW		**Detailed Weight Estimation**	
		• L.E. sweep angle • Airfoil type • Airfoil positon • Aerodynamic Efficiency		**CFD Analysis**

Table 4: N2 Chart illustrating the main design parameters computed and exchanged during the various steps of the conceptual design process

Operative Condition	*Assumptions*	*T/W*	*T (kN)*	*P (MW)*
Cruise	• $C_{D0c} = C_{D0} + 0.03$ • v = 236.3 m/s • h = 11000 m	0.053	457 @ h 1254 @ s.l.	108 300
Maneuver	• $n_{max} = 2.5$ • h = 11000 m • v = 236.3 m/s	0.17	1458	**344.5**
Take-off	• $X_{TO} = 3000$ m • Sea level			
Landing	• $v_{st} = 43.73$ m/s • Sea level			
Rate of Climb	• $C_{LTO} = 1.4$			
Ceiling	• $RC_{ceiling} = 1.5$ m/s	0.0273	234 @ h 637 @ s.l.	55.3 150
Climb Gradient	• 4 engines • $C_{LTO} = 1.4$ • $C_{LL} = 2.2$ • $v_2 = 1.2^* v_{st}$	Initial climb 0.157 Transition climb 0.165 Second part climb 0.174 Route climb 0.151 Aborted landing 0.184 Aborted landing 0.222	**1900**	100

Table 5: T/W needed in different flight conditions

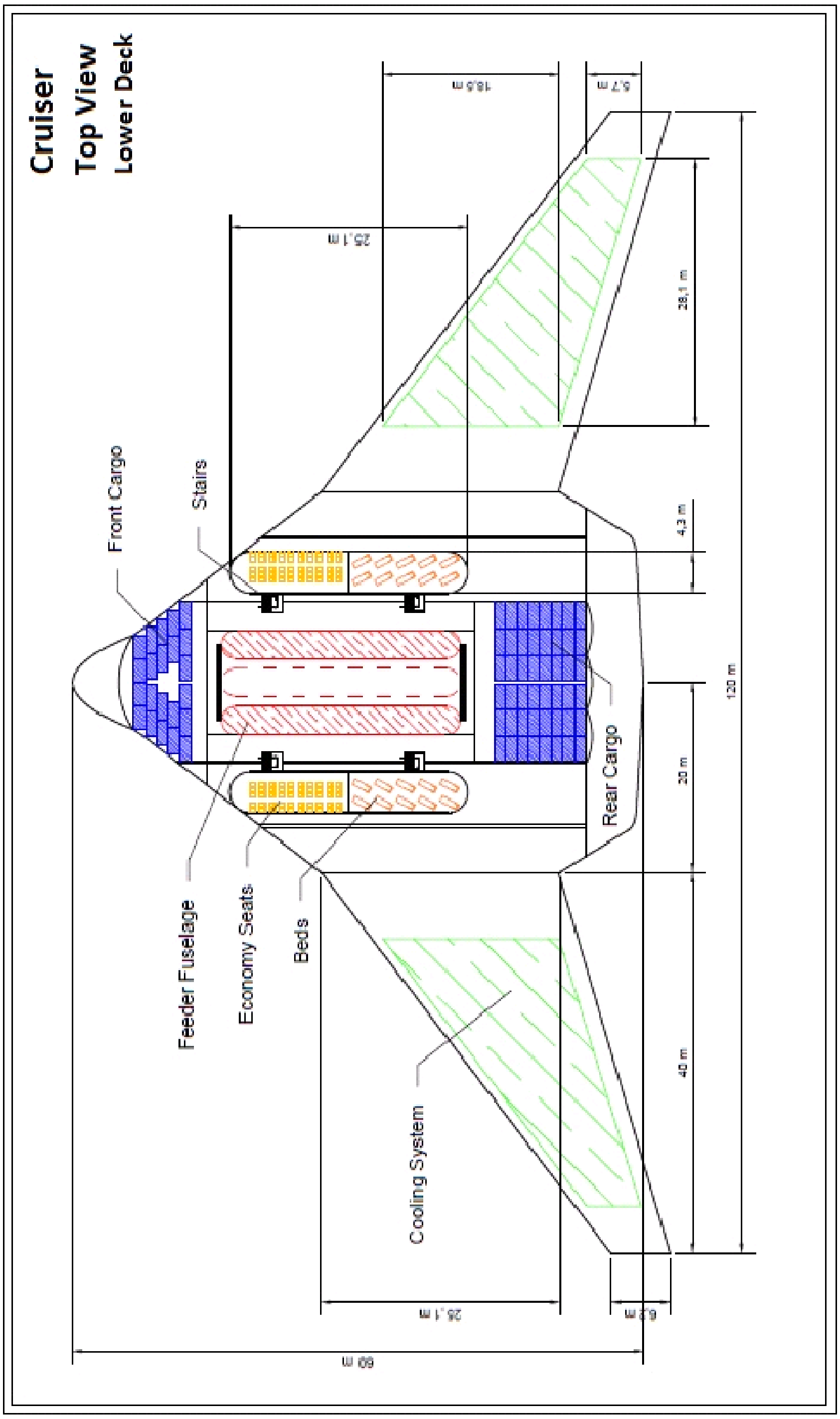

Figure 8: top view of the cruiser

Figure 9: top view of the upper and middle deck

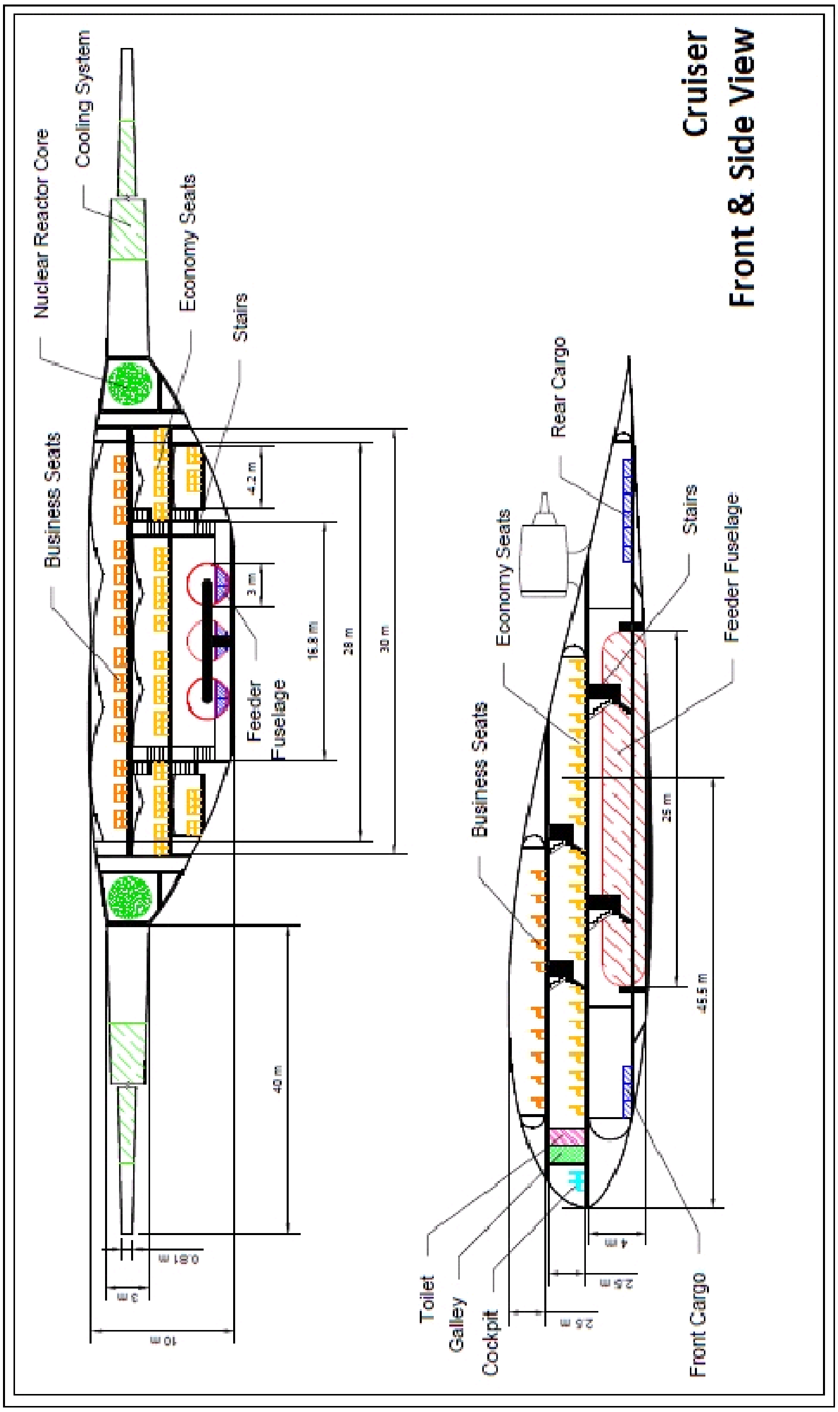

Figure 10: front and side view of the cruiser

Personal Jet
A student project

C. Jouannet, P. Berry, T. Melin, D. Lundström
Linköpings University, Sweden Affiliation 1, Country

Keywords: *Student project, demonstrator, aircraft design*

Abstract

The presented work considers designing, building and flight test of a demonstrator of a personal jet aircraft realized as a student project. The goal is to allow student to participate in an aircraft project from design to flight test in order to acquire aircraft design knowledge from theoretical and practical means. A first theoretical part consists of creating a sizing program for studying different concepts. Then the gathered knowledge will result in the realization of a flying demonstrator. This was realized during a student project over a 5 month period..

1 Background

Since the development of the BD5J, a kit plan, no personal jet has been available to the market. The possibilities for developing a new personal jet is studied, in order to reach a broader market an investigation on certifications regulation is performed. The project aim is to design a single seat sport jet aircraft based on a TJ100A turbine engine. To prove the design a radio controlled sub scale demonstrator will be built and flown, powered by a Funsonic FS70 jet engine.

2 Educational Challenge

Over the years there has been a dramatic reduction in ongoing aircraft projects. Today's aircraft design engineers are lucky if they will be involved in one or two complete projects during their entire careers. This is in sharp contrast to the "golden age", when an engineer was likely to be part of several projects during his career, see Table 1.

This situation creates an issue regarding the education of aircraft design engineers. When they start their professional life they will be assigned to an ongoing project and they may be involved in that for a long time before starting on a new project. The teaching approach as proposed by Linköping University is to allow future aircraft engineers to participate in a complete aircraft design project, from requirements to flight testing, as a preparation for their very first steps into industry.

The other major challenge in aerospace education is changing demands from the industry regarding the type of knowledge the yet to be engineers should be educated for. Most of university aerospace educations are focused on

Table 1 Aircraft project through an aerospace engineer's career [1]

Time Span	Aircraft projects
1950-1980	XP-5Y, A-2D, XC-120, F-4D, F-3H, B-52, A-3D, X-3, S-2F, X2, F-10F, F-2Y, F-100,B-57, F-102, R-3Y1, F-104, A-4D, B-66, F-11F, C-130, F-101, T-37, XFY, F-8U, F-6M, U-2, XY-3, F-105, X-13, C-133, F-107, B-58, F-106, F-5D, X-14, C-140, T-2, F-4, A-5, T-39, T-38, AQ-1, X-15, F-5A, X-1B...
1960-1990	A-6, SR-71, SC-4A, X-21, X-19, C-141, B-70, XC-142, F-111, A-7, OV-10, X-22, X-26B, X-5, X-24
1970-2000	F-14, S-8, YA-9, A-10, F-15, F-18, YF-17, B-1B, YC-15, YC-14, AV-8B, F/A-18
1980-2010	F-117, F-20, X-29, T-46, T-45, B-2, V-22
1990-2020	YF-22, YF-23, JSF, C-17
2000-2030	UCAV, B-3?...

developing students analytical skills and not as much to develop the synthesis capabilities nor the innovative perspective needed for aircraft design. Recent changes in educational perspective, such as the CDIO initiative[2], initiated by the Aerospace institute at MIT and tree Swedish universities, Linköping University being one among them, try to apply a more synthetical view on engineering education, by introducing small practical assignments into the regular courses. This approach is adopted in a larger scale for the aircraft design education at Linköping University, and was adopted before the creation of the CDIO initiative [2].
Nowadays team-work is increasingly important. Being able to present results and ideas in a selling manner is also an important skill, as well as to be able to convert ideas into something practical and useful. This is something which Universities seldom care much about, but that is certainly important, i.e. to bridge the cliff between the students mostly theoretical life into the more practical life in industry. One of the most important issues is to be able to gain a holistic viewpoint from the very start in working life, i.e. to possess a kind of "helicopter view" with regard to the product or project one is involved in. One way of preparing for that insight is to carry out projects like the aircraft design project at Linköping University.

3 Project Task

The project will be divided into the following phases:

- First phase: Concept generation and design competition
  - o The group will be divided in teams and will compete for the best design
  - o An advisory board will select 1 or 2 designs for further studies.
- Second phase: Conceptual and preliminary design
  - o Further study of the selected designs
  - o Sizing and performance calculations
  - o CAD design
  - o The advisory board will select one design for final development
- Third Phase: Detailed design and demonstrator development
  - o Detailed studies of the final configuration.
  - o Demonstrator development
  - o Design
  - o Manufacturing
  - o Flight testing

3.1 Design specifications

The main characteristics are:

- Appealing design
- Good handling qualities
- Performance level similar to BD5J

Following must be included in the design of the fullscale and demonstrator must be represented in CATIA V5 R21

- Landing gear studies
    - retractable landing gear
    - steering on nose wheel
- Brakes
- Cockpit layout
    - Instrumentation and instrument panel
    - Adjustable pedals to accommodate different pilot sizes
    - all necessary information for the cockpit¨
    - Field of view for the pilot
- Mechanism for control surfaces/Flight control system
- Fuel system designed for advanced flight
- Engine installations
    - Duct design
    - Outlet design
- Emergency escape mechanism
- Electrical system Sizing for
    - Navigation light
    - ECU/engine start
    - Avionics

4 Certification and regulations

To be allowed to fly the airplane and make it profitable for production the airplane needs to be certified by competent authorities. Different certifications categories were studied, it appeared that the categories CS-VLA (Very Light Airplanes),
CS-LSA (Light Sport Airplanes) and Experimental could not be used for this project for different reasons. The CS-VLA is for non-aerobatic aircraft and the CS-LSA does not allow turbine engines, making both of these regulation categories unavailing. In addition, the experimental category is different in every country witch is not optimal for export possibilities.
The two remaining categories were CS-23 (Normal, Utility, Aerobatic, and Commuter Airplanes) [3]and FAR, another category for experimental aircraft. It was decided to use the CS-23 as certification basis for the aircraft, mainly because this category allows aerobatic and jet aircrafts and also commercial sales.
Once the aircraft regulation category was decided, it was necessary to further study the associated regulation in order to extract the information needed and ensures that the aircraft is in accordance with the regulations.

5 Concept development

The conceptual phase started as a sketch exercise to present various ideas around a personal jet, examples of those sketch are illustrated in Fig. 1.

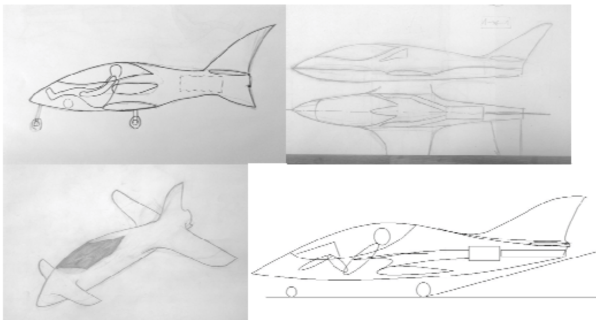

Fig. 1 Early concept sketches

Further discussion and development gave the airplanes more aggressive contours and keeping an aerodynamic shape. Inspiration from nature and animals gives a shark-shaped outlines and tiger eyes shaped canopy, illustrated in fig.2.

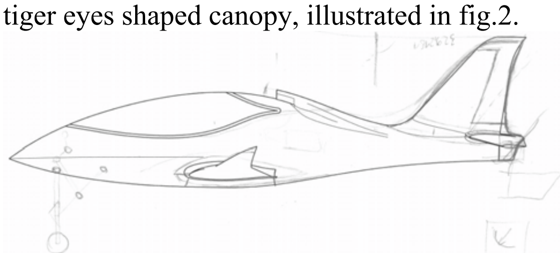

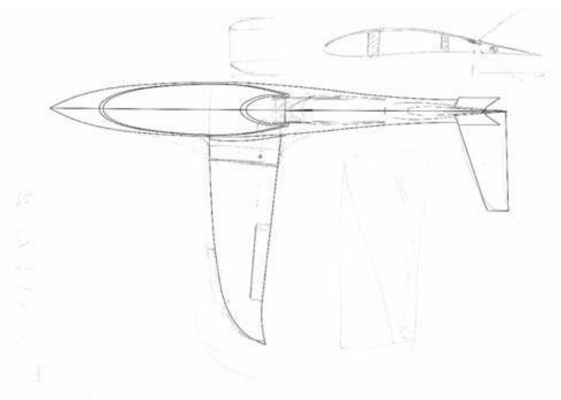

Fig. 2 Final Concept

5.1 Sizing

The sizing was performed around a given engine, the TJ100 from První brněnská strojírna Velká Bíteš. It is a single shaft, single stage radial compressor of about 20 kg's and has a static thrust of 1200N. The sizing program used is a Linköpings university in house sizing tool. The sizing tool was calibrated with the actual BD5J [4]. Weight factors were added in order to take into account composite usage instead of metal such as used in BD5J.

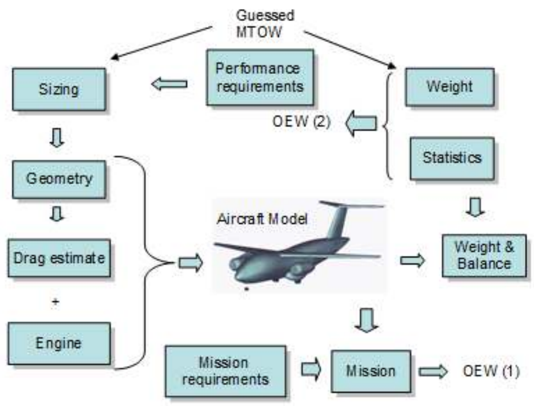

Fig. 3 sizing flow

The following characteristics were obtained from the sizing.

	MidJet	BD5J
MTOW [kg]	320	386
OEW [kg]	146	163
Vcruise [km/h]	437	386
Stall speed [km/h]	104	107
Wing loading [kg/m2]	100	137
Sref [m2]	3,2	2,8
Wing span [m]	5,2	4,36
Length [m]	4,8	3,6
Height [m]	1,46	1,68

The new design called MidJet is lighter than the original BD5J and has a lower wing loading. In order to improve handling characteristics the fuselage was stretched. The stretching of the fuselage provides a smother overall shape and gives a more modern look to it.

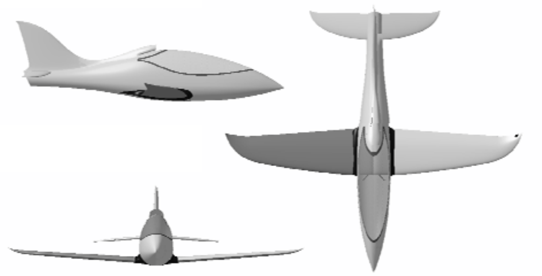

5.2 Engine specifications

The TJ100 is designed and manufactured by První brněnská strojírna Velká Bíteš. It is a single shaft, single stage radial compressor of about 20 kg's and has a static thrust of 1200N.

6 Preliminary design

6.1 Landing gear

A study on a retractable landing gear was performed, see Fig. 4. The landing gear has a classic nose configuration with a steerable nose wheel and hydraulic brakes on the main landing gear. The tires have a diameter of 220 mm. Retraction is performed by a mechanical system of rods and levers controlled by the force of the pilot’s hand motion. The weight distribution is 92% for the main landing gear and 8% for the nose wheel.

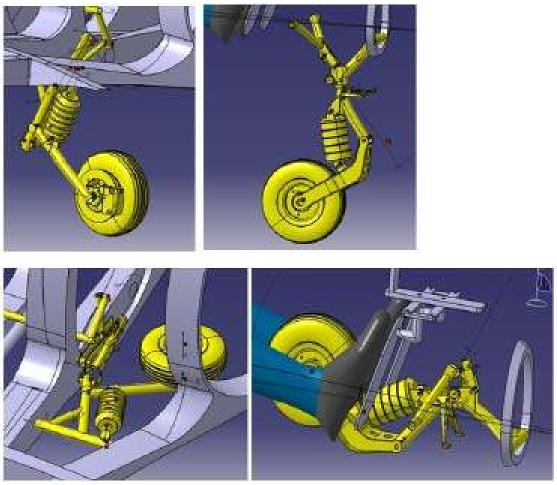

Fig. 4 Landing gear

6.2 Flight control system

In order to move the control surfaces, a linkage between the stick and pedals and the surface is required. A lot of research was done on the design of the stick. The challenge was to make a mechanism that allows the transfer a lateral and rotational movement at the same time, while being compact and robust.

The pedals are moving the rudder in the vertical tail as well as the nose wheel while it is extended.

Since the landing gear takes up a lot of space it was decided to have a lever on the stick for activating the brakes rather than toe brakes. The joint for the pedals which is usually placed underneath the pilots feet had to be repositioned to be able to fit the nose wheel.

The restrained space and rather complex routing for rods leads to a fly-by-wire system. The intention was to keep the wire as straight as possible to avoid friction between the pulleys and the wires. This was limited by the many components that had to be avoided between the stick and the control surfaces such as the fuel tank, the seat, the duct, the landing gear and the different frames.

6.3 Structure

The first thing that was considered when designing the structure was to think "composite". Then, since the fuselage and the wings are built using sandwich technique, there is neither need for stringers or longerons in the fuselage nor multiple ribs in the wings. The skin shell is stiff by itself for the fuselage but needs some reinforcements for the wings, horizontal and vertical stabilizer since they are thin parts and large bending moments are involved.

6.3.1 Fuselage design

The fuselage needed numerous frames to attach the internal components of the aircraft and this also offers more torsional stiffness (for loads that come from the vertical stabilizer), illustrated in Fig.5. The frames, regarding their location, are made with different thickness. The thin ones are used for carrying components such as engine, fuel tank or rudder pedals. Two big frames are used for the front (main) and rear spar of the wing. The main spar can then cross through the frame and therefore be very stiff. The two main frames were extended to carry the loads from the landing gear. The last spars in the rear part of the aircraft are realizing two functions: carrying the exhaust pipe and also acting as a spar for the vertical stabilizer and bring bending stiffness.

6.3.2 Wing design

Since the wing is mostly constructed from carbon fibre, there is no need for multiple ribs to support the skin. This skin links the main and rear spar and allows to form a "wing box" design and then creates something very stiff in a torsional and bending point of view. First, two ribs are needed: one at the root and one at the tip, illustrated in Fig.5. They enable to carry the hinge rod around which will swivel the flaps and ailerons. Between those two components (not on Catia) it is also required to have a hinge attached on the rear spar because of the aerodynamic forces that will tend to bend the hinge rod.

The main spar is made of two parts that are bolted together and on the frame. It was placed at the chord-wise thickest part so the web could be made as high as possible. The way of splitting the spar was to proceed with a shallow angle (as done on some gliders) to avoid sharp corners that could generate structural problems. Therefore, the two parts bolted together that are crossing through the fuselage and allow a large bending and shear stiffness. The rear spar cannot cross the fuselage since there is the landing gear. Therefore, it is attached to a frame without going through it.

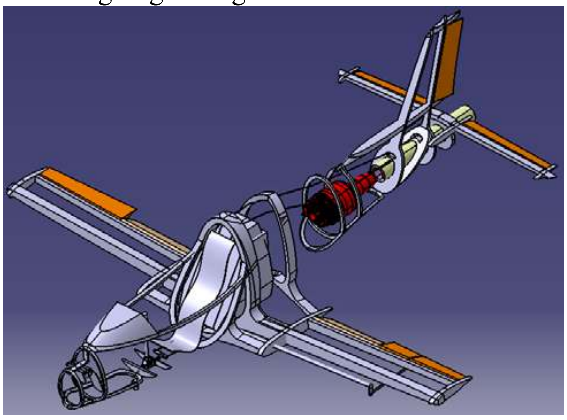

Fig. 5 Structure layout

7 Demonstrator

The scale of the demonstrator was determined by sizing down the full scaled aircraft to fit a engine (and its nozzle) that was already chosen, called FS70 made by the company Fun Sonic. The scale of the demonstrator was then set to 1:2,8. To get the center of gravity at the desired position the components had to be placed in a good way, the lightweight of the main component and the lack of “pilot” inside the demonstrator forced to use ballast in the nose in order to have a balanced aircraft.

The fuselage consists of three parts. The main and biggest part of fuselage is made out of composite sandwich with two millimeters foam core and glass fibre cloth, structure is showed in Fig.6 and molding of the fuselage is seen in Fig.7. The wings are attached wings to this part as well as the horizontal tail and the part of the inlet made out of glass fibre. On this part is glued third part of the fuselage - top part of the inlet made out of plastic on 3D-printer, see Fig.9.

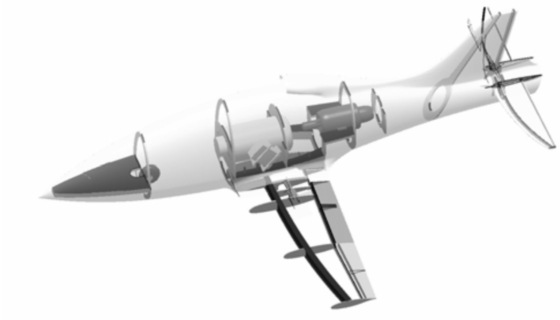

Fig. 6 Structure layout of demonstrator

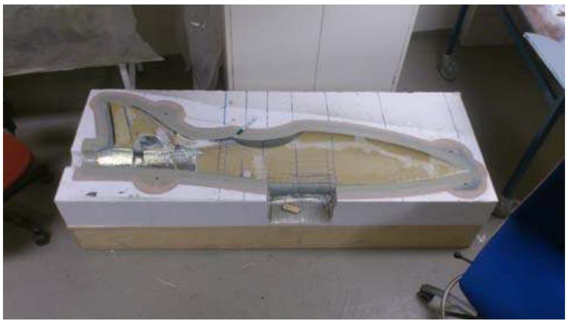

Fig. 7 Molding of the fuselage

Further stiffening of the fuselage is not required, so the structure inside is focused mainly on holding components. The front part of the structure is the frame and floor for attaching nose landing gear, batteries and extra weight for keeping center of gravity at the right place. Behind the nose landing gear there is space where regulators and remote control receiver will be attached. The wing will be attached on floor which is held by two frames from each side. The wing itself is attached to the floor by four screws. This part of the fuselage also holds the fuel tank, hopper tank and floor where the engine is attached. After the engine follows exhaust pipe that is held by four frames, where second frame is reinforced and used also as a vertical tail beam. The third frame is used to hold rudder hinges.

Fig. 8 Molding of the wing

The wing is made from composite structure and is undivided, see Fig.8. The wing attachment is done via 4 bolts, going into the fuselage wing attachment floor, made as a plywood sandwich. The bending moment is transferred by the main spar, specially by flanges of the main spar. Shear stress is transferred in the web of the main spar and finally the torsion moment is taken by the skin.

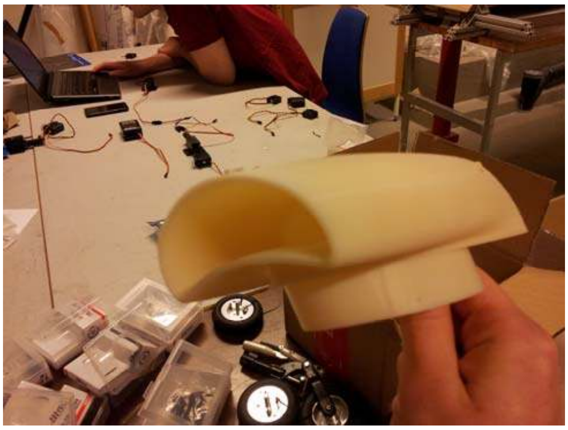

Fig. 9 3D printed inlet

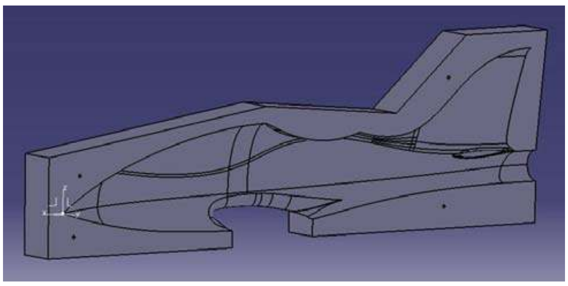

8 Conclusion

Realization of a student project is a dual challenge. Education and the success of the project. The goal in this case is to give the student a broad understanding of the aeronautical challenges and the interaction between disciplines. The usage of a flight demonstrator, an advanced RC model is sufficient to allow students to acquires a sense for the challenges while applying there theoretical skills. The manufacturing phase remind the students that manufacturing is time consuming and that system installation is a large part of the finalization of aircraft project prior to flight testing. This makes this kind of project very suitable for education of broad aeronautical engineers.

Fig. 10 Artistic illustration of the MidJet

References.

[1] Scott, W. B., “Industry’s Loss Expertise Spurs Counterattack - Aerospace in Crisis” Aviation Week & Space Technology, March 13, 2000, pp. 60-61

[2] http://www.cdio.org

[3] EASA Certification CS-23: http://www.easa.europa.eu/agency-measures/certificationspecifications.php#CS-23 (retrieved 2013-04-1)

[4] BD-5 info: http://www.bd5.com/bd5info13.htm

4:th CEAS Air & Space Conference
FTF Congress: Flygteknik 2013

Open Access Publishing in Aerospace – Opportunities and Pitfalls

D. Scholz

Aircraft Design and Systems Group (AERO),
Hamburg University of Applied Sciences,
Germany

Keywords: *aerospace, paper, journal, publisher, open access*

Abstract

The first Open Access (OA) peer reviewed online journals in aerospace were all established after 2007. Still today more and more OA aerospace journals get started. Many publishers are located in less developed countries. The benefits of OA publishing are undisputed in the academic community, but there is disagreement if the new publishers can work to required standards. The current situation is evaluated based on an Internet review. OA journals in aerospace are listed with their major characteristics. Well know OA publishers charge high publication fees, whereas less known OA publishers tend to charge relatively low fees. All publishers need to be carefully checked for their level of rigor in peer review and their offered service in the scholarly publication process. Authors should evaluate OA journals and publishers against provided lists of criteria before submitting their work.

1 Introduction

1.1 Objective

Intension is to explain the background and to systematically present possibilities for researchers in aerospace to have their work published on the Internet so that it can be read without access fees by anybody. Such Open Access (OA) publishing is growing at fast pace. Many models of OA exist and will be presented and discussed to enable subsequent application to OA publishing in aerospace.

Fig 1: Open Access Logos [2], [14]

1.2 Definition of Basic Terms

This contribution is about publishing an academic paper in contrast to publishing an academic books or a thesis. Several terms are defined in this context.

Open Access (OA) means "to provide the public with unrestricted, free access to scholarly research – much of which is publicly funded. Making the research publicly available to everyone – free of charge and without most copyright and licensing restrictions". [1] The Budapest Open Access Initiative [1] recommends establishing the "goal of achieving Open Access as the default method for distributing new peer-reviewed research". Open Access Initiatives are often marked with a logo as presented in Fig 1.

Publishing means "the activity of making information available" [3] and includes everything from development to distribution (e.g. in paper, online or both in parallel), including e.g. copy-editing, graphic design, production, and marketing.

Academic Publishing (of scholarly journals) is peer reviewed publishing. [4] An academic publisher has to be able to manage the peer review process and will index his journals.

Publication has two meanings [5]:
(a) *legal meaning*: anything that is made public,
(b) *scientific meaning*: only what is meeting the quality standards and acceptance for publication by a peer reviewed journal or peer reviewed proceedings. Journals will only accept submitted papers not having been published before (according to scientific meaning b).

2 Self-Archiving

Self-archiving is a possibility to make research results public on the Internet independent of a publisher. Self-archiving is sometimes also called *Green OA* and means "to deposit a digital document in a publicly accessible website" [6]. Self-archiving does not include anything else as to make the content available online. It is done for the purpose of maximizing the paper's accessibility, usage and citation impact. [7] The paper can be uploaded

- to the *website of the researcher*,
- to the *website of an organization*, or better
- to a *repository* [8].

Self-archiving is done in parallel to traditional academic publishing. A publisher with established reputation is used for providing the peer review process. The paper is made public in a print journal (with limited visibility). The author uses the possibilities granted by the rules of the publisher for self-archiving and enhanced visibility.

Possibilities for self-archiving granted by the publisher depending on **what** is allowed to go online [9]:

- *Green OA*
  - preprint (paper before the review process)
  - postprint (paper after the review process) or publisher-generated PDF file
- *Blue OA*
  - postprint (after review process) or publisher-generated PDF
- *Yellow OA*
  - preprint (before review process)
- *White OA*
  - Archiving not formally supported by the publisher.

Possibilities for self-archiving granted by the publisher depending on **when** it is allowed to go online:

- *instant self-archiving*: no time delay required
- *delayed self-archiving* (Delayed OA). Typical required elapsed times between journal publication and self-archiving are 6, 12 or even 24 month.

Repository is a systematic online collection of digital documents with "all stages of research from pre-refereed preprint, through successive revisions, till the refereed postprint" [10] and if (in rare cases) allowed for upload also with publisher-generated PDF files.

Eprints are either preprints or postprints.

3 OA Conference Publications

An Open Access conference publication is a publication based on a conference presentation or poster. The conference offers

- a peer-review process for the papers and
- to publish the papers online after the conference without access restrictions.

One example of such a conference in aerospace is the "Congress of the International Council of the Aeronautical Sciences" (ICAS) [11] offering paper review and uploading. However, most aerospace conferences seem not to fulfill both criteria. In that case, it is possible to go to a suitable journal after the conference for publication. The journal (OA journal or classic journal) will accept the proposed paper, because – so far without a review process or without wider dissemination – the paper is not considered a scientific publication yet. Conference publications are not further considered here.

4 Business Models

Business models have been established for OA and for traditional journals and their publishers:

- **OA journals** [12], [13], [2]:
  - *subsidized* (paid by: academic institution or learned society; eventual in most cases by the government)
  - *authors charged* (paid by: authors or their funding agencies; eventual in most cases by the government)
  - *institutional membership* (institutions pay a flat rate for a certain volume of publications of their members)
  - *advertisement on website*
- **Traditional journals**:
  - *subscription-based* (paid by libraries, eventual by the government)
  - *pay per view* (paid by readers for download of a single paper)
  - *Hybrid OA* (paid by author for the benefit that readers do not need to pay per view for his/her paper)
  - *advertisement in journal*.

OA and traditional journals tend to combine some or all of the listed options in their category to maximize revenues.

OA means **free access for the reader** to the papers, but the authors may need to pay instead. The subsequent classification looks at different **author payment models** depending also on the amount of delay (embargo) requested by the publisher [14]:

- Free OA (no payments by authors)
- Gold OA (*moderate payments* by authors)
- Hybrid OA (often *expensive payments* by authors)
- Delayed OA (embargo period, often no payments by authors)

Moderate payments: normally around 1000 €, but vary from 500 € to 2500 €.
Expensive payments: around 3000 $.
Linköping University says: "Virtually all the major subscription-based publishers offer a scheme whereby you can pay them $3000 (or thereabout) to make your article freely available in their otherwise subscription-based operation. As an author, you often receive an offer for this service just after your paper has been accepted for publication. We strongly do not recommend this option." [15]

5 Open Access Spectrum

The Open Access Spectrum [16] has been defined by the organizations SPARC [17], PLOS [18] and OASPA [19] to answer the question "How open is it?" (see logo in Fig. 3 and definitions in Fig 4). Together they point out: "Open Access is a means of disseminating scholarly research that breaks from the traditional subscription model of academic publishing. It has the potential to greatly accelerate the pace of scientific discovery, encourage innovation, and enrich education by reducing barriers to access. Open Access shifts the costs of publishing so that readers, practitioners, and researchers obtain content at no cost. However, Open Access is not as simple as 'articles are free to all readers'. Open Access encompasses a range of components such as readership, reuse, copyright, posting, and machine readability. Within these areas, publishers and funding agencies have adopted many different policies, some of which are more open and some less open. In general, the more a journal's policies codify immediate availability and reuse with as few restrictions as possible, the more open it is. Journals can be more open or less open, but their degree of openness is intrinsically independent from their: Impact, prestige, quality of peer review, peer review methodology, sustainability, effect on tenure & promotion, article quality."

The Open Access Spectrum embraces six core components with their most open characteristics they are:

1. *Reader Rights*: Free readership rights to all articles immediately upon publication.
2. *Reuse Rights*: Creative Commons License CC BY (see Chapter 6).
3. *Copyrights*: Author holds copyright with no restrictions.
4. *Author Posting Rights*: Author may post any version to any repository or website.
5. *Automatic Posting*: Journals make articles automatically available in trusted third-party repositories (e.g. PubMed Central) immediate upon publication.

6. *Machine Readability*: Article full text, metadata, citations & data, including supplementary data, provided in community machine readable standard formats through a community standard API or protocol.

The first of these six open access components is at the heart of OA, but also the second component "reuse rights" is heavily demanded already in form of "CC BY".

6 Creative Commons License CC BY

Creative Commons [20] – in short CC – has evolved as the accepted free provider of reuse right licenses. The most liberal reuse license is CC BY (except from CC0). CC BY [21] stands for

"You are free:

- to Share – to copy, distribute and transmit the work,
- to Remix – to adapt the work,
- to make commercial use of the work.

Under the following conditions:

- Attribution – You must attribute the work in the manner specified by the author or licensor (but not in any way that suggests that they endorse you or your use of the work)"

Its logo is given in Fig 2.

Fig 2: Creative Commons CC BY logos [22]

Research funders like RCUK [23] demand CC BY. If they have paid the research, they should have the right to dictate that everyone should ultimately benefit from it. Organizations of librarian like SPARC-Europe [24] strongly support CC BY. They have an interest to foster the widest possible information exchange. The Directory of Open Access Journals (DOAJ) [25] inspires the use [26]. Objection could come from those authors who have written their paper in their own time and have paid publication fees from their own pocket and do not want to see others to commercially exploit their work. Creative Commons offers for them e.g. CC BY-NC [27] and CC BY-NC-SA [28], but these licenses are not considered a "Free Culture License".

7 Current Debate

Without doubt, a paradigm shift in the business model of academic publishing (see Chapter 4) got started in the US [29], in Europe [30] and beyond. That ultimately means that not all of the traditional publishers may survive, if they can not quickly enough adapt. On the other hand the "gold rush" in starting new OA journals has not always brought quality. Sound and established processes have yet to be found by the newcomers. Repositories are increasing at a rapid rate [8]. For this reason at the heart of the debate [31], [32] is the fear of traditional publishers to loose market share and profit.

The open access newcomers are under heavy observation. Two possibilities exist:

- **To black-list** journals and publishers who do not perform up to established standards. "Beall's List of Predatory Publishers 2013" [33] is the current prominent blacklist with 242 OA publishers and 126 OA journals listed. A less prominent black list is [34] with only 7 OA journals listed (but also linking to [33]).
- **To white-list** journals and publishers who have undergone a minimum check by a respected organization and are listed with this organization. If an open access journal or publisher is listed in the Directory of Open Access Journals (DOAJ) [25] it is a first good sign. DOAJ lists currently almost 10000 OA journals. If the publisher is listed as a member of Open Access Scholarly Publishers Association (OASPA) [19] it has undergone an even more detailed check. OASPA lists currently (only) about 40 OA professional publishing organizations.

8 Pros and Cons of Blacklisting versus Whitelisting Publishers and Journals

The pros and cons of blacklisting and whitelisting have been discussed in [35].

"Beall says ... he is sceptical about whether a white list would be able to keep up with the surge of new publishers, and believes that his blacklist provides more immediate warning" [35].

“ ‘One of the major weaknesses of Jeffrey Beall's methodology is that he does not typically engage in direct communication with the journals that he has classified as predatory,’ says Paul Peters, chief strategy officer at Hindawi Publishing Corporation, based in Cairo, and president of the Open Access Scholarly Publishers Association (OASPA), based in The Hague, the Netherlands. A set of Hindawi's journals appeared on a version of Beall's list because he had concerns about their editorial process, but has since been removed. ‘I reanalysed it and determined that it did not belong on the list,’ he [Beall] says.” [35]

“ ‘Some [publishers] are embarrassingly ... amateurish, but predatory is a term that, I think, implies intent to deceive,’ says Jan Velterop, a former science publisher at Nature Publishing Group” “Damage could be done if ‘a damning verdict is given to otherwise honest, though perhaps amateurish, attempts to enter the publishing market’, he says.” [35]

“Publishers in developing countries and emerging economies are at particular risk of being unfairly tarred by Beall's brush, critics say. Many open-access publishers are springing up in India and China, for example, where swelling researcher ranks are creating large publishing markets.” [35]

“ ’It is important that criteria for evaluating publishers and journals do not discriminate [against] publishers and journals from other parts of the world,’ says Lars Bjørnshauge, managing director of the Directory of Open Access Journals (DOAJ), based in Copenhagen, which lists open-access journals that have been reviewed for quality. ‘New publishing outfits may legitimately use aggressive marketing tactics to recruit authors, and they may have yet to polish their websites, editorial boards and peer-review procedures.’ ” [35]

“Bjørnshauge feels that the entire problem needs to be kept in perspective. He estimates that questionable publishing probably accounts for fewer than 1 % of all author-pays, open-access papers – a proportion far lower than Beall's estimate of 5 ... 10 %. Instead of relying on blacklists, Bjørnshauge argues, open-access associations such as the DOAJ and the OASPA should adopt more responsibility for policing publishers. He says that they should lay out a set of criteria that publishers and journals must comply with to win a place on a 'white list' indicating that they are trustworthy.” [35]

9 Criteria for OA Publishers and Journals

9.1 Criteria of the Directory of Open Access Journals (DOAJ)

To be (white) listed as journal on DOAJ, criteria as follows have to be met [25] (summary):

- Open Access Journal: We define open access journals as journals that use a funding model that does not charge readers or their institutions for access. From the BOAI definition of "open access", we support the rights of users to "read, download, copy, distribute, print, search, or link to the full texts of these articles" as mandatory for a journal to be included in the directory.
- Registration: Free user registration online is acceptable.
- Open Access without delay (e.g. no embargo period).
- Research Journal: Journals that report primary results of research or overviews of research results to a scholarly community.
- Periodical: A serial appearing, or intending to appear, indefinitely at regular intervals and generally more frequently than annually, each issue of which is numbered or dated consecutively and normally contains separate articles, stories, or other writings. The journal should have an ISSN (International Standard Serial Number). Online journals should have an eISSN.
- Content: a substantive part of the journal should consist of research papers. All content should be available in full text.
- Quality: For a journal to be included it should exercise quality control on submitted papers through an editor, editorial board and/or a peer-review system. Describe the process on the web site.
- Metadata: Journal owners are encouraged to supply article metadata.

- Necessary information: The journal's aims and scope, presentation of the editorial board, author guidelines, description of the quality control system and information about Open Access, information about the specific journal should be available on its own URL.
- Commercials: If for financial reasons it is necessary to have commercials on the journal's web site make sure the commercial is not in any way offensive or includes information that could decrease the credibility of the journal. Please note that blinking and/or moving objects can distract a reader.
- Transparency: Be as transparent as possible when presenting your editorial board. Provide:
  - a contact address for the journal,
  - the affiliation of the editorial board members,
  - the contact addresses to the editorial board members,
  - add a link to the web site where the specific editorial board member is presented by his or her employing institution.
- Author guidelines: Provide
  - information on journal charges, handling fees, publication fees with the amount clearly stated,
  - a CC-license for the journal papers; the SPARC Europe Seal is given for a journal with CC BY and provision of metadata,
  - information about copyright – please note the importance of informing authors about whether the journal will be the copyright holder after publication of an article or if the copyright remains with the author(s),
  - description of how to submit an article,
  - a detailed style guide.

9.2 Criteria of the Open Access Scholarly Publishers Association (OASPA)

To be (white) listed as publisher with the OASPA, criteria as follows have to be met [19] (summary):

- The publisher's website demonstrates that care has been taken to ensure high standards of presentation.
- Published articles can be read without the requirement for registration of any kind.
- Full contact information is visible on the website and includes a business address.
- Clear and detailed Instructions for Authors are present and easily located from the homepage. The guidelines include details of the Open Access policy for this publication.
- All articles shall be subjected to some form of peer-based review process. This process and policies related to peer-review shall be clearly outlined on the journal or publisher web site.
- Journals shall have editorial boards or other governing bodies of sufficient size to support the journal, whose members are recognized experts in the field(s) that constitute the scope of the publication.
- Any fees for publishing in the journal are clearly displayed. If there are no charges to authors this should also be highlighted.
- The journal website and published articles, including PDF, should clearly show the licensing policy of the journal. Ideally, the policy should be equivalent to CC BY (also CC BY-NC is acceptable).
- The publisher should not indulge in any practices or activities that could bring the Association or open access publishing into disrepute.
- Any direct marketing activities publishers engage in shall be appropriate and unobtrusive.
- Where appropriate, OASPA will request information about the legal status of the publishing organization, for example, whether it is a privately-owned or public company, a not-for-profit organization or a charity. OASPA will request company registration information.
- Demonstration of the following is also desirable: A&I services that index the journal(s), availability of DOIs for published content, COPE membership [36] and archiving policy.

9.3 Criteria of LiU Electronic Press for Evaluating a Journal

Before publishing it is important to determine whether a journal is serious or not writes Linköpings University Electronic Press [37]. It is important to check if a publication in the journal under investigation "counts" in an academic evaluation exercise in the author's home country. This includes checking the journal being appropriately indexed. The following criteria are worth checking in addition:

- Is the publisher a member of OASPA?
- Is the journal listed in the Director of Open Access Journals (DOAJ)?
- Who is on the editorial committee?
- Who produces the journal?
- Do they give clear contact information?
- Is there a clear and detailed description of the peer-review process?
- Is there regular publishing of articles, no periods of inactivity?
- Are articles found by Google, when searching by using their full titles?
- Is transfer of copyright required? (Should not be required)
- Is the right to parallel publishing (preferably with an embargo period of 6 months or less) retained? (Should be retained)
- Are DOIs (Digital Object Identifier) assigned to all articles?
- Do well established authors in the field publish in the journal?

Also [35] includes "A checklist to identify reputable publishers" which however does not give new criteria compared to the criteria listed so far. Also [35] sees DOAJ and OASPA as the two organizations that check OA journals respectively OA publishers.

9.4 Criteria to Put a Publisher on Beall's Black List

There are many things a publisher can do wrong. Accordingly, Beall's "Criteria for Determining Predatory Open-Access Publishers" [38] is quite long and will not be reproduced here in full. Some (interesting) criteria not mentioned before are selected to illustrate the pitfalls that publishers and authors should watch out for:

1. The publisher depends on author fees as the sole and only means of operation with no alternative, long-term business plan for sustaining the journal through augmented income sources.
2. The publisher provides insufficient information or hides information about author fees, offering to publish an author's paper and later sending a previously-undisclosed invoice.
3. The publisher sends spam requests for peer reviews to scholars unqualified to review submitted manuscripts.
4. The publisher dedicates insufficient resources to preventing and eliminating author misconduct, to the extent that the journal or journals suffer from repeated cases of plagiarism, self-plagiarism, image manipulation, and the like.
5. The publisher asks the corresponding author for suggested reviewers and the publisher subsequently uses the suggested reviewers without sufficiently vetting their qualifications or authenticity.
6. Operate in a Western country chiefly for the purpose of functioning as a vanity press for scholars in a developing country.
7. Do minimal or no copyediting.
8. Have a "contact us" page that only includes a web form, and the publisher hides or does not reveal its location.

"The following practices are considered to be reflective of poor journal standards ..., while they do not equal predatory criteria" [38]:

9. The publisher copies "authors guidelines" verbatim (or with minor editing) from other publishers.
10. The publisher lists insufficient contact information, including contact information that does not clearly state the headquarters location or misrepresents the headquarters location (e.g., through the use of addresses that are actually mail drops).
11. The publisher publishes journals that are excessively broad (e.g., Journal of Education) in order to attract more articles and gain more revenue from author fees.

12. The publisher requires transfer of copyright and retains copyright on journal content. Or the publisher requires the copyright transfer upon submission of manuscript.
13. The publisher has poorly maintained websites, including dead links, prominent misspellings and grammatical errors on the website.
14. The publisher engages in excessive use of spam email to solicit manuscripts or editorial board memberships.
15. The publishers' officers use email addresses that end in .gmail.com, yahoo.com some other free email supplier.
16. The publisher includes links to legitimate conferences and associations on its main website, as if to borrow from other organizations' legitimacy, and emblazon the new publisher with the others' legacy value.
17. The publisher displays prominent statements that promise rapid publication and/or unusually quick peer review.
18. The publisher uses text on the publisher's main page that describes the open access movement and then foists the publisher as if the publisher is active in fulfilling the movement's values and goals.
19. None of the members of a particular journal's editorial board have ever published an article in the journal.

These criteria should suffice to illustrate how publishers can fall in traps and should give an overview of how badly some publishers are organized apparently. However, it seems not clear how to apply some criteria in practice to black-list publishers:

1. Every publisher with a business model base only on author fees is black-listed? How to obtain the business plan from the publisher?
6. To distinguish between "Western country" and "developing country" is imprecise. What about Japan? The term "vanity press" seems to be used in a subjective way. Possible questions for a distinction could be based on: Is vanity press "self-publishing" in contrast to "self-archiving"? [5] Is vanity press defined as "without peer-review"? [10] Is vanity press based on "correlation between publishers' quality standards and the fees charge"? Will positive or negative correlation cause black-listing? [39]
7. Business models can vary, including extensive copyediting in the publication fee, charging for copyediting in addition, handing over this task to another company specialized it this field. Hence more details need to be included in a verdict on this point.
11. To establish broad-spectrum journals seems to be common accepted practice. PLOS ONE's publication criteria state "We welcome submissions in any discipline" [40]. Similarly, SAGE Open spans "the full extent of the social and behavioral sciences and the humanities" [41].
14. It is not defined what "spam emails" are. Commercial electronic mail messages are legal e.g. in the USA according to the CAN-SPAM Act of 2003 [42] if they observe unsubscribe, content and sending behavior compliance.
16. What may be allowed for a "white" publisher seems not to be allowed for a "black" publisher. A more precise statement would be: Including links to other organizations should (preferably) require that these organizations also link back to the publisher.
17. Ok, but some traditional publishers should be blamed for dragging on publication in a way that should not be tolerated.
18. Here the evaluation will be subjective.

Some criteria may show a "Western" bias:

10. A publisher showing its (say) Indian origin will be blamed for being Indian. An Indian publisher trying to hide its origin will be blamed for not being transparent. This is a catch-22.
12. Grammar and spelling: Only English language journals seem to be investigated. Journals published by employees with English not a native language are treated like journals published by native English employees. However, journals publishing in a language other than English do not run the danger of being blacklisted, they are not even considered.

15. This may be normal in "developing countries".

These *remarks do not attempt to be a full criticism* of [38], but may show how problematic it is to come to a verdict. It may be asked, if [38] has been applied only to publishers already in focus to produce Bell's list [33]. *Applying [38] also to established publishers* may reveal more candidates for the list. Applying [38] to Springer's "European Transport Research Review" would probably reveal "predatory behavior" according to criteria 2 (fees, see below). Yet Springer is not listed in [33]. The journal writes: "Manuscripts that are accepted for publication will be checked by our copyeditors for spelling and formal style. This may not be sufficient if English is not your native language and substantial editing would be required." [43] The journal links to an external service which is charging extra. Is this "predatory behavior" according to criteria 7 (minimal or no copyediting)?

After all, it is not made public how many and which of the criteria a black-listed publisher was found guilt of.

10 Review of Open Access Aerospace Journals

Listed are primarily journals that are only dedicated to aerospace. Given is the journal name and with web link to the journal. The publisher's origin is given according to the web page information and from the registration of the domain name. If the domain name information is hidden this is indicated ("hidden"). White or black listings are indicated of the publisher. If the publisher and the journal is listed on DOAJ three numbers are given (number of journals listed / number of articles listed / number of articles of the aerospace journal listed). If only one journal exists two numbers are given. Information is provided, if ISSNs are assigned for the journal, if DOIs are assigned to articles of the publisher, in which format the articles are presented, reuse and copyright details according to the publisher's information. Listed is further how many articles have been published in the journal and in how many databases the journal is indexed. Since all these journals are quite new, none has an impact factor. A subjective indication is given about the web page appearance with regards to clear design, structure and necessary information for an OA journal (according to Chapter 9).

International Journal of Aerospace Engineering
Hindawi Publishing Corporation
http://www.hindawi.com/journals/ijae
Origin: Egypt
Started: 2008
Fees: 600 USD
Publisher and journal white-listed:
DOAJ (SPARC Europe Seal) (405/73000/79), OASPA
Publisher black-listed: none
ISSN, eISSN, DOI, PDF, HTML, CC BY, copyright ret.
Articles: 84 (≈ 14 per year)
Indexed in databases/resources: 28
Editor-in-Chief: none
Members on Editorial Board: 75
Reviewers acknowledged: 340
Web page appearance: good

Open Aerospace Engineering Journal
Bentham open
http://www.benthamscience.com/open/toaej
Origin: USA / United Arab Emirates, ... / hidden
Started: 2010
Fees: 250 USD
White-listed: DOAJ (106/139/0)
Black-listed: Beall (no comments given),
Linköpings Universitet
ISSN, PDF, CC BY-NC, copyright retained
Articles: 20 (≈ 3 per year)
Editor-in-Chief: Dan Mateescu, Canada
Members on Editorial Board: 84
Web page appearance: "less convincing"

Journal of Aeronautics & Aerospace Engineering
OMICS Group
http://www.omicsgroup.org/journals/jaaehome.php
Origin: USA / India
Started: 2012
Fees: 919 USD
White-listed: DOAJ (1/207/0)
Black-listed: Beall (no comments given),
Linköpings Universitet
ISSN, HTML, PDF, Audio, CC BY, copyright retained
Articles: 21 (≈ 10 per year)
Indexed in databases/resources: 4
Editor-in-Chief: Prof. Raffaele Savino, Italy
Members on Editorial Board: 47
Web page appearance: "less convincing"

Frontiers in Aerospace Engineering (FAE)
Science and Engineering Publishing Company
Journal: http://www.fae-journal.org
Publisher: http://www.seipub.org
USA / China
Started: 2012
Fees: 0 USD (in 2013)
Publisher white-listed: none
Publisher black-listed: Beall (comments outdated)
ISSN, eISSN, PDF, CC BY-NC-ND, copyright ret.
Articles: 22 (≈ 22 per year)
Indexed in databases/resources: 15
Editor-in-Chief: Prof. Pizhong Qiao
Members on Editorial Board: 10
Web page appearance: good

Advances in Aerospace Science and Technology (AAST)
Scientific Research Publishing
http://www.scirp.org/journal/aast
USA (registration) / China (offices)
Started: 2013, Fees: 300 USD
Publisher white-listed:
DOAJ (127/19000/0), application: OASPA
Publisher black-listed: Beall (no comments given)
CC BY or CC BY-NC, copyright retained
Editor-in-Chief: Prof. Dieter Scholz, Germany
Members on Editorial Board: 10
STARTUP!

American Journal of Aerospace Engineering
Science Publishing Group (SciencePG)
http://www.sciencepublishinggroup.com/journal/news.aspx?journalid=309
Origin: USA / hidden
Started: 2012
Fees: 170 USD
White-listed: none
Black-listed: Beall (no comments given)
Editor-in-Chief: none
Members on Editorial Board: none
Web page appearance: good
STARTUP!

Journal of Aeronautical Engineering (JAeE)
Trans Stellar Journal Publication Research Consultancy
http://tjprc.org/journals.php?jtype=1&id=2
India
White-listed: none
Black-listed: Beall (no comments given)
STARTUP!

Not considered in full detail, because the scientific field is broader than “aerospace”:

International Journal of Research in Aeronautical and Mechanical Engineering (IJRAME)
IJRAME Aero Team, Hyderabad
http://www.ijrame.com
(http://www.mlrinstitutions.ac.in/aeronautical-engineering.html)?
Origin: India / hidden
Started: 2013
Fees: 50 USD
Publisher white-listed:
DOAJ (SPARC Europe Seal) (1/17)
Publisher black-listed: none
eISSN, PDF, CC BY, copyright transferred
Articles: 17 (≈ 17 per year)
Editor-in-Chief: Mr. Mohammad Salahuddin (student?)
Members on Editorial Board: 2
Reviewers acknowledged: 8
Web page appearance: simple but ok

Journal of Mechanical, Aerospace and Industrial Engineering
Publisher: Scientific Journals International (SJI)
http://www.scientificjournals.org/Journals2011/j_of_mechanical1.htm
Origin: USA / hidden
Started: 2011
White-listed: none
Black-listed: Beall (no comments given),
Linköpings Universitet
Articles: 1 (≈ 1/2 per year)
Web page appearance: very confusing, little information

International Journal of Mechanical and Aerospace Engineering
World Academy of Science, Engineering and Technology
http://www.waset.org/journals/ijmae
Origin: USA / hidden
Started: 2012
White-listed: none
Black-listed: Beall (no comments given)
Articles: 79 (≈ 79 per year)
Web page appearance: very dubious, little information

On DOAJ there are also aerospace journals listed that are published by their own institution – probably more for own purposes then for international authors. All three journals do not charge fees, because they are sponsored by their founding institution (but note the Springer journal!):

INCAS Bulletin
National Institute for Aerospace Research (INCAS)
http://bulletin.incas.ro
Origin: Romania
Started: 2009
Fees: 0 USD (according to DOAJ), no information given on web page, response to email: **no fee**, international authors welcome
Publisher white-listed: DOAJ (1/277)

Journal of Aerospace Technology and Management
Institute of Aeronautics and Space
http://www.jatm.com.br
Origin: Brazil
Started: 2009
Fees: 0 USD (according to DOAJ), no information given on web page, not further checked
Publisher white-listed: DOAJ (1/97)

European Transport Research Review
Springer
http://www.springer.com/engineering/civil+engineering/journal/12544
for the
European Conference of Transport Research Institutes (ECTRI)
http://www.ectri.org
Origin: Germany
Started: 2009
Articles: 110 (≈ 28 per year)
Fees: 0 USD (according to – information delivered to – DOAJ), no information given on web page, response to email: **1250 EUR** (if not sponsored by ECTRI)
Publisher white-listed: DOAJ (1/0)

11 Conclusions

It makes sense for everyone that **OA is the way for the future** and to let everyone participate from the common knowledge. As long as the traditional publishers with their subscription-based business model dominate and control the market only **Green OA and self-archiving is possible**. **This however is not a final solution**. The rate with which self-archiving is done is only 20 % on a world average [45]. With full implementation of OA the rate would be 100 %.

Commercial OA Journals obviously **need to charge publication fees in some form** to be viable as an enterprise. Low cost publishing can be performed better in countries with low labor rates (Egypt, China, India), but errors occur caused by lack of experience of startup companies. Undoubtedly there are various difficulties in these countries to overcome, and off course financial pressure exists in these companies as in companies of other countries.

The *International Journal of Aerospace Engineering* by Hindawi Publishing Corporation is fully white-listed and not black-listed. No other commercial OA journal is without blemish. The startup standalone journal International Journal of Research in Aeronautical and Mechanical Engineering (IJRAME) from Hyderabad, India seems to be lucky not to have been spotted by any watchdog, but needs still to mature. Institutes working on limited public funding may not be capable of handling large numbers of manuscripts for free in the long run flowing in from all over the world.

To develop a journal that gets accepted and earns a reputation over time it seems to be advisable to meet all quality and publication standards and display them on the journals website in a way that the statements can be proven by the reader. Get the journal listed in DOAJ [25] with SPARC Europe Seal [24], [26] and in Sherpa RoMEO [46]. Publishers should become a member of OASPA [19] and COPE [36] following COPE guidelines and flowcharts. Editors should become members of e.g. the Council of Science Editors (CSE) [47] or the European Association of Science Editors (EASE) [48] and should follow their recommended and other accepted standards preferably the ISO [49] standards that should find world wide acceptance.

Beall's statement "... we recommend that researchers, scientists, and academics avoid doing business with these publishers and journals. Scholars should avoid sending article submissions to them, serving on their editorial boards or reviewing papers for them" **can be seen as libel** without prove (prove seems missing), can have immense consequences for the companies and can destroy them. This is probably what Beall intends. I can think of **two different approaches**:

1. Instead of seeking to have a few major commercial OA aerospace journals in the world, many organizations (universities, research establishments, societies) could handle smaller OA aerospace journals (like the INCAS Bulletin) based on basic and simple HTML or based on the Open Journal Systems (OJS), a journal management and publishing system serving more than 14000 journals around the world [50]. In this way fees could be kept low.
2. In the same way as companies like e.g. Airbus are cooperating with China [51], editors-in-chief can get active and can build quality into existing or startup journals from such countries. Publishers seem to have their

doors wide open for such co-operation and volunteer work. Also in this way fees could be kept relatively low.
Let every nation bring in their strength.

Let's not destroy, but rather let's work together in this world, share our knowledge and let's live in peace!

Fig 3: Logo of the Open Access Spectrum [16]

Access	Reader Rights	Reuse Rights	Copyrights	Author Posting Rights	Automatic Posting	Machine Readability	Access
OPEN ACCESS	Free readership rights to all articles immediately upon publication	Generous reuse & remixing rights (e.g., CC BY license)	Author holds copyright with no restrictions	Author may post any version to any repository or website	Journals make copies of articles automatically available in trusted third-party repositories (e.g., PubMed Central) immediately upon publication	Article full text, metadata, citations, & data, including supplementary data, provided in community machine-readable standard formats through a community standard API or protocol	OPEN ACCESS
	Free readership rights to all articles after an embargo of no more than 6 months	Reuse, remixing, & further building upon the work subject to certain restrictions & conditions (e.g., CC BY-NC & CC BY-SA licenses)	Author holds copyright, with some restrictions on author reuse of published version	Author may post final version of the peer-reviewed manuscript ("postprint") to any repository or website	Journals make copies of articles automatically available in trusted third-party repositories (e.g., PubMed Central) within 6 months	Article full text, metadata, citations, & data, including supplementary data, may be crawled or accessed through a community standard API or protocol	
	Free readership rights to all articles after an embargo greater than 6 months	Reuse (no remixing or further building upon the work) subject to certain restrictions and conditions (e.g., CC BY-ND license)	Publisher holds copyright, with some allowances for author and reader reuse of published version	Author may post final version of the peer-reviewed manuscript ("postprint") to certain repositories or websites	Journals make copies of articles automatically available in trusted third-party repositories (e.g., PubMed Central) within 12 months	Article full text, metadata, & citations may be crawled or accessed without special permission or registration	
	Free and immediate readership rights to some, but not all, articles (including "hybrid" models)	———	Publisher holds copyright, with some allowances for author reuse of published version	Author may post submitted version/draft of final work ("preprint") to certain repositories or websites	———	Article full text, metadata, & citations may be crawled or accessed with permission	
CLOSED ACCESS	Subscription, membership, pay-per-view, or other fees required to read all articles	No reuse rights beyond fair use/ limitations & exceptions to copyright (all rights reserved copyright) to read	Publisher holds copyright, with no author reuse of published version beyond fair use	Author may not deposit any versions to repositories or websites	No automatic posting in third-party repositories	Article full text & metadata not available in machine-readable format	CLOSED ACCESS

Fig 4: The Open Access Spectrum – A systematic way of showing the openness of a journal [16]

References

[1] Budapest Open Access Initiative. – URL: http://www.opensocietyfoundations.org/openaccess
[2] Open Access to Scholarly Information: "Business models", 2013-06-13. – URL: http://open-access.net/de_en/general_information/business_models
[3] Wikipedia: "Publishing". – URL: http://en.wikipedia.org/wiki/Publishing
[4] Wikipedia: "Academic publishing". URL: http://en.wikipedia.org/wiki/Academic_publishing
[5] eprints: "Self-Archiving FAQ". – URL: http://www.eprints.org/openaccess/self-faq/#self-archiving-vs-publication
[6] eprints: "Self-Archiving FAQ". – URL: http://www.eprints.org/openaccess/self-faq
[7] Wikipedia: "Self-archiving". – URL: http://en.wikipedia.org/wiki/Green_Open_Access
[8] ROARMAP: Registry of Open Access Repositories. – URL: http://roarmap.eprints.org/
[9] University of Nottingham: "RoMEO colours", 2011. – URL: http://www.sherpa.ac.uk/romeo/definitions.php?la=en&fIDnum=|&mode=simple&version=#colours
[10] Harnad, Stevan: "For Whom the Gate Tolls?", 2003. – URL: http://eprints.soton.ac.uk/258705/1/resolution.htm#1.4
[11] International Council of the Aeronautical Sciences. – URL: http://www.icas.org
[12] Wikipedia: "Open-access journal". – URL: http://en.wikipedia.org/wiki/Open_access_journal
[13] Open Access Directory: "OA journal business models", 2013. – http://oad.simmons.edu/oadwiki/OA_journal_business_models
[14] Wikipedia: "Open access". – URL: http://en.wikipedia.org/wiki/Open_access
[15] Linköpings Universitet: "Open Access", 2013-06-24. – URL: http://www.ep.liu.se/openaccess/
[16] PLOS: How open is it? – URL: http://www.plos.org/about/open-access/howopenisit/
[17] Scholarly Publishing and Academic Resources Coalition (SPARC). – URL: http://www.sparc.arl.org

[18] Public Library of Science (PLOS), 2013. – http://www.plos.org
[19] Open Access Scholarly Publishers Association (OASPA), 2013. – URL: http://oaspa.org
[20] Creative Commons: “About”. – URL: http://creativecommons.org/about
[21] URL: http://creativecommons.org/licenses/by/3.0/deed.en
[22] URL: http://creativecommons.org/about/downloads
[23] Research Councils UK: “RCUK Policy on Open Access and Supporting Guidance”, 2013-05-24. – http://www.rcuk.ac.uk/documents/documents/RCUKOpenAccessPolicy.pdf
[24] SPARC-Europe: “SPARC Europe Seal”, 2013. – URL: http://sparceurope.org/our-work/sparc-europe-seal-for-open-access-journals
[25] Directory of Open Access Journals (DOAJ). – URL: http://www.doaj.org
[26] Directory of Open Access Journals (DOAJ): “FAQ, How do I get the SPARC Europe Seal for Open Access Journals?”. – URL: http://www.doaj.org/doaj?func=loadTemplate&template=faq&uiLanguage=en#getseal
[27] URL: http://creativecommons.org/licenses/by-nc/3.0/deed.de
[28] URL: http://creativecommons.org/licenses/by-nc-sa/3.0/deed.de
[29] Office of Science and Technology Policy: “Increasing Access to the Results of Federally Funded Scientific Research”, 2013-02-22. – URL:http://www.whitehouse.gov/sites/default/files/microsites/ostp/ostp_public_access_memo_2013.pdf
[30] Foreign & Commonwealth Office, UK: “G8 Science Ministers Statement”, 2013-06-13. – URL: https://www.gov.uk/government/news/g8-science-ministers-statement
[31] Wikipedia: “Elsevier”. – URL: http://en.wikipedia.org/wiki/Elsevier#Criticism_and_controversies
[32] Wikipedia: “Open access journal”. – URL: http://en.wikipedia.org/wiki/Open_access_journal#Debate
[33] Beall, Jeffrey: “Beall’s List of Predatory Publishers 2013”. – URL: http://scholarlyoa.com/2012/12/06/bealls-list-of-predatory-publishers-2013
[34] Linköpings Universitet: “Dubious Open Access”, 2013-04-05. – URL: http://www.ep.liu.se/authorinf/dubiousjournals.en.asp
[35] Butler, Decan: “Investigating journals: The dark side of publishing – The explosion in open-access publishing has fuelled the rise of questionable operators”. *Nature*, Vol. 495, pp 433 - 435 (2013-03-28). – DOI:10.1038/495433, URL: http://www.nature.com/news/investigating-journals-the-dark-side-of-publishing-1.12666
[36] Committee on Publication Ethics (COPE): “About COPE”. – URL: http://publicationethics.org/about
[37] Linköpings Universitet: “Evaluating a Journal (as a Potential for Publishing an Article)”, 2013-07-05. – URL: http://www.ep.liu.se/authorinf/evaluating_a_journal.en.asp
[38] Beall, Jeffrey: “Criteria for Determining Predatory Open-Access Publishers”, 2nd edition, 2012. – URL: http://scholarlyoa.com/2012/11/30/criteria-for-determining-predatory-open-access-publishers-2nd-edition/
[39] Davis, Phil: “Open Access and Vanity Publishing”, *The Scholarly Kitchen*, 2009-10-21. – URL: http://scholarlykitchen.sspnet.org/2009/10/21/open-access-and-vanity-publishing
[40] Public Library of Science (PLOS): PLOS ONE – For Authors. – URL: http://www.plosone.org/static/publication
[41] SAGE: SAGE Open. – URL: http://www.sagepub.com/sageopen/landing.sp
[42] Federal Trade Commission: Definitions and Implementation Under the CAN-SPAM Act, 16 CFR Part 316, Project No. R411008, RIN 3084-AA96, 2004-05-19. – URL: http://www.ftc.gov/os/2005/01/050112canspamfrn.pdf
[43] Springer: “English Language Editing”. URL: http://www.springer.com/engineering/civil+engineering/journal/12544
[44] Edanz: “Welcome Springer Authors”. – URL: http://www.edanzediting.com/springer
[45] Admin, Blog: *Why the UK Should Not Heed the Finch Report*, 2012. – URL: http://blogs.lse.ac.uk/impactofsocialsciences/2012/07/04/why-the-uk-should-not-heed-the-finch-report
[46] University of Nottingham: “Sherpa RoMEO”. – URL: http://www.sherpa.ac.uk/romeo
[47] Council of Science Editors (CSE). – URL: http://www.councilscienceeditors.org
[48] European Association of Science Editors (EASE). – URL: http://www.ease.org.uk
[49] International Organization for Standardization (ISO). – URL: http://www.iso.org
[50] Public Knowledge Project: Open Journal Systems. – URL: http://pkp.sfu.ca/ojs
[51] Airbus: Airbus in China, 2013. – URL: http://www.airbus.com/company/worldwide-presence/airbus-in-china

All sites accessed on 2013-08-12.

UAV Joined-Wing Test Bed

Dimo Zafirov, Hristian Panayotov
Technical University – Sofia, Plovdiv Branch, Department of Transportation and Aviation Engineering, Bulgaria

Keywords: joined-wing, UAV, design, test bed, studies

Abstract

The future green aircraft will meet demanding weight reduction, energy and aerodynamics efficiency, a high level of operative performance, in order to be compliant regards to pollutant emissions and noise generation levels. The joined-wing concept is considered as a trade-off variant for green design. This is because of its lower cruise drag and lower structural weight. On the other hand the requirements for low pollution and noise could be met using all-electric aircraft. Hence the aim of the present study is to design and produce joined-wing unmanned aircraft – test bed or flight laboratory. The basic design incorporates tip-joined front and rear wings with wing-tip vertical joints. The airframe is mainly of carbon and glass-fiber composite materials. The power plant consist of electrical ducted fan, speed controller and Li-Po batteries. The aircraft integrates Piccolo II Flight Management System which offers a state-of-the-art navigation and flight data acquisition. Prior to production and flight testing of the prototype, aircraft aerodynamics and flight dynamics are being analyzed. Potential models together with wind tunnel tests have been used to determine aircraft aerodynamics. One of the major problems found during simulation and flight experiments is the Dutch roll effect. This is thoroughly discussed in the paper. Some problems that concern autopilot tuning are also described.

1 Introduction

The joined-wing is a relatively new concept that in general represents a configuration of a “front” and “rear” wings that are joined structurally in spanwise direction to form a diamond-shaped box. Starting form 1970s a great deal of works [1,3] has been published on joined-wing concept, aerodynamics, structure and multi-disciplinary optimization (MDO). However, recently most of aircraft design organizations are recalling this concept due to its serious advantages compared to cantilevered wings. These are lower aerodynamic drag, increased structural strength and/or lower structural weight, supermaneuverability features (direct lift and side force control). Thus the joined-wing concept is a contemporary trade-off variant for green transport aircraft or unmanned aerial vehicles (UAV). In order to design, produce and operate joined-wing aircraft a numerous research is involved – both theoretical and experimental. Hence the abovementioned implies the necessity of a development of a joined-wing test bed aircraft or a flying laboratory that could yield real-time flight data stream for analysis and characteristics determination.

To fulfill this task a team was formed in the Department of Transportation and Aviation Engineering in Technical University – Sofia, Plovdiv Branch. The main objectives and expected results are in the area of aerodynamics, aircraft structure and flight dynamics. In the present paper related investigations are reviewed and published.

2 JoWi-2 Test Bed

Figure 1 shows joined-wing UAV – JoWi - 2FL (FL=Flight Laboratory).

The basic design incorporates tip-joined front and rear wings with wing-tip vertical joints. The front and rear wing root chords are structurally connected using a keel-like element which starts with the fuselage trough propulsion mounting and ends at the vertical stabilizer. The role of the keel is to increase the strength and the stiffness of the wing. The airframe is mainly of carbon and glass-fiber composite materials.

Fig. 1 JoWi-2 FL

Since the main concept aims at all-electric aircraft the power plant of the UAV is represented by a modern carbon-fiber electrical ducted fan (Fig. 2), powered by Li-Po batteries.

The core of the Flight Control System (FCS) of JoWi-2FL is Autopilot Piccolo II (Fig. 3) which offers a state-of-the-art navigation and flight data acquisition.

Fig. 2 Schübeler DS77 DIA HST

Fig. 3 Cloud Cap Piccolo II Autopilot

The joined-wing is appropriate to locate and use a great number of control surfaces with different assignment. For example JoWi-2FL has nine control surfaces – two at each quarter of the wing and a rudder. It is known that when the control surfaces are used as elevators and ailerons they are referred to as elevons [elevon=elev(ator)+(ailer)on]. When they are used as flaps and ailerons they are referred to as flaperons [flaperon= flap+(ail)eron]. With the joined wing scheme the rear edge flaps and ailerons can be used as elevators, slope rudders and direct control of the lift and side-force. This could result in the introduction of a new term for joined-wings such as flapeleron [flapeleron = flap+ele(vator)+(aile)ron] [2,3].

The flight controls of JoWi-2FL are: front wing inboard section – flaps and elevator (fl.); front wing outboard section – ailerons (ail); rear wing inboard section – elevators (elev.); rear wing outboard section – elevator and/or ailerons (elevon); rudder on the vertical stabilizer (rudd.).

The main design parameters of JoWi-2FL are given in Table 1.

Table 1 JoWi-2FL design parameters

Parameter	Value	Dimension
Wing Gross Area	0.55	m^2
Wing Span	1.8	m
Rear-to-Front Wing Areas	1	-
Take-off Weight	7.5	kg
Ducted-fan Thrust	10(98)	kgf(N)

3 Aerodynamics

In order to investigate and determine the aerodynamics and its properties of the discussed aircraft potential vortex-lattice methods and wind tunnel experiments are involved.

3.1 Potential methods

Athena Vortex Lattice or commonly referred to as AVL by Mark Drela from MIT is used as a potential low-speed wing aerodynamics method and software. The vortex-lattice model is shown on Fig. 4. Only the lifting surfaces are modeled altogether with the control surfaces. The fuselage is not considered as it could yield a methodological error in the results for the lifting system.

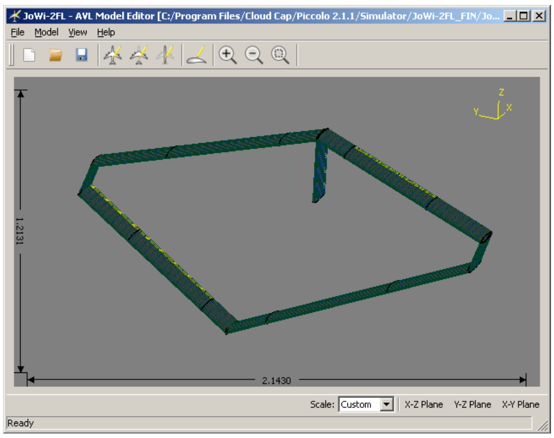

Fig. 4 JoWi-2FL AVL model

The calculated results of the desired aerodynamics characteristics in terms of the angle of attack (AOA) are given in Table 2. These values are necessary for flight dynamics simulations and autopilot tuning.

Table 2 Aerodynamics properties vs AOA

	$\propto = -2°$	$\propto = 2°$	$\propto = 6°$	$\propto = 10°$
C_D	0,015	0,021	0,033	0,052
C_L	0,046	0,342	0,634	0,920
$C_{L\propto}$	4,254	4,223	4,149	4,035
$C_{m\propto}$	-0,368	-0,402	-0,425	-0,442
$C_{Y\beta}$	-0,579	-0,545	-0,508	-0,468
C_{lp}	-0,497	-0,495	-0,489	-0,479
C_{mq}	-1,345	-1,383	-1,413	-1,437
$C_{L\delta_{fl}}$	0,522	0,506	0,486	0,462
$C_{m\delta_{fl}}$	0,164	0,163	0,160	0,156
$C_{l\delta_{ail}}$	-0,048	-0,046	-0,044	-0,041
$C_{L\delta_{elev}}$	0,702	0,695	0,681	0,660
$C_{m\delta_{elev}}$	-0,351	-0,353	-0,350	-0,345
$C_{l\delta_{elevon}}$	-0,068	-0,067	-0,066	-0,064
$C_{L\delta_{elevon}}$	0,410	0,406	0,396	0,382
$C_{m\delta_{elevon}}$	-0,153	-0,153	-0,152	-0,149
$C_{Y\delta_{rudd}}$	0,131	0,129	0,126	0,121
$C_{n\delta_{rudd}}$	-0,044	-0,043	-0,042	-0,040

The following nomenclature is used in Table 2 and further in the text (ISO 1151):

– c -coefficient of aerodynamic force or moment;
– α, β -angle of attack and sideslip angle;

- L -aerodynamic lift force;
- D -aerodynamic drag force;
- X, Y, Z -projections of the aerodynamic force on the axes of body coordinate system;
- L, M, N -projections of the aerodynamic moment on the axes of body coordinate system;
- $\bar{p}, \bar{q}, \bar{r}$ -dimensionless angular rates ($\bar{p} = pb/2V$, $\bar{q} = q\bar{c}/2V$, $\bar{r} = rb/2V$ Where $\bar{c}$ is the mean aerodynamic chord and b is wingspan);
- δ -angle of control surface deflection.

For example C_{L_α} will be the private derivative of lift coefficient with respect to the angle of attack or the lift curve slope. The $C_{m\delta_{elev}}$ will be the private derivate of the pitch moment coefficient with respect to the angle of deflection of elevator etc.

3.2 Wind tunnel tests

Wind tunnel test are conducted to validate the accuracy of potential methods. The test wind tunnel model is shown on Fig. 5.

Fig. 5 Wind tunnel joined-wing model

The experimental results are given on Fig. 6 to Fig. 8. The effective Reynolds number is $Re = 129886$ calculated using wind tunnel airspeed, joined-wing standard mean chord and wind tunnel turbulence factor.

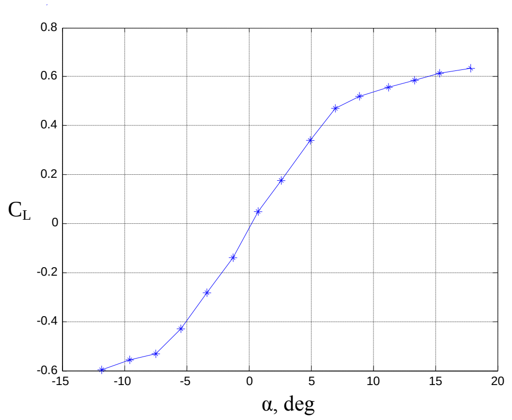

Fig. 6 Lift coefficient vs AOA (Experimental)

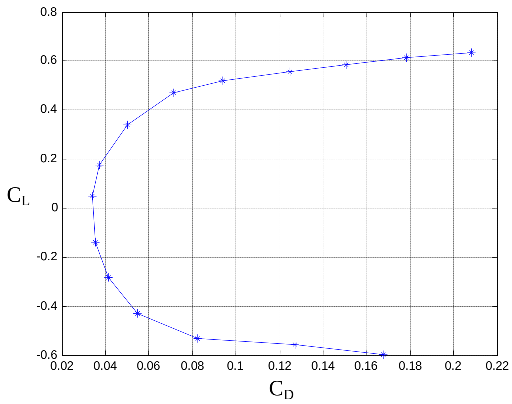

Fig. 7 Drag polar (Experimental)

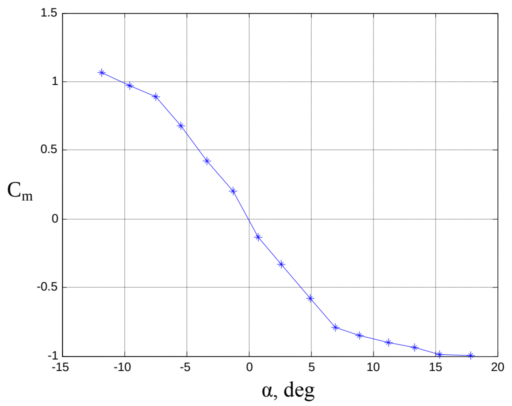

Fig. 8 Pitch moment coefficient (Experimental)

3.3 Ducted fan aerodynamics

Electrical ducted fan (Fig. 2) is used as a propulsion unit on JoWi-2FL. For the purpose of flight dynamics simulations and flight experiments the thrust of the power plant is need to be known a priori.

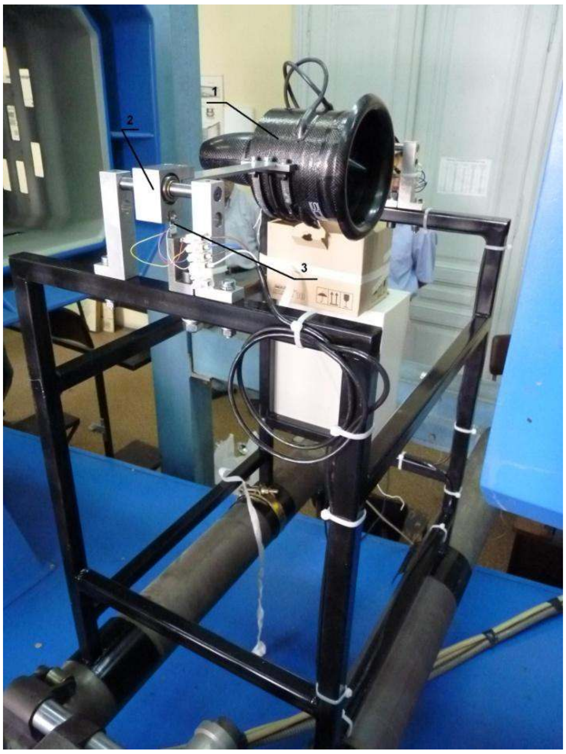

Fig. 9 Ducted fan thrust measurement equipment

1-ducted fan; 2-linear bearing; 3-load cell

Because the geometry of fan blades is not known, theoretical research is obstructed. In this study the dependence of the thrust and fan efficiency is determined experimentally in wind tunnel. Specially designed thrust measurement equipment is used so that the propulsion unit is placed in the working area of the wind tunnel (Fig. 9). The results for the ducted fan thrust are shown on Fig. 10. The power of the electrical motor is given with percents. Figure 11 gives the efficiency as a function of airspeed. The efficiency is calculated using the following formula:

$$\eta_{EDF} = TV/P \qquad (1)$$

where T is the thrust, [N]; V is the airspeed, [m/s]; P is the electrical power of the engine, [W].

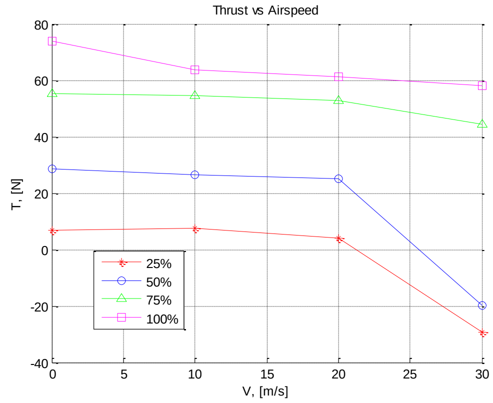

Fig. 10 Thrust vs airspeed

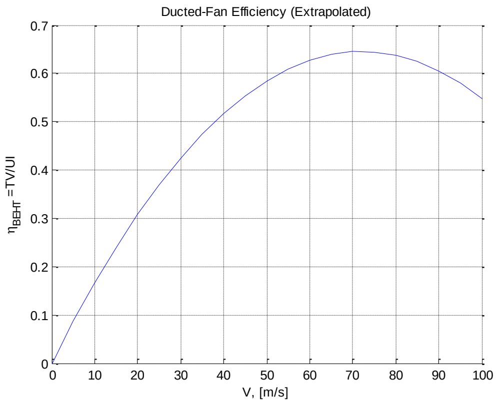

Fig. 11 Ducted fan efficiency

4 Simulations

Simulations are conducted in order to estimate aircraft flight dynamics characteristics and to analyze flight performance. This is done at early design stages such as conceptual design to eliminate undesired flight behavior. As it will be described later the simulations showed that at low airspeeds and high angles of attack Dutch roll occurs.

The simulations are run using MATLAB Simulink Aerospace Blockset and using Piccolo II Simulation Environment. The first one gives more freedom to analyze aircraft flight using various configurations of control surfaces while the second one allows flying the aircraft in integrated aircraft-autopilot simulation environment.

4.1 Simulation models

The simulation model of aircraft flight dynamics is shown on Fig. 12. It generally consists of the following submodels that are designed in MATLAB Simulink Aerospace Blockset:

1. Longitudinal movement
2. Side-lateral movement
3. Propulsion
4. 6 degree-of-freedom flight dymanics
5. Standard atmosphere
6. Earth gravity
7. Flight controls
8. Flight Gear interface

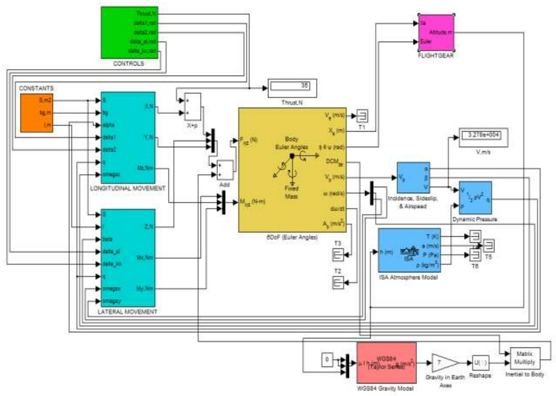

Fig. 12 Simulation model

Since we have previously determined the aerodynamics coefficients and derivatives, ducted fan characteristics and desired flight modes one could examine the flight of JoWi-2FL.

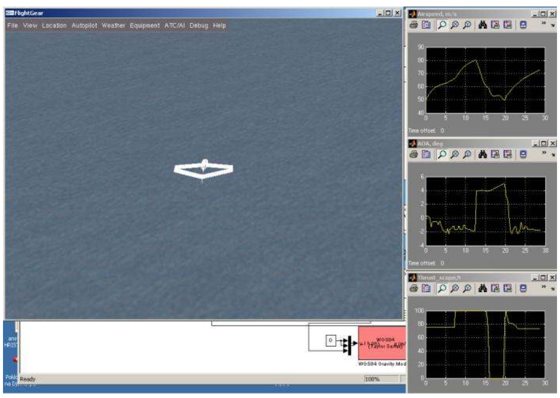

Fig. 13 Visualization with FlightGear

Interface with FlightGear flight simulator is established and the flight is visualized during the simulation (Fig. 13). As an input for the flight controls a joystick is used.

4.2 HiL and SiL simulations

Piccolo II autopilot offers its own simulation environment tools that include hardware-in-the-loop (HiL) and Software-in-the-loop (SiL) simulations (Fig. 14).

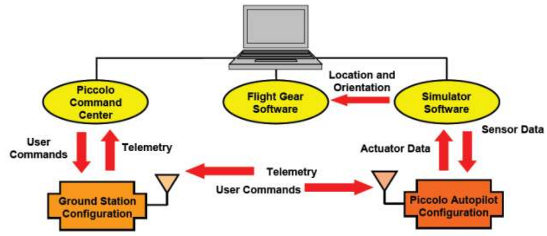

a)

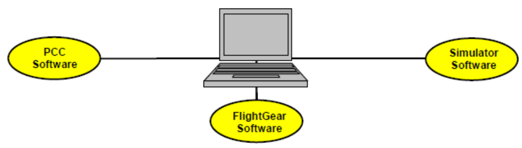

b)

Fig. 14 HiL a) & SiL b) configurations

HiL-simulation uses Piccolo II autopilot and Ground Control Station (GCS) hardware during flight simulation and the aircraft is responding as if it is flying. SiL-simulation uses software models for the autopilot and GCS. Simulation allows flight control laws for the aircraft and mission functionality to be tested without risking a real aircraft in test flight.

4.3 Piccolo II autopilot tuning

Autopilot tuning requires certain vehicle data as an input [7]. These are geometrical properties, mass and inertial properties, propulsion characteristics and aerodynamics characteristics. The last are the most critical. Piccolo CGS-software – Piccolo Command Center is designed to automatically calculate these values from AVL data but in the case of the joined-wing configuration with nine control surfaces errors occur and the output XML-file is empty. Therefore these values are manually calculated. Namely they are:

1. Elevator power – change in pitch moment coefficient per change in elevator [/rad]. Increasing elevator angles should produce decreasing pitch moments, hence this number is negative. If only elevators are used for pitch control it is equal to $C_{m\delta_{elev}}$ from Table 2. If elevons are used with elevators then the superposition rule should be applied.
2. Elevator effectiveness – steady state change in lift coefficient per change in elevator position [/rad]. This is the primary elevator control power term. The change in the lift is both due to change in the lift from the elevator and from the respectful change in the angle of attack. This value is calculated using the formula:

$$\sum c_{L\delta_{elev}} = c_{L\delta_{elev}} + c_{L\alpha}\frac{c_{m\delta_{elev}}}{c_{m\alpha}}. \quad (2)$$

3. Aileron effectiveness - dimensionless roll rate per change in aileron position [/rad]. This is the primary aileron control power term.

$$\bar{p}_{\delta_{ail.}} = \frac{\partial \bar{p}}{\partial \delta_{ail.}} = \frac{\partial c_l / \partial \delta_{ail}}{\partial c_l / \partial \bar{p}} = \frac{c_{l\delta_{ail.}}}{c_{lp}}, \quad (3)$$

where $\bar{p}$ is the dimensionless roll rate.

4. Rudder power - yawing moment coefficient per change in rudder position [/rad]. This is the primary rudder control power term. It equals $C_{n\delta_{rudd}}$ from Table 2.
5. Rudder effectiveness - change in sideslip per change in rudder position [rad/rad]. In combination with the tail moment arm this number is used to estimate the amount of rudder deflection required to coordinate a turn.

$$\beta_{\delta_{rudd}} = \frac{\partial \beta}{\partial \delta_{rudd}} = \frac{\partial c_Y / \partial \delta_{rudd}}{\partial c_Y / \partial \beta} = \frac{c_{Y\delta_{rudd}}}{c_{Y\beta}} \quad (4)$$

6. Sideslip effect - change in side force coefficient per change in side slip [/rad]. This term is used to scale the side force integral feedback for feedback turn coordination. It equals $C_{Y\beta}$ from Table 2.

The values for the discussed autopilot tuning coefficients are given in Table 3.

Table 3 Autopilot tuning coefficients

Elevator power	Elevator effectiveness	Aileron effectiveness
-0.36	**-4.37**	**0.09**
Rudder power	Rudder effectiveness	Sideslip effect
0.09	**-0.35**	**-0.74**

4.4 Dutch roll considerations

It might be of use to discuss that during simulations the initial JoWi-2FL design showed strong Dutch roll effect at low speeds. This made the landing difficult and risky. The Dutch roll effect is mainly due to increased lateral stability coefficient ($C_{l\beta}$) compared to directional stability coefficient ($C_{n\beta}$). The joined-wing design having back swept forward wing and fore swept rare wing both of which obtaining specific dihedral/anhedral angle could seriously suffer Dutch roll. One might erroneously consider that the front and rare wing have approximately the same dihedral/anhedral and thus the roll stability of both wings should be compensated. However the pattern of the flow over the front and rare wings differs due to the sweepback angle. Previous investigations [4,5] show that generally the lift coefficient at same angle of attack of the front wing is significantly higher compared to the rare wing's. Respectively the roll stability effect of the front wing is expected to be higher than the roll stability effect of rare wing and finally a joined-wing with a typical diamond-shape front view is highly potential to show Dutch roll mostly at low speeds and high angles of attack (Table 4). The Dutch roll effect is likely to occur when the parameter $\kappa > 2$:

$$\kappa \approx \frac{C_{l\beta}}{C_{n\beta}} \cdot \frac{J_z}{J_x}, \tag{5}$$

where J_x, J_z are the mass inertia moments for the specified axes of body reference system.

Table 4 shows that at angles of attack more than 4 this parameter highly exceeds the norm.

This periodic instability is also visible from simulation data [6] on Fig. 15 at airspeed of 15 m/s.

Table 4 Lateral and directional stability

α, deg	$C_{l\beta}$	$C_{n\beta}$	κ
-2	-0,088	-0,056	1,918
0	-0,099	-0,052	2,331
2	-0,111	-0,049	2,769
4	-0,123	-0,047	3,210
6	-0,135	-0,045	3,629
8	-0,148	-0,045	3,998
10	-0,160	-0,045	4,292

This problem was resolved [6] when the vertical stabilizer area was increased significantly.

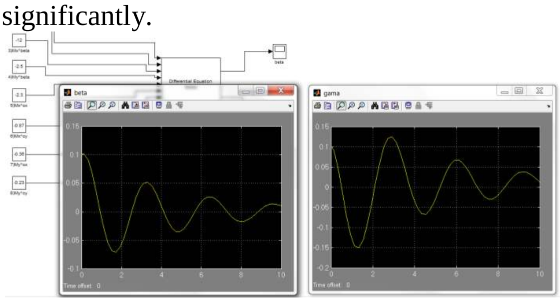

Fig. 15 Yaw and roll angles at Dutch roll

5 Flight experiments

The first flight of JoWi-2FL test bed was done at Cheshnegirovo airport near the city of Plovdiv, Bulgaria (Fig 16).

Fig. 16 JoWi-2FL maiden flight

The flight mission is shown on Fig. 17. The aircraft was flown entirely manually to check aircraft performance, stability and control. Thou the vertical stabilizer area was increased because of simulation results there was still weak Dutch roll effect at landing.

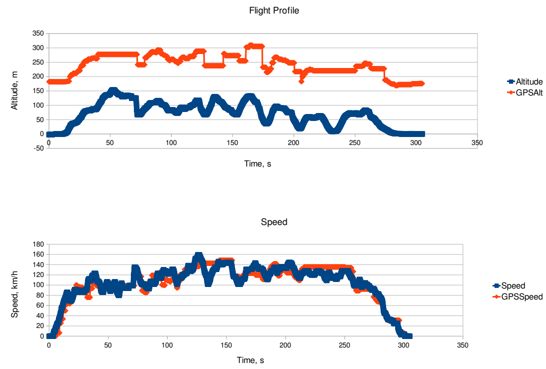

Fig. 17 Manual control

Further flights were done with Piccolo II autopilot. In autonomous mode the aircraft was holding its mission precisely and without any human interaction. Figure 18 shows the accuracy of airspeed, altitude and engine RPM stabilization in autopilot mode.

During the preliminary phase of preparation of the flight experiments SiL and HiL-simulation were extremely helpful. Thanks to precisely build simulation model a lot of mistakes were found and corrected. This was critical for safety and successive first flight. Also precise calculation of aircraft aerodynamics, propulsion and mass and inertia properties is necessary for good results.

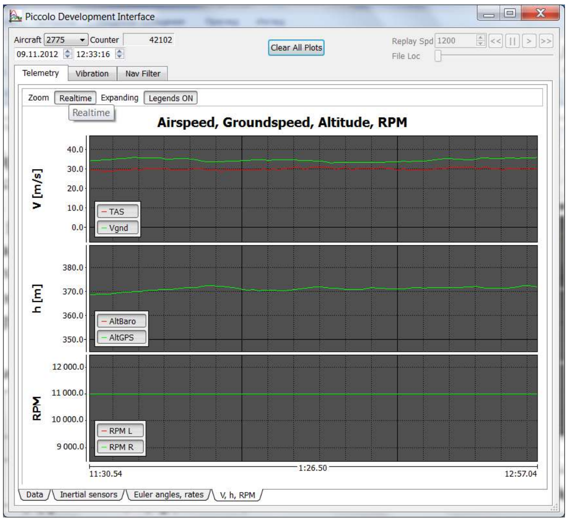

Fig. 18 Autopilot control

6 Conclusion

A joined-wing UAV test bed was designed, produced and flown. A numerous simulations, ground and flight experiments were conducted to precisely determine aircraft performance. JoWi-2FL is capable to be fully autonomously operated as an on-board experimental test bed. It is planned to be used for real-time flight data acquisition for aerodynamics and flight performance analysis. Also it could be used to solve tasks related to autonomous control and navigation.

References

[1] Wolkovich, J., “The Joined Wing: An Overview,” Journal of Aircraft, Vol. 23, No. 3, 1986, pp. 161-178.

[2] Zafirov D., “Joined Wing with Ducted Fan”, UAV World Conference on Disc [CD-ROM], Frankfurt am Main, 2009.

[3] Zafirov, D., “Joined Wings Thrust Vectored UAV Flight Envelope”, AIAA-2010-7509, AIAA Atmospheric Flight Mechanics Conference, Toronto, 2010

[4] Panayotov H., Zafirov D., “Aerodynamic Optimization of Joined-Wing for Unmanned Aerial Vehicle”, Journal of the Technical University at Plovdiv, *“Fundamental Sciences and Applications”*, Vol. 13(8), Plovdiv, Bulgaria, 2006, pp. 12-19

[5] Zafirov D., Panayotov H., “Experimental results analysis of joined-wing aircrafts”, Scientific Conference on Aeronautics, Automotive and Railway Engineering and Technologies BulTrans-2012, Sozopol, Bulgaria, 2009, pp. 82-85

[6] Panayotov H., “Investigation of Dutch Roll of a Joined-Wing Aircraft”, Scientific Conference on Aeronautics, Automotive and Railway Engineering and Technologies BulTrans-2012, 26-28 September 2012, Sozopol, Bulgaria, pp. 84-87

[7] B. Vaglienti, R. Hoag, M. Niculescu, “Piccolo User’s Guide v2.1.1”, Cloud Cap Technology, 2010

4:th CEAS Air & Space Conference
FTF Congress: Flygteknik 2013

Battery Pack Modeling Methods for Universally-Electric Aircraft

Patrick C. Vratny, Corin Gologan, Clément Pornet, Askin T. Isikveren and Mirko Hornung
Bauhaus Luftfahrt e.V., Germany

Keywords: *battery pack model, discharge analysis, universally-electric aircraft, aircraft conceptual design*

Abstract

Stimulated by ambitious emission reduction goals like FlightPath 2050 established for the aviation sector, radical technologies and revolutionary design approaches are required for future transport aircraft to fulfill those targets. One approach could be performed with the totally electrification of an aircraft. As one future promising technology advanced battery systems have been identified as potential energy and power suppliers for those concepts. The objective of this paper is to give a deeper insight in battery modeling within a universally-electric aircraft and will describe one approach of how the required battery capacity for a certain mission can be determined. Based on the results of this paper a simplified approach for battery capacity estimation is proposed for a standard mission profile making an error less than 2% compared to the exact model. The proposed methodology can serve as baseline for future research topics like sizing of thermal management systems or flight profile optimizations.

1 Nomenclature

1.1 Abbreviations

BCU	Battery Control Unit
DOD	Depth of Discharge
EIS	Entry Into Service
GPU	Ground Power Unit
HTS	High Temperature Superconducting
MTOW	Maximum Take-Off Weight
OC	Open Circuit
OEW	Operating Empty Weight
SOA	State of the Art
SOC	State of Charge
SRIA	Strategic Research and Innovative Agenda
SSPC	Solid-State Power Controller
UEA	Universally-Electric Aircraft
UESA	Universally-Electric Systems Architecture

1.2 Symbols

C	[Ah]	Battery Capacity
η	[-]	Battery Efficiency
ε	[-]	Convergence Limit
I	[A]	Electric Current

m	[-]	Number of Battery Modules
n	[-]	Number of Cells in Series
P	[W]	Power
ρ	[Wh/kg]	Specific Power
R	[Ω]	Resistance
r_C	[%]	Relative Available Capacity
S	[m²]	Wing Area
t	[s]	Time
U	[V]	Voltage
w	[kg]	Total Battery Mass
ζ	[1/h]	Discharge Rate
#	[-]	Number of Battery Packs

1.3 Subscripts

Act	Actual
Bat	Battery
ElecSys	Electrical System
i	Internal
Nom	Nominal
OC	Open Circuit
Ref	Reference
TL	Transient Long Time
TS	Transient Short Time

2 Introduction

Aircraft conceptual design for future transport aircraft is currently driven by fulfilling ambitious environmental targets such as the Strategic Research and Innovative Agenda (SRIA) published by the Advisory Council of Aeronautics Research in Europe [1] or the NASA N+3 [2] goals. For example, SRIA stipulates an improvement of the energy efficiency of aircraft technologies (airframe and propulsion) of 68% of the total 75% in the year 2050 to the baseline year 2000. Using evolutionary improved technologies to fulfill those reduction potentials seems questionable. Therefore revolutionary concepts are required allowing maybe greater improvement steps than with a further development of state of the art (SOA) technology. One approach could be followed with the electrification of the aircraft systems. This trend is already shown with the Boeing 787 [3]. But beyond, the electrification of the subsystems, the embedding of the entire propulsion system within the electrical systems architecture seems to be the most promising approach to reduce or even dispense with inflight emissions altogether. Beside fuel cells and photovoltaic cells, solely battery-powered aircraft are growing in interest. The current problem of SOA battery technology is the relative low specific energy (amount of energy stored in one kilogram of the energy carrier). Current high energy Lithium-Ion batteries have a storage capacity of around 200 Wh/kg at pack level [4] (compared to kerosene with 12.0 kWh/kg). Nevertheless, although the specific energy of batteries is relative low, there are already numerous studies focusing on battery powered transport aircraft utilizing either hybrid as well as full electric propulsion systems. For example NASA investigated a hybrid aircraft called SUGAR Volt [5], which is powered by batteries and gas turbines. There are also Universally-Electric Aircraft (UEA) such as the EADS VoltAir regional aircraft concept for 70 passengers [6] or the Bauhaus Luftfahrt Ce-Liner study [7], a short to mid-range aircraft with a passenger capacity of about 190. Even with very aggressive yet reasonable assumptions for battery cell properties, battery systems still end up heavier than conventional kerosene based systems. Therefore, there is the attempt to further increase the efficiency and to decrease the mass of battery systems.

The main objective of this paper is the present method to introduce battery discharge characteristics into the aircraft sizing process. Furthermore, the degrees-of-freedom available when designing a battery system will be discussed as listed below:

- Adaption of a discharge profile
- Impact of different cell configurations

Finally, it will be shown what simplifications can be made in the context of aircraft conceptual design.

3 Battery Systems within Aircraft Sizing

Fig. 1 shows a proposed strategy of introducing a battery model within an existing aircraft sizing and flight performance simulation environment. The aim of this approach is to determine the required battery mass and, therefore, the required battery capacity, to fly a specified mission. Within the aircraft simulation environment the shaft power demand profile (denote as power profile here) is the basis for the prediction of required battery mass and capacity. The simulation starts with an initial Maximum Take-Off Weight (MTOW) and battery mass. During the sizing process the MTOW and battery mass is gradually adapted to meet the mission requirements. Such an approach is also shown by Pornet et.al. [8] using the here described methodology within hybrid electric aircraft.

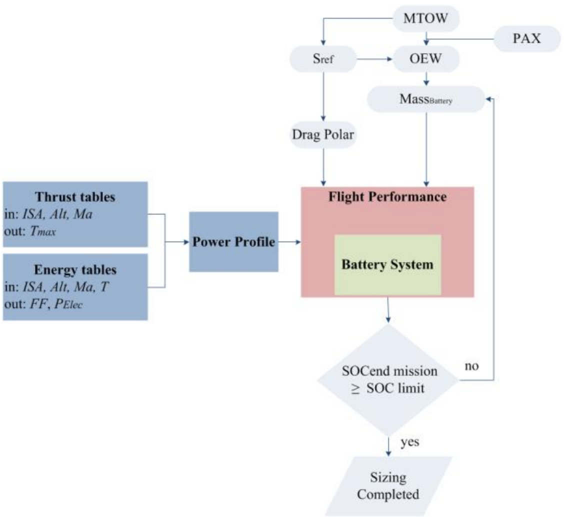

Fig. 1: A battery model within the aircraft sizing process

The power profile represents the power demand at the electric motor shaft(s). For the estimation of the required battery capacity it has to be corrected by the efficiency chain of the electrical system plus additional power off-takes such as for subsystems. The battery capacity represents in this case the theoretical maximum energy available during the mission. It is comparable to that of the available fuel capacity in a conventional aircraft. With an available battery weight, w_{Total}, a specific energy, ρ_{Bat}, and the system operating voltage, $U_{ElecSys}$, the maximum available capacity of one battery pack can be calculated with Eq. *(1)*. In this case also the total number of installed battery packs $\#_{Pack}$ is considered.

$$C_{Pack} = \frac{w_{Total} \cdot \rho_{Bat}}{\#_{Pack} \cdot U_{ElecSys}} \qquad (1)$$

The battery system has to be integrated within the flight performance calculation to define at each mission point the battery performance characteristics. For the assumption of the specific energy Table 1 summarizes different values of battery specific energies, ρ_{Bat}, and specific powers, which were already used in different UEA and hybrid electric aircraft concepts for future application. For comparison SOA battery systems have around 200 Wh/kg at pack level [4]. An estimation of specific energies of possible future Lithium based battery systems have been performed by Kuhn and Sizmann [9].

Table 1: Specific energy and specific power assumptions for battery

Aircraft	Specific Energy	Specific Power	Source
SUGAR Volt	0.7 kWh/kg	0.3 kW/kg*	[5]
VoltAir	1.0 kWh/kg	0.9 kW/kg*	[6]
Ce-Liner	2.0 kWh/kg	1.3 kW/kg	[7]

* calculated at cell level; further assuming an efficiency of 95% for the total electric systems chain (excl. battery efficiency)

With the calculated battery capacity and the power profile the battery performance can be simulated as described in the next section. The simulation process (shown in Fig. 1) checks to see if the installed battery mass is sufficient for the specified mission. As figure of merit the state-of-charge (SOC) is used. The SOC is an indicator for a battery showing how much energy is still available (further described in Section 4). If the SOC is below a certain limit, which would effect the operational life and could cause irreparable damage the electrodes of the battery [10] thus inferring the initial battery mass was estimated to be too low and needs to be increased. If the SOC is above the specified limit the battery pack is oversized, meaning the mass could be reduced. This mass iteration process can be repeated until a targeted SOC value is reached.

4 Battery Pack Modeling

The following section will describe the electrochemical discharge behavior of Lithium-Ion batteries and the most important parameters required for an accurate estimation of the necessary battery capacity for a given power profile. A power profile in this case defines the power demand of the propulsion system and subsystem at each time step over the design mission. The estimation of the battery capacity is explained in the subsequent subsection.

4.1 Characteristics of the Electrochemical Battery Cell Performance

A battery cell is a simple energy storage system consisting of an anode and a cathode separated by an electrolyte, but the discharge behavior shows strong non-linearity behavior overleaf concerning the available output voltage (cf. Fig. 2). The output voltage of a battery cell depends up on the one hand of the actual discharge rate (or C-Rate), which is an indicator of the amount of electrical current the battery delivers based on its nominal capacity, and of the SOC or equivalent depth of discharge (DOD) of the battery, which shows how much energy is available or was already consumed. A battery cell is, furthermore, characterized by its nominal voltage, U_{Nom}, and its nominal capacity, C_{Nom}, which are normally defined at a discharge rate of C/5 and SOC of 50% [11]. An example of a battery discharge curve is shown in Fig. 2, where the cell voltage development is shown over the DOD and different C-Rates.

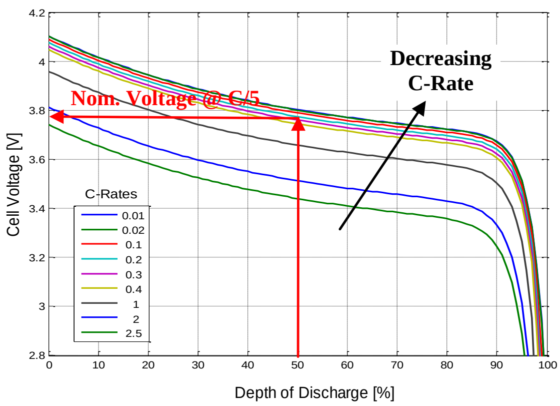

Fig. 2: Example of a discharge curve of Lithium Polymer battery extracted from [12]

Another parameter, which has to be considered, especially when discharging a battery at high discharge rates, is the cut-off voltage. The cut-off voltage represents the minimum voltage of a battery cell, where it is assumed that the battery cell is empty. It is normally given by the manufacturer of the battery cells. The cut-off voltage also defines the maximum available discharge capacity at a certain discharge rate.

The DOD is defined according to Eq. *(2)* valid for a start SOC of 100%:

$$DOD = 1 - SOC \tag{2}$$

In Fig. 2 above it can be recognized that the available output voltage of battery cell depends up on the SOC and different discharge rates as mentioned before. This voltage drop is caused by the internal resistance of a battery cell, where a part of the available voltage is consumed for internal electrochemical processes (according to Ohm's Law). The discharge behavior of a battery cell can also be represented by an equivalent circuit consisting of a voltage source and a resistance network as shown in Fig. 3.

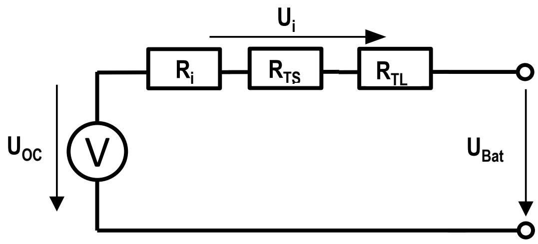

Fig. 3: Simplified equivalent circuit of a battery cell with considered impedances based on [12]

The single resistances represent different electrochemical processes like ohmic losses, activation losses or concentration losses as described in [13]. The single resistances can be summed up to the total resistance $R_{i,Total}$ according to [12]. The available output voltage (incl. the voltage drop) at current SOC and discharge rate can be calculated with Eq. *(3)*:

$$U_{Bat} = U_{OC} - R_{i,Total} \cdot I \tag{3}$$

The resistances and the available maximum battery voltage, which are functions of SOC, are taken from [12] and summarized in Table 2.

Table 2: Overview of battery cell parameters taken from [12] and used for Fig. 2

U_{OC} [V]	$-1.031 \cdot e^{-35 \cdot SOC} + 3.685 + 0.2156 \cdot SOC - 0.1178 \cdot SOC^2 + 0.321 \cdot SOC^3$
R_i [Ω]	$0.1562 \cdot e^{-24.37 \cdot SOC} + 0.07446$
R_{TS} [Ω]	$0.3208 \cdot e^{-29.14 \cdot SOC} + 0.04669$
R_{TL} [Ω]	$6.6030 \cdot e^{-155.2 \cdot SOC} + 0.04984$

Due to this voltage drop a battery cell delivers a decreasing power according to Eq. *(4)*, when discharging a battery with a constant discharge current (or constant C-Rate).

$$P_{Bat} = U_{Bat} \cdot I \qquad (4)$$

The actual C-Rate of a battery can be calculated with Eq. *(5)*.

$$\zeta = \frac{I}{C_{Nom}} \qquad (5)$$

Because the available battery capacity also depends up on the discharge rate of the battery, as shown in Fig. 2 previously, the C-Rate can be used to determine the relative available capacity, r_C, from the diagram, Fig. 4.

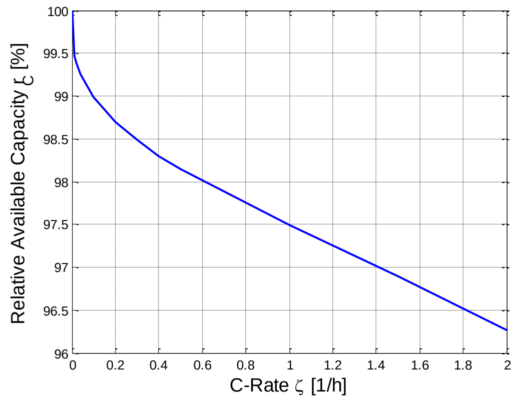

Fig. 4: Available battery capacity depending on discharge rate of the battery (extracted from Fig. 2)

With Eq. *(6)* the available capacity, C_{Act}, can then be calculated.

$$C_{Act} = C_{Nom} \cdot r_C \qquad (6)$$

The SOC change over the total mission time, *T*, for each time step, *dt*, is calculated with Eq. *(7)*.

$$SOC = SOC_{Start} - \int_0^T \frac{I(t)}{C_{Act}(t)} dt \qquad (7)$$

The discharge efficiency of the battery is calculated with Eq. *(8)*, where the voltage drop at the internal resistance is completely treated as losses.

$$\eta_{Bat} = 1 - \frac{I^2 \cdot R_{i,Total}(SOC)}{U_{OC}(SOC) \cdot I} = 1 - \frac{U_i}{U_{OC}} \qquad (8)$$

4.2 Design of a Battery Pack

A battery pack consists of cells connected in series and parallel. The numbers of *n* cells, which are connected in series, define the required nominal system output voltage and can be combined to a *battery module*. The *m* battery modules connected in parallel increase further the capacity of a battery pack at a defined system operating voltage. The schematic design of this package is sketched in Fig. 5.

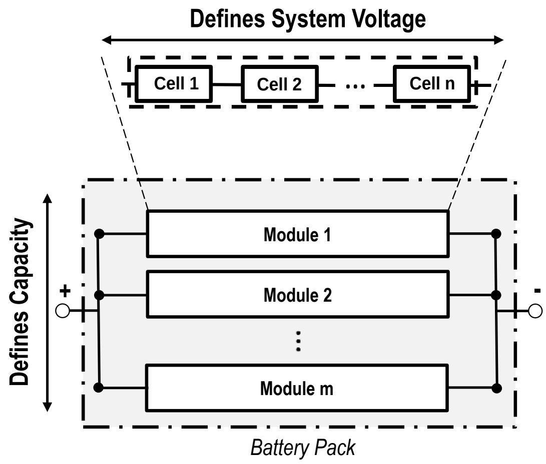

Fig. 5: Design of a battery pack consisting of n-cells in series and m-modules in parallel

The number of cells in series and in parallel defines the acting power demand at cell level (according to Kirchhoff's Law) and is important to determine the battery cell performance. The power is distributed to all battery containers and their modules. Therefore one battery module has only to handle the m-th power of the total power demand of one battery pack according to Eq. *(9)*:

$$P_{Bat}(t) = \frac{P_{Shaft}(t) + P_{Offtakes}(t)}{\#_{Pack} \cdot m \cdot \eta_{ElecSys}} \qquad (9)$$

$\#_{Pack}$ represents the total number of installed battery packs, m the number of modules per pack, $\eta_{ElecSys}$ the total efficiency from the electric motors to the batteries and $P_{Offtakes}$ additional power off takes required by subsystems, e.g environmental control system, flight controls, cabin etc.

4.3 Estimation of the Battery Pack Capacity

Fig. 6 overleaf the block diagram for the process of the determination of the SOC for a given battery capacity and power profile of one battery module is presented. As input parameters the actual SOC, the battery capacity of one battery cell and the power demand for each time step, *dt*, (as shown in Eq. *(9)*) are required (1). The simulation starts with an initial voltage estimation of a battery module, in this case the nominal voltage of a battery cell times the number of n cells connected in series. With this voltage and the power demand, the discharge current and the discharge rate are calculated (2). With these parameters the actual voltage of a battery cell is determined according to the used battery model (e.g. equivalent circuit or look-up table of a discharge curve; 3). With the new estimated voltage the actual power output of the battery is calculated (4) according to Eq. *(4)* and the process is repeated with the new determined voltage. The iteration is completed when the required battery output power has converged to a certain convergence limit ε. Simulations have shown that convergence limits up to E-06 are practicable. If the cut-off voltage is reached, the initial capacity was estimated too low and iteration process stops. If the voltage is above the cut-off voltage (5), the time is increased by the time step *dt*, the available capacity is determined according to the current C-Rate and the new SOC is calculated according to Eq. *(7)*. If the end of the simulation has reached, the process returns the SOC at the end of the power profile. A lower limit constraint check is finally performed within an installed system sizing loop as described in Section 3.

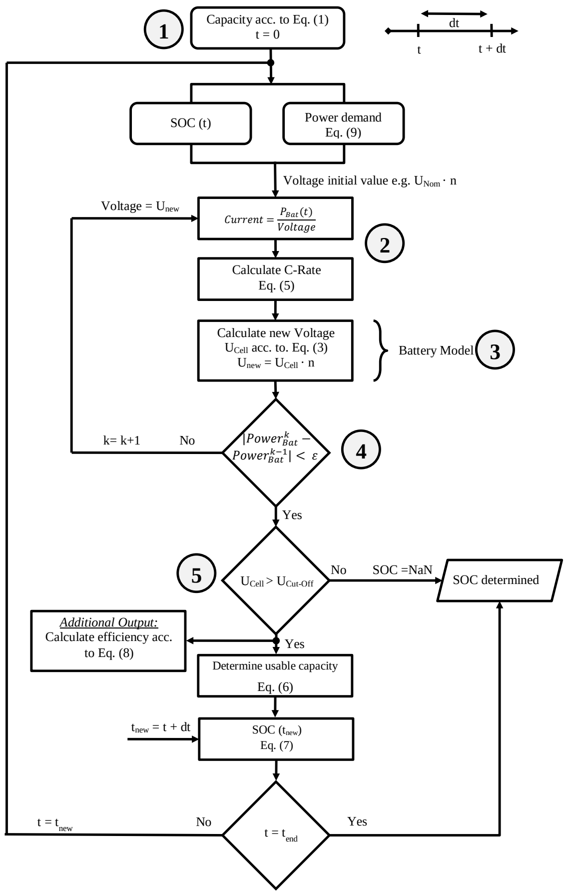

Fig. 6: Flow chart for the estimation of the end of state of charge for a given power demand and battery capacity. Extended from [14]

5 Application of Methodology

The following section shows an example where the above described methodology is applied. As a simulation platform the Ce-Liner concept [7] was used. Finally, the battery simulation parameters are described here as well as the results of one battery pack, or in this case, a battery container called a Charge Carrying Container or 3C.

5.1 Baseline Aircraft Description

The Bauhaus Luftfahrt design of the Ce-Liner (illustrated in Fig. 7) is born from an interdisciplinary group design project whose objective was to perform the conceptual design and initial technical assessment of a short range aircraft application featuring electro-motive power.

Fig. 7: The Universally-Electric Aircraft Ce-Liner is solely powered by batteries housed in 14 battery containers within the fuselage. [7]

Conceived for an entry-into-service (EIS) 2035, the Ce-Liner is a medium capacity short range UEA accommodating 189 PAX over 900 nm (1666 km). The power demand overleaf this design mission is shown in Fig. 8 including the additional reserves 30 min hold, 10% of total trip time as extended cruise and an alternate airport section (diversion section) of 100 nm. The concept features two Silent Advanced Fans utilizing Electrical energy (SAFE) mounted on the aft fuselage, driven by High Temperature Superconducting (HTS) motors. For the design mission fourteen battery containers, housed in standardized LD3 containers, provide the electrical energy required for the flight. The electrical system itself is sized for nine battery containers which correspond to the minimum required installed battery mass. With 109300 kg MTOW, the total installed battery mass corresponds to 27.6% of MTOW. Consequently, the aircraft is equipped with a Universally-Electric Systems Architecture (UESA).

The low speed performance, and particularly, the second segment climb requirement sized the 22.2 MW of the HTS motor (in total 44.4 MW installed), resulting in a 0.407 kW/kg power-to-weight ratio and the nominal power provided by the UESA with a power-to-weight ratio of 0.267kW/kg (based on maximum UESA power). One HTS motor is sized for the one engine inoperative case. Due to weight saving issues the UESA is rated to meet the take-off requirements, which results in a lower power demand than actually installed by the electric motors. The power profile of the design mission (shown in Fig. 8) is used for the further battery simulations. The cruise and also hold segments show a constant power demand, which is the result of a non-changing aircraft mass during the mission and a constant flight altitude and speed.

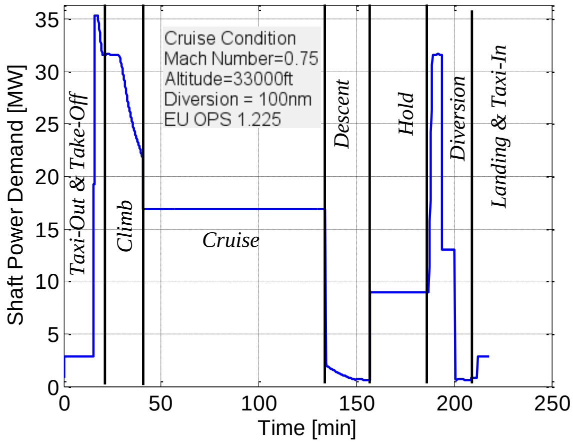

Fig. 8: Power profile at shaft of electric motors for the design mission of the Ce-Liner

5.2 Universally-Electric Systems Architecture

The UESA is one key element within an UEA. It connects all important consumers within a UEA and has, furthermore, the function of managing the power supply to the consumers and protecting the entire system from failure cases. The following section describes the components comprising UESA and how the battery packs are connected to the entire system.

5.2.1 Overview of Components and Layout

Fig. 9 gives an overview of the architectural layout of the UESA of the Ce-Liner. It consists of three power levels, which also represent three different voltage levels. The operating voltage of the propulsion system is 3,000 VDC, for the major subsystems like the Environmental Control System, cabin or flight controls a voltage of 540 VDC is used and finally for the conventional avionics the standard voltage level of 28 VDC is taken. The high voltages are a trade-off between mass savings and lightning arcs, which can occur according to Paschen's

Law. The voltage levels are taken form [7]. The 3C battery containers of the propulsion system are connected in parallel, which have the advantage that if a battery container fails the other containers are not influenced (expect due to a higher power demand). Furthermore, all batteries are monitored and controlled by Battery Control Units (BCU) and additional protected by Solid States Power Controllers (SSPCs). The SSPC has the further advantage of isolating a battery pack from the entire network.

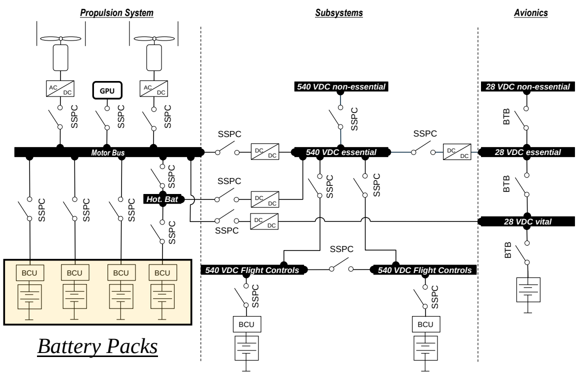

Fig. 9: The high power batteries are located at the propulsion section within the universally-electric systems architecture of the Ce-Liner [7]

Furthermore for the propulsion system advanced electrical components and transmission systems are used, for example HTS motors and cables as well as cryogenically cooled power electronics. These advanced electrical components lead to a transmission systems efficiency $\eta_{ElecSys}$ of 97.7 % (excluding the batteries) [7].

5.2.2 Battery Specifications

As input for the power demand the power profile shown in Section 5.1 is used including an average subsystem power of 720 kW and an electrical system efficiency $\eta_{ElecSys}$ of 97.7%. The battery cells from the Ce-Liner are housed in 3Cs, which allow an ease of exchange of the batteries at the airport against fully charged ones. Table 3 summarizes the most important battery and system parameters used for the capacity simulation. For the simulation it was further assumed that the thermal management system of the battery packs keeps the battery cells on a constant temperature of 25°C.

Table 3: Overview of used battery parameters

Parameter	Value
Nominal Voltage	3.75 V
Cut-off Voltage	2.8 V
Specific Energy	2000 Wh/kg
SOC_{End} Block Mission	20.0 %
SOC_{End} Reserve Mission	5.0 %
System Nominal Voltage	3000 V

5.3 Results of the Integrated Study

The battery cell performance of one battery container is plotted in Fig. 10 (in total 14 3Cs are installed for the design mission). This section will discuss the characteristics of each flight segment.

During **Take-Off** the battery cells have their highest output voltage of about 3250V (see plot b), which is caused by the high SOC (plot a) during this flight phase. The high output voltage is advantageous in this case, because during take-off the maximum power output of 35.4 MW occurs, which the batteries have to deliver caused by the take-off field requirement.

During **Climb** phase the power demand decreases slightly (about 10.0%), which has a direct effect on the discharge rate (see plot c). Therefore the battery pack efficiency during this flight phase is higher than during take-off.

In the **Cruise** phase the power demand reduces to about 17 MW, which can be also recognized with the slightly increased voltage in plot (b) caused by the reduced C-Rate. Due to the reduced C-Rate the efficiency of the battery during cruise is 1.0% higher than compared to the climb phase. It can also be recognized that the battery efficiency decreases slightly, although the power demand for this flight phase is constant. This is the result of the decreasing voltage output of the battery cells, which is dependent on the actual SOC, which also changes during the mission. As consequence the discharge current and, therefore, the discharge rate has to be increased to meet the required output power.

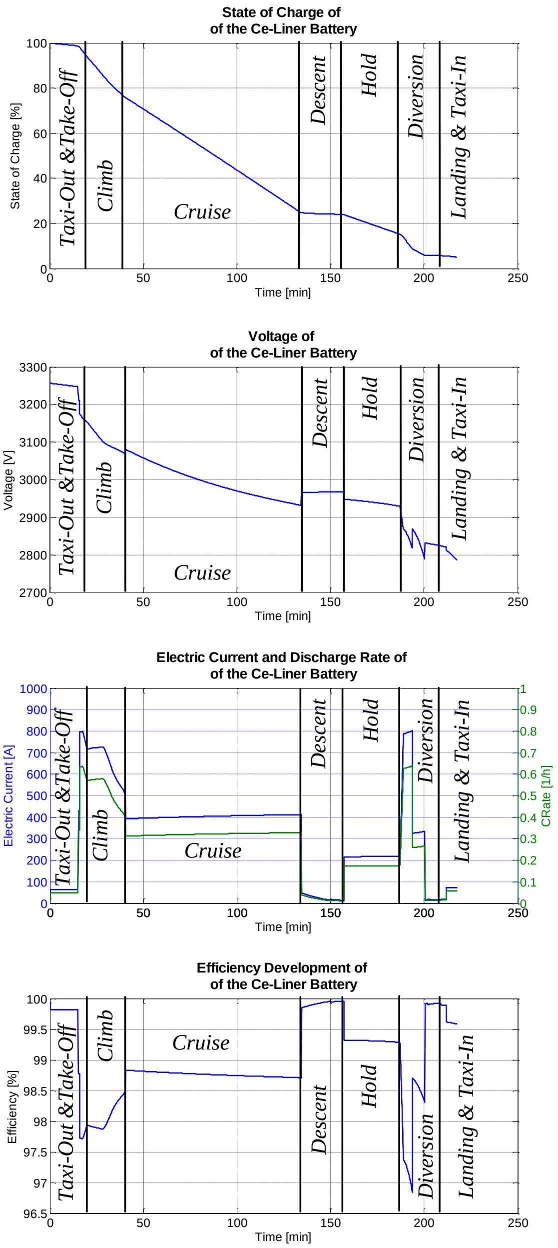

Fig. 10: Battery characteristics for the design mission of the Ce-Liner

The highest efficiency is reached during **Descent**, where the battery has only to deliver the power demand for the subsystems. The efficiency reaches nearly the 100% during this phase caused by the very low discharge rate.

During **Hold** the power demand increases again to maintain a constant flight altitude. Therefore the voltage and also efficiency drops about 1% compared to the descent phase, but still higher than in the cruise phase due to the lower discharge rate.

The climb phase after the beginning of the **Diversion** section causes even higher discharge rates than during take-off although the power demand is around 10% lower. This is the result of the low SOC during this segment and therefore the low output voltage, which has to be compensated with a higher electric current to meet again the required power demand. Because the diversion segment consists also of a climb, cruise and descent phase, the power demand changes during these phases relatively fast. These changes in power can be recognized by the steps in the output voltage plot (b) as well as the required electric current plot (c) and the efficiency plot (d).

During **Landing** as well as the taxi-in phase the battery has the lowest SOC, therefore the lowest output voltage. But due to the relative low power demand during these segments the efficiency is, nevertheless, relative high compared to the Diversion. In plot (a) it can be also seen that after the taxi-in procedure there is still a residual capacity of 5%, which was set as a target value at the beginning of the sizing process.

Fig. 11 shows the characteristic mission points mentioned above on cell level. The total voltage drop from take-off to landing is 0.5 V.

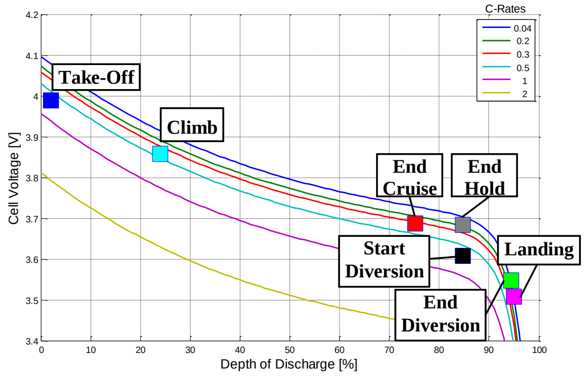

Fig. 11: Discharge characteristic of one battery cell corresponding to specific operating points

Table 4 summarizes the results of the battery pack simulation of the most important parameters of one 3C.

Table 4: Summary of one battery container of the Ce-Liner

Total Capacity	3760 kWh
Mean Efficiency	99.1 %
Mean Voltage	3000 V
Mean C-Rate	0.26 per hour
SOC End Block Mission	20.0 %
SOC End Reserve Mission	5.0 %
Cell mass*	1880 kg
* without structure, power electronics and thermal management	

6 Findings

The following section summarizes additional findings of this paper. The first section shows a simplification of the battery model applicable for conceptual design. The second section describes an idea of increasing the battery pack efficiency during low efficiency operations.

6.1 Simplification of the Battery Model

Fig. 12 shows a comparison of the proposed battery model and a simple integration of the power over the time of a power profile including different flight times (varying only cruise duration) to determine the necessary battery capacity. For the energy integration of the battery the same target values of the SOC is used as for the battery model plus a constant battery efficiency η_{Bat} of 99.0%. For the capacity estimation using the energy integration method over the total mission time T Eq. *(10)* is used:

$$C_{Bat} = \frac{m}{(1-SOC_{End}) \cdot \eta_{Bat}} \cdot \int_0^T P_{Bat}(t)dt \qquad (10)$$

The maximum error between the battery model and the energy summation is between +2% and -1% for flight time up to 500 min. Therefore, for an estimation of the battery capacity and mass it is sufficient in aircraft conceptual design to use a simple integration of the power profile over time, which also decreases overall simulation time.

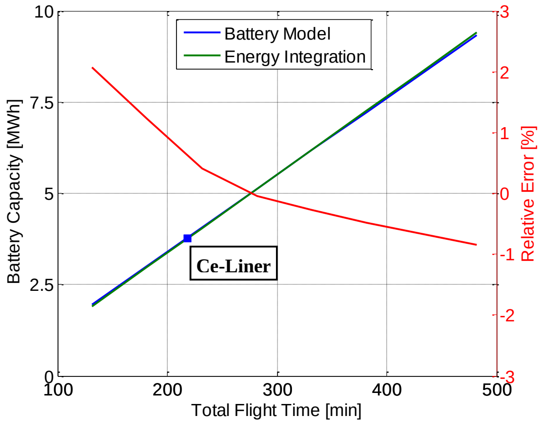

Fig. 12: Comparison of the capacity estimation with battery model and simple power integration over time

A battery model comes into play, when the exact development of any parameter is required over the flight time. This is important for example when sizing the thermal management system or conducting a flight profile optimization. But this simplification is only valid for typical power profiles. For aerobatic or combat aircraft, where quick changes in power can occur, this simplification has to be verified. Also noticeable is the slightly increasing error of the energy integration method at increasing flight time. This is caused due to the increasing capacity of the batteries at the same maximum power demand, which causes therefore, higher efficiencies (as shown in Fig. 13) of the batteries due to the lower discharge rates. This can be adapted via the assumed battery efficiency of the energy integration method.

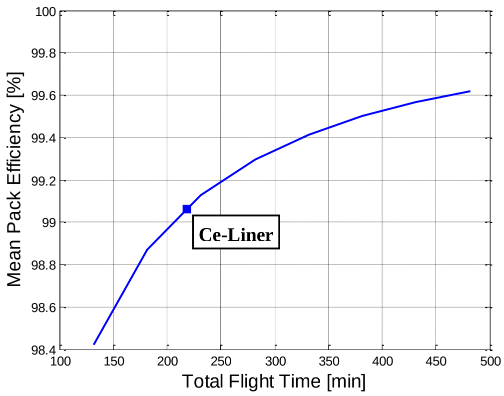

Fig. 13: Mean efficiency of battery pack for typical flight profiles

6.2 Reconfiguration of Battery Pack Layout

When thinking to increase the efficiency during take-off and missed approach, one idea is to reconnect two battery packs from parallel to series in such phases in order to increase the voltage output. The higher available voltage should reduce in turn the discharge current and increase therefore the battery efficiency. This could be managed by an Active Battery Management System (ABMS). Such an approach is illustrated in Fig. 14.

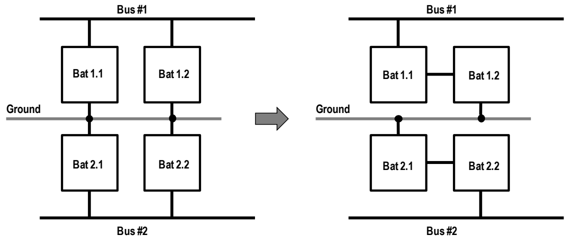

Fig. 14: Reconfiguration of battery packs to increase voltage during take-off and missed approach

This approach was identified as not suitable, because it has no impact on the battery discharge characteristic, when keeping the total number of battery cells constant. Although, the total voltage has been increased, the number of packs, to which the electric current has been distributed (according to Kirchhoff's Law), has been reduced. In sum and according to Eq. *(2)* the discharge current and, therefore, the discharge efficiency stay the same.

7 Conclusion and Future Work

This paper has shown one possibility of integrating a battery discharge characteristic into an aircraft sizing loop for a UEA to estimate the required battery capacity for a certain design mission. As a result typical characteristics of battery parameters are shown for a given power profile like the voltage drop over the flight time as well as a simplified method for capacity estimation usable for aircraft conceptual design.

The presented methodology is applicable for all battery types and configurations. With an exchange of the battery discharge model any battery type can be simulated.

References

[1] ACARE, "Strategic Research & Innovation Agenda - Volume 1," 2012.

[2] M. K. Bradley and C. K. Droney, "Subsonic Ultra Green Aircraft Research : Phase I Final Report," Huntington Beach, California, 2011.

[3] L. Faleiro, "Beyond the More Electric Aircraft," *Aerospace America*, pp. 35–40, 2005.

[4] J. Christensen, P. Albertus, R. S. Sanchez-Carrera, T. Lohmann, B. Kozinsky, R. Liedtke, J. Ahmed, and A. Kojic, "A Critical Review of Li/Air Batteries," *Journal of The Electrochemical Society*, vol. 159, no. 2, p. R1, 2012.

[5] M. Bradley, C. Droney, D. Paisley, B. Roth, S. Gowda, and M. Kirby, "NASA N+3 Subsonic Ultra Green Aircraft Research SUGAR Final Review," 2010.

[6] S. Stückl, J. van Toor, and H. Lobentanzer, "VOLTAIR - The All Electric Propulsion Concept Platform – A Vision For Atmospheric Friendly Flight," in *28th International Congress Of The Aeronautical Sciences*, 2012, pp. 1–11.

[7] A. T. Isikveren, A. Seitz, P. C. Vratny, C. Pornet, K. O. Plötner, and M. Hornung, "Conceptual Studies of Universally- Electric Systems Architectures Suitable for Transport Aircraft," in *Deutscher Luft- und Raumfahrt Kongress 2012, Berlin, Germany*, 2012.

[8] C. Pornet, C. Gologan, P. C. Vratny, A. Seitz, O. Schmitz, A. T. Isikveren, and M. Hornung, "Methodology for Sizing and Performance Assessment of Hybrid Energy Aircraft," in *AIAA Aviation 2013*, 2013, pp. 1–20.

[9] H. Kuhn and A. Sizmann, "FUNDAMENTAL PREREQUISITES FOR ELECTRIC FLYING," in *Deutscher Luft- und Raumfahrt Kongress 2012, Berlin, Germany*, 2012, pp. 1–8.

[10] Air Force Space Command, "LITHIUM-ION BATTERY FOR SPACECRAFT APPLICATIONS," 2008.

[11] Y. Harats, B. Koretz, J. R. Goldstein, and M. Korall, "The Electric Fuel TM System Solution for an Electric Vehicle," Jerusalem Israel, 1995.

[12] M. Chen and G. A. Rincon-Mora, "Accurate Electrical Battery Model Capable of Predicting Runtime and I–V Performance," *IEEE Transactions on Energy Conversion*, vol. 21, no. 2, pp. 504–511, Jun. 2006.

[13] W. Tahil, "How Much Lithium does a LiIon EV battery really need ?," Meridian International Research, 2010.

[14] P. C. Vratny, *A Battery Powered Transport Aircraft*. Saarbrücken: AV Akademikerverlag, 2012.

4:th CEAS Air & Space Conference
FTF Congress: Flygteknik 2013

Comparison of traditionally calculated stability characteristics with flight test data of PW-6U sailplane

Tomasz Goetzendorf-Grabowski, Ewa Marcinkiewicz, Cezary Galiński
Warsaw University of Technology, Warsaw, Polandy

Keywords: flight test, stability

Abstract

The paper presents results of flight test and dynamic analysis of PW-6 glider, which was designed and built in Warsaw University of Technology. The stability characteristics obtained in the course of experiment were compared with computational results using traditional methods. The observed differences were discussed.

1 Introduction

For many years the only method available for dynamic stability analysis lead through aerodynamic derivatives calculations to the analysis of equations of motion. Aerodynamic derivatives were calculated with application of data contained in reports databases like ESDU [1]. Unfortunately data available there have several important limitations like narrow range of aspect ratios or constraint choice of aerodynamic configurations. Recent development of numerical methods allows calculating aerodynamic derivatives for any configuration and any combination of geometrical parameters. However, numerical method provides only approximate solution due to the assumptions and simplifications incorporated in it. Moreover, traditional method of equations of motion analysis assumed minor disturbances and small range of angles of attack. Both of these assumptions are questionable. Therefore an effort was undertaken under SIMSAC program [2] to develop better software intended for dynamic stability analysis. Results provided by this software [3] have to be validated with application of flight test data. Some of this data were already available to software authors; others however had to be collected. This paper presents an example of experiment undertaken to collect such data. Results obtained in the course of this experiment are compared with data calculated with application of traditional methods to observe the differences between them.

Figure 1: PW-6U sailplane during experiment

2 An object of the experiment

PW-6U [5] sailplane prototype was used to conduct this experiment as it was easily available for authors of this paper. Not only the ship itself was available but also complete documentation, including inertial data and previous flight tests results were available since PW-6 was developed by WUT a few years ago.

The PW-6U is a glass-epoxy two-seater glider with a mid-set wing and a conventional tail. It was designed for beginner instruction, and training of young pilots including cross-country flights and basic aerobatics. According to the catalogue PW-6U can be described by the following parameters:

General characteristics:

- Length: 7.85 m
- Wingspan: 16.0 m
- Height: 2.44 m
- Wing area: 15.25 m2
- Aspect ratio: 16.8
- Empty weight: 360 kg
- Gross weight: 546 kg

Performance:

- Never exceed speed: 260 km/h
- Stall speed: 68 km/h
- Maximum glide ratio: 34
- Rate of sink: 0.75 m/s

However, after several years of operations and modifications, including application as airfoils flying laboratory, some degradation of performances was expected.

3 Measurement system

To conduct the experiment the sailplane was equipped with additional sensors and data acquisition system. The following parameters were measured and tested:

- Airspeed
- Altitude
- 3 orthogonal linear accelerations
- 3 orthogonal angular velocities
- Temperature

Airspeed and altitude sensors were connected to the standard measurement system of the glider in the rear cockpit. Accelerometers and gyroscopes were installed in the common box, at the shelve, behind the rear pilot back. This allowed installing them almost in the same place and almost in the glider's centre of gravity. The whole measurement system was calibrated in various temperatures to make sure that MEMS sensors were well compensated against temperature effects. Temperature was measured during flight testing to make sure that it does not exceed those used for calibration. Data logger APEK AL154RE03.2 was used to record data [7]. It allows to record data from 16 channels with frequency of 1 kHz. 10 channels and frequency no smaller than 33Hz were used in this experiment. Moreover head-up bank angle indicator was installed in front cockpit to make sure that certain bank angles were achieved.

4 Manoeuvres and test procedures

The following flight modes were tested: phugoid oscillations, short period oscillations, spiral and Dutch roll and rolling. Sailplane reaction to the rolling input was also explored. Finally several points of velocity polar were measured to check the level of performances degradation mentioned above. The last measurement could have appeared critical for comparison of theoretical and flight test results of phugoid oscillations. Flight test programme was developed according to [8]. The following procedures were used to excite each flight mode:

PHUGOID OSCILLATIONS:

1. Glider was trimmed at defined airspeed
2. Airspeed was gently increased by 20-25 km/h
3. Stick was slowly moved backwards to neutral position
4. Stick was kept in neutral position for 250s

SHORT PERIOD OSCILLATIONS:

1. Glider was trimmed at defined airspeed
2. Stick was quickly moved forward and backward to neutral position
3. Stick was kept in neutral for 50s

SPIRAL:

1. Glider was trimmed at defined airspeed
2. Glider was banked with a rudder to bank angle of 15°
3. Rudder was moved to the neutral position
4. Stick was released and kept free for time necessary to double the bank angle

DUTCH ROLL - method 1:

1. Glider was trimmed at defined airspeed

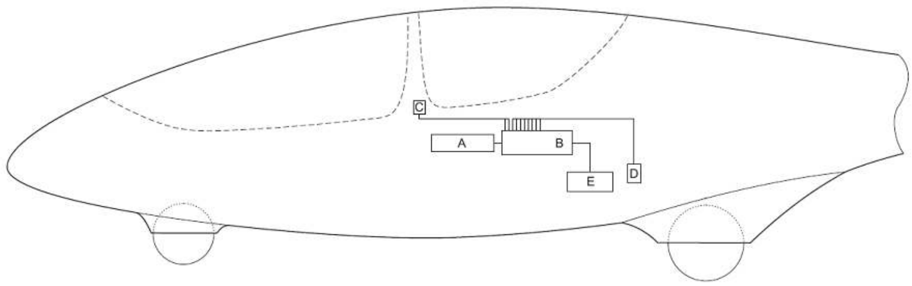

Figure 2: Measurement system: A - data logger, B - adapter box, C - pressure sensors, D - accelerometers and gyroscopes, E - battery.

2. Rudder was quickly moved to the bumper and immediately withdrawn to the neutral position
3. Controls were kept in neutral for 50s

DUTCH ROLL - method 2:
1. Glider was trimmed at defined airspeed
2. Rudder was moved quickly to the left and right bumper
3. Rudder was stopped in neutral position
4. Controls were kept in neutral position for 50s

ROLLING:
1. Glider was trimmed at defined airspeed
2. Coordinated turn with bank angle of 45°was initiated
3. Glider was rolled as quickly as possible to the opposite bank angle.

AILERON SENSITIVITY:
1. Glider was trimmed at defined airspeed
2. Aileron was deployed as quickly as possible
3. Controls were kept motionless up to 45°of bank angle was achieved.

5 Simplified stability analysis

Eigenvalues of each flight mode of PW-6U sailplane, resulting from approximate analytical formulae, were calculated with application of dimensional and nondimensional aerodynamic derivatives computed before [9]-[13]. The task was performed twice. For the first time it was done before flight test campaign, to estimate periods of oscillations for each flight mode. It was necessary to excite oscillations properly, but results were perceived as inaccurate since some data (like airspeed) were assumed, not measured. Then, after flight test campaign, eigenvalues were calculated again, with application of weather and flight parameters experienced during flight test campaign. Moreover, flight testing was conducted for sailplane weights 513kg and 540kg, therefore all eigenvalues were calculated for these two configurations. These second set of eigenvalues was compared with flight test results [14]. Eigenvalues were calculated for each mode separately according to the following model. They depend on aerodynamic derivatives i.e. sailplane geometry, it's weight and weight distribution as well as flight parameters like airspeed and altitude (air density). Analysis starts from the indicial equation of dynamic stability. It is a differential equation with constant parameters, which can be written as follows:

$$\lambda^2 + 2\zeta\omega_n\lambda + \omega^2 = 0 \tag{1}$$

Complex solutions of this equation are the following:

$$\lambda_{j,j+1} = \xi_{j,j+1} \pm i\eta_{j,j+1} \tag{2}$$

where:

$$\xi = Re\lambda = -\zeta\omega_n \quad \left[\frac{1}{s}\right] \tag{3}$$

$$\eta = ln\lambda = \omega_n\sqrt{1-\zeta^2} \quad \left[\frac{1}{s}\right] \tag{4}$$

Real part of each solution is marked as ξ and has an influence on motion damping. Imaginary part η (sometimes marked as ω) is equal to the damped oscillation frequency, therefore it is equal to zero for each aperiodical flight mode. Sailplane is dynamically stable if each real part is smaller than zero. For periodical oscillations (phugoid, short period oscillations, Dutch roll) period of oscillations T, time to half $T_{1/2}$ or time to double T_2 and frequency of undamped oscillations ω_n were also calculated. The following formulae were used to conduct these calculations:

The period of oscillation:

$$T = \frac{2\pi}{\eta} \tag{5}$$

Time to half ($\xi < 0$):

$$T_{1/2} = -ln(2)/\xi \tag{6}$$

Time to double ($\xi > 0$):

$$T_2 = ln(2)/\xi \tag{7}$$

Damping ratio and undamped natural frequency can be found using:

$$\omega_n = \sqrt{\xi^2 + \omega_D^2} \tag{8}$$

$$\zeta = \frac{\xi}{\omega_n} \tag{9}$$

Frequencies of undamped oscillations and damping coefficient depend on dimensional aerodynamic derivatives resulting from: weight, weight distribution, airspeed, air density and dimensionless aerodynamic derivatives characteristic for each flight mode. Relevant formulae are given below.

Phugoid

$$\zeta_p = \frac{X_u}{2\omega_{np}} \tag{10}$$

$$\omega_{np} = \sqrt{\frac{-Z_u g}{u_0}} \tag{11}$$

or

$$\zeta_p = \frac{1}{\sqrt{2}}\frac{1}{L/D} \tag{12}$$

$$\omega_{np} = \sqrt{2}\frac{g}{u_0} \tag{13}$$

Short Period oscillations

$$\zeta_{SP} = -\frac{M_q + M_\alpha + \frac{Z_\alpha}{u_0}}{2\omega_{nSP}} \tag{14}$$

$$\omega_{nSP} = \sqrt{\frac{-Z_\alpha M_q}{u_0} - M_\alpha} \tag{15}$$

Dutch roll

$$\zeta_{DR} = -\frac{1}{2\omega_{nDR}}\frac{Y_\beta + u_0 N_r}{u_0} \tag{16}$$

$$\omega_{nDR} = \sqrt{\frac{Y_\beta N_r - N_\beta Y_r + u_0 N_\beta}{u_0}} \tag{17}$$

Rolling

In this case the imaginary part of eigenvalue η is equal to zero, so:

$$\lambda = \xi = L_p \tag{18}$$

Moreover velocity of constant rolling p_{ss} can be estimated for this flight mode:

$$\frac{p_{ss}b}{2u_0} = -\frac{C_{l_{\delta a}}}{C_{l_p}}\Delta\delta a \tag{19}$$

Spiral

In this case also the imaginary part of eigenvalue η is equal to zero, so:

$$\lambda = \xi = \frac{L_\beta N_r - L_r N_\beta}{L_\beta} \tag{20}$$

In the case of aperiodical modes time to half or time to double $T_{1/2}$ and T_2 are calculated similarly to periodical modes according to equations (6,7), however interpretation is slightly different. In the case of periodical modes amplitude of oscillations is halved/doubled; In the case of aperiodical modes roll angle is halved/double. Formulae listed above were used to calculate eigenvalues for each particular manoeuvre executed during flight tests campaign; therefore they can be directly compared with results of measurement recorded during this manoeuvre.

6 Flight test data processing

Three periodic modes of motion (phugoid, short period, Dutch roll), which were taken under consideration, can be analyzed in the similar way. The following formula was assumed to derive the typical variables, which describe the oscillation, from recorded flight parameters:

$$p = e^{-\zeta t} sin(\omega t + \varphi) + A_0 \tag{21}$$

where:
p - flight parameter,
A - the initial amplitude of oscillation,
A_0 - the initial value of p parameter,
ζ - damping coefficient,
ω - angular frequency,
φ - phase shift.

The variables mentioned above where computed using least squares approximation. The approximated time history of selected state parameters allows to compute the period and time to half amplitude, which are usually taken to assess an aircraft handling qualities. The appropriate formulas are as follows:

$$T = 2\pi/\omega \tag{22}$$

$$T_{1/2} = ln(2)/\zeta \tag{23}$$

The aperiodic modes characteristics, selected flight parameters, recorded during test flights were analyzed directly to obtain halve/double time.

7 Comparison of flight test data and simplified stability model

7.1 Phugoid

The phugoid mode is relatively easy to identify due to regular oscillations, however it requires a long test to record a few maxima. Figure 3 presents the true airspeed in time recorded during one flight test and obtained from computation. Numerical results are presented in Table 1. The results show good conformance for damping characteristics and a little worse for period (relative error 20%).

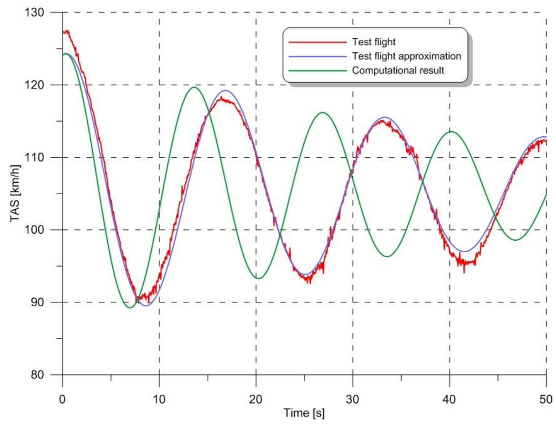

Figure 3: PW-6 phugoid test - True airspeed in time

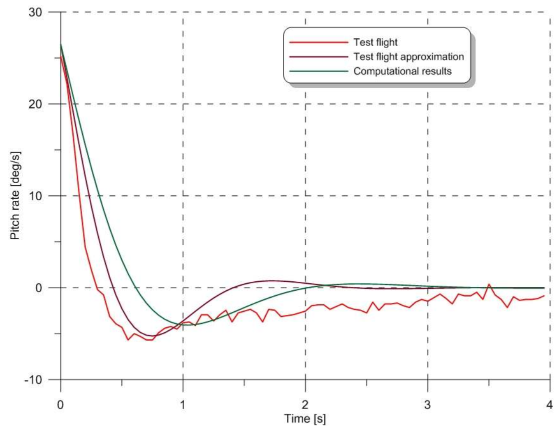

Figure 4: PW-6 Short Period test - pitch rate in time

7.2 Short Period

The Short Period oscillations are the most difficult to identify due to very strong damping. It causes, that identification of at least two maxima of recorded signals could be impossible. The attempt to identify short period characteristics is presented in Fig. 4 and the numerical values are in Table 2.

7.3 Dutch roll

A number of Dutch roll oscillations were recorded during test flights. Two of them are presented on the time history (yaw rate) graphs - Fig. 5. The numerical results are in the Ta-

Table 1: Phugoid characteristics obtained from flight and computation

Flight No.	TAS [km/h]	Altitude [m]		T [s]	Rel. Error [%]	$T_{1/2}$ [s]	Rel. Error [%]
1	103	1123	test flight	16.02	17.37	35.89	9.59
			computation	13.24		32.45	
2	104	1201	test flight	15.98	17.92	30.81	5.30
			computation	13.11		32.45	
3	105	1305	test flight	16.45	19.26	36.23	10.44
			computation	13.28		32.45	

Table 2: Short Period characteristics

Case	T [s]	$T_{1/2}$ [s]
test flight No. 1	1.905	0.341
test flight No. 2	1.963	0.350
computation	2.810	0.427

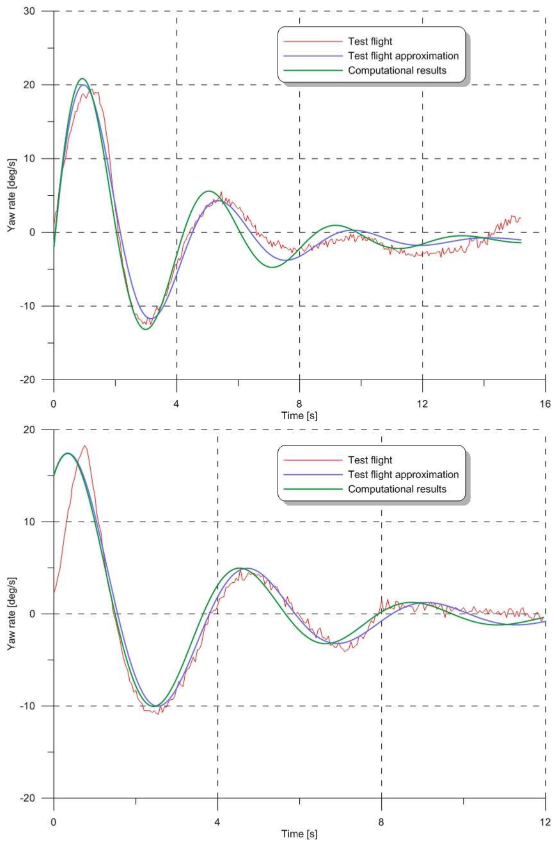

Figure 5: Dutch roll oscillations

ble 3. The results show very good conformance especially for the first and fourth flight (Fig. 5).

7.4 Roll

The result of flight test and computational are presented on Fig. 6. These are the results for the eight tests. The time required to reach the angle of about 90°was measured and calculated. Very good conformance was achieved.

8 Final remarks

The results presented in the previous chapter show, that the conformance between experiment and computation is different for different modes of motion. The best results are for lateral motions (roll and Dutch roll). The results for longitudinal modes are a little worse. Although the phugoid is quite easy for modelling, the assumption about small disturbance can be not satisfied due to long period and big amplitude (initial amplitude is about 20 km/h, what is about 20% of the airspeed). Despite this, computed damping coefficient of phugoid is very close to experimental one and relative error doesn't exceed 10% in most cases. The Short Period mode is very difficult to identify. Very strong damping and associated phugoid oscillation cause, that the identification of the period and damping coefficient is very difficult, so the results of identification (approximation) should be taken only as general information, that Short Period oscillations are strongly damped, what is good from airworthiness regulations point of view [15].

Table 3: Dutch roll characteristics obtained from flight and computation

No.	V [km/h]	H [m]	Flight test		Computation		Relative error	
			T	$T_{1/2}$	T	$T_{1/2}$	T	$T_{1/2}$
1	101.0	988	4.382	2.222	4.120	2.398	5.98%	7.92%
2	102.5	1070	4.667	1.869	4.160	2.407	10.87%	28.77%
3	102.0	950	4.700	2.160	4.140	2.398	11.91%	11.06%
4	101.5	1022	4.376	2.502	4.200	2.407	4.03%	3.82%
5	100.2	1005	4.263	2.607	4.200	2.407	1.47%	7.69%

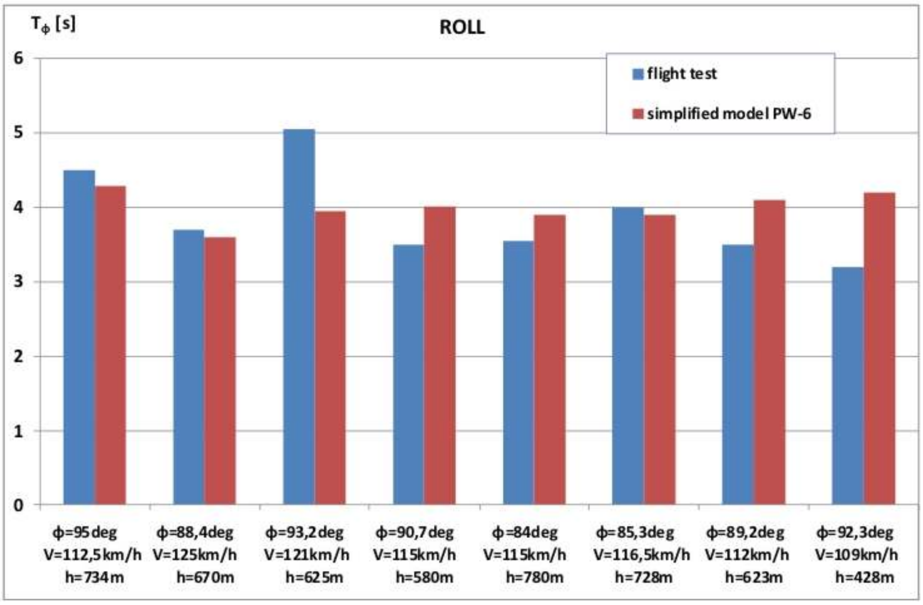

Figure 6: Roll characteristics

Acknowledgments

This work was supported by Dean of Mechanical Faculty of Power and Aviation at Warsaw University of Technology through the grant 503R11320264004. Authors would also like to express their thanks to PhD eng. Maciej Lasek, and MSc. eng. Jerzy Kędzierski who worked as test pilots and helped to organize the experiment.

References

[1] ESDU (Engineer Science Data Unit) reports, http://www.esdu.com/

[2] SIMSAC (Simulating Aircraft Stability And Control Characteristics for Use in Conceptual Design) http://www.simsacdesign.org/

[3] Goetzendorf-Grabowski T., Mieszalski D., Marcinkiewicz E. "Stability analysis using SDSA tool", *Progress in Aerospace Sciences*, Vol. 47, Issue 8, November 2011, Pages 636-646

[4] von Kaenel R., Rizzi A., Oppelstrup J., Goetzendorf-Grabowski T., Ghoreyshi M., Cavagna L., and Berard A., "CEASIOM: Simulating Stability & Control with CFD/CSM in Aircraft Conceptual Design", *26th International Congress of the Aeronautical Sciences*, Anchorage, Sept 2008, Paper 061

[5] Ewald J., "Flight Test: PW-6", *Sailplane and Gliding*, Feb-Mar 2001

[6] Rodzewicz M., Sierputowski P., "EB-2, the FlyLab of the Warsaw University of Technology", *XXIX OSTIV Congress*, Lüsse, Germany, 6-13 August 2008

[7] APEK: http://www.apek.x.pl/pl/re.html (in Polish)

[8] Kimberlin R. D., *Flight Testing of Fixed-Wing Aircraft*, AIAA Education Series, 2003

[9] Goraj Z., *Calculations of equilibrium, manoeuvrability and stability of an aircraft in subsonic range of speed (in Polish)*, Warsaw University of Technology, Warszawa 1984.

[10] Nelson R.C., *Flight Stability and Automatic Control*, 2^{nd} ed., McGraw-Hill, 1998.

[11] Etkin B., *Dynamics of Flight - Stability and Control*, John Wiley & Sons, Inc., New York 1982.

[12] Cook B.H., *Flight Dynamics Principles*, Butterworth Heinemann, Cranfield 1997.

[13] Smetana F. O., Summey D. C., Johnson W. D., "Riding and handling qualities of light aircraft - a review and analysis", NASA Contractor Report - NASA CR-1975, Washington, 1972

[14] Marcinkiewicz E., "The dynamic stability analysis of PW-6U glider", BSc thesis, Warsaw University of Technology, Warsaw, Poland 2009

[15] EASA - CS-22 (Sailplanes and Powered Sailplanes), http://www.easa.europa.eu

4:th CEAS Air & Space Conference
FTF Congress: Flygteknik 2013

SESAR and Military Aircraft: Human Machine Interface definition for 4D Trajectory Management and ASAS Spacing functionalities

G.A. Di Meo
Politecnico di Torino,Italy

A.Cavallo and A.Lunghi
Alenia Aermacchi S.p.A., Italy

Keywords: *SESAR, Military Aircraft, Human Machine Interface, Initial 4D, ASPA*

Abstract

Single European Sky ATM Research (SESAR) is an ambitious research program funded by European Community and Eurocontrol whose aim is to renovate the European ATM (Air Traffic Management) system toward a Single European Sky (SES). SES will involve not only civil/commercial air traffic but also military air traffic. The integration of military aircraft into a collaborative ATM environment leads to the necessity to solve the problem of making the military aircraft systems interoperable with the Air Traffic Management framework. SESAR procedures identified for a minimum interoperability level are Initial 4D (I4D) and ASAS SPAcing Sequencing and Merging (ASPA S&M) where ASAS stands for Airborne Separation Assistance System. The aim of the paper is to study the accommodation of selected SESAR functionalities (i.e. I4D and ASPA S&M) in the military cockpit configuration of Transport-type and Fighter-type. Typical military cockpit configurations have been analyzed in order to identify cockpit item which could accommodate requirements of SESAR functionalities. By analyzing military cockpit items as well as requirements of Initial 4D and ASPA S&M, a design solution has been identified in concurrence with industry military pilots.

1 General Introduction

SESAR (Single European Sky ATM Research) is a research programme co-funded by the SJU (SESAR Joint Undertaking) the European Community and Eurocontrol. The aim of SESAR is to reform ATM (Air Traffic Management) rules and procedures in order to realize the following goals as indicated in the SESAR ATM Master Plan [1]:

- Enable a 3-fold increase in capacity which will also reduce delays, both on the ground and in the air;
- Improve safety performance by a factor of 10;
- Enable a 10% reduction in the effects flights have on the environment and;
- Provide ATM services to the airspace users at a cost of at least 50% less.

The realization of SESAR goals is based on ATM concepts here reported:

- Moving from an airspace to trajectory based operations so that each aircraft achieves its preferred route and time of arrival;

- Collaborative planning so that all parties involved in flight management from departure gate to arrival gate can plan their activities based on the performance the system will deliver;
- Dynamic Airspace Management through enhanced coordination between civil and military authorities;
- New Technologies providing more accurate airborne navigation and optimized spacing between aircraft to maximize airspace and airports capacity
- Central role for the human, widely supported by advanced tools to work safely without undue pressure.

By analyzing ATM concepts for SESAR realization and in particular the Dynamic Airspace Management it is possible to understand that the future ATM scenario, delineated by SESAR concepts of operations, shall consider the presence of military aircraft within the airspace in a collaborative environment. This requirement leads to the necessity to solve the problem of making the military aircraft systems interoperable with the Air Traffic Management framework in accordance with results of interoperability assessments presented in [2] and [3].

1.1 Mission Trajectory

The SESAR target concept of operation is a trajectory-based concept. All partners involved in the Air Traffic Management will share in real time all relevant trajectory information through SWIM (System Wide Information Management). In accordance with what Eurocontrol/DCMAC affirms in its “Introduction to the Mission Trajectory” [4] a Business Trajectory (BT) for civil aviation or a Mission Trajectory (MT) for military operation is elaborated and agreed for each flight between the user and the Air Navigation Service Provider (ANSP). It has to be highlighted that BT and MT are 4D Trajectories so that each waypoint of the trajectory is unambiguously defined by: latitude, longitude, altitude and Requested Time of Arrival (RTA).

The most relevant peculiarity of Mission Trajectory is the possibility to consider dynamic Areas Reserved (ARES) for military activities (e.g. firing, training and air refueling) as a part of the whole 4D Trajectory agreed with ANSP. Military aircraft will fly in ARES only where requested by specific military activities whereas, the remaining part of the trajectory will be shared with Air Traffic Control (ATC).

It has to be noticed that Mission Trajectory concept concerns innovative flight procedures and consequent on-board functionalities. The complete set of ATM procedures and functionalities in order to realize a minimum and sufficient level of Civil-Military interoperability is wide and its definition is ongoing in the SESAR research program. At the moment the procedures identified in SESAR for a minimum interoperability level are Initial 4D and ASAS SPAcing Sequencing and Merging (ASPA S&M) where ASAS stand for Airborne Separation Assistance System. This paper is focused on the presentation of the technological solutions for allowing military avionics to implement on-board functions requested by the Initial 4D and ASPA S&M procedures. Transport and Fighter aircraft are the platform types here considered. Following paragraphs describe Initial 4D and ASPA S&M flight procedures as they find application to civil air traffic, the paragraph “Military ATM Environment” describes how these procedures can be applied to military air traffic and to the Mission Trajectory concept.

1.2 Initial 4D

In accordance with the SESAR – WP 9 Description of Work (DoW) [5] 4D Trajectory Management is an aircraft function that enables to build, guide, predict and communicate a 3D trajectory where waypoints are described also by a time constraint. In SESAR target concept Initial 4D is the first implementation step of 4D Trajectory Management.

Initial 4D is a flight procedure which applies in the final en-route and Terminal Maneuver

Area (TMA) within the Arrival Manager (AMAN) Horizon. In accordance with the description of Initial 4D found in [2] and [6] it is possible to decompose the nominal flight procedure in the following main steps:

- The aircraft downlinks via ADS-C (Automatic Dependent Surveillance-Contract) EPP (Extended Projected Profile) report [7] its preferred 4D Trajectory composed by a waypoints defined by latitude, longitude, altitude and time prediction.
- A 3D route clearance is uplinked to the aircraft via CPDLC (Controller Pilot Data Link Communications) [7]. This clearance is issued in order to communicate if the ATC can accommodate aircraft preferred 3D route or modifications to aircraft preferred 3D route are requested;
- After the 3D route is synchronized, the Flight Management System (FMS) of the aircraft estimates on a defined waypoint of the Trajectory the ETA (Estimated Time of Arrival) maximum and ETA minimum. These values represent the time interval in which the aircraft is confident to overfly the defined waypoint. ETA maximum and ETA minimum are downlinked via ADS-C ETA min/max report [7];
- The ATC receives downlinked ETA minimum and maximum values and determines a Single Time Constraint to assign to the aircraft. The Single Time Constraint takes the name of Required Time of Arrival (RTA). The ATC uplinks via CPDLC [7] the assigned RTA;
- The aircraft receives the assigned RTA and automatically uploads it into the FMS. If the crew agree with the received RTA value, they activate the RTA function in the FMS;
- The RTA function steers the aircraft by adjusting the speed so that RTA value is respected with a given tolerance of ±10 seconds (if the waypoint is in TMA) or ±30 seconds (if the waypoint is in En-Route) [7].

1.3 ASPA S&M

In accordance with the SESAR – WP 9 Description of Work (DoW) [5] ASPA S&M is expected to improve capacity and flight regularity in terminal areas by having the aircraft to maintain a defined time spacing from a target aircraft. ASPA S&M will contribute to suppress the use of vectoring instructions by reducing ATC controllers and pilot workload.

ASPA S&M is a flight procedure which applies in the final en-route and Terminal Maneuver Area (TMA). In accordance with the description of ASPA S&M found in [8] and [9] it is possible to decompose the nominal flight procedure in the following steps:

- The ATC communicates via voice or CPDLC to the aircraft that an ASPA S&M maneuver shall be executed and clearance instructions for the requested maneuver.
- The flight crew inserts in the FMS the received instructions for the ASPA S&M maneuver. The FMS processes all instructions and identifies the lead aircraft to follow with the requested time spacing by accessing its received ADS-B (Automatic Dependent Surveillance – Broadcast) reports.
- Once identified the target aircraft to follow, the FMS uses leader aircraft data contained in the ADS-B reports in order to steer the aircraft by adjusting current speed so that requested time spacing is achieved before ABP (Achieve By Point) waypoint.
- Once the time spacing is achieved the FMS uses ADS-B reports of the leader aircraft to regulate velocity and maintaining the time spacing constant with a required tolerance.
- ASPA S&M is interrupted when TER (i.e. termination) waypoint is reached or the Air Traffic controller communicates the interruption via voice or CPDLC.

1.4 Military ATM environment

Initial 4D and ASPA S&M as described above are applicable to the civil Air Traffic environment. As far as Military Air Traffic is concerned the above mentioned procedures can be used as enablers of the Mission Trajectory concept. It is possible to find applicability of Initial 4D and ASPA S&M to military typical use of airspace which often concerns the presence of a dynamic reserved area (ARES) in accordance with what Eurocontrol states in [10]. The following figure adds details on what has been stated above.

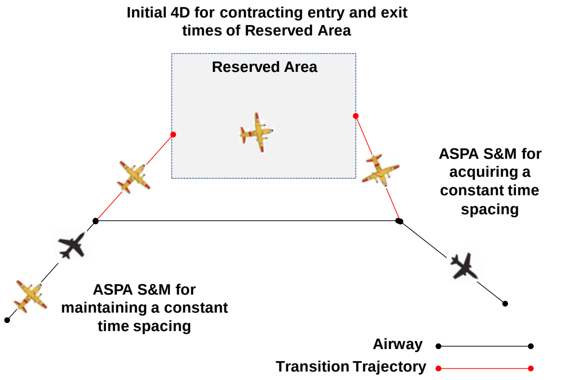

Fig 1. Applicability of Initial 4D and ASPA S&M to military airspace use.

As it is possible to see in Fig. 1 the idea is to exploit existing SESAR procedures for enabling the Mission Trajectory concept described by EUROCONTROL/DCMAC in [10]. The ASPA S&M procedure can be exploited, indeed, for maintaining constant time spacing while the military aircraft is flying its GAT (General Air Traffic) in en-route. Then during the transition segment for arriving to ARES the aircraft could perform an Initial 4D procedure for negotiating the time of arrival at the entry point of the reserved area. The same can be done for the exit point of the ARES. The negotiation of entry and exit points with ATC in this way can enhance predictability of ARES occupancy by the military aircraft by allowing better management of the dynamic generation and removal of Reserved Areas in the airspace. At ARES exit ASPA S&M could be used during transition segment between the ARES and the airway as a useful tool for allowing the ATC to better reinsert the military aircraft in the GAT on the airways.

2 Military Cockpit Configurations

This paragraph analyzes military cockpit configurations for Transport-type and Fighter-type aircraft. The strong commonality among cockpit configurations of Transport aircraft together with similarities among Fighter aircraft cockpit allow to define a general cockpit configuration where it is possible to design an accommodation of SESAR functionalities which could be applicable to the vast majority of military Transport and Fighter aircraft.

2.1 Transport-type

Transport are those military aircraft used by national Air Forces or Armies for tactical and strategic transportations. This category of aircraft is distinguished by high capacities of the cargo bay and high take-off and landing performance on a wide variety of surfaces. Some examples of modern transport military aircraft are:

- Alenia Aermacchi C-27J Spartan
- Airbus A400M
- EADS CASA C-295M

Fig 2. C27J Spartan Cockpit

Transport aircraft usually adopt pilot and copilot side-by-side configuration. Positioning of Displays and Control Panels are often very similar to commercial civil transportation aircraft.

Transport aircraft in the modern glass cockpit configurations are equipped with Multi Function Displays (MFD) located on the main instrument panel in front of the pilot flying and pilot not flying seats. In particular both pilot and co-pilot are provided with a PFD (Primary Flight Display), Navigation Display and Systems' displays where aircraft status parameters are showed. An Alert page is usually presented in these displays in order to show to the crew the malfunctions, abnormal conditions or systems' relevant states.

Multipurpose Control Display Units (MCDUs) provide the primary operator interface via an alphanumeric keyboard, mode select keys, line select keys, annunciators and a flat panel display. Usually two MCDUs are positioned in the pedestal panel providing the pilots with a redundant and centralized control of the avionic systems. Some Transport aircraft like C27J Spartan include an additional control panel called CMD (Communication Management Display) for a more efficient management of communication system.

Head-Up Display (HUD) is being adopted also in modern Transport aircraft. The HUD is a transparent display of flight data that allows the pilots to maintain an "out-the-window" viewpoint.

2.2 Fighter-type

Fighters are those military aircraft whose main role is to cope with the national air forces needs for air-to-air and air-to-ground defense. This paper considers only 4th Generation Fighter due to the limited information available on 5th Generation Fighters. Some examples of European modern 4th generation Fighters are:

- Eurofighter Typhoon
- Dassault Rafale
- Saab Gripen

Modern fighter aircraft typically concern single-seat configuration. It has to be noticed that, differently from Transport aircraft, fighters' cockpit configurations are not homogeneous among the several platforms, even if it is possible to identify some common elements which will be the focus of the present study.

Fig 3. Eurofighter Typhoon Cockpit

Three Multi Function Displays (MFD) are usually located on the main instrument panel in front of the pilot; he is able to select the information to be showed by manually setting formats of each display. During navigation flight phase these displays are able to provide the pilot with information in PFD, Navigation display and System Display format.

Fighter pilots are not provided with a MCDU interface where control of avionic function is centralized; here these are distributed on the left and right glare shields where buttons for avionic systems control are located.

An HUD is also adopted for showing flight data for navigation and flight control.

3 Human Machine Interface design solutions

The description of SESAR functions in paragraphs 1 gives the possibility to define basic HMI functions to be implemented in the cockpit for allowing flight crew to interact with Initial 4D and ASPA S&M.

HMI main functions to be implemented are:

- Activation of the functionality
- Visualization of speed commands to autopilots
- Visualization of time estimates

- CPDLC communication management
- Target aircraft visualization for ASPA S&M function
- Navigation management

The following sub-paragraphs show examples of design solutions for the above mentioned HMI functions. Paragraph 4 discusses the applicability and allocation of design solution to Transport and Fighter cockpits.

3.1 Activation of the functionality

Both Initial 4D and ASPA S&M function concern the need to be manually armed by flight crew once ATC requests to the aircraft such maneuvers and the flight crew agree with their execution. This function can be performed by using a dedicated pushbutton whose general aspect is shown in Fig. 4. The same pushbutton could be used for arming Initial 4D or ASPA S&M, the system will engage the first or the latter depending on the one that the flight crew has associated to the active flight plan.

Fig 4. Pushbutton for Initial 4D and ASPA S&M arming

The flight crew, by pressing the 4D NAV button, arms Initial 4D or ASPA S&M functions and, as already happens with common autopilot modes activation, the aircraft FCS (Flight Control System) engages Initial 4D or ASPA S&M in the autopilot on the condition that specific preliminary checks give positive results.

3.2 Visualization of speed commands

When Initial 4D and ASPA S&M are engaged by FCS the aircraft speed is automatically adjusted for achieving CTO constraint (i.e. Initial 4D engaged) or an assigned spacing with a target aircraft (i.e. ASPA S&M engaged). As for autopilot modes involving autothrottle the speed commanded shall be shown to the flight crew. Figure 5 give examples of two possibilities for visualization.

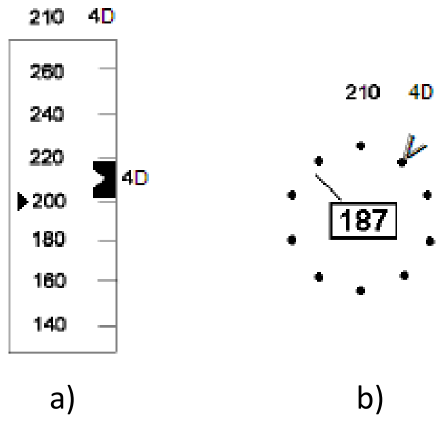

Fig 5. Possibilities for indication of speed commands to autopilot

In Figure 5.a the visualization of the commanded IAS is realized through a digital readout and a caret moving along the IAS moving tape; according to specific cockpit philosophy these indications might respect a defined color coding. In Figure 5.b, the visualization of the commanded IAS is realized through a digital readout and a caret moving around the IAS indicator.

3.3 Visualization of time estimates

While Initial 4D and ASPA S&M functions are active there is the need for visualizing time estimates on waypoints.

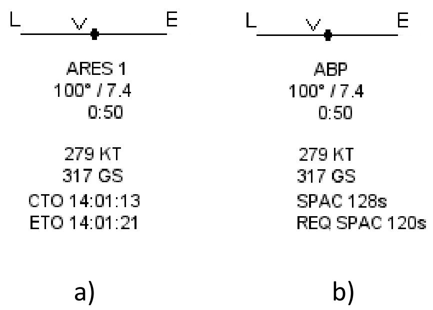

Fig 6. Visualization of aircraft time estimates for Initial 4D a) and ASPA S&M b)

Figure 6.a shows a concept of time estimates visualization for Initial 4D function that is composed from top to bottom by:

- a caret that moves between E (i.e. Early) and L (i.e. Late) indications for giving fight crew a graphical representation of difference between CTO assigned by ATC and ETO (Estimated Time Overfly) on the ARES1 waypoint;
- a waypoint box containing ID, bearing and range of the constrained waypoint;
- an indication of IAS commanded to autopilot together with associated Ground Speed (GS);
- CTO constraint assigned by ATC together with aircraft ETO (Estimated Time Overfly).

Figure 6.b shows a concept of time estimates visualization for ASPA S&M function, this is very similar to the one conceived for Initial 4D. The only difference is that labels in bottom part indicate actual spacing between the aircraft and the target together with spacing required in ATC instructions for ASPA S&M.

3.4 CPDLC communication management

Initial 4D function calls for a CPDLC communication between flight crew and ATC in order to negotiate and assign a time constraint (i.e. CTO) on waypoint.

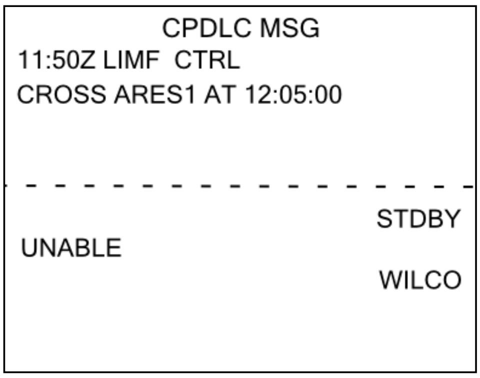

Fig 7. MCDU Page for CPDLC messages management

Figure 7 shows the concept for a MCDU page for managing CPDLC communications. As it is possible to notice, in the upper part of the display, CPDLC message appears with related time and sender. In accordance with [7], in the lower part of the display three labels indicate three standard downlink messages to ATC. Flight crew can choose the one to be downlinked by using lateral pushbuttons on MCDU frame:

- WILCO: flight crew downlinks this message in the case they understand the instruction and they will comply. In this case the CTO contained in the uplink CPDLC message is automatically associated to the waypoint contained in the same message;
- UNABLE: flight crew downlinks this message in the case the instruction is not applicable to the aircraft flight plan;
- STDBY: flight crew downlinks this message to acknowledge the receipt of the message and for declaring to the ATC to wait for a response.

3.5 Target aircraft visualization

During ASPA S&M maneuver there is the need for visualizing the position of the target aircraft on the active flight plan.

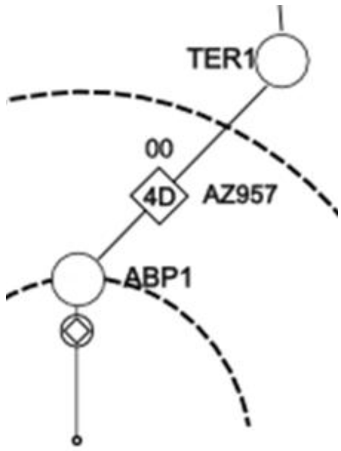

Fig 8. Visualization of Target Aircraft for ASPA S&M function

In Figure 8 the position of target aircraft is shown as a square between ABP and TER waypoints with a 4D label inside it in order to distinguish it from aircraft detected by TCAS (Traffic Collision Avoidance System). The figure also shows the point on the active flight plan where the navigation system estimates the spacing will be achieved; the associated symbol consists in a square inside a circle.

3.6 Navigation management

Flight crew need to manage some data prior and during the execution of Initial 4D and ASPA S&M maneuvers.

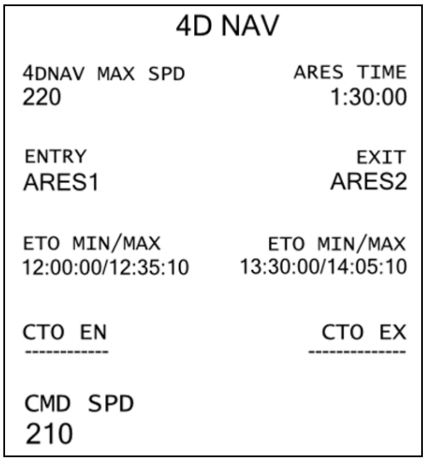

Fig 9. MCDU Page for Initial 4D function management

Figure 9 shows a concept of MCDU page for Initial 4D function management. Flight Crew can interact inserting:

- 4D NAV MAX SPD: maximum speed reachable by the aircraft during the maneuver. This mainly depends on the fuel consumption policy of aircraft operator;
- ARES TIME: this is the time that the military aircraft is confident to remain in the reserved area. This is an important input for time estimations of the exit point from the reserved area;
- ENTRY and EXIT waypoints of the reserved area that the aircraft uses for its military operations;

The same interface gives the flight crew the possibility to visualize:

- ETO Minimum and ETO Maximum estimations on Entry and Exit Waypoints;
- CTO on Entry and Exit points of ARES;
- CMD SPD: speed commanded to autopilot for satisfaction of CTO constraint (only once the Initial 4D function becomes active).

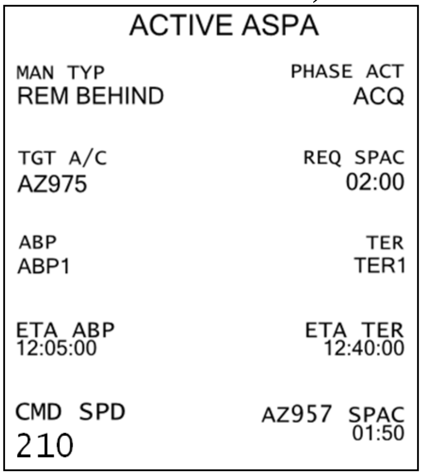

Fig 10. MCDU Page for ASPA S&M function management

Figure 10 shows a concept of MCDU page for ASPA S&M function management. Flight Crew can interact inserting:

- MAN TYP: type of ASPA S&M maneuver demanded by ATC through clearance instructions;
- TGT A/C: the target aircraft to follow
- REQ SPAC: spacing required by ATC through clearance instructions;
- ABP (Achieve By Point) and TER (Termination Point) for the ASPA S&M maneuver.

The same interface gives the flight crew the possibility to visualize:

- PHASE ACT: this is the indication of the actual ASPA S&M phase (i.e. spacing achieving or spacing maintaining);
- ETA (Estimated Time of Arrival) estimations on ABP and TER waypoints;

- AZ957 SPAC: actual spacing with the selected target aircraft (i.e. AZ957 in Figure);
- CMD SPD: speed commanded to autopilot for spacing acquisition and maintaining (only once the ASPA S&M function becomes active).

4 HMI allocation to military cockpit configurations

This paragraph discusses the allocation of HMI concepts defined in the paragraph 3 to military cockpit configurations of Transport and Fighter-type aircraft. Table 1 presents the results of the allocation.

HMI function	Allocation on Transport-type cockpit	Allocation on Fighter-type cockpit
Pushbutton for Initial 4D and ASPA arming (i.e. Fig. 4)	Pushbutton for arming Initial 4D and ASPA can be allocated on the autopilot panel typically located in the upper part of military Transport cockpit. This concerns the addition of a pushbutton, so both hardware and software modifications.	As for Transport aircraft, pushbutton for arming Initial 4D and ASPA can be allocated on the autopilot panel typically located in the glareshield of Fighter cockpit. The addition of a pushbutton, even if desired, is considered critical due to lack of spare space on fighter glareshields.
Indication of speed commands to autopilot (i.e. Fig. 5.a and 5.b)	Visualization of speed commands to autopilot as shown in Figure 5 shall be allocated to PFD (Fig.5.a), and HUD (Fig.5.b) for those Transport aircraft equipped.	Visualization of speed commands shall be allocated at first to HUD (Fig.5.b) and to PFD visualization (Fig.5.a) in the MFD.
Visualization of aircraft time estimates for Initial 4D and ASPA (i.e. Fig. 6.a and 6.b)	Visualization of time estimates as in Fig. 6.a and 6.b should be allocated to Navigation Display, and HUD for those Transport aircraft equipped.	As for Transport visualization of time estimates as in Figure 6 should be allocated to Navigation Display and HUD.
CPDLC messages management (i.e. Fig. 7)	Management of CPDLC messages can be realized by adding proposed HMI as a new page of MCDU, or as new page of CMD for those Transport aircraft equipped.	Fighter cockpit typically includes a display for managing tactical messages on MIDS/Link 16. HMI concept presented in Fig. 7 can be adapted for being allocated on this display.
Visualization of target aircraft for ASPA function (i.e. Fig. 8)	Visualization of Target Aircraft should be allocated to Navigation Display where active flight plan is shown.	As for Transport aircraft, visualization of Target Aircraft should be allocated to Navigation Display where active flight plan is shown.
Initial 4D and ASPA navigation management (i.e. Fig. 9 and Fig.10)	Concepts in Fig. 9 and Fig. 10 have been conceived as new pages of the existing MCDU control panel.	Fighter aircraft does not concern the presence of a former MCDU. Typically MCDU functions are allocated to pushbuttons on glareshield. For this reason navigation management could be allocated to buttons of glareshield by exploiting functions of already existing buttons. Even if critical, the implementation of this function strongly depends on the specific fighter platform considered.

Table 1. Allocation of HMI function to Fighter and Transport cockpits

Transport aircraft, as already said in paragraph 2.1, typically concerns a cockpit configuration very similar to commercial civil aircraft and as a consequence this allows an easier allocation of the defined HMI concepts.

Fighter aircraft, instead, concerns a cockpit configuration very different from civil aviation together with limited space for hardware modifications. This leads to a more difficult adaptation of fighter cockpit to SESAR HMI functions.

5 Conclusions

The paper has presented conceptual HMI design solutions for Initial 4D and ASPA S&M implementation on military cockpit aircraft with particular attention to military Transport and Fighter cockpit configurations. Civil-Military Interoperability is under development in the context of the SESAR research programme under the responsibility of Alenia Aermacchi.

Proposed solutions showed that the above mentioned ATM functionalities can be integrated on existing military cockpit configurations by upgrading available displays and controls and by minimizing hardware modifications. This aspect is relevant for military aircraft due to the often limited space for additional hardware that their cockpit offers, especially for the fighter aircraft case.

The HMI concept solutions indicated in this paper are the result of presentations and discussions performed with Alenia Aermacchi pilots and Alenia Aermacchi HMI specialists.

Future perspectives of the presented work consist in integrating HMI solutions and SESAR navigation functions into a stand-alone hardware solution and test them in Alenia Aermacchi flight simulators before the end of 2014. In the end of 2015 a flight test campaign will be performed on C-27J platform to tests the CNS (Communication Navigation Surveillance) and HMI solution in a real ATM environment.

Acknowledgments

The Authors would like to thank the SESAR Joint Undertaking, European Commission and EUROCONTROL for the important commitment in sustaining the interoperability aspects among military and civil users for the future Single European Sky.

Alenia Aermacchi S.p.A.

Disclaimer

The activities developed to achieve the results presented on this paper, were created by Alenia Aermacchi for the SESAR Joint Undertaking within the frame of the SESAR Programme co-financed by the EU and EUROCONTROL. The opinions expressed herein reflects the author's view only. The SESAR Joint Undertaking is not liable for the use of any of the information included herein.

References

[1] SESAR Joint Undertaking, "European Air Traffic Management Master Plan", SESAR Joint Undertaking Avenue de Cortenbergh 100-B-1000 Brussel, Belgium, Edition 2, 2012

[2] Di Meo G.A., Montrucchio C., and Medici G., "Interoperability of Military Aircraft versus Future Air Navigation System(FANS)", *28th Congress of International Council of the Aeronautical Sciences*, Brisbane, Australia, 2012

[3] Di Meo G.A., Medici G., Chiesa S., Viola N., Cavallo A., "Benefits and Technological Impacts of the Future ATM Scenario for Civil and Military Aircraft", *10th Conference of Research and Education in Aircraft Design*, Brno, Czech Republic, 2012

[4] Eurocontrol DCMAC, "Introduction to Mission Trajectory", EUROCONTROL Headquarters 96 Rue de la Fusée B-1130 Brussels, Belgium, 2010.

[5] SESAR Joint Undertaking, "WP9 – Aircraft Description of Work (DoW)", Version 4.0, SESAR Joint Undertaking Avenue de Cortenbergh 100-B-1000 Brussel, Belgium, 2008

[6] Eurocontrol DCMAC, "Initial 4D - 4D Trajectory Trajectory Data Link (4DTRAD) Concept of Operations", EUROCONTROL Headquarters 96 Rue de la Fusée B-1130 Brussels, Belgium, 2008.

[7] RTCA SC-214 EUROCAE WG-78 "Data Communications Safety and Performance Requirements - Version I", RTCA ,Inc. 1828 L Street, NW, Suite 805, Washington, DC 20036-5133, USA 2011

[8] Eurocontrol Experimental Centre, "Flight Deck

User Requirements for Airborne Spacing (Sequencing and Merging)" Volume 1 Version 2.3, EUROCONTROL Headquarters 96 Rue de la Fusée B-1130 Brussels, Belgium, 2006

[9] DFS, Eurocontrol, "Sequencing & Merging Simulations – Final Report" Volume 1 Edition 1.0, DFS Deutsche Flugsicherung GmbH Forschungszentrum / Research Center Am DFS-Campus 5 D-63225 Langen, Germany

[10] Eurocontrol CMAC/ATM, "Mission Trajectory Detailed Concept in SESAR", EUROCONTROL Headquarters 96 Rue de la Fusée B-1130 Brussels, Belgium, 2012

Towards Optimized Profile Descents at Malta International Airport through Revised Approach Procedures

Matthew Micallef and Kenneth Chircop
Department of Electronic Systems Engineering, University of Malta, Malta

David Zammit-Mangion
Department of Electronic Systems Engineering, University of Malta, Malta
School of Engineering, Cranfield University, UK

Andrew Sammut
Department of Electronic Systems Engineering, University of Malta, Malta

Keywords: *trajectory optimisation, SIDS, STARS, PBN, OPD*

Nomenclature

ADS-B = Automatic dependent surveillance-broadcast
AIP = Aeronautical information publication
AMSL = Above mean sea level
ARP = Aerodrome reference point
ATC = Air traffic control
ATCO = Air traffic control officer
BADA = Base of aircraft data
CI = Cost index
CO_2 = Carbon dioxide
FAF = Final approach fix
FMC = Flight management computer
FTE = Flight technical error
GNSS = Global navigation satellite system
GRIB = General regularly-distributed information in binary form
IAF = Initial approach fix
IF = Intermediate fix
ICAO = International civil aviation organization
IFR = Instrument flight rules
ILS = Instrument landing system
LMML = ICAO CODE for Malta International Airport
MCDU = Multifunctional control display unit
MIA = Malta International Airport
NCEP = National centers for environmental prediction
NOTAM = Notice to airmen
OPD = Optimal profile descent
PBN = Performance based navigation
PDF = Probability density function
RF = Fixed radius
RNAV = Area navigation

RNP	= Required navigation performance
RNP-AR	= Required navigation performance authorization required
SID	= Standard instrument departure
STAR	= Standard instrument arrival route
TF	= Track to fix
TOD	= Top of descent
VFR	= Visual flight rules

Abstract

Traditionally, aircraft descend from cruise level towards the aerodrome in a stepped manner as directed by Air Traffic Control to ensure safe separation between aircraft, particularly in the terminal area. A descent methodology that is now being preferred is that of optimised profile descents (OPD). In OPDs, the aircraft descends from the top-of-descent (TOD) point towards the aerodrome following a smooth, continuous descent profile that is optimal from an operational perspective of choice, until it intersects the final approach glide path such as that of the Instrument Landing System (ILS). OPDs are advantageous because they consume less fuel and generate fewer emissions than their stepped counterparts.

This paper presents a proposal of new approach procedures for use in the approaches to Malta International Airport (MIA) that will facilitate the introduction of OPDs. With around 28,000 aircraft movements per annum at MIA, this can be achieved by giving Air Traffic Control Officers (ATCOs) a selection of approach procedures on which to direct in-trail inbound and outbound aircraft without imposing altitude constraints. The discussion includes a study of current procedures, a statistical analysis of historical radar plots, the presentation of the proposed approaches, and a forecast of the potential gains in terms of fuel burn and emissions expected through fast-time simulation.

1 Introduction

Malta International Airport (MIA) is a small to medium sized airport having a peculiar characteristic in that the overwhelming majority of flights operate via north-westerly routes overflying western Sicily. The work associated with this paper has been carried out within the CLEAN-FLIGHT project, a research project funded by the Maltese National Research & Innovation Programme involving the University of Malta and QuAero Ltd., an aerospace consultancy company focusing on aircraft operations. The project aims to lead the way to the introduction of optimal approaches to and departures from MIA for the reduction of greenhouse gases in the Maltese airspace.

The work presented in this paper follows on earlier work in which the methodologies associated with the design of standard instrument departures (SIDs) and standard arrival routes (STARs) for the Maltese airspace have been presented [1]. In this paper, new approach procedures for runways 13 and 31, which are the two most heavily used runways, are presented. These runways are equipped with Instrument Landing Systems (ILS) certified to CAT I, but flight checked to CAT II standards [2]. An in-depth study that has been conducted to quantify the economic and environmental gains expected with the adoption of the proposed procedures is also discussed.

2 Performance Based Navigation

There is a global initiative to improve the efficiency of aircraft operations whilst still ensuring safety, regularity, expedition and sustainability. The implementation of the performance-based navigation (PBN) concept has been recognized as a key enabler to improved flight efficiency, as identified by major programmes such as NextGen in the US and SESAR in Europe [3].

PBN incorporates the area navigation

(RNAV) and the required navigation performance (RNP) concepts. RNAV is defined as a method of instrument flight rules (IFR) navigation that permits aircraft operation on any desired flight path within a particular navaid coverage zone. RNAV has been further improved through the introduction of RNP procedures, which use the Global Navigation Satellite System (GNSS) and on-board technology to monitor in real time the aircraft position and the achieved navigation performance. PBN allows aircraft to fly three dimensional routes in the most flexible and accurate way currently considered possible. ICAO Doc 9613 states that: “The PBN concept represents a shift from sensor-based to performance-based navigation” [4]. PBN routes are defined by the minimum required navigation performance in terms of accuracy, integrity, availability, continuity and functionality required for operation within a given airspace.

One of the key-enablers of the PBN concept is the capability that allows the aircraft to fly a predefined ground track with consistency, predictability and reliability and in different weather conditions. The fixed radius (RF) leg manoeuvre is an integral part of flying such a predefined ground track, as it allows aircraft to follow a circular track defined by a constant radius traversing from an initial fly-by waypoint to another fly-by waypoint [5].

In PBN, turns can also be performed through the connection of three waypoints using track to fix (TF) segments. For fly-by waypoints, the flight management computer (FMC) calculates the turn anticipation distance required to connect to the following leg based on the current ground speed, the programmed bank angle and the change in track required. From observation studies conducted by the MITRE Corporation of the United States, it has been shown that due to different implementation of standards adopted by the FMC, aircraft compute the anticipation distance for TF-TF legs differently. This results in variations in the flight paths followed when executing such a turn [6]. This lack of accuracy and predictability compromises the concept defined by PBN and is an issue when predicting the optimal flight path, particularly in 4D navigation.

In another study for turns using the RF leg, also carried out by MITRE Corporation [7], it was concluded that an aircraft established on the tangential path leading to a RF turn will have a flight technical error (FTE) that falls within the limits provided by the relevant RNP. The FTE represents the extent of the ability of the aircraft guidance system to follow the flight path defined within the navigational database. Lateral conformance was also proven when RF turns were performed in the presence of a tail wind. The authors of [6] suggest that turns in the terminal area should be defined using the RF legs when possible, due to the accuracy and predictability associated with such procedures being greater than that of turns performed using TF-TF segments. The accuracy provided by the RF turn makes it suitable for use in the design of PBN routes.

Currently, use of RF legs is limited to aircraft with FMCs that are approved for Required Navigation Performance Authorization Required Approach (RNP-AR APCH) navigation. However, ICAO is working towards establishing an RNP Advanced Navigation System incorporating the RF leg without the need of an authorization approval [3]. RNP-AR APCH is a navigation method that allows a higher level of navigation performance with the improved capacity to solve accessibility problems to airports located in environments with complex obstacles. This is possible due to the precision, integrity and functional capacities of the equippage of RNP-AR APCH approved aircraft. The high precision provided by this type of approach is ensured by redundant systems through dual GNSS sensors, dual FMS systems, dual air data systems, dual autopilots and a single inertial reference unit [8].

3 Problem Definition

The Boeing 737 and Airbus A320 aircraft families constitute the large majority of the traffic flying in and out of MIA (ICAO code LMML). Although the flight management systems (FMSs) installed on such aircraft are capable of computing an appropriate TOD point for a particular cost index (CI) and upper wind forecasts, the computation, being aircraft centered, does not include considerations such as ATC constraints and aircraft separation. When air traffic controllers instruct changes in headings, altitude, and speed in order to maintain adequate separation from other aircraft, the actual route flown, deviating from that planned by the FMS, becomes inefficient in terms of fuel and carbon emissions [9].

The effect of this limitation is further aggravated by the fact that LMML lacks published arrival routes, making it more difficult to plan and implement optimal descents. The lack of arrival routes causes dispersion in the flight paths followed by aircraft flying towards the final approach fix, with the result that sub-optimal trajectories are being followed both laterally and vertically. The trajectories followed may include lateral extensions and stepped descents due to the lack of planning strategies, which, in turn, result in an increase in the fuel burn and emissions.

The initial approach into Malta International Airport can be performed under either VFR or IFR, with the final approach on the main runways often being performed with the aid of the ILS. Recently, Malta's AIP was updated with a number of RNAV waypoints forming a T-bar structure for the main runways as seen in Fig. 1 [2]. These waypoints give both pilots and air traffic controllers additional flexibility to support the better planning of a descent. They are used by ATC to issue direct clearances to arriving traffic to one of the fly-by waypoints before intersecting the final approach fix. However, the inherent limitation of fly-by waypoints still causes dispersion in the tracks flown when approaching the ILS glide slope. The variation in the flight paths followed during the approach is mainly noticed from the recordings of aircraft performing the base turn.

The design of accurate and predictable flight paths is required as the first step towards optimized profile descents into LMML. In this paper, the revised approach routes at a strategic level are presented for runway 13 and runway 31. A new STAR, named EKOLA 1A, is proposed for arrivals from the entry point EKOLA, which is situated to the the north-west of Malta (Fig. 2).

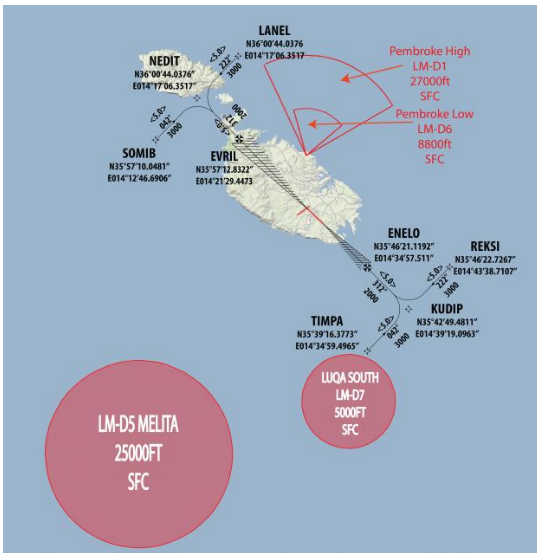

Fig. 1 The current T-bar approaches to runways 13 and 31 at LMML [2].

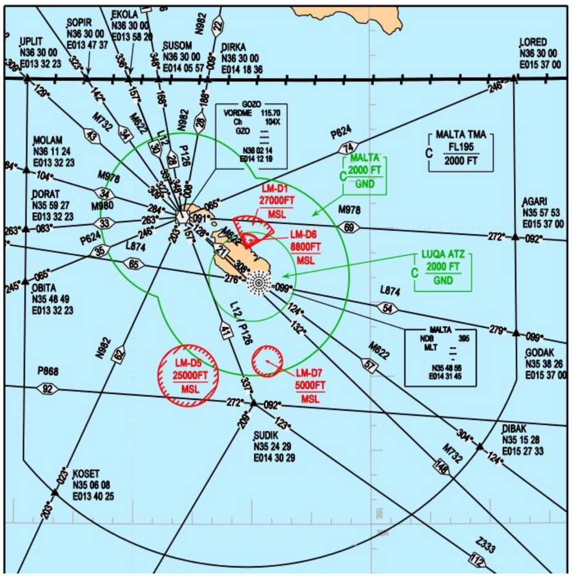

Fig. 2 Malta's Terminal Area [2].

This STAR is connected to one of the new proposed approaches to runway 31 and, through statistical analysis of actual recorded arrival trajectories, the maximum gains that could be achieved by following the proposed new route path are identified and presented as the potential gains in terms of reduction of track miles flown, reduced fuel burn and emissions.

4 Design Methodology

ICAO document 9905 (Required Navigation Performance Authorization Required (RNP AR) Procedure Design Manual) [10] was used as the guideline document to design the new instrument approaches to LMML and to connect entry points to the final approach fix, thus utilizing the expected aircraft RNP capabilities to the greatest extent.

In line with the methodology of [1], the entry points around LMML were connected directly to an initial approach fix. For changes in track of up to 90 degrees between one segment to the next, the turn was designed through TF-TF segments. In the case of turns requiring a track change greater than 90 degrees (typically base turns), these were designed using the RF leg.

Section 3.2 of ICAO Doc 9905 identifies two methods for finding the tailwind component when calculating the turn radius, namely either by using a standard tail wind component as given in Table 3-2(a) in that document, or by using statistical winds [10]. In this work, the tail wind at various altitude intervals was analysed in a statistical manner, thus avoiding the need to use over-conservative values. This approach ensures the design of the tightest RF turn for the expected range of meteorological conditions.

The Malta International Airport Meteorological Office does not currently perform radiosonde launches and only provides surface weather data from various locations around the Maltese islands. The upper winds are currently being obtained through a service provider and this data is then passed on to ATC. The meteorological data used for the analysis of the tailwind component was obtained from the National Centers for Environmental Prediction (NCEP) Climate Forecast System, which provides a six hour forecast, four times per day. Forecasts from 1st January 2005 to 31st December 2012, providing an 8 year history, were downloaded for this analysis. The forecast is provided in General Regularly-distributed Information in Binary 2 (GRIB2) format, which was decoded using *wgrib2*[1] and the *degrib*[2] software. The GRIB2 file stores forecast weather data in a grid format with a defined resolution for a number of isobaric levels. The files obtained to analyse the wind over Malta have a spatial resolution of 0.5° by 0.5° at altitudes corresponding to isobaric pressure levels ranging from 1,000mb to 1mb as well as at mean sea-level. The horizontal and vertical components of wind were also obtained at the aerodrome reference point (ARP) through a bi-linear interpolation of the forecast values at the edges of the sub-grid in which the ARP lies. The altitude above mean sea level (AMSL) for each isobaric level was calculated using the recorded mean sea level pressure and the temperature forecast at the interpolated isobaric level. For altitudes below the tropopause (i.e. below 11,000m), the geo-potential height above mean sea level h in meters was found using Eq. (1), where P_0 is the recorded mean sea pressure in hPa, P is isobaric pressure level in hPa and T is the forecast temperature in $°C$.

$$h = \frac{\left(\left(\frac{P_0}{P}\right)^{\frac{1}{5.257}} - 1\right) \cdot (T + 273.15)}{0.0065} \qquad (1)$$

ICAO Doc 9905 includes the minimum and maximum speeds for different aircraft categories allowed for when following a RF turn. An analysis on the collected wind data was performed to find the maximum forecast tail wind component expected for each possible track and for an altitude interval between the start and the end of the turn. A 3° glide slope from the aerodrome's threshold was assumed to determine the altitudes along the descent trajectory. The maximum tail wind found was then used to calculate the maximum bank angle

[1] Available at : http://www.cpc.ncep.noaa.gov/products/wesley/wgrib2/
[2] Available at: http://www.nws.noaa.gov/mdl/degrib/

that would be required to correctly follow the RF leg with a 2.5 NM radius as adopted in the current T-bar structure. This resulted in a bank angle of 20.7 degrees. Section 3.2.8 of ICAO Doc 9905, however, stipulates a maximum bank angle of 20 degrees for altitudes above 492ft AGL. In order to meet this constraint, a new turn radius needed to be identified. This was done by increasing the turn radius in steps of 0.1 NM, each time finding the altitude at the start of the turn and the associated altitude interval in the turn, the maximum expected tailwind component in this interval and the resulting maximum bank angle required by a CAT D aircraft[3] to perform the turn. This process was repeated until the maximum resulting bank angle with the minimum allowed indicated airspeed was less than 20 degrees.

The analysis of the tailwind was based on the wind speed and direction and the altitudes of the forecasts recorded within the analysed period. The winds were sorted by altitude in order to create a sub-list of wind forecasts within the altitude interval being analysed. The wind records within an altitude interval were then sorted out in ascending order in terms of wind strength. A 95% confidence interval was used to discard wind records with low and high wind speeds. For each possible track the maximum recorded speed for the said confidence interval was found and these were plotted on a wind rose at 1 degree intervals (Fig. 3). For each of the maximum wind speeds measured, the tail wind component for each possible track was calculated as suggested in [11]. The resulting maximum tail wind component for each possible track was calculated and this was also plotted on a wind rose (Fig. 4).

The tail wind component was found using Eq.(2) as suggested in [11], where V_{TW} is the tail wind component in *kts*, Θ_W is the wind direction in degrees and Θ_T represents the track followed by the aircraft in degrees.

$$V_{TW} = V \cdot cos(\Theta_W - \Theta_T - 180) \qquad (2)$$

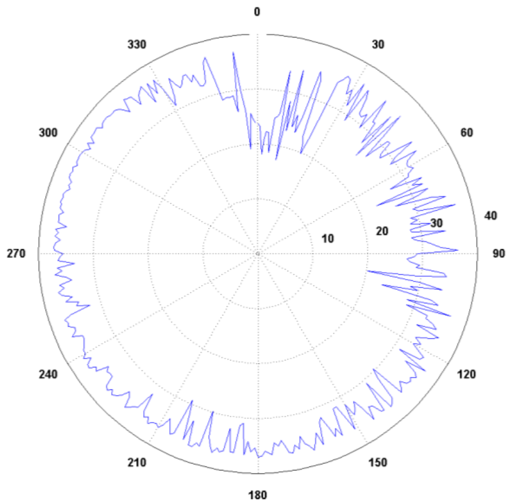

Fig. 3 Polar plot of the maximum wind speed (95% limit) over Malta at 1900-4800 ft AMSL between 1st January 2005 and 31st December 2012.

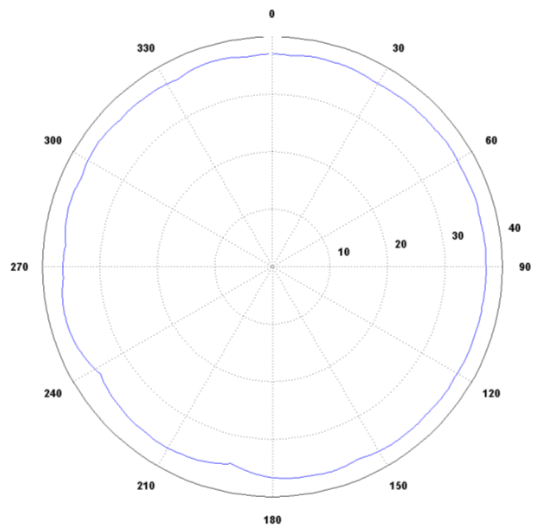

Fig. 4 Polar plot of the maximum tail wind component for each track at an altitude interval of 1900-4800 ft AMSL between 1st January 2005 and 31st December 2012.

For approaches requiring a 180 degree base turn to align the aircraft with the runway extended centreline, it was decided to start the turn abeam the final approach fixes EVRIL and ENELO

---

[3] Category D aircraft have a runway threshold speed (V_{at}) of between 141 kts and 166 kts.

shown in Fig. 1. To reduce the track miles flown to a minimum, the tightest possible turn radius had to be designed. To this effect, the process described above was used. The first attempt was to try to overlay the designed tracks on the existing T-bar structure shown in Fig. 1. The altitude intervals considered were 1,900 ft to 4,500 ft for runway 31 and 2,900 ft to 5,400 ft for runway 13. These altitude intervals were determined by applying a 3 degree glide slope from the runway threshold to the start and end of the RF turn respectively. The difference in the two intervals is due to position of the 13 and 31 FAFs with respect to the runway thresholds. For both intervals, the resulting maximum tail wind component was found to be 37 kts. ICAO Doc 9905 recommends that a CAT D aircraft performing a RF turn within the initial approach stage should have a minimum indicated airspeed of 210 kts. Converting this to true airspeed at 4,800 ft and adding a tail wind component of 37 kts, the maximum bank angle required to perform an RF turn with a radius of 2.5 NM was found to be 20.7 degrees. As explained, this bank angle just exceeds the maximum bank angle of 20 degrees suggested for RNP-AR equipped aircraft by ICAO Doc 9905. Using the incremental procedure described, a radius of 2.8 NM was found to satisfy the 20 degree bank angle limitation and therefore more suitable to connect the downwind leg to the final approach fix before intersecting the ILS glide slope.

A speed restriction of 210 kts was also introduced within the turn to ensure the aircraft does not exceed the 20 degree bank angle suggested by ICAO Doc 9905. This restriction is applied at the initial waypoint of each RF turn. It is relevant to note, however, that the maximum design bank angle allowed by ICAO Doc 9905 is conservative. Indeed, the Airbus A320 is capable of banking at an angle of 30 degrees while performing a RF leg [11]. The conservative bank angle adopted by ICAO Doc 9905 introduces an additional safety margin which, however, if not applied could result in a tighter RF turns to be flown at higher speeds. A tighter radius would reduce the total track distance flown and therefore could be considered advantageous at the cost of reducing safety margins, whilst a higher speed constraint would allow the aircraft to be flown in a clean configuration for longer before extending flaps to slow down [11]. Nevertheless, the conservative bank angle recommended by ICAO Doc 9905 was adopted in this work.

Once the turn radii were defined, the turns were connected to the relevant FAFs of the two runways. In order to obtain standardised approach patterns, IAFs were placed at least 2.5 NM upwind (parallel to the runway) from the respective turns. This distance was calculated to be that required to ensure an adequate minimum stabilisation distance between the RF turn and the IAF fly-by waypoint, following guidance material published by Eurocontrol [12]. The IAFs could then be connected to the different entry waypoints, which, in the case of this work, was EKOLA.

Holding patterns were added at the initial approach fixes (IAFs) to allow holding when required. This effectively also influenced the positioning of the IAFs, because holding patterns have 3-dimensional buffer zones around them that must not be traversed by other operational routes or holding points, etc. Given the extent of the lateral separations required, vertical separations, which, under current procedure allow for a minimum of 1,000 ft [13], were preferred. IAFs and associated holding points were consequently designed to ensure departing aircraft could procedurally be kept at least 1,000ft below the holding patterns. These holding patterns, of course, could compromise optimal flight profiles for both arriving and departing traffic but these have been introduced only with a view to provide an additional operational buffer to ensure separation should this be tactically required, with aircraft not normally requiring to hold. Indeed, the traffic density at LMML is low enough to rarely require arriving aircraft to enter a hold. In addition, it is envisaged that emerging ATM technologies based on 4-D PBN navigation will further reduce the need for their use. In this context, therefore, it has been considered acceptable for a hold pattern to also impact an outbound traffic by introducing an altitude constraint to keep it below the holding pattern

when the pattern is occupied by an inbound aircraft.
The minimum altitude of the holding points was set to 6,800 ft to ensure safe separation from the earth's surface (the holding points are all above the sea). The holding patterns were designed in line with the recommendation in Section 4-10 of ICAO Doc 9905, which suggests the inbound leg to be tangential to the start of the turn. They were also designed for RNAV equipped aircraft, using the design guidelines within ICAO Doc 8168 Vol II [14] and using a minimum RNP of 1. A design speed of 280 KIAS was used to define the turn radius of the holding pattern, which is the maximum allowed speed in turbulent conditions defined for holds below 14,000 ft. In line with ICAO Doc 8168 Vol II, a design bank angle of 23° was used to determine the turn radius, taking into account a tail wind components using estimated values calculated from Eq. (3) [14]:

$$w = 2h + 47 \tag{3}$$

where h is the altitude in thousands of feet and w is the tail wind in kts. The length of the parallel segments was calculated for a flight time of 1 min at 230 KIAS, which is the maximum IAS allowed in still air up to 14,000 ft in accordance with RNP holding design rules [12]. This equates to a true still air speed of 249.2 kts and results in a leg length of 4.15 NM.

5 The New Approaches

The proposed new approaches to runways 31 and 13 resulting from the discussed design methodology are presented in Figs. 5 and 6 respectively.

5.1 Approaches to Runway 31

For the approaches to runway 31 (Fig. 5), five IAFs have been identified, namely CEKCI for approaches from the north-east, CONAD for the south-east, ZERKI the south-west and MINDI and HARVY for approaches from the north-west, for the left-hand and right-hand downwind legs respectively. These IAFs have been located in such a way as to ensure adequate vertical separation between aircraft using adjacent arrival and departure routes whilst assuming a 3 degree descent gradient. The right-hand IAF (HARVY) is further upwind than its left-hand counterpart (MINDI) due to there being more arrival routes from the west (not shown in Fig. 5), requiring merging at a point further downwind on the left-hand circuit.

Two T-bar structures for runway 31 have been designed, one having the existent waypoint ENELO as the FAF, 5.3 NM from the runway threshold, and having the newly designed XERRI 3.14 NM further out. The waypoints PALMA, MOLLY, EREND and FARUN, all situated 5.6 NM laterally from their respective FAF, complete the T-bar structures, thus allowing for a 2.8 NM radius turn to be initiated at these waypoints to bring the aircraft aligned with the runway extended centreline at the respective FAF. The two T-bar structures have been implemented to facilitate traffic separation, in the event an extended downwind leg would be required. Indeed the outer T-bar structure results in an extension of the approach by 6.2 NM with respect to the shorter (inner) approach pattern, which, at a nominal speed of 180kts, translates to an extension of just over 2 minutes in flying time.

The north-easterly and south-westerly approaches are designed to merge with the paths of the inner T-bar structure, thus ensuring the shortest possible ground track to be flown. Accordingly, IAFs CECKI and ZERKI are followed by IFs DELLY and FERGI respectively, both situated at the apex of the base turn of the north-westerly approaches.

The south-easterly approach is straight-in, requiring no IF past the IAF CONAD, but XERRI, designed for the outer T-bar structure, also acts as the IF for this approach route.

Fig. 5 illustrates the danger zones LM-D1 and LM-D6 to the north of the airfield. These are activated by a NOTAM [2], making the right hand down wind route temporarily unavailable. This is already the procedure adopted by ATC in Malta. Likewise, when danger zones LM-5 and LM-D7, situated to the south-west of the airfield, are active, arrivals will not be allowed via ZERKI and traffic will need to be re-routed.

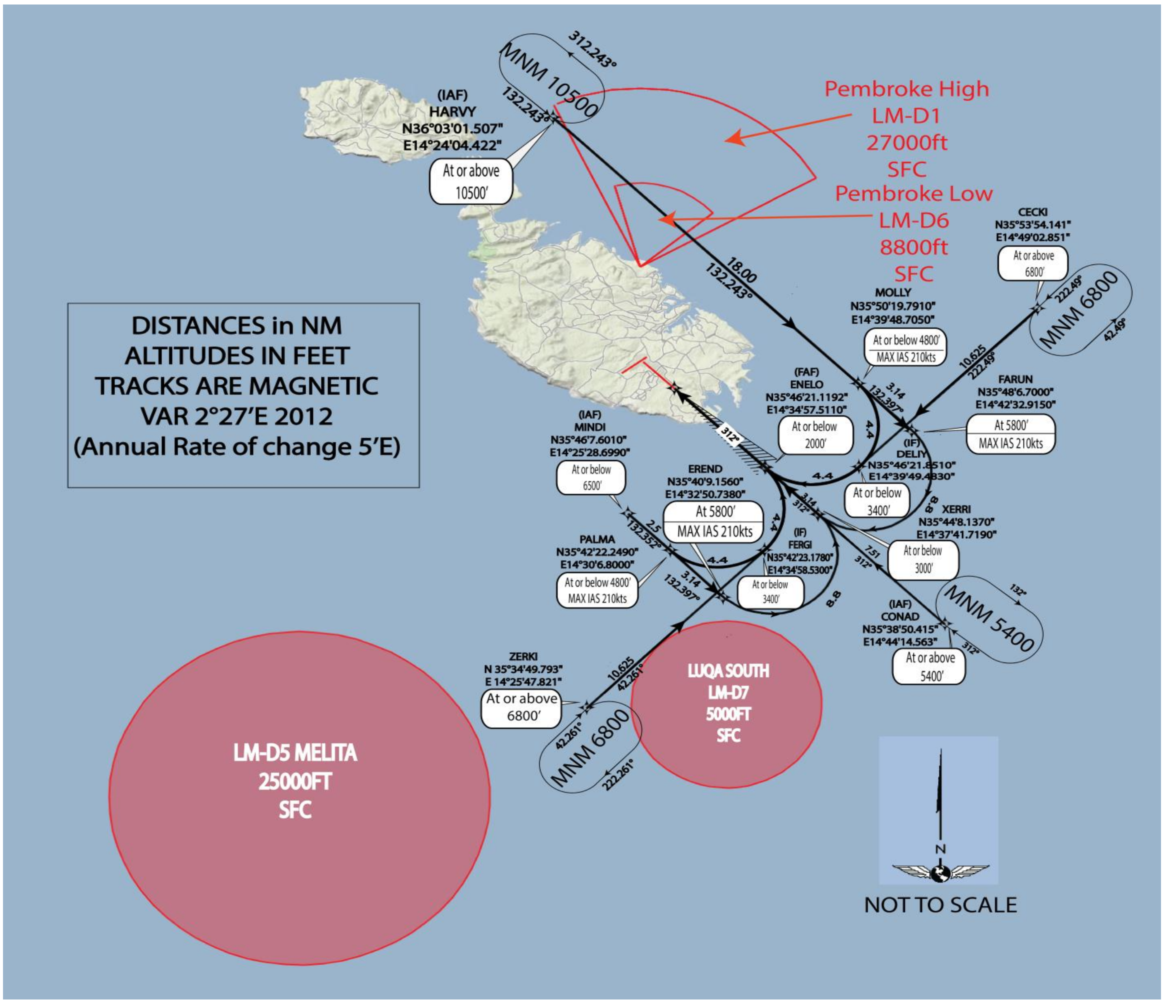

Fig. 5 The proposed revised approach routes to runway 31.

Holding patterns were placed at the IAFs, except at MINDI when runway 31 is use and DEXER when runway 13 is in use. In the latter cases, holds were designed within the STARs connecting to these IAFs. The IAFs having a holding pattern were geographically placed such as to allow aircraft to proceed to the next waypoint by maintaining a continuous descent with a glide path of 3°, equivalent to a descent rate of 320ft/NM. On the other hand MINDI and DEXER were placed 2.5NM away from the start to the RF turn. This distance was calculated using the formula for the minimum distance allowed between a fly-by turn and a fixed radius turn as specified in [12], which would allow an aircraft with an indicated airspeed of 250 KIAS to make a track change smaller or equal to 90° to intercept the track which aligns aircraft tangentially to the start of the RF turn.

5.2 Approaches to Runway 13

For the approaches to runway 13 (Fig. 6), six IAFs have been designed. These are FERRO and DEXER for approaches from the north-east, JOLLY and SERRA for the south-east (left hand and right hand downwind circuits respectively), CUBAN the south-west and QUEEN for straight-in approaches from the north-west.

Two approaches are provided for the north-east primarily so that arrivals could be routed via DEXER instead of FERRO when danger zone LM-D1 is active. In contrast with the design for runway 31, only one T-bar structure has been designed for runway 13. This is primarily because arrivals from the south are not very common and as a result it is considered that extended downwind legs will rarely be required.

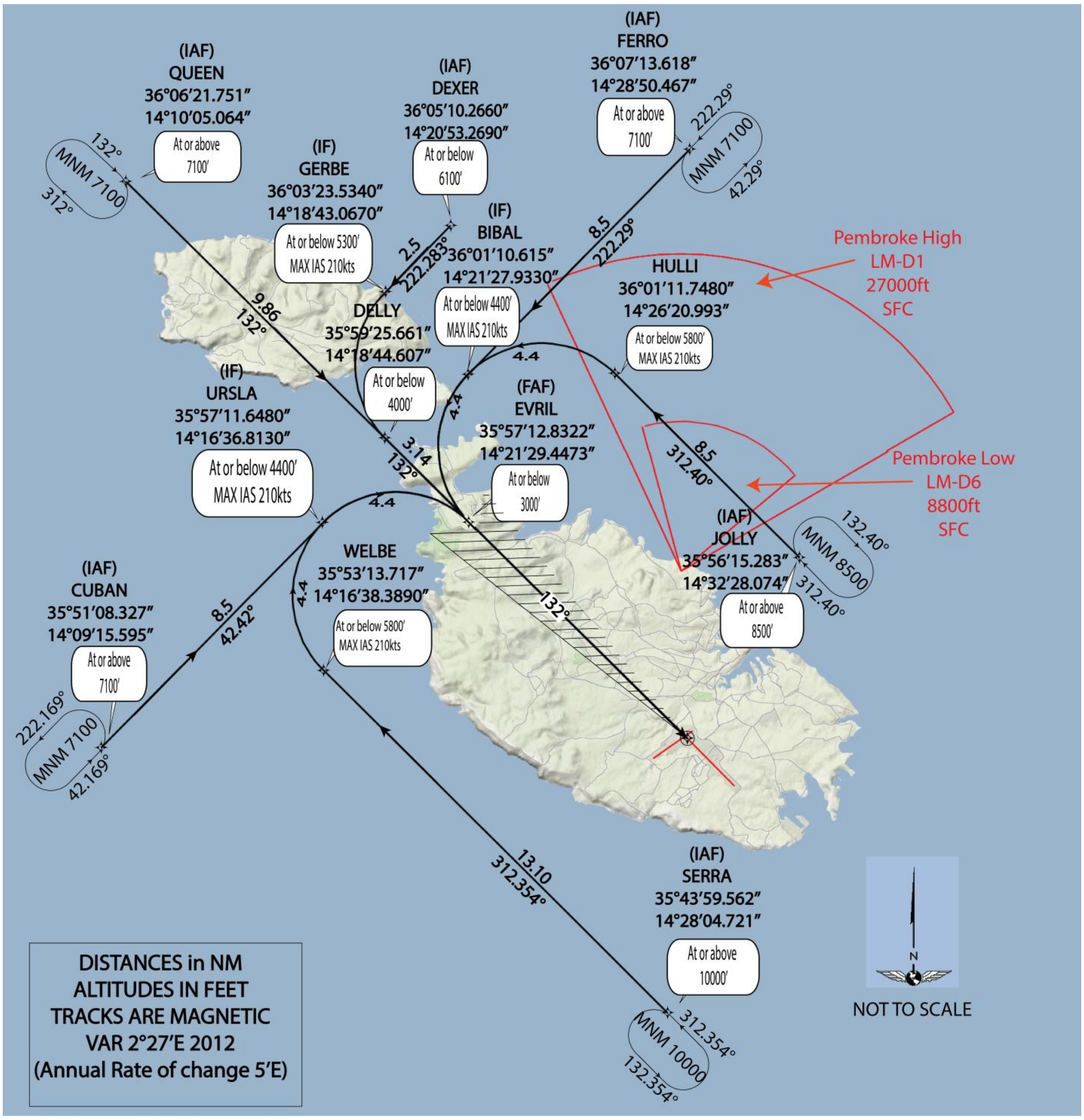

Fig. 6 The proposed revised approach routes to runway 13.

As for the approaches to runway 31, the north-easterly and south-westerly approaches have been designed to merge with the paths of the T-bar structure, thus again ensuring the shortest possible ground track to be flown. Accordingly, IAFs KUBAN and FERRO are followed by IFs URSLA and BIBAL respectively, both situated at the apex of the base turn of the south-westerly approaches. The IF GERBE follows the IAF DEXER.
Holding patterns were again placed at the IAFs, except at DEXER.

6 The EKOLA 1A STAR

The analysis presented in this paper focuses on arrivals from the EKOLA entry point, landing on runway 31 after flying a right hand downwind leg over the eastern coast of the island from HARVY to MOLLY, turning in to fly by the IF DELY and intercepting the ILS from the right. Consequently, this paper also presents a proposal of the EKOLA 1A STAR, (Fig. 7). From EKOLA, a track of 137.6° (Magnetic) leads directly to the HARVY IAF, 34 NM away. Combined with the HARVY approach via DELIY (ie: using the inner T-bar structure), the EKOLA 1A STAR results in 65.37 track miles (NM) from the entry point to the runway threshold.

7 Quantification of Gains

Quantification of the economic and environmental gains that can be achieved with the introduction of the proposed procedures can only be performed against a reference baseline. The reference baseline chosen was the actual paths taken by aircraft flying in via EKOLA and landing on runway 31 via a right-hand downwind leg. To this extent, the Kinetic SBS-3 ADS-B receiver, which decodes ADSB transmissions transmitted on Mode-S (1090MHz) was used to log the trajectories flown by aircraft as they approached the runway to land. This allowed the reconstruction of the trajectories flown by each aircraft logged which, in turn, enabled the determination of the track miles of each trajectory flown. The ADS-B receiver used has a coverage range of 200 NM, making it suitable to analyse the descents from the top of the descent (TOD) point down to the moment of touchdown. The ADS-B receiver outputs a data stream of the decoded Mode-S signal, including the aircraft call sign, altitude, ground speed, track, latitude, longitude, vertical rate, squawk code and a flag that indicates whether the aircraft is airborne or otherwise. The receiver outputs the data stream for each aircraft at a base rate of, on average, 1Hz.

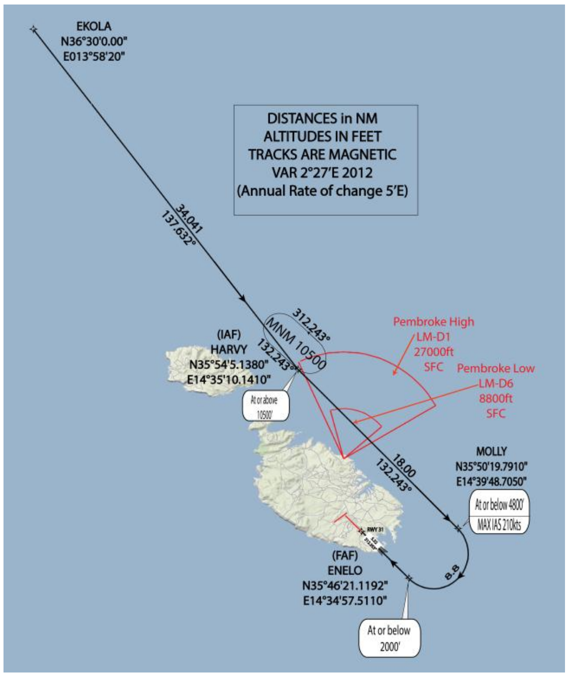

Fig. 7 The proposed EKOLA 1 STAR and arrival route for runway 31 via HARVY and DELIY (not shown).

The data stream was processed with software developed in JAVA and this facilitated the organisation of the recorded trajectories into separate files held within folders for each day. Lateral profiles are reconstructed using the logged geographic location given by the latitude and longitude, while vertical profiles are reconstructed using the recorded altitude and timestamp.

The constructed trajectories were then processed in Matlab®. Processing included filtering of data, which was necessary due to ADS-B transmission outages and other log discontinuities that resulted in unusable records. As the ADS-B receiver receives transmissions of all aircraft, the filtering also facilitated discrimination between aircraft approaching LMML and all other traffic, including en-route aircraft and aircraft outbound from LMML. In order to reduce memory space and processing time, the ADS-B logs were then reformatted so that successive records were only stored if the aircraft track changed by half a degree, as intermediate points proved redundant.

Analysing the logged trajectories, it became evident that aircraft often do not overfly the entry points, but tend to fly past them, often having a lateral displacement of several miles. In the new proposed STAR, however, it is assumed that the aircraft will overfly the entry point EKOLA. Consequently, it was necessary to 'normalise' the recorded trajectories so that a fair comparison in track miles flown could be made with the EKOLA 1A STAR. This normalisation involved identifying, for each logged flight, the point where the base turn started and this was used as the centre of a circular arc that passed through EKOLA. Then, the start of the arrival for the recorded flight was taken to be the intersection point between this arc and the actual trajectory flown. This effectively generated an arrival path equal in length if the aircraft had actually flown over EKOLA. Thus a fair comparison between the track miles flown in the proposed new STAR EKOLA 1A (65.37 NM) and the logged flights could be made.

The baseline trajectories from each entry point were plotted to display the lateral profiles flown by logged flights, as seen in Fig. 8. Trajectories that were identified to have followed a longer route due to lateral vectoring or having flown a hold pattern were discarded, as this would have skewed results. Trajectories that were identified to exhibit any errors, including offsets in the reported positions were likewise considered as outliers and discarded. Trajectories that exhibited gaps in the timestamp were further scrutinised and their correct trajectories were reconstructed only if the time gap between the records occurred at altitudes above 10,000 ft. Otherwise they were discarded. This was done because it could be fairly assumed that above 10,000ft, the aircraft would be flying at constant CAS, allowing the fuel burn to be correctly estimated.

8 Results and Discussion

The analysis included in this paper is based on trajectories recorded from the 22nd of March until the 24th of June 2013. From the trajectories recorded, 135 arrivals from EKOLA landing on runway 31 via a right-hand downind leg were extracted and these baseline trajectories were plotted as seen in Fig. 8. The associated track miles flown were also calculated for each trajectory. On no flight was any danger zone active and all flights flew direct to REKSI, the current RNAV waypoint that forms part of the T-bar structure for the approach to runway 31 (Fig. 1). The variation (dispersion) in the paths followed by aircraft is clearly visible in the trajectories plotted in Fig. 8. This is also captured in the histogram of the track miles flown (Fig. 9), which indicates the number of track miles that could have been gained had the aircraft followed the proposed EKOLA 1A STAR and HARVY arrival route. The variaiton in paths is primarily associated with the fact that there are no established arrival routes leading to the T-bar approaches and aircraft follow trajectories at the flight crew's discretion .

Of the 135 normalised flights recorded, 74 (54.8%) exhibited a longer trajectory than the proposed new STAR EKOLA 1A, indicating that savings could be made with the introduction of the new procedure. The remaining flights will have flown tighter base turns, as evidenced in Fig. 8. It is probable that visual approaches would have been made on these flights, a common practice in Malta, given the extent of good weather the island enjoys. This, naturally, allows pilots to fly with less leeways than standard instrument approach procedures allow for, and naturally distracts from the overall gains that can be achieved. However, for optimal descent approaches, the track miles to be flown need to be known prior to top of descent in order to plan the vertical profile too besides the plan path. Given that the proposed procedure results in the shortest track miles path that can be formally published to ensure safe operation in all expected operating conditions, it does offer savings and improvement over current procedure. Furthermore, it is not envisaged that OPDs will be operationally planned based on visual approaches that fly tighter base turns than those published.

The shortest normalised recorded trajectory had a total of 57.3 track miles (NM) to the runway threshold, 8.1 NM shorter than the proposed route. The longest was 79.9 NM, 14.6 NM longer than the proposed route. When all paths were analyzed, the average track miles flown were found to be 66.9 NM, 1.5 NM more than the proposed trajectory. This means that, if all flights were to follow the proposed new route (EKOLA 1A STAR and the HARVY approach via DELEY), an average of 1.5 NM on each flight would be saved.

Assuming that flights flying shorter tracks than the proposed STAR and approach were flown under VFR (61 of the 135 recorded flights), these would probably also not have followed the proposed route once operational and another analysis can be made with these flights ignored, focussing only on those flights that would have benefited from the new procedure. Results show that these latter flights flew, on average, 70.57 track miles. This means that these flights would, on average, benefit from a 5.2 NM reduction in the total track miles flown had they followed the new proposed route.

The vertical profiles of the recorded flights were also generated from the recordings and these are plotted in Fig. 10. Aircraft that exhibit a longer trajectory than the new proposed procedure appear to have a tendency of arriving higher than those trajectories that flew shorter trajectories. This is reasonable, as aircraft that remain high for any reason will need to extend their flight path to intercept the glideslope correctly. This extension is typically implemented in the form of an extended downwind leg.

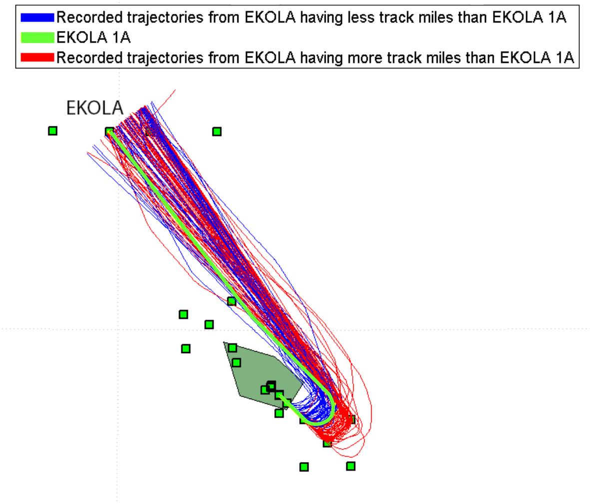

Fig. 8 Recorded trajectories over the period 22nd March 2013 to 24th June 2013 and the proposed new EKOLA 1A STAR and HARVY arrival route.

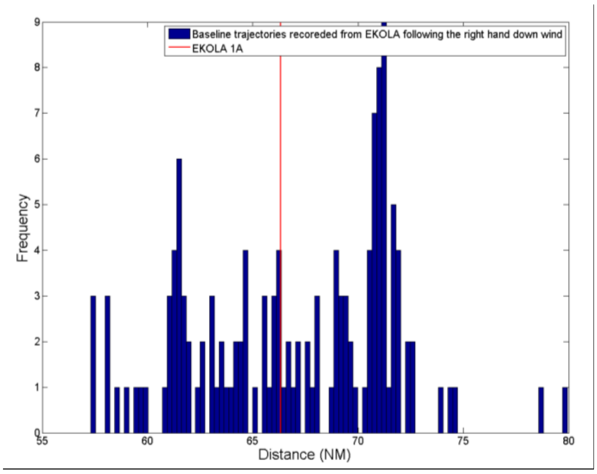

Fig. 9 Histogram of the total track miles flown in the recorded trajectories arriving from EKOLA (22nd March 2013 to 24th June 2013).

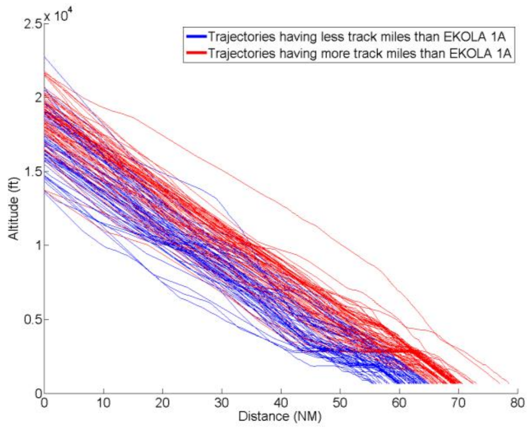

Fig. 10 The vertical profiles of the recorded trajectories arriving from EKOLA (22nd March 2013 to 24th June 2013).

Whilst Fig. 10 indicates that there are a number of flights that descended early to have segments of shallow glides or level flight whilst others that have had stepped descents, for the purpose of the quantification of gains in terms of fuel burn (and ensuing CO_2 emissions), it was assumed that the extra track miles were flown at cruise altitude. Whilst this simplified the assessment, it results in conservative estimates, as flying at lower altitudes would result in higher fuel burn. As a comparison, the analysis was repeated with the assumption that all the extra distance was flown at 3,000ft which, of course, then resulted in optimistic forecasts of savings.

Since the logged trajectories did not contain information on aircraft type, gains had to be calculated using the fuel consumption of a typical aircraft. Single aisle aircraft the size of the Airbus A320 and Boeing 737 families constitute the large majority of the traffic flying in and out of Malta and conseqeuntly the A320 was chosen for the analysis. To this extent, the BADA Revision 3.7 performance files of the A320 with CFM-56 engines at nominal weight (64,000kg) were used for all calculations.

The histograms of the potential fuel savings that could have been achieved by the 74 flights were the extra track miles not flown are shown in Fig. 11 and Fig. 12.

In Fig. 11, results are based on the assumption that the savings were achieved at cruise level. The calculations have been made using the ground speed recorded on each flight, which allowed the estimation of the reduction in flight time that would have resulted had the flight been flown on the proposed STAR/arrival route combination. Using the fuel flow data for cruise from the BADA performance files, the total fuel that would have been saved was then calculated for each flight.

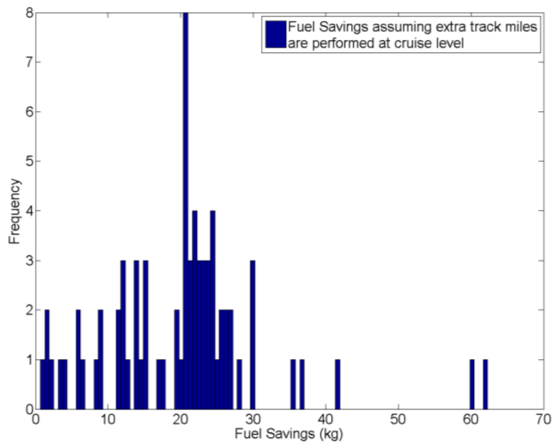

Fig. 11 Histogram of the potential fuel savings of the recorded flights, assuming that the reduction in track miles is gained at cruise level.

In total, for the 74 trajectories that could have benefited from the shorter suggested route, 1,487 kg of fuel would have been saved if the extra distance was not flown at cruise level. This corresponds to an average saving of 20.1 kg per flight. Given that 3.15 kg of CO_2 are produced for every 1kg of jet fuel burned [15], every flight, on average, would then have benefited from a reduction of 63.3 kg of generated greenhouse gases.

Fig. 12 shows the histogram of the same analysis were the savings in track miles flown to be made at 3,000 ft.

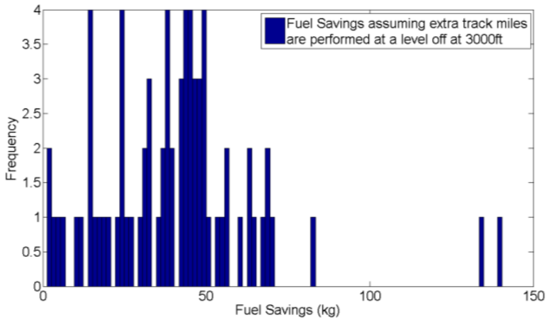

Fig. 12 Histogram of the potential fuel savings of the recorded flights, assuming that the reduction in track miles is gained at 3,000 ft.

In total, the same 74 flights would have benefited from a reduction of 2,991 kg in fuel burn, which corresponds to an average saving of 40.4 kg per flight. This, in turn, corresponds to an average reduction of 127.3kg of CO_2 generated per flight.

Using these results, it is interesting to consider the total impact the introduction of the EKOLA 1A STAR used in conjunction with the proposed arrival routes for runway 31 could have on all traffic. In an unpublished study carried out by the authors, it was found that about 40% of all traffic tend to arrive from EKOLA and land on runway 31. Taking the 135 trajectory records logged in this study as typical, 54.8% of all flights could be expected to benefit from a reduction in track miles flown. Considering then that Malta International Airport experiences just under 15,000 arrivals of scheduled and un-scheduled flights (ie: excluding cargo, mail and general aviation) annually [16], it can be expected that around 3,300 flights would benefit from the proposed new route annually. This would amount to a total fuel saving of the order of 65 tons were the gains made at cruise altitude, corresponding to a saving of over 200 tons of man-made greenhouse gases annually. Were the savings to be exploited from 3,000 ft, the corresponding values would be about 130 tons and 420 tons respectively. This, of course, assumes no further gains due to the introduction of OPDs, which is where the major gains can be expected to be achieved.

9 Conclusion

This paper presented, at a strategic level, a proposal for revised approach routes for the main runways (31 and 13) at Malta International Airport (LMML). These approach routes have been designed to allow aircraft to fly the shortest possible routes into Malta, with the intention of increasing the repeatability of the path followed by the aircraft over current levels, thus ultimately leading to reduced fuel burn and emissions. To achieve this, fixed radius (RF) turns were used for base turns, whilst TF turns were allowed where heading changes of less than 90° were required.

In order to obtain an indication of the improvement the new proposed routes could be expected to bring about, an experiment was designed in which trajectories of actual flights arriving from the north-west (via EKOLA) were recorded using an ADS-B receiver and compared to the the standard track of the new proposed route. The analysis focused on the amount of track miles reduced and associated reduction in fuel burn and CO_2 emissions that could be expected were the inbound aircraft to follow the route proposed in this work. The results show that a small but significant gain can be achieved. Greater benefits can, of course, be expected with the implementation of ODPs in conjunction with the proposed route and this work lays the foundations to facilitate aircraft to accurately plan such profiles as a step towards greater gains in the reduction of fuel burn and CO_2 emissions in the approaches to Malta International Airport.

Acknowledgments

The work presented in this paper was conducted as part of the CLEAN-FLIGHT project which is financed by the Malta Council for Science and Technology through the National Research and Innovation Programme 2011 (Grant Agreement R&I-2011-021). The authors also wish to acknowledge the contributions of QuAero Ltd., partners in the project.

References

[1] Micallef M., Zammit-Mangion D., Chircop K. and Muscat A. "A proposal for revised approaches and procedures to Malta International airport", *Proceedings of the 28th Congress of the International Council of the Aeronautical Sciences (ICAS), Brisbane,* ICAS, 2012. ISBN 978-0-9565333-1-9.

[2] *Aeronautical Information Publication (AIP) Malta*, 4th ed., Civil Aviation Directorate, Transport Malta, Malta, 2012.

[3] Miller S. and Bruce J., "Integration of the "constant radius arc to a fix" (RF) navigation leg type into NextGen", *Proceedings of the 30th Digital Avionics Systems Conference*, *Seattle, WA*, Institute of Electrical and Electronic Engineers (IEEE), 2011.

[4] *Doc 9613 AN/937 – Performance-Based Navigation (PBN) Manual*, 3rd ed., ICAO, Montreal, 2008.

[5] *ARINC Specification 424-19 - Navigation System Database*, Aeronautical Radio, Inc., Annapolis, MD, 2008.

[6] Herndon, A.A., Mayer, H.R., Ottobre, C.R. and Tennille, F.G, "Analysis of Advanced Flight Management Systems (FMSs)", The MITRE Corporation, McLean, VA, 2006. Also available at: http://www.mitre.org/work/tech_papers/tech_papers_06/06_1013/06_1013.pdf Accessed on 30/8/2013.

[7] Herndon, A.A., Cramer, M. and Sprong, K., "Analysis of advanced Flight Management Systems (FMS), Flight Management Computer (FMC) field observations trials, Radius-to-Fix path terminators", *Proceedings of the 27th Digital Avionics Systems Conference, Saint Paul, MA,* Institute of Electrical and Electronic Engineers (IEEE), 2008.

[8] Medeiros, M.C.D, Silva, M.R.J. and Bousson K., "RNAV and RNP AR approach systems: the case for Pico Island airport", *Int. J. of Aviation Management*, Vol.1, No.3, 2012, pp.181 – 200.

[9] Coppenbarger R., Dyer G., Hayashi M., Lanier R., Stell L. and Sweet D., "Development and testing of automation for efficient arrivals in constrained airspace", *Proceedings of the 27th Congress of the International Council of the Aeronautical Sciences (ICAS)*, Nice, ICAS, 2010. ISBN 978-0-9565333-0-2.

[10] *Doc 9905 AN/471 – Required Navigation Performance Authorization Required (RNP AR) Procedure Design Manual*, 1st ed., ICAO, Montreal, 2009.

[11] Wiklander N., Cadot E., Maier T., et al., "The VINGA Project Final Report", The VINGA Consortium, 2011. Also avialable at: http://www.sesarju.eu/sites/default/files/documents/reports/AIRE_-_Vinga.pdf?issuusl=ignore. Accessed on 30/8/2013.

[12] *Guidance Material for the Design of Terminal Procedures for Area Navigation (DME/DME, B-GNSS, Baro-VNAV & RNP-RNAV)*, 3rd ed., Eurocontrol, 2003. Also available at: http://www.skybrary.aero/bookshelf/books/243.pdf. Accessed on 30/8/3013.

[13] *Doc 4444 – Procedures for Air Navigation Services, Air Traffic Management*, 5th ed., ICAO, Montreal, 2007.

[14] *Doc 8168 OPS/611 – Procedures for Air Navigation Services, Aircraft Operations, Volume II, Construction of Visual and Instruments Flight Procedures*, 5th ed., ICAO, Montreal, 2006.

[15] Kar. R, Bonnefoy, A.P, and Hansman, J.R, "Dynamics of implementation of mitigating measures to reduce CO_2 emissions from commercial aviation", Report No. ICAT-2010-01, MIT International Center for Air Transportation, Cambridge, MA, 2010.

[16] "2012 Annual Statistical Summary", Malta International Airport, Malta, 2013. Avialable at: http://corporate.maltairport.com/downloads/747/2012%20Annual%20Statistical%20Summary.pdf. Accessed on 30/8/2013.

The Russian Federation Airspace Structure Analysis with the Use of ATM Research Simulation Tool

Andrey Popov, Larisa Vishnyakova, Oleg Degtyarev, Elena Filenkova, Vladimir Sikachev
Research Department
State Research Institute of Aviation Systems (GosNIIAS)
Moscow, Russian Federation

Keywords: *air traffic control, airspace structure, route network structure, simulation tool*

Abstract

Airspace usage effectiveness assessment research is a significant component of airspace structure design and modernization. This paper is devoted to this type of research in the Russian Federation with the use of a set of research Air Traffic Management (ATM) simulation tools (KIM OrVD). Key features of KIM OrVD program, which provide an opportunity to conduct the complete cycle of simulation, are considered in this paper following the example of modernized airspace usage effectiveness assessment. The methodology (scheme) describing all the stages of the research is presented. Research results show the benefits of Moscow air traffic control center (ACC) route network and airspace structure.

1 Introduction

The measures of the Russian Federation Airspace structure modernization are performed as part of the Federal target program "Modernization of the Russian Federation Unified system of Air Traffic Management (ATM) (2009-2015)". They involve air traffic control centers (ACC) enlargement, airways structure upgrade, new Standard Instrumental Departure (SID)/Standard Terminal Arrival Route (STAR) schemes generation for airports.

The need for measures is based on the following factors. The area of Russian Federation Airspace which is served by the ATM system exceeds 25 million square kilometers, the length of airways is about 800,000 km including about 500,000 km of international airways. The use of the airspace of the Russian Federation constantly increases due to the geographical position of the Russian Federation and the growth of the number of flights in the direction of South-East Asia - Europe, South-East Asia - the United States through the Russian Federation Airspace. Also, the number of international flights to/from the airports of the Russian Federation is growing, and the need in domestic flight operations increases.

The existing Russian Federation Airspace structure does not allow of conflict-free flights within its most overloaded areas. There is a problem of conflicts at intersections of transit flights and arrival/departure flows close to major airports. At low intensity of the traffic such problems are almost invisible, but because of the growth of traffic now there are already problems at the intersection of routes of such flights.

These problems are particularly acute in Moscow's center, through which more than 50% of all transit flights across the Russian Federation Airspace pass. The majority of the traffic flows to the Moscow airports

Sheremetyevo, Domodedovo and Vnukovo, located relatively close to each other. For various reasons, the direction of flights from the airports of Moscow Terminal Maneuvering Area (TMA) does not correspond to the geographical location of the airport. In addition the Moscow ACC has many areas that are closed to flights. All this leads to the need for airspace structure reorganization in airspace approach sectors and aerodrome airspace to achieve efficient operations.

One of the reasons for the modernization of the system is the organization of major events such as the XXII Olympic Winter Games of Sochi in 2014 which imply a transition of large domestic and international passenger flows. The Games require restructuring of the Sochi airport, its terminal airspace area and the introduction of new systems both in the air and in the airports.

One of the drawbacks of the ATM system is the large number of air traffic control centers (at the beginning of 2013 the Russian Federation Airspace is divided into 53 centers). Such a number of centers were created due to the following factors: Russian Federation Airspace has a very large area of service, different levels of automation of various air traffic control centers, different weather conditions in different centers. This greatly affects the operating conditions in different regions, which leads to uneven load of the airspace. At the same time the global air navigation concept provides for a "seamless" airspace. Large number of centers hinders the achievement of "seamlessness" because of frequent transfer of control of an aircraft from one center to another.

Currently we are working on the enlargement of ACCs - reducing their number from 120 (in 2005) to 12 air traffic control centers (in 2015). But simultaneous modernization of all the elements of the airspace is impossible. It is necessary to undertake gradual improvement of the air traffic control centers structure from one center to another. However, this upgrade is associated with certain difficulties, for example, joining the new structure of the district center with neighboring areas. On the other hand, it is necessary to develop an integrated route network across the airspace of the Russian Federation. This is caused by the need to create optimal routes for transit flights passing through most of the Russian Federation Airspace.

To estimate the changes in the airspace structure a number of indicators is defined. First of all it's safety and efficacy of airspace use indicators.

A flight safety should be provided by the ATM system, so the safety performance of the system is considered such as: the number of potential conflicts in sectors, at waypoints, at segments of the airways. Performance indicators of airspace use (the length of the route, the use of optimum flight levels, etc.) are estimated mainly from the airspace users' point of view.

2 Features and Requirements for Research Tool

ATM system of the Russian Federation has a number of peculiarities compared with other countries' ATM systems. It's a large amount of airspace, extreme irregularity of air traffic in space and time, poor information in the number of ACCs, peculiarities of Air Traffic Flow Management (ATFM) and Air Traffic Control (ATC). It's impossible to use existing foreign simulation tools and generates a need to create advanced simulation tools for Russian Federation's ATM System.

The modernization of the Russian Federation Airspace structure research task is to evaluate the efficiency and safety of airspace use under various constraints. First of all, the subject of such research is changes in the airspace structure. Research method can be relative if there is a comparison of the advanced structure in relation to the existing structure or absolute if there is a completely new structure or the proposed structure for whatever reason can't be compared with the existing structure.

Such research should answer the following questions:

- are the research goals achieved;
- are the results consistent with the effect of structural changes according to the chosen metrics expected by the researcher; and, if not, for what reasons;
- what are the possible solutions of the problems identified.

Computer simulation tools, designed for research in the field of airspace structure improvement, must meet the following general requirements:

- enabling of research of the ATM systems and air traffic flows that correspond to en-route and "free" flights;
- creation and choice of the necessary air traffic flow, convenient and simple adjustment to the required structure and state of the airspace and the ATM system;
- possibility to change the capacity of individual elements of the ATM system;
- possibility to investigate the conditions of flight operations, such as weather conditions;
- possibility to form the areas of airspace restrictions;
- possibility to form key performance areas: safety, productivity, regularity, economic efficiency;
- simulation rate acceptable for the researcher.

To meet the above requirements the simulation tools must:

- be universal (able to be used for assessment of efficiency of various measures taken to improve the structure of various elements of the airspace);
- take into account the peculiarities of the specific elements of the ATM system and the specifics of individual research tasks;
- have friendly human-machine interface.

To solve the problem the support tools should use both calculation-based analytical modeling and simulation. When a precise description of a simulated process is possible a calculation-based mathematical modeling should be used. If a process can't be described and if you want to follow the dynamics of the process simulation should be used. Both types of modeling can be used at different stages of the design and validation of decisions process. Thus, different types of modeling can be implemented for research in the framework of one tool.

Research scenario generation tools also play a significant role. There are two major parts in the preparation of the research scenario: formation of air traffic flow and formation of the airspace structure. The tool should provide either an exact match of data on the air traffic flows and the airspace structure, or have the ability to synthesize the two types of data with controlling their integrity.

Given the above, there are several key requirements that tools created for design of the airspace structure research should meet. First, it is the flexibility to configure the necessary simulation scenario and conditions of research. Second, it is the adequacy of the presented results, which depend on the input data by 50% and depend on the way of the research by 50%. Third, it is the processing and presentation of results. This factor affects the perception of the results by a researcher and, eventually, affects the conclusions based on these results.

3 Research Tool for Airspace Usage Efficiency Assessment

At present, there are a number of complexes of mathematical modeling of systems and processes for air traffic management in the world.

The ATM simulation tools "KIM OrVD" is developed in the State Scientific Centre of Russian Federation «GosNIIAS» in 2006 [1]. KIM OrVD was created in behalf of the national ATM system from the "State ATM Corporation" and is now widely used for research.

The different studies on airspace usage effectiveness have been and are carrying out at present at KIM OrVD facility.

- Analysis of ACCs proposals and development of options for the configuration of sectors of the St. Petersburg ACC, 2007.
- Analysis of the effectiveness (benefit analysis of proposals) of Rostov ACC, Samara ACC and Moscow ACC proposals to change the airways structure in these areas in 2008-2009.
- The development of options for sectors configurations in the enlarged Khabarovsk ACC, 2008-2009.
- Analysis of ACCs proposals to change the airways structure and sectors configurations and the development of alternatives for the St. Petersburg and Irkutsk ACCs in 2009-2010.
- Evaluation of the reduced vertical separation minima (RVSM) implementation in

the Russian Federation and neighboring countries, 2010-2011.

- Research and analysis of airspace use features for the period of transition to the reduced vertical separation minima (RVSM) in Russia and neighboring countries, 2011.
- Assessment of advanced airspace structure of the Moscow ACC, 2012.
- Prediction of the characteristics of the terminal area of Sochi airport during the XXII Winter Olympic Games, identification of problems, evaluation of the effectiveness of measures for its use, 2012-2013.

It should be noted that the KIM OrVD meets the requirements for similar tools for conducting research for airspace usage assessment. It has a number of features associated with the modeling of Russian Federation Airspace. First of all, KIM OrVD is a tool to support ATM experts in the following research areas:

- to develop and evaluate of measures taken to improve the ATM system, including the modernization of the airspace system structure and the change of measures to manage and regulate the air traffic flows;
- to assess the efficacy and safety of airspace by a set of indicators and for different conditions of flight operations;
- to assess the impact of changes in the state of the ATM system, the airspace and the conditions of flight operations on the effectiveness of the airspace use.

Different tools for research included in KIM OrVD allow for closed-loop studies on the development of proposals for airspace structure improvement, options of rational airspace area division into ATC sectors for improved airways structure with taking into account the air traffic flow re-routing, existing or future traffic intensity in the investigated ACC.

The KIM OrVD is based on several incorporated solutions that allow a meaningful multidisciplinary study.

First, in the KIM OrVD the synthesis of traffic flows and airspace structure are implemented in a single software tool. This concept enables flexible settings for any modeling scenario and provides efficiency of this configuration. The traffic flows and airspace structure always form the basis of the research. KIM OrVD uses air traffic flow model with wide capabilities for air traffic flow generation and structure synthesis, which distinguishes it from other similar tools in this area, where the issue of creating traffic flows receive little attention.

Secondly, specialized algorithms for specific tasks, including the ones for solving optimization problems are used in KIM OrVD. The following, tasks are solved: synthesis of the optimal 4-D route (flight plan) with the imposed restrictions, the optimal division of the ACC airspace into air traffic control sectors and other tasks. Algorithms designed for specific tasks consider various constraints unique to this task. On the other hand, all models in which the algorithms are implemented interact with each other through a KIM OrVD database. This allows usage of the results of one study in other models in the series of studies or in outside research.

Third, data storage technology for simulation results and source data is based on library format. Thus, the researcher can make adjustments by selecting the scenario data options.

KIM OrVD consists of five software tools connected via KIM OrVD Database. Each tool is aimed to solve separate tasks in the research cycle framework:

- Research ATM – tool aimed for the preparation of basic data (flight plans, airspace structure, ATM system, weather, capacity and airspace usage restrictions) airspace usage and system effectiveness assessment, and results analysis.
- Administration database – tool aimed for integrity database control and coordination of its usage by all users.
- Import data – tool aimed for copying data from central database, transferring data to the KIM server and importing restrictions and weather data.
- Flying Simulation – tool aimed for proposals on ATM and reconfiguration of routes with account for implementation of Area Navigation (RNAV) and Required Navigation Performance (RNP) en-route, TMA and aerodrome assessment.

- Safety evaluating simulation tool is aimed for safety evaluation predictive assessment and revelation of decrease tendencies due to ATM system structure modernization or flight conditions.

Over the last years the KIM OrVD modernization was associated with a dynamic flight simulation in TMA and aimed at accuracy of flight operations on SID/STAR evaluation and safety level assessment, both at en-route and take-off/landing. The "aircraft model" program allows to simulate flight operations with flight performance characteristics corresponding to the Base of Aircraft Data (BADA), as well as to work out flight operation conditions effect on flight trajectory holding accuracy (meteorological conditions, etc.). It's possible to trace the simulation dynamics in 3D in real time and in post simulation mode. Such a feature is intended to identify some essential singularities that you won't be able to see in the integrated results. 3D visualization allows displaying all "traffic" in the Russian Federation Airspace which amounts to more than a thousand aircrafts under ATC.

4 Key Features, Solutions and Research Opportunities KIM OrVD

There are two important parts of the research - a methodology and a research tool.

A. Methodology

One of the main components of the methodology is the description of research stages. First of all, the research should be based on a research plan, which should include all the stages. Research can be divided into three main parts:

- preliminary data preparation for modeling scenarios;
- simulation;
- comparison and results analysis.

More detailed description of these steps is stated below.

1) Stage 1. Preliminary data preparation for modeling scenarios (yellow block in Fig. 1). Initial data for the modeling are to be presented in the form of task for modeling. It must be formed according to certain rules, and includes the following:

- qualitative description of problems requiring changes to the current airspace structure and ATM system;
- data for the proposed structure of airspace elements, and for changed flight operation conditions;
- indicators for measuring the effectiveness of the proposed changes;
- the expected effect of the changes.

Data preparation for modeling scenarios is:

- to set airspace structure on a given date for the simulation;
- to choose flight plans for the simulation (and adaptation of plans for the airspace structure if necessary).

2) Stage 2. Simulation as well as planning and flight operations effectiveness analysis with the calculation of airspace usage indicators (blue block in Fig. 1).

Simulation is carried out for three cases:

- initial system structure with the initial flight plans;
- new system structure with the initial (or adapted) flight plans;
- new system structure with predicted forecasted flight plans.

3) Stage 3. Comparison of simulation results, the analysis of prospects. At this stage, we carry out the comparative analysis of simulation results and analysis of the prospects of a proposed airspace structure (with projected changes in the intensity and structure of the flight plans). The effectiveness of proposed changes must be evaluated. According to results the research conclusions are formulated.

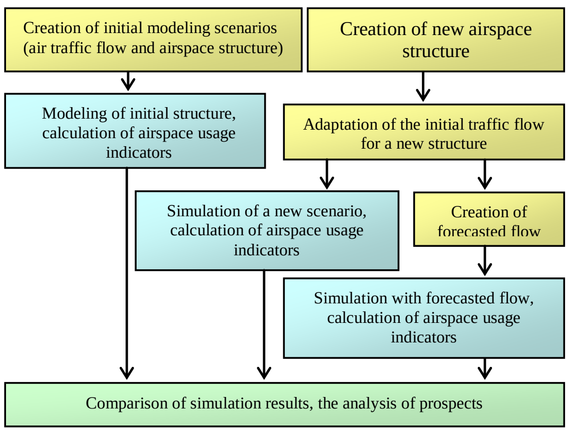

Fig. 1 Research chart

After research development plan is formed, the question of choosing of indicators to measure changes in the airspace structure arises. Depending on the research purpose performance indicators are selected from the group of Key Performance Area (KPA) [2].

Research tool selection depends on the task. There are a number of research tasks to evaluate the airspace structure, which requires simulation:

- evaluation of proposals for improving the airspace structure;
- development and justification of proposals for improving the airspace structure;
- evaluation of proposals for the ACC airspace division;
- development and justification of proposals for the choice of efficient routes to suit different restrictions for airspace usage;
- future studies to assess the airspace usage in conditions of airspace structure and air flows change;
- development and justification of proposals for configuration and sectors ACC Centers work schedule;
- analysis of the effectiveness of the proposals for airport or TMA airspace structure;
- development and justification of proposals for a new route network of the Russian Federation and/or an enlarged ACC Center;
- safety estimation in a given sector airspace structure for ACC Center and used system structure.

KIM OrVD block diagram is shown in Fig. 2.

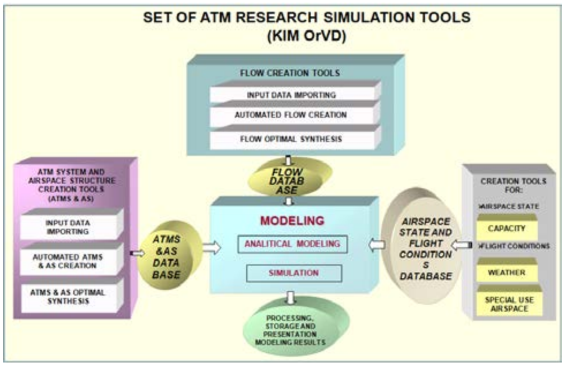

Fig. 2 KIM OrVD block diagram

To solve the task of analysis the airspace structure KIM OrVD is provided by the following features (Fig. 3).

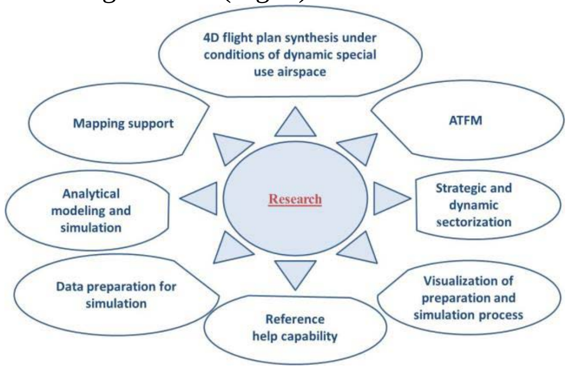

Fig. 3 KIM OrVD functionality

B. Research tool functionality

KIM OrVD uses two options to prepare data for simulation:

1) Set up a research scenario using libraries.

Implemented features allow KIM OrVD off-line options to configure various data imported from “State ATM Corporation” database. With the appropriate tools we can choose:

- flights data (flow);
- ACC Centers structure and ATC sectors structure;
- route network (includes date setup, and the route network variant);
- ATC sectors capacity;
- special use airspace data.

2) Automated data generation options.

The researcher can generate data in accordance with the research task.

One of KIM OrVD’s most important parts is the creation of research flows. This model allows us to shape the flow for any specified requirements, for example, to work out the methods of flow planning and management. KIM OrVD allows creating of research flows by modifying the base flow:

- the flow creation by varying intensity from base flow. Various intensity variants are implemented: uniform change in all directions, a change in a given direction, between the specified airport groups, between the specified regions;
- the flow creation, based on the characteristics of a set of selected daily flows. An example of using this function is the random

flow synthesis for forecasting research in the reorganization of the ACC Center ATM system. In particular, random flows can be formed with changed intensity for the next planning period for 5-10-15 years. Using this look-ahead flow data, the researcher can determine the needs of the ATM system;

- the flight plans creation, which correspond to different criteria and airspace usage according to the scenario;
- the flow creation to meet the specific research task requirements;
- the flow creation for ACC Center, this flow contains all original intensive hour flows, but less, that all original flows. Representative flows used in solving various research tasks, such as:
- full-scale study of ACC Center airspace;
- studies evaluating the effectiveness of forecasting route network;
- research on the effectiveness of ATFM;
- division of ACC airspace into ATC sectors (sectorization task).

Also, the researcher can create pseudo free-flight zones of different configurations and special use airspace zones.

KIM OrVD provides great opportunities for route network data. Route network can be edited from an original, or can be entirely created. During this process researcher can create, edit or delete data for points, segments and airways.

There are also tools for the automated generation of data on the ACC Centers and ATC sectors structure. This feature is in demand at many research stages. Starting from complete creation of ACC Center structure and finishing with ATC sector boundaries editing in the latter stages of research. When working with ATC sectors the researcher can create a new sector with the following data: sector code, schedule, boundaries, standard capacity. If you need to change any of the sector characteristics, it is possible to edit the data on the ATC sector. During research, the researcher can combine sectors from the existing ones in various ways.

Similar tools have been provided for use with ACC Centers. One possibility - the integration of the ACC Centers, for example, used in research tasks with integrated ACC Centers.

Model for navigation and surveillance equipment allows you to create, edit and delete data for this equipment (type and characteristics of the equipment, the location, mode, schedule).

The complex uses analytical and simulation types of modeling. Depending on the tasks, they can be used separately; both types of modeling can also be used for one task.

Analytical modeling is used in research to assess, for example, route network or ACC Center structure efficiency or in the evaluation or assessment of conflicts. KIM OrVD uses the following indicators for estimation:

- air traffic intensity at airspace elements (points, segments, airports);
- load of ATC sector;
- workload of ATC sector controller;
- potential conflicts;
- the influence of special use airspace on airspace structure;
- the influence of special use airspace on air traffic flow.

KIM OrVD provides the following visual elements for the analysis of the simulation data and display the results:

- diagram of the air traffic intensity of the airspace elements, an example of such a diagram is shown in Fig. 4;
- controller workload diagram;
- diagram of the conflicts in the ATC sector and at the points of airways;

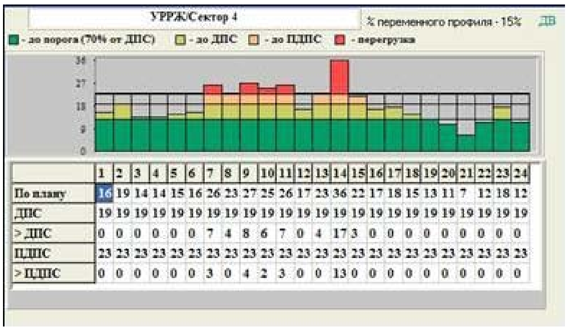

Fig. 4 Diagram of sector load counts

- tools for analysis of the following flow intensity indicators: cyclogram of the daily flow intensity, the integrated flights intensity of the airspace elements, flight plans involved in ATC sector overload; the maximum and the average number of flights managed by the controller simultaneously, average and overall flight time in the ATC sector, the statistical characteristics of the ATC sectors flights intensity, overall flight distance in the ATC sector.

At the simulation stage a researcher can control the process, the simulated aircraft flight is modeled with regard to the navigation errors, various random factors are considered, including the operation time characteristics of the controller as well as random conditions, such as wind.

It is possible to analyze the results either directly during the dynamic simulation of flight operations, or after the end of the simulation (post-simulation analysis). To make this possible KIM OrVD implements flights performance, security and regularity analysis tools, which present results in chart, tabular and graphical form. These tools are designed both for obtaining integral estimates, and more detailed analysis of the airspace elements or system, separate flights and separate events.

KIM OrVD has separate optimization procedures to solve some research tasks, such as the optimal 4-dimensional (4-D) routes creation [3], optimal sectorization [4] and flow management [5].

5 Solving Research ATM Problems on the Example of Evaluation of the Proposals on the Modernization of Moscow Airspace Area Structure Using KIM OrVD

Several researches on airspace usage assessment were made with the use of KIM OrVD. The example given below refers to KIM OrVD usage for Moscow ACC airspace prospective structure assessment.

A research on proposed airspace structure assessment based on KIM OrVD usage for performance evaluation of airspace management application methodology was held on demand of the “State ATM Corporation” in 2012. The prospective Moscow ACC structure designed by State Research Institute “Aeronavigation” consisted of more than 60 new airways and 21 ATC sectors.

This research was aimed to produce independent (from structure designer assessment) quantitative and qualitative performance evaluation of one of the proposed variants of the new route network and Moscow ACC airspace structure.

The whole research cycle consisted of initial data and scenarios preparation, criteria choice, simulation with airspace usage criteria calculation and the following results analysis (Fig.5 shows the research scheme).

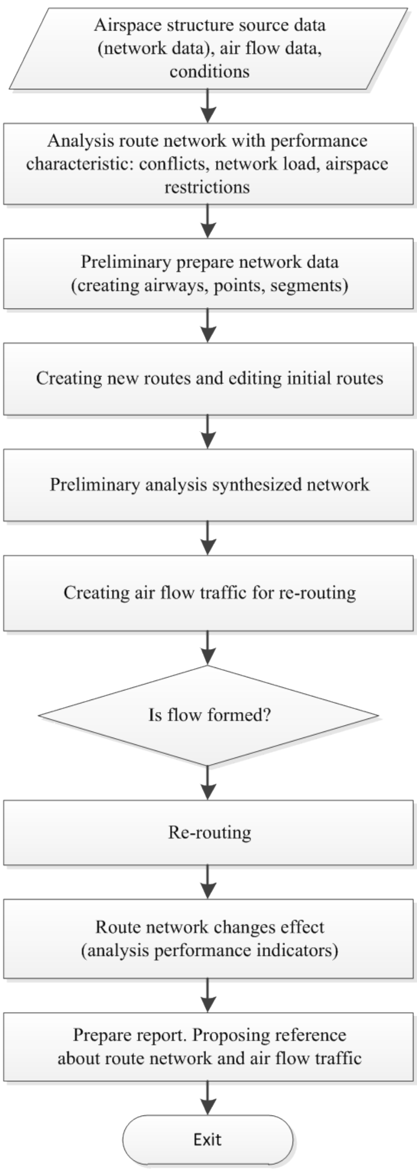

Fig. 5 Research scheme

At the first stage of the analysis the initial data consisted of: air traffic flow through the modernized Moscow ACC route network data analysis, Moscow ACC ATC sectors analysis, SID/STAR data analysis. In particular, the air flow data analysis showed growth in the number of flights in 2011 relative to 2008 by 13%.

Data was prepared and recorded into the database with the use of KIM OrVD capabilities at the second stage.

After data preparation and recording, a preliminary qualitative estimation route structure and comparison with existing route structure was made by the researcher.

One component of the qualitative evaluation was the air traffic flow direction through the existing and modernized Moscow ACC route structure analysis, example of transit traffic flow through the modernized structure is shown in Fig. 7.

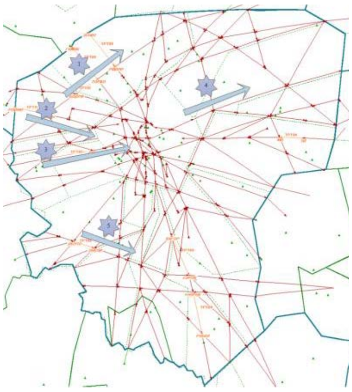

1 - airway is designed for Europe – Japan, China air flows;
2 - airway is designed for Central Europe – Japan, China air flows;
3 - airway is designed for Central and Southern Europe – China, Japan air flows;
4 - converged from 2 and 3;
5 - airway is designed for Central Europe to Hong Kong

Fig. 7 Flow distribution

Quantitative effectiveness and safety assessment of current and modernized route networks was conducted based on qualitative effectiveness assessment of current and modernized Moscow route networks. Comparative analysis was made after that.

Current structure analysis revealed problems in Moscow ACC route network structure and ATC sectors structure management. Unbalanced sector load counts and overload capacity in some sectors during the rush hours were identified when analyzing the sector's structure. Several “bottlenecks” existing due to the high air traffic flows at some directions in the route network structure were identified. One of such problems occurs due to the flow from Moscow airports (Domodedovo, Vnukovo, Sheremetievo) to airports of Southern Russia. From the point of ATM safety levels conflicts at the same flight level occur in the most loaded directions and crossing points, where transit flow crosses arrival/departure flow from/to Moscow hub.

The synthesis of the newly introduced route structure and the air traffic flow passing through a given structure was necessary to produce quantitative evaluation.

The synthesis involved re-routing of the whole air traffic flow through Moscow airspace to a new route network.

Some problems at the Moscow ACC sector border were identified while attempting to re-route, e.g. new airways in Moscow airspace and old nearby airways connection was not provided. Additional work to connect boundary areas was done at this stage. For the re-routing purposes the whole air flow has been divided by directions and re-routed partially. Re-routed sub air flows were finally put together to form one “research air flow”.

Analysis of the modernized Moscow ACC airspace and route network structure conducted using the "research air flow" showed the following results: the proposed Moscow ACC sector structure is characterized by a considerably balanced load; one-way airways organization in the modernized structure reduces problematic directions load.

The modernized airspace and route network structure contains less heavy air traffic flow crossing points, than the current one. Safety level assessment showed a significant reduction of conflicts, including the full absence of "opposite course" conflicts.

The use of forecast flows under the conditions of a 50% intensity level increase was analyzed to assess the sector's modernized structure capacity reserve. The similar assessment made for the increased flow demonstrated a capacity reserve reaching 87%.

Finally, the comparison showed advantages and disadvantages of the proposed new Moscow ACC route network and airspace structure. Airspace structure management decisions have mainly positive effect on effectiveness and safety performance, which was evaluated during the research. Route network structure (points, segments, airways) load decreased (at some airways decrease is up to 50%), opposite conflicts disappeared and other conflicts counts decreased due to one-way airways usage. These advantages lead to an increase in the safety level. Different performance indicators comparison results also indicate unsuccessful decisions which lead to safety and effectiveness level decrease. Such solutions are: “non-geographical” flights structure management and the airway for the West direction departure flow. In the first case conflicts appeared due to “non-geographical” directions flow. In the second case the problem is high airspace elements load.

And at the last stage conclusion was made based on the results of research.

The proposed new Moscow airspace structure enables to achieve the settled goals and target criteria. The Moscow ACC structure organization solution introduced is aimed to solve the following current issues:

- to decrease problematic arrival/departure directions load;
- to increase safety level mostly by one-way airways organization;
- to make sector’s load more proportional.

The disadvantages of the new structure are as follows:

- non-geographical air flows organization in one of the Moscow TMA area sectors resulting in safety level decrease and arrival routes extension;
- connection of the airways structure at the Moscow ACC border is not provided;
- West departure airway direction is overloaded.

6 Summary

Research simulation tool named KIM OrVD was designed by the State Research Institute of Aviation Systems and implemented in the “State ATM Corporation”, Russian Federation. It is used for conducting various researches. First of all, KIM OrVD is intended for effective airspace usage assessment. Development of the KIM OrVD is currently aimed at TMA operations and surface operations at airport simulation. On the volunteer initiative a research aimed to comprehensive evaluation of Sochi airport TMA usage predictive performance and airfield surface usage at the time of the XXII Winter Olympic Games, is being currently conducted. It helps to reveal bottleneck and assessing airfield surface usage effectiveness.

KIM OrVD consists of five software tools which are designed to solve separate tasks. Interaction via KIM Database allows data exchange between the tools during the research. Complex structure allows upgrading and expanding of the complex functionality for various research types. The KIM OrVD contains a large number of algorithms, including optimization algorithms for 4-D flight plan synthesis under conditions of dynamic special use airspace, slot allocation, optimal sectorization, dynamic sectorization. Automated tools allow creating airspace and route network structure (points, segments, airways, ACC, restrictions airspace usage, free flights areas, SID/STAR routes). Analysis and visualisation tools allow getting the necessary results and present them in a user-friendly format.

The KIM OrVD allows conducting research on behalf of the Russian ATM system. It's particularly significant in view of traffic growth in Russian Airspace.

References

[1] Agreement №020/06-825 from 31.07.06 . Design a first version of the set of ATM research simulation tool “KIM OrVD”

[2] SESAR Consortium. Air Transport Framework. The Performance Target. – EUROCONTROL, Doc 2, 2006.

[3] Degtyarev O.V., “Methodical and Algorithmic Issues of Constructing Four-Dimensional Flight Routes for Long-Range Aircrafts.” *Journal of Computer and System Sciences International*, Vol. 45, No 5, 2006

[4] Degtyarev O.V., Minaenko V.N., Orekhov M.O., “Solution of Sectorization Problems for an Air Traffic Control Area. I. Basic Principles and Questions of Airspace Sectorization and its Formalization as an Optimization Problem”, *Journal of Computer and Systems Sciences International*, Vol. 48, No. 3, 2009

[5] Kan A.V., “Development of Algorithms of Air-Traffic Flow Management”. *Journal of Computer and System Sciences International*, Vol. 45, No 5, 2010

Unmanned collaborating autonomous aircraft

Lars Rundqwist, MSc, PhD
Saab AB, Linköping, Sweden

Florian Grässel, Dipl. Ing
Cassidian, Manching, Germany

Gilles Ruel, MSc
Dassault Aviation, St Cloud, France

Keywords: UAV, UCAV, autonomy, collaboration

Abstract

This paper describes the results of a project that was performed within the framework of the European Technology Acquisition Programme (ETAP), by Saab AB, Cassidian (part of EADS Deutschland GmbH) and Dassault Aviation. The project was mainly financed by the Swedish Defence Material Administration (FMV), the German Federal Office of Bundeswehr Equipment, Information Technology and In-Service Support (BAAINBw), and the French Direction Générale de l'Armement (DGA), but also partly funded by industry.

In this study a group of five Unmanned Combat Air Vehicles (UCAV) perform a ground attack mission against three targets. By using collaboration and a high level of autonomy the group is able to re-plan and execute the mission despite "opposing" activities and events, e.g. air defense or malfunctions or losses of systems or vehicles. Due to the high level of autonomy and the low level of operator interaction required, only a single or a small number of operators are sufficient to control the whole group of five UCAV.

1 Introduction

Current types of unmanned aircraft are typically remotely piloted or follow a pre-programmed route with the possibilities to upload new routes, or switch between remote piloting and up-loaded routes. They usually have a low level of autonomy and thus require frequent or constant operator interaction, and they are designed to operate alone. Cooperation, if any, is achieved on the operator level, not by inherent vehicle functions. On top of this, each vehicle typically requires 2-3 operators during the mission.

By contrast the present project, performed in collaboration by Saab AB, Cassidian and Dassault Aviation, studied and developed functions for a group of collaborating unmanned combat aircraft, with specific focus on air-ground missions. The intention was that a single operator should be able to plan the entire mission and a single (the same) operator should be able to supervise the aircraft group during the mission.

The study is performed entirely in a real-time software simulator, which could allow reaching a Technology Readiness Level (TRL) of 5, but not higher, see [1].

1.1 Paper organization

The paper is organized in the following way. First the purpose of the study is explained, high-lighting the main capabilities that were studied. Then the Demonstrator system will be described, both in terms of what a “real UCAV system” would look like, and the simulator implementation. Then the Flight Management and the Mission Management functions are described. After that an Evaluation Mission is described followed by Evaluations Results and Conclusions.

2 Purpose of the study

The purpose of the study was to “explore, demonstrate and verify the system-level technologies for mission planning, guidance and control of Unmanned Combat Air Vehicle (UCAV) operations”. Thus it was not the intention to study single technologies or algorithms on their own, but rather to put them together in a system and to demonstrate the system capability in a reasonable mission scenario. Due to the complexity of the scenario it was not sufficient with one UCAV to perform the mission, and it was judged as infeasible to use the current approach with remotely piloted vehicles. Instead a group of UCAV was used to perform the mission in collaboration, with a high level of autonomy and only a small amount of operator interaction.

The study focused on some specific problems or capabilities. For the Flight Management the focus was on the capabilities for

- Rendezvous
- Refueling
- Flight in the target area

For the Mission Management the study focused on the following capabilities.

- Survivability (Long Term and Short Term)
- Prepare for Weapon release
- Manage and update the mission
- Monitor and execute the mission

Some of these capabilities are usually governed by Rules of Engagement (ROE), which typically define conditions for when attacks are allowed, etc, see [2].

The goal of the design was to demonstrate that a cooperative system of UCAV platforms will be able to perform the mission in the presence of stressors.

2.1 Stressors

Any event or condition that has a potentially adverse effect on the mission goal is defined as a stressor. The stressors range from environmental conditions (winds, visibility, etc) through equipment malfunctions (sensor failures, etc) and failed actions (target missed, no operator clearance, etc) up to hostile actions (new threats, fired missiles, moved targets, lost vehicles, etc). Thus the stressors may have effect on both the Flight Management and the Mission Management, and include anything that prevents or may prevent the group from fulfilling the Mission Goal

2.2 Limitations and Exclusions

The focus of the study was to explore the capabilities in the target area, and the areas immediately before and after (i.e. the ingress and egress phases). Thus no aspects of flying in controlled airspace, taxiing, take-off or landing were studied. For these aspects the current state-of-the-art was either quite high or they are studied in other projects, e.g. MIDCAS, see [3] and [4]. Instead this project focused on the target area capabilities where the TRL was low, around 2, which means that technical concepts exist only in paper versions, but the capabilities have not been proven in any experimental way.

The operator control was modeled in a simple way, and mainly consisted in granting or rejecting requests from the UCAV group in a pre-programmed way. The mission planning was also not covered, except that the necessary mission plan data was produced manually.

3 System descriptions

As mentioned above the study was performed in a real-time software simulator. The simulator then needs to contain both the “on-board mission system” software functions, together with models of the vehicles, other tactical entities as well as simulator services for start/stop/hold, data logging, visualization, etc. But before describing the simulation system the tentative "real world" UCAV system will be described, as well as the system architecture for the on-board mission system.

3.1 UCAV System

The tentative UCAV system that was modeled in the simulator consists of

- UCAV platforms, all of identical type, with avionics and communication systems
- Identical onboard sensors
- Variable weapons payload
- Ground components for Pre-flight mission planning and Operator control

The UCAV platforms are a twin engine, tailless "stealthy" delta wing configuration, for subsonic speed only. They are designed for a quite large combat radius and maximum 2000 kg of internal weapons payload, which resulted in a platform length of 12 m, wing span of 12 m and maximum take-off weight around 16 metric tons.

The tactical sensor suite consists of Electro-Optical/Infrared (EO/IR) sensor, radar and Electronic Support Measures with Surface-Air Missile (SAM) detection, radar and missile warning.

The weapons include Precision Guided (GPS) munitions and Laser Guided munitions.

The UCAV may also carry chaff and flares for self-defense.

For the operators there are Ground Stations for Pre-flight Mission Planning and Operator Control.

A high bandwidth tactical data link is used for internal communication, within line-of-sight.

In the current study the modeling of these items focused on the platforms with their avionics and communications systems. Simple models were used for the EO/IR sensor, the radar, SAM detection, radar and missile warning and the weapons, while chaff/flares were not used at all.

3.2 Avionics System Architecture

The avionics architecture on-board one of the platforms is shown in Fig. 1 below.

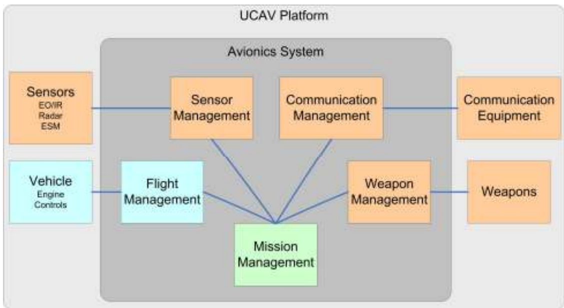

Fig. 1 On-board avionics architecture

The Mission Management component is the main on-board component in the architecture and interacts with the components for Flight, Sensor, Weapon, and Communications Management on this platform. All the Management components manage either the entire platform (vehicle) or a specific set of equipment, e.g. sensors or weapons. The architecture for the entire UCAV system is shown in Fig. 2.

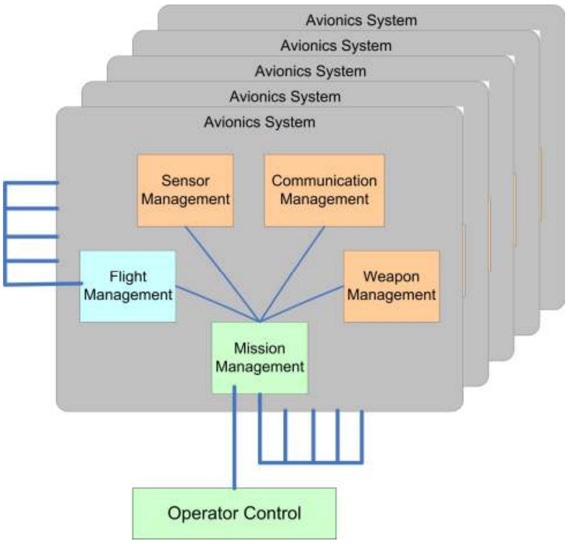

Fig. 2 UCAV System architecture

Before take-off the Mission Plan is uploaded to the Mission Management component in all the platforms. During the mission the operator control station interacts with only one of the UCAV platforms, designated as the Mission Group Leader (MGL). Further, the Mission

Management component is then responsible for all communication and coordination between the platforms on tactical level.

The Flight Management components also interact across the platforms. In this case the Flight Management communication is limited to flight coordination, e.g. to ensure safety of flight and coordinated trajectory computations.

All functionality for each of the components is implemented on-board every vehicle. They exchange information in order to maintain an updated database in all vehicles with respect to vehicle status and tactical situation.

3.3 The demonstrator system

The demonstrator system has the following architecture.

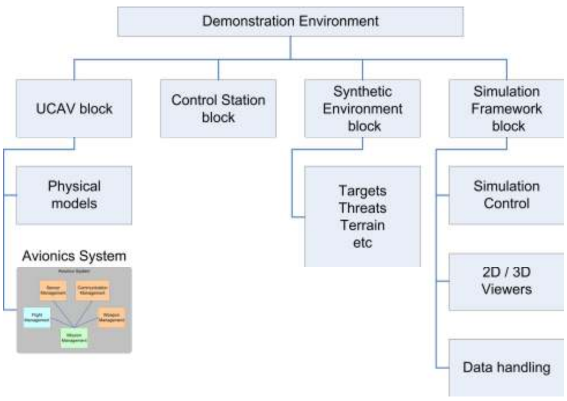

Fig. 3 Demonstrator architecture

In addition to the Avionics System (Flight, Sensor, Weapon, Communications and Mission Management functions), which is the main item to demonstrate, and the Operator Control, the demonstrator system includes vehicle models, sensor models, weapon models, tactical entities (targets and threats), simulation controls, visualization, data logging, etc. It was implemented in a group if high-end PC computers, running a Linux OS. The simulation can be configured to run on one computer only or to be distributed on more computers.

Through this arrangement it is possible to achieve a Technology Readiness Level (TRL) of 5, but not higher. This level requires that both functionality and performance of the technology is demonstrated in a relevant environment. TRL6 requires a realistic simulated operational environment, which probably would require the use of avionics computers, or something representative of such computers, integrated in a demonstrator rig.

Actual achieved TRL is mixed. All demonstrated items can be stated as having passed at least TRL3, meaning that proof-of-concept has been demonstrated for critical functions. Most items have also been demonstrated in an integrated fashion, and thus passing TRL4. For some individual items you may state that they have been implemented with higher fidelity and tested in a realistic environment, and thus passed TRL5. But it should be noted that no formal TRL process was followed, and thus the achieved TRL is based on an assessment of overall results and the test environment.

4 Flight Management

The Flight Management (FM) component of the Avionics is the part “responsible” for executing all tasks related to the flight plan, i.e. to pass all necessary waypoints, coordinate the flight of the UCAV group, ensure flight safety, refueling, etc. For FM the focus in this study was on the capabilities for

- Rendezvous
- Refueling
- Flight in the target area

5 Mission Management

The Mission Management (MM) component of the Avionics is the part “responsible” for executing all tasks in the mission plan, despite stressors. In this study MM focused on the following capabilities:

- Survivability (Long Term and Short Term)
- Prepare for Weapon release
- Manage and update the mission
- Monitor and execute the mission

In the MM component a number of functions were implemented and integrated in order to provide all capabilities above, and to be demonstrated together with the FM functions in an integrated system and not individually. This was necessary in order to comply with the main purpose of the study, i.e. to work with “system level technologies”.

The MM functionality is divided into 2 main parts. The first part is to execute a plan, and the second part is to adapt the plan in case the current plan is not feasible anymore. There is a set of sub-functions to both these main parts, which will be further detailed below. Thus the MM function has the following overall architecture, see Fig. 4.

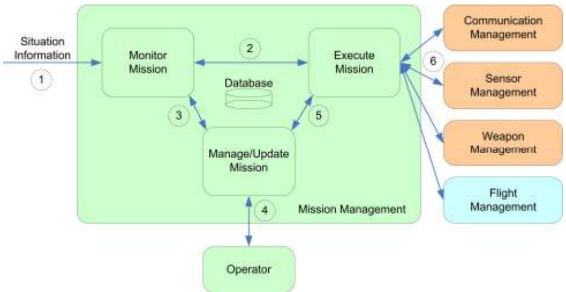

Fig. 4 Mission Management architecture

5.1 Mission Monitoring and Execution

The upper part in Fig. 4 implements the capability

- Monitor and execute the mission

As part of the monitoring all vehicles collect information from their sensors (1), both about the vehicle and system health status as well as sensor inputs, e.g. new threats and targets. The data is stored in a database, and represents the Local Situation Awareness (LSA). A subset of this information, judged necessary for the group to know is sent to all the other Mission Group members as a broadcast message. All members then compute its Mission Group Situation Awareness (MGSA), based on own and received parts of the MGSA. Then a checksum is computed for the latest MGSA in each vehicle, and broadcasted. If all Mission Group members have computed the same checksum, they “know” that they all have the same consolidated MGSA. As a fallback the MGSA of the Mission Group Leader is distributed to all group members. This coordination principle is similar to that of “implicit coordination with shared belief”, see e.g. ref [5].

The MGSA is then searched for deviations, meaning any sign of a stressor acting the system, In case a deviation is found, the adaptation function is triggered, see Section 5.2, by (3) in Fig. 4.

Irrespective of if a deviation is found or not, MM continues to execute the current plan, i.e. (2) in Fig. 4, e.g. via the sub-plans for sensors, weapons, etc, until a new plan is received from the adaptation part.

5.2 Adaptation of Mission Plans

The concept of stressors was explained in Section 2.1. When a stressor induces a deviation, (3) in Fig. 4, the MM is responsible for adaptation of the Mission Plan such that the Mission Goal still can be fulfilled by the group. This update of the Mission Plan is handled by the Manage/Update Mission function in a similar fashion to the MGSA above.

Since all group members have the same MGSA, they can all compute the new Mission Plan. It was chosen to let all members compute the new plan, and then exchange a checksum in order to verify that all new Mission Plans are identical. As a fallback the new Mission Plan of the Mission Group Leader is distributed to all group members.

5.2.1 Impact and reaction

The first step when an adaptation is triggered is to analyze the impact of the deviation, and determine a suitable reaction type. This is done by calling the functions responsible for

- Short Term Survivability
- Long Term Survivability
- Weapon Release

Both Survivability functions want to stay away from threats. They differ in that the Short Term function may trigger an immediate response to a threat if a vehicle is inside a threatened area or will get inside this area within a predefined time interval. This immediate response is a quick turn and new heading away from the threat, and bypasses the ordinary adaptation. While the immediate response is executed the ordinary adaptation continues.

The Long Term Survivability function checks if the current flight plan passes through any threatened area, and if so it proposes to update the flight plan. It will also provide constraint areas to be avoided.

The Weapon Release functions checks if there are any constraints affecting the weapon release waypoints, and if so it proposes to move the weapon release points. It will also provide a constraint area, inside which the weapon release point must be located in order to hit the target.

5.2.2 Constraints

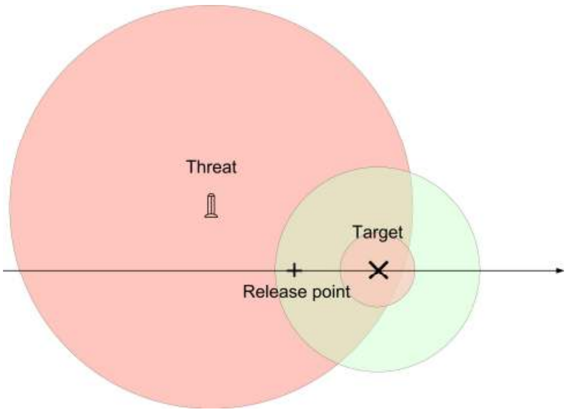

Fig. 5 Constraints from threat and target

The new plan needs to be constrained in a number of ways. The survivability functions typically give constraints of where **not** to be, (prohibited areas) while weapon functions give constraints of where to be (required areas). And such constraints typically overlap since any party in a conflict tends to put a defense (threat) nearby a valuable asset (target), see Fig. 5. In this figure it is quite obvious that you should avoid the red circle around the threat (prohibited), while still wanting to release a weapon in the green area (required). Releasing the weapon in the red area over the target will cause an overshoot and miss the target.

5.2.3 Solution finding

In the situation in Fig. 5 you need to find a new weapon release point in the green area outside the threat area and compute a new route with a flight direction towards the target. This implies that the solution should look something like in Fig. 6.

In the process of finding this solution all the known constraints have to be merged into a set which includes all required areas and excludes all prohibited areas. The solution is then computed using this set of merged constraints, taking solution constraints into account. E.g. as mentioned above the flight direction on the weapon release point shall be towards the target.

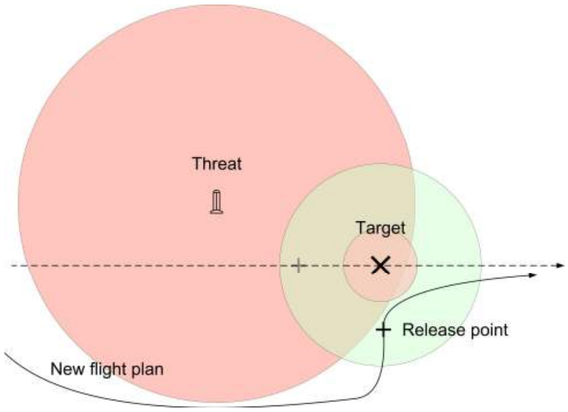

Fig. 6 Solution with new release point

5.2.4 Adaptation in general

The adaptation above covers one simple and obvious case for one platform, and handles the trajectory versus areas to be avoided or used, respectively. In the studied scenario there are five platforms performing a coordinated attack on three pre-defined targets. Each attack is a sequence of tasks:

- Target identification
- Weapon release
- Illumination, in case of laser guided weapon
- Battle damage assessment (BDA)

Each task can be performed by different platforms, and thus the tasks need to be synchronized between the platforms. When stressors are present these tasks may need to be reallocated

- In space, e.g. new release point
- In time, e.g. new time interval for BDA due changed release point and release time
- Into new platform, e.g. if a platform is lost or has lost a capability

MM tries to minimize the reallocation, and thus avoid a combinatorial explosion of possible solutions by keeping all tasks with the original platform, and thus only shift the tasks in space and/or time. However, when a task is shifted to another platform, there may be many possible solutions.

5.3 Rules of Engagement

One important aspect, specifically asked for by the customers, was the ability for the UCAV group to obey Rules of Engagement (ROE), see e.g. [2]. Note, however, that ROE is not one fixed set of rules. ROE are typically defined for each conflict/mission and may also change over time. ROE define the means you, if needed, are allowed to use and when in order to achieve a goal. ROE is often defined at political level.

ROE typically lists conditions for when targets may be attacked, e.g. depending on their physical location, type of target, type of weapon to be used, etc. Such conditions can be parameterized in e.g. lists of allowed target types, lists of allowed targets, lists of allowed weapons for each target type, lists of geographical areas where a weapon is allowed, etc. This way the MM function can handle these conditions as parameters and/or constraints, both when executing a plan and when adapting a plan.

But ROE typically also use terms like hostile intent, imminent attack, contributes to an attack, etc, when the conditions for attack are stated. And it is not easy for a machine to evaluate if there is a hostile intent or not; it is sometimes hard also for humans. The chosen solution in this study was then to call the operator for clearance to proceed with the task. The mechanism used for this was to define an autonomy level for each task (in each geographical area), which will be explained in the next section.

5.4 Autonomy Levels

As stated in the title of this paper, Autonomy is one of the key concepts for this study about collaborating unmanned aircraft. In principle this group of UCAV could operate completely autonomous, i.e. without any human intervention at all during a mission. However, most recent conflicts are at a relatively low scale, e.g. peace-enforcing or peace-keeping operations, where most of the people and property in an area should be considered friendly or neutral, and should not be damaged.

Thus it is necessary to restrict some of the tasks such that they are not unconditionally executed, but instead requires interaction with a human operator. The method used for this was to assign each task an Autonomy Level (AL).

In this study three Autonomy Levels were used, shortly described as follows.

- AL5 – Full autonomy
    - Operator can only interrupt the entire mission
    - Cannot reject the individual task
- AL4 – Rejection possible
    - Operator can reject the task before time-out
    - Else the task is approved
- AL3 – Approval necessary
    - Operator must approve the task before time-out
    - Else the task is rejected

These 3 autonomy levels above are the 3 higher levels of autonomy defined in [5] for Pilot Authorizing and Control of Tasks. The 3 lower levels in [5], AL2, AL1 and AL0, require more operator input and commanding, and were excluded in this study.

The Autonomy Levels were then used as follows:

- AL3 was used for tasks where there was a risk for causing unintended damage, e.g. weapon release. This way there would be no weapon release without explicit operator approval, as may be required by ROE
- AL4 was used for Target Identification and Illumination, mainly just for illustration that a task can be actively rejected by the operator
- AL5 was used for BDA and regular navigation, i.e. no operator intervention was needed for performing BDA or passing waypoints.

This way any task may be constrained such that it is not executed without explicit operator approval, or the operator at least has a possibility to reject the task, without interrupting the entire mission.

6 Developed/prototyped functions

Since the purpose of the study was to explore and demonstrate system-level technologies, at TRL 4-5, it was judged necessary to implement all required functions in software in a real-time simulator. This implies that also a number of supporting functions are needed.

6.1 Main functionality for Flight Management

For the Flight Management (FM) part of the system the following functions were developed/ prototyped in order to handle rendezvous and flying in the target area:

- Trajectory definition functions to provide 4D trajectories, including waypoint constraints, e.g. on altitude, speed, course, time, and vehicle synchronization and separation
- Vehicle control functions to follow the defined trajectory, including vehicle synchronization and separation
- Vehicle separation functions to ensure collision avoidance within the group

From this list you can see that vehicle separation is handled in a number of steps. The first step is to plan for separated trajectories. Due to disturbances these trajectories will not be perfectly followed. Therefore a control function was implemented that causes the vehicles to "repel" each other in case they get closer than a predefined distance. The third step in anti-collision is a more drastic maneuver in cases where the vehicles quickly get very close.

The detailed trajectories are calculated from the waypoints using the Dubins path method, see ref [7], i.e. as a sequence of straight lines and circular arcs.

Together these functions allow the vehicles to fly individual routes, coordinated routes, and routes for packages of vehicles.

For refueling the sequencing according to the NATO ATP-56(B) procedure was implemented, but the refueling details, e.g. catching the basket, was not studied. During the sequencing the general Flight Management functions presented above were used.

6.2 Functionality for Mission Management

The main developed/prototyped functionality in Mission Management has already been described above, i.e. functions for

- Monitoring and executing the mission
- Adaptation of the mission plan in case of deviations.

These adaptations consists of, e.g.

- Moving routes
- Moving tasks between vehicles and in time
- Moving e.g. weapon release points and associated tasks for illumination and Battle Damage Assessment

And with all changes respecting defined Rules of Engagement and Autonomy Levels.

As support to these functions the following functions have also been developed/ prototyped (not exhaustive).

- Merger of reaction types and constraints
- Cost calculations for proposed solutions
- Evasive maneuver (turn rate and new heading) for Short Term Survivability
- New weapon release points, based on release basket computation
- Layered communication function (inter and intra vehicle)
- Route planner, a modified version of a 3D A* algorithm, see ref [8]
- Threat/danger calculation, estimating the survivability of the vehicle as exponential decay based on the time/distance travelled inside a threat with threat level λ

7 Evaluation mission

A specific air-ground mission was defined where 3 targets were to be attacked, with Target Identification for all of them, Target Illumination for one of the targets, and Battle Damage Assessment for all of them. The mission was to be performed with 5 UCAV, all with the same sensor suite, and 1 Laser guided and 1 GPS guided weapon each. The absolute minimum for the mission is 2 UCAV; otherwise all targets cannot be attacked. But then the Mission Goal might not be fulfilled in case one or more of the defined stressors would occur.

The stressors used in this mission were e.g. pop-up threat affecting the target area, malfunction of EO sensor, malfunction of weapon, loss of vehicle(s), operator rejection of weapon release, target not destroyed, target moved, etc.

8 Results

Two examples of evaluation results will be shown, where the first demonstrates the Long Term Survivability function reacting to a new threat, and the second demonstrates re-planning when a new threat pops up, affecting the target area.

8.1 Long Term Survivability

In this scenario there is an unplanned threat, a Surface/Air Missile (SAM) site, activated very close to a preplanned merge point. This event takes place before reaching the target area in the Evaluation Mission, see Section 7. The UCAV group of 5 platforms is within detection range for the SAM site but outside the missile range, see Fig. 7.

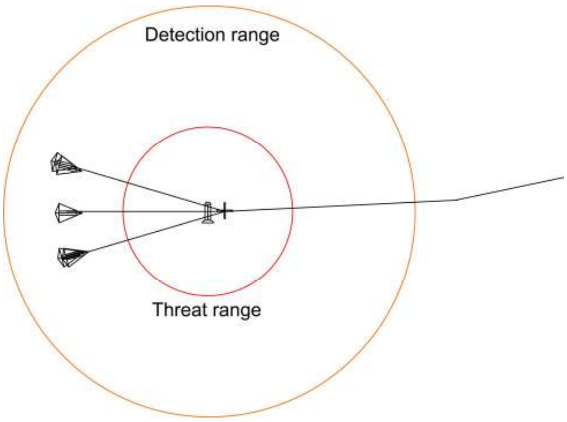

Fig. 7 A new threat pops up at a merge point

The threat is detected and a deviation is triggered by the Monitor Mission function. In the mission adaptation it is noted that the merge point is threatened, and this point is then moved outside of the threat area and the routes affected by the threat are recalculated, see Fig. 8.

From the A* algorithm we get sequences of waypoints for each of the 3 UCAV groups, leading to the new merge point.

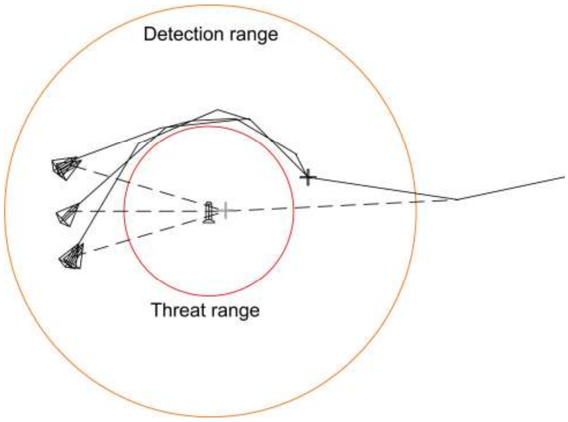

Fig. 8 Moved merge point and recalculated routes

8.2 New threat in target area

This scenario takes place in the target area of the Evaluation Mission, see Section 7. UCAV 1 and 4 will both perform Target Identification and release a weapon. UCAV 2 will perform Target Identification and Illuminate a target while UCAV 3 will release a laser guided weapon against this target, see Fig. 9. The new pop-up threat affects UCAV 1 and 2 directly, and UCAV 3 and 5 indirectly due to the coordination between different tasks.

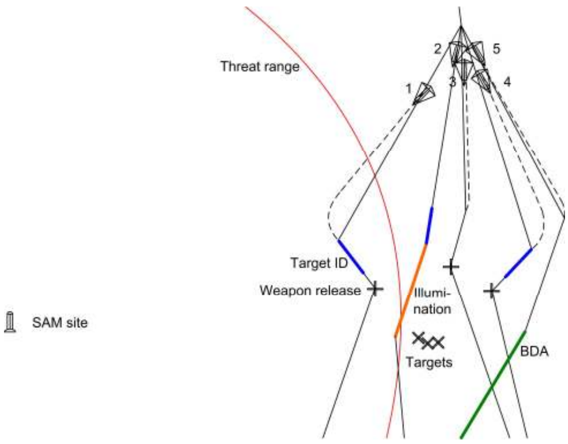

Fig. 9 Pop-up threat affecting 2 UCAV in target area. Dashed lines indicate flight (Dubins) paths, colored lines indicate different tasks, and crosses indicate weapon release points, all for the original plan.

When the unplanned threat, a SAM site, is activated this is detected and this deviation triggers an adaptation of the plan. As a minimum UCAV 2 needs a new flight plan during the illumination task and UCAV 1 needs a new flight plan for the complete attack.

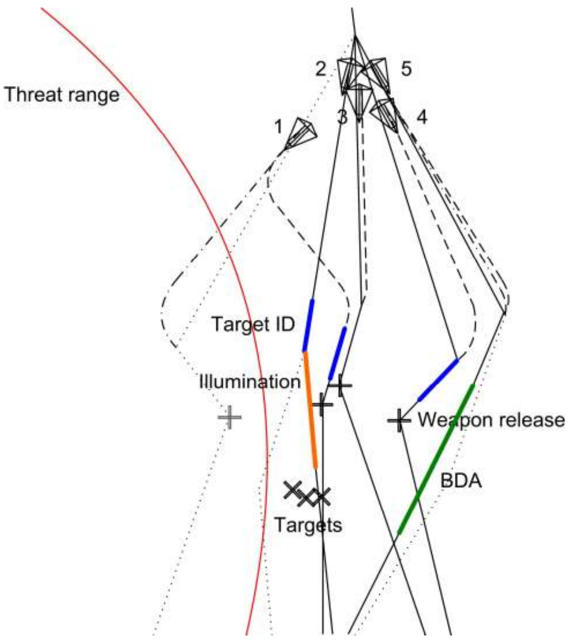

Fig. 10 Adapted plan, shown together with the original plan (dotted and dash-dotted lines).

The adapted plan is shown in Fig. 10. The plan is unchanged for UCAV 3 and 4, while it is updated for the others. UCAV 2 performs Target Identification as in the original plan, but has a new flight path for Illumination. UCAV 1 has a completely new flight plan and releases the weapon from a new direction. For UCAV 5 there is a slight change in flight path, and the BDA tasks are moved to start and finish earlier than before.

8.3 Other results

For other selected demonstrations the results are similar, a reasonable adapted mission plan is computed. However, due to the limited scope of the project and the demonstrations a number of functions in the system are very simplified or incomplete. Thus it is quite easy to find examples where there is room for improvement.

9 Conclusions

In the evaluations above it has been shown that the system works as expected and comes up with solutions to handle the selected stressors. Thus the results from this project can be used as a baseline for further development. Due to the constrained scope of this project there are still necessary functions/capabilities for the selected scenario which were not implemented and demonstrated. The overall robustness of the system also needs improvements, e.g. by running more scenarios and variants of them in order to increase the maturity of the system. Further the complexity/realism for sensor and weapon models and their management needs to increase. Operator Control is another topic to study further, e.g. in order to assess how many operators you would need for this kind of scenario using a collaborating UCAV group with this level of autonomy.

References

[1] Mankins, J., “Technology Readiness Levels”, NASA, 1995.

[2] Cole A., et al, “Sanremo Handbook on Rules Of Engagement”, International Institute of Humanitarian Law, 2009.

[3] Pellebergs, J., “The MIDCAS Project”, 27th Congress of ICAS, Nice, France, 2010, paper ICAS-2010-6.5.1.

[4] http://www.midcas.org

[5] Stulp F., et al; “Implicit coordination with Shared Belief: A heterogeneous Robot Soccer Team Case Study”. Advanced Robotics, Vol 24, 2010, pp 1017-1036

[6] Taylor, R.M. “Technologies for Supporting Human Cognitive Control”, DERA, Paper presented at RTO HFM Specialists’ Meeting on “Human Factors in the 21st Century”, Paris, France, 11-13 June 2001

[7] Dubins, L. E., “On curves of minimal length with a constraint on average curvature, and with prescribed initial and terminal positions and tangents”, American Journal of Mathematics, Vol 79, 1957, pp 497–516.

[8] Hart, P. E.; Nilsson, N. J.; Raphael, B. (1968). "A Formal Basis for the Heuristic Determination of Minimum Cost Paths". IEEE Transactions on Systems Science and Cybernetics SSC4 4 (2), 1968, pp 100–107.

The Servitization of the Aerospace Industry and the Affects on its Product Development

Johanna Wallin
GKN Aerospace Engine Systems, Sweden
Department of Product and production development, Chalmers University of Technology, Sweden

Keywords: *Product-Service Systems (PSS), Servitization, Product development*

Abstract

The aerospace industry is facing a servitization as the service integration is increasing in the product development and product-service systems (PSS) offers become more and more common. This change implies new challenges for the development teams as well as for the whole organization and its network. This research has studied this servitization at GKN Aerospace Engine Systems. The research has focused on the collaborative issues and the findings show examples of methods and activities that support the organization and its teams in the servitization of the product development.

1 Introduction

The long life cycles and product complexity of aircraft engines imply that every engine is an opportunity to supply a stream of spare parts and maintenance services. And since availability of the engine is increasingly valued, rather than the ownership of it, offers such as TotalCare by Rolls Royce has arisen [1]. In these “power by the hour” offers, the functionality of the engine is sold, but the ownership remains with the OEM (Original Equipment Manufacturer). This business model provides a steadier revenue stream for the OEM during the life cycle of the engine.

The safety issue is also of large concern in an industry that risks several lives at engine failure. This implies the regular schedule of maintenance and overhaul, which are services of large cost to the engine owner. It has also lead to large investments in monitoring systems to predict the need for services and exchange of spare parts prior to failure [2].

These are some examples of the “servitisation” of the aerospace industry and the increase of complex Product-Service Systems (PSS) [3] [4]. With this emerges the need for the companies in the industry to build the capability to develop PSS in a systematic way similar to the “traditional” product development.

However, a product development that includes the development of services, software and business models demands a higher complexity of team composition, ways of working, processes, methods and tools for an integrated connection between business development, service development, software development and product development.

The presence and co-creation with users and end customers is critical in service development. This is one of the known difficulties to manage in complex product development processes where the focus is on requirements establishment and verification. To involve the end customer directly in development is hindered by the de-composition of requirements.

This study point to challenges in PSS development and suggest changes in order to integrate a PSS mindset in the development processes and support practitioners and organizations in their transitions to integrated PSS development and increased customer value.

2 Theoretical Framework

Product development has by Kennedy, Harmon & Minnock (2008) [5] been divided into two value streams; a product value stream and a knowledge value stream (Figure 1). The product value stream consists of the flow of tasks, people and equipment needed for creating the product. Whereas the knowledge value stream represents the capture and reuse of knowledge within the organization regarding for example markets, customers, technologies, products and manufacturing.

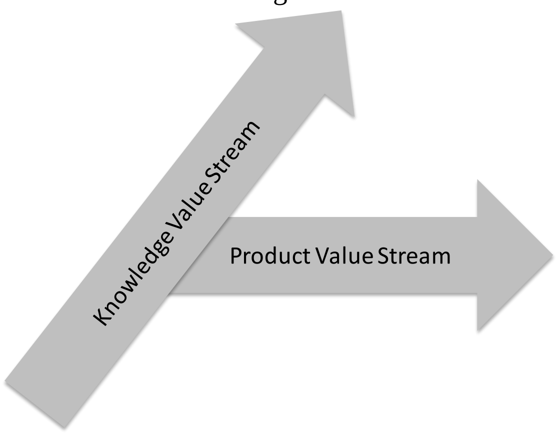

Fig. 1 The value stream in product development (after [Kennedy et al, 2008]).

The servitization of the industry is not something that is happening to the aerospace industry alone. This phenomenon can be noted in all kind of manufacturing companies and industries. One example is IBM that has transitioned from a hardware manufacturing company to a global service provider and software company [6] or Volvo Group that has increased their focus on 'Soft Products' meaning products and services that enhances the satisfaction of customer beyond the core/hard product [7].

There are three main factors that drive companies to PSS development according to Baines et al (2007) [3]; financial (for a higher profit margin or more stable income), strategic (to gain competitive advantage) and marketing (to use services to sell more product).

Literature on the topic has also claimed that there are ecological and sustainable aspects since services can extend the product's life cycle [8], manufacturers become more responsible for upgrades and material recycling [9], it contributes to a more conscious product usage and increases resource productivity [10].

The different characteristics of products and services challenge the development of PSS. There are three main differences between products and services: (1) Products are first produced and then used, whereas services are produced and used at the same time [11]. This also has its affects on the lead time, product design is longer compared to service design, and products are therefore harder to adjust to a changing environment compared to services [12]. (2) Products and services are conducted by different areas of expertise [12] and the ownership of a product is transferred to the customer when the product is sold; whereas the ownership of a service is not generally transferred [11]. (3) Products have hard technical variables (material, dimensions etc.) whereas services soft variables (time, place etc.) [12].

These differences imply barriers for the development of integrated product-service systems.

3 Methodology

The purpose with this research has been to advance our knowledge and support methodology of PSS innovation capability in the aerospace industry. Therefore a qualitative approach was chosen since it is appropriate for obtaining insights into the experiences of individuals and groups. To enable an in depth understanding of the conditions regarding organization, culture, processes and challenges, it was conducted as a single case study.

3.1 The case company

The case company GKN Aerospace Engine Systems (previously known as Volvo Aero). The company has three main businesses; First, the largest, the commercial market, where the company develops components to aircraft engines in partnership with the engine Original Equipment Manufacturer (OEM). The second market is the military, where the company develops the engines to the military aircrafts, such as the Swedish Gripen fighter. Thirdly, the company develops components and subsystems to European space rockets.

In addition to product developments, the company provides services such as maintenance and product support.

This research has focused on the military and commercial business side. The military business side has integrated more service offers to their military engines compared to the commercial business side (Figure 2). This has to do with the fact that on the military side, the company is engine OEM, on the commercial side the OEM is their partner.

3.2 Data collection

Data has been collected through three years of observations at the case company as well as 35 semi-structured interview sessions with stakeholders of business, product, service and PSS development that are distributed across several functions and hierarchy levels at the company. Workshops have also been held to test creative methods for PSS development teams.

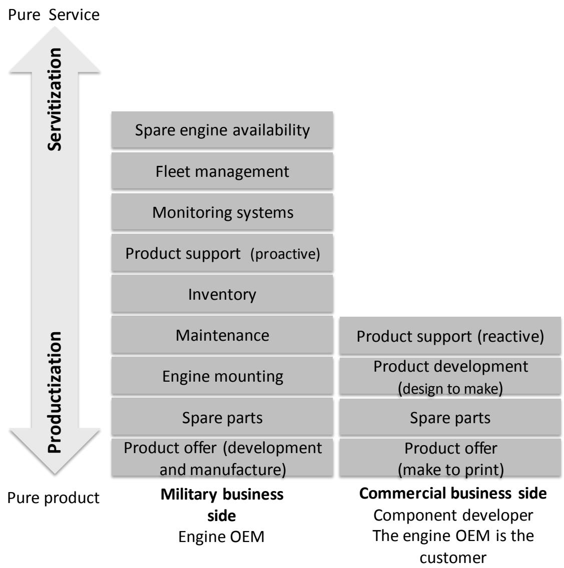

Fig. 2 Service integration in product development at case company.

4 Findings

4.1 The PSS challenge

When talking about 'products' it is not always a clear definition. Sometimes the word includes more than hardware and is rather a definition of PSS:

> *"Product, it actually means more than just hardware, for what we sell, and have done for many years, that is our product expertise, our process technology in production, and our understanding of how the product works on engine level. /../ But I think 90% think of the hardware. And that is a problem in itself".*

The definition of product as hardware only, limits the value creation. It has its history from the traditional business models of selling engines rather than "power by the hour" and the increased value of availability that is recently happening in the aerospace industry.

> *"Adapt to trends, that's perhaps the only way to survive, to keep up with the trends and bring more value. And the*

value may exist on other levels than pure hardware".

The value is considered to be in the product and its functionality. In the aerospace industry there is for example a focus on making the product as light as possible to reduce thrust which leads to a reduction of the fuel consumption.

"Our task is to deliver something that the customer wants. And they want it [the product] to be lighter and cheaper. That's what they want. Then there may be other things, those sorts of things that they do not know that they want".

The product development projects are initiated by the customer in the engine programs and requirements are received from the OEM.

"We shall comply with the requirements. Customers have expressed their expectation. So, the process is not about surprising the customers".

However the same respondent later explained:

"To only do what the customer says is perhaps not sufficient".

4.2 PSS strategies and business models

In a product-focused organization there are ideologies that influence the decisions and strategies in the organization, for example:

"We shall operate in the aerospace industry" or *"We shall not develop software".*

Although, software can be a link between product and services and can therefore be important for the development of PSS offers. A strategy that encourages focus on value propositions or product-service systems strengthens the PSS teams. One project manager of a PSS team described the introduction of a "Soft product" strategy (soft products being products and services that enhance the satisfaction of the customer beyond the core product):

"we got quite a boost, people talked about it quite high up in the company. And it was relatively easy to obtain resources"

This indicates that strategies can change product-focused ideologies in the organization, which is a step forward to find ways to support the PSS transition in the organization.

The development of PSS provides new opportunities to explore new markets. For the case company it has been considered important to provide services that are close to their own core business, but in the periphery of the customers' business. To create long-term value for their customers, the company puts great effort in their relationship with their various customers.

However, it is important to note that the integration of service to their product offer can lead to a position of being competitor to their customers/partners since their customers of their products is the engine OEM, while the customer of certain services are the airlines.

A previous study has analyzed a well known business development tool, The Business Model Canvas [13], from a PSS perspective [14]. The tool is commonly used to design business models. This study concluded that the tool is appropriate for PSS development since is focuses on Value Proposition, however for PSS development it would need a larger focus on a change perspective to widen the business scope, as well as including attention on risks since the transition towards PSS development involves business risks.

4.3 Organizational structures and networks for PSS development

Even though the company is focused on developing and manufacturing of product, they also provide services such as maintenance and overhauls. However the service organization is separate from the product development organization with weak ties between them. One reason is that the services that are provided are often connected to other products/engines then the products that the company is developing.

These weak ties between divisions mean that the two divisions do not directly affect each other in the organization. Although, more close connected to the product development organization is the department of Life Cycle Data Management, which deals with Customer Support and Maintenance Development. This department has increased the strength of the tie between product and service development which is important for the support of the servitization. The department has for example developed software for monitoring systems of users' behavior to maximize product use. Software development falls in the middle of service and product development and is coupled to both.

In PSS development project it has been evident that people with double competences or experience from both product development and software/service development have gotten key roles. They have been important for the communication between different areas of expertise and therefore strengthen the ties between divisions and departments.

The challenges that rise in the process of PSS innovation need to be met with both internal and external routines within the process, such as establishing an innovative PSS culture and have continuous customer interaction. This study has indicated the importance of interaction, collaboration and communication between disciplines internally within the organization as well as externally with customer, in a higher degree compared to product development.

Building PSS innovation capability involves the development of new PSS competence. This research has shown that this can happen through job-rotation, bringing in external recourses and emerge competences.

4.4 Workshops for PSS teams

When the solutions to the problem not only involve the design of a product but also could include the design of services, this opens up the design space for new innovative solutions. The differences of products and services characterize and challenges PSS innovation. However, these challenges can be handled using certain workshops methods with the cross-functional design team which has been shown in previous findings [15].

The differences between product and service development implies challenges for the PSS design team, which can be handle by appropriate workshop methodology. For example:

1. The time perspective is different. This implies that the PSS design team need to visualize the time perspective of history and foresight of the problem and the whole life cycle of the product.
2. The ownership of products and services is different. This implies the importance of having a cross-functional team that includes product, service and business expertise and the importance of having a contact and collaboration with the customer as well as the user of the products and services in order to ensure value creation.
3. The design of products and services are different. Products have hard technical variables of a product, such as material, dimensions etc., whereas services soft variables of services, such as a time and place etc. Therefore there is a need to visualize not only the product but also the services with prototypes for example, in order to unify the cross-functional team and support communication about value creation. *"With the prototype, we could show the value and use it as a tool for communication"* described one interviewee regarding the importance of prototyping.

5 Discussion and conclusion

This research has shown how the servitization of the aerospace industry is evident not only for OEM but also for 1st tier suppliers as the case company.

As the offers no longer consist of products (hardware) only but also of various value adding services, this changes the view of the value stream within the organization. The value stream of services runs in parallel with the value stream of products.

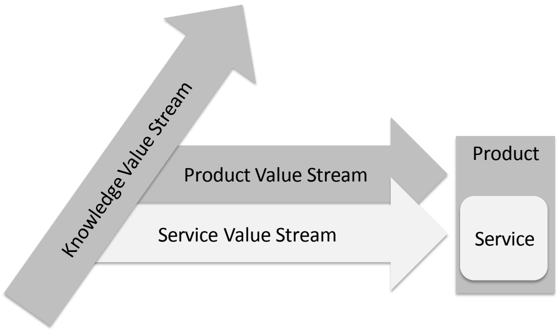

Fig. 1 The value stream in of product-service system development.

This research has exemplified the importance of strategies that is communicated through the organization. This can support the team as they handle the new challenges of servitization and get the right mindset for value creation that is not limited to products.

This research has shown an increased need for collaboration and a larger degree of complexity in the collaborative network as the aerospace industry is servitized. The collaboration involves more stakeholders, which including the customer and user who need to collaborate for a longer period of time, through the whole life cycle of the PSS. To handle the challenges of servitization it is importance to have a larger degree of cross-functionality in the teams compared to product development. Hence, includes product, service and business expertise within the team.

Individuals with double competences or experience from more than one area deserve special attention, because they can play an important role in the communication between different areas of expertise that are new to this collaboration.

Further, this research has shown that the teams need to focus more on the time perspective of products and services, discuss the ownership and value creation of products and services through the lifecycle and preferable visualize this for better communication.

Acknowledgements

Financial support from NFFP5 (Nationella Flygtekniska Forskningsprogrammet) through VINNOVA for the PLANT-project is greatly acknowledged.

References

[1] Harrison, A. (2006). Design for service - Harmonising product design with a services strategy. The ASME Turbo Expo 2006, 6-11 May, Barcelona, Vol. 2, pp. 135-143

[2] Ward, Y., Graves, A. (2007). 'Through-life management: The provision of total customer solutions in the aerospace industry'. J. Services Technology Management, 8(6), 455–477

[3] Baines, T. S.; Lightfoot, H. W.; Evans, S.; Neely, A.; Greenough, R.; Jeppard, J.; Roy, R., Shehab, E.; Braganza, A.; Tiwari, A.; Alcock, J. R.; Angus, J. P.; Bastl, M.; Cousens, A.; Irving, P.; Johnson, M.; Kingston, J.; Lockett, H.; Martinez, V.; Michele, P.; Transfield, D.; Walton, I. M.; Wilson, H. (2007). 'State-of-the-art in product-service systems', J. Engineering Manufacture, Vol. 221, Part B.

[4] Tukker, A. & Tischner, U., 2006. *New Business for Old Europe*. Sheffield, UK: Greenleaf Publishing.

[5] Kennedy, M., Harmon, K. & Minnock, E., (2008). *Ready, set, dominate - Implement Toyota's Set-Based Learning for Developing Products and Nobody Can Catch You*. Richmond: The Oaklea Press.

[6] Dittrich, K., Duysters, G., & de Man, A.-P. (2007). Strategic repositioning by means of alliance networks: The case of IBM. *Research Policy , 36*, 1496-1511.

[7] Remneland-Wikhamn, B. (2011). Path dependence as barrier for 'soft' and 'open' innovation. *International Journal of Business Innovation and Research, 5* (6), 714-730.

[8] Vandermerwe, S., & Rada, J. (1988). Servitization of Business: Adding Value by Adding Services. *European Management Journal, 6* (4), 314-324

[9] Mont, O. (2002). Clarifying the concept of product-service system. *Journal of Cleaner Production,10*, 237-245

[10] Aurich, J., Fuchs, C., & Wagenknecht, C. (2006). Life cycle oriented design of technical Product-Service Systems. *Journal of Cleaner Production, 14*, 1480-1494

[11] Morelli, N. (2002). 'Product-service systems, a perspective shift for designers: A case study: the design of telecentre', Design Studies, Vol.24, No.1, pp. 73-99.

[12] Brezet, J.C., Bijma, A.S., Ehrenfeld, J. and Silvester, S. (2001). 'The Design of Eco-Efficient Services', Design for Sustainability Program, Delft University of Technology, June 2001.

[13] Osterwalder, A. and Pigneur, Y. (2010). 'Business Model Generation'. NJ: John Wiley.

[14] Wallin, J., Chirumalla, K. and Thompson, A. (2013). 'Developing PSS Concepts from Traditional Product Sales Situation: The Use of Business Model Canvas'. To be presented at the 5th CIRP International Conference on Industrial Product-Service Systems, Bochum, Germany, April 14th-15th, 2013.

[15] Wallin, J. and Kihlander I. (2012). 'Enabling PSS development using creative workshops', proceedings at the International Design Conference – DESIGN 2012, Dubrovnik, Croatia, May 21-24.

4:th CEAS Air & Space Conference
FTF Congress: Flygteknik 2013

A New Safety Net for Tower Runway Controller: Preliminary Results from SESAR Exercise at Hamburg Airport in Detection of Conflicting ATC Clearances

Karsten Straube[1], Marcus Biella[1], Marcus Helms[1], Steffen Loth[1], Heribert Lafferton[2], Stephen Straub[2], Benjamin Weiß[2], Felix Schmitt[2], Paul Diestelkamp[2], Roger Lane[3] & Stéphane Dubuisson[3]

[1]DLR Institute of Flight Guidance, Braunschweig, Germany
[2]DFS Deutsche Flugsicherung GmbH, Langen, Germany
[3]EUROCONTROL Experimental Centre, Brétigny, France

Keywords: **ATC Clearances, Runway Controller, Runway Incursions, Hamburg Airport**

Abstract

One of the most serious safety concerns in air traffic control are runway incursions. A runway incursion is defined by International Civil Aviation Organization (ICAO) as "any occurrences at an aerodrome involving the incorrect presence of an aircraft, vehicle or person on the protected area of a surface designated for the landing and take-off of aircraft" [1]. Traditional Advanced Surface Movement Guidance and Control Systems (A-SMGCS) level 2 safety systems detect runway incursions and potential collisions. The subsequent alerts to controllers often require immediate reaction. A new, additional safety net for tower runway controllers was developed to provide longer reaction times for certain kinds of imminent runway incursions. This new safety net detects if controllers give a clearance to an aircraft or vehicle contradictory to another clearance already given to another mobile. The new safety net, developed in context of SESAR, was tested in a shadow mode validation exercise at the operational environment of Hamburg Airport (Germany). Operational feasibility was tested in order to clarify if operational requirements in terms of usability are fulfilled. At the same time operational improvements regarding safety were studied e.g. if the new safety net detects all defined conflicts.

A data logging was made to measure reaction time of the developed Conflicting Air Traffic Control Clearances System (CATC), in interaction with the electronic flight strips (EFS) system.

1 Introduction

Chicago Midway International Airport, December 1st 2011, runways in use are 31C for take-off and landing and runway 22L for take-off. There are two air traffic controllers, one is handling the regular traffic, a second is plugged in as "ground control 2" monitoring the tower frequency and working a VIP arrival checklist.

The tower runway controllers know that a VIP arrival is planned for later the day, which would effectively shut down the airport. This creates a lot of pressure to get as many departures and arrivals through as possible. For this reason the tower runway controllers decide to open runway 31R as an additional departure runway. Figure 1 shows the runways in use at Chicago Midway Airport.

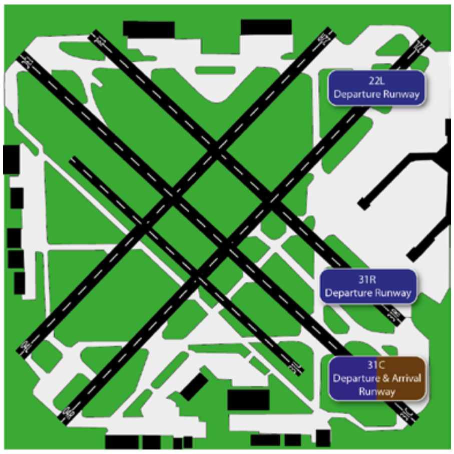

Figure 1: Runways in Use at Chicago Midway Airport

It is 09:06 in the morning. A Boeing 737 of Southwest Airlines flight SWA844 gets the landing clearance for runway 31C. During the landing the first officer of SWA844 observes a Learjet 45 lining up on runway 31R. After the landing of SWA844 the tower runway controller gives take-off clearance to the Learjet on runway 31R. After that he gives SWA844 the instruction "*vacate runway 31C via taxiway Bravo, cross runway 31R and contact ground*". The monitoring tower runway controller recognizes the conflict of the two instructions and queries his colleague whether he would give SWA844 an instruction to hold short of runway 31R on taxiway November. The runway controller does not answer his colleague. The monitoring controller points out for a second time that there is a conflict between SWA844 and the Learjet 45; however he receives no reply by his colleague. In the meantime SWA844 is taxiing at high speed on taxiway Bravo. At 09:08 the pilot of SWA844 calls the tower and advises that "*we have a plane taking off from 31R and you cleared us to cross runway 31R*" The runway controller responds "*SWA844 cross 31R, contact ground*". "*Okay if you just copied you cleared us to cross a runway where there is a plane taking-off*" respond the cockpit crew of SWA844. The tower runway controller does not cancel the take-off nor issue an instruction to SWA844 to hold short of runway 31R on November. At this moment the first officer of SWA844 spots the Learjet which is taking-off from runway 31R and yells to the captain to stop. The SWA844 Boeing stops just short of the runway edge. At this moment the Learjet overflies the Boeing with a vertical separation of 62 feet/ 19 meters and a lateral separation of 267 feet / 81 meters. [2], [3]. Figure 2 illustrates the runway incursion at Chicago Midway Airport.

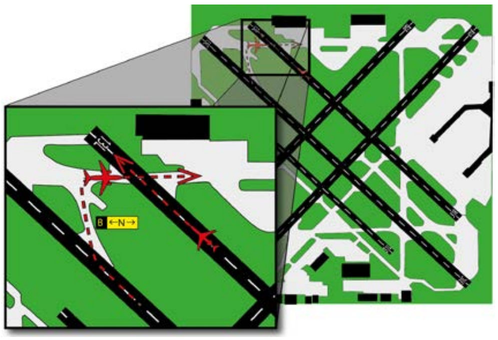

Figure 2: Runway incursion at Chicago Midway Airport

This incident illustrates the risk of conflicting air traffic control (ATC) clearances and their potential consequences.

Another pair of conflicting ATC clearances was given on May 17th 2013 at Hartford airport (Connecticut, USA). In this case simultaneous clearances for take-off and landing on crossing runways were given. In both cases (Chicago and Hartford), fatal collisions could be prevented.

Unfortunately, this was not always so. On February 1st 1991 in Los Angeles conflicting ATC clearances led to a collision between two aircraft where 34 people lost their lives. [4]

In 2011, altogether 66 runway incursions - not leading to an accident - have been reported in Germany. Only 12% of these rare events were caused by tower runway controllers [5] but it can be presumed that conflicting clearances were given before. In order to prevent this cause for a potentially dangerous situation, an additional "Conflicting ATC Clearances Safety Net" (CATC) was created. This safety net detects if clearances given to aircraft or vehicles could lead to a runway incursion.

2 Concept

2.1 Background

The “Single European Sky Air Traffic Management Research” (SESAR) programme is one of the most ambitious research and development projects ever launched by the European Union. The programme is the technological and operational dimension of the Single European Sky (SES) initiative to meet future capacity and air safety needs, i.e. an improvement of safety by a factor of 10 [6]. In this context runway incursions shall be reduced.

The Conflicting ATC Clearances Safety Net concept as well as the prototypes used for validation were developed under the SESAR programme and co-financed by the European Community and EUROCONTROL.

The sole responsibility of this paper however lies with the authors. The SJU and its founding members are not responsible for any use that may be made of the information contained herein.

2.2 The Conflicting ATC Clearances Safety Net Concept

Currently the only safety net available to tower runway controllers to avoid runway incursions is the Runway Incursion Monitoring System (RIMS). It uses Advanced Surface Movement Guidance and Control System (A-SMGCS) surveillance data to detect dangerous situations within the runway protection area. Detections and subsequent alerts to controllers are often provided at the very last moment and require immediate reaction.

The new CATC Safety Net will not replace the existing RIMS but is intended as an additional layer of safety. It will give tower runway controller more time to react by detecting conflicting ATC clearances much earlier – typically at the moment when the tower runway controller inputs clearances into the Electronic Flight Strips (EFS), which are already in operational use in many control towers. To do so, it will perform crosschecks with previous clearances input on the EFS, and in most cases the aircraft position, to check whether one of the situations described in the subsequent paragraphs occurs which could lead to a runway incursion or other hazardous situation [7].

Below we define the types of “conflicting clearances”. Our definition follows the one in [9], which in turn is based on the one in [7]. We consider 4 types of runway related ATC clearances: Line Up (LUP), Cross (CRS), Take-Off (TOF) and Land (LND). Based on these four clearances we define the following conflicting clearance situations:

LUP/LUP: two aircraft are cleared to line up from opposing runway entries on the same end of a runway; or: two aircraft are cleared to line up on opposite ends of the same runway; or: two aircraft are cleared to line up on the same or adjacent runway entries on the same runway, and multiple line-up is not authorized.

LUP/CRS: one aircraft is cleared to line up and another mobile is cleared to cross the same runway from an opposing runway entry.

LUP/TOF: one aircraft is cleared to line up and another is cleared to take-off on the same runway, and the runway entry of the aircraft lining up is in front of the position of the aircraft taking off.

LUP/LND: one aircraft is cleared to line up and another is cleared to land on the same runway, and the runway entry of the aircraft lining up is in front of the position of the landing aircraft, and the landing aircraft is not expected to vacate the runway before the line up point.

CRS/CRS: two mobiles are cleared to cross the runway from opposing runway entries.

CRS/TOF: one mobile is cleared to cross and another is cleared to take-off on the same runway, and the runway entry point of the crossing mobile is in front of the position of the aircraft taking off.

CRS/LND: one mobile is cleared to cross and another aircraft is cleared to land on the same runway, and the entry point of the crossing mobile is in front of the position of the landing aircraft, and the landing aircraft is not expected to vacate the runway before crossing point.

TOF/TOF: two aircraft are cleared for take-off on the same runway or on dependent runways.

TOF/LND: one aircraft is cleared to take-off and another aircraft is cleared to land on the same runway or on dependent runways.

LND/LND: two aircraft are cleared for land on the same runway or on dependent runways.

A CATC system provides an alert to the responsible tower runway controller whenever it detects one of these conflicts. In the introductory example at Chicago Airport, a CRS/TOF conflicting alert would have been given.

Furthermore, definitions of alert types were made [10]:

False Alert: an alert is given but no conflict exists. No alert should be indicated in this case.

Wrong Alert: an alert is given and a conflict exists (e.g. LUP/LUP) but a wrong type of alert is indicated (e.g. LUP/TOF). The correct type of conflict should be indicated instead (e.g. LUP/LUP).

Nuisance Alerts: in contrast to false alerts and wrong alerts, there is no objective definition for "nuisance alerts", but we use this name to label alerts which are not false alerts, but which at least one tower runway controller in the validation subjectively considered this alert as a nuisance.

2.3 Recommendations from Real Time Simulation

A first CATC prototype had already been successfully tested in a SESAR real time simulation exercise [8] with three tower runway controllers from the airports Paris Charles de Gaulle (France) and Leipzig (Germany) in 2011. As a result of this exercise, the definition of the LUP/TOF conflict was changed: previously, the situation had been considered to be a conflict if the position of the lining up aircraft was in front of the taking-off aircraft, as opposed to its runway entry being in front of the taking off aircraft. This lead to nuisance alerts in situations when the aircraft that was due to line up would be still taxiing on the taxiway parallel to the runway but was in front of the aircraft taking off, while the planned line up point was behind the aircraft taking-off.

Furthermore, the real time simulations lead to the recommendation to make the safety net more proactive instead of reactive. A “what-if tool” would be capable to highlight potential conflicting ATC clearances before these clearances are actually given. This would eliminate some alerts and therefore the need for the tower runway controller to revise clearances.

2.4 Description of DFS’s Prototype

The prototype that supported the final validation was developed by DFS Deutsche Flugsicherung GmbH. It is based on the flight data processing system (FDPS) *SHOWTIME* and on the surveillance data processing system (SDPS) *PHOENIX*. In contrast to other CATC implementations, the prototype employs a novel detection logic based on *ground routes:* essentially, a conflict is detected by noting that the cleared parts of two routes overlap somewhere on a runway. See [9] for more details on this approach.

Detected conflicts lead to alerts that are displayed both in the FDPS HMI (Figure 3) and in the SDPS HMI (Figure 4) for as long as the conflict persists. When a new alert occurs, this event is also accompanied by an audible beep.

Figure 3: TOF/LND alert in FDPS

The tower runway controller may *acknowledge* an active alert by clicking on the "ACK" button the very right of a flight strip. Acknowledged alerts continue to be displayed, but become less obtrusive.

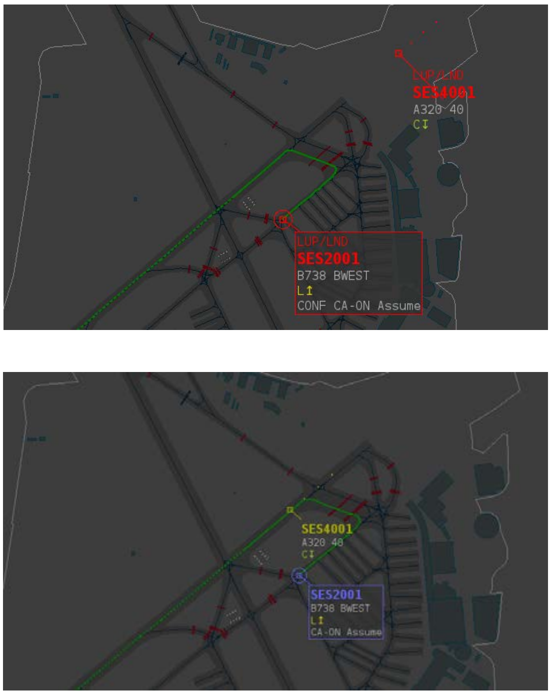

Figure 4: LUP/LND alert in SDPS display (first image), neutralized after SES4001 passes the runway entry of SES2001 (second image)

Tower runway controllers enter relevant information such as holding points, assigned thresholds and clearances via the FDPS HMI. For example, the typical "next" clearance according to standard procedures at the airport can be entered by clicking on the square at the very left of a flight strip.

Following a recommendation that resulted from the real time simulation (see Section 2.3), the prototype includes a predictive indication of conflicts in addition to the regular alerting mechanism. The system continuously checks for every active mobile whether entering the typical next clearance (according to standard procedures) would, at this point in time, cause a clearance conflict or not.

Figure 5: Predictive conflict indication: two possible clearance conflicts indicated by red dots in the flight strips of UAE25 and DLH1MA

The result is shown as a little red or green dot in the flight strip. For example, in Figure 5, the system indicates that giving a LUP clearance to UAE25 or to DLH1MA would currently create a clearance conflict, whereas giving a LUP clearance to GEC9834 would not.

2.5 Validation Objectives for Shadow Mode Trials

First of all, the operational feasibility in terms of fulfillment of operational requirements (as stated in the Operational Services and Environmental Description (OSED) [7]) had to be checked, mainly by controllers' feedback on the usability of the different alerts and the HMI design.

Secondly operational improvements in terms of safety had to be studied. Also, it was crucial that the new safety net detected all defined conflicting situations. Furthermore the safety net should allow the controller to solve detected situations timely. In addition to that the false alert rate and also the nuisance alert rate had to be acceptable for the controller.

Furthermore, in this paper we consider in detail one of the objectives, derived by SESAR P16.06.01 and SESAR P06.07.01 on the basis of [12] and [13], which validates if the CATC system is able to provide alerts to the tower runway controller in not more than 1 second following the reception of the conflicting clearance from the EFS system.

3 Method

3.1 General Description of the Trials

The shadow mode trials were performed with different controller teams each day at the airport environment at Hamburg airport between the 26th and 30th November 2012. A controller team consisted of a ground and a runway controller.

In total eleven tower controllers took part in the study. Six were active Hamburg controllers, one had recently retired in 2011. Additional controllers came from the airports in Hamburg Finkenwerder, Leipzig (both Germany), Klagenfurt (Austria) and Lamezia Terme (Italy). Eight of them were male, three were female. Their average age was 35.5 years. For the six active Hamburg controllers the mean reported experience was 6.3 years.

3.2 Shadow Mode Environment

The exercise was located outside the control tower environment to not interfere the active controllers and pilots communication. All data was copied and re-routed to a separate, temporary control room set up for the duration of the exercise.

3.3 Traffic

Real live traffic of Hamburg Airport was used. Additional synthetic traffic was produced to create pre-conditions for conflicting clearances in case the live traffic did not allow for a CATC situation. The participating controllers were informed that these synthetic targets could be injected to increase the number of critical situations in the trials.

3.4 Task

Due to the nature of a shadow mode trial both controllers of a team had to act as if they were in charge but without any intervention to the real traffic. One of the two controllers started as tower runway controller, assisted by a technical supporter from DFS on his left, and the validation supervisor from DLR on his right. The other controller had to act as a ground controller, dealing with all other clearances. Together with the validation co-supervisor they created potential conflicting situations for the tower runway controller.

The inherent problem of the validation exercise was that the controllers had to be forced to produce conflicting ATC clearances situations to test the concept. The tower runway controller was briefed to make an input to the EFS for an aircraft in accordance to a clearance by the real operational tower runway controller in the control tower. The validation supervisor identified a second aircraft and asked the tower runway controller in the validation scenario to give now a pre-defined conflicting ATC clearance. For example, the tower runway controller made a TOF clearance input on the EFS for an aircraft. After that he gave – on order of the validation supervisor – a CRS clearance to another aircraft on the same runway in front of the taking-off aircraft. This resulted in a TOF/CRS conflict.

The first part of each day was dedicated to brief both controllers on the scope and objectives of the shadow mode trials and to train them on the equipment and environment. Most of them already had an additional pre-training the week before.

3.5 Scenarios

Every day, three shadow mode trials lasting seventy minutes each were performed. After 35 minutes controllers were told to switch roles (from tower to ground controller and vice versa). The first of the three trials focused on scenarios with the first clearance being “LND”. The second trial took into account scenarios with the first clearance being “LUP” or “TOF”. The third and final trial dealt mainly with CRS scenarios and any other conflicting clearance situation which had not been tested before or which was regarded as particularly interesting by the participating controllers.

3.6 Data Logging and Measurements

Data logging was made to check if the objective and the resulting requirements were fulfilled. To this end, the message-oriented middleware of the DFS prototype had been wiretapped such that all messages throughout the trials were sorted (with respect to their origin), time stamped, and written to disk. These messages carried information about:

- flight plans,
- flight plan changes,
- selections, i.e., a mouse click on a specific target,
- CATC alerts,
- CATC alert acknowledgements (cf. chapter 2.4).

Furthermore, tailor made questionnaires had been prepared to capture controllers‘ feedback and comments. Each controller had to complete the questionnaire in an Excel spreadsheet after the last of the three shadow mode trials on each day. Controllers were asked how far they could agree to each proposition by choosing answers amongst six categories ranging from 1 (strongly disagree) to 6 (strongly agree) on a Likert scale. Mean values (M) and standard deviations (SD) were calculated to describe the result. Furthermore, by use of a binomial test [14] for a single sample size, each item was proven for its statistical significance by following conditions:

Expected mean value = 3.5
Test ratio: 0.50
Alpha = 0.05
Probability (p) values are classified as follows:

$p<0.01$: the agreement with a statement has been highly significantly unambiguous because the p-value is equal or less than the critical error probability which is 0.01.

$p<0.05$: the agreement with a statement has been significantly unambiguous because the p-value is equal or less than the critical error probability which is 0.05.

$p<0.10$: the agreement with a statement has at least a significantly unambiguous trend because the p-value is equal or less than 0.10. More tests are needed to clarify if this trend is really unambiguous significant.

Furthermore, the questionnaires asked whether the correct type of alerts had been triggered and to what amount false and nuisance alerts had been observed.

The complete results of the final debriefing questionnaire including comments can be found in the SESAR Validation Report [10].

4 Results

4.1 Operational Feasibility

The tower runway controllers agreed in the post trials questionnaire that they appreciate the conflict information (M=4.7 on a six point Likert scale, SD=0.9, N=10, p=0.02). Furthermore, the tower runway controllers gave positive feedback for the HMI design aspects. They agreed that the configuration of the alert indicating was fine with them regarding size (M=4.7, SD=0.6, N=11, p=0.01), the use of the alert color “red” (M=4.9, SD=0.8, N=11, p=0.01), and contrast (M=4.8, SD=0.4, N=11, p=0.00). Further, audio alarms were rated as usable (M=4.8, SD=0.4, N=10, p=0.00) by the controllers.

Detailed feedback for conflicting clearances alerts regarding operational feasibility is provided in [10] and [11].

4.2 Operational Improvements

4.2.1 Operational Improvements in Terms of Safety

4.2.1.1 Detection of Conflicting Situations

Based on observation by experts the correct type of alert was triggered in each case. In detail, the following alerts were triggered successfully during the week of shadow mode exercise: 55 LND/LND; 55 LUP/LND; 96 TOF/LND; 25 CRS/LND; 35 LUP/LUP; 27 LUP/TOF; 18 LUP/CRS; 39 TOF/TOF; 25 CRS/TOF; and 4 CRS/CRS [10].

In addition all controllers highlighted that no alerts were missing in the different trials.

Furthermore it could be shown that multiple alerts with more than two aircraft can be displayed comprehensibly.

4.2.1.2 Timely Detection of Alerts

Based on observation by the expert team, on the controllers' statements during the debriefing session and the results in the questionnaires, it can be said that the alerts are generally displayed in time. (M=5.0 on a six point Likert scale, SD=0.5, N=9, p=0.00) [10].

4.2.1.3 Acceptability of False Alert Rate

Based on observation by experts no alerts were given by the system in case that no conflict existed. Therefore no false alerts can be reported [10].

4.2.1.4 Absence of Nuisance Alerts

The controllers were asked if the CATC system gave alerts in situations where the alert is not necessary, for instance according to local procedures.

The controllers agreed in the post trials questionnaire that the number of nuisance alerts was acceptable (M=4.8 on a six point Likert scale, SD=1.2, N=8, p=0.07 indicating a statistically significant trend).

Furthermore the number of alerts that were displayed "too early" was sufficiently low (M=5.3, SD=0.5, N=6, p=0.03) [10].

The controllers of Hamburg airport reported that two LUP/CRS alerts were not necessary in some cases because the width of these particular two taxiways allows a simultaneous line up and cross of two aircraft depending on aircraft size.

4.2.2 Validation of Average Time of Alerts' Provisions

The average provision time of an alert was calculated with the average time between a change in the flight plan and the time when the alert message occurred. In this case a flight plan change means when the second clearance was given. The system logged this time only in seconds not in milliseconds. During the validation exercise we had 379 alerts (cf. chapter 4.2.1.1).

In 61.18% of all cases the alert occurred within the same second in which the conflicting clearance was given which means that the time between the flight plan change and the alert was somewhere between 0 seconds and 1 second.

In 38.03% of all cases the alert occurred within two consecutive seconds which means that the time between the flight plan change and the alert was somewhere between 0 seconds and 2 seconds. It is also possible that the value could be less than 1 second[1].

In only 0.79% the alert needed more than two consecutive seconds which means that the time was somewhere between 1 second and 3 seconds[1].

This result was also supported by observations through DLR experts. The observation and the data logging revealed that the most of the average provision of alerts took no longer than one second.

Furthermore, this topic was discussed with controllers. They gave a positive feedback about this topic during the discussion in debriefing sessions and within the questionnaires. The result of controller questioning about the average provision of alerts was a positive feedback with a mean=4.0 on a 6-point Likert scale (SD=1.5, N=6) [10].

[1] The reason for this inaccurate information is the lack of milliseconds during the data logging.

5 Discussion

Overall the validation can be considered as very successful. The technical feasibility of the safety net within a real airport environment could be shown. The display of alerts simultaneously on SDPS and FDPS and the use of an audio alert were appreciated by the controllers [10].

Even though, for obvious reasons, the experimental setup on site at Hamburg Airport did not allow for real-time interaction with aerodrome traffic, the trial was able to demonstrate the potential of an additional safety net of this kind.

The controllers' feedback given in the questionnaires and debriefing sessions was very positive regarding the new safety net. Every expected alert was generated and displayed by the system. During the exercise no false alert occurred. This is an important result, because few false alerts within a period of time could lead to total distrust, followed by ignorance of the controllers, thus making the entire safety net void.

Furthermore, false alert events are noted yet more intensely. The workflow would be interrupted, actions might be taken possibly even creating new and additional risks, as no conflict existed in the beginning – a result that is not acceptable and thus is strongly remembered by the user.

It therefore is crucial to allow for individual configuration, decreasing nuisance alerts and to invest into the elimination of false alerts before introducing a safety net of any kind.

According to the controllers and observers and after evaluating of the data logging the alerts occurred in an acceptable time.

The concept in general was considered to be a useful predictive safety support tool that would work in conjunction with additional safety nets (e.g. RIMS).

In the next step the use of the underlying routing function as part of the concept could be discussed as a part of the next OSED. This function is an added value to suppress nuisance alerts this was also shown in the Hamburg shadow mode trials. Furthermore the necessity of additional real time simulations was stressed by the validation team, controllers and observers. They should involve the above mentioned safety nets, and include visual flight rules traffic and helicopters to test more complex situations (e.g. traffic without flight plans). This will certainly increase workload for the controller and probably create more safety critical situations. Conflicting taxi clearances could be tested in this environment as well [10].

A new objective concerning the acknowledgement of alerts should be derived. This new objective could validate in which situations the controller acknowledges an alert, to adapt the safety net on local procedures.

Furthermore, data logging in future validations should use milliseconds in order to validate the reaction times of the system much more precisely.

In the validation exercise conflicting ATC clearances were caused on purpose in order to test the concept. However, in the real operational environment the new safety net would act as a kind of watchdog in the background, and would be visible only in the rare occasion of a clearance conflict. It would be a revealing test to let the system run silently and unattendedly by the controller in shadow mode linked to the EFS inputs of the real operational tower controllers. This would allow one to measure how often conflicting clearance alerts occur in practice with real controllers acting normally. The goal being that this happens almost never.

In summary, the implementation of the safety net is capable to assist the controllers to perform their tasks even more safely while maintaining the efficiency of the airport operations.

In combination with other safety tools in use and under development, decreasing the risk of potential conflicting clearances is one step in the effort to maintain and increase safety in air traffic despite continuously increasing traffic numbers and growing demand especially at international airports as bottlenecks in the air transport system.

References

[1] ICAO Document 4444 - *Procedures for Air Navigation Services - Air Traffic Management* (14th Edition), 2001.

[2] Hradecky, S.: Incident Southwest B737 at Chicago on Dec 1st 2011, ATC error causes runway incursion (Jan 10th 2012) http://avherald.com/h?article=4490d65e&opt=6912 [June 7th 2012]

[3] National Transport Safety Board. Final report OPS12IA167B File No.:30492 11/07/2012

[4] National Transport Safety Board. Aircraft Accident Report Runway. PB91-910409 NTSB/AAR-91/08

[5] Deutsche Flugsicherung: *Luftverkehr in Deutschland*. Mobilitätsbericht, 2011. http://www.dfs.de/dfs/internet_2008/module/presse/dfs_mobilitaetsbericht_2011_de.pdf

[6] SESAR: *The Roadmap for sustainable Air Traffic Management: European ATM Master Plan (2nd Edition)*, 2012.

[7] R. Lane, M. Bonnier, S. Dubuisson, B. Morizet. *SESAR P06.07.01 D16 Updated Operational Service and Environment Definition (OSED) for Conflicting ATC Clearances, Version 1.0*, 2012.

[8] R. Lane, M. Bonnier, S. Dubuisson, M. Biella, K. Straube *SESAR P06.07.01 D15 V2 VALR ATC Conflicting Clearances Validation Report (VALR)* – Version 1.0, 2012.

[9] B. Weiß, F. Centarti, F. Schmitt, S. Straub (2013). *Route-Based Detection of Conflicting ATC Clearances on Airports.* In International Symposium on Enhanced Solutions for Aircraft and Vehicle Surveillance Applications (Proceedings ESAVS 2013).

[10] M. Biella, K. Straube, M. Helms. *SESAR P06.07.01 D19 VALR V3 ATC Conflicting Clearances Validation Report* (VALR) – Version 00.01.00, 2013.

[11] M. Biella, K. Straube, M. Helms, S. Straub, B. Weiß, F. Schmitt, H. Lafferton, S. Dubuisson, R. Lane. *How can a future safety net successfully detect conflicting ATC clearances – yet remain inconspicuous to the Tower runway controller? First results from a SESAR exercise at Hamburg Airport.*

[12] D. Fowler, E. Perrin, R. Pierce *2020 Foresight – a system-engineering Approach to Assessing the Safety of the SESAR Operational Concept* – 2011

[13] E. Perrin *SESAR P16.06.01 Safety Reference Material* Ed. 2.01 – 2012

[14] Handbook of Biological Statistics: Exact test for goodness-of-fit http://udel.edu/~mcdonald/statexactbin.html [29.07.2013]

Automatic Landing System for Civil Unmanned Aerial System

C. Grillo and F. Montano
University of Palermo, Italy

Keywords: *Ground Effect, Automatic Landing, UAS*

Abstract

Taking ground effect into account a longitudinal automatic landing system is designed. Such a system will be tested and implemented on board by using the Preceptor N3 Ultrapup aircraft which is used as technological demonstrator of new control navigation and guidance algorithms in the context of the "Research Project of National Interest" (PRIN 2008) by the Universities of Bologna, Palermo, Ferrara and the Second University of Naples.

A general mathematical model of the studied aircraft has been built to obtain non–linear analytical equations for aerodynamic coefficients both Out of Ground Effect and In Ground Effect. To cope with the strong variations of aerodynamic coefficients In Ground Effect a modified gain scheduling approach has been employed for the synthesis of the controller by using six State Space Models. Stability and control matrices have been evaluated by linearization of the obtained aerodynamic coefficients. To achieve a simple structure of the control system, an original landing geometry has been chosen, therefore it has been imposed to control the same state variables during both the glide path and the flare.

1 General Introduction

In spite of a number of potentially valuable civil UAS applications The International Regulations prohibit UAS from operating in the National Air Space. Maybe the primary reasons are safety concerns. In fact their ability to respond to emergent situations involving the loss of contact between the aircraft and the ground station poses a serious problem. Therefore, to an efficient safe insertion of UAS in the Civil Air Transport System one important element is their ability to perform automatic landing afterwards the failure. At the present, a few number of UAS is fully autonomous from takeoff to landing [1]. Moreover, the mathematical model of ground effect is usually neither included in the model of the aircraft during takeoff and landing nor in the design requirements of the control system [1], [2], [3], [4]. Some authors take into account the ground effect using a mean value of down-wash angle [5]. To cope with strong variation of aerodynamic characteristics most of papers make use of two different mathematical models of the aircraft during landing: the first Out the Ground Effect (OGE) and the second In Ground Effect (IGE).

Besides for an automatic longitudinal landing control, two different control systems are used:

a glide path control system during the glide slope phase and a flare control system in order to execute the flare maneuver [2], [3], [4] [5]. Usually ,during the glide slope glide path angle, pitch attitude and air speed are controlled [2], [3], [4] .Other authors use normal acceleration, air speed and pitch rate [5]. A lot of paper employees altitude and descent velocity. Recently, because of either GPS use or the increase of sensor's performances for the angular rates measurement, pitch angle and pitch rate are often used [2], [3], [6], [7], [8]. Sometimes, instead of airspeed (V) , because of the small values of the glide slope angle, aircraft velocity along the longitudinal axes (u) and elevation are controlled and the altitude is employed to tune the control laws[9]. As the airplane gets very close to the runway threshold, the glide path control system is disengaged and the flare control system is engaged. This one controls either the vertical descent rate of the aircraft, or the air speed and altitude [2], [3], [4], [5]. To control height accurately in the presence of wind and gust the perpendicular distance and velocity from the required flight path are used to calculate a demanded maneuver acceleration, this one, by means of aircraft speed and orientation is converted to pitch rate [10].

Obviously the above mentioned approach leads to a complex structure of the control system, therefore it could give rise to significant system errors due to unmodelled ground effect. To overcome these complexities, the objective of this paper is the design of a longitudinal control system having the following characteristics:

a. The controlled variables are the same during both the glide path and the flare;
b. According to previous papers [11], [12]; the aerodynamic coefficient vs. altitude are modeled during takeoff instead of using a mean value [13], [14];
c. Indirect flight path control is carried out by controlling the velocity vector (Airspeed V and glide path angle γ);

Item a. allows to achieve a simple structure of the control system independently of the actual flight phases. Item b. permits to take into account the actual ground effect. Item c. implies that the elevator and the throttle control the velocity vector, during the whole path.

Because of high angles of attack during landing, a nonlinear mathematical model of the aircraft should be used for designing the controller [15], [16]. As a consequence, to obtain satisfactory performance, nonlinear controllers should be developed [17]. To overcome the difficulties due to the use of nonlinear models of the aircraft in ground effect, a gain scheduling flight control system has been designed using the following approach:

– The Landing flight path has been divided into two segments: the glide path for aircraft altitudes $h >$ *of the* wing span b (OGE) and the flare for $h <= b$ (IGE);
– The flare manoeuvre starts for $h = b$;
– An acceptable number of linear models has been obtained by means of linearization of the original nonlinear model in various flight conditions: one in OGE condition (from 300 ft to $h = b$) and five in IGE conditions (during flare). (These ones are necessary to employ the linearization through the small disturbance theory).
– A modified gain scheduling approach has been employed for the synthesis of the controller. Initially, by using the obtained linear models, various PID controllers have been designed. Afterwards the obtained PID gains have been modelled by using analytical equations,taking into account the hyperbolic variations of the aerodynamic coefficients. Finally, by linearization of the obtained equation for the gains a set of control gains matrix has been calculated.
– A flight control system has been implemented consisting of the above PID controllers and a supervisor which schedules one of them to be inserted online, depending on the actual flight condition.

The contributions of this paper are: the general model of the aerodynamic coefficients in the whole range of altitude from OGE to IGE condition, the original landing geometry, the simple structure of the control system. Therefore, the system is easily configurable since to control the velocity vector only a small set of sensors are necessary. In fact, by using both Inertial Measurement Unit (IMU) and air data boom, pitch attitude (ϑ) ,airspeed (V) and angle of attack (AOA, α) are easy obtainable. Otherwise a low rate GPS may be used to obtain glide path angle (γ) airspeed (V) and vertical ground speed (V_Z).

2 Flight Control Research Laboratory

The studied research aircraft is used for the Italian National Research Project PRIN2008.

The subject vehicle is an unpressurized 2 seats, 427 kg maximum take of weight aircraft. It features a non retractable, tail wheel, landing gear and a power plant made up of reciprocating engine capable of developing 60 HP, with a 60 inches diameter, two bladed, fixed pitch, tractor propeller. The aircraft stall speed is 41.6 kts, therefore it is capable of speeds up to about 115 kts (Sea level) and it will be cleared for altitudes up to 10.000 ft. (Fig. (1))

Because of it is used as a Flight Control Research Laboratory (FCRL) the studied aircraft is equipped with a research avionic system composed by sensors and computers and their relative power supply subsystem. In particular the Sensors subsystem consists of :

- Inertial Measurement Unit (three axis accelerometers and gyros)
- Magnetometer (three axis)
- Air Data Boom (static and total pressure port, vane sense for angle of attack and sideslip)
- GPS Receiver and Antenna
- Linear Potentiometers (Aileron, Elevator, Rudder and Throttle Command)
- RPM (Hall Effect Gear Tooth Sensor)
- Outside air temperature Sensor

Geometrical characteristics of the subject vehicle are:

- Wing area S: 120 ft^2
- Wing chord c: 3.934 ft
- Wing span b: 30.5 ft

Fig. 1 Flight Research Laboratory L.A.U.R.A.

3 UAS Mathematical Model

When an aircraft flies close to the ground, this imposes a boundary condition which inhibits the downward flow of air associated with the lifting action of wing and tail. The reduced downwash mainly reduces both the downwash angle ε and the aircraft induced drag, therefore it increases both the wing-body and the tail lift slope. Therefore, the lift increases, the neutral point shifts, the pitching moment at zero lift varies. So, stability derivatives In Ground Effect must be used during take-off and landing for aircraft altitudes similar to the wing span b.

Because of these effects, stability derivatives have to be modified and so it is very important a mathematical model which afford to evaluate their behavior in ground effect.

Therefore, for ground distance h ≤ b it's necessary to evaluate the h-derivatives.

In previous researches [11], [12], a mathematical general methodology has been tuned up to evaluate the aerodynamic characteristics variation laws due to the altitude. Such a methodology permits the calculation of aerodynamic coefficients either OGE or IGE. It has been found that aerodynamic coefficients can be expressed by means of hyperbolic equations [11].

According to [18], to evaluate the influence of ground effect on aerodynamic coefficients the variation of either angle of attack (α), or downwash angle (ε) or aspect ratio (A) due to flight altitude have been modeled by using classical methodologies [13], [19] by:

$$\Delta\alpha = -F_{tv}\left[\frac{9.12}{A} + 7.16\frac{c_r}{b}\right]c_{L_{wf}} - \frac{A}{2c_{L_{\alpha_{wf}}}}\frac{c_r}{b}\left[\frac{L}{L_0} - 1\right]c_{L_{wf}} r_g \quad (1)$$

where:

- F_{tv} represents the vortex effect on the lift;
- A represents the aspect ratio;
- c_r represents the cord in the wedge wing section;
- $c_{L_{wf}}$ represents the lift coefficient, in this case it is the value in the equilibrium position;
- $\frac{L}{L_0} - 1$ represents a correction factor that take into account of the vortex non linear effects on the lift;
- r_g represents the non linear correction factor for taking into account that the wing is finite

$$\Delta\varepsilon = \frac{b_{eff}^2 + 4(H_h - H_w)^2}{b_{eff}^2 + 4(H_h + H_w)^2} \quad (2)$$

where:

- H_h e H_w represent the tail and wing height from the ground;
- b_{eff} represents a non linear term that links contributes due to the wing span in IGE condition. It can be expressed by:

$$b_{eff} = \frac{c_{L_{wf}} + \Delta c_L}{\frac{c_{L_{wf}}}{b_w^I} + \frac{\Delta c_L}{b_f^I}}$$

where:

- $c_{L_{wf}}$ represents the lift coefficient in OGE condition;
- Δc_L represents the lift increase in OGE condition;
- b_w^I is calculated by $b_w^I = b\left(\frac{b_w^I}{b}\right)$ and the $\frac{b_w^I}{b}$ ratio is known in literature;
- b_f^I is calculated by $b_f^I = b\left(\frac{b_f^I}{b_w^I}\right)\left(\frac{b_w^I}{b}\right)$ and the $\frac{b_f^I}{b_w^I}$ ratio is in literature.

$$-\frac{1}{\pi A_e} = \frac{c_{L_{\alpha_{IGE}}}}{c_{L_{\alpha_{OGE}}}}\frac{1}{c_{L_{\alpha_{airfoil}}}}\left(1 - \frac{c_{L_{\alpha_{airfoil}}}}{\pi A_{OGE}}\right) - \frac{1}{c_{L_{\alpha_{airfoil}}}} \quad (3)$$

By using Eq. (1), Eq. (2) and Eq. (3) the longitudinal stability derivatives may be determined as:

$$c_{L_\alpha} = 3.7931 + 0.01091\left(\frac{h}{b}\right)^{-1.416}$$
$$c_{M_\alpha} = -0.8798 - 0.03147\left(\frac{h}{b}\right)^{-1.405}$$
$$c_{L_{\dot\alpha}} = 0.9452 - 0.05758\left(\frac{h}{b}\right)^{-1.406}$$
$$c_{M_{\dot\alpha}} = -2.4528 - 0.1501\left(\frac{h}{b}\right)^{-1.403}$$
$$c_{L_q} = 4.5086\, rad^{-1} \qquad (4)$$
$$c_{M_q} = -7.3647\, rad^{-1}$$
$$c_{T_V} = -0.0896\, rad^{-1}$$
$$c_{L_h} = -0.006653\left(\frac{h}{b}\right)^{-2.463}$$
$$c_{D_h} = -0.0001002\left(\frac{h}{b}\right)^{-2.685}$$
$$c_{M_h} = 0.001339\left(\frac{h}{b}\right)^{-2.717}$$

4 Flight Path Model

As it is known, the landing procedure is constituted of a slope segment and a flare. Obviously the glide slope phase start out of ground effect, afterwards ground effect is to take into account. Therefore because of, as previous stated, strong variation of aerodynamic coefficients are due to ground effect, a non linear model of the studied aircraft should be used. To overcome this difficulty an original landing geometry has been chosen:

- The first part starts when UAS is at h=300ft and it is a constant speed descent until $h=b$ with a glide slope angle γ=-6° (because there are not passengers, and so it's not necessary take into account some wealth requirement, it's possible don't consider flight path angle γ limitations);
- the second part is a constant speed flare which start when $h=b$ (UAS in IGE condition).

Therefore it has been divided the second condition in five steps based on the values of the h/b ratio. Each one of these steps have a 0.2 h/b ratio size. So the first step is from h/b=1 to h/b=0.8 and so on (in this way there are not strong variation of flight altitude in each step).

This subdivision has been necessary to employ the linearization at several equilibrium flight conditions over the desired flight path; then the small disturbance theory may be applied. In this way difficulties due to the use of nonlinear models of the aircraft in ground effect have been overcome and, in particular, it has been obtained six stability matrices and six control matrices (one for OGE condition and five for IGE condition for each kind of matrices).

The studied flight path is governed by the two following equations:

$$h = -0.1051x + 91.44$$
for $0 \le x \le 766.8\, m$

$$h = \frac{1}{2}\left(3952.4 - \left(3952.4^2 - 4(x^2 - 1927.6x + 932880)\right)^{\frac{1}{2}}\right) \qquad (5)$$
for $x > 766.8\, m$

where x=0 h= 300 ft represents the beginning of the landing path.

5 Automatic Landing System

Because of the small disturbance theory permits to decouple longitudinal and lateral motion only longitudinal equations have been used in the present study.

$$\dot V = \frac{T}{m}cos(\alpha_T + \alpha) - \frac{D}{m} - gsin(\alpha_T + \alpha)$$
$$\dot\alpha = \frac{T}{mV}sin(\alpha_T + \alpha) - \frac{L}{mV} + \frac{g}{V}cos(\alpha_T + \alpha) + q \qquad (6)$$
$$\dot q = \frac{M}{I_y}$$

Considering Eq. (4), stability derivatives have been calculated in one value of *h/b* inside each of the five steps considered. Because of altitude variation inside each step is small, it has been possible to consider derivatives constant inside each step.

The above hypothesis bring to the following linear state space equation:

$$\dot{x}(t) = A(h)x(t) + B(h)u(t) \qquad (7)$$

where the state vector is

$$x(t) = [\Delta V\ \Delta\alpha\ \Delta q\ \Delta\theta\ \Delta h]^T \qquad (8)$$

and the control vector is

$$u(t) = [\delta_{el}\ \delta_{th}] \qquad (9)$$

Air speed and flight path angle has been controlled during the whole procedure. In particular deflection of elevator is used to control the speed while the deflections of elevator and throttle together are used to control the flight path angle.

Besides following requirements have been imposed:

- maximum tracking error less than 10% during the studied flight path;
- rise time smaller than 5 seconds;
- settling time smaller than 15 seconds.

Because of during the landing flare it is necessary to correlate the vertical speed to the instantaneous distance from ground, an altitude control has been effected through an external P feed forward control loop. Such a system is engaged from flight altitude from 6 m to touch down. Elevator deflections are employed to control flight altitude. Obviously such a system improves the precision of the controller in flight path following.

Because of, as stated in the previous paragraph, six linear models of the studied aircraft have been obtained six multiple PID controllers have been designed by using time domain specifications.

In particular the elevator PID controllers are MISO systems, whereas the throttle PID controllers are SISO systems.

Each one of the obtained sets of gains belongs to one value of the h/b ratio.

Afterwards a supervisor, has be implemented. This one, by using the actual flight altitude, schedules the set of gains to be inserted online, depending on the real flight condition.

In this way it is possible to take into account the ground effect.

6 Results

Before its implementation on board the Flight Control System has been tested in MATLAB Simulink environment, Fig. (1-a) shows the flight path of the center of mass (notice that because of the presence of the landing gear the touchdown corresponds to h=1.1 m). As previous stated, the landing has been divided in descent (that starts when UAS is at h=300ft) and flare covered both at constant speed. According to JAR VLA the approach speed is equal to 1.3 times stall speed.

To test the system ability to perform autonomous landing in case of remote control failure, it has been decided to use a horizontal flight condition as equilibrium condition. The selected initial conditions are:

h = 300ft
V = 54.08 kts
$\alpha_e = 0.072$ rad
q = 0
$\vartheta_e = \alpha_e$

The beginning of Fig. (2-a) shows transition from horizontal flight to descent with a little knee and it's possible to see such a transition also in Fig. (2-c) where the glide path angle is shown.

In the center-right side of Fig. (2-a) it's possible to note that the studied control system tracks the desired path with minimal error. In fact in Fig. (2-b) it's possible to see that the maximum error is about 1.9 m ,when the UAS altitude is 94m: This error is due to the selected equilibrium condition. Then, during descent, the tracking error is constantly about 0.05 m. When the flare start, at about 26 seconds, tracking error comes to 0.09 m but it quickly come back to values less than 0.05 m. So it's possible to say that the FCS permits to track the desired trajectory with noticeable precision.

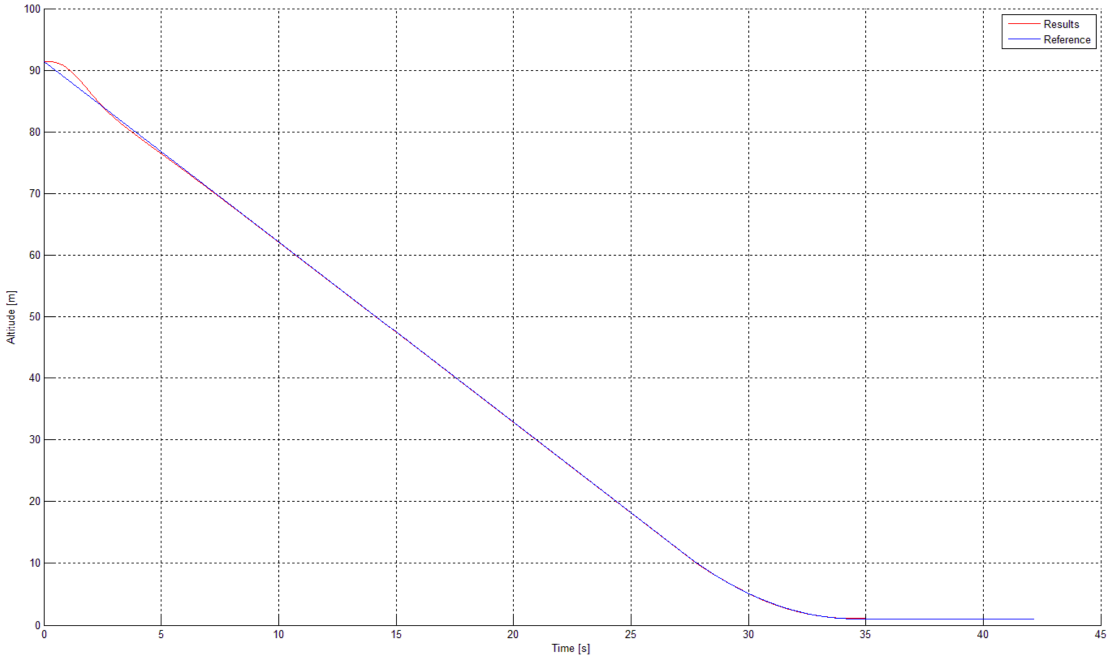

a)

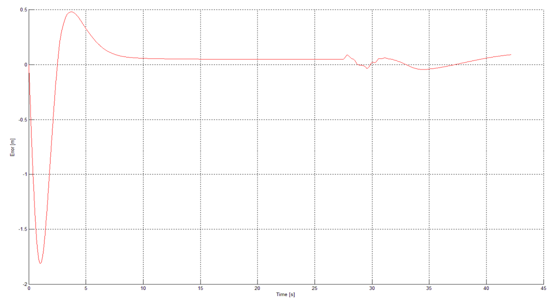

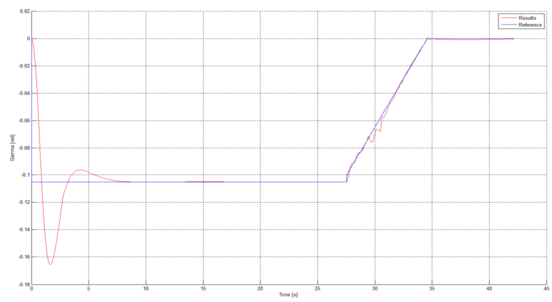

b) c)

Fig. 2 Indirect flight path following:

a) desired and controlled flight path, b) tracking error, c) desired and controlled flight path angle.

This affirmation is comforted also with the Fig (2-c) observation, in fact it's possible to note that desired flight path angle and real flight path angle are overlapped except for few. seconds when the descent starts and when the flare starts.

Obviously, to design the Automatic Landing System the classical hypotheses of air at rest has been made. To verify either robustness properties of the controller or its ability to reject disturbances several operating situations such as flight in the presence of gust, rear or front wind and atmospheric turbulence have been considered. Some of the most relevant results are shown in Fig. (3). It refers to a vertical gust that modifies the aircraft angle of attack of $\Delta\alpha$= -1 deg. The vertical gust is inserted into the model at the start of the flare maneuver. Despite of the angle of attack reduction, due to the gust, it is interesting to note that the aircraft performs the flare with a noticeable precision. In fact either the desired flight path or the flight path angle (Fig. 3-a) are followed with negligible errors. Figure (3-b) shows a comparison between tracking errors. It is possible to note that the maximum error is 0.08 m. The mean value of the tracking error is 0.049 m during the whole flare phase. Near the touch down the stabilized tracking error is about 0.02 m.

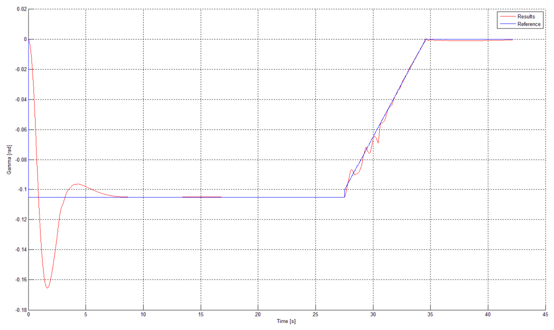

a)

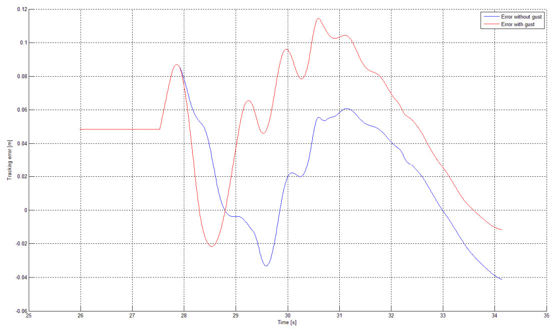

b)

Fig. 3 Indirect flight path following with gust:

a) desired and controlled flight path angle, b)tracking error comparison

7 Conclusion

The obtained results show the effectiveness of the designed Automatic Landing System. Therefore these ones show a good accuracy of the control system for trajectory tracking in ground proximity. In fact the UAS follows the desired flight path with a noticeable precision. The following original contributions can be highlight: 1) the obtained model of the aerodynamic coefficient In Ground Effect that afford to evaluate stability and control derivatives variations during the landing 2) the use of airspeed and glide path angle as controlled variables during the whole landing 3) the landing geometry.

Further developments of the present research will be the extension of the designed control system to the take-off phase.

Afterwards the aircraft model will be improved by evaluating both lateral stability derivatives variations In Ground Effect and the bank angle derivatives (ϕ derivatives). Since the present methodology will be employed to design a Lateral Automatic Landing System.

At the present flight tests are performing to verify the effectiveness of the designed Automatic Longitudinal Landing System by means of the above described Flight Control Research Laboratory. The obtained results could be used later on, with the purpose to realize a fully autonomous UAS.

Acknowledgements

This paper has been realized with the financial support of the Italian University and Scientific Research Minister in the context of the PRIN 2008.

References

[1] Schawe D., Rohardt C. -H., Wichmann G., “Aerodynamic design assessment of Strato 2C and its potential for unmanned high altitude airborne platforms”, *Aerospace Science and Technology* Vol .6,2002, pp.43-51

[2] Nelson,R.C., *Flight Stability and Automatic Control,* McGraw-Hill Book Company, NewYork, 1989

[3] Stevens,B.L., Lewis F.L., *Aircraft Control and Simulation*, John Wiley & Sons,Inc., New York, 1992

[4] Blakelock J.H., *Automatic control of Aircraft & Missiles*, John Wiley & Sons, Inc., New York, 1992

[5] Ohno M., Yasuhiro Y., Hata T., Takahama M., Miyazawa Y., Izumi T., “Robust flight control law design for an automatic landing flight experiment”, *Control Engineering Practice* , Vol 7, 1999, pp. 1143-1151

[6] Che J., Chen D., “Automatic landing control using H-inf control and stable inversion”, Proceedings of *The 40th Conference on Decision and Control*, 2001, pp.241-246

[7] Pashilkar A.A., Sundadadajan N.,Saratchhandran P.A., ”Fault-tolerant neural aided controller for aircraft auto-landing”, *Aerospace Science and Technology*, Vol. 10 N.1,2006, p.p. 49-61

[8] Rong H.J. et al., “Adaptive fuzzy fault-tolerant

control for aircraft autolanding under failure", *IEEE Transactions on Aerospace and Electronic Systems* Vol. 43 No. 4, 2007, pp.1586-1603

[9] Lungu L.,Lungu M. Grigorie L.T.," Automatic Control of Aircraft in Longitudinal Plane During Landing", *IEEE Transactions on Aerospace and Electronic Systems* Vol. 49 No. 2,2013, pp.1338-1350

[10] Riseborough P., "Automatic Take-off and Landing Control for Small UAV's", Proceedings of *The 5th Asian Control Conference,* 2004,Vol 2,pp.754-762

[11] Grillo C., Gatto C.," Dynamic Stability of Wing in Ground Effect Vehicles: a General Model", Proceedings of *The 8th International Conference on Fast Sea Transportation*,2005*(on CD-ROM)*

[12] Grillo C., Gatto C.Caccamo C. Pizzolo A., "A Non Conventional UAV In Ground Effect: Synthesis of a Robust Flight Control System", *Automatic Control in Aerospace* Vol. 2,2008, p.p.1-8

[13] Roskam J., *Airplane Design , part VI , Preliminary calculation of Aerodynamic, Thrust and Power Characteristics*, The University of Kansas, 1990

[14] Curry R.E., Moulton B.J., Kresse J., "An in-flight investigation of ground effect on a forward-swept wing airplane", NASA T.N. 101708, 1989.

[15] Amato F., Mattei M., Scala S., Verde L., "Robust flight control design for the HIRM based on Linear Quadratic Control", *Aerospace Sciences & Technologies*, Vol. 4, 2000, pp.423-438

[16] Hata T., Onuma H., Miyazawa Y., Izumi T., "Flight control system for ALFLEX", Proceedings of The second Asian Control Conference, Seoul ,2004, Vol. 2,pp.31-34

[17] Kovacic Z., Bogdan S., *Fuzzy Controller Design-Theory and Applications*, Taylor and Francis,2006

[18] Rozhdestvensky K. V, *Aerodynamics of a lifting system in extreme ground effect,* Springer,2000

[19] AA.VV. "Engineering Data" ESDU, IHS, 1972

4:th CEAS Air & Space Conference
FTF Congress: Flygteknik 2013

Route Optimization for Commercial Formation Flight Using PSO & GA

F. Asadi, S.M. Malaek, S.A. Bagherzadeh
Department of Aerospace Engineering, Sharif University of Technology, Iran

Keywords: *Formation Flight, Particle Swarm Optimization Algorithm, Genetic Algorithm, Path Optimization, Catch-up Point*

Abstract

This paper focuses on the first step of flying in a formation which is forming a group. There are several ways to form the group and fly in a formation. One of these ways is the scheduled take off from a single runway which in all launched aircraft after reaching the cruise altitude must meet one another at certain coordinates to create a formation. In this article, the optimum flight trajectories of aircraft which take off from a runway and want to participate in a formation flight is designed by using Particle Swarm Optimization (PSO) algorithm and the best points for aircraft rendezvous in cruise flight is determined. For ensuring about reliability of resulting trajectories, Genetic Algorithm is implemented beside the PSO. Cases involving a formation consisting of three commercial jets show that a total fuel efficiency of 10% is quite achievable.

1 Introduction

Fuel consumption and fuel cost are generally known as the main contributing factors in the aircraft direct operating cost (DOC) [1]. On the other hand, recent experiments suggest how flying in some types of formation would help reduce fuel consumption dramatically, at least for the follower aircraft [2, 3]. In fact, the idea of commercial formation flight has been introduced in recent years and various studies have been done to probe different challenges of formation flight implementation in transport aircraft [4,5]. Most researches in the field of formation flight have focused on a number of topics, including the aerodynamic benefits of formation flight and control strategies for maintaining the formation [6-12]. Also, several efforts on the subject of finding the best formation geometry and optimal routing for commercial formation flight have been arisen recently [13-15].

Almost all the rout optimizing studies in this area have focused on the specific approach for forming a group which is taking off from different airports and joining to each other in the cruise altitude. However, there is another option for handling this issue which is taking off from a runway in one airport with retardation and forming the group in the cruise altitude. This work will examine this idea which is elaborated in next session.

2 Problem Statement

The first step for flying in formation is forming a group which can be done in several ways. Three possible scenarios exist for forming a group which are as follows [4, 5]:

- Case (a): Coordinated take off from several airports in different locations [13-15].
- Case (b): Coordinated take off from parallel runways in a same airport.
- Case (c): Scheduled take off from a single runway in the same airport.

For case (b) the problem is rather a safety issue as compared to that of any trajectory calculations. In fact, we need to consider the incoming traffics who desire to land. So, it may not be seen as an attractive idea, especially for crowded airports.

For case (c), all launched aircraft must meet one another at certain coordinates to create a formation. Regarding the constraints, three promising conditions may exist [5]:

1. The aircraft are waiting in a typical holding pattern at the cruise flight level, and as soon as an aircraft arrives, it can join-up while the formation is turning on the holding pattern. Then the formation continues flying the holding pattern. Certainly, this procedure results in improper fuel consumption and wasting time. This is therefore not a recommended procedure except when airspace restrictions preclude the other options.
2. Followers accelerate to join the leading aircraft once reaching a desired cruise altitude. This strategy becomes inefficient, if either aircraft is forced to cruise faster or slower than its economy speed. In addition, depending on number of aircraft the distance to catch-up point will be long. Extra acceleration and less beneficial formation flight will waste the fuel.
3. Aircraft that have taken off from a single runway with retardation ascend with different climb angle to meet at the desired cruise altitude. Here, it is required to consider the lower and upper bounds of rate of climb and climb angle.

Aforementioned scenarios have their own pros and cons. Nevertheless, they all describe a possibility in which we still need to find the optimum solution. In this work, it is shown that how Particle Swarm Optimization (PSO) algorithm and Genetics Algorithm (GA) can be used to generate the optimal trajectories for case (c) [16-20].

Here, the objective is to determine near optimal minimum fuel trajectories of all *n* aircraft participating in a formation based on Case(c-2, c-3) scenario. Assume that *n* aircraft take off from a runway in time intervals of Δt_i and coincide at catch-up points. The number of these points which are located in cruise altitude may be from *1* to *n-1*. The first aircraft (the leader) takes-off at t_0, then the i^{th} aircraft takes-off at t_i. Here, Δt_i denotes the time interval between t_0 and t_i.

Flight trajectory of every aircraft is divided into *m*+2 sectors (with *m* catch-up point). As depicted in Fig. 1, the first sector refers to a climbing trajectory. The second sector of flight begins from the cruise altitude and ends at the first catch-up point. In the third sector, aircraft which have formed a formation flight, precede to the second point. In this sector the percentage of fuel consumption which depends on the location of aircraft in formation flight, will decrease. Aircraft that have not joined the formation continue their individual flight to adjoin to the group in a suitable point.

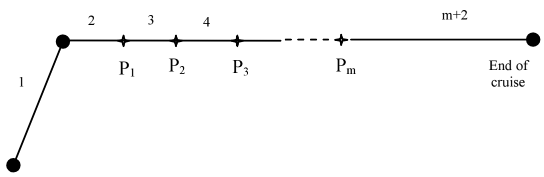

Fig. 1 Partitioning of aircraft trajectory in formation flight

Aircraft velocities may alter during flight from one section to another but it is constant in each section and it's obvious that for keeping formation, all aircraft in a group must have same velocity. In each catch-up point, two or more aircraft can joint each other. Multiplicity and location of these points will be determined by PSO/GA algorithm. Another issue arises when scheduling take-off time of each aircraft. The least time interval between two aircraft take-off is around 2 to 3 minutes. Of course, this minimum time interval depends on the aircraft types.

2.1 Problem Formulation

Climb is the first operational phase of flight after take-off. Therefore, climbing equation is derived which considers the aircraft as a point mass [21]:

$$\dot{\gamma} = \frac{g}{V}(n_{l.f.} - cos\gamma) \tag{1}$$

$$\dot{V} = \frac{g}{W}(\eta T - D) - g sin\gamma \tag{2}$$

$$\dot{x} = V\, cos\gamma \tag{3}$$

$$\dot{y} = 0 \tag{4}$$

$$\dot{z} = V\, sin\gamma \tag{5}$$

$$\dot{W} = -\eta T_{Max}(M,h)C(M,h) \tag{6}$$

Where:

$\dot{\gamma}$ Rate of climb angle changes
V Aircraft velocity
$n_{l.f.}$ Load factor
W Aircraft Weight
M Mach number
h Flight altitude
T Thrust as a function of mach & altitude
C Fuel consumption as a function of mach & altitude

In the suggested model for this phase, climb trajectory is divided into np sectors and variations in altitude are determined in each sector.

By taking account current problems in air traffic and high levels of work pressure on controllers below altitude of 3 km (10,000ft), the number of commands given to an aircraft in this zone is limited. Therefore, the first sector extends to 3 km with a constant angle that its optimum magnitude must be determined. So, the state variables include the $\dot{\gamma}$ in the sectors between 2 and np-1, initial flight path angle to 3 km and required time for climbing in each sector (Δt). By assuming that an aircraft at the end of climb trajectory begins cruise phase, the flight path angle at the end of climb will be zero. Considering this assumption, it is not necessary to assign a random value to $\dot{\gamma}$ in the last section of climb. Eventually the angle of trajectory in other sectors may be calculated by $\dot{\gamma}$ and the relevant time intervals in the following manner:

$$\gamma_{j+1} = \dot{\gamma}_j \Delta t + \gamma_j \quad (j = 2, \dots, np - 1) \tag{7}$$

The velocity in each sector is computed as follows:

$$V_j = -\frac{dh_j\, \dot{\gamma}_j}{(\cos\gamma_{j+1} - \cos\gamma_j)} \quad j = (1, \dots, np) \tag{8}$$

Having aircraft velocity, longitudinal distance surveyed in each sector and load factor may be calculated:

$$dx_j = \frac{V_j}{\dot{\gamma}_j}(\sin\gamma_{j+1} - \sin\gamma_j) \tag{9}$$

$$n_{l.f_j} = \frac{V_j\, \dot{\gamma}_j}{g} + cos\,(\frac{\gamma_{j+1} + \gamma_j}{2}) \tag{10}$$

According to FAA standards (FAR 25.337), maximum positive load factor for commercial civil and transport aircraft is 3 to 4 and maximum negative magnitude is -1 to -2. However, passengers may have a better feeling if this factor is taken to be 1.

Another important parameter for us is required thrust. If required thrust for flying in certain trajectory exceeds maximum thrust, then that trajectory would be unacceptable. Therefore η is always less than one and only in urgent situations it can be equal to 1. Since, η depends on aircraft weight, variation of this factor must be considered.

Time intervals between commands are another issue. Jet engines having a high inertia are slow in response. For example, in the most amenable jet engines this time is about 5 seconds. It seems that this delay may have a higher magnitude in commercial civil jets. Other control surfaces like ailerons, elevators and rudders that use hydraulic actuators, also lead to delays in response. Delays in commands issued from autopilot on one hand and aircraft oscillations after changing of input variables on the other hand, beside time required for transition from this situation as the third factor, necessitates a minimum time to accomplish and settle. This required time varies for different aircraft; for most commercial civil aircraft, it is about 30-45 seconds. Therefore, for this type of aircraft, commands must be issued more than 45 seconds in advance. This problem introduces $t_{command}$ as a computational factor that imposes commands to not pursue each other more closely [22].

When reaching the cruise altitude, the individual flight of aircraft continues to catch-up points. After meeting at catch-up points, depending on situation of aircraft in formation, fuel consumption may reduce significantly, except for the leader aircraft.

The weight of fuel which is consumed by the all aircraft in the whole flight including the climb and individual/grouping cruise may be formulated as follows:

$$Wf_{formation} = \sum_{i=1}^{n} Wf_i = \sum_{i=1}^{n}\sum_{j=1}^{m+2} Wf_{i,j} \qquad (11)$$

Wf_i is fuel consumption of each aircraft in its flight trajectory (climbing and cruise flight).

$$Wf_i = Wf_{climb,i} + Wf_{cruise,i} = \sum_{j=1}^{m+2} Wf_{i,j} \qquad (12)$$

$Wf_{climb,i}$ is fuel consumption of the i[th] aircraft in climbing flight. Climbing trajectory of flight itself is composed of several sectors. It yields:

$$Wf_{climb,i} = \sum_{z=1}^{np} \eta_z T\max_z(M,h) C_z(M,h) \frac{\sqrt{dh_z^2 + dx_z^2}}{V_z} \qquad (13)$$

Fuel consumption in cruise phases (individual and formation flight), can be calculated as below:

$$Wf_{cruise,i} = \sum_{j=2}^{m+2} \left(\eta_j T\max_j(M,h) C_j(M,h) \frac{dx_j}{V_j} \right) \times (1 - K_{i,j}) \qquad (14)$$

$K_{i,j}$ is the proportion of reduction in fuel consumption for the i[th] aircraft as a result of flying in j[th] sector in formation. This coefficient in individual flight is zero and after arrival to formation, depending on formation topology and aircraft location in the group, can increase to a magnitude of 0.2. *K* is assumed to be equal of the drag force reduction which should be determined from wind tunnel experiments.

2.2 Particle Swarm Optimization

Decision variables in PSO are listed as follows:

$$\begin{array}{lc} i,j,z,k,p \in (\mathbb{N}) & \\ \gamma_{0i} & i = (1,\dots,n) \\ \dot{\gamma}_{i,j} & j = (2,\dots,np-1) \\ t_{i,z} & z = (1,\dots,np) \\ V_{i,k} & k = (2,\dots,m+2) \\ x_p & p = (1,\dots,m) \end{array} \qquad (15)$$

Where:

γ_0 Initial flight path angle in climb

t Time duration of each sector in climb

x_p Horizontal locations of catch-up points

Here, aircraft operational constraints include: maximum and minimum velocity, load factor, maximum angle of climb, maximum rate of climb and required thrust for flying in the specific trajectory. The cost function will be weight of consumed fuel by the group.

2.3 Genetic Algorithm

Mathematical model for climbing trajectory in GA is similar to model selected in PSO, but because of natural behavior of GA in constraint problems, flight path angle and velocity in each sector of climb are treated as decision variables instead of $\dot{\gamma}$ and *t*.

3 Case Studies

In this sector, we suppose three Boeing 727-200s take off from a runway and form a group for formation flight (n=3). Destination of aircraft is located at a distance of 3000 km. The cruise altitude is supposed 10 km. It is assumed that drag force reduction for follower aircraft will be 20 percent (Having accurate magnitude of this coefficient requires wind tunnel experiments).

For comparison, the fuel usage of one aircraft in individual flight is determined. All results for range of 3000 kilometers are presented in table 1 and 2.

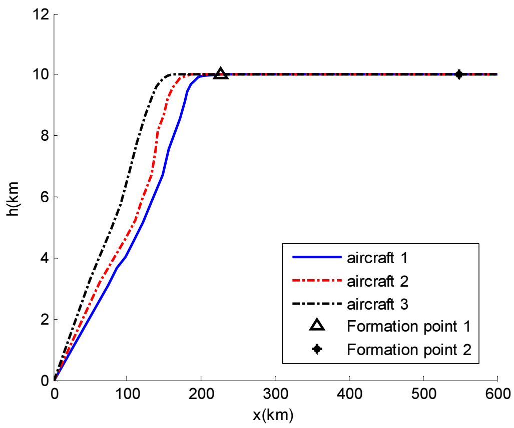

Fig. 2 Optimum trajectories in formation flight for three Boeing 727-200 with PSO

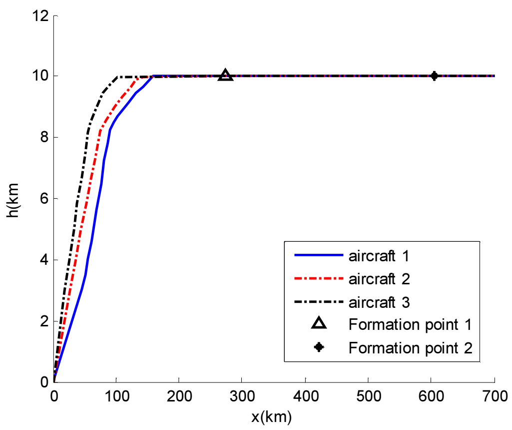

Fig. 3 Optimum trajectories in formation flight for three Boeing 727-200 with GA

Tab. 1 Comparison between consumed fuel of each aircraft in formation

	Consumed fuel of the leader aircraft (kg)	Consumed fuel of the second aircraft (kg)	Consumed fuel of the third aircraft (kg)
PSO	21240	17544	18287
GA	21990	17896	18922

Tab. 2 Comparison between fuel usage of individual and formation flight

	Consumed fuel of three aircraft in individual flight (kg)	Consumed fuel of group in formation flight (kg)	Fuel consumption benefit
PSO	21240*3 = 63720	57071	10.4 %
GA	21990*3 = 65970	58808	10.9 %

4 Conclusion

This paper has produced optimum trajectories for climbing and cruise flights of a group of aircraft in formation and their catch-up points with GA and PSO. Results from the two algorithms are close; therefore, it is assumed that these results are not local minima and are trustworthy. Based on the results, total aircraft fuel consumption in formation flight can be reduced about 10% through finding the best trajectories and suitable joining points. This benefit is more appreciated over long ranges. Considering the better fuel efficiency in formation flight, can open new windows in fleet design. For example, having three 200-seats aircraft which fly in formation can be considered as an alternative instead of one aircraft with capacity of 600-seats. Of course, the overall DOC and other related issues must be studied. It is the first step and more efforts must be taken.

In this work, all the aircraft had same amount of fuel at the take off time (same W_{TO}). However, calculations can be done based on required fuel for flying in the formation for each aircraft. This absolutely will increase the fuel efficiency, because the follower aircraft can take off with fewer amounts of fuel and smaller W_{To}.

References

[1] Barnhart S., Belobaba P., OdoniA., “Global Airline Industry”, First Edition , John Willy & Sons, 2009, Chap-5, page 115.

[2] Weimerskirch H., Martin J., Clerquin Y., Alexandre P. and Jiraskova S., “ Energy saving in Flight Formation”, Nature, Vol. 413, No. 6857, 10 2001, pp. 697-698.

[3] Jake Vachon M., Ronald J., Kevin R., Kimberly E., "F/A-18 Performance Benefits Measured During the Autonomous Formation Flight Project", NASA Dryden Flight research Center , Edwards, California, 2003.
[4] MIT Open course, "Air Transportation Systems Architecting", http://www.ocw.mit.edu, Spring 2004.
[5] Brachet J.B., Cleaz R., Denis A., Diedrich A., King D., MitchellP., Morales D.,"Reference Material for a Proposed Formation Flight System", Department of Aeronautics & Astronautics MIT, 2004.
[6] Lissaman PBS, Shollenberger CA, "Formation flight birds", Science 168:1003–1005, 1970.
[7] Hummel D., "Aerodynamics Aspect of Formation Flights in Birds", Journal of Theoretical Biology, Vol. 104, No. 3, 1983, pp. 321-347.
[8] Iglesias S., Mason W. and Blacksburg V., "Optimum Span load in Formation Flight", AIAA paper 2002-258, 2002.
[9] Eugene H., Wanger Jr., Major USAF, "An analytical Study of T-38 Drag Reduction in Tight Formation Flight", Thesis, Department of the Air Force, Air University, Air Force Institute of The Technology, USA, 2002.
[10] Frazier J. and Gopalarathnam A., "Optimum Downwash Behind Wings in Formation Flight", Journal of Aircraft, Vol. 42, No. 4, 2003, pp. 799-803.
[11] Giulietti F., Pollini L. and Innocenti M., "Autonomous Formation Flight", Control system Magezine, IEEE, Vol. 20, No. 6, 2000, pp. 34-44.
[12] Pachter M., D'Azzo J., and Proud A., "Tight Formation Flight Control", Journal of Guidance, Control and Dynamics, Vol. 24, No. 2, 2001, pp. 246-254.
[13] Bower G.C., Flanzer T.C., Kroo I.M., "Formation Geometries and Rout Optimization for Commercial Formation Flight", 27th AIAA Applied Aerodynamics Conference, June 2009, San Antonio, Texas.
[14] Xu J., Ning S.A., Bower G. and Kroo I., "Aircraft Route Optimization for Heterogeneous Formation Flight", 53rd AIAA/ASME/ASCE/AHS/ASC Structures, Structural Dynamics and Materials Conference, 2012, Hawaii.
[15] Kent T. and Richards A.G., "A Geometric Approach to Optimal Routing for Commercial Formation Flight", AIAA Guidance, Navigation and Control conference, August 2012, Minneapolis, Minnesota.
[16] Eberhart R.C., Kennedy J., "Particle Swarm Optimization", Proceedings of the IEEE International Conference on Neural Networks, Australia, NJ, IV: 1942 – 1948, 1995.
[17] Eberhart, R.C., and Shi, Y., "Particle Swarm Optimization: developments, applications and resources", Proc. Congress on Evolutionary Computation, Seoul, Korea. Piscataway, NJ: IEEE Service Center, 2001.
[18] Clerc M., Particle Swarm Optimization, ISTD Ltd, UK, 2006.
[19] Coley D., an Introduction to Genetic Algorithm for Science and Engineering, McGraw-Hill, 1999.
[20] Vose M.D., the Simple Genetic Algorithm Foundations and Theory, McGraw-Hill, 1999.
[21] Malaek S.M, Marzaabaadi M.A., Sadati S.H., "Minimum Fuel Trajectory in a 3D Time Scheduled Climb", Iranian Aerospace Society, JAST, Vol. 2, No. 2, pp 11-1, 2005.
[22] Sadrayi, M.H. , Flight Dynamics, Imam Hossein University Publication, First Edition, 1997.

Validation of a numerical simulation tool for aircraft formation flight.

T. Melin
Fluid and Mechatronic Systems, Department of Management and Engineering, the Institute of Technology, Linköping University, Linköping, Sweden.

Keywords: Formation flight, drag reduction, panel methods.

Abstract

The use of formation flight for increased fuel efficiency has received a lot of attention in the last couple of years.

This paper covers a numerical simulation of a NASA test flight utilizing a formation of two F18A Hornet aircraft. The numerical simulation was made using an adapted version of the vortex lattice method TORNADO, allowing for several aircraft to be simulated in a trimmed condition. The numerical results showed good agreement with the flight test data. Some discrepancies due to the numerical model not covering viscous diffusion was found as expected but not quantified or analyzed.

1 Background

The physical phenomenon behind the drag reduction encountered in formation flight has been understood for a long time, but formation flight has never seriously been employed in civilian airline traffic. On the military side, formation flight has been extensively used for tactical considerations such as navigation or suppressive fire coverage and only exceptionally as a fuel saving measure. The increased fuel efficiency is due to the decrease in induced drag caused by the upwash formed by the vortex system of a lifting wing. The formation flight then becomes a virtual extension of the span of the constituent aircraft thereby increasing the aspect ratio.

Several studies have been performed showing large potential savings in fuel consumption; The NACA study supplying the flight test date used in this paper reported a reduction in fuel consumption of 20% for a fighter type aircraft, the McDonnell Douglas (now Boeing) F/A-18 Hornet. This is a number significantly higher than the potential fuel savings from design changes.

As an example of the systematic benefits of employing formation flight for fleet operations in the north Atlantic, a conservative stance on what the in-operation fuel savings would be to assume a 5% save, based on the NASA results. Just for the trans-Atlantic routes with 385 flights a day, each direction, each burning 50 tons of fuel this would mean that in absolute numbers a flight-in-formation scheme would save 2000 ton of aviation fuel saved, each day.

While Flight tests results are closer to a real situation, they are also prohibitively expensive for mapping out a large array of tests, and some data may be inaccessible for measurement. This paper aims at showing the validity of using a Vortex Lattice Method (VLM) to assess benefits and drawbacks of employing formation flight in fleet operations and to explore what types of results would be beneficiary for future studies, such as autopilot controller design or aircraft formation movement procedures.

The numerical study was set up using the VLM implementation Tornado, modified to cater for multiple aircraft computational meshes. The code has been developed for linear aerodynamic wing design applications in conceptual aircraft design. By modeling all lifting surfaces as thin plates and modeling the flow as a potential flow, Tornado can solve for most aerodynamic derivatives for a wide range of aircraft geometries. With a very high computational speed, Tornado gives the user immediate feedback on design changes, making quantitative knowledge available earlier in the design process.

The aircraft geometry in Tornado is fully three dimensional with a flexible, free-stream following wake. Tornado allows a user to define most types of contemporary aircraft designs with multiple wings, both cranked and twisted with multiple control surfaces. Each wing may have taper of both camber and chord.

Based on the polar equation (eqn 1), a simple model of maximum achievable induced drag reduction for a multi aircraft formation would simply be based on a virtual increase of the aspect ratio.

$$C_{Di} = \frac{C_L^2}{\pi e \cdot AR} \quad (1)$$

By assuming that the Oswald factor, e, remains constant the induced drags of the formation ($C_{Di,2}$) can be written as a function of the single ship induced drag, ($C_{Di,1}$) and the corresponding aspect rations, as in eqn 2:

$$C_{Di,2} = C_{Di,1} \frac{AR_1}{AR_2} \quad (2)$$

Plotting this relation for up to a ten aircraft formation, as in figure 1, it becomes evident that that the marginal benefit of adding one more aircraft when already having 4 in formation diminishes.

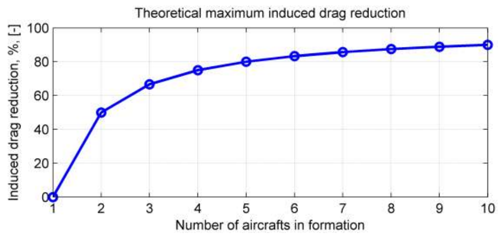

Fig. 1 Expected theoretical maximum induced drag reduction from formation flight, based on increased virtual aspect ratio.

1.1 Formation flight code modifications

The VLM code needed some modifications before a formation of aircraft could be modeled. In the single aircraft case, the lattice, or mesh is a list of coordinates describing vortex lines, collocation points, normal and panel corners. When adding one or more aircraft to the lattice, the connectivity is based on the number of panels on each aircraft. The coordinate system of secondary aircraft placement is shown in figure 2, were the origin is placed at the apex of the main wing of the lead AC and one half-span outboard.

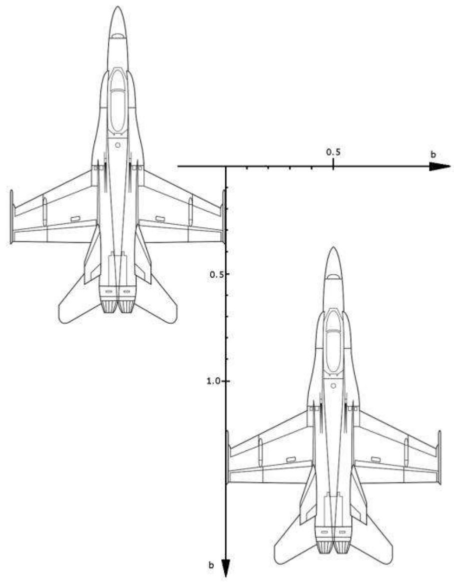

Fig. 2 Coordinate system. When the aircraft are line abreast, wing tips touching, they are at origin position. [0 0 0].

The aerodynamic state of the aircraft: angle of attack, sideslip angular rotations and so on, becomes properties of the formation in the multi aircraft case. This means that instead of changing the angle of attack to achieve heave trim, the code instead rotates the individual aircraft sub lattice for heave trim. In order to achieve useful drag reduction results, all aircrafts in the formation were trimmed in heave and pitch, while partial trim drag components from roll and yaw trim were estimated from a single ship control derivatives.

The result vector contains forces on each panel, and by using the same connectivity as for the lattice, forces and moments can be distilled out and an integrated for forces on each aircraft used for generating the individual aerodynamic coefficients.

1.2 Experiments

A NASA study performed in 1998 [2],[3] Used two F18A aircraft flying in close formation to evaluate the drag reduction. What was actually measured was the fuel consumption, which via an advanced thrust model could be equated to drag decrease. Maximum recorded value was decrease in overall drag by approximately 20%, see figure 3, corresponding to a decrease in induced drag by around 40%, close to the theoretical maximum of 50% for a two ship formation.

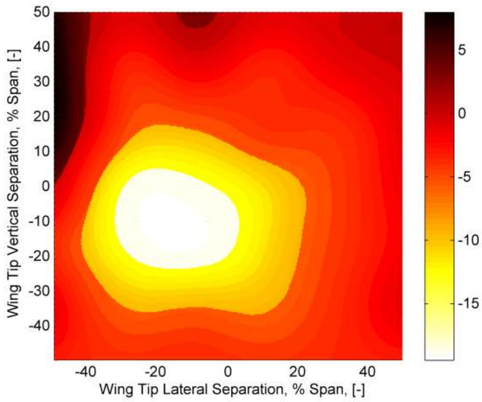

Fig 3: Overall drag reduction. in %, as a function of wingtip separation as reported by [3].

As these tests were performed under a certain timespan, the weight of the fuel remaining, thus aircraft weight varied throughout the experiment. This in turn means that the lift required for heave trim is unknown, thus the actual drag due to lift is unknown.

When evaluating the drag from the flight tests in this study, it was assumed that the weight of the aircraft was the average weight of the aircraft during the flight tests. As start and stop weight were available, the errors of this approach could be quantified.

1.3 Numerical model

The flight test parameters were modeled with the following accuracy:

The aircrafts, the F18A was modeled in Tornado as a system of lifting surfaces, according to figure 4. The geometrical data was compiled from a list of resources [5],[6],[7]

A grid convergence study was performed to ensure good grid quality. The convergence was performed on a single aircraft geometry. The cutoff level for changes between iterations was set to 0.01 delta in Lift-, Drag- and pitching moment coefficients. The grid convergence history can be seen in figure 5.

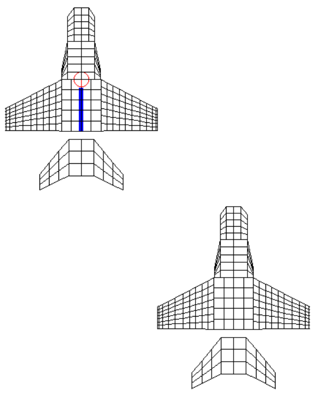

Fig 4: Mesh distribution of the numerical simulation with the following aircraft in position [1.3 0 0].

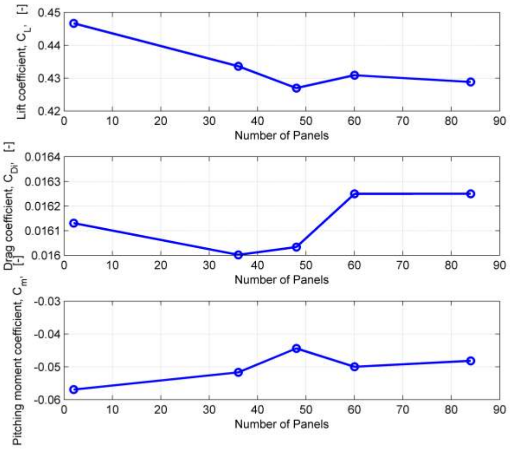

Fig 5: Grid convergence history. Number of panels in the entire geometry.

The converged grid had 18 panels semi-span wise on the main wing, and 4 panels chord wise.

The horizontal tail was modeled as an all-moving tail. The nosecone of the aircraft was not modeled at all, as the angles of attack and sideslip in this study were low enough to prevent detached vortex formation from the nose.

The solver was set to give both aircraft a prescribed C_L by changing their individual angle of attack in an iterative loop. Once heave convergence was found, the horizontal taileron was deflected in an inner loop to achieve pitch trim. When this was done, the heave loop was entered again to ensure that heave convergence was still valid. When exiting the loop, rudder and aileron deflections were computed form the control power derivatives, and the associated trim drag increase was computed from a single aircraft computation.

2 Results

There was good agreement between the simulated and experimental results; Figure 6 shows the numerical induced drag reduction at flight level 250 with a 2.75 span longitudinal separation. The cruise C_L was 0.42. The box shows the region of available flight test data.

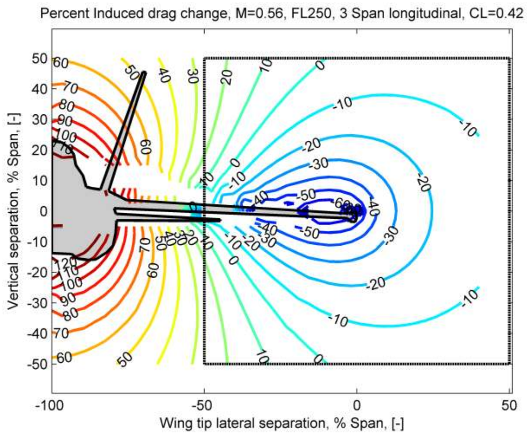

Fig 6: Iso curves of induced drag reduction., showing the F/A 18 outline.

Figures 7 and 8 shows the induced drag reductions in the test space available from the flight test, for the numerical and for the experimental results, respectively. The numerical results show a higher drag reduction which is more centered on the trailing edge. This is to be expected as the numerical model does not take any viscous losses into account, nor employs any wake relaxation schemes.

Furthermore, the induced drag reduction in the numerical results is slightly higher than the theoretical maximum, but as these areas are also coupled with a large condition number in the numerical solver, hence a larger error is expected.

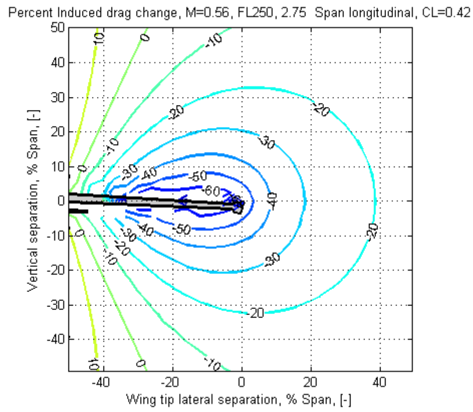

Fig 7: Iso curves of induced drag reduction from the numerical simulation.

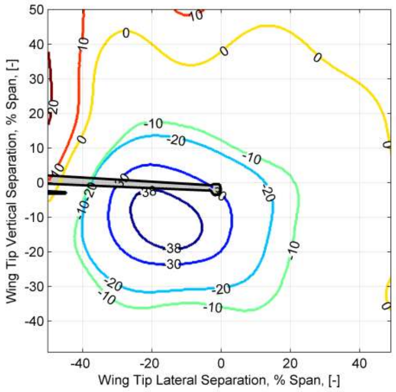

Fig 8: Iso curves of induced drag reduction from NASA flight tests.

When assessing the similarity between the incremental rolling moment on the wing aircraft caused by the tip vortices of the lead aircraft a relation similar to the drag reduction comparison. Figure 9 show the numerical results and figure 10 show the experimental results. Both methods have the maximum influence zone at around -10% wing tip offset. In the numerical results, the data for zero vertical offset were omitted as it contained large numerical errors due to badly conditioned matrices. The numerical results were also more closely centered on the zero offset vertical position. As with the drag this is due to the numerical methods inability to model wake relaxation.

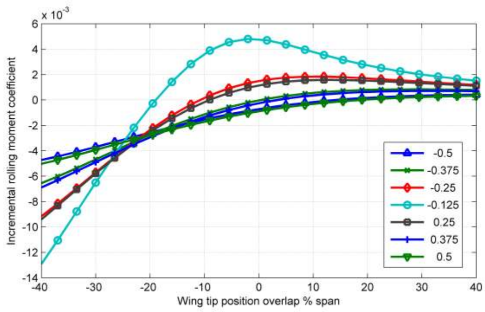

Fig 9: Incremental rolling moment coefficient at different wing tip overlaps and height offset, numerical results.

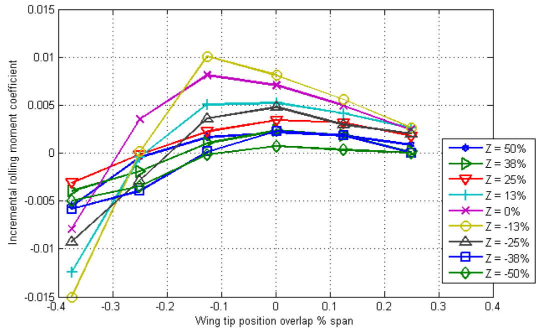

Fig 10: Incremental rolling moment coefficient at different wing tip overlaps and height offset, numerical results.

Figure 11 show the numerical data for the incremental rolling moment coefficient in iso-curve format. Interestingly there are two iso lines valued zero approaching the wing from the top and bottom. These paths could serve as approach vectors when joining a formation in order to minimize the need for excessive control input during formation forming.

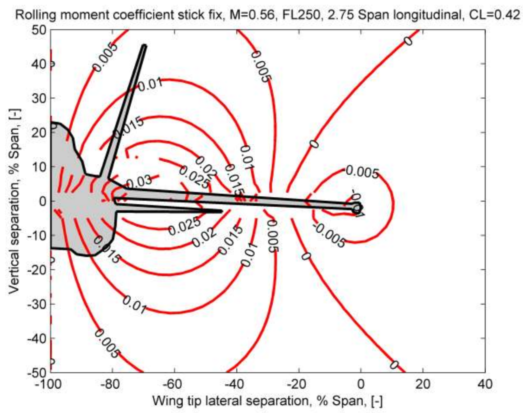

Fig 11: Incremental rolling moment coefficient

Other interesting results are shown in figure 12, where the rudder and aileron deflections needed for trim in yaw and roll are displayed. This data also shows the zero-influence approach paths as suggested by the rolling moment is also valid for the yawing moment., and as shown in figure 13 the side force coefficients.

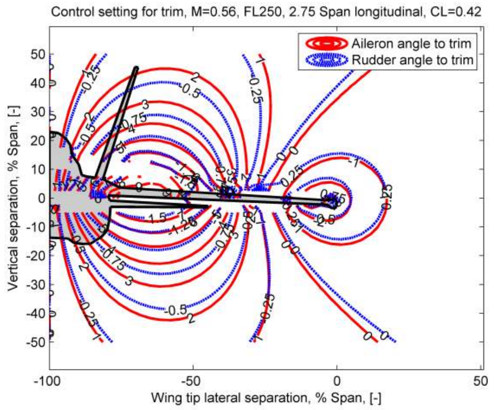

Fig 12: Incremental rolling moment coefficient

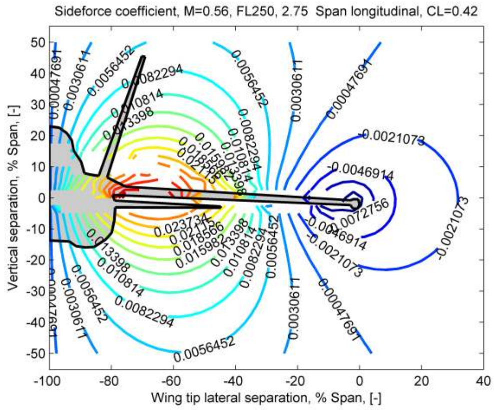

Fig 13: Incremental rolling moment coefficient

It appears as if there exists equilibrium point at [-20, 0] where rotational and translational derivatives are zero. The nature of this equilibrium point is dependent of the coupling derivatives of the individual aircraft. For example, an aircraft with no side-yaw coupling, and a very stiff roll axis, it would be a stable point with oscillations in spanwise overlap, with a frequency dependent on dynamic pressure. With a weaker roll inertia, the aircraft would start rolling out from the equilibrium pointafter disturbance.

3 Discussion

The numerical model did not cover the effects of vortex dissipation which will account for the indicated reduction of induced drag as computed numerically is slightly higher than the experimental data.

Furthermore, as no wake relaxation scheme is employed. The wake is static downstream and is not influenced by mutual interaction the vortex pair or by the vortices of the following aircraft. This in turn accounts for the misalignment of the position of the maximum drag reduction position in the y-z plane.

As no wake relaxation is done, the proposed method cannot be used to study the wake-aircraft interaction in detail.

The drag increments due to aileron and rudder deflections needed to attain trim in roll and yaw were computed using a single aircraft, therefore any effects on the drag increase due to the distorted flow field of the formation is not modeled. This effect though, is assumed to be small.

4 Conclusion

The validation study performed shows that the multi aircraft modification of Tornado can replicate flight test results with good accuracy. This means that further studies of other configurations will be encouraged.

References

[1] http://atwonline.com/international-aviation-regulation/article/open-skies-last-0229

[2] M. Jake Vachon, et.al. F/A-18 Performance Benefits Measured During the Autonomous Formation Flight Project, NASA/TM-2003-210734, 2003

[3] Cole. J, et al., Autonomous Formation Flight Project Overview, NASA Dryden Flight Research Center 2008.

[4] Hansen, J Cobleigh, B.R. Induced moment effext of Formation Flight Using Two F/A 18 Aircraft. NASA/TM-2002-210732, 2002.

[5] Jane's All the World's Aircraft 1984/85, Janes Publishing Company Limited, England, 1985.

[6] Waclawicz. K, From A to F: The F/A-18 Hornet, Virginia Tech, 2000:04:28

[7] Anon. F-18A 3- View, Dryden Research Center, NASA, 1998

Innovative Airport and ATM Concept (Operating an Endless Runway)

H.H. Hesselink
(henk.hesselink@nlr.nl)
NLR, The Netherlands

S. Loth
(steffen.loth@dlr.de)
DLR, Germany

M. Dupeyrat, S. Aubry, P. Schmollgruber
(maud.dupeyrat@onera.fr)
ONERA, France

M. Vega Remírez
A. Remiro Bellostas
(vegarma@inta.es)
INTA, Spain

Abstract

This paper presents an innovative and radical new concept for future airport operations, consisting of an airport with one circular circumventing runway, called The Endless Runway. This runway is used for take-off and landing in any direction from any point on the circle and offers through this the unique characteristic a sustainable capacity in all wind conditions through the possibility for an aircraft to operate with headwind during the take-off and landing phase. By placing airport facilities inside the circle, the airport will be more compact, runway crossings can be avoided and taxiing aircraft will be able to shorten their global trajectory through optimised arrival and departure routes. The project, the Endless Runway, is partly funded under EC FP7 [1].

1 Introduction

Where SESAR expects a three-fold increase in air traffic for the year 2020, vision statements beyond that date [1][3][4] expect an even further increase to a five-fold increase of aircraft use by 2050, based on the growth of the world population and a progressed mobility. The global fleet of aircraft is expected to grow fivefold from 19,800 in 2011 to a 100,000 aircraft in 2050! As was identified by ACARE, the Advisory Council for Aeronautics Research in Europe, the lack of capacity at airports is a major constraint to growth in air transport today and in the following decades. These numbers demonstrate that without a radical new airport concept providing fast and efficient aircraft handling with capacities beyond state-of-the art, the expected growth in air traffic cannot be realised.

A number of physical constraints on runways and runway operations, such as wake vortex separation minima and cross- and tailwind limits, and of societal and environmental constraints limiting airport and traffic expansion (new runway, night traffic, etc.), make it hard to improve the performance of conventional airport configurations significantly.

Directionality of runways results in a dependency to the wind direction and speed and using the same approach path results in trailing aircraft having to avoid wake vortices from leading aircraft.

This paper presents a fundamentally new and innovative approach to runway operations, where the major motivation of the study is to provide a sustainable airport capacity under all wind conditions whilst maintaining a high level of safety, reducing operating costs, and keeping environmental considerations in mind: *the Endless Runway*. The aim of the project is to investigate, through simulations, the feasibility of the concept.

2 The concept

A novel and radical concept is proposed here: *the Endless Runway*, a concept which consists of an airport with one circular circumventing runway, that fits for both seasonal and hub airports [5] [6]. This runway is used for take-off in any direction and landing from any direction and will allow aircraft to shorten their global trajectory through optimized departure and arrival routes and will offer the unique characteristic that the runway can be used under any wind condition through the possibility for an aircraft to operate always with headwind during take-off and landing. Moreover, runway crossings are avoided and runway overruns cannot occur since the runway has no end.

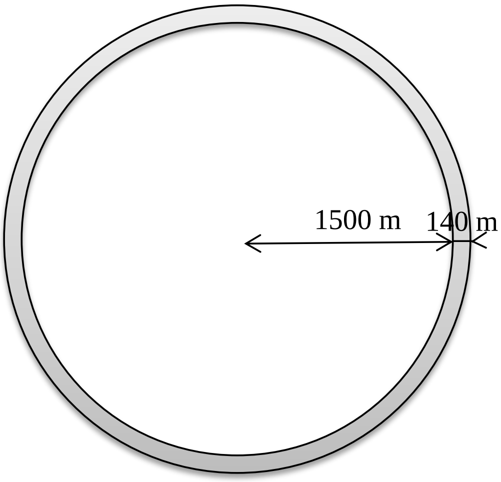

Figure 1 - Top view of the Endless Runway

The design of *The Endless Runway* consists of a banked circular track with all facilities for aircraft, passengers, baggage and freight handling located inside the circular runway. The circle of the runway has an inner radius of 1.5 kilometres, see Figure 1: it is large enough to provide room for airport infrastructure inside the circle and this magnitude should allow current-day aircraft to use the circular runway without significant structural modifications due to the turn. This compact airport design will allow aircraft to efficiently move from the runway to the gate and vice versa, reducing the taxiing phase and thus optimising global aircraft trajectories. In addition, passenger fast transfer times can be achieved. Moreover, it makes the airport footprint smaller than a conventional one: around 850 hectares compared to 3,257 hectares for a comparable hub airport in terms of traffic like Roissy CdG airport [7].

Wind direction, wind speed, and visibility conditions are the major factors in the decision of air traffic control to use a certain runway configuration. Limits on tailwind and crosswind components determine whether runways can be used or not, and low visibility limits the use of dependent runways. The fixed direction of the runways results in a dependency to the wind direction, and to the fact that following aircraft must use the same approach path, resulting in the need for wake turbulence separation. *The Endless Runway* operates a concept consisting of a circular runway that allows take-off in any direction and landing from any direction, avoiding the constraints mentioned before.

3 Airport layout

The proposed airport design is more compact than a conventional airport as most of the airport facilities are located inside the circle to avoid runway crossings. Access to the airport is provided through tunnels passing under the runway. *The Endless Runway* studies large airports where the circle size should allow a sufficient number of operations for the following categories of airports:

- *Large hub airports* with a mix of traffic, including mid-size and large aircraft. Roissy Charles de Gaulle is considered as our reference.
- *Seasonal non-hub airports*, with a mix of traffic, but where mid-size aircraft are predominant. Palma de Mallorca is considered as our reference.

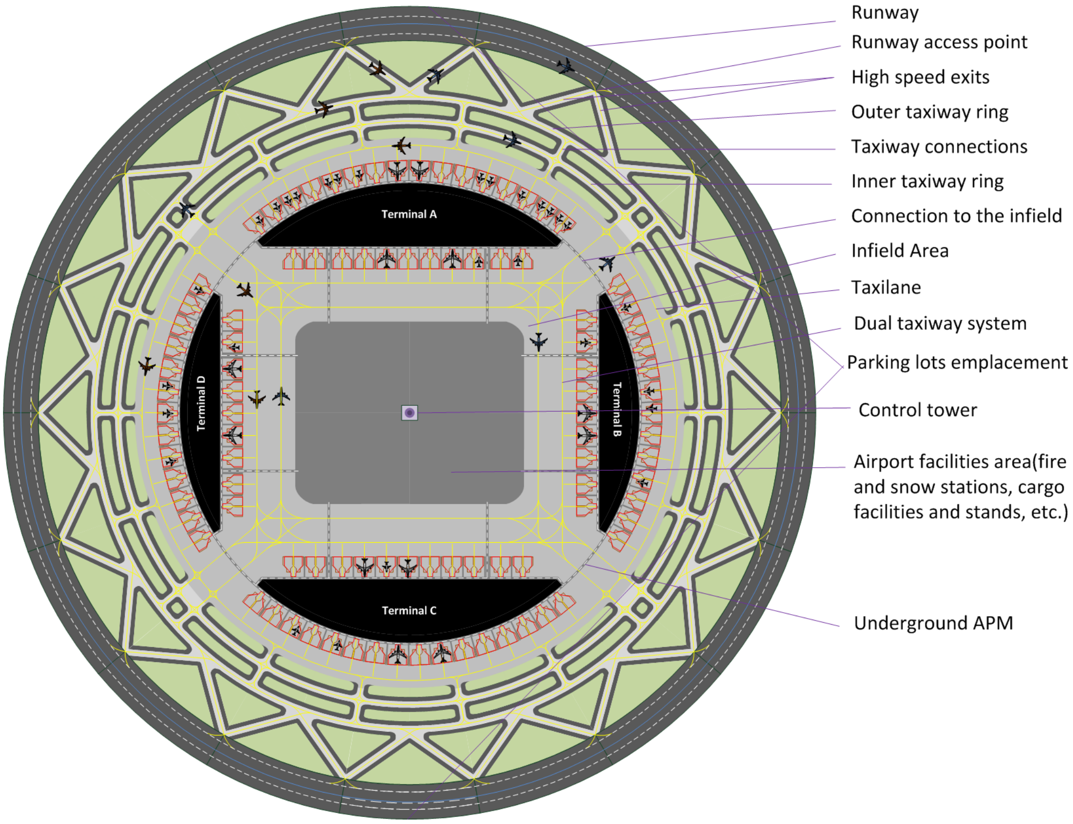

Figure 2 - Endless Runway airport airside elements

The following design principles are applicable to both airport types, see Figure 2.

The runway is a banked circle with a radius of 1,500 meters at the inside of the track. This size affords to operate several aircraft at the same time on the runway. It is small enough to keep the airport compact in terms of surface and to minimize taxiways and runway construction and maintenance costs.

The width of the banked track is set to 140 meters and its transversal profile is defined considering aircraft constraints (speed and ground clearance). Eighteen runway access points are provided. Thus, runway exists are located every 524 meters, which is optimal for runway occupancy time. In fact, airport design rules state that a long runway (3,500 m) at a busy airport should have exit taxiways located every 450 to 600 meters ([8])

To deal with peak periods, the number of stands for the reference airport is 133. Four terminal buildings are located in such a way that aircraft taxiing distances are limited and passengers experience an easy flight transfer (hub-airport) through a dedicated Automated People Mover (APM).

The airport's taxiway system consists of two taxiway rings just inside the runway: an outer and an inner taxiway ring. The taxiways connecting the runway with the outer circular taxiway are high-speed exit taxiways. They are 318 meters long and make a 45° angle with the tangent to the runway. The high speed exits will preferably be used as high speed entries for departing aircraft as well and aircraft can already start their take-off roll early. The length of the entry provides sufficient space for one aircraft waiting for take-off without interfering with aircraft on the runway

The outer taxiway ring (centerline radius: 1,275 m) is connected with the inner taxiway ring (centerline radius: 1,177.5 m) with single connection taxiways except at the entries/exits to the inner airport area, where a double connection taxiway forms a roundabout to avoid congestion between departing and arriving aircraft.

The connection between the inner and outer ring is located differently from the connections of the runway to the outer ring to avoid mistakes. Indeed, all connections are 10 degrees shifted with respect to the point joining the high speed exit and the outer ring taxiways. Moreover, it avoids complex taxiway junctions and facilitates aircraft crossings through better separation of inbound and outbound flows.

Between the terminals a dual taxiway system is available (yellow lines on Figure 2). The taxiways in between the airport's buildings link the inner circular ring to this inner airfield area. An additional circular taxi lane is available on the outside of the terminal stands to allow pushback operations independent from the outer taxiway rings.

The inner area thus measures around one million m^2 providing sufficient room for the major different facilities and for aircraft manoeuvring towards the inner gates.

4 Aircraft and passengers

The proposed radical change in the airport layout is directly affecting the aircraft and its passengers. Just as well, the aircraft characteristics during ground runs, end of take-offs and final approaches generate a number of requirements on the circular runway design. This section summarizes the outcomes of the concept studies that have been performed in order to assess the feasibility of aircraft operations on a circular runway, to identify the most promising runway cross section and to define the main characteristics of a specific aircraft tailored to this innovative layout.

As a first point, it must be noted that aircraft operating on a circular runway will, with increasing speed during take-off, move to the outside because of the centrifugal force. In order to limit the forces on the aircraft structure and passengers, the runway is banked. The used part of the runway depends on aircraft speeds: aircraft ground roll takes place between the inner flat part of the runway where its speed is null until part of the runway circle where the angle corresponds to its lift-off speed (and vice versa during landing roll). In other words, the aircraft will touchdown/lift-off on the outer part of the runway and will then move to the inside/outside. Given this unconventional aspect, the classical longitudinal performance models cannot be used. All analyses must then be based on six-degrees-of-freedom simulations in order to assess asymmetric conditions.

It has been decided to use the free and open-source simulator Flight Gear coupled with JSBSim to solve the equations of motion. Advantage of the choice is that models of aircraft are already available and the tool offers good visualisation means. Disadvantage is that models would have to be heavily modified to perform automatic landing manoeuvres, hence landings need to be performed “by hand”.

With the objective of validating the simulation environment and assessing the possibility for an existing aircraft to operate a circular runway, a Boeing 747-100 has been modelled based on NASA data [9] and a semi-empirical engine model. The choice of this reference aircraft has been driven by the necessity to have an extensive and reliable database of the aircraft characteristics and to be conservative during this exploratory phase (its specific configuration results in a reduced ground clearance for the outboard engines). Simulations performed on a classical straight runway provided extremely good results when compared with the real data, thus validating the virtual models. The subsequent parametric studies enabled to evaluate the take-off performance of the B747-100 on banked runways with different cross sections. The first conclusions from these tests are:

- It seems feasible to take-off and land on a circular runway with a Boeing 747-100. However, there is a non-negligible risk to have a contact between an outer engine and the track given the small ground clearance.
- The lateral accelerations observed during the ground runs are below 0.47 m/s² and thus acceptable for passengers ([11]).
- The landing gear characteristics recorded during Flight Gear simulations did not show critical behaviour.
- The take-off field length on a circular runway is about 15% higher than the one on a straight and flat track (duration of take-off is about 59 seconds).
- The landing distance on a circular runway is about 23% higher than the one on a straight and flat track (duration of landing phase is about 58 seconds).

Figure 3 gives an impression of using Flight Gear for operating *the Endless Runway*.

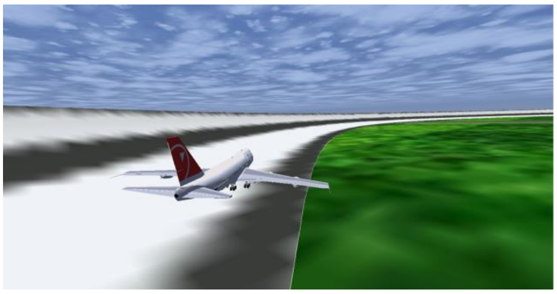

Figure 3 - Simulation with Flight Gear of the Boeing 747-100 at take-off on a circular runway

In addition, these simulations provided key inputs to the design and development of *the Endless Runway* concept:

- The runway cross section should provide a linear relationship between the aircraft position on the runway and its speed. This selection is a compromise between the overall size of the runway and the aircraft dynamic behaviour.
- The runway width is fixed to 140 m (see Figure 1), considering that the cross section allows speeds up to 20% more that the lift-off speed of the B747-100 for safety;

With this selected geometry, see Figure 4, in the case of the reference aircraft, the take-off rotation is made at a speed of 160 kts that is reached on the circle with a radius of 1616 m. At this point, the runway bank angle is 20°. During landing, touchdown is performed with a speed of 150 kts on the circle with a radius of 1,605 m where the bank angle is about 24°.

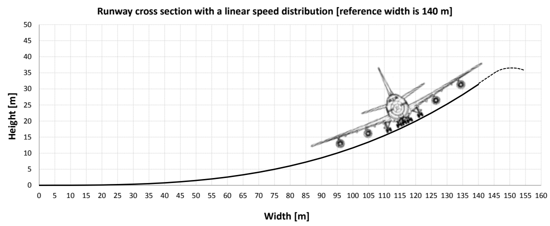

Figure 4 - The Boeing 747-100 on the banked runway at lift-off point

Following these initial studies on the shape of the runway and its impact on the aircraft performance, a few key requirements have been identified when preparing the design of an aircraft tailored to *the Endless Runway* concept. In order to reduce the risk of contact between the aircraft and the runway, the span is limited and the engines are located at the rear of the fuselage instead of under the wing. In addition, to increase the ground handling of the aircraft on the circular runway, the track of the landing gear must be increased. Thus, a larger fuselage may be selected. From a performance point of view, the higher take-off distance can be compensated by the selection of powerful engines to achieve a thrust-to-weight ratio higher than the one observed in today's classical configurations. These requirements lead to the following conceptual view of the aircraft tailored to *the Endless Runway* concept, see Figure 5.

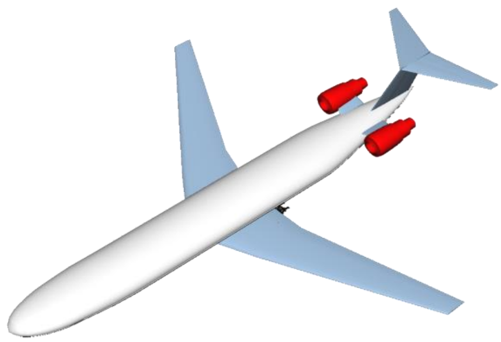

Figure 5 - 3D model of an aircraft tailored to the Endless Runway Concept

5 Runway operations

Today's operation follows the rule that the runway can only be used by one aircraft at any given time. To achieve the required capacity of the airport, simultaneous use of different parts of the runway should be allowed at *the Endless Runway*.

To allow the most flexible use of the system the runway can be operated in any direction if wind conditions allow so.

For ATM scheduling, we have subdivided the runway into 18 segments, see Figure 6, which correspond to the 18 access points on the runway defined in the Airport layout chapter.

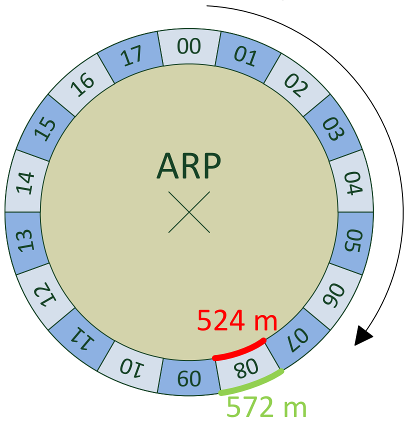

Figure 6 - The Endless Runway segments

These segments can be claimed in continuous strips by aircraft that want to use the runway. A booking system coordinates the available runway segments for operation and schedules the aircraft on the runway. For each flight, depending on the airspace user preferred trajectory, the aircraft performances (take-off and landing length and duration, wake-vortex category) and of other traffic constraints, a temporary runway strip is booked during a certain time period. The booking system accounts for avoiding possible wake turbulence encounters through adding additional time reservation when needed.

The taxiway system consists of two parallel rings that are used to coordinate the traffic to and from the runway. While the outer ring is operated in the same direction as the runway, the inner taxiway ring is operated in the opposite direction. The connection to the apron is provided by a number of taxiways, whereas four main entries to the inner part of the apron are available, see Figure 2.

For the operation a distinction has been made between two wind scenarios.

a) If the wind exceeds 20 kts, aircraft aiming at landing or taking-off at some points of the circular runway would experience a crosswind that is not acceptable. Therefore, in strong wind conditions, the aircraft will fly in two streams towards *the Endless Runway* to allow for landing at the touchdown point where dependency from the wind is at a minimum, that is to say as close as possible to headwind, see
b) Figure 7.

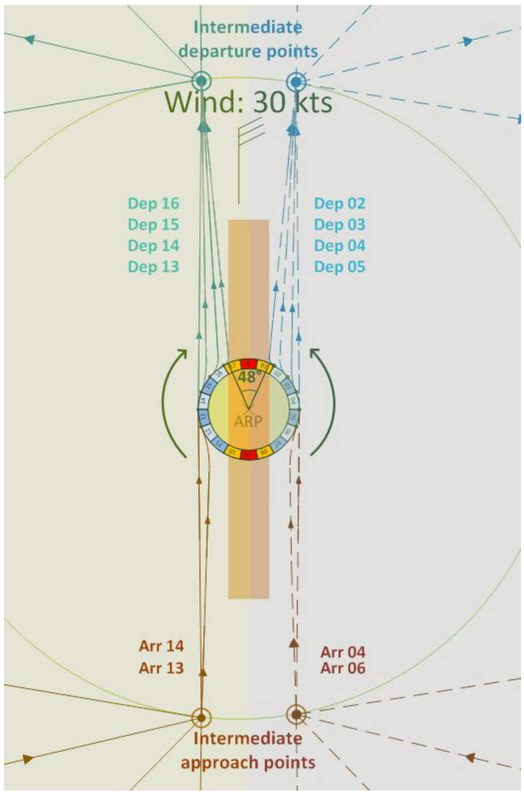

Figure 7 Operations in strong wind conditions (example 30 kts; the numbers in the arrival and departure routes indicate the touchdown and lift-off segments)

Aircraft will have to avoid segments with high crosswind during take-off and landing, so that only a limited number of segments of the runway can be use; segments with crosswind above 20 kts will be closed for lift-off and touchdown. Traffic flows must be directed towards the operational lift-off and touchdown points. The high wind scenario is similar to operating two parallel independent runways.

c) In low wind conditions (speed below 20 kts), aircraft can be operated in a flexible manner as all segments are available for take-off and landing, as presented in Figure 8).

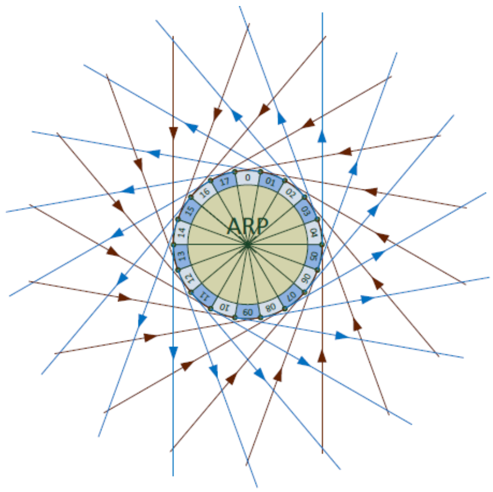

Figure 8 - Flexible sequencing of aircraft on the Endless Runway

With changing wind direction where speed remains below 20 kts, the runway continues operating uninterrupted at the full circle. In case of a direction change in strong wind conditions, the open TMA routes gradually "move" with the wind direction. No break in the sequence occurs as is the case with conventional runway configurations, where runways need to be opened or operational directions need to change with changing wind direction. No costly operation for tactical runway changes or runway directions change during operation will be necessary at *the Endless Runway*.

In combination with multiple runway operations and 4D operations, a controller decision support system will need to be available that allows negotiations between aircraft, airport, ATC and the ATM network.

6 TMA design

The TMA (Terminal Manoeuvring Area) is a controlled area around busy airports that is intended to coordinate the traffic that is climbing out from and descending towards the airport. The limits of a TMA are not standardized and differ from country to country.

The typical 3,000ft height of arriving aircraft performing an Instrument Landing System (ILS) approach was taken as a requirement to calculate the dimensions of *the Endless Runway* TMA [10]. With a standard 3° glide path angle the distance can be calculated where the final approach (descending from 3,000 ft) starts:

$$final\_dist = \frac{3000ft}{\tan(3°)}$$

For the calculations the touchdown and lift-off points for all segments are defined to be 100 m from the inner runway edge[1]. This corresponds to a distance of 1,600 m (*rwy_radius*) from the airport reference point (ARP) at the centre of the airport. With the final distance and the offset, the radius for the TMA can then be calculated:

$$TMA_{radius} = \sqrt{final\_dist^2 + rwy\_radius^2}$$

Based on these calculations, the TMA around the Endless Runway will cover a circular area around the centre of the airport with a radius of 17,521 m (9.46 NM).

For departures an average climb angle of 5° is defined. Taking this, the departure_height at the TMA exit can be calculated again using the final_dist as departure distance.

$$dep\_height = final\_dist \times \tan(5°) = 5000ft$$

[1] The touch-down and lift off points are related to the approach/lift-of speed of the aircraft. As a simplification of the calculations a common value of 100m was chosen.

Summarizing the calculations, the TMA has a minimum lateral dimension of 9.46 NM around the Airport Reference Point (ARP) and vertical limits from the airport height to 5,000ft. Figure 9 presents these dimensions. The departure and arrival routes start/end tangential at the start/end of a runway segment.

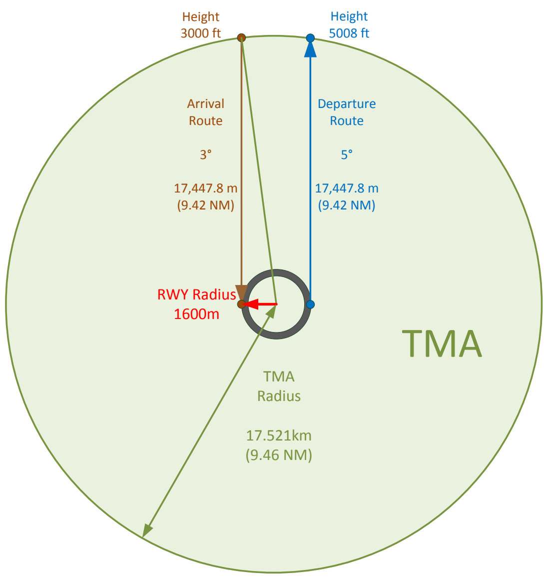

Figure 9 - TMA dimensions

With a number of 18 segments on the runway, there are also 18 different arrival and 18 different departure routes. Every route starts at the border of a segment. Figure 10 shows the 18 segments (00-17) of the runway, the routes and the start/end points at the borders of the segments. The picture displays the definition of the routes in a counter-clockwise operation mode. In a clockwise operation the lateral profile of the routes are mirrored. The departure routes become arrival routes and vice versa[2].

[2] The vertical profile changes as well. While all arrival routes start at 3000ft the departure routes end at around 5000ft. Therefore the vertical position of the start/end point is also dependent on the direction of operation

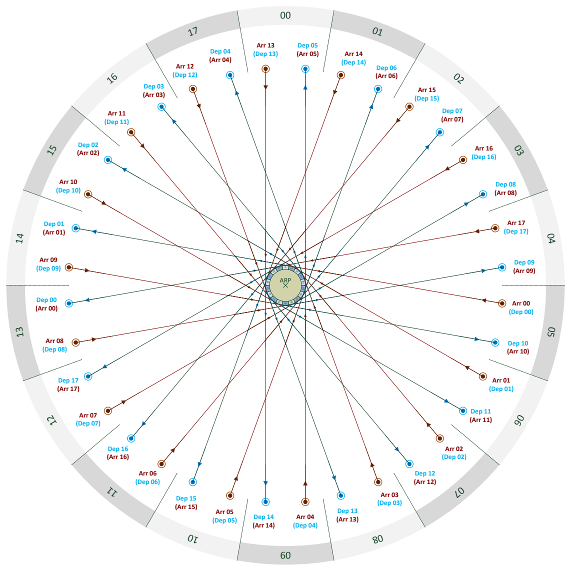

Figure 10 – TMA Arrival / departure route structure

Aircraft in the TMA are separated either vertically (from 4.9 to 10 NM, where no intersections between the routes exist) or laterally (within 4.9 NM, where several crossings in the routes occur). For vertical separation 1000ft was used and for lateral separation 1.5 NM

7 Results

Simulations have been performed to evaluate the proposed TMA and runway operations. The objectives of the simulations concerned calculation of capacity and delay and the use of the runway booking system.

Capacity calculations have been performed through running a typical high density CdG scenario at Paris Roissy Charles de Gaulle – the reference hub airport. The first simulation has been organised such that the first aircraft was able to book a number of segments on the runway (cf. its length necessary for take-off or landing), including one or two additional segments for safety. The following flights were able to book the necessary segments if there was no conflict with other flights on the runway or in the air (TMA). If a conflict occurred, the flight was delayed until no conflict existed anymore.

Several traffic density scenarios have been set up and planned on the available runway segments. Aircraft performance (the number of segments necessary per aircraft type) has been taken into account. All scenarios have then been evaluated with respect to the average delay. With this methodology, for a traffic demand similar to a hub airport in terms of aircraft mix, the following result is observed.

From a capacity point of view, *the Endless Runway* seems to be advantageous compared with a classical runway system: a first evaluation shows that 109 movements per hour are possible in the low wind case, decreasing to 60 movements per hour in the high wind case for a total runway length of about 10,000 m. The average delay in the low wind case was 39 seconds. When allowing a higher average delay, the number of movements could increase, see table below.

Max flights per hour	Average delay (h:min:s)
109	00:00:39
118	00:01:33
129	00:04:27
137	00:19:24
140	00:38:25
151	01:06:27
261	03:09:38

As a comparison with the 13,815 m total runway length of Roissy Charles de Gaulle airport and a capacity of 115 movements per hour in 2011, *the Endless Runway* scored similar in number of movements, but on a considerable shorter total runway structure.

8 Related work

The idea of a circular runway to avoid cross- and tailwind operations has been considered earlier. The first reference found is an impression from 1919 of a circular structure that would be built on top of skyscrapers in New York [12]. It would allow business travellers to enter the city without delay. In the 1960's flight trials on a circular banked runway were performed by the U.S. Navy, leading to some (expired) patents [13]. The trials proved to be positive as the runway's bank angle kept the aircraft on the right track avoiding them from being swept out of the runway.

Several other patents have been filed e.g. [14][15], based on the idea of a circular track, mostly concerned with new ideas for taking off and landing at some straight segment outside or inside the circle and only using the circular track for the lower speed segments of the take-off and landing roll.

9 Conclusions

This paper describes an innovative concept for designing and operating an airport with an *Endless Runway*. An initial operational concept is proposed, based on earlier experiences with a circular banked track; the work performed so far has not demonstrated any show stoppers. ATM simulations are planned in the near future to further assess the impact *the Endless Runway* may have.

It can be concluded that a runway of 1.5 km radius will fit the requirements for the size of the circle. The total runway length is equivalent to about three conventional runways and can accommodate sufficient movements for a large hub airport or a seasonal airport. Also, sufficient space is available inside the circle to cater for gates, terminal buildings, and other necessary infrastructure, such as fire stations. All non-essential facilities will be positioned outside of the circle.

The simulations showed that today's aircraft can take-off and land on a circular runway. However, performances are degraded and the risk of contact between the track and the aircraft is not negligible. Regarding the development of future aircraft, *the Endless Runway* concept implies a limit on the aircraft span associated to the necessary ground clearance. This constraint might be critical since recent studies showed that next generation airplanes would have higher aspect ratios.

ATM procedures will require a high level of automation. Air traffic controllers will need assistance for calculating the optimum take-off and touchdown point for each aircraft, taking other traffic and meteorological conditions into account. Simultaneous aircraft movements for arrivals and departures, both in clockwise and counter-clockwise directions may be possible, where more than one aircraft can occupy the runway at the same time.

10 Acknowledgments

The authors would like to thank A. De Giuseppe for his work regarding the assessment of today's aircraft capability to take-off and land on a circular runway and the conceptual design of *the Endless Runway* tailored aircraft.

11 References

[1] www.endlessrunway-project.eu

[2] ACARE (Advisory Council for Aeronautics Research in Europe), *Aeronautics and Air Transport: Beyond Vision 2020 (Towards 2050)*, Background Document, Issued: June 2010

[3] *Flightpath 2050, Europe's Vision for Aviation Report of the High Level Group on Aviation Research*, EUROPEAN COMMISSION, Directorate-General for Research and Innovation, Directorate General for Mobility and Transport, Luxembourg: Publications Office of the European Union, 2011, ISBN 978-92-79-19724-6, doi 10.2777/50266, © European Union, 2011

[4] http://www.boeing.com/boeing/commercial/cmo/market_developments.page

[5] Loth, S, et.al., *D1.2 The Endless Runway State of the Art, runway and airport design, ATM procedures and aircraft*, version 2.0, November 2011

[6] Hesselink, H.H. et.al., *D1.3 The Endless Runway concept: High-level overview*, version 2.0, December 2012

[7] Wikipedia article on Aéroport de Paris-Charles-de-Gaulle: http://fr.wikipedia.org/wiki/A%C3%A9roport_de_Paris-Charles-de-Gaulle

[8] Richard de Neufville and Amedeo Odoni, *Airport Systems*, Second Edition, 2013

[9] C. R. Hanke, D. R. Nordwall, *The simulation of a Jumbo Jet Transport Aircraft Volume II: Modeling data*, 1970

[10] S. Loth; H. Hesselink; R. Verbeek; M. Dupeyrat, *D4.2 The Endless Runway ATM Operational Concept*, version 1.0, June 2013

[11] E. M. Greitzer, H. N. Slater, *Volume 1: N+3 Aircraft Concept Designs and Trade Studies, Final Report*, The MIT, Aurora Flight Sciences, and Pratt&Whitney Team, 2010

[12] *Roosts for City Airplane : Would This Circular Track Solve the Landing Problem?*, in Popular Science, June 1919

[13] *Navy Tests Design for Airport With Circular, Banked Runway*, The Milwaukee Journal, Dec 1965

[14] US Patent 3157374, *Airport Design*, James S. Conrey, Nov 1964

[15] US Patent 3333796, *Closed Track Airport with Straight Runways for Instrument Landing and Take-off*, A. Woldemar, August 1967

Early assurance of the Gripen E combat performance by mission simulation

J. Jeppsson
Operational analyst, Saab Aeronautics, Sweden

Keywords: Mission simulation, Gripen, aircraft development

Abstract

In the development of the new Gripen E(Echo version) fighter aircraft an early operational evaluation of system design is an essential way of making the right decisions regarding design, functionality and HMI (Human Machine Interface).
Traditionally an operational evaluation of a Gripen version has been done when the aircraft has been about to be delivered to the air force. Because of that some operational remarks were discovered late and could only be adjusted in the next edition release.
In recent years Saab Aeronautics has developed a simulation tool called OpVal (Operational Validation Simulator). This is a facility with eight Gripen cockpit stations collocated and interconnected. It is possible to change the design and functionality in the OpVal cockpit in a short time and compare different concepts to each other.
With this facility it is possible to try out and evaluate new functionality, together with the end-user, in a realistic scenario and therefore send the feed-back direct to the design team before the aircraft is built. For the manufacturer and end user this means gained operational value, reduced development time and reduced cost by making the right design from the beginning.

1 Introduction

Producing fighter systems is a complex and expensive process and has traditionally resulted in a global trend of military aircraft projects that has exceeded time lines and financial limits. Saab Aeronautics has changed the direction of this trend when introducing the Gripen aircraft in the beginning of the 90’s.

With the next Gripen project Saab Aeronautics has an ambition to continue in this direction. The key is to identify the system functions and HMI design issues in an early phase of the project and have a close cooperation with the customer to ensure fulfilled operational needs.

Modeling and simulations is an essential way of identifying these issues by investigating the aircraft model in its combat environment.

2 Gripen E

Saab Aeronautics is developing the next generation Gripen fighter aircraft – the “Echo” version for the Swedish Air Force.

The Gripen E aircraft is the enhanced version of today's operational Gripen C. It will be equipped with a stronger engine (GE 414) and have a new structure that allows it to carry more external stores and internal fuel. But the biggest changes are in the system architecture and capabilities of the aircraft. New sub systems like AESA (electrically scanned array)-radar, IRST (Infra Red Search and Track), ESM/ECM (Electric Support & Counter Measures) and communication system will provide this fighter with a capability that will encounter challenges of a future combat environment such as hostile stealth aircraft and agile surface-to-air missile systems.

Fig 1 The Gripen Demonstrator

However, all these new sub system may overwhelm the pilot with information if not integrated correctly. The design of the tactical system must be modeled and simulated to be able to prioritize level of access and presentation of sensor data. The HMI (Human Machine Interface) is the interface from the aircraft system that provides the pilot with correct and time sensitive information for making decisions. The best way to optimize this mix of information, sensor fusion, access levels, presentation modes and system layout is to try it out with operational pilots in a multi aircraft realistic scenario.

Additionally it is important to know if the aircraft has a correct balance between sensor performance, weapon performance and communication system so the full range of the weapon system can be used efficiently when the aircraft is provided with sensor information or data link information.

3 Gripen E Mission Simulation

The project is currently in the design phase and there are several design choices are to be made. The Swedish Air Force has an early insight into the project by participating in the operational evaluations simulations at Saab Aeronautics.

These evaluations take place in the OpVal (Swedish- Operationell Validering) simulator facility at Saab that consists of eight simulator stations representing Gripen E and/or its adversaries, two Command & Control sites (fighter controller that provides the fighter unit with tactical information via speech and data link) and a scenario overview.

In this design and evaluation phase the requirements of high fidelity simulators are limited to the display interfaces and a fully represented flight model is not crucial. Instead, a short cycle of system upgrades is used in order to evaluate suitable system solutions.

Fig 2 Saab OpVal

The Swedish Air Force has provided Saab with a number of CONOPS (Concept of Operation) that are to be evaluated. From these CONOPS a scenario with manned and unmanned entities is built in the OpVal simulator.

The main goal is to try out the concept of the Gripen E weapon system in an early stage to evaluate its operational usability and lethality and to identify design choices to be made. During these yearly evaluations participating pilots represent the SwAF, FMV and Saab.

Typical simulation sessions run for a week and are initiated after the pilots have been trained in the new HMI and system concept.

Saab has a long experience of using modeling and simulation as a part of in the verification and validation process but this has traditionally only been made in stand-alone simulators where the pilots could focus on the individual cockpit functionality and aircraft behavior.

Using the new method of early evaluating in the OpVal-simulators in a realistic scenario, the aim is that the aircraft weapon system will come into full operational service as a mature aircraft 2023, with a design made of combat training experiences

4 Spinoffs from the evaluating simulations

The aim is to Design Once by a) making the right choices from the beginning and hereby saving time and money in the project and b) being able to reuse system code and models to the final product e.g. the operational mission trainer simulators.

The results from the evaluations are taken from the pilot’s digital debriefing forms, recording of combat results and recording of the aircraft performance regarding sub-systems.

Fig 3 Debriefing

But most important are the face-to-face debriefings and discussions in the end of the days.

The results from the simulations are reported back to the organizations of the Swedish Air Force, FMV and Saab Aeronautics. Critical findings are used to convince management to make adjustments in the design and for the customer it is also a valuable knowledge to look into the future and assess future challenges, like impacts of a future operational issues such as tactics, joint mission support, command & control and organization..

5 The way ahead

The evaluations will continue annually at least until the Gripen E enters operational service in Swedish Air Force 2023. Based of flight test data from the Gripen E test aircraft starting 2015, models of the aircraft and its subsystem will be refined and the output will be more accurate for every year.

Initially the cockpits had a HMI similar to the Gripen C/D aircraft which was familiar to the pilots who normally fly this version. But when after modifying the HMI and HOTAS (Hands on throttle and stick) concept to utilize the new sensors and fusion tools it has been noticed that a longer familiarization phase of the pilots is needed to achieve a smooth and realist use of the cockpit and the weapon system and therefore also make the right tactical decisions.

The annual operational evaluation of Gripen E has started a new era at Saab Aeronautics where the system engineers and developers have achieved a mindset that is more focused on the entire operational capability of the platform than before. The cooperation with the customer is a collaboration that will gain time and money and provide the Swedish Air Force with a formidable fighter aircraft able to meet the future threats.

Concept Assessment for Remotely Piloted Commercial Aircraft using Multi-Attribute Nonlinear Utility Theory

Amina Malik, Xiaoqian Sun, and Florian Linke
Institute of Air Transportation Systems, DLR and TUHH, Hamburg, Germany

Keywords: *Remotely Piloted Commercial Aircraft, Remotely Piloted Aircraft, Multi-Attribute Non Linear Utility Theory, Stakeholders*

Abstract

This paper outlines the research on Remotely Piloted Commercial Aircraft (RPCA) using multi-attribute nonlinear utility theory, from the perspective of multiple stakeholders in air transportation systems, including airlines, regulating authorities, pilots, and passengers.

In this research, RPCA implies cockpit crew reduction for future commercial passenger aircraft. With ongoing increase in automation, commercial aircraft would be able to fly autonomously without on-board pilots. However, for the backup and safety of the system, pilots would be positioned on the ground for remotely monitoring and controlling the aircraft from a Ground Control Station (GCS). The concept is similar to the currently operated Remotely Piloted Aircraft (RPA).

In order to evaluate the maximum potential of the concept, a long range passenger aircraft is considered as the use case for this study. Major stakeholders and key criteria are identified for this preliminary research. Furthermore, a widely used multi-criteria analysis method: nonlinear utility theory is applied to evaluate a set of scenarios based on number of pilots on-board and on ground.

1 Introduction

Remotely Piloted Aircraft Systems (RPAS) have evolved as an increasingly growing industry over the last decade. The worldwide RPAS forecast indicates that the market will double over the next decade with an annual procurement and R&D market of $11.3 billion in 2020. These estimates predict a total of 35,000 RPAS to be produced worldwide in the next 10 years [1].

Over the decades, the RPAS industry has been mainly focused on military applications however in recent years, civil and commercial applications are becoming increasingly popular. From the statistics of worldwide survey, 20% of RPAS produced in 2011 comprised of civil and commercial usage [2]. The emerging civil and commercial applications range from civil security, search and rescue, firefighting, meteorological, precision agriculture and fisheries, power/gas line monitoring, infrastructure inspection, communications and broadcast services to research missions.

This increased growth has been pushing the authorities to accept RPAS as legitimate users of airspace. U.S. Federal Aviation Administration (FAA) has set a timeline to integrate RPAS in the National Airspace System (NAS) by year 2015 [3]. Similarly in Europe, several initiatives have been undertaken by European Union, in close collaboration with other commission services and international organizations. It is anticipated that by 2016, current RPAS will be able to fly in Europe in non-segregated airspace [1].

Once the milestone of safely integrating the different classes of RPAS in airspace will be achieved, the requirements for new commercial applications will emerge. A Remotely Piloted

Commercial Aircraft carrying passengers seems a radical concept at present but it might become a reality in future. It is likely that single piloted commercial aircraft will come into service as the transition from current aircraft to pilotless aircraft. Airlines have already shown interest in reduction of cockpit crew to a single pilot for commercial aircraft [4]. National Aeronautics and Space Administration (NASA) conducted a meeting of different stakeholders, research and industry partners to identify potentials and challenges of single piloted commercial aircraft operation. A diverse feedback was provided, from various stakeholders in favor of the concept whereas regulating authorities anticipated safety issues. Public acceptance and pilot boredom were also highlighted as significant areas [5].

It can be stated that, if automation would prove to be safe enough, a fully autonomous aircraft with no pilots on board would eventually become a reality. However, the safety standards of technology would have to match or even supersede the existing requirements. In addition to safety, there are other issues such as public acceptance, ground pilot's responsibility, liability, insurance, data-link protection etc. The objective of this research is to incorporate these key criteria for feasibility analysis of a RPCA based on three alternative scenarios of on-board and ground pilots.

2 Literature Review

Slingerland et al. conducted research on an environmental friendly pilotless freighter aircraft. The removal of pilots from cockpit resulted in modifying some subsystems of aircraft, particularly environmental control system. The economics tradeoffs for redesigned environmental control system showed a 3.5% reduction on direct operating costs [6].

Innovative Future Air Transportation System (IFATS), an EU research project which considered the revolutionary step changes in the Air Transportation System (ATS). The concept was based on fully automated ATS, with pilot-less transport aircraft controlled and monitored by ground operators with a network-centric communication system. The key findings of the project were that the concept is technologically not far from reality, though modifications would be required in aircraft and ground infrastructure. Various technologies e.g. Automatic Dependent Surveillance – Broadcast Out, (ADS-B Out) has already been implemented on various aircraft and the development of ADS-B In is required for Airborne Separation Assurance System (ASAS). Availability of frequency spectrums and communication architecture would be complex, however lower number of voice messages will provide simplicity and other advantages to the IFATS concept. Meanwhile, security risks were mentioned as open questions.

IFATS highlighted that current regulations could be made re-usable for highly automated ATS and aircraft but some additions would be required for new systems and operations. These would include new on-board equipment, data-link for ground station, operator responsibilities, software, communication and data integrity of the systems. Public opinion was also considered and it was concluded that public would possibly accept to fly in pilot-less aircraft.

The research in this project also proved the concept to be economically profitable. Operational costs of the system were estimated however ground control segment was not modeled in the overall operating costs. The increase in depreciation, maintenance, insurance, interest costs due to ground control station could be significant, however it was not included. Other incurring costs like data link charges were also not considered [7].

3 Methodology

The single economic criterion, such as Direct Operating Cost, is not the only metric for final technology evaluation. In addition to the economic consideration, there are several other criteria which need to be taken into account. However, it is often difficult to derive a reliable transfer function to convert these non-monetary criteria into monetary values. One solution is to apply Multi-Criteria Decision Analysis (MCDA) techniques. As an important field in Operational Research (OR), MCDA is a process that allows one to make decisions in the presence of multiple, potentially conflicting criteria [8]. Common elements in the decision analysis process are a set of candidate alternatives, multiple decision criteria, and preference information representing the attitude of a decision maker in favor of one criterion over another, usually in terms of weighting factors. MCDA techniques can help a decision maker to evaluate the overall performance of the candidate alternatives [20], [21].

Multi-Attribute Utility Theory is one widely used MCDA method. This method is based on the concept of utility function, which represents a mapping from the decision maker's preference into a mathematical function [9]. The most widely used form is the additive multi-attribute utility method, with two assumptions stating that utility functions of all attributes are independent and the weighting factor of an attribute can be determined regardless of the weighting factors of other attributes. Ramani et al. assessed the impact of accounting nonlinearity in multi-attribute utility theory for transportation planning applications [10]. The authors found that employing nonlinear functions had a significant impact with the comparison of the commonly assumed linear scaling. Furthermore, Macharis et al. presented a multi-actor multi-criteria analysis method to evaluate transport projects, with emphasis on the inclusion of multiple stakeholders [11].

3.1 Stakeholders and Scaling of Criteria

There are multiple stakeholders involved in air transportation systems and reduced crew operation would impact all of them. In this research, we assess the Remotely Piloted Commercial Aircraft by using multi-attribute nonlinear utility theory, from the perspectives of four stakeholders: airlines, regulating authorities, pilots, and passengers. Other stakeholders including aircraft manufacturers, air traffic control and air navigation service providers are out of scope for current study. Table 1. identifies the set of criteria relevant for each stakeholder, based on literature research. Criteria were further broken down into sub-criteria; however, sub-criteria are not incorporated in this study due to unavailability of data.

Table 1 Stakeholders and Criteria.

Stakeholder	Criteria	Sub-criteria
Airlines	C.1.1 Direct Operating Cost C.1.2 Passenger Acceptance C.1.3 Pilot Acceptance	
Regulating Authorities	C.2.1 Safety/ Airworthiness C.2.2 Passenger Acceptance	C.2.1.1 Increased number of incidents/accidents C.2.1.2 Pilot Workload and Situational Awareness C.2.1.3 Data link Protection C.2.1.4 Emergency Situations C.2.1.5 Liability/legal Issues
Pilots	C.3.1 Job Acceptability	C.3.1.1 Salary C.3.1.2 Boredom Issues C.3.1.3 Workload and Situational Awareness
Passengers	C.4.1 Passenger Acceptance	

Table 2. lists the reference values for baseline aircraft A330-203, from Los Angeles International (LAX) to Stockholm Arlanda airport (ARN) [12] .

Table 2 Baseline Aircraft Specifications.

MTOW	Block Distance	Block Time	Block Fuel	No. of Passengers
233000kg	9000km	11hours	90000kg	260

For transition from three pilots on board (two pilots flying and a third relief pilot) for a long haul flight to a fully autonomous aircraft, we selected three alternative scenarios, listed in Table 3.

Table 3 Reduced Crew Alternatives.

	Baseline Case	Alternative I	Alternative II	Alternative III
Pilots on-board	3	2	1	0
Pilots on ground	0	1	2	2

One onboard pilot is subsequently moved from the cockpit to Ground Control Station (GCS). Alternative III is assumed to operate autonomously without any on-board pilot, while two ground pilots monitor the aircraft and take over the aircraft in case of emergencies.

3.2 Direct Operating Cost

Direct Operating Cost (DOC) is a significant criterion for airlines for aircraft operations. DOC can be generally segmented into:

a. Depreciation Cost – Aircraft and Spares
b. Interest
c. Insurance
d. Fuel
e. Maintenance Airframe
f. Maintenance Engine
g. Flight Crew
h. Cabin Crew
i. Landing Fees
j. Navigation Charges

The cost fractions from (a) to (c) are categorized as ‘ownership costs’, whereas (d) to (j) are grouped as “cash operating costs”, according to Liebeck et al. [13].

For the DOC estimation of RPCA, Ground Control Station segment is added in the conventional DOC. The cost fractions for airframe and engine are kept unchanged. This assumption is not fully valid as new on board avionics and sensors would increase the aircraft price and increase all segments of aircraft DOC. However, due to unavailability of required data, it is kept constant at this stage. For further studies, technology factors can be assumed to predict increase in DOC, similar to IFATS approach [7].

GCS depreciation, interest and insurance costs are modeled using Liebeck et al. method [13]. GCS price is S6.0 million, for the current in use technology for RPAS [14]. Depreciation costs for GCS are a percentage of the total investment in spares. As GCS is less complex and has less number of parts, compared to the airframe, investment in GCS spares is taken as 3% of GCS cost. Insurance rate for GCS is kept at 0.05% [14]. For simplicity, maintenance costs for GCS are not included in the model yet. For RPCA, ground pilots/operators are assumed to be paid 60% of flying pilots’ salary. Landing fee is also decreased to 15% due to autonomous systems, based on IFATS [7]. SATCOM fee is an additional segment of DOC. This fee is based on the in service RPA data link operation charges, which is 420$ per flight hour [14].

According to IFATS study [14], 10 additional passengers can be flown due to removal of cockpit for fully autonomous aircraft. This assumption is used for DOC estimates for Alternative III. A more precise calculation can be performed for added number of passengers for each alternative, by estimating the exact volume gained due to removal of cockpit. However, this level of accuracy was not required for this study. Another assumption in current DOC modeling is that only one aircraft is controlled by one GCS. If multiple aircraft are to be controlled, DOC for GCS and the cost for ground pilots would distribute on multiple aircraft, hence decreasing the overall DOC.

Table 4 DOC Estimations for Alternatives.

	Alternative I	Alternative II	Alternative III
Decrease in DOC	0.3%	2.2%	6.5%

Table 4. shows the estimated DOC decrease for each alternative from baseline A330-203. A 6.5% reduction in DOC is achieved for a fully autonomous aircraft, having no pilot onboard and two pilots on ground.

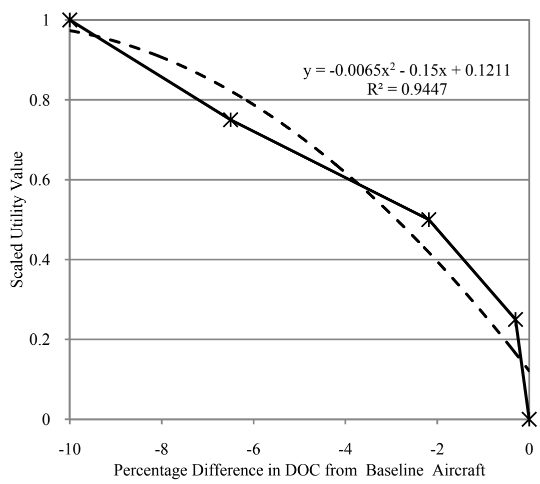

Fig. 1 Utility Curve for Decrease in DOC

Figure 1. represents the utility values corresponding to percentage reduction in DOC. A piecewise linear graph depicts the estimated DOC reduction. For deriving the scaled utility value corresponding to each DOC value, we projected the best case as 10% decrease in DOC from the baseline aircraft. No reduction in DOC is taken as the Worst case in this study. Based on the piecewise linear graph, a second order nonlinear curve is generated for scaled utility value. A 10% decrease in DOC (best case) has a utility value of 1.0, whereas the worst case corresponds to utility value of zero.

3.3 Equivalent level of Safety

The implementation of RPCA is improbable without fulfilling the safety requirements. Safety standards for manned aircraft are a set of requirements defined for various aircraft subsystems, for all stages of aircraft design, manufacturing and final operation of the aircraft. CS 1309 contains these requirements for different classes of aircraft with corresponding AMC sections. Any event where a fatality or injury can occur, is categorized as hazardous (< 10^{-7} events per flight hour). A catastrophic event where multiple fatalities can be caused should have a probability of 10^{-9} per flight hour [15].

The International Civil Aviation Organization (ICAO) Safety Report shows that, 2011 has been the safest year since 2004. This comparison states the lowest number of fatalities which decreased to 41.4% [16]. On the other hand, if we look at RPAS industry, safety standards have not been so stringent. However, the RPA industry been trying to implement the Equivalent Level Of Safety (ELOS) to unmanned aircraft. The ELOS requirements for RPAS vary from 10^{-6} to 10^{-8} per flight hour, depending on the application. However it's not yet close to the standards of commercial aircraft. Table 6 shows the comparison of failure data for a military RPAS to Boeing 747 and Boeing 777 aircraft [17].

Table 5 Comparison of Failure Data of of Commercial Aircraft and RPA.

Aircraft	Mishap Rate (per 100k hrs)	MTBF (hours)	Availability	Reliability
Boeing 747	0.013	532.3	98.6%	98.7%
Boeing 777	0.13	570.2	99.1%	99.2%
Predator/RQ-1	32	55.1	93%	89%

For the RPCA concept, we selected two extreme values for reliability. The best case corresponds to the prevalent current safety standards for manned aircraft as 10^{-9} per flight hour whereas the worst case is set for current commercial RPAS as 10^{-7}per flight hour [18].

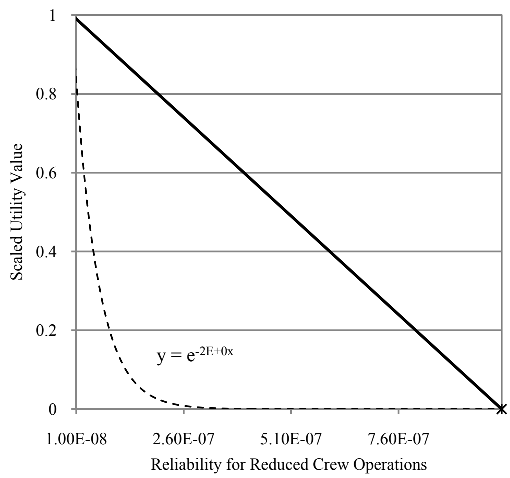

Fig. 2 Utility Curve for Reliability

A linear graph and its resulting exponential curve are drawn based on the extreme values (Fig. 2.). Exponential curve best describes the scaled utility representation of safety requirements. With RPCA having a reliability of 10^{-7} per flight hour is unacceptable for regulating authorities and with increased reliability up to 10^{-9} per flight hour, utility value would increase exponentially to 1.0.

3.4 Job Acceptance for Pilots

Job acceptance as ground pilots is a challenging criterion to quantify. The question, as how pilots would react to losing their jobs or switching the jobs as ground pilots is of major concern. The ground pilots in military RPAS often have to deal with boredom because they are not physically present inside the aircraft. This also relates to situational awareness of pilot. However, commercial pilots are mostly monitoring the aircraft and not flying the aircraft physically, so boredom issues might be less prevalent than in military ground pilots.

Due to unavailability of any data of how pilots would accept jobs as ground pilots, we assumed the best and worst case values. Assuming 25% of pilots willingly accepting the new jobs defines the worst case. This high percentage is chosen because pilots might find advantages in this job for staying close to family and not flying all the time. The best case is assumed as all pilots willing to take new jobs as ground pilots.

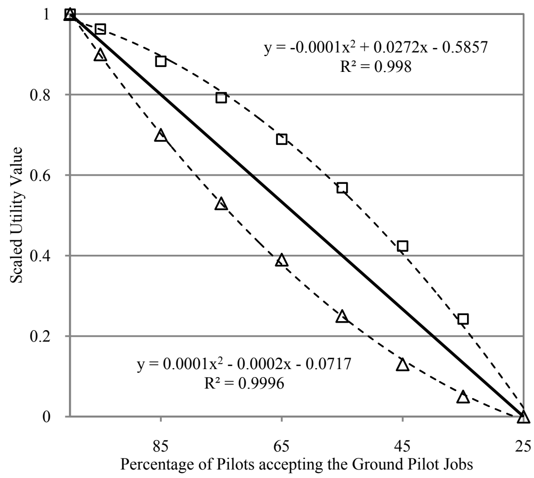

Fig. 3 Utility Curve for Pilots' Acceptance

The best and worst cases are then linearly scaled to utility values. Two best fitting second order non-linear curves are drawn to replicate two possible scenarios. Top curve in Fig. 4. represents the optimistic scenario for passenger acceptance while the bottom curve shows a pessimistic scenario for pilots' acceptance to take jobs as ground pilots.

3.5 Public/Passenger Acceptance

Passenger acceptance/public opinion is a very common question being asked whenever there is a discussion of RPCA aircraft. In general, public has a perception of safety assurance related to pilots on board. MacSween-George[19] conducted a survey among 200 random men and women, asking their opinion about travelling in unmanned automated aircraft. The survey included four different questionnaires providing different level of information about automated aircraft. The survey with more information about unmanned automated aircraft yielded higher willingness to accept automated aircraft and to support the regulating authorities. We aggregated the results of all questionnaires. Out of 200, a total of 21 agreed to flying in an unmanned aircraft. This approximation of 10% of passengers willing to fly in such aircraft defines the worst case scenario for our study, yielding a utility value of zero. Figure 4. represents the linear line joining the best and worst cases for passenger willingness. The second order non-linear curves depict the optimistic scenario (top curve) and pessimistic scenario (bottom curve) for passenger acceptance to fly in RPCA.

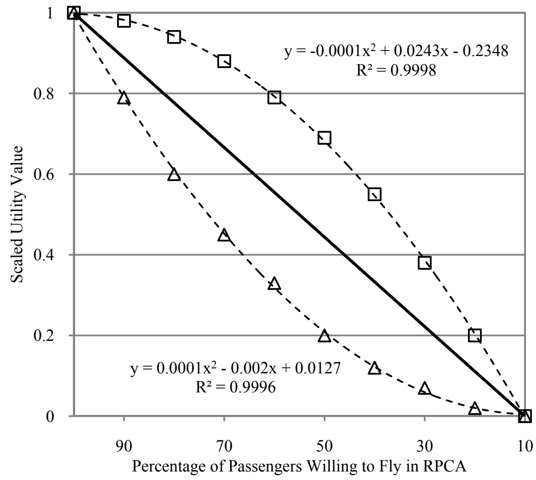

Fig. 4 Utility Curve for Passenger Willingness

4 Assessment Results

The results are generated based on two cases. For Case I (Fig. 5.), we selected a pessimistic scenario for reduction in DOC while taking optimistic nonlinear curves (Fig. 3. and Fig. 4.) for pilots and passenger acceptance. The utility values for DOC reduction for Case I are taken from the estimated piecewise linear graph, see Fig. 1. Case II shown in Fig. 6. is based on the opposite approach to Case I, by utilizing the optimistic scenario for DOC reduction while using the pessimistic curves for pilot acceptance (Fig. 3.) and passenger acceptance (Fig. 4.)

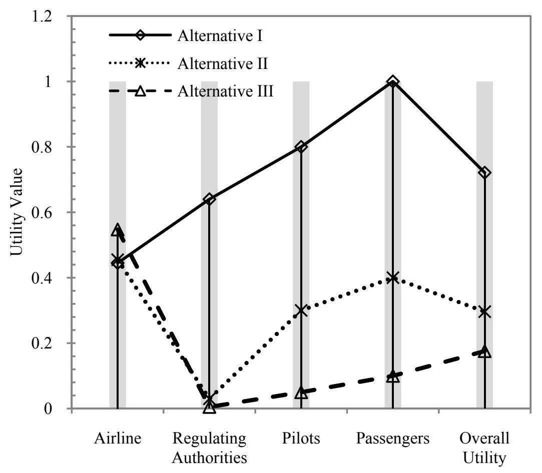

Fig. 5 Overall Utility Value for Case I

Figure 5. and Fig. 6 show the utility values for each stakeholder for three RPCA alternatives. The utility value for stakeholders represents the aggregated sum calculated by multiplying the utility values for respective criterion to weighting factor of each criterion. For example, in Fig. 5, Alternative I has an assigned utility value of 0.25 for difference in DOC. Passenger acceptance for this alternative, where one pilot is on ground and two pilots flying is nearly equivalent to the current aircraft. Thus, a utility value of 1.0 is taken as passengers would still feel safe having two pilots on board. However, pilots might not accept this change fully; though an optimistic value of 0.8 was chosen. A weighting factor of 0.7 is given to DOC reduction whereas passengers' and pilots' acceptance are given equal weighting factors of 0.15 from airlines' perspective. For regulating authorities, a utility value of 0.6 for safety is taken for this alternative as third pilot will only be monitoring or taking role while one on-board pilot is resting. Though, in case of any emergencies, the on-board pilot would take control. However, new failure modes might appear due to system addition and complexity of GCS. Thus a weighting factor of 0.9 is assigned to equivalent level of safety because of its importance to regulatory authorities as a stakeholder. The remaining percentage of 0.1 is assigned to passenger acceptance. From pilots and passengers point of view, utility remains the same as given in the airline case, except the weighting factors are given as 1.0. The overall utility value is then obtained by an averaged sum of the utility values for all stakeholders.

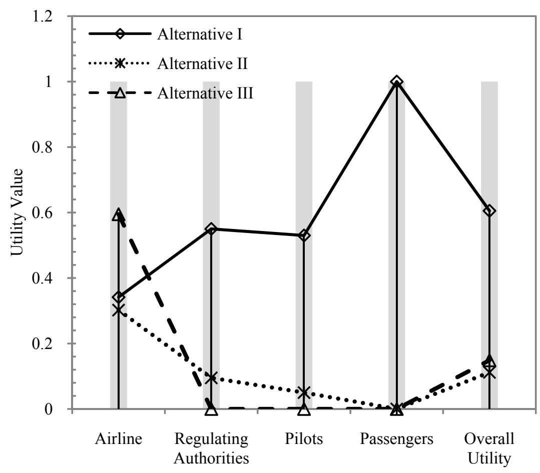

Fig. 6 Overall Utility Value for Case II

The details of utility values taken for Case I and Case II along with weighting factors are given in Appendix. The approximation for utility values and weighting factors are solely based on authors' opinion. No stakeholders were directly involved in this research as the purpose of this study is to visualize the importance of each criterion with respect to different stakeholders. Both cases (Fig. 5. And Fig. 6.) clearly show that Alternative I has highest overall utility. Although it has a lesser utility value for airlines but other stakeholders, it proves to be of best value. Thus, it can be considered a more favourable alternative for regulating authorities, pilots and passengers when compared to Alternative II or III.

To further visualize the effect of weighting factors in this study, we took one stakeholder, i.e. airlines and performed a sensitivity analysis. Figure 7. shows equal weighting factors of 0.33 assigned to all three criteria for airlines. The utility values for each criterion are kept the same as for Case I. When equal weighting factors are given to each criterion, Alternative I has the highest overall utility value of 0.225 whereas Alternative III has the lowest, shown in Fig. 7.

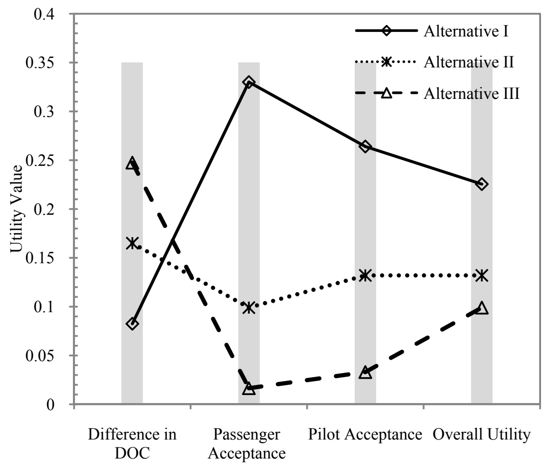

Fig. 7 Equal Weighting Factors for Airline Criteria

Figure 8. shows the result of unequal weighting factors for individual criterion. For airlines, DOC being the most important criteria is assigned a weighting factor of 0.7. A weighting factor of 0.2 is given to passenger acceptance, whereas pilots are given 0.1 weighting factor.

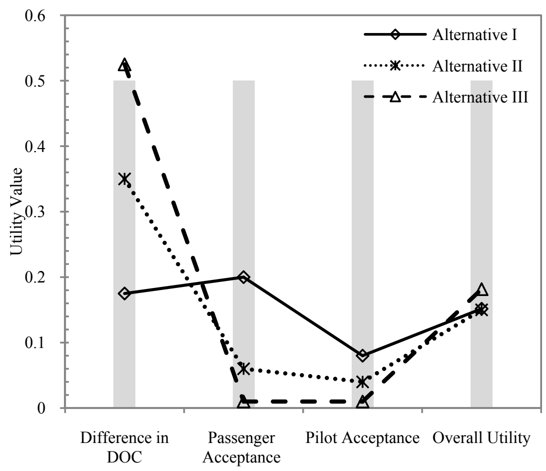

Fig. 8 Unequal Weighting Factors for Airline Criteria

A high weighting factor for DOC results in an increased utility value for Alternative III, which is logical for airlines. Although the difference in overall utility value is relatively small with comparison to Fig. 7, but change in weighting factors could lead to a different outcome of the analysis, thus providing different scenarios for feasibility of a concept.

5 Conclusions and Future Work

The goal of this paper is to assess the Remotely Piloted Commercial Aircraft (RPCA) concept from the perspective of multiple stakeholders in air transportation systems. With a long range passenger aircraft as the use case, major stakeholders and key criteria in air transportation systems are identified for this preliminary research. Furthermore, a widely used multi-criteria analysis method: nonlinear utility theory is applied to evaluate a set of scenarios based on number of pilots on-board and on ground. Based on the results of this study, Alternative I (two pilots on-board and one pilot on ground) has the highest overall utility than the other two alternatives. Alternative III (zero pilot on-board and two pilots on ground) might have the highest advantage in terms of DOC reduction for airlines.

The current DOC modelling showed a reduction for each Alternative compared to the baseline aircraft; however, the increase in operational costs due to massive ground infrastructure to support individual RPCA aircraft is an open question. The concept could only be feasible in case of having multiple aircraft being controlled from one Ground Control Station (GCS). One visionary concept could be air traffic controllers controlling the aircraft from ground which can be assumed in further studies.

A detailed breakdown of criteria into sub-criteria can be used to predict realistic utility values. For example, for projection of safety, pilot workload and situational awareness, data link protection, handling of emergency situations, legal issues can be added as sub-criteria for utility function. In this study, the utility value for safety for Alternative II (one pilot on-board and two pilots on ground) and Alternative III (zero pilot on-board and two pilots on ground) is nearly zero, however this might actually change due to potential benefits associated with this concept, e.g. lesser incidents/accidents due to pilot error, fatigue and indecision. For Alternative III, no accidents will occur due to loss of life support to pilots. Technology can play an important role in increasing the safety e.g. automated takeoffs and landing can eliminate the risk of pattern related accidents. Such factors can be taken into account into more detailed analysis.

References

[1] European Commission, "Towards a European strategy for the development of civil applications of Remotely Piloted Aircraft Systems (RPAS)", SWD (2012) 259, Brussels, 2012.

[2] UVS International, "Remotely Piloted Aircraft Systems: The Global Perspective", 10th Edition, 2012.

[3] Joint Planning and Development Office, "NextGen UAS Research, Development and Demonstration Roadmap", Version 1.0, 2012.

[4] Flight global, "Embraer reveals vision for single-pilot airliners", accessed on 10.08.2013 http://www.flightglobal.com/news/articles/embraer-reveals-vision-for-single-pilot-airliners-343348/

[5] National Aeronautics and Space Agency, "Proceedings of Single Pilot Operations (SPO) Technical Interchange Meeting", NASA Flight Deck Display Research Lab, 2012, http://humansystems.arc.nasa.gov/groups/FDDRL/SPO/agenda.php

[6] Slingerland, R., Zandstra, S., Scholz, D., and Seeckt, K., "Green Freighter Systems", *46th AIAA Aerospace Sciences Meeting and Exhibit*, American Institute of Aeronautics and Astronautics, Virginia U.S., 2008.

[7] CLT., AJ. and HJ. et al., "Innovative Future Air Transport System", EU Sixth Framework Programme, 2007.

[8] Ehrgott, M., Figueira, J. and Greco, S., *Trends in Multiple Criteria Decision Analysis*, Springer, 2010.

[9] Keeney, R.L. and Raiffa, H., *Decision with Multiple Objectives: Preferences and Value Tradeoffs,* Cambridge University Press, 1993.

[10] Ramani T., Quadrifoglio L., and Zietsman J., "Accounting for Nonlinearity in the MCDM Approach for a Transportation Planning Application", *IEEE Transactions on Engineering Management*, Vol. 57, No. 4, 2010, pp. 702-710.

[11] Macharis, C., De Witte, A. and Ampe, J., "The multi-actor, multi-criteria analysis methodology (MAMCA) for the evaluation of transport projects: Theory and practice". *Journal of Advanced Transportation,* Vol. 43, No. 2, 2009, pp. 183-202.

[12] Owner's & Operator's Guide A330-200/-300, Aircraft Commerce, Issue No. 57, April/May 2008.

[13] Liebeck, R.H., Andrastek, D. A., Chau, J., Girvin, R., Lyon, R., and Rawdon, B., et al., "Advanced Subsonic Airplane Design & Economic Studies", NASA CR-195443, 1995.

[14] Moir'e Inc., "Cost and Business Model Analysis for Civilian UAV Missions", Final report prepared for NASA, 2004.

[15] European Aviation Safety Agency (EASA), "Certification Specification 25 (CS25)", Amendment 3, 2007.

[16] International Civil Aviation Organization, "Safety Report © 2012", 2012.

[17] DeGarmo, M. T., "Issues Concerning Integration of Unmanned Aerial Vehicles in Civil Airspace", MITRE Center for Advanced Aviation System Development, McLean, Virginia, 2004.

[18] Dalamagkidis, K., Valavanis, K. P. and Piegl, L. A., "On unmanned aircraft systems issues, challenges and operational restrictions preventing integration into the National Airspace System", *Progress in Aerospace Sciences*, 44, 503-519, 2008.

[19] MacSween-George, S. L., "A public Opinion Survey – Unmanned Aerial Vehicles for Cargo, Commercial, and Passenger Transportation", *2nd AIAA Unmanned Unlimited Systems, Technologies and Operations*, 15-18 Sep. San Diego 2003.

[20] Sun, X., Gollnick, V., Li, Y., and Stumpf, E., "An Intelligent Multi-Criteria Decision Support System for Systems Design", American Institute of Aeronautics and Astronautics (AIAA), *Journal of Aircraft*, 2013, in press.

[21] Sun, X. et. al., "Multi-Criteria Decision Analysis Techniques in Aircraft Conceptual Design Process", *28th Congress of the International Council of the Aeronautical Sciences (ICAS)*, Brisbane, Australia, September, 2012.

Appendix - Scaled Utility Values for Cases

Stakeholder	**Case - I Alternative I**	**C1.1**	**C1.2**	**C1.3**	**C1.4**	**Total**	**Case - II Alternative I**	**C1.1**	**C1.2**	**C1.3**	**C1.4**	**Total**
Airlines	Scaled Utility Value	0.25	1.0	0.8	-		Scaled Utility Value	0.16	1.0	0.53	-	
	Weighting Factor	0.7	0.15	0.15	-		Weighting Factor	0.7	0.15	0.15	-	
	Aggregated Sum	0.175	0.15	0.12	-	**0.445**	Aggregated Sum	0.112	0.15	0.0795	-	**0.3415**
Regulating Authorities	Scaled Utility Value	-	1.0	-	0.6		Scaled Utility Value	-	1.0	-	0.5	
	Weighting Factor	-	0.1	-	0.9		Weighting Factor	-	0.1	-	0.9	
	Aggregated Sum	-	0.1	-	0.54	**0.64**	Aggregated Sum	-	0.1	-	0.45	**0.55**
Passenger Acceptance	Scaled Utility Value	-	1.0	-	-		Scaled Utility Value	-	1.0	-	-	
	Weighting Factor	-	1.0	-	-		Weighting Factor	-	1.0	-	-	
	Aggregated Sum	-	1.0	-	-	**1.0**	Aggregated Sum	-	1.0	-	-	**1.0**
Pilots' Acceptance	Scaled Utility Value	-	-	0.8	-		Scaled Utility Value	-		0.53	-	
	Weighting Factor	-	-	1.0	-		Weighting Factor	-		1.0	-	
	Aggregated Sum	-	-	0.8	**-**	**0.8**	Aggregated Sum	-		0.53	-	**0.53**
Stakeholder	**Case - I Alternative II**	**C1.1**	**C1.2**	**C1.3**	**C1.4**	**Total**	**Case - II Alternative II**	**C1.1**	**C1.2**	**C1.3**	**C1.4**	**Total**
Airlines	Scaled Utility Value	0.5	0.3	0.4	-		Scaled Utility Value	0.41	0.05	0.05	-	
	Weighting Factor	0.7	0.15	0.15	-		Weighting Factor	0.7	0.15	0.15	-	
	Aggregated Sum	0.35	0.045	0.06	-	**0.455**	Aggregated Sum	0.287	0.075	0.075	-	**0.302**
Regulating Authorities	Scaled Utility Value	-	0.3	-	0		Scaled Utility Value	-	0.05	-	0.1	
	Weighting Factor	-	0.1	-	0.9		Weighting Factor	-	0.1	-	0.9	
	Aggregated Sum	-	0.03	-	0	**0.03**	Aggregated Sum	-	0.005	-	0.09	**0.095**

Passenger Acceptance	Scaled Utility Value	-	0.4	-	-		Scaled Utility Value	-	0.0	-	-	
	Weighting Factor	-	1.0	-	-		Weighting Factor	-	1.0	-	-	
	Aggregated Sum	-	0.4	-	-	**0.4**	Aggregated Sum	-	0.0	-	-	**0.0**
Pilots' Acceptance	Scaled Utility Value	-	-	0.3	-		Scaled Utility Value	-		0.05	-	
	Weighting Factor	-	-	1.0	-		Weighting Factor	-		1.0	-	
	Aggregated Sum	-	-	0.3	-	**0.3**	Aggregated Sum	-		0.05	-	**0.05**
Stakeholder	**Case - I Alternative III**	**C1.1**	**C1.2**	**C1.3**	**C1.4**	**Total**	**Case - II Alternative III**	**C1.1**	**C1.2**	**C1.3**	**C1.4**	**Total**
Airlines	Scaled Utility Value	0.75	0.05	0.1	-		Scaled Utility Value	0.85	0.0	0	-	
	Weighting Factor	0.7	0.15	0.15	-		Weighting Factor	0.7	0.15	0.15	-	
	Aggregated Sum	0.525	0.075	0.015	-	**0.5475**	Aggregated Sum	0.595	0	0	-	**0.595**
Regulating Authorities	Scaled Utility Value	-	0.05	-	0		Scaled Utility Value	-	0	-	0	
	Weighting Factor	-	0.1	-	0.9		Weighting Factor	-	0.1	-	0.9	
	Aggregated Sum	-	0.005	-	0	**0.005**	Aggregated Sum	-	0	-	0	**0.0**
Passenger Acceptance	Scaled Utility Value	-	0.1	-	-		Scaled Utility Value	-	1.0	-	-	
	Weighting Factor	-	1.0	-	-		Weighting Factor	-	0	-	-	
	Aggregated Sum	-	0.1	-	-	**0.1**	Aggregated Sum	-	0	-	-	**0.0**
Pilots' Acceptance	Scaled Utility Value	-	-	0.05	-		Scaled Utility Value	-		0.0	-	
	Weighting Factor	-	-	1.0	-		Weighting Factor	-		1.0	-	
	Aggregated Sum	-	-	0.05	-	**0.05**	Aggregated Sum	-		0	-	**0.0**

Terminal Route Optimization for Cumulative Noise Exposure

Sander Hartjes, Joeri Dons and Dries Visser
Delft University of Technology, The Netherlands

Keywords: *trajectory optimization, noise abatement, aircraft performance*

Abstract

This paper presents a study on the development of a methodology for the optimization of multi-event aircraft trajectories. The new optimization framework – an extension of the NOISHHH tool originally developed for the environmental optimization of single-event aircraft trajectories – can be employed to synthesize multi-event terminal routes that minimize the community noise impact in near-airport communities due to the aggregated noise exposure of all inbound and outbound traffic over an extended time period. The new framework has been applied to traffic flows on a representative day at a large international airport. The numerical example revealed a significant decrease in the number of people highly annoyed due to aircraft noise in the vicinity of the airport.

1 Introduction

The ever increasing demand for civil aviation traffic has in many countries led to increased awareness with respect to the environmental impact of aviation on near-airport communities, especially with respect to the noise nuisance. At Amsterdam Airport Schiphol (AMS) – the fourth largest airport by traffic movements in Europe – continued public debate has led to a proposition for significant changes in the noise regulations for the neighboring communities. The new regulatory system, which is currently being implemented for a two-year trial period – is expected to accommodate a 15% growth in the number of movements whilst maintaining acceptable noise exposure levels in surrounding communities. The proposed regulatory system is based directly on site-specific, population-based criteria, and aims to limit the number of people being exposed to given aggregated (annual) noise levels. With the new system in place, the opportunity arises to developed new noise abatement terminal routes in an effort to minimize the community noise impact, and hence to still allow the projected growth in the number of movements.

Research aimed at optimizing terminal routes and procedures to minimize the noise exposure has been quite extensive in the last decade. Prats [2] focused on single-event trajectories using optimal control theory, aiming to minimize the noise exposure in a number of highly noise-sensitive areas. Visser and Wijnen [3], Hogenhuis [4], Fernandes de Oliveira [5] and Richter [6] have all considered community noise impact in their optimization studies. In all of these studies, however, only single event aircraft trajectories were considered, whereas the noise regulations around airports are generally expressed in terms of the aggregated noise exposure over a longer time period. With a focus on cumulative noise impact, Braakenburg [7] has shown a significant reduction of noise exposure by applying optimal control theory to arrival ground tracks at a regional airport, taking into consideration the entire yearly fleet mix.

Previous research has mainly focused on single-event noise abatement, or was limited to only arrival routing. Based on the NOISHHH optimization tool developed at Delft University of Technology, this study aims to extend the work of [7] by applying trajectory optimization techniques to all traffic movements on a major airport during a given reference period. As an example, this paper shows the results of the methodology applied to a number of arrival and departure streams at Amsterdam Airport Schiphol, which have been optimized with respect to the community noise impact. The results show a significant potential reduction in the people highly annoyed.

The structure of this paper is as follows. First the NOISHH optimization framework is introduced. Next the community noise impact modeling is discussed, and in Section 4 the example scenario is presented. Section 5 discusses the results of the example scenario, followed by conclusions and recommendations in Section 6.

2 Optimization Framework

2.1 NOISHHH

The NOISHHH optimization framework [3, 4] applies optimal control theory based on collocation to convert the continuous time optimal control problem into a finite-dimensional non-linear programming (NLP) problem. Thereto, the continuous problem is discretized into segments with linear state and constant control variables. The state and control variables at the intersections of the segments – called nodes – are treated as NLP variables. The objective function and problem differential equations are discretized as well and transformed into algebraic equations. Finally, path constraints and boundary conditions are treated as algebraic inequalities in the resulting NLP problem. In addition to the dynamic trajectory optimization algorithm, NOISHHH comprises a dynamic aircraft model, an aircraft noise model, a Geographic Information System (GIS) and a noise dose-response relationship.

2.2 Aircraft Dynamics

In previous studies performed with the NOISHHH tool, only single-event trajectories were assessed. In this study, however, the aim is to optimize the cumulative noise impact of all movements during a given reference period. To extend the tool to represent all movements at a large international airport is by no means a trivial task. As a first step to reduce the computational burden of the optimization problem, the aircraft types operating during the reference period have been grouped into 11 representative categories based on acoustic class and Maximum Take-Off Weight (MTOW) [8], where a higher acoustic class indicates a more silent aircraft type. Next, based on the acoustics/MTOW classes, 11 representative aircraft types are selected to be modeled in the optimization framework. The 11 representative aircraft types are presented in Table 1.

Table 1: Representative aircraft types

MTOW [tons]	Noise class	Repres. A/C type	Dep.	Arr.
Turboprop	4	F50	4	5
<15	4	C550	10	8
15-40	4	F70	83	82
40-60	3	F100	79	77
60-100	3	B734	59	58
60-100	3	B738	159	150
60-100	3	A320	99	101
100-160	3	B752	6	7
160-230	3	B763	15	13
230-300	4	B772	51	52
300-400	3	B744	36	37
Total			601	590

Still, modeling the complete dynamics of 11 different aircraft types would still require unacceptable computational times, as each aircraft type would require its own set of state and control variables. Therefore, an approach was chosen to optimize only the terminal route (ground track) with prescribed (representative) procedures (altitude and airspeed). With this approach, essentially only the ground track kinematics need to be optimized, which are shared by all aircraft types on a given terminal route. Based on a point-mass dynamic model, sufficiently small flight path angles, and using along track distance s as the independent variable, the kinematic equations can be written as:

$$\frac{dx}{ds} = \cos\chi \tag{1}$$

$$\frac{dy}{ds} = \sin\chi \tag{2}$$

$$\frac{d\chi}{ds} = \dot{\chi}_s = \frac{1}{R} \tag{3}$$

where χ is the heading angle. The position *(x,y)* is expressed in an Earth-fixed Cartesian reference frame. The control variable $\dot{\chi}_s$ in the optimal control formulation is the reciprocal of the turn radius R and is chosen to ensure continuity of the heading state history, and to allow constraints on the turn rate and the bank angle in the optimized routes.

The kinematic equations defined above apply to all aircraft types on a single route. The next step is then to determine the required thrust level as input for the noise model. The airspeed *V(s)* and altitude *h(s)* are derived from the prescribed procedures and with the heading rate $\dot{\chi}_s$ known from the control history, the bank angle can be determined using:

$$\mu = \arctan\left(\dot{\chi}_s \frac{V^2}{g_0}\right) \tag{4}$$

The bank angle can in turn be used to determine the lift increment due to banking as well as the corresponding drag increment. Then the required thrust levels are defined as follows:

$$\begin{aligned} T &= \frac{dV}{dt}\frac{W}{g_0} + C_D \frac{1}{2}\rho V^2 S + WV\sin\gamma \\ &= V\dot{V}_s \frac{W}{g_0} + C_D \frac{1}{2}\rho V^2 S + W\dot{h}_s \end{aligned} \tag{5}$$

where C_D is the drag coefficient and W is the aircraft weight. The airspeed and altitude derivatives, $\dot{V}_s$ and $\dot{h}_s$ can also be extracted from the prescribed procedures.

In order to obtain more realistic trajectories, a number of operational constraints is imposed on the problem. Since airspeed and altitude constraints are already accounted for in the prescribed profiles, only constraints relating to heading changes need to be considered. First, the turn rate is constrained as follows:

$$\left|\dot{\chi}_s\right| \le \frac{\left.\dot{\chi}_t\right|_{\max}}{V(s)} \tag{6}$$

where it is noted that $\dot{\chi}_t = \dot{\chi}_s V(s)$ is the heading rate with respect to time. In addition, the bank angle is constrained using Eq. 7:

$$\left|\dot{\chi}_s\right| \le \frac{g_0 \tan\mu_{\max}}{V(s)^2} \tag{7}$$

It is noted that these constraints both depend on the airspeed. As the airspeed at a given location s can be different for different aircraft type, the aircraft with the highest airspeed defines the limiting values for $\dot{\chi}_s$. In addition, at any given airspeed V one of the constraints will be dominant.

3 Community noise impact

With the complete trajectories now defined for all 11 aircraft types, the next step is to determine the noise impact in near-airport communities. The ground track following from the optimization, the prescribed procedures and the thrust levels from Eq. 5 are then evaluated by the noise model integrated in NOISHHH. This model, the Integrated Noise Model version 7.0b [9] has been the FAA's standard tool for airport noise assessment for decades, and is probably the most widely used noise modeling tool available. NOISHHH contains a direct transcription of the noise model employed in INM, which is used to determine the Sound Exposure Level (SEL) for each individual representative aircraft type on a regular grid on a ground surrounding the airport. To determine the cumulative noise impact over a given reference period, the contribution of each individual aircraft type is aggregated in the day-evening-night average level (L_{den}), which can be defined as:

$$L_{den} = 10\log_{10}\left[\sum_{i=1}^{N_{A/C}} w_i n_i 10^{\frac{SEL_i}{10}}\right] - 10\log_{10} T \qquad (8)$$

where $N_{A/C}$ is the number of different aircraft types, n_i is the number of movements by that aircraft type and T is the reference time period in seconds. In addition, w_i is a penalty factor for movement during evening and night hours. For evening flight (19.00-23.00 hours) the penalty is 3.16. For night movements (23.00-6.00 hours) the penalty factor is 10, which essentially means that each night movement counts as 10 movements.

With the noise exposure on the ground defined, the next step is to determine the community noise impact in terms of the number of people highly annoyed. Therefore, NOISHHH contains a Geographic Information System (GIS) containing population density data of the area surrounding the airport. An example of the GIS can be seen in Fig. 1.

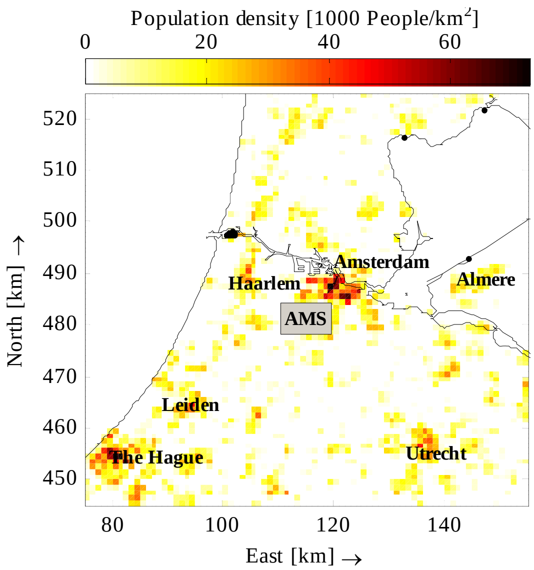

Figure 1: Population density, AMS area

The data points in the GIS coincide with the regular grid on which the noise exposure was calculated. The cell size in the grid is 500x500 m, and the total grid size used in the optimization runs depends for instance on the general direction of the route and its length. A Typically, grid sizes of up to 80x80 km have been used.

Next, a dose-response relationship is used to determine the percentage of people highly annoyed as a result of the noise exposure. This relationship, developed by Dutch research institutions TNO and RIVM is considered the standard relationship in The Netherlands, and is based on a large-scale research effort in 2002 [10]. The relationship can be expressed as:

$$\%HA = \left(\frac{e^{-8.11001+0.1333L_{den}}}{1+e^{-8.11001+0.1333L_{den}}}\right)\cdot 100 \qquad (9)$$

where $\%HA$ is the number of people highly annoyed. Figure 2 shows this relationship, which is valid from the threshold value of 39 dBA.

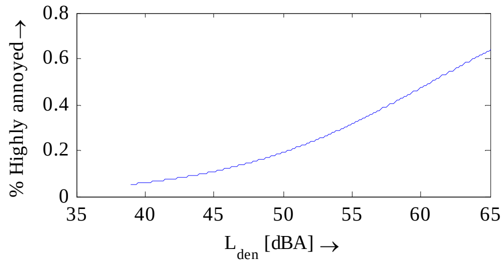

Figure 2: Annoyance dose-response relationship

Multiplying this percentage with the number of people living in each grid cell and summating for all cells then yields the total number of people highly annoyed (PHA), which is used as the main noise optimization criterion in this study.

In most noise abatement studies the approach is to optimize individual trajectories or routes, hence accounting only for a part of the total noise exposure around an airport. In this study, however, a novel approach is used where – although still individual routes are optimized – the noise from all other movements is accounted for to assess the impact of existing traffic flows on the optimized routes. To achieve this, first the existing total noise exposure levels have been determined. For these reference noise levels historical ground track data has been used, but for consistency the same representative aircraft types and procedures are projected onto the recorded ground tracks. In the next step, the noise contribution of all movements on the terminal route that needs to be optimized is removed from the reference noise. During the optimization process, the remaining background noise levels are added to the noise contribution of the optimized route, hence accounting for all noise contributed by both existing and optimized traffic flows.

Apart from optimizing with respect to community noise impact, in this study also the total path length s_f has been taken into account to represent airline economic interests, local air quality considerations, etc. This then yields the following objective function for this study:

$$J = s_f + k_{noise} PHA \qquad (10)$$

where k_{noise} is a weighting factor. By varying this weighting factor the relative contribution of noise to the objective function can be changed. It is noted that as different routes can have significantly different total path lengths s_f, the weighting factor can vary significantly as well to ensure a comparable relative contribution of noise for all optimized routes.

4 Example scenario

The proposed methodology has been applied to Amsterdam Airport Schiphol for the reference day of October 22, 2010. On this day, a total of 590 arrivals were recorded on 4 different runways, as well as 601 departures from 3 runways. The arrival (white) and departure (blue) tracks can be seen in Fig. 3. The historical flight data results in a total of 220,010 people highly annoyed based on the prescribed airspeed and altitude procedures, and the 11 representative aircraft classes.

For the sake of brevity, in this example only arrivals at runway 18R are explored. In total, 405 flights arrive on runway 18R on 3 Standard Terminal Arrival Routes (STARs) from the east, west and south. It is noted that given the penalty factor w_i for evening and night operations in Eq. 10 this leads to an effective number of 1309 movements. For departures, only the southbound LEKKO Standard Instrument

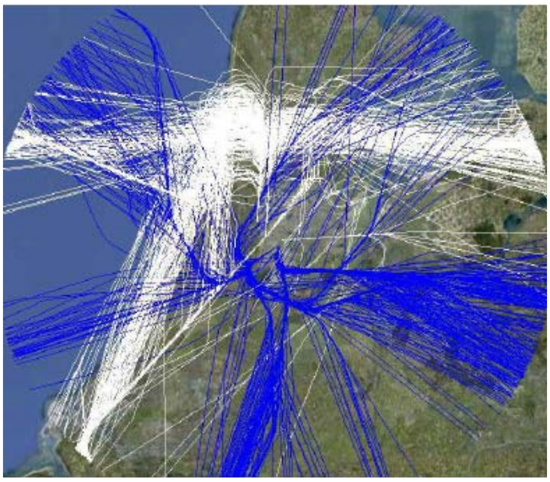

Figure 3: Arrival and departure tracks, 22-10-2010

Departure (SID) is assessed, from runways 24 and 18L, which accommodated 122 movements (394 effective movements, due to a high number of night departures). The reference noise levels, containing the noise contribution of all 1191 (3515 effective) movements on the reference day, can be seen in Fig. 4. The number of movements for each of the acoustic/MTOW classes can be found in Table 1.

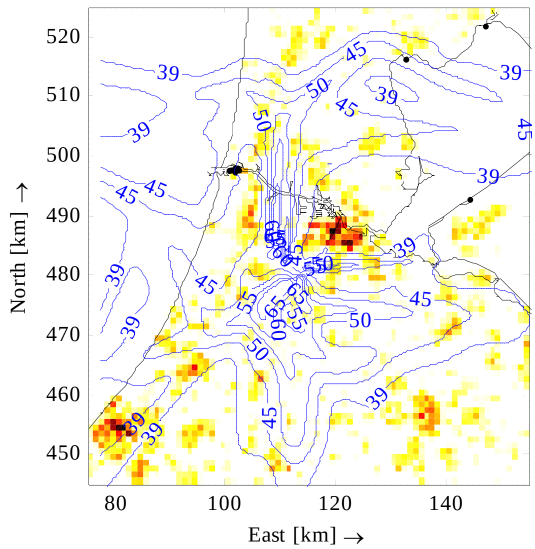

Figure 4: Reference L_{den} levels, 22-10-2010

Hence, in total 5 terminal routes will be optimized in this example. These terminal routes will be optimized sequentially. Therefore, the first step is to remove the historical noise contribution of one of the 5 routes from the

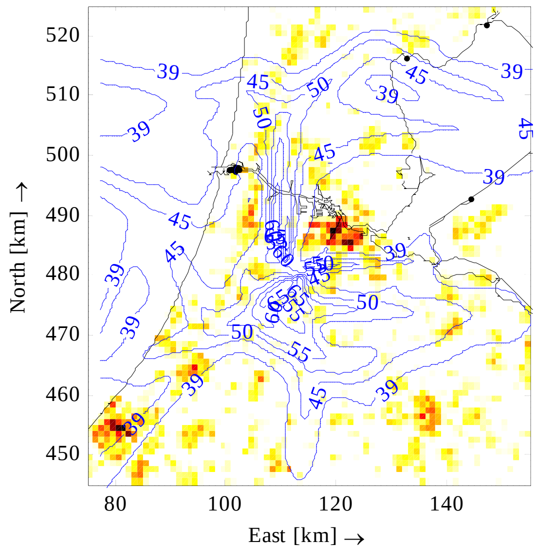

Figure 5: Reference L_{den}, minus LEKKO from R24

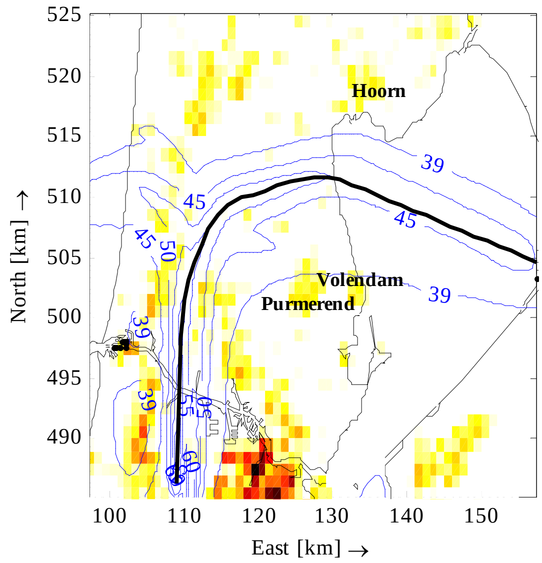

Figure 6: Optimized ARTIP arrivals

background noise levels. An example of this can be seen in Fig. 5. This figure shows the background noise levels after removing the contribution of the southbound departures from runway 24 along the LEKKO SID. Next all movements on that route are assumed to follow the same ground track, and to use the prescribed procedures. The ground track is then optimized for a weighted combination of track length and the number of people highly annoyed (which includes the noise contribution of all other movements from Fig. 5).

5 Results

First, the results for the arrivals to runway 18R on the ARTIP STAR are presented. The route, accommodating 399 effective arrival movements, has been optimized for noise weighting factors up to k_{noise} = 13. Major results for this route are presented in Table 2.

It is noted that the table contains both the total number of people highly annoyed, PHA,

Table 2: Results for optimized ARTIP STAR

Parameter	Reference	k_{noise} = 13
Track distance [km]	67.0	68.1
PHA (route)	18,328	10,224
PHA (total)	212,010	203,325

and the number of people highly annoyed without taking the reference noise levels into account. The results reveal that the optimized route results in a 4.1% reduction in the total PHA, or almost 9,000 in absolute numbers. This can be explained by considering the trajectory and contour plots seen in Fig. 6. As compared to the reference noise levels in Fig. 4, the concentration of all inbound movements on a single ground track has led to a narrower contour, which results in noise levels in the communities of Hoorn, Volendam and Purmerend below the threshold level of 39 dBA.

In addition, the high intensity noise levels directly below the flight track are projected upon a less densely populated area. The result is highly concentrated noise levels in a rural area.

In the next step, the same process of extracting the historical contribution and replacing it by an optimized ground track is repeated for the other two arrival streams to runway 18R. These routes, following the RIVER STAR from the southwest and the SUGOL STAR from the west, accommodate 403 and 506 effective movements respectively. As a result of the relatively long total track distance compared to the number of PHA, in these cases the weighting factor k_{noise} is significantly higher, up to 33 for the RIVER arrivals, to ensure a similar ratio between noise and track distance in the objective function. Major results for both cases are presented in Table 3 and 4.

Table 3: Results for the optimized RIVER STAR

Parameter	Reference	k_{noise} = 33
Track distance [km]	107.3	111.8
PHA (route)	10,462	6,159
PHA (total)	212,010	206,930

Table 4: Results for the optimized SUGOL STAR

Parameter	Reference	k_{noise} = 30
Track distance [km]	59.3	55.5
PHA (route)	17,030	11,559
PHA (total)	212,010	210,236

As can be seen from Fig. 7 and 8, again high noise levels are concentrated in less densely populated areas. When compared to the historical data in Fig. 2, especially the RIVER arrivals avoid major cities such as The Hague and Leiden by displacing the ground track over the North Sea to completely avoid noise exposure in these communities. However, over these cities the altitude and airspeed are relatively high, leading only to a relatively small reduction in the absolute number of people highly annoyed as compared to the ARTIP arrivals. Although the SUGOL intersection lies over the North Sea, and only a small section of the arrival stream should lie over populated areas, still a significant reduction in the PHA is achieved. This can be explained by a closer inspection of the historical data in Fig. 9. The figure reveals that a significant part of the arrival movements is vectored parallel to the coast line, near the communities of Haarlem, Beverwijk and Castricum, and is diverted further north as compared to the optimized trajectories. This extended path close to densely populated areas naturally results in relatively high number of PHA. After optimization, the SUGOL STAR resulted in a 2.4% reduction in PHA, and in a 6.4% shorter total track distance. The RIVER STAR was extended by 4.2%, which resulted in only 0.8% reduction in the total number of PHA. This can also be explained by considering that the number of

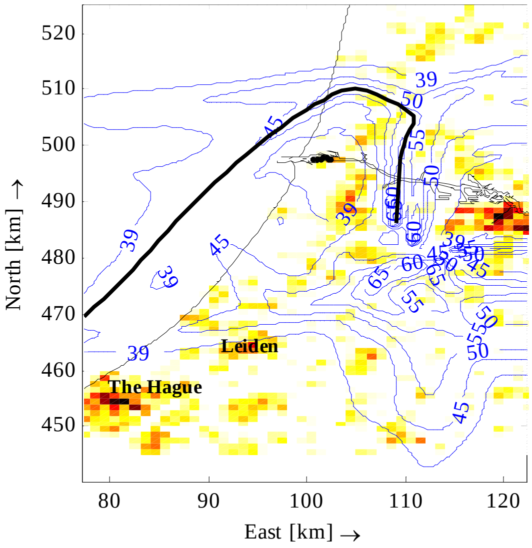

Figure 7: Optimized RIVER arrivals

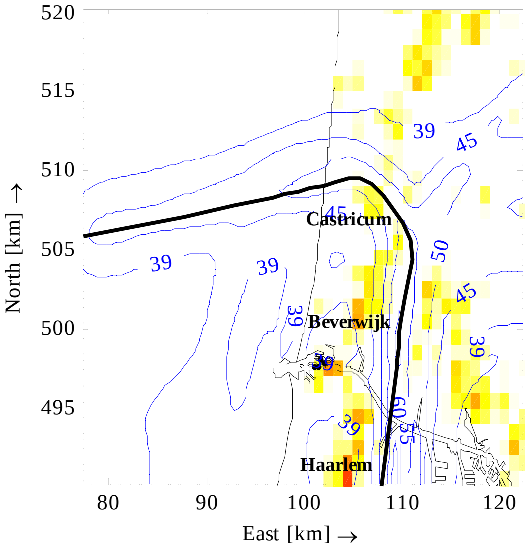

Figure 8: Optimized SUGOL arrivals

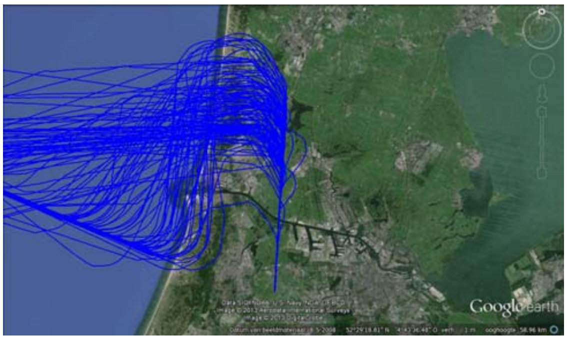

Figure 9: SUGOL arrivals to runway 18R, 22-10-2010

PHA caused by this arrival route (hence disregarding reference noise levels) is relatively small.

Finally, the departure streams are considered. Major results for both LEKKO SIDs from runways 24 and 18L are presented in Table 5 and 6 and Figure 10 and 11. When first the results of the departure route from runway 18L is considered, it can only be concluded that the current departure is procedure is already very efficient in terms of noise exposure, and hardly any reduction in the number of PHA can be achieved. However, the results for runway 24 do reveal a significant improvement, both in the number of PHA for the isolated route and the cumulative PHA. When the historical ground tracks in Fig. 12 are compared to the optimized routes for the LEKKO SID from both runways, this difference can be explained. Instead of following an individual ground track as can be seen in the historical data, the departures from runway 24 circumvent the community of Aalsmeer to further share the same ground track as the departures from runway 18L. As it was already concluded that the existing LEKKO SID from runway 18L was efficient in terms of noise exposure, sharing the ground track leads to a reduction in the total number of people highly annoyed of about 3.8% at the cost of an increased track distance of 6.0%.

Table 5: Results for the optimized LEKKO SID, R24

Parameter	Reference	$k_{noise} = 7$
Track distance [km]	42.3	44.9
PHA (route)	24,711	16,275
PHA (total)	212,010	203,875

Table 6: Results for the optimized LEKKO SID, R18L

Parameter	Reference	$k_{noise} = 2$
Track distance [km]	40.0	40.2
PHA (route)	10,689	10,423
PHA (total)	212,010	211,917

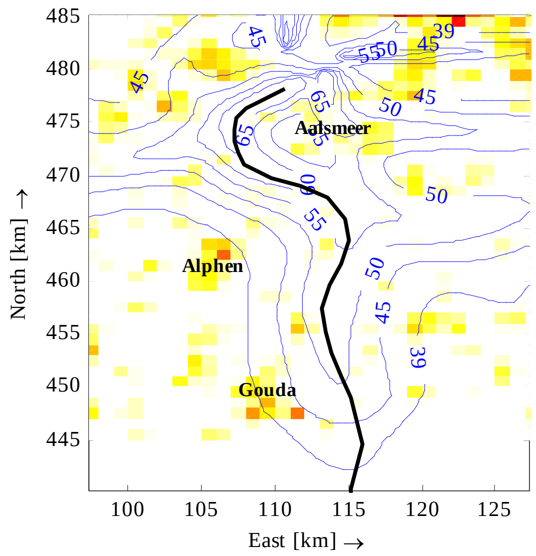

Figure 10: Optimized LEKKO SID, runway 24

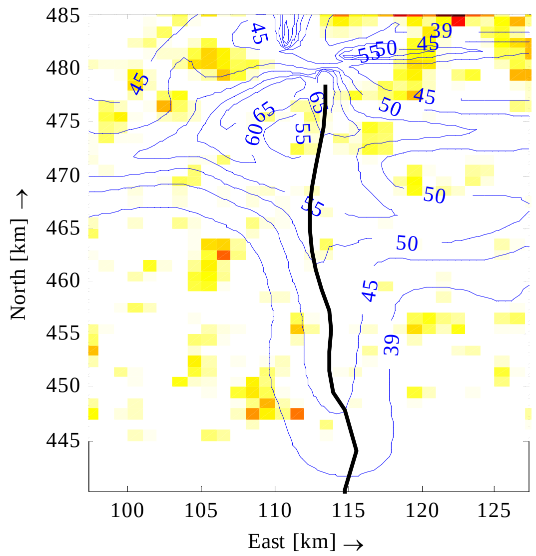

Figure 11: Optimized LEKKO SID, runway 18L

Figure 12: Historical departure streams

Finally, the results after optimizing all five terminal routes are presented in Fig. 13. This figure shows the complete area surrounding Amsterdam Airport Schiphol, and reveals in which areas the total L_{den} levels have increased or decreased after concentrating the movements on optimized ground tracks. It can be seen that although in less densely populated areas noise levels have increased by up to 11 dBA, significant and comparable reductions can be seen in more densely populated areas. In total, the number of people highly annoyed was reduced by 23,361 or 11% after optimizing the 5 routes presented above. This was mainly achieved by reducing the number of people being exposed to relative low noise levels, farther away from the airport. As an indication, the number of people exposed to 39-43 dBA L_{den} was reduced by 34.5%, whereas the number exposed to levels between 59 and 63 dBA actually increased by 6.0%.

6 Conclusions

Work is presented on the development of a methodology for multi-event trajectory optimization in an effort to minimize the cumulative noise impact in the vicinity of a large international airport. The presented methodology optimizes ground tracks shared by all movements from/to a given general direction, and takes into account the complete noise contribution of all movements in a reference time period.

Results are presented where a number of arrival and departure routes at Amsterdam Airport Schiphol are optimized with respect to the total number of people highly annoyed due to aviation noise.

From the example scenario it can be concluded that concentrating traffic on a single ground track leads to high peak noise levels below this shared ground track,. However, this also reduces the width of the contours, and hence allows to avoid exposing noise-sensitive areas to high noise levels. Essentially, the ground tracks are positioned such that they expose rural areas to very high noise levels, thus reducing the total number of people highly annoyed in urban areas.

Although the example scenario considered both arrival and departure streams, constraints relating to terminal route design where not yet imposed. In addition, each of the terminal routes was optimized sequentially. Already concentrating all movements on a single ground track might lead to significant capacity issues, and this can only be further exacerbated if different departure or arrival routes are sharing the ground track. These effects need to be taken into account in further research.

In addition, although the absolute number of people highly annoyed is reduced, exposing different and possibly new parts of the population to significant noise levels might result in more annoyance. Furthermore, the effect of concentrating flights on a single ground track might also lead to unacceptably high noise levels in some areas.

Acknowledgements

The authors would like to thank Air Traffic Control the Netherlands (LVNL) for supplying the historical flight data used in this study.

References

[1] Alders, H., “Advies van de heer Alders over toekomst Schiphol en de regio tot 2010”, Dutch Government Report, br.8977, June 2007.

[2] Prats, X., Puig, V., Quevedo, J., and Nejjari, F., “Multi-objective optimisation for aircraft departure trajectories minimising noise annoyance”, *Transportation Research Part C*, Vol. 18, No. 6, 2010, pp.975–989.

[3] Visser, H. G., and Wijnen, R. A. A., “Optimization of Noise Abatement Departure Trajectories”, *Journal of Aircraft*, Vol. 38, No. 4, 2001, pp. 620–627.

[4] Hogenhuis, R.H, Heblij, S.J., Visser, H.G., “Optimization of RNAV Noise Abatement Approach Trajectories”, *Proceedings of the Institution of Mechanical Engineers – Part G - Journal of Aerospace Engineering*, Vol. 225, Issue 5, 2011, pp.513-521.

[5] Fernandes de Oliveira and R., Büskens, C., “On-board Trajectory Optimization of RNAV Departure and Arrival Procedures Concerning Emissions and Population Annoyance”, *Aerospace Technology Conference and*

Exposition, Toulouse, France, 2011.

[6] Richter, M., Fisch, and F., Holzapfel, F., “Noise-minimal landing and take-off trajectories under procedural and safety regulations”, *Air Transport and Operations Symposium*, Delft, The Netherlands, 2012.

[7] Braakenburg, M.L., Hartjes, S., Visser, H.G., and Hebly, S.J., “Development of a Multi-Event Trajectory Optimization Tool for Noise-Optimized Approach Route Design”, *11th Annual Aviation Technology, Integration and Operations (ATIO) Technical Forum*, Virginia Beach, U.S.A., 2011.

[8] Heppe, G.J.T., “Appendices van de voorschriften voor de berekening van de geluidsbelasting in Lden en Lnight voor Schiphol en in Lden voor de overige burgerluchthavens bedoeld in artikel 8.1 van de de Wet luchtvaart, NLR-CR-96650 L - Versie 12.1”, National Aerospace Laboratory NLR, 2011.

[9] E.R. Boeker, et al., “Integrated Noise Model (INM) Version 7.0 Technical Manual, FAA-AEE-08-01”, Federal Aviation Administration, Office of Environment and Energy, 2008.

[10] Engelen, J.A.J. van, et al., “Evaluatie Schipholbeleid - Trends milieu-effecten Schiphol, NLR-CR-2005-551”, National Aerospace Laboratory NLR, 2006.

DORATHEA: AN INNOVATIVE SECURITY RISK ASSESSMENT METHODOLOGY TO ENHANCE SECURITY AWARENESS IN ATM

F. Matarese, P. Montefusco
SESM S.c.a.r.l. A Finmeccanica Company, Italy

J. Neves, A. Rocha
GMV Skysoft, Portugal

Keywords: *Security, Risk, Methodology, ATM*

Abstract

The increasing complexity of systems that support navigation and surveillance, due to the pervasiveness of emerging technologies and growing number of flights, create the conditions for the rise of unpredicted threats that may potentially turn into dramatic events. This is also driven by the on-going update of legacy systems with new technologies and their connection to innovative systems, which creates a new environment with new threat vectors, for which these systems were not prepared when they were designed.

DORATHEA is a research project co-funded by European Commission Directorate-General Home Affairs with the aim of developing a common methodology for carrying out risk, threat and vulnerability assessments for ATM protection.

DORATHEA aims at increasing the awareness of ATM operators through an innovative security risk assessment methodology for ATM systems, because only a common methodology can provide the necessary basis for a coherent implementation of measures to protect European ATM Critical Infrastructure and clearly define the respective responsibilities of all relevant stakeholders.

1 General Introduction

Concerns about security were already being raised in the past, but the tragic events of 9/11 thrust the issue of security into public domain as never before and set in motion responses that are re-shaping transportation in unforeseen ways.

Physical security of airports has been the focus of security concerns for many decades. Hijacking aircraft came to the fore in the 1970s, when terrorist groups in the Middle East exploited the lack of security to commandeer planes for ransom and publicity. Refugees fleeing dictatorships also found taking over aircraft a possible route to freedom. In response, the airline industry and the international regulatory body, ICAO, established screening procedures for passengers and bags. This process seems to have worked in the short run at least, with reductions in hijackings, although terrorists changed their tactics by placing bombs in un-accompanied luggage and packages, as for example in the Air India crash off Ireland in 1985 and the Lockerbie, Scotland, crash of Pan Am 103 in 1988.

Because passengers were being routed by hubs, the numbers of passengers in transit through the hub airports grew significantly. Concerns were being raised by some security experts, but the costs of improving screening and the need to process ever larger numbers of passengers and maintain flight schedules caused most carriers to oppose tighter security measures.

The situation was changed irrevocably by the events of September 11, 2001. Security involves many steps, from restricting access to airport facilities, fortifying cockpits, to the more extensive security screening of passengers. Screening now involves more rigorous inspections of passengers and their baggage at airports. The imposition of these measures has come at a considerable cost. The purchase of improved screening machines and the re-designing of airport security procedures have been important cost additions. These measures have also had a major influence on passenger throughputs. Clearing security has become the most important source of delays in the passenger boarding process. Security issues have had a negative effect on the air transport industry as costs increased with delays and inconveniences to passengers increasing as well.[1]

Moreover, cyber security became an issue for many civil aviation organisations because they rely on electronic systems for critical parts of their operations, and for many organizations their electronic systems have safety-critical functions.

There are a number of reasons why risks to civil aviation from malicious cyber activity are increasing, principally because:

- Much of the new IT technology being introduced raises potential security issues which are unfamiliar in the civil aviation industry; and
- IT systems are becoming increasingly interconnected and interdependent, so organisations are exposed to risks caused by security weaknesses in other people's systems.

Today air traffic is controlled using instructions issued from the ground by radio, with aircraft position determined by radar, and things have not substantially changed for 70 years. With increasing air traffic, today's ATM system is beginning to hit its physical limits, particularly in terms of the number of aircraft that can be managed by human controllers within a given airspace. The industry has designed solutions to automate the routine part of ATM, which if put into place, would greatly increase the number of aircraft that can be managed within a given airspace. This would leave the air traffic controller with the executive role rather than having to issue all the routine control instructions, which would be produced automatically by the system.

The expected widespread use of Unmanned Aerial Vehicles (UAVs) in the near future also raises new issues due to the increased importance of remote linkages and ground control stations.

These and other air traffic control issues are being solved by the introduction of new communication methods and technologies, which includes the use of internet based solutions. The use of these increases the role of cyber security and exposes numerous vulnerabilities that do not exist in today's more closed, proprietary, civil aviation systems. These cyber security vulnerabilities have the potential to jeopardize civil aviation safety and efficiency.[2]

The setting and implementation of security measures come at a cost that must be assumed by ATM operators and eventually by the costumers. It has been estimated that an increase of 1% in the costs of air transport would cause a decrease in flows of in the range of 2 to 3%. But, security based measures could increase total costs between 1% and 3%. Given budgetary and other constraints, integrating secure/safe and cost-effective design objectives oftentimes requires compromise and tradeoffs.[3]

DORATHEA (Development Of a Risk Assessment meTHodology to Enhance security Awareness in ATM) is a research project co-funded by European Commission Directorate-General Home Affairs, in the frame of the Prevention, Preparedness and Consequence Management of Terrorism and other Security related Risks Programme, with the aim of developing a common methodology for carrying out risk, threat and vulnerability assessments for

ATM protection. It is envisaged that only a common methodology can provide the necessary basis for a coherent implementation of measures to protect European ATM Critical Infrastructure and clearly define the respective responsibilities of all relevant stakeholders.

DORATHEA aims at increasing the awareness of ATM operators through an innovative security risk assessment methodology for ATM systems that:

- Can be adopted either by state-of-the-art ATM systems as well as legacy/proprietary systems allowing the assessment of the new risks that their interconnection may (and will) introduce.
- Is based on existing and well established security standards already in use by the industry, including the ICAO [7], the CC [8], the ISO 27005 [9] and extend them to cover the ATM security scenario.
- Is complementary with the risk assessment methodology currently being developed within SESAR and other EU projects in ATM security.

2 Need for a DORATHEA Security Risk Assessment Methodology

Recent vulnerabilities discovered and attacks executed (e.g. refer to [4]), prove that the security of ATM systems is always under the spotlight, which is also confirmed by public entities (e.g. refer to [5]). Furthermore, the increasing complexity of ATM systems due to the pervasiveness of emerging technologies and growing number of daily flights create the conditions for the rise of unpredicted threats that may potentially turn into dramatic events. This is also driven by the on-going update of legacy/proprietary systems with new technologies and their connection to innovative systems, which creates a new environment with new threat vectors, for which these systems were not prepared when they were designed. Thereby, given that the ATM plays a critical role in supporting the overall airspace/aviation system, the security risk assessment of ATM should be a major concern and a top priority.

Presently, the ICAO Security Manual for Safeguarding Civil Application, one of the main references for threat and risk assessment in the ATM domain, offers little help in identifying and prioritising threats according to time and budget constraints. On the other side, new guidelines are on the way, such as those currently being developed in the Sub Work Package (SWP) 16.2 of the Single European Sky ATM Research (SESAR) project, which focus on ATM security framework, methodology, tools and best practices.

The proposed methodology is an extension of ICAO ATM security guidelines and it is based on the strength points of the Safety Assessment Methodology defined by EUROCONTROL.

It comprises three phases (see Figure 1):

- **Security Functional Hazard Assessment** (**SecFHA**) aims at evaluating how secure the system need to be in order to achieve a tolerable risk. It is a process that, evaluating system functionalities, identifying potential Security Hazards and assessing the consequence of their occurrence on the system, produces the system Security Objectives. Therefore SecFHA inputs are the system functionalities and knowledge about Security Hazards consequences and SecFHA outputs are the Security Objectives of the system.
- **Preliminary System Security Assessment** (**PSSecA**) aims at evaluating if the proposed architecture is expected to achieve a tolerable risk. It is a process that produces system requirements related to Security (Security Requirements) in order to satisfy all the Security Objectives defined in SecFHA process.
- **System Security Assessment** (**SSecA**) is a process to demonstrate that the system as implemented achieves a tolerable risk, i.e. satisfies the Security Objectives identified in the SecFHA and the system elements meet the Security Requirements specified in the PSSecA.

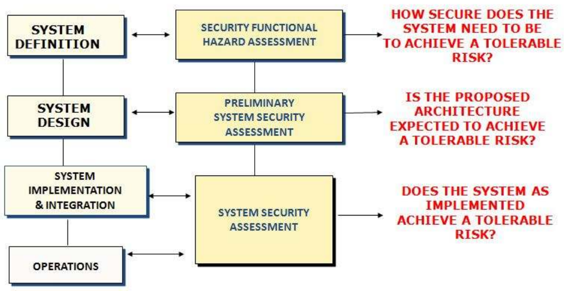

Figure 1. DORATHEA Security Risk Assessment Methodology Overview

2.1 Security Functional Hazard Assessment (SecFHA)

The SecFHA is a top-down iterative process, starting at the beginning of the development or modification of an Air Navigation System that aims at *determining how secure the system needs to be.*

The steps to be performed during the SecFHA are:

- To identify all potential Security Hazards associated with the system;
- To identify Security Hazard effects on system functionalities;
- To assess the impact of Security Hazard effect(s);
- To derive Security Objective, i.e. to determine their acceptability in terms of Security Hazard's maximum likelihood of occurrence, derived from the impact and the maximum likelihood of the Security Hazard's effects.

2.1.1 Identification of all potential Security Hazards

The identification of all potential Security Hazards is performed through the:

1. Identification of all the functionalities that the system under evaluation is expected to provide;
2. Definition of a sub-set of functionalities containing only the system functionalities that are relevant from a security point of view, i.e. the functionalities that have to be protected.

The selection of these functionalities will take into account:

- How critical the functionality is from a security point of view, i.e. the loss or the corruption of such functionality due to an attack would have a high impact on people, equipment and procedures.
- How "attractive" is the functionality from an attacker point of view: an attacker could decide to attack a functionality on the basis of the effort needed to perform the attack in terms of costs, time needed to prepare the attack, skills required to achieve the attack, equipment required to be able to perform the attack, the likelihood of being identified during the attack.

3. Definition of all the potential Security Hazards as any condition, event, or circumstance which could lead to the loss or the corruption of such functionalities.

2.1.2 Identification of Security Hazard's effect Impact

All the possible consequences of the Security Hazard on the system will be identified and the impact of these consequences will be established.

This impact is a number from 1 to 5 as reported in Table 1. To obtain this evaluation, the impact of the Security Hazard's effect(s) must be evaluated on each of the SESAR Security Impact Areas (refer to [6]). Comparison shall not be done between impact areas, they should be evaluated independently.

	5	**4**	**3**	**2**	**1**
Impact Areas	**Catastrophic**	**Critical**	**Severe**	**Minor**	**No impact**
IA1: Personnel	Fatalities	Multiple Severe injuries	Severe injuries	Minor injuries	No injuries
IA2: Capacity	Loss of 60%-100% capacity	Loss of 60%-30% capacity	Loss of 30%-10% capacity	Loss of up to 10% capacity	No capacity loss
IA3: Performance	Major quality abuse that makes multiple major systems inoperable	Major quality abuse that makes major system inoperable	Severe quality abuse that makes systems partially inoperable	Minor system quality abuse	No quality abuse
IA4: Economic	Bankruptcy or loss of all income	Serious loss of income	Large loss of income	Minor loss of income	No effect
IA5: Branding	Government & international attention	National attention	Complaints and local attention	Minor complaints	No impact
IA6: Regulatory	Multiple major regulatory infractions	Major regulatory infraction	Multiple minor regulatory infractions	Minor regulatory infraction	No impact
IA7: Environment	Widespread or catastrophic impact on environment	Severe pollution with long term impact on environment	Severe pollution with noticeable impact on environment	Short Term impact on environment	Insignificant

Table 1. SESAR Security Impact Areas

The final impact value for each Security Hazard's effect will be the maximum impact level from this evaluation.

2.1.3 Security Objectives Identification

The Security Objective specifies, for each identified Security Hazard, the maximum tolerable likelihood of its occurrence, given its assessed impact.

In particular, it will be linked to the likelihood of a loss or corruption of functionality due to an attack.

For each identified Security Hazard, the Security Risk associated to it will be evaluated as follows:

$$Security\ Risk = L_{sh} * I_c \qquad (1)$$

Where:

- L_{sh} indicates the likelihood to have a given Security Hazard;
- I_c indicates the impact of the consequence of the vulnerability on the security of the system (people, procedures, equipment).

The Risk Classification Scheme (see Table 2) is used in order to fix the maximum acceptable likelihood of a given Security Hazard, given its assessed Impact, in order *to achieve a tolerable risk.*

The likelihood of an attack is defined as follows:

– **Very Frequent**: Likely to occur often;
– **Frequent**: Likely to occur several times;
– **Occasional**: Likely to occur sometime;
– **Rare**: Unlikely but may occur exceptionally;
– **Extremely Rare**: Unlikely to occur during the lifetime of the system.

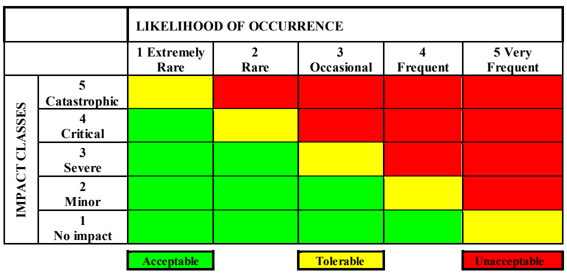

Table 2. Risk Classification Scheme

2.2 Preliminary System Security Assessment (PSSecA)

The objective of the PSSecA process is *to evaluate if the proposed architecture is expected to achieve a tolerable risk.*

PSSecA is a top-down iterative process, conducted during the System Design phase of the system life cycle. A PSSecA should be performed for a new system or each time there is a change to the design of an existing system. In the second case, the purpose of PSSecA is to identify the impact of such a change on the architecture and to ensure the ability of the new architecture to meet either the same or new Security Objectives.

The essential pre-requisite for conducting a PSSecA is a description of the high level functions of the system.

This phase aims at deriving the Security Requirements for each individual system element under evaluation (People, Procedure and Equipment), in order to satisfy the Security Objective of the system.

The system architecture can only achieve the Security Objectives established during the SecFHA, provided the architecture elements meet their Security Requirements.

The PSSecA starts with the Identification of all the Assets that provide the functionalities associated to the Security Objectives, identified during the SecFHA.

According to [6] the Assets will be classified as:

- **Primary assets**: they are the intangible activities, information and services that contribute to have the functionalities of the system to be protected (the ones specified in the Security Objectives).
- **Supporting assets**: they are the physical entities which enable the primary assets.

They are of various types, including for example, hardware, software, operating systems, business applications, networks, storage media, relays, communication interfaces, personnel, sites, premises, utilities, subcontractors, authorities and organizations.

A Security Objective is satisfied if the Primary Assets that provide the functionalities associated to it are protected.

The Primary Assets are protected if and only if the Supporting Assets supporting them are not attackable.

Then, the apportion of Security Objectives into Security Requirements allocated to the system elements is performed through two analyses:

- **Attack Tree Analysis** (**ATA**): it is a functional analysis that aims at identifying that identifies the logical combination of consequences coming from attacks, leading to the non-fulfilment of the security objectives. The focus is on the consequences on Primary Assets. The output of this analysis will be the list of attacks that can impact on a given Security Objective (linked to one or more Primary Asset) with an assigned likelihood.
- **Identification of Vulnerability and Effects Analysis** (**IVEA**): it is a physical analysis and aims at evaluating if the Supporting Assets linked to a given Security Objectives are vulnerable to the identified threats.

The combination of ATA and IVEA analyses allows to identify how critical are the Supporting Assets and consequently to define the Security Controls in a cost-effective way The security controls will be traced to the System Requirements that will become Security Requirements.

Figure 2 shows an overview of the PSSecA process.

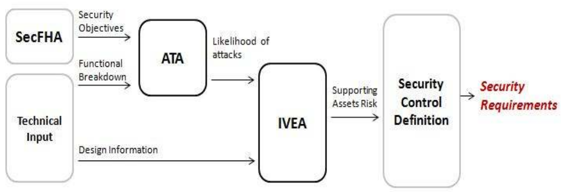

Figure 2. PSSecA Overview

2.2.1 Attack Tree Analysis (ATA)

The ATA is a functional analysis that identifies the logical combination of consequences coming from attacks, leading to the non-fulfilment of the security objectives.

The focus is on the consequences on Primary Assets. Starting from the likelihood of the Security Objective (Top Event), the Attack Tree Analysis allows identifying the likelihood that the attacks successfully lead to the non-fulfilment of the security objective. If an attack is associated to two different values of likelihood, the most stringent value is considered.

2.2.2 Identification of Vulnerability and Effects Analysis (IVEA)

IVEA is performed on the physical components. The objective of this analysis is to identify the system vulnerabilities, evaluates how an attacker can use them (i.e. a threat exploits the vulnerability) and which are the consequences of this attack.

The input of this analysis will be the design information of the system that allows establishing which Supporting Assets support the Primary Assets that provide the functionality associated to a given Security Objective. The analysis follows the following steps:

1. The list of Supporting Assets is considered
2. The vulnerabilities of these supporting Assets are identified.
3. The list of potential threats is considered.
4. Each threat in (3) will be traced to the Supporting Assets in (2) if they are vulnerable to it, i.e. if the threat can exploit the vulnerability of the supporting asset
5. The effect of threat will be evaluated (in order to identify the Primary Asset affected by it).

The IVEA will be in table format:

Supporting Assets	Vulnerabilities	Threats	Threats effect	Threats likelihood	Security Controls	Likelihood after mitigation
Name of the physical component	Vulnerability of the supporting asset	Threat that exploits the vulnerability of the Supporting Asset	It reports the consequences of the threat inherited by the Primary Asset	It indicates the likelihood associated to the effect on Primary Asset resulting from ATA.	It describes the possible security control to be applied to the Supporting Asset in order to mitigate the threat effect	It indicates the risk associated to the Supporting Asset affected by the threats after the application of the Security Controls.

Table 3. IVEA

2.3 System Security Assessment (SSecA)

System Security Assessment is the last phase of the methodology, through Verification and Validation of the System Security.

Verification assess if the implementation is according to the requirements. Validation demonstrated that the implemented product accomplishes its purpose. This phase aims at evaluating *if the implemented architecture achieves a tolerable risk.* It is a top-down iterative process led during system integration, validation and on-site acceptance. The process produces assurance that the Security Objectives are satisfied and that system elements meet their Security Requirements.

The objective is to collect evidences and to provide assurance that:

Verification:

– each system (people, procedure, equipment) element as implemented meets its Security Requirements;
– the system as implemented satisfies its Security Objectives throughout its operational lifetime (till decommissioning);

Validation:

– the system satisfies users expectations with respect to Security;
– the system achieves a tolerable risk.

The correct implementation of Security Measures will be demonstrated through Verification and Validation activities.[11][12]

3 Case study Application: Controller-Pilot Data Link Communications system

The Air Ground Data Link (AGDL) communication system has been selected to evaluate the methodology.

In particular the Controller-Pilot Data Link Communications system (CPDLC) application provides a means of communication between the controller and pilot, using data link for ATC communication. Then CPDLC is a mean of digital communication between aircraft and Air Traffic COntroller (ATCO), allowing data exchange in digital text format.

There are two types of CPDLC messages:

- Downlink messages, which are CPDLC messages sent from aircraft;
- Uplink messages, which are CPDLC messages sent from a ground system.

The CPDLC application is used by the following services[9]:

– **ATC Communication Management (ACM)** service provides automated assistance to the aircrew and current and next controllers for conducting the transfer of ATC communications. The ACM Service encompasses the transfer of all controller/aircrew communications, both the voice channel and the data communications channel used to accomplish the ACM Service. The ACM service is completed prior to using any other CPDLC service.
– **ATC Clearance (ACL)** for exchanging clearances and requests between the current data authority Air Traffic Service Unit (ATSU) and flight crew. An aircraft under the control of an ATSU transmits reports, makes requests and receives clearances, instructions and notifications. The ACL service describes the dialogue procedures to be followed to perform these exchanges via air/ground data communications. The service description states the exchanges that could be conducted via data communications, the rules for the combination of voice and data link communications and abnormal mode requirements and procedures.
– **ATC Microphone Check (AMC)** for instructing pilots to check the aircraft is not blocking a given voice channel. The AMC service allows a controller to send an instruction to all CPDLC equipped aircraft in a given sector, at the same time, in order to instruct flight crews to verify that their voice communication equipment is not blocking the sector's voice channel. This instruction will be issued only to those aircraft for which the controller currently has responsibility
– **Departure Clearances (DCL)** for exchanging departure clearance, request and start up combined messages between

the current ATSU and grounded aircraft to prepare its departure. Where local procedures or flight category require, flights intending to depart from an airport must first obtain a departure clearance from the C-ATSU. The process can only be accomplished if the flight operator has filed a flight plan with the appropriate ATM authority. The DCL Service provides automated assistance for requesting and delivering departure information and clearance, with the objective of reducing aircrew and controller workload and diminishing clearance delivery delays.

3.1 SecFHA: Identification of Security Objectives

An analysis of CPDLC functionalities is performed in order to identify Hazards. According to the classification of effects, Security Objectives are identified in Table 4.

Security Objectives (SO)	Description
SO-1	The likelihood of out-of-sequence CPDLC message shall be less than Occasional
SO-2	The likelihood of denial of CPDLC Services shall be less than Extremely Rare
SO-3	The likelihood of loss of integrity of CPDLC messages exchange shall be less than Rare
SO-4	The likelihood of theft of a CPDLC message shall be less than Rare
SO-5	The likelihood of reception of a fake CPDLC message shall be less than Rare

Table 4. CPDLC Security Objectives

3.2 PSSecA: Identification of Safety and Security Requirements

ATA is performed in order to analyse Primary Assets potentially affected by the identified Security Objectives. An example is presented in Figure 3.

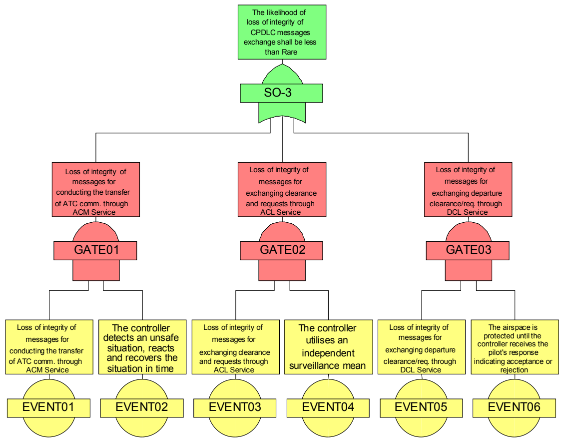

Figure 3. ATA example for SO-3

IVEA is performed in order to analyse Supporting Assets potentially affected by the identified Safety and Security Objectives and to identify Safety and Security Requirements. An example is presented in Table 5.

Supporting Assets	Vulnerability	Threats	Effect	Likelihood	Security Controls	Likelihood after mitigation
Controller Working Position (CWP)	Unsecured protection of integrity of data	Corruption of data	If the message is related to a clearance, the flight crew and ground are out of sync	Rare	Requirements for ensuring authenticity and protecting message integrity	Occasional
CWP	Lack of data validity checks	Corruption of data	If the message is related to a clearance, the flight crew and ground are out of sync	Rare	Automatic checks shall be incorporated to detect any corruption of information through processing errors due to deliberate acts	Occasional
Dual Data Link Server (DLS)	Unsecured protection of integrity of data	Corruption of data	The situation will develop slowly: not all aircraft will receive corrupted messages and take action at the same time. The controller will have time to deal with all impacted aircraft.	Rare	Requirements for ensuring authenticity and protecting message integrity	Occasional
DLS	Services running with unnecessary privileges	Corruption of data	The situation will develop slowly: not all aircraft will receive corrupted messages and take action at the same time.	Rare	The allocation and use of privileges shall be restricted and controlled	Occasional

Table 5. IVEA example for SO-3

3.3 SSecA: Verification and Validation

SSecA has to be performed after development phase, for this reason DORATHEA third step is not finalized for the time being.

4 Conclusions

The objective of this paper is the definition of a new methodology for carrying out security risk assessment in the ATM domain.

Countermeasures must be considered at design phase, identifying areas of synergy and potential conflicts between safety and security approaches, and highlighting cost-effectiveness opportunities within certain security and safety strategies.

The proposed methodology allows the identification of countermeasures in a systematic way. Countermeasures can be adopted as security system requirements at design level.

For demonstrative purposes, the methodology has been applied to the real case study of approach and landing flight phases scenario, with a special focus on Controller-Pilot Data Link Communications systems.

Acknowledgments

The research leading to these results is carried out with the financial support of the Prevention, Preparedness and Consequence Management of Terrorism and other Security related Risks Programme of the European Commission – Directorate-General Home Affairs (Registration number HOME/2010/CIPS/AG/030, DORATHEA Project).

References

[1] Slack B., Rodrigue J.P., "Transport Security", 2012.
[2] UK Centre for the Protection of National Infrastructure (CPNI), "Cyber Security in Civil Aviation", 2012.
[3] Paradis R., Tran B., "Balancing Security/Safety and Sustainability Objectives", National Institute of Building Sciences, 2010.
[4] Federal Aviation Administration, "Review of Web applications security and intrusion detection in Air Traffic Control Systems", U.S. Department of Transportation, 2009.
[5] SESAR Definition Phase Project, "D1 Air Transport framework – The current situation", v3, SESAR Consortium, 2006.
[6] EUROCONTROL, Deliverable 16.02.03 – "SESAR ATM Security Risk Assessment Method", Ed.01.01, SESAR WP16.2 ATM Security, 2013.
[7] ICAO, Security Manual for Safeguarding Civil Aviation Against Acts of Unlawful Interference, Seventh Edition, 2010.
[8] IEC 15408, Information Technology – Security Technique – Evaluation Criteria for IT Security, 2005.
[9] IEC 27005, Information Technology — Security Techniques — Information Security Risk Management, Second Edition, 2011.
[10] ICAO, Manual of Air Traffic Services Data Link Applications, First Edition, 1999.
[11] ESA "Information Systems Verification and Validation", Guide Issue 2.0 29, December 2008.
[12] IEEE 1012-2004 "Standard for Software Verification and Validation", 2004.

4:th CEAS Air & Space Conference
FTF Congress: Flygteknik 2013

Optimal Spot-out Time – Taxi-out Time Saving and Corresponding Delay

R. Mori
Electronic Navigation Research Institute, Japan

Keywords: *Taxi-out; Taxiing; Spot-out time control; Uncertainty; Airport operation*

Abstract

A departure queue management strategy has been proposed to reduce fuel burn and emission at the airport operation. If this strategy is implemented, departure aircraft can wait at the spot with engine off instead of waiting on the taxiway. However, at the same time this strategy can potentially delay the take-off time compared to the nominal take-off time, which has not been addressed in detail so far by other researchers. From airlines' perspective, it is important how often and how much take-off delay could occur in return of taxi-out time saving. Therefore in this paper, the trade-off relationship between the expected taxi-out time saving and corresponding expected take-off delay is revealed quantitatively at Tokyo International Airport. To reveal this relationship, a stochastic simple airport simulation model considering various uncertainties is developed based on actual traffic data, and a simple departure queueing algorithm is proposed. The simulation result shows the quantitative relationship between taxi-out time saving and take-off delay.

1 Introduction

Airport congestions are recently becoming a critical problem at many airports in the world. The bottleneck of airport operations is usually found on the runway, because the number of take-off and landing aircraft is limited due to the required minimum aircraft separation. As a result, there are long waiting queues of aircraft both on the ground taxiway and in the air, which leads to an increase in both fuel burn and emissions. Arrival aircraft are often considered in airport congestions because any additional flight time obviously requires extra fuel. Even if not so apparent, departure aircraft burn sufficient amount of fuel during taxiing, too, so departure queue management can help to reduce fuel burn. Compared to arrival queues, departure queues can be controlled easily by allocating appropriate spot-out time. Departure aircraft waiting at the gate can stop its engines and therefore save fuel. Efficient taxiing has been a subject of several research teams. Pujet et al[1] apply a simple queuing system to control the departure queue. Balakrishnan et al[2] develop N control strategy to control the pushback rate based on the statistical analysis of departure throughput. This algorithm is realized at Boston airport and proven effective. Briton et al[3] introduce the Collaborative Departure Queue Management concept, where the allocation of the slot is determined based on the Generalized Ration by Schedule algorithm. Burgain et al[4] analyze the effect of available information for optimal pushback times. However, these researches focus on taxi-out time saving, and do not seem to investigate its negative effect. One such possible negative effects caused by departure queue management is take-off delay.

If the spot-out time is controlled to save taxi-out time, the take-off time can be potentially delayed due to various uncertainties. Here, "taxi-out time" is defined as the time between pushback start and take-off, and "delay" is defined as the difference of take-off time between the nominal case and the spot-out time controlled case. Even if a large margin is set to absorb uncertainties, the expected delay will be close to 0, but not definitely 0. According to most researches mentioned before, the taxiing time is reduced as long as further delay is not caused, but strictly speaking, this cannot happen. Even if delay is caused, it is usually attributed to a "rare unexpected event". However, from airlines' perspective, it is important to know how much take-off delay is caused as well as how much fuel saving is expected. Therefore, it is reasonable to investigate the trade-off relationship between the expected taxiing time reduction and the corresponding take-off delay.

In this research, the relationship between taxi-out time saving and take-off delay at Tokyo International Airport is revealed quantitatively. Delays are caused only when an unexpected situation happens which is a probabilistic occurrence, so first, in section 2 a stochastic simple airport operation model is developed based on the actual data at Tokyo International airport. The model validation is also performed. In section 3, the assumed ATC operation for departure queue management is explained, and a simple queue management algorithm is proposed. Using the proposed model and algorithm, the expected trade-off relationship between taxi-out time saving and take-off delay is shown.

2 Stochastic Airport Simulation Model at Tokyo International Airport

Tokyo International Airport is the target airport of this research. First of all, the airport operation is briefly explained in subsection 2.1, and a stochastic simulation model is developed. To conduct a Monte Carlo simulation, the model itself is simplified as much as possible. Error distribution models for stochastic components are introduced in subsection 2.2, and stochastic simulation parameters are obtained in subsections 2.3 and 2.4. Finally, the simulation flow is shown in subsection 2.5 and simulation accuracy is investigated compared to the actual data in subsection 2.6.

2.1 Tokyo International Airport and its operation

Tokyo International Airport is the busiest airport in Japan, and is mostly used for domestic flights. In 2010, the traffic volume was 303,000 flights per year, and is expected to increase to 447,000 flights per year (earliest by 2014) with the opening of the new runway[5]. Figure 1 shows the airport map and typical operation under north wind. There are four runways at the airport. A runway is used for arrival and D runway is used for departure, but C runway is shared by both departure and arrival aircraft. Due to the arrangement of the runways, aircraft departing from D runway cannot take-off while a landing aircraft is approaching C runway. B runway is usually not used under north wind.

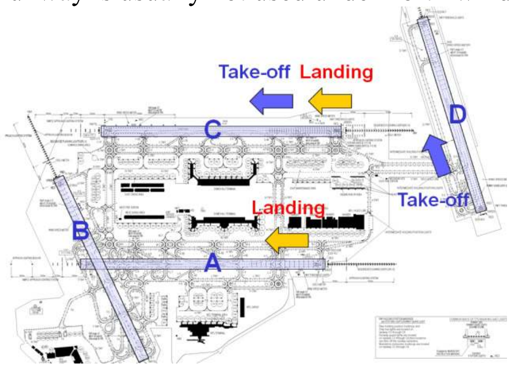

Fig. 1 The airport map and runway operation under north wind.

In order to model taxiing correctly, knowledge of the procedures during which departure aircraft undergoes before take-off is necessary. The ATC flow of departure aircraft is summarized in Fig. 2. First, about 5 minutes before the aircraft is ready for starting engine, the pilot calls clearance delivery. If the flight plan is approved, the pilot will get a departure clearance from ATC. When the aircraft is ready for block off, the pilot requests pushback to ATC. Once the pilot gets pushback approval, the aircraft starts pushback. During or after the pushback, the pilot requests taxiing to the runway. If the taxiing is approved and the aircraft is ready for taxiing, the aircraft will start taxiing. When the aircraft approaches the runway, the pilot requests runway clearance. Only after the runway clearance is approved, the aircraft can take-off.

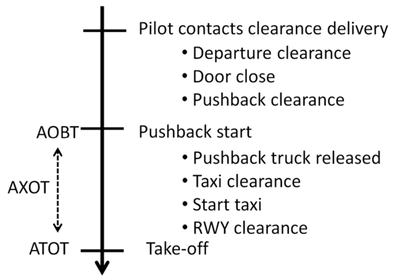

Fig. 2 Flow of departure.

Here, several variables are defined. The time when the pilot contacts clearance delivery is defined as ACDT (actual contact clearance delivery time), and the time when the pilot starts pushback is AOBT (actual off-block time). Actual take-off time is defined as ATOT. "ATOT–AOBT" is defined as AXOT (actual taxi-out time). Airport operation is not completely deterministic, and there are probabilistic factors. Therefore, considering certain uncertainty, AXOT is determined probabilistically in the simulation. The distribution of AXOT is examined in subsections 2.4, respectively.

As for arrival aircraft, a certain time before arrival, the ELDT (estimated landing time) is obtained. However, ELDT does not consider congestions, so the aircraft tends to land later than ELDT, at ALDT (Actual Landing Time). Even if the arrival aircraft airspace is not so congested, ELDT and ALDT are different due to estimation uncertainty.

This time, the data used to determine the simulation parameters in this research is obtained based on the smoothened airport surface movement data for six days in March 2012, when north wind operation was conducted throughout a day.

2.2 Error Distribution Model

To consider the error factor, several error distribution models are applied. In this research, normal distribution and Erlang distribution are used. Normal distribution, also known as Gaussian distribution, is a symmetric distribution. The detailed explanation is not given here, but it has two parameters, average μ and standard deviation (SD) σ. The probability density function of normal distribution is given by the following equation.

$$N(x;\mu,\sigma)=\frac{1}{\sqrt{2\pi}\sigma}\exp\left(-\frac{(x-\mu)^2}{2\sigma^2}\right) \tag{1}$$

Furthermore, to account for error's asymmetry, Erlang distribution is also introduced. This distribution is asymmetric and is defined only when x is greater than 0. This function is often used in the field of stochastic processes. There are two parameters; average and shape n (positive integer). The probability density function of Erlang distribution is given by the following equation.

$$E(x;\mu,n)=\frac{n^n x^{n-1} e^{-nx/\mu}}{\mu^n (n-1)!} \quad (x>0) \tag{2}$$

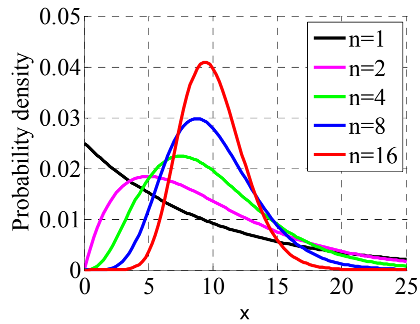

Fig. 3 Erlang distribution for various n. (average = 10).

Figure 3 shows the shape of the probability density function for various n. This distribution is close to the normal distribution as n increases.

2.3 Distribution of Taxi-out Time (AXOT)

Taxi-out time is defined as the time between pushback start and take-off. To determine the taxi-out time, it is divided into several stages, and the duration of each stage is determined. Figure 4 shows the flow of taxi-out. First, the aircraft has to complete pushback, defined as "pushback time" ($\Delta t_{pushback}$). Next, the aircraft has to be released from the pushback truck and prepare for taxiing, defined as "preparation time" ($\Delta t_{prepare}$). Then, the aircraft goes taxiing to the runway, defined as "taxiing time". If there is a queue before the runway, the aircraft will need additional waiting time. The minimum time which an aircraft needs to cover the distance between its spot and the runway even when no congestion is observed is defined as "minimum taxiing time" (Δt_{taxi}). The difference between total "taxiing time" and "minimum taxiing time" is defined as "additional waiting time" (Δt_{wait}). Finally, taxi-out time (AXOT) is calculated by the following equation. Each time is estimated based on the data available.

$$\mathrm{AXOT} = \Delta t_{pushback} + \Delta t_{prepare} + \Delta t_{taxi} + \Delta t_{wait} \qquad (3)$$

Here, some variables are defined. PTOT (earliest possible take-off time) is defined as the time when the aircraft is ready for take-off assuming there is no congestion. PTOT is calculated by the following equation.

$$\mathrm{PTOT} = \mathrm{ATOT} - \Delta t_{wait} \qquad (4)$$

PXOT (earliest possible taxi-out time) is also defined in the same way by the following equation.

$$\mathrm{PXOT} = \mathrm{AXOT} - \Delta t_{wait} \qquad (5)$$

As for the pushback time, it is expected to depend on the pushback distance. The pushback distance is usually determined by the spot position, so it is easily obtained in advance. Figure 5 shows the relationship between pushback distance and pushback time, and the red line represents the best fit obtained by least squares linear regression. The figure shows that the two variables are linearly dependent, but there is still a residual. The residual is fitted with Erlang distribution by maximum likelihood estimation (MSE) method. Finally, the probability density function of the pushback time is calculated by the following equation. $d_{pushback}$ indicates the pushback distance [m].

$$\Delta t_{pushback} = 0.6279 d_{pushback} - 27.23 + E(x; 100.5, 13) \qquad (6)$$

Another variable defined in this research is $\Delta t_{prepare}$. It includes the time for the pilot to receive a taxiing clearance and the time needed to release the pushback truck from the aircraft. There is no predictor variable, so the probability density of the preparation time is fitted by the combination of normal distribution and Erlang distribution. After adjusting the parameters by MSE method, the probability density function of the preparation time is given by the following equation.

$$\Delta t_{prepare} = 0.2438 E(x; 205.7, 8) + 0.7562 N(x; 169.0, 25.10) \qquad (7)$$

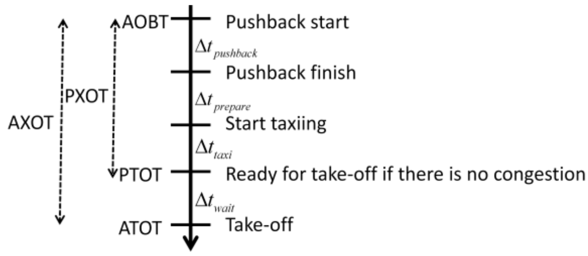

Fig. 4 Taxi-out flow.

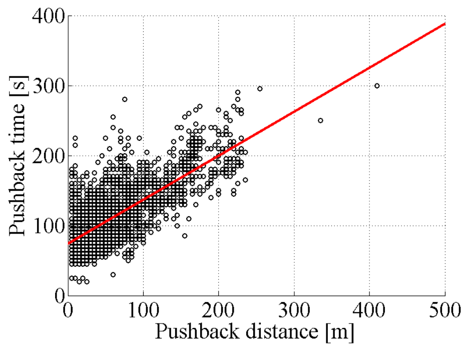

Fig. 5 Relationship between pushback distance and pushback time.

The last element needed to be defined in order to determine the earliest possible taxi-out time is the minimum required taxiing time. The minimum taxiing time varies with each pilot, and some aircraft go faster taxiing while others go slower. However, the minimum taxiing time is basically related to taxiing distance. Although it is difficult to estimate the minimum taxiing time of the congested aircraft, for non-congested aircraft the minimum taxiing time is equal to the total taxiing time. In this paper, the minimum taxiing time also includes the conflict between two aircraft after they start taxiing, which is calculated as uncertainty. Figure 6 shows the relationship between taxiing distance and taxiing time of non-congested aircraft departing from D runway. This figure shows that there is a correlation between these two factors, and the residual tends to increase with the taxiing distance. Therefore, the distribution of the normalized residual (residual per 1km taxiing distance) is fitted by a normal distribution. Finally, the probability density function of the minimum taxiing time is calculated by the following equation when the taxiing distance (d_{taxi}) is given. The taxiing time of aircraft departing from D and C runways are given in Eqs. (8) and (9).

$$\Delta t_{taxi} = 0.0939 d_{taxi} + 108.22 + N(x; 0, 16.58 d_{taxi} / 1000) \quad (8)$$

$$\Delta t_{taxi} = 0.1162 d_{taxi} + 57.26 + N(x; 0, 16.58 d_{taxi} / 1000) \quad (9)$$

Taxiing differs between C runway and D runway, so the minimum taxiing time is calculated in a different manner. Once the spot position and the departure runway are determined, the taxiing distance is easily obtained, so the minimum taxiing time is also obtained.

Finally, the additional waiting time is considered. The additional waiting time is caused by the waiting queue at the runway, so it is strongly affected by take-off and landing separations. In addition, the departure and arrival traffics are affected by each other due to the arrangement of the runways at this airport, so the mutual interaction between the runways should also be considered. In addition, the effect of wake turbulence should be considered. The take-off separation depends on the size of preceding aircraft and the take-off aircraft[6]. According to our prior analysis, the take-off separation does differ with the wake turbulence category[7], so the take-off separation is calculated separately. Note that aircraft from the ICAO light category are very rare at Tokyo International Airport, so "light" category is not considered in this research.

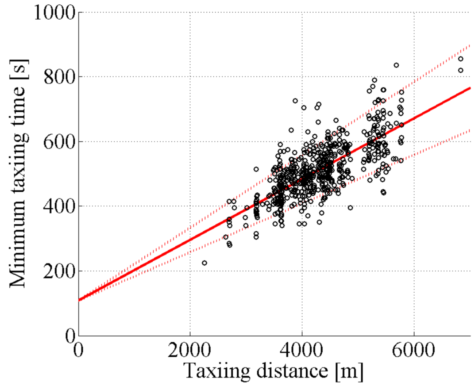

Fig. 6 Relationship between taxiing distance and minimum taxiing time on D runway.

Figure 7 shows the probability density distribution of take-off separation normalizing the effect of wake turbulence. Only aircraft which are caught in the congestion and are not affected by landing aircraft are chosen. The distribution is well fitted by the Erlang distribution, and the probability density function of take-off separation is given by the following expression. "H" denotes ICAO heavy aircraft while "M" denotes ICAO medium aircraft. The landing separation is also calculated in the same way.

$$\Delta t_{takeoff} = 50.28 + E(x; 45.75, 7) + \begin{cases} -5 & M-H \text{ or } M-M \\ 5 & H-H \\ 10 & H-M \end{cases} \quad (10)$$

$$\Delta t_{land} = N(x; 114.6, 16.33) \quad (11)$$

In terms of the mutual interaction between departure and arrival traffic, the effect of landing aircraft at C runway to departure aircraft on each runway must be considered. Arrival aircraft are assumed not to shift the landing time, so prohibited departure time relative to the landing time on C runway is defined. This time, it is set to a constant time. The restriction is summarized in Table 1 according to the data.

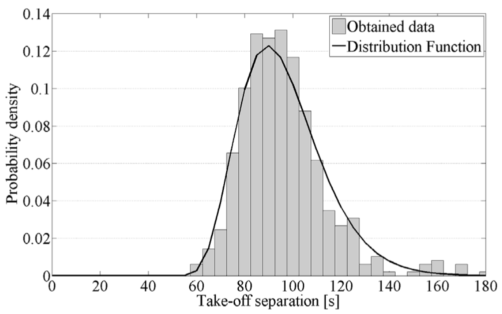

Fig. 7 Probability density and fitted function of take-off separation for congested case.

Table 1 Prohibited Departure Time Relative to the Landing Time on C Runway.

	Prohibited start	Prohibited end
Departure from C runway	–125 s	+70 s
Departure from D runway	–130 s	+0 s

2.4 Estimation of Arrival Uncertainty

It is difficult to obtain arrival uncertainty from actual data, because ELDT is assumed when no arrival traffic congestion occurs but most aircraft are stuck in congestion. Therefore, this time, the uncertainty is assumed to be normally distributed with average of 0 second and standard deviation of 2 minutes, written in the expression form as follows. ELDT is assumed to be available 30 minutes before ALDT.

$$\text{ELDT} = \text{ALDT} + N(x; 0, 120.0) \qquad (12)$$

2.5 Simulation Flow

In order to conduct a simulation, initial conditions must be specified. As for the departure aircraft, once AOBT is obtained, the PTOT can be calculated considering the uncertainty explained before. Even though PTOT is also calculated from ACDT, ACDT is currently not available, so ACDT is also estimated from AOBT for taxi-out time reduction strategy. In the simulation, each departure aircraft is assumed to come to the runway at PTOT, and ATOT is decided based on the runway separation on first-come-first-served (FCFS) basis. For arrival aircraft, ALDT is obtained from the data, so ALDT is fixed in the simulation, but ELDT is calculated based on ALDT with uncertainty by Eq. (12). Note that the arrival aircraft is always assumed to be prioritized over departure aircraft. The flow of the calculation of each variable is summarized in Fig. 8.

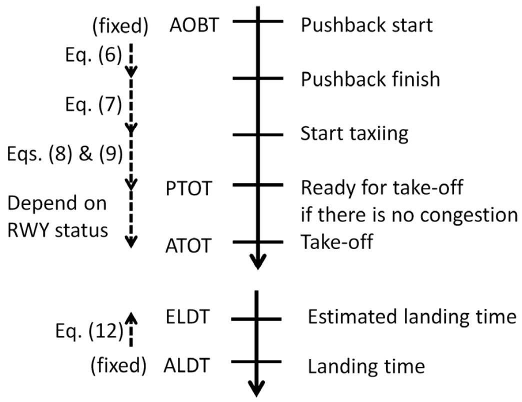

Fig. 8 Simulation flow.

The simulation can be conducted if the following data is obtained: AOBT, pushback distance, and taxiing distance of each departure aircraft and ALDT of each arrival aircraft. Although it is possible to estimate these data as randomly distributed, the actual traffic is not random but based on the flight schedule, so these data are obtained by actual data.

2.6 Simulation Accuracy

The proposed model is a stochastic model, so no single result should be expected. Therefore, Monte Carlo simulation is conducted to validate the model accuracy, and the Monte Carlo simulation results are compared to the actual data. Total six days between 6 pm and 8 pm in March 2012 are chosen for the validation. Table 2 shows the taxi-out time on each day and time. Although little difference of the number of aircraft, i.e. traffic volume, is found among the days, the average taxi-out time is different. It means that the waiting time at the runway varies significantly. This difference seems to come from the traffic randomness since the traffic volume is similar for most days. In addition, it is the waiting time at runway that can be potentially reduced by spot-out time management, so the larger runway waiting time means that it is easier to reduce the taxi-out time. In terms of the time, 7 pm is obviously the most congested and 8 pm is the least congested time judging from the total waiting time at runway. The simulation can be validated for both non-congested time and congested time by simulating between 6 pm and 8 pm.

Table 2 Statistics of Taxi-out Time and Runway Waiting on Each Day and Time.

Date	Average of taxi-out time	SD of taxi-out time	Total waiting time at runway (Δt_{wait})	Number of departure aircraft
March 5	15.00 min	3.18 min	223.5 min	96
March 6	14.76 min	3.31 min	211.5 min	99
March 7	16.86 min	5.07 min	402.0 min	99
March 8	15.38 min	3.60 min	262.0 min	98
March 9	16.04 min	3.79 min	320.2 min	102
March 10	15.43 min	4.23 min	274.8 min	99
6pm	14.96 min	3.38 min	462.3 min	203
7pm	17.37 min	4.24 min	1008.8 min	230
8pm	13.82 min	3.15 min	222.8 min	160

Table 3 shows the simulation result. Taxi-out time of each aircraft is compared between actual data and simulation, and the average and standard deviation of error is shown. In addition, total waiting time at runway is also compared between actual data and simulation. Average of taxi-out time is estimated with about 0.5 minutes at most, but the standard deviation of the error still remains about 1.5 minutes. However, this value is not so significant because of the following reasons. First, the actual data is just a single result, and it should not be the same as the average. Second, the order of take-off is determined by FCFS rule based on the PTOT in the simulation, but the take-off order affects the taxi-out time very much. Actually, the take-off order is not necessarily decided by FCFS rule. Besides, PTOT is also calculated probabilistically in the simulation, so the take-off order is different between simulations and actual data. In this research, total taxi-out time reduction is discussed, not an individual aircraft's reduction. Even if the take-off order is changed, the total waiting time at runway is not changed, which is more important in this research. According to the table, average error of total waiting time is estimated to be 14% at most. This infers that the proposed model can simulate the runway operation appropriately.

Table 3 Monte Carlo Simulation Results.

	Average error of taxi-out time	SD of error of taxi-out time	Average error of total waiting time at runway	
March 5	0.20 min	1.51 min	20.1 min	9.0%
March 6	0.24 min	1.26 min	23.6 min	11.2%
March 7	–0.55 min	1.78 min	–54.5 min	–13.6%
March 8	0.21 min	1.99 min	20.3 min	7.7%
March 9	–0.07 min	1.62 min	–7.2 min	–2.3%
March 10	0.05 min	1.78 min	4.9 min	1.8%

In order to validate the model further, the relationship between actual waiting time at the runway and average simulated waiting time of individual aircraft at runway is shown. Fig. 9 shows that the waiting time is well estimated for most aircraft. Some negative actual waiting time is observed, but that is because the actual waiting time is calculated as the difference of AXOT and standard taxi-out time. Therefore, if an aircraft goes taxiing faster to the runway than average and does not wait at the runway, the actual waiting time becomes negative. Considering overall simulation results, it is concluded that the proposed simulation model works to estimate the waiting time at runway and is applicable for evaluating the spot-out time management strategy.

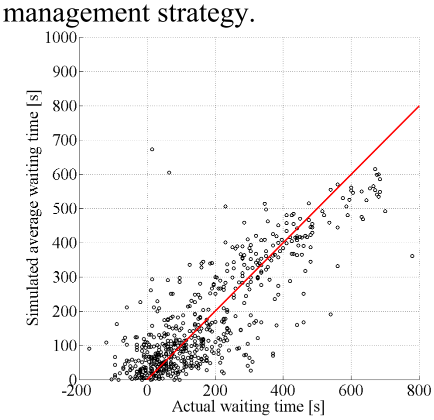

Fig. 9 Relationship between actual waiting time and simulated waiting time at runway.

3 Simple Spot-out Time Management Algorithm and Its Performance

3.1 Assumed ATC Operation

When the spot-out time management is implemented, the management strategy should be based on possible ATC operation. Shifting the spot-out time is controlled by ATC, so

ATCs or an alternate system need some information of each aircraft so they can provide the appropriate spot-out time to each aircraft. Therefore, simply obtaining an optimal solution without considering its application is insufficient. The proposed operation flow is shown in Fig. 10. Here, only the flow is explained, and the calculation details are explained in the next section.

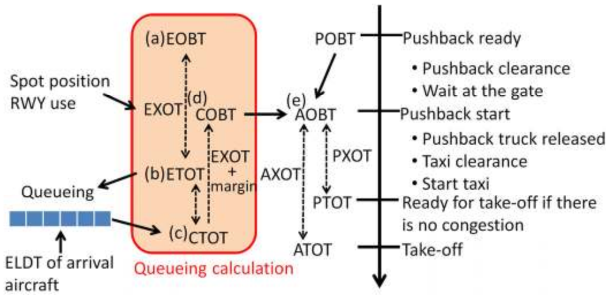

Fig. 10 Flow of Spot-out Time Management.

First, at a certain timing, EOBT (Estimated Off-Block Time) is obtained from a departure aircraft (See (a) in Fig. 10). Using EOBT and the aircraft's spot position and runway data, EXOT (Estimated Taxi-Out Time) is calculated, then ETOT (Estimated Take-Off Time) is obtained (b). Based on ETOT information, a queueing algorithm calculates the appropriate take-off time (CTOT: Controlled Take-Off Time) (c). Based on CTOT, the appropriate off-block time (COBT: Controlled Off-Block Time) is calculated and is sent to the pilot (d). Note that COBT is not necessarily assigned to all aircraft. If COBT is not assigned, ATC gives a pushback clearance without delay, and the aircraft leaves the spot as early as possible, i.e. AOBT = POBT. However, if COBT is provided by ATC, the aircraft should not leave the spot earlier than COBT. Finally, AOBT is calculated by the following equation (e).

$$\mathrm{AOBT} = \max(\mathrm{POBT}, \mathrm{COBT}) \qquad (13)$$

Once AOBT is determined, ATOT is calculated based on the flow shown in Fig. 8.

To shift the spot-out time, the take-off time and order should be estimated in advance. If ETOT is exactly estimated, the take-off time and order can be exactly controlled, but uncertainty exists as explained in the previous section, and ETOT with uncertainty must be used.

The accuracy of ETOT depends on the uncertainty of both EOBT and EXOT. Although the uncertainty of EXOT is constant, the uncertainty of EOBT usually depends on the timing when EOBT is obtained. If EOBT is obtained long before the estimated take-off, ETOT is not accurately estimated and vice versa. However, if EOBT is available close to the actual take-off time, the estimated sequencing of runway might not work well. This time, to minimize the uncertainty effect, it is assumed that ETOT is obtained just before the aircraft is ready for pushback (POBT), and EOBT is assumed to be equal to POBT, i.e. there is no uncertainty effect coming from EOBT. When pilot contacts ATC to request pushback clearance, system calculates COBT.

This research considers the delay caused by spot-out time management, so here its definition is clarified. The delay of each aircraft is calculated based on the following equation:

$$delay_i = \mathrm{ATOT}_i^{\mathrm{mng}} - \mathrm{ATOT}_i^{\mathrm{nominal}} \qquad (14)$$

where "mng" indicates the case of controlled spot-out time, and "nominal" indicates the case of uncontrolled spot-out time, i.e. current practice. i denotes each aircraft. Total delay is also defined in the same way as follows.

$$delay_{total} = \sum_i delay_i \qquad (15)$$

The delay of each aircraft can be negative if the take-off time becomes earlier than that of the nominal case, which usually happens when the take-off sequence is changed. However, the total delay is the sum of all delays, so the total delay remains almost the same even if the take-off sequence is changed. Therefore, the total delay is closely linked to the efficiency of the runway utilization.

3.2 Simple Spot-out Time Management Algorithm

In order to calculate COBT of each aircraft, aircraft are sequenced by obtained ETOT and ELDT. If the runway is used by departure aircraft only, only departure aircraft information is required, but that is not the case at Tokyo International Airport. Here, it is assumed that ELDT is available 30 minutes before landing with standard deviation of 2 minutes, as written in Eq. (12). It is assumed that ELDT is directly obtained, but ETOT should be estimated based on some information available. In the previous section, PXOT is calculated probabilistically, so EXOT is calculated as PXOT on the condition that the uncertainty is 0.

Once ETOT or ELDT is obtained, the aircraft is sequenced and CTOT or CLDT (calculated landing time) is obtained. Each runway has virtual slots divided by equal length of time, which is set to 90 s this time. Both departure and arrival aircraft use a single runway slot. Arrival aircraft is given priority over departure aircraft. Even if the slot for the arrival aircraft is already allocated to a departure aircraft, the arrival aircraft gets the slot and the departure aircraft which had already received the slot is shifted to the next slot. On the other hand, the departure aircraft is allocated to the earliest vacant slot after ETOT. In addition, at Tokyo International Airport, there are two runways (C and D runways) used by departure aircraft, but an aircraft arriving at C runway affects an aircraft departing from both C and D runways. Therefore, a single arrival aircraft on C runway occupies a slot on both runways at the same time window. A sample flow of runway slot allocation is shown in Fig. 11. If an aircraft takes off or lands earlier than its allocated slot, it is deleted from the list and all following aircraft are shifted earlier only when new CTOT/CLDT is larger than ETOT/ELDT. On the other hand, if an aircraft does not take off or land before the allocated slot, it is shifted to the next time slot. All following departure aircraft are shifted later, too.

Once an aircraft is allocated to a runway slot, CTOT is obtained, so COBT is calculated based on CTOT. The simplest method to calculate COBT is obtained by the following equation.

$$\mathrm{COBT} = \mathrm{CTOT} - \mathrm{EXOT} - m \tag{16}$$

where m denotes the margin to absorb uncertainty. If the margin is too small, take-off delay is likely to occur due to uncertainty. On the other hand, if the margin is too large, taxi-out time cannot be reduced sufficiently. Therefore, there is a trade-off between take-off delays and taxi-out time saving.

To absorb uncertainty efficiently, it is effective to have some aircraft waiting at the runway, which means that ATC makes some aircraft wait at the runway on purpose. Even when an aircraft cannot reach the runway at the allocated take-off time (CTOT), another aircraft can take off, which means that the allocated runway slot is not missed. To implement this idea, CTOT is set to the aircraft only when there are n or more consecutive aircraft ahead in a virtual runway slot. Here, n is a parameter, and set to 7 this time.

Fig. 11 Sample flow of runway slot allocation. (black: departure, red: arrival)

In addition, in this algorithm, each aircraft has an allocated runway slot, i.e. the take-off order is determined in advance, but actual runway operation is done on FCFS basis. Although each aircraft has COBT linked to CTOT, the actual sequence at runway might be changed due to uncertainty in each phase. Therefore, the actual take-off order and the planned take-off order on virtual queues do not necessarily match in order to avoid the decrease in runway usage.

3.3 Simulation Results

To clarify the relationship between the expected taxi-out time saving and corresponding take-off delay, Monte Carlo simulation is conducted. The possible reduction of taxi-out time varies depending on the initial conditions. Although AOBT and ALDT are set constant as explained before, ETOT and ELDT are distributed randomly, which affects virtual queueing. The average taxi-out time saving and the average delay are discussed here and 10,000 simulations are conducted. This time, the result of March 6 is shown, when the expected taxiing time saving is the smallest among 6 days. Figure 12 shows the simulation result of average taxi-out time saving and average take-off delay with various margin (m) on March 6.

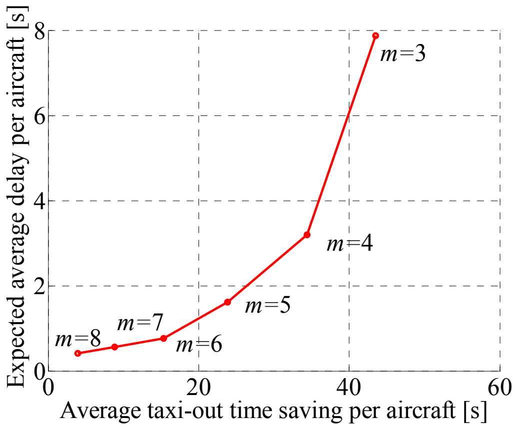

Fig. 12 Average taxi-out time saving and average delay with various m on each day.

According to the figure, there is a trade-off between taxi-out time saving and corresponding delay. If m is set large, the expected delay is small, but the taxi-out time saving is also small, and vice versa. However, among these solutions, if one objective function is better, the other objective function is worse, so all solutions can be optimal depending on the weight of the factors.

Assume that the acceptable average delay is 1 s, about 20 s average taxi-out time saving is expected, which is in total 33 minutes taxi-out time saving for 3 hours. According to Table 2, the estimated total waiting time at runway is 211.5 minutes, so only 15% of potential saving margin is used. However, the current solution shown in Fig. 12 is not necessarily a optimal solution set. This time, it is assumed that ATC makes some aircraft wait at the runway on purpose, but another method might be more efficient, which will be a subject to future work.

Besides, as expected, a certain take-off delay is unavoidable to reduce taxi-out time because of the trade-off relationship. However, it is unclear which the best solution is in this solution set. If large delay is acceptable, the solution with large error and large saving will be the optimal one, and vice versa. The opinion might differ between ATC and airlines, so this kind of information will help discuss a "real" optimal strategy. This research might provide a different perspective for "optimal" operation.

References

[1] Pujet, N., Delcaire, B., Feron, E., "Input-output modeling and control of the departure process of congested airports," *AIAA Guidance, Navigation and Control Conferences and Exhibit*, AIAA-1999-4299, 1999.

[2] Simaiakis, I., Khadilkar, H, Balakrishnan, H. et al, "Demonstration of Reduced Airport Congestion Through Pushback Rate Control," *9th USA/Europe Air Traffic Management Research and Development Seminar*, 2011.

[3] Brinton, C., Provan, C., Lent, S., Prevost, T., Passmore, S., "Collaborative Departure Queue Management: An Example of Airport Collaborative Decision Making in the United States," *9th USA/Europe Air Traffic Management Research and Development Seminar*, 2011.

[4] Burgain, P., Pinon, O. J., Feron, E., Clarke, J-P., Mavris, D. N., "Optimizing Pushback Decisions to Valuate Airport Surface Surveillance Information," *IEEE Transactions on Intelligent Transportation Systems*, Vol. 13, No. 1, pp. 180-192, 2012.

[5] Japan Civil Aviation Bureau, http://www.mlit.go.jp/kisha/kisha04/12/120226/03.pdf (in Japanese)

[6] International Civil Aviation Organization, "Procedures for Air Navigation Service - Air Traffic Management (PANS-ATM)," Doc 4444.

[7] Mori, R., "Aircraft Ground-Taxiing Model for Congested Airport Using Cellular Automata," *IEEE Transactions on Intelligent Transportation Systems*, IEEE, Vol. 14, No. 1, pp. 180-188, 2013.

Enabling Uncertainty Quantification of Large Aircraft System Simulation Models

M. Carlsson, S. Steinkellner, H. Gavel
Saab Aeronautics, Linköping, SE-581 88, Sweden

J. Ölvander
Linköping University, Linköping, SE-581 83, Sweden

Keywords: *Model validation, uncertainty analysis, uncertainty quantification*

Abstract

A common viewpoint in both academia and industry is that that Verification, Validation and Uncertainty Quantification (VV&UQ) of simulation models are vital activities for a successful deployment of model-based system engineering. In the literature, there is no lack of advice regarding methods for VV&UQ. However, for industrial applications available methods for Uncertainty Quantification (UQ) often seem too detailed or tedious to even try. The consequence is that no UQ is performed, resulting in simulation models not being used to their full potential.

In this paper, the effort required for UQ of a detailed aircraft vehicle system model is estimated. A number of methodological steps that aim to achieve a more feasible UQ are proposed. The paper is focused on 1-D dynamic simulation models of physical systems with or without control software, typically described by Ordinary Differential Equations (ODEs) or Differential Algebraic Equations (DAEs). An application example of an aircraft vehicle system model is used for method evaluation.

1 Introduction to Uncertainty Quantification

Uncertainty Quantification (UQ) or Uncertainty Analysis (UA) refers to the process of identifying, quantifying, and assessing the impact of uncertainty sources embedded along the development and usage of simulation models. According to Roy and Oberkampf (2011), all uncertainties originate from three key sources:

1. *Model inputs*: e.g. input signals, parameters, and boundary conditions.
2. *Numerical approximations*: e.g. due to the numerical method used by the solver.
3. *Model form*: e.g. model simplifications or fidelity level of underlying equations.

This is in line with the definitions provided by Coleman and Steele (2009). Commonly, a distinction is made between aleatory uncertainty (due to statistical variations, also referred to as variability, inherent uncertainty, irreducible uncertainty, or stochastic uncertainty) and epistemic uncertainty (due to lack of information, also referred to as reducible uncertainty or subjective uncertainty). See

Padulo (2009) for an extensive literature review of uncertainty taxonomies.

It may be questioned whether the term *uncertainty* or *error* should be used, and in the literature these terms are sometimes used interchangeably. To avoid misinterpretation, uncertainty here refers to the nature of the source, i.e. if it is aleatory, epistemic or a mixture, and is often characterized as a Probability Density Function (PDF) or an interval. Error on the other hand does not concern the nature of the source, and is often seen as a single realization of an uncertain entity.

For the common case of using measurement data for validation purposes, the uncertainties of the data used for validation are as important as the uncertainties of the model itself. Sometimes the uncertainty of the validation data is deemed too hard to assess and is ignored without justification, or simply understood as the measurement error of a specific sensor. The following basic equations provide the fundamental relationships between the simulation result *S*, the validation data D, the validation comparison error E, and the true (but unknown) value T. The error in the simulation result δ_S and the error in the validation data δ_D are also defined. The equation variables may be either time-series or single values, such as steady-state values. The equations originate from Coleman and Steele (2009), and corresponding equations are found in Oberkampf and Roy (2012).

$$E = S - D \tag{1.1}$$

$$\delta_S = S - T \tag{1.2}$$

$$\delta_D = D - T \tag{1.3}$$

Hence, the validation comparison error is the combination of all errors in the model and in the validation data.

$$\begin{aligned} E &= (\delta_S + T) - (\delta_D + T) \\ &= \delta_S - \delta_D \end{aligned} \tag{1.4}$$

With the three model uncertainty sources described at the beginning of this section, the error in the simulation result can be defined as follows.

$$\delta_S = \delta_{S\,input} + \delta_{S\,num} + \delta_{S\,model} \tag{1.5}$$

In addition to sensor measurement error (which may also include A/D conversion implying finite resolution), the total error in the validation data may depend on various characteristics of the physical test setup, e.g. uncertain boundary conditions, experimental simplifications, or placement of sensors. An example might be when comparing airstream temperatures obtained from a 1-D simulation model with experimental results. In such a case, the model typically does not take local effects and inhomogeneous flow patterns into account. Therefore, to obtain useful validation data, the placement of the temperature sensor should be carefully chosen, e.g. in terms of downstream distance from a mixing point or radial positioning in a pipe. To emphasize this, the equations provided by Coleman and Steele (2009) can be expanded by defining the total error in the validation data as a combination of sensor measurement error $\delta_{D\,sensor}$ and errors due to the experimental setup $\delta_{D\,setup}$ itself.

$$\delta_D = \delta_{D\,sensor} + \delta_{D\,setup} \tag{1.6}$$

Combining equations (1.4) to (1.6) and solving for the model form error $\delta_{S\,model}$ yields:

$$\begin{aligned} \delta_{S\,model} = E &- (\delta_{S\,input} + \delta_{S\,num}) \\ &+ (\delta_{D\,sensor} + \delta_{D\,setup}) \end{aligned} \tag{1.7}$$

There are methods to estimate $\delta_{S\,input}$ and $\delta_{S\,num}$, but according to Coleman and Steele (2009) no way to independently observe or calculate the effects of $\delta_{S\,model}$. In most cases, the knowledge of $\delta_{D\,sensor}$ is available, but the knowledge of $\delta_{D\,setup}$ is often limited. In some sense, the error due to the experimental setup $\delta_{D\,setup}$ is the experimental counterpart to the model form error of the simulation $\delta_{S\,model}$. Roy and Oberkampf (2011) and Coleman and Steele (2009) agree that the objective of model validation is to estimate the model form uncertainty.

2 UQ During System Development

In large part, model validation commonly involves comparison of simulation results and measurement data. The added value of UQ changes with the system development phase and the availability of measurement data for model validation purposes.

Figure 2-1: Typical A/C system development phases.

In early phases, i.e. conceptual and preliminary design, measurement data are scarce and UQ is the main means to gain an understanding of the credibility of a simulation model. As system development continues, the availability of measurement data increases – starting with measurement data for separate equipment or smaller subsystems, on to test rig data, and in later phases flight test data.

Even though later phases enable model validation against measurement data, it is often difficult to obtain satisfactory coverage of the *validation domain*, or *domain of applicability*. See e.g. Hemez et al. (2010) for an illustrative description of a model with a domain of applicability spanned by two parameters. In such cases UQ is a useful support also in later development phases.

It should be noted that for some models, to actually define the validation domain might be a problem in itself. Another problem is how to visualize the validation domain, as well as the coverage and the goodness-of-fit throughout the validation domain when the validation domain is spanned by multiple parameters. This is the case for the Environmental Control System (ECS) used as an industrial application example.

3 Method for UQ

Roy and Oberkampf (2011) describe a comprehensive framework for UQ as a six-step procedure. The framework is described in detail and includes an application example, which makes it suitable as reference process in this paper. Briefly described, the six steps are as follows:

1. *Identify all sources of uncertainty:* Locate uncertainties in parameters, inputs, and boundary conditions.
2. *Characterize uncertainties:* Classify the identified uncertainties as either aleatory, epistemic, or a mixture. Assign precise DPFs for the aleatory uncertainties, intervals for the epistemic uncertainties, and imprecise PDFs for the mixed type of uncertainties. *Imprecise* here refers to when the parameters of the PDF, for example the mean and standard deviation, are given as intervals or PDFs themselves.
3. *Estimate uncertainty due to numerical approximations:* Use for example post-processing based methods such as Richardson extrapolation to estimate numerical uncertainty of all model outputs.
4. *Propagate input uncertainties through the model:* As aleatory and epistemic uncertainties are two different types, it is recommended to use Probability Bounds Analysis (PBA) to treat them independently. Briefly described, the interval of the epistemic input is divided into a number of sub-intervals, and for each sub-interval of each epistemic input a complete propagation of aleatory inputs is carried out, typically with Monte Carlo sampling based techniques. The result is one Cumulative Distribution Function (CDF) for each epistemic sub-interval. The complete set of CDFs for a model output is referred to as a probability box, or a *p*-box.
5. *Estimate model form uncertainty:* Use a well-defined validation metric to compare model output with measurement data. In this framework, the measurement data for a specific system characteristic as well as the corresponding model output are described as two CDFs.

6. *Determine total uncertainty in the model outputs:* To the *p*-box generated from the uncertainty propagation, add the model form uncertainty and the numerical uncertainty as epistemic uncertainties.

4 Industrial Application Example

A detailed Modelica model of the Gripen C/D Environmental Control System (ECS) is used as an application example of realistic industrial size. The main purpose of the ECS is to provide sufficient cooling of the avionics equipment, as well as tempering and pressurizing the cabin. In addition to this, essential tasks are to enable pressurization of the fuel system and anti-g system, and to provide conditioned air to the On-Board Oxygen Generating System (OBOGS), which provides breathing air to the pilots. Briefly, this is achieved by means of a bootstrap configuration using engine bleed air which is decreased in pressure and temperature and dried prior to distribution. The main H/W components in the ECS are heat exchangers, compressor, turbine, water separator, pipes, and control valves. The ECS S/W, which is physically located in the General systems Electronic Control Unit (GECU), controls and monitors pressure, temperature, and flow levels in various parts of the system.

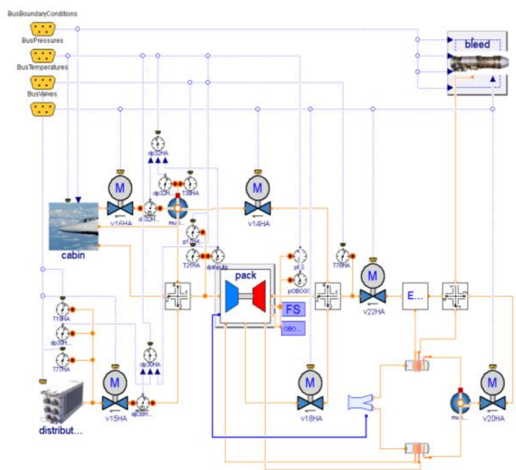

Figure 4-1: A graphical overview of the ECS H/W model.

The model is mainly used for:

- Concept studies
- Detailed equipment specifications
- Control system design
- Performance analysis
- Incident analyses
- System safety analyses
- Computation of loads

The model is developed in the modeling and simulation tool Dymola using the modeling language Modelica (Dymola 2013, Modelica 2013). A system equipment component library for aircrafts is used. The component parameters are based on information from drawings, vendor sheets, bench test measurement data, and experience. The control code integrated in the Modelica model is C-code automatically generated from a Simulink control code specification.

5 Effort Estimations of UQ

The intention of this section is to make an estimation of the effort required to carry out (as far as possible) each step in the methodology described in section 3 on the ECS model. The following sub-sections describe each step from a practical viewpoint including estimations of work effort.

Figure 5-1 shows a typical layout of a closed-loop model of a specific aircraft vehicle system. System S/W and ECU H/W denote system-specific software and hardware placed in an Electronic Control Unit, and are typically modeled in Simulink. System H/W is a model of the physical system, typically developed in Modelica using Dymola. BC denotes boundary conditions in terms of for example flight case and climate profile, and the gray-dashed arrows indicate communication with other systems.

The UQ dealt with in this paper is performed on the red-dashed part of the closed-loop model. That is, the models of ECS S/W and GECU H/W are seen as specifications (with possible errors or “bugs”) rather than descriptive models subject to uncertainty (Andersson 2009). However, to obtain interpretable results, the full closed-loop model is used when propagating uncertainties during the UQ.

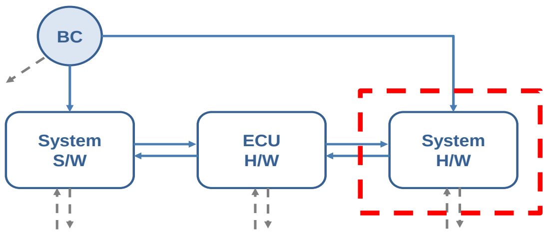

Figure 5-1: Typical layout of an aircraft vehicle system closed-loop model. UQ delimited to ECS H/W model.

A prerequisite for the UQ is that the current development phase is preliminary design or early detailed design. In this phase, there is typically rig test data available to some extent, while flight test data is unavailable or very limited.

Another prerequisite is that model verification is already performed as a continuous part of the model development, i.e. the effort estimation of the UQ does not include typical verification tasks. This means that all nominal parameter values are verified against supporting documentation, which is also referred to and available. Without this verification having been performed and documented, the step “Identify all sources of uncertainty” will be much more time-consuming than assumed below.

Informal model validation against available test rig data is assumed to be performed. The purpose of the informal model validation is to check that nominal simulation results are reasonable. The purpose of the following UQ is to increase the understanding of the uncertainties embedded in the model, and how these affect simulation results. In other words, the purpose of the UQ is to go from nominal simulation results to simulation results with an estimated uncertainty.

The UQ performer is assumed to be a person in close relationship with the people who performed all the above mentioned requisite activities but the UQ performer did not actually participate. This person has adequate knowledge of tools and some knowledge of the component library. His or her ECS system knowledge and professional skills are assumed to be on a senior level although he or she has not performed any UQ analysis on a large system model. The following sub-sections follow the structure of section 3.

5.1 Identify all sources of uncertainty

By categorizing all model parameters and inputs as either certain or uncertain the workload downstream the process can be reduced. Which of the parameters and inputs are certain or uncertain, respectively, is preferably and pragmatically decided through experience. Concerning parameters, this work is straightforward, e.g. a pipe diameter is easy to find and has a high manufacturing accuracy compared to a pump performance that can differ between pumps and as a function of wear. The categorization of inputs is trickier. For example, an ECS model may have engine bleed temperature and pressure as input via an engine model. If the simulation results are presented in the context of engine bleed data, the engine bleed data can obviously be categorized as certain inputs. On the other hand, if the engine bleed data is a consequence of flight case specified by inputs such as Mach, altitude, and thrust to an engine model and presented in the context of the flight case, the uncertainties in the engine model must be considered and the engine bleed data should consequently be treated as uncertain inputs.

The estimation of work effort required for the UQ is based on the following categorization of parameters and input signals. The list includes number of parameters or input signals representative of the ECS H/W model described in section 4.

A) Geometry parameters considered certain (e.g. pipe diameter): 92
B) Geometry parameter considered uncertain (e.g. hose length or pipe surface roughness): 76
C) Physical parameters considered certain (e.g. pressure loss coefficient of simple pipe bend): 31

D) Physical parameters considered uncertain (e.g. participating thermal mass or pressure loss coefficient of complex geometry): 196
E) Input signal considered certain (e.g. one-seater or two-seater): 7
F) Input signal considered uncertain (e.g. engine bleed pressure): 4

Naturally, the effort of identifying and categorizing parameters and input signals is dependent on the model's size. Currently, Dymola provides information about the total number of parameters in a model, but does not provide support for categorization. This step therefore requires some manual work possibly supported by scripting. For the ECS H/W model, the effort involved in this step is estimated to be 16 hours.

5.2 Characterize uncertainties

This step concerns characterization of the uncertainties of parameters and input signals in categories B), D), and F) from the previous section. Categorization begins with defining parameters and inputs as either epistemic, aleatory, or a mixture of the two. Supporting information like data sheets, drawings, CAD-models, or bench test data is used to assign intervals, PDFs or imprecise PDFs.

A rough, experience-based estimate of the time needed to characterize each parameter type is given below. Fully representative estimates cannot be obtained without performing the actual characterization, which is beyond the scope of this paper. The estimates are however believed to give a reasonably good indication of the total work effort required.

Category	**Number**	**Time/par. [hours]**	**Time total [hours]**	**Comment**
B) Geometry parameter considered uncertain	76	6	456	4 hours for obtaining necessary information, e.g. from installation drawing, CAD-model, or repeated measurements on several equipment individuals. 2 hours for characterization of interval or PDF.
D) Physical parameter considered uncertain				
D-1) Information available	117	10	1170	8 hours for obtaining necessary information, e.g. from existing bench test measurement data or assessment using basic physics. 2 hours for characterization of interval or PDF.
D-2) New bench testing or CFD simulations required	79	22	1738	80 hours for conducting new bench tests or new CFD-simulations. However, significant synergies are obtained by for example coordination of physical testing. The estimation is therefore reduced to 20 hours. 2 hours for characterization of interval or PDF.
F) Input signal considered uncertain	4	8	32	6 hours for obtaining necessary information from e.g. model description of connected models or assessment by applicable domain expert. 2 hours for characterization of interval or PDF.

Table 5-2: Typical layout of an aircraft vehicle system closed-loop model. UQ delimited to ECS H/W model.

To simplify the estimation, it is assumed that uncertainties in geometry parameters are related to tolerances in production and assembly and thus dominated by a stochastic behavior. The geometry parameters are therefore treated as aleatory and are assigned PDFs. It is assumed that uncertainties in physical parameters and input signals are mainly due to limited knowledge, and are therefore treated as epistemic and assigned intervals. In reality, most uncertainties in the model are a mix of aleatory and epistemic behavior and according to section 3 should be assigned imprecise PDFs. However, this implies additional complexity to an already complicated UQ and is not deemed a feasible approach for the type of model used in this paper. All in all, we have 76 aleatory uncertainties and 200 epistemic uncertainties.

Since an input can differ from one simulation to another (unlike the model parameters), its accuracy may also differ. As with the engine bleed pressure which varies with boundary conditions in terms of altitude, Mach, Power Lever Angle (PLA), and climate profile, the *uncertainty* of the engine bleed pressure may also vary. To ease the workload in this phase, a reasonable simplification is to assume that the input uncertainties are constant rather than functions of inputs/boundary conditions.

5.3 Estimate uncertainty due to numerical approximations

As long as the solver tolerances are sufficiently strictly chosen, the effect of numerical approximations are normally marginal for this type of simulation model and are therefore typically ignored. This is also what has been done for the ECS H/W model; an assessment using different solvers (Dassl and Radau) and varying tolerances ($1\cdot10^{-6}$ to $1\cdot10^{-4}$) shows maximum deviations in the investigated temperature, pressure, and mass flow levels of 0.04°C, 0.39 kPa, and 0.002 kg/s, respectively. This indicates that the numerical errors are insignificant compared to other simulation result uncertainties for the model under study. In addition to comparing a set of model outputs for varying solver tolerances, a good indicator in this type of model is to check that conservation of mass and energy is fulfilled for a set of connection points or branches in the model.

For the ECS model, the effort involved in this step is estimated to be 4 hours.

5.4 Propagate input uncertainties through the model

The uncertainty propagation methods applicable for the type of model used are Monte Carlo based sampling techniques. To decrease the number of simulation runs needed, Latin Hypercube Sampling (LHS) is used instead of brute force Monte Carlo sampling.

Due to the physical relations embedded in the model, it may well be the case that uncertainties in the simulation results vary throughout the validation domain. Due to the multidimensionality of the validation domain of the ECS H/W model, complete coverage is practically impossible. In this effort estimation it is assumed that *one* compressed flight mission covering the main parts of the flight envelope (Mach, altitude) for *one* climate profile with *one* fixed relative air humidity is analyzed. Later on, only the one-seater A/C configuration is considered. The flight mission is constructed in such a way that uncertainties at both steady-state levels and transients are considered. Steady-state levels are obtained by keeping Mach and altitude constant during a specified time interval, and transients are obtained by positive and negative changes in Mach, altitude, and Power Lever Angle (PLA). The compressed flight mission used in the uncertainty propagation is 5 minutes real-time, which for the model under study means approximately 8 minutes execution time.

Purely epistemic uncertainties have no structure over the uncertainty interval, i.e. there are no PDFs, and the only values considered known are the limits of the interval. In line with this, Roy and Oberkampf (2011) propose LHS with at least three samples for each epistemic uncertainty. In addition to this, for *each* combination of epistemic uncertainties, the aleatory uncertainties are sampled using a number of Monte Carlo samples. This implies nested sampling, with an outer LHS loop for the epistemic uncertainties and an inner Monte Carlo loop for the aleatory uncertainties. For m epistemic uncertainties with l LHS intervals and s inner loop samples, the total number of samples n is computed as:

$$n = m^l \cdot s \tag{5.1}$$

With, say, as few as 100 inner loop samples, the total number of samples for the ECS model would be $8\cdot10^8$. That is, $8\cdot10^8$ simulations of 8 minutes each, which certainly confirms the conclusion drawn by Roy and Oberkampf

(2011) that *"for more than a handful of epistemic uncertainties, the total number of samples required for convergence becomes extraordinarily large, and other approaches should be considered"*.

An alternative approach is to lump aleatory and epistemic uncertainties together in one single sampling scheme, preferably using a sampling technique more efficient than brute force Monte Carlo, e.g. LHS. This requires deviations from the above methodology in terms of also assigning PDFs to the epistemic uncertainties. Since the true nature of the parameters earlier classified as epistemic probably is a mix of aleatory and epistemic, assigning uniform PDFs may be seen as a middle road.

As described in Carlsson et al. (2012), LHS using 250 intervals proved to provide reasonable output distributions for a simulation model with 10 uniformly uncertain inputs, i.e. 25 simulation runs per parameter. Using this number for the ECS model results in $297 \cdot 25 = 7425$ simulation runs. This number is not scientifically justified but may still provide practical guidance as to what sample size to expect. With 8 minutes per simulation run this implies 990 hours (41 days) execution time (using one CPU). The actual work effort involved in this step is estimated to be 40 hours, consisting mainly of setting up a framework for LHS and results post-processing.

5.5 Estimate model form uncertainty

Two major contributors to model form uncertainty are simplifications in the model and in the components' underlying equations. The two contributions are much the same thing but on different scales. For example, the component's equations cannot represent the domain of interest, e.g. can handle turbulent but not laminar flow, or may be used in the domain of interest but with low accuracy. On model level, the components' equations correspond to system functions/parts not modeled or, for example, lumped together.

Due to the incompleteness of the measurement data, consisting of poor coverage in the flight envelope, few tests in the same test point, tests performed by a system rig or bench test and sometimes with immature prototype system equipment, a compilation of CDFs according to step 5 in section 3 is not feasible. What can be done is the following.

First of all, the question *"Has the components' equations capability to describe the physical phenomena of interest?"* must be asked. For example, if a valve component lacks an equation for chocked condition, then it is not of any interest to quantify the model form accuracy for simulation results including large pressure ratio between valve inlet and outlet. The components used for the ECS model are a mix of standard Modelica components and a commercial component library developed for aircraft fluid systems. The standard Dymola components are assumed not to contribute to the model form accuracy since they are often of a mathematical and logical nature, e.g. tables, gains, and switches without "physical behavior" equations. In our case, the commercial component library documentation will support the phase "Estimate model form uncertainty". What then remains is to analyze the underlying physical equations in the components concerning their contribution to the model form, e.g. to what extent heat transfer coefficients are described and in which regions they are valid.

Circumstances that may complicate the analysis are whether some components' code is IPR-protected and therefore not accessible. Component equations can also be difficult to find if inheritance technique has been used intensively for the component structure. The ECS model contains 16 different component types assumed to be relevant for this step, sensors and mathematical components excluded. For each component it is assumed that 3 days are needed to find documentation, read, understand model code, evaluate by simulating components, and finally document the result. For the ECS model, the effort is estimated to be $16 \cdot 8 \cdot 3 = 384$ hours, which is rounded down to 350 hours since some synergies are assumed to exist.

The lack of suitable measurement data in early phases makes it hard to estimate the uncertainty originating from model simplifications. A manageable strategy for the ECS model is to estimate the uncertainty with the help of experience based on other more mature models. For the ECS model, the effort is estimated to be 40 hours to read model documentation and compare it to the real system layout, and another 40 hours for comparison, via documentation and interviews, with other models; 40 + 40 = 80 hours.

For the ECS model, the effort involved in this step is estimated to be 350 + 80 = 430 hours. This type of analysis and experience can at best lead to reasoning that the model form uncertainty is probably lower/higher relative to the effects of parameters and inputs.

5.6 Determine total uncertainty in the model outputs

Once the earlier steps have been carried out, this final step mostly involves compilation of results, visualization, and documentation. For the ECS model, the work effort involved in the final step is estimated to be 40 hours.

5.7 Total workload for the UQ framework

The estimations in steps 1 to 6 are summarized in the table below.

Step	**Engineering workload [hours]**	**Machine execution time [hours]**
1) Identification	16	N/A
2) Characterization	3396	N/A
3) Numerical approx.	4	N/A
4) Propagation	40	990
5) Model form	430	N/A
6) Total uncertainty	40	N/A
Total:	**3926**	**990**

Table 5-3: Summary of estimated work effort.

As can be seen from the table, a comprehensive UQ of a detailed simulation model is time-consuming and human-/skill-intensive. Naturally, there is an uncertainty in the estimation but the workload is not believed to be overestimated. The total workload is primarily dominated by the step *characterize uncertainties*, followed by *estimate model form uncertainty*.

The uncertainty propagation is demanding when it comes to computational resources. The time required can however be shortened by distributing a number of batch simulations over several machines. That is, the 990 hours of execution time for the uncertainty propagation can be significantly reduced.

6 Simplifications Enabling UQ of Large A/C System Simulation Models

With time and budget constraints typical for A/C development programs, the figures presented in section 5.7 are not acceptable. That is, for a UQ to be carried out, the workload has to be significantly reduced. If not, the resources are surely seen to be better spent on activities other than UQ. Also, if numbers of this magnitude are included in the estimation of model development time, there is a risk that needed early sponsors of the model will never spend resources on model-based system development and consequently no model will be developed.

As a comparison, the total time for development, verification, and steady-state validation of the ECS model was approximately 2000 hours. Adding around 4000 hours for UQ alone cannot be considered realistic. Furthermore, the UQ should be updated when new measurement data is available or if the model or the component library is updated. Therefore, the intention of this section is to discuss simplifications, compromises, and methods to ease the UQ workload.

The estimation performed is representative of a comprehensive UQ. However, a number of simplifications are already performed:

1) Geometry parameters and physical parameters are treated as purely aleatory and purely epistemic, respectively. The more realistic mix of aleatory and epistemic behavior is not considered.
2) Uncertainties in inputs and parameters are treated as constant PDFs or intervals,

and not as functions of other inputs or boundary conditions.
3) Minimalistic assessment of uncertainty due to numerical approximations.
4) Uncertainty propagation is performed using single loop LHS instead of nested sampling with strict separation of aleatory and epistemic uncertainties.
5) Model form uncertainty is assessed by analysis of underlying equations rather than extensive validation against measurement data.

In addition to the above, two main measures for reducing the workload are to reduce the number of parameters considered uncertain and to simplify the characterization of uncertainties. These two measures are treated in the subsections below.

6.1 Reducing the number of uncertain parameters

This fundamental measure reduces the workload in both characterization and propagation, and may be done using local sensitivity analysis and/or experience. As an example, for the ECS model experience tells us that production tolerances causing aleatory uncertainty in geometry parameters such as pipe diameter can be safely ignored. Uncertainties in for example efficiency characteristics of compressor, turbine, and heat exchangers are significantly larger. Regarding local sensitivity analysis and how it may be applied in the context of aircraft vehicle system models, see Steinkellner (2011).

An alternative method for reducing the number of parameters considered uncertain is *output uncertainty* (Carlsson 2013). Briefly described, each component in a model, e.g. a compressor, a pipe, or a heat exchanger, is typically validated against some available data. The result from this low-level validation is information concerning component-level uncertainty. In the output uncertainty method, this information is integrated directly into the components. The uncertainties in a component's original parameters are aggregated and expressed in a smaller set of uncertainty parameters. In this way, the level of abstraction is raised from uncertainty of component input parameters to uncertainty of component output characteristics. It should be noted that the output uncertainty for each component may include not only parameter uncertainty but also estimations of model form uncertainty.

6.2 Simplify characterization of uncertainties

As seen in section 5, the characterization of uncertainties is a main contributor to the total UQ workload. Therefore, in addition to reducing the number of uncertain parameters, it is beneficial to simplify the characterization itself as far as possible. An approach that is reasonable for the ECS model is to abandon the use of PDFs of several different types and instead consistently use uniform distributions throughout the UQ – or even simpler, only use intervals with upper and lower bounds. Naturally, while this approach results in a less precise UQ, it is more worthwhile to make an approximate UQ than no UQ at all.

7 Conclusions

Uncertainty Quantification (UQ) is commonly seen as a value adding activity that increases the credibility of a simulation model. However, analysis of industrial applicability and estimations of the UQ workload are rare. This work has shown that a comprehensive but not excessive UQ of a large aircraft system simulation model may be very time-consuming. The UQ workload of the ECS model is estimated to be twice the time for the model development, verification, and steady-state validation.

As a comparison, our gut feeling of what a model sponsor may consider affordable in terms of UQ workload is, say, 10% relative to the sum of model development, verification, and steady-state validation. Furthermore, UQ does not have all the answers. Questions such as *"How uncertain is UQ?"* can always be asked. Will the system design be better and sounder and will we become wiser with much more UQ data? It should not be forgotten that even with poor or unknown accuracy of the simulation results, models are useful for many activities during the development phase.

To find a way forward, simplifications, compromises, and methods to ease the UQ workload have been discussed in this paper. Without adding too much uncertainty to the UQ, a number of simplifications are available. The most significant measures proposed in this paper concerns reducing the number of uncertain parameters, simplifying the characterization of uncertainties, and simplifying the uncertainty propagation. All in all, these simplifications make UQ of large aircraft system simulation models more feasible.

Despite the proposed simplifications, a comprehensive UQ will remain a significant part of the model development budget. However, if the UQ implies that a physical system-level test rig is no longer necessary or can be significantly simplified, a large UQ workload can motivated.

Finally, the NASA Standard for Models and Simulations describes factors that affect the credibility of the results, i.e. how useful they are (NASA 2008). In this case, “Result uncertainty” is only one of eight factors. “M&S management” and “People qualification” may be mentioned as two other factors. In other words, although a UQ is carried out in detail with high quality, it is still a fact that if the simulations that will be a basis for design decisions have been carried out with poor configuration management of the model and its inputs and by inexperienced personnel, the risk of large uncertainties and even errors in simulation results is high. A balance of available funds between the various factors that affect the credibility of the simulation result is desirable.

Acknowledgements

The research leading to these results has received funding from Saab Aeronautics and the Swedish Government Agency VINNOVA’s National Aviation Engineering Research Programme (NFFP5 2010-01262).

References

Andersson, H. (2009), *Aircraft systems modeling, model based systems engineering in avionics design and aircraft simulation*, Tekn. Lic. Thesis No. 1394, Linköping University, Sweden.

Carlsson, M. (2013), *Methods for Early Model Validation – Applied on Simulation Models of Aircraft Vehicle Systems*, Tekn. Lic. Thesis No. 1591, Linköping University, Sweden.

Carlsson, M., Steinkellner, S., Gavel, H., Ölvander, J. (2012), ‘Utilizing Uncertainty Information in Early Model Validation’, *Proceedings of the AIAA Modeling and Simulation Technologies Conference*, Minneapolis, MN, USA.

Coleman, H. W., Steele, W. G. (2009), *Experimentation, Validation, and Uncertainty Analysis for Engineers*, 3rd ed., John Wiley & Sons, Hoboken, NJ, USA.

Dymola (2013), http://www.3ds.com/se/products/catia/portfolio/dymola

Hemez, F., Atamturktur, H., S., Unal, C. (2010), ‘Defining predictive maturity for validated numerical simulations’, *Computers and Structures*, 88: 497-505

Modelica (2013), https://www.modelica.org

NASA (2008), *Standard for Models and Simulations*, NASA-STD-7009, National Aeronautics and Space Administration, Washington, DC 20546-0001, USA.

Oberkampf, W. L., Roy, C. J., (2012), *Verification and Validation in Scientific Computing*, Cambridge University Press, Cambridge, UK.

Oberkampf, W. L., Trucano, T. G., Hirsch, C., (2003), *Verification, Validation, and Predictive Capability in Computational Engineering and Physics*, SAND2003-3769, Sandia National Laboratories, Albuquerque, New Mexico 87185 and Livermore, California 94550, USA.

Padulo, M. (2009), Computational Engineering Design Under Uncertainty – An aircraft conceptual design perspective, PhD diss., Cranfield University: 127-144.

Roy, C. J., Oberkampf, W. L. (2011), ‘A comprehensive framework for verification, validation, and uncertainty quantification in scientific computing’, *Computer Methods in Applied Mechanics and Engineering*, 200: 2131-2144.

Steinkellner, S. (2011), *Aircraft Vehicle Systems Modeling and Simulation under Uncertainty*, Tekn. Lic. Thesis No. 1497, Linköping University, Sweden.

Process for Evaluation and Validation of Non-Original Components for Aircraft Hydraulic Systems

Jussi Aaltonen, Vänni Alarotu, Kari T. Koskinen
Department of Intelligent Hydraulics and Automation, Tampere University of Technology
PL 589, FI-33101 Tampere, Finland

Capt. Mika Siitonen
Finnish Air Force Materiel Command, Finland

Keywords: *Supplementary type certificate, Hydraulic system, Hydraulic Pump, Simulation*

Abstract

This paper presents an efficient evaluation and validation process which can be used to determine suitability of non-original components for aircraft systems in order to apply for the supplementary type certificate (STC).

In the process a non-original component is compared against the original one. Goal in the comparison is to prove that the non-original component has at least equal performance and safety and reliability characteristics than the original component has.

Key performance characteristics are usually well defined in aircraft's documentation or can otherwise be defined relatively easily. Also the testing of them is usually relatively straight forward process and can be carried out with test equipment used depot level maintenance. Usually also component testing procedures specified in depot level maintenance documentation can be applied.

Comparing safety and reliability characteristics of non-original and original component is however less straight forward task. There can be general component specifications available (such as MIL-specifications for military equipment of US origin) which define baseline requirements for these characteristics. Baseline however is definition of absolute minimum and there usually is no data available how much above it the original component lays. Comparison is most cost effectively made by comparing the safety and reliability performance of components in a life test which replicates the load spectrum of the real application as closely as possible or accelerated life test of some kind.

The complete evaluation and validation process is presented and discussed using the case of a twin engine aircraft hydraulic pump as an example. In this case the load spectrum of hydraulic pump is generated by extracting flight control system command data from real mission data and converting it to pump load spectrum using combined flight simulation and system simulation model. This load spectrum is then used as load spectrum in life testing of both original and non-original hydraulic pumps in a test rig.

1 Introduction

Components of aircraft systems go through long and thorough evaluation and validation procedures before they are approved and included in the initial aircraft design [1]. The type certificate, issued by the aviation regulating body to manufacture certifies that the initial aircraft design fulfills airworthiness requirements. All aircraft produced under this type certified design are then issued a standard airworthiness certificate. If the initial design is changed by the type certificate holder either a service bulletin (SB) is issued (minor changes) or amendment to type certificate is requested from regulating body (major changes). Any design changes or alterations to type certified aircraft made by other party than the type certificate holder, need an approved supplementary type certificate (STC).

Continuous airworthiness based on type certificate requires also usage of original spare- and replacement parts and rigorous following of maintenance programme and repair procedures specified by the manufacturer. Thus all deviations from these are typically issued under SBs. For these purposes STCs are typically needed due to the type certificate holder's refusal or other inability to meet aircraft operator's requirements. For STC typically similar validation and verification procedures are required than for type certificate.

STCs are often needed with aged and out-of-production aircraft types for conversions to new roles. Also application of non-original spare- and replacement parts or maintenance and repair procedures not specified in original documentation is usually considered needing a STC.

Evaluation and validation of non-original replacement and spare parts for applying the STC is in many cases even more complicated process than validation and evaluation of original parts because there usually is no certain knowledge on original design requirements and specifications available. Also component and system evaluation and validation programs followed with the original design usually are more or less unknown. To overcome these problems and also to keep all testing involved in evaluation and validation as simple and as cheap as possible a new systematic approach is needed.

2 Non-Original Component Evaluation and Validation Process

Process is divided into four distinct phases. Each phase acts as a prerequisite for the following phase and also produces information which supports making decision whether to continue to next phase. Process outline as a flowchart is shown in Figure 1.

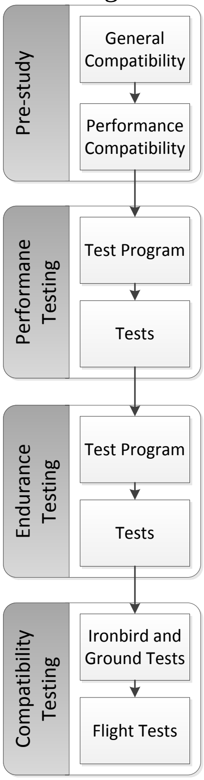

Figure 1 Evaluation process flowchart

Component evaluation begins with the pre-study phase which is followed by the performance testing. After performance is evaluated follows endurance or life testing. Final compatibility tests are first done either in ironbird environment or as ground testing and then followed by flight testing.

2.1 Pre-study Phase

Pre-study phase concentrates on verifying and evaluating component compatibility and performance on basis available documentation and experiences on the specific application and aircraft type.

General information, such dimensions, weight etc., and performance data of the non-original component are gathered from data supplied by manufacturer or by measuring from the actual component sample. In case the component is used in some other aircraft type and there is access to its technical documentation it is also possible to use them as an information source.

Requirements against which the non-original component is validated and verified are gathered from technical documentation of the specific aircraft type, general specification (such as MIL-specifications), standards and usage experiences.

In this phase it is important to notice that there is safety margins already incorporated in the performance of the original component and thus there usually is no need to apply safety margins again in this phase. However, if there is some specific short coming or flaw in the original component it must be carefully considered whether the requirements have been originally set too low or the original component just does not meet the requirements.

2.2 Performance Testing Phase

Performance testing consists of tests which evaluate and validate that the performance of the non-original component meets the requirements.

These tests can be simply the tests used in the depot level maintenance of the component. Test routinely done in depot level maintenance are typically well specified and explained the technical documentation and test benches are also usually readily available somewhere. It should however be noted that depot level maintenance tests do not always test all necessary performance criteria, but some aspects of component performance could have been considered always to be satisfactory if component has gone through some specific maintenance or repair.

In cases where there will be a significant change in component design, i.e. operation principle, materials etc., the test program must be carefully planned to guarantee all necessary performance criteria becomes thoroughly evaluated and validated.

2.3 Endurance Testing Phase

The purpose of endurance testing is to verify and validate the component endurance and life-time in the specific application. Ultimate goal is to prove that the reliability of the component is at least on the level of the original one and that it does not cause any flight safety risks. On the other hand testing also proves that components usable service life fits to maintenance schedule and targeted availability.

Planning of the endurance test program requires extensive and profound knowledge on the aircraft in question and its typical usage, i.e. mission profile, environmental conditions etc. One viable approach on planning these tests is to find out component stresses and loads during various flight operations either by measuring or by simulations. Test program and necessary tests can be then designed on the basis of stress and load data.

In some cases it might be possible to use some method of accelerated life testing with close to real load and stress spectrum to simulate complete component lifecycle or even run entire lifecycle in real-time in the endurance test with satisfying accuracy and reliability. Result of the accelerated test can be then compared to experiences on the original component in the specific aircraft.

In cases where this is not a possible approach a comparative test, where original on non-original component are compared against each other, must be planned. In the comparative test both components are run under same load and stress spectrums for specified time after which the wear and tear of them is measured in terms of for weight loss, change in dimensions of critical wear interfaces, changes in performance and efficiency etc.

2.4 Compatibility Testing Phase

Final actions towards airworthiness are taken in the compatibility testing phase. In this phase the component compatibility with aircraft systems is tested first by ground testing and finally by flight testing. Due to extensive bench testing prior to this phase ground testing can mainly concentrate on general systems and mechanical compatibility issues. After successful completion of ground tests it is possible to enter flight testing.

Planning the flight testing program must be done considering the lifecycle of the component in the specific usage. Typically it is not reasonable to plan flight testing to last for a component life cycle but it should be determined how long testing is needed to prove the modification reliably enough.

In cases where there is two identical components in aircraft and both of them run under same stresses and loads flight testing is best done by replacing only one of them with non-original component and observing wear and tear in them periodically during flight testing.

In cases where there is only one component or components run under different stresses and loads it is best to employ two aircrafts in testing. The non-original component is installed on most stressed and loaded point. During flight testing both aircrafts are used in same kind of missions for the same time and wear and tear in components is observed periodically.

3 CASE: Twin Engine Aircraft Hydraulic Pump

Case presented in this paper describes evaluation and validation process which targets on qualifying a non-original hydraulic pump to be used as a spare part alternative in a twin engine aircraft. Non-original pump originates to another aircraft of the same type and same manufacturer but which is targeted to different customer base. Thus it is designed to meet general aerospace specifications as well as manufacturer specific specifications but customer specific specifications may differ.

Comparison of available technical data and design specifications as well as weighting and measuring general dimensions proved that the non-original pump was very similar to the original one and there is no need for any additional design changes related to changing the hydraulic pump type.

3.1 Performance Testing

Basic performance characteristics of both pumps were compared by a set of tests where pumps were run at constant drive speed on maximum pressure in six different deliveries from zero to full delivery in a test bench. Supply and case drain pressures were kept constant during tests. Test bench used resembles very closely the one specified for pump depot level maintenance testing but test sets were designed to reveal out any fundamental differences critical to specific application. Parameters studied in tests were:

- Delivery flow
- Case drain flow
- Delivery pressure
- Case drain line pressure
- Supply pressure
- Drive torque
- Drive rotational speed
- Mechanical vibrations in the direction of the pump axis

Dynamic characteristics of pumps and their regulators were studied in second test set by inducing fast flow demand changes of variable magnitude (both increasing and decreasing) with fast response on/off-valves.

As a result of the first test set basic performance characteristics such as could be compared:

- Pump efficiencies
- Controller operation curves
- Delivery and drain flow rates
- Level of delivery pressure pulsation

Generally detecting pressure pulsation generated by hydraulic pump accurately is relatively complicated task since dynamics of pressure line tend to effect on results. In this case so-called secondary source method was used to measure the pressure ripple [2]. Minimum supply pressure of the pump is also a very important characteristic for this application. It was however decided that it will be tested in later stage of the process due to the fact testing it inevitably causes damage to pump which could not be afforded before endurance testing phase.

Second test set enables comparing:

- Controller operating curve (pressure as a function of flow rate)
- Step response
- Case drain flow dynamics

Figure 2 shows basic performance characteristics of both pumps as percentages of nominal values of the original pump. Example test response to 50% - 0 - 50% flow demand change is shown in Figure 3.

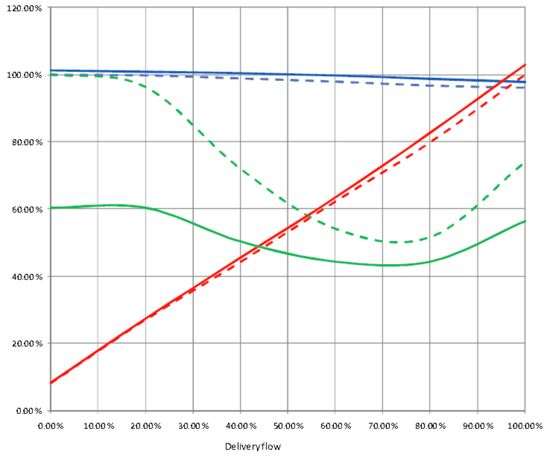

Figure 2 Basic performance characteristics (dotted line – original, solid line – non-original). Blue – pressure, red – drive torque, green – drain flow.

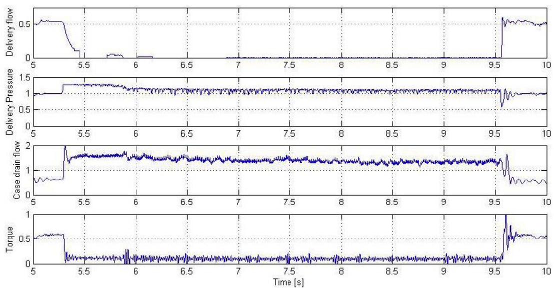

Figure 3 Example step response of the non-original pump

3.2 Endurance Testing

Hydraulic pump lifetime in real application is far too long to be reasonable to be replicated in laboratory tests and on the other hand hydraulic pump is too complicated piece of machinery to undergo any kind of accelerated life test with satisfying reliability. Even though overhaul cycle of the pump could be reached also in the laboratory and there naturally are a lot of experiences on the condition of the original pump when it enters overhaul there is no possibilities to replicate same service cycle to the non-original pump in laboratory so that comparable results would be possible. Therefore it was decided that endurance test will comparative test where both pumps undergo same test program.

Generation of the load spectrum for endurance test begun with extensive simulations using combined hydraulic system and flight simulation model to find out operating points where the load for the hydraulic system and particularly for the pump is the harshest [3]. Simulations indicated, as could be expected, that the harshest load spectrums could be found during dog fight and aerobatic manoeuvring. Load spectrum finally used in the test was generated by extracting flight control system commands related to continuous 8 min aerobatic manoeuvring from real mission data and running them through the simulation model to translate them to corresponding hydraulic system flow demands. Endurance test used this load spectrum as a continuous loop. Length of test was set either to hydraulic pump service interval, or to malfunction or failure.

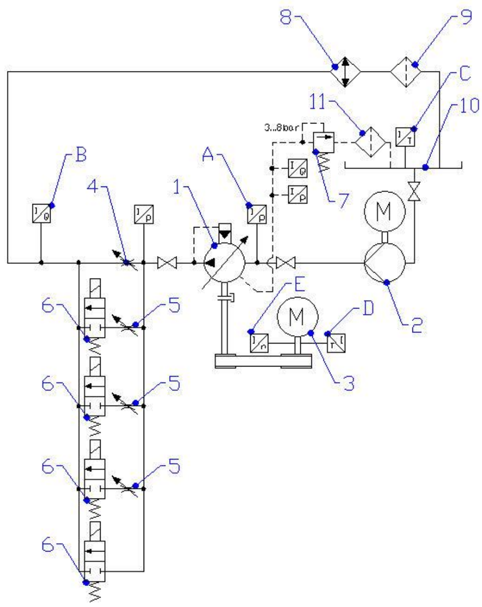

Figure 4 Hydraulic diagram of the test bench

A special test bench was manufactured for endurance testing phase. Hydraulic diagram of the bench is shown in Figure 4. Main components of the bench are frequency converter driven electric motor (3), supply pressure pump (2), digital flow control unit (5,6) and the pump itself (1). The goal in designing the bench was to create a pump test environment which can resemble real operating conditions as closely as possible. Test bench control and data acquisition system consisted of two separate programmable logic controllers and a pc-computer to guarantee reliability in prolonged operation without immediate human supervision.

Goal of the endurance test was to find out if there is a significant difference in between the reliability and life time of pumps and if there is any differences in how their performance evolves during long usage time in harsh conditions. Also the minimum supply pressure tests were incorporated in this test since load spectrum naturally included several points in every cycle where supply pressure drops down to zero. Thus it is possible to investigate behaviour on low supply pressure in these points. Other parameters investigated in this test are related to wear on critical wear surfaces measured as weight loss during the test and change in overall performance measured as efficiency.

Due to harshness of load spectrum used neither of pumps reached full time but tests ended prematurely to minor failure (leakage) in both cases.

Error! Reference source not found. shows, as an example, volumetric and mechanical efficiencies of non-original pump during the first 450 test hours.

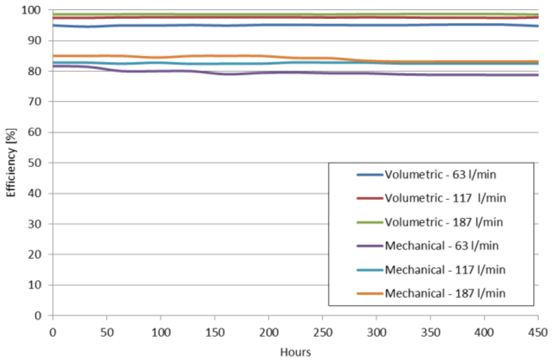

Figure 5 Volumetric and mechanical efficiency of the non-original pump during the first 450 h of endurance test

An example of the supply pressure curve (delivery flow as a function of pump supply pressure) is shown in **Error! Reference source not found.**.

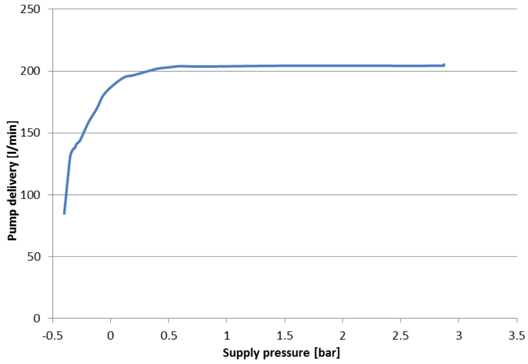

Figure 6 Supply pressure curve of the original pump

3.3 Final Steps towards Airworthiness

After successful completion of endurance testing phase follows the final compatibility testing. It is planned to begin with short ground test program which consists of tests sets known to put hydraulic pump into operating points where extensive controller vibrations and other adverse effects are likely to occur [4]. There will be two separate ground tests in which non-original pump is tested in both aircraft's hydraulic systems.

If ground tests are succesfully completed follows two sets of flight testing. In these test sets non-original pump will be tested in both hydraulic systems so that in another system there is the original pump.

These final steps are however yet to be taken, but they will be taken in very near future. Upon completion of the process the non-original pump will be qualified to be used as a spare part in combination with the original one.

4 Conclusions

The evaluation and validation process has been developed and it has proven to be effective in the terms of costs and time as well as producing information for decision making support.

It is noted that even though this process is cost effective and straight forward it still requires extensive expertise on the specific aircraft type and aircraft systems and components in general. Also the importance of experience base and research data gained in earlier systematic research programs cannot be overlooked since developing for example advanced simulation models is hardly justified for the sole purpose of a single spare part evaluation and validation.

References

[1] I. Moir ja A. Seabridge, Aircraft Systems: Mechanical, Electrical and Avionics Subsystems Integration, Reston, Virginia: American Institute of Aeronautics and Astronautics, 2001, p. 344.

[2] N. Johnston ja K. Edge, ”The ‘secondary source’ method for the measurement of pump pressure ripple characteristics Part 1 : description of method,” *Proceedings of the Institution of Mechanical Engineers, Part A:Journal of Power and Energy,* p. 8, 1990.

[3] J.-P. Hietala, J. Aaltonen, K. T. Koskinen ja M. Vilenius, ”Aircraft hydraulic system model integration to fligh simulation model,” *The Twelfth Scandinavian International Conference on Fluid Power, SICFP'11*, Tampere, 2011.

[4] J. Aaltonen, K. T. Koskinen ja M. Vilenius, ”Pump supply pressure fluctuations in the semi-closed hydraulic circuit with bootstrap type reservoir,” *The Tenth Scandinavian International Conference on Fluid Power, SICFP'07* , Tampere, 2007.

PRESAGE: VIRTUAL TESTING PLATFORM APPLICATION TO THRUST REVERSER ACTUATION SYSTEM

RODOLPHE DENIS
AIRCELLE, France

ACHOUR DEBIANE, JULIEN DACLAT
CERTIA, France

GENEVIEVE DAUPHIN-TANGUY
EC-LILLE, France

JEAN-CHARLES MARE
INSA-TOULOUSE, France

- *Virtual platform & Virtual testing*
- *Electrical actuation system*
- *Modeling and simulation*
- *Mechatronic*
- *Thrust reverser*

Abstract

The purpose of this article is to demonstrate the interest and the need to rely on modeling and simulation of mechatronic systems in case of testing application and to contribute to the "democratization" of the use of models and "virtual testing".

Indeed, the systems are becoming increasingly complex: more dynamic, more optimized. Add for that the development schedules are more and more restricted with reduced budgets. These constraints which are antagonistic tend to emerge a new generation of designing and testing: the "virtual test platform".

We propose industrial methods and appropriate tools to develop this virtual test platform.

It is with this objective that CERTIA (Provider of test benches and studies) and the company AIRCELLE (designer and integrator of nacelles), with significant experience in their respective fields, have developed the platform "PRESAGE" for virtual testing in collaboration with academic partners such as Ecole Centrale de Lille, INSA Toulouse and ESIGELEC Rouen.

1 Introduction and background

It is now established that world of new equipment and systems design and world of tests means technologies both evolve towards more innovation and more specificity to electrical systems.

However, these steps forward associated with more electric systems induce several difficulties such as:

- The increase in complexity of the power system,
- New thermal-mechanical coupling,
- Interaction between electromechanical system and flexible structure.

- The difficulty to establish a global optimization process and build bridges over the multiplicity of softwares in specific fields.

As a consequence, it is necessary to find palliative improvements in terms of cost concepts and of new processes to perform tests.

The virtual testing platform is clearly identified as the future evolution of testing means, integrating HIL & SIL concepts.

This platform allows virtual test benches to be reusable and reconfigurable.

2 PRESAGE Platform

The design of new equipment and complex systems, particularly in the field of tests resources, are evolving towards more and more innovative technologies. The integration of concepts such as HIL (Hardware In the Loop) and SIL (Software In the Loop) is clearly identified as a way to reduce the costs of test bench manufacturing, integration, monitoring and maintenance. In this context, the "virtualization" of design cycles and tests platforms is a key factor to satisfy the existing constraints in the long term. Testing platforms that we propose to develop and integrate in the industry are based on the following concepts:

- ✓ Platforms for testing HIL / SIL;
- ✓ Reduction of the resources in testing laboratories;
- ✓ Transfer of activities to the engineering services;
- ✓ Reusable and reconfigurable test bench.

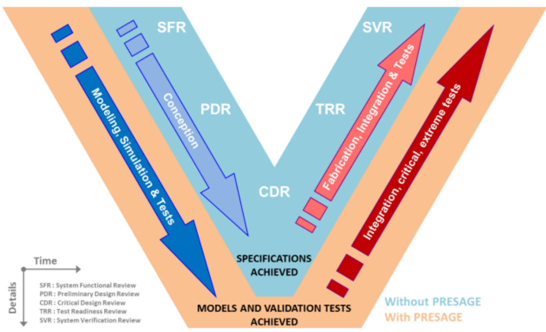

Fig. 1 V-cycle production process with/without PRESAGE.

The advantage of this approach is no longer working on a product but on a process which describes methods of integrating new types of test equipment in civilian or defense area.

The main objective of PRESAGE is to develop a modular and virtual test bench platform, in order to simulate the test scenarios required for the validation and verification of the complex systems behaviors and prepare the final system integration in the real environment.

3 PRESAGE Application case

In the context of thrust reverser electrical actuation system development for aircraft engine, the verification and validation process induces the development of specific test bench means to validate system behavior in operational conditions.

As a consequence, PRESAGE platform was used as a virtual test bench to model and virtually test an electrical thrust reverser actuation system coupled with a two doors thrust reverser structure.

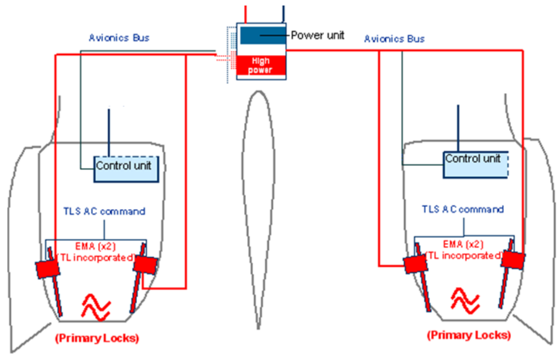

Fig. 2 Integrated electrical T/R actuation system architecture.

A schematic representation of electrical thrust reverser actuation system integrated in aircraft configuration is provided in Fig. 2.

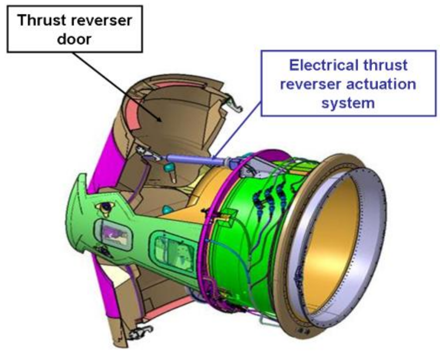

Fig. 3 Integrated T/R actuation system in aircraft environment.

Two configurations in terms of system integration are considered:

- ✓ Thrust reverser actuation system integrated in aircraft environment
- ✓ Thrust reverser actuation system integrated in tests bench environment

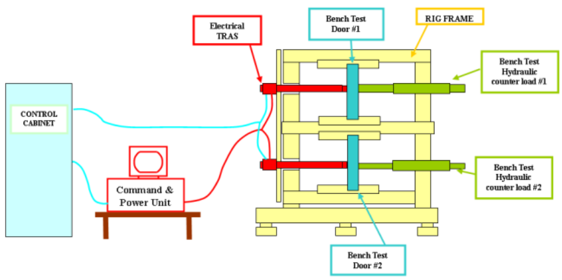

Fig. 4 Integrated T/R actuation system in bench test environment.

The approach is to ensure that test bench is representative of the aircraft environment through PRESAGE platform as explained on Fig. 5.

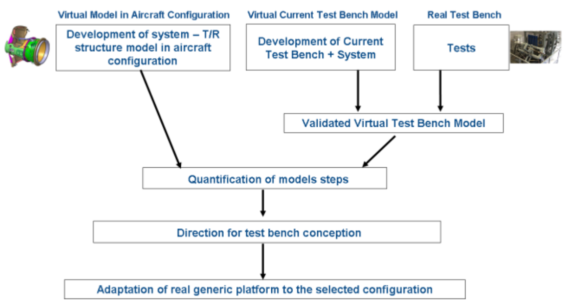

Fig. 5 PRESAGE Application case approach.

A validated virtual test bench platform, representative of aircraft environment, leads to pre-validate actuation system and coupled flexible T/R structure behaviors.

Moreover, PRESAGE virtual platform ensures the observation of several variables which are not accessible on real bench tests and lead to consider failure cases without risk of system deterioration.

3.1 T/R actuation system

The electrical T/R actuation system is defined by:

- Two innovative electromechanical actuators integrating an electrical motor, a brake, a gear stage, an inverted screw-nut system and a position sensor.

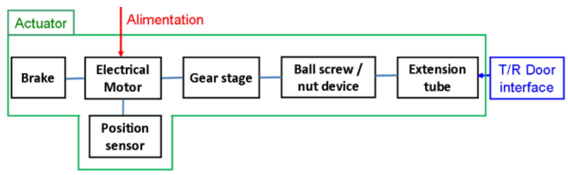

Fig. 6 Actuator functional architecture.

- A power supply unit, based on classical voltage converter architecture: A voltage inverter is used for converting DC voltage to three-phase voltage modulated in frequency and amplitude in order to drive the electric motor.

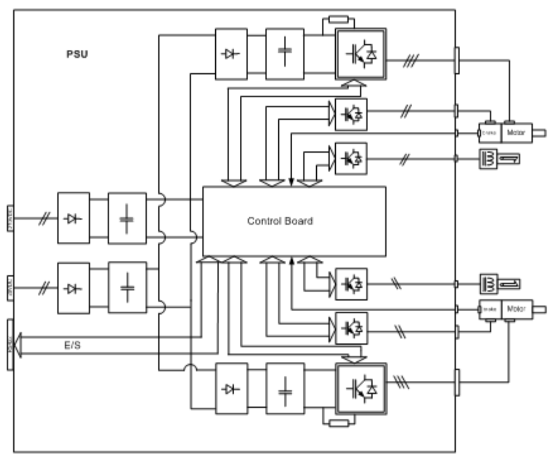

Fig. 7 Power electronic architecture.

- An electronic control unit, to regulate the positions of the two actuators. The control loop is based on electric motor position, speed and current sensors.

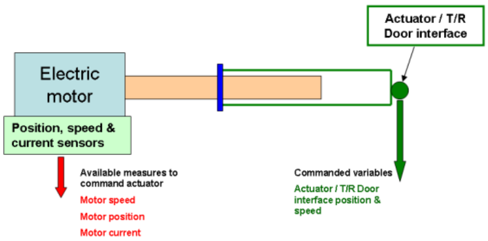

Fig. 8 Control loop inputs & adjusted variables.

Electric motors are commanded based on speed profiles defined in Fig. 9 in order to meet good performances in terms of thrust reverser deployment and stowage time under operational loading conditions.

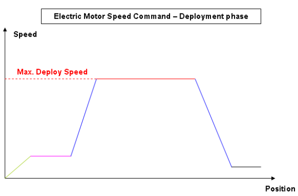

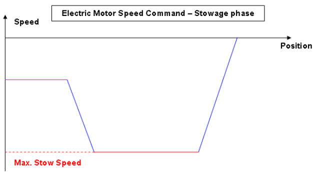

Fig. 9 Electric motor speed profile command – Deployment & Stowage phases.

The strategy of command is based on two regulations loops: a speed and a current regulation loop. Each one is defined by a Proportional Integrator (PI) controller, as presented hereunder.

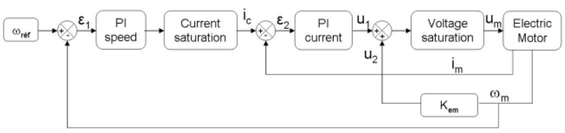

Fig. 10 Electric motor regulation architecture.

3.2 Aircraft and test bench configurations

In aircraft environment, the electrical actuation system is coupled with a thrust reverser structure, composed of two independent doors (mobile parts) and a fixed structure.

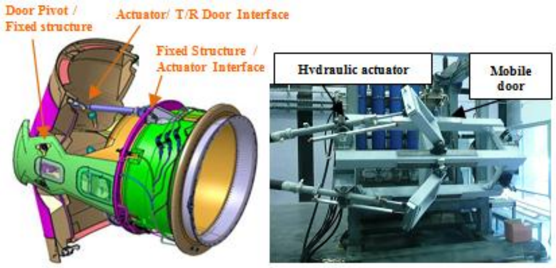

Fig. 11 System integration in Aircraft configuration.

For test bench configuration, each electrical T/R actuator is coupled with a mobile door consistent with T/R door in terms of kinematics and inertia. Aerodynamic loadings are expressed through hydraulic actuators.

4 PRESAGE virtual platform architecture and simulation tools

The aim of the platform is to validate and verify the integration of the equipment in the aircraft environment, based on virtual testing leading to consider all variables and to accommodate specific cases.

In case of the thrust reverser application, the virtual platform leads to define and check:

- Thrust reverser actuation system performance, translated by:
  - The time to deploy and stow the thrust reverser under specific environment conditions (loading and temperature conditions, in particular)
  - The consumed energy and electric power on the aircraft on-board electrical network.
  - The absence of coupling between the thrust reverser flexible structure and the actuation system.
  - The capacity of the actuation system to react external loads with accuracy, stability and rapidity.
- The sizing loads for actuator / thrust reverser interface and actuation components.

- The actuation system behavior, coupled with the flexible T/R structure, under operational conditions

In order to meet these requirements, PRESAGE virtual platform has to allow:

- The representation of the actuation system kinematics
- The representation of the detailed actuation system load path
- The capture of each actuation components loads
- The representation of the electric motor energetic behavior
- The integration of the motor control laws
- The representation of the electronics of power

As a consequence, modeling activities consist in:

- Modeling of tested actuation system
- Modeling of the 3D thrust reverser flexible structure and ensure the coupling with actuation system 1D modeling
- Modeling of the 3D bench test flexible structure and ensure the coupling with actuation system 1D modeling
- Modeling of the counter load bench test actuation system

4.1 Modeling procedure

The considered PRESAGE application case is a multi-physical domains system which includes several physical aspects such as mechanical, electronic, signal, hydraulic, thermal, etc.

In order to achieve a virtual model representing as accurately as possible the behavior of the real system, it is recommended to consider each physical aspect during modeling. Such task requires special modeling and simulation tools. Selecting a virtual platform simulation tool is crucial: a benchmark was conducted during PRESAGE project which has led to define two platforms deserving to be tested along the project.

Selected modeling and simulation tools are:

- LMS (AMESim, VlabMotion) + MathWorks (Simulink)
- Dassault (Dymola) + MathWorks (Simulink)

Using these two virtual platforms models are classified as follows:

- 1D multi domain representation (mechanics, electric, hydraulics, thermal).
- 3D flexible structure representation.
- Command and state flow representation.
- Co-simulation capabilities
- Real time capabilities.

The platforms architecture and simulation tools are presented in Fig. 12.

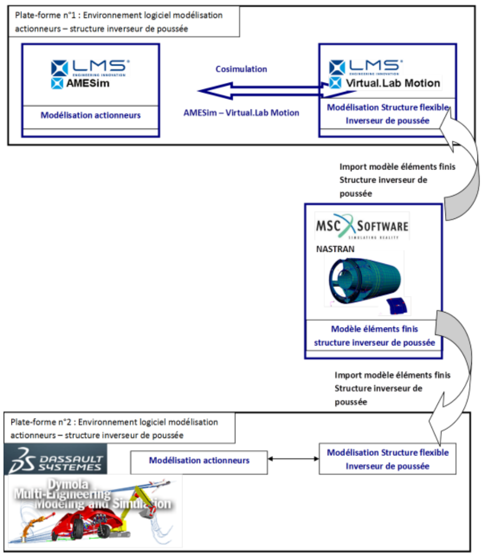

Fig. 12 PRESAGE platforms.

The diversity and complexity of the studied system involve a deep and complex modeling to obtain the adequate level of accuracy in representing the real system. Achieving such a model step may cause several defaults and simulation deviation. That's why a progressive modeling procedure is established:

- Phase 1: completion of elementary independent models
- Phase 2: coupling realized on elementary models
- Phase 3: elaboration of global co-simulation between all models (all simulation tools)

- Phase 4: adding generic bloc to coupled model in order to consider more physical aspects that were neglected during Phase 1

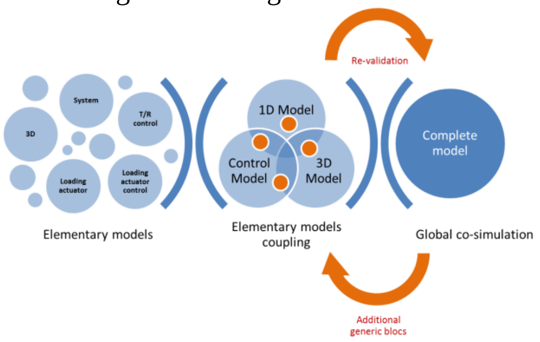

Fig. 13 Progressive modeling procedure.

To model electrical actuation system kinematics and load path, generic power transmission components (motor, screw-nut, axial stop, bearing components…) have been developed including a thermal port for energetic analysis ([1]).

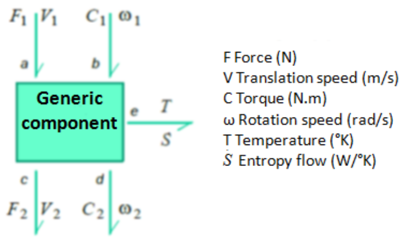

Fig. 14 Generic power transmission component.

4.2 Platform-1: AMESim (1D), Simulink (control) and VlabMotion (3D) coupling

Modeling under platform-1 consists in developing three models: 1D, 3D and Control model.

4.2.1 1D T/R actuation system and bench test counter load modelling (AMESim)

AMESim model contains two basic parts:

- Hydraulic actuator submodel
- Electromechanical thrust reverse actuator submodel

To simulate the hydraulic actuator, it is sufficient to consider a hydraulic power source, a servovalve, an actuator (inertia, stiffness, and dimensions). However, the electromechanical actuator submodel is quite complex to simulate regarding the multi-physical domains involved in the system: electronic power, electric motor, rotational and translational dynamics. All these aspects were indeed considered in the 1D AMESim model.

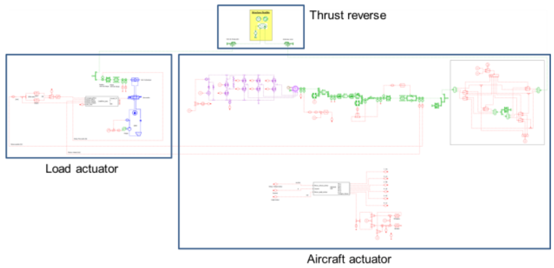

Fig. 15 AMESim 1D model.

4.2.2 3D model (VlabMotion)

Thrust reverser flexible structure representation is translated by the modeling of stiffness and inertia characteristics of thrust reverser fixed and mobile parts.

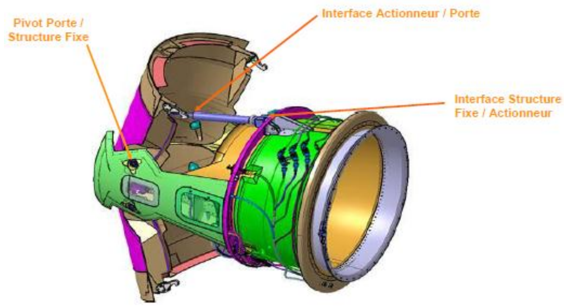

Fig. 16 Thrust reverser structure interfaces.

The following interfaces were selected to translate thrust reverser flexible structure characteristics:

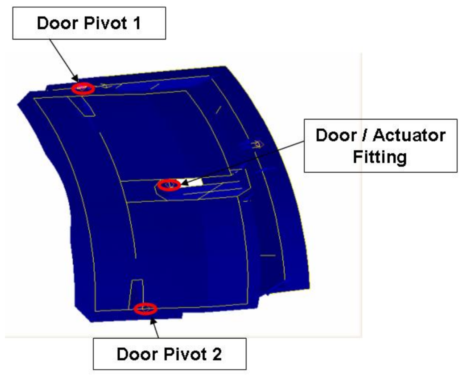

Fig. 17 Flexible structure – thrust reverser door.

- Thrust reverser door / actuator interface
  Aerodynamic loads are reacted by the actuators at the door / actuator interface. As a consequence, it is necessary to integrate thrust reverser structure characteristics at door / actuator interface level in order to comprehend system / thrust reverser structure behavior.
- Thrust reverser fixed structure / actuator interface.
- Door pivots / fixed structure interfaces.
  Deformation of the fixed structure at door pivots level influences door behavior itself and, by consequence, have an effect on actuation system.

Representation of thrust reverser structure characteristics is summarized in Fig. 18.

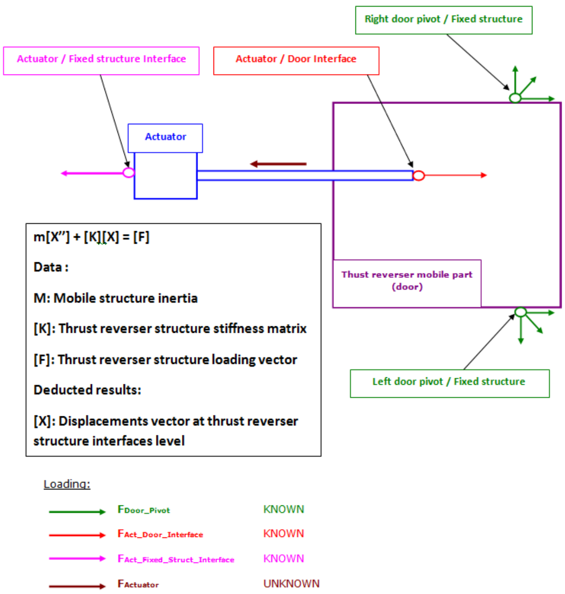

Fig. 18 Actuator applied forces statement.

4.2.3 Control model (Simulink)

Control model provides the control loops for both hydraulic and electromechanical actuators. These control loops are basically performed using PID-controllers. In addition, the control model pilots the co-simulation process between Simulink (control), AMESim (1D) and VlabMotion (3D). To achieve this, a communication bloc with other simulation tools is used.

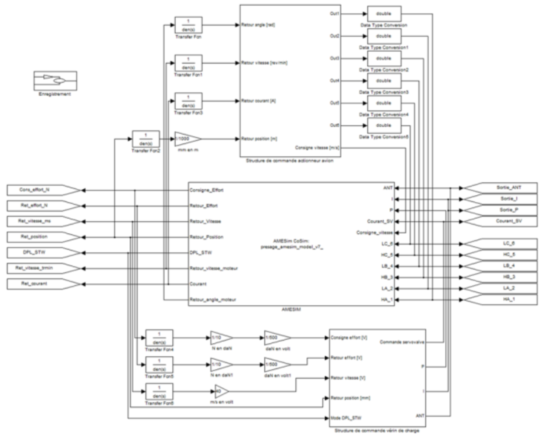

Fig. 19 Control model (Simulink).

Coupled simulation between these three models offers three principle results that explicit a good convergence of the developed models.

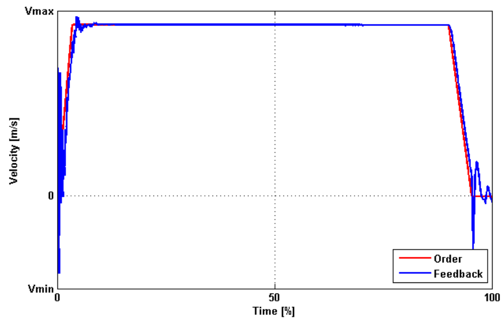

Fig. 20 Thrust reverser actuator longitudinal velocity.

Fig. 20 represents the order and feedback translational velocity of the electromechanical actuator, during a deployment sequence under operational loads. Excepted some oscillations that are due to hydraulic opening valve at the beginning of the curve, we notice the convergence between order and feedback.

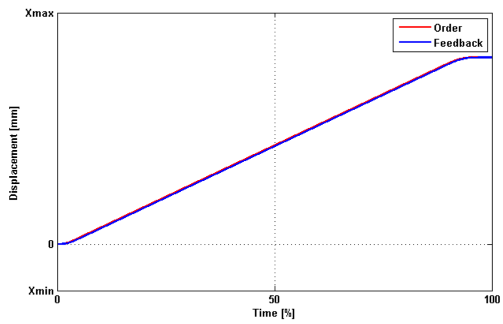

Fig. 21 Thrust reverser actuator longitudinal displacement.

Fig. 21 shows the longitudinal position of the actuator rod. This position curve corresponds to the desired displacement defined using the velocity order curve.

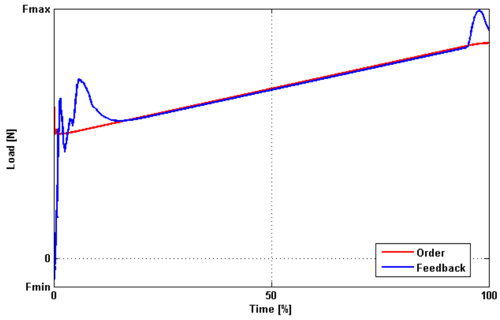

Fig. 22 Aerodynamic load on thrust reverser.

The order and feedback of aerodynamic load, translated through bench test hydraulic counter load actuator, is represented in Fig. 22.

4.3 Platform-2: Dymola (1D and FE flexible structure) and Simulink (control) coupling

Contrarily to platform-1, modeling under platform-2 consists in developing only two models:

- 1D model (Dymola): this model contains bench test hydraulic actuator submodel, electromechanical thrust reverser actuator submodel, as well as an imported finite element model of the 3D flexible thrust reverser structure (opening door).

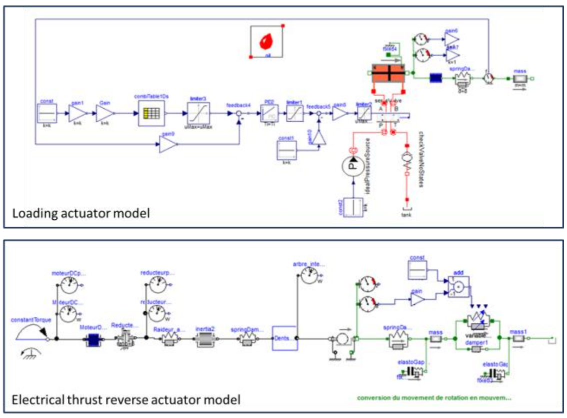

Fig. 23 Dymola 1D model.

- Control model (Simulink): control loops for hydraulic and electromechanical actuators

Due to the fact that model development was started on Platform-1, the realized models on platform-2 are not enough mature to give improved simulation results.

4.4 Introducing generic bloc components models

Electromechanical actuators generate secondary loads (parasitic torque) on the fixed structure and loading system. These secondary loads are basically caused by the presence of rotary components in the actuator. Considering the PRESAGE electromechanical actuator, the secondary loads are produced by:

- ✓ Reaction torques on the electric motor stator, or even on the reducer body;
- ✓ Friction torque in the rotational/translational transformation component;

Loading system and fixed structure should be able to support these secondary loads in addition to functional acting forces. In order to quantify and consider the cause and consequences of secondary loads generated in the electromechanical actuator, it is recommended to use 2 degrees of freedom components: translation and rotation along the translation axis (for example: rotational friction force on a longitudinal endstop, friction torque is a function of applied axial force).

Components actually used in available modeling and simulation tools are not considering these 2 degrees of freedom. Developing such an elementary component under generic bloc can lead to an evolution of the virtual test platform.

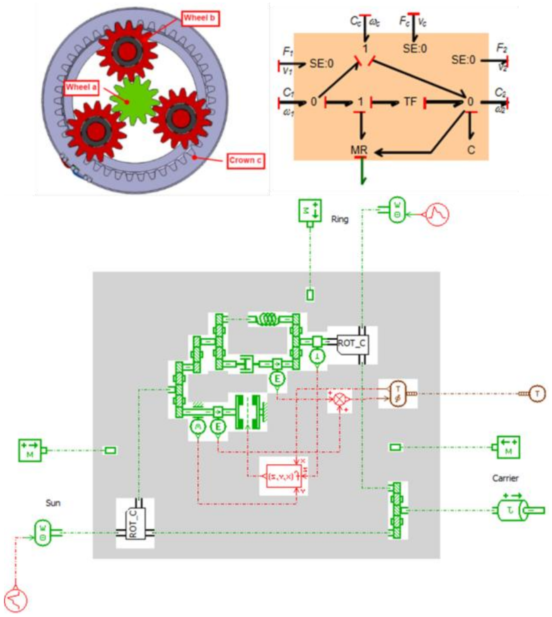

Fig. 24 Epicycloid gear generic model.

Applying this configuration on the PRESAGE thrust reverser actuator leads to develop 2 main generic blocs representing:

- ✓ An epicycloid gear generic bloc
- ✓ Screw-nut generic bloc

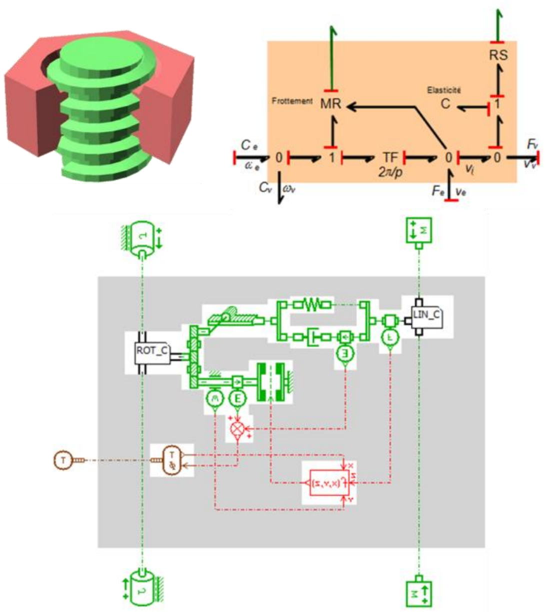

Fig. 25 Screw-nut generic model.

5 Conclusion

The results were validated by correlation with a real test platform.

The PRESAGE platform reaches industrial expectations in terms of "genericity" of testing means, reducing costs, time and integration of complex multi-physic systems.

So, we appreciate, through this project, the support of the virtual test means in order to reach the first objective which is to launch the first bases of the virtual testing.

Sure, we have to define the most adaptive simulation platforms which not were an easy work, because of the many existing platforms.

We had to benchmark all these platforms and select 2 or 3 of them. We have selected 2 whom seem to be the most used, the most robustness and the most adaptive for our request: virtual testing.

By the PRESAGE project, we are happy to propose for the industrial our works in order to help him to integrate the virtual platforms on their testing process

References

[1] R3ASC 2012: 2-D lumped-parameters modelling of EMAs for advanced virtual prototyping / J-C. Maré, Université de Toulouse; INSA-UPS, Institut Clément Ader, France

Abbreviations

PRESAGE: Plate-forme Réelle Et Simulée d'Actionnement Générique et Evolutive
HIL: Hardware In the Loop
SIL: Software In the Loop
T/R: Thrust Reverser

Integration of On-Board Power Systems Simulation in Conceptual Aircraft Design

Ingo Staack, Petter Krus
Division of Fluid and Mechatronics Systems
Linköping University
ingo.staack@liu.se

Keywords: *Conceptual aircraft design, system simulation, onboard power systems, knowledge based engineering*

Abstract

This paper describes the methodology of generating simulation models out of basic information, available during conceptual design phase. The implementation of an aircraft system is shown as an example using the simulation software HOPSAN.

Because of the limited direct project-related data available at the conceptual stage, the traditional method of creating physical simulation models by the bottom up approach with the help of (standard) component libraries is not applicable. Instead, the respective systems' architecture as well as their composition has to be descriptively predefined in a flexible, wide-range applicable manner, known as the knowledge base (KB) approach. These system technology driven design declarations – combined with project related data – result in roughly pre-tuned system simulation models, which may help when conducting more detailed investigations of the project such as performance analysis.

This (system architecture) knowledge-based approach is shown on the whole aircraft system level down to the detailed implementation of the control surface actuator systems of the primary flight control system.

0 Nomenclature

In this paper, the following naming convention is used to describe a physical system (simulation model) composition:

model layout	the way in which a model consisting of (sub)systems or components is arranged
model topology	schematic description of the arrangement of a (sub)system, including its nodes, connecting lines and in-/output ports
model architecture	the structure and design of a model/system

1 Introduction

Classical aircraft conceptual design explained in the literature is mainly based on statistics of existing aircraft or basic physical effects (e.g. [1]). The natural limitation of these methods makes it necessary to perform more advanced, complex and more direct project property related analytical analysis, for example CFD and FEM if the product properties definition has reached a certain level of accuracy.

In a modern aircraft with its electrically driven subsystems, the entire systems become closely integrated and both positive and negative cross-couple effects arise. This, combined with the enlarged system architecture complexity – owing to the higher overall efficiency – makes it almost impossible to investigate these effects without simulation. Taking into consideration all limiting factors and requirements might overload the engineer and require too detailed an input, which is not possible during the conceptual design phase where – apart from certification regulations – even central requirements are often vaguely formulated and negotiable.

A typical case is the primary flight control system (PFCS) with its control modes, which are normally not defined during conceptual design but are needed to some extent when simulating the total aircraft.

2 Related Work

This paper – with its focus on application – is related to a wide area of research within systems engineering and system architecture development and metamodelling.

Within model-based system engineering, the model creation and validation process is a major topic in addition to the system declaration. [2] shows the use of UML/SysML for system declaration within model-based development.

More focused on the requirement to product-function coupling, [3] defines a process that maps the requirements towards functions and the related means of the product (function-means tree) by generic object inheritance. The result can be seen as a configurable product data management (PDM) system that allows traceability to the requirements. [4] developed such a traceability (thus between models) with the help of the eXtensible Markup Language, XML [5]. Here, in the software engineering domain, related work focuses on reusable pattern definitions for the metamodelling process in XML, such as for example [6] with an overview of different pattern definitions.

Application examples of the whole process using UML for the graph-based metamodelling are given in [7] and [8].

3 Architectural Design Process

A simulation, together with model result investigations like stability and robustness analysis, helps the developer to understand the properties and behaviour of the design. Complex models, however, may veil or draw attention away from the important parameters; it requires a great amount of time to fine-tune all system parameters. Besides building the simulation model, system tuning (and if applicable system verification) is the most time-consuming and expertise-demanding process in system modelling. The target of the architectural design process is thus the generation of an already pre-tuned simulation model by knowledge reuse in combination with the project data.

3.1 Model Translation Methodology

Within the transition step from pure project data towards a simulation model, the combination of two processes is essential:

- **Transforming the project data** by an interpreter into the simulation system with its components and parameters.
- **Adding additional information** by pre-known knowledge such as for example the general architecture of a subsystem and the required components that are not explicitly described in the (conceptual aircraft) data setup.

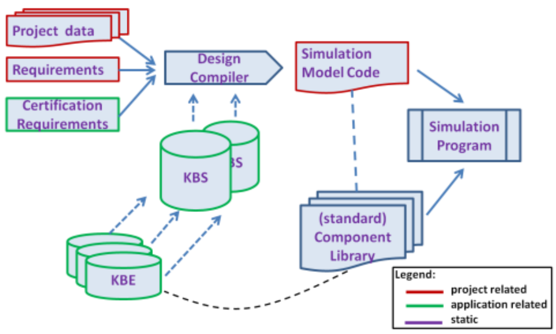

Figure 1: Flow diagram of the translation process.

Figure 1 shows a comprehensive overview of this process where the project-related data (shown in red) are extended by the application of more generally formulated application-related data (shown in green). The application-related data might for example be a KBS library for JAR/FAR-25 airplanes.

3.2 System Architecture Design Definition

The definition of the system and its layout can be seen as a metamodel of the simulation model, containing the necessary translation rules. These rules enable the design compiler to translate the aircraft project data in conjunction with the project-specific requirements and the general certification requirements[1] into the executable simulation model.

Under closer scrutiny, the metamodel information can be split up into two parts:

1. the meta-data and the meta-process, dealing with the model (layout) generation
2. the data transfer processes in order to transfer the project data towards the (simulation) model systems and component properties.

3.3 KBS Level Definition

The system layout definitions used, in the following referred to as *knowledge base system(s)* (KBS), can be divided into four categories:

I. **Fixed ports, static system**
This represents a static system layout with fixed defined system ports. This type can be handled as a (complex) single component (KBC) but is matched towards a system. These types require only parameter adaption during instantiation, e.g. a simple propulsion system model, where only the engine deck data is updated.

II. **Fixed Port, repetitive system**
A fixed system component composition with an adaptable number of occurrences. An example is the mission system, defined by a state machine (with static number & functionality of in-/output ports) but with a flexible number of the repetitive elements of the same shape but different parameter settings.

III. **Fixed port, flexible system**
System with flexible internal component composition but with a fixed defined number (and functionality) of the in-/output ports. An example is the PFCS controller with its roll/pitch/yaw commands (fixed ports!) but with significant changes in the controller layout between different projects (e.g. stable vs. unstable configuration).

IV. **Flexible port, flexible system**
Systems with flexible system component composition and varying number and functionality of the in-/output ports. Example is the hydraulic actuator system.

These KBS categories define and limit the possible actions within the meta-process.

Although automatic simulation model generation is the primary objective, this may not be applicable for every complex system (KBS category III or IV) definitions. In this case, the KBS translation may require user interaction, integrating the engineer (with his or her expertise) into the system architecture generating process [9]. This interaction can be defined by a configurator process; within the configurator, different design rules can be implemented to support the user during the designing process by preventing impossible combinations.

3.4 Simulation Compiling Process

Necessary inputs for the translation process, here called compiling, are:

- system topology definition (STD)[2]
- KBS definitions (with the embedded configurator/adaption rules, mainly for KBS categories III and IV)
- KBE definitions establishing the connection to the simulation component libraries used

[1] In the example implementation in this paper, certification requirements have not been included.

[2] The STD might be integrated in the system's KBS.

- the project-related dataset (in a known setup)

The process itself is then:

- instantiate the KBS
- conduct the configurator process (if applicable)
- apply the (project data) adaption rules
- create the inter-KBS connections, defined by the STD.

These steps can be conducted iteratively top-down on the different subsystem levels.

3.5 Linkage and Coupling Adaptation

With the presence of type IV KBS, the overlying system description has to be capable to establish valid connections according to both the KBS definition and the simulation program's needs. For this purpose, it might be necessary to define one's own "connection" KBS that are added by the STD.

In the case of HOPSAN [10], this is especially tricky because of its underlying TLM solver[3] and the fact that most connector ports of the standard library components are not multi-connection capable. In the latter, the KBS has to include the process information on how to merge these ports. This merging process can be solved either by adding only a KBC with the required number of ports or a multiport functionality, or by adding one's own subsystem (of KBS type IV). A similar approach can be used for split-up processes.

In the aircraft example, these merging processes are used for the distribution (and signal gain adaption) of the roll, pitch and yaw PFCS commands for the control surface actuators.

[3] The simulation software HOPSAN is based on a distributed system solver method (TLM) with two different component type definitions which have to be alternating connected. For more information see [12].

3.6 Simulation Parameter Tuning

In addition to the system layout modelling process, the respective component properties have to be set. These may be fairly easy parameter aliases in high-level systems or components that directly match a subset in the existing (conceptual design) project data; this is the case in the 6DOF aircraft model, where the aerodynamic coefficients, geometry and weight properties of the simulation model (which is a single component defined by the related KBC definition) are directly linked with the project data. This process can be seen as a simple data translation and can thereby easily be performed by for example an XSLT [11] file.

This topic becomes more complex on the detailed subsystems and components that are not explicitly or implicitly defined in the project data. This is the case where new information is added to the project using the knowledge base approach, for example the respective actuators and the mechanic actuator – control surface linkage: This can be solved by a complex approach making use of the (system, design space and requirements) limitations, the model (analysis result) data and the KBS definitions.
In the case of actuator and linkage sizing these are:

- available space for the actuator and linkage (defined by the wing and airfoil shape) [*geometrical scaling*].
- control surface hinge moments and forces from the aerodynamic analysis [*power scaling*], together with:
- (general knowledge of) usual control surface deflection and deflection angle [*geometry & power scaling*]

Iteratively, the connected parent systems can be built up and tuned in the same manner (bottom-up approach) like e.g. the hydraulic power supply system scaling according to the flow requirements of the connected actuators.

3.7 Model tuning by Simulation

This method has not been applied to the project yet, but has to be named because of its importance and powerful capabilities:

Because the outcome of the process shown above is an executable simulation, the retrieved simulation results can be used to apply a simulation based optimization on the generated system, not primarily focused on a real system optimization but in order to retrieve a well-functioning (and thereby hopefully well-tuned) simulation model.

4 Use Case: Total Aircraft and Hydraulic System Simulation

For this paper, a use case has been chosen to demonstrate the implementation of the methodology shown above: a total aircraft system simulation with the primary flight control (hydraulic power) system, based on conceptual aircraft data.

4.1 Aircraft System Topology Definition

A flexible aircraft system top level architecture can be defined as shown in Figure 2.

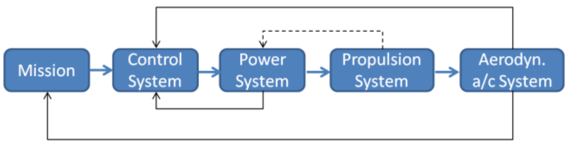

Figure 2: Top level aircraft system description.

This architecture is a logical composition of the physical instances needed to describe a whole aircraft.

4.2 Aircraft Hydraulic System Topology

The (normally hydraulic) actuator power system of the PFCS can be described by three different system layouts (see Figure 3):

- Centralized system
- Distributed system
- Hybrid systems [12]

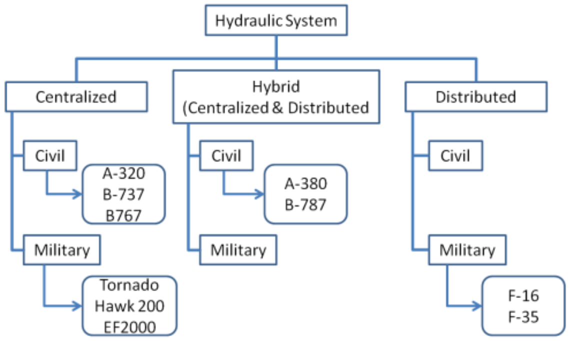

Figure 3: Hydraulic system top level architecture layout concepts.

The naming refers to the supply power generation concept. In civil applications, the centralized layout is usually realized with the trend towards hybrid systems in the latest aircraft generations, whereas in military applications both centralized and distributed systems can be found (see Figure 3).

4.3 Centralized Hydraulic System Definition

The following application example will focus only on the centralized system layout.

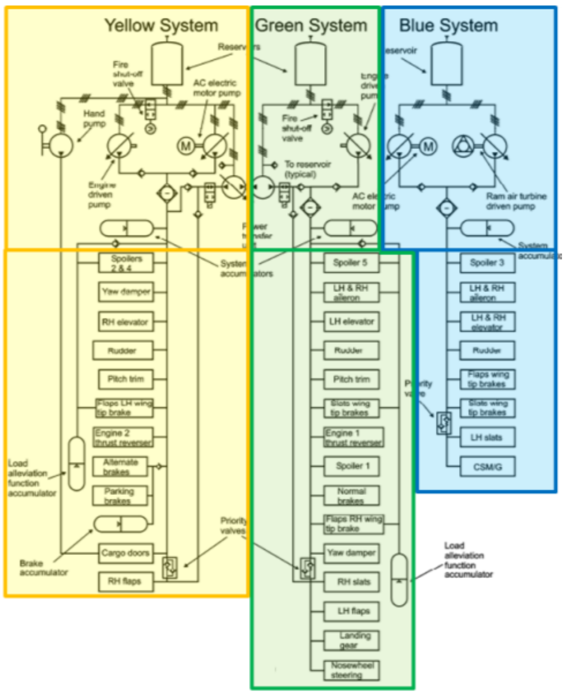

Figure 4: Airbus A-320 Hydraulic system layout [13]**.**

A typical system in a civil JAR/FAR-25 certified aircraft, the Airbus A-320/321 family, is shown in Figure 4 [13]. These types of systems usually consist of three independent hydraulic systems, here called yellow, green and blue.

As described in Chapter 3.2, the system-designing process has to be described in STD/KBS declarations. Here, XSD, an XML schema language notation, has been used [14] for these definitions. This offers the potential to use the file during the whole process; for the system architecture (rules) development, the documentation and the instruction source for the design compiler.

The definition (of the PFCS related parts) of one of the centralized hydraulic systems in the Airbus A-320 shown above can be described as shown in Figure 5, where each element beginning with the prefix *KBS* refers to a system layout definition devised by the designer. The *KBC* prefix denotes elements that are directly linked towards simulation components and thus represent the smallest possible unit that cannot contain any subsequent KBS/KBE definitions.

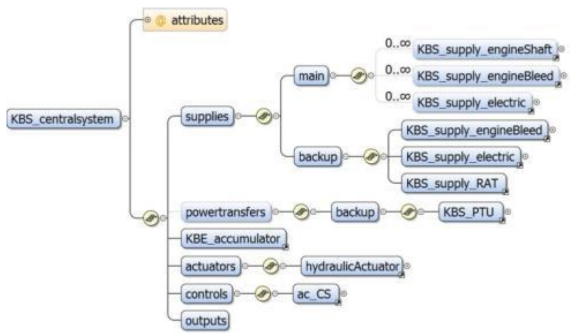

Figure 5: System architecture description of one centralized hydraulic system branch (XSD based).

4.4 Hydraulic Actuator Model Definition

By defining the global system layout as “centralized”, the actuator type used can be only of hydraulic input type. Figure 6 shows a hydraulic actuator configuration tree, which can be easily simplified for the PFCS case to:

- linear type only
- civil: usually single or double type
military: usually tandem type [15]

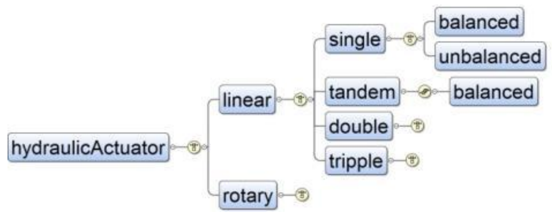

Figure 6: Hydraulic Actuator design tree. Double and triple linear actuator can be seen as a combination of single actuators; rotary type branch not shown.

The configured actuator therefore encapsulates no further KBS definitions (KBC only), this system can be instantiated by the compiler process. In the case of the following selection

```
hydraulicActuator(type=”linear” housing=”single”
                  subtype=”unbalanced”);
```

this declaration is translated into the following actuator subsystem:

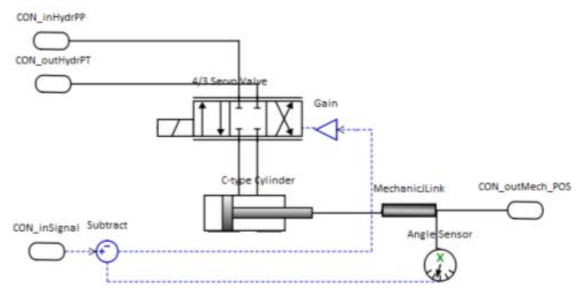

Figure 7: Example of the KBS instantiation of a linear single actuator (KBS Type I) in HOPSAN.

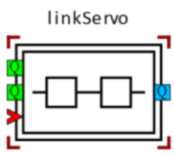

Figure 8: Top level view of the linear actuator system (without defined system symbol) with the highlighted system ports hydraulic (green), mechanical (blue) and control signal input (red).

For the overlying KBS, this object appears as a black box with the defined system in-/output ports visible as shown in Figure 8.

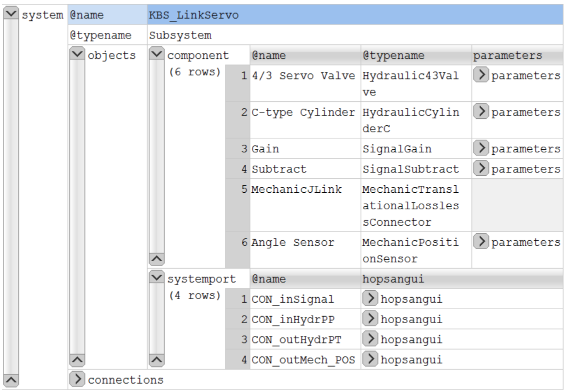

system		
@name	KBS_LinkServo	
@typename	Subsystem	
objects	component (6 rows)	

	@name	@typename	parameters
1	4/3 Servo Valve	Hydraulic43Valve	parameters
2	C-type Cylinder	HydraulicCylinderC	parameters
3	Gain	SignalGain	parameters
4	Subtract	SignalSubtract	parameters
5	MechanicJLink	MechanicTranslationalLossesConnector	
6	Angle Sensor	MechanicPositionSensor	parameters

systemport (4 rows)

	@name	hopsangui
1	CON_inSignal	hopsangui
2	CON_inHydrPP	hopsangui
3	CON_outHydrPT	hopsangui
4	CON_outMech_POS	hopsangui

connections

Figure 9: Table presentation of the created HOPSAN system definition XML code (insignificant details such as GUI information hidden).

The actuator KBS therefore contains no further KBSs. The created simulation object code, shown in Figure 9, consists only of library components with their parameters and connections and the system ports.

5 Model-Framework Implementation

In this example, Matlab scripts have been used as the design interpreter, with the following inputs:

- TANGO aircraft data (Matlab class or XML).
- the KBS (including the STD), implemented in Matlab.
- Configurator with GUI (also Matlab).

5.1 Conceptual Aircraft Design Framework

The aircraft data has been generated with the conceptual aircraft design tool TANGO, developed at the Division of Fluid and Mechatronic Systems (FluMeS) at Linköping University [16]. This Matlab application saves the aircraft sizing output in a parametric-based datasheet in XML format, similar to the CPACS definition from DLR [17].

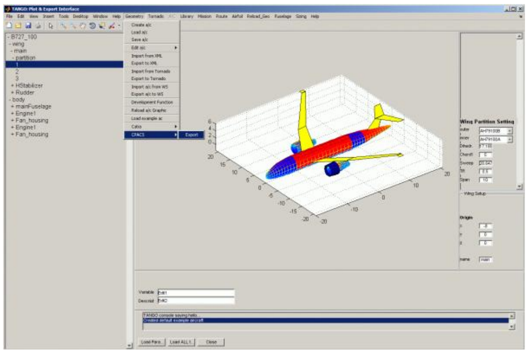

Figure 10: Screenshot of the TANGO GUI with example aircraft.

Together with the panel method program Tornado [18] included in TANGO and the CATIA based RAPID program these tools form a powerful framework for conceptual aircraft design [16].

5.2 HOPSAN Simulation Environment

The in-house developed multi-domain system simulation tool HOPSAN [10] was used for the simulation.

HOPSAN works with a distributed, fixed time step solver for each component, using the transition line method [19]. Using the HOPSAN standard library, a six degree of freedom aircraft simulation model, including mission controller, prolusion and the PFCS, can be simulated [20]. On a standard PC, simulation time is approximately 30 seconds for a whole mission.

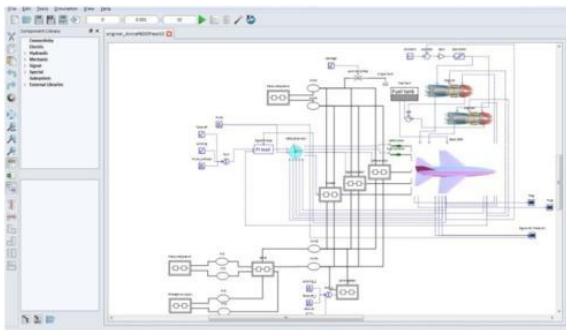

Figure 11: HOPSAN screenshot of the 6DOF airplane simulation model [20]**.**

5.3 The Model Generation Process: Model Description and Translating Action

The project-related model data, i.e. the aerodynamic properties, are achieved during the conceptual aircraft design with help of a vortex lattice method program, Tornado [18], and classical textbook methods. By means of these parameters, a six degree of freedom (6DOF) aircraft model can be created and placed into the simulation as the central part in the highest system layer. More details about the 6DOF model and the total aircraft system simulation can be found in [20].

Executing the Matlab design interpreter script starts the KBS defined system with the top layer architecture according to Figure 2. During the compilation process, the user is integrated in the hydraulic system layout configuration through configurator GUIs.

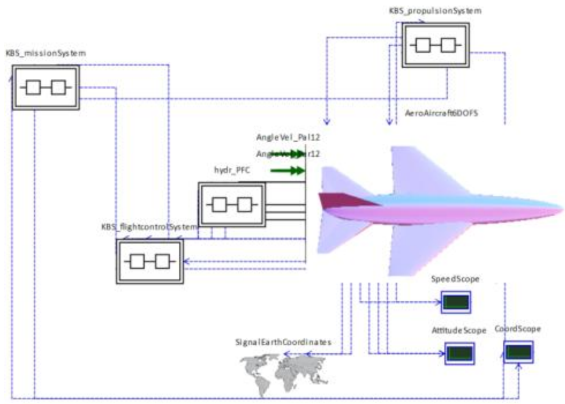

Figure 12: The generated HOPSAN simulation model (top level view).

Components are placed within the subsystems using a simple algorithm that is not capable of fulfilling the need for good, human readable component placement and connector line shape. Figure 13 shows the manually realigned hydraulic system with its colour-coded connections and the connection subsystems created (see in Chapter 3.5) which serve to merge the actuator position outputs to the control surfaces.

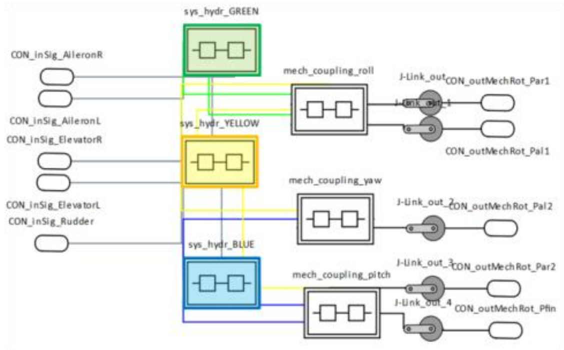

Figure 13: The generated centralized hydraulic system with three hydraulic systems; comparable with Figure 4 (components manually rearranged).

5.4 Simulation Results, Analysis and Representation

In addition to the HOPSAN GUI and the simulation result analysis, the simulation model (setup) can be directly analysed during instantiation: Figure 14 shows different model analysis and access methods that are available to the developer during the simulation model generation process. These are (from left to right) the Matlab class(es) instance of the model, a component connection analysis (connection matrix) and a tree view of the subsystems and component hierarchy. It should be noted that this hierarchy differs from the original (TANGO XML style sheet) dataset hierarchy. In order to fit industrial (documentation) standards, this analysis data can also be exported in for example Microsoft Excel or HTML format.

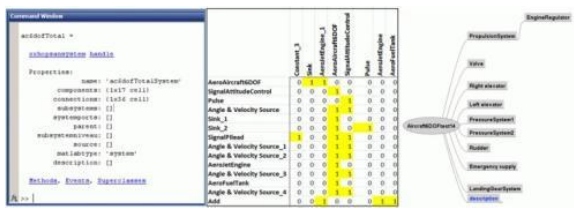

Figure 14: Overview of different simulation representation and analysis in Matlab, Microsoft Excel or XML-based mind maps.

5.5 Limitation and Use Case Review

The use case implementation shown was performed with a rather crude implementation in Matlab with a focus on testing the suggested methodology and developing the KBS/KBE/SDK nomenclature. The following problem areas were detected during this work:

- graphical representation of the generated system; requires complex component placing algorithm.
- insufficient KBE definition assistance for the developer: Other program languages and development environments should be tested for the KBS/KBE definition.
- aircraft system layout is mainly driven by reliability. This makes it necessary to involving fault tree analysis (FTA) and failure mode and effect analysis (FMEA) during the KBS definition process.
- Time-consuming KBS definition; only justifiable if the KBS definitions are reusable in other/future projects or are integrated in an iterative (optimization) process.

6 Conclusions

Simulation within aircraft conceptual design is – to some extent – state-of-the-art. This paper shows that with additional effort, even complex and detailed simulation models can be created by applying knowledge-based engineering methods. Primarily this is shown as a support tool for the engineer, but the (automatic) breakdown of systems in particular enables a more accurate system efficiency and weight prediction and will thereby enhance the project benchmark prediction accuracy.

In the PFCS use case shown above, using a robust default (knowledge-based) topology for these (kinds of) systems might not get the full capability the aircraft will attain later but gives the engineer a chance to evaluate the aircraft.

A key prerequisite for this approach is a parametric, well-defined (input) dataset that allows parsing of the original data into simulation component properties or whole system architectures. The XML format in combination with its related style and translation languages (XSLT and XSD, both XML-based) suits very well; theoretically, the translation might be performed directly by a XML Transformation Sheet (XSLT), but initial proves highlighted the limitations of this language regarding mathematic operations and complex parsing actions[4]. The KBE description and design compiling were performed by means of Matlab scripts instead. Future work will include replacing these scripts with an appropriate language (e.g. SysML, UML or XSD) and specifying the KBS nomenclature.

References

[1] D. P. Raymer, *Aircraft Design - A Conceptual Approach*, 2nd ed, American Institute of Aeronautics and Astronautics (AIAA), 2006.

[2] H. Andersson, *Aircraft Systems Modeling: Model Based Systems Engineering in Avionics Design and Aircraft Simulation*, Lic. Thesis No.1394, Linköping University, Department of Management and Engineering, 2009.

[3] O. Johansson, H. Andersson, and P. Krus, “Conceptual Design using Generic Object Inheritance”, *Proceedings of the AMSE Intern. Mechanic Engineering Congress*, New Orleans, USA, November 2002, pp. 931-941

[4] J. I. Maletic, M. L. Collard, and B. Simoes, “An XML based approach to support the evolution of model-to-model traceability links”, *Proceedings of the 3rd international workshop on Traceability in emerging forms of software engineering – TEFSE 05*, Long Beach, CA. 2005, pp. 67-74

[5] XML 1.0 Language Definition http://www.w3.org/XML (2013.08.17)

[6] Z. Hu and G. Vollmar, “Towards XML Metamodel Patterns for XML Data Modeling”, *Proceedings of the 12th International Workshop on Database and Expert Systems Applications*, IEEE, Munich, Germany, 2001, pp. 71–75.

[7] J. Groß and S. Rudolph, “Generating Simulation Models from UML – A FireSat Example”, *Proceedings of the Symposium on Theory of Modeling & Simulation - DEVS Integrative M&S Symposium*, DEVS, Orlando, FL, USA, 2012.

[8] S. Rudolph, S. Hess, J. Beichter, M. Motzer, and M. Eheim, “Architectural Analysis of Complex Systems with Graph-Based Design Languages”, *Proceedings of the 4th International Workshop on*

[4] using the XSLT Version 1.0 in combination with XPath Version 1.0; Currently existing XSLT Versions 2.0 (and Version 3.0 announced) may offer greater functionality.

Aircraft System Technologies (AST), TUHH, Hamburg, Germany, 2013, pp. 159–168.

[9] C. Haskins, K. Forsberg, and M. Krueger, *Systems engineering Handbook*, Version 3, International Council on Systems Engineering, INCOSE, 2007, p. 304.

[10] Software: P. Nordin, R. Braun, B. Eriksson, and P. Krus, "Hopsan Program" http://www.iei.liu.se/flumes/system-simulation/hopsanng?l=en, Linköping, Sweden, 2012 (2013.08.17)

[11] XSL Transformations (XSLT) Version 1.0, http://www.w3.org/TR/xslt (2013.08.17)

[12] D. Chuenprapai and K. Panyaboon, "Centralized and Distributed Hydraulic Systems Design in Generic Future Fighter Aircraft", Master Thesis, Linköping University, LIU-IEI-TEK-A--12/01429--SE, 2012.

[13] A-6a1 Commercial Aircraft Committee, "SAE-AIR5005A: Commercial Aircraft Hydraulic Systems", SAE Aerospace Information Report (AIR), 2010.

[14] XML Schema, Version 1.1: http://www.w3.org/TR/xmlschema11-2/. (2013.08.17)

[15] V. R. Schmitt, J. W. Morris, and Jenney Gavin D., *Fly-by-Wire: A Historical and Design Perspective*, 1st ed., SAE International, Warrendale, PA, USA, 1998, pp. 1–132.

[16] I. Staack, R. Chaitanya.M.V, K. Amadori, P. Berry, T. Melin, C. Jouannet, D. Lundström, and P. Krus, "Novel Parametric Aircraft Conceptual Design Framework", *Proceedings of the 28th Congress of the International Council of the Aeronautical Science(ICAS)*, Brisbane, Australia, 2012.

[17] C. Liersch, "A unified approach for multidisciplinary preliminary aircraft design", *Proceedings of the 2nd CEAS European Air and Space Conference*, Manchester, UK, 2009, pp. 1-18.

[18] Software: T. Melin, "Tornado Program", 2001, http://www.redhammer.se/tornado/index (2013.08.17)

[19] M.Axin, R. Braun, A. Dell'Amico, B. Eriksson, P. Nordin, K. Pettersson, I. Staack, and P. Krus, "Next Generation Simulation Software using Transmission Line Elements", P*roceedings of the ASME Symposium on. Fluid Power and Motion Control*, FPMC, Bath, UK, 2010.

[20] P. Krus, "Whole Mission Simulation for Aircraft Systems", *Proceedings of the CEAS European Air and Space Conference*, CEAS, Manchester, UK, 2009.

4:th CEAS Air & Space Conference
FTF Congress: Flygteknik 2013

Coupled CFD simulation of gas turbine engine core

Alexander V. Krivcov, Leonid S. Shabliy, Oleg V. Baturin, Daria A. Kolmakova
Samara State Aerospace University named after academician S.P. Korolyov (National Research University), Russian Federation

Keywords: CFD, gas turbine engine core, coupled simulation, operating

Abstract

The experience in *gas turbine engine core's* workflows simulation using modern computational fluid dynamics is described in the paper. The capabilities of software for coupled simulation of gas turbine engine core workflows are shown. Advantages and disadvantages of the methods used are pointed out. The results of coupled CFD simulation of simplest gas turbine engine in single software package are given. It is shown that the results of the coupled CFD simulation are in good agreement with the results of calculation using calibrated one-dimensional thermodynamic model.

1 Relevance

Core (fig. 1) is most important part of the gas turbine engine (GTE), and can operate as a standalone single-shaft engine, or can be a part of more complex engines. This element of GTE performs the basic engine workflow as a heat engine. Also it significantly determines all the main GTE characteristics, namely efficiency, cost, cost effectiveness and environmental friendliness. Therefore the study of the engine core workflow is an important task for aircraft and power engine technology.

The main elements of GTE core are compressor, combustion chamber and turbine. Usually, each engine component is designed separately in in detached company department according to own procedures. In this case the evaluation of engine components mutual influence and matching of their operation is performed only during the finished product testing. This way is long, expensive and complicated. In addition, it does not take into account the influence of neighboring components during design stage, reducing the development quality and increasing the expenses for identified problems overcoming.

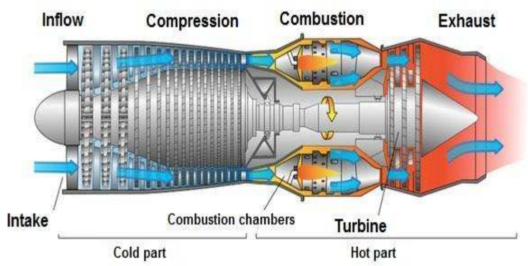

Fig. 1 Engine core image [4]

Recent year progress of computational fluid dynamics (CFD) methods and capabilities of computers enabled to change a significant part of the test to rapid and cheap calculations that are able to predict characteristics and structure of the flow with permissible accuracy in the separate components of the GTE. Based on these capabilities, the authors suggested that the simultaneous CFD simulation of coupled workflows of all GTE core components will provide more accurate distribution patterns of parameters along gas-dynamic duct with the mutual influence of engine components on each other. In addition, it will be possible to estimate the impact of different regime, external and internal factors on the GTE characteristics and the laws of its collaboration, and also to simulate the engine parameters changing under different conditions.

As the analysis of the available literature has shown, this approach is investigated by various research groups in different countries [1...3], but none of them have solved it completely and this idea is far from practical use.

2 Approaches to end-to-end CFD simulation of gas turbine engine core workflow

It is known [5] that three conservation laws: mass, power, and rotor frequency must be carried out for GTE operating at steady state mode. Therefore while gas turbine engine core's workflow CFD modeling the following base patterns must be followed:

- work fluid mass flow rate must be equal at the boundaries of adjacent computational domains;
- the value of bulk total enthalpy of the flow must be kept constant at the boundaries of adjacent computational domains;
- the pressure, temperature and velocity values, as well as their distribution at the boundaries of adjacent computational domains must be identical;
- rotor speeds must be equal in compressor and turbine;
- power (torques) in the compressor and turbine models' rotors must be the same at all of steady modes.

Two approaches to CFD simulation of gas turbine engine core [4] were stated by the authors:

- simulation approach using a number of special programs each of which are best suited to describe the workflow of a particular engine component;
- simulation approach in one universal program that allows to modeling all the core's components simultaneously at once.

The first approach allows to calculate each component's workflow in the most appropriate program with the optimal model and solver settings and involving the most appropriate physical models. This provides a better simulation of the processes and requires less computational resources because the GTE elements are calculated separately. The disadvantage of this approach is the necessity of data exchange between engine components that are modeling in different programs. This is complicated by the fact that they usually have a different format description of the input / output data and the properties of the working fluid. Another drawback is the unilateral influence of the previous element parameters to downstream element in a single data transmission. It is necessary to organize a series of iterative calculations with multiple specifications of boundary conditions for a full simulation of the gas turbine engine core in different programs [4] (fig. 2).

The second approach (fig. 3) is free from such disadvantages. The computational model is created in a single universal CFD software package, consisting of several separate components, and data exchange is organized easily with standard tools of the program. However, the settings of the model are "universal" and certainly not optimal for each component in this case [4].

The lack of standard software tools for automatic GTE rotor power balancing in CFD programs one of the major problems in modeling the engine core. Therefore it is necessary to achieve the equality of compressor and turbine power by correcting the fuel consumption or the rotor speed independently or by means of automatic tool that implements the control algorithm. Selection of control algorithm is caused by variant of simulation (the operating of the engine control system): constant fuel consumption rate while changing rotor speed or constant rotor speed while correcting fuel consumption.

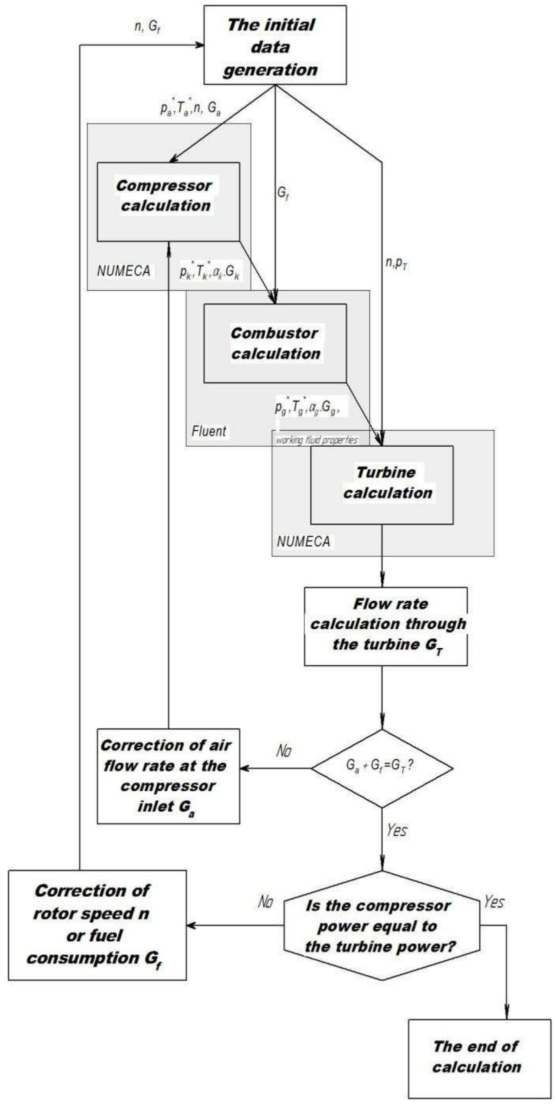

Fig. 2 Computation algorithm for uniform engine core workflow with application specialized software

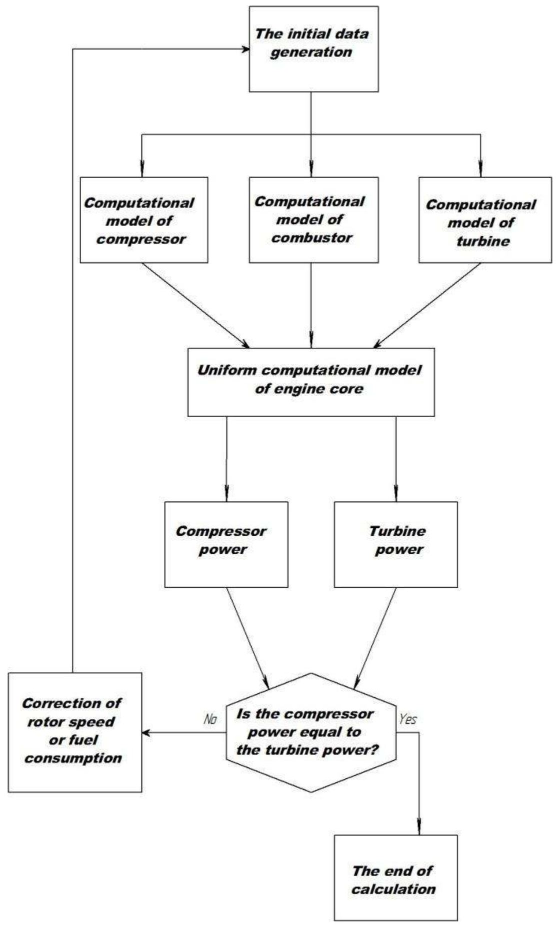

Fig. 3 Computation algorithm for uniform engine core workflow in one universal program

3 Simulation of single-shaft gas turbine engine workflow in in one universal program

3.1 Key data on engine under investigation

To illustrate the feasibility of end-to-end simulation of GTE workflow in universal software package, the authors calculated in CFD program the gas flow in core of the simplest single-shaft gas turbine engine. This engine was designed at Samara State Aerospace University' (SSAU) department of Theory of Engines For Flying Vehicles (fig. 4). This engine has the following characteristic parameters:

– compressor pressure ratio , pr = 4,5;
– turbine inlet temperature, T_g*=1100K;

- air flow rate G_a=0,756 kg/s;
- fuel consumption rate G_f=0,013 kg/s;
- rotor speed n=72600 rpm;
- outer diameter of the compressor wheel D_{2k}=135 mm;
- outer diameter of the turbine wheel D_{2t}=116*мм*.

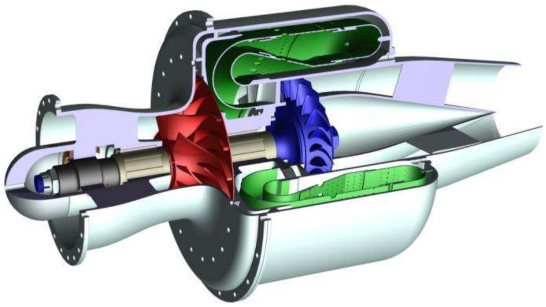

Fig. 4 Test gas turbine engine appearance

3.2 Description of the numerical model

Simulation of engine workflow was performed in a universal software package ANSYS CFX, implementing the second approach described (Fig. 3). The computational model consisted of grid models of intake, the centrifugal compressor rotor wheel, vaned diffuser, reverse-flow combustion chamber, turbine, axial turbine nozzle guide vane and rotor wheel and also nozzle. The models of all turbomachinery elements took into account the tip clearance and consisted of one blade passages with periodic boundary conditions on the side walls.

The model did not allow for leakage and fluid bleeding. Heat exchange between the flow and the air-gas channel walls was not taken into account.

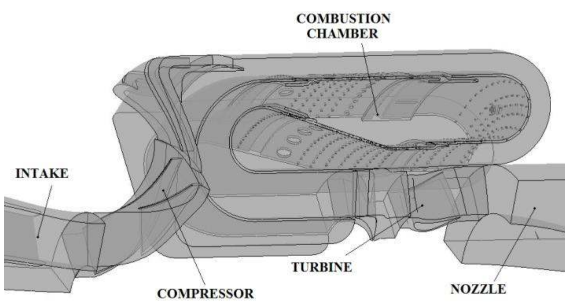

Fig. 5 Computation model of gas turbine engine appearance

Combustion chamber grid model were provided by group of combustion processes studying of Gas Dynamic Research REC of SSAU, team leader - Candidate of Science {Engineering}, Associate Professor, Sergei G. Matveev. The computational domain of combustor was a sector of 45°.

Data transfer from one model to other downstream components was performed by means of interface Stage in which flow parameters averaging in circumferential direction takes place.

A gas mixture of oxygen O_2, nitrogen, N_2, carbon dioxide CO_2, water H_2O and conventional kerosene Jet A was used as the fluid in the simulation.

The combustion was modeled with eddy dissipation model (Eddy Dissipation) which is based on the assumption that the chemical reaction is much faster than the transfer processes in the flow. Reagents instantly form chemical reaction products as soon as they are mixed at the molecular level. The mixing time is determined by the eddy properties in turbulent flows. Consequently, the reaction rate is proportional to the mixing time, determined by the turbulent kinetic energy and energy of dissipation.

The following chemical reaction equation is the basis of kerosene combustion process calculation:

$$\text{Jet A} + 17{,}75O_2 = 12\ CO_2 + 11{,}5H_2O + Q$$

The boundary conditions were applied to created uniform model of engine core workflow:

- total pressure, total temperature and flow direction at the inlet of intake;
- static pressure at the nozzle exit;
- rotor speed that is equal for the compressor and turbine;
- gaseous fuel consumption rate in combustor.

K-epsilon model with scalable wall functions was used as a model of turbulence.

The problem was solved in steady state statement.

The total number of model nodes was of 5 million. Turbomachinery had structural finite element mesh. The combustion chamber, the nozzle and an intake had unstructured mesh.

The flow in the engine was obtained without fuel combustion in the combustion chamber in the first stage. Then this solution was used for the initialization the calculation taking into account the combustion. The experience gained form the calculation showed that the solutions process with Ansys CFX uniform computational model has low stability. This is particularly evident in the calculations taking into account the burning so it is difficult to obtain the result. For example, temperature fluctuations reach 30° relative to the mean value in hot engine parts. This may indicate the transient nature of investigated process or instability of applied solution mathematical methods. Solution process requires constant monitoring by estimator for these reasons.

The most important parameters describing GTE workflow and calculation process were visualized in the solution process: the flow temperature in characteristic sections, the imbalance of mass flow and compressor and turbine power. Decision of solution completing was made based on these parameters. The fuel consumption was adjusted manually during the calculation so that the compressor and turbine torque values matched within 5%.

3.3 The simulation results

The throttle performance calculation of investigated engine’s (Fig. 4) was performed using the model described above under standard atmospheric conditions. Ten equally spaced points was calculated. Rotor speed was varied from 15,000 to 100,000 rpm. Calculation time of one engine mode was 11 hours on 48 cores of supercomputer "Sergei Korolev". Thrust P, the air flow through the engine Ga and specific fuel consumption Csp dependencies, as shown in Fig. 6 were obtained in the calculation. The joint working line obtained in the CFD calculations is shown in Fig. 7 on compressor map of considered engine.

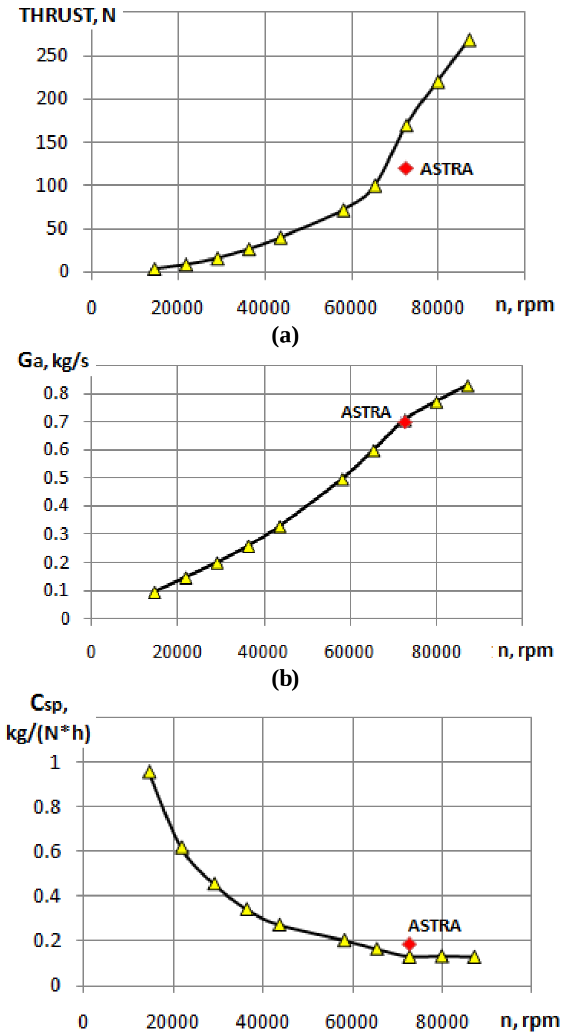

Fig. 6 The basic parameters of the GTE workflow dependencies (a - thrust, b - air flow rate through the engine, c - specific fuel consumption) on the rotor speed obtained using a uniform CFD workflow model

The same GTE workflow was also investigated at takeoff mode with a one-dimensional thermodynamic model developed in the program ASTRA [6]. This program was developed by A. Yu. Tkachenko, the associate professor of SSAU and allows to estimate the GTE parameters on the basis of the conservation laws and analysis of the GTE thermodynamic cycle [5]. The program has been extensively tested. It shows good agreement between the calculation results and experimental data [6]. The loss factors and efficiency values of components were assumed equal values that were calculated using CFD models in the thermodynamic calculation. The results of thermodynamic calculation in the program ASTRA are shown in Fig. 4 and 5 as a red diamond.

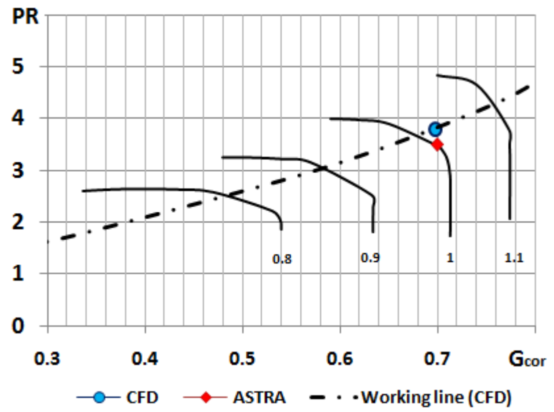

Fig. 7 Joint working line obtained in the CFD calculations on compressor map of considered engine

Comparing the results of thermodynamic calculations with the CFD data it can be concluded that they are in good agreement with each other. The difference between the results is no more than 7%. This conclusion is supported by graphic dependences of total pressures and temperatures changing along the flow passage, obtained by means of thermodynamic and CFD models. These dependences are shown in Fig. 8.

Thus it can be concluded that the CFD calculations results do not contradict existing physical concepts of GTE workflow and can be used for its parameters calculation and simulations under various conditions.

However, the end-to-end numerical simulation of the engine core workflow allows to find the value of the flow parameters in all points of the computational domain, and not only in the control sections (Fig. 9, 10, 11) compared with the thermodynamic model that allows to solve the same problems. Moreover the CFD model allows to take into account the effect of any geometrical parameters on the GTE performance.

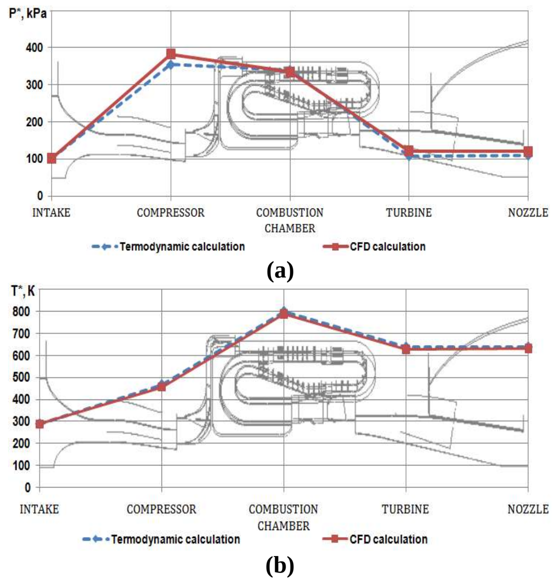

Fig. 8. Comparison of the graphs of total pressures (a)and temperatures (b) changing along the flow passage, obtained by means of thermodynamic and CFD models.

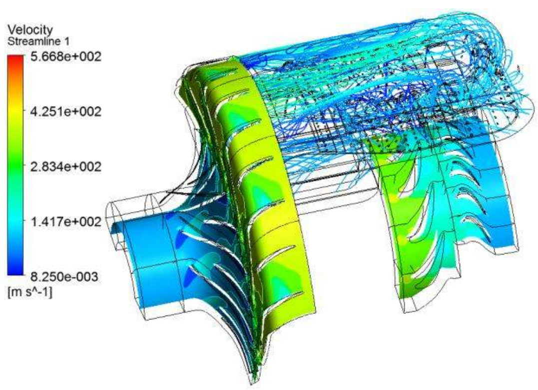

Fig. 9 The flow pattern of working fluid in a gas turbine engine

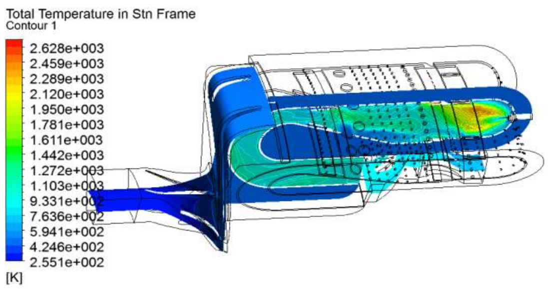

Fig. 10 Variation of temperature field in a gas turbine engine

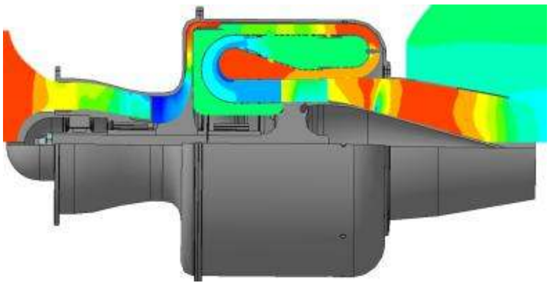

Fig. 11. Results of calculation

4 Conclusion

The first step in the CFD simulation of the GTE core was made in the present work. The computational studies shows that the results obtained using the computational model are in good agreement with the existing physical concepts and thermodynamic calculations. However, the significant problems were identified in the course of work. These difficulties do not allow to use the end-to-end numerical simulation of GTE workflow in a real design process today. The difficulties are primarily due to the large computation time and the needs of computing resources, the instability of the solution process, a lot of the assumptions used. In addition estimator, conducting the study, must have a high qualification and be equally well-versed in numerical simulation of gas flow and combustion processes, workflows of all GTE components and their joint work, thermodynamics, etc.

However, the numerical modeling of engine core workflow is very promising. It allows to model the mutual influence of engine components to each other, to investigate the impact of any working conditions and changes of passage elements on the GTE characteristics and all the nodes. For this reason, the research in this field will be continued in the future.

Acknowledgements

This work was supported by the Ministry of Education and Science of the Russian Federation, the agreement 14.B37.21.0297.

References

[1] Russell W. Claus, Scott Townsend, “A review of high fidelity, gas turbine engine simulations” ICAS 2010, 2010. 27th International Congress of The Aeronautical Sciences.

[2] Claus, R.W. “A review of high fidelity, gas turbine engine simulations” ICAS 2010 Paper, 2010, 27th International congress of the aeronautical sciences.

[3] Turner, M., Reed, J.A., Ryder, R., Veres, J.P., “Multifidelity Simulation of a Turbofan Engine with Results Zoomed into Mini-Maps for a Zero-D Cycle Simulation,”ASME GT2004-53956.

[4] Krivcov A.V., Shabliy L.S. Problemy modelirovaniya rabochego protsessa gazogeneratora v edinom CFD-pakete i otdel'nykh programmakh (Problems of engine core workflow modeling in a single CFD-package and separate programs), Mezhdunarodnyi nauchno-tekhnicheskii forum, posvyashchennyi 100-letiyu OAO «Kuznetsov» i 70-letiyu SGAU, Samara 5-7 sentyabrya 2012 goda: Sbornik trudov v 3-kh tomakh. Tom 3. Vserossiiskaya molodezhnaya nauchno-tekhnicheskaya konferentsiya «Kosmos - 2012». - Samara: Izdatel'stvo Samarskogo gosudarstvennogo aerokosmicheskogo universiteta, 2012. Vol. 3, p. 51-52.

[5] Kulagin V.V. Teoriya raschet i proektirovanie aviatsionnykh dvigatelei i energeticheskikh ustanovok: Uchebnik. Osnovy teorii GTD. Rabochii protsess i termogazodinamicheskii analiz. Kn.1. Sovmestnaya rabota uzlov vypolnennogo dvigatelya i ego kharakteristiki. Kn.2.,2. (The theory, calculation and design of aircraft engines and power plants: Textbook. The basic theory of the GTE. Workflow and thermal gas analysis. Book 1. Join work of performed engine and its performance. Book.2), Moskow Mashinostroenie, 2002. – 616 p.

[6] Kuz'michev V.S., Tkachenko A.Yu., Rybakov V.N. , Krupenich I.N. , Kulagin V.V. “Metody i sredstva kontseptual'nogo proektirovaniya aviatsionnykh GTD v CAE-sisteme «ASTRA»” (Methods and tools for the conceptual design of gas turbine engines in the CAE-systems "ASTRA"), Vestnik Samarsk.gos. aerokosm. unta. - 2012. - №5(36). part.1. – p. 169-173.

A unified method of identification and optimization of airfoils for aircrafts, turbine and compressor blades

S. Zietarski, S. Kachel, A. Kozakiewicz
Military University of Technology (WAT), Faculty of Mechatronics and Aviation,Warsaw, Poland

Keywords: airfoils, design optimization, combinatorial-cyclic method, turbine engines.

Abstract

Topics below are rather undesired, but important, outcome not yet completed research on the aircraft airfoils, turbine and compressor blades, parametric design of airfoils, establishing the relationships based on the results of experiments in a wind tunnel, developing databases for determining the relationships between airfoil parameters and lift and drag coefficients. Reliable database created as a result of the research work allows to simulate the wind tunnel. Very early on, however, was necessary to extend the developed specialized software for a new applications, and it meant the need for generalization of software, e.g. for gas turbine engines, propellers, etc. But after some time it turned out, that in order to achieve the required accuracy, the changes are needed in the underlying assumptions, set decades ago. In addition, coordinate measuring machines and systems, and associated software were not always as accurate as expected. Concepts how to solve it and develop software carrying out these tasks are presented in the article. It is like to withdraw from the old path and look for a new path that will lead to the reliable data base. Processes related to air or gas flow should be similarly defined in all the specialized software applications (e.g. aircrafts and turbine engines). Accuracy (10^{-9}mm) achieved in virtual measurements within the integrated system can be used to verify the results of CMM and other measuring systems, provided that an appropriate software has been developed.

1 Introduction

Over the last two decades, passenger and military aircrafts, became a fully high technology products, and design, engineering, manufacturing of these aircrafts is carried out entirely within integrated CAD/CAM/CAE systems. It should be emphasized that in these systems, all the tasks related to the definition of the geometric shape of the structure are realized by Nurbs geometry concepts. Because this geometry can define all surfaces, and solids that occur in engineering practice, therefore, the software-based identification and optimization of even the most complex shapes have become feasible, at least, by a virtual prototyping approach. There is a meaningful difference, as far as time-consuming factor is concerned, whether an interactive mode is used or program-oriented definition of any engineering problem, described by using a build-in basic system language (e.g. GRIP in Siemens NX system, updated APT, etc.). Such a programming is becoming the necessary qualification for engineers of high technology products, particularly, when the highest quality, optimization, CNC manufacturing, and reverse engineering are of a primary concern.

The main role in the developed software, needed to solve given tasks, plays the combinatorial-cyclic method of optimization. The structure of subprograms in the method is fit to different area of applications, since one subprogram is treated as target-oriented and defining the objective function as well as selecting either a deterministic model or artificial intelligence model. There has been gathered a considerable experience in the following main areas of applications:

(1) Analysis of all errors in manufacturing processes, even on the most complex surfaces (eg. airplanes, turbines, propellers, car bodies, etc.), moreover, on each stage of CAD/CAM technology; eliminating the necessity of a precise set-up of the part being measured on a CMM table or for scanning system; verifying the accuracy of CMM itself and applied software. The specialized software is of a great importance for effective calculation of dimensional deviations between the virtual product model and the part machined, defined by a cloud of points (even more than 2 million).In assembled physical objects the total error can be divided on errors of surfaces machined and assembling errors.

(2) Design optimization, according to required accuracy of location and orientation of principal axes of inertia or other design objective functions, e.g. minimizing the deviation between principal axis and axis of rotation; optimization of parametric design, where parameters are optimization variables; it enables us to effectively apply reverse engineering techniques (max. number of optimization variables=15).Virtual balancing, as a variety of design optimization, has become a necessity in virtual prototyping of gas turbine engines.

(3) Establishing the optimal mathematical formula for interrelationships among variables, based on experimental data or parametric design data; it works as an extension to multiple regression analysis not requiring the linearity. Usually, we can consider additionally 2nd or 3rd degree, power or exponential equations.

(4) Solving the equation systems, linear and non-linear, particularly, where the number of unknowns is less than number of equations; mostly applied to analytically defined surfaces (eg. a sphere, plane, cylinder, cone, ellipsoid, etc.). The method identifies these surfaces and solid bodies with high accuracy from a cloud of points, obtained from coordinate measuring systems. Measuring the reference sphere (30, 50, or 100 points) , we can effectively determine the current accuracy of the CMM.

To achieve higher geometric accuracy of complex shapes, airfoil shapes included, and overall increase in surface quality it is necessary to take full advantage of capabilities available in integrated CAD/CAM/CAE systems as well as in a new generation of CNC production equipment and coordinate measuring machines. It should be remembered that one of the main advantages of Nurbs geometry is that we can easily calculate the shortest distances between points and solid body models, and more importantly, give them signs '+' or '-', what means –outside- or -inside- of the body. But in this context, if we want to accurately measure the airfoil we have to replace it with the solid body model, even if it is virtual measurement.

Rules for the airfoil analysis and experimental research in aerodynamics were established decades ago, when computer systems, based on Nurbs geometry, were not tools of everyday use for engineers, and therefore, these rules should be revised. These revised rules must provide two main features that could not be guaranteed in the existing computational procedures and practical steps of implementation.

The two main features are:

- building an accurate CAD airfoil model from the point set, wherein, high accuracy is achieved by the optimization of curves that make up the model surfaces, and then analyzing the CAD model errors by using combinatorial-cyclic method of optimization;

- the ability to accurately verify the geometric errors of the physical model, manufactured by CNC machine tools according to the CAD model, and then measured by coordinate measuring systems.

When the CAD / CAM / CAE system is extended by specialized programs ensuring these two features, then even the geometry of the aircraft, directly from the manufacture or repair, can be geometrically identified by a coordinate measuring. Combinatorial-cyclic method of optimization [1,2] provides computation of the differences in position and orientation of the two systems, the coordinate system of the CAD model and the measurement coordinate system, which, as yet, had been replaced by the time-consuming and geometrically inaccurate set-up of the object being measured. It should be noted that the accuracy achieved with such an approach in the virtual prototyping allows to determine permanent deformations after extreme testing in flight

To achieve these new features the addition of a new specialized software for almost all the major modules of the system, is required.

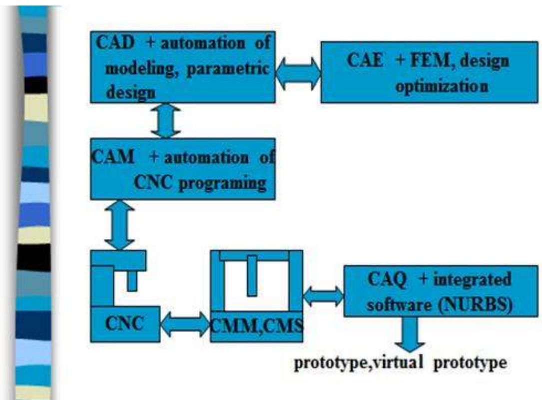

Fig 1. COMPUTER INTEGRATED MANUFACTURING CAD+/CAM+/CAE+/CAQ+ (= CIM)

Fig.1 shows the developed specialized software in different modules of the system to meet the challenges of identifying and optimizing processes in various stages of CAD, CAM and CAE. The new software is presented after sign '+'. This software is also generalized in nature and allows by the same definitions to describe computational processes for aircrafts and turbine engines. Of course, the range of applications can be relatively easily extended to other similar products, especially, to those where a reverse engineering and accuracy of complex shapes plays an important role, e.g. airscrews, ships and yachts, cars, satellite dishes, etc.

2 A revised method of airfoil definitions

When we want to increase the accuracy of the airfoil fitting to the given set of points and also to extend definitions on turbine blades, compressor blades, airscrews, and ship propellers we need to make changes to the previously applied rules in an airfoil design process, airfoil manufacture process, and coordinate measurement of the airfoil shape machined. A new approach for defining the airfoils from the set of points has already been presented in [2], but in practice, the verification and the need to adapt the airfoils for the turbines and compressors, required significant modification. The contents of current description, though apparently similar, differs in details and in the sequence of steps.

Points, underlying the accurate calculations of airfoils, are derived from the published tables of standardized airfoils (NACA), from airfoils tested in wind tunnels, and, more and more often, from digitization or scanning of real objects, photographs or images on the internet, from available technical documentations or specifications on the internet. Assuming that in this approach coordinate errors of points are inevitable, absolutely the first step must be to reduce to the maximum impact of these errors.

The key to accurately determine the location, orientation and length of the chord and camber line is a calculation of two extreme segments of the given airfoil, i.e. the leading edge and trailing edge segments. The leading edge segment is always the curve of 2.degree, mostly circles, but ellipses, parabolas, and hyperbolas are also possible. The trailing edge segment is a line or the curve of 2.degree as in the previous edge. The main assumption is that, at first, we start with circles only and compute the first segment of camber line, which also determines the axis of symmetry. Then we go to circles and ellipses, to compute the first segment of the camber line, which is a straight line. The standard deviation gives an indication what is the best fit, a circle or ellipse. It is worth to notice that in a definition of an ellipse, a circle is the specific case only. The procedure can be extended to parabolas and hyperbolas.

As the results of this initial step, we get:

- a point that marks the beginning of a new X-axis, the beginning of a new chord, the beginning of the first segment of a camber line; this point is so calculated that determines the first segment of the camber line and also the axis of symmetry of the2.degree curve, which was not previously possible for ellipses, parabolas, and hyperbolas;.

- a point that marks the end of a new X axis, the end of a new chord, the end of the last segment of a camber line;

- two points of tangency on the leading edge and two points of tangency on the trailing edge (or two intersection points).

If the new X axis is not the same as in the coordinate system of the points, the set of points must be transformed by rotation and translation. So far, there were no such transformations, and errors arising from that, even more than 0.5 mm or 0.5 degree, could not be determined by the coordinate measurement. Now, by applying the method presented in this paper, it is no longer impossible.

After the corrected coordinate system has been established, upper and lower segments of the airfoil are optimized to fit to the transformed set of points. To optimize the airfoil as a whole (four segments), the combinatorial-cyclic method of optimization is necessary.

It is worth noting that all the airfoils consist of four different segments, each of these segments should be a separate curve with clearly defined beginning and end of the segment. Each of the four segments is determined from a given set of points, and the number of points can be very different- tens, hundreds, or even thousands.

There are well-defined geometric constraints for particular segments of the profile, resulting from research in aerodynamics and gas dynamics, and determining the approximate number of points required to define the optimal curve for each segment. The key to accurately determine the location, orientation and length of the chord is a calculation of two extreme segments of the given profile, i.e. the leading edge and trailing edge segments. The leading edge segment is always the curve of 2.degree, mostly circles, but ellipses, parabolas, and hyperbolas are also possible. The trailing edge segment is a line or two lines or the curve of 2.degree as in the leading edge.

To generalize algorithms for all airfoils, either airplane or turbine and compressor blades, in both segments the starting, ending, and midpoints are precisely calculated. Therefore, the chord must be defined as the straight line joining the midpoint of the leading edge and the midpoint of the trailing edge, and these points may not always be the extreme points of the profile. It is worth repeating that if the starting point of the chord or the angular position of the chord are not exactly in line with the chord established from the set of points, e.g. joining the extreme points , then you need to transform the existing set of points to the coordinate system of the new chord.

The airfoil as the optimal curve can be presented in the Nurbs geometry definition:

nurbs1=bcurve/fit, p(1..n),toler,t,degree,d

where: p, t, d - obtained from the optimization process, p- selected points (e.g.15 to 25 points), t- max. distance between the selected points and curve, d– degree of the upper and lower segments of the airfoil (mostly 3). The method used to optimize the profile curve can be extended to solid bodies of an airplane wing, stabilizer, and fuselage. Also, turbine blades, compressor blades, etc. are optimized by this method, but, of course, the software for an automatic generation of geometric models must be developed. The optimal airfoil with the mean chord length (e.g. 100 mm, 1000 mm or any other) are then parameterized. The main aim of parameterization is establishing the optimal mathematical formula for interrelationships between characteristics of the airfoil and parameters, e.g. c_l or c_d as a function of p(1..n). It is possible, to read parameters from the airfoil and, inversely, to build the airfoil from parameters. The airfoils can be divided into classes, depending on the specific properties of airfoils or standard length of the chord. Usually, for increasing the accuracy of the calculation of aerodynamic characteristics, e.g. c_l, c_d for all airfoils resulting from scaling the basic airfoil.

Of course, the complete and reliable database enables to develop the software simulating a wind tunnel. Instead of manufacturing a physical model of airfoil shape for a wind tunnel, it is possible to predict c_d and c_l from airfoil parameters. The detailed procedure has been presented in the paper [2], but after have gathered some databases, it turned out that some modifications and extensions are required.

Successes of CFD software encourage to a new approach to aerodynamic research, particularly, to problems hitherto unsolved. The unified method for all airfoils, i.e. of wings, stabilizers, longitudinal section of an aircraft fuselages, turbine blades, compressor blades, airscrews, etc.makes it easy to extend the application of wind tunnel research. Before we start the wind tunnel research, we have to know accuracy of the designed CAD model and accuracy of the CNC machined physical model.

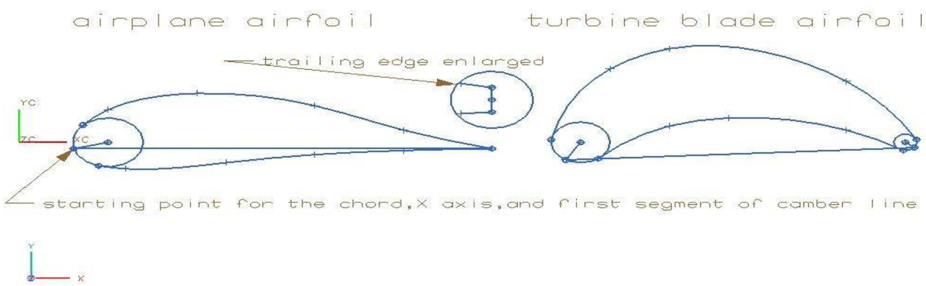

Fig.2. Accurate calculation of leading and trailing edges of the wing airfoil and of the turbine blade airfoil. As a result, we may adjust the length and position of the chord, what enables to transform points defining the airfoil. Then the airfoil as a Nurbs curve can be optimized in relation to the transformed set of points. The middle point and two boundary points in edge curves or edge lines are of great importance in the presented concept. The figure has been generated by the optimization program from a cloud of points (hundreds of points). Airplane thin airfoils and compressor airfoils are similar to left and right airfoils, respectively, except that the edge radius can be as small as 0.5 mm. Heretofore, because of the large camber angles on the leading edge of the turbine and compressor blades, the same method of defining the edges, as for airplane airfoils, could not be used.

```
============================================
General conic:
CIRCLE(0,1),ELLIPSE(1),PARABOLA(3),HYPERBOLA(2
A*x**2 + B*x*y + C*y**2 + D*x + E*y + F = 0
n1= 8, n2= 5, n3= 1 n4=15, n5=12
Conic index (as above): ehp=1, first point p( 8)
ellipse center:  149.7212,  26.0472,    .0000
semimajor:  150.0000
semiminor:  149.8732
  tilt angle:   10.0000
start angle:  211.3381
 end angle:  542.8950
 start point:   19.8343, -51.8256,    .0000
  end point:   -2.0562,  18.4729,    .0000
standard deviation for all points p( 8..12): sigma=  0.1312
OPTIMUM GCONIC-CURVE:p( 8),p( 5),p( 1),p(15),p(12);

Remove all points below and insert the middle, and two
boundary points
p( 8)=POINT/  -2.0562,  18.4729,  .0000
p( 5)=POINT/   5.8911,  73.4382,  .0000
p( 1)=POINT/  46.8690, 135.1525,  .0000
p(15)=POINT/  57.6299, -92.7142,  .0000
p(12)=POINT/  19.8343, -51.8256,  .0000
```

Fig.3 Printout from the program showing the outline of algorithms for the general conic optimization, i.e. for both edges of the airfoil. The middle point and two boundary points (tangency points) are also computed in the program.

Points for design and points from CMM measurement are the base for computing sigma, as the error measure. It is especially important when the geometric CAD model has not been defined in the same system as the CNC program. A generalized geometric identification of all airfoils in use, is presented graphically on the example of an airplane airfoil and the airfoil of a turbine blade, Fig.2. A thin airfoils of airplanes and airfoils of compressors actually differ only in leading edge radii and thickness in relation to two airfoils presented, but the leading and trailing edges have a significant impact on the chord. A geometrically accurate airfoil, optimized in relation to a set of points, is an essential condition for the transition to solve other tasks, carried out by the dedicated software.

It is recognized that almost always when we get an airfoil as a cloud of points, we have no certain information about the precision with which the X-axis of measurement system coincides with the airfoil chord .To indicate the validity of the problem of airfoil accuracy, the most important aspects have already been presented in the Introduction above. Circles, ellipses, parabolas or hyperbolas are computed from 15 to 30 points taken from the area around both edges.

The results of iterative computations with the ever decreasing number of points are as shown in the printout after each run with a new number of points from e.g.30 to 5. Therefore, to minimum 5, because the curves of second degree are defined as general conics, Fig.3. This is actually the first step in identifying the leading edge and, in particular, to determine the angle of the first segment of camber

Similarly, it can also be shown the optimization of the airfoil as one NURBS curve, linking together three segments, i.e. the segment of leading edge with upper and lower segments. The results of combinatorial-cyclic method are printed in paper [2]. Airfoil geometry has been optimized as CAD solid body model. Precise identification of the airfoil geometry means that the geometrical model requires only the development of a tool path for CNC milling machines with 3- or 5-axis controlled. The presented sequencing gives a very large guarantee, that we can achieve a high accuracy and repeatability, assuming that we proceed within the integrated system.

3 Accuracy of CAD models and CNC machined parts, and developed CAQ extensions for assemblies

CAD model surfaces shaped for air or gas flow around, could not be measured, so far, that it was clear that each point of the measurement is above or below the concerned surface. Introducing the combinatorial-cyclic method to the CAQ module allows it. Analysis of errors is carried out both for the CAD model and physical object machined. Even the surfaces of analytic geometry as spheres, general cones, slanted cylinders can be used to test the accuracy of the hardware and software of CMM used.

In the paper [2] we presented the wide range of goals, which could not be fully achieved, because of errors in an early stage of the research. Parametric design is necessary for an optimization but even optimized model cannot be manufactured by any standardized machining processes. Some CAD models for wind tunnel tests (e.g. airplane fuselage, wings, blades) should be, if possible, machined according to the direction of air flow. Experiences from these approach necessitated adjustments in specialized software, and it is introduced below.

This way of presenting the results is a standard for the combinatorial-cyclic method of optimization, which was applied to the analysis of coordinate measurement of F-16 airplane model, designed for research in a supersonic wind tunnel. There is not known any other method that would result in an accurate calculation of the surface errors from hundreds, or even hundreds of thousands, of points from coordinate measurement (CMM) of the physical object (3D). Surface errors, measured at a given points, are obtained after the CAD model (which is the base for the CNC program) has been positioned inside the set of points, so that the sum of squared distances from all points of measurement to the surface reached minimum.

.

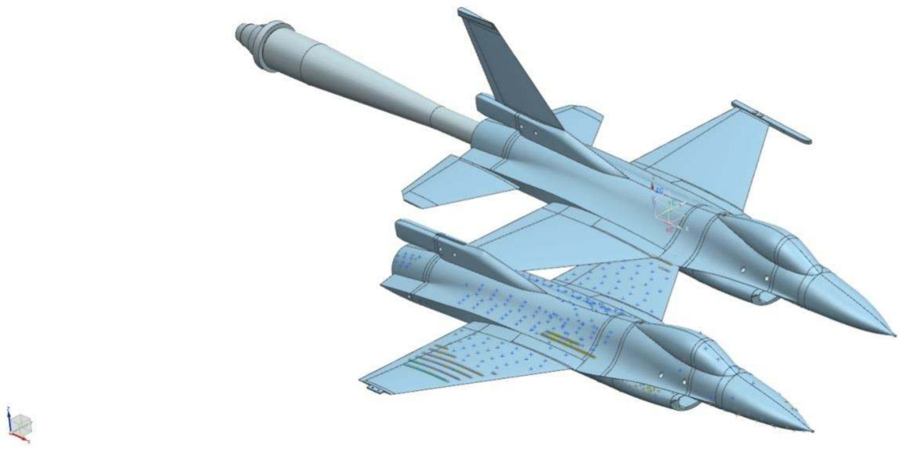

- Fig.4. Graphical presentation of the results from the applied combinatorial-cyclic method of optimization. Two objects are: the complete CAD model of F-16 airplane, including extensions for mounting in the supersonic wind tunnel and incomplete physical F-16 model, which was CNC machined and then measured by a coordinate measuring system. Visible points on the surface, depending on the color, indicate errors above sigma, 2 *sigma and 3 * sigma and inside or outside as well. Points below |sigma| are invisible and if 80% of points is invisible means, approximately, that on 80% of the surface there are errors below |sigma|.
-

Effective visualization of errors on the measured surface is only possible because each rotation and translation of the CAD model in relation to the points changes visible points and its colors. Of course, the colors represent error values into and out of the material. Reading the text with detailed documentation takes more time, but, in general, it is essential in practice.

Previously, it was possible to only measure the distance between the characteristic points of the design, which could be a large number, but it is not comparable to what is currently giving digitizing or scanning the surface of the design. For example, to identify the sphere meant coordinates of the center and the radius of the sphere. For this, it was enough 4 to 10 CMM points, but when these points was 100 or more, we had no effective mathematical tools to determine the surface errors. It must be remembered that the arithmetic mean is not a good criterion, but the accepted criterion is the minimum sum of squares and resulting from that sigma.

It should be emphasized that the combinatorial-cyclic method eliminated the need to set the object to be measured in accordance with the coordinate system of the CAD model, which accounted for over 50% of the time-consuming process of measurement, and the measurement involved only, a dozen or more, specific points or sections of the design. The method can also be used when the object as a whole must be measured with different reference points, i.e. with different origins of the coordinate system for the measurement. The same problems are also present in these technical objects like airliners (Boeing, Airbus), gliders, helicopters (Sikorsky), car body dies, turbine and compressor blades, yacht hulls, hip replacements, reflectors and satellite dishes, etc For these objects, this method has been used and modified since 1998.

Attention must be drawn that not only the outer surface of the airplane has a lot of surfaces composing the whole, whichare machined separately and then assembled. Car body outer surface is composed of, at least, 11 surfaces, which are pressed by different dies, and dies, generally, do not produce sheetmetal with the same accuracy. If we want to achieve a drag coefficient c_d<0.30, we need to test the model of the car in the wind tunnel, and before that check the accuracy of the model. Very often this requires that the complex coordinate measurements are performed on work surfaces of dies to accurately determine the shape errors. Determining the differences between the sheetmetal surfaces and working surfaces ofdies allows to compute springback errors, as indeed it was the first field applications of combinatorial-cyclic method.

Before we use the geometric CAD model in the CAM module,in order to prepare CNC machining program, first we should also analyze CAD model errors, except that the base of comparison is then the same points that were used to define the model. Scaling errors or other size errors can be corrected. The final inspection of CAD solid body model is the mass analysis, where we check if model is not encumbered by a serious mass distribution errors, which could then be transferred to programs for CNC milling machines. The most important is whether the center of mass is in the plane of symmetry of the solid body model and whether the two principal axes of inertia are in the plane of symmetry, and whether one of these axes, at least with the permissible error, coincides with the principal axis along a fuselage in right-hand coordinate system.

Coordinate measurements were made in one setup with possibility to group points: (1) F-16 model as a whole, (2) the center and rear fuselage, (3) the front fuselage with the cockpit and nozzle inlet,(4) wings as a whole, right and left, (5) the right wing, (6) the left wing. First and foremost is the error analysis of the model as a whole, and it means that we sum up the machining errors and assembling errors of all components. It was not until the next steps we submit further analysis of surfaces (2,3,4,5,6) that make up the model. This increases the time-consuming research, but also the results of these analyzes are crucial to assess the reasons for the resulting errors, and allows the separation of the surface errors from the assembling errors of errorsof parts that make up the multi part object, which is the airplane model.

In the technical metrology a measure of error is the standard deviation sigma and 3 * sigma. Since the central and rear fuselage are the one part of the model to which are mounted the front fuselage and wings, so it can be assumed that the errors sigma and 3 * sigma of this part are 100%, and in relation to this part are measured translations and rotations of all other parts, which are assembling errors.

In the case of a milling the part in one setup on the CNC milling machine, sigma is a measure of the surface errors arising from the quality and accuracy of the machine, CNC program quality, but so far these errors were measured in selected sections of the part machined. In current approach the part machined is measured and then compared with the CAD model throughout its volume. Errors resulting from failure to accurate setup of the part in relation to the coordinate system of the model also affect the assembling errors.

Of course, each integrated CAD / CAM / CAE system accomplishes the modeling and manufacturing within the CAD and CAM modules and never redefines the geometric model, from which the CNC program is developed. After any change of the model all optimization analyses must be repeated.

The analysis takes into account errors that the model is composed of many parts machined separately and comparative analysis of these parts is given in the table as a sigma / sigma fuselage (2).The short comparative analysis of parts within the airplane assembly model has been shown in Tab.1.

In order to fully understand all of the errors in the CNC machining and in the assembling the model, it is necessary to present an analysis of the errors in the various parts that make up the model. It only indicates the cause of errors.

3.1 Assembling errors in relation to fuselage (2)

(1) F-16 model as a whole(2)
dx=101.1733-x(2)=-0.1833mm
dy=-188.2687-y(2)=0.0022mm
dz=-1.9083-z(2)=-0.0863mm

Summary of the results of error analysis

Model surface errors:

	sigma	% of points -/+ sigma	3*sigma	% of points -/+ 3*sigma	sigma/ sigma fuselage(2)
(1) F16 model	0.1276mm	81.42%	0.3828mm	98.17%	365.61%
(2) Fuselage central	0.0349mm	77.35%	0.1046mm	99.94%	100.00%
(3) Fuselage front	0.1423mm	88.41%	0.4270mm	97.98%	407.74%
(4) Wings as a whole	0.1107mm	73.00%	0.3322mm	99.32%	317.19%
(5) Wing right	0.0408mm	66.51%	0.1224mm	99.42%	116.91%
(6) Wing left	0.0547mm	96.42%	0.1641mm	99.87%	156.73%

Fuselage central(2):

translation	x(2)= 101.3566mm	y(2)=-188.2709mm	z(2)=-1.8220mm
rotation (degrees)	alfa_x(2)=0.6452	beta_y(2)=-3.2590	gama_z(2)=-0.0744

Tab.1. The analysis of F-16 model errors.

dalfa_x=0.6686-alfa_x(2)= 0.0234 degree
dbeta_y=-3.2725-beta_y(2)=0.0765 degree
dgama_z=-0.0575-gama_z(2)=0.0169 degree

(3) Front fuselage
dx=100.8614-x(2)=-0.4952mm
dy=-188.4025-y(2)=-0.1316mm
dz=-2.0163-z(2)=-0.1943mm
dalfa_x=0.6358-alfa_x(2)=-0.0094 degree
dbeta_y=-3.3172-beta_y(2)=-0.0682 degree
dgama_z=-0.0110-gama_z(2)=0.0634 degree

(4) Two wings as a whole
dx=99.8758-x(2)=-1.4808mm
dy=-188.7938-y(2)=-0.5229mm
dz=-1.9488-z(2)=-0.1268mm
dalfa_x=0.6968-alfa_x(2)=0.0516 degree
dbeta_y=-3.4490-beta_y(2)=-0.1900 degree
dgama_z=-0.2243-gama_z(2)=-0.1499 degree

Asymmetry error of two wings dy=-0.5229 mm, requires a thorough error analysis for the two wings separately. Error indicates that the two wings are moved along the Y-axis dy =-0.5229 mm from the XZ symmetry plane; the problem is the first, but not the only, indicating that the two wings as a whole does not meet the symmetry condition in relation to the symmetry plane of the airplane model.

(5) Right wing
dx=100.8611-x(2)=-0.4955mm
dy=-187.0223-y(2)=-1.2486mm
dz=-1.3273-z(2)=0.4947mm
dalfa_x=1.0144-alfa_x(2)=0.3692 degree
dbeta_y=-3.3280-beta_y(2)=-0.0690 degree
dgama_z=0.5747-gama_z(2)=0.6491degree

(6) Left wing
dx=102.7037-x(2)=1.3471mm
dy=-190.8077-y(2)=-2.5368mm
dz=-1.5773-z(2)=0.2473mm
dalfa_x=0.5148-alfa_x(2)=-0.1304 degree
dbeta_y=-3.2849-beta_y(2)=-0.0259 degree
dgama_z=0.0034-gama_z(2)=0.0778 degree

3.2 Closing remarks on computed results

Validation and verification of the method is carried out as follows:

- around 1000 points are measured on the CAD model surface using system tools, the same as in the virtual coordinate measurement;
- the points are subjected to transformation in the space;
- the applied combinatorial-cyclic method identifies the transformation, i.e. translation and rotation around the axis of the model system, and the resulting standard deviation sigma = 0, namely 0.00000000, i.e. (10^{-9}), since this is the accuracy of Siemens NX7.5 system.

Rules applied to the analysis of CMM measurements of airplane models can also be used to other multi-part objects (assemblies) in full scale. Of course, the full scale of the object often means that we cannot use coordinate measuring machines (CMM) but laser measuring systems with larger measurement errors.

Verification of results of CMM measurement by the virtual measurement, as described above, confirmed the results for all parts from which has been assembled the model.

. Results of the analysis can be verified by virtual measurements for all parts of the model, including the model as a whole, but the results are the same, sigma=0. Therefore, the front fuselage was chosen, because in this part the CNC machining errors are maximum. The last part of this analysis has been shown below:

OUTSIDE AND INSIDE ERRORS
Ten maximum outside distances:
ptm(84): x= 148.7551 y= 42.0552
z= -4.6323 dist= .000000001
ptm(82): x= 122.7822 y= 45.2660
z= -3.5096 dist= .000000001
ptm(77): x= 158.8327 y= -24.9500
z= -6.1918 dist= .000000001
………………..
……………….
Ten minimum inside distances:
ptm(98): x= 140.1554 y= 6.5764
z= 39.1135 dist= .000000000
ptm(97): x= 157.5730 y= 7.4581
z= 40.2845 dist= .000000000
ptm(92): x= 251.3148 y= 12.9132
z= 5.9603 dist= .000000000
……………….
……………….

Tab.2. Excerpt from the printout; .- dist-means an error.

Since the use of software requires to know a running time for the computing task, below are given approximate times, if prerequisites are met.

Prerequisites:

- the computer at least 4 GB of RAM;
- the complexity as of the airplane model consisting of more than one component, machined separately;
- the number of points from coordinate measurements around 5000

When the required accuracy: 0.1 mm,
the computation time from 15 min. to 1 hr. depending on initial values of iteration.
When the required accuracy: 0.01 mm,
the computation time ca. 1.5 hr
When the required accuracy: 0.001 mm,
the computation time ca. 3 hr
When the required accuracy: 0.0001 mm,
the computation time ca. 4.5 hr

In mobile workstations of such class as Dell Precision M4700, you can, at the same time, calculate the model as a whole, and three or four other components, which significantly speeds up the execution of calculations for all components of the measured object.

Conclusions

In recent years, almost all achievements in aircraft technology are connected with the development of a new class of specialized software. This software is built mostly in languages relevant to a particular engineering system, specific to the industry. These languages are derived from Fortran and C + +, but for engineering applications are much more efficient. Still, the software is never 100% reliable and requires constant testing and modifications. Thus, in the present study was paid so much attention to the results of the verification and testing After all, even in the most modern aircraft we often encounter failures, resulting from the operation of the software.

References

[1] Zietarski S.**:** **"**AI-based optimization method for the analysis of coordinate measurements within integrated CAD/CAM/CAE systems". Computer Aided Production Engineering, CAPE 2003. Professional Engineering Publishing Limited, London and Bury St Edmonds, UK, 2003

[2] Zietarski S., Kachel S., Kozakiewicz A.: "A new approach to identification and optimization of airfoils by using the combinatorial-cyclic method". 28th International Congress of the Aeronautical Sciences, Brisbane, Australia, 2012

4:th CEAS Air & Space Conference
FTF Congress: Flygteknik 2013

Numerical simulations of two-phase turbulent reactive flows

A.C. Petcu, C. Sandu
National Research and Development Institute for Gas Turbines COMOTI, Romania

C. Berbente
Politehnica University of Bucharest, Faculty of Aerospace Engineering, Romania

Keywords: *3D RANS, ANSYS CFX, combustion chamber assembly, Jet-A*

Abstract

In order to develop a new multiple-fuel combustion chamber, a series of numerical simulations has been conducted on an existing combustion chamber, in order to determine the modifications required to allow its proper operation for multiple liquid fuels and fuel mixtures. The combustion chamber used in the simulations comes from a Garrett gas turbine engine, model GTP 30-67. A three-dimensional unsteady RANS numerical integration of the Navier-Stokes equations has been carried out, using an Eddy Dissipation combustion Model (EDM) and the k-ε turbulence model, implemented in a numerical simulation conducted using the commercial software ANSYS CFX. To verify the numerical simulations accuracy, the outlet temperature has been recorded along 600 time-averaged iterations and compared with the designed turbine inlet temperature. Numerical simulations results have a good accuracy in this particular case, so it can be concluded that the used numerical models are valid and appropriate for use to simulate the combustion process under different conditions. Thus the results obtained in these simulations will help adapt the existing combustion chamber to different fuels and fuel mixtures.

1 Introduction

In order to develop a new combustion chamber, a series of numerical simulations have been conducted on an existing combustion chamber, in order to determine the modifications required to allow its proper operation for multiple liquid fuels and fuel mixtures.

The combustion chamber used in the simulations comes from a Garrett gas turbine engine, model GTP 30-67. Garrett GTP 30-67, a shaft power gas turbine engine, is a compact, lightweight, shaft power source which is readily adapted to fit various types of enclosures and installations. The engine provides a mounting pad and drive shaft for installation and drive of an AC generator. The ambient air is compressed by a single stage centrifugal compressor, mixed with fuel in the combustion chamber and the mixture's ignited. The resultant high energy gases drive a radial inward-flow turbine wheel. The rotating shaft power of the turbine wheel drives the compressor impeller and an accessory gear train to provide reduced rpm shaft power. The remaining power is the engine power output. This gas turbine was used mainly to drive the alternator in military, portable, generator sets.

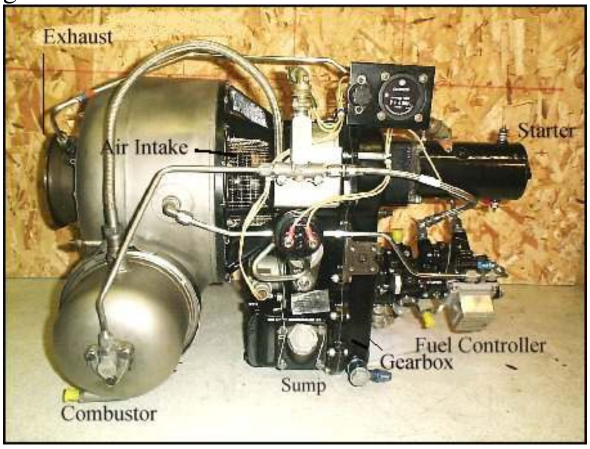

Fig.1 Garrett gas turbine model GTP 30-67

In table 1 are presented a few of the gas turbine engine's technical characteristics.

Table 1. GTP 30-67 technical characteristics [1]

	Characteristics	Value	Unit
1	Idle rotation speed	52800 ± 200	rpm
2	Output drive shaft rotation speed	8000±15	rpm
3	AC generator power	20	kW
4	Compressor inlet maximum temperature	325	K
5	Exhaust gases maximum temperature	1091	K
6	Load functioning regime rotation speed limits	55400 - 58000	rpm
	Fuel		
7	Main: MIL-T-5624, JP4, Alternative: JP5, Kerosene – VV-K-211, Emergency: MIL-G-5572, Gasoline, Diesel VV-F-800		
8	Fuel inlet pressure	0.35 – 1.38	bar
9	Fuel maximum inlet temperature	330	K
10	Maximum fuel consumption at nominal regime	0.0075	kg/s
11	Maximum fuel consumption at idle regime	0.0044	kg/s

2 Numerical simulations

2.1 Geometry

The figures below present the whole combustion chamber assembly and the fire tube used in the simulations.

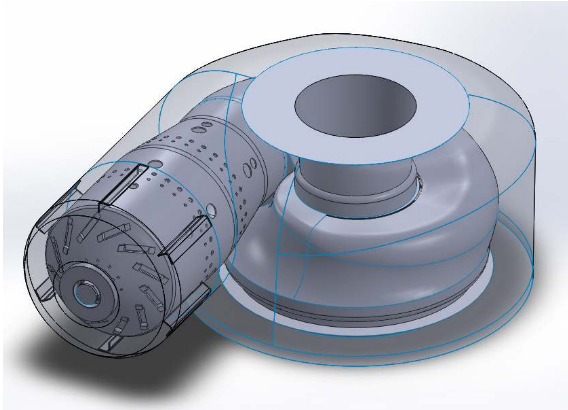

Fig. 2 The combustion chamber assembly

Fig. 3 The fire tube

2.2 Mesh

Based on the geometry of the combustion chamber assembly presented in fig. 2 an unstructured computational grid of 3.576.588 tetrahedral cells and 592465 nodes has been created using ICEM CFD (fig. 4).

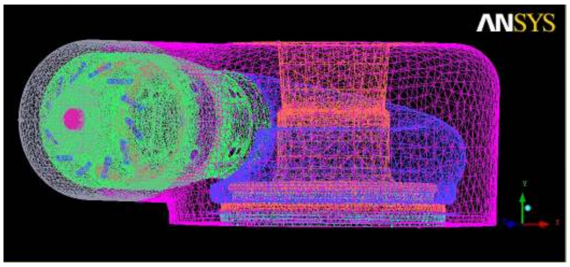

Fig. 4 The computational grid

2.3 Boundary conditions

Separated fuel and air inlets have been used in the numerical simulations. The air inlet is considered the exit from the compressor – the entrance in the combustion chamber assembly. This is an annular surface of 7540 mm^2. The air mass flow is of 0.9 kg/s [2]. The combustor inlet temperature is of 423K which is the corresponding temperature for the engine's compression ratio of 3 [2]. The fuel, in our case Jet-A, is injected directly in the fire through an orifice of 0.017 mm^2. It has been considered that the fuel is injected at a purely axial velocity 1200 m/s. The fuel's velocity has been determined from the following relations:

$$\left.\begin{aligned} \dot{m}_{fuel} &= \frac{\dot{m}_{air}}{\lambda * \min L} \\ \dot{m}_{fuel} &= \rho * \dot{V}_{fuel} \\ \dot{V}_{fuel} &= v * A \end{aligned}\right| \Rightarrow v = \frac{\dot{m}_{fuel}}{\rho * A} \qquad (1)$$

where:

$\dot{m}_{fuel}$ - fuel mass flow (kg/s)

$\dot{m}_{air}$ - air mass flow (kg/s)

λ - air excess

minL – the stoichiometric quantity in kg of oxidizer needed to burn 1 kg of fuel

ρ - fuel density (kg/m^3)

$\dot{V}_{fuel}$ - fuel volumetric flow (m^3/s)

A – fuel inlet orifice area

v - fuel inlet velocity (m/s)

In our case: $\dot{m}_{air}$ =*0.9 kg/s*, λ =*3.5*, *minL =14.67 kg, A= 0.017*mm^2. By substituting these values in Eq. (1) a fuel's velocity of 1200 m/s has been obtained. The fuel temperature at the entrance in the computational domain is of 300K.

The air enters the fire tube through a series of holes made in the fire tube's wall. The air which enters the fire tube through the holes situated in its upper region, the primary air flow, is used in the combustion reaction. The air which enters the fire tube through the lower situated holes, the secondary air flow, is used to cool the fire tube's walls.

The exit from the combustion chamber assembly – entrance in the turbine is the subsonic outlet of the domain. The outlet pressure is set at 2.83 bars.

The fuel, Jet-A, is uniformly injected into the fire tube, in the form of droplets. The values of the droplets diameter have been chosen based on the diagram presented in reference [3] (fig.5).

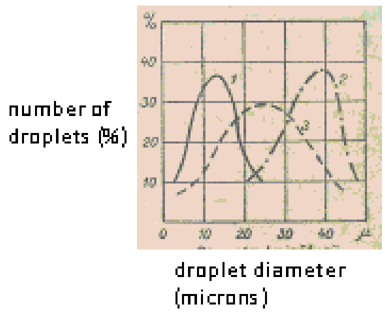

Fig. 5 Droplet distribution in a section of the liquid jet, in 3 cases [3]

2.4 CFD simulation used settings

A three-dimensional unsteady RANS numerical integration of the Navier-Stokes equations has been carried out using the commercial software ANSYS CFX. In these numerical simulations an Eddy Dissipation combustion Model (EDM), based on a one step kerosene-air reaction mechanism from the ANSYS library [4], and an k-ε turbulence model have been used.

To simulate the transformation of the Jet A droplets into Jet-A vapours a Liquid Evaporation Model from the ANSYS library is used [4].

3 Results

In the figure below are presented the residuals of the numerical simulation after 2900 iterations. It can be noted that, after an initial decrease, the simulation residuals oscillate around a mean value, without further decreasing, as an effect of the unsteady nature of the highly turbulent reactive flow.

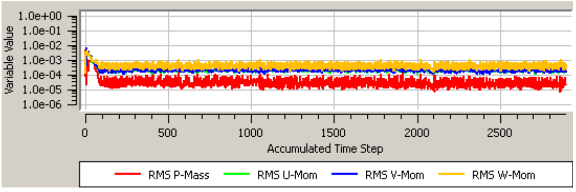

Fig. 6 The residuals after 2900 iterations

To account for the residuals seen above, the pressure and temperature were averaged along 100 iterations using the TECPLOT software [5]. The results in fig. 7 show that the mean pressure is quasi-constant, verifying the typical hypothesis of constant pressure combustion in a gas turbine combustor.

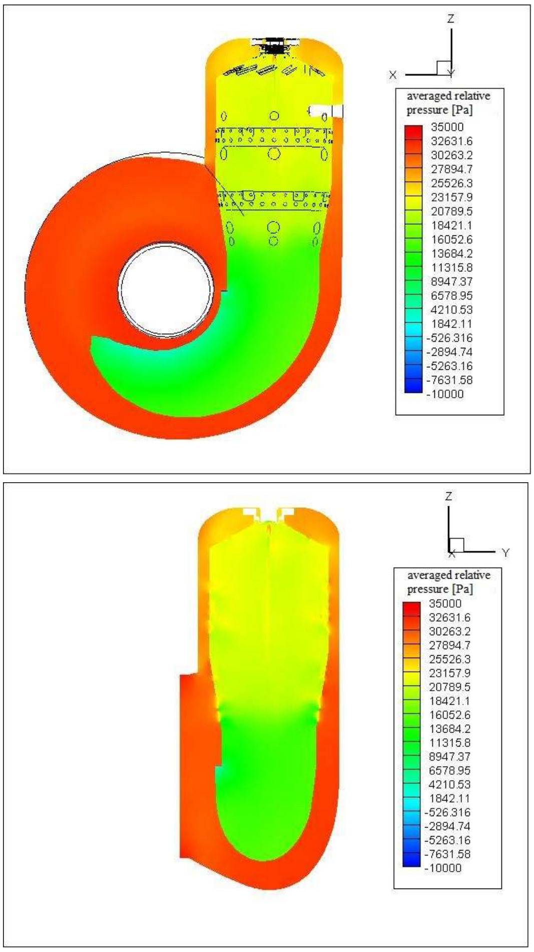

Fig. 7 The averaged relative pressure along 100 iterations (reference pressure = 2.92 bars)

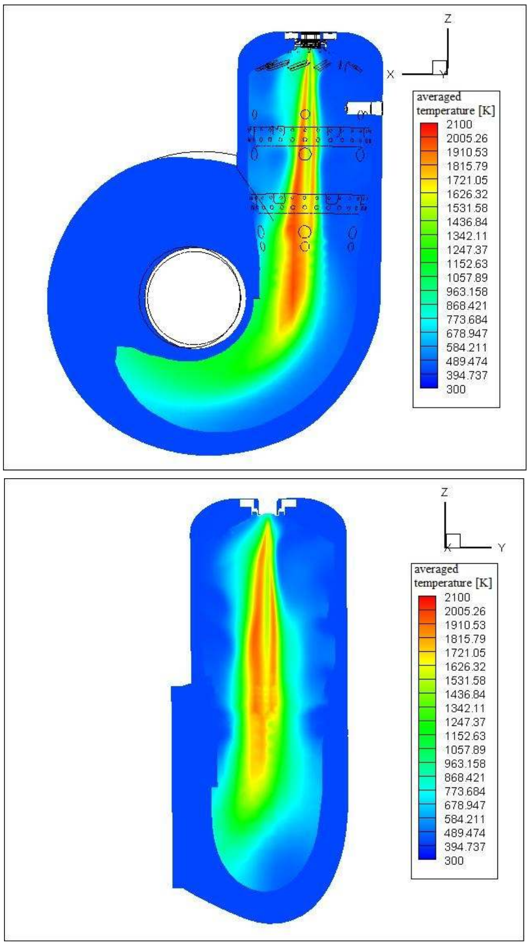

Fig.8 The averaged temperature along 100 iterations

The mean temperature field, presented in fig. 8, shows that the high temperature region is contained in the axial region of the combustor and does not extend into the volute that directs the burned gas to the downstream turbine, thus not endangering the physical integrity of the engine.

To verify the numerical simulations accuracy, the average outlet temperature has been recorded along 500 iterations and compared with the engine’s constructive turbine inlet temperature. The engine’s turbine inlet temperature is around 1100 K, while the average outlet temperature obtained in the numerical simulations is near 1200 K, as it can be observed in fig. 9. The accuracy of the numerical simulation is quite good, and the temperature oscillations are small, indicating proper operation of the combustor.

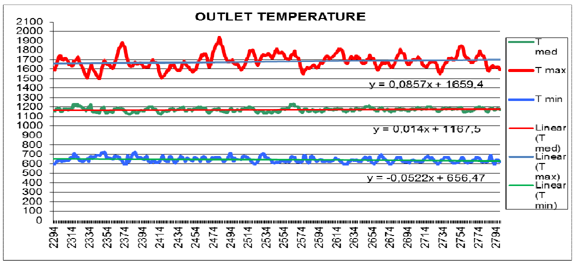

Fig. 9 Outlet temperature

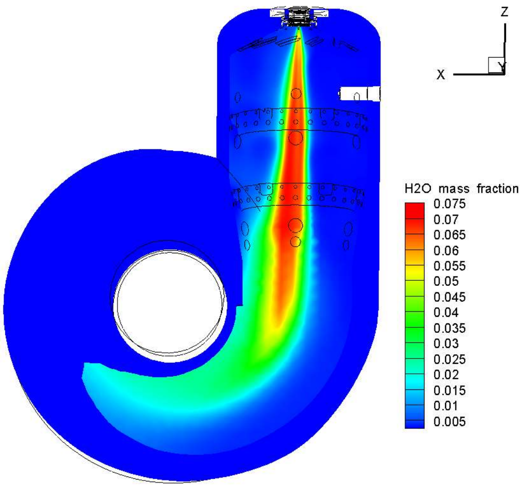

Fig. 10 Avereged H_2O mass fraction field

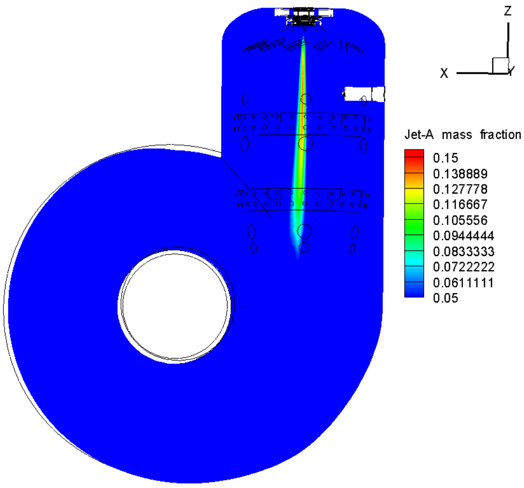

Fig. 11 Avereged Jet-A mass fraction field

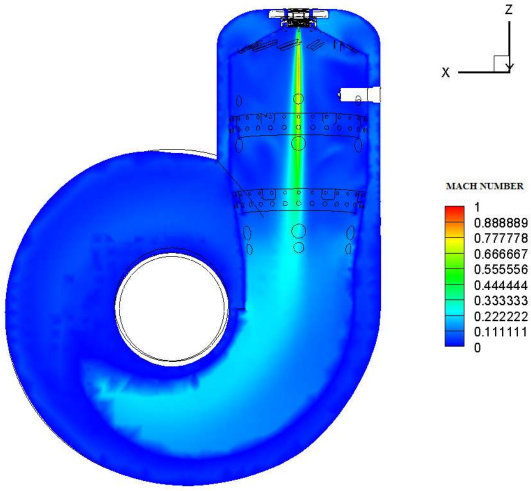

Fig. 12 Avereged Mach number field

In the above figures are presented the averaged H_2O mass fraction field (fig.10), averaged Jet-A mass fraction field (fig.11), respectively the averaged Mach number field (fig. 12).

It can be noted that the fuel is completely consumed inside the combustor, thus validating the design. The maximum velocity value is reached in the fuel jet and in the surrounding region, but the velocity decreases downstream fast enough to provide complete combustion inside the flame tube, as indicated by fig. 12.

4 Conclusion

Taking in consideration that the above numerical simulations results have a good accuracy, in this particular case, it can be concluded that the used numerical models can also be used to simulate the combustion process in other combustion chambers. Thus the results obtained in these simulations will help adapt the existing combustion chamber to different fuels and fuel mixtures.

References

[1] "Shaft Power Gas Turbine Engine. Model GTP 30-67", Technical Manual, 1966.

[2] Bose T., *Airbreathing Propulsion: An introduction*, Springer, 2012, Appendix: Engine Data Tables

[3] Pimsner V., Vasilescu C.A., Radulescu G.A., *Energetica turbomotoarelor cu ardere interna*, Ed. Academiei Republicii Populare Romania, Bucuresti, 1964, Chap. 4.
[4] ***, Product-Manual for ANSYS CFX v11, ANSYS INC., 275 Technology Drive Cannonsburg, PA, November 2010.
[5] ***, Tecplot 360 User's manual, Tecplot Inc., Bellevue, WA, 2012.

C^*-Efficiency Evaluation of Transpiration Cooled Ceramic Combustion Chambers

A. Herbertz, M. Ortelt, I. Müller and H. Hald
DLR, Germany

Keywords: Ceramic Combustion Chamber, Transpiration Cooling, Characteristic Velocity

Nomenclature

a	Sonic velocity, m/s
A	Cross section area, m^2
c^*	Characteristic velocity, m/s
C_F	Thrust coefficient
d	Diameter, m
F	Thrust force, N
g_0	Gravitational acceleration, m/s^2
I	Specific impulse, m/s
k_T	Transpiration cooling coefficient
l	(Chamber) length, m
l^*	Characteristic chamber length, m
$\dot{m}$	Mass flow, kg/s
p	Pressure, Pa
R	Mass mixture ratio (oxidizer to fuel)
V	Volume, m^3
η	Efficiency
ρ	Density, kg/m^3
τ	Coolant ratio

Subscript

0	Initial, injection
c	Chamber
e	Exit (nozzle)
fu	Fuel
id	Ideal
k	Coolant
ox	Oxidizer
t	Throat (nozzle)
vac	Vacuum

Abstract

Achievable benefits of the transpiration cooled ceramic thrust chamber are the reduction of weight and manufacturing cost, as well as an increased reliability and higher lifetime due to thermal cycle stability. The transpiration cooling principle however reduces the engine performance. In order to evaluate the performance losses a c^*-analysis is performed.

Due to the transpiration cooling the characteristic velocity decreases with increasing coolant ratio. The goal of the chamber development is therefore to minimize the required coolant mass flow.

The paper discusses the test specimen set up for the ceramic thrust chamber tests. Chamber operating parameters are listed. The paper discusses the impact of transpiration cooling on the calculated c^* efficiency. The evaluation is based on test results with the ceramic combustion chamber conducted in four separate test campaigns between 2008 and 2012.

1 Introduction

The transpiration cooling principle, while slightly reducing the specific impulse, highly increases chamber wall lifetime. Furthermore, depending on the ceramic materials used in thrust chamber construction, it is possible to substantially reduce the engines mass and manufacturing cost, compared to that of metallic engines. A small fraction of propellant is routed to the wall cooling channels. The coolant passes through the porous wall and exchanges heat with the wall. A film layer on the inner side of the chamber wall is created by the transpiration flow, further protecting the wall from the hot gases.

The *Deutsches Zentrum für Luft- und Raumfahrt* - German Aerospace Center (DLR) concept of a transpiration cooled ceramic thrust chamber consists of an outer load-carrying Carbon Fibre Reinforced Plastic (CFRP) shell and an inner porous and permeable Ceramic Matrix Composites (CMC) liner, which is actively cooled. The concept leads to a functional split between outer shell and liner. The outer CFRP structure carries the mechanical loads created by inner chamber pressure and longitudinal compression and bending moments induced by nozzle movements and thrust. The permeable liner provides the cooling functionality and acts as an interface to the combustion area. The use of CFRP for the outer jacket avoids or reduces problems created by materials with high thermal expansion coefficients or mismatches, as are present in case of combined application of CMC and metal. The coolant mass flow is provided by a tap-off valve. The pressure difference between the coolant distribution reservoir and the chamber adjusts itself, according to the material properties, during operation. Figure 1 shows the functional principle of the ceramic rocket engine thrust chamber. The manufacturing process and the ceramic materials are described in more detail in previous publications [4, 6]

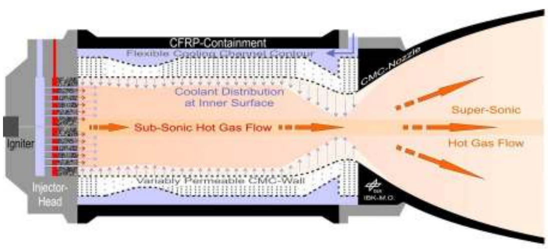

Fig. 1: Functional principle of a transpiration cooled ceramic thrust chamber.

Based on test results scaling analyses have been performed in the past, indicating that for large diameter and high pressure applications it is possible to build ceramic chambers operating with coolant ratios of less than 1% of the chamber mass flow [8]. This paper discusses the expected impact on chamber performance in relation to the applied coolant ratio.

2 DLR Test Campaigns with Ceramic Thrust Chambers

Experiments with porous CMC materials for rocket engine chamber walls have been conducted at the DLR since the end of the 1990s at various testbenches under a wide varity of test conditions. Table 1 lists the test campaigns of DLRs ceramic thrust chamber. The test cases used for the analysis described in the following section were part of the DLR projects *Keramische Schubkammer* - Ceramic Thrustchamber (KSK) and *Keramische Bauweisen für Experimentelle Raketenantriebe von Oberstufen* - Ceramic Design of Experimental Rocket Engines for Upper Stages (KERBEROS). Project KSK was conducted from 2007 to 2010. Project KERBEROS started in 2012 and is ongoing. Figure 2 shows test operation of the ceramic thrust chamber during the test campaign *MT5-A*. The test campaigns and the specimen thrust chambers are described in more detail in a previous publication [7].

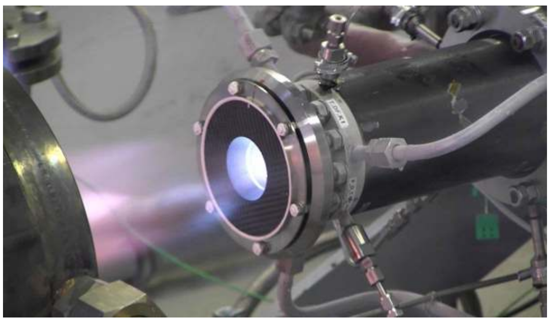

Fig. 2: MT5-A thrust chamber at the P6.1 test bench in Lampoldshausen (March 2012).

Table 1: DLR ceramic thrust chamber test campaigns.

	KSK-KT	KSK-ST5	MT5-A	WS1
Year	2008	2010	2012	2012
Test bench	P8	P8	P6.1	P6.1
Propellant combination	LOX/LH2	LOX/LH2	LOX/GH2	LOX/GH2
Injection temperature (fuel)	≈ 55 K	≈ 55 K	≈ 135 K	≈ 150 K
Injection temperature (oxidiser)	≈ 155 K	≈ 155 K	≈ 125 K	≈ 140 K
Coolant	H_2	H_2	H_2	H_2
Wall material	C/C	Al_2O_3 and C/C	Al_2O_3 and C/C	various
Nozzle material	copper	C/C	C/C	C/C
Injector	API	API	TRIK	TRIK
Chamber diameter (d_c)	50 mm	50 mm	50 mm	50 mm
Throat diameter (d_t)	31.6 mm	32.5 mm	20 mm	20 mm
Characteristic chamber length (l^*)	0.86 m	0.68 m	1.75 m	1.83 m

3 Analysis of Test Data

This section discusses the performance impact of transpiration cooling based on available test results. In all campaigns a substantial amount of hydrogen was used for chamber wall cooling. This resulted in very cold wall temperatures. The transpiration coolant flow rate is defined in this paper as the ratio of coolant mass flow to total mass flow:

$$\tau = \frac{\dot{m}_k}{\dot{m}_k + \dot{m}_{fu_0} + \dot{m}_{ox_0}} \tag{1}$$

As can be noted (cf. table 2 on page 6) the amount of coolant was in those sub-scale campaigns of the same order as the hydrogen used for combustion in the injector. In order to operate the chamber of a full-size rocket engine efficiently, much lower coolant ratios are required [5]. However due to favorable scaling effects, the cooling of large diameter and/or high pressure combustion chambers requires much lower coolant fractions. This is further discussed in previous publications [6, 8].

No direct measurement of thrust degradation due to transpiration cooling has been performed in the DLR test campaigns. The thrust can be expressed as a function of the thrust coefficient (cf. Eq. (3)).

$$I = \frac{F}{\dot{m}\, g_0} \tag{2}$$

$$F = C_F\, A_t\, p_c \tag{3}$$

The characteristic velocity (c^*) is defined as:

$$c^* = \frac{A_t\, p_c}{\dot{m}} \tag{4}$$

Along with the definition of c^* (cf. Eq. (4)) this leads to the relation of the specific impulse and the characteristic velocity.

$$I = \frac{c^*\, C_F}{g_0} \tag{5}$$

For a fixed nozzle (i.e. constant value for C_F) the specific impulse is therefore in theory proportional to the characteristic velocity. Experimental studies performed in the 1990s however indicate that the impact of transpiration cooling on the specific impulse is lower than on the characteristic velocity [3]. The c^*-efficiency is therefore a conservative estimation for the I_{vac}-efficiency.

The characteristic velocity is an indicator for chamber performance. It is mainly influenced by the quality of the injector and the characteristic chamber length.

The characteristic chamber length (l^*), defined as the ratio of chamber volume to throat area ratio, is related to the stay time of the propellants in the combustion chamber. For the propellant combination LOX/LH2 a choice of $l^* = 1$ m is a conservative value, while a choice of $l^* = 0.75$ m represents an aggressive value [9].

$$l^* = \frac{V_c}{A_t} \tag{6}$$

3.1 c^* Efficiency

The characteristic velocity (c^*) is independent of nozzle characteristics and therefore commonly used as a figure of merit for comparison of combustion chamber designs [10]. In order to evaluate the thrust chambers performance the characteristic velocity is compared with the ideal characteristic velocity.

$$\eta_{c^*} = \frac{c^*}{c^*_{id}} = \frac{A_t\, p_c}{(\dot{m}_k + \dot{m}_{fu_0} + \dot{m}_{ox_0})\, c^*_{id}} \tag{7}$$

Here the ideal characteristic velocity is determined for each test case according to Eq. (8) based on measured chamber pressure.

$$c^*_{id} = \frac{p_{c_{id}}}{\rho_{t_{id}}\, a_{t_{id}}} \tag{8}$$

Typical values for the efficiency η_{c^*} range from 92% to 99.5% [10]. The density and velocity required to calculate the ideal characteristic velocity, according to Eq. (8), are obtained by use of the NASA code Chemical Equilibrium with Applications (CEA) [1]. The thermal transport properties (specific heat, thermal conductivity and the resulting Prandtl numbers) are generated in two sets by CEA. In this study properties for shifting equilibrium (eql) are used in all calculations.

The ideal c^* is determined according to the current total mixture ratio. For a fixed injection mixture ratio R_0, an increasing coolant ratio τ (coolant mass flow per total chamber mass flow) reduces the total chamber mixture ratio R_e. Figure 3 shows the resulting chamber mixture ratio and inherent increase in c^* for a variation of the coolant ratio. For an initial mixture ratio of $R_0 = 5.5$ the ideal characteristic velocity reaches a maximum value at a total mixture ratio of $R = 2.7$. This corresponds to a coolant ratio of $\tau = 13.75\%$. The calculations presented in this paper therefore do not normalize the characteristic velocity with a theoretic value for the injection conditions. Instead for each dataset the ideal characteristic velocity is calculated separately, taking into account variations in injection temperatures and total mixture ratio.

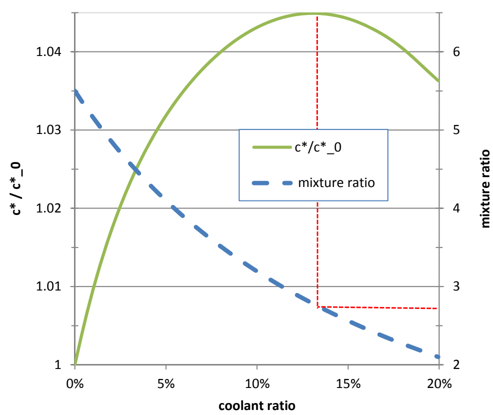

Fig. 3: Ideal characteristic velocity as a function of the coolant ratio, for an initial mixture ratio of $R_0 = 5.5$.

The total or final mixture ratio is calculated according to equation Eq. (9).

$$R_e = \frac{\dot{m}_{ox_0}}{\dot{m}_{tot}} = \frac{R_0\,(1-\tau)}{1+\tau\, R_0} \tag{9}$$

3.2 Available Test Data

In order to obtain suitable data for the performed analysis, the test data was processed. The averaged signals at steady state operation were taken as a basis for calculation. Figure 4 shows an example of original signal, the averaging and the selection of the test data. The reference time for the steady state data is arbitrarily selected immediately before the initiation of the shutdown sequence. Table 2 lists test runs used for the c^*-evaluation presented in this paper.

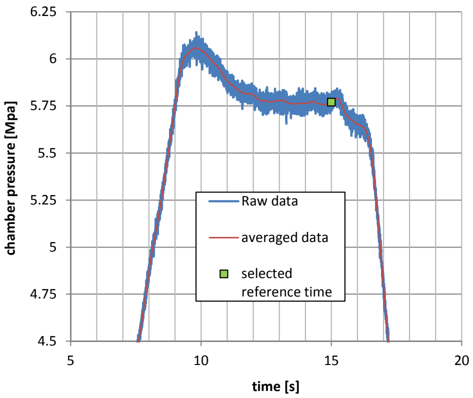

Fig. 4: Signal averaging and selection of steady state test data.

4 Resulting Dependencies of c^*

Relating the characteristic velocities to the ideal characteristic velocity leads to the efficiency calculated according to Eq. (7). Figure 5 shows the calculated efficiencies of the characteristic velocity.

4.1 Transpiration Cooling Coefficient

By applying linear regression to the data, for extrapolation of the impact of the transpiration cooling on c^*, an off-set for the characteristic velocity can be determined. For a coolant ratio of $\tau = 0\%$ (i.e. no transpiration cooling), the

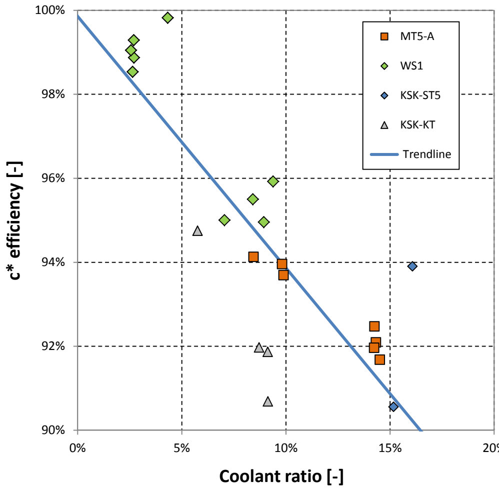

Fig. 5: Efficiency η_{c^*} as a function of the coolant ratio τ for different test campaigns.

efficiency is extrapolated from test data. It is assumed that the impact on the characteristic velocity can be assessed by use of Eq. (10).

$$\eta_{c^*} = (1 - k_T\ \tau) \tag{10}$$

For campaigns with few performed tests (e.g. KSK-ST5), the regression analysis may provide incorrect values with extrapolated initial efficiencies above 100%. In such cases the regression analysis is performed with a fixed value of $\eta_{c_0^*} = 100\%$. Calculated values for the derived cooling coefficients and initial efficiencies are shown in table 3. Based on the test data extrapolation, the averaged transpiration cooling coefficient for all DLR ceramic thrust chamber campaigns is $k_T = 0.6$.

4.2 Error Discussion

Several uncertainties remain with this approach and leave room for further investigation. The exact value of the transpiration cooling coefficient k_T will likely depend on the chamber design and its interaction with the injector. Modeling and analysis of each chamber there-

Table 2: Selected reference chamber conditions during the test campaigns of DLR's ceramic thrust chamber.

campaign	test #	ref. time	chamber pressure	injection mixture	coolant ratio	total mass flow	char. velocity
KSK-KT	081208	25 s	9.1 MPa	5.5	8.71 %	3.148 kg/s	2269.4 m/s
KSK-KT	081212a	25 s	9.11 MPa	5.5	9.13 %	3.157 kg/s	2267.2 m/s
KSK-KT	081212b	28 s	9 MPa	5.5	9.14 %	3.159 kg/s	2238.2 m/s
KSK-ST5	100629a	6 s	5.34 MPa	6.68	17.63 %	2.069 kg/s	2139.3 m/s
KSK-ST5	100629b	15 s	5.7 MPa	5.78	16.08 %	2.049 kg/s	2306.5 m/s
KSK-ST5	100702a	60 s	5.54 MPa	5.45	15.15 %	2.066 kg/s	2224.6 m/s
MT5-A	120222a	16 s	4.73 MPa	6.27	14.51 %	0.649 kg/s	2287.5 m/s
MT5-A	120223b	14 s	5.87 MPa	6.23	14.23 %	0.804 kg/s	2294 m/s
MT5-A	120224b	14 s	5.68 MPa	6.22	9.89 %	0.765 kg/s	2330.7 m/s
MT5-A	120227b	15 s	5.79 MPa	5.6	9.82 %	0.777 kg/s	2340.7 m/s
MT5-A	120301	15 s	5.71 MPa	5.59	8.45 %	0.766 kg/s	2342.1 m/s
WS1a	121031a	14 s	5.8 MPa	5.33	9.38 %	0.761 kg/s	2395 m/s
WS1a	121031b	15 s	5.67 MPa	5.66	8.41 %	0.75 kg/s	2375.6 m/s
WS1a	121107	15 s	5.55 MPa	5.5	7.05 %	0.74 kg/s	2357.9 m/s
WS1b	121120a	16 s	5.68 MPa	5.67	8.94 %	0.755 kg/s	2364.6 m/s
WS1b	121120c	20 s	4.52 MPa	2.05	4.32 %	0.577 kg/s	2457.7 m/s
WS1b	121122	22 s	4.4 MPa	2.05	2.7 %	0.566 kg/s	2440.6 m/s
WS1b	121126a	8 s	4.34 MPa	1.91	2.56 %	0.563 kg/s	2423.9 m/s
WS1b	121126b	8 s	4.36 MPa	1.9	2.64 %	0.568 kg/s	2409.2 m/s
WS1b	121127	8 s	4.37 MPa	2.08	2.69 %	0.563 kg/s	2439.9 m/s

Table 3: Transpiration cooling coefficient for the ceramic thrust chamber.

campaign	initial η_{c^*}	coefficient k_T
KSK-KT	$\eta_{c_0^*} = 100\%$	$k_T = 0.94$
KSK-ST5	$\eta_{c_0^*} = 100\%$	$k_T = 0.59$
MT5-A	$\eta_{c_0^*} = 97.5\%$	$k_T = 0.38$
WS1	$\eta_{c_0^*} = 100\%$	$k_T = 0.50$

fore requires the use of unique coefficients.

Concerning the uncertainties in the measurement it has to be noted that the evaluation of η_{c^*} depends on several measured quantities, as described by Eq. (7) and Eq. (8). The characteristic velocity directly depends on the accuracy of the measurement of chamber pressure and mass flow. The ideal characteristic velocity also depends on the injection temperatures. Due to the chosen implementation of the pressure measurement, the associated uncertainty is the largest of the above. Taking everything together individual errors of up to 3% are expected. While this is a substantial margin of error for the considered ranges, the regression analysis still provides a good basis for performance evaluation.

4.3 Comparison with Metallic Transpiration Cooled Chambers

In the frame of the German-Russian research program *Technologien für Hochleistungs-Raketenmotoren* - Technologies for High-Performance Rocket Engines (TEHORA) several tests with transpiration cooled metallic combustion chambers were conducted between 1995 and 1998 [2, 3]. Obviously the configuration in those test was substantially different from that used in ceramic thrust chamber tests. The resulting linear regression (applying the same normalizing process as described in section 4.1) leads to similar cooling coefficients as those listed in table 3.

In the frame of the TEHORA program thrust measurement of the test chamber was performed. The degradation of the specific impulse was therefore measured independently of the c^* performance. Losses in the specific impulse efficiency were observed to be only about half as large as those of the characteristic velocity efficiency [3].

5 Conclusion and Outlook

Test data generated between 2008 and 2012 in DLR's ceramic thrust chamber development projects has been analyzed concerning c^*-efficiency. The test campaigns were performed with different mixture ratios, different components and different geometries. Each configuration therefore exhibits a different relation between coolant ratio and performance loss. In general however it can be concluded that for coolant ratios below 1 % of the total mass flow, the expected reduction of the characteristic velocity is less than 0.6 %.

The associated reduction of the specific impulse was not measured in DLR's test campaigns. According to results of past experimental studies it is significantly lower than the loss in the characteristic velocity. Consequently based on available test data the losses in specific impulse can be expected to be 0.3 - 0.6 of the transpiration coolant mass flow rate. Scaling analysis of the transpiration cooled ceramic thrust chamber has shown that for large scale and high pressure applications coolant ratios below 1% are well feasible. Expected losses in the specific impulse for high performance cryogenic rocket engines will therefore range in the order of 1.5 s.

This loss in performance is the price to pay for the introduction of a new technology that will reduce the manufacturing effort and increase chamber life time. Whether this is economical worthwhile is subject of further investigation, taking into account a detailed analysis of expected manufacturing costs, as well as the impact on the payload mass of selected space transportation systems.

References

[1] S. Gordon and B. J. McBride. *Computer Program for Calculation of Complex Chemical Equilibrium Compositions and Applications Vol.II: Users Manual and Program Description.* NASA Lewis Research Center, June 1996. NASA RP-1311.

[2] J. Görgen, O. Knab, D. Haeseler, and D. Wennerberg. Impact of intentional and unintentional combustion chamber porosity on rocket engine characteristics. In *Fourth International Symposium on Liquid Space Propulsion*, Mar. 2000.

[3] D. Haeseler, C. Mäding, V. Rubinskiy, V. Gorokhov, and S. Khrisanfov. Experimental investigation of transpiration cooled hydrogen-oxygen subscale chambers. In *34th Joint Propulsion Conference*, July 1998. AIAA 98-3364.

[4] H. Hald, A. Herbertz, M. Kuhn, and M. Ortelt. Technological aspects of transpiration cooled composite structures for thrust chamber applications. In *16th AIAA/DLR/DGLR International Space Planes and Hypersonic Systems and Technologies Conference*, Bremen, Nov. 2009.

[5] A. Herbertz. *Systemanalytische Untersuchung einer Brennkammer in faserkeramischer Bauweise von Raketenantrieben.* PhD thesis, RWTH Aachen, Sept. 2008.

[6] A. Herbertz, M. Ortelt, I. Müller, and H. Hald. Potential applications of the ceramic thrust chamber technology for future transpiration cooled rocket engines. *Transactions of the Japan Society for Aeronautical and Space Sciences, Aerospace Technology Japan*, 10(ists28), 2012.

[7] A. Herbertz, M. Ortelt, I. Müller, and H. Hald. Transpiration-cooled ceramic thrust chamber applicability for high-thrust

rocket engines. In *48th Joint Propulsion Conference*, Atlanta, Georgia, July 2012. AIAA-2012-3990.

[8] A. Herbertz and M. Selzer. Analysis of coolant mass flow requirements for transpiration cooled ceramic thrust chambers. In *29th International Symposium on Space Technology and Science*, Nagoja, June 2013.

[9] R. Humble, G. Henry, and W. Larson. *Space Propulsion Analysis and Design*. McGraw-Hill, 1995.

[10] G. P. Sutton and O. Biblarz. *Rocket Propulsion Elements*. John Wiley & Sons, 7th edition, 2001.

4:th CEAS Air & Space Conference
FTF Congress: Flygteknik 2013

Sustainable Alternative Fuels for Aviation: International Emission Targets vs. Corporate Sustainability Aspirations

Christoph Jeßberger and Sebastian Wolf
Bauhaus Luftfahrt e.V., Germany.

Keywords: alternative fuels, sustainability criteria, supply chain management, risk management, corporate responsibility

Abstract

Alternative fuels are seen as a major enabler by the aviation industry to achieve its emission reduction goals in the coming decades. However, vast quantities are needed, potentially leading to significant social and ecological side-effects. This situation is aggravated by the multi-tiered character of most alternative fuel supply chains. Respective fuels are sourced and produced by a multitude of providers in various regions around the globe, affecting a wide range of stakeholders. As such, although the final users are seen responsible for the sustainability of "their" alternative fuels, they can hardly guarantee that no impacts were incurred along the process. Therefore, an active sustainable supply chain management is needed to address the root-causes of inter-organizational sustainability issues. In this context, following an introduction of the role and challenges of biofuel for aviation's emission targets, a structural framework is used to discuss the corporate role in ensuring the sustainability of alternative fuels. Findings imply, that much more intense partnerships along the supply chain from the airlines down to agricultural players are needed, making the aviation industry jointly responsible to help improve structural and individual supplier capabilities for a sustainable alternative fuel production. Taking these developments into account we propose a change towards more industrial vertical integration as this would facilitate the provision of sustainable jet fuel.

1 Introduction

International commercial aviation operates around 23 000 aircraft world-wide. With passenger traffic expected to grow around 5% annually in the next twenty years, this number is expected to increase to almost 40 000 by 2031 [2, 8]. Closely linked to this growth are aviation's greenhouse gas (GHG) emissions and thus public concerns about the increasing impact of global aviation on climate change. Although aviation currently only accounts for about 2% of global emissions, a more than threefold increase is expected by 2050 [7] making this the fastest growth within the transport sector [15, 19, 16, 46]. This, in turn, leads to rising concerns among public and private stakeholders.

This paper aims at discussing a sustainable supply chain management in the context of aviation biofuels and is organized as follows. Sections 2 and 3 describe the challenges of sustainable alternative drop-in fuels in the context of aviation's emissions targets. Section 4 outlines the supply chain risk and costs mitigation analysis. Section 5 discusses these findings in the context of an increased upstream corporate responsibility, which we see as a major driver for a public acceptance of alternative fuels. Finally, Section 6 offers concluding remarks.

2 Aviation's Emissions Targets

Due to the fast growth of the aviation sector and respective CO_2 emissions, a range of industrial as well as political actors have agreed on ambitious emission reduction goals. As an industrial initiative, IATA has committed itself to a net carbon neutral growth from 2020 onwards and to a 50% net CO_2 emission reduction by 2050 compared to 2005 values [27]. On a European level, the EU has declared to reduce aviation's CO_2-footprint by 75% until 2050 (vs. 2000) in its "Flightpath 2050" document [17]. Additionally, national governments strive to reduce CO_2 emissions in the respective transport sectors. The German mobility- and fuel strategy, for example, aims at a decrease of 40% in total transport emissions by 2020 and 80% by 2050 (relative to the base year 1990) [13].

Air transport is challenged to contribute to these goals. Operational improvements (i.e. higher load factors, Single European Sky, Continuous Descend Approach), infrastructural means (i.e. optimized or zero-emission taxi procedures) as well as technical progress (i.e. more efficient engines, lighter airframes) have greatly increased aircraft efficiency in the last years. However, these measures cannot, even under the most aggressive technology forecast scenarios, sufficiently decouple the rising demand for air transportation from the sector's fuel burn and related carbon emissions. In this context, a 2011 EU Whitepaper formulates a CO_2 emission reduction of 60% by 2050 (relative to 1990 levels), which is to be achieved using 40% "low-carbon sustainable fuels" in the aviation sector [20]. Especially the use of alternative fuels is thus seen as a key factor to reduce aviation's impact on climate change.

3 The Challenge of Sustainable Biojet

Besides achieving the ambitous emissions targets with the aid of alternative fuels, sustainable biojet needs to meet huge challenges and strict specifications. These aspects are shown in the subsequent subsections.

3.1 Biofuel Specifications

With aircraft being long-lived assets, kerosene and kerosene-like fuels will be used for many years to come. As such, initiatives are currently underway to search for alternative sourcing options, which are able to foster the development and implementation of sustainable fuels to meet the industry's demand while at the same time diversifying the sectors fuel supply [16]. Respective jet fuels must meet an array of specifications to enable the safe operation of current aircraft [5, 34]. In this context, the approval of hydroprocessed esters and fatty acids (HEFA) as well as Fischer-Tropsch based biomass to liquid (BTL) to be used by aviation has made alternative fuels based on plant oils or biomass a tangible reality for the airline industry. Already today, up to 50% of bio-derived components and other synthesized hydrocarbons can be added, resulting in a blend which is essentially identical to conventional aviation fuel in performance and operability, i.e. "drop-in" without limitations or the need for special handling or re-certification of aircraft [6]. The use of biofuels, however, leads to a number of other challenges for the industry as discussed in the following.

The production of large quantities of drop-in biojet will require a tremendous amount of plant oil or woody biomass every year. According to the industry, a 6% share of alternative fuels is needed by 2020 to achieve the targeted carbon-neutral growth [28]. With a projected annual fuel burn of 320 Mt, this would lead to an annual demand of 19 Mt from 2020 onwards [29], accounting for about 12% of todays total global plant oil production from soy, rapeseed, sunflower and oil palms [21, 35]. A significant scaling up of respective feedstock production is therefore needed to provide sufficient quantities of biofuel to meet aviation's short- and mid-term demand alone. These vast quantities are expected to lead to tremendous negative externalities [23, 36, 12], increasing the public concern aviation actors face. Already, airlines have come under pressure, being held accountable for the negative impacts incurred by the (test) usage of biofuels [10, 30, 11]. Currently, the use and continuous development of certification schemes is seen as the only method to minimze the risks when employing biofuel. The challenges of certification will be discussed in the following section.

3.2 Limits of Biofuel Certification

Initiatives like the 'International Sustainability and Carbon Certification' (ISCC) [31], the 'Roundtable on Sustainable Biofuels' (RSB) [39] or the 'Roundtable on Sustainable Palm Oil' (RSPO) [40] define voluntary sustainability standards as well as supervise and monitor respective certification processes. Technically, to avoid conflicting interests and to ensure the validity of a certification, independent on-site auditors perform the actual certification process. However, the set of sustainability criteria to be used can lastly be chosen by the demanders of a certificate, as long as it is in accordance with the limitations imposed by the subsequent usage – e.g. conform to the EU Renewable Energy Directive (EU RED) for biofuels used in the EU [14]. In this context, the aviation initiative for renewable energies in Germany (aireg e.V.) working group "sustainability" is developing a comprehensive set of sustainability criteria to ensure an equally sustainable global sourcing of alternative aviation fuel, independent of the region where the feedstock is produced, converted and blended [3].

Despite the multitude of (voluntary) sustainability standards, the certification process is neither prone to error nor totally fail-save. Especially the wide range of different schemes make the compliance with respective criteria extremely difficult. In Europe alone, 14 different EU RED conform certification schemes can be equivalently applied to certify the "sustainability" for one or more production steps within a biofuel production process [18]. These certification schemes mutually acknowledge the sustainability certificates of each other for individual steps along a value chain. Although, this enables companies to freely chose a certification scheme, it signifcantly impedes the traceability and transparency of a certification process. For example, a feedstock has been cultivated and certified according to the RED Bioenergy Sustainability Assurance Scheme (RBSA) [1]. This feedstock is further processed and certified according to RSB EU RED. Finally, the respective biofuel is produced, certified according to ISCC EU, and transported to the end-user. As RBSA, RSB and ISCC mutually acknowledge their sustainability certificates, the final product is rightly labled "sustainable". However, RBSA only implements ecological criteria, while social aspects do not need to be complied with. As such, although the final product has succesfully been certified along the entire process chain, the ultimate buyer cannot be sure that social sustainability criteria (e.g. labor and human rights) are implemented upstream.

Even certified end-products can thus not guarantee the high environmental and social quality needed for a mass usage of respective fuels. In accordance with the "polluter pays" principle (i.e. the party responsible for producing a negative externality also pays for the damage done) biofuel end-users are seen jointly responsible for a pro-active engagement along the supply chain *before* contractual agreements are made, processes established and operations begun. Managing the risks from a global supply by developing sustainable production chains will thus play a key role for an ecologically benign and socially accepted utilization of aviation biofuel. However, although the consideration of sustainability criteria is vital when it comes to planning and developing new biofuel production chains, a systematic framework to address underlying hazards is oftentimes missing [4]. The following approach aims at providing a tool to be used in concurrence with other impact assessment guidelines (i.e. the RSB [37]).

4 FMEA as a Tool for Supply Chain Risk & Cost Mitigation

True to the adage that "a danger foreseen is half avoided", the *Failure Modes and Effects Analysis* (FMEA) is a methodology used to identify unwanted events early in a product or process development phase. The aim is to tackle potential problems before a process is started or implemented, thereby enhancing *reliability through design*. Otherwise high process non-conformity costs may occur. These include monetary as well as non-monetary expenses (e.g. time, reputation) incurred by necessary corrective or compensatory measures. In this context, the ten-folding-rule of non-conformity costs implies that one dollar spent on prevention will save 10 dollars on correction and 100 dollars on failure costs (cf. Fig. 1) [22].

Figure 1: Ten-Folding-Rule of Non-Conformity Costs

A FMEA is thus used for troubleshooting and identifying counteractive actions in a process development phase. It is implemented to identify potential forms of failure, determine their impact and identify root-causes before a process is started. This makes the FMEA an attractive preventive planning tool to test in the context of a sustainable biofuel supply chain. Figure 2 shows the structural framework used. Each (1) process step of a generalized biofuel supply chain is individually analysed according to possible (2) "failure modes". These are potential undesirable and unsustainable developments which could occur due to a specific process step. These "failure modes", in turn, lead to (3) "failure effects", which were defined as impacts on key (4) sustainability criteria. For these, the set of sustainability criteria of the aireg strategy paper were used [3]. This leads to a systematic identification of (5) underlying root-causes which can promote or stimulate the breaching of ecological, social as well as economical criteria.

A systematical scoping of all process steps for underlying risks and impacts could help an organisation identify whether a proposed operation is in "an area of high risk" concerning sustainability impacts and possible noncomformity costs. In this context, with its emphasis on problem prevention, a FMEA analysis can help raise the awareness among biofuel users for the risks of negative externalities incurred along the supply chain. An example of the FMEA principle and results for the first process step of land conversion is given in the Annex in Table 2. In accordance with the given example, all process steps have been analysed. Table 1 provides a summary of underlying root-causes along a complete biofuel production chain.

The identified root-causes summarized in Table 1 clearly illustrate, that a reliance on certification measures which mainly focus on ecological aspects cannot address the underlying problems which are *always* of a socio-economic nature. This is critical due to the above noted wide range of certification schemes, which are usable along different stages of a single production chain. For example, an inherent problem of certification schemes is to control the use, expansion and conversion of the land used for feedstock cultivation [9]. However, a destruction of high-value conservation areas, biodiversity loss, soil erosion or sinking groundwater levels, are fundamentally caused by a combination of lacking knowledge as well as misguiding local policies, behaviours and market structures. As such, sourcing biofuels from a powerful agro-industrial operator in an area with weak or corrupt governance structures and ambiguous land-rights must be considered highly risky. This is often aggravated by a focus on fast profit maximization leading to short-term planning horizons. As such, even if a certification is as-

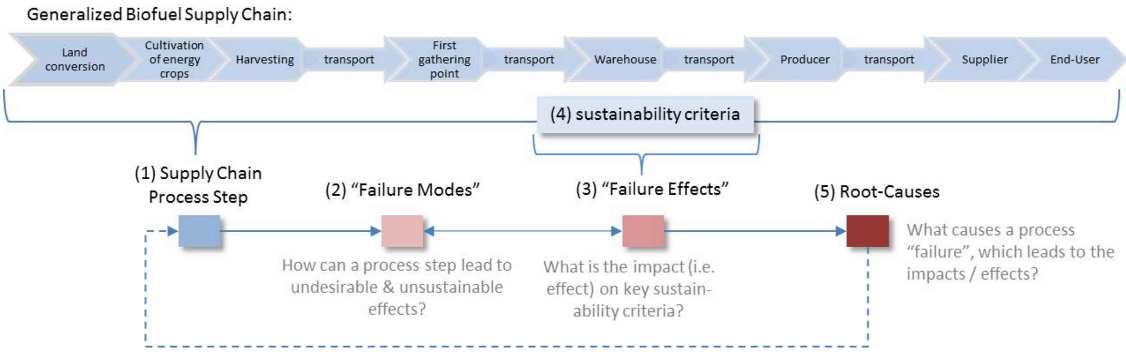

Source: own compilation.

Figure 2: FMEA Structural Framework

sured by a respective provider, effective controls cannot be genuinely guaranteed. Therefore, although formally enabling companies to assure due diligence, certification schemes are not fail-safe, particularly in multi-tiered processes encompassing numerous subcontractors. Recent examples within the textile chain show that companies face high risks of reputational losses when making sustainability claims which their suppliers cannot comply with or may not be equally committed to.

Especially in the context of an increasing demand for alternative fuel, the sole reliance on certification schemes does not facilitate the development of new, sustainable sourcing solutions [42, 38]. These, however, are lastly needed to provide aviation with the amount needed to meet the future demand as well as meet the industry's sustainability aspirations. As such, requesting certification can only be part of a corporate strategy when it comes to looking for and building new alternative fuel pathways. To address the root-causes of inter-organisational sustainability issues, the implementation of sustainability standards must be complemented by other activities. Rather than merely relying on third-party auditing and checking, the adoption of preventive measures is necessary to ensure socially and environmentally benign as well as economically succesful production practices. In this context, the industry must pro-actively identify social and environmental impacts and incorporate respective prevention measures into the sourcing process. How this could be achieved is discussed in the following.

Table 1: Underlying root-causes of sustainability impacts

- "powerful" agro-industrial actors - weak national power - high corruption - no (effective) controls - very high economic margins from alternative fuels production - focus on short-term profit maximization - poverty-driven pressure - missing knowledge & technology - missing/not-implemented nature protection schemes - short-planning horizons due to short-term contracts - lack of understanding of smallholder structures by policy makers - ambiguous land-rights, missing land register	- inappropriate crop selection - excessive land-usage, large-scale monocultures - lacking knowledge of benign agricultural practices - strong hierarchical social structures - missing or lacking controls of water-sharing rights - (locally) not adapted cultivation methods - lacking infrastructure (e.g. transport, sewage) - lacking process management skills/knowledge - lacking logistic management skills/knowledge - outdated, input intensive technology - overestimation of harvest expectations - lacking awareness for social responsibility or socially benign management practices

Source: own compilation.

5 An "Upstream" Corporate Responsibility

The industry is challenged to take on an increased responsibility for a pro-active engagement of a longer part of the biofuel supply chain. Only an engagement of the root-causes of many sustainability impacts ultimately helps to build capacities to enable processing practices which are environmentally, socially and economically beneficial. This, however, requires a far greater level of supplier development and supply chain commitment than merely relying on third-party auditing and checking [26]. Much more intense vertical partnerships along the supply chain from the airlines down to agricultural players are needed [46], making the aviation industry jointly responsible to help improve structural as well as individual supplier capabilities. Therefore, supplier collaboration and development measures are not only essential to promote new, promising biofuel pathways [24], but are also seen to lie within the responsibility of the industry as part of the sector's commitment towards carbon neutrality.

In this context, two corporate sustainable supply chain strategies have been identified, which should be pursued parallely [42, 43]. Figure 3 presents a generalized overview of the strategies for (1) *"risk avoidance"* and (2) *"sustainable products"* in the context of aviation's sustainability aspirations to offer air transport services based on biofuel. From a supply chain perspective, especially airlines are seen as the focal entities of the aviation industry. These, however, currently either rely on external fuel suppliers, with fuel "ownership" not changing until the fuel is pumped into the aircraft or they organize their fuel supply from the refinery to the aircraft themselves. Although the first case is more common, the main focus lies on the responsibility for the "downstream" part of their fuel supply chain in terms of cost, speed, quality and dependability. However, in line with the fuel comes the environmental, economic and social burden incurred during different stages of its production. The corporate responsibility for alternative fuels thus does not start with the ownership of the fuel at the refinery or the aircraft, but at a much earlier stage of the supply chain. With the main root-causes of environmental and social impacts lying far "upstream", a longer part of the fuel supply chain must be taken into account by focal actors than needed for "pure" economic reasons.[1]

The priorly depicted root-causes of many negative social and ecological externalities, illustrate that lastly only a two-fold approach can lead to the sourcing of genuinely sustainable fuels. Although, certification schemes or the introduction of contractual clauses are necessary to ensure due diligence in terms of compliance with sustainability requirements, stakeholder pressure and the responsibilities for environmental and social impacts are simply passed "upstream". Additionally, there are limits to what monitoring can achieve. Particularly its capacity to encourage advanced performance outcomes is limited [43, 44].

To tackle many of the identified root-causes supplier development measures are thus necessary to, for example, improve structural capacities, empower local land-users or accelerate the diffusion of knowledge. A complementary strategy should therefore be the pro-active development of an inherently sustainable process by supporting suppliers via increased cooperation and collaboration. This, in turn, requires that "upstream" suppliers are not viewed as interchangeable entities to be managed for risk avoidance, but as vital value-adding partners. Lastly, both aspects, auditing and checking as well as supplier engagement and cooperation, must be seen as integral parts of a single genuine sustainable supply chain strategy, requiring a more pro-active and higher level of collaboration between all actors [32, 42].

[1]Note: For example, similar strategies have been implemented within the textile/cotton chain [25, 33].

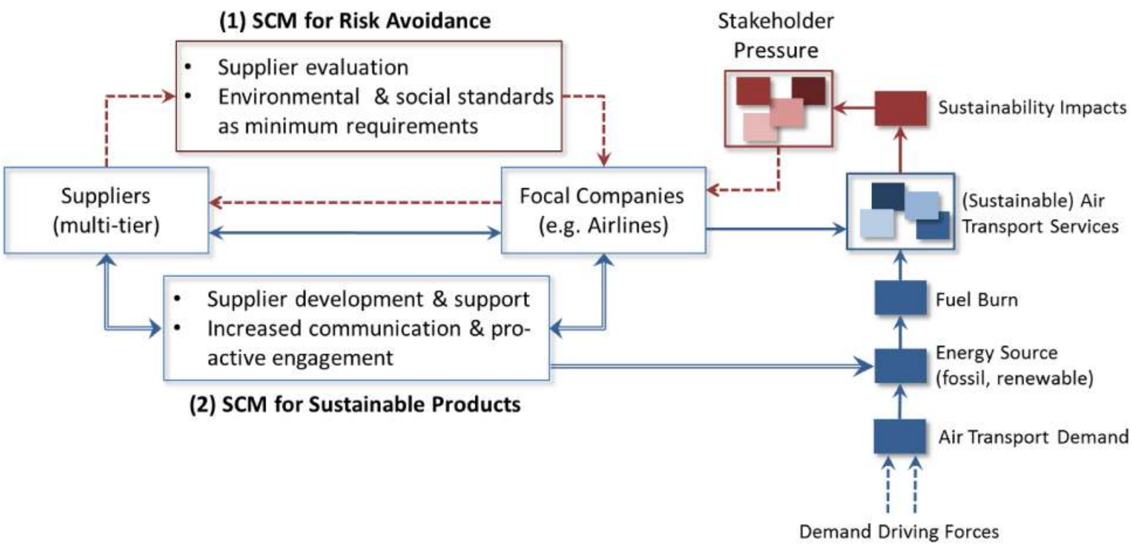

Note: SCM: Supply chain management. Source: own compilation based on [32, 42].

Figure 3: Strategies & Responsibilities for Sustainable Aviation

6 Conclusion

Today, aviation faces the challenge *and* responsibility to support the development of inherently sustainable alternative jet fuel. Surely, the use of environmental and social standards plays an important role, but aviation's carbon commitment extends the industries obligations beyond this scope. Pro-actively developing suppliers as well as respective operating environments will help lead to win-win situations, which are far more likely to integrate the three dimensions of sustainability than trade-offs. This will enable long-term strategic benefits for all sides [41, 42, 45]. As such, only by actively managing all phases of biofuel production can the integrity of sustainability claims be maintained and the targeted aspirations of the aviation sector be guaranteed. Thus, we propose a change towards more industrial vertical integration as this would facilitate the provision of sustainable aviation fuel.

Acknowledgements

Special thanks to Jenny Walther-Thoss and Lydia Pforte, and thanks to all aireg members of the aireg working group "Sustainability" for the fruitful discussions about the mutual acknowledgements of sustainability certificates along the production chain.

This paper benefited from the financial support of the Federal Ministry of Economics and Technology (BMWi) due to a decision of the German Bundestag.

Gefördert durch:

Bundesministerium für Wirtschaft und Technologie

aufgrund eines Beschlusses des Deutschen Bundestages

A Annex

Table 2: FMEA for the Process Step of "Land Conversion"

Process Step (What is the process step?)	**Potential "Failure Mode"** (In what ways can the process step fail in terms of sustainability performance?)	**Potential Failure Effects** (What is the impact on key sustainability criteria once it fails?)	**Potential Root-Causes** (What causes the process to go "wrong"? What is a cause of the potential "failure modes"?)
Land Conversion	- (uncontrolled) expansion of the area for feedstock cultivation	- conversion of HVC areas, natural, non-HVC area & land used for food production (LUC) - displacement of area used for food prod. (ILUC) - GHG-emissions - biodiversity loss - soil erosion - impact on (ground-) water household - danger to the local population's nutritional base	- weak national power - high corruption - no (effective) controls - very high economic margins from biofuel prod. - limited productive land - missing/not-implemented nature protection schemes - short planning horizons due to short-term contracts - missing knowledge & technology - high pop. density & growth - missing stakeholder consultation
	- Displacement & Exexclusion of small land-users	- loss of livelihoods - regional & social conflicts - loss of regional cultural & agricultural structures	- weak national power - high corruption - lack of understanding smallholder structures by decision makers - ambiguous land-rights, missing land register - missing stakeholder consultation - "powerful" agro-industrial actors

Note: HVC - high value conservation, Source: own compilation

References

[1] Abengoa Bioenergia. *The RED Bioenergy Sustainability Assurance Scheme (RBSA)*. 2011. URL: `http://www.abengoabioenergy.com/web/es/index.html`.

[2] Airbus. *Delivering the future. Global market forecast 2011-2036*. Toulouse, 2011.

[3] Aireg. *The future of climate-friendly aviation: Ten percent alternative aviation fuels by 2025*. 2012. URL: `http://www.aireg.de/images/downloads/aireg/aireg_climate_friendly_aviation.pdf`.

[4] R. A. Anggara. Implementation of risk management framework in supply chain: A tale from a biofuel company in indonesia. *Manchester Business School Working Paper*, 614, 2011.

[5] ASTM. *ASTM D1655. Standard Specification for Aviation Turbine Fuels*. 2010.

[6] ASTM. *ASTM D7566. Standard Specification for Aviation Fuels Containing Synthesized Hydrocarbons*. 2011.

[7] ATAG. *Beginner's guide to aviation efficiency*. 2010. URL: `http://www.enviro.aero/AviationEfficiency.aspx`.

[8] Boeing. *Current market outlook 2012-2031*. Seattle, 2012. URL: `http://www.boeing.com/commercial/cmo/`.

[9] S. Bringezu, H. Schtz, M. O'Brien, L. Kauppi, R. W. Howarth, and J. McNeely. *Towards sustainable production and use of resources: Assessing biofuels*. UNEP, Nairobi, 2009.

[10] BUND. Biosprit macht fliegen nicht umweltfreundlich lufthansa wscht sich mit testflgen zwischen hamburg und frankfurt grn. *BUND. Friends of the Earth Germany - online*, July 2011. URL: `http://www.bund.net/nc/presse/pressemitteilungen`.

[11] C. de Boni. Hochfliegende plne, absturz der nachhaltigkeit. *Magazin Greenpeace*, (3):28–30, 2011.

[12] K. Deininger, D. Byerlee, J. Lindsay, A. Norton, H. Selod, and M. Stickler. *Rising global interest in farmland*. Washington, 2011.

[13] Dena. *Entwicklung einer Mobilitts- und Kraftstoffstrategie fr Deutschland Voruntersuchung*. 2011. URL: `http://www.bmvbs.de/cae/servlet/contentblob/81938/publicationFile/56440/mksdenastudie.pdf`.

[14] European Commission. Directive 2009/28/ec of the european parliament and of the council of 23 april 2009 on the promotion of the use of energy from renewable sources and amending and subsequently repealing directives 2001/77/ec and 2003/30/ec. 2009. URL: `http://eur-lex.europa.eu/LexUriServ/LexUriServ.do?uri=OJ:L:2009:140:0016:0062:EN:PDF`.

[15] European Commission. *Fuel and air transport. A report for the European Commission*. Cranfield, 2010.

[16] European Commission. *2 million tons per year: A performing biofuels supply chain for aviation*. Brussels, 2011.

[17] European Commission. *Flightpath 2050: Europes Vision for Aviation*. 2011. URL: `http://www.acare4europe.org/docs/Flightpath2050_Final.pdf`,.

[18] European Commission. *The recognised sustainability schemes and the assessment reports*. 2011. URL: `http://ec.europa.eu/energy/renewables/biofuels/sustainability_schemes_en.htm`.

[19] European Commission. *Sustainable way for alternative fuels and energy in aviation*. Brussels, 2011.

[20] European Commission. *WHITE PAPER: Roadmap to a Single European*

Transport Area - Towards a competitive and resource efficient transport system. 2011. URL: http://eur-lex.europa.eu/LexUriServ/LexUriServ.do?uri=COM:2011:0144:FIN:EN:PDF.

[21] FAPRI-ISU. World agricultural outlook. *FAPRI Outlook*, 2011. URL: http://www.fapri.iastate.edu/outlook/2011/.

[22] A. V. Feigenbaum. *Total Quality Control.* New York, 2004.

[23] Food and A. O. of the United Nations. *Bioenergy and Food Security.* 2010.

[24] S. Gold. *Sustainable Supply Chain Management: Theoretische Reflexion und Anwendungsfeld Bioenergie.* Kassel, 2011.

[25] M. Goldbach, S. Seuring, and S. Back. Coordinating sustainable cotton chains for the mass market - the case of the german mail-order business otto. *Greener Management International*, 43:65–78, 2003.

[26] E. G. Hansen, D. Harms, and S. Schaltegger. Sustainable supply chain management im globalen kontext. *Die Unternehmung*, 62:87–110, 2011.

[27] IATA. A global approach to reducing aviation emissions. *IATA. Environment*, 2009. URL: http://www.iata.org/SiteCollectionDocuments/Documents/Global_Approach_Reducing_Emissions_251109web.pdf.

[28] IATA. *Fact sheet: Carbon-neutral growth.* December 2011. URL: http://www.iata.org/pressroom/facts_figures/fact_sheets/pages/carbon-neutral.aspx.

[29] ICAO. *U.S. fuel trends analysis and comparison to GIACC/4-IP/1.* Montreal, 2009.

[30] INKOTA. Pressemitteilung: Lufthansa heizt mit biokerosin landkonflikte an. *INKOTA-online*, July 2011. URL: http://www.inkota.de/presse/pressemitteilungen/pressemitteilung-lufthansa-biokerosin/.

[31] ISCC. *International Sustainability and Carbon Certification (ISCC).* 2013. URL: http://www.iscc-system.org/en/.

[32] M. Janic. *The sustainabiliy of air transportation. A quantitative analysis and assessment.* Ashgate Publishing, Hampshire, 2007.

[33] A. Meyer and P. Hohmann. Other thoughts; other results? - remei's biore organic cotton on its way to the mass market. *Greener Management International*, 31:59–70, 2000.

[34] MoD. *Defence Standard 91-91. Issue 6. Turbine Fuel, Aviation Kerosine Type, Jet A-1. NATO Code: F-35. Joint Service Designation: AVTUR.* 2008.

[35] OECD and FAO. *Agricultural outlook 2011-2020. Biofuels.* Paris, 2011.

[36] D. Rajagopal, S. Sexton, D. Roland-Holst, and D. Zilberman. Challenge of biofuel: Filling the tank without emptying the stomach? *Environmental Research Letters*, 2, 2007.

[37] Roundtable on Sustainable Biofuels, editor. *RSB Guidelines for Land Rights Respecting Rights, Identifying Risks, Avoiding Disputes and Resolving Existing Ones and Acquiring Lands through Free, Prior and Informed Consent.* 2012. RSB-GUI-01-012-01 (version 2.1).

[38] S. Roy, K. Sivakumar, and I. F. Wilkinson. Innovation generation in supply chain relationships: A conceptual model and research propositions. *Journal of the Academy of Marketing Science*, 32(1):61–79, 2010.

[39] RSB. *Roundtable on Sustainable Biofuels (RSB).* 2013. URL: http://rsbservices.org/.

[40] RSPO. *Roundtable on Sustainable Palm Oil (RSPO).* 2013. URL: http://www.rspo.org/.

[41] S. Seuring and M. Mller. Core issues in sustainable supply chain management a delphi study. *Business Strategy and the Environment*, 17:455–466, 2008.

[42] S. Seuring and M. Mueller. From a literature review to a conceptual framework for sustainable supply chain management. *Journal of Cleaner Production*, 16:1699–1710, 2008.

[43] D. Simpson and D. Samson. Developing strategies for green supply chain management. *Production / Operations Management*, pages 12–15, July 2008.

[44] C. Sisco, B. Chorn, and P. M. Pruzan-Jorgensen. *Supply chain sustainability. A practical guide for continuous improvement*. UN Global Compact Office and Business for Social Responsibility, 2010.

[45] S. M. Wagner. Supplier development and the relationship life-cycle. *International Journal of Production Economics*, 129:277–293, 2011.

[46] WEF. *Policies and collaborative partnership for sustainable aviation*. Geneva, 2011.

Efficiency improvement of a multistage compressor by optimization stagger angles of blade rows

Valeriy N. Matveev, Oleg V. Baturin, Grigorii M. Popov
Samara State Aerospace University named after academician S.P. Korolyov (National Research University), Russian Federation

Igor N. Egorov
Sigma Technology, Russian Federation

Keywords: *optimization, CFD, gas turbine engine, compressor, blades*

Abstract

Modern computer technologies now allow to conduct rather complex numerical calculations in a relatively short period of time. Thus, it has become possible to employ optimization methods in the design of various parts of gas turbine engines.

The results of two optimization tasks of seven-stage high pressure compressor are presented in this paper. The goal of the first optimization task was to improve the compressor efficiency at one operating mode (100% rotation frequency) by optimizing the blade stager angles of the guide vanes of the three first stages. As a result of solving this task, the HPC efficiency increase by 0.3% was achieved at required rotation frequency. This result was confirmed by experimental test.

The goal of the second optimization task was to improve the compressor efficiency at two operating modes (80% and 100% rotation frequencies) by optimizing the blade stager angles of all blade rows. As a result of solving this task, the HPC efficiency increase up to 1.2% was achieved at required rotation frequencies.

1 Introduction

Compressor, as gas turbine engine (GTE) component, determines the power (thrust), economical efficiency, external dimensions, weight, reliability and engine service life to a large extent [1]. The design and development of modern compressors are very complex technical tasks [2]. It should be considered contradictory requirements of reliability and gas-dynamic efficiency, as a rule, in different operation modes when solving these tasks. This process is an iterative and is to test the influence of various design measures on the required compressor characteristics (efficiency, stability margin, pressure ratio, air flow). Modern numerical simulation methods, implemented in software such as NUMECA FineTurbo [3], can accelerate the compressors development and allow to use optimization methods one of which, in particular, is implemented in the software package IOSO [4].

Optimization of multistage compressors and their components has a number of features [2]. Firstly, the optimization process is usually necessary to provide the improvement of compressor parameters (efficiency, stability margin) at different operation modes. Thus, optimization is a multi-criteria problem. Moreover, it is necessary to consider various design, technological, thermodynamic constraints during the optimization process.

Second, the optimization criteria and constraints in optimization task are determined by mathematical modeling of the compressor operation. Therefore, the numerical model of the compressor flow has to describe work processes with a required accuracy rate. Alternatively, the hundreds optimizer call to the mathematical model can be required to solve the optimization task. For this reason, the numerical model should have a reasonable computation time. Also, the compressor numerical model should be parametric and automatically, without user intervention should reconstruct the compressor geometry for all possible combinations of input data.

This work is aimed to test the application of optimization techniques to improve the efficiency of seven-stage GTE high-pressure compressor (HPC) (Fig. 1). The testing was performed on the solution of two optimization problems.

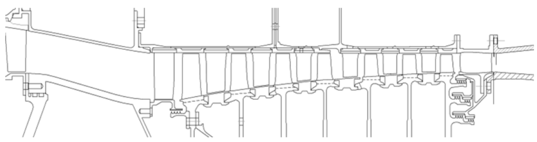

Fig. 1 Seven-stage HPC

The goal of the first optimization task was to increase the HPC efficiency for the operating mode that corresponds to the relative rotor speed 100% by optimizing the stagger angles of the guide vanes (GV) of the three first stages.

The goal of the second optimization task was the increasing of the HPC efficiency at two operating modes (rotation frequencies 100% and 80%) by optimizing the stagger angles of all blade rows.

Optimization solution of each task consisted of the following steps:

1. Optimization problem statement.
2. Creation and validation of the HPC parametric gas dynamic numerical model, which allows to change the HPC geometry in accordance with the optimization problem statement.
3. Solving of the optimization task.
4. Analysis of the HPC optimization results.

2 HPC optimization by variation of the three first stages GV blades stagger angles

2.1 Optimization problem statement

The goal of the first optimization task was to increase the HPC efficiency at the 100% rotation frequency. That is a reason why the maximum efficiency points on the branch, corresponding to the rotation frequency of 100% at the performance map, have been chosen as the optimization criteria.

There were not any constraints in optimization task statement.

The optimization problem statement is shown in Fig.1.

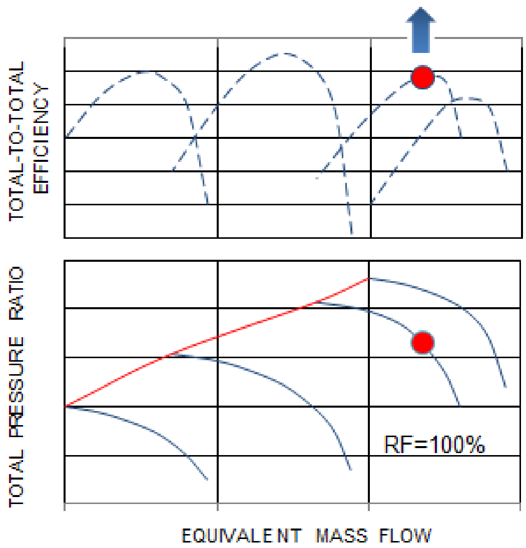

Fig. 2 First optimization problem statement

The blade stagger angles of the three first stages GV have been chosen as optimization variables (Fig.3). The choice of these variables (blade stagger angles of the 1st, 2nd and 3rd GV) was explained by the technological capabilities of the manufacturing, on the one hand, and the limited time to solve the optimization problem, on the other hand. Angle variation range has been chosen so that modified blade fits into the existing root for each GV. The blade number was not changed. It was allowed not to change compressor case details. So, the total number of variables was 3.

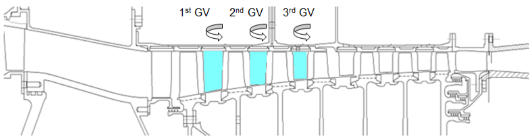

Fig. 3 Variables of the first optimization task

2.2 Creation and validation of the HPC parametric CFD-model

The HPC numerical model was created using NUMECA FineTurbo software. The model included domains of all HPC blade rows and bearing which is located before compressor (Fig.4). The created numerical model took into account existing tip clearances in the HPC.

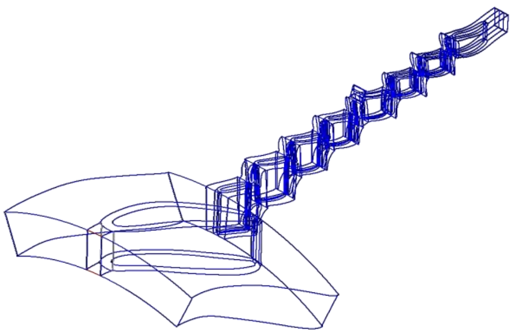

Fig. 4 HPC model

Construction of the structured mesh was accomplished by using program Numeca Autogrid5 with O4H-topology. The first to wall element size provided y + value of 1. The mesh size of each blade row domain was approximately 320000 elements. The total mesh size of entire model was approximately 5 million elements.

The program Profiler [5] integrated with mesh construction was used to modify the stagger angles of blade rows. This allowed to rebuild HPC numerical model automatically during the optimization process.

The HPC numerical model calculation was performed in a steady statement with using the Spalart-Allmaras turbulence model. The calculations in rotor blades domain were accomplished in rotating reference frame. Their rotation frequency corresponded to modeling operation mode. The total pressure and total temperature values at the inlet as well as static pressure at the outlet (which is corresponded to required characteristic point), were used as the boundary conditions.

The HPC numerical model validation was performed before optimization start by the comparison of the calculated (solid lines) and the experimental (dashed line) HPC performance maps at rotation frequencies of 89%, 94%, 100% and 103% (Fig. 5). The numerical model allows to describe the efficiency performance behavior, although it has the error in efficiency values predicting about 4% as shown in Fig. 5. The numerical model describes the pressure performances with greater accuracy. The conclusion that the HPC numerical mode can be used for the optimization was made on the basis of this.

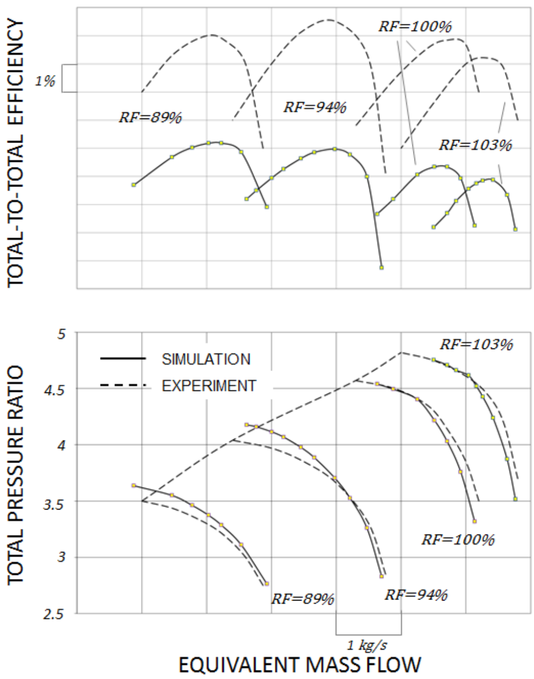

Fig. 5 Validation of HPC model

2.3 Solving of the optimization task

IOSO software needed 102 references to HPC numerical model to solve the optimization task. One reference to numerical model was a calculation of the max efficiency point at the 100% rotation frequency at the HPC performance map. The dynamics of the efficiency changes during optimization is shown on Fig. 6.

The blades stagger angles of the 1st, 2nd and 3rd GV were obtained as a result of solving this optimization task. These new optimal blades stagger angles allowed to increase HPC efficiency by 0.3% at 100% rotation frequency. As an example, the comparison of initial and optimized blade of 1st GV is shown in Fig. 7.

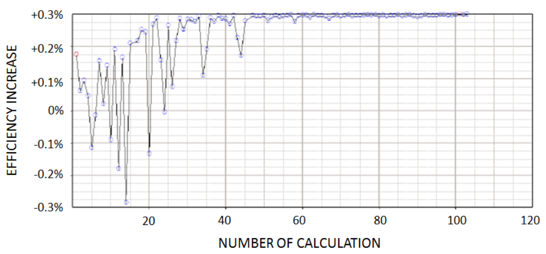

Fig. 6 The dynamics of solving the problem

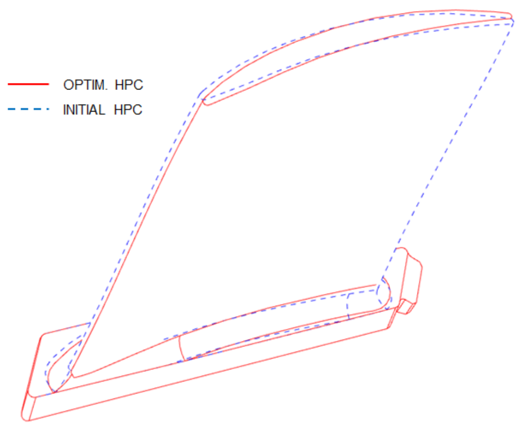

Fig. 7 Comparison of the airfoils of the first guide vane

2.4 Analysis of the optimization results

The numerical model of optimized HPC was created for the optimization results analysis. The performance map at 94% and 100% rotation frequencies were calculated for optimized HPC and then were compared with corresponding performance map of initial HPC (Fig. 8). The dashed lines correspond to the initial HPC and solid lines correspond to the optimized HPC on Fig. 8. The comparison of performance maps showed:

1. The stability margin of the optimized HPC configuration did not decrease in comparison with basic HPC configuration at the investigated rotation frequencies;
2. The equivalent mass flow rate through the optimized HPC was lower than equivalent mass flow through the initial HPC configuration by 1.3% at both rotation frequencies (94% and 100%);
3. The HPC efficiency increased by 0,3% at the 94% and 100% rotation frequencies.

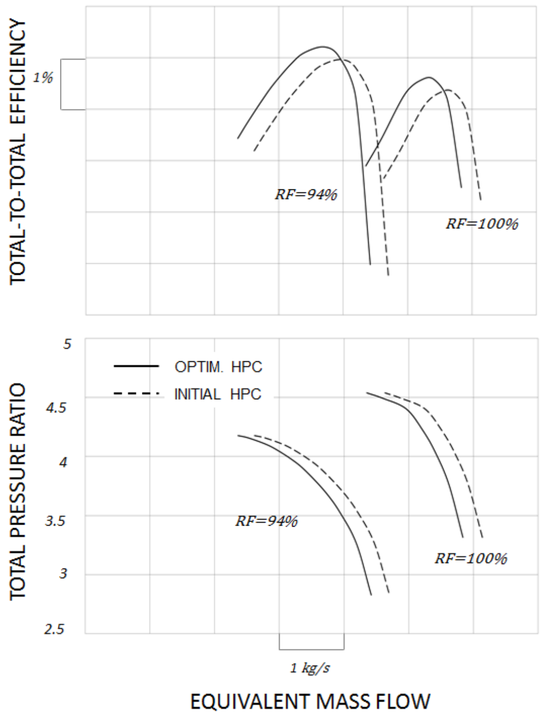

Fig. 8 Comparison of the HPC performance maps for the initial and optimal HPC configurations

The optimized blades of 1st, 2nd and 3rd GV were manufactured. HPC with these optimized blades within engine core (Fig. 9) was tested on rig of JSC KUZNETSOV [6]. The test results confirmed the HPC efficiency increase by 0.3% at 94% and 100% rotation frequencies.

Fig. 9 Engine core of GTE

3 HPC optimization by variation the stagger angles of all blade rows

3.1 Optimization problem statement

Since the results of the first optimization task have been confirmed experimentally, it was concluded that the developed optimization methodology is appropriate and workable.

For this reason it was decided to revisit the problem of compressor efficiency increasing the in a more complex formulation and taking into account the shortcomings that were identified in the first problem solution.

In particular, it was assumed that the variation of all the blades stagger angles allows to achieve greater efficiency gain. Therefore, the stagger angles of the seven guide vanes, seven rotor blades and inlet guide vane were ranged in solving the second problem of optimization. The total number of variable parameters was 15 (Fig. 10).

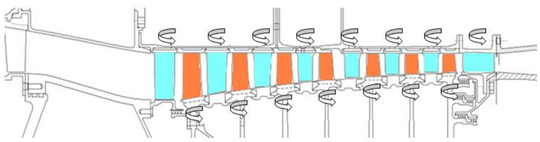

Fig. 10 Variables of the second optimization task

The variation range of each blade row stagger angle was chosen so that the turned blade profiles fit into the existing root as in the first optimization problem solving. The blade number also was not changed. This decision was allowed to find the variant of HPC efficiency increasing without compressor disks design and case details changing.

Secondly, the solution to maximize the efficiency at two modes (relative speeds at 80% and 100%) was taken. It was allowed not to impair the effectiveness at the one operating modes (80% of rotor speed), while increasing the efficiency at another mode (100% rotor speed).

Furthermore, the pressure ratio and equivalent mass flow rate changing at operating conditions was unacceptable when analyzing the results of the first optimization task. This disrupts the setting of engine components joint work and can lead to a substantial engine performances changing as a whole. Therefore, additional constraints were introduced in the optimization process:

1. The equivalent mass flow rate through the compressor at the maximum efficiency point of 100% rotation frequency may vary within ±0,6% of the original;
2. The equivalent mass flow rate through the compressor at the maximum efficiency point of 80% rotation frequency may vary within ±1,3% of the original;
3. The total pressure ratio at the maximum efficiency points of both rotation frequencies may vary within ±1,5% of the original.

The HPC stability margin on both rotation frequencies were not taken into consideration during optimization problem statement and appointment of constraints (in contrast to [7]), because it could complicated the optimization task and increasing solution time. The HPC stability margin on both rotation frequencies were evaluated at the stage of the optimization results analysis.

The optimization criteria and constrains used in the optimization problem statement are shown schematically in Fig. 11.

3.2 The HPC parametric numerical model

The same HPC numerical model was used to solve this optimization problem as in the optimizing the GV stagger angles of the HPC first three stages (section 2.2) task.

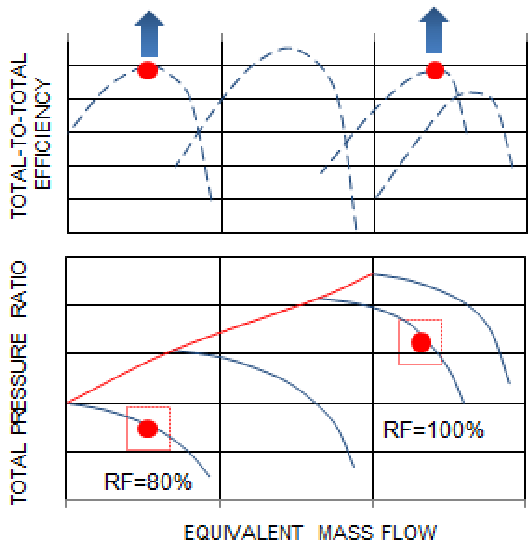

Fig. 11 Second optimization problem statement

3.3 Solving of the optimization task

IOSO software needed 446 references to HPC numerical model to solve the stated optimization task. One reference to numerical model consisted of calculation of two points at the HPC performance map in the programming software NUMECA FineTutbo: max efficiency points at the 100% and 80% rotation frequencies.

Set of unimprovable solutions (Pareto set) was obtained as a result of solving optimization task. Pareto set was a compromise between efficiency increase at the 100% and 80% relative rotation frequencies (Fig. 12). Each point from Pareto set had a correspondence with HPC unique geometry represented as stagger angles massive of all HPC blade rows.

Analysis of Pareto set extreme points showed that maximum efficiency improvement at the 80% relative rotation frequency was 1,8% with almost unchanged maximum efficiency at relative rotation frequency of 100% (point 1 at Pareto set, Fig. 12). The highest efficiency improvement at the 100% relative rotation frequency was 0,6% with maximum efficiency increasing of 1% at the 80% relative rotation frequency (point 2 at Pareto set, Fig. 12). However one of the middle points of Pareto set (point 3, Fig. 12) was chosen for further investigation. This point allowed to achieve efficiency increase by 0,5% at the 100% relative rotation frequency and by 1,2% at the 80% relative rotation frequency.

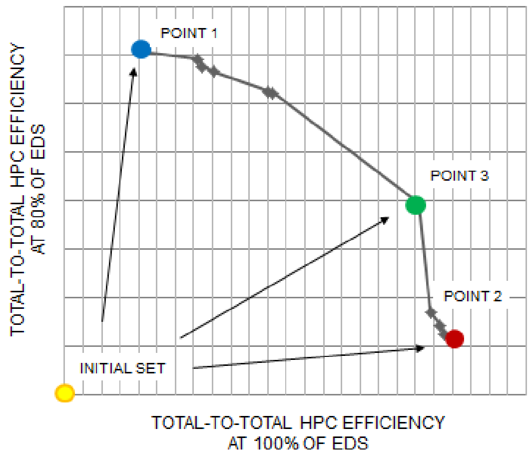

Fig. 12 Pareto set

3.4 Analysis of the optimization results

The HPC numerical model corresponding to the selected point 3 of the Pareto set was built to analyze the optimization results. The performance maps for optimized HPC at both rotation frequencies (100% and 80%) were obtained using this numerical model. And their comparison with the performance of the initial HPC was carried out (Fig. 13). The dashed lines correspond to the initial HPC performance, solid - optimized HPC in Fig. 15.

The performances comparison established the following:

1. The stability margin of optimized HPC variant did not decrease in comparison with basic HPC variant at the investigated rotation frequencies;
2. The air flow rate and pressure ratio values changing of optimized HPC at points of maximum efficiency for the investigated rotor speeds are in the constraints range;
3. The HPC efficiency increased by 0,5% at the 100% rotation frequency and by 1,2% at the 80% rotation frequency.

The flow structure analysis of optimized HPC at maximum efficiency and at 100% relative rotation frequency showed that optimization of blade stagger angles allowed to eliminate flow separation near hub of 4th and 5th HPC rotor (Fig. 14).

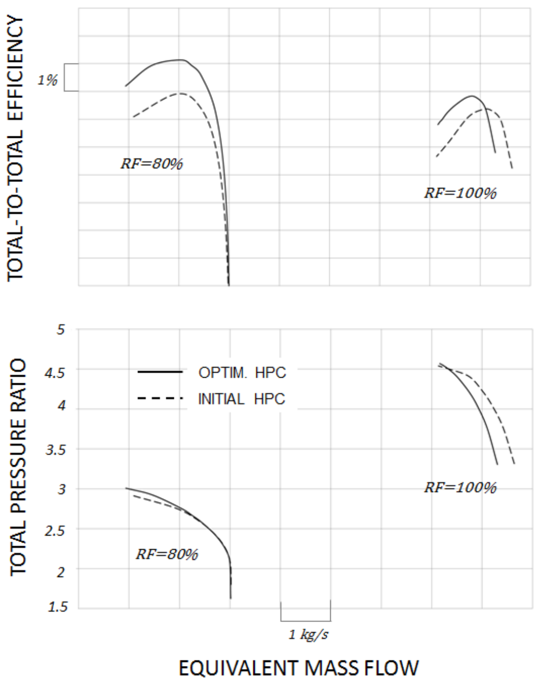

Fig. 13 Comparison of the HPC performance maps for the initial and optimal HPC configurations

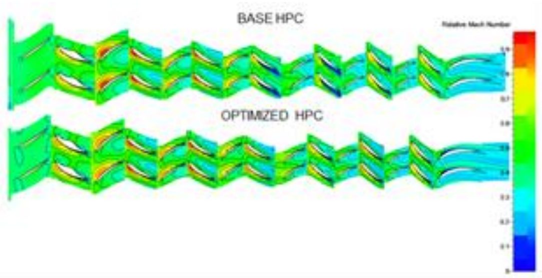

Fig. 14 Mach number field near hub for base and initial HPC

4 Conclusion

Thus, the following results were achieved as a result of work:

1. The methodology for improving the multistage axial compressor efficiency using multi-objective optimization methods has been developed and practically worked out.
2. The adequacy of used physical and mathematical models has been confirmed by a successful comparison of the calculated and experimental data, both the basic and optimized design.
3. The HPC efficiency increase of 0.3% at 100% rotor speed by optimizing the stagger angles of the first three stages blades is achieved. This result was confirmed experimentally by testing the optimized HPC within engine core at the JSC KUZNETSOV.
4. It is shown that the HPC efficiency can be increased by 1.2% at the relative speed 80% and up to 0.5% at the relative speed 100% increase in efficiency of due to the change in the stagger angle of the all HPC blades within the existing roots while maintaining the position of the operating points on the performance map.

Acknowledgements

Authors wish to express profound gratitude to Prof. Charles Hirsch and the whole team of NUMECA Company for the help in mastering Numeca FineTurbo software.

Also The authors gratefully acknowledge the comprehensive support in carrying out this work of JSC KUZNETSOV, in particular Dmitry G. Fedorchenko, Mr. Anton N. Shatsky, Mr. Gennadii N. Chursanov and Mr. Maxim G. Miheev.

This work was financially supported by the Government of the Russian Federation (Ministry of Education and Science) based on the Government of the Russian Federation Decree of 09.04.2010 № 218.

References

[1] Inozemcev A.A., M.A. Nihamkin, V.L. Sandrackij, Osnovy konstruirovanija aviacionnyh dvigatelej i jenergeticheskih ustanovok (tom II): Uchebnik dlya VUZov (The basic design of aircraft engines and power plants (Volume II): Textbook for High Schools), Moskow, Mashinostroenie, 2008. 198 p.
[2] Kuzmenko, M.L., Egorov, I.N., Shmotin, Yu.N., "Axial Fan Optimization Using 3D Codes", ASME GT2005-68209.
[3] NUMECA Int., http://www.numeca.com/en
[4] SIGMA technology, http://www.iosotech.com
[5] Shablii, L.S., Dmitrieva, I.B., Popov, G.M.,

Avtomatizatsiya postroeniya modelei lopatochnykh ventsov dlya CAE-raschetov v programme Profiler (Automation modeling blade rows for CAE-calculations in the program Profiler), Vestnik Samarsk.gos. aerokosm. unta. - 2012. - №1(28). part.1. – p. 82-90.

[6] JSC KUZNETSOV ,http://www.kuznetsov-motors.ru/en

[7] Kuzmenko, M.L., Egorov, I.N., Shmotin, Yu.N., Fedechkin, K.S., "Optimization of the Gas Turbine Engine Parts Using Methods of Numerical Simulation", ASME GT2007-28205.

Development of a preliminary design method for hybrid propulsion aircraft

S. Bagassi, F. Lucchi and F. Persiani
sara.bagassi@unibo.it, f.lucchi@unibo.it, franco.persiani@unibo.it

DIN – Industrial Engineering Department,
University of Bologna, Italy

Keywords: *diesel, hybrid propulsion, aircraft sizing, Weight Fractions Method*

Abstract

Standard design procedures are not readily applicable to aircraft that use multiple energy sources; innovative concepts like hybrid propulsion systems require new approaches in weight and performance prediction. Therefore, developing green propulsion concepts for aviation requires changes in standard procedures for the preliminary aircraft design.
In this paper the application of a new methodology to account for the changes in the governing equations when using hybrid propulsion is explored.
The focus is on hybrid propulsion systems based on diesel heavy fuel ICE (Internal Combustion Engine) combined with electric motor in a parallel configuration. This study relies on simple structure and material performance indexes, neglects stability and control analysis, and uses simplified aerodynamic models.

1 Introduction

Aircraft environmental impact has emerged as a key factor in aircraft design. Since air passengers are projected to grow at a rate of 5 percent per year through 2020, aircraft design will require new solutions and concepts to meet environmental requirements: in this context “green design” paradigms should play a key role, in order to describe actions to reduce emissions and noise, defining green aircraft technologies.
In particular, environmental impacts from hydrocarbon fuels have adverse effects both on global warming and local air quality: this is leading to the introduction of cleaner energy sources and systems. Research on unconventional aircraft propulsion systems is now advancing, with the aim to reduce aircraft emissions and noise.
Hydrogen [1], [2], [3] solar energy systems [4], electric systems, fuel cells [5] and power management and distribution are currently the most investigated alternative energy sources for aircraft applications [6].
With the energy crisis still looming, initiatives such as More Electric Engine (MEE) and More Electric Aircraft (MEA) are promoted [6]: in this context hybrid combustion-electric power, helping in reducing fuel usage, is considered because of its potential advantages. Reduced emissions, increased performances (especially at altitude, since air density does not affect electric motor performances), lower operating costs, increased safety due to redundancy, reduced risk of explosion or fire in the event of an accident

and less noise are some main advantages expected from its employment.
Despite some all-electric aircraft have been developed [7], the installation of an all-electric propulsion system is limited by the energy storage capability; the hybrid electric motor-ICE propulsion technology seems to be a good compromise between reduced fuel consumption, emissions and high power to weight ratio needed for aircraft propulsion.
The ratio between the electric motor power and total power (ICE plus electric motor) is defined as the Hybridization Factor (HF), which defines both full and mild hybrid designs, ranging from 0.3 to 0.5. Mild-hybrid propulsion systems are characterized by the lower values, while full-hybrid systems have higher values, near 0.5.
Hybrid technology combines the advantages of two or more power sources to create a more efficient propulsion system for a vehicle: three basic architectures are usually considered: series, parallel and power-split [8]. In particular, in most systems an internal combustion engine is the primary power source and the battery packs, to power electric motors, are combined to generate power [9].
Usually the ICE is a gasoline engine: this study proposes a diesel engine as the ICE subsystem, the target is to further reduce fuel consumption and emissions with respect to a gasoline ICE, optimizing safety and limiting fuel costs.
Unconventional design strategies are at the basis of such propulsion systems. In order to implement the hybrid concept, the most relevant aspects of aircraft sizing, impacting on the overall size of aircraft and installed engines, must be adapted to the new technology.
Aircraft design is a highly iterative process: by incorporating a hybrid propulsion system, new design parameters enlarge the domain of feasible solutions and the complexity for finding an optimal solution increases further.
The design process for traditional aircraft using internal combustion engines can be used as a reference framework, but must be modified properly.
The starting point of the work presented in this paper is described in [10] and [11]. It is developed elaborating on constrained static optimization formulation to study hybrid diesel-electric propulsion system design on a UAV application.

2 Methodology

Two configurations of the same aircraft, equipped with two different propulsion systems, are compared, in terms of performances, consumptions and weights. In particular, a traditional diesel engine and a parallel hybrid diesel-electric propulsion system are evaluated. The parallel hybrid diesel-electric propulsion system consists in a diesel internal combustion engine, an electric motor/generator, a rechargeable battery pack and a propeller (Fig.1).

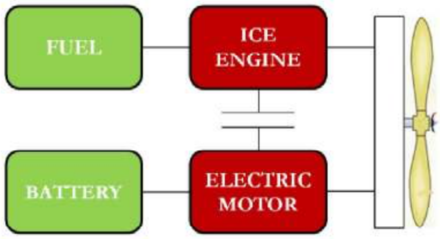

Fig.1 Parallel hybrid diesel-electric propulsion layout

2.1 Hybrid conceptual design

The methodology consists in three main blocks [11]: a weight estimation module, an optimization module and a post – processing module (Fig.2).

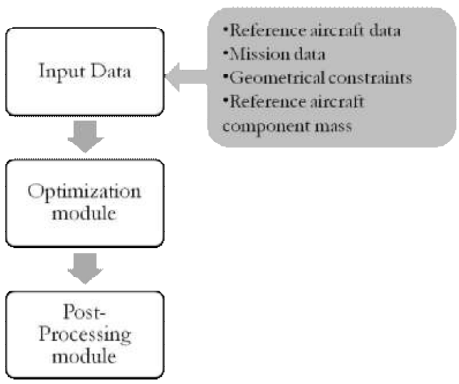

Fig.2 System architecture

The weight estimation module estimates the weight fractions of the hybrid engine aircraft (*Hybrid Configuration*) starting from data of diesel–engine aircraft (*Reference Configuration*).
The Reference Configuration provides input data, which consists in:

- reference aircraft data (*wing efficiency, max. lift coefficient, stall speed, propeller efficiency, mechanical efficiency, battery specific energy, specific motor power*);
- mission data (*takeoff altitude, mission altitude, maneuvering speed, ref. cruise speed, ref. SL rate of climb, ref. TO ground distance, reference range*);
- wing geometry constraints (*maximum wing area, minimum wing area, maximum wingspan, minimum wingspan*);
- reference aircraft component mass breakdown (*max. take-off weight, fuel weight, engine weight, payload weight, empty weight, battery weight*).

Such input parameters are at the basis of the weight of the glider, which is defined as the difference between the empty weight and the engine weight, in the reference configuration.
Weight fractions are evaluated for each mission segment on the basis of the statistical data form as discussed in [12]. The take-off weight and the input dataset are thus estimated, to be used in the second module.
The optimization module elaborates the solution proposed by the weight estimation module by optimizing a selected objective function: the required power for cruise. The function (1) is minimized under stall limit constraint (2) and structural limit constraint (3).

$$P = \frac{1}{\eta_{Prop}\eta_{Mech}}\left(\frac{1}{2}\rho V_{cr}^3 S c_{D0} + \frac{KW}{\frac{1}{2}\rho V}\frac{W}{S}\right) \qquad (1)$$

$$\frac{W_0}{S} - \frac{1}{2}\rho V_{stall}^2 c_{L,max} \le 0 \qquad (2)$$

$$AR - \left(\frac{2nW_0}{\rho V_a^2 S}\right)^2 \frac{1}{c_{D0}\pi_e} \le 0 \qquad (3)$$

Where:

$$K = \frac{1}{\pi e AR}$$

P	Power
η_{Prop}	Propeller efficiency
η_{Mech}	Mechanical efficiency
ρ	Density
V_{cr}	Reference cruise speed
S	Wing Cross Sectional Area
W	Weight
c_{D0}	Zero-lift drag coefficient
$c_{L,max}$	Maximum lift coefficient
V_{stall}	Stall speed
V_a	Manoeuvring speed
AR	Aspect Ratio
e	Oswald efficiency factor

The performance are thus computed and the power excess need is evaluated, considering as design requirements the take-off distance and the rate of climb. An Hybridisation Factor is defined for the proposed hybrid configuration.
In the last post processing module, the reference and hybrid configuration are quantitatively compared.

3 Hybrid aircraft preliminary design: a case study

The case-study consists in an UAV's conceptual design. The reference design is a MALE UAV equipped with an ICE Diesel engine. The study goal is evaluating the retrofit of the propulsion system through an hybrid system in parallel configuration with the aim to minimize the in–flight fuel consumption in terms of the "environmental factor" (see Eq.4) defined as the mass of fuel burnt FB per kilogram of payload per mile, sacrificing maximum 40% endurance and increasing minimum 30% payload with respect to the reference design.
The diesel engine is expected to be a good compromise to obtain energy more efficiently

and it should lead to an even more green propulsion.

$$EF = \frac{FB}{kg_{Payload} \cdot mile} \qquad (4)$$

As previously described, the input data are the reference aircraft design parameters to be kept constant and a certain number of variables of the hybrid propulsion.

4 Results and discussions

Table 1 and 2 show the main results.

Different distributions of the weight fractions are reported in terms of source energy components weight fraction (Figure 3).
The battery mass needed was too large for enough fuel to be carried on board to support the original range. The high reduction of fuel mass is due to the lower range and the more efficient propulsion: fuel consumption per NM of range drops from 0.3125 to 0,1 kg/NM.

Weight	*Unit*	*Reference Configuration*	*Hybrid Configuration*
MTOW	kg	1200	1132
Fuel weight	kg	250	50
Engine weight	kg	200	141
Payload weight	kg	140	182
Battery weight	kg	10	134
Glider weight	kg	600	600
Electric Motor weight	kg	--	25

Table 1 Weight estimation for the optimized configuration

The battery weight fraction increase was comparable to the total loss in fuel and engine weight fractions. One of the problems of the reference aircraft is due to the over-size of the ICE engine in cruise condition. This has been solved because the electric motor was designed to supply the surplus power needed to take off, while in cruise the hybrid UAV relies only on the power of the smaller ICE diesel engine.
Since there were demonstrated fuel savings, the hybrid solution should lead to fuel savings also with a different amount of range reduction.

Performance	*Unit*	*Reference Configuratior*	*Hybrid Configuratior*
ICE Engine Power	kW	121	104
Wingspan	m	12	12
TO Distance	m	500	483
ROC	m/min	304,5	304,5
Range	NM	800	500
Cruise speed	m/s	65	65
Electric Motor Power	kW	--	56
Hybridization Factor	**0**	--	**0,36**
EF	**kg/kg NM**	**22 x 10^{-4}**	**5.5 x 10^{-4}**

Table 2 Performances estimation for the optimized configuration

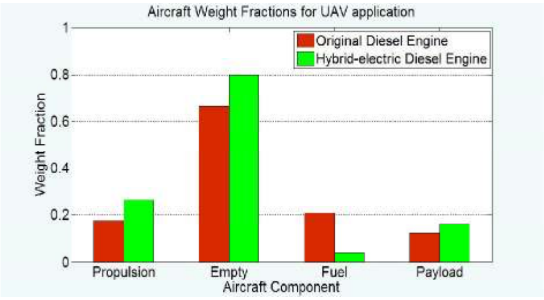

Figure 3 Weight fractions results

5 Conclusion

The hybrid conceptual design code is based on a modified weight fraction method.
The presented case – study shows that the fuel consumption has dramatically decreased in despite of a significant range reduction. As a consequence, Mild Hybrid Electric design

shows fuel saving potential and improvements of the overall efficiency of energy delivery.
Comparing the weight fractions before and after hybridization, the UAV case study has shown that a percentage of range was sacrificed, while gaining in fuel burnt per mile of range per kg of payload. In the next future, the battery specific energy is expected to be improved, so less range would need to be sacrificed.
It is considered that the efficiency of diesel engines is around 40%: the high specific energy of the chemical fuel is wasted on thermal inefficiency. Specific energy of batteries needs to reach 40% of hydrocarbon fuel's specific energy to be just as effective. If more fuel is replaced by batteries, the efficiency of the energy stored on-board would increase. Based on these considerations, the improvement of the UAV propulsion design to satisfy multiple mission profiles seems to be supported by this research. Moreover, considering that electric power is independent from altitude, the added performance provided by the electric motor could get the flying platform to altitude quickly and provide boost power when requested.

For better understanding of the advantages of hybrid propulsion, many more specific simulations need to be run so the mild hybrid-electric system can be more effectively designed for specific mission profiles. During a typical reconnaissance mission a UAV may perform climbs, sustained turns, slow flight, and missed landing operations that may need extra power. To simulate these conditions, different fuel fractions can be calculated for each mission taking into account the different mission segments .

In next studies we aim to analyze the performance of the transmission system, in terms of additive torque from power sources. Additive torque is essential for the conceptual design code to be accurate.

References

[1] Westenberger, A., Hydrogen Fuelled Aircraft. *AIAA/ICAS International Air and Space Symposium and Exposition: The Next 100 Y*, 2003.

[2] Brand J, Sampath S.F, Potential Use of Hydrogen in Air Propulsion. *AIAA/ICAS International Air and Space Symposium and Exposition: The Next 100 Y*, 2003.

[3] Renouard-Vallet G, Saballus M, Schumann P, Kallo J, Friedrich K.A, Müller-Steinhagen H, Fuel cells for civil aircraft application: On-board production of power, water and inert gas. *Chemical Engineering Research and Design*, Vol 90, Issue 1, January 2012, pp 3-10.

[4] Vashishtha V.K, Kumar A., Makade R., Lata S. Solar power the future of aviation industry. *International Journal of Engineering Science and Technology (IJEST)* Vol. 3 No. 3 March 2011, pp. 2051-2058.

[5] T.H. Bradley, B.A. Moffitt, D. Mavris, D.E. Parekh, *Aviation: Fuel Cells*, Encyclopedia of Electrochemical Power Sources, 2009, Pages 186-192.

[6] A. Sehra and W. Whitlow, *Propulsion and power for 21st century aviation*, Prog. Aerosp. Sci., vol. 40, no. 4, pp. 199–235, 2004.

[7] Gohardani A.S, Doulgeris G and Singh R, *Challenges of future aircraft propulsion: a review of distributed propulsion technology and its potential application for the all electric commercial aircraft*, Progress in Aerospace Sciences-Elsevier, Vol 47, Issue 5, July 2011, pp 369-391.

[8] Momoh O.D and Omoigui M.O, An overview of hybrid electric vehicle technology. *Vehicle Power and Propulsion Conference*, 2009, pp. 1286 – 1292.

[9] Glassock R.R., Hung J.Y., Walker R.A. and Gonzalez L, *Design, modeling and measurement of hybrid power plant for unmanned aerial systems (UAS)*, 5th Australasian Conference on Applied Mechanics, 10-12 December, 2007, Brisbane, Australia.

[10] Hiserote, R., Harmon, F., *Analysis of Hybrid-Electric Propulsion Systems for Small Unmanned Aircraft Systems*, AIAA-2010-6687, AIAA's 8th International Energy Conversion Engineering Conference, Nashville, TN, July 25-28, 2010.

[11] S. Bagassi, G. Bertini, D. Francia, F. Persiani, Design Analysis for Hybrid Propulsion, ICAS 2012, 28th International Congress of the Aeronautical Sciences, September 23rd – 28th, 2012, Brisbane, Australia, ISBN 978-0-9565333-1-9.

[12] Raymer, D.P., *Aircraft Design: A Conceptual Approach*, 1st Edition, American Institute of Aeronautics and Astronautics, 1989.

4:th CEAS Air & Space Conference
FTF Congress: Flygteknik 2013

Feasibility Study of small Satellite Launcher Vehicle launched from atmospheric Carrier Aircraft

Dr. N. Viola and A. D'Ottavio
Department of Aerospace Engineering, Politecnico di Torino, Italy.

Prof. S. Chiesa
Department of Aerospace Engineering, Politecnico di Torino, Italy

Keywords: Space Vehicle, carrier aircraft, air launch

Abstract

The paper deals with the feasibility study of an air-dropped small satellites launcher vehicle. A conceptual design methodology has been defined and then applied to various case-studies, in order to evaluate the main flight, mission and system performances of the unconventional space vehicle (SV) that may be either launched from a supersonic fighter aircraft or from a subsonic cargo aircraft. The SV concept presented is a fast and affordable solution able to access space from any sites of the world in all weather conditions. It is a missile-like solution able to inject in Low Earth Orbits a small payload (mass lower than 200 kilograms) in a few hours, through a low cost mission. At the beginning, the paper presents a short investigation of traditional European space launch capabilities, highlighting the lack of dedicated transport solutions for Nano and Micro-satellite families and proceeding with the analysis of the state of the art of new concepts of unconventional launch solutions. The paper then describes the conceptual design methodology developed, used to accomplish the feasibility study of the SV. This proposed methodology has been translated into a flexible numerical program in Matlab® language, which allows evaluating the main flight and system performances of the SV, after being dropped from its carrier aircraft. The most promising design alternatives, which may be air-dropped either in subsonic or in supersonic flight regimes, are finally described and shown in the paper. Eventually main conclusions are drawn.

1 Introduction

Generally, the ability to insert a limited payload mass in Low Earth Orbits (LEO) from an air-dropped spacecraft is extremely interesting and stimulating for the aerospace research community, especially for small satellites developers. Space is playing an increasingly important role in the leverage and execution of military, scientific and civil protection missions. For these reasons since the last few years the increasing demand and consolidated capability of accessing space have been generating a high request for affordable, strong, continuous, and flexible space access solutions. The "help from space", in general the need to use space technologies and space systems, is typically required for particular events sometimes defined as hostile environments. In these circumstances the capability of inserting in a very short time a dedicated payload mass into orbit may be crucial. Critical scenarios may therefore require the capability of being highly responsive. This specific capability can be considered as a new mission requirement for space systems. An innovative concept of space system, able to match the new mission requirement, is the Space Vehicle (SV), which is a fast and affordable solution able to access space from any sites of the world in all weather conditions thanks to an air-dropped launch from its carrier aircraft. The SV is a missile-like solution able to inject in LEO a small scientific or military payload, i.e. small satellites whose mass does not exceed 200 kilograms, in a few hours, through a low cost mission. For these reasons, the SV can be considered as an innovative concept for space transport and it represents the most affordable, easily available and flexible solution for a continuous access to space for small payload missions.

The paper deals with the feasibility study of a SV, i.e. a small satellites launcher, launched from a carrier aircraft. A conceptual design methodology has been defined and then applied to various case-studies, in order to evaluate the main mission and system performances of the unconventional satellites launcher that may be either launched from a supersonic fighter aircraft or from a subsonic cargo aircraft.

A brief investigation of the European space launch capabilities has been accomplished, in order to understand the launch capability of the European space launchers. Figure (1) [1] shows the rationalization of the satellites market, which has been divided in seven different satellites categories, according to their mass at launch. The analysis that has been performed highlights the lack of a dedicated transport solution for the families of Nano and Micro-satellite, whose mass respectively extends up to 10 kg and 100 kg. Nano and Micro-satellites, for which a high increase in launch demand is expected in the next years (especially for Nano-satellites) nowadays are typically considered and operated as secondary payloads.

The Federal Aviation of Administration (FAA), as reported in [2] and in accordance with other space market forecasts ([3], [4], [5] and [6]), has certified that a new market sector in the aerospace industry has born, mainly focused on the development of small space launchers, able to insert limited payloads masses into LEO. The certification of this new market sector is the direct consequence of the increasing launch demands of Nano and Micro-satellites families.

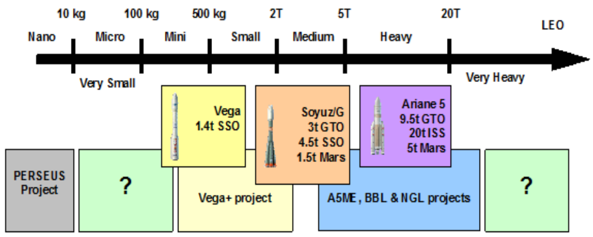

Fig. 1 European space launch capabilities.

In 2012 about 57 launches of Nano and Microsatellites have been registered; the same value is expected also for the 2013. Generally, all market outlooks show a constant and positive trend in launch demand for Nano and Micro satellites for the next 7 years, with 142 launches forecast for the year 2020. Figure 2 [6] shows the percentage of types of uses for Nano and Micro-satellites families related to their 2020 market forecast.

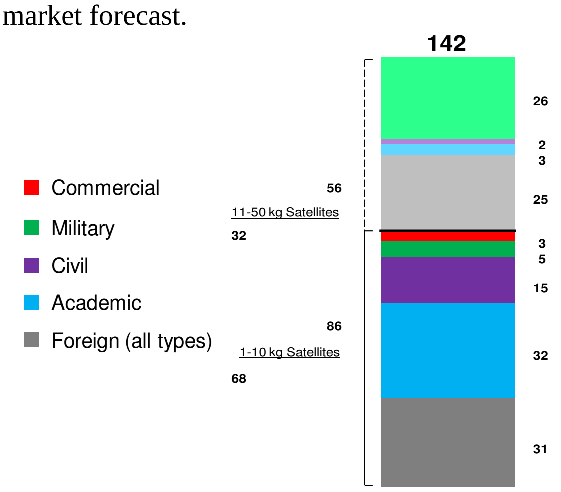

Fig. 2 Micro and Nano satellite market forecast.

Taking all these considerations into account, it can be said that the unconventional launcher concept, presented in the paper, could have a tremendous impact on the satellites market today, filling the gap of dedicated transport solutions for Nano and Micro-satellites categories. This consideration lays behind the main purpose of this work, i.e. the feasibility study of an unconventional solution for small satellites launchers, launched from an atmospheric carrier aircraft.

2 State of the art and general considerations

Today research activities and international programs focused on the development of new space transportation solutions, such as the SV, are growing. An updated list of these studies and programs can be found in [7], which describes 115 international projects since 1962. For the aim of this work, only 14 international programs have been considered acceptable references (some of them are not listed in [7]), as reported in Table 1.

Table 1 Selected international projects. In the fourth column the letter A, B and C indicate the design level: A means "feasibility study"; B means "prototype"; C means "operative".

Concept name	Program Acronym	Nation	Project phase (*)	Performer	Year of introduction
Minuteman	M-ICBM	🇺🇸	B	USAF	1974
Pegasus	--	🇺🇸	C	Orbital	1984
Ishim	--	🇷🇺	B	--	1998
F-15 MLV	MLV	🇺🇸	B	Boeing-USAF	2003
Air Start	--	🇷🇺	B	Antonov	2003
RASCAL - Coleman	RASCAL	🇺🇸	A	DARPA-Coleman	2003
Peregrine	--	🇺🇸	A	Andrews Aeros.	2004
QuickReach	SLV	🇺🇸	B	DARPA-USAF	2005/2006
ALDEBARAN	MLA	🇫🇷	A	CNES	2008/2009
DEDALUS	--	🇫🇷	A	CNES	2008/2009
EFA Launcher System	--	🇮🇹	A	Univ. di Roma	2008/2009
Tornado Launc. Sys.	MURALM	🇮🇹	A	Università, MBDA, Alenia	2008/2009
LauncherOne	--	🇺🇸	B	Virgin Galactic	2010
NanoLaunch LLC conc.	--	🇺🇸	A	Premier Sp. Sys.	2010

Among these 14 reference programs, our attention has focused on the following SV concepts: Aldebaran and EFA-Launch System (EFA-LS) projects, as they represent the two most significant European projects currently under development (see [8] and [9]), F-15 Microsatellite Launch Vehicle-MLV (see [10], [11] and [12]) and Pegasus project (see [13]).

The SV reference configuration (baseline missile) that has emerged from this analysis is a three-stage launch solution. The baseline missile summarizes the most important technical characteristics, like number of stages, thrust level, specific impulse and propellant mass of each propulsive stage. The typical mission profile starts with an air launch performed at medium altitude. Through the analysis of each mission profile we understand that the SV is a delivery system, which combines the best performance of two types of missile families: the Intercontinental Ballistic Missiles, ICBM, from the point of view of space performance, and the Tactical Missiles, from the point of view of weight and size. Main disadvantages of air launch are severe criticalities in the design and operations of the system. As far as the design is concerned, the integration between the SV, i.e. the missile, and the carrier aircraft, is a critical issue, which affects the final weight and size (length and diameter) of the spacecraft as well as its aerodynamic configuration (tails, wings or canard) and is one of the keys for the final success of the SV. As far as the operations are concerned, the separation of SV from the carrier aircraft is again a critical issue. Main advantages of air launch are here briefly listed. The launch from a carrier aircraft allows injecting the payload into the desired orbit and it eliminates any geographical, weather and political launch constraints. The total velocity increment that is required to reach the orbit is a sum of the velocity increments of both the SV and the carrier aircraft. Lower values of velocity increment allocated to the SV imply higher SV payload capability. Typical values of velocity increment for a fighter aircraft as launch aircraft range between 300 to 800 m/s, while for a cargo aircraft as launch aircraft range between 150 to 200 m/s. As well as the velocity increment given by the launch aircraft, the release altitude is also a crucial issue for the SV sizing activity: higher values of release altitude imply lower dynamic pressure and consequently lower drag and thermal loads acting on the spacecraft structures. From the point of view of the thrust, higher values of release altitude reduce the engine pressure losses with direct benefits on the final values of the expansion ratios of the engine nozzles.

3 The design process: general guideline

In this section the design process that has been used to accomplish the conceptual design of the SV is presented (see Fig. 3). The conceptual design methodology, presented in the paper, has been translated into a flexible simulation program in Matlab® language, which allows evaluating the main performance of orbit insertion of the SV, after being air launched by its carrier aircraft.

The first step of the conceptual design process is represented by the definition of the mission and system requirements of the carrier aircraft that can be chosen between fighter and cargo family. Once the carrier aircraft has been selected, the first-guess geometrical configuration and propulsion performance of the SV can be extrapolated on the basis of the baseline missile. The SV, for sake of simplicity, can be thought of as a missile system divided into three different parts: nose section, center body and boattail, as shown in Fig. 4. For each section analytical formulas are used, in order to evaluate drag and normal force coefficients at each time-step of the simulations. In particular it is worth mentioning that for the nose section, which accommodates the payload, six different aerodynamic models or nose shapes (cone profile, tangent ogive, parabolic series, elliptical shape, Von Karman profile and Haack series) are implemented into the program's code. The best nose configuration can therefore be selected by the operator for every payload of interest and its effects on the performances of the spacecraft, like the maximum attainable altitude, can be immediately evaluated. For example, the conical shape guarantees the minimum values of drag coefficient at high speed and therefore the highest final altitude of the SV but, at the same time, it does not represent the best solution for payload integration. For these reasons, trade-off analyses may be necessary, in order to choose the best nose shape. Apart from the missile sections, aerodynamic surfaces can be added by simply introducing their geometrical values and position. As for the spacecraft body, also for these surfaces (canard, wings and tails) specific aerodynamic formulas are implemented in the program's code.

It has to be remembered that each final configuration of the SV is subjected to several missile-aircraft integration constraints (for more details, see [14]). As an example, the length of the SV depends on the free volume between the aircraft's engine and landing gear, and the maximum value of the cross sectional diameter depends on the height of the aircraft and on the clearance required for the takeoff maneuver.

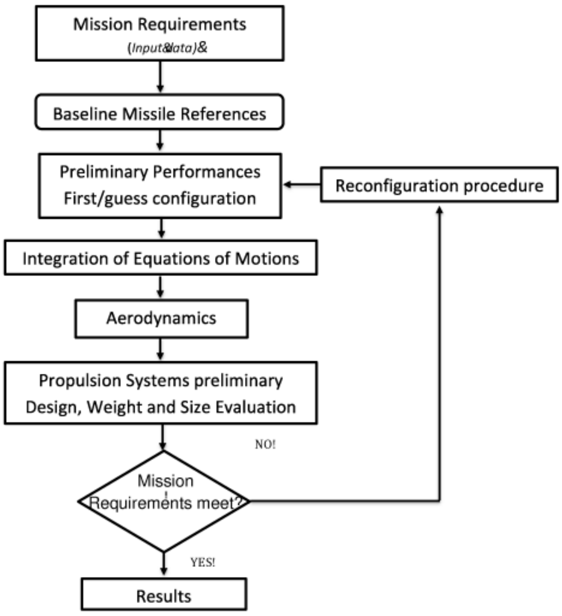

Fig. 3 The design process.

When the external configuration of the SV has been frozen, the integration of the equations of motion can be performed. Thanks to the integration of the equations of motion, the outputs of the program provide the users with the possibility of evaluating the flight path trajectories and the time history of flight path angles, altitude and Mach number, with an estimation, at the same time, of the trend and magnitude of the aerodynamic and thermal loads acting on the external structure of the spacecraft during its ascent to orbit. Additional output of the program is the preliminary sizing of the SV and particularly of its rocket system [15]. Apart from the dynamic equations of motion, also the cinematic equations of motion are integrated in the simulation program. In this way also the latitude and longitude time history are known.

Once the SV configuration meets all requirements, the solution can be frozen, otherwise some parameters have to be modified and the system sized again.

3.1 The Space Vehicle: configuration and aerodynamic

Fig. 4 [16] shows **the** **n**ose, **b**ody and **b**oattail, and the most important parameters that have been taken into account in the design process.

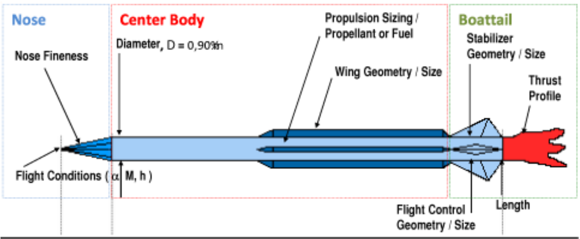

Fig. 4 – Example of Spacecraft missile-like solution

One of the most important parameter of the sizing activity is the drag force, D. Considering a cylindrical configuration of the central body section of the spacecraft, D can be expressed as follows:

$$D = C_D \cdot q \cdot \left(\frac{\pi}{4}\right) \cdot d^2 \qquad (1)$$

From Eq. (1) we can see that the drag force acting on the SV is a function of two main parameters: the cross-sectional diameter of the spacecraft, d, and the dynamic pressure, q.

The total value of the zero-lift drag coefficient, $(C_{D0})_{SV}$, is the sum of three different terms: the skin friction drag, $(C_{D0})_{Body,Friction}$, the base drag, $(C_{D0})_{Base}$, and the wave drag, $(C_{D0})_{Body,Wave}$, as expressed by Eq. (2).

$$(C_{D0})_{SV} = (C_{D0})_{Body,Friction} + (C_{D0})_{Base} + (C_{D0})_{Body,Wave} \qquad (2)$$

The zero-lift skin friction drag coefficient is associated to friction phenomena between the airflow and the metal skin of the spacecraft. Generally, its value depends on the structure of the boundary layer and on the air flow viscosity. The zero-lift base drag coefficient is related to the geometrical layout associated to the separation flow or stall flow phenomena on it. Eventually the zero-lift body-wave drag coefficient, the most important term in Eq. (2), is related to shocks waves phenomena. Its values becomes higher than the sum of the first two coefficients of Eq. (2) (right hand side) during supersonic and hypersonic flight, i.e. the main flight regime experienced by the spacecraft.

For the final evaluation of the total value of the zero-lift drag coefficient of the entire missile configuration all aerodynamic surfaces of the SV have also to be considered. Hence, Eq. (2) yields Eq. (3):

$$(C_{D0}) = (C_{D0})_{SV} + (C_{D0})_{Wing} + (C_{D0})_{Tail} + (C_{D0})_{Canard} \qquad (3)$$

Most flight regimes experienced by the spacecraft are characterized by high values of dynamic pressure, which allow to generate high values of aerodynamic efficiency (L/D), necessary to control and sustain the spacecraft without large aerodynamic surfaces. For these reasons the SV configuration typically does not need wings or canard surfaces, whose presence increases also the values of the aerodynamic drag and the radar osservability of the space system. Eventually, the absence of great aerodynamic surfaces has also some advantages for the final integration of the SV on the carrier aircraft. The combination of tail control surfaces and Thrust Vector Control System (TVC) allows to have a better control attitude of the SV during all flight phases.

3.2 The Space Vehicle: propulsion system

The general SV configuration that has been considered is a three-stage rocket system, in which the first two stages of propulsion are Solid Rocket Motors (SRM), while, for a better attitude control and orbit insertion, the third stage is a Liquid Rocket Motor (LRM). Liquid Rocket Propulsion Systems (LRPS) and Solid Rocket Propulsion Systems (SRPS) are therefore the propulsion technologies that have been selected for this work. Hybrid Rocket Propulsion Systems (HRPS) can however be considered as valid alternative.

Typically the fuel mass represents more than 80% of the entire gross mass of the spacecraft. The ideal Rocket Equation (Eq. (4)) permits to estimate the size of each rocket system characterized by a definite value of total velocity budget (ΔV):

$$\Delta V_{ideal} = c \cdot ln\left(\frac{m_{start}}{m_{end}}\right) \tag{4}$$

where c is the velocity of the exhaust gases expulsed through the exit nozzle section and is given by the product of the specific impulse (I_{sp}) and the acceleration of gravity at sea level. Eventually m_{start} and m_{end} represent respectively the total gross mass of the rocket launcher, before the manoeuvre, and its final mass, after the manoeuvre, i.e. when the fuel mass (m_{fuel}) has been burned. As the total velocity budget and the gross mass of the launcher are known values, we can calculate the final mass, by solving the Tsiolkowsky equation for m_{end}. Eventually the propellant mass, m_{prop}, which has been burned during the manoeuvre, can be computed simply by subtracting the final mass from the gross mass.

Generally the value of the velocity budget for each mission phase is unknown to the designer. As simplifying hypothesis, both the thrust of the rocket and its specific impulse may be considered constant values throughout the flight. In order to obtain a more accurate estimation of the total velocity budget, ΔV_{LEO}, Eq. (5) has been considered.

$$\Delta V_{LEO} = v_{Orbital} + \Delta V_{Drag} + \Delta V_{Grav.} \tag{5}$$

$$v_{Orbital} = \sqrt{\frac{G \cdot M_E}{r_{Orbital}}} \tag{6}$$

The first term on the right hand side of Eq. (5) is the orbital velocity and it is expressed by Eq. (6), where G is the universal constant of gravity, M_E is the mass of the Earth and $r_{Orbital}$ is the magnitude of the position vector that identifies (during the ascent flight) the altitude of the spacecraft with respect to the Earth centre of mass. The second and the third term on the right hand side of Eq. (5) represent the losses due to drag, ΔV_{Drag}, and gravity forces, $\Delta V_{Grav.}$ during the ascent mission phase. The loss due to drag force and to gravity force can be expressed respectively by Eq. (7) and Eq. (8).

$$\Delta V_{Drag} = \int_0^{t_{Orb}} \left(\frac{D}{m(t)}\right) dt \tag{7}$$

$$\Delta V_{Grav} = \int_0^{t_{Orb}} \left[\frac{(g_0 \cdot r_{Earth})}{r^2} sin\,\gamma\right] dt \tag{8}$$

Once the total velocity budget has been calculated, the main performance characteristics of each propulsive stage can be evaluated through several non-dimensional parameters. Eq. (9) expresses the propellant mass fraction, φ, defined as the ratio of the propellant and the initial mass. The propellant mass fraction can be associated to the mass fraction, Λ, of the spacecraft, defined as the ratio of the initial and the final mass (Eq. (10)).

$$0.5 < \varphi = \frac{m_{prop}}{m_{start}} < 0.9 \tag{9}$$

$$2 < \Lambda = \frac{m_{Start}}{m_{End}} = \frac{1}{(1-\varphi)} < 10 \tag{10}$$

Launchers are usually characterised by the payload mass fraction, λ, defined as the ratio of the payload and the initial mass (Eq. (11)).

$$0{,}01 < \lambda = \frac{m_{Payload}}{m_{start}} < 0{,}2 \qquad (11)$$

The length, l_{grain}, of an end-burning (cigarette-types) solid grain can be calculated by Eq. (12) [14], where d is the diameter and ρ_{prop} is the propellant density.

$$l_{grain} = \frac{4 \cdot m_{prop}}{\pi \cdot d^2 \cdot \rho_{prop}} \qquad (12)$$

An internal burning propellant grain has been considered in this work. Hence, its length can be estimated by Eq. (13) [14].

$$l_{grain,IB} = \frac{l_{grain}}{0{,}85} \qquad (13)$$

Each nozzle throat section can be calculated as follows [15] (Eq. (14)), where the burn-out time (tBO) of each stage of propulsion can be initially estimated through Eq. (15):

$$A_t = \frac{c \cdot m_{prop}}{p_c \cdot t_{BO}} \qquad (14)$$

$$t_{BO} = \frac{I_{SP}}{(T/W)}\left(1 - \frac{1}{\Lambda}\right) \qquad (15)$$

Then, from the nozzle throat area and the burn-out velocity, the cross-sectional throat diameter, D_t, can be calculated as follows (Eq. (16)) [15]. Eventually each single nozzle length can be finally calculated as follows (Eq. (17)) [15], where θ_{nozzle} is the so-called aperture angle selected for the cone nozzle.

$$D_t = \sqrt{\frac{4\, c\, m_{prop}}{\pi\, p_c \cdot t_{BO}}} \qquad (16)$$

$$L_{Nozzle} = \frac{D - D_t}{2\, tan(\theta_{nozzle})} \qquad (17)$$

3.3 Equations of motions

During each ascent trajectory, the spacecraft ranges from low-speed at low-altitude to close-to-orbital velocities at high altitude. In presence of the atmosphere, this results in subsonic, supersonic and hypersonic flight regimes. These flight phases are characterised by rarefied gas at very high altitude or dense gas at low altitude. Consequently mission and flight performances are seriously affected by the atmosphere and thus by the atmospheric model.

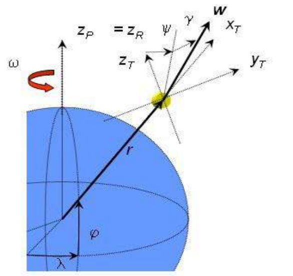

Fig. 5: LVLH Spacecraft Reference Frame

In the present work a rotating planet-centric frame with an exponential model of the atmosphere has been assumed as the reference frame for the motion of the space vehicle. The reference frame is fixed with the Earth and rotates at the same angular speed of the planet. The spacecraft is a point-mass and the mass value changes with time, $m(t)$. A second local reference frame centred in centre of mass of the spacecraft, known as local-vertical local-horizontal frame, LVLH, has also been assumed (see Fig. 5). In Fig. 5 the symbols λ and φ indicate, respectively, the longitude and the latitude of the spacecraft, while h is its altitude with respect to the surface of the Earth. The cinematic equations of motion, which allow evaluating the position of the space vehicle over the spherical reference frame (r,λ,φ) are expressed by Eq. (18).

$$\begin{cases} \dot{r} = \dot{h} = v \sin\gamma \\ \dot{\lambda} = \dfrac{v}{r} \dfrac{\cos\psi \sin\psi}{\cos\varphi} \\ \dot{\varphi} = \dfrac{v}{r} \cos\gamma \cos\psi \end{cases} \tag{18}$$

The dynamic equations of motion for the flight over a spherical rotating Earth are given by Eq. (19):

$$\begin{aligned} \dot{v} &= \frac{T\cos\varepsilon - D}{m} - g\sin\gamma \\ &\quad + \omega^2 r\cos\varphi\,(\cos\varphi\sin\gamma \\ &\quad - \cos\gamma\cos\psi\sin\varphi) \end{aligned}$$

$$\begin{aligned} v\dot{\gamma} &= \frac{T\sin\varepsilon + L}{m}\cos\sigma - \left(g - \frac{v^2}{r}\right)\cos\gamma + \\ &+ 2\omega v\cos\varphi\sin\psi + \omega^2 r\cos\varphi\,(\cos\gamma\cos\varphi + \\ &+ \cos\psi\sin\gamma\sin\varphi) \end{aligned} \tag{19}$$

$$\begin{aligned} v\,\dot{\psi} &= \frac{T\sin\varepsilon + L}{m\cos\gamma}\sin\sigma \\ &\quad + \frac{v^2}{r}\cos\gamma\sin\psi\tan\varphi + \\ &+ \frac{\omega^2 r}{\cos\gamma}\cos\varphi\sin\varphi\sin\psi + 2\omega v(\sin\varphi \\ &\quad - \cos\varphi\cos\psi\tan\gamma) \end{aligned}$$

The parameters L and D in Eq. 19 indicate, respectively, the lift and drag forces acting on the spacecraft. The thrust force, T, produced by the rocket engine, typically cannot be throttled. Its magnitude is considered as constant value during all flight phases. The spacecraft can be equipped with a TVC system, which allows varying the thrust moment arm with respect to the spacecraft's centre of mass. For the purpose of this work a general TVC system that provides the spacecraft with longitudinal attitude control has been assumed. The ε angle is the so called thrust angle of attack, defined as the angle between the thrust and the velocity vector, as shown in Fig. 6. For an axis-symmetric body (no TVC) simply results that ε is equal to α, the angle of attack, whereas for the cases with TVC, here investigated, ε is equal to the sum of α and δ, which is the angle the nozzle has been tilted. Taking into account the high values of dynamic pressure experienced by the spacecraft during the mission, it is desirable to reach values of the angle of attack close to zero, in order to generate lower aerodynamic loads on the spacecraft's structures. It is worth noting that low values of δ greatly affect the final mission performance of the spacecraft, especially in terms of the final orbit altitude.

The simulations have been run with a null value of the thrust angle of attack, ε, and with an angle of attack that remain close to zero ($\alpha \ll 1°$) throughout the flight. Then, the angle δ can be considered equal to zero.

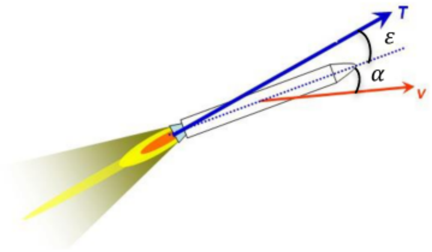

Fig. 6: Thrust Vector Control, reference angles

4 Simulations results

As mentioned above, the most significant design solution, here investigated, is a three-stage rocket solution, which consists of two initial stages, equipped with a SRM, and a third stage with a liquid propellant motor, LRM, in order to optimize orbit insertion. The most common third liquid stage is a small monopropellant Hydrazine stage, which provides a precise orbit insertion as well as attitude control.

The total length missile is fixed equal to 6 meters with a cross sectional diameter of 0.9 m, and a total gross mass of 6 tons. The fairing of the spacecraft, which contain the payload equal to 100 kg, has an elliptical profile and is one meter long. The first stage is equipped with four fins or tail surfaces, in order to guarantee the small static stability margin needed for a safe release maneuver from the carrier aircraft when the rocket motor is still switched off. It has to be underlined that the static stability reduces the performance of the TVC system. The size of the tails surfaces has been selected, in order to achieve the minimum value of the static stability margin necessary to stabilize the rocket during the time interval between separation and the ignition of the first stage of propulsion. Subsequently, once the first stage is switchedon, the TVC system automatically stabilizes the rocket. The selected fins have a triangular geometrical layout, with a root chord of 40 cm and a span value of 30 cm from the root. The carrier aircraft selected is the Eurofighter Typhoon characterized by: an absolute ceiling of 19800 m and by a service ceiling of 16700 m, a maximum speed equal to Mach 2 and a loaded capacity equal to 16 tons. Table 2 reports the initial release condition performed by the carrier aircraft, while Table 3 shows the main characteristics of the SV considered.

Table 2 Initial Condition.

Mission Parameter	Initial Condition
Altitude (km):	16
Mach:	0.8
Path Angle (deg):	45
Orbit altitude (km):	400
Payload Mass (kg):	100

Table 3 SV main characteristics.

	Stage 1	Stage 2	Stage 3
Length (m):	2.25	1.80	1.95
Diameter (m):	0.9	0.9	0.9
Mass (kg):	4800	600	600
Fuel Mass (kg):	4320	540	540
Prop mass fr. (φ):	0.90	0.90	0.90
Structural Ef. (ε):	0.09	0.09	0.09
Thrust (kN):	206	31	0.432
Spec. Imp. (sec):	290	290	300

Table 4: Mission Top Events.

Event:	Time (s)	Altitude (km)	Velocity (km/s)	Mass (kg)
Separation:	0	16	0.24	6000
Stage-1 BO:	77.14	52.34	4.33	1680
Coasting:	92	63.07	4.32	1248
Stage-2 BO:	200	122.5	7.62	708
Coasting :	800	349	7.33	654
Stage-3BO-1:	802	400	7.96	114

The SV ascent trajectory starts few seconds after the separation from its carrier aircraft. The separation maneuver is performed from an altitude of 16 km with a velocity of 236 m/s and a flight path angle of 45°. The first stage of propulsion is ignited for 77 sec and it reaches a final altitude of 52 km at 4.33 km/s with a flight path angle of 0.17°. After the first stage burns out and separates, a coasting flight of 15 sec is performed. At the end of this phase, the second stage of propulsion starts burning and the spacecraft reaches an altitude of 122 km with a flight path angle of 0,07° and a velocity of 8.35 km/s. After the second stage separation, another coasting phase of 600 seconds is performed.

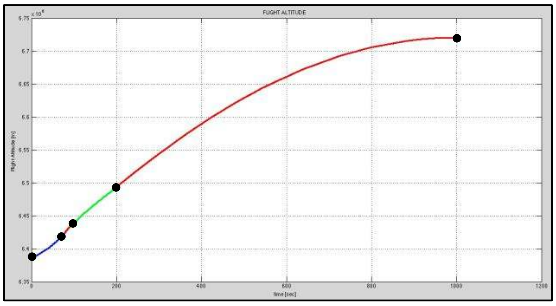

Fig. 7: Ascent flight Trajectory

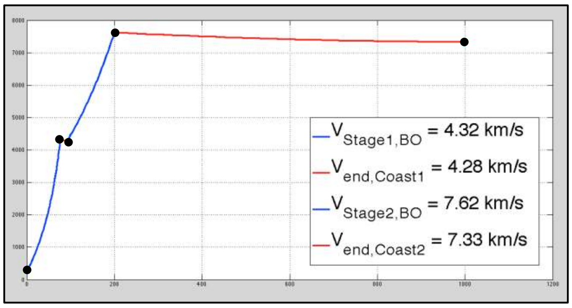

Fig. 8: Mission Velocity Profile

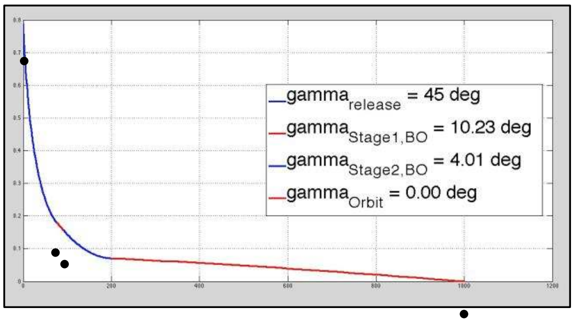

Fig. 9: Mission Path Angle Profile

The LRP third stage performs the last burn able to ensure the requested orbit insertion.

Finally, the space vehicle is inserted in a circular orbit at an altitude of 400 km with a final mass of 114 kg (14 kg are for the structural mass of the third stage). Table 4 reports the main events that describe the presented launch mission profile.

Figures 7-10 show the flight path, velocity, altitude and mass time history of the entire launch mission evaluated.

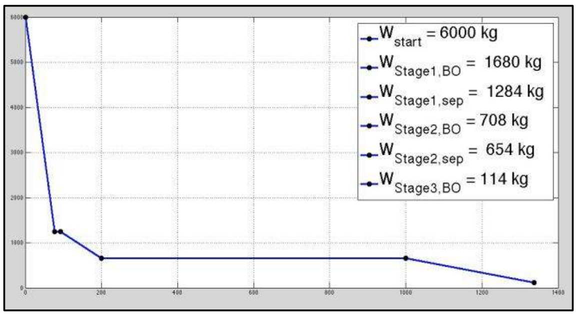

Fig. 10: Mission Mass Profile

5 Conclusion

This paper presents the design and the analysis of the performance of an air-launched system that can be dropped from an high performance carrier aircraft with different flight conditions. The results show that the SV solution is able to insert in LEO a payload mass of 100 kg and it thus appears to be a very appropriate choice for small space payloads. By setting different combinations of mission and performance parameters payload mass is likely to be improved. However, it must be remember that the fighter aircraft are subjected to strictly size and weight constraints, which limit the range of possible payloads. Nevertheless, today, the progressive reduction of the satellite mass and size (see standard Cubesat) through the adoption of improved technologies, makes the SV solutions more and more attractive. Moreover the Fighter aircraft represents, more than the Cargo aircraft, the suitable answer to the responsive requirement for space launch demand, both for their readiness on demand and their fast turnaround capability.

References

[1] CNES, “Air Launch Solution for Microsatellites”, Surrey University, 2008.

[2] FAA Commercial Space Transportation (AST) and Commercial Space Transportation Advisory Committee (COMSTAC), “2012 Commercial Space Transportation Forecast”, Federal Aviation Administration, 2012.

[3] Futron, “2010 Futron Forecast of Global Satellite Service Demand”, Futron, 2010.

[4] Christensen I., Vaccaro D., Kaiser D., “Market Characterization: Launch of very-small and Nano sized Payloads enabled by new Launch Vehicles”, International Astronautical Congress 2010, Prague, Czech Repubblic, 2010.

[5] DePasquale D., Charania A.C., “Nano/Microsatellite Launch Demand Assessment 2011”, Space Works Commercial, 2011.

[6] DePasquale D., Matsuda J., Kanayama H., “Analysis of the Earth-to-Orbit Launch Market for Nano and Microsatellites”, AIAA Space 2010 *Conference and Exposition”*, Anahelm, CA, United States, 2010.

[7] NASA and DARPA, “Report of the Horizontal Launch Study”, NASA/DARPA, 2011.

[8] Talbot C., Gotor P.G., Merino R.A, Froebel L., “ALDEBARAN, A Launch Vehicle System Demonstrator”, 7th Responsive Space Conference, AIAA, Los Angeles, CA, United States, 2009.

[9] Ridolfi F., Pontani M. and Teofilatto P., “Effect of different flight conditions at the release of small spacecraft from high performance aircraft”, Acta Astronautica, Vol. 66, 2010, pp. 665-673.

[10] Timothy T., P.W. Ferguson, D.A. Dreamer and Hensley J., “Responsive Air Launch using F-15 Global Strike Eagle,” 4th Responsive Space Conference, Los Angeles, CA, United States, 2006.

[11] Capt. Hague N., Lt. Siegenthaler E., Lt. J. Rothman, “Enabling Responsive Space: F-15 Microsatellite Launcher Vehicle”, Airspace Conference 2003, Vol. 6, 2003, pp. 2703-2708.

[12] Socher A. and Gany A., “Investigating of Combined Air-Breathing/Rocket Propulsion for Air Launch of Micro-Satellites from a Combat Aircraft”, 6th Responsive Space Conference, Los Angeles, CA, United States, 2008.

[13] Orbital Sciences Corporation, “Pegasus User’s Guide”, Orbital, 2010.

[14] CHIN S. S., Missile Configuration Design, McGraw-Hill Book Company, United States, 1961, Chaps. 11.

[15] Humble R. W., Henry G. N. and Larson J. W., Space Propulsion Analysis and Design, McGraw-Hill Book Company, United States, 1995, Chaps. 5,6.

[16] Fleeman E. L., Tactical Missile Design, AIAA Series, 2nd ed., 2006.

4:th CEAS Air & Space Conference
FTF Congress: Flygteknik 2013

Environmental impact assessment of the PROBA 2 mission

T. Geerken, K. Boonen and A. Vercalsteren
VITO, Belgium

J. Leijting
PRé Consultants, The Netherlands

L. Bierque and F. Preudhomme
QinetiQ Space nv, Belgium

Keywords: *Life Cycle Assessment, hybrid LCA, Input Output database*

Abstract

A Life Cycle assessment (LCA) of the PROBA 2 satellite mission was performed in order to elaborate a methodological framework and database for ESA space missions and to identify environmental hot spots of the PROBA 2 mission from a life cycle perspective.

The LCA model which we applied for the space mission uses a combination of physical and cost data in a so called hybrid LCA. Physical data were derived from an LCA (process) database, while cost data were used from an Environmentally Extended Input Output (EEIO or IO) database. LCA databases contain products and processes with the related environmental flows, such as emissions and use of energy. The units in an LCA database can be mass (product) or distance (transport). Input-output databases describe the sale and purchase relationships between economic sectors (agriculture, industry, services) within an economy and link them to the environmental flows resulting from these activities. Monetary units such as Euros or dollars are used to express the environmental flow per economic sector.

Modelling the environmental impact of man-hours in high-tech contexts with LCA databases is very time consuming and still might cause an underestimation of their impacts. Therefore, the environmental impact of man-hours is modelled with IO data.

The results of the hybrid LCA show that, when the launch is not taken into account, the environmental impact of the PROBA 2 mission is mostly generated in phase C & D (production, verification and testing). The contribution of phase E1 (launch preparation and commissioning) and B (design) to the total impact of the mission is also significant. The remaining phases, A (design) and E2 (use), have a minor influence on the environmental profile.

For the PROBA 2 mission excluding launch, the impact on climate change is ten times higher for the hybrid LCA than for the process-based LCA. The results are similar for all other impact categories for which all resources and emissions are included in the IO database (radioactive emissions, some toxic emissions, some specific metals and land use data are not included in the US IO database).

This study indicates that using only easily retrievable process-based data may lead to an underestimation of the environmental impact of a space mission.

1 Introduction

The European Space Agency (ESA) is aware of the importance and strategic interest of comprehensively quantifying the environmental impact of its activities and products. ESA issued a number of studies to determine the environmental impact of space missions. This paper is based on the study of the PROBA 2 space mission.

A recognized method to estimate environmental impacts is Life Cycle Assessment (LCA), where the whole life cycle of a product or service is taken into account. In the case of this space mission, the life cycle begins with the extraction of the raw materials needed and ends with the end-of-life of the satellite. An inventory of inputs (materials and energy) and outputs (emissions, waste and by-products) is made for each step of the life cycle. The assessment of the life cycle impacts of space missions can be very challenging due to sector-specific characteristics, such as the use of special materials and the custom made components which have a much lower product output/overhead ratio compared to mass produced products. Furthermore, data collection on space missions can be rather difficult due to confidentiality issues and limited time availability to model a very complex life cycle. LCA databases contain data on generic processes and materials but generally not on space specific processes and materials.

2 Methods

Before starting the full life cycle data inventory of the PROBA 2 mission, a specific pilot case on solar panels was performed to better understand the challenges of applying LCA to space applications.

The specificity of the space sector can be illustrated with the example of solar panels. The environmental impact of *domestic solar panels* can be estimated with process-based LCA or with IO. In this example, data is taken from the Ecoinvent 2.2 database, which is a process-based LCA database, and from the US Input Output database 2002. Figure 1 shows the comparison of both approaches, calculated with the ReCiPe Endpoint method, which allows the presentation of a single score result. One m² of the Ecoinvent record “Photovoltaic panel, multi-Si, at plant/RER/I U” was compared with the estimated market price for one m² of solar panel, modelled with the US IO database record “Semiconductor and related device manufacturing”. Both results have the same order of magnitude, which shows that IO data can be used for domestic solar panels.

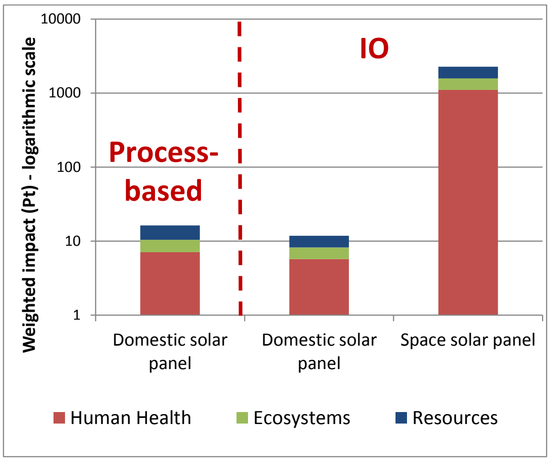

Fig. 1 Comparative environmental profile of 1 m² of domestic and space solar panel, process-based data and IO data, calculated with the ReCiPe Endpoint (H) / Europe H/A method

Space solar panels are very different from domestic solar panels. While domestic panels are made of commonly used materials (e.g. Si and PVC), space panels are made of materials that allow to reach a high efficiency (e.g. GaAs) and of plastics that do not decompose in space environments (e.g. Teflon, Mylar). Domestic panels have only one cluster, while space panels consist of individual cells with separate diodes. Domestic solar panels are mass produced; space solar panels have to be custom made and require a lot of individual testing. All these factors result in a much higher price (and associated environmental impacts) for space solar panels.

When space solar panels are modelled with the same IO record as used for the domestic solar panels (“Semiconductor and related device manufacturing”), their impact shows to be much higher than that of domestic solar panels, as costs are much higher too (Fig. 1, a logarithmic scale is used for visibility reasons). The impact of the space panels is about 170 times larger. The high costs of these panels is in reality probably mostly due to the large amount of (technical) man-hours attributable to these space solar panels, higher share of overhead costs and, to a lesser extent, to special materials. A process LCA approach would require a lot of specific data on many different contributing processes, associated to working in a laboratory environment.

In the context of the space sector the IO approach offers, with realistic (cost) data inventory efforts, a more complete inclusion of impacts compared to a process LCA approach with similar data inventory efforts.

We must make sure that the materials and processes that contribute most to the cost of a space mission are included in our environmental assessment.

2.1 Hybrid LCA

Modelling the entire supply chain of the space sector with LCA is not possible (with a reasonable effort), therefore cut-off rules are used. Cut-off criteria are commonly used in LCA to ensure that all relevant environmental impacts are represented in the study. For example, a cut-off rule may state that the process flows (inputs and outputs) that contribute to 90% of the impact in each environmental impact category must be taken into account. However, it is not possible to know when 90% is reached if information on the remaining flows is lacking. According to Lenzen [1], applying cut-offs may lead to truncation errors in the order of 50%. In the space sector this error might be even higher, as it is a sector with specific supply chains, small order quantities and a large amount of man-hours (including energy, travel and buildings, but also office equipment and supplies etc.). Lenzen [1] suggests avoiding errors caused by cut-offs by using a hybrid assessment method, combining (physical) process data with input-output data.

In this study, the combination of LCA with environmentally-extended input-output (EE-IO) databases is used. Input-output databases describe the sale and purchase relationships between economic sectors (agriculture, industry, services) within an economy. They are as such expressed in cost figures, such as Euros or Dollars. These databases can be extended with environmental tables (environmental accounts), which include environmental data linked to each of the economic sectors.

IO databases are developed top-down. That is why they offer a complete picture of all environmental impacts (all inputs, no truncation errors) throughout the complete supply chain (macro level), while LCA databases focus on the most important input flows (micro level). For example, in process-based LCA the environmental impacts related to services, such as financial services or research and development, are often neglected and not taken into account [1, 2]. Using IO data can solve this problem, since IO databases include the whole supply chain (and its environmental impact).

Using IO data also has some disadvantages, such as the high level of aggregation [3, 4, 5] and the dependence of the result on prices, since market prices vary over time, in different regions, per customer, etc. [1, 4, 5].

Several EE-IO databases are available. One interesting database in the context of this study is the EE-IO database developed for the US and containing data for the year 2002. This database includes data on environmental interventions like emissions to air, land use etc. and divides the US economy in about 500 economic sectors, which include the ‘guided missile and space vehicle manufacturing’ sector. Figure 2 shows the total product flow (in US dollar) to this sector from the linked economic sectors. A cut-off has been used in order to display the sectors with the highest contributions. The size of the arrows and the indicators in the boxes relate to the size of the monetary flow. This figure illustrates the importance of service sectors in the US space supply chain.

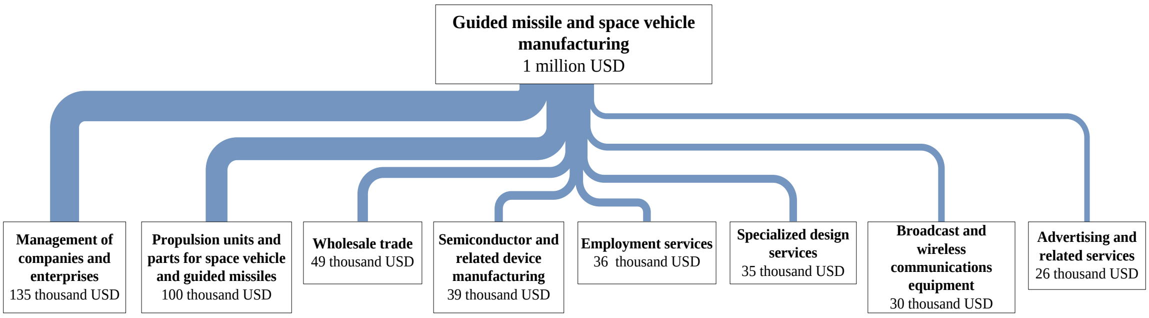

Fig. 2 Sectors with highest monetary contribution to the guided missile and space vehicle manufacturing sector (cut-off 2%)

The figure also shows that the sectors contributing more than 2 % together represent 45 % of the total value. Hundreds of other sectors each contribute less than 2 %, which would make a process-based LCA approach a time consuming effort. As an example the largest (13.5 %) contributing sector is "management of companies and enterprises". In process based LCA studies on mass produced goods and services this activity usually can be ignored due to its lower significance. The high sectoral level of detail and the existence of space specific sectors make this US IO database a valuable source of information for background data in this study.

2.2 Life cycle data inventory of the PROBA 2 mission

The *functional unit*, which has been defined for this specific LCA is "one space project in accordance with the mission's requirements". The space project considered in this study is the PROBA 2 mission.

The *life cycle phases* which have been distinguished are phase A (design), phase B (design), phase C & D (production, verification and testing), phase E1 (launch preparation and commissioning), E2 (use) and phase F (disposal).

Primary data (both physical and cost data) were delivered by QinetiQ Space nv, the producer of the PROBA 2 satellite. *Secondary data* for the satellite production, testing and transport were used from LCA databases (Ecoinvent 2.2); data for man-hours were retrieved from the US Input Output database 2002. The most suitable IO data records were selected for each type of worker and combined with their specific cost data. These types of worker are office workers, computer system designers and programmers, scientific researchers and developers. To evaluate the impact of using IO data in the analysis, a fully process-based version is also made. In this case, the impact of the man-hours of phases A, B, CD and E1 is based on QinetiQ Space nv averages and approximated by the energy use of offices and clean room (natural gas and electricity), infrastructure (building only) and travel. The modelling of man-hours of phase E2 is based on ESA average environmental data for 2009 on 3 ground stations: Redu, Kiruna and Cebreros [6]; including energy use (electricity and natural gas), infrastructure (rough estimates for buildings and antennas), business travel, water use and treatment, paper use and waste disposal.

The impact of the *launch* is calculated with data of the VEGA launcher which has been studied by BIO Intelligence Service.[1]. The PROBA 2 (estimated mass of 124 kg) is launched together with the SMOS satellite (estimated weight 658 kg). Weight allocation is done to distribute the impact of the launch over these 2 satellites; which means that 16% of the impact is assigned to the PROBA 2. The impact of the launch is not shown in the results for confidentiality reasons.

[1] Private communication of BIO Intelligence Service

Not much is known about the environmental impact of the *end of life* phase of the PROBA 2 satellite. Therefore a worst case waste scenario is modelled for phase F, separately from the rest of the phases with environmental impacts. It is assumed that all non-metals are incinerated completely when the satellite re-enters earth's atmosphere. Metals are assumed to fall into the ocean and disintegrate completely into emissions of the metal or its ion to the sea water. The model includes ocean deposition of aluminium, copper, iron, lithium, chromium, tin, silver, brass, lead, zinc, steel, nickel and molybdenum. Due to the large uncertainty, the results for phase F are not discussed in this paper.

3 Results and discussion

Various *life cycle impact assessment methods* can be used to assess the environmental effects of products and systems. The Recipe Midpoint (H, V1.07) method and the ILCD Midpoint (V1.00) method were selected for this study.

The environmental profile (Fig. 3) shows the contribution of the various *phases of the life cycle* excluding launch, per environmental impact category. Phase CD has a major contribution to the environmental impact (83 to 100% of the total impact). Phase E1 and B generate up to 17% and 9%, respectively, of the total impact. The remaining phases have a minor influence on the environmental profile (contributions of about 1% for phase A and 0,4% for phase E2). The reason that the impact is entirely related to phase CD in some impact categories, is that in those categories the Ecoinvent (LCA) database includes inputs/emissions that are not included in the US 2002 (IO) database (radioactive emissions, some toxic emissions, some specific metals and some land use data). As phase A, B and E2 are entirely modelled with IO data records, and E1 mostly, their impact is zero or negligible for those categories. Overall, the relative results for the ReCiPe impact assessment method are quite similar to the ILCD method and therefore not shown in Fig. 3.

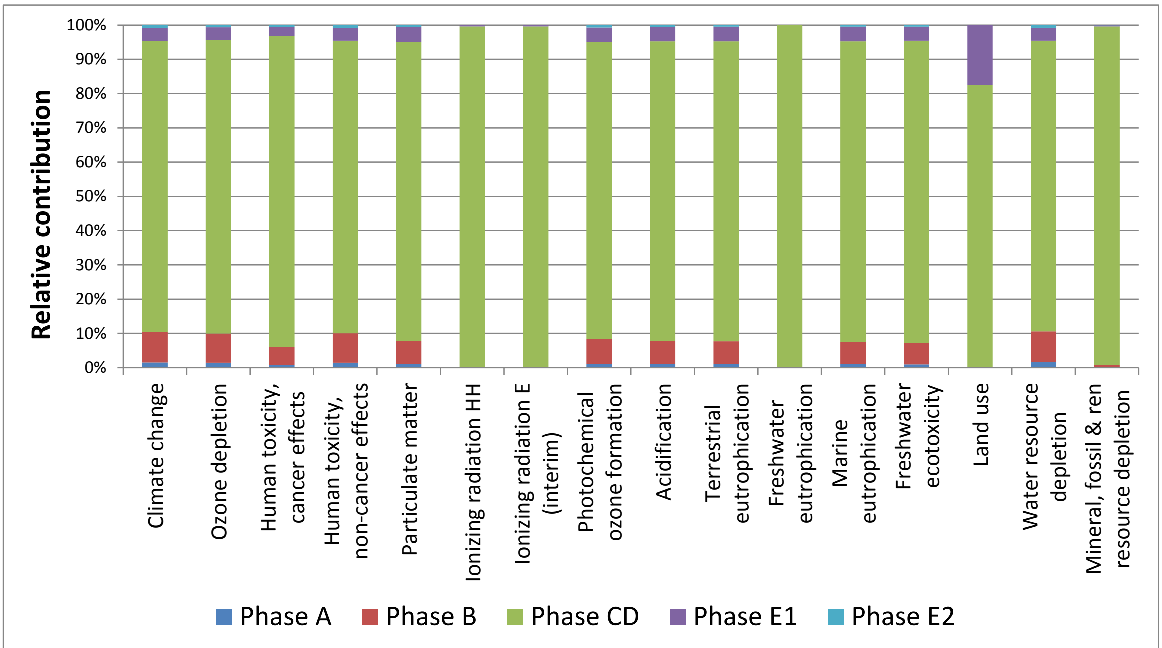

Fig. 3 Environmental profile of the PROBA 2 mission excluding launch, hybrid LCA, calculated with the ILCD method

The results show the environmental importance of the phases with a lot of man-hours. Most of the working time is needed for the production and testing of the satellite, therefore phase CD is the phase with the largest environmental impact (launch is not included in the analysis).

Even when modelled with *process-based LCA* only, the R&D man-hours have a major contribution to the environmental impact of the satellite mission. Their impact is mainly generated by the consumption of energy and the infrastructure used (both land use and the production of buildings).

A *comparison* of the results of the *hybrid and process-based LCA* is shown in Fig. 4. This figure focusses on climate change, as it is considered one of the most important categories, and the same greenhouse gas emissions are included in both LCA and IO databases. The hybrid LCA approach shows a higher impact for the PROBA 2 mission compared to the process-based LCA approach. The difference is around a factor ten. The results are similar for other impact categories for which all resources and emissions are included in the IO database. This indicates that using only easily retrievable process-based data where cut-off is applied may lead to a strong underestimation of the environmental impact of the mission. We believe that the results from the hybrid LCA offer the most accurate estimation of impacts for the PROBA 2 mission.

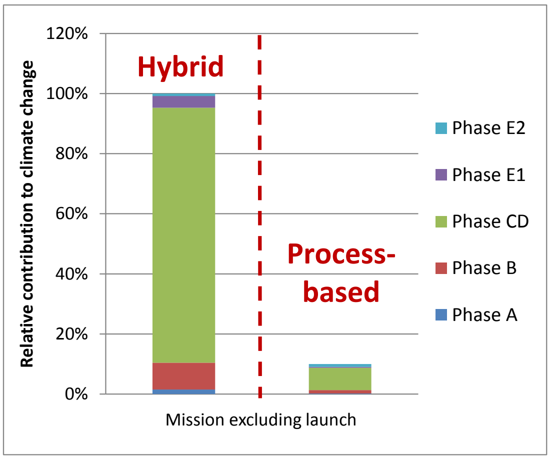

Fig. 4 Environmental profile of the PROBA 2 mission excluding launch, focussing on climate change only, comparison of hybrid and process-based LCA

4 Conclusions

The hybrid LCA approach is a very useful and cost-efficient method for estimating environmental impacts from the space sector, as the truncation errors in process-based LCA may be very high due to the complexity of the supply chains and the importance of services (environmental impact of man-hours). IO-databases are based on a top-down approach and include the whole supply chain.

The combination of process-based LCA data on better known materials and processes and IO (cost-based) data on the not-included materials and processes provides the best of two worlds: details and completeness.

Further work on European IO databases can improve the accuracy of hybrid LCAs for application within the European space sector.

References

[1] Lenzen M., "Errors in Conventional and input-output-based life-cycle inventories", Journal of Industrial Ecology, Vol. 4(4), 2001, pp. 127-148.

[2] Müller B. and Schebek L., "Input-Output-based Life Cycle Inventory", Journal of Industrial Ecology, 2013, doi: 10.1111/jiec.12018

[3] Suh S. and Huppes G., “Methods for Life Cycle Inventory of a Product”, Journal of Cleaner Production, Vol. 13 (7), 2005, pp. 687-697.

[4] Rebitzer G., “Enhancing the application efficiency of life cycle assessment for industrial use”, Ph.D. dissertation, Institut des sciences et technologies de l'environnement, Ecole polytechnique fédérale de Lausanne, Switzerland, 2005.

[5] Williams E. D., Weber C. and Hawkins T. R., “Hybrid Framework for Managing Uncertainty in Life Cycle Inventories”, Journal of Industrial Ecology, Vol. 13, 2009, Issue 6, pp. 928-944.

[6] ESA, "Sustainable development - 2009-10 report", 2011, ESA SP-1319.

Guidance Systems for Sounding Rockets

Anders Helmersson
RUAG Space AB, Sweden

Keywords: *Boost Guidance Systems, TVC, Canard, Cold gas.*

Abstract

RUAG Space has a long history of guidance systems for sounding rockets. In total more, than 240 sounding rockets have been guided with a system by RUAG Space AB.

1 S19

S19 Boost Guidance System is a family of guidance systems for sounding rockets. NASA launches typically five to ten sounding rockets every year guided with S19 from White Sands Missile Range in New Mexico, USA. The purpose of using a guidance system is that the impact dispersion can be reduced and the number of launch opportunities are increased since the wind constraints are highly relaxed. The rockets are mainly used for solar, stellar and related deep-space research,

Typically, the S19 is used during the first 18 seconds of the flight or up to an altitude of 5-8 km. The rocket is controlled by measuring the attitude using the onboard gyro. The canards on the S19 module produce the control torques to guide the rocket. The sounding rockets reach altitudes of 200-450 km.

Several versions of the S19 have been used. The original system was analog and was later replaced by digital versions using rate-integrating gyros.

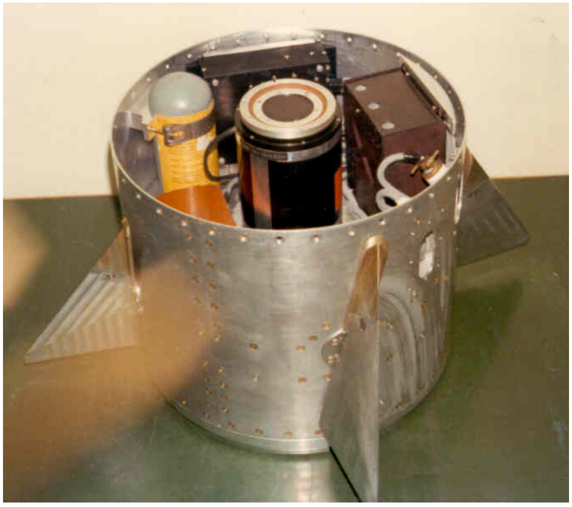

Figure 1: The very first S19 system.

2 Spinrac

Spinrac was our first digital guidance system. It is used for guiding the upper stage of a sounding rocket while it flies outside the atmosphere. Spinrac uses two small cold gas thrusters that are used to redirect the spinning rocket before igniting the motor and at the same time removing any coning motion that may have been produced during the flight. The reference attitude is computed based on the measured position and velocity in order to reduce the impact point dispersion.

Figure 2: The Spinrac Module.

The Spinrac system flew twice in 1990. During the second flight, the so called Maxus Test flight in November that year, it reached an altitude of 532 km, which was a record at that time for Esrange, Kiruna.

3 Maxus GCS

The *Maxus Guidance, Navigation and Control System* is a family of guidance systems for the Castor IVB motor. The Castor IV motor was originally used as strap-on boosters for the Delta launcher. The Castor IVB is equipped with thrust vector control (TVC), which means that the nozzle of the motor can be swiveled using hydraulic actuators. The same control concept can be used throughout the flight, both inside and outside the atmosphere. The Maxus sounding rocket is launched from Esrange and reaches altitudes of above 700 km.

Figure 3: The Maxus GCS module.

The guidance concept is to control the vehicle in order to reduce the impact dispersion. During the flight the position and velocity is measured and the rocket is directed in order to achieve the designated impact point, which is located about 80 km north of Esrange.

Figure 4: Maxus ready for launch.

4 Guidance

Essentially the same guidance and control principles are used in all our guidance systems for sounding rockets. The attitude is measured using gyros. Originally, in our analog systems, the gyro was a gimbaled gyroscope that measured the attitude relative to its position on the launcher just before liftoff. The attitude was then kept constant throughout the guided portion of the fight. Two sets of parameters were used and the gain switch occurred when the first and second stages separated.

Table 1: Overview of sounding rocket guidance systems by RUAG Space AB.

Year	#	Name	Actuators	Remarks
1976-2006	185	S19	Canards	Analog version
1990-	2	Spinrac	Cold gas thrusters	High altitude rockets
1991-2001	5	Maxus 1-4	TVC	TVC 1st generation
1998-	4	DS19	Canards	S19 digital version
2002-2010	16	S19D	Canards	
2002-2009	4	Maxus 5-8	TVC	TVC 2nd generation
2006-	24	S19L	Canards	Strapdown gyro
2014?		S19E	Canards	Electrical servos
2014?		Maxus 9	TVC	TVC 3rd generation

Today, an inertial measurement unit is used as attitude reference. In addition, the measured velocity and position are used. The control action is today implemented in software, and allows for a continuous change of the control parameters. Also tailored filters for avoiding excitation of flexible modes in the rocket are implemented.

Before each launch a preflight analysis is performed in order to determine the most appropriate control parameters. There exist a number of standard parameter sets that can be used and, if so required, a new set of parameters can be implemented.

The guidance system provides a continuous monitoring of the flight. For instance, the *instantaneous impact point* is computed onboard and transmitted via a telemetry link to the launch site. These data can be compared to the radar predictions for monitoring the status of the rocket and its onboard systems.

5 Conclusion

RUAG Space AB provides guidance systems for sounding rockets since 1976. Three different guidance principles are used: canards, cold gas and TVC. In total, more than 240 sounding rockets have been guided with our guidance systems.

SKYLON D1 Performance

Roger Longstaff
Reaction Engines Ltd. United Kingdom

Keywords: *SKYLON, upper stage, mission strategies)*

Abstract

For over 20 years Reaction Engines Ltd. (REL) studied the design of a Single Stage to Orbit (SSTO) reusable launch vehicle with a fixed take-off mass of 275 tonnes – SKYLON C1. The take-off mass was fixed for historical reasons (from the HOTOL programme) and the payload mass was allowed to vary as the project progressed, culminating with the result of a 10.25 tonne payload into a 300 km, low inclination, circular orbit.

Since 2010 REL have been working on their final design – SKYLON D1. The design requirement for this vehicle is very different – a SSTO reusable launch vehicle with a payload of 15 tonnes to the standard LEO orbit - having been derived from REL market analysis between 2005 and 2010. In 2012 REL started work to evaluate this system in the context of a European market, and the interim results of REL analysis are reported showing that payloads into GTO of 6.4 tonnes can be achieved with a fully reusable system and when combined with onboard electric propulsion on station masses of 5.6 tonnes.

1 Introduction

For 30 years engineers in the UK have investigated the design, manufacture and operation of a reusable spaceplane, that would operate from a runway and deliver and retrieve payloads to and from Earth orbit. The premise for this work has been that a Reusable Launch Vehicle (RLV) will always be more cost effective than an expendable launch vehicle in the medium to long term, and that a Single Stage To Orbit (SSTO) RLV will always be more cost effective than a two stage to orbit RLV system providing it has a reasonable payload fraction.

2 Background

Work on the SSTO / RLV concept started in the 1980s with the British Aerospace / Rolls Royce HOTOL project (see Figure 1)[1]. This was a concept for a SSTO spaceplane powered by a combined cycle, pre-cooled, airbreathing rocket engine that transitioned to pure cryogenic rocket propulsion at Mach 5 in order to complete its ascent into orbit. At the time a payload of 7 tonnes into low inclination, Low Earth Orbit (LEO) was targeted, and in order to standardise the design process a Gross Lift Off Mass (GLOM) of 275 tonnes was fixed, and the payload allowed to vary from one design iteration to the next. In the 5 year lifetime of the project the best calculated payload performance of HOTOL was estimated to be about 5.5 tonnes.

Following the termination of the HOTOL project in 1989 a group of engineers, led by Alan Bond (the inventor of the RB545 engine used in HOTOL), formed Reaction Engines Ltd (REL), a company dedicated to act as a repository for the knowledge gained during the HOTOL project, and to improve the design. The new system, designated SKYLON [2 & 3], retained a GLOM of 275 tonnes but now targeted a payload of 12 tonnes – believed to be possible with performance gains made by moving the wings and engines to the centre of the vehicle (thereby reducing the control requirements), improving aerodynamic efficiency and by a more efficient propulsion cycle that introduced a closed helium loop in the new SABRE engine [4]. In addition SKYLON dispensed with the takeoff trolley adopted by HOTOL and featured a takeoff capable undercarriage for improved operational flexibility (made possible by the above performance gains). The eventual result was the SKYLON C1 vehicle (Figure 2), with a final calculated payload of 10.25 tonnes.

Fig. 1 BAe HOTOL

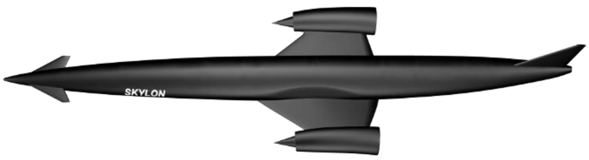

Fig.2 SKYLON C1 Configuration

This system was reviewed in 2010 by almost 100 invited experts from ESA, NASA, JAXA and Roscosmos and worldwide industry and academic institutions. ESA was conducting the review for the UK Space Agency and they concluded that no impediment had been identified that would prevent the development of either the SKYLON vehicle, or the SABRE engine [5].

3 SKYLON D1

Following the SKYLON Requirements Review Reaction Engines began work on what they believe to be the final design of the SKYLON airframe – configuration D1, and the engine – SABRE 4 [6]. In 2008 market analysis by REL determined that a growth in payload performance was required in order to address the majority of the predicted market, and determined a performance requirement of 15 tonnes to low inclination LEO. This new requirement, together with almost 20 years of knowledge gained during the study of SKYLON variants A to C1 and engine variants SABRE 1 to SABRE 3, gave an initial estimate of a GLOM of 325 tonnes for the final (REL) system, as shown in Table 1.

SKYLON D1 will be a vehicle that has a payload performance of 15 tonnes by design. If it is discovered that mass and performance margins are insufficient to guarantee this payload the GLOW will be increased until the target has been achieved. The design methodology is shown in Figure 3. However, REL are confident that the final design of SKYLON D1 will be at least 50 tonnes lighter that a Boeing 747 at takeoff, and at least 200 tonnes lighter than an Airbus A380 at take off

Vehicle	Propulsion	Design GLOW	Payload Requirement	Final Calculated Payload
HOTOL A-K 1984 - 1989	RB545	**275 t**	7,000 kg	5,500 kg
SKYLON A – C1 1990 - 2009	SABRE 3	**275 t**	12,000 kg	10,250 kg
SKYLON C2 /D1 2010 - Present	SABRE 3 / 4	340 t / 325 t	15,000 kg	**15,000 kg**

Table 1: Comparison of HOTOL, SKYLON C1 and SKYLON D1
(Bold indicates the parameter is a design driver)

The SABRE 4 engines on which the D1 configuration is based requires some new technologies that are in the final stages of validation. In the event the required technical maturity of these technologies cannot be shown then SKYLON would revert to a SABRE 3 engine and a C2 configuration which fundamentally would be a scaled C1 with a GLOM of 340 tonnes.

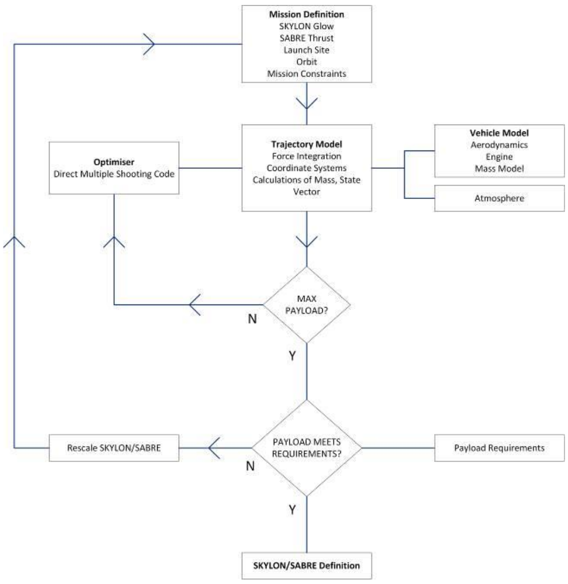

Fig. 3 Design Methodology for SKYLON

Figure 4 shows the orbital payload performance of SKYLON D1 to other orbits, with the vehicle scaled to deliver 15 tonnes to a low inclination, 300 km altitude orbit, following a due East launch from ESA's CSG launch site in French Guiana. The payload diminishes with increasing inclination (as a higher MECO velocity is required as a consequence of a lower contribution from Earth rotation), and altitude (as a consequence of more orbital manoeuvring system (OMS) propellant required to circularise, and de-orbit the vehicle).

4 European Launcher Performance Requirements

European performance requirements are assumed to be those given by ESA for the Ariane 6 system in Reference 7.

- GEO, either directly or through intermediate orbits, in particular GTO and LEO
- Polar/SSO
- MEO or MTO
- other

The targeted payload performance is 4 t for polar/SSO missions at 800 km altitude and 3 – 6.5 t, with two mission segments (3 – 3.5 t and 6 – 6.5 t) in GTO equivalent.

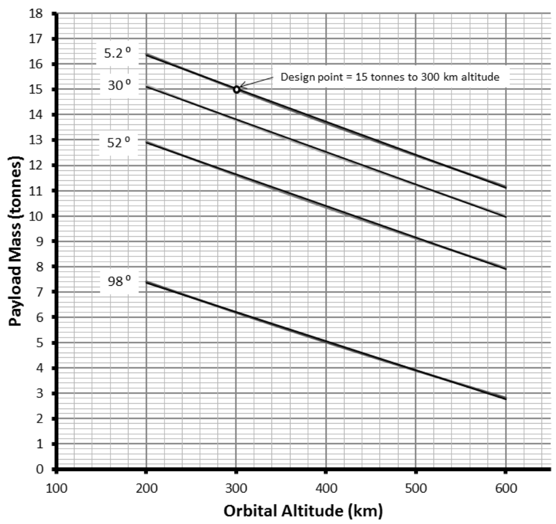

Fig. 4 Payload Performance of SKYLON D1 from CSG Kourou.

5 The SKYLON Polar / SSO Mission

Figure 4 gives the performance of SKYLON D1 to a 98 degree inclination orbit for a launch from CSG in French Guiana. Although a payload of over 7 tonnes can be delivered to a 200 km altitude orbit, performance to higher orbits diminishes rapidly with altitude. In order to place a 4,000 kg satellite into an 800 km altitude orbit either a small upper stage would need to be added, or the satellite would be required to carry extra propellant to perform an orbit raising manoeuvre. As the satellite must provide a propulsion system for its orbit and attitude control during its active mission, and extra propellant to de-orbit at the end of its operational life, the second option of adding extra propellant to the satellite itself is seen by REL as the best option

REL calculations show that a satellite of mass 4,700 kg deployed at 300 km would have a start of life mass of 4,250 kg in its operational 800 km orbit, after allowing for roughly 400 kg of extra propellant and 50 kg of additional tankage and structure mass.

6 The SKYLON / SUS Standard GTO Mission

Clearly, by far the most important performance requirement for SKYLON is the GTO / GEO case, with satellite payloads of up to 6.5 tonnes GTO equivalent required. The most important technical task for REL is therefore to determine if its 15 tonne LEO payload performance for SKYLON D1 matches the European requirement of 6.5 tonnes into GTO. For a LEO vehicle like SKYLON, an upper stage is clearly required to achieve this, and in common with long established REL philosophy it is the intention that the upper stage will be reusable, and collected by SKYLON after its mission for return to Earth and subsequent reuse.

REL has produced a design for an upper stage – the SKYLON Upper Stage [8]), with the characteristics

- 1,500 kg end of mission mass
- Up to 7,500 kg of hydrogen / oxygen propellants
- Engine SI 4,562 m/s

A representation of SKYLON deploying a SUS / satellite stack in LEO is shown in Figure 5.

Fig. 5 SKYLON Deploying Upper Stage

REL originally selected a 300 km altitude for defining SKYLON/SUS GTO performance as it has a 7:1 resonance with GTO (as reported in Reference 8). That is, the period of a GTO is 7 times longer than that of a 300 km circular orbit. The mission sequence for a reusable GTO is shown in Figure 6.

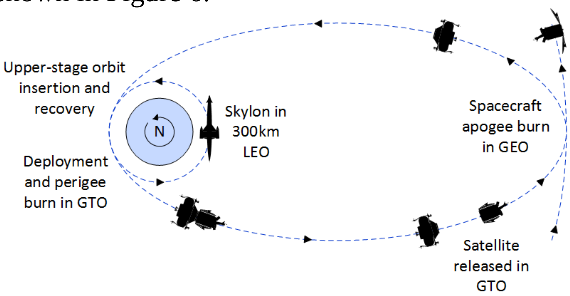

Fig. 6 Nominal GTO Mission Sequence

The SUS / satellite stack is deployed in LEO and after checkout and separation from SKYLON performs a perigee burn to place the stack into GTO. The SUS and satellite then separate and the launch function is then complete, with the satellite circularising its orbit in GEO, with an apogee burn as is traditionally the case. The SUS, however, continues alone in GTO for a whole orbit, when it will perform a perigee burn in order to circularise its orbit at 300 km, in phase with the waiting SKYLON (which well have completed exactly 7 orbits). The SUS will rendezvous and dock (RVD) with SKYLON, and return to Earth in the payload bay for reuse in a later mission. SKYLON carries Air Support Equipment (ASE), of estimated mass 1,050 kg, in its payload bay in order to facilitate RVD operations with the SUS. It is calculated that SKYLON / SUS can launch satellites with a mass of up to 5,628 kg into GTO in this mission.

Clearly, The SUS could be used in an expendable mode (without propellant to return to RVD with SKYLON) and deliver heavier satellites to GTO. In this mode it is calculated that satellites of maximum mass 7,500 kg could be launched by this approach. However, with the REL philosophy of total re-usability of launch infrastructure, another method has been investigated in order to meet the European requirements of 6,600 kg into GTO.

7 The SKYLON / SUS Low Altitude Deployment Mission

Figure 7 shows the mission sequence for a low altitude deployment SKYLON / SUS mission. An altitude of 185 km has been selected as NASA often use 100 nautical miles to gauge the performance of future launch vehicles (and indeed the Apollo missions used this LEO prior to departure into a trans-lunar trajectory). The SKYLON achieves an extra 1.5 tonnes of payload performance to this LEO (as a consequence of a lower MECO velocity, and less OMS propellant required to circularise and de-orbit the vehicle). The problem in this case, however, is adjusting the period of the SUS return transfer orbit to enable a perigee burn that will allow the phasing required for a RVD with SKYLON.

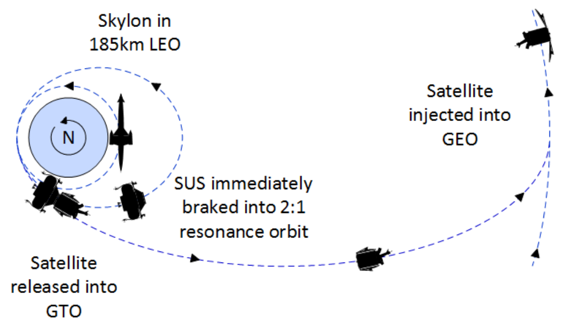

Fig. 7 Low Altitude Deployment Mission Sequence

The SUS performs a 3 burn mission:

i. A perigee burn to place the SUS / satellite stack into GTO (the satellite then separates)
ii. A rapid SUS near-perigee burn into a 2:1 resonance orbit with SKYLON (apogee 7,890 km).
iii. A final perigee burn to circularise its orbit at 185 km circular, in – phase with SKYLON.

The SUS then performs RVD operations with SKYLON for return to Earth. With this mission sequence it is calculated that SKYLON / SUS can launch satellites with a mass of up to 6,428 kg into GTO, virtually meeting the European requirement.

8 The SKYLON / SUS Electric Propulsion Satellite Mission

REL recently began to consider the launch of "all electric" satellites into GEO. The mission sequence derived by REL is show in Figure 8. Again, fully reusable launch infrastructure is used in the analysis

In this case the SUS performs a 4 burn mission, raising the satellite to a circular, Medium Earth Orbit (MEO) of altitude 5,900 km in a two burn Hohmann transfer, deploying the satellite, and then performing a scheduled two burn Hohmann transfer timed to phase with the waiting SKYLON in LEO. As before, the SUS can then be recovered to Earth for subsequent reuse.

The selection of the MEO of 5,900 km by REL for this operation was specifically to deploy the satellite above the lower (proton) Van Allen radiation belt. Flight data from ESA's SMART-1 mission to the Moon [9]) – which employed electric propulsion for orbit raising - showed that no further degradation of the solar arrays occurred when the perigee of the orbit rose above 5,900 km (having initially been deployed into GTO). Fortuitously, there is another advantage in operating from this circular MEO – the power available from the solar arrays matches well with Hall Effect thruster performance to give a satellite transit time from MEO to GEO of approximately 120 – 150 days, which REL believe is commercially acceptable for a GEO communications satellite with a 15 year lifetime. REL calculations show that an EP satellite with a beginning of mission mass of up to 5,644 kg into GEO can be delivered with this mission sequence.

9 An Example - Alphabus

To explore whether the promise of the theoretical case examined above can be realised, the impact of high power Hall Effect thrusters that are now being developed and tested was examined. A specific example of an Alphabus, equipped with two 20kW Snecma Hall Effect thrusters (required for redundancy), flying from a 5,900 km circular MEO (deployed by SKYLON & SUS) to GEO was examined.

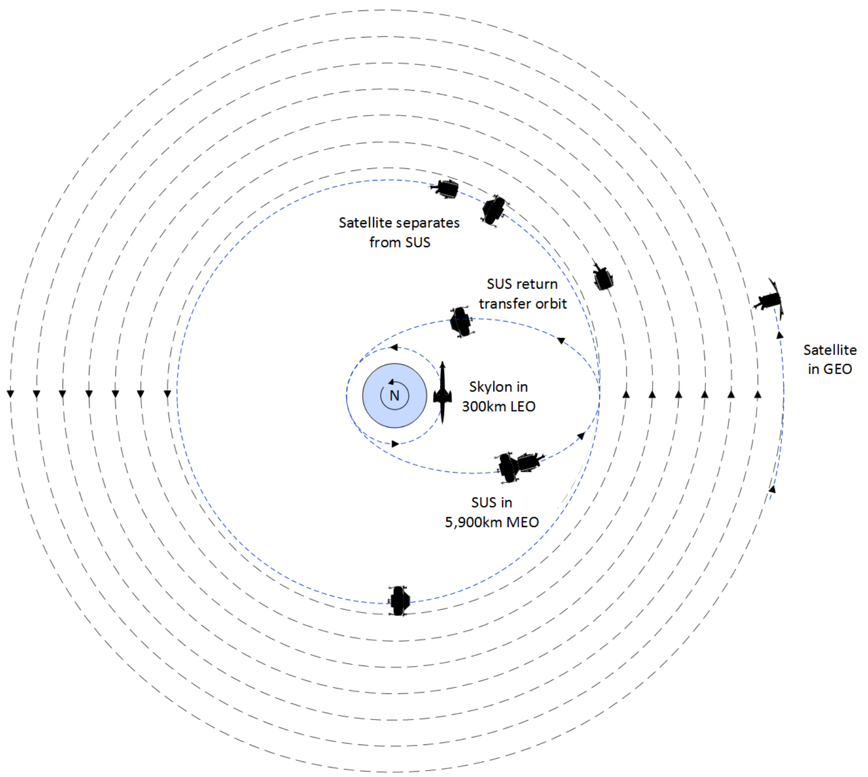

Fig.8 On Board Electric Propulsion Mission Sequence

The characteristics for the Alphabus from Reference 10 are:

- Max GTO mass = 8,800 kg
- Max propellant load = 4,200 kg
- Assumed max BOL GEO mass = 4,600 kg
- Max power = 22 kW

The characteristics for the Snecma 20 kW thruster used on Alphabus from Reference 11 are:

- Max thrust of single unit = 1.05 N
- Assumed total thrust @ 22 kW = 1.155 N
- SI = 2,700 sec (Vex = 26,478 m/s)

For this analysis we will retain the assumed maximum BOL GEO mass of 4,600 kg, with the assumption that the apogee engine and associated hypergolic propellant tanks have been removed and replaced with an EP system comprised of propellant tankage, two 20 kW thrusters and additional payload.

REL calculations show that a deployed satellite mass of 5,097 kg in a 5,900 km MEO is required to obtain a final mass in GEO of 4,600 kg, which is easily achievable by SKYLON / SUS which can deliver up to 5,644 kg into this orbit, as previously calculated. In this case the transit time from MEO to GEO is 127 days. Therefore, it is concluded that SKYLON, with the reusable SUS, can comfortably deliver the largest European Alphabus satellite planned, when equipped with current technology Hall Effect thrusters, with little or no degradation to its solar arrays or electronic systems.

SKYLON / SUS Mission	Maximum Mass of Satellite into GTO	Maximum Mass of Satellite into GEO (with 320s SI apogee engine)
300 km LEO deployment Reusable SUS, 7:1 resonance return transfer orbit (GTO)	**5,626 kg**	(3,525 kg)
185 km LEO deployment Reusable SUS, 2:1 resonance return transfer orbit	**6,428 kg**	(4,028 kg)
185 km deployment Expendable SUS, destructive re-entry	**7,500 kg**	(4,699 kg)
300 km LEO deployment Reusable SUS 5,900 km circular MEO EP satellite, 20 kW HE thruster, 154 day transit to GEO	N/A (9,008 kg GTO equivalent)	**5,644 kg**

Fig.8 Summary of Geostationary Satellite Launch Strategies

10 Conclusions

A summary of the performance of all of the upper stage missions described in this paper is shown in Table 2. Any future revisions to SKYLON D1, and the final design of the SUS, combined with detailed numerical trajectory analysis, will be required in order to finally evaluate the proposed launch system. However, this preliminary analysis indicates that SKYLON D1, with its SUS upper stage, appears capable of performing all of the geostationary satellite missions required by Europe, using a fully reusable launch system infrastructure

References

[1] B.R.A. Burns, "HOTOL space transport for the twenty first century", *Proceedings of the Institute of Mechanical Engineers, Part G – Journal of Aerospace Engineering*, Vol 204, pp.101-110, 1990.

[2]. R.Varvill, and A. Bond, "The SKYLON Spaceplane", *Journal of the British Interplanetary Society*, Vol 57, pp.22-32, 2004.

[3]. A. Bond, R. Varvill, J. Scott-Scott and T. Martin, "SKYLON - A Realistic Single Stage Spaceplane", *Spaceflight*, Vol 45, pp.158-161, 2003.

[4]. R. Varvill and A. Bond, "A Comparison of Propulsion Concepts for SSTO Reuseable Launchers" *Journal of the British Interplanetary Society, Vol 56, pp. 108-117, 2003*

[5] "SKYLON Assessment Report", European Space Agency, TEC-MPC/2011/946/MF, Issue 1 Rev 2, 6th May 2011.

[6] Mark Hempsell, Robert Bond, Roger Longstaff, Richard Varvill "*The SKYLON D1 Configuration* " IAC-10.D2.4.7 presented at the 61st International Astronautical Congress. Prague, September 2010

[7]. Mark Hempsell and Alan Bond, "Technical and Operational Design of the SKYLON Upper Stage", *Journal of the British Interplanetary Society*, Vol. 63, pp.136-144, 2010.

[8] Ariane 6 performance requirements: http://www.esa.int/Our_Activities/Launchers/Launch_vehicles/Ariane_6 (accessed August 2013)

[9] Electric Propulsion on SMART–1, http://www.esa.int/esapub/bulletin/bulletin129/bul129e_estublier.pdf (accessed August 2013)

[10] Alphabus Fact Sheet, http://telecom.esa.int/telecom/media/document/Alphabus%20factsheet%2010-5-2011%20JH%20%281%29.pdf (accessed August 2013)

[11] Performance Evaluation of a 20 kW Hall Effect Thruster, http://erps.spacegrant.org/uploads/images/images/iepc_articledownload_1988-2007/2011index/IEPC-2011-020.pdf (accessed August 2013)

Time-Triggered Ethernet Communication in Launcher Avionics

T. Hult, A. Petersén, S. Eriksson
RUAG Space, Sweden

Keywords: *Time-Triggered Ethernet, launcher avionics*

Abstract

Experiences and results from using Time-Triggered Ethernet technology in two studies on launcher avionics are presented. In the first study, a protocol implementation in software was used, with an evaluation system using COTS hardware. In the second study, a Time-Triggered Ethernet IP block was integrated within a system-on-chip in an FPGA.

1 Introduction

Current European launchers Ariane5 and Vega have similar avionics architectures resulting from work performed in the late 1980-ies. The main principle is a flight control system based around a MIL-STD-1553 data bus and an independent telemetry system having local communication links. The operation life time for this avionics architecture will be more than 25 years, from first launch in 1995 with last launch after 2020.

The next generation launcher, Ariane6, is planned to be operational before 2025. For this launcher a new avionics concept with higher performance and lower cost is envisaged. One of the main methods to reach the cost objective is to integrate several functions in the same hardware, for instance by using the same computer and network both for flight control and telemetry. Fig. 1 below shows a possible avionics configuration for a launcher with such a common network.

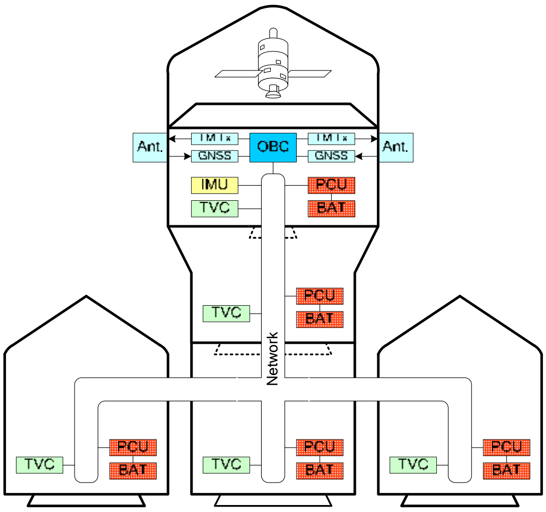

Fig. 1 Tentative launcher avionics configuration

The baseline configuration selected for Ariane6 will be a three-stage vehicle. The lower stage consists of three motors with 135 tonnes of solid propellant. The second stage has one motor, which is identical to the bones in the first stage. The upper stage is based on the Vinci cryogenic engine. Finally there will be a 5.4 m diameter fairing that provides the same volume for satellite payloads as the Ariane5 launcher. Ariane 6 is targeted for a payload capacity of 3 – 6.5 tonnes while Ariane5 can handle payloads of more than 10 tonnes.

The motor control will be electric and thus there will be batteries and power control units in all stages, feeding power to the main thrust vector control units and the rest of the avionics.

2 Time-Triggered and Segregated Communication

The functional integration for next generation launcher is to a large extent solved by using data communication links with high performance and a capability of handling both critical and non-critical communication on the same link. The trade-offs made in earlier studies have resulted in an initial selection of Time-Triggered Ethernet [1] (TTEthernet) as the main communication link.

With a TTEthernet network, multiple virtual links (Critical Traffic IDs) are used for communication; each assigned a specific traffic class:

* Time-Triggered (TT) traffic, for communication with a deterministic latency and fixed period
* Rate Constrained (RC) traffic, for communication with a guaranteed minimum bandwidth. This is communication following the AFDX protocol.

In addition to this, TTEthernet also supports Best Effort (BE) traffic, for non-critical communication. This is legacy Ethernet communication, which does not use the virtual link concept.

Fig. 2 below shows a possible TTEthernet launcher network topology in line with the avionics configuration described in Fig. 1. The dashed lines indicate where the network will be cut off during flight as the lower stages are separated. The network is also connected to the launch pad ground support equipment during the launch preparations.

3 Studies

RUAG Space has gathered experience from using TTEthernet technology within the frame of two still ongoing ESA and CNES studies concerning launcher avionics, as summarised below.

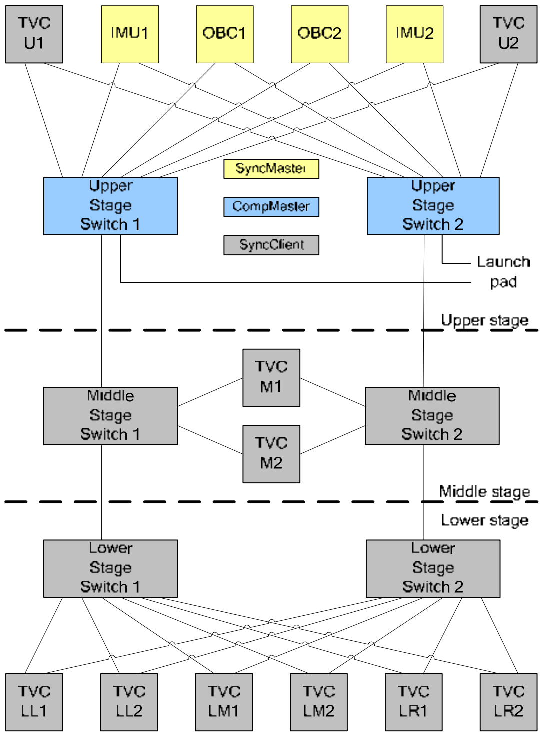

Fig. 2 Tentative launcher TTEthernet topology

3.1 Early TTEthernet Development System

During the first step of the ESA study, a TTEthernet development system was used to demonstrate key communication aspects with the same redundancy concept as is used in Ariane5 today, i.e. with two computers operating in warm redundancy and communicating on one network at a time.

The TTEthernet development system that was used for this study is based on a software implementation of the TTEthernet protocol in end system nodes consisting of COTS PCs running Linux and using 100 Mbps Ethernet links. This software implementation of the protocol has imposed large limitations on achievable period and jitter comparable to what would be achievable with a hardware implementation. For the study, two message cycles of 5 ms and 50 ms were used and the accuracy achieved for the time-triggered transfers was better than 200 µs.

The development system switches that were used in this study does not support the Rate Constrained traffic class, so only the Time-Triggered and Best-Effort traffic classes have been used.

To schedule the TTEthernet network traffic and to configure all TTEthernet network switches and end systems, configuration tools are needed. The tools available for this study were of prototype quality and had several limitations, which lead to multiple vendor iterations.

3.2 Flight Representative Demonstrator

In the second ongoing step of the ESA study the COTS PCs simulating the launcher On-Board Computers (OBCs) have been replaced with more functionally representative units using FPGA prototypes of what can finally be real flight hardware. The system now looks similar to what is shown in Fig. 3 but excludes the RTU elements as all actuators and sensors are simulated by two PCs. An On-Board Computer now consists of:

* An Application Processor Module based on a quad-core LEON4 FPGA breadboard of ESA's Next Generation Microprocessor.
* An I/O Module having a Virtex-6 FPGA with a commercial TTEthernet IP block supported by a high-speed interface to the Application Processor and a local I/O Processor, local communication memory and external interface circuitry.
* A Supervisor hardware that is programmed to monitor the OBC operation and autonomously reconfigure the pair of OBCs in case of detected errors.
* A Backplane connecting the various OBC modules inside a standard 19" rack

The two PCs used to simulate actuators and sensors are enhanced with 100 Mbps TTEthernet PMC NIC cards in order to handle the improved speed and accuracy that a hardware-controlled TTEthernet can give. The software running in these PCs is modified accordingly to be able to handle up to 2000 TTEthernet frames per second.

3.3 Use of TTEthernet IP Block

During the CNES study, all nodes, including the end systems used hardware implementations of the TTEthernet protocol using a setup similar to what is described in §3.2. Linux based test PC end system nodes used 100 Mbps TTEthernet PMC NIC boards and the on-board computer (OBC) end system nodes used a commercial TTEthernet IP block integrated with a System-on-Chip design in a large FPGA.

For this study, a two-channel redundant TTEthernet network was used, with one switch per channel. In such a network, there are two independent communication paths between all interconnected end systems, and all frames are sent on both channels in parallel. Fig. 3 below shows the used topology.

In addition to the switches and the OBC and test PC nodes, a monitor node (MON) was used to passively monitor network traffic on a switch port. Using TTEthernet, Time-Triggered and Rate Constrained frames are sent using Ethernet multicasting, where part of the destination address field of the frame encodes the virtual link, or Critical Traffic ID. The switches use this information to route multicast frames to the associated end systems. To allow for monitoring, all virtual links used in the study simply included the MON node as a destination in addition to the intended target node(s). For a system with a higher bandwidth utilisation than here, this might not be feasible, as the sum of the bandwidth requirements for all virtual links may be too large for the link towards the monitor node. The open-source Wireshark tool includes a dissector plug-in capable of analysing TTEthernet traffic, and has been used to capture and interpret the monitored traffic.

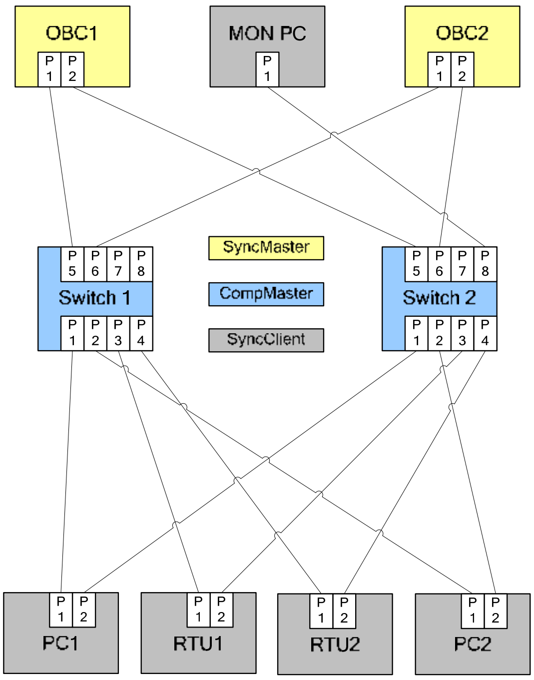

Fig. 3 TTEthernet topology used for study

To simplify the software, the redundancy management support of the TTEthernet IP block was used. For Time-Triggered traffic, each frame is concurrently transmitted on both channels of the network. The properties of TTEthernet ensure that both of them are received during the same time slot on the two channels of the end system. Therefore, one of the frames can be discarded, and the TTEthernet IP block was configured to do so automatically. For Rate Constrained traffic, there are no guarantees on concurrent reception on the two channels, but since each Rate Constrained frame includes a sequence number, the redundancy management of the IP block can use this to discard a received Rate Constrained frame, which was already received on another channel.

The IP block was used in a configuration where it has no direct access to external memory, but only to a limited amount of FPGA on-chip memory. This memory is used to both host the IP block configuration and schedule as well as for dynamic frame buffers for transmission and reception on each virtual link. With this configuration, the software driver needs to copy all frame data to and from the IP block buffers for frame transmission and reception. A dedicated DMA controller assisting this copying could be one way of off-loading the software and achieve an implementation with higher performance.

The TTEthernet configuration tool suite used for this study is more mature than the one used for the first step of the ESA study, and is provided as plug-ins for the Eclipse Integrated Development Environment (IDE). Despite its relative maturity, one major limitation of the tool suite during this study was the lack of support for the used TTEthernet IP block. This lack of tool support has lead to the need for iterative vendor involvement to reach a working configuration.

The TTEthernet protocol is based on a distributed clock synchronisation mechanism to agree on a common global time between all nodes, as knowing when to transmit and receive frames is essential for all participating nodes. Briefly, with this scheme, Synchronisation Master nodes periodically transmit synchronisation messages to Compression Master nodes which calculate a weighted average time and then distribute synchronisation messages with this time to all nodes, including Synchronisation Masters and Synchronisation Clients.

The approach that was used for this study is to run the OBC end system nodes as Synchronisation Masters, the switches as Compression Masters and other nodes as Synchronisation Clients, in line with Fig. 3. The on-board computer (OBC) nodes also host local reference clocks used for software scheduling, and for scheduling reasons, the OBC local clocks and the TTEthernet global time need to be synchronised and in-phase. The TTEthernet IP block allows a correction term to be applied to its contribution to the global clock synchronisation, such that it attempts to slow down or speed up the global time in accordance with the correction term. In the study, this mechanism was used in a periodical regulation loop on each OBC to minimise the phase difference between the local and global clocks, under the assumption that the OBC local clocks do not drift relative to each other. Here, the

OBC local clocks were free running, but in a real launcher application, GNSS receivers could be used as high-precision time references for the OBCs.

The failure hypothesis considered was that one synchronisation master (OBC), but not both could fail, and hence the network was configured such that synchronisation could be maintained with down to a single operational synchronisation master. If employing multiple synchronisation masters, the TTEthernet network is capable of handling a failure in one or more (depending on the total number of synchronisation masters) of the synchronisation masters through the synchronisation algorithm, using voting mechanisms. For the configuration used in the study, however, this is not feasible, as only two synchronisation masters are available. Instead, for such a system, a synchronisation master could e.g. stop participating in the network when it detects a local failure, such as excessive clock drift, or loss of synchronisation to external reference. In the study, no such fault containment mechanism was implemented.

4 Ongoing Work

The current work is focused on extending the scope of the TTEthernet evaluation to a Demonstrator that is more representative of a real launcher computer and network:

* Operating the main flight computers both in warm and hot redundancy.
* Hot redundant network communication.
* Operation at up to 500 Hz packet rate from a selected number of sensors.
* Examining end-to-end communication latency via the network for critical messages like booster separation commands.
* Further evaluation of the tools used to establish the network communication schedule and to distribute it to all network nodes.

The work to be carried out in the beginning of the next year will be focused on:

* Examining ways to achieve higher failure coverage, e.g. fail silence mechanisms to prohibit propagation of erroneous frames
* Further examination of how to implement synchronisation to reference time
* Electrical vs. optical link trade-off

References

[1] "SAE Aerospace Standard AS6802, Time-Triggered Ethernet", SAE International, 2011

4:th CEAS Air & Space Conference
FTF Congress: Flygteknik 2013

Swedish and European research collaboration in simulation supported POD

Anders Rosell and Per Henrikson
GKN Aerospace Engine Systems, Sweden

Keywords: *Nondestructive evaluation, Simulation, Eddy current, Probability of detection (POD), EU collaboration project*

Abstract

This paper summarizes the main contributions from GKN Aerospace Engine Systems (GKN) and Chalmers University of Technology within the European collaboration project PICASSO. PICASSO is a recently finished research project within the 7th European framework programme. The project goal was to develop mathematical models and methodologies in order to carry out capability estimations of non-destructive testing procedures regarding their probability to detect defects of various sizes. Mathematical models were developed and successfully validated against representative experimental cases.

This paper starts with a description of the overall objectives of the project and describes the Swedish collaboration. We will then go through the main results, conclusions and finally discuss the continuation of GKN and Chalmers research within the 6th Swedish National Aeronautical Research Programme.

1 Introduction

PICASSO is a recently finished research project within the 7th European framework programme [1]. The name PICASSO is an acronym for *improved reliability inspection of aeronautic structure through simulation supported probability of detection*. The goal of this project was to build a new and novel concept of simulation supported probability of detection (POD) curves.

The POD methodology is generally used for quantitative non-destructive testing (NDT) process capability assessments within aerospace. The NDT performance is evaluated in order to ensure the desired level of safety. The estimation of a POD curve is based on statistical treatment of inspection data and a confidence level is conventionally used in order to have a conservative estimate, see Fig 1.

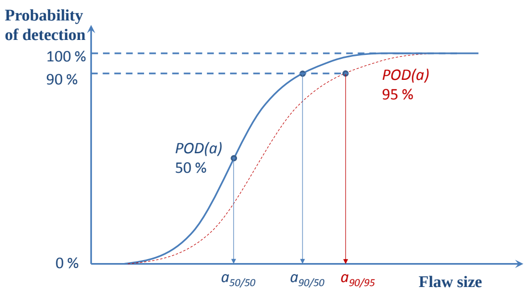

Fig. 1 POD curve with 95 % lower confidence limit.

The project has included the conventional methods of NDT eddy current, ultrasound and radiography. The approach has been to couple mathematical modelling of these methods to estimate their performance in terms of probability of detection in simple but realistic inspection procedures. The project has addressed development at technology readiness level (TRL) 1-4 and, as final objective, to demonstrate the developed tools and methodologies towards simple but representative cases selected for validation.

The POD assessment estimates the probability for a NDT procedure to detect a certain flaw type as a function of the flaw size. The POD curves provide thus a powerful and quantified measurement of the capability of NDT procedures. POD curves are used as a basis for establishing design acceptance requirements and for definition of inspection maintenance intervals according to damage tolerance concepts. The performance of the NDT process is then summarized into a single value often taken as the flaw size that is detected with 90 % probability estimated with 95 % confidence ($a_{90/95}$). This value is then used as input to design according to the damage tolerance requirements.

The POD result is usually obtained by extensive experimental work. The basis for the experiments is often a large set of relevant defects of known sizes. Such experimental results are often associated with significant costs and long lead times for establishment of flaw population and NDT measurements. The experimental campaign is usually technically difficult and often not feasible to realize in the desired way. This can e.g. be related to lack of relevant defects in the desired geometry. The specific challenge related to a POD assessment is that instead of showing the smallest defect possible to detect we must estimate the largest defect that can be missed. This is directly related to the specific NDT procedure including the flaw characteristics, component and inspection system.

The objectives of PICASSO were:

- to have more accurate and reliable POD curves,
- to overcome the cost and lead time issues of the experimental work needed for POD assessment, by using NDT simulation techniques,
- to increase the knowledge and understanding of NDT capability.

2 PICASSO strategy

The PICASSO project consisted of 6 partners from aerospace industry, 3 SMEs, and 5 universities and research organisations, representing 5 countries within the European Union (France, Germany, United Kingdom Sweden and Poland). The overall project strategy is presented in Fig. 2. The technology developments and demonstrations are tested and evaluated by a set of validation cases proposed by the engine manufacturers.

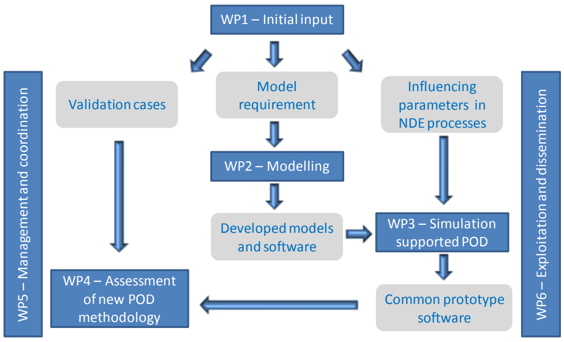

Fig. 2 Overall project strategy of PICASSO.

The first four work packages (WP1-4) have specific technical challenges coupled to them. WP1 gives the initial input which includes all parameters of relevance for the NDT procedure and also their estimated variability. WP2 then address the mathematical modelling, which must handle all the input parameters. The models must then be able to include the variation in order to propagate the uncertainty of input to the variation in signal response of the NDT procedure. WP3 address the use of simulated input data and WP4 is focused on evaluation and validations comparing results to experimental work, validation cases and between different software. WP 5 is concerned with management aspects and finally WP6 is focused on exploration and dissemination of project results.

3 Results from the collaboration between GKN and Chalmers

GKN Aerospace Engine Systems (GKN) has had a close collaboration together with Chalmers University of Technology within the project. The work has focused on the eddy current method applied to the overall project objectives, presented previously. The research effort has mainly been carried out by two PhD students, one industrial at GKN and one academic at Chalmers, with the main results summarized in two licentiate thesis's [2] and [3]. This working strategy has been very successful as the research developments directly strengthen GKN in NDT knowledge and tools as well as Chalmers research group *advanced NDT* at the department of Materials and Manufacturing technology.

3.1 Model development

There are several possible approaches to model eddy current NDE. Both finite element modelling and analytical methods are used within the project. This particular inspection method relies on the principles of electromagnetism which is described by Maxwell´s equations. Regardless of the mathematical method used in order to describe the underlying physical model, it is important to consider the validity and ability to include the required probe-flaw interaction parameters. The model must be able to handle the relevant parameter space that is relevant during the inspection process. Figure 3 shows how the mathematical model must be set up to capture the essence of the NDT procedure. The NDT process is described by parameters divided into two sets. A detailed description is needed of both the Set 1 parameters, that are important regarding their absolute value, as well as the Set 2 parameters which also have an important variation coupled to them. The variation must be described with probability density functions (pdf's) for such parameters. In our work we have validated the mathematical models against benchmark problems from literature as well as with own experimental work [4]. The validation should show that the model is valid within the parameter space relevant for the inspection procedure. However, some validations (e.g. crack tilt) is only technically justified at this stage and left for detailed experimental validation in the future. The primary focus of the model developments has been to be able to include all relevant procedure parameters.

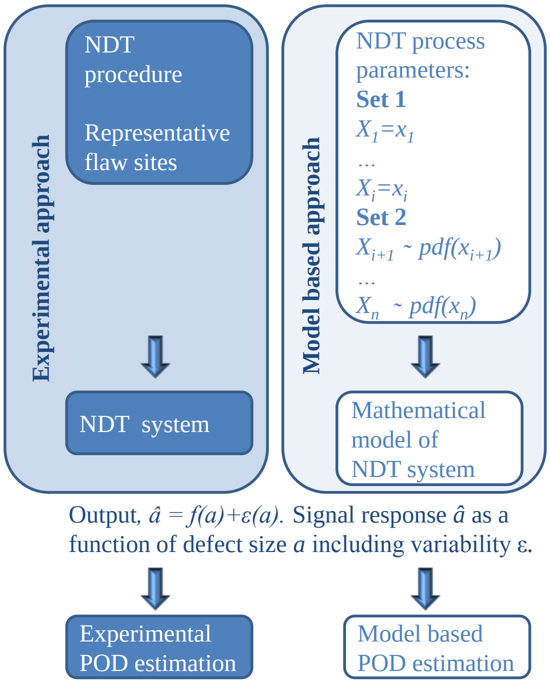

Fig. 3 Steps in the approach to model inspection variability for estimation of POD.

In order to build model based POD curves for eddy current procedures we have to address the parameters of the inspection that can have an impact on the final inspection result. The human influence on data collection and interpretation of the collected response data are left out as a simplification within the project. The result of this is that we treat still treat automated or manual inspections but only as the signal reading on the screen of the eddy current instrument (which applies analogously to the other NDT methods). There are then a number of parameters that have an impact on the final eddy current measurement. Such parameters can be related to the location and orientation of the probe or the defect as well as the specific physical or geometrical properties of the defect or the bulk material. By knowing the parameters and their variation in terms of statistical distributions then allow us to sample a number of inspection configurations and calculate these in the mathematical model.

3.2 Comparing simulated and experimentally based POD

A flat surface eddy current inspection procedure was set up for experimental validation purposes [5]. A laboratory system was set up and 53 fatigue cracks were used in order to gain information about the procedure performance through estimation of the POD curve. The experimental work was repeated with a change in one procedure parameter. The goal with this was to investigate if the change in POD (ΔPOD) can be estimated by the model. The selected parameter was L_{scan} which represents the distance between sequential scans with the eddy current probe. Estimations of variability in procedure parameters based on both measurements and judgments were used as input to the model. The comparison between experimental and model based estimations is shown in Fig. 4. Simulated data using a finite element model is used for input to the calculation of the POD curves in the figure. Similar results are also presented using the commercial software CIVA in [6].

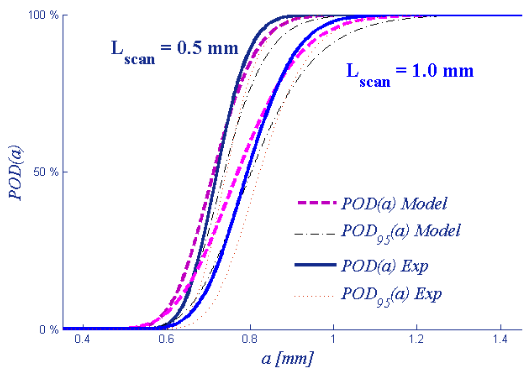

Fig. 4 Comparison between experimental and model based POD estimations, from [7].

The result in Fig. 4 is showing good agreement also for the estimated change in POD due to the procedure change in L_{scan}. A limitation of this model is that all signal response variation is occurring as a consequence of probe flaw interactions. This reduces the possibility to study variations in the model as input for estimation of the probability of false calls (PFA) [7].

3.3 Extend procedure knowledge from simulations

A good agreement in the simple geometry (flat surface) procedure was shown in Fig. 4. This result can now be the baseline for further studies of a similar procedure applied on complex surfaces. In such cases, experimental data may be restricted due to the difficulty or cost to generate relevant defects in the new geometry. However, these steps are not demonstrated within the frame of the project. Simulations can also be used in order to understand the impact for various process variables. Figure 5 shows a comparison between two different flaw types with variation in depth. These flaws have the same surface length but the POD curves are shown to be significantly different [8]. The figure includes also the simulated change due to a variation in the selected frequency of the eddy current procedure. This parameter is shown to have a minor impact on the method performance regarding the probe – flaw interaction within the specified range. The background noise will of course be different but this is not included in the model.

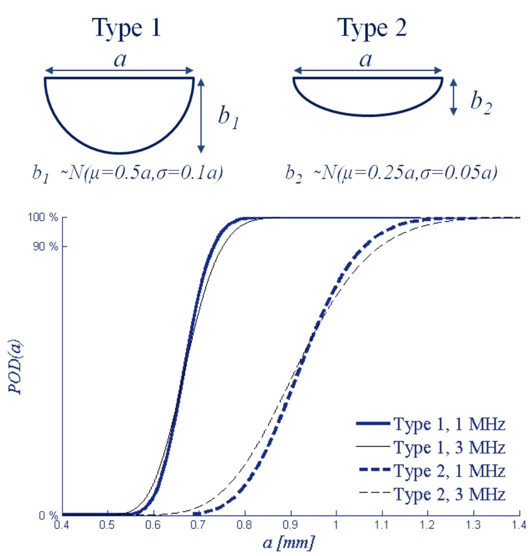

Fig. 5 Simulated estimation of POD curves for the same procedure applied to half-circular and elliptic crack characteristics, from [8].

Figure 6 is showing the change in POD as a result of changes in scan index distance regarding cracks that are oriented perpendicular and parallel to the scan respectively. The figures 5 and 6 illustrates how we can use simulations both to increase our knowledge in method sensitivity due to different flaw characteristics and to better apply effective procedures.

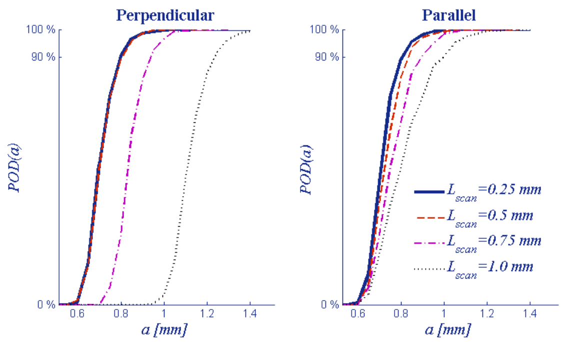

Fig. 6 Simulated estimation of the change in POD resulting from different probe scan densities, from [7].

4 Summary of PICASSO conclusions

The project has demonstrated that mathematical modelling can give fast and accurate POD estimations. The model can give quantitative results and understanding of the procedure capability but requires good knowledge of the NDT process. First the procedure knowledge is important, as the adequate variables have to be assessed in the model with reasonable distributions coupled to them. Secondly the defect model needs to be accurately defined in order to be relevant for the final model of the NDT procedure. The results have also shown that the concept of ΔPOD can be aided by mathematical modelling. In that case the change of a parameter is studied in the model and the change in POD is added to an existing experimental data set, thus combining model based and experimental data. The result includes then the crucial confidence of having real experimental data as a baseline for the POD. A list of conclusions related to the presented work is given below.

Advantages using model assisted POD:

- Quantitatively understand the capability of NDT procedures.
- Investigate factors that influence NDT performance.
- Fast estimations of POD, on new inspection procedures (e.g different geometry, material, equipment, …).
- Reduced cost of samples.
- Support capability estimations using limited number of experimental data or if such data don't apply to the conventional statistical models.
- Improve or aid in selection of defect size distributions.
- Using ΔPOD allow simulated data to be combined with experiments.

Limitations and challenges:

- Full understanding of physics is needed in order to be able to create model.
- Parameter space of the validation shall cover the variables of the procedure.
- Complex models may require time consuming set up and calculations.
- Uncertainty parameters need to be determined and quantified.
- The relevant parameters need to be included in the model.
- Development for handling of calibration as an uncertainty parameter is needed.
- Developments for estimating confidence levels based on model accuracy is needed.
- Developments are needed to understand and include the human impact on POD in models.

The model based approach is schematically presented in Fig. 7. The left side in the figure is showing how model data is applied similar to experimental input. In that case the POD curve is estimated from a limited number of signal response data. However, there exist also new possibilities using simulations. If a large number of simulations are feasible then there is a possibility to estimate the POD value pointwise for different flaw sizes. This will result in a non-parametric POD curve, which then will allow investigations in cases where signal response data does not apply for analysis using the conventional statistical techniques [9].

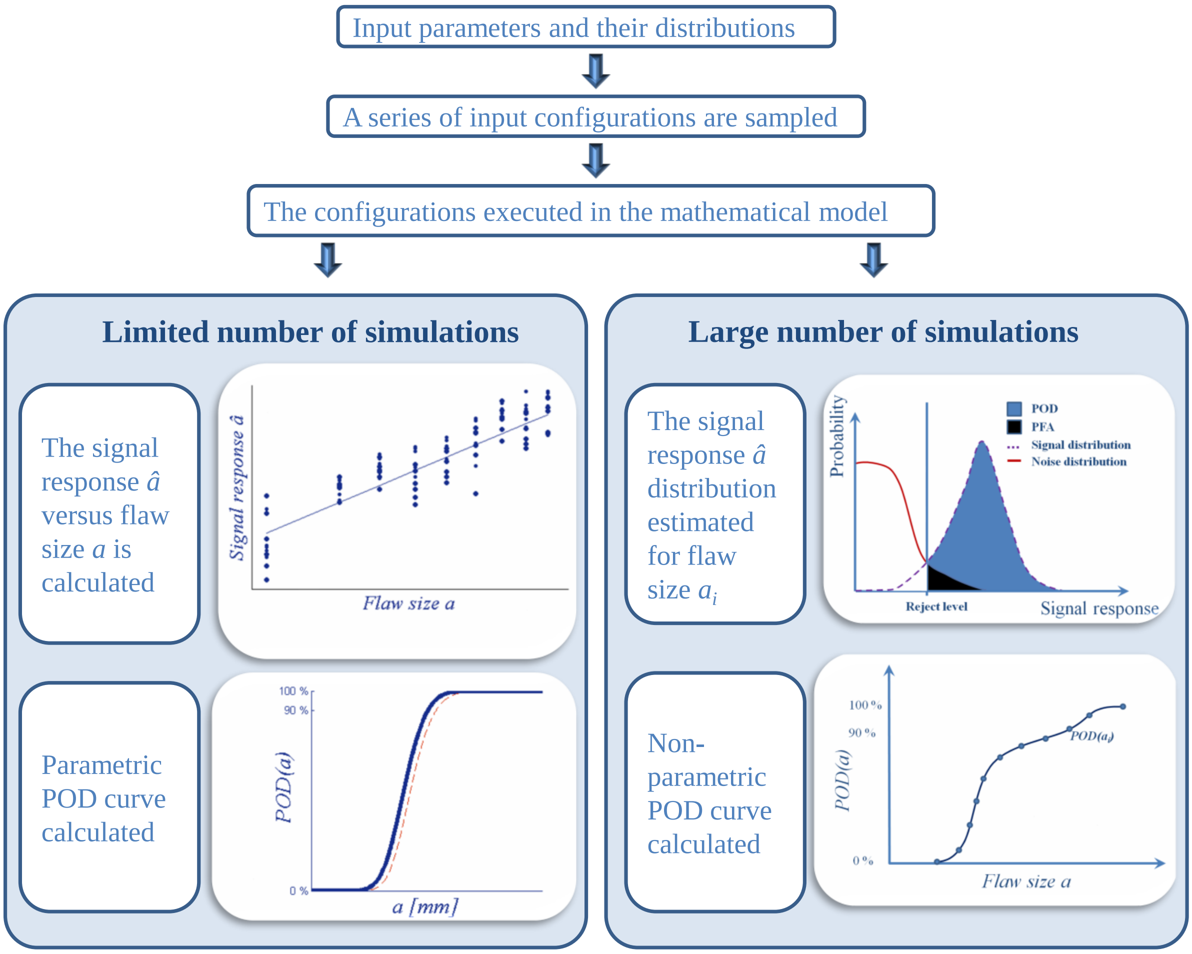

Fig. 7 General approach of using mathematical modelling of NDT to support POD assessments. Uncertainties of process variables are propagated through the mathematical model to give variation in signal response. The data is on the left side treated in the standard statistical model in order to build a parametric POD curve. The right side shows schematically the calculation of a non-parametric POD based on a large number of data and hit/miss criteria.

5 Continuation of research within NFFP6

As PICASSO has been a project focused on low level TRL, the utilization of the technology to its full potential relies on further developments. The main focus for this, with regard to eddy current NDT, is to be able to apply the methodologies to complex geometries, welded material, more complex equipment and procedures. These demands are proposed to be addressed by GKN and Chalmers within the 6th National Aeronautical Research Programme (NFFP6), sponsored by the Swedish innovation agency VINNOVA. The continuation of GKN and Chalmers work started in PICASSO will focus on developments toward higher TRL levels, and demonstrate the developments on relevant and novel product inspection procedures. The project will also take the new developments further to study the connection between NDT and fracture mechanical characteristics on components used in service. This will be achieved by increased knowledge of defect characteristics as influencing both component fracture mechanics and NDT performance in POD, schematically shown in Fig. 8.

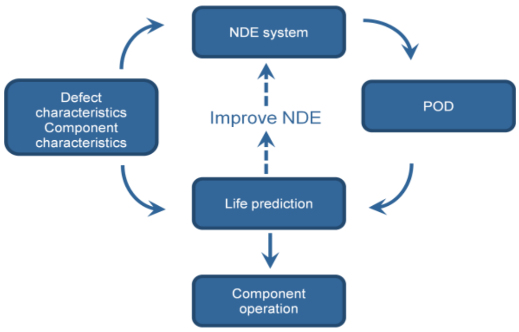

Fig. 8 Coupling between defect characteristics NDT system and component operation.

Special probes such as sender – receiver type are commonly used in eddy current procedures for crack detection. This type of probe can be found in array configurations but also with the receiver coil replaced with another type of magnetic field sensor. These possible options make this configuration especially interesting for future eddy current procedures. However, the sender - receiver probes give in general a non-linear signal response as a function of the crack size. This presents a problem since the Berens approach, which is the classical method to derive the POD curve, requires that the signal response versus crack size can be predicted with a linear relation [9]. The collected input data must also show a constant variance around the linear regression line, which in general does not hold for sender - receiver probes. One approach which can be used to overcome these limitations is to use a mathematical model of the eddy current probe – flaw interaction and use this to estimate the detection probability at specific crack sizes. Such estimation requires a large number of calculations. However, this approach is more general and can increase the understanding of the NDT system and its capability. These issues will be addressed in the proposed project.

6 Summarizing remarks

Mathematical modelling can give fast and accurate POD estimations and thus reduce the costs for POD investigations. The model based approach does demand a more thorough technical justification of the inspection procedure by the judgement of variation in parameters. This is of course a challenge but results in increased process knowledge. It can also be a possibility to test and evaluate the procedure settings with respect to method capability and reliability.

To summarize, we propose that mathematical modelling is a key for increased reliability of future NDT processes within aerospace. The tools of modelling are giving the possibilities not only to improve NDT systems but also to optimize them in order to meet increasing demands on component operation and safety.

References

[1] PICASSO website, www.picasso-ndt.eu, 2013.
[2] Rosell, A., "Finite Element Modelling of Eddy Current Non-Destructive Evaluation in Probability of Detection Studies", Thesis for the degree of Licentiate of Engineering, Chalmers University of Technology, Sweden, 2012.
[3] Larsson, L., "Analytical methods of solution to eddy current interaction problems", Thesis for the degree of Licentiate of Engineering, Chalmers University of Technology, Sweden, 2012.
[4] Rosell, A. and Persson, G., "Finite Element Modelling of Closed Cracks in Eddy Current Testing", *International Journal of fatigue*, 41, 2012, pp. 30-38.
[5] Rosell, A. and Persson, G., "Comparison of Experimental and Model Based POD in a Simplified Eddy Current Procedure", *18th World Conference on Nondestructive Testing*, 2012.
[6] Rosell, A. and Persson, G., "Simulation supported POD methodology and validation for automated eddy current procedures", *4th symposium on NDT in Aerospace*, Augsburg Germany 2012.
[7] Rosell, A. and Persson, G., "Model Based Capability Assessment of an Automated Eddy Current Inspection Procedure on Flat Surfaces", *Research in Nondestructive Evaluation*, 24:3, 2013, pp. 154–176.
[8] Rosell, A. and Persson, G., "Eddy Current Signal Response Predictions for Use in Model Assisted POD Estimations Based on Different Flaw Characteristics", *4th symposium on NDT in Aerospace*, Augsburg Germany 2012.
[9] Berens, A. P., *NDE reliability data analysis*. In: Nondestructive Evaluation and Quality Control. Vol. 17. ASM Metals Handbook. ASM International, pp. 689-701, 1989.

4:th CEAS Air & Space Conference
FTF Congress: Flygteknik 2013

Buckling and Modal Analysis of Rotationally Restrained Orthotropic Plates

Abajo D. and Villarreal E.

Keywords: *Buckling, Orthotropic Lay-Out, Dynamic Load Factor, Rotationally Restrained Plate*

Abstract

The results of this study have been performed at Aernnova Aerospace inside the European project DAEDALOS. The analysis is focused on the static buckling, modal analysis and vibration buckling of orthotropic plates with four-edges simply supported, rotationally restrained and linearly biaxial loaded.

The parametric solution of this problem allows making a more accurate initial sizing of typical aerospace structural components, like stiffened panels, where both static and dynamic buckling loads for composite structures are fundamental for the final design.

The parametrically restrained four edges allows a more suitable solution than known buckling curves of simply supported or clamped metallic plates. The obtained results show an important buckling factor gauge respect the simply supported plates due to rotationally stiffness.

Finally, the dynamic analysis of the problem shows the buckling factor gauge for load frequencies higher than the first natural frequency taking into account the initial plate imperfection.

1 Approximate Analysis

The approximate analysis carried out in this study is based on the general linearly biaxial loaded case shown in Figure 1. This analysis includes a static buckling [section 2.1], modal [section 2.2] and dynamic or vibration buckling analysis [section 2.3]. These analyses are carried out considering composite linear continuum mechanics [section 1.1], variation methods of the system energy [section 1.2] and solving the system of equations assuming shape functions as Ritz-method [section 1.2.2].

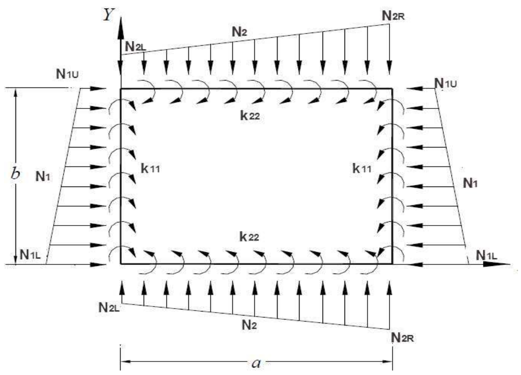

Figure 1: Model of Rotationally Restrained Plate

1.1 Continuum Mechanics

The continuum mechanics considered in this analysis are basically the kirchhoff hypothesis ([1] Clebsch 1883):

Linear behavior	$\varepsilon_{ij} = \frac{1}{2}\left(\frac{\partial u_i}{\partial x_j} + \frac{\partial u_j}{\partial x_i}\right)$
Thin plates theory	$t \ll a, b$
No coupling	$U_{strain} = f(D_{ij}, w)$
Orthotropic material	$D_{ij} = 0$ for $ij = [16,26]$
Middle surface	Unstrained after bending

The necessary relation between loads and strains is simplified according to previous hypothesis.

$$\begin{Bmatrix} M_x \\ M_y \\ M_{xy} \end{Bmatrix} = \begin{bmatrix} D_{11} & D_{12} & 0 \\ D_{12} & D_{22} & 0 \\ 0 & 0 & D_{66} \end{bmatrix} \begin{Bmatrix} k_x \\ k_y \\ k_{xy} \end{Bmatrix} \qquad 1.1$$

The curvatures of a thin plate, assuming linear behavior, can be expressed as follows ([3] Kollar):

$$\begin{Bmatrix} k_x \\ k_y \\ k_{xy} \end{Bmatrix} = \begin{Bmatrix} -\dfrac{\partial^2 w}{\partial x^2} \\ -\dfrac{\partial^2 w}{\partial y^2} \\ -\dfrac{2\,\partial^2 w}{\partial x \delta y} \end{Bmatrix} \qquad 1.2$$

The strain energy of an orthotropic plate in pure bending case ([4] Whitney 1987):

$$U_{sb} = \frac{1}{2}\int_0^a \int_0^b D_{11}\left(\frac{\partial^2 w}{\partial x^2}\right)^2 + D_{22}\left(\frac{\partial^2 w}{\partial y^2}\right)^2 + +2D_{12}\left(\frac{\partial^2 w}{\partial x^2}\right)\left(\frac{\partial^2 w}{\partial y^2}\right) + 4D_{66}\left(\frac{\partial^2 w}{\partial x \delta y}\right)^2 dxdy \qquad 1.3$$

The energy due to the rotational stiffness applied in all four edges is as follows:

$$U_{sBC} = \frac{1}{2}\left(\int_{\Gamma_{10}} k_{11}\left(\frac{\partial w}{\partial x}\right)^2_{x=0} dy + \int_{\Gamma_{1a}} k_{11}\left(\frac{\partial w}{\partial x}\right)^2_{x=a} dy\right) + \frac{1}{2}\left(\int_{\Gamma_{20}} k_{22}\left(\frac{\partial w}{\partial y}\right)^2_{y=0} dx + \int_{\Gamma_{2b}} k_{22}\left(\frac{\partial w}{\partial y}\right)^2_{y=b} dx\right) \qquad 1.4$$

The work done by biaxial load N_1 and N_2, illustrated in Figure 1 , is computed as integral

$$W_{nc} = \frac{1}{2}\int_0^a \int_0^b \left(N_1(y,t)\left(\frac{\partial(w_0 + w)}{\partial x}\right)^2\right) dxdy + \frac{1}{2}\int_0^a \int_0^b \left(N_2(x,t)\left(\frac{\partial(w_0 + w)}{\partial y}\right)^2\right) dxdy \qquad 1.5$$

Where w_0 is the initial imperfection and $N_1(y,t)$ and $N_2(x,t)$ the biaxial loads with separated variables:

$$w_0(x,y) = w_0^{max} F_w(x,y)$$
$$N_1(y,t) = N_{1L} Y_{N1}(y) T(t)$$
$$N_2(x,t) = N_{2L} X_{N2}(x) T(t)$$

The kinetic energy due to out of plane displacements:

$$T = \frac{1}{2}\int_0^a \int_0^b \rho\, t\, \dot{w}^2\, dxdy \qquad 1.6$$

1.2 Energy Variation and Ritz-Method

The solution of the general problem is reached by Hamiltonian Mechanics and the Ritz Method that means the first variation of the energy functional *F* should be equal to 0:

$$min(\epsilon) = \int_{t_1}^{t_2} (T - U + W_{nc})dt$$
$$\int_{t_1}^{t_2} \{\delta(T) - \delta(U) + \delta(W_{nc})\} dt = 0 \qquad 1.7$$

1.2.1 Boundary Conditions

The boundary conditions of plate presented Figure 1 are four edges with out-of-plane displacement null, $w(\Gamma_i) = 0$ and four edges rotationally restrained, RRRR.

$$w(0,y) = 0; \; w(a,y) = 0$$
$$w(x,0) = 0; w(x,b) = 0$$
$$\mp k_{11}\left(\frac{\partial w}{\partial x}\right)_{x=0||a} = -D_{11}\left(\frac{\partial^2 w}{\partial x^2}\right)_{x=0||a} \qquad 1.8$$
$$\mp k_{22}\left(\frac{\partial w}{\partial y}\right)_{y=0||b} = -D_{22}\left(\frac{\partial^2 w}{\partial y^2}\right)_{y=0||b}$$

Where k_{11} and k_{22} are the rotational stiffness presented in the Figure 1, D_{ij} are the flexure stiffness coefficients of the plate and w the out plane displacement.

1.2.2 Assumed Functions

The below assumed functions fulfill the boundary conditions expressed in equation 1.8, it is a further development of assumed functions proposed by Shan L. [7] and allows to calculate the buckling coefficient for a larger aspect ratio range .

$$w(x,y)=\sum_{m=1}^{M}\sum_{n=1}^{N}q_{mn}(t)X_m(x)Y_n(y)=$$
$$=\left\{(1-\psi_1)\,sin(m\pi\tilde{x})+\frac{\psi_1}{2}(1-cos(2m\pi\tilde{x}))\right\} \tag{1.9}$$
$$\left\{(1-\psi_2)\,sin(n\pi\tilde{y})+\frac{\psi_2}{2}(1-cos(2n\pi\tilde{y}))\right\}$$

Where ψ is the parameter that allows set the rotational stiffness to fully clamped CC, simply supported SS or rotational restrained RR and m, n define the buckling modes in X and Y axis.

$$\psi_1=\frac{\tilde{k}_{11}}{\tilde{k}_{11}+2m\pi};\quad \psi_2=\frac{\tilde{k}_{22}}{\tilde{k}_{22}+2n\pi}$$

1.2.3 Variational Development

The variational development becomes to an M·N equations system and is carried out considering the suggested dimensionless parameters presented in [5] Mittlested C

$$\alpha=\frac{a}{b}\sqrt[4]{\frac{D_{22}}{D_{11}}};\ \eta_1=\frac{D_{12}}{\sqrt{D_{11}D_{22}}};\ \eta_2=\frac{2D_{66}}{\sqrt{D_{11}D_{22}}} \tag{1.10}$$
$$\tilde{k}_{11}=\frac{k_{11}a}{D_{11}};\quad \tilde{k}_{22}=\frac{k_{22}b}{D_{22}}$$

The dimensionless degrees of freedom can be expressed as follows:

$$\tilde{x}=\frac{x}{a};\ \tilde{y}=\frac{y}{b};\ \tilde{w}_0=\frac{w_0}{t}\quad \tilde{q}=\frac{q}{t} \tag{1.11}$$

Moreover, the dimensionless external loads are considered as follows:

$$\tilde{N}_{1L}=\frac{N_{1L}b^2}{\pi^2\sqrt{D_{11}D_{22}}};\quad \tilde{N}_{2L}=\frac{N_{2L}a^2}{\pi^2\sqrt{(D_{11}D_{22})}};$$
$$\gamma_{21}=\frac{\tilde{N}_{2L}}{\tilde{N}_{1L}}\qquad \omega_a^2=\frac{\sqrt{D_{11}D_{22}}}{\rho(ab)^2t} \tag{1.12}$$

The biaxial loads are considered as a linear function shown in Figure 1:

$$Y_{N1}=1-\left(1-\frac{N_{1U}}{N_{1L}}\right)\tilde{y};\quad X_{N2}=1-\left(1-\frac{N_{2U}}{N_{2L}}\right)\tilde{x} \tag{1.13}$$

The next step is applying the first variation to each energy term expressed in equations 1.3 to 1.6 and introducing the previous dimensionless parameters. The first variation of the strain energy depends on α, η_1, η_2 and shape functions X_m and Y_n:

$$\frac{\delta\tilde{U}_{sb}}{\delta\tilde{q}_{jk}}=\sum_m^M\sum_n^N\tilde{q}_{mn}\left[\alpha^{-2}\int_0^1\frac{\partial X_m^2}{\partial\tilde{x}^2}\frac{\partial X_j^2}{\partial\tilde{x}^2}d\tilde{x}\int_0^1 Y_nY_kd\tilde{y}\right.$$
$$+\alpha^2\left\{\int_0^1 X_mX_jd\tilde{x}\int_0^1\frac{\partial^2Y_n}{\partial\tilde{y}^2}\frac{\partial^2Y_k}{\partial\tilde{y}^2}d\tilde{y}\right\}$$
$$\eta_1\left\{\int_0^1 X_m\frac{\partial X_j^2}{\partial\tilde{x}^2}d\tilde{x}\int_0^1\frac{\partial^2Y_n}{\partial\tilde{y}^2}Y_kd\tilde{y}+\int_0^1\frac{\partial X_m^2}{\partial\tilde{x}^2}X_jd\tilde{x}\int_0^1 Y_n\frac{\partial^2Y_k}{\partial\tilde{y}^2}d\tilde{y}\right\} \tag{1.14}$$
$$\left.+2\eta_2\left\{\int_0^1\frac{\partial X_m}{\partial\tilde{x}}\frac{\partial X_j}{\partial\tilde{x}}d\tilde{x}\int_0^1\frac{\partial Y_n}{\partial\tilde{y}}\frac{\partial Y_k}{\partial\tilde{y}}d\tilde{y}\right\}\right]$$

The first variation of the boundary conditions energy depends on $\tilde{k}_{11}$, $\tilde{k}_{22}$, α and shapes X and Y:

$$\frac{\delta\tilde{U}_{sBC}}{\delta\tilde{q}_{jk}}=\sum_m^M\sum_n^N\tilde{q}_{mn}\left[\tilde{k}_{11}\alpha^{-2}\int_0^1 Y_nY_kd\tilde{y}\left\{\left(\frac{\partial X_m}{\partial\tilde{x}}\frac{\partial X_j}{\partial\tilde{x}}\right)_{\tilde{x}=0}\right.\right.$$
$$\left.\left.+\left(\frac{\partial X_m}{\partial\tilde{x}}\frac{\partial X_j}{\partial\tilde{x}}\right)_{\tilde{x}=1}\right\}\right] \tag{1.15}$$
$$+\tilde{q}_{mn}\left[\tilde{k}_{22}\alpha^2\int_0^1 X_mX_jd\tilde{x}\left\{\left(\frac{\partial Y_n}{\partial\tilde{y}}\frac{\partial Y_k}{\partial\tilde{y}}\right)_{\tilde{y}=0}+\left(\frac{\partial Y_n}{\partial\tilde{y}}\frac{\partial Y_k}{\partial\tilde{y}}\right)_{\tilde{y}=1}\right\}\right]$$

Doing the same with the external loads, the first variation depends on $\tilde{N}_{1L}$, γ_{21} and shapes X_m and Y_n:

$$\frac{\delta\tilde{W}_{nc}}{\delta\tilde{q}_{jk}}=\sum_m^M\sum_n^N\tilde{q}_{mn}\pi^2\tilde{N}_{1L}\left[\int_0^1\frac{\partial X_m}{\partial\tilde{x}}\frac{\partial X_j}{\partial\tilde{x}}d\tilde{x}\int_0^1 Y_{N1}Y_nY_kd\tilde{y}\right]$$
$$+\tilde{q}_{mn}\pi^2\tilde{N}_{1L}\left[\gamma_{21}\left\{\int_0^1 X_{N2}X_mX_jd\tilde{x}\int_0^1\frac{\partial Y_n}{\partial\tilde{y}}\frac{\partial Y_k}{\partial\tilde{y}}d\tilde{y}\right\}\right]$$
$$+\pi^2\tilde{N}_{1L}\tilde{w}_0^{max}\left[\int_0^1\int_0^1 Y_{N1}\frac{\partial F_w}{\partial\tilde{x}}\frac{\partial X_j}{\partial\tilde{x}}Y_kd\tilde{x}d\tilde{y}\right] \tag{1.16}$$
$$+\pi^2\tilde{N}_{1L}\tilde{w}_0^{max}\left[\gamma_{21}\left\{\int_0^1\int_0^1 X_{N2}\frac{\partial F_w}{\partial\tilde{y}}X_j\frac{\partial Y_k}{\partial\tilde{y}}d\tilde{x}d\tilde{y}\right\}\right]$$

The variation of the kinetic energy depends on ω_a and shapes $X_m\ Y_n$

$$\frac{\delta \tilde{T}}{\delta \tilde{q}_{jk}} = -\sum_{m}^{M}\sum_{n}^{N}\frac{\ddot{\tilde{q}}_{mn}}{\omega_a^2}\left[\int_0^1 X_m X_j d\tilde{x}\int_0^1 Y_n Y_k d\tilde{y}\right] \qquad 1.17$$

Substituting the first variation(1.14) to 1.17 into *1.7* an MN equations system is reached:

$$\begin{aligned}\frac{-1}{\omega_a^2}\left[\tilde{\tilde{\tilde{M}}}\right]\{\ddot{\tilde{q}}\} - \left[\tilde{\tilde{\tilde{K}}}_{sb} + \tilde{\tilde{\tilde{K}}}_{sBC}\right]\{\tilde{q}\} + \pi^2 \tilde{N}_{1L}\left[\tilde{\tilde{\tilde{Q}}}_1\right]\{\tilde{q}\} \\ = -\pi^2\,\tilde{N}_{1L}\left[\Delta\tilde{\tilde{\tilde{Q}}}_o\right]\{w_0{}^{max}\}\end{aligned} \qquad 1.18$$

Where $\left[\tilde{\tilde{\tilde{M}}}\right]$ is the dimensionless mass matrix; $\left[\tilde{\tilde{\tilde{K}}}_{sb} + \tilde{\tilde{\tilde{K}}}_{sBC}\right]$ is the dimensionless stiffness; $\left[\tilde{\tilde{\tilde{Q}}}\right]$ is the dimensionless external force matrix, $\left[\Delta\tilde{\tilde{\tilde{Q}}}_o\right]$is the dimensionless forced vector due to initial imperfections and $\{\tilde{q}\}$ is the generalized coordinates vector. Each term of these matrixes corresponds to a defined m and n term of previous variations:

$$\begin{aligned}
\tilde{M}^{jkmn} &= \frac{\delta\tilde{T}^{mn}}{\delta\tilde{q}_{jk}}\left(\ddot{\tilde{q}}_{mn}\left(\frac{\omega^2}{\omega_a^2}\right)\right)^{-1};\\
\tilde{K}^{jkmn} &= \left(\frac{\delta\tilde{U}^{mn}_{sb}}{\delta\tilde{q}_{jk}} + \frac{\delta\tilde{U}^{mn}_{sBC}}{\delta\tilde{q}_{jk}}\right)(\tilde{q}_{mn})^{-1};\\
\tilde{Q}_1^{jkmn} &= \left(\frac{\delta\tilde{W}^{mn}_{nc}}{\delta\tilde{q}_{jk}}\right)_1\left(\tilde{q}_{mn}\pi^2\tilde{N}_{1L}\right)^{-1};\\
\tilde{Q}_0^{jk} &= \left(\frac{\delta\tilde{W}_{nc}}{\delta\tilde{q}_{jk}}\right)_0\left(w_{0mn}^{max}\pi^2\tilde{N}_{1L}\right)^{-1}
\end{aligned} \qquad 1.19$$

The static buckling problem can be solved by Eigenvalues methodology neglecting kinetic terms, see section 2.1. The pure modal analysis also is solved by same methodology neglecting external forces work, or including in-plane loads and neglecting initial imperfection terms, see section 2.2. The vibration buckling analysis applies a Runge-Kutta of whole system, see section 2.3.

2 Solution & Results

The analytical or approximated solution of different proposed analysis has been carried out using an own MATLAB code. This code computes the different matrixes and solves the Eigen value problem for static buckling and modal analysis or the Runge-Kutta integration for vibration buckling. The results have been obtained for different boundary conditions, adjusting stiffness k_{11} and k_{22}, different plates, modifying the aspect ratio α and the materials adjusting stiffness parameters η_1 and η_2.

2.1 Static Buckling Analysis

The static buckling analysis is solved applying an Eigen Value problem to the equation 1.18 with neglected kinetic terms and no initial imperfections

$$\left[\tilde{\tilde{\tilde{K}}}_{sb} + \tilde{\tilde{\tilde{K}}}_{sBC}\right]\{\tilde{q}\} - \pi^2\tilde{N}_s\left[\tilde{\tilde{\tilde{Q}}}_1\right]\{\tilde{q}\} = 0 \qquad 2.1$$

The static buckling load N_{1sb} corresponds to the lower Eigen Value λ_{min} which matches with a particular buckling mode m and n.

$$\lambda_{min} \to m, n, \tilde{N}_{1sb} \to N_{1sb} = \frac{\tilde{N}_{1sb}\pi^2\sqrt{D_{11}D_{22}}}{b^2} \qquad 2.2$$

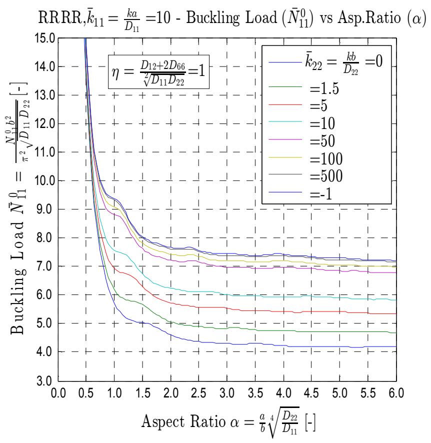

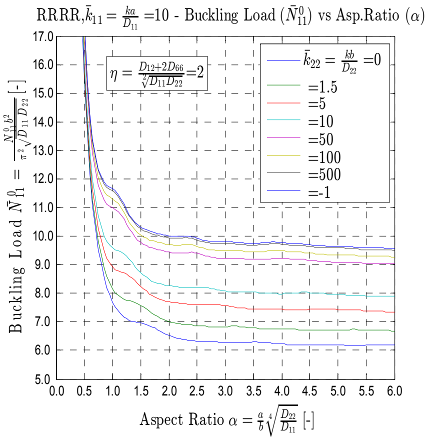

Figure 2: Buckling Factor for different conditions

The static buckling load factor $\tilde{N}_{1sb}$ is higher for CCRR case due to its higher global stiffness. The difference increases when the aspect ratio α decrease and it is due to the clamped edge is b which is relatively longer when α decrease.

2.2 Modal Analysis

The general modal analysis including axial in-Plane loads is solved applying an Eigen Value problem to the equation 1.18 neglecting initial imperfection terms:

$$\tilde{\omega}^2 \left[\tilde{\tilde{M}}\right]\{\tilde{q}\} - \left[\tilde{\tilde{K}}_{sb} + \tilde{\tilde{K}}_{sBC}\right]\{\tilde{q}\} + \pi^2 FC \cdot \tilde{N}^0_{1L} \left[\tilde{\tilde{Q}}_1\right]\{\tilde{q}\} = 0 \qquad 2.3$$

Where FC is the in-plane compression factor in reference to the axial allowable buckling $\tilde{N}^0_{1L}$. The first natural frequency f_{1st} corresponds to the lower Eigen Value λ_{min} which matches with a particular mode m and n.

The first natural frequency f_{1st} increases with rotational stiffness $\tilde{k}_{22}$ and also from SSRR to CCRR due to its higher global stiffness except for long aspect ratios, α, where there is no practical difference. In case of $\tilde{k}_{22}$, the difference increases with the aspect ratio α and it is due to the rotationally restrained edge a is longer for high values of α. In case of $\tilde{k}_{11}$, happens the opposite effect, the difference increases when the aspect ratio α decreases because the clamped edge b is longer for low values of α.

Figure 3 shows the square of the dimensionless angular frequency for different in plane load ratios in reference with the static buckling load of the panel. The results obtained are according with results shown in ([10] 1969 NASA-SP-160) where values for isotropic materials ($\eta = 1$) and several aspect ratios are shown.

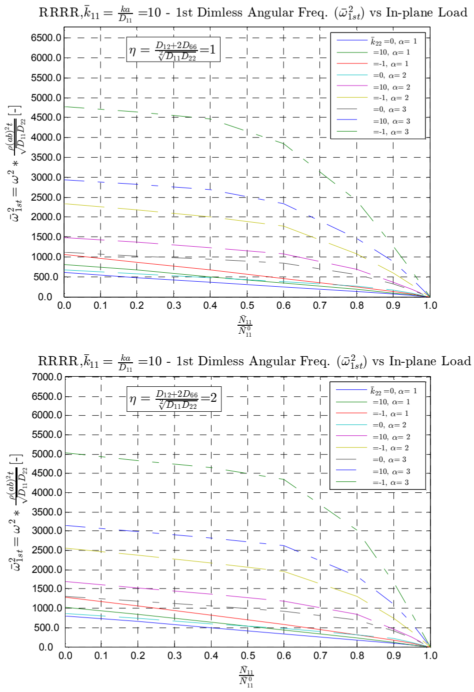

Figure 3: First Angular Freq. vs in-Plane Load Ratio

2.3 Vibration Buckling Analysis

The vibration buckling is solved applying a Runge-Kutta method to the equation 1.18 which expressed in time field becomes:

$$(\tau\omega_a)^{-2}\left[\tilde{\tilde{M}}\right]\{\tilde{q}\,''\} + \left[\tilde{\tilde{K}}_{sb} + \tilde{\tilde{K}}_{sBC}\right]\{\tilde{q}\} = \pi^2 \tilde{N}_{1L}\left[\tilde{\tilde{Q}}_1\right]\{\tilde{q}\} + \pi^2 \tilde{N}_{1L}\left[\Delta\tilde{\tilde{Q}}_o\right]\{\tilde{w}_0{}^{max}\} \qquad 2.4$$

Where the dimensionless time $\tilde{t}$ is expressed as $\tilde{t} = t/T_{exc} = tf_{exc}$,$(\tau = T_{exc})$, and the external dynamic load $\tilde{N}_{1L} = \tilde{N}_{1L}T(t)$ has been analyzed as follows:

$$\tilde{N}_{1L}(t) = \begin{Bmatrix} \tilde{N}_{1L}^{st}\, n_{Alt} \sin(\pi \tilde{t}) \\ 0 \end{Bmatrix} \quad \begin{matrix} 0 < \tilde{t} < 1 \\ \text{otherwise} \end{matrix} \qquad 2.5$$

Where $\tilde{N}_{1L}^{st}$ is the corresponding static buckling factor and n_{Alt} the dynamics factors. An important parameter in the vibration buckling analysis is the load period, n_T, defined as the ratio between the excitation period to first plate vibration period with no in plane compression.

The following results consider the next parameters:

2-1 Loading and Initial Deformation Parameters

Parameters	Definition	Plots	Parametric
Load Period	T_{exc}/T_{1st}	[50, 0.7]	[0.25 ,4]
Load Magnitude	$\tilde{N}_1^d/\tilde{N}_{1L}^{st}$	[0.7]	[0.25, 0.95]
Initial Def	$\lvert w_0^{Max} \rvert$	[t, t/2, t/5]	t/5
Def Shape	F(x, y)	{[X5, Y1]}	{[X5, Y1]}

The vibration buckling results are based on the maximum out of plane displacement w_{Max} versus dimensionless time $\tilde{t}$.

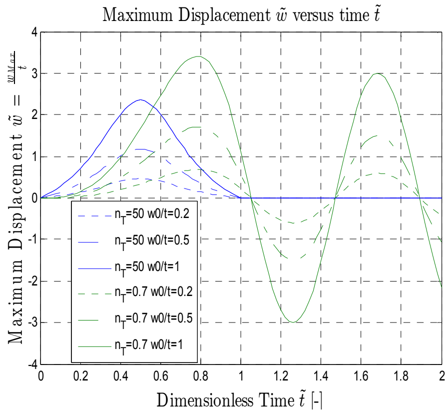

Figure 4: Out-plane displacement w_{Max} versus time $\tilde{t}$.

The maximum displacement increase when the load period is near to first natural frequency as shows the above figure. Moreover, these results are quite sensitive to magnitude and initial imperfection shape, so statistical imperfection analysis should be done.

In order to show as the buckling load factor is higher than 1 for short period loads, the out plane displacement at critical time t_{Max} for $n_{Alt} = 1.2$, $n_T = 0.3$ and $\tilde{w}_0 = 0.2$ of a particular plate problem with aspect ratio $\alpha = 3.67$ is shown in the next figure:

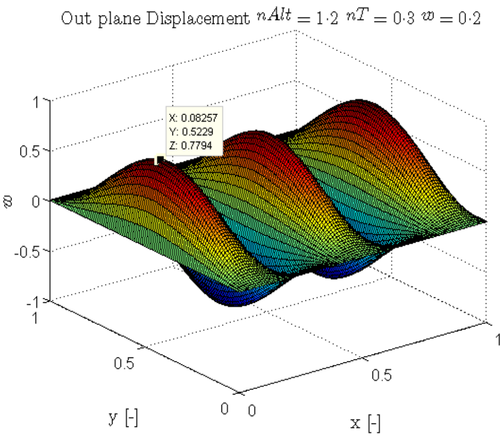

Figure 5: Out-plane displacement at critical time t_{Max}

The maximum out displacement $\tilde{w}$ is lower than $\tilde{w} = 1$ even for loading values higher than static buckling N_{1L}^{sb} ($n_{Alt} > 1$). The most critical maximum plate deformation is produced when the initial imperfection shape fits with the static buckling mode, for this case, $m = 5$ $n = 1$. Moreover, the critical mode is the shown in Figure 5, $m \approx 5n$ due to the plate dimensions $a \approx 4b$ for this particular example of simulation.

In the following, a parametric analysis has been performed. Figure 6 shows the maximum out of plane displacement w_{Max} versus nT for different n_{Alt}. Results shown are related to dimensionless parameters specified in table 2-1.

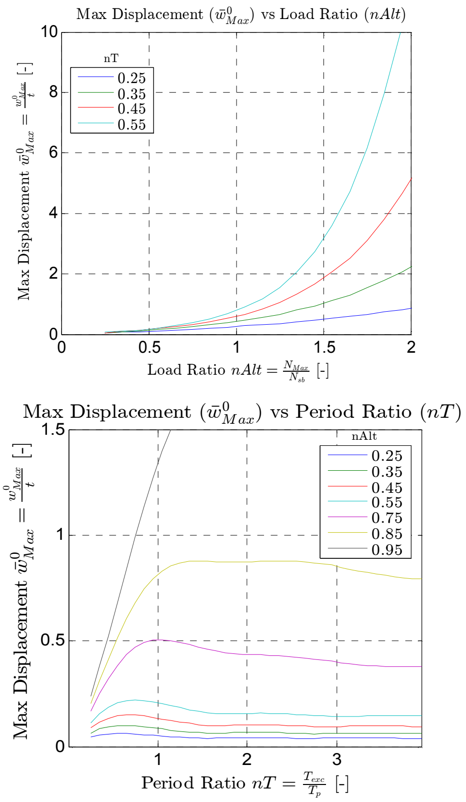

Figure 6: Out plane disp. versus nT for different nAlt

The out plane displacement reaches its maximum value for n_T close to 1 due to resonance effects. The minimum values are reached for low values of n_T due to dynamics effects and wave propagation, for example the figure shows the plate does not buckles for compression load near static buckling load, $n_{Alt} = 0.95$ and low load period $n_T < 0.5$.

It is important to reminder that all results here presented consider the initial imperfection shape proportional to the first static buckling mode. From the point of view of the analysis, if this is not true the buckling is reached at higher n_{Alt} . Obviously nothing is perfect and always exist a component of imperfection with the shape of the first buckling mode, so is a factor to reconsider in this analysis.

However, it is necessary take into account that this simulation use linear theory, according to [9] when w/t is around 40% the assumption regarding the inextensibility of the middle plane is not true, so plate deflection bigger than 40% should be re-analyzed with non-linear theory.

Another important aspect is the criteria used to predict the vibration buckling effect. The classical criteria used in dynamic buckling analysis is the Budiansky-Roth criteria, according to this, the buckling is reached when a suddenly change is produced in the plate deflection at a critical instant of time. However in this parametric analysis the considered dynamic buckling criterion is based on dimensionless maximum displacement $\widetilde{w}_{Max}$ and in this study is assumed the plate buckles for $\widetilde{w} > 1$.

Finally, the most representative curves for vibration buckling show dynamic load factor DLF versus load period ratio nT.

$$DLF = N^{db}_{Max}/N^{sb} \qquad 2.6$$

Where N^{db}_{Max} is the dynamic buckling load and N^{sb} the static buckling load calculated in section 2.1.

The next figures show DLF curves for different boundary conditions SSSS, SSRR, CCRR, equal initial deformation magnitude $\widetilde{w}_0^{Max} = 0.2$ and equal initial deformation shape X_5, Y_1.

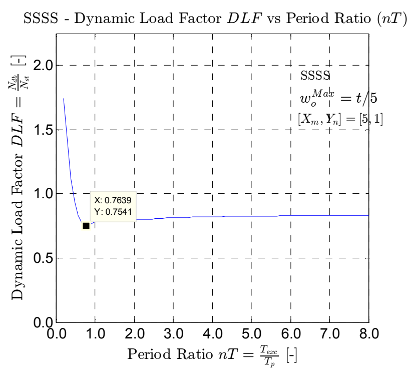

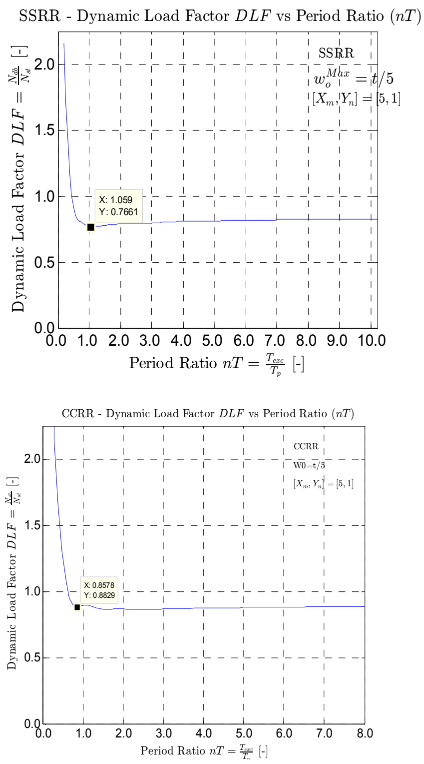

Figure 7: Dynamic Load Factor DLF versus period ratio n_T

All figures show as for short periods the DLF reach values higher than 1 therefore the plate would withstand without buckling higher compression loads. For loads periods close to natural period, the DLF reach the minimum value, whereas for large load periods the DLF tends to one.

The typical spectrum axial loads in aircrafts structures, i.e. a stiffened composite panel, has frequencies inputs below 10 Hz even lower, so we normally have period ratio n_T bigger than 150 typical. So the typical DLF are close to one in typical aerospace structures, however the analysis of a typical stiffened panel, from the dynamic point of view, is very sensitive to initial imperfections and the analysis should be reconsidered with non linear theory and a most exhaustive analysis taking into account the practical imperfections found.

3 Validation of Results

The validation of the previous results obtained by the approximated Ritz method is done in two ways; first, comparing them with a specific analytical solution and second, comparing them with a finite element analysis of a rotationally restrained orthotropic plate.

3.1 Analytical Solution of a Static Buckling SSRR

The available analytical solution for a rotationally restrained orthotropic plate RROP considers a uniform axial load, simply supported loaded edge and rotationally restrained unloaded edge, it means SSRR case. The next figure shows a scheme:

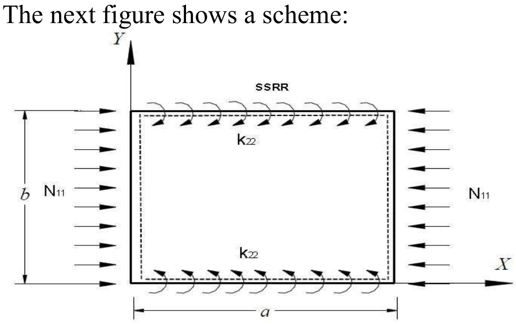

Figure 8: SS loaded edges and RR unloaded edges

3.1.1 Newtonian Mechanics Equation

The equilibrium differential equation for buckling of a RROP and uniform axial load was reached by Whitney 1987 and can be expressed using the dimensionless parameters defined in equation 1.10.

$$\alpha^{-2}\frac{\partial^4 w}{\partial \tilde{x}^4} + \alpha^2\frac{\partial^4 w}{\partial \tilde{y}^4} + 2\eta\frac{\partial^4 w}{\partial \tilde{x}^2\,\partial \tilde{y}^2} + \pi^2\tilde{N}_{11}\frac{\partial^2 w}{\partial \tilde{x}^2} = 0 \qquad 3.1$$

Where α = aspect ratio, η = flexure stiffness parameter, w = out-plane displacement and N_{11} = uniform axial load

3.1.2 Boundary Conditions

The boundary conditions of the structural situation shown in Figure 8 can be expressed as simply supported in axis $x = 0$ and $x = 1$ and rotationally restrained on axis $y = 0$ and $y = 1$.

$$w(0,y) = 0;\ \ w(1,y) = 0;\ \ w(x,0) = 0; w(x,1) = 0$$
$$M_{11_{x=0||a}} = 0\,;\ \ M_{22} = \left(\frac{\partial^2 w}{\partial \tilde{y}^2}\right)_{y=0||1} = \mp\tilde{k}_{22}\left(\frac{\partial w}{\partial \tilde{y}}\right)_{y=0||1} \qquad 3.2$$

Where, $\tilde{k}_{22}$ is the equivalent dimensionless rotational stiffness in axis $\tilde{y} = 0$ and $y = 1$.

3.1.3 Exact Solution

The exact solution of the equation 3.1 was reached by Bleich on 1952 [2] and for symmetric boundary conditions from axis $\tilde{y} = 1/2$ can be expressed as:

$$w(\tilde{x},\tilde{y}) = \sin(m\pi\tilde{x})[C_1\cosh(k_1 m\pi\tilde{y}) + C_3\cos(k_2 m\pi\tilde{y})] \qquad 3.3$$

Where k_1 and k_2 are parameters defined as:

$$k_{1,2} = \frac{1}{\alpha}\sqrt{\sqrt{\eta^2 + \tilde{N}_{11}\left(\frac{\alpha}{m}\right)^2 - 1} \pm \eta} \qquad 3.4$$

Applying the boundary conditions system of 2 equations is reached and the the static load factor $\tilde{N}_{11}$ is achieved doing the determinant equals to zero and solving the resultant transcendental equation following:

$$k_1\tanh\left(\frac{k_1 m\pi}{2}\right) + k_2\tan\left(\frac{k_2 m\pi}{2}\right) + \frac{m\pi}{\tilde{k}_{22}}(k_1^2 + k_2^2) = 0 \qquad 3.5$$

The solution of this transcendental equation has been achieved using a own Matlab code based on Newton Raphson numerical method with parametric initial value.

3.1.4 Static Buckling Comparison

The exact buckling load factor $\tilde{N}_{11}$results are omitted due to its similarity with Ritz method results shown in Figure 2. The results comparison has been done plotting the relative error $\delta\tilde{N}_{11}$ for the same range specified in Figure 2 with the exception of $\tilde{k}_{11} = \infty$ for which there is not analytical solution. Finally the relative error has been defined as follows:

$$\delta\tilde{N}_{11} = \frac{|\tilde{N}_{11}^{\mathrm{Exact}} - \tilde{N}_{11}^{\mathrm{Ritz}}|}{\tilde{N}_{11}^{\mathrm{Exact}}} \qquad 3.6$$

The next figure shows the relative error $\delta\tilde{N}_{11}$between Ritz method and exact method results for different number of assumed functions:

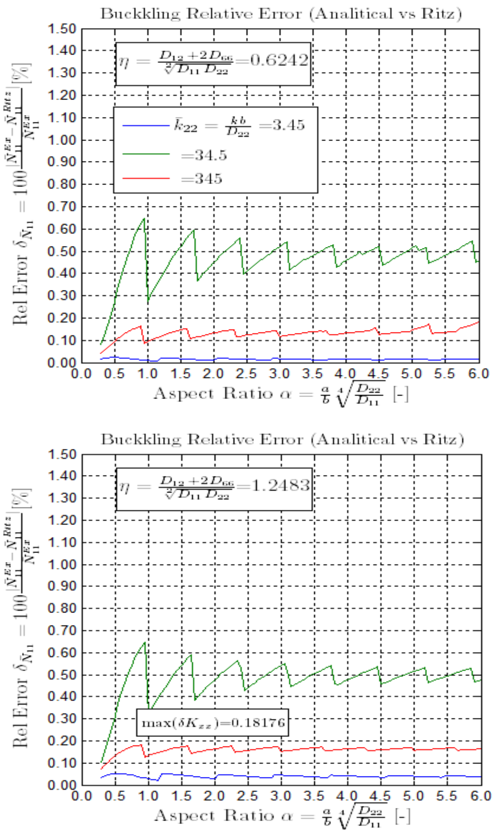

Figure 9 Error between Exact and Ritz Method

3.1.5 Modal Analysis Comparison

According to [10] an isotropic plate with no in plane compression load has a non dimensional angular frequency:

$$\tilde{\omega}_{th1st} = \frac{\pi^2}{\alpha}\sqrt{\frac{K}{N}} \qquad 3.7$$

Where K is a function of aspect ratio α and N is a constant. Both parameters depends the boundary conditions analyzed. Below are shown for CCCC and SSSS.

CCCC:: $$K = 12 + 8\alpha^2 + 12\alpha^4$$ N=2.25

SSSS: $$K = 0.25 + 0.50\alpha^2 + 0.25\alpha^4$$ N=0.25

Figure 10 shows the comparison between the Ritz method used and the corresponding theoretical analysis. It can be seen the perfect agreement for SSSS however a little deviation of no more than 3.25% depending the aspect ratio is produced for CCCC boundary conditions.

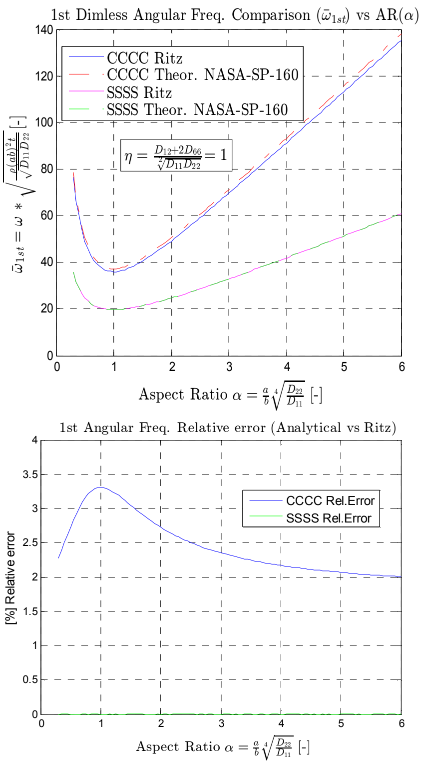

Figure 10 Comparison between Exact and Ritz Method for SSSS and CCCC

Acknowledgments

The research leading to these results has partially received funding from the European Union's Seventh Framework Programme [FP7/2007-2013] under grant agreement "DAEDALOS - Dynamics in Aircraft Engineering Design and Analysis for Light Optimized Structures" No. 266411.

References

[1] Clebsch,A. Theorie de lÉlasticite des Corps Solids, Avec des Notes Extendues de Saint-Venant, Dunoid, Paris, pp. 687-706 (1883).
[2] Bleich F. , *Buckling strength of metal strctures*, New York 1952
[3] Kollar L., *Mechanics of composites* structures, Cambridge 2003
[4] Withney J.M., *Structural analysis of laminated anisotropic plates*, Lancaster 1987
[5] Mittlested C. and Beerhorst M., *Closed-form buckling analysis of omega stringer stiffened composite panels,* Germany 2010
[6] Qiao P and Wanf J., *Local buckling of FRP shapes by discrete plate analysis*, 2001
[7] Shan L., *Explicit buckling analysis of FRP composite structures*, Washington 2007
[8] Barbero, E J. and Raftoyiannis , *Local buckling of FRP beams and columns*, 1993
[9] Timoshenko P and Gere J., *Theory of elastic stability* – Stanford 1936
[10] NASA-SP-160, A.W.Leissa, Vibration of Plates

4:th CEAS Air & Space Conference
FTF Congress: Flygteknik 2013

Variable Fidelity Loads Process in a Multidisciplinary Aircraft Design Environment

R. Liepelt, G. P. Chiozzotto, H. Schmidt
Institute of Aeroelasticity, German Aerospace Center (DLR), Göttingen, Germany

Keywords: *Aircraft Loads. Multidisciplinary Design. Aeroelasticity. Finite Element Model.*

Abstract

Multidisciplinary design is transforming the way aircraft design is performed. New challenges include the integration of several disciplines with increasing complexity of methods and processes in design frameworks. Loads and aeroelastic effects strongly influence these design tasks in early design stages. This paper presents the development of a two-level loads process integrated into a multidisciplinary design environment. The process includes the option for a fast and simplified rigid loads analysis, as well as a more complex process with a fully parameterized aeroelastic model. Case studies are presented for a conventional 150 passenger aircraft and an alternative forward swept laminar flow concept.

Nomenclature

α_{l0}	Zero-lift angle
$\alpha_{l0,\delta}$	Zero-lift angle derivative due to control surface deflection
c_{m0}	Moment coefficient about the aerodynamic centre
$c_{m,\delta}$	Moment coefficient due to control surface deflection
$\Lambda_{50\%}$	wing sweep at the 50% chord line
η	Dimensionless coordinate in spanwise direction
ξ	Dimensionless coordinate in x direction
CG	Centre of gravity
EI	Bending stiffness
FEM	Finite element method
LC	Load case
M	Bending moment
MLM	Maximum landing mass
MTOM	Maximum take-off mass
MZFM	Maximum zero fuel mass
OEM	Operational empty mass
S	Shear force
T	Torsion
t/c	Profile thickness ratio
$k_{t/c}$	Profile thickness ratio factor
V_A	Manoeuvre speed
V_C, M_C	Cruise speed
V_D, M_D	Dive speed
VEAS	Velocity, equivalent air speed
Vs	Stall speed

1 Introduction

One of the current main efforts in the development of more efficient aircraft is the integration of different disciplines in collaborative design activities. To increase the fidelity of aircraft preliminary design, the use of physics-based methods is of great importance.

In this context, aircraft loads and aeroelasticity play a critical role, determining reliable and not too conservative loads as early as possible in the design. The capability of handling several load cases with different mass configurations and flight points is also essential to correctly describe the expected loads on the aircraft. Design tasks such as trade studies and optimization require reliable parameterized processes and models.

In this paper, a fully automated process for the estimation of aircraft flight loads in a multidisciplinary design framework being developed at the DLR is described. Design space „zoom" functionalities [1] are provided through the combination of simplified methods capable of handling thousands of load cases in a few seconds and more advanced methods including aeroelastic models and structural optimization. To demonstrate the capabilities of the prescribed loads process two design concept studies and sensitivity analyses will be presented.

An example of a multidisciplinary design framework into which the presented loads process is integrated is depicted in Fig. 1. The framework includes other disciplinary analysis tools such as aerodynamics, mass estimation, propulsion and flight performance.

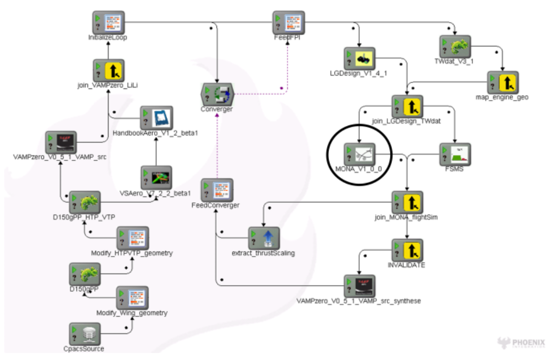

Fig. 1 Multidisciplinary design framework in ModelCenter® with the presented tool position circled.

One of the enablers for the integration in flexible frameworks is the use of a common language for aircraft description. For this purpose, the CPACS data format (Common Parametric Aircraft Configuration Schema) [2] has been developed at the DLR. It is an xml-based aircraft parametric representation with auxiliary tools for data processing and is currently integrated into the ModelCenter® design software. The presented loads process gathers the necessary data from the CPACS input, which include geometry, masses and operational characteristics of the aircraft, returning loads at the wings and fuselage for further use. Load Reference Axes (LRA) are defined in CPACS for each component, containing the geometric definitions where loads models are built and results are calculated. The load case definitions and results are stored in CPACS, as depicted in Fig. 2. Through this unified language, loads results can be exchanged between different tools.

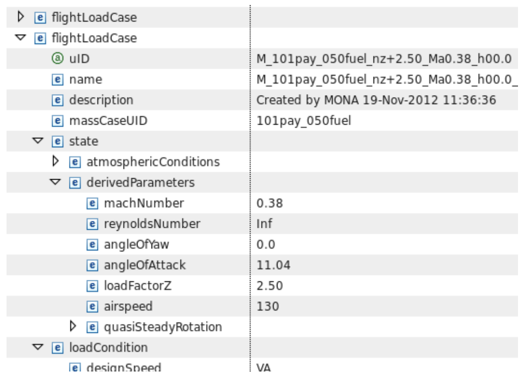

Fig. 2 Load case description in CPACS.

2 Loads Process: Two-Level Approach

A two-level fidelity approach is used for the loads analysis. The first level consists of a rigid aircraft analysis for the first design loads, stiffness and mass estimations. The second level involves an FEM based method for aero-structural coupled analysis. Both levels are integrated in the same tool and can be chosen according to the design task. The developed loads process includes: model generation, load case definition and selection, aircraft trim, component loads calculation as well as stiffness and mass estimation. An overview of the loads process and its two level approach is illustrated in Fig. 3, at which the first level procedure can

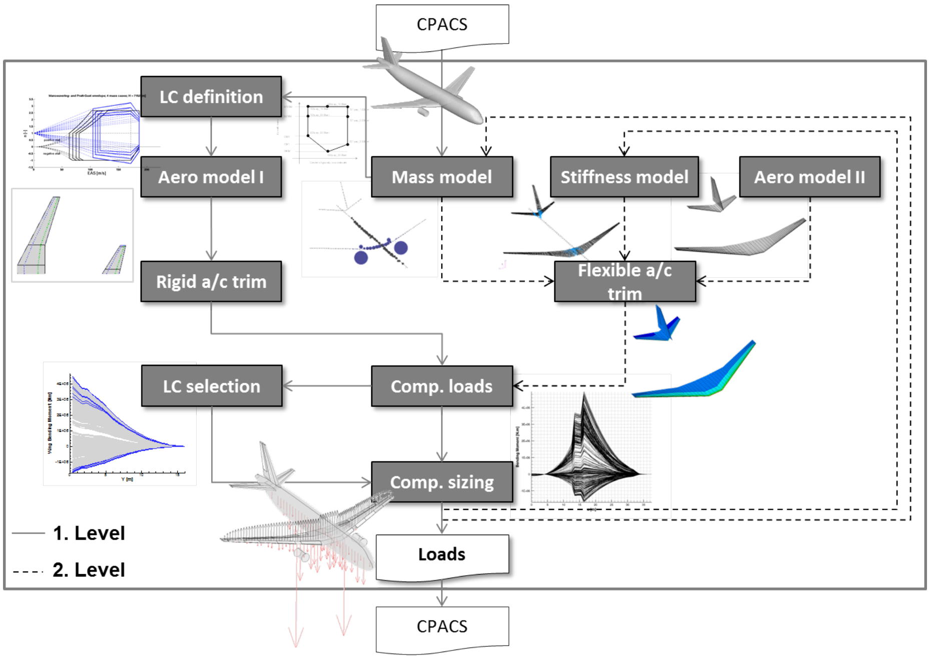

Fig. 3 Overview of the developed loads process.

be followed through the solid lines, the second level cycle by the dashed lines.

The next sections include the description of each process step and methods employed.

2.1 Mass Model

Two main tasks are accomplished in the mass model step of the process: distribution of estimated point masses and definition of mass cases for analysis.

In the multidisciplinary design framework, other tools perform the estimation of the aircraft masses and update the results in the CPACS data as point masses. For the loads estimation, it is necessary to have distributed masses to account correctly for the inertia effects. Each given point mass is then distributed as lumped masses over the geometry according to four methods:

1. Exposed area: point mass distributed over the component (wing, fuselage or control surface) as lumped elements with mass proportional to the exposed area;
2. Volume: mass distributed as lumped elements with mass proportional to the enclosed volume, e.g. fuel;
3. Uniform distribution: mass distributed as lumped elements with constant mass over the component, e.g. passengers;
4. Concentrated mass: no distribution, the mass is included as one single lumped mass at the required position, e.g. engines, landing gears.

A mass model with distributed lumped masses is shown in Fig. 4.

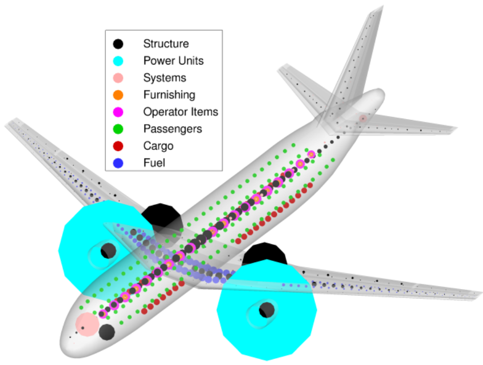

Fig. 4 Lumped masses model.

After the mass distribution, ten mass cases are generated to cover critical loading conditions according to the weight and balance diagram, as shown in Fig. 5 and described in

Table 1. To achieve the CG limits defined, an optimization algorithm modifies the payload and fuel lumped masses densities within defined restrictions.

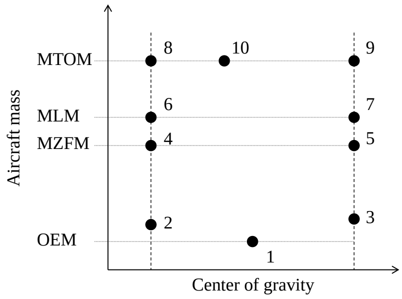

Fig. 5 Mass cases and weight and balance diagram.

Table 1. Mass cases description.

Nr	Description
1	OEM
2	OEM + Min. Payload @ fwd CG
3	OEM + Min. Payload @ aft CG
4	OEM + Max. Payload (MZFM) @ fwd CG
5	OEM + Max. Payload (MZFM) @ aft CG
6	OEM + Max. Payload + Fuel (MLM) @ fwd CG
7	OEM + Max. Payload + Fuel (MLM) @ aft CG
8	OEM + Max. Payload + Fuel (MTOM) @ fwd CG
9	OEM + Max. Payload + Fuel (MTOM) @ aft CG
10	OEM + Payload + Max. Fuel (MTOM)

A mass model is generated for each mass case in MSC.Nastran format. The distributed masses are condensed to the nearest load reference axes (LRA) points.

2.2 Load Cases Definition

In the current implementation, the load cases considered include symmetric balanced manoeuvre, following the aviation certifications [3], and vertical discrete gust cases, defined in the former JAR requirements [4]. The definition of load cases starts with the calculation of the necessary structural design speeds and flight envelope according to the CS25.335.

The cruise speed (V_C, M_C) is defined according to aircraft design requirements, all other relevant design speeds are calculated. Aerodynamic data, including compressibility effects is used in the definition of the stall (V_S) and manoeuvre speed (V_A). The design dive speed (V_C, M_D) is computed with a margin of 0.07 Mach to the cruise speed M_C.

For each combination of mass case and altitude, a total of seven manoeuvre and six gust cases are defined, as shown in Fig. 6. The gust cases are simplified with the Pratt [5] method for a fast assessment of gust effects.

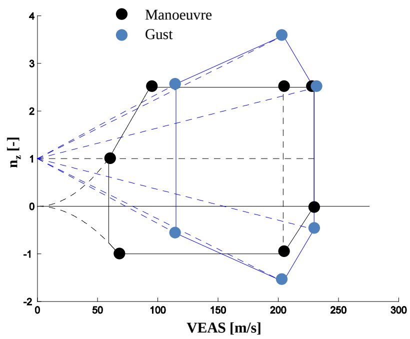

Fig. 6 Flight load cases defined for one altitude and one mass case.

2.3 Rigid Loads

To initiate the loads process and to provide fast loads estimations, an adapted vortex lattice method (VLM) is used to trim the aircraft at each load case and to provide the aerodynamic loads. The condensed mass models are used in the inertia static loads computation.

The aerodynamic method employed is a combination of planform (horseshoe vortices) and two-dimensional airfoil aerodynamics, as shown in Fig. 7.

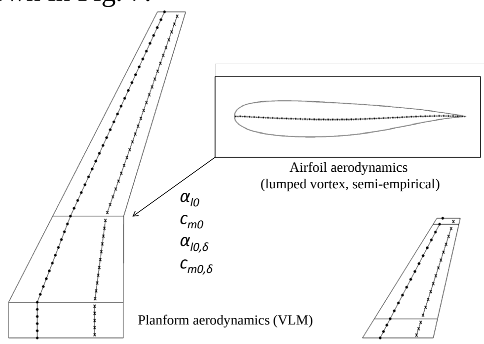

Fig. 7 Fast aerodynamic model.

Horseshoe vortices are placed at the quarter chord lines of all wings and are used to calculate the aerodynamic influence coefficients matrix (AIC matrix) at the three-quarter chord control points [6]. No panels are placed in the chord direction (lifting line simplification [7]), the airfoil aerodynamics are accounted for through the airfoil zero-lift angle, α_{l0}; moment coefficient about the aerodynamic centre, c_{m0} and their derivatives with respect to control surface deflection: $\alpha_{l0,\delta}$ and $c_{m,\delta}$. Airfoil zero-lift angle and moment coefficients are calculated with the camberline lumped-vortex method from Katz and Plotkin [8], whilst the control surface derivatives are calculated with the semi-empirical method from Phillips [9].

A system of linear equations is formed with the angle of attack and elevator deflection as unknowns and all load cases definitions in the right–hand side (trim equations), which can be solved in one step for all loads cases.

The internal loads (cut loads) at the wings and fuselage load reference axes are calculated and either one or two-dimensional loads envelopes [10] are used to filter the critical load cases for further analysis.

2.4 Preliminary Stiffness Estimation

A simplified estimation of wings and fuselages stiffness and masses is performed with an analytical cross-section sizing method valid within the limitations of beam theory [11].

The wing cross-sections geometry is idealized as a box with skins resisting bending and torsion, stiffened with stringers resisting only bending and webs resisting shear and torsional loads. The stringers are idealized as a fraction of skin area. An approximate shear flow distribution is assumed for multi-cell wings.

A circular cross-section is used to represent the fuselage with the same skin/stringer idealization of the wing. Constant thickness is assumed along the whole fuselage cross-section. The fuselage direct loads are calculated with and without the cabin pressure differential, CS25.365(a), including an extra load case according to the CS25.365(d).

All structural allowables are based on material properties and buckling constraints. The material properties are defined in CPACS and include: ultimate, yield and fatigue strengths. Since all load cases computed are limit load cases, the ultimate strength is divided by the safety factor and the fatigue allowable is adapted to limit loading conditions. Buckling is accounted for with the assumption of simultaneous local and global buckling [11, 12] and is also divided by the safety factor. The non-linear tangent modulus of the material is represented by the Ramberg-Osgood equation [13] and is used in the buckling allowable estimation.

The skins and webs are sized to achieve a fully stressed condition in the most critical loading case. Stringers are sized with the equivalent area factor to the skin area. Analytical bending and torsional stiffness are then calculated at each section.

2.5 Models for Aeroelastic Analysis

To increase the fidelity of the loads analysis and account for flexible aerodynamic- structural coupled behaviour, the second level loop of the process can additionally be started, as illustrated by the dashed lines in Fig. 3. The flexible process includes a parameterized FEM model generation, an aerodynamic model based on the doublet-lattice method (DLM) [14] and the flexible aircraft trim analysis with MSC.Nastran [15].

For the model generation an in-house fully parametric model generator ModGen [16, 17] is used, which includes the generation of the FEM and aerodynamic model, as well as the aero-structural coupling model. It also enables an optimization model to be defined for structural sizing.

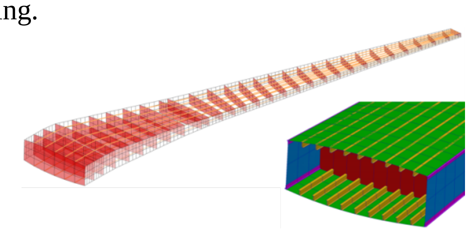

Fig. 8 FEM wingbox model representation.

As inputs for the structural model, either the former analytical sizing results or pre-established structural data available in CPACS can be used. The wings are modelled as box models representing the load carrying wing structure, defined by spar, ribs, skins and stringer. The skins, ribs and spar webs are modelled as shell elements, while stringers, spar caps and other stiffeners are beam elements, as shown in Fig. 8. The fuselage is modelled with beams, the properties are derived from the first level preliminary design concept. The model is then assembled to a global FEM.

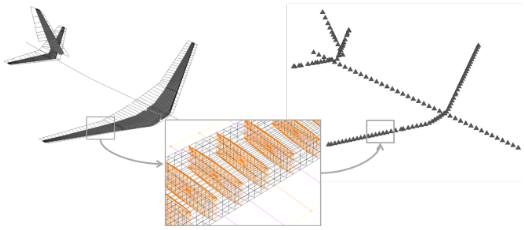

Fig. 9 FEM model reduction.

To reduce the computing time of the loads, a model reduction of the stiffness box model and the mass model is performed at the load reference axis points (Fig. 9). The aircraft model obtained is also one of the outputs of the tool and can be used for structural dynamic analysis and aeroelastic assessment. A representation of the aeroelastic models is given in Fig. 10.

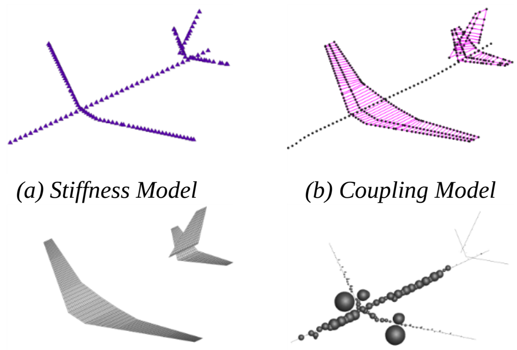

(a) Stiffness Model *(b) Coupling Model*

(c) Aerodynamic Model *(d) Mass Model*

Fig. 10 Aeroelastic Models.

2.6 Elastic Loads and Structural Optimization

After the set-up of the parameterized structural, aerodynamic and optimisation model of the second level approach, the loads and sizing process is performed, which is an iterative process, repeated until convergence of the mass is achieved. The elastic trim calculations are accomplished with MSC.Nastran, obtaining the nodal and internal loads at the components.

The structural sizing method can be chosen between a preliminary cross section sizing approach (PCS), as described in section 2.4, a fully stressed design (FSD) or the optimisation method, using the capabilities of MSC.Nastran [18]. The beam elements, like the stringer and spar caps are sized with PCS. If chosen, the skins, ribs and spar webs are sized with FSD or the optimization method, to achieve minimum weight.

Usually only the selected load cases are considered in the second level analysis. Since the process is running inside a framework for aircraft preliminary design, computation speed is of great importance. An analysis with the fast method is accomplished in the order of seconds, while the FEM based analysis is finished in the order of minutes up to one or two hours depending on the complexity and number of iterations.

3 Design Studies

As application of the prescribed loads process a design study between two different aircraft concepts for similar requirements and a sensitivity analysis are presented. For the stiffness estimation, the structural sizing is realised with the analytical cross section sizing combined with the MSC.Nastran Sol200 optimisation for the design analysis and FSD for the design sensitivity studies.

3.1 Configuration Study

Two different aircraft configurations with similar operational requirements are evaluated with the developed process. Both aircraft are designed for a typical short to mid-range 150 passengers design mission and are conceived as typical metal construction, using the same materials. The loads of the different fidelity approaches are compared as well as the influence of the aircraft configuration.

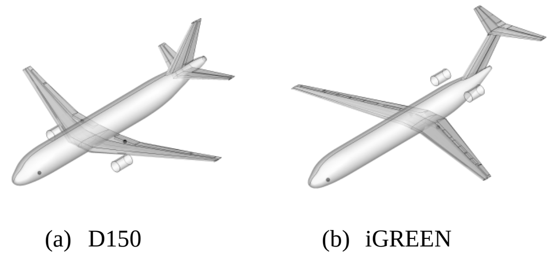

Fig. 11 Aircraft concepts used in the configuration study.

One configuration is conventional with an aft swept wing, conventional tail and engines mounted under the wing, as depicted in Fig. 11a. This configuration was developed in the DLR project VAMP and is called D150 [2].

Table 2 Extract of configuration study aircraft data

	D150	iGREEN
Wing area	122 m^2	132 m^2
Wing aspect ratio	9.4	9.7
Wing sweep 1/4c	24°	-23°
Wing span	34 m	35.8 m
Fuselage length	37.6 m	37.6 m
Fuselage width	3.95 m	3.95 m
Payload	19200 kg	19250 kg
MTOW	73000 kg	73365 kg
MOEM	40640 kg	43712 kg
M_{cruise}	0.78	0.78

The second concept is primarily designed to reduce fuel consumption. Besides others, this should be achieved by an aerodynamic design of the wing geometry in order to preserve laminar flow condition. This is achieved by a laminar flow wing design with optimized airfoils, forward sweep and rear mounted engines, for a clean wing configuration. Horizontal and vertical tailplanes are arranged in a T-tail format. The configuration was developed in the DLR project LamAiR [19, 20], and was used for aeroelastic analysis within the DLR project iGREEN [21]. As follows, this configuration is named iGREEN and is shown in Fig. 11b.

From the aeroelastic point of view such a configuration holds some challenges. The forward swept wing is prone to divergence. Further the wing twist deformation under load normally leads to higher maneuver and gust loads, which have to be adressed in the dimensioning and analyses process.

An excerpt of the dimensions and the requirements of the transport mission for both concepts is given in Table 2. A representation of the applied aeroelastic models is presented in Fig. 12 and Fig. 13.

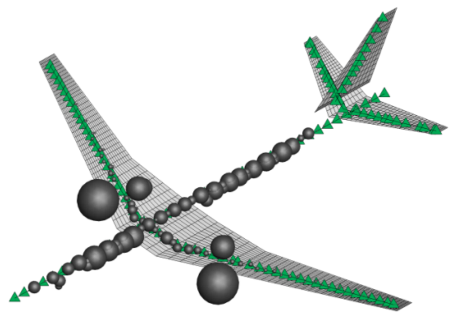

Fig. 12 Aeroelastic Models D150: Stiffness (green) and Mass (grey) Model plotted over the Aerodynamic Model.

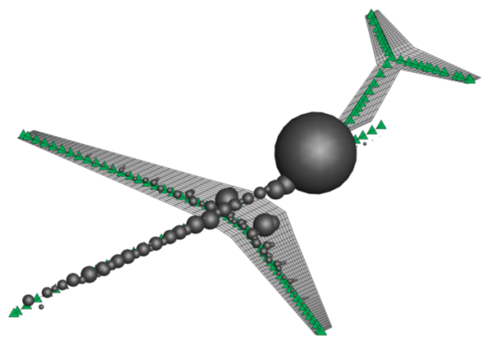

Fig. 13 Aeroelastic Models iGREEN: Stiffness (green) and Mass (grey) Model plotted over the Aerodynamic Model.

The FEM loads and sizing process shows good convergence behaviour for the D150, since the structural masses converge after four iteration steps (Fig. 14).

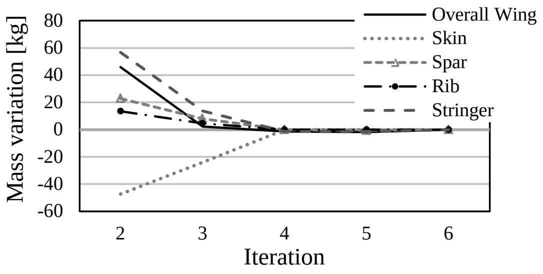

Fig. 14 Iteration overview of D150.

The iGREEN loads and sizing process display a different convergence behaviour. The examination of the resulting loads (or equivalently the structure masses) of each iteration step demonstrate an alternation between high loads, resulting in a stiff structure, and low loads, resulting in a flexible structure, which declines after seven iteration steps (see Fig. 15).

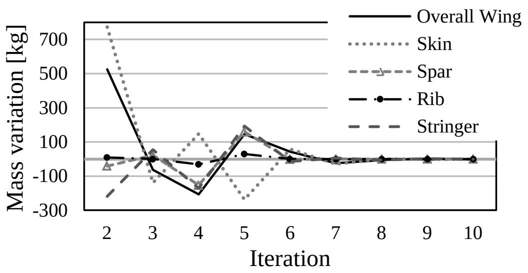

Fig. 15 Iteration overview of iGREEN.

The internal wing loads envelopes obtained for both configurations using the first and the second level approaches are presented in Fig. 16 to Fig. 18. Illustrated are the envelopes from the wing fuselage attachment (η=0.1) to the wing tip (η=1.0). It can be seen that both methods predict higher shear forces and bending moments for the iGREEN configuration. Even though this concept has a lower absolute wing sweep (lower wing box structural span), it has a higher taper ratio, slightly higher wingspan and has no inertia relief due to the engines. All these rigid aircraft effects combine and cause the higher loading identified with both methods. This is an important conclusion, showing a great impact on the loads even without consideration of typical flexibility effects of forward swept configurations. Analysing the differences between the two fidelity methods, one can then identify the flexibility effects. Shear forces are lower next to the wing tip for the elastic D150 results and higher for the elastic iGREEN results. This is caused by the differences in lift distribution due to the elastic deformation and has a significant impact on the bending moment loads.

The internal torsion loads are quite different for both configurations. The D150 has an approximately symmetric distribution of positive and negative torsion moments and the iGREEN has higher negative torsion loads than positive. This is caused by the structural arrangement and airfoil aerodynamics. The iGREEN wingbox is placed closer to the wing leading edge due to the bigger flaps required and to reduce the distance between the wingbox shear centre and the local aerodynamic centre. This in turn reduces the amount of torsional moment caused by the lift. Most of the torsional moment is therefore caused by the airfoil pitching moment, which is higher for the iGREEN airfoil.

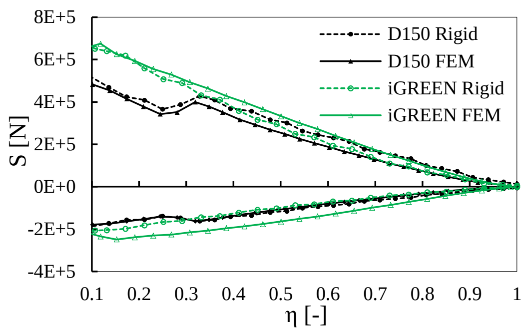

Fig. 16 Wing shear force envelope of D150 and iGREEN.

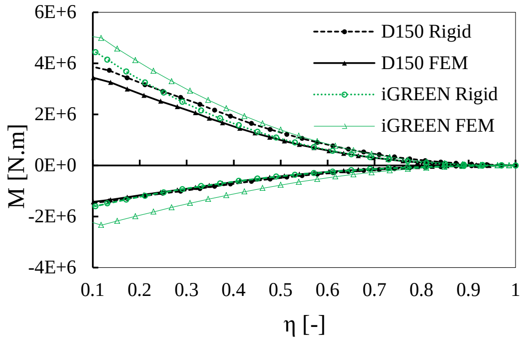

Fig. 17 Wing bending moment envelope of D150 and iGREEN.

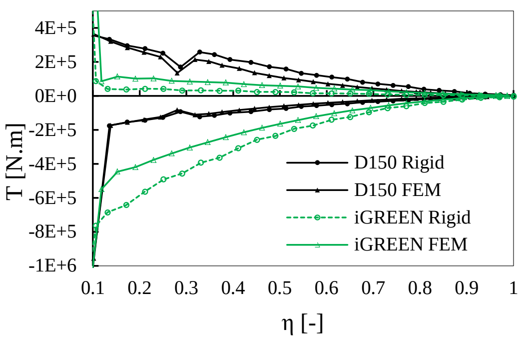

Fig. 18 Wing torsion moment envelope of D150 and iGREEN.

The fuselage bending moment distribution is shown in Fig. 19. Due to the forward sweep, the iGREEN has the wing intersection with the fuselage further aft, which increases the bending moment peak. The rear engines also increase the loads in the rear fuselage portion.

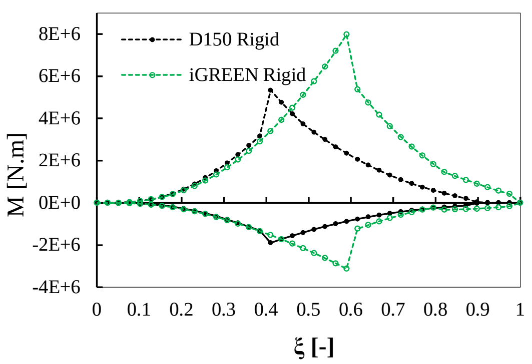

Fig. 19 Fuselage moment envelope of D150 and iGREEN.

The relative wing masses obtained are shown in Fig. 20, compared to the D150 as reference. It can be seen that the iGREEN has considerably higher wing mass for rigid and elastic calculations, the mass obtained with the elastic calculations being even higher. These differences illustrate the conclusion of the previous loads discussion.

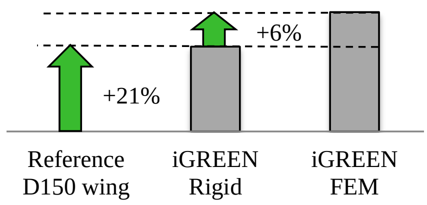

Fig. 20 Relative wing masse comparison.

3.2 Sensitivity Analysis

To investigate the capabilities of the loads process integrated to a multidisciplinary design framework, a sensitivity analysis of the iGREEN configuration is performed. The aim is to check the reliability and robustness of the rigid and elastic loads processes in the analysis of parametric variations of an initial aircraft.

A framework was built in ModelCenter® including geometry pre-processors to perform the necessary changes to the CPACS data.

Two sensitivity studies were conducted: wing mass sensitivity to taper ratio variation and trade-off between sweep ($\Lambda_{50\%}$) and airfoil thickness (*t/c*) effects on the wing mass. The parameterization used also modifies the wing attachment position to the fuselage in order to keep the aircraft aerodynamic centre approximately in the same position.

The taper ratio sensitivity analysis results are shown in Fig. 21. As expected, wings with lower taper values are lighter, which can be explained due to structural sizing constraints, thus more inertia is available to resist the loadings next to the root, and it has to resist lower aerodynamic loading at the tip. This effect is shown by both processes, rigid and elastic. It is also possible to identify the clear offset between the rigid and elastic results, as expected for the forward swept configuration. A third effect is the higher sensitivity of the wing mass in the elastic calculations in comparison to the rigid ones. For rigid aerodynamics, lower taper values results in less lift close to the wing tip. This effect becomes more pronounced for an elastic wing since the deformation due to the aerodynamic loads is also reduced.

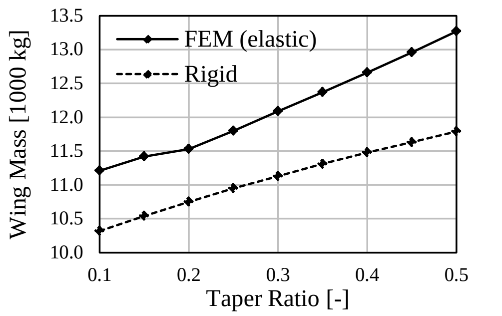

Fig. 21. Wing mass sensitivity to taper ratio variations for the iGREEN configuration. Fast (rigid) and FEM loads processes.

The trade-off results between wing sweep and airfoil thickness are shown in Fig. 22. For this analysis the wing sweep at 50% of the chord length was varied ±20% around the iGREEN design point [20]. All wing airfoils *t/c* were also varied ±20% around the design point. In the carpet plot, the multiplying factor ($k_{t/c}$) applied to the airfoils *t/c* is shown (e.g. 0.8 lower and 1.2 higher thickness).

An offset between the rigid and elastic processes is present, as expected. The offset reduces for lower wing sweep angles and higher airfoil thickness as seen in the lower right corner of the carpet plot.

Reducing the airfoil thickness increases the wing mass due to structural limitations, as seen by the similar behaviours of the rigid and elastic sensitivities. It also increases the wing flexibility and consequently the static loads for the forward swept wing as seen by the higher sensitivity of the elastic results.

The wing sweep effects include a higher wingbox structural span (higher mass) and lower aerodynamic rigid loading at the wingtip for higher forward sweep angles (lower mass). These opposing effects seem to cancel each other in the rigid results, as seen by the low sensitivities. When elastic effects are included, the aerodynamic loading increases at the wing tip (higher mass) due to the higher deformation. This effect can be seen by the higher mass sensitivity of the elastic results.

Divergence problems appear already inside the operational envelope for very low airfoil thickness and high negative sweep angles, as seen in the upper left corner of the carpet plot elastic results. The process needs a considerable higher number of iterations until convergence is achieved. For the lowest thickness and highest sweep, convergence was not achieved in acceptable time during the sensitivity study.

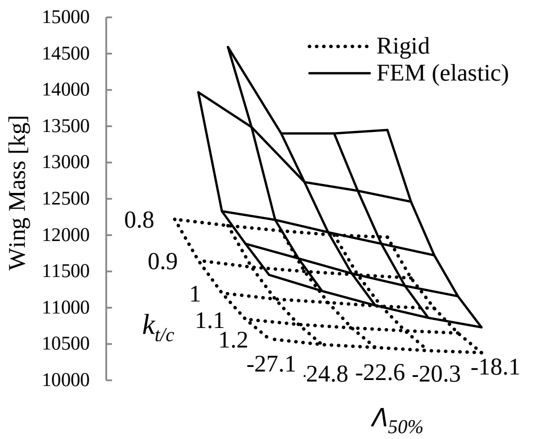

Fig. 22. Wing mass sensitivity to airfoil thickness and wing sweep angle variations for the iGREEN configuration. Fast (rigid) and FEM loads processes.

4 Conclusion

An integrated and automated loads process was presented for multidisciplinary analysis and design. The complexity of creating an automated loads process was assessed and a two level approach was proposed. The capabilities as a tool to support design decisions were proven with the analysis of two aircraft concepts and sensitivity studies of key design parameters. The importance of considering the disciplines of loads and aeroelastics early in design is emphasized by the results and the discussion presented.

References

[1] A. Keane and P. Nair, *Computational Approaches for Aerospace Design: The Pursuit of Excellence*. Wiley, August 2005

[2] T. Zill, D. Böhnke, and B. Nagel, "Preliminary aircraft design in a collaborative multidisciplinary design environment," in *AIAA Aviation Technology, Integration, and Operations (ATIO)*, Virginia Beach, USA, 2011.

[3] *Certification Specifications and Acceptable Means of Compliance for Large Aeroplanes CS25*, 12th ed., European Aviation Safety Agency, July 2012.

[4] *Joint Aviation Requirements JAR-25 Large Aircraft*, Joint Aviation Authorities, 5. October 1989.

[5] K. Pratt, *A Revised Formula for the Calculation of Gust Loads*, ser. National Advisory Committee for Aeronautics technical note, U. S. N. A. C. for Aeronautics, Ed. National Advisory Committee for Aeronautics, 1953.

[6] R. Bisplinghoff, H. Ashley, and R. Halfman, *Aeroelasticity*, ser. Dover Books on Aeronautical Engineering Series. Dover Publications, 1996.

[7] W. F. Phillips and D. O. Snyder, "Modern application of prandtl's classic lifting-line theory," *Journal of Aircraft*, vol. 37, no. 4, pp. 662–670, July–August 2000.

[8] J. Katz and A. Plotkin, *Low-Speed Aerodynamics*, ser. Cambridge Aerospace Series. Cambridge University Press, 2001

[9] W. Phillips, *Mechanics of Flight*, ser. Aerospace/Engineering. Wiley, 2004

[10] J. R. Wright and J. E. Cooper, *Introduction to Aircraft Aeroelasticity and Loads*. Wiley, 2007.

[11] D. Howe, *Aircraft loading and structural layout*, ser. Aerospace series. Professional Engineering Publishing, 2004.

[12] B. Budiansky, "On the minimum weights of compression structures," *International Journal of Solids and Structures*, vol. 36, no. 24, pp. 3677 – 3708, 1999.

[13] W. Ramberg and W. R. Osgood, "Description of stress-strain curves by three parameters," Tech. Rep. NACA TN-902, 1943.

[14] W. P. Rodden, P. F. Taylor, and S. C. M. Jr., "Further refinements of the subsonic doublet-lattice method," *Journal of Aircraft*, vol. Vol. 35, No. 5, pp. 720–727, 1998.

[15] W. Rodden and E. Johnson, *MSC/NASTRAN Aeroelastic Analysis: User's Guide, Version 68*. MacNeal-Schwendler Corporation, 1994.

[16] T. Klimmek, "Parameterization of topology and geometry for the multidisciplinary optimization of wing structures," in *CEAS*, 2009.

[17] T. Klimmek, "Development of a structural model of the CRM configuration for aeroelastic and loads analysis," in *IFASD 2013 - 16th International Forum on Aeroelasticity and Structural Dynamics*, 24 - 27 June 2013.

[18] G. Moore and M.-S. Corporation, *MSC/NASTRAN 2012 Design Sensitivity and Optimization User's Guide*. MacNeal-Schwendler Corporation, 2012.

[19] M. Kruse, T. Wunderlich, and L. Heinrich, "A conceptual study of a transonic NLF transport aircraft with forward swept wings," in *30th AIAA Applied Aerodynamics Conference*. AIAA, 25. - 28. Jun 2012.

[20] A. Seitz, M. Kruse, T. Wunderlich, J. Bold, and L. Heinrich, "The dlr project lamair: Design of a NLF forward swept wing for short and medium range transport application," in *29th AIAA Applied Aerodynamics Conference 2011, Honolulu, Hawaii*, no. 3526. AIAA, 27 - 30 June 2011.

[21] W. R. Krueger, T. Klimmek, R. Liepelt, H. Schmidt, S. Waitz, and S. Cumnuantip, "Design and aeroelastic assessment of a forward swept wing aircraft," in *IFASD 2013 - 16th International Forum on Aeroelasticity and Structural Dynamics*, 24 - 27 June 2013

A Combined Numerical and Statistical Approach to Crack Propagation Modeling and Prediction of Crack Propagation Rates

M. Rembeck and A. Sjöblom
GKN Aerospace Engine Systems Sweden, Sweden

Keywords: *Fatigue crack propagation, Crack closure*

Abstract

In order for the engineer to correctly predict the operational life of a component it is important to understand the physical background to fatigue, i.e. the growth of fatigue cracks. In the industry, the dominating models used for crack propagation analyses are based on either a pure curve fit procedure or models that intend to capture the physical phenomenon related to the crack growth. The present study attempts to make more accurate life predictions of aircraft engine components by employing a more physical approach to crack propagation modeling. In particular, the paper deals with the derivation of five parameters in the NASGRO® equation for crack growth. Four of these parameters were derived by curve fitting to experimental data and one parameter, the crack closure, was derived by means of finite element analysis. This differs from the empirical method, currently in industrial use, determining life where all five parameters are obtained from curve fitting. Both methods were evaluated and compared to experimental data for cast Inconel 718 using statistical tools. The crack closure, here assumed to be induced by plasticity, was determined by numerical simulations of fatigue crack growth of a semi-circular surface crack in a 3D domain. The objective was to obtain an unequivocal value of Newman's plane stress/strain constraint factor, α, which is directly related to the closure level. In this study experimental data of cast Inconel 718 test specimens at different temperatures, and for three R-ratios, was utilized. The numerical analysis used a kinematic multi-linear hardening constitutive model and crack propagation was modeled by releasing all nodes at the crack front after unloading in a one-node-per-one-cycle debonding scheme. Different values of the plane stress/strain constraint factor were found for each of the three R-ratios, i.e. an unequivocal value was not obtained and instead an average was used. The predicted lives were calculated by use of the established parameters in the NASGRO® equation and were compared to the actual lives observed in the experimental testing. The proposed method gave similar results as to the empirical pure curve fit method, although the models credibility is increased due to the better understanding of the crack closure phenomenon. Hence, the model can be expanded for different geometries with different crack closure levels resulting in more accurate life predictions. Consequently, the study provides a basis for further improvements of the crack propagation modeling.

1 Notations

The notations used in the paper are listed and explained in Table 1 below.

Table 1 Notations used in the paper.

Notation	*Unit*	*Description*
R	[-]	Stress ratio
T	[°C]	Temperature
K	$[\mathrm{MPa}\sqrt{\mathrm{mm}}]$	Stress intensity factor (SIF)
K_{max}	$[\mathrm{MPa}\sqrt{\mathrm{mm}}]$	Maximum SIF
K_{min}	$[\mathrm{MPa}\sqrt{\mathrm{mm}}]$	Minimum SIF
ΔK	$[\mathrm{MPa}\sqrt{\mathrm{mm}}]$	Stress intensity range
ΔK_{eff}	$[\mathrm{MPa}\sqrt{\mathrm{mm}}]$	Effective stress intensity range
ΔK_{th}	$[\mathrm{MPa}\sqrt{\mathrm{mm}}]$	Threshold stress intensity range
K_c	$[\mathrm{MPa}\sqrt{\mathrm{mm}}]$	Material fracture toughness
K_{op}	$[\mathrm{MPa}\sqrt{\mathrm{mm}}]$	SIF at crack opening
K_{cl}	$[\mathrm{MPa}\sqrt{\mathrm{mm}}]$	SIF at crack closure
f	[-]	Crack opening function
α	[-]	Plane stress/strain constraint factor
σ_{max}	[MPa]	Maximum stress
σ_y	[MPa]	Material yield strength
σ_u	[MPa]	Material ultimate strength
σ_0	[MPa]	Material flow stress
L_e	[mm]	Element length ahead of crack tip in propagating direction
φ	[-]	Angle in the circumferential direction in the crack plane
a	[mm]	Crack width
c	[mm]	Crack length
Δa	[mm]	Crack propagation increment
da/dN	[mm/cycle]	Crack growth per cycle
C	[-]	Constant in the NASGRO® equation
n	[-]	Constant in the NASGRO® equation
p	[-]	Constant in the NASGRO® equation
q	[-]	Constant in the NASGRO® equation

2 Introduction

It is important to understand the fatigue phenomenon in order for the engineer to correctly predict the operational life for any design and material. Fatigue crack growth is often described by semi-empirical equations, many of which contain a large amount of material, geometry and load related parameters. Some equations describe only specific parts of the crack growth life, such as the Paris law [1] which is limited to the crack growth in the linear part of the logarithmic relationship between crack propagation rate and stress intensity range. At GKN Aerospace Engine Systems (GAES) the NASGRO® equation is used to describe the entire crack growth life.

This study deals with the derivation of five parameters in the NASGRO® equation. Four of these parameters are derived by curve fitting to experimental data and one parameter, the crack closure is derived by means of finite element analysis. This differs from the current method used at GAES for determining life where all five parameters are obtained from curve fitting.

The goal is to obtain an unequivocal value of the plane stress/strain constraint factor, α, which is directly related to the closure level. When all five parameters from the NASGRO® equation are established together with α as well as material data for cast Inconel 718, life predictions can be made by use of the NASGRO® software.

The method is evaluated and the predicted lives are compared with the actual lives observed in the experimental testing of cast Inconel 718 Kb-specimens.

3 Theory

Experiments of crack propagation during cyclic loading reveals striation on the fracture surface of ductile materials. The striations represent the increment of growth occurring in one load cycle, which reflect the operation of slip planes at a crack tip causing plastic blunting and sharpening. During reverse loading compressive stresses at the crack tip reverse slipping, but the newly created surface cannot be removed by reconnection of the atomic bonds. At cyclic loading, as the crack propagates, a plastic wake is formed behind the crack tip and will induce crack closure.

If the plastic zone at the crack tip is sufficiently small compared to other length scales, such that it is embedded in the elastic singularity zone, the condition at the crack tip is uniquely defined by the current stress intensity [2]. The typical fatigue crack growth behavior in metals is illustrated in Fig. 1, showing the logarithmic relationship between crack propagation rate and stress intensity range. The curve consists of three distinct regions. Below a threshold ΔK_{th}, *da/dN* approaches zero and the crack will not grow (Region I). In the intermediate part a linear trend is evident (Region II). At high ΔK-values the crack growth rate escalates rapidly as the stress intensity factor increases towards a critical value K_c, the fracture toughness of the material (Region III). The crack growth can, under small scale yielding (SSY) condition, be defined in a general form as:

$$\frac{da}{dN} = f(\Delta K, R) \qquad (1)$$

where:

$$\Delta K = K_{max} - K_{min} \qquad (2)$$

$$R = \frac{K_{min}}{K_{max}} \qquad (3)$$

$$\frac{da}{dN} = crack\ growth\ per\ cycle \qquad (4)$$

A number of equations have been developed similar to this form, most of which are empirical, describing both short and long cracks. Paris and Erdogan [3] were the first to establish an equation of such a form. This equation, called Paris law, only describes the linear part of the logarithmic relationship between crack propagation rate, *da/dN*, and stress intensity range, ΔK. Once the crack growth law is determined the equation can be integrated to compute the operational life of a component, given a critical crack size and a fracture criterion. The parameters that influence the crack growth rate are the loading conditions, component geometry, material and its microstructure, temperature and environment.

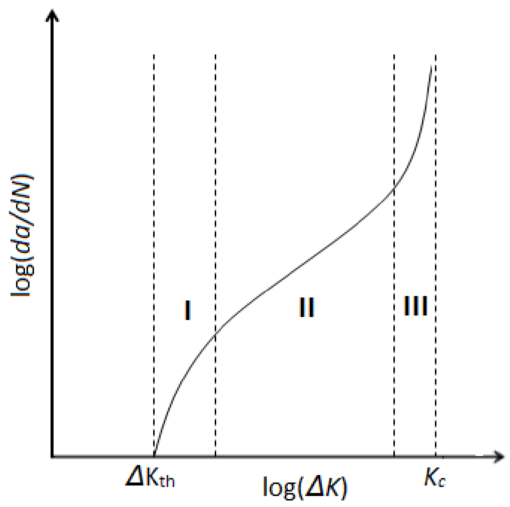

Fig. 1 Typical fatigue crack propagation behavior in metals, showing the logarithmic relationship between crack propagation rate (*da/dN*) and stress intensity range (ΔK).

3.1 Crack closure[1]

The crack closure is here assumed to be plasticity induced crack closure (PICC) only. The PICC level is a complex relation between plastic strains occurring in the vicinity of the crack tip and the growth of the crack through this plastically deformed material. The residual stretch in the plastic wake brings forth the crack surface to close at the tip at a certain fraction of the maximum load. Elber [4] was the first to discover crack closure at tensile loading and suggested that the crack tip deformation and crack propagation rate are controlled by an effective stress intensity range, ΔK_{eff} defined by:

$$\Delta K_{eff} = K_{max} - K_{op} \qquad (5)$$

[1] Usually most authors do not distinguish between crack closure and crack opening, which may cause some confusion. In this paper the mix of the terms is strived to be avoided, however depending on the context one or the other term is more suitable to use.

Here K_{op} is the stress intensity factor corresponding to the case when the crack surface is completely opened. Following Elber [4], ΔK can be replaced by ΔK_{eff} in Eq. (1) and the crack growth rate can now be expressed as:

$$\frac{da}{dN} = C(\Delta K_{eff})^n \tag{6}$$

where C and n are material parameters and are derived empirically.

3.2 NASGRO® equation

The NASGRO® equation, Eq. (7), is an extension of Eq. (6) and describes the entire crack growth life, taking account of both the threshold stress intensity range, ΔK_{th} , and the material fracture toughness, K_c [5] The crack propagation rate is evaluated from the stress intensity factor range, ΔK, the R-ratio, threshold levels and fracture toughness. The equation is given by:

$$\frac{da}{dN} = C\left[\left(\frac{1-f}{1-R}\right)\Delta K\right]^n \frac{\left(1-\frac{\Delta K_{th}}{\Delta K}\right)^p}{\left(1-\frac{K_{max}}{K_c}\right)^q} \tag{7}$$

where the C, n, p and q are empirically derived parameters.

Newman [6] suggested that crack closure is a function of the stress ratio, as well as the stress-state and the maximum stress level, σ_{max}. He defined the crack opening function, f, as:

$$f = \begin{cases} \max(R, A_0 + A_1R + A_2R^2 + A_3R^3), & R \geq 0 \\ A_0 + A_1R, & -2 \leq R < 0 \end{cases} \tag{8}$$

where the polynomial coefficients are given by:

$$A_0 = (0.825 + 0.34\alpha + 0.05\alpha^2)\left[\cos\left(\frac{\pi}{2}\frac{\sigma_{max}}{\sigma_0}\right)\right]^{\frac{1}{\alpha}} \tag{9}$$

where $1 < \alpha < 3$ and $0 < \frac{\sigma_{max}}{\sigma_0} < 1$)

$$A_1 = (0.415 - 0.071\alpha)\frac{\sigma_{max}}{\sigma_0} \tag{10}$$

$$A_2 = 1 - A_0 - A_1 - A_3 \tag{11}$$

$$A_3 = 2A_0 + A_1 - 1. \tag{12}$$

The parameter, α, is the plane stress/strain constraint factor and $\frac{\sigma_{max}}{\sigma_0}$ is the ratio between maximum stress and the material flow stress. The material flow stress is usually defined as the average between the material yielding and ultimate strength [7], and the same definition is used in this paper:

$$\sigma_0 = \frac{\sigma_y + \sigma_u}{2} \tag{13}$$

Given a value of the closure level, f, the plane stress/strain constraint factor, α, can be solved for by use of equations (8) - (12).

4 FE-analysis to determine crack closure level, *f*

A numerical analysis to establish the crack closure of a surface crack, along a 3D crack front has been simulated for different R-ratios and temperatures. The analysis provides an understanding of how the closure level varies along the crack front of a Kb-specimen and the potential to describe crack closure, and thereby α, with only one value for such a geometry. The model is subjected to mode I loading, which makes it possible to utilize two-fold symmetry allowing modeling of only one-quarter of the specimen. The crack is assumed to be semi-circular, i.e. $a = c$, at all times (assumption supported by the experimental results). The mesh is built 8-noded solid elements and a typical mesh consists of 55 000 nodes and 70 000 elements. The crack propagation scheme is essential for accurate crack closure results and a thorough investigation of current research has been performed. To accurately confine crack growth and contact leading to closure and opening behavior, the load steps for every cycle need careful designs. It is refined in areas where the closure and opening levels are expected to be found since the finite sized load step will resolve the opening level to the same magnitude as the load increment. Preliminary studies points out a requirement of 40 increments for $R = 0$ and $R = 0.5$ and 65 increments for $R = -1$. The analysis uses a multi-linear kinematic hardening constitutive model that incorporates the Bauschinger effect to describe the cyclic elastic-plastic response of the material. The backstress uses a stepwise linear relation to plastic strain. The material data used in this work was produced by GAES for cast Inconel 718.

The size of the forward- and the reversed plastic zones are main parameters to consider and there are many papers on mesh criteria for 2D FE-analysis of fatigue crack growth (see Fig. 2 for clarity on forward plastic zone).

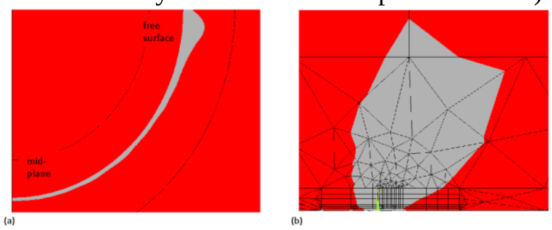

Fig. 2 Forward plastic zone (a) along the crack front indicating larger forward plastic zone near the free surface and (b) at the free surface.

However, many researchers have neglected this issue for their 3D models. Skinner and Daniewicz [8] investigated closure in a finite rectangular plate with a semielliptical surface flaw subjected to remote tension loading. They concluded that five elements in the forward plastic zone at the deepest point of penetration are sufficient for mesh independent closure loads. Roychowdhury and Dodds [9] found in their small scale yielding analysis that 10 elements in the forward plastic zone in fact could give an adequate solution. The mesh also needs to have sufficiently small elements to capture reversed yielding at the crack tip upon unloading [10]. Roychowdhury and Dodds [9] suggest that 2-3 elements should be fully contained within the reversed plastic zone at the end of the first cycle. This study suggests that 2 or more elements are contained in the reversed plastic zone and 5-10 elements in the forward plastic zone.

The crack propagates uniformly over the crack front by an increment of one element ($\Delta a = L_e$) in each cycle after releasing all the nodes at the crack front after the last unloading step. L_e is the element length ahead of the crack tip in propagating direction. As a criterion for minimum crack extension required in order to obtain steady state values for crack closure the initial forward plastic zone is used as a measure. Figure 3 shows how crack closure develops through crack growth and Fig. 4 shows saturated values (typically the last value seen in Fig. 3) through the crack front. To achieve convergence the crack should propagate all through the initially deformed material [8], [9], [11], [12]. The reasoning is that a material point right behind the crack tip needs to accumulate all plastic strain from a complete deformation history.

Closure is defined based on when the first node behind the crack tip comes into contact according to [11], [13].

The stress intensity factor is captured both at crack closure (K_{cl}) and at crack opening (K_{op}). The numerical analysis shows a difference between the two, however K_{op} is commonly regarded to be more important in a physical sense to the crack propagation mechanism, and will thus be used in the analytical calculations.

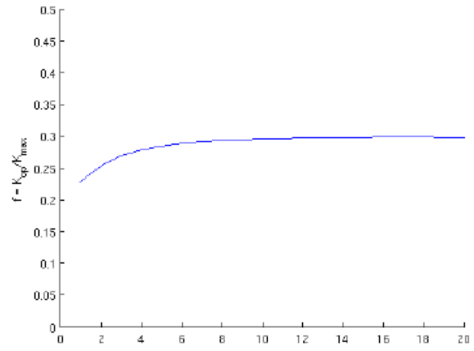

Fig. 3 A typical graph for crack closure (*f*) vs. crack growth increments (Δa).

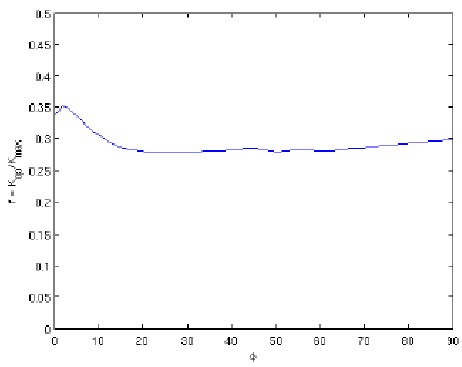

Fig. 4 Typical graph for stabilized opening levels, *f*, as a function of φ (angle in the circumferential direction in the crack plane, where $\varphi = 0^{o}$ at the free surface).

The result from the FE-analysis is presented in Table 2. It can be seen that the closure value does not change considerably for the two different temperatures. Even if the material properties are changed with increasing temperature, the applied loads have been changed accordingly in the experimental testing as well in the numerical analysis. Values of α varies from 1 to 3 leading to that determining an unequivocal value is not straightforward. Simply, an average of these values is chosen as the best method.

Table 2 Results from the numerical analysis.

Temperature [^{o}C]	R	f	σ_{max}/σ_0	α
20	0	0.29	0.52	1.95
20	0.5	0.59	0.56	1*
20	-1	0.09	0.47	3*
650	0	0.31	0.45	1.93
650	0.5	0.59	0.54	1*
650	-1	0.13	0.42	3*

*An α could not be found within the range of Newman's crack opening function and the closest value is used.

5 Experimental data

Crack growth is a stochastic process, often showing considerable scatter even in controlled environments. The scatter increases for longer fatigue lives. The crack is initiated where there are stress concentrations due to microstructural inhomogeneities, grain structure influences and/or other influences at micro- or macro scale From this point of view it is important to analyze the scatter in fatigue crack growth rates in a statistical manner.

As mentioned before, at GAES the NASGRO® equation is used to characterize the crack growth behavior of a material. The parameters of the NASGRO® equation, both for mean behavior and to account for the scatter, are established from the experimental results through a statistical analysis.

5.1 Experimental set-up

GAES has performed crack propagation experimental tests of surface crack specimens of cast Inconel 718 at several different temperatures and R-ratios. The experiments produced measured da/dN-data as a function of ΔK, along with threshold values for different temperatures and R-ratios of interest.

In the numerical analysis only two different temperatures, 20 ^{o}C and 650 ^{o}C, with corresponding R-ratios have been considered (R = 0, 0.5 and -1).

5.2 Least mean square fit to determine C, n, p and q

With the closure level, f, established through finite element analysis a curve fit process, based on the experimentally obtained values of da/dN versus ΔK, is used to obtain the parameters C, n, p and q. Values of the parameters K_{th} and K_c have been obtained by GAES for cast Inconel 718. The method chosen uses a least-squares minimization of error in the log-log domain. By taking the logarithm of Eq. (7), a linear relation with respect to the predictors can be established:

$$\log\left(\frac{da}{dN}\right) = \log(C) + n\log\left(\frac{1-f}{1-R}\Delta K\right) + p\log\left(1-\frac{K_{th}}{\Delta K}\right) - q\log\left(1-\frac{K_{max}}{K_c}\right) \quad (14)$$

The coefficients are estimated by least squares, thus minimizing the sum of squares of the residuals. With this procedure the parameters C, n, p and q can be obtained. However, an option is to move the terms including p and q to the left hand side of Eq. (14) and use fixed, standard values of p and q, thus making the least square fit with respect to only C and n. This is a more common procedure since experimental data is lacking in the two extreme regions, corresponding to parameters p and q. Both procedures are applied and compared in the following sections to check which gives the best prediction of crack propagation rates. However, for the future, additional experimental crack growth rate data in region I and III is needed to get more accurately fitted constants as well as additional and more thorough measurements of the threshold level to avoid uncertainties in the threshold stress intensity range.

Figure 5 shows the *da/dN*-data versus (a) ΔK and (b) $\Delta K_{\mathrm{eff}} = \frac{1-f}{1-R}\Delta K$ for T = 20 ^{o}C. As can be seen, the *da/dN*-data merges quite well if plotted against ΔK_{eff}, indicating the validity of Elber's assumption and the numerically obtained *f*.

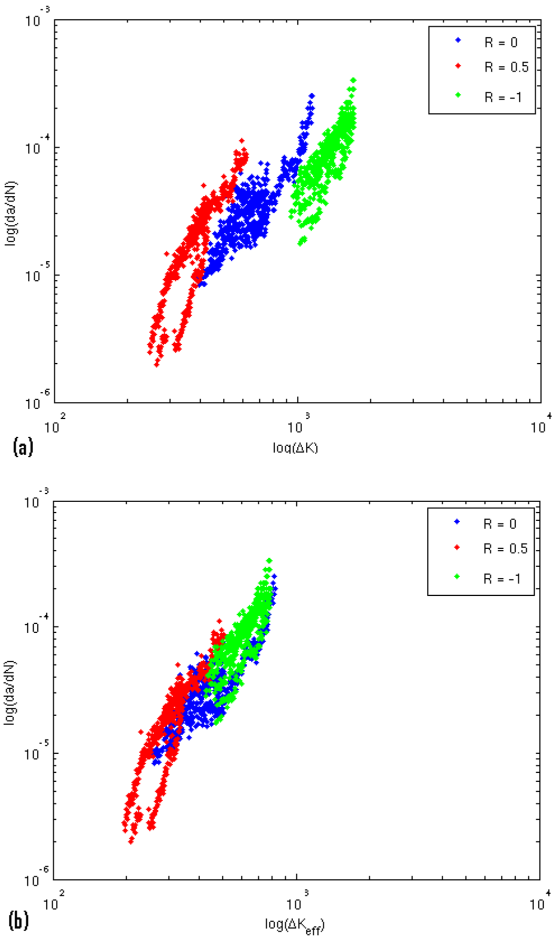

Fig. 5 Experimental data, T = 20 ^{o}C (a) *da/dN* versus ΔK, (b) *da/dN* versus ΔK_{eff}.

Figure 6 shows the corresponding plots for T = 650 ^{o}C. The data merges quite well, however not as good as for T = 20 ^{o}C.

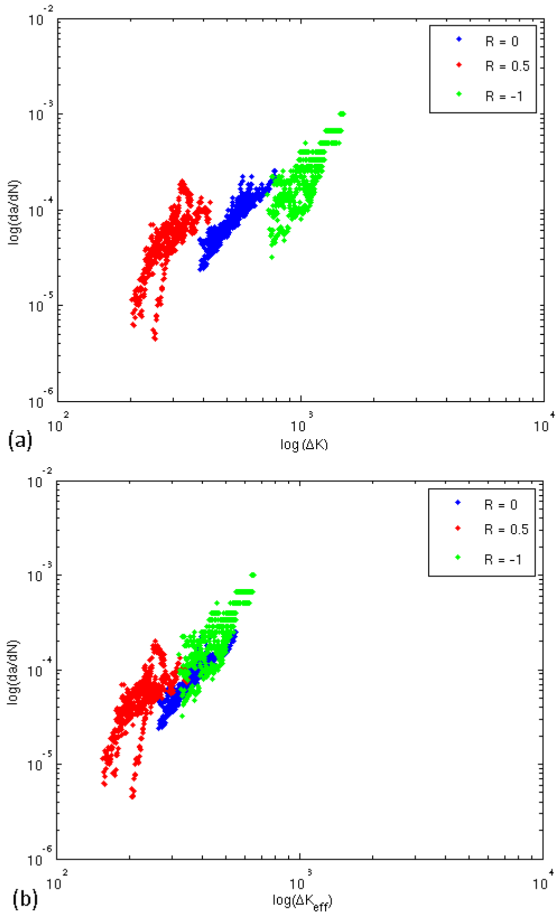

Fig. 6 Experimental data, T = 650 ^{o}C (a) *da/dN* versus ΔK, (b) *da/dN* versus ΔK_{eff}.

Figure 7 shows a generated curve fit with ΔK_{eff} ranging from ΔK_{th} to $K_{\max} = K_c$ for (a) when letting *p* and *q* be free and (b) locking them as $p = 0.25$ and $q = 0.75$. The two procedures clearly give different estimation of the crack propagation rates. However, in both cases it is evident that the experimental data mainly covers Region II of the crack propagation rate curve.

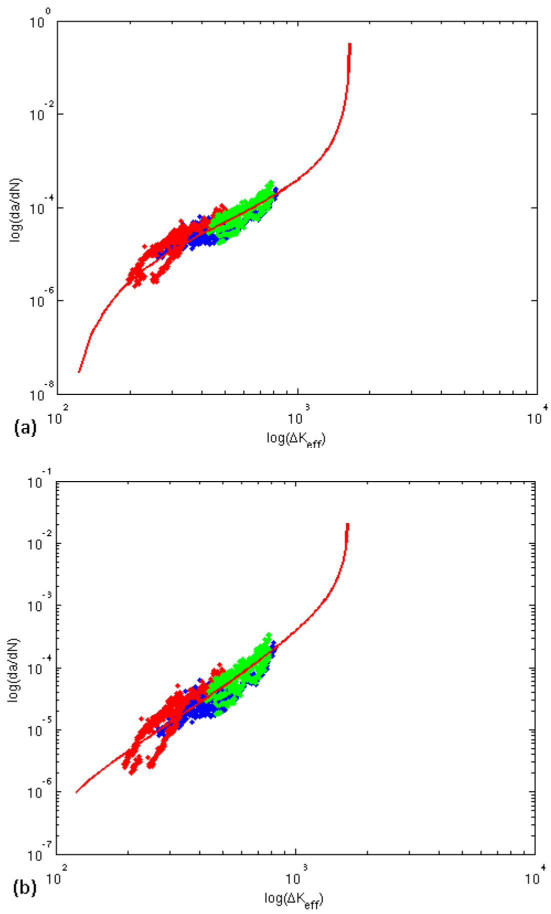

Fig. 7 Generated curve fit with ΔK_{eff} ranging from ΔK_{th} to $K_{max} = K_c$ for (a) when letting *p* and *q* be free and (b) setting $p = 0.25$ and $q = 0.75$ (T = 20°C).

The obtained values of the fitted parameters for the respective temperature are shown in Table 3 for the two proposed methods as well as for GAES's current method (where all five parameters are obtained through curve fitting). The parameters *C* and *n* have been scaled so that $n = 1$. Note that, there are other parameters with differing values between the methods that are not shown in the table, e.g. α. A clear difference of *C* and *n* can be seen for the two proposed methods. The acquainted reader of fracture mechanics will, by studying the numbers when letting *p* and *q* be free, observe unusually high values. Recall that *p* and *q* control the shape of the asymptote in the threshold and critical crack growth region, respectively. Thus, the two methods show very different behavior for the threshold crack growth region as is evident in Fig. 7.

Table 3 The fitted parameters *C, n, p* and *q* for the two temperatures considered, and both proposed methods as well as GEAS's current method. Top: *p* and *q* free, middle: *p* and *q* locked, bottom: GAES's current method. The parameters *C* and *n* have been scaled so that n = 1.

	Proposed method (*p* and *q* free)	
	T = 20°C	T = 650°C
C	3.37E-08	6.13E-07
n	1	1
p	2.9042	2.7386
q	1.6647	1.119

	Proposed method (*p* and *q* locked)	
	T = 20°C	T = 650°C
C	1.07E-11	1.38E-10
n	1	1
p	0.25	0.25
q	0.75	0.75

	GAES's current method	
	T = 20°C	T = 650°C
C	9.17E-14	5.94E-13
n	1	1
p	0.25	0.25
q	0.75	0.75

6 Evaluation of the proposed method

One way to determine the validity of the model is to compare the predicted life (P) with the actual life (A) observed in the experimental testing. For each case the actual life over the predicted life (A/P) is calculated. An A/P-value of around 1 is obviously desirable, a value less than one implies a non-conservative estimate of life and a value above one implies a conservative estimate of life. Comparing the predicted life using GAES's current method will reveal if the more thorough analysis, used in the proposed method, will increase the accuracy of the life predictions.

To illustrate the accuracy of the predicted lives, Minitab probability plots are used. They show the probability distribution of acquired A/P-values. If the method used for life predictions is good, it should have an A/P of 1 at 50% probability. The distribution should also deviate from A/P = 1 as little as possible, i.e.

have a vertical shape. Figure 8 shows the Minitab probability plot for the proposed method (p and q free) versus the current method used at GAES. Figure 9 shows the proposed method (p and q locked) versus the current method used at GAES.

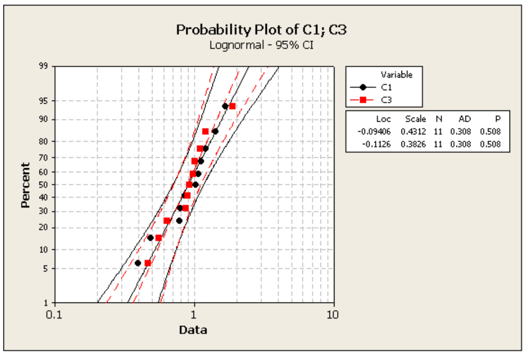

(a)

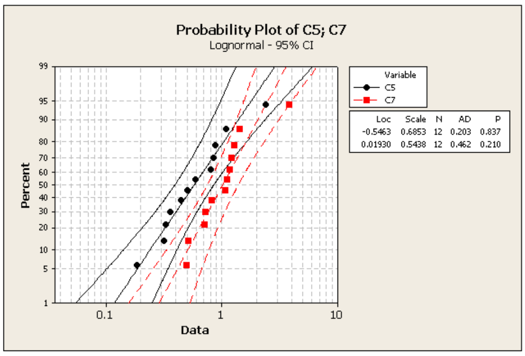

(b)

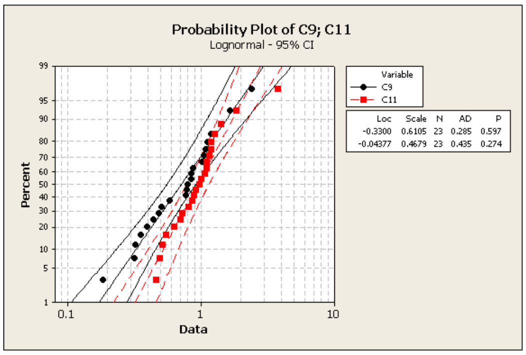

(c)

Fig. 8 Minitab probability plot; the proposed method (p and q free) (black) versus current method used at GAES (red). (Vertical axis: probability, Horizontal axis: A/P-value), (a) T = 20°C, (b) T = 650°C and (c) both temperatures.

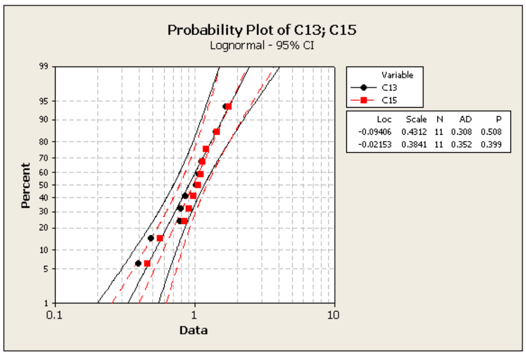

(a)

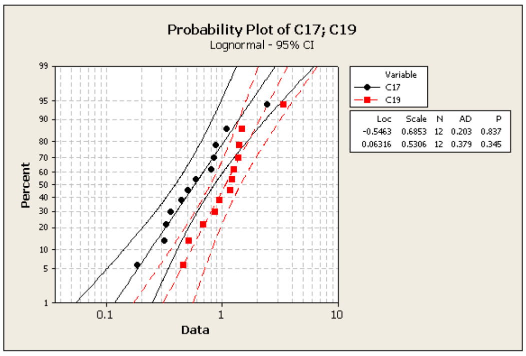

(b)

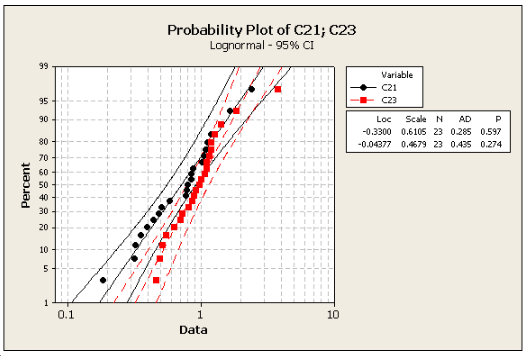

(c)

Fig. 9 Minitab probability plot; the proposed method (p and q locked) (black) versus current method used at GAES (red). (Vertical axis: probability, Horizontal axis: A/P-value), (a) T = 20°C, (b) T = 650°C and (c) both temperatures.

For T = 20 °C both proposed methods as well as the current method used at GAES show good life predictions. However for T = 650 °C all three methods show somewhat less accurate predictions. The proposed method (p and q locked) and the current method used have an A/P-value of 1 at 50% probability which is desirable. This is not the case for the proposed method (p and q free).

7 Conclusions

This paper examines whether it is possible to make more accurate life predictions of aircraft engine components by employing a more physical approach to identifying parameters in crack propagation models as compared to a pure curve fit method. The objective was to statistically evaluate the predictions of these two methods and compare to experimental data.

The physics-based method shows promise, as the predicted lifetime on average is similar to the pure curve fit method. The model can be expanded for different geometries with different crack closure levels resulting in more accurate life predictions.

Other conclusions are:

- With the model and crack propagation scheme used in this paper, an unequivocal value of α cannot be directly established. A further understanding of this parameter is desired.
- Crack closure and thereby α do not seem to have a direct relation to temperature.

References

[1] Dowling, N.E., "Mechanical Behavior of Materials – Engineering methods for Deformation, Fracture, and Fatigue", 2007, Third Edition, Pearson Education International, USA.

[2] Suresh. S., "Fatigue of Materials", 1991, Cambridge University Press, Cambridge, UK.

[3] Paris, P.C. and Erdogan, F., "A Critical Analysis of Crack propagation Laws", *Journal of Basic Engineering*, 1960, **85** pp. 528-534.

[4] Elber, W.,"Fatigue crack closure under cyclic tension", 1970, *Engineering Fracture Mechanics*, **2**(1), pp. 37-44.

[5] T.L. Anderson, "Fracture Mechanics – Fundamentals and applications", 1991, Taylor & Francis group, Florida, USA.

[6] Newman, J.C., "A Crack Opening Stress Equation for Fatigue Crack Growth". *International Journal of Fracture*, Mars 1984, **24**(3), pp. R131-R135.

[7] NASGRO® Manual, Version 6.2, 2011.

[8] Skinner, J.D., and Daniewicz, S.R., "Simulation of plasticity induced fatigue crack closure in part-through cracked geometries using finite element anal ysis", 2002, *Engineering FractureMechanics,* **69**, pp. 1-11.

[9] Roychowdhury, S., Dodds, R.H., "A numerical investigation of 3D small scale yielding fatigue crack growth", Engineering Fracture Mechanics, 2003, 70, pp. 2363–83.

[10] McClung, R.C., Thacker, B. H and Roy, S., "Finite element visualization of fatigue crack closure in plane stress and plane strain", 1991, International Journal of Fracture, 50, pp. 27-49.

[11] Borrego L.F.P., Antunes F.V., Costa J.D., Ferreira, J.M., "A numerical study of fatigue crack closure induced by plasticity", 2004, Fatigue & Fracture of Engineering Materials & Structures, 27(9), pp. 825 – 835.

[12] Antunes , F.V., Rodrigues D.M., "Numerical simulation of plasticity induced crack closure: Identification and discussion of parameters", Nov 2008, Engineering Fracture Mechanics, 75, pp. 3101-3120.

[13] Kiran Solanki, S.R. Daniewicz, J.C. Newman Jr., "Finite element analysis of plasticity-induced fatigue ecrack closure: an overview", 2004, Engineering Fracture Mechanics, 71. pp. 149–171.

Studies on manufacturing-related management accounting

Myrelid A.
GKN Aerospace Engine Systems, Sweden
andreas.myrelid@gknaerospace.com

Keywords: *operations management, performance measurement, decision making.*

Abstract

The purpose of this paper is to provide perspectives on some aspects concerning the relationship between manufacturing operations management and management accounting. This will increase the knowledge and understanding of how management accounting information supports manufacturing decision making.

Findings from four studies designed to investigate the informational relationship between management accounting and operations management in companies is reported. Results show that there are many factors to consider when choosing and designing an appropriate management accounting system. Contextual factors include market, manufacturing strategy, technology, and organization.

This paper contributes with some explanatory aspects on the practical problem and investigates some potential ways forward concerning manufacturing-related management accounting.

1 Introduction

In companies with complex products and complex production systems it is hard to see economic consequences of activities made in production. In order to create a financially successful company there is a need to understand the economic consequences of decisions and actions in production. Consequently, there is a need for good transparency between the production and accounting/finance functions. The purpose of this paper is to provide perspectives on some aspects concerning the relationship between production and management accounting. This study is concerned with the informational relationships between management accounting and operations management of manufacturing firms, particularly advanced manufacturing technology companies.

In 1987, Johnson and Kaplan wrote that more or less all the management accounting practices used at that time had stopped their development in 1925. The manufacturing environment as well as the competitive environment has changed since then and much research shows that the traditional way of managing the operations is not suitable in this new environment [1-5]. Different management accounting systems seem to be needed for different types of manufacturing systems. For a management accounting system to be utilized to its full potential to support the manufacturing decision making it needs to be used in the right context for which it has been developed. Figure 1 on next page shows an illustration where information to support decision making flows between production/manufacturing functions and accounting/finance departments through the management accounting system. This paper focuses on the bold arrows between the management accounting system and the production.

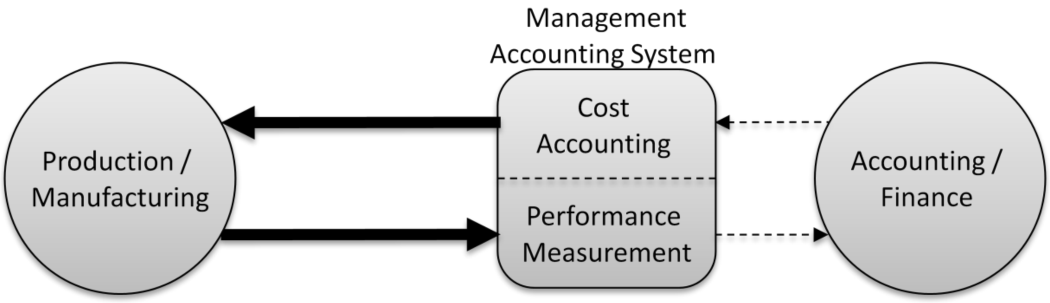

Fig. 1 Information flow between Production and Finance department through the management accounting system.

Management accounting is the part of the management process that is focused on adding value to organizations by attaining the effective use of resources in dynamic and competitive contexts [6]. Management accounting consists of both cost accounting and performance measurement.

There is often a mix up between management accounting and financial accounting [6]. Financial accounting has an external purpose for external stakeholders and should not be used for internal decision making in the daily operations management. While financial accounting is regulated when it comes to what to include and how to calculate, management accounting has no regulations at all. Financial accounting has to be done by law and has to follow generally accepted accounting principles (GAAP) to be transparent enough and understandable for shareholders, authorities and others who might have an interest in the financial situation at the company. This means it involves compliance with common and standard rules and regulations established by external authorities, maintaining official records, preparing reports responding to questions defined by external bodies, and coordinating and responding to audits. Financial accounting also deals with managing financial transactions and valuations such as balance sheet valuation as well as processing cash interactions with suppliers, customers, tax, and other authorities [6]. They are similar in the way that they are both based on financial information and non-financial quantitative information about the operations [7]. But as shown in **Error! Reference source not found.** there are some important differences.

Tab. 1 Financial accounting vs Management accounting

	Financial Accounting	Management Accounting
Perspective	Retrospective – Summarizing the financial result of past decisions and transactions.	Both retrospective and prospective – Both providing feedback of past operations and help to plan for future events.
Role	Report to external stakeholders such as shareholders, investors, creditors, and tax authorities.	Help employees and managers internally in their decision making in how to run the operations.
Content	Has to follow external standards (GAAP) for how to be developed and presented.	No prescribed regulations. Can contain and be presented in any way found suitable for the purpose of manage the operations.

Cost accounting is the process of accumulating and accounting for the flows of costs in a business. It is defined as a technique or method for determining the cost of a project, process, or thing through direct measurement, arbitrary assignment, or systematic and rational allocation. The appropriate method of determining cost often depends on circumstances that generate the need for information [1].

Performance measurement is the process of quantifying actions, where measurement is the process of quantification and performance is the result of action [8]. These measurements show how well the production is performing in categories such as quality, delivery precision, service level, time per operation, set up time and so on. The direction of which an organization is heading is influenced by the chosen performance measures. The attention is given to what is measured, sometimes on the cost of more important criteria that are not being measured [1].

The more traditional accounting systems worked as support for decision making in more traditional manufacturing context. The management accounting system should be designed to fit the organizational context. Two research questions were formulated for this research. What contextual factors need to be considered when designing a cost accounting system for organizations with advanced technology products and manufacturing systems? What contextual factors need to be considered when designing a performance measurement system for organizations with advanced technology products and manufacturing systems?

Traditional costing systems are widely used by about 75% of manufacturing companies but only appropriate for some specific manufacturing environments [9]. Traditional costing systems are often used where there are standardized processes, limited number of products which are similar, and direct costs are high [9, 10]. Earlier in the 20th century the total production cost consisted of 70-80% of direct costs such as labour and material [11-13]. Then it seemed logical for the management to use direct labour as their allocation key by which to allocate other overhead. Logical or not, misapplication did not really matter since overhead was such a negligible part of the total production cost [14]. Today most manufacturing companies consist of a totally different cost structure compared to when traditional costing systems developed. Overhead cost today is often the single largest part of the total cost. It is to a large extent driven by large investments in advanced manufacturing technologies, more of indirect activities such as planning, quality control, maintenance and research and development. The development to a more modern and advanced production has led to that the overhead is no longer proportional to production volume. Practices used in traditional costing systems use incentives for overproduction since managers feel a need to maximize standard labour hours to spread out the overhead [15]. Due to the allocation of the overhead by direct labour it influences managers to focus on the direct labour variances to control the allocation of overhead to the products, not control of the direct labour costs [9].

2 Methodology

To gain better understanding in the processes the researcher has participated in education and meetings with topics such as budgeting and controlling held by the finance/accounting department for production managers at a primary case company. The researcher has also been a member in projects teams with different purposes in improving manufacturing. Initially there was a need to review the literature to understand the current position in the body of knowledge. The search strategy to find relevant literature included a selection of databases: Academic search premier, Business source premier, Scopus, and Web of Science. These are partly overlapping, but together they make a full coverage of international scientific journals of high reputation. In these databases, three types of selected keywords were used for search in the abstract: (i) one of management accounting, product costing, and cost accounting, (ii) in combination with one of manufacturing, production, and operations, (iii) and with decision making. In the literature review different methods and comparisons of these were identified. But there was no sufficient comparison between two of the most recently developed ones. The literature review was followed by three case studies. This resulted in the first study which comparing lean accounting and throughput accounting applied at the primary case company to be able to get an understanding of their advantages and disadvantages compared to the existing and more traditional accounting method. Two case studies with focus on the performance measurements were also carried out, one at the primary case company concerning the design of the entire performance measurement system, and one at another company focusing only at the performance measurement related to inventory management.

3 Findings

When searching for literature it was decided to have the year of 1987 as the limit of how far back to go. This due to that the book Relevance lost [2] was published this year and basically started the era of questioning the old way of management which initiated many new ways of thinking. The publications were classified in one of three categories; factors to consider, description of a single management accounting system, and comparisons between different management accounting systems. Based on this review, a conceptual model (cf. Fig.2) is proposed for the relationships among contextual factors, the choice and design of management accounting systems and performance.

The model in Fig. 2 depicts the relationships among the contextual factors, the choice and design of costing/accounting approach, and the potential impact on performance. Arrow (a) represents the level of consideration of contextual factors when choosing an approach and designing the corresponding system. The two (b) arrows represent the congruence between costing and accounting information and manufacturing decision-making. Higher levels of congruence should have a positive effect on manufacturing performance, as represented by relationship (c). Arrow (d) indicates that the contextual factors per se may have a direct impact on manufacturing performance. Correspondingly, arrow (e) indicates that the choice and design of approach and system may have a direct impact on manufacturing performance.

From the initial literature review and the insight from the company a study was initialized and carried out to look deeper into and compare lean accounting and throughput accounting. In recent years, lean accounting and throughput accounting have emerged as viable options for management accounting in manufacturing firms, replacing traditional accounting systems and activity-based costing (ABC) systems. In the first case study the applications of lean accounting and throughput accounting to GKN are analyzed, as potential systems replacing the

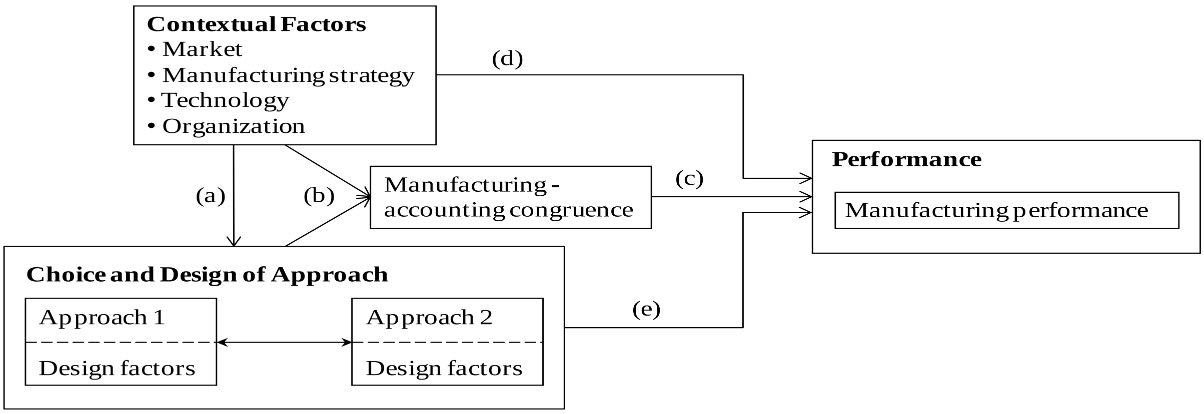

Fig. 2 Conceptual model describing relationship among contextual factors, the choice and design of accoutning method, congruence between the accoutning methods and the manufacturing environment, and performance.

existing system. It was found that neither of the two systems can fully replace the current accounting system without other adoptions in the company, but both lean and throughput accounting can offer some advantages and can be more viable in the future. Since the company is currently incorporating some lean initiatives, lean accounting can become more relevant in the future. Also, since bottleneck management is becoming more important for the company, throughput accounting can become relevant in the near future.

The second case study is about performance measurement in inventory management executed at a component manufacturing company within the automotive industry with sites all over the world. The objective is to study how a company structure their performance measurements related to inventory management. It is shown that the company uses the performance measurements proposed in the literature but not in the right way. At the case company it is seen that the different functions and different sites have variances of the measurements making it less useful for both comparison and aggregation. It was found that people in finance and production had different definitions on the same key performance indicator. The reason for this is that finance is looking in the mirror to report what has happened the last period while production is looking forward and planning for the future. While finance wants to have historical data input production wants to have forecasted future data input in the same performance indicator.

The purpose of the third case study is to outline how the case company works to incorporate the overall strategy through the entire organisation and how the strategy also can be seen in the design of the performance measurement system. Compared to the second case study presented above, this study has a wider view and looks into the performance measurements system overall design. The findings from the study are that the organisation deploys two processes for developing the performance measurement system. There is one top-down approach with the starting point in the business plan and another more bottom-up approach within an operational development program. Several challenges are highlighted relating to the IT-system, culture and involvement. From the study it is concluded that even though the processes are theoretically sound, the scarcity of time and focus in practice derail their purposes.

4 Discussion

This research finds that there is a lot to consider when choosing which management accounting system to apply in a company. Some contextual factors, such as market, manufacturing strategy, technology, and organization are identified. A comparison of lean accounting and throughput accounting where they are applied in a real manufacturing company shows that neither lean accounting nor throughput accounting can be fully applied due to the existing context. Both lean accounting and throughput accounting have elements that can be useful and provide useful information for decision making in manufacturing in the case company. Although the results may be limited to the case company, companies with similar products and manufacturing systems may experience similar problems. A traditional accounting system is not automatically wrong, but it is not automatically correct either just because it has been working for the last decades. The structure of the company as well as the production philosophy is most likely not the same as it used to be. Using a management accounting system from an old era can cause more damage than it do good.

The studies concerning the performance measurement system shows how unclear definitions of performance measure causes problem. In one case study it is found that the company has two processes to design a performance measurement system. They are well thought through in theory but it has been hard to apply in practice. This shows that it is not strange that the problem with misalignment between production and management accounting systems still exists. After more than 20 years where both practitioners and academia have spent resources into the problem and suggesting development of existing management accounting systems as well as to introduce new management accounting systems the problem is not solved. This shows that the problem might not be in the theories themselves, but among practitioners not implementing and using them as initially intended by the researchers developing them.

5 Contribution

This paper shows some implications for practice. It shows that contextual factors such as market, manufacturing strategy, technology, and organization aspects should be taken into account when selecting and designing a management accounting system. Lean accounting and throughput accounting adds some perspectives concerning value streams and bottlenecks. The paper also shows that there might be appropriate performance measurements used, but lack of standardization regarding definition and phrasing can cause disinformation in the decision-making process. The IT system, employee involvement, and the culture have to be considered when designing a performance measurement system. While this paper does not provide the full view on how to link management accounting and manufacturing decision making, it provides some explanatory aspects on the practical problem and investigates some potential ways forward.

The literature review and the first case study show there is a lot to consider when choosing which management accounting system to apply in a company. From the literature review some contextual factors are identified, those are market, manufacturing strategy, technology, and organization. The first case study is a comparison of lean accounting and throughput accounting where they are applied in a real manufacturing company. It is found that neither lean accounting nor throughput accounting can be fully applied due to the existing context.

References

[1] Swamidass, P.M., ed. *Encyclopedia of production and manufacturing management*. Kluwer Academic Publishers, Norwell, MA, 2000.

[2] Johnson, H.T. and R.S. Kaplan, *Relevance lost: the rise and fall of management accounting*: Harvard Business School Press, 1987.

[3] Bhimani, A., "Modern cost management: putting the organization before the technique", *International Journal of Production Economics*, Vol. 36, No. 1, 1994, pp. 29-37.

[4] Chen, C.-C. and W.-Y. Cheng, "Customer-focused and product-line-based manufacturing performance measurement", *International Journal of Advanced Manufacturing Technology*, Vol. 34, No. 11/12, 2007, pp. 1236-1245.

[5] Fry, T.D. and D.C. Steele, "Wall Street, accounting, and their impact on manufacturing", *International Journal of Production Economics*, Vol. 40, No. 1, 1995, pp. 37-44.

[6] Sharman, P.A., "Bring on German Cost Accounting", *Strategic Finance*, Vol. 85, No. 6, 2003, pp. 30-38.

[7] Atkinson, A.A., et al., *Management accounting: information for decision-making and strategy execution*. 6th ed: Prentice Hall Upper Saddle River, NJ, 2012.

[8] Slack, N., ed. *The Blackwell encyclopedic dictionary of operations management*. Blackwell, Cambridge, MA, 1997.

[9] Fry, T.D., D.C. Steele, and B.A. Saladin, "The use of management accounting systems in manufacturing", *International Journal of Production Research*, Vol. 36, No. 2, 1998, pp. 503-525.

[10] Kaplan, R.S., "Measuring manufacturing performance: a new challenge for managerial accounting research", *Accounting Review*, Vol. 58, No. 4, 1983, pp. 686-705.

[11] Seed, A.H., "Cost accounting in the age of robotics", *Management Accounting*, Vol. 66, No. 4, 1984, pp. 39-43.

[12] Turk, W.T., "Management accounting revitalized: the Harley-Davidson experience", *Journal of Cost Management for the Manufacturing Industry*, Vol. 3, No. 4, 1990, pp. 28-39.

[13] Friedl, G., H.U. Küpper, and B. Pedell, "Relevance Added: Combining ABC with German Cost Accounting", *Strategic Finance*, Vol. 86, No. 12, 2005, pp. 56-61.

[14] Ruhl, J.M. and T.A. Bailey, "Activity-based costing for the total business", *CPA Journal*, Vol. 64, No. 2, 1994, pp. 34-38.

[15] Hutchinson, R., "Linking manufacturing strategy to product cost: toward time-based accounting", *Management Accounting Quarterly*, Vol. 9, No. 1, 2007, pp. 31-42.

Fatigue Crack Propagation with Peridynamics: a sensitivity study of Paris law parameters

M. Zaccariotto, F. Luongo, G. Sarego, D. Dipasquale and U. Galvanetto
Department of Industrial Engineering, University of Padova, v. Venezia 1, 35131 Padova, Italy

Keywords: *computational mechanics, non-local methods, peridynamics, crack propagation*

Abstract

Structural failure is a phenomenon that has to be anticipated and possibly avoided by designers and engineers. The modeling of damage propagation phenomena is usually a difficult task because it is necessary to have the capability of describing generation and growth of material discontinuities. Recently a general and powerful method based on the peridynamic non-local theory has been introduced. This approach is more general in the sense that the crack is free to appear in every part of the structure, following only physical and geometrical constraints. In this paper a high cycle fatigue model has been introduced using the peridynamic approach. A method to study the correlations between the peridynamic fatigue model parameters and the classical Paris law parameters will be presented.

1 General Introduction

For structural components it is of the highest importance to be able to describe the damage process in order to evaluate their life expectancy for a safe use and to define a proper repair and maintenance program. The numerical approaches used in structural mechanics face always the problem of dealing with discontinuities since the underlying theory, continuum mechanics, is based on a differential approach and the derivatives involved in the formulation are not well defined across discontinuities. In the past such limitation was not perceived as strong as nowadays because the first manifestation of a crack was often chosen as failure condition. Furthermore in advanced engineering fields, such as aeronautics and aerospace, cracks were closely monitored on the field with very limited attempts to simulate their evolution.

In the last thirty years a few approaches have been proposed to deal with discontinuities in structural materials: interface elements and Cohesive Zone Models (CZM) [1] can only be applied if the path of the discontinuity is known a priori and it is limited by the element discretisation; the extended finite element method (XFEM) [2] is more recent and, although overcoming some of the CZM drawbacks, requires ad-hoc strategies for the definition of the node sets for enrichment and the evaluation of the enrichment functions and it is not easily applicable to 3D cases. Similar approaches are presented as an ad hoc modifications of techniques originally based on a differential formulation of continuum mechanics.

Recently a powerful method based on the peridynamic theory [3] has been introduced; in such theory internal forces are expressed through nonlocal interactions (named bonds) between pairs of material points within a continuous body, and damage may be introduced as a part of this interaction. The peridynamic equation of motion is formulated using spatial integral equations. The integral equations remain valid at discontinuities which enables to model crack initiation and propagation in a natural way [4] even when cracks take place simultaneously at multiple locations. The theory is also able to foresee the dynamic crack branching [5] and the mutual crack interaction without any special additional criteria.

The peridynamic theory seems a natural approach for the study of fatigue failure phenomena. A previous work on this topic [6] presents an extension of the bond damage by means of the concept of bond weakening: the fatigue damage is considered as a cycle-dependent reduction of bond stiffness. In this paper the parameters used for the fatigue model with the peridynamic approach and the correlation between these parameters and the classical Paris law coefficients will be presented.

2 Fundamental concepts

In bond-based peridynamics a solid body is interpreted as a collection of material points. Each point interacts with others within a finite distance δ called horizon. The interaction between any pair of points exists even when they are not in contact. This physical interaction is referred to as “bond”, which can be seen as a mechanical, generally non-linear, spring.

The equations that govern the motion of the points of the structure assume the following form:

$$\rho\ddot{\mathbf{u}}_i = \int_{Hi} \mathbf{f}\left[\mathbf{u}(\mathbf{x},t)-\mathbf{u}(\mathbf{x}_i,t),\mathbf{x}-\mathbf{x}_i\right]dV_j + \mathbf{b} \qquad (1)$$

$$\forall j \in Hi$$

where Hi is the neighbourhood of the point $\mathbf{x_i}$ limited by the horizon length, $\mathbf{u}$ is the displacement vector field, $\mathbf{b}$ is a body density force vector and $\mathbf{f}$ is called pairwise force function (with unities of force per unit volume squared), that represents the force that point $\mathbf{x}$ exerts on point $\mathbf{x_i}$. To assure the conservation of linear and angular momentum the force vector $\mathbf{f}$ between these particles (inside a bond) has to be parallel to their relative position vector. With this assumption, the following vectors $\boldsymbol{\xi}$ and $\boldsymbol{\eta}$ can be defined in Eq. (2). They represent the relative position and displacement respectively.

$$\boldsymbol{\xi}=\boldsymbol{x}-\boldsymbol{x}_i\ ,\ \boldsymbol{\eta}=\boldsymbol{u}-\boldsymbol{u}_i \qquad (2)$$

The bond stretch s (the relative elongation of a bond) can be obtained by the following formula

$$s=\frac{|\boldsymbol{\xi}+\boldsymbol{\eta}|-|\boldsymbol{\xi}|}{|\boldsymbol{\xi}|} \qquad (3)$$

The pairwise (PW) force function depends on the bond stretch: many laws can be used to describe the material behavior. For an elastic brittle material the PW force is proportional to the bond stretch itself; when the stretch reaches a given limit value (s_c) the bond breaks: once a bond fails, it cannot be recovered. The constitutive law for a brittle material is shown in Fig. 1. It is possible, comparing the elastic energy for a homogeneous deformation [3], relate the slope c (micromodulus) with the material elastic properties for the 2D case (see Eq. (4)).

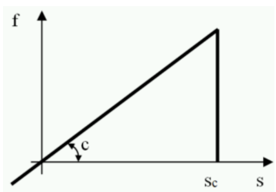

Fig. 1 Pairwise force function for a brittle material

$$c=\frac{48\cdot E}{5\cdot\pi\cdot t\cdot\delta^3}\quad \text{2D plane strain}$$
$$c=\frac{9\cdot E}{\pi\cdot t\cdot\delta^3}\quad \text{2D plane stress} \qquad (4)$$

The limit stretch s_c is estimated by the evaluation of the energy required to break all the bonds that initially connect points in the opposite sides of a fracture surface. This energy is related with the equivalent material property

G_{Ic}; the relevant formula (see [3] for more details) are reported on Eq. (5).

$$s_c = \sqrt{\frac{5\pi G_{Ic}}{12E\delta}} \quad \text{2D plane strain}$$
$$s_c = \sqrt{\frac{4\pi G_{Ic}}{9E\delta}} \quad \text{2D plane stress} \tag{5}$$

The local damage in a material point $\mathbf{x_i}$ is proportional to the ratio between the numbers of cracked bonds and the number of bonds initially connected to $\mathbf{x_i}$. Using a bilinear (or a more complex tri-linear, as for example shown in Fig. 2) PW force function, the concept of fatigue bond weakening can be introduced (see Fig. 3).

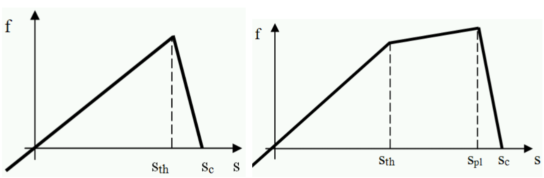

Fig. 2 Example of bi-linear and tri-linear pairwise force function

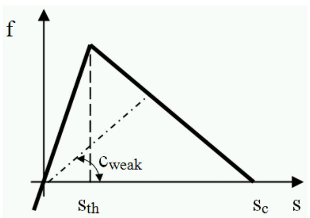

Fig. 3 Example of bi-linear and tri-linear pairwise force function

When the bond stretch exceeds a threshold level (s_{th}) the nominal bond stiffness c is reduced

$$c_{weak} = c \cdot (1 - D_N) \tag{6}$$

where c_{weak} is the weakened bond stiffness, c is the pristine bond stiffness and D_N is the fatigue damage after N cycles. The bond weakening process is irreversible. The total load will be composed by blocks of cycles, each block will be characterized by a fixed load amplitude and a number of cycles ΔN_i. Two components of damage increment are considered: static damage, ΔD_s, and fatigue damage ΔD_f, defined in Eq. (7). The fatigue damage formulation is inspired by previous work reported in references [7,8]. The sum of static and fatigue damage rates will be the total weakening damage rate for a bond.

$$\Delta D_s = \frac{s_{th} s_c}{s_c - s_{th}} \cdot \left(\frac{1}{s(N)} - \frac{1}{s(N + \Delta N)} \right)$$
$$\Delta D_f = \Delta N_i \cdot \frac{B}{1+\beta} e^{\lambda D_\mu} \left(\frac{s_\mu}{\delta} \right)^{1+\beta} \tag{7}$$

The static damage term is related to the increase of the resulting bond stretch s, whilst the fatigue damage term is related to the block number of cycles. The constants B, β and λ are related to the material fatigue behavior. For the numerical implementation an incremental approach has been adopted, the number of cycles will be considered as a real-valued variable and a rate-independent model is assumed, so in Eq. (1) inertia effects are neglected. The solution of the Eq. (1), including the bond fatigue weakening, is found using a standard Newton-Raphson technique.

2.1 Paris' law parameters

Life prediction for fatigue cracks was made easier and quantitative with the introduction of the Paris' law. The fatigue behavior of a material is usually represented with a diagram in which the rate of a crack growth is plotted against the stress intensity factor range ΔK on a log-log graph. The graph (see Fig. 4) shows three areas corresponding to the different crack propagation speeds: a regime with slow crack growth rate (near threshold), a regime with mid-growth rate (Paris' regime) and a last part with an high growth rate.

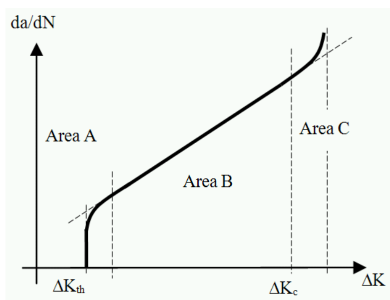

Fig. 4 Typical crack propagation diagram (log-log scale) Area A: slow growth rate regime, Area B: mid-growth rate, Area C: high growth rate.

Paris' law is reported in Eq. (8)

$$\frac{da}{dN} = C'\Delta K^{m'} \tag{8}$$

where a is the crack length, N is the number of the cycles, ΔK is the stress intensity factor range, C' and m' are empirical parameters evaluated by tests.

A modified version of the previous equation will be used for our purposes; in this version the strain energy release rate, G, is preferred to a local stress intensity factor, so the Eq. (8) can be rewritten as

$$\frac{da}{dN} = C\Delta G^{m} \tag{9}$$

In this paper the results obtained by implementing at bond level the damage model of Eq.(7) will be presented. Two main issues will be studied: the first one will be to verify if at macro scale the material behavior is similar to the one described by the Paris' law, and the second one will be to perform a sensitivity analysis on some of the peridynamic fatigue constants B, β and λ of Eq. (7).

3 Numerical simulations

To investigate the effectiveness of the fatigue model presented above, numerical simulations of fatigue driven crack growth have been performed in typical fracture toughness specimens.

3.1 Model for numerical simulation

The studied system for the fatigue crack simulation analysis is shown in Fig. 5

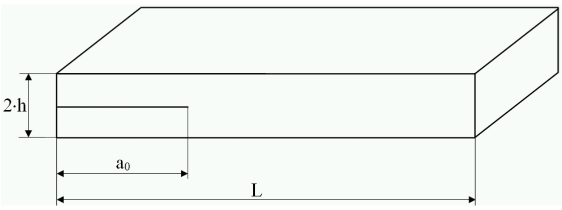

Fig. 5 System studied in the numerical simulations.

In this system an external moment is applied (see Fig. 6), in this way the loading condition at the crack tip is independent from the crack length itself.

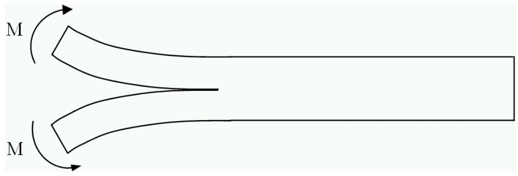

Fig. 6 Opposite external moment has been applied on the system.

As reported in [8] the energy release rate for this loading case is

$$G_I = \frac{M^2}{B_w EI} \tag{10}$$

In the Eq.(10) B_w is the specimen width, E is the longitudinal flexural Young's modulus and I is the second moment of area of the specimen arm. The numerical model is shown in Fig. 7; it is composed by 1212 nodes and 30080 bonds, the main material properties are: E=70 GPa, and G_c = 260 J/m^2, while the geometrical parameters are the following 2h=2.75 mm, a_0=7.25 mm and L=25mm.

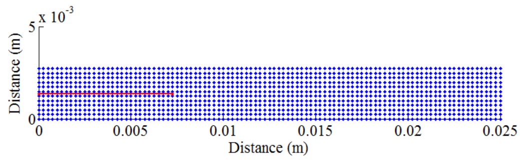

Fig. 7 Numerical model: the nodes are shown as dot points.

All simulations have been carried out using a Matlab code written by the authors, which implements the peridynamic theory. The fatigue simulations are performed with a static solver based on an implicit Newton-Raphson method and using the small displacement assumption.

3.2 Numerical simulation results

A first set of analyses has been performed in order to verify if the adopted fatigue model applied at bond level is able to describe the Paris' law behavior. The preliminary parameter set for the Peerling law is: B = 0.75, β = 2, λ = 0.5

Many values of external applied moments have been considered, in order to obtain the data for the Paris' law diagram.

For example, applying an external moment that makes G_I= 29 J/m^2 after 50000 cycles, the cracked bonds are shown in Fig. 8.

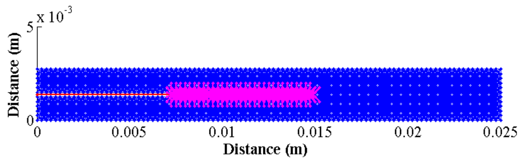

Fig. 8 Cracked bond propagation due to fatigue damage effect.

The displacements are shown in Fig. 9 (amplification factor 20) it is possible to see that the crack propagates along the specimen.

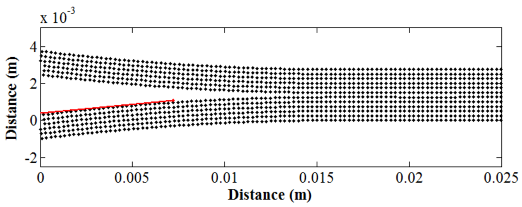

Fig. 9 Deformed structure after the fatigue crack propagation

The crack length versus the applied load cycle number is shown in Fig. 10, the analysis has been performed until a total crack length twice as long as the initial length.

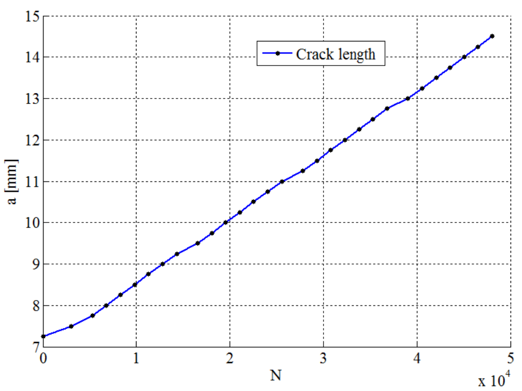

Fig. 10 Typical crack propagation diagram (log-log scale)

From these results it is possible to evaluate the crack speed (da/dN) for the applied external moment (G_I). Repeating the analysis for other external moment values, it is possible to build the diagram of da/dN versus G_I. The obtained results are shown in Fig. 11 which corresponds to the Paris' diagram (Area B in Fig. 4).

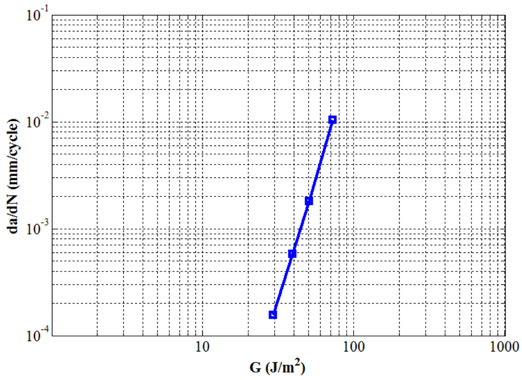

Fig. 11 Crack speed versus strain energy release diagram

Then, it has been shown that the fatigue damage model reported in Eq. (7) applied at bond level is able to describe, at macro level, a behavior as expected by the Paris' law.

To correlate the Peerlings' fatigue damage model parameters with the Paris' law parameters a set of preliminary analyses has been performed.

The influence of parameter B has been studied (the other parameters β and λ have been maintained at the their initial value β = 2, λ = 0.5). In Fig. 12 the effect of the B_{Peer} variation on the C parameter of the Paris law is shown. While in the Fig. 13 the influence of B_{Peer} on the m exponent of Paris' law is shown.

To obtain each point of the diagrams it was necessary to build a corresponding Paris law graph similar to the one shown in Fig. 11 in order to get the Paris' law coefficients.

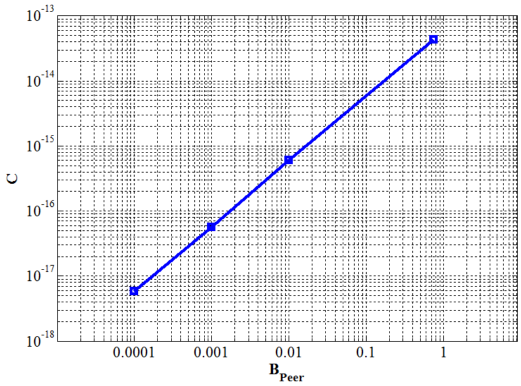

Fig. 12 Effect of B_{Peer} parameter on the C parameter of the Paris law.

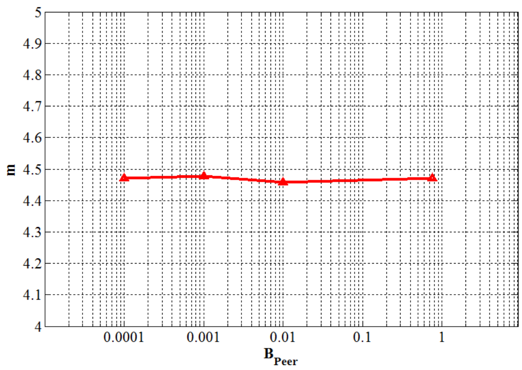

Fig. 13 Effect of B_{Peer} parameter on m exponent of the Paris' law.

The B_{Peer} parameter influences mainly the C parameter of the Paris law of Eq. (9) while the m exponent is slowly modified. This gives the possibility to identify the B_{Peer} parameter starting from the C coefficient of the Paris' law. Additional analyses must be carried out in order to study the effect of β and λ coefficients, using an similar approach.

4 Conclusion

The peridynamic theory is a recent theory of continuum based on integral equations. This theory is able to describe the behavior of bodies in presence of discontinuities such heterogeneities or cracks. The theory is also able to manage the crack interaction or branching without any other additional criteria. In this paper a fatigue damage model at bond level has been introduced and it has been shown that at macro scale it is possible to reproduce the Paris' law behavior. Then a strategy to study the effects of the bonds fatigue damage model on the Paris law coefficients has been presented. In particular, it has been shown that the B_{Peer} parameter significantly influences the C coefficient of Paris' law and only slightly the m exponent.

Acknowledgement

The financial support of the University of Padova PRAT-CPDA111598 is gratefully acknowledged.

References

[1] G. Alfano and Crisfield M. A., "Finite element interface models for the delamination analysis of laminated composites: mechanical and computational issues", *Int. J. Numer. Meth. Engng*, Vol 50, No. 7, 2001, pp. 1701-1736.

[2] G. Zi, T. Belytschko, "New crack-tip elements for XFEM and applications to cohesive cracks", *Int. J. Num. Meth. Engin.*, Vol. 57, No. 15, 2003, pp. 2221-2240.

[3] S.A. Silling, "Reformulation of elasticity theory for discontinuities and long-range forces", *J. Mech. Physics Solids*, Vol. 48, No. 1, 2000, pp. 175-209.

[4] Silling S. A., Weckner O., Askari E., Bobaru F., "Crack nucleation in a peridynamic solid", *Int J Fract*, Vol. 162, 2010, pp. 219–227.

[5] Y.D. Ha, F. Bobaru, "Studies of dynamic crack propagation and crack branching with peridynamics", *Int. Journal of Fracture*, Vol. 44, 2010, pp. 162-229.

[6] M. Zaccariotto and U. Galvanetto, "Modeling of Fatigue Crack Propagation with a Peridynamics Approach", *8th European Solid Mechanics Conference*, Graz, Austria, 2012

[7] R. H. J. Peerlings, W. A. M. Brekelmans, R. de Borst and M. G. D. Geers, "Gradient-enhanced damage modelling of high-cycle fatigue", *Int. J. Num. Meth. Engin.*, Vol. 49, No 12, 2000, pp. 1547–1569.

[8] Galvanetto U., Robinson P., et. al. ," A Simple Model for the Evaluation of Constitutive Laws for the Computer Simulation of Fatigue-Driven Delamination in Composite Materials", *SDHM*, Vol.5, No. 2, 2009, pp. 161-189.

A400M Aeroelastics and Dynamic Tests

M. Oliver[1], **G. Pastor**[1], **M.A. Torralba**[1], **S. Claverías**[1], **J. Cerezo**[1] and **H. Climent**[1]

[1] *Structural Dynamics and Aeroelasticity Domain*

Airbus Military, John Lennon s/n, 28906 Getafe (Madrid) Spain

Mercedes.oliver@military.airbus.com

Keywords: *Dynamic Loads, Aeroelasticity, Structural Dynamics, Flight Test, Ground Vibration Test.*

Abstract

Between December 2009, with the Airbus A400M First Flight, and the recent delivery of the first A400M to the French Air Force in August 2013, a fruitful flight test campaign has involved four prototypes and the first series aircraft.

This paper is devoted to present the A400M ground and flight tests used in the aeroelastics and dynamic loads models validation. Dynamic loads are among the A400M sizing critical load cases. For this reason the dynamic loads model validation is a critical issue in the certification path.

The first ground test that will be presented is the complete aircraft (A/C) Ground Vibration Test (GVT) that will be briefly described, to continue with Finite Element (FE) model updating to match test results. Next test will focus on Landing Gear (LG): the Drop Test, used to validate the isolated LG model and to demonstrate the LG target characteristics.

Taxi tests were performed in August 2010 at Francazal runway near Toulouse. The runway was equipped with an artificial (1-cos)-20-meters obstacle to validate the taxi loads model. A set of taxi runs with different speeds, with and without braking and/or reverse were performed. Flight test results will be compared with numerical simulations and the model update process will be described.

During all the flight test campaign, every severe landing was registered and analyzed. Several "hard landings" with sink speeds close to 12 ft/s will be compared with the numerical simulations. The LG and A/C coupling for dynamic loads calculation validation by using the controlled flight test firm landings will be shown.

The aeroelastic model for gust calculations has been validated using the same Flight Vibration Test (FVT) used for flutter envelope expansion. The FVT will be briefly described and the aircraft response to control surface sweeps and pulses compared with the numerical simulations.

The wake vortex model for wake encounter loads has been the last aeroelastic model to be validated, following a dedicated flight test campaign involving two A400M prototypes and a jet airliner.

In all cases, the paper will briefly describe the modelling techniques, the pre-test numerical simulations and the post-test updates when needed.

1 Introduction to Airbus A400M tests

Figure 1 shows a summary of the tests presented in this paper. These tests results are used to validate the different A400M dynamic loads models needed for Certification:

— The GVT is used to validate the A/C dynamic FE model.

— The Drop Test is used to validate the isolated LG model and to demonstrate the LG target dynamic characteristics.

— The resulting preliminary dynamic ground loads model needs to be validated separately for dynamic landing (Firm Landings) and dynamic taxi (Taxi Tests over obstacles) models.

— On the other hand, the A/C dynamic FE model is coupled with the unsteady aerodynamic model and the Flight Control System (FCS) model to obtain the dynamic flight loads model, which is validated with the FVT results by means of control surfaces frequency sweeps.

— Although not regarded in any certification specification from loads point of view, dedicated Wake Encounter Tests have been performed to be used for the wake vortex loads model validation.

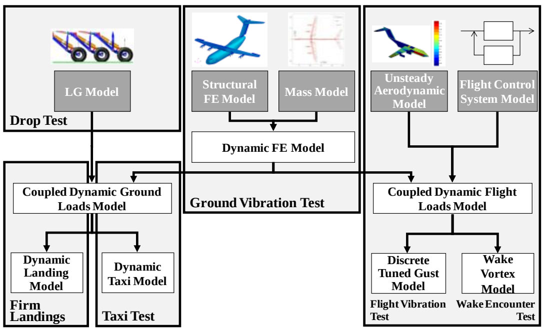

Figure 1 A400M dynamic loads models validation flow chart

2 A400M Ground Vibration Test

The A400M GVT was performed in Airbus Military facilities at Seville in October-2008, [1] and [2]. The objective of the GVT was to experimentally obtain the complete aircraft normal modes and in particular:

— Frequencies & mode shapes.

— Damping & modal mass.

— Non-linearities ([3]).

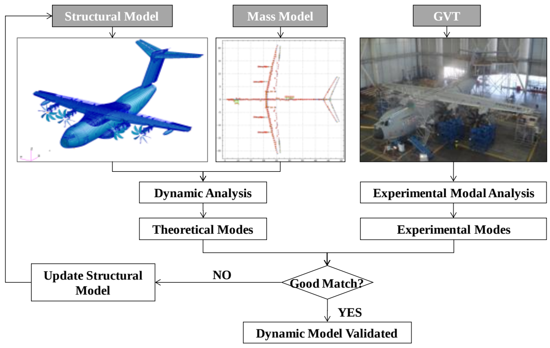

Figure 2 A400M GVT flow chart

Different types of excitation (random, sweep sine and phase resonance method) are used in the different test execution phases (structure global response overview, frequency range of interest and single normal mode tuning), [4].

GVT results can be shown in a plot that compares theoretical modal frequencies (obtained from a FE model, for instance) with experimental data. Ideally, test results should be aligned with the 45° division line (continuous red line in Figure 3). The closer these data are to this line, the better the model is behaving and fewer changes will be needed.

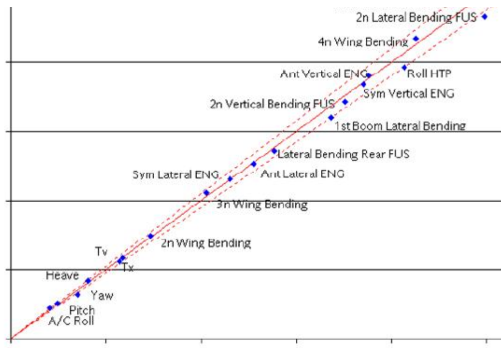

Figure 3 Typical GVT results plot

The test results have been used in turn to validate and update the structure FE model. Modes frequencies and shapes obtained in the GVT have been matched by means of beams connecting the fuselage and lifting surfaces elastic axis points superimposed to the FE model. Those beams stiffness modify the FE model global stiffness, [5].

3 A400M Landing Gear Drop Test

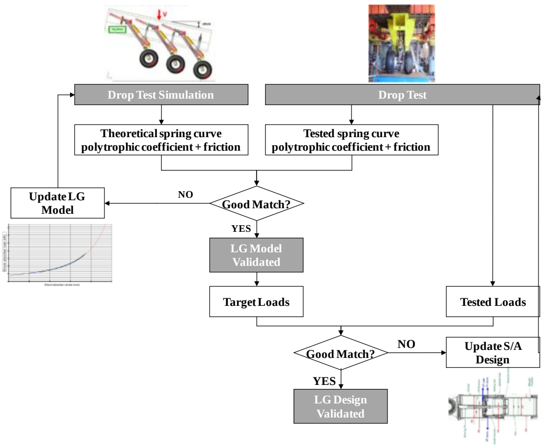

Figure 4 A400M LG model and design validation flow chart

Relevant parameters for Dynamic Landing (DL) and Taxi adjusted in this test:

— Vertical load on the leg vs. strokes.

— Shock absorbers (S/A) loads vs. S/A strokes.

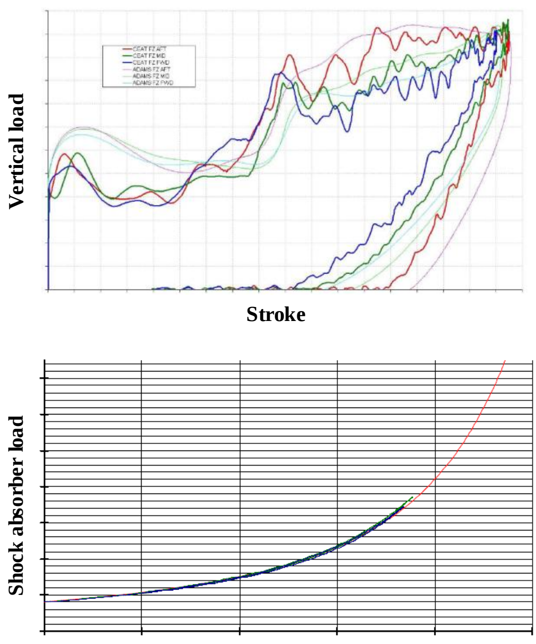

Figure 5 A400M Landing Gear adjustment curves

4 A400M Dynamic Loads Tests instrumentation

4.1 Loads measurements

Different kinds of loads have been monitored among the entire A/C in order to compare the Flight Tests (FT) results with the computed values:

— Integrated loads: The measurements at the extensometers placed along the wing, the fuselage, the horizontal tailplane (HTP) and the vertical tailplane (VTP) (Figure 7, red lines) are post processed with the method suggested by Skopinski [6] to obtain the integrated loads (Figure 6). The total amount of measured load magnitudes is 54.

	FX	FY	FZ	MX	MY	MZ	TOTAL
Wing	-	-	10	10	10	-	30
Fuselage	-	3	3	3	3	-	12
HTP	-	-	2	2	2	-	6
VTP	-	2	-	2	-	2	6
							54

Table 1 Integrated loads measurements summary

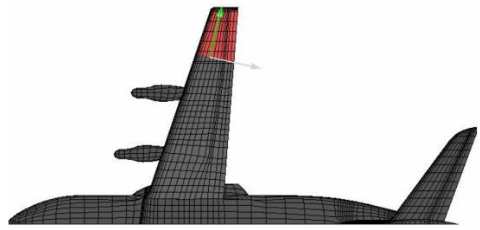

Figure 6 Example of integrated load on wing

— Interface loads: 112 magnitudes measured:

	FX	FY	FZ	FXZ	TOTAL
LG to aircraft (pintles)	26	26	26	-	78
Wing to fuselage	4	-	4	4	12
EMS to wing	8	-	8	-	16
VTP to HTP	2	2	2	-	6
					112

Table 2 Interface loads measurements summary

4.2 Accelerometers

In addition to the loads, the 114 accelerometers shown in Figure 7 (green dots) and Table 3 have been selected to monitor the aircraft behaviour during the flight test campaign:

	NX	NY	NZ	TOTAL
Wing	12	-	28	40
Fuselage	6	6	6	18
HTP	6	-	16	22
VTP	4	9	-	13
LG	7	7	7	21
				114

Table 3 Accelerometers summary

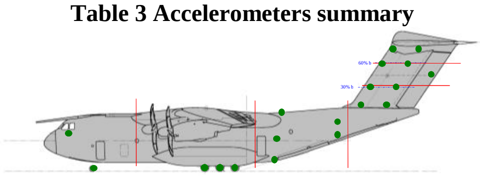

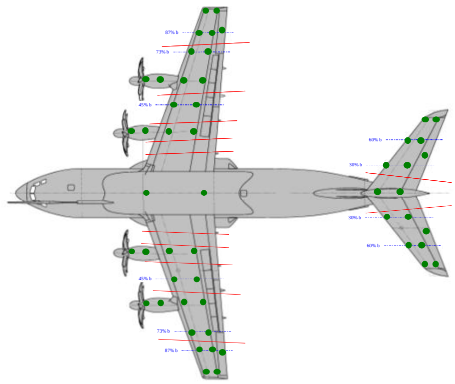

Figure 7 Accelerometers (dots) and loads (lines) recorded during flight tests

4.3 Other measurements

Other 111 LG magnitudes have been measured and used for the model validation:

— Pressures on different chambers
— Temperatures on different parts
— Shock absorbers strokes, speeds and forces

	Press	Temp	Stroke	Speed	Load	TOTAL
NLG	3	2	1	1	6	13
MLG	12	2	6	6	72	98
						111

Table 4 LG measurements summary

5 A400M Firm Landings

5.1 Coupled A/C-L/G Dynamic Landing model validation process

Actual aircraft firm landing tests are used to validate the mathematical coupled approach, [7].

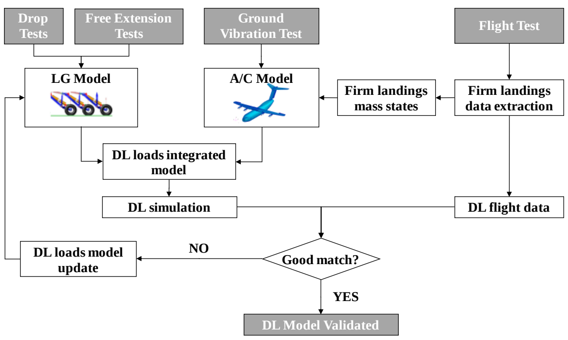

Figure 8 A400M dynamic landing loads model validation flow chart

5.2 Brief description of the DL numerical simulation model

During landing, the airplane vertical velocity is quickly reduced to zero when wheels strike the ground. This process transfers the sinking airplane kinetic energy to internal energy in the shock absorption system. The rapid change in velocity and equally rapid forces application causes dynamic phenomena in the airplane structure.

The LG non-linearities, related with its kinematics and some of its components elastic characteristics, constitute the main difficulty in these loads determination. The non-linear coupled system of equations that defines the A/C-LG system movement should be solved numerically in an iterative process in the time domain, [8]. In addition, the LG flexibility is an essential feature for an accurate determination of DL loads.

The problem can be solved either uncoupled (conservative) or coupling the LG with the A/C. Airbus Military has been using the modern coupled approach for some years in the A400M design, an aircraft in which dynamic landing cases are sizing large parts for some structural components like forward and rearward fuselage or wing down bending. The approach uses the FE Method (FEM) technique to model completely the L/G (MSC.ADAMS), the A/C (MSC.NASTRAN) and the coupling (MSC.ADAMS).

Component Mode Synthesis technique is used to obtain LG-A/C attachment loads with both the effect of A/C flexibility and attachment effects. Craig-Bampton reduction output, obtained with MSC.NASTRAN SOL103, is introduced to MSC.ADAMS to solve the coupling (non-linearities and mechanisms) and provide the pintle loads.

These loads are subsequently introduced to an A/C model without the LG model to obtain the A/C modal response (MSC.NASTRAN SOL 112). From that modal response, the integrated distribution of internal loads is obtained using in-house software (DYNLOAD).

5.3 Firm landings results and comparison with pre-test numerical simulations

A firm landing is an event in which an aircraft performs a controlled landing with a large sink rate. These events are particularly suitable for validating Dynamic Landing models because they allow loading the model with high loads and so, assessing how accurate limit load levels are. Figures below show comparisons between numerical simulation model and flight test measured firm landings for both loads and accelerations at a 10.9 ft/s firm landing.

Figure 9 shows two time-histories corresponding to fuselage shear force and bending moment. Continuous blue line represents the numerical simulation (fully coupled A/C & L/G) while the red line is the measured test results.

Figure 10 shows four time-histories: front and rear fuselage, as well as wing and HTP tip vertical accelerations comparison.

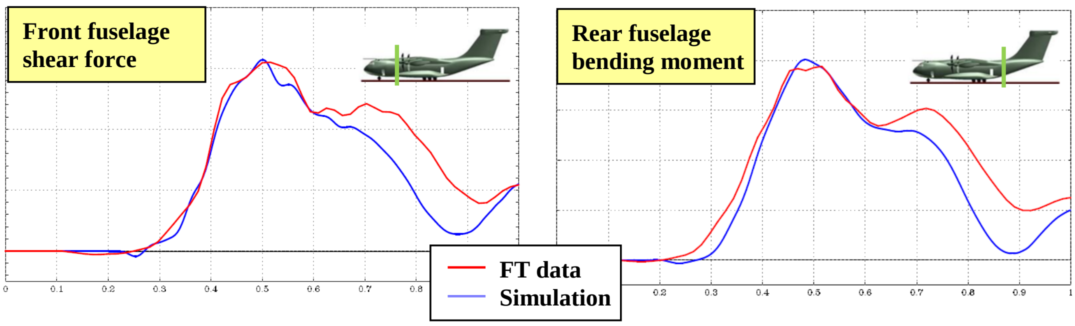

Figure 9 A400M test-simulation loads comparison. 10.9 ft/s landing

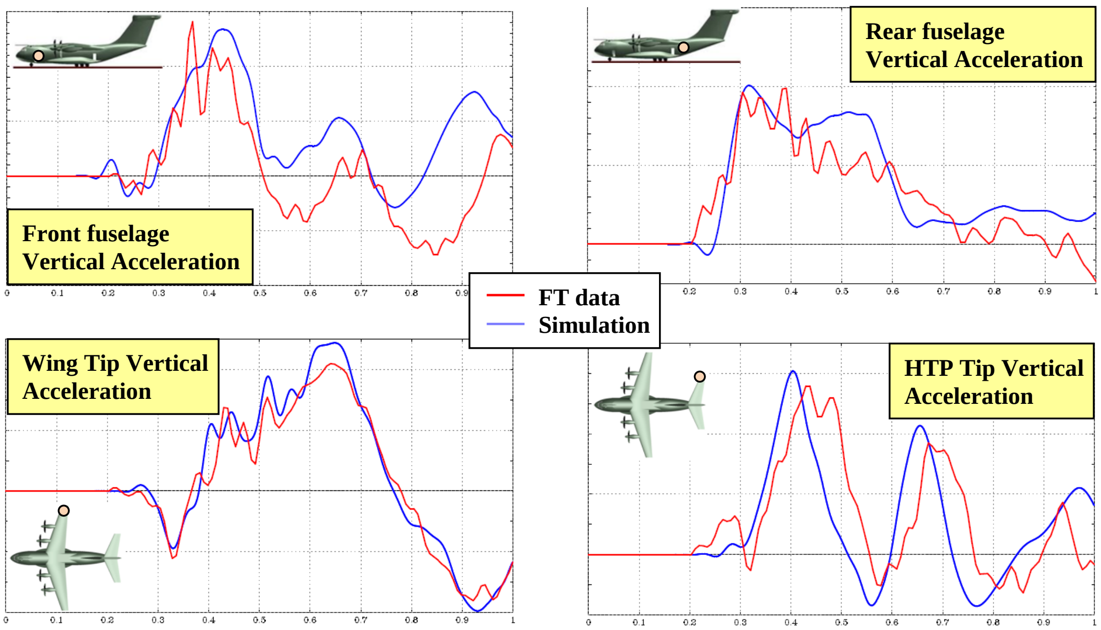

Figure 10 A400M test-simulation accelerations comparison. 10.9 ft/s landing

5.4 Comparison remarks

— Results match between test and simulation is better for high sink rates than for low sink rates. As high sink rate cases provide sizing loads, they are the most relevant cases to be successfully matched. The better agreement in these cases increases confidence in the design load levels obtained.

— **Damping**: There is no unsteady aerodynamic effect in Dynamic Landing model, so it is introduced by increasing modal damping. Beware that this damping increase is not used within cargo hold elements because they are not in contact with the external flow and consequently they are not benefited from that extra damping.

— **1P loads:** The incremental contribution of 1P load depends on the variation of the in-flow angle (not on its stationary value) and on the A/C speed. The in-flow angle typical variation during a landing touch-down is less than 1 degree, and the A/C speed is low, so the contribution of 1P incremental loads to DL loads is considered negligible.

— The pre-test fully coupled DL model was considered enough accurate or conservative to provide certification loads.

6 A400M Taxi Tests

6.1 Coupled A/C-L/G Taxi model validation process

Runs over runway irregularities (bumps and troughs) are used to validate the taxi model, [7].

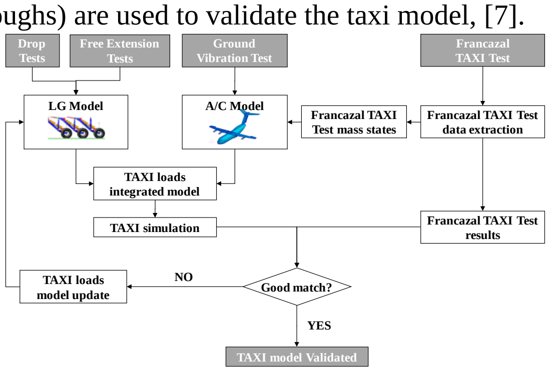

Figure 11 A400M taxi loads model validation flow chart

6.2 Brief description of the taxi numerical simulation model

During A/C take-off, rejected take-off (RTO) and landing taxi runs, the A/C low frequency modes can couple (at certain speeds and A/C configurations) with runway irregularities, increasing the internal loads due to dynamic phenomena.

Airbus Military has a long tradition of working with the taxi dynamics loads problem. The first version of the tool was developed in the late 80's and successfully applied to the CN-235 aircraft. With significant improvements, the current tool (DYNTAXI) is suitable to deal with very complex landing gears like those of the A400M. The A/C structure is considered a linear system governed by a set of equations in modal coordinates. The LG equations keep all the kinematic and elastic non-linearities of tires and S/A, considering as rigid all the structural components of the LG. The coupling of these two systems leads to a system of LG equations that takes into account its non-linear behavior and its interaction with the flexible A/C structure, [8].

The LG is considered like a mechanism of rigid elements on which the tires, the S/A and the rest of the A/C structure actuate. The LG elements mass characteristics are represented by lumped masses.

As a result of the system integration, DYNTAXI obtains the loads in the L/G elements, the parameters defining its behavior (tire deformation, S/A displacement…) and the interaction forces between the A/C and the LG. These loads can be applied directly to the aircraft structure to obtain the aircraft response on the considered runway (MSC.NASTRAN SOL 112). From the modal response, the integrated distribution of internal loads is obtained using in-house software (DYNLOAD).

6.3 Description of the taxi test in Francazal

The A400M tests campaign has included taxi runs over standard obstacles. This test was performed in the Francazal airfield near Toulouse in August 2010. One of its main objectives was validating the A400M dynamic taxi loads model. Figure 12 shows the A400M

MSN2 running over one of the obstacles used at this test.

Figure 12 A400M running over the (1-cos) bump during Francazal test

Three kinds of wooden obstacles were tested. Their shape and size are defined below:

— Single bump (1-cos): used to validate the dynamic taxi loads model.

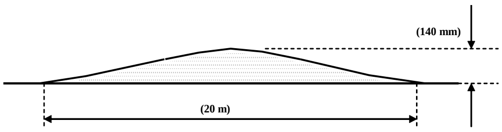

— Single repair-plate MAT-2: used to study the response of the system to a single impact.

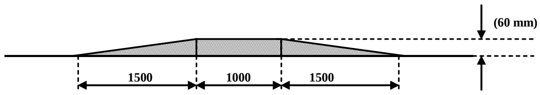

— Single step: used to study the maximum tire deformation.

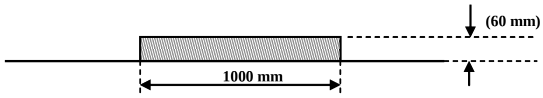

The Francazal runway profile was measured in order to assure the usage of the right input to the dynamic taxi simulation. The test consisted of successive trials over each obstacle, varying the A/C speed, centre of gravity position, thrust, brakes and flaps deflection.

6.4 Taxi test results and comparison with pre-test numerical simulations

Next figures show comparisons between simulation model and one of the trials over the (1-cos) bump for both loads and accelerations.

The taxi test run selected to be presented in this paper corresponds to particularly severe conditions for both the wing down bending moment and the NLG vertical force, two of the A400M magnitudes sized by taxi.

Figure 13 shows two time-histories corresponding to the NLG (left) and Front Right MLG (right) legs vertical force. Continuous blue line represents the numerical simulation while the red line is the measured test results:

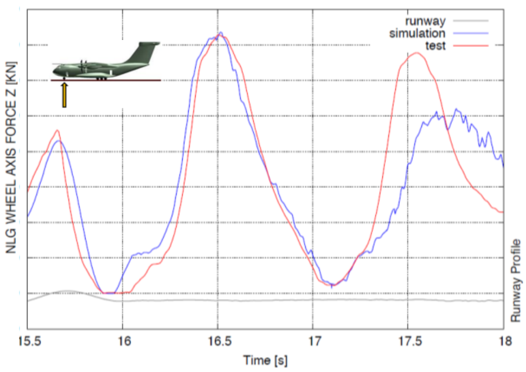

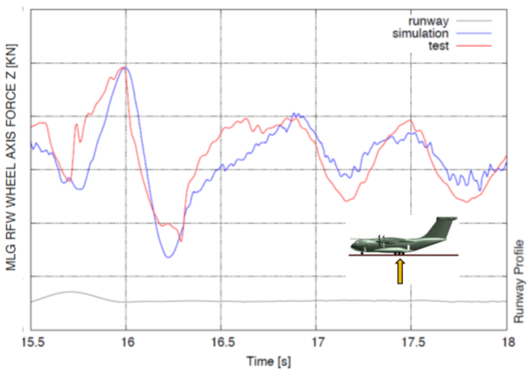

Figure 13 A400M test-simulation LG loads comparison. (1-cos) bump

Figure 14 shows the comparison of four loads and accelerations time-histories in representative points of the A/C structure:

— Wing tip vertical acceleration.
— Front fuselage shear force.
— Wing root bending moment.
— Wing root torsion moment.

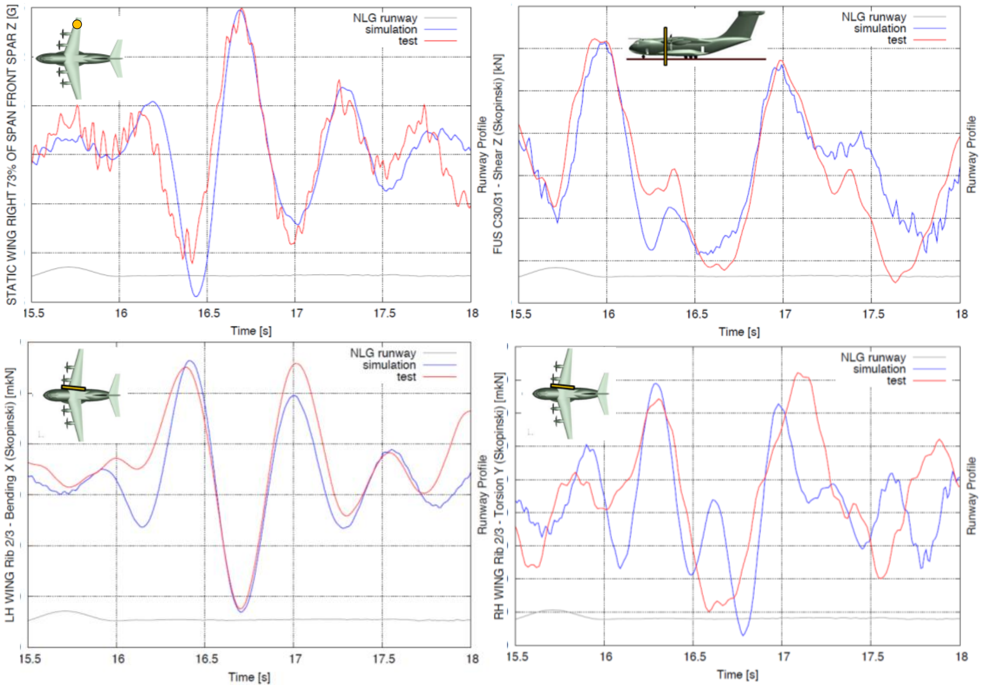

Figure 14 A400M test-simulation A/C loads and accelerations comparison. (1-cos) bump

6.5 Comparison remarks

— Dynamic taxi simulations show better correlation with test results for the trials that produce high A/C and LG loads (near to the sizing loads) rather than for those that produce low loads. The better agreement in these cases increases confidence in the design load levels obtained.

— **Damping**: There is no unsteady aerodynamic effect in Dynamic Taxi model, so it is introduced by increasing modal damping with A/C speed.

— **1P loads**: The incremental contribution of 1P load depends on the variation of the in-flow angle (not on its stationary value) and on the A/C speed. The typical variation of the in-flow angle during a landing touch-down is less than 1 degree, and the A/C speed is low, so the contribution of 1P incremental loads to taxi loads is considered negligible.

— The pre-test fully coupled Dynamic Taxi model was considered enough accurate or conservative to provide certification loads.

7 A400M Flight Tests (control surfaces frequency sweeps)

7.1 Aeroelastic model validation process

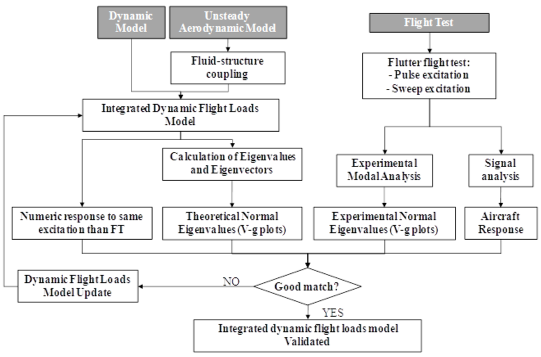

Figure 15 A400M fight loads model validation flow chart

7.2 Brief description of the aeroelastic numerical simulation model

The general aeroelastic equation can be expressed as:

$$\left(-M_{hh}\omega^2 + iB_{hh}\omega + (1+ig)K_{hh} - \frac{1}{2}\rho V^2 Q_{hh}(M,k)\right)\{u_{hh}\} = \{P(\omega)\} \quad (1)$$

Where M_{hh}, B_{hh} and K_{hh} are, respectively, the modal generalized mass, damping and stiffness matrices. Q_{hh} is the modal generalized aerodynamic force matrix, function of Mach (M) and reduced frequency (k). $\{P\}$ is the non aerodynamic generalized loads vector.

When the second term of (1) is equal to zero, the aeroelastic equation represents a stability problem (the flutter equation) and when the second term is different from zero, the aeroelastic equation represents a response problem (e.g. gust response or, in this paper, the oscillation of the control surfaces).

Both approaches can be used for validation of the aeroelastic model:

— Theoretical V-g plots (evolution of modal frequency and modal damping with flight speed) can be compared vs. the experimental modal analysis results measured in flight.

— Simulation of the aircraft response to controlled oscillations from different control surfaces can be compared with measured values from flight test.

Unsteady aerodynamic forces Q_{hh} are computed using the Doublet Lattice Method (DLM) [9]. The DLM model includes:

— Flat panels to model lifting surfaces (wing, horizontal tail and vertical tail) and control surfaces (Ailerons, Elevator, Rudder).

— Engine modelled as a flying ring plus pylon.

— Fuselage modelled as a cross of panels.

Structure-aerodynamic interpolation is made by using surface splines. The lift of each panel is adjusted for tuning the aerodynamic derivatives obtained in wind tunnel tests.

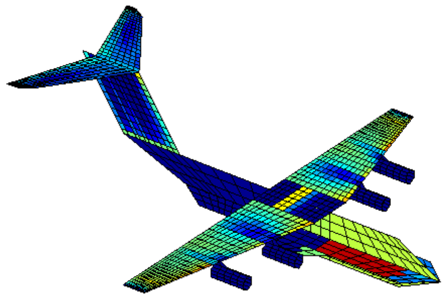

Figure 16 A400M aerodynamic model

7.3 Description of the Flight Vibration Tests

In a Flight Vibration Test, the aircraft flying -normally- at constant speed and altitude is excited by control surfaces pulses or sweeps.

The A/C response to this excitation is measured in the accelerometers and loads monitoring stations. The aircraft envelope is expanded by progressing successively increasing the dynamic pressure, Mach number, etc.

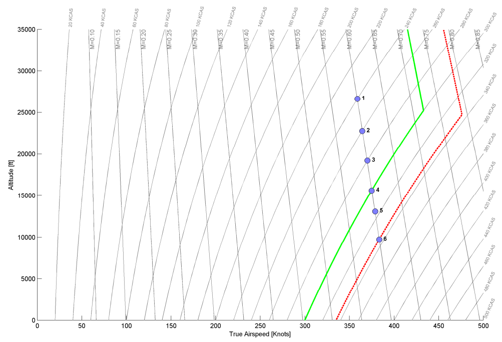

Figure 17 Typical flight envelope for flight vibration tests

The control surfaces excited are:

— Aileron (Symmetric & Antisymmetric).

— Elevator (Symmetric & Antisymmetric).

— Rudder (Antisymmetric).

The numerical analysis should simulate the actual motion of the control surfaces measured in flight post processed by means of a high-pass filter.

The results presented in this paper correspond to a flight devoted to aeroelastic model calibration performed at M=0.6. Table 5 shows the three different type of excitations used in the A400M Flight Vibration Tests.

A400M Excitations	Frequency (Hz)	Pulse	Amplitude
Low frequency sweeps	1.5-6.0		~0.5º
High frequency sweeps	4.0-8.0 & 6.0-12.0		~0.5º
Pulses		200 ms with 10 ms ramp	1º,2º & 3º

Table 5 Type of excitations

7.4 FVT test results and comparison with numerical simulations

Two types of test results can be obtained:

— V-g plots.

— Aircraft response to control surfaces oscillations.

The V-g plots comparison in Figure 18 and Figure 19 shows the evolution of the damping with the speed for the first symmetric and antisymmetric wing bending modes. The experimental values match the curve theoretical behavior. The mode experimental frequency also matches the theoretically stable value.

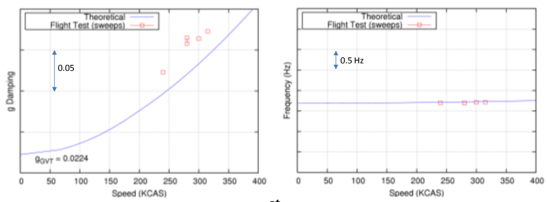

Figure 18 V-g plots for 1st symmetric wing bending mode

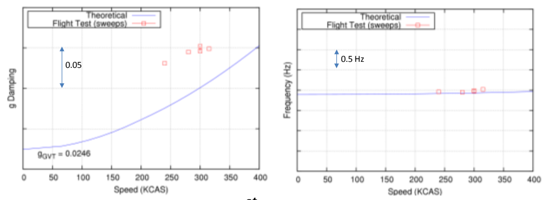

Figure 19 V-g plots for 1st antisymmetric wing bending mode

Similar V-g plots have been obtained for the most important symmetric and antisymmetric modes (i.e. for 6 symmetric and for 7 antisymmetric). Comparison between analytical predictions and test was good in all cases.

With respect to A/C response to control surfaces oscillations, the aileron antisymmetric oscillation has been selected to compare test and numerical results. Figure 20 shows this comparison for accelerations (Nz) and loads (Fz) in wing tip.

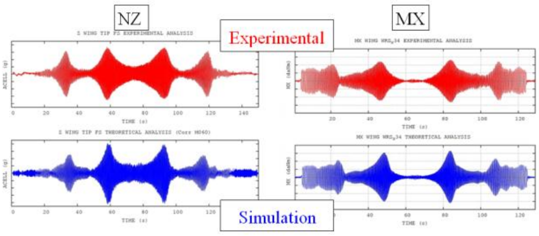

Figure 20 Comparison Experimental data vs. Numerical simulation (Wing tip dynamic loads & accelerations)

7.5 Comparison remarks

For each mode, the V-g plots show good matching for damping and frequency evolution with the speed.

Aircraft response to sinusoidal sweeps generates longer signals with less noise that allow a better analysis and produces better results than the short pulses.

The sinusoidal sweep of control surface is also used to validate the aeroelastic model. More quantity of aircraft modes is excited with the symmetrical aileron movement (Table 6). For this reason, the comparison obtained is better, although the other control surface excitations produce good results as well. The comparison is also better for low frequencies than for high frequencies but the differences are not very large.

Symmetric main modes	Difference
First wing bending	0.02 Hz
Pylon pitch with four engines down	0.07 Hz
Pylon pitch with outer engines down and inner engines up	0.13 Hz
First wing chordwise	0.23 Hz

Table 6 Symmetric main modes and differences between numerical and experimental frequency

The numerical results for symmetric aileron oscillation are generally conservative: 7% in peak accelerations and 2.5 % in peak loads. This conclusion can be extended for other control surface oscillations: antisymmetric aileron, symmetric elevator and antisymmetric rudder.

8 A400M Wake Vortex Encounter Flight Tests

8.1 Wake vortex model validation process

Wake vortex encounter (WVE) is a dynamic phenomenon occurring when an aircraft (the follower or crossing aircraft) crosses the vortex velocity field previously generated by itself or by another aircraft (the leader or generating aircraft). Apart from the controllability and handling quality aspects, this encounter may yield significant loads that should be studied in a similar way to that of discrete tuned gust, except that the velocity field is much more complex now.

In addition to the aeroelastic model validation, required for gust and turbulence loads analyses, the wake model requires an additional validation process through dedicated flight tests.

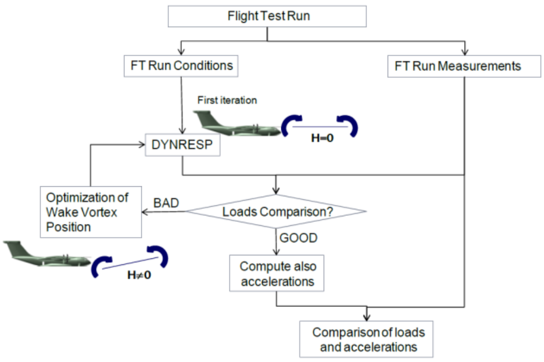

Figure 21 A400M wake encounter loads model validation flow chart

In these tests, the leader aircraft is equipped with smoke-generators to provide a visual location of the wake. Despite the smoke threads, it is quite difficult for the follower aircraft to achieve a full hit of the wake and usually there is a deviation of some meters from the target. Thus, the strategy to fit the numerical simulations to flight test results (Figure 21) involves an iterative process to find out the actual distance of the crossing aircraft with respect to the vortices. Other uncertainties, like the vortex decay or the vortices separation, can be determined as part of this iterative process. Predictive models of vortex core radius increase due to vortex aging can also be included in the analysis.

8.2 Brief description of the wake vortex simulation model

The wake vortex model, from the Prandtl slender wing theory, consists of a couple of counter-rotating vorticity tubes (Figure 22). This is more accurate the longer the streamwise distance travelled from the generating aircraft is. The present work is focused only on encounters that happen in the far wake, where the assumption of a pair of counter-rotating vorticity tubes is valid, [10].

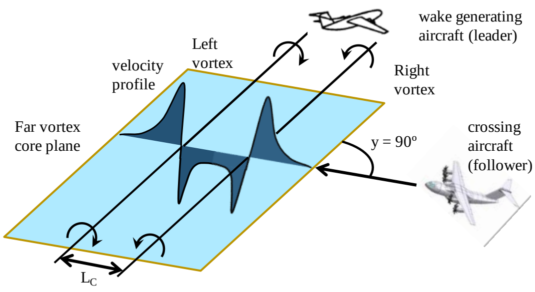

Figure 22 Far wake model

The resultant velocity at point P is the combination of the azimuthal velocities and induced by the right and left vortex tubes. To avoid the singularity of the classical potential theory at the vortex core, some expressions have been developed to represent the actual fact that the velocity is finite at the vortex centre. For this work, the azimuthal velocities are given by the Hallock–Burnham model.

Once the wake model has been characterized by the vortex core radius *rc*, the vortex separation L_C and the vortex circulation Γ, the velocity field induced by the wake is known at any point of space. The problem of determining the velocity profile seen by each point on the crossing aircraft is the problem of determining the path of each point along the wake.

In the general case of an aircraft crossing the wake at a height $H \neq 0$ from the vortex core plane at an angle $\Psi \neq 90^o$ (Figure 23), the velocity at a point of the aircraft has two components:

— A vertical velocity w.

— A lateral velocity v.

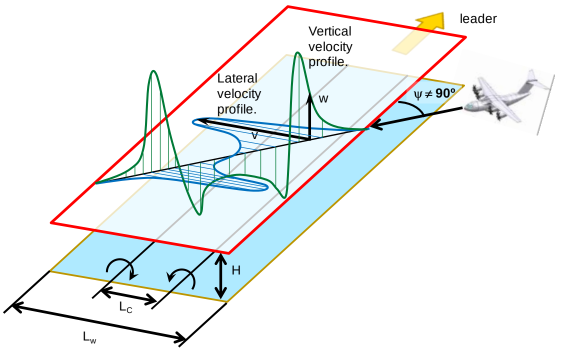

Figure 23 Case H ≠ 0, Ψ≠ 90º

The Airbus Military in-house software WESDE (Wake Encounter Speed Distribution Evolution) has been programmed so as to provide the velocity field to the dynamic equations of motion solver, DYNRESP (aeroservoelastic package), [11].

8.3 Wake vortex encounter Tests Description

The methodology presented in §8.1 has been validated with an extensive flight test campaign in the A400M MSN1 prototype. 249 wake encounters devoted to WVE loads measurements, split in two separate parts, have been performed by both crossing large airliner wakes and the wakes generated by another A400M (MSN3 prototype), for different flight conditions and Ψ angles:

Part 1: A400M crossing the wake of a jet airliner (140 runs).

Part 2: A400M crossing the wake of another A400M 109 runs. It is a way to replicate, for instance, the aircraft crossing its own wake in a wind up turn.

The airliner wake was already well known in advance from previous FT campaigns. Therefore Part 1 allowed assessing the response of the A400M to an already known wake. Part 2 was also used to characterize the wake of the A400M.

Two kinds of hits were performed: (Figure 24): Nose hits, aimed to measure wing high load cases and Tail hits, aimed to measure T-tail high load cases.

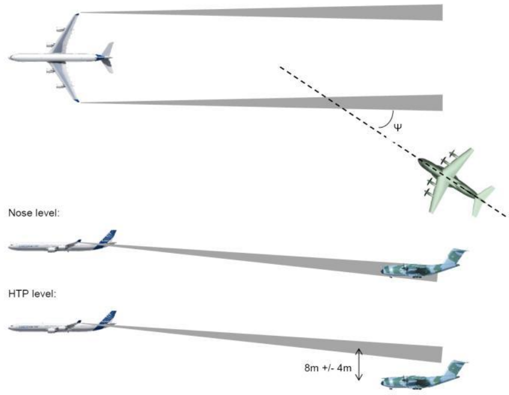

Figure 24 Two types of WVE: nose and tail

8.4 Wake vortex encounter test results and comparison with numerical simulations

Two different numerical tools were used for WVE loads calculation: DYNRESP and VARLOADS. A more detailed description of these tools approach can be found in [12].

Comparison between test measurements and DYNRESP and VARLOADS numerical simulations are presented herein. Red lines in next figures correspond to FLIGHT TESTS time histories (THs), green lines to VARLOADS and blue lines to DYNRESP.

Figure 25 shows an example of shear and bending THs at the wing root, corresponding to a run with Ψ≈90º in which high response at the wing was measured.

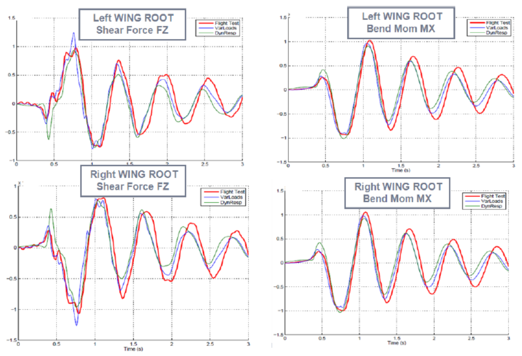

Figure 25 Incremental wing root shear and bending THs during a Ψ≈90º WVE (wing hit)

Figure 26 shows an example of shear and bending THs at the wing root, corresponding to a non-perpendicular crossing with Ψ≈40º.

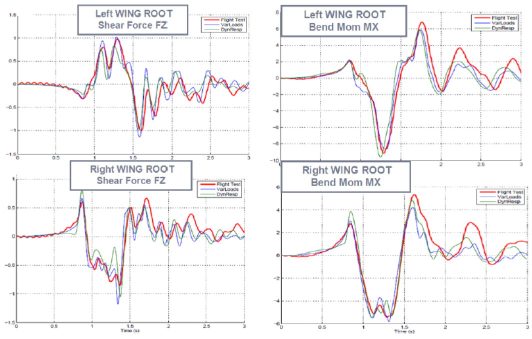

Figure 26 Incremental wing root shear and bending THs during a Ψ≈40º WVE (wing hit)

Figure 27 illustrates an example of shear and bending THs at the HTP root, corresponding to a run hitting the T-tail of the aircraft with Ψ≈50º and high response at the HTP.

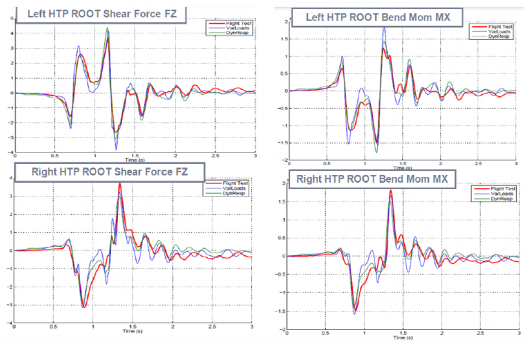

Figure 27 HTP root shear and bending THs during a Ψ≈50º WVE (T-tail hit)

Last case presented corresponds to a WVE run with high VTP response. Figure 28 shows the comparison of shear, bending and torque at the VTP root in a run with Ψ≈40º.

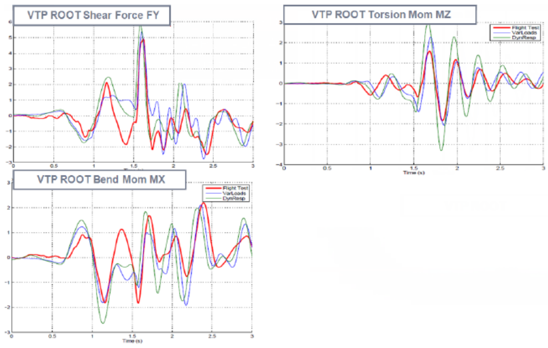

Figure 28 VTP root shear, bending and torsion THs during a Ψ≈40º WVE (T-tail hit)

8.5 Comparison remarks

— Perpendicular crossings (Ψ≈90º) are verified through the symmetry of results between left and right side. In those runs there is a very good matching between Flight Tests and numerical simulations using both VARLOADS and DYNRESP.

— Non-perpendicular crossings (Ψ≈40º-50º) are much tougher runs to match. The asymmetry between left and right sides is evident as it should be for a non-perpendicular crossing of the wake.

— Runs hitting the wing and runs hitting the T-tail of the aircraft with high response at the HTP show very good matching between FTs and simulations.

— Runs with high VTP response have shown to be the most difficult magnitudes to match. Shear and bending moment time histories correlate fairly well and there is a good representation of the peak values of both magnitudes. On the other hand, although shape of the torsion moment time history is also correct, peaks are conservative for this magnitude. Two reasons have been envisaged as a possible explanation of this conservatism: Lack of damping in the DLM in-plane movements and T-tail effect.

9 Conclusion

Dynamic Ground Loads

In general, the isolated models (i.e. aircraft FE model and landing gear FE model) needed some level of adaptation. Once the models were matched to isolated test results, the numerical simulation of the coupled models (dynamic landing and taxi) proved to be accurate enough or slightly conservative without need of updating.

Dynamic Flight Loads

Discrete Tuned Gust model is more difficult to check directly because there is no possibility in exciting the aircraft with an (1-cos) gust. Nevertheless the use of flight flutter tests provides a way of indirect validation by comparing the sets of results:

— V-g plots.
— A/C response to control surface oscillations.

It was found that pre-test models were accurate enough or slightly conservative without need of matching for the computation of the incremental part of the DTG analysis.

Validation of Wake Vortex loads model has required innovative FT. The procedures envisaged to hit the wake of the generating aircraft were adequate. The instrumentation, test data acquisition system and subsequent post processing were suitable for the purposes of the tests. The iterative process to adjust the wake model parameters has fully validated the numerical simulation tools.

References

[1] Oliver, M., Rodriguez Ahlquist, J., Martinez Carreño, J. and Climent, H. “A400M GVT: the Challenge of Nonlinear Modes in Very Large GVT’s”. *Proceedings of the International Forum of Aeroelasticity and Structural Dynamics, IFASD 2009,* Seattle. June 2009. Paper 40.

[2] Peeters, B. and Climent, H. “Optimisation of Ground Vibration Testing using Structural Dynamic Models”. *Showcase 2010 Special issue of the Aerospace Testing Magazine*, pp 96-98.

[3] Rodriguez-Ahlquist, J., Martinez-Carreño, Climent, H., De Diego R. and De Alba, J. “Assessment of Nonlinear Structural Response in A400M GVT”. *Proceedings of IMAC 28, the International Modal Analysis Conference,* Jacksonville, Florida USA. February 2010. Paper 94.

[4] Peeters, B., Climent, H., de Diego, R., de Alba, J., Rodriguez-Ahlquist, J., Martinez-Carreño, J., Hendricx, W., Rega, A., García, G., Deweer, J., and Debille, J., “Modern Solutions for Ground Vibration Testing of Large Aircraft”. *Proceedings of IMAC 26, the International Modal Analysis Conference, Orlando (FL), USA.* February 2008.

[5] Sanchez-Zabala, F., Oliver, M. and Climent, H. “Influence of High Performance Computing on Aeroelasticity and Structural Dynamics”. *Proceedings of the CEAS 2011 European Air and Space Conference.* Venice. October 2011.

[6] Skopinski, T. H., Aiken, W. S., Jr. and Huston, W. B. “Calibration of strain-gauge installation in aircraft structures for the measurements of flight loads”. *NACA Technical Report* 1178, 1953.

[7] Pastor, G., Pérez-Galán, J.L., Climent, H., Rodriguez-Jimenez, A.J., Pérez de la Serna, A. and Veguillas, S. “A400M Tests used for Dynamic Loads Model Validation”. *Proceedings of the International Forum of Aeroelasticity and Structural Dynamics IFASD 2011.* Paris, June 2011. Paper 166.

[8] Pérez-Galán, J.L, Benitez, L., Oliver, M. and Climent, H. “Survey of Aircraft Structural Dynamics Non-Linear Problems and some Recent Solutions”. *CEAS 2009 European Air and Space Conference,* Manchester. October 2009. Paper 132.

[9] Albano, E. and Rodden, W. P. “A doublet-lattice method for calculating lift distributions on oscillating surfaces in subsonic flows”. *AIAA Journal, vol. 7, issue 2, pp. 279-285*. February 1969.

[10] Claverías, S., Karpel, M., Cerezo, J., Torralba, M.A., Reyes, M. and Climent, H. " Wake Vortex Encounter Loads Numerical Simulation". *International Forum of Aeroelasticity and Structural Dynamics IFASD2013*. Bristol, June 2013.

[11] Karpel, M., Shousterman, A., Reyes, M. and Climent, H. "Dynamic Response to Wake Encounter". *54th AIAA/ASME/ASCE/AHS/ASC Structures, Structural Dynamics, and Materials Conference.* Boston, April 2013.

[12] Climent, H., Lindenau, O., Claverías, S., Viana, J.T., Oliver, M., Benítez, L., Pfeifer D. and G. Jenaro-Rabadán. "Flight Test validation of Wake Vortex Encounter Loads". *International Forum of Aeroelasticity and Structural Dynamics IFASD2013*. Bristol, June 2013.

4:th CEAS Air & Space Conference
FTF Congress: Flygteknik 2013

Advantages of an Integrated Simulation Environment

Markus Kunde and Andreas Schreiber
Simulation and Software Technology
German Aerospace Center (DLR)
51147 Cologne, Germany

Keywords: Simulation, MDAO, Integration, CPACS, RCE

Abstract

Numerical simulation software in the field of aircraft design can be classified as first, second or third generation Multi-Disciplinary Analysis and Optimatzion (MDAO) system. The most challenging task nowadays is to create a third generation MDAO because there are no good-practice rules how to create a useful software system. The prerequisite for a success-story of such a software is a successful consideration of the dependency of simulation scenario (workflow), simulation models and the simulation data. Some good-practice rules for developing a third generation MDAO can be extracted from monolithic first generation systems regarding this dependency. The still under development software *RCE for CPACS* is a system for applied numerical aviation pre-design simulations and a technology carrier for evolving a third generation MDAO. The current state of *RCE for CPACS* regarding the good-practice rules will be outlined. A future state will be sketched considering possible next steps on the way to a successful third generation MDAO.

1 Introduction

Simulation in the aircraft engineering domain is a challenging task. Different knowledge domains have to work together to fulfill the requirements each domain has regarding the aircraft. From a historical view there are three generations of systems which meet this challenging task [1]. First generation Multi-Disciplinary Analysis and Optimization (MDAO) systems are described as single user operating a monolithic simulation workflow. The second generation is described as a distributed system with different simulation models but with a single user. The third generation consist of a distributed system with multiple users, representing design or model experts.

In this paper, we describe the third generation MDAO system of the German Aerospace Center (DLR). It is developed, maintained and used by most aeronautic institutes of DLR, especially the institutes for Aerodynamics and Flow Technology, Air Transportation Systems, and Simulation and Software Technology.

2 Advantages of an Integrated Simulation Environment

Third generation MDAO systems are still under development and therefore there is no best practice answer how such a system should be designed. In the following we will focus on third generation MDAO systems as this research is done in the field of distributed simulation systems. It may be possible to transfer the results to monolithic systems as well, but usually their internal structure follows the concept we want to achieve in a distributed system. Within third generation MDAO systems there is a collaborative point of view onto multidisciplinary scenarios which include the relationship and dependency of each domain to the others. Ques-

Table 1: Structure of simulation aspects

Aspect	Technical View
Workflow	Simulation environment for execution of simulation workflows. Software which is able to perform simulations. Needs integration possibility of simulation models. Should be able to combine models and describe their relationship.
Model	Algorithm which represents domain specific knowledge. Possibility to insert data, calculate algorithm and receiving a result.
Data	Data item which describes the knowledge domain(s).

tions like "how should a simulation perform?" or "what supporting features are needed to build up a simulation scenario?" should be answered [2]. But there is also a technical view on these simulation scenarios possible. Each simulation consists of three aspects:

Simulation Workflow. A simulation workflow represents the complete simulation scenario and consists of simulation models and their relations.

Simulation Models. A simulation model describes a self-containing (coherence) simulation aspect. Combining two or more models result in a simulation workflow description.

Simulation Data. The data representing the result of each simulation model and therefore the result of the simulation workflow.

This collection represents the lowest common denominator for any simulation and without one of them a simulation scenario is not possible. Having a closer technical look at each aspect shows the usual structure (see Table 1).

It is obvious that each simulation aspect has a relationship to another (see Figure 1). The typical relationship observed in many distributed simulation environments is: "Simulation workflow knows simulation model which knows simulation data". This approach has some disadvantages because no aspect has knowledge about the others. The workflow has no knowledge about the current content of the simulation data and the complete simulation cannot react on it. The simulation model does not have any knowledge about the workflow system and cannot act well in the workflow context. In the following we will describe our approach with its advantages to tackle this disharmonic situation. These benefits touch the observed drawbacks in the typical relationship mentioned above.

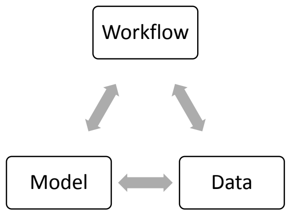

Figure 1: Dependency cycle of simulation aspects.

2.1 Structural View on MDAO systems

In a third generation MDAO system where workflow, model and data are integrated into each other several advantages exist. The structure of such a solution will be described in the following. A concrete solution will be introduced in section 3.3.1. From an engineers point of view the integrated solution looks as follows:

Simulation Workflow. The simulation workflow system is a software where simulation models and data are integrated. The system considers at least a concept how to integrate a model with its specifics, e.g., their data connections or computer environment. It shows specific views onto the model and let the user make use of the model in its native or in a predefined conceptual way. The data format is considered in the system as well. Specific possibilities for choosing data items out of the data or specific views are necessary. In the highest integration dimension data format specifics are hidden and an aircraft engineers view onto the data appears.

Simulation Model. The simulation model is aware about the data format. It integrates in a naturally way into the internal algorithm of the model. There is no conversion to own data format(s) necessary regarding any loss of information during conversion. The model considers the simulation workflow system. It uses its advantages and its way to integrate a model into the workflow system.

Simulation Data. The simulation data consist of all data artefacts all models need. It describes the full dimension of the simulation task.

Supporting Simulation Software Libraries. Supporting libraries are a very common way to centralize parts of the simulation algorithms. The access to the data format or basic calculations can be made at this point and simulation models and workflow system can make use of it.

The following set of rules describe the advantages of an integrated MDAO system. They were extracted from the described structure above and evolved to our approach.

Hiding data format specifics in simulation workflow system. Hiding data specifics in a workflow system under a more engineers related view implies a flat learning curve instead of a high initial effort. Persons who are new to this research topic are affected as well as every involved person when, e.g., a change in the data format is made.

Way of working fits to data format, models and workflow. Every workflow system, every simulation model and even a data format have their own way how they work and how they should be used. When all aspects have the same view on data, model and workflow, they act in the same way and do not contradict in their processing. This is the case when a model-driven approach meets a data- oder process-driven one. These different approaches fit rarely together.

Affecting changes in data format usually results in changes of simulation environment. The direct dependency from data format to model and workflow system results in a direct change of both when something meaningful is changed in the data format. This is in most situations a good approach for the user because he always has the most up-to-date information about the data format. There is of course also a direct dependency between workflow system and model. These dependencies have the manner to be loosely coupled and therefore have a continous modification character instead of being too much or to less regarding their frequency and substantial.

Same calculation basis. The same calculation basis (regarding the supporting software libraries) have a very high effect to the quality of the results. When using a common shared software library there is no discrepancy between the simulation models with respect to their internal assumptions about the data. The same access to the data format can be used as well as some shared calculation algorithms. This affects a single point of failure regarding results.

Working direct on data. As each aspect, workflow system and simulation models, have direct access to the data format they can make use of it as their internal data model. This has the benefit that no conversion irreversibilities can occur. This sort of error has the same high effect on the quality of calculation results like the same calculation basis.

React on data internals. Then the workflow system is aware of the data format and is able to comprehend data changes it is possible to create a more intelligent system. It can prevent the user from mistakes or may react on changes regarding the workflow.

2.2 Generic Proposal of MDAO System

In a more concrete detailed view, a typical MDAO system should not regard only some rules of how workflow, models and data fit together. It should consider also different kind of insights how such a system should act with respect to some software usability guidelines. Therefore a workflow containing models which interact with data is only one view onto a simulation. Depending on the fact that there are several different disciplines with different perspectives onto a simulation or a part of a simulation, each of these different groups should be considered with a special view on a simulation. During designing an MDAO system a clear identification of every user group and its look onto the simulation should be made. Table 2 shows an extract of some possible user groups.

In general each discipline should work on their

Table 2: Extract of possible user groups.

User Group	View Description
Engine Designer	Should see the engine in detail. Engine parts or fluids flow are in focus of interest.
Aero-dynamics Designer	Interested in a detailed geometry view, e.g., with some dynamics. Possibility to modify geometry should be given.
Economics Designer	Valueing the aircraft or fleet with some boundary conditions. View on data is a strong calculation and formula one.
Aero-elastics Designer	Has a similar view on geometry like the aerodynamics designer, but with some other focus.
Simulation Designer	Is interested in the complete simulation workflow. Should see the dependencies between different disciplines.
Data Quality Analyst	The consistency and correctness of the data are in main focus. The main question is if the simulation outcome is valid and trustable.

own topics with their own 'natural' view onto their special part of the simulation. This makes it more easy to create a simulation and to evaluate the results.

The separation into views and the underlying simulation structure has a strong decoupling effect which is neccessary for avoiding too heavy maintenance effort. The simulation aspects itself (workflow, models and data) should be strongly coupled together as there is a strong dependency to each other.

2.3 Benefiting Effects of Coupling

As already described in section 2.1 the coupling of workflow, models and data has some benefiting effects we will focus more concrete in the following. Therefore a closer look at the roles of each aspect should be made.

Simulation Workflow. The simulation workflow has some more tasks than connecting simulation models and the regulation of data flow. Following the main topics a workflow should be aware of:

- Knows dependencies between models or models and data
- Prevents user from usage-errors
- Assists of design task
- Knows how a model works (for control) and for what tasks it can be used
- Gives statement to quality of results
- Represents data in adequate way
- Reacts in a smart (intelligent) way on any changes (with, e.g., modified process execution)

All of these points ensure the outcome of the simulation regarding consistency and correctness of data. In other words, the simulation workflow is responsible for trustability of the result.

Simulation Models. The simulation model represents a specific aviation discipline. Nethertheless it needs knowledge of the outside environment. Following the main topics a model should be aware of:

- Knows how workflow works (model-, data- or process-driven) and support this behavior
- Ensures consistency of data regarding all data which are adressed by the model

These points affect the model and its outcome. A model is thereby always responsible for the quality of the result.

Simulation Data. The simulation data represents at least the complete simulation data-artefacts. But it has some more tasks as being a container for aviation-results:

- Knows which data items influence each other

- Knows which models access to specific data items and therefore data knows the dependencies between the models
- Knows every change of a data item and track the changes each model performs

Summarizing the aspects of the workflow (responsible of trustability of the result), models (responsible of quality of the result) and data (the outcome of the simulation) are equally important to a simulation environment. As all of them have dependencies to the outcome it is necessary that every aspect is aware of the other two aspects.

2.4 Example "VAMPzero"

The advantages can best shown on a monolithic system because the concept described above takes the advantages of a monolithic system to a third generation MDAO system with its distributed nature. The reference example is the simulation model "VAMPzero" [3]. VAMPzero is a conceptual aircraft design tool based on handbook methods. It integrates the CPACS data format [4] and is model and workflow system in one tool. VAMPzero is able to trace changes on data because it directly tracks relationships between the used algorithm and the underlying data item. Therefore it can resolve dependency forward ("what data item/algorithm is based on the current calculated algorithm") and backward ("from what data item/algorithm is the current calculated algorithm addicted"). There is a full recognition of what is happening during calculation and therefore the trust and quality of the outcome is extremly high. Changes in the workflow or model or data aspect is directly available to the other aspects as well because they are related to each other. We transfered this integrated concept to a third generation MDAO system.

3 Integrated third generation MDAO system

The integrated third generation MDAO system of German Aerospace Center (DLR) consist of all three simulation aspects and one additional

Table 3: Simulation aspects at DLR

Aspect	Concrete DLR Software
Workflow	RCE for CPACS
Model	Several simulation algorithms which implement the "CPACS-"way of integration into RCE
Data	CPACS data format
Libraries	TiXI & TiGL

aspect. The simulation aspects are identified in 2.4 while the additional aspect (supporting software libaries) is introduced in the same section. To come to the concrete simulation environment at DLR, a mapping to concrete names of software should be introduced (Table 3).

The section will describe each aspect on its own.

3.1 Data Format - CPACS

The Common Parametric Aircraft Configuration Scheme (CPACS) [4] is

> "one potential step towards a unified data model".

B. Nagel et al. introduce CPACS as the data format which is designed for performing collaborative MDAO simulations in aircraft design. The format of CPACS is human readable and provides a computer a structured access. It is based on Extensible Markup Language (XML) and is defined as a schema definition (XSD). CPACS has a hierarchical structure based on the parts of an aircraft and can describe, beside the entire vehicle, many related aspects of aircraft design (e.g., missions or fleets). The format handles product and process information. Each part of the aircraft is called component. In the hierarchical structure assemblies can be defined which are based on components. They can be used multiple times via a referencing approach with Unique Information Identifiers (UIDs). This avoids redundancies in the data format. On top of W3C XML specification [1] two techniques are added. At first external data-files can be referenced in the XML data format and will included

[1] http://www.w3.org/XML, 01.03.2013

during reference into a sub-node of the CPACS data. The second addition is CPACS-support for multi-dimension arrays which can be specified. More information about CPACS can be found in [5, 6].

3.2 Supporting Libraries - TiXI & TiGL

There are two supporting libraries based on CPACS data format.

TiXI. TiXI [2] provides an Application Programming Interface (API) for access to CPACS data. As CPACS is based on XML-technology with some additions, these specifics are hidden behind one interface. TiXI is available for several programming languages such as C, C++, Python, Java and Fortran.

TiGL. TiGL [3] provides an Application Programming Interface (API) for higher functions regarding CPACS data. TiGL is the geometry library related to CPACS, based on open-source CAD-kernel OpenCASCADE [4]. It provides access to geometry information and several basic calculation algorithms.

3.3 Simulation Workflow System - RCE

The simulation framework *RCE* [5] (Remote Component Environment) is an open-source product from the DLR institute Simulation and Software Technology [6], department Distributed Systems and Component Software and the Fraunhofer Institute for Algorithms and Scientific Computing (SCAI). *RCE* is a workflow component framework for distributed computing based on the Eclipse Rich Client Platform (RCP) and provides core functions needed in a distributed environment [7, 8]. It executes a distributed workflow which looks and acts like a data flow diagram. These simulation workflows consist of several components which represent different simulation models. These simulation models can be system and data independent. That means each component wraps the specific simulation code with its special data or operating system dependencies and provides an interface to the simulation framework *RCE*. This has several advantages:

- The Simulation model is independent from other models. The interfaces between them are *RCE* internal
- Possibility to mix different technologies (e.g., programming languages)
- Simulation models are network-compatible regardless of their technology
- Other actors cannot see implementation details of a simulation model
- Programmer can define a fixed interface to their simulation model
    - Reduce possibility of wrong usage
    - Possibility to change interface of the simulation model without interfering *RCE* interface

In the workflow editor area (Figure 2), rectangles represent the simulation models and edges represent the data flow. In general it is possible to create and execute simulation workflows with these two elements. On the right side different available components can be chosen to build more complex workflows, e.g., Python component or other simulation models provided at DLR. The lower part of the screenshot shows three different viewparts. On the lower left side all data available from a simulation workflow can be displayed, analyzed or compered with previous workflow-runs. The lower middle shows the console output of all simulation models involved in a simulation workflow. In the lower right corner a graphical representation of the geometry information in CPACS is presented. Nethertheless there are more functionalities in *RCE* (e.g., options for pre- and post processing of data or execute parametric studies or doing optimization).

[2] http://tixi.googlecode.com, 01.03.2013
[3] http://tigl.googlecode.com, 01.03.2013
[4] http://www.opencascade.org, 01.03.2013
[5] http://www.rcenvironment.de, 01.03.2013
[6] http://www.dlr.de/sc, 01.03.2013

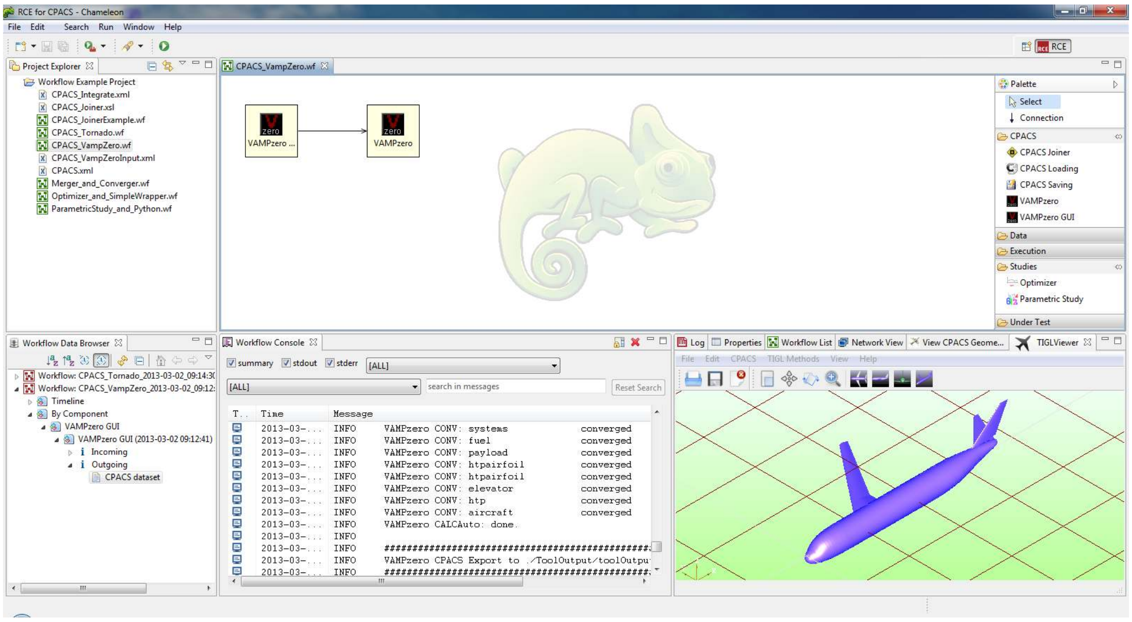

Figure 2: Workflow editor view of *RCE for CPACS*.

3.3.1 RCE for CPACS

RCE for CPACS is a special distribution of RCE regarding the CPACS data format. It has several additions for a more common way to work with CPACS in a workflow and simulation model environment. From a workflow systems point of view there are two simulation aspects which should be taken care of. The integration of a simulation model into the workflow system is necessary with respect to its behavior and its interface to CPACS. Simulation data should be integrated into the workflow system as well.

ToolWrapping. A wrapping approach was developed and evolved many times (see [8], [9], [10] and current documentation [7]). It connects the simulation model with a special CPACS-related concept to the simulation workflow system. This concept has a contractual manner and ensures that both parts have enough understanding of each other. The concept includes an abstraction layer. All simulation aspects (workflow, model and data) are related to each other but there is a well defined interface which ensures that small changes do not affect other parts.

XPathChooser. The main tasks of the engineer need that he is able to address one specific data item in the complete CPACS data format. The XPathChooser dialogue window let him choose the correct node in CPACS for further processing. It provides a special hierarchical view on CPACS data with its specific approach to point to one data item. This graphical element is used at several points in RCE for CPACS, every time the user should have access to a specific data item in CPACS.

TiGLViewer. TiGL as a geometry library has an on-top build viewer for CPACS geometry. This viewer component is integrated into RCE for CPACS to have a look onto the current CPACS geometry during execution of a simulation workflow (Figure 2, right lower corner). It is often used for quick error recognition as a specialized view on data is much more intuitive and easier to use than a textual or hierarchical representation.

XML Editor and Compare. CPACS is based of XML. Therefore it is obvious to add a specific XML editor to RCE for CPACS. It can be used to show or edit CPACS data. There is

[7]www.rcenvironment.de, 01.03.2013

also a comparing view available for comparing two CPACS datasets, e. g., at different times or locations in a workflow.

4 Next Steps on the Road to MDAO

The road to a success-story of third generation MDAO systems is already stepped on even the finish-line is not overstepped yet. This also concerns *RCE for CPACS* as well as other simulation systems. The goal of a useful and accepted MDAO system can be achieved with two different approaches. The first one is to sketch how a possible final software should work and look like and how it should be developed. The second approach is to evolve a software with involving aviation pre-design engineers until the software reaches the goal. We chose the second approach as there is a strong learning curve for aircraft engineers and MDAO software vendors. Also there is no accordance in the community how a third generation MDAO system should look like and therefore no complete concept-description is available. In our opinion it is neccessary to learn from each other and fullfilling little steps towards a final system. This is the reason we want to share our good-practice rules and discuss it.

To come to an outlook of our next steps two aspects should be considered. The first one is understanding MDAO in the context of a distributed simulation including different persons and knowledge domains and how they want to work together. The second aspect is to enhance *RCE for CPACS* as a technology carrier with experience gained in understanding MDAO as a collaborative and interdisciplinary process.

But how we want to move forward in the next months?

- Collecting more good-practice rules via analyzing current available software regarding similarities and distinctions

- Analyzing current working process with *RCE for CPACS* with respect to what performs well and what problems and drawbacks we should face

- Sharing experience with users, researchers and other aviation pre-design engineers

- Enhancing *RCE for CPACS*
  - Bind dataset CPACS in a more intuitive and integrated way in graphical user interface
  - Performing usability studies with respect to pre-design work-tasks
  - Bind pre-design work-tasks in a more intuitive and integrated way in graphical user interface
  - Focus common dataset more into center of simulation (checking validity, consistency)

In our opinion a consistent and trustable dataset is one of the key features of an intelligent MDAO system. The second key feature is to face every work-task of every involved person and to integrate it into the software. The challenge is hereby to identify the important tasks from an avation pre-design view, implement a task-supporting approach in the software and to map it to the mental model of the each involved engineer. This becomes even more important and complex when different approaches of performing pre-design will collaborate.

5 Conclusion

Current third generation MDAO systems do not consider the relationship between the simulation workflow, its underlying simulation models and the data processed in the simulation. There are several drawbacks this situation brings into effect. Some effects are related to the quality trustness of the simulation outcome while others affect the control concept of the simulation. If the relationship between these aspects can be considered in a simulation environment many quality-decreasing aspects can be reduced. In addition to the three simulation aspects "workflow", "models" and "data" a fourth aspect "supporting software libraries" is introduced. Our answer to the question how a third generation MDAO system should be designed is to consider the relationships and peculiarities of the workflow system, the simulation models and the data format in every part of the whole simulation environment.

The German Aerospace Center (DLR) developed a third generation MDAO system with consideration of the relationship of all four simulation aspects. It is based on the CPACS data format which holds process and product information, a concept for integrating CPACS into simulation models and a concept to combine CPACS and simulation models into a simulation workflow system called "RCE for CPACS". This solution is a collaborative work of most aeronautic institutes of DLR. The key roles maintain within the Institute for Aerodynamics and Flow Technology, Institute of Air Transportation Systems and Simulation and Software Technology. DLR pursues the objective to evolve this solution to a standard simulation environment for us and all our partners in research and industry. It is still under development and will enhance in the future with ideas from inside DLR and from the growing open source community. Especially collaboration with partners and the integration of their solutions into our software environment is part of our interests.

References

[1] I. Kroo
Multi-Disciplinary Design Architectures: History and Status. *Multidisciplinary Design Consortium, Stanford University*, 2006.

[2] D. Boehnke et al.
Challenges for Collaborative Data Management in an MDAO Process. *DLRK 2012. German Aeronautics and Space Congress*, 10.-12. September 2012.

[3] D. Boehnke et al.
Towards a Collaborative and Integrated Set of Open Tools for Aircraft Design *ASM 2013. 51st AIAA Aerospace Sciences Meeting*, January 7.-10. 2013.

[4] B. Nagel et al.
Communication in Aircraft Design: Can We Establish a Common Language? *ICAS 2012. 28th International Congress of the Aeronautical Sciences*, September 23.-28. 2012.

[5] D. Boehnke et al.
Evaluation of Modeling Languages for Preliminary Airplane Design in Multidisciplinary Design Environments. *DLRK 2012. German Aeronautics and Space Congress*, 31. August - 2. September 2010.

[6] C. Liersch, M. Hepperle
A Distributed Toolbox for Multidisciplinary Preliminary Aircraft Design. *CEAS 2011. CEAS Aeronautical Journal p. 57-68*, 2011.

[7] D. Seider et al.
Open Source Software Framework for Applications in Aeronautics and Space. *IEEE 2012. Aerospace Conference*, March 2012.

[8] A. Bachmann, M. Litz, M. Kunde, and A. Schreiber
Advances in Generalization and Decoupling of Software Parts in a Scientific Simulation Workflow System. *ADVCOMP 2010. Fourth International Conference on Advanced Engineering Computing and Applications in Sciences*, October 25.-30. 2010.

[9] A. Bachmann, M. Litz, M. Kunde, and A. Schreiber
A dynamic data integration approach to build scientific workflow systems. *IWWM 2009. In: 4th International Conference on Grid and Pervasive Computing: International workshop on workflow management*, May 04.-08. 2009.

[10] A. Bachmann, M. Litz, M. Kunde, Lothar Bertsch and A. Schreiber
Automation of Aircraft Pre-design Using a Versatile Data Transfer and Storage Format in a Distributed Computing Environment. *ADVCOMP 2009. Third International Conference on Advanced Engineering Computing and Applications in Sciences*, October 11.-16. 2009.

PLIF experiments in a turbulent reactive flow using an afterburner

Florin G. Florean, Ionut Porumbel and Cristian Carlanescu
Romanian National Institute Research and Development Institute for Gas Turbines, Bucharest, 061126, Romania

Gheorghe Dumitrascu
"Gheorghe Asachi" Technical University, Iasi, 700050, Romania

Keywords: *Afterburner, Planar LIF, radical species concentration fields, flame stability*

Abstract

The paper presents Planar Laser Induced Fluorescence (PLIF) measurements in a premixed methane-air turbulent flame in an afterburner system installed on a gas turbine engine. The PLIF measurements are based on capturing the fluorescence of Hydroxyl (OH).

The afterburner system used here was designed and manufactured at INCDT - COMOTI and was installed downstream of a Garrett 30-67 gas turbine engine used as a gas generator. A description of the afterburner is included. The flame stabilization in the afterburner is achieved by means of a bluff body that creates a recirculation region in the flow, serving as a source for the continuous ignition of the fresh mixture.

The measured mean and fluctuating fields of the OH concentration are presented both in an axial, and in a transversal direction, at several locations downstream of the bluff body flame stabilizer. The measurements indicate a highly turbulent flame, with an extensive turbulent flame brush, and high turbulent fluctuations of the flame front. The flame is found to be stable, thus validating the afterburner design.

1 Introduction

The PLIF technique is an optical spectroscopic diagnosis technique used for the non-intrusive investigation of reactive gas flows in order to determine the concentrations (mass or molar fractions) of various chemical species in the flow. Briefly, when tuned to specific wavelengths, the LASER radiation will excite certain species (molecules), in our case OH, to a higher energy level. Fluorescence occurs when this excited state decays and emits radiation of a longer wavelength than the incident laser radiation. Quenching is negligible and the fluorescence signal is proportional to the OH concentration. The colors of the images captured using the LIF system represent absolute concentrations of OH and not just relative fluorescence intensities. More details on the PLIF technique can be found in the literature [1, 2]. The equipment used for the measurements presented herein, as well as the software used for data processing was produced by the German company LaVision GmbH [3]. The PLIF measurement installation is briefly described in Fig. 1:

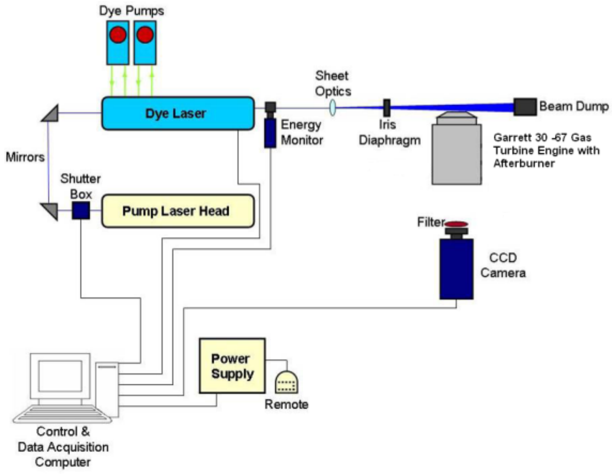

Fig. 1 – Schematic diagram of the PLIF measurement equipment

2 Experimental apparatus

The experimental apparatus used for the results presented herein is presented in Fig. 2.

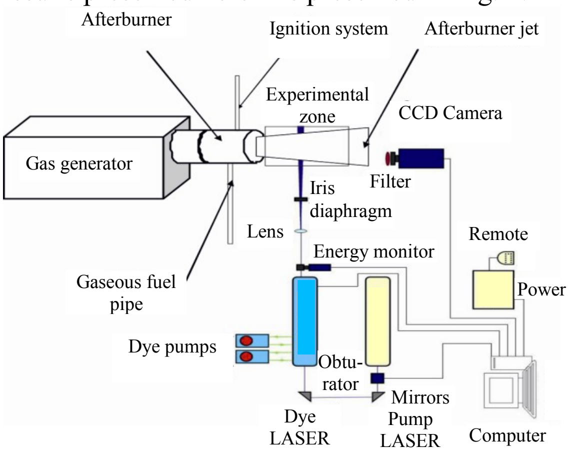

Fig. 2 – Schematic diagram of the experimental apparatus

The experimental setup uses a gas turbine engine model Garrett 30–67 (Fig. 3) as the gas generator for the afterburner. The gas turbine engine is capable of providing a maximum exhaust velocity of 150 m/s and a maximum exhaust temperature of 600 K.

Downstream of the gas generator, an afterburner system, design by the authors and manufactured by INCDT COMOTI is placed. The afterburner system is able to raise the exhaust gas temperature up to 1800 K and will be described in more detail in the following.

Fig. 3 – The Garrett 30-67 gas turbine engine

The overall dimensions of the afterburner are 168 mm in width, 228 mm in height and 330 mm in length. A general view of the afterburner assembly is provided in Fig. 4. The afterburner is equipped with a bluff body flame stabilizer of the shape of letter "V".

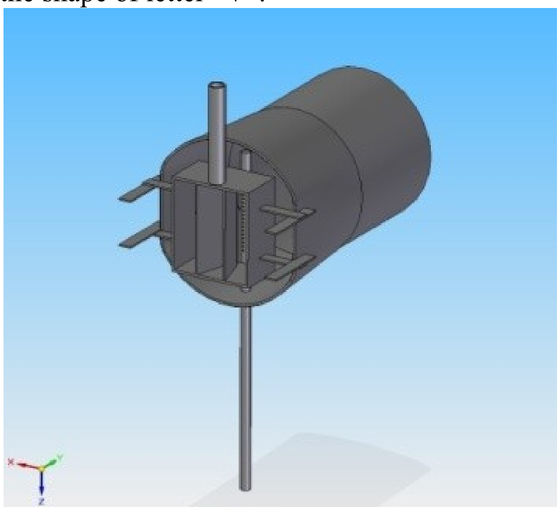

Fig. 4 – General view of the afterburner

The afterburner consists of an outer casing (Fig. 5), of dimensions 330 x 228 mm, the stabilizer assembly (Fig. 6), and the gas fuel pipe of diameter Ø = 10 mm and height 200 mm. The gaseous fuel is fed into the afterburner through 20 holes, equally spaced on the gas fuel pipe, of diameter Ø = 2 mm.

The stabilizer assembly includes the V-shaped bluff body stabilizer, with a tip angle of 60°, a width of 117 mm, and a side of 51 mm in length, the flame entrainment ignition system pipe, of diameter Ø = 16 mm and 115 mm long, and the stabilizer casing (Fig. 7), including the mounting lugs, of dimensions 103 mm x 60 mm x 120 mm.

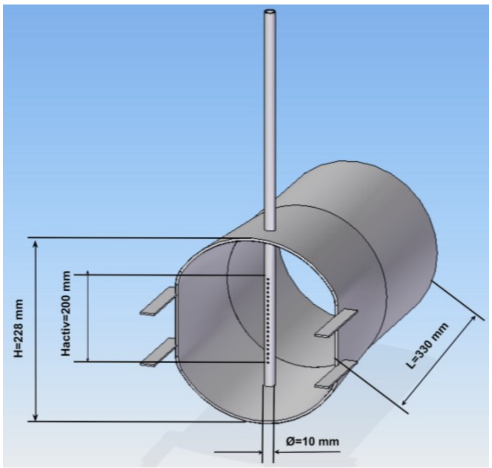

Fig. 5 – Afterburner outer casing

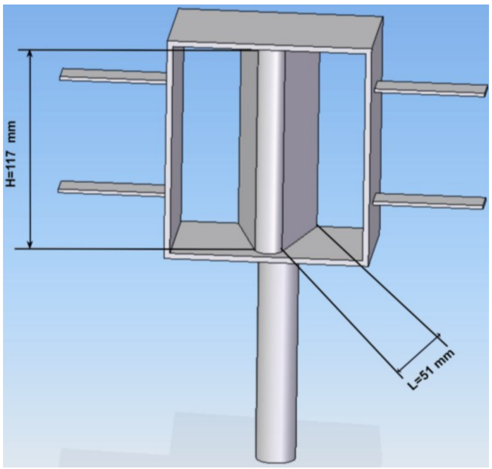

Fig. 6 – Afterburner stabilizer assembly

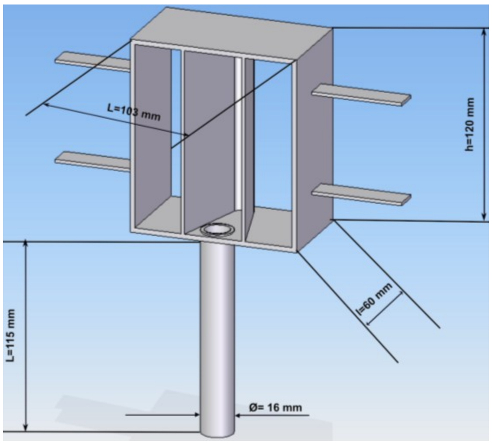

Fig. 7 – Afterburner stabilizer casing

Figure 8 presents a cross section of the afterburner.

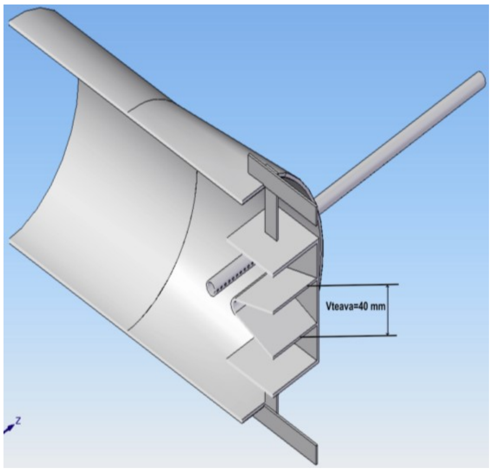

Fig. 8 – Afterburner outer casing

The initial coherent light beam is provided by a Quanta-Ray pump LASER that uses an intermittent lamp to stimulate a Nd:YAG crystal in the absorption bands in the red region, bordering on infrared. The absorption of the lamp photons creates an inversion in the atomic population of the crystal, exciting them to a higher, unstable, energy level. The transition probability towards an intermediate, meta-stable, energy level is higher than the transition probability towards the initial energy level, so the excited atoms will remain on this level for a relatively long time, of about 230 µs [1, 2]. When the atoms finally leave the meta-stable energy level for a lower one, they will emit LASER light on the fundamental frequency of 1064 nm [1]. The pump LASER uses a Q-switch to produce short bursts of high intensity beams, allowing the Nd:YAG to reach a maximum of population inversion before the switch opens and allows a sudden release of energy. The resulting high energy coherent light beam is sent through a Harmonic Generator either to polarize the fundamental frequency, or to generate sub-harmonics. Finally, the beam is reflected by two dichroic mirrors that will reflect only the desired light wavelength [1].

The dye LASER is a Sirah Dye Laser - Cobra Stretch model [3], operating on a similar principle as the pump LASER, except it cannot generate its own coherent light beam and needs to be fed by an external source (in this case, the pump LASER). Its main purpose in PLIF is to selectively emit on a given wavelength. The emission wavelength is tunable to the specific wavelength of the tracked molecule. The dye LASERs use liquids as LASER emission media, being able to generate a larger range of wavelengths compared to the solid emission medium LASERs, such as the Nd:YAG crystal based ones [1]. The pump LASER beam is led, via a mirror system, inside the dye LASER. A separator deflects a small part of the beam into a 20 mm quartz dye cell, exciting the dye inside and causing the emission of fluorescent light of known wavelength range and efficiency, depending on the dye and according to a known calibration curve. For the OH measurements presented here, the Coumarin 153 dye was used.

From the realizable range of wavelengths, a Prismatic Expander and a couple of grated mirrors allow the selection of the desired wavelength. Together, the dye cell, the prismatic expander and the mirrors for the Resonator [1]. The beam emitted by the resonator is led through a series of Brewster polarization plates and through a directional prism, and reflected back into the dye cell. The rest of the original beam is reflected through two prisms into a second separator and intersected with the resonator beam in the dye cell, creating a stimulated emission. The stimulated emission beam is expanded through a telescope and led into a second dye cell, where the emission is further amplified. The resulting coherent light beam is led into a Frequency Conversion Unit that doubles the frequency, a Compensator, restoring the original light beam direction after its passage through the frequency convertor, and a wavelength separation unit, formed by four Pellin- Broca prisms that deviate the residual fundamental wavelengths, allowing only the second harmonic to pass through [1].

The fluorescent light photons are captured by an Intensified Charged Coupled Device (ICCD) camera equipped with a filter that lets through only the fluorescent light wavelength. The focusing range of the lenses installed on the camera is the limiting factor for the size of the measurement domain and the spatial resolution of the measurements.

3 Experimental results

The experimental measurements to be presented in this section were carried out under the conditions below:

- Engine speed: 52.800 ± 200 rpm (idle, no electrical loading);
- Exhaust gas temperature at the afterburner inlet: 550 K;
- Exhaust gas pressure at the afterburner inlet: 1.05 bar absolute;
- Exhaust gas mass flow rate 0.45 kg/s;
- Afterburner fuel (natural gas) temperature: 300 K;
- Afterburner fuel pressure: 3,5 bar absolute.

Figure 9 presents an image taken during the experimental measurements on the previously described afterburner, and Fig. 10 shows the PLIF LASERs setup.

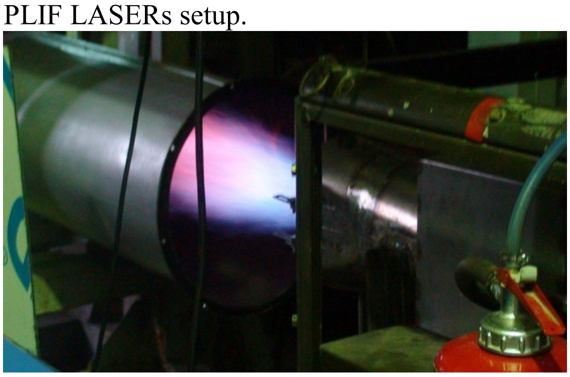

Fig. 9 – Afterburner in operation during experimental measurements

Fig. 10 – PLIF LASERs setup during experimental measurements

The results of the experimental program measurements are presented in the following.

Figures 11 and 12 present the mean, respectively the fluctuating fields of the OH concentration in a plane containing the symmetry axis of the afterburner.

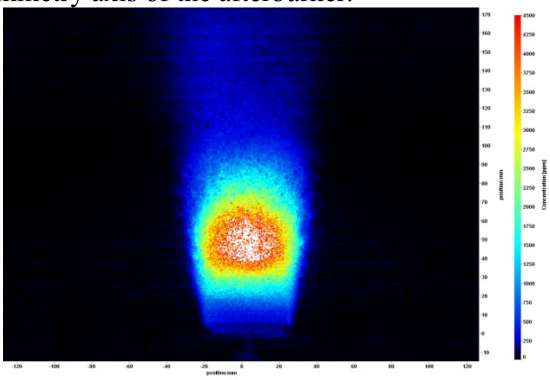

Fig. 11 – Mean OH concentration in the axial plane

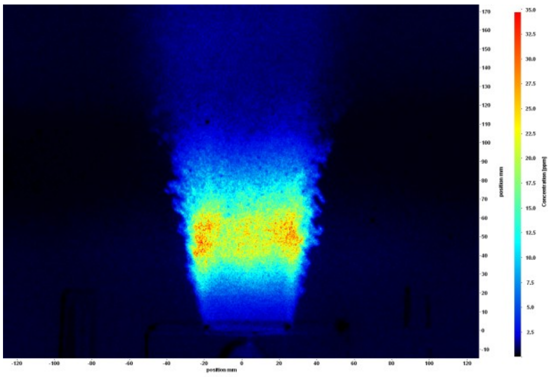

Fig. 12 – Fluctuating OH concentration in the axial plane

It must be noted from the beginning that the OH radical is a very fast radical, that is created and destroyed rapidly in the combustion process [4]. For this reason, its presence can be detected in the flame front only, being a very precise indication on its position. For this reason, in the reminder of this paper, discussions on the flame front position and behavior will be based on this observation, and will not be reiterated.

As seen in Fig. 11, the position of the mean flame front coincides to the recirculation region that forms downstream of the flame stabilizer, as noted in previous studies [5]. The turbulent flame brush, clearly visible in Fig. 11, determines a significant increase of the mean flame front, as compared to its instantaneous thickness. The turbulent flame brush is an effect of the turbulent intermittency, which causes, through the effect of the turbulent fluctuation of the flame, a given point in space in the flame front region to be part of the time inside the flame front, and part of the time outside it. Therefore, the averaging process leads to region much thicker than the very thin flame front characteristic to a laminar flame, where the mean fields have characteristics corresponding partially to the flame front, partially to the preheating region, and partially to the oxidation zone [4].

The turbulent OH concentration fluctuations (Fig. 12) present a maximum value over a ring shaped region around the centerline, corresponding to the intersection of the turbulent flame brush region with the high turbulent intensity shear layer delimiting the recirculation region occurring downstream of the flame stabilizer from the free stream that by-passes the flame stabilizer through the afterburner casing.

For a better evaluation of the experimental measurements results, Figs. 13 and 14 present the mean, and respectively, the fluctuating OH concentration profiles along the afterburner symmetry axis, while Figs. 15 and 16 show the mean, and respectively, the fluctuating OH concentration profiles along several transversal lines placed at 25 mm, 50 mm, 75 mm, and 100 mm from the afterburner flame stabilizer trailing edge.

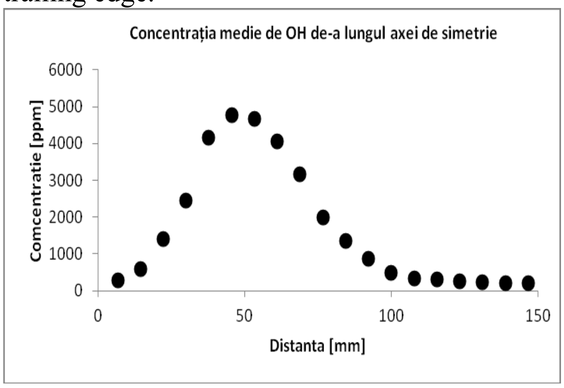

Fig. 13 – Mean OH concentration along the afterburner symmetry axis

In the axial direction, the maximum OH concentration, of about 5,000 ppm, is reached at about 50 mm from the flame stabilizer trailing edge, and the turbulent flame brush extends between 0 and 100 mm with respect to the same axial coordinate origin.

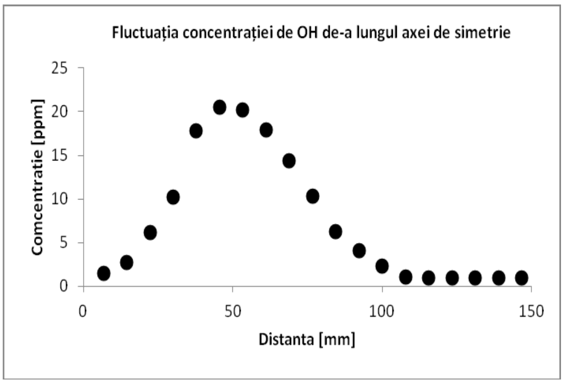

Fig. 14 – Fluctuating OH concentration along the afterburner symmetry axis

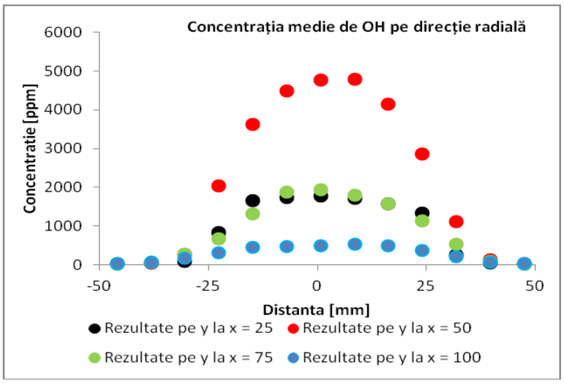

Fig. 15 – Mean OH concentration along the transversal direction

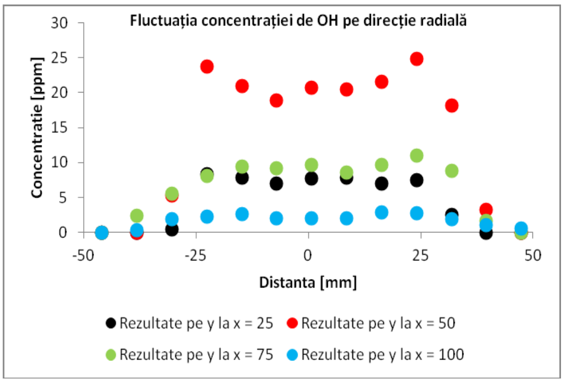

Fig. 16 – Fluctuating OH concentration along the transversal direction

Generally, the literature [6, 7] indicates that a turbulent premixed flame stabilized by a prism shaped bluff body has the shape of letter "V", with the opening towards the stabilizer downstream, and the two arms anchored at a short distance downstream of the stabilizer trailing edge. The distance between the stabilizer and the flame front anchoring point is controlled by the characteristic ignition delay of the flame.

Figure 13 reveals that, on the average, the maximum OH concentration, corresponding to the maximum flame front mean intensity occurs, in this case, at 50 mm downstream of the flame stabilizer. Upstream and downstream of the maximum position, the OH concentration gradually decreases to zero, as the probability that the respective spatial location to be in the instantaneous flame front decreases.

It is important to note that the profile in Fig. 13 do not represent the instantaneous turbulent flame front, which is much thinner, but the turbulent flame brush.

The turbulent fluctuations profile, presented in Fig. 14, confirm the previous observations, placing the maximum value of the turbulent fluctuation of the OH concentration axial profile, of about 20 ppm, in the same position.

In the transversal position, all mean profiles show maxima on the symmetry axis (at 0 mm). Again, since the figure presents mean values, the shown OH concentration distribution characterizes the turbulent flame brush, and not the instantaneous turbulent flame front.

Close to the flame stabilizer trailing edge, the OH concentration mean radial profile presents a large and clearly defined flat zone, where the mean OH concentration is nearly constant. Downstream, the flat zone tends to disappear, and the profile tends to become parabolic in the region where the mean OH concentration reaches its axial direction maximum (Fig. 15). Further downstream, as the mean OH concentration decreases, the shape of the transversal profiles tends to flatten again.

As before, this behavior is characteristic to the turbulent flame brush, and not to the classical laminar flame profile. The experimental data show that, on the average, the flame extends over the entire recirculation region, due to the turbulent eddies that detach from the sharp flame stabilizer trailing edge and force the instantaneous flame front to wrap around them [6], thus transporting the OH molecules created in the flame front throughout the entire recirculation region.

Over the entire upstream to downstream evolution of the reactive flow, the transversal region where the mean OH concentration is non-zero expands, along with the spreading of the recirculation region downstream of the bluff body, in good correlation with the velocity profiles presented elsewhere [5].

As opposed to the mean profiles that tend to a parabolic profile in the intermediate field, with a maximum in the central region, the turbulent fluctuations of the OH concentration along the transversal direction present maxima in the shear layer region, where the turbulent intensity also peaks [5].

It is also noteworthy that both in the near, and in the intermediate fields (at distances below 75 mm from the bluff body trailing edge) the OH concentration turbulent fluctuation profiles reach significant values in the regions around the symmetry axis, corresponding to the recirculation region. This observation confirms that the presented profiles represent the turbulent flame brush created by the intermittency phenomenon. The intensity of the turbulent fluctuations changes in correlation with the velocity turbulent fluctuations [5], reaching a maximum of about 30 ppm at 50 mm from the flame stabilizer trailing edge (Fig. 16).

4 Conclusion

The OH concentration measurements carried out through the Planar LASER Induced Fluorescence method reveal the instantaneous, mean, and fluctuating position of the flame front. The experimental results show that the turbulent intensity is significant enough to create a large turbulent flame brush, the turbulent eddies transporting the OH molecules created in the flame front throughout the entire recirculation region, The mean flame position coincides, for this reason, with the recirculation region. The turbulent fluctuations of the OH concentration peak in an annular region placed at the intersection between the turbulent flame brush and the shear layer delimiting the recirculation region.

The maximum mean OH concentration is of about 5,000 ppm and is reached at about 50 mm from the bluff body trailing edge.

The flame in the afterburner is found to be stable, validating the afterburner design.

References

[1] Fredette C.F., “Quantitative hydroxyl (OH) concentration calibration by use of a flat flame burner, thermocouple and planar laser induced fluorescence (PLIF) system”, M.S. Dissertation, Department of Mechanical and Industrial Engineering, Northeastern University, Boston, MA, USA, 2009

[2] Andrews, R., “Measurement of Hydroxyl (OH) Concentration of Transient Premixed Methane-Air flames by Planar Laser Induced Fluorescence (PLIF) Method”, M.S. Dissertation, Department of Mechanical and Industrial Engineering, Northeastern University, Boston, MA, USA, 2008

[3] ***, “Product-Manual for DaVis 7.2, LIF in Gaseous Fluids”, LaVision GmbH, Göttingen, Germany, 2009

[4] S.R. Turns, An *Introduction to Combustion. Concepts and Applications*. McGraw-Hill, London, 2000

[5] F.G. Florean, C. Sandu, I. Porumbel ”Experimental measurements in reactive and non-reactive turbulent flows” *AIAA Conference*, Atlanta, Georgia, 2012, USA

[6] I. Porumbel, *LES of Bluff Body Stabilized Premixed and Partially Premixed Combustion*. VDM Verlag Dr. Muller, Saarbrucken, Germany, 2007

[7] S. Nair, “Acoustic characterization of flame blowout phenomenon” ,Phd Dissertation, Georgia Institute of Technology, Atlanta, GA, USA, 2006

Novel Pulse Detonation Engine Concept

Cleopatra F. Cuciumita, Bogdan G. Gherman and Ionut Porumbel
Romanian National Institute Research and Development Institute for Gas Turbines, Bucharest, Romania, 061126

Keywords: *propulsion, detonation, supersonic combustion, rotating combustor*

Abstract

The presentation introduces the ongoing research efforts carried out by the National Research and Development Institute for Gas Turbines COMOTI, in collaboration with the Von Karman Institute of Fluid Dynamics, the Lund University, and the Academy of Sciences of Moldova, towards developing a new, breakthrough, high speed propulsion system technology envisioned to trigger a step change in air transportation in the second half of this century and based on the principle of pulsed detonating combustion. This new, radical approach to create propulsion power aims at reducing the weight, the complexity, and the cost of the classical, air breathing, aero-engine and, thus, at significantly reducing the overall fuel consumption and, consequently, the total amount of pollutants emission. The research efforts are carried out as part of a European research project, funded in by the European Commission within the Framework Programme 7.

1 Introduction

The central idea of the investigated propulsion technology is the replacement of the gas turbine in a typical aviation engine of today by a simpler, and at least as effective system.

The advantages of the approach are multiple. Firstly, the gas turbine represents about 25 % of the total weight of the engine, so, its replacement by a simpler system will lead to a decrease in engine weight. Secondly, the most important limitations for the modern gas turbine engines are related to the maximum temperature at the turbine inlet. As the turbine blade material can only withstand a certain maximum temperature, in order to maximize the temperature of the burned gas at the combustor exhaust, and therefore the performances of the engine, the turbine blades, especially for the first rows, need to be cooled. Given the dimensions and the complex geometry of the typical turbine blade, the design and machining of the cooling channels to and through the blades is a difficult and expensive process. The replacement of the turbine by a simpler power device would, therefore, simplify the design and the manufacturing of the engine and lower its costs. Thirdly, a gas turbine is a very complex machine, including a large number of rotating parts subjected to high temperature, and typically made from expensive and hard to machine materials. A simpler power device would lower significantly the time and the costs allocated to design, manufacturing and maintenance, while reducing the failure risks in both manufacturing and exploitation by reducing the number of parts. Finally, the dimensions of the engine, particularly its length, can also be reduced by replacing a series of turbine disks and stators by a more compact solution.

A power device able to replace the gas turbine in an aviation engine must, while providing the advantages discussed earlier, fulfill the functional role of the turbine. This role consists in converting the working fluid kinetic energy (velocity) and potential energy (pressure) into work used to propel the aircraft and to compress the air upstream of the combustor by means of blade rows forming divergent channel. The conversion of the fluid energy into work is achieved by changing the direction of the flow (impulse turbines), and by expanding the fluid (reaction turbines). Modern turbines use both approaches in varying degrees.

2 Description of Concept

2.1 The Rotating Combustor Concept

The concept proposed here uses the conservation of impulse for the combustor exhaust jet released tangentially, to rotate the entire combustor assembly. The combustor assembly contains several can combustors rotating together and connected together through a disk to a central shaft and enclosed in a stationary pressurized shroud. The shaft of the combustor assembly is connected, and provides power, to a compressor upstream of the combustor that provides pressure to the combustor shroud. The remaining energy will be used to power the aircraft. The typical approaches to extract this energy are via a propeller connected, possibly through a gear box, to the main shaft, via a main exhaust nozzle that collects the flow from the combustors re-axialize it, and accelerates it to provide reactive thrust, or via a combination of the two. If the propeller solution is used, like in a turboprop, after the momentum transfer to the rotating combustor assembly, the low kinetic energy, high pressure jet is collected into an exhaust chamber, connected to a nozzle that further extracts the potential energy from the burned gas, providing additional thrust for the aircraft, such that a full expansion of the exhaust gas is achieved. The solution has the disadvantage of requiring the addition of a gearbox, to match the optimal propeller speed and the speed of the compressor and of the rotating combustor disk. If the reactive nozzle solution is preferred, like in a turbojet, the losses incurred through the re-axialization of the flow are higher. To diminish them, the fraction of the energy transferred to the shaft can be controlled through the shape of the rotating combustor nozzles, and the direction of the jet exiting the combustors. Thus, as the jet direction is closer to the axial direction, the tangential impulse transmitted to the central shaft decreases, up to a point where only the energy required to balance the compressor work is converted into rotational speed. The remaining energy, both potential (pressure) and kinetic (velocity) is extracted from the flow by means of the engine exhaust nozzle. A diagram illustrating the proposed concept is provided in Fig. 1.

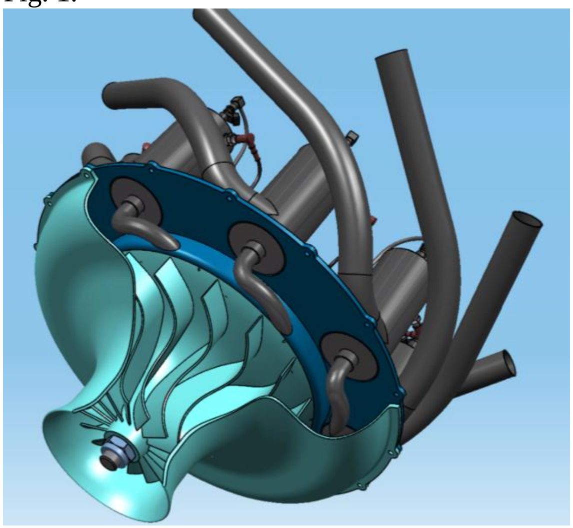

Fig. 1 The engine diagram. Exhaust nozzle removed for clarity

One of the main difficulties raised by the proposed concept is fuelling the rotating combustor assembly. Obviously, rotating the entire fuel supply system, including lines and pumps (and, possibly, the entire fuel tank) is practically impossible. Instead, the concept proposes a fuel supply installation through the combustor disk, as described in Fig. 2.

The fixed part of the engine is the bearing casing 1 that contains the main shaft 2, supported by the bearing 3. The fuel enters through the channel 4 in the stuffing box 11.

From here, through a circular channel 14, the fuel enters the rotor and leaves towards the electronically controlled injectors, through channels 6 and pipes 7.

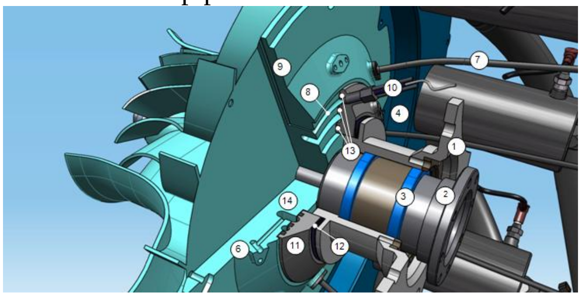

Fig. 2 Fuel supply diagram

A number of radial channels equal to the number of combustors is machined into the rotor. Through these channels, pressure information is transferred from the combustor inlet, through the circular channel 8, to a pressure transducer 10 that controls, through different timers, the successive opening of the injectors. A solution where separate pressure channels provide the signal to separate transducers that would compensate for possible out of sync combustors will be analyzed.

The sealing of the circular fuel channel and of the pressure channel is ensured by the stuffing box 11, placed between the bearing casing and the rotor. The stuffing box is guided by a series of slide bars that prevent its rotation with respect to the casing 1, but allow the axial movement. Between the bearing casing 1 and the stuffing box 1, two conical springs provide the sealing pressure force, by means of the graphite rings 13.

The ignition system consists of an induction coil mounted on the rotor above the channels 6 exit. The coil, as well as the injectors are controlled by means of mobile brush contacts.

Even though the rotating combustor concept is, in itself, a breakthrough new technology, reducing the weight and size of the engine, increasing the maximum temperature of the cycle, or its efficiency are important goals, but in order to trigger a step change in the propulsion technology of the future air transportation more radical approaches are needed. One such approach is supersonic combustion, that will allow efficient propulsion for supersonic and hypersonic flight. The approach proposed here to supersonic combustion is the Pulsed Detonation Combustor (PDC).

2.2 The Pulsed Detonation Combustor

A pulsed combustor is a constant volume combustor operating under oscillatory conditions, based on the so-called Humphrey cycle [1], which is significantly more efficient than the constant pressure combustion, Brayton cycle, typical for the modern gas turbine engines[2].

If a detonation wave is used instead of a regular flame to burn the combustible mixture, as in a PDC, the speed of the burning process increases by several orders of magnitude and the thermal efficiency further increases [2, 3]. A recent theoretical comparative study [2] of the efficiencies of the three cycles (constant pressure, constant volume, and detonation), indicates a thermodynamic efficiency of 27% for the Brayton cycle, of 47% for the Humphrey cycle, and of 49% for the detonation cycle. However, more recent research studies indicate that the superior efficiency of a pulsed detonation based cycle is only maintained up to flight Mach numbers of 3 [4]. Furthermore, NOx production is expected to be lower in a PDC, due to the significantly lower residence time and to the recirculation of the combustion products back into the combustion region [5].

A diagram of the PDC is presented in Fig. 3.

If the detonation wave is assumed steady, planar, and one-dimensional, and if state 1 denotes the conditions for the reactants upstream of the detonation wave, while state 2 denotes the conditions for the products downstream of the detonation wave, then the Hugoniot relationship describing the energy release in a compressible flow is [6]:

$$\Delta h = h_2 - h_1 = \frac{1}{2}(p_2 - p_1)\left(\frac{1}{\rho_1} - \frac{1}{\rho_2}\right) \quad (1)$$

where h is the enthalpy, p is the pressure, and ρ is the density.

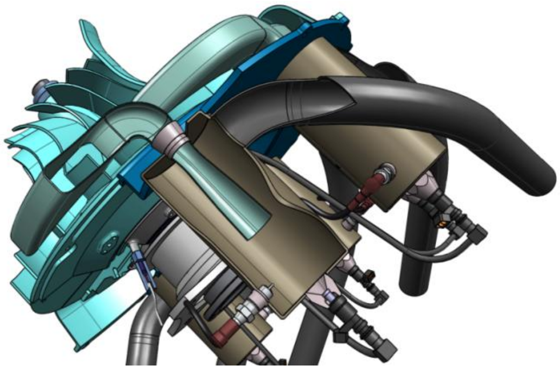

Fig. 3 PDC diagram

A graphical representation of Eq. (1) for a given initial state 1 with, and without (pure shock) energy release is presented in Fig. 4.

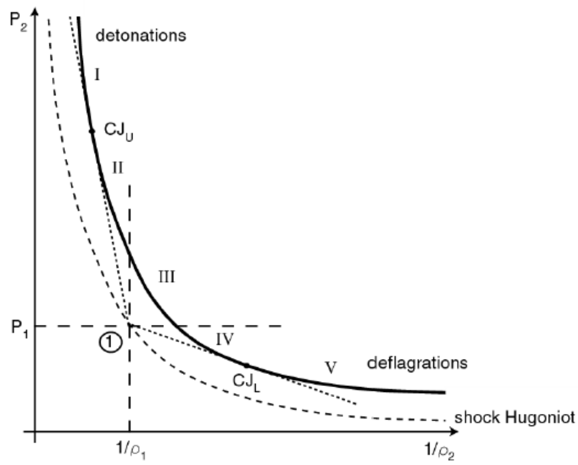

Fig. 4 The Hugoniot curve without (dotted curve) and with energy release (solid curve) [6]

The dotted lines (1) - CJL and (1) CJU are the Rayleigh lines [7], tangent to the Hugoniot curve.

The solutions located in regions I and II correspond to supersonic waves (detonations), while the solutions located in regions IV and V correspond to subsonic waves (deflagrations). Region I (strong detonations) can only be achieved if there is a piston forcing the compression behind the wave [7]. Region II (weak detonations) can only be found in extreme situations (eigenvalue solutions) [7]. Thermodynamically, point CJU represents the only readily achievable solution for detonation waves [6]. At point CJU, the flow behind the wave is sonic relatively to the wave ($M_2 = 1$). It can also be shown that the same point corresponds to a minimum entropy point [8], with positive implications on the combustion related entropy raise, which is the most significant contribution to the total entropy raise that determines the engine thermal efficiency [9]. The solutions in region III are not real [7]. Region IV (weak detonations) corresponds to laminar flames. Region V (strong deflagrations), cannot be achieved in a constant area duct [7]. For deflagrations, the propagation speed is a function of the combustion wave structure and of the turbulent and diffusive transport properties. For detonations, the propagation speed is determined by gas dynamic considerations. A point similar to CJU, CJL, exists on the lower, deflagration, branch, but, as the entire region IV is acceptable thermodynamically, this point does not represent a special case.

The planar detonation wave is periodically initiated at one end of the combustor and travels at the Chapman - Jouguet velocity [6] towards the opposite end. After the detonation wave leaves the chamber, a set of expansion waves forms, decreasing the pressure and evacuating the combustion products. If the detonation wave travels from the open end of the combustor towards the closed end, the pressure behind the expansion waves drops below the ambient pressure, absorbing a new volume of fresh air into the chamber without the need for controlling valves [10]. Conversely, if the detonation wave is initiated at the closed end, the confinement existing here benefits the initialization of the detonation wave [11]. Since the specific thrust of the PDC does not depend on the detonation wave initiation location [12], this choice is not considered critical. However, it has been decided that the project described here will initiate the detonation at the closed end.

The thermal efficiency of the detonation cycle was found to be further increased by an increasing compression of the fresh gases before detonation, which increases the work done during the expansion process [3]. This observation justifies the preservation of the compressor upstream of the rotating combustion assembly, as indicated in Fig. 1.

In order to further increase the new engine efficiency, the rotating PDCs will be equipped with nozzles aimed at increasing the thrust during the ignition phase. These nozzles should not be confused with the engine nozzle that discharges the exhaust chamber into the air. Previous studies [13, 14] have shown that the presence of a nozzle of proper shape at the combustor exhaust positively influence engine efficiency. To further increase the thrust of the gas exiting the PDC, ejector devices, based on the Venturi effect can be added to the PDC nozzles to convert the potential energy stored in the high pressure burned gas into kinetic energy.

Compared to a deflagration wave Pulse Jet Engine (PJE), the PDC has a significantly higher efficiency, because the explosive combustion process is able to burn the whole volume of combustible mixture fed inside it while still at constant volume, contained in the combustor.

Compared to the classical Pulse Detonation Engine (PDE), the proposed concept has several advantages. The most important novel approach that improves the classical PDE is the presence of the compressor upstream of the PDC inlet. The high air pressure facilitates the safe and stable operation of the PDC, increases the combustion efficiency and completeness. Consequently, the PDE is significantly more fuel efficient. Even more important, combined with a careful design and timing of the PDC operation, the upstream high pressure allows the design of a valveless PDC. As a result, the operating frequency can be higher than the usual tens of Hz [15], increasing the specific impulse of the engine and allowing for a more compact combustor. Due to inertial effects, high frequency, PDCs will also smooth out the mechanical vibrations in the engine and will improve the operating conditions for the compressor, which operates with fluctuating back-pressure.

The use of multiple PDCs operating out-of-phase will reduce the overall noise emitted by the engine, which may be a significant problem, since detonations are much louder than classical deflagrations. Furthermore, the mechanical vibrations of the engine and the velocity fluctuations transmitted upstream are damped by the use of opposite phase pairs of PDCs. A secondary advantage of the concept, compared to PJEs is that it allows simple extraction of auxiliary power for the engine from the main shaft.

3 Progress Beyond the State-of-the-Art

3.1 Current State-of-the-Art

Pulse Detonation Engines are not a novel research issue. The detonation and deflagration processes have been studied intensely in the last century. The detonation process was observed for the first time in gaseous fuels by Bertolet in 1881. Later on, Chapman [8] and Jouguet [16, 17] discovered that the products resulted from the detonation propagate at sonic speed relative to the detonation wave. The studies showed a fast energy convergence rate that occurs during detonation corroborated to a much higher thermodynamic efficiencies compared to the deflagration process. One of the first theories that deals with PDE cycle analysis was the Chapman - Jouguet theory [18, 19, 20] developed for the one-dimensional propagation of detonation waves.

While remaining an exotic phenomenon, of strictly academic interest for quite a while, the study of the processes associated to the detonation took an important step forward in the interest of combustion researchers in the mid-XX century, as supersonic flight appeared as an achievable possibility. A first approach was the definition of various thermodynamic cycles aiming at modeling the detonation powered engine, improving on the Chapman - Jouguet theory. A first attempt was the development of the Humphrey cycle [18], based on constant volume heat addition with an isentropic expansion and an isobaric heat rejection. Another cycle used for shocks and detonation wave engines is the ZDN (Zeldovich–von Neumann–Doring) cycle [19, 20, 21]. The theory defines an intermediate state, the von Neumann state or ZND point, defining the chemical reaction start point. Compared to the C-J theory where the reactions start immediately, here the heat release take place from ZND to CJ point. Another cycle worth mentioning is the Fickett-Jacobs cycle [21]. The novelty of the cycle is a special piston-cylinder arrangement, with the reactants and products located inside a cylinder, between pistons.

Over the last decade, the application of the above mentioned cycles in PDEs was studied in several analyses [22, 23, 24, 25, 26, 27, 28] performed with various degrees of success. In another study, a comparison of three shock wave based cycles is performed for both nonreactive and reactive mixtures [29].

On the experimental side, a review on the measurements of deflagration and detonation waves velocities was provided by Sutton [30]. The interaction between the shock wave and the flame front and unstable dynamic behaviour of the wave was theoretically studied by Winterberger [8]. Experimental observations of the detonation wave front confirming Winterberger's findings were reported by Ficket and Davis [31]. Austin [32] made experimental inquiries into the detonation wave structure, reporting a characteristic cellular pattern created by the oscillatory nature of the wave.

During the space race in the ’70 new types of detonation based thrusters was studied [33, 34, 35, 36]. Later research [37] studied the applicability of detonation in high frequency operation, beyond the audible range.

A detailed review of the work carried out in the field of PDE design, including theoretical and experimental approaches can be found in [2]. The application of detonation waves in propulsion system dates back to the 1940s [38, 39], but the complexity of the problem delayed the first successful demonstrator flight to as late as 2008 (DARPA's Blackswift [40]). The demonstration flight was, however, at low speed, and the project was soon cancelled. During this time, a significant number of constructive solutions and approaches has been proposed, however none completely successful. There are three types of PDE configurations: pure [33, 34, 35, 36] combined-cycle PDE [41, 42] and hybrid PDE [35, 43]. The pure PDE is comprised of one or more detonation tubes an inlet and a nozzle. The main problem of the solution is the low inlet pressure at high altitudes. The combined-cycle PDE is typically used for ramjets or scram jets. However this type of engine only works efficiently until Mach 5 [44]. The hybrid PDE replaces the classical deflagration combustor with a PDE to enhance the engine performance, reduce flight time and, possibly, decrease pollutant emission.

To generate the propulsion force, two approaches have been proposed: the direct use of the reactive jet exiting the PDC, or the discharge of the PDC jet into a properly design gas turbine. In this last case, the very high pressure achieved through detonation in the combustor allows the total, or partial, elimination of the compressor, but the main problem is the high jet temperature of the jet impinging the turbine blades. Even worse, the thermal load of the turbine blades is oscillatory, adding thermal fatigue to the already harsh operating conditions. Multiple combustor solutions have been proposed to alleviate this problem, increasing the uniformity of the jet entering the turbine.

The optimal PDC operating frequency has been a research objective. To approach the performances of a classical gas turbine engine, the PDC operating frequency must be of at least 75 Hz for a near stoichiometric fuel air mixture [44]. Further increasing the frequency allows for a reduction in the combustor size, reducing the weight and drag of the engine. One solution [45] to obtain higher frequencies proposes a series of out-of-phase detonation initiation chambers that are connected to a main PDC. Another frequency increasing solution, applicable for mechanical valves DDT initiation PDCs, is to reduce the deflagration phase time by enhancing the fuel-air mixing, either through increasing the turbulence level [46], or through controlling the geometry [47].

Aerodynamic valve solutions have also been used in some PDE applications. The most important requirement related to this approach is to prevent the flashback. Proposed solutions were to place a detonation initiator equipped with an aerodynamic isolator at the chamber inlet [48], or to accelerate the flow to the supersonic regime upstream of the combustor inlet [49, 50]. Other valveless high frequency solutions [51, 52, 53, 54] propose the generation of high frequency oscillations at the combustor inlet, though the interaction of supersonic jets, or by using stationary or moving walls. A wedge-shaped object detonation wave stabilization concept [66] proposed the initiation of the detonation wave through the coupling of the reaction waves with the leading shock waves. The solutions present several important advantages related to better mixing, ease of initiation, flashback prevention, detonation control, reduced size, low emissions and stability[56]. Rotating, tangential exhaust PDEs has also been recently proposed [57, 58] based on a quite old pioneering idea [59], but, opposed to the one proposed here, using mechanical valves, operating at low frequency and without a compressor to provide high inlet pressure.

An extensive review of the evolution and current PDE state-of the art can be found in the literature [60].

3.2 Expected Progress

In order for the presented technology to become a viable solution for commercial flight in the second half of this century, several aspects need to be investigated and clarified. The main question that, in the author's view, arises is the issue of operating frequency. The typical detonation frequency in PDEs is of the order 10 Hz [15]. As discussed earlier, high frequency PDC have several important advantages, and the efforts towards increasing it are needed. Obviously, mechanical limitations of the rotational speed of the PDC in the case proposed here must also be considered, and the impact of these supplementary limitations on the engine performance must be assessed and minimized.

On a related topic, the selection of a valved, or valveless solution must also be addressed. To ensure the correct air flow through the combustor, the classical PDE design proposes a set of valves that open and close the admission of the air, or air-fuel mixture, in the combustor. The main problem in this approach is the high wear experienced by the valves, even more so at high frequencies. Additionally, the valves are subject to very high operating temperatures, and will induce pressure losses in the flow. Valveless designs, based on carefully timed pressure gradients in the flow, are an obvious goal for the future PDC development. Also, the use of a high frequency supersonic jet at the combustor inlet may play the role of an aerodynamic valve, and the effect of this jet on the combustion wave remains an open research topic.

Nonetheless important is the fuel supply system, which needs to provide the fuel in close correlation with the PDC operating frequency. For this, the fuel will be provided continuously through the disk supporting the rotating PDCs. The disk will also include the ignition system. The approach has also the advantage of providing sufficient space to premix the air and fuel, and to achieve vaporization and possibly preheating in the case of liquid fuels. By monitoring the pressure inside the combustor, feedback signal can be provided to the fuel injection and ignition automation system, to ensure the correct synchronization. A rotating sealing system will have to be designed in order to avoid fuel leakage.

Maybe the most important outstanding issue is the initiation of the detonation wave, strongly dependent on the inlet conditions. One possible solution is the use of a very energetic spark, but further research is needed into assessing how practical for an aircraft engine this solution is. Another possibility is to use the so-called deflagration-to-detonation transition (DDT) [61]. In this approach, a spark initiates a high-energy deflagration that is further accelerated to become a detonation. The process is not trivial, due to resistance encountered by the wave front, and to the long acceleration ducts that may render the solution inappropriate for aircraft engines.

Another problem that needs investigation is the optimal geometry of the PDC exit nozzle. Considering the fact that, in order to increase the overall TIDE engine efficiency, the combustors must provide the highest possible impulse on a direction other than along the combustor axis, the optimal direction with respect to the engine performances and constructive solution, as well as the minimization of pressure losses due to the deflection of the flow have to be studied. The addition of ejectors on the PDC nozzle should also be considered. The internal design of the PDC flow path is critical for the optimal detonation wave travel. A design with multiple detonation chambers of increasing wave intensity, serially connected, may provide further engine efficiency increase. The stability and completeness of the supersonic combustion, strongly dependent on the combustor geometry, must also be optimized. Of special interest is the production and emission of NOx. The high temperatures in the PDC favors the NOx production, while the very short residence time in the combustor will tend to decrease the effect, hence a quantitative approach will have to be used to determine NOx emissions. Related to this issue, it must also be noted that supersonic combustion models for finite rate kinetics numerical simulations, as well as the limitations of the existing models applied to detonations are still an open research topic.

Also important is the definition of the optimal compressor geometry, taking into account the rotation of the downstream combustor, and the discontinuous discharge of the combustor shroud. A high frequency PDC will alleviate the problem, but the effect on compressor stability remains to be assessed. Furthermore, since the combustion process is supersonic, the need to decelerate the flow upstream of the combustor disappears. Therefore, the presence of the compressor stator vanes may no longer be required, thus reducing the pressure losses during the passage between the rotating and fixed blading.

The noise generated by the TIDE engine is also an issue that needs to be studied, and solutions for noise damping must be sought, as the noise levels of the new technology may be expected to be high. The effect of opposite phase pairs of PDCs and the optimal interference of the resulting sound waves needs to be investigated. Also, the presence of detonation waves inside PDCs raises questions on the vibration levels of the new engine, which need further evaluation, understanding and solution finding.

Finally, the optimal fuel selection for the PDCs such as to allow the reliable initiation of the detonation wave, is also an open research field. Most of the research studies carried out up to the present focus on gaseous fuels [2], mostly Hydrogen, methane, and propane. However, experimental studies conducted on PDCs using liquid fuels (kerosene) have been reported in recent years [2, 62]. The main problems when considering liquid fuels for PDC are the increased difficulty to initiate the detonation and the required very high mixing velocity of the air and fuel to be supplied to the combustor.

The specific fuel consumption of the engine is lower than in the case of a PJE. By reducing the overall engine weight, by optimizing the supersonic combustion process, and by maximizing the engine power, the overall fuel consumption can be further minimized, but the engine cycle design has to be carefully centered on this issue.

Novel materials, able to withstand the high temperatures in the PDC, together with the mechanical solicitations (mainly centrifugal load and vibrations) for a number of cycles large enough to provide an engine resource economically viable need to be developed in order to bring the engine concept from a breakthrough technology to a market ready product.

4 Project Objectives

Given the complexity of the task, and the limited resources available through the project, its scope is also limited, and it does not try to tackle all the problems raised by the new engine concept. Instead, the main goal of the project is to prove the functionality and feasibility of the concept, opening the road towards developing a mature technology over the next 50 years.

The most important result expected from the proposed project is to demonstrate, both numerically and experimentally, that the power provided by the rotating PDCs can provide the energy to accelerate the compressor to the speed required for its design performance, with sufficient excess energy to power up the aircraft.

A second achievement is expected to be the practical realization of a high frequency, self supporting ignition PDC. To achieve this, the combustor inlet has to be valve free, and the solution selected to control the inlet must be proven to prevent the detonation wave to propagate upstream. A high frequency PDC is expected to be compact, both in diameter and in length, allowing a significant reduction in engine dimensions and weight.

As mentioned earlier, the constant volume cycle is of higher efficiency than the classical Brayton cycle. Due to the elimination of the classical engine turbine, the most important limitation of a gas turbine engine cycle, the maximum temperature, will be removed, thus allowing an overall increase in the engine performance and efficiency. The project aims at demonstrating the increase in theoretical cycle efficiency.

Finally, the project will provide an integrated solution for the proposed concept, validated through numerical simulation, and laying the foundation for building a demonstrator engine concept in the future.

References

[1] Hrițcu C.E., "Reseaarch on Pulsed Operation Combustion Chambers", Ph.D. Thesis, "Gh. Asachi" Technical University, Iași, Romania, 2004

[2] Kailasanath K., "Review of Propulsion Applications of Detonation Waves", *AIAA Journa*l, Vol. 38, No. 9, 2000

[3] Wintenberger E. and Shepherd J.E., "Thermodynamic Cycle Analysis for Propagating Detonations", *Journal of Propulsion and Power*, Vol. 22, No. 3, pp. 694 - 697, 2006

[4] Heiser W.H. and Pratt D.T., "Thermodynamic Cycle Analysis of Pulse Detonating Engines", *Journal of Propulsion and Power*, Vol. 18, No. 1, pp. 68 - 76, 2002

[5] Plavnik G., "Pulse Combustion Technology", *14th North American Waste to Energy Conference, NAWTEC14-3195*, Tampa, Florida, USA, 2006

[6] Turns S.R., *An Introduction to Combustion*, McGraw - Hill, London, 2000

[7] Anderson J.D., *Modern Compressible Flows*, McGraw-Hill, Second Edition, 1990

[8] Chapman D.L., "On the Rate of Explosions in Gases", *Philosophy Magazine*, Vol. 47, pp. 90 - 104, 1899

[9] Wintenberger E., "Applications of Steady and Unsteady Detonation Waves to Propulsion", Ph.D. Thesis, California Institute of Technology, Pasadena, CA, 2004.

[10] Eidelman S., Grossmann W. and Lottati I., "Review of Propulsion Applications and Numerical Simulations of Pulsed Detonation Engine Concept", *Journal of Propulsion and Power*, Vol. 7, No. 6, pp. 857 - 865, 1991

[11] Bussing T. and Pappas G., "Introduction to Pulsed Detonation Engines", *AIAA - 94 - 0263*, 1994

[12] Zitoun R., Gamezo V., Guerraud C. and Desbordes D., "Experimental Study on the Propulsive Efficiency of Pulsed Detonation", *21st International Symposium on Shock Waves*, Paper 8292, Great Keppel Island, Australia, 1997

[13] Cambier J.L. and Tegner J.K., "Strategies for PDE Performance Optimization", *AIAA - 97 - 2743*, 1997

[14] Eidelman S. and Yang X., "Analysis of the Pulse Detonation Engine Efficiency", *AIAA - 98 - 3877*, 1998

[15] Schwer S. and Kailsanath K., "Numerical Investigation of the Physics of Rotating-Detonation-Engines", *Proceedings of the Combustion Institute*, Vol. 33, pp. 2195-2202, 2011

[16] .Jouguet E.., “Sur la propagation des reactions chimiques dans les gaz” *Journal des Mathematiques Pures et Appliquees*, Vol. 1, pp. 347–425. 1905

[17] Jouguet E.., “Sur la propagation des reactions chimiques dans les gaz” *Journal des Mathematiques Pures et Appliquees*, Vol. 2, pp. 5–86, 1906

[18] Zeldovich Y.B., “K Teorirasprostraneniadetonazi v gasoobrasnikhsystemakh”, *Zhurnal Experimentalnoi i Teoreticheskoi Fiziki*, Vol. 10, pp. 543–568, 1940.

[19] Lee J.H.S., *The Detonation Phenomenon*, Cambridge, New York, 2008

[20] von Neumann J., “Theory of Detonation Waves", Progress Report to the National Defense Research Committee, Div. B, OSRD-549, April 1, 1942. PB 31090, *John von Neumann: Collected Works*, 1903–1957, edited by A. H. Taub, Vol. 6, Pergamon, New York, 1963

[21] Heiser W.H. and Pratt D.T., “Thermodynamic Cycle Analysis of Pulse Detonation Engine,” *Journal of Propulsion and Power*, Vol. 18, No. 1, pp. 68–76, 2002

[22] Kentfield J.A.C., “Thermodynamic Cycle Analysis of Pulse Detonation Engine,” *Journal of Propulsion and Power*, Vol. 18, No. 1, pp. 68–76, 2002

[23] Talley D.G. and Coy E.B., “Constant Volume Limit of Pulsed Propulsion for a Constant Ideal Gas,” *Journal of Propulsion and Power*, Vol. 18, No. 2, pp. 400–406, 2002

[24] Hutchins T.E. and Metghalchi M., “Energy and Exergy Analyses of the Pulse Detonation Engine,” *Journal of Engineering for Gas Turbines and Power*, Vol. 125, No. 4, pp. 1075–1080, 2003

[25] Wu Y., Ma F. and Yang V., “System Performance and Thermodynamic Cycle Analysis of Airbreathing Pulse- Detonation Engines,” *Journal of Propulsion and Power*, Vol. 19, No. 4, pp. 556–567, 2003

[26] Bellini R. and Lu F.K,, “Exergy analysis of a pulse detonation power device” *Journal of Propulsion and Power*, Vol. 26, No. 4, pp. 875–878, 2010

[27] Li J.L., Fan W., Wang Y.Q., Qui H. and Yan C.J., “Performance Analysis of the Pulse Detonation Rocket Engine Based on Constant Volume Cycle

Model," *Applied Thermal Engineering*, Vol. 30, No. 11 – 12, pp. 1496–1504, 2010

[28] Braun E.M., Lu F.K., Wilson D.R. and Camberos J., "Detonation Engine Performance Comparison Using First and Second Law Analyses," *AIAA Paper 2010–7040*, 2010

[29] Gordon S. and McBride B.J., "Computer Program for Calculation of Complex Chemical Equilibrium Compositions and Applications, I: Analysis," NASA RP 1311, 1994

[30] Sutton G.P., *Rocket Propulsion Elements: An Introduction to the Engineering of Rockets*, Sixth Edition. John Wiley & Sons, pp. 17 - 539, 1992

[31] Fickett W. and Davis W.C., *Detonation Theory and Experiment*, Dover Publications Inc, 2001

[32] Austin J.M., "The Role of Instability in Gaseous Detonation", Ph. D. Thesis, California Institute of Technology, Pasadena, California, 2003

[33] Back L.H., "Application of Blast Wave Theory to Explosive Propulsion" *Acta Astronautica*, Vol. 2, pp. 391–407, 1975

[34] Varsi G., Back L.H. and Kim K., "Blast Wave in a Nozzle for Propulsion Applications," *Acta Astronautica*, Vol. 3, pp. 141–156, 1976

[35] Kim K., Varsi G. and Back L.H., "Blast Wave Analysis for Detonation Propulsion," *AIAA Journal*, Vol. 10, No. 10, pp. 1500–1502, 1977

[36] Back L.H., Dowler W.L. and Varsi G., "Detonation Propulsion Experiments and Theory," *AIAA Journal*, Vol. 21, No. 10, pp. 1418–1427, 1983

[37] Eidelman S. and Grossmann W., "Pulsed Detonation Engine Experimental & Theoretical Review", *AIAA Paper No. 92-316, AIAA/SAE/ASME/ASEE 28th Joint Propulsion Conference & Exhibit*, Nashville TN, July 6-8, 1992

[38] Hoffmann N., "Reaction Propulsion by Intermittent Detonative Combustion", German Ministry of Supply, AI152365, Volkenrode Translation, 1940

[39] Roy M., "Propulsion par Statoreactuer a Detonation", *Comptes-Rendus de l'Academie des Sciences,* Vol. 222, pp. 31-32, 1946

[40] Shachtman N., *Explosive Engines Key to Hypersonic Plane*, Wired, San Francisco, CA, U.S.A., Conde Nast Publications, 2008

[41] Dabora E.K., "Status of Gaseous Detonation Waves and Their Role in Propulsion," *Fall Technical Meeting of the Eastern States Section of the Combustion Institute*, Combustion Inst., Pittsburgh, PA, pp. 11–18, 1994

[42] Menees G.P., Adelman H.G., Cambier J.L. and Bowles J.V., "Wave Combustors for Trans-Atmospheric Vehicles," *Journal of Propulsion and Power*, Vol. 8, No. 3, pp. 709–713, 1992

[43] Butler L., Dunbar L.W. and Johnson J.E., "Combined cycle pulse detonation turbine engine" , European Patent EP1433946, 2004

[44] Pegg R.J., Couch B.D. and Hunter L.G., "Pulse detonation engine air induction system analysis" *AIAA Paper 96-2918, AIAA Meeting Papers on Disc*, 1996

[45] Dean A.J., McManus K.R. and Tangirala V.E., "Multiple detonation initiator for frequency multiplied pulsed detonation combustion", US Patent US7131260, 2006

[46] Lee S.Y., Watts J., Saretto S., Pal S., Conrad C., Woodward R. and Santoro R., "Deflagration to Detonation Transition Processes by Turbulence-Generating Obstacles in Pulse Detonation Engines," *Journal of Propulsion and Power*, Vol. 20, No. 6, 2004

[47] Smirnov N. ,"Pulse Detonation Engines: Advantages and Limitations", *Advanced Combustion and Aerothermal Technologies, NATO Science for Peace and Security*, Series C: Environmental Security, Vol. 6, pp. 353-363, 2007

[48] Ma F., Choi J.Y. and Yang V., "Internal Flow Dynamics in a Valveless Airbreathing Pulse Detonation Engine", *Journal of Propulsion and Power*, Vol. 24, No. 3, 2008

[49] Reingold V.L., Quillevere A. and Delange G., "Perfectionnements apportés aux foyers à circulation interne supersonique, notamment aux chambres de combustion pour moteurs à réaction d'aérodynes", French Patent FR1008660, 1952

[50] Reingold V.L., "Combustion Chambers Operating on a Supersonic Stream Chiefly for Jet Engines", UK Patent GB1541408, 1968

[51] Li C. and Kailsanath K., "Method and apparatus using jets to initiate detonations", US Patent US6964171, 2005

[52] Tew D.E., Anderson T.J., Guile R.N., Sobel D.R., Twelves Jr. W.V. and Jones G.D., "Pulse detonation engine having an aerodynamic valve", US Patent US6584765, 2003

[53] Denne A.W., "Pulse Jet Engines" WIPO Patent WO/2005/106234, 2005

[54] Shmelev V.M. and Frolov S.M., "Method and Device for Developing Thrust", Russian Patent RU2179254, 2010

[55] Lee J.H.S., "Dynamic parameters of gaseous detonations", *Annual Review of Fluid Mechanics*, Vol. 16, pp. 311- 336, 1984

[56] Bychkov I.M., Vyshinsky V.V. and Nosachev L.V., "Investigation of the flow pattern in a gas-jet Hartmann resonator", *Technical Physics*, Vol. 54, No. 8, pp. 1110-1115, 2009

[57] Brouillette M. and Plante J.S., "Rotary Ramjet Engine", US Patent US7337606, 2008

[58] van Holstyn A., "Reflective Pulse Rotary Engine, US8132399, 2012

[59] Kramer B.G., "Rotary Explosion Engine" US Patent US1287049, 1918

[60] Roy G.D., Frolov S.M., Borisov A.A. and Netzer D.W., "Pulse Detonation Propulsion: Challenges, Current Status, and Future Perspective," *Progress in Energy and Combustion Science*, Vol. 30, No. 6, pp. 545–672, 2004

[61] Oran E.S. and Gamezo V.N., "Origins of the Deflagration-to-Detonation in Gas-Phase Combustion", *Combustion and Flame*, Vol. 148, No. 1 - 2, pp. 4 - 47, 2007

[62] Brophy C., Netzer D. and Forster D., "Detonation Studies of JP-10 with Oxygen and Air for Pulse Detonation Engine Development", *AIAA - 98 - 4003*, 1998

THE SUPPORT PROCESS, SIMULATION RESERCH DESIGN AND STRUCTURE OF THE NEW HELICOPTER'S CONSTRUCTION SCHEMATICS WITH SPECIAL EMPHASIS ON GROUND RESONANCE PHENOMENON

Tomasz Gorecki
Institute of Aviation
Al. Krakowska 110/114, 02-256 Warsaw, Poland
email:togor@ilot.edu.pl

Introduction

During design work on the new construction of a light unmanned helicopter an attempt was made to map the actual design of the helicopter and built the helicopter mode using the finite element method. Calculations made using this method were intended as a support for construction work. In addition, this model could be used as a simulator for the real resonance tests and the first attempts to disassemble the rotor. Such an approach to the design and testing of the real structure allowed us to examine in detail the dangers that may occur when tested on a real object. The main reasons for using the model were to determine the natural frequency of the structure, reproduction attempts resonance (excitation harmonic force) simulations of the rotor to detach from zero to nominal speed and landing simulations of asymmetric structures on the ground.

1. MODEL

2.1. Basic parameters.

Presented at work computational model helicopter has been modeled using finite element software ANSYS. It contains a carefully mapped grid helicopter skid landing gear with the characteristics of the shock absorbers, shaft rotor mast with driving gears, rotor, along with those of the deviations silencers main rotor. The composite beam tail was imaged using beam elements in terms of mass. The remaining items of equipment such as engine, fuel tanks, equipment design, the front part of the hull were modeled using the masses gathered and assigned to the appropriate nodes on the structure. The components used to build the model are: Shell43, Pipe20, Mass21, Link8, Pipe16, Beam189, BEam4, Link10, Beam44. An important element of the presented work is to introduce a model reaction contact between the chassis and the ground and the possibility of taking your skids off the ground. It is very important while analyzing the phenomenon of resonance, which is impossible using classical analytical methods.

Basic data calculation model:
Weight - 1100 [kg]
Center of gravity:
XC = 3.5413 - 0.0413 [m] from the point of intersection of the axis of the rotor shaft and the tail rotor along the axis X,
YC = 0.86332 - 0.00086 [m] from the point of intersection of the axis of the rotor shaft and the tail rotor along the Y axis,
ZC = 1.9441 [m] - from the point of intersection of the axis of the rotor shaft and the tail rotor axis Z and the moments of inertia were:
IXX = 0.3867 kgm 2 +07
IYY = 0.1587 E 08 kgm 2
IZZ = 0.1229 E 08 kgm 2
IXY = -2429 kgm 2
IYZ = -1299 kgm 2
IZX = -0.6341 E 07 kgm 2
Weight of main rotor 39 [kg].

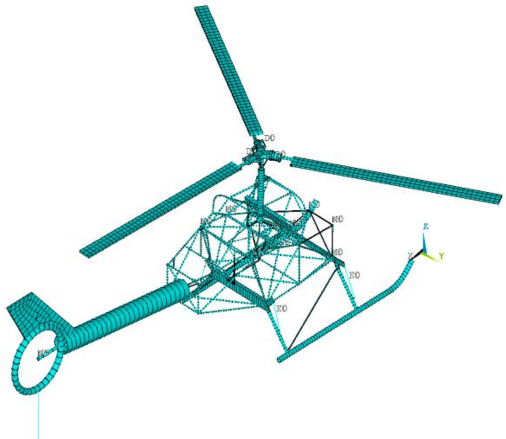

Fig. 1 The Helicopter model prepared in finite element method.

Fig. 2 Model of the helicopter in finite element method.

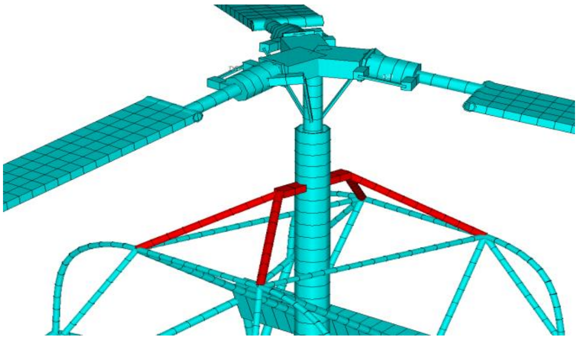

Fig. 3. The change in the construction after simulation.

2. Analisys.

2.1 Modal Analisys.

The primary goal of modal analysis in the finite element method is to determine the frequency and form of vibration of the system in this case, the supporting structure helicopter. For the calculation method, the issue boils down to mapping the real object by a finite number of elements described in the adopted coordinate system and assigning them appropriate for each degree of freedom. Each of the elements of defined mass is described by the following equation.

(1) $M(\frac{d^2q}{dt^2}) + K \cdot q = 0$

where:
M - matrix mass (inertia)
K - stiffness matrix
q - generalized displacement vector (vector degrees of freedom of the system)
t - time
The solution of the above system will have the following form:

(2) $q = q_0 \cdot \cos(\omega t)$

where:
q_0 - vector amplitude vibrations
ω - circular frequency of self-
The second time derivative of the above equation after inserting it into the equation (1) gives the following linear equation:

(3) $(K - M\omega^2) \cdot q_0 = 0$

This equation makes sense with a non-zero solution when the characteristic determinant is equal to 0:

(4) $Det(K - M\omega) = 0$

After expanding the above determinant we obtain a polynomial of n - the point of the ω^2. When setting the roots of this polynomial, e.g. Lanczos method in the finite element method we obtain the frequency of vibration of the structure.

Table 1. The frequency of vibration of the structure.

No.	Frequency [Hz]
1	1,07
2	1,10
3	1,18
4	2,57
5	3,32
6	4,05
7	8,29
8	11,52
9	13,27
10	13,49
11	20,43

In order to illustrate the structure below shows the deformation of deformation of the structure for the chosen vibration frequency.

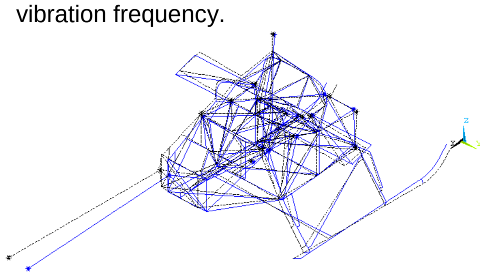

Fig. 4 The figure for the frequency of 1,074 Hz. Tail beam deviations in the XY plane.

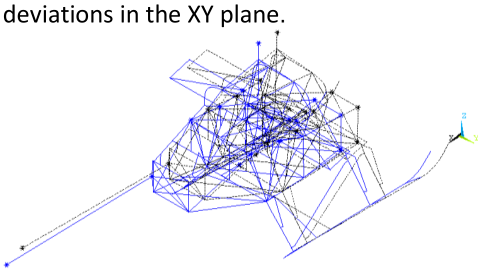

Fig. 5 The figure for the frequency of 1.10 Hz. The Vertical movements of the fuselage.

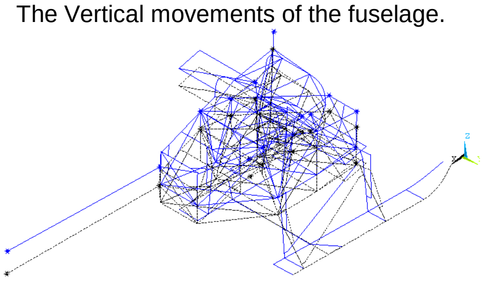

Fig. 6 The figure for the frequency of 1,10 Hz. The Vertical movements of the fuselage.

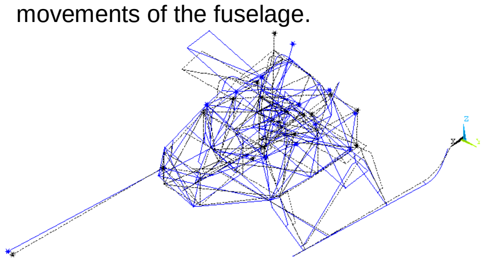

Fig. 7 The figure for the frequency of 3.32. Movements the center of the hub in ZY plane directions.

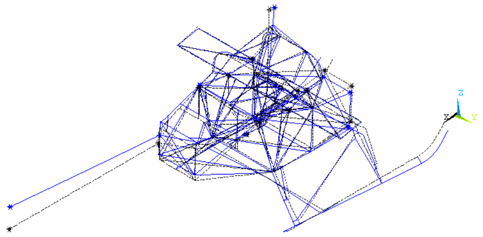

Fig. 8 The figure for the frequency of 4,05Hz. Movements the center of the hub in ZX plane directions.

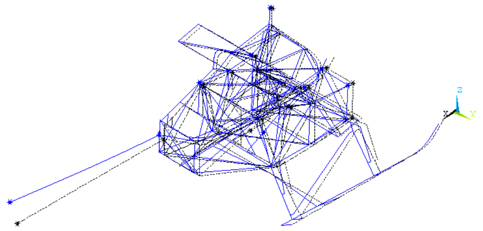

Fig. 9 The figure for the frequency of 8.29 Hz. Tail beam deviations in the XY plane.

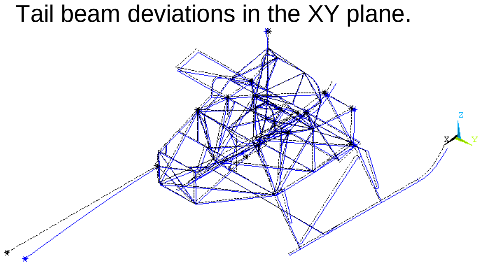

Fig. 10 The figure for the frequency of 11.52 Hz. Tail boom deviations in the XY plane.

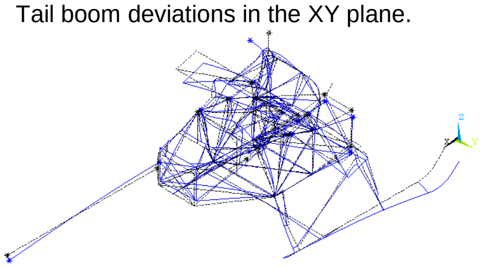

Fig. 11 The figure for the frequency of 20,43 Hz. Tail boom deviations in the XY plane.

2.2 Harmonic Analisys.

Despite the many simplifications that have occurred in this model, changes in vector vibration (vibration frequency and form) due to changes in structural parameters (changes in characteristics of the shock absorbers) should be an order of magnitude more accurate than the "zero" vector vibration and therefore should be useful for adjusting subsequent phases of the experimental trials. The following charts show the relationship amplitude [mm] of the frequency Hz] extortion for excitation of longitudinal hull strength of 200N. These results are only indicative because, based on the study we will be able to accurately assess the size of the amplitudes through appropriate selection of the damping factor in the construction of the finite element method. The presented model is the next stage of development for simulation of ground resonance.

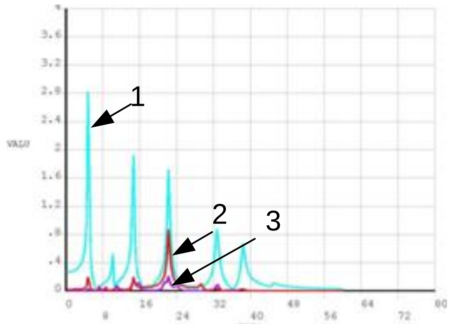

Fig. 12 The amplitude of the X(1)Y(2)Z(3) – axis as a function of frequency Hz.

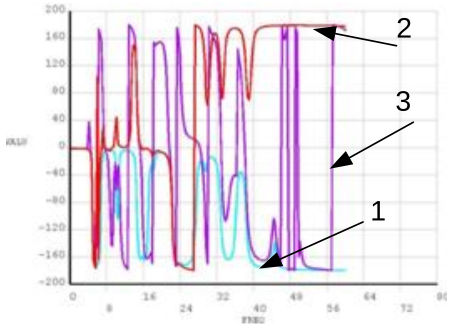

Fig. 13 Phase displacement X(1)Y(2)Z(3) as a function of frequency Hz.

2.3 Simulations.

Calculations of an unbalanced helicopter landing simulation were performed for two cases of helicopter design. The first case, the results of which are shown in figures (Pictures No. 15, 17, 19, 21, 23, 25, 27) was a case of a helicopter without members supporting the rotor shaft. By chance, the second was the case with additional support elements rotor shaft (Fig. 3), the results presented graphs (Pictures No. 14, 16, 18, 20, 22, 24, 26) The simulations were performed for the construction of descent speed of 2.5 m / s The angle of the structure was 20 °. In both variants of computational helicopter after contact with the ground at the end of the first second analysis followed by a decrease to zero lift. Introduction of additional elements to the structure was designed to eliminate the resonance surface.

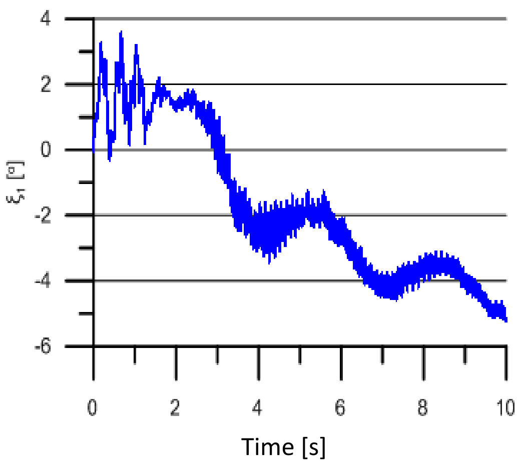

Fig. 14 The angle of deviations fluctuations blade in the plane of the rotor as a function of time for the blade no 1 for the helicopter with changes in the construction(Fig. 3).

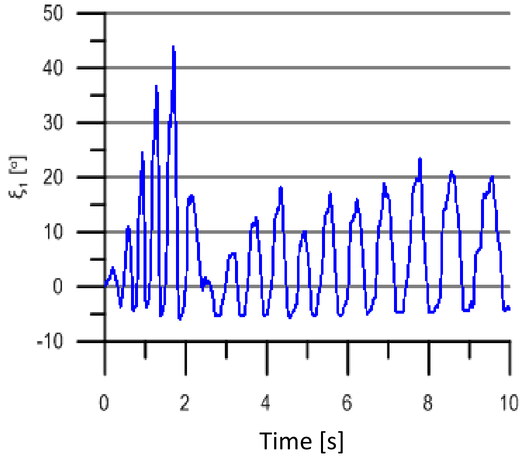

Fig. 15 The angle of deviations fluctuations blade in the plane of the rotor as a function of time for the blade no 1 for the helicopter without changes in the construction.

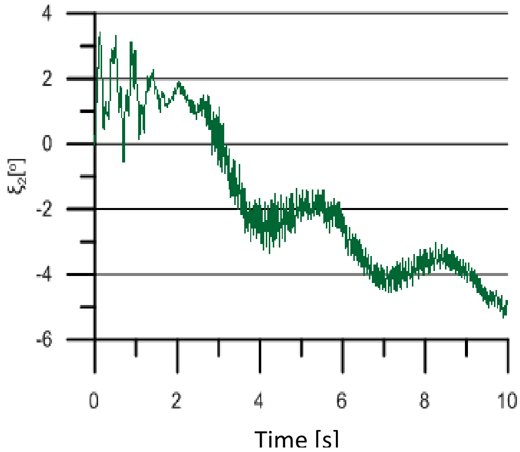

Fig. 16 The angle of deviations fluctuations blade in the plane of the rotor as a function of time for the blade no. 2 for the helicopter with changes in the construction (Fig. 3).

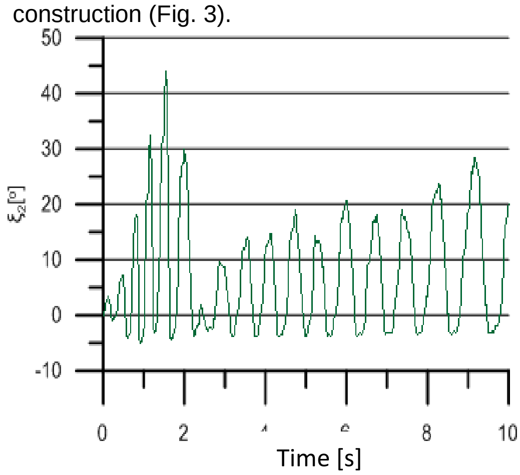

Fig. 17 The angle of deviations fluctuations blade in the plane of the rotor as a function of time for the blade no 2 for the helicopter without changes in the construction.

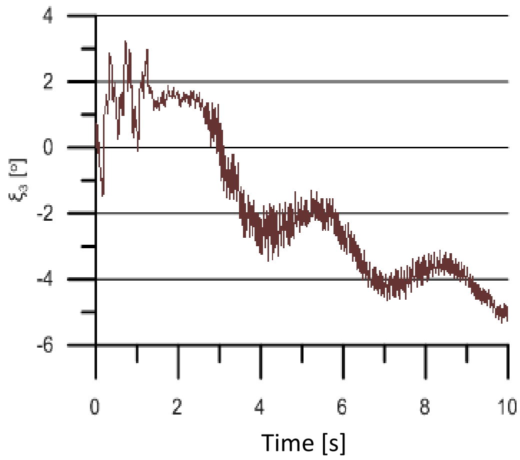

Fig 18 The angle of deviations fluctuations blade in the plane of the rotor as a function of time for the blade no 3 for the helicopter with changes in the construction (Fig. 3).

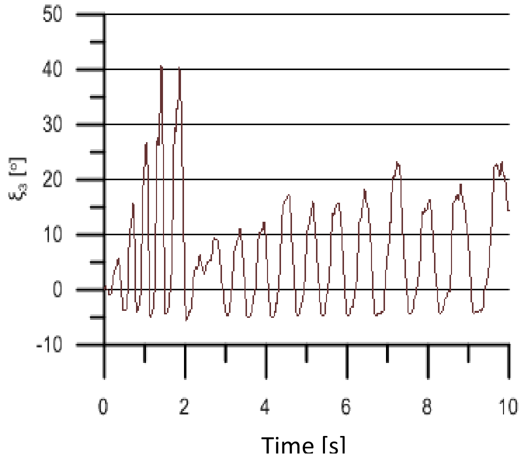

Fig. 19 The angle of deviations fluctuations blade in the plane of the rotor as a function of time for the blade no 3 for a helicopter without changes in the construction.

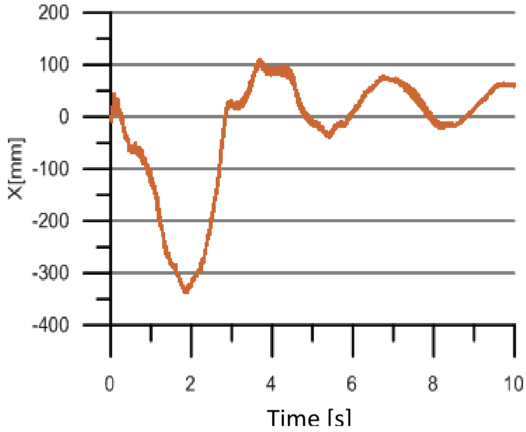

Picture No. 20 The amplitude of the displacement of the rotor hub in the X direction for the helicopter with changes in the construction (Fig. 3).

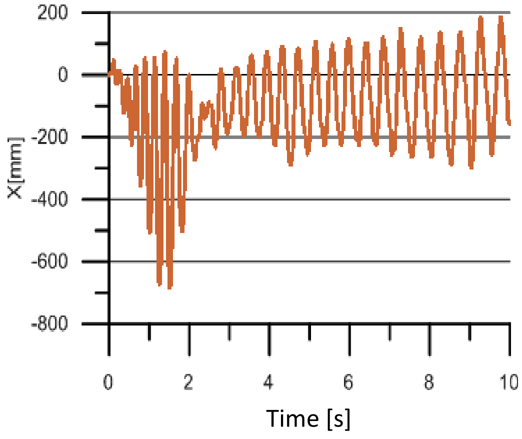

Fig. 18 The amplitude of the displacement of the rotor hub in the X direction for the helicopter without changes in the construction.

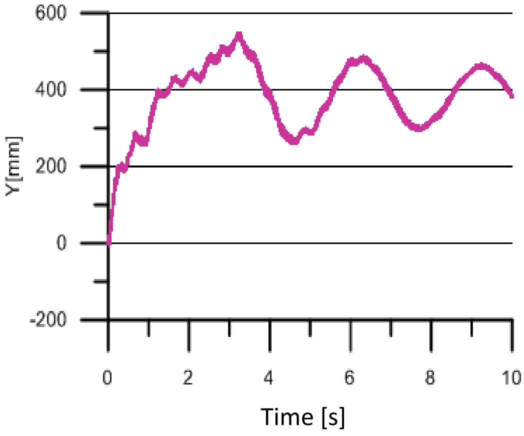

Fig. 19 The amplitude of the displacement of the rotor hub in the Y direction for the helicopter with changes in the construction (Fig. 3).

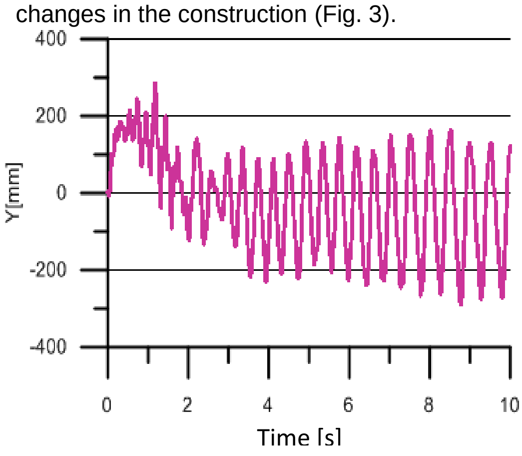

Fig. 20 The amplitude of the displacement of the rotor hub in the Y direction for the helicopter without changes in the construction..

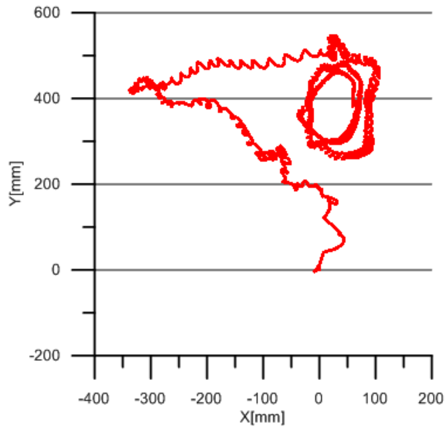

Fig. 21 Displacement of the rotor hub in the plane of the rotor (Fig. 3).

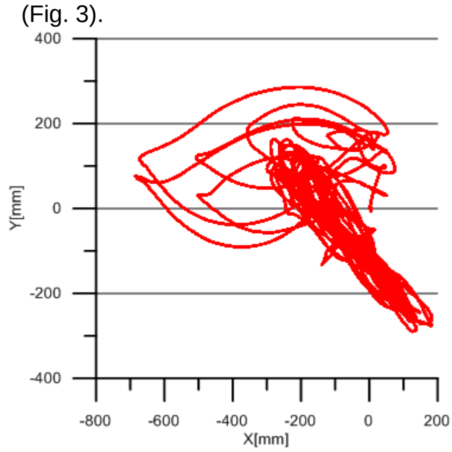

Fig. 22 Displacement of the rotor hub in the plane of the rotor.

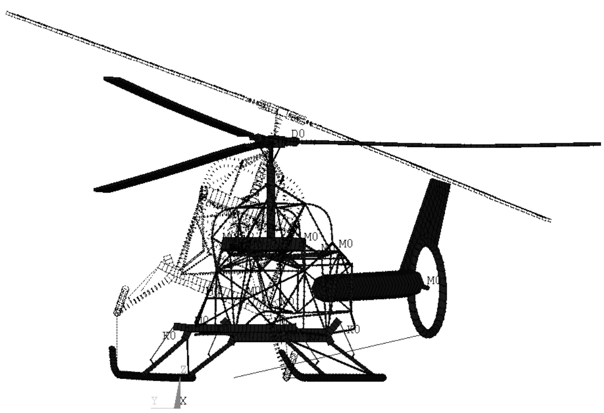

Fig. 23 View of the model helicopter at the start of the analysis (black intermittent) and end (black). for the helicopter with changes in the construction (Fig. 3).

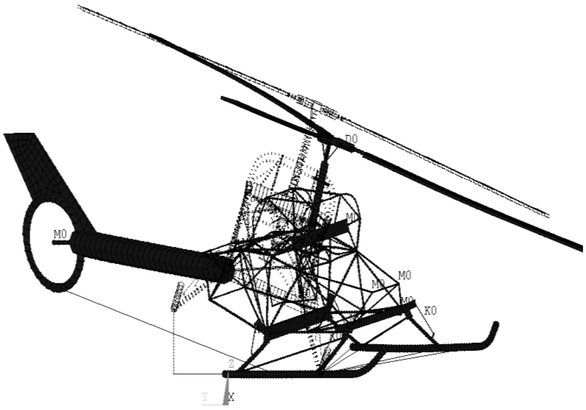

Fig. 24 View of the model helicopter at the start of the analysis (black intermittent) and end (black). for the helicopter without changes in the construction.

4. Conclusions.

Presented in this paper FEM model helicopter fuselage structure can be used to support the testing ground for ground resonance imaging system (free standing on bench), to simulate the potential risks that may occur during the rotor detaching from zero to nominal speed and for the analysis of potential unsymmetrical helicopter landing on the ground. Through the use of simulation models we can accurately (depending on the tuning of the model to the real object) predict the behavior of the structure during the test, and evaluate the safety based design solutions. Based on the results of the analysis carried out for a number of cases, which may have influenced the design of the helicopter we achieved fairly reliable results. As a result, we failed to predict the occurrence of resonance in the areas of design and test their character. It is very important when performing tests on actual construction. In the event of instability in the structure ≈ 6 Hz for the construction the danger can be avoided by quickly moving through the danger of resonance. This took place both during and after the detachment of the brake rotor. On this basis, it can be assumed that the application of the finite element method in implementing the project of light unmanned helicopter made a huge difference to the pace of the work of construction and safety during testing.

Bibliography:

1. Bramwell A. R. S., Done G., Blamford D., „Bramwell`s Helicopter Dynamics", Butterworth-Heinemann, 2001
2. Gorecki T. „Symulacja niesymetrycznego lądowania śmigłowca jako źródło potencjalnego zagrożenia rezonansem naziemnym" Modelowanie Inżynierskie, Gliwice 2013
3. Gorecki T. „Model dynamiczny mes struktury śmigłowca do badań rezonansu naziemnego z uwzględnieniem warunków kontaktowych podwozie – podłoże", Modelowanie w mechanice, Warszawa 2012
4. Szabelski K. „Wstęp do konstrukcji śmigłowców", WKiŁ, 1995
5. Szrajer, M. „Badanie symulacyjne rezonansu naziemnego", Prace Instytutu Lotnictwa , nr 119, Warszawa 1989.
6. Żerek, L. , „Rezonans naziemny śmigłowca o doskonałej i przybliżonej symetrii z uwzględnieniem drgań łopat w płaszczyźnie ciągu", Prace I.Lot. , nr 119, Warszawa 1989.

Advanced Strategic Planning Regarding the Development of a Turbopump System for a Liquid Fuel Rocket Engine

Valentin Silivestru, Radu Mihalache, Cristina Silivestru,
Jeni A. Popescu, Cleopatra F. Cuciumita, Virgil Stanciu
COMOTI Romanian Research and Development Institute for Gas Turbines, Romania

Keywords: *strategic planning, liquid rocket engine, turbopump, turbine*

Abstract

Since Oberth in the 1920's and von Braun in the 1930's, the rocketry has developed into an industry covering areas like space exploration, Earth observation, telecommunications. Within the framework of the Cosmic Vision 2015 – 2025 Programme, the current cycle of long-term planning for space science missions, one of the directions on which the European Space Agency focuses is involving the diversification of suppliers at European level, aiming to develop new generations of liquid propulsion systems for launch vehicles.

Aligning to the European axis and to the Plan for European Cooperating States, designed to help European contries particularly those joining EU after 2004, such as Romania, DevPump is a new national project financed through Romanian Space Agency, implemented by COMOTI Romanian Research and Development Institute for Gas Turbines, Bucharest, in collaboration with National Research and Development Institute for Cryogenic and Isotopic Technologies - ICSI Rm. Valcea and Institute for Theoretical & Experimental Analysis of Aeronautical Structures – STRAERO, Bucharest. Following a technical audit evaluating COMOTI capabilities in the aerospace field, the Head of Sourcing and Analytical Database from EADS Astrium acknowledged COMOTI as potential turbopump system developer due to its execution, calculus and design capabilities. An element in development remains a cryogenic testing facility dedicated for turbopumps, which could easily be implemented with the direct support of ESA.

The main objectives of the project consist in: developing and promoting the Romanian research capacities in the field of turbopumps for liquid rocket engines; multidisciplinary training of specialists at the highest level in hydro-gas-dynamics, structural analysis, cryogenics, materials' study and innovating technologies.

DevPump aims to elaborate a logical succession of operations involved in the development of a turbopump system, covering all phases of the process, upgrading the cycle and therefore contributing to the advance in the state-of-the-art of rotating machinery, bearing and dynamic seal technology, fabrication methods, material development, using time and cost reducing computational tools, such as CFD and FEM methods, focusing on improving and optimizing the performances of the turbopump system. These will be achieved by strategic planning for developing the main components of the turbopump system (pump, turbine, shaft, bearing, seals), the turbopump assembly and technology and a test bench facility for turbopump testing.

1 Introduction

In 1898, the Russian professor Konstantin Tsiolkovsky brought into attention the idea of exploring space with the help of rockets. In a report published in 1903, he suggested using the liquid propellants in rocket propulsion in order to achieve a higher flight range. In the beginning of the XX-th century, the American Robert H. Goddard proved through practical experiments that the liquid fuels are more efficient for rocket propulsion than the solid ones, leading to the first liquid fuel rocket flight in 1926. It was a 2.5 seconds flight, with liquid oxygen and gasoline, that opened the road for a rocket new era. [1]

Nowadays, considering the fuel storage capacity, the manufacturing technologies for liquid rockets represent a mature field on which most launchers in use are based on.

The international space industries, as well as the European space industry, continue the development in fields such as space exploration, Earth observation, science and telecommunications. In order to ensure this development, there is a need for modern transportation systems (rockets) propelled by high performances engines.

The present trend is to minimize the volume of the fuel tanks inside the rockets in order to ensure a power/weight ratio as high as possible for the entire rocket, leading to a higher load. The liquid rocket engines ensure a specific momentum higher than the solid or hybrid fuelled ones, present a high efficiency regarding the fuel storage, as well as the stop/start capability during the mission.

2 The liquid fuel rocket engine

A liquid fuel rocket engine is an engine using cryogenic fuels or oxidants stored at very low temperatures as liquefied gases. This type of engine had a significant contribution to the success of the Saturn V mission in reaching the Moon.

Different combinations of cryogenic fuel-oxide have been used, but the one with liquid hydrogen (LH2) as fuel and liquid oxygen (LOX) as oxidant is the most used in present. Both components are affordable and their combustion reaches a high entropy value producing a specific momentum above 450 [s], at an exit velocity of 4.4 [km/s]. There is a great difference between the fuel density, LH2, of 75 [kg/m^3], and the oxidant density, LOX, of 1,200 [kg/m^3], requiring different properties of the equipments ensuring the pressure in the combustion chamber.

The liquid rocket engines operate based on different cycles, the differences consisting in the flow channel in the system's components, the method of providing the hot gases for one or more turbines and the method of their exhaustion from the turbine. The closed cycle is characterized by the fact that the hot gases from the turbine are exhausted into the atmosphere or introduced into the rocket engine nozzle. The closed cycle is characterized by the injection of the hot gases from the turbine into the combustion chamber in order to achieve a more efficient utilization of the remaining energy. The closed cycle is slightly more efficient due to the complete expansion of the gases in the turbine. The performance differences are usually in the range of 1 - 8 % of the specific momentum, fact more visible in the performance of the entire rocket performance. The "best cycle" must be chosen considering the mission type, the existing engines performances and the criteria established for the rocket performing the mission, therefore finding the optimum combustion pressure and mixture ratio for each application and the engine cycle to achieve maximum autonomy, low cost or maximum load.

Only six countries are presently developing liquid fuel rocket engines, as presented in Table 1. [2, 3, 4, 5, 9, 10, 11]

The European Space Agency develops the Vinci rocket engine, to be used on the higher stage of ESC-B for the European rocket Ariane 5, increasing its load up to 12 [t]. Once finalized the development and testing of the Vinci engine, estimated for 2016, it will replace the cryogenic engine HM-7B. The engine is characterised by an expander cycle, variable nozzle manufactured from composite materials and ignition system capable to be restarted up to 5 times. [6, 7, 8]

Table 1 Rocket engine producers

Country	Rocket	Engine	Cycle	F [kN]	I_{sp} [s]
U.S.A.	Space Shuttle	SSME	SC	2,279	453
	Saturn IB Saturn V	J-2	GG	890	426
	Atlas/Titan/ Delta IV/ Saturn I	RL-10	EC	110	462
	Delta IV	**RS-68**	GG	3,370	410
	Delta IV	RS-83	GG	3,370	446
Russia	Energia	RD-0120	SC	1,961	455
	Rus -M	RD -180	SC	4,150	338
	Rus - M	RD-0146	EC	98,100	463
France	Ariane 5	Vulcain	GG	1,340	434
	Ariane 2,3,4,5	HM7-B	GG	70	447
	In dev.	VINCI	EC	110	465
China	Long March 5	YF-50t	SC	700	432
	Long March/ CZ-3	YF-73	GG	44.15	420
	Long March/ CZ-3A/ CZ-3B/ CZ-3C	YF-75	GG	78.45	470
	Long March/ CZ-5	YF-77	GG	699.5	304
Japan	H-II	LE-7/7A	SC	1078	446
	H –I, H-II	LE-5/5A/5B	EC	137.2	447
India	GSLV	CE-15	SC	73	454
	GSLV	CE-20	GG	200	443

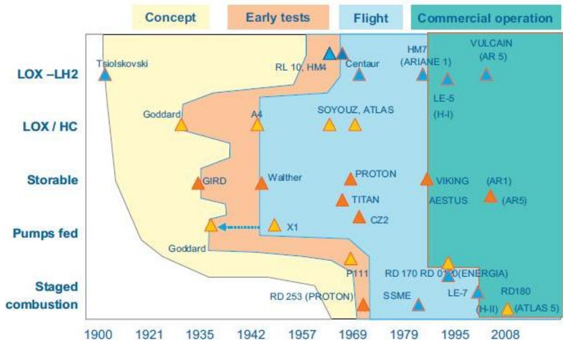

Fig. 1 Liquid fuel propulsion evolution [1]

3 Strategy for developing the turbopump configuration, performances and characteristics

A strategic plan of development for a product includes several essential components: identifying the necessities, establishing the characteristics and performances, preliminary planning of the design and development, development and testing the final product. The development planning for high complexity products focus on reducing the costs on all components and processes and increasing the reliability.

The advanced strategic plan regarding the development of a turbopump system for a rocket engine operating on liquid fuel will take as reference the liquid hydrogen pump of the Vulcain 2 engine, equiping the first stage of the rocket Ariane 5 (SNECMA), with 20% higher power than Vulcain. [9, 10]

Table 2 Vulcaine 2 turbopump characteristics

Vulcain 2	Characteristics
Turbine type	2 transonic axial stages
Power [MW]	9.9 – 20.4
Speed [rpm]	31,800 – 39,800
Inlet pressure [bar]	60 -122
Outlet pressure [bar]	4 – 7.5
Inlet temperature [K]	770 – 960
Average diametre [m]	0.24

3.1 Turbopump

The role of the turbopump in the liquid fuel rocket engine is that of increasing the pressure of the fuels from the low one in the tanks and of introducing them in the combustion chamber at the required pressure and mass flow in order to reach a specific momentum as high as possible. The energy necessary to the turbine is ensured by the expansion of the gases at high pressure from the combustion chamber.

The turbopump of the liquid fuel rocket engines is a unique rotational system compared to turbojets, turbofans or turboprops due to the fact that the pump compresses the cryogenic fuels with low density while the gas turbine is driven by the gases at high temperatures, leading to a high difference in temperature between the pump and the turbine, the main components of the turbopump. The pump must avoid the cavitation phenomenon and ensure a high pressure in its outlet section and the combustion chamber inlet section.

There are several possible configurations for the turbopump systems, with centrifugal or axial pump and radial or axial turbine. The most used configuration is the one with centrifugal pump and axial turbine due to a higher compression ratio in the pump for the fluids specific to liquid rocket engines. It is usually used only one centrifugal stage for liquid oxygen pump and two centrifugal stages for liquid hydrogen pump. [1, 2, 3, 4, 5, 6, 7, 8, 9, 10, 11]

Table 3 Turbopumps characteristics

Engine	Fuel	Pump	Stages	Pin [bar]	Pout [bar]	W [kg/s]	N [rpm]
RL10A-3-3	Ox	C	1	4.2	41	13	12,100
	H2	C	2	2.1	68	2.7	30,250
J-2	Ox	C	1	2.7	77	209	8,753
	H2	A	7	2.1	85	38	27,130
SSME	Ox	C	1/2	340	585	54	31,000
	H2	C	3	13	481	73	37,400
Vulcain	Ox	C	1	7	153.9	265.6	12,300
	H2	C	2	-	182	40.9	35,800
Vinci	Ox	C	1	-	86.5	33.7	18,000
	H2	C	2	-	225	5.8	90,000
HM7-13	Ox	C	1	2	50	12.4	13,000
	H2	C	2	3	55	2.4	60,800

The DevPump project aims to elaborate the strategy for a pump, identified as the DevPump, with a configuration similar to the ones produced in Europe, motivated by the fact that the involvement of Romania in the design of such complex assemblies will be made most probably by European partners.

It has been chosen a liquid hydrogen pump for a rocket engine, able to equip the first stage of Ariane 5 rocket, therefore the rocket engine must be able to achieve 1,340 [kN] thrust and 431 [s] specific momentum.

First step in setting the configuration of the turbopump consists in the pump analysis, by choosing the maximum speed as the highest value allowing the lowest turbopump mass without excess cavitation. In case of excess cavitation occurrence in the section of the first rotor's leading edge (inducer of main rotor), the flow becomes unstable and variable leading to a lower thrust of the rocket engine and a possible instability of combustion.

Because of the difference in densities of the working fluids, liquid hydrogen and liquid oxygen, there is a difference in the pumping height, much higher for the low density liquid. Therefore different pumps are used for hydrogen and oxygen, the hydrogen pump, with more than one stage, working at higher speed.

The chosen characteristics of the hydrogen pump are: 36,000 [rpm] speed, 40.4 [kg/s] mass flow rate and 200 [bar] discharge pressure, in order to ensure the necessary pressure in the combustion chamber and to cover the pressure losses on the feeding line. The initial pressure of the hydrogen, in the storage tank, is approximately 3 [bar]. The centrifugal pump includes two stages for which a pre-dimensioning calculation and then a CFD calculation are to be performed. In order to decrease the manufacturing costs, both stages will have identical rotor geometry and radial diffusers. [12, 13]

In order to avoid cavitation, an inducer is used, allowing minimum pressures in the fuel tanks. The inducer is a special pump component, on the same shaft with the centrifugal rotors, operating at the same 36,000 [rpm] speed. Its rotor is in fact an axial spiral pump usually operating in slight cavitation conditions. Two stator stages will follow the rotor for an increase in hydrogen pressure to approximately 15 [bar], in order to ensure the optimum pump operation.

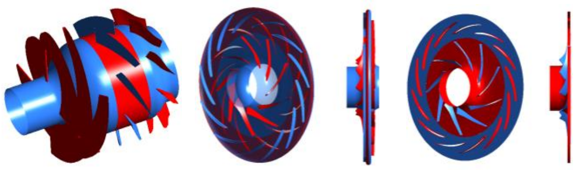

Fig. 2 The main components of the pump: inducer, first stage, second stage

3.2 Gas properties in front of the turbine

The first stage in establishing the calculation methodology for a turbine equipping a liquid hydrogen turbopump is to know the properties of the burned gases from the gas generator in front of the turbine. For this reason it must be analysed the combustion of the bi-component carburant mixture in the gas generator.

The combustion of the bi-component carburant takes place at constant pressure and it's the process producing the increase in the temperature of the working fluid passing through the gas generator. The two components are stored in different tanks and mixed before the combustion chamber.

The theoretical combustion analysis has been accomplished using the program CEAexec (Chemical Equilibrium with Applications), elaborated and developed by NASA Lewis Research Center, which allows obtaining the chemical equilibrium for thermodynamic states imposed by the user through defining the parameters, completed with data bases included in the program, related to the composition of substances and thermodynamic data common to all applications. [14]

It has been used the *hp* problem (constant pressure combustion), imposing:

- the pressure of the mixture at the inlet of the combustion chamber – three cases: 60 [bar], 101 [bar], 122 [bar];
- the fuel: $H_2(L)$;
- the oxidant: $O_2(L)$;
- the number of moles of each component entering the reaction;
- the inlet temperatures of the two components: 20.27 [K] for $H_2(L)$ and 90.17 [K] for $O_2(L)$;
- the tracked reaction products: H_2O, H_2, O_2.

The algorithm has started with the stoichiometric reaction:

$$H_2(L)+0.5O_2(L)\rightarrow H_2O \qquad (1)$$

for which the reached turbine inlet temperature (TIT) is 3,984.27 [K].

In order to decrease the temperature in the 750÷960 [K] range, two cases have been considered: the supplementation of hydrogen, respectively that of the oxygen. The turbine inlet temperature variation with the modification of the proportions in the mixture is presented in Fig. 3 and 4, for the increase of hydrogen, respectively oxygen proportion.

It can be noticed that the influence of the pressure on which the combustion process takes place decreases with the modification of the composition from the stoichiometric reaction, becoming insignificant in the 750÷960 [K] range.

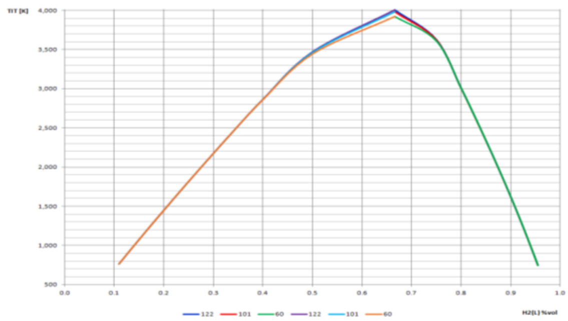

Fig. 3 TIT depending on $H_2(L)$ volume

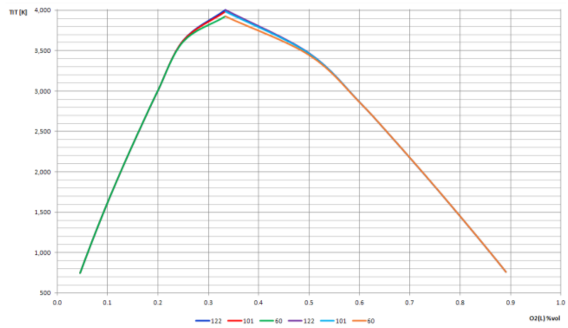

Fig. 4 TIT depending on $O_2(L)$ volume

For a oxidant/fuel massic ratio of 0.9 [15] the reaction takes the form:

$$17.2H_2(L)+16O_2(L)\rightarrow 18H_2O+15.2\,H_2 \qquad (2)$$

For this reaction, the combustion analysis has been made with the help of the same CEA program, the turbine inlet temperature of the gases reaching 892.9 [K] at 100 [bar] pressure.

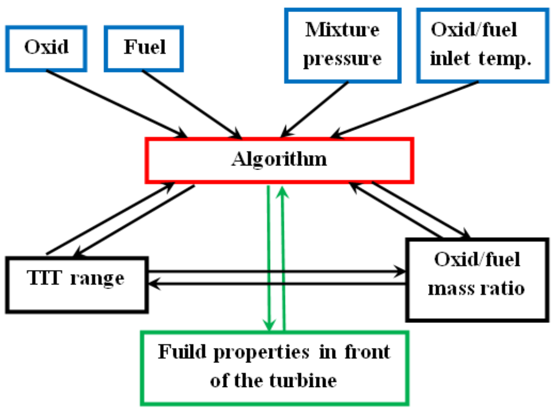

Fig. 5 Algorithm for calculating the fluid properties at the turbine inlet

3.3 Turbine design

Although several elements are common for the design of the turbines for turbopumps equipping liquid fuel rocket engines, there are no unique, well defined, procedures or design methods. The entities designing and manufacturing these components have different approaches regarding the stages and the steps to follow due to their previously acquired experience. The approach regarding the design of a turbine is also affected by the quantity of the available data concerning the fuels, the gases properties in front of the turbine, the necessary materials, the novelty degree, the identification of necessary software’s, as well as the identification of the materials providers.

Usually the following elements are part of the preliminary design process and they contribute to the setting of the configuration, performances and characteristics of the turbine.

Table 4 Requirements for turbine

Requirement	Example
Application	Defining the mission, vehicle and propulsion system requirements, manoeuvrability, operating environment
Functionality	Total momentum, thrust to time characteristic, start delay, initial engine mass, specific momentum, fuel ratio, time and tolerances for the above parameters.
Interfaces	Transmitting equipments, command and control systems, power sources, launching and transportation characteristics, structural inspection, signal control
Operation	Storage, launching, flight environment, temperature limitations, transportation loads, vibrations, radiation, reliability, etc.
Structure	Imposed loads for the vehicle (flight manoeuvrability), rigidity at rocket oscillations, safety factor
Cost and manufacturing time	Limitation in allocated time and budget
Constraints	Volume, length or diameter limitations, minimum accepted performances

The algorithms for determining the general configuration and the turbine specifications are presented in Fig. 6 and 7, along with the steps of the design process for one axial stage, Fig. 8. [16]

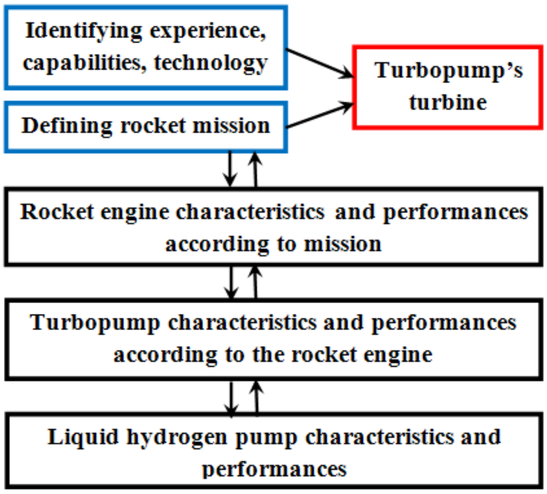

Fig. 6 General configuration/ concept

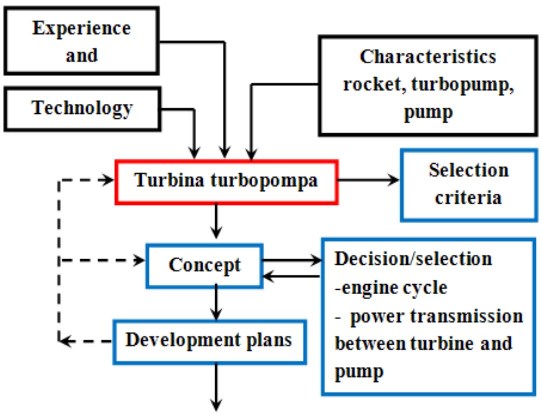

Fig. 7 Algorithm for determining the turbine specifications

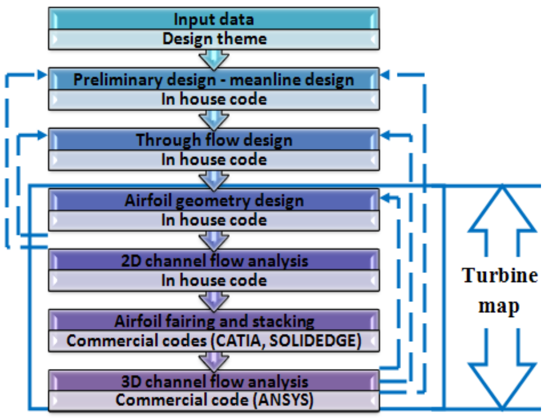

Fig. 8 Design process of one stage of axial turbine

For pre-dimensioning a turbine to equip a liquid hydrogen turbopump, reaching these steps is aimed by using computational resources existing at COMOTI. Therefore, for each of the main stages of the design process, the equations are solved using dedicated in house codes. The turbine characteristic obtained using these programs is validated by numerical simulations in CFD environment, in commercial codes, made using the 3D model obtained by stacking the profiles for different radius

4 Identification of suitable materials

As consequence of high requests for improving the performances and increasing the lifespan of the turbines equipping turbopumps, there have been developed several studies regarding the use of optimum materials for manufacturing the turbine assembly, such as the use of super-alloys (mono-crystal, rapid solidification, fibre reinforced or even ceramic structure super-alloys). [17]

For the turbopumps operating on liquid hydrogen, few materials are suitable due to liquid hydrogen's corrosive effect in contact with other materials, when the atomic hydrogen dissolves into the material's surface. The absorption of the atomic hydrogen in the molecular structure of the material leads to a decrease in the mechanical properties. The materials used in such environments are: Aluminium, stainless steel, Ni and Ti alloys. When choosing the material for a component of the turbopump, it must be taken into consideration the following: operating temperature (high temperature or cryogenic environment), the exposure to the working fluid, the forces acting upon the respective component and its transfer to the turbopump case, etc. The rotational components are subject to the most difficult conditions as a consequence of high operating speed, direct contact with the working fluid, high temperature gaps, requiring high strength. The most used materials for these components are Ni based alloys, with a high strength to mass ratio. Depending on the environment and the operating conditions, the turbine blades are protected through thermal treatment and sometimes coating.

The following table presents the materials used on different turbopumps for the case, helix and rotor of the turbine.

Table 5: Materials used in turbine manufacturing

Engine	Turbine case	Turbine helix	Turbine rotor
RL-10	-	-	Ni alloy 5667
VINCI – LH2	Inconel 718	Inconel 718	Ti 6-4
VINCI - LOX	Inconel 718	Inconel 718	Al alloy
ALH	Waspaloy	Waspaloy	PWA Ti-1240
Vulcain	Inconel 718	Waspaloy	Super - Waspaly

5 Conclusions

The paper presents several aspects of an on-going project, financed through national funds by the Romanian Space Agency, aiming to develop a strategy to design the turbopump system to equip a rocket engine. The main identified stages in order to establish the general configuration are related to the main gas-dynamic components, pump and gas turbine, for which the background has been researched and a series of design algorythms have been developed.

Future work will consist in finalizing the gas-dynamic design methodology, along with developping the mechanical design one and correlating the processes in order to be able to elaborate a complete strategy, including a logical succession of operations involved in the development of a turbopump system, covering all phases of the process, upgrading the cycle and contributing to the advance in the state-of-the-art of rotating machinery, bearing and dynamic seal technology, fabrication methods, material development, using time and cost reducing computational tools, such as CFD and FEM methods, focusing on improving and optimizing the performances of the turbopump system.

References

[1] Caissoa P. et al., A Liquid Propulsion Panorama, *Acta Astronautica*, vol. 65, 2009, pp. 1723-1737
[2] ***, NASA, Turbopump Systems for Liquid Rocket Engines, NASA SP-8107, U.S.A., 1974
[3] ***, http://www.b14643.de/Spacerockets_2/ Diverse/U.S._Rocket_engines/engines.htm
[4] ***, http://www.b14643.de/Spacerockets_2/ Diverse/U.S._Rocket_engines/engines.htm
[5] ***, http://www.b14643.de/Spacerockets_2/ Diverse/ U.S._Rocket_engines/engines.htm
[6] ***, www.snecma.com/Safran/Space propulsion VULCAIN2/Fiche technique/
[7] ***, http://www.capcomespace.net//dossiers/ espace_europeen/ariane/
[8] ***, www.snecma.com Space propulsion VINCI prospect, 2012
[9] Alliot P, Dalbies, E, Delange, J-F, Ruault, J-M, „Development status of the VINCI engine for the Ariane 5 Upper Stage" *AIAA 2003-4484*, 2003, Austin, U.S.A.
[10] Brodin S., J. Steen, I. Ljungkrona, N. Edin, B. Laumert, "Vinci Engine Development Testing, A Summary of Turbine Testing Results", *AIAA-2005-3949*, 2005, San Francisco, U.S.A.
[11] ***, Pratt & Whitney Aircraft, "Design Report for RL10A-3-3 Rocket Engine", PWA FR-1769, 1966
[12] Sutton G.P., Biblarz O., *Rocket Propulsion Elements*, John Wiley & Sons Ltd. Publications, USA, 2001, Chap. 10
[13] Dorney D.J., Sondak D.L., Marcu B., „Application of a real-fluid turbomachinery analysis to rocket turbopump geometries", *AIAA 2005-1007*, 2005, Reno, USA
[14] Gordon S., McBride B.J., „Computer Program for Calculation of Complex Chemical Equilibrium Compositions and Applications. I Analysis", NASA Reference Publication 1311, 1994
[15] Ley W., Vittman K., Hallmann W., *Handbook of Space Technology*, John Wiley & Sons Ltd. Publications, Singapore, 2009
[16] Moustapha H., Zelesky M.F., Baines N.C. & Japikse D., *Axial and Radial Turbines*, Concepts ETI, Inc. D.B.A. Concepts NREC, Vermont, U.S.A., 2003
[17] Petrasek D.W., Stephens J.R., "Fiber reinforced superalloys for rocket engines", NASA-TM-1000880, Lewis Research Center, Cleveland, Ohio, 1988

4:th CEAS Air & Space Conference
FTF Congress: Flygteknik 2013

Anisogrid technology made available for the west – a cooperation between RUAG, KTH and CRISM

Michael Thuswaldner
RUAG Space AB, Sweden

Keywords: *Anisogrid, Adapter, NRFP, KTH, RUAG*

Abstract

This paper describes how Russian anisogrid technology and design philosophy has been made available for western space applications through cooperation within the NRFP (Nationellt Rymdtekniskt Forskningsprogram) between RUAG Space AB, The Royal Institute of Technology (KTH) and Central Research Institute of Special Machinery (CRISM) .

1 Introduction

1.1 History

Lattice structures (or truss structures) have been frequently used through history. Larger structures like bridges, cranes and towers are very visible examples. Older race cars (with tube chassis) and aircrafts are medium sized but more invisible examples.

These structures are built up from rigidly connected ribs to globally form load carrying structures.

The most common topology used for such lattice structures is a triangle pattern like the classical isogrid pattern. There are however other topologies in use as well. Examples are orthogrid and anglegrid which together with isogrid structures were used in early projects (see fig. 1). In Russia a designer named Vladimir Shukhov used other topologies like the anisogrid (Anisotropic grid), which will be the focus of this paper.

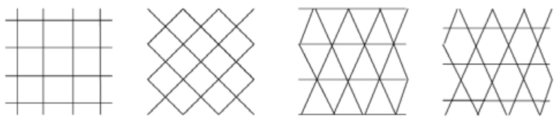

Fig. 1 From left to right: Orthogrid, Anglegrid, Isogrid and Anisogrid

The first hyperboloid lattice structure was a 25 m high tower built by Shukhov for the 1896 All-Russian Industrial and Handcraft Exhibition [1]. The same Shukhov later (1920 - 1922) built the 160 m high radio tower in Moscow (named the Shukhov Tower). This tower was originally projected to be 350 m high but due to the lack of material it came out smaller [2].

The Shukhov tower has a topology which combines strength and lightness. Compared to the 350 m high Eifel tower, the projected 350 m high Shukhov tower would use three times less material!

1.2 The Modern CFRP Anisogrid Adapter

The Russian company and institute CRISM 30 years ago proposed anisogrid structures made from Carbon Fibre Reinforced Plastic (CFRP) based on the work done by Shukhov [3]. The original Hyperboloid geometry has in this case been adapted to fit a filament winding manufacturing process. Mathematically this is no longer a hyperboloid geometry but it is the closest match possible.

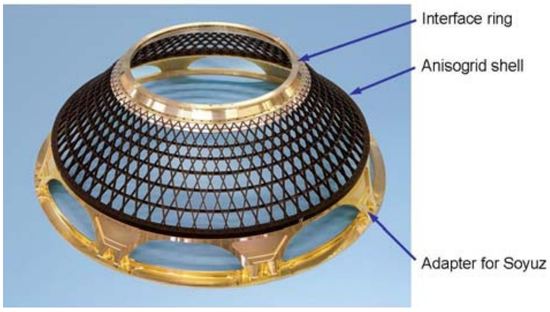

Fig. 2 Anisogrid adapter (LAS).

Since filament winding is a highly automatic process it is possible to reduce the man hours for each manufactured structure unit. This is what, together with the mechanical properties, gives this lattice structure its edge. A robust structure produced with an automatic process!

Due to the nature of the winding process, the finished structure becomes a so called interlaces structure. This means that the amount of fibre is doubled at the rib intersection points compared to the rest of the rib. Therefore the mechanical properties are limited by the highest possible fibre volume fraction at these intersections [4].

Although there are no rigorous comparisons of different design methods and topologies, numerical optimizations often give structures with high specific stiffness and strength for cylindrical and conical structures. It is possible to make CFRP honeycomb structures with better properties but they are usually more expensive and more sensitive to imperfections (buckling) or damage. According to Vasiliev [5], properly designed lattice structures are self-stabilizing in a way that reduces its sensitivity to shape imperfections.

Today these CFRP lattice structures have been used in various space applications. The Russian Proton launch vehicle e.g. has both interstage structures and payload adapters built with this method. To this date they have flown on more than 40 missions.

2 Russian Design Philosophy vs. Western Design Philosophy

RUAG was introduced to CRISM in 2006 by a common customer, Khrunichev State Research and Production Space Center, Russia (KhSC). KhSC, the manufacturer of the Proton Launch Vehicle had by then had a long experience with this company and its anisogrid lattice structures.

RUAG entered an agreement with CRISM which gives exclusive rights to market and sell anisogrid lattice technology products manufactured by CRISM to the west. This is however not as straight forward as it sounds. Despite the obvious cost and performance benefits of these structures there are some complicated hurdles to overcome.

The space industry is due to historical and reliability reasons very conservative. A launch failure must be avoided and this to almost any cost.

How this is handled comes down to design philosophy and this is a point where (traditionally) Russian and western engineers have different approaches. Both have their merits and, ultimately, the end result is the same. Usually it is however difficult to convince western customers to accept the Russian approach.

2.1 Western Design Philosophy

Western space industry is based on the aircraft industry and the early rocket development in the United States and Europe. In the beginning the design approaches were just based on the theoretical knowledge of the engineers and their common sense.

Over the years sets of rules and guidelines have developed. Some of these are due to failure investigations and some have been developed as the result of quality control programs. The body of rules and guides to follow has become quite extensive and more are continuously added.

The development of a typical space structure begins with a design phase where all the rules and guidelines are strictly followed. Types of analyses and allowed materials and components are specified.

The manufacturing is controlled from the material source to the assembly of the finished structure. Every step has traceability.

The completed structure is first built as a prototype that is subjected to a qualification test program where the foreseen flight loads (including numerous test factors) are applied. The test results are used to correlate mathematical models of the structure.

After this the structure is considered qualified for flight. Slight modifications are usually allowed, if accompanied by detailed mathematical modelling. If however the structure fails the tests in a bigger sense, the process starts over.

All subsequently built structures are then never tested before delivery. There are however strict controls on source material, manufacturing processes and end item controls before shipping. High finish everywhere is required.

This approach is thorough but costly and time consuming.

2.2 Russian Design Philosophy

The Russian approach also has its origin in the aircraft industry and early rocket development. Also here a vast body of knowledge has been documented into guidelines and rules.

However, there seems to be a more pragmatic approach than in the west. Although there usually is a strong theoretical background to design solutions the emphasis is on testing.

Russian designs are often characterised by robust designs proven through testing. High quality finish is only applied where it is needed. Testing and flight heritage triumphs everything.

Normally it is also difficult to get the type of certificates and documentation required in the west. Instead it is implied that one should have faith in the knowledge of the subcontractor.

2.3 Implications for the Anisogrid Adapter

Specifically for the anisogrid structures designed and manufactured by CRISM this means:

- High finish only where needed - Inclusions, porosity and matrix are not important; only the fibre volume content and the interfaces to surrounding structures.
- Proof load instead of qualification and analysis – Every delivered unit is subjected to proof load. Every 12th unit is loaded to failure. This ensures a good control over the manufacturing process.
- Robust, simple design.
- Limited documentation.

3 Cooperation During the Development Program

Before RUAG was able to market and sell the anisogrid structures designed and manufactured by CRISM we had to understand them. RUAG therefore invested in a development program prior to any marketing activities.

One of the most common payload adapter structures delivered by RUAG is the PAS 937S. This system includes a conical aluminium shell with a bottom diameter of 1780 mm, a top diameter of 945 mm and a height of 447 mm. This adapter is traditionally turned out of a single massive forging. The end result is an adapter with a mass of 48 kg.

The development program specified the same adapter but made with the anisogrid technology. The idea was to test the technology on a known product.

The resulting adapter is a two piece structure (shown in fig. 2). One lower conical grid structure and one upper aluminium ring (for interfacing the spacecraft). The weight of the complete LAS (Lattice Adapter System) ended up at 39 kg where 29 kg is from the lattice structure.

Two units of the LAS were manufactured. As per the Russian philosophy, the first unit was destroyed in a rupture test (2008) while the second unit (the delivery unit) was proof loaded (2009).

In the frame of NRFP, RUAG started a cooperation with KTH. This cooperation aimed at gaining a theoretical/analytical understanding of the anisogrid adapter structure.

This cooperation resulted in three master thesis and one test correlation report:

1. Generic modelling and optimization, [6] – This work shows that the anisogrid structure is rather robust with respect to its geometrical definition. Also, a automatic model generation script was developed
2. Structural analysis, [7] – The stiffness properties of the lattice intersections were studied as well as the model fidelity.
3. Post-test FE-modelling, [8] – A FE model correlation to the rupture test was done in order to identify detailed structural properties of the LAS.
4. Design of a dual launch adapter, [9] – This was a study made to evaluate the possibility of replacing the current Ariane 5 dual launch structure, SYLDA, with a less costly and more structural effective anisogrid structure.

All these mentioned activities have given RUAG a detailed understanding of the properties and capabilities of anisogrid structures for payload adapter applications. This has been an important step towards introducing this technology to the western space community.

4 The First Commercial Application

As a result of the work done the first commercial application of the anisogrid technology in the west was realised in 2013 when NASA launched its Lunar Atmosphere and Dust Environment Explorer (LADEE) mission.

For this mission RUAG was awarded a contract to deliver an anisogrid payload adapter manufactured by CRISM. The adapter specified was a conical structure with a diameter of approximately 1 m and a height of 0.5 m. Low cost together with a low mass was required.

The resulting structure weighs only 4.5 kg and is able to sustain loads up to 32 metric tons!

5 Conclusion

The anisogrid technology allows for cheaper, optimized space structures.

Through the cooperation between RUAG and KTH, supported by NRFP funding, the CRISM anisogrid technology has been made available for the west.

References

[1] http://en.wikipedia.org/wiki/Hyperboloid_structure

[2] http://www.shukhov.org/tower.html

[3] Vasiliev V.,Barynin V.,Razin A., “Anisogrid composite lattice structures – Development and aerospace applications”, Central Research Institute of Special Machinery, 2011

[4] Köll J, “Composite lattice structures for space launch vehicle applications – Review of history and development”, KTH Lightweight Structures, Stockholm 2008

[5] Vasiliev, V. V: Anisogrid lattice structures – survey of development and application, Composite Structures 54, , 2001, pp. 361-370.

[6] Köll J., “Generic FE-Modeling and Weight optimization of Lattice Payload Adapter Structures”, Master Thesis, Lightweight Structures, KTH, Sweden, 2008.

[7] Arvidsson J., “Structural analysis of composite payload adapter”, Master Thesis, Lightweight Structures, KTH, Sweden, 2008.

[8] Köll J., “Post-test FE-modeling of the LAS 937 lattice adapter structure under full-scale test conditions”, Lightweight Structures, KTH, Sweden, 2009.

[9] Kockum P., “Basic design of lattice dual launch adapter”, Master Thesis, Lightweight Structures, KTH, Sweden, 2010.

Enhanced methods for warping, edge blending and colour correction when projecting in domes

Mats Elfving, Carl Andersson, Joakim Hägvall and Olov Wilander
Sjöland & Thyselius, Sweden

Keywords: Flight Simulator Dome, Geometric alignment, Photometric alignment, Camera projector calibration, Automatic calibration

Abstract

When working with flight simulation for the Swedish Armed Forces we have developed methods to improve quality and decrease time spent when setting up a simulator.

It is very common to use multiple projectors to project the environment image in an aircraft simulator. Any change in the configuration of these simulators amounts to time consuming, often manual, work to adapt and improve the quality of the projections, to give a good simulator experience to the user.

By using different more or less automatic methods to map, calibrate and warp the picture we can reduce this time consuming work and at the same time achieve an improvement of image quality.

Experience from the development work indicates that the methods we have developed at Sjöland & Thyselius reduces the manual workload to about 20% of the work of the usual methods, and at the same time noticeably improve the image quality.

1 General Introduction

When projecting pictures from multiple projectors and/or onto any surface you will likely encounter several problems with the picture that you want to create. You will get errors in the picture, distortions, unwanted shadows, and other problems. It is a painstaking process to correct these problems, often with very time-consuming hands-on processes.

At Sjöland & Thyselius we have, during our work with flight simulators, discovered several different methods which simplify the work of adjusting pictures and of merging several projected pictures to form a continuous picture on any smooth surface. Several different methods have been developed to solve different problems that you may come up against in such situations, for example correcting colour and mapping coordinates.

2 General description of warping

Warping, or image warping, covers methods for distorting one or several pictures, mainly to correct the image as projected onto a viewing surface. In the case of several pictures, the pictures can also be integrated into one large picture. The integration can be done with edge blending methods.

A common use for warping is to arrange one or several pictures onto a curved surface with image projectors. The purpose is to create one large picture that gives the impression of a "window" where you look through the picture into the surrounding world.

Image projectors are normally built to project a large rectangular grid of pixels, with equal distances between neighbouring pixels, onto a flat viewing surface perpendicular (or nearly perpendicular) to the direction of projection. If the projector is turned or if the surface is not flat, the picture is going to be distorted. In the same way, the perceived picture will be distorted if a person looking at it changes position relatively to the projected picture (for example, in a cinema the end seats of the first row may have a noticeable distortion effect from the poor viewing angle). If you want to create an environment without perceived distortion for a viewer, you need to compensate for all the distortions mentioned above.

A warping system normally consists of three things:

1. The possibility to move pixels in the picture (i.e. warping)
2. The possibility to attenuate the pixel intensity (i.e. blending)
3. The possibility to change and calibrate the modifications in 1 and 2

The two first parts are known technology and are described briefly below. The focus of this paper will be to describe several different methods for calibrating and enhancing the effectiveness of the warping and blending.

2.1 Warping

Warping is used for correcting image distortion and is done by digitally moving pixels. To manually move pixels one-by-one is an infeasible process and even if the great effort is made, it does not usually produce a satisfactory result. Instead you use a transformation with a limited degree of freedom. A common transform is a "spline patch", that is a number of bidirectional splines. The original picture is mapped onto this spline patch so that when the patch is changed the picture changes along with it.

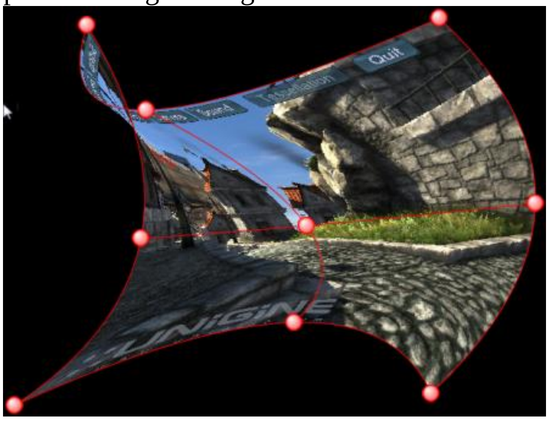

Figure 1, Unigine Heaven warped across a spline patch

2.2 Edge blending

To merge two pictures using an edge blending technique you first need to locate the region where the two pictures overlap. A point in this region is lit by both projectors, making it much brighter compared to the rest of the projected image. Edge blending defines a function on the overlapping area, used to reduce light intensity from the projectors, so that the final intensity at any point corresponds to the light intensity of the original scene. These functions are constructed so that one picture is faded out across the overlapping area and the other picture is faded in, creating a single image with the light intensity of the original scene.

Figure 2, Two edge blended pictures that are merged

2.3 Calibration

Today, the calibration of warping and antialiasing is usually done in the simplest way, by a person who manually adjusts some control points and parameters. The disadvantage of this method is that the person doing the calibration needs a long time for these adjustments, and that the results are not optimal (particularly with respect to the time spent).

3 How to improve the effectiveness

The paper is going to describe different ways to calibrate and make certain that a pixel in a picture is placed by the projector in the right place to reduce distortion and other negative effects. It will describe methods that are semiautomatic (that is, where manual steps are reduced but not eliminated) but also methods that are fully automatic where no human effort is needed. This because the main factor to enhance the effectiveness both in time and result is to exclude the human as much as possible, both in terms of work done and in terms of decisions made.

3.1 Geometrical calibration

To be able to get the right pixel at the right place you need to map the surface and correlate it to the picture you want projected. This is really a two-step process, where both steps can require significant effort, and any errors tend to accumulate into visible artefacts. The first step is to collect geometrical information – where in the intended viewer's field of view are the projector pixels located – and the second is to fit the images, so that the virtual objects in the images end up in the correct place in the field of view.

3.1.1 Mapping spherical coordinates

In order to convert the image to any surface, information about the surface geometry is needed. The method we propose therefore gives each projector a polar coordinate system by calibrating the projectors against a calibrated camera.

The calibration of the camera is made from images taken from different positions. The camera takes pictures of a check board image in which OpenCV [1] finds the corners. Based on these corners, OpenCV calculates the camera model parameters with the help of an algorithm by Zhang [2]. All pictures captured hereinafter are undistorted with those parameters.

The calibration of a projector requires a transform between the camera space and the projector space.

To filter out irrelevant pixels a mask is created for the camera. The mask holds information about which projector(s) each camera pixel covers. Each projector displays a black and a white image captured by the camera. The difference between the images is filtered with a threshold to remove e.g. secondary light artifacts from the projector. The biggest blob in the image is marked as the area of interest in the mask.

The projector's pixels are identified in the camera using Gray code patterns produced by the projector. Gray codes are less sensitive to spurious readings compared to ordinary binary code. Each pixel coordinate in the projector screen is coded to strings of bits similar to the process listed in Jordan[4], Raskar [3] and Zhang[2].

The patterns correspond to bit planes of the Gray coded projector coordinates, starting with the most significant bit. The camera detects two images: first the pattern and then its inverse. If the difference between the pattern and its inverse, for a given pixel, is less than a threshold, then the pixel is assumed to lie on the border between a black and a white area and is thereby complete. Current bit depth of the bit plane, together with the bits found this far, then uniquely determines the pixel's Gray code. If the pixel difference is greater than the threshold, the pixel bit is set to 0 or 1, depending on which image's pixel intensity was greatest. The process of Gray code detection is repeated for all bit planes both vertically and horizontally. Finally the Gray codes are transformed to binary form.

At this point, a camera image is created, where each camera pixel (inside the previously created mask) has a dedicated projector pixel. Detected projector pixels are marked in a projector image along with the camera pixel that detected them. All camera pixels have a corresponding vertical and horizontal angle. These angles can be calculated as gnomic projection coordinates with the help of the principal point and the focal length of the camera, as in Eq. (1)

$$\begin{pmatrix} x_g \\ y_g \end{pmatrix} = \frac{\left(\begin{pmatrix} x_m \\ y_m \end{pmatrix} - \begin{pmatrix} x_0 \\ y_0 \end{pmatrix}\right)}{f} \qquad (1)$$

Where x_g and y_g are the gnomic projection coordinates. The values x_0 , y_0 and f are taken from the camera model expressed in pixels, and finally x_m and y_m are the measured image pixels.

The stored values from a single view are called a camera view. One such camera view contains all visible projectors pixels and the gnomic projection coordinates in the camera space that detected that projector pixel.

3.1.2 Fitting the warping transformation

Once we have found where the projector images fall in the camera's field of view, warping transforms for the projectors are created.

One such transform is created by finding a transform from projector space to gnomic space, finding a quaternion relation between camera images capturing the same projector, and finally describing all projectors' gnomic coordinates in the same reference frame.

The transform from the projector space to the measured gnomic coordinate space is expressed as a 2D spline function. The spline is found by doing a least square fit in gnomic space. The process for this is described in Figure 3.

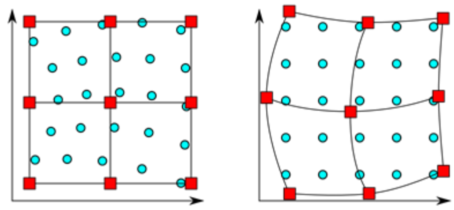

Figure 3, Spline transform function from projector space (left) to gnomic coordinates (right). Cyan dots in left figure are projector pixels detected by the camera, with a corresponding dot in gnomic representation to the right. Left red square grid is equidistant control points of the spline. Right Corresponding red square grid is the spline fitted to the gnomic coordinates using linear regression.

When the projector display is not covered by one camera view, multiple views are needed. The relation between views is described with a quaternion. Measures from different camera views can then be added together to increase the resolution and area covered. To calculate the relation between two intersecting views all the known pixels in one of the camera views are matched with the corresponding interpolated pixels in the other camera view. The pixels from the second view are then transformed to the first camera view using a test quaternion, q_t. The sought quaternion q_t is the one minimizing the error. The error is calculated through Eq. (2)

$$\sum_i \left| f(q_1^i) - f\left(q_t q_2^i\right) \right|^2 \qquad (2)$$

Where q_1^i is the quaternion to the first measurement in the first views reference frame, q_2^i is the quaternion to the second measurement in the second view's reference frame, and f is a function that removes the roll from the quaternions and gives values that corresponds to pitch and yaw or x and y coordinates after a gnomic projection. Due to the non-linearity of f, it's not possible to easily solve this with linear regression.

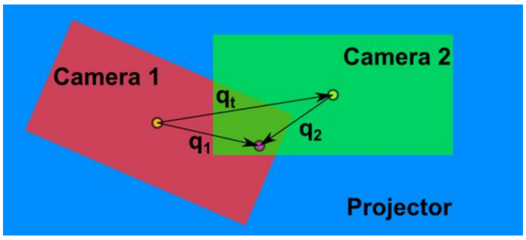

Figure 4, Relation between two camera images described as a quaternion (q_t). Common dots (purple) are described in each camera image as a quaternion related to camera image center (q_1 and q_2). Note that the quaternions exist in SO(3) and not in R(2).

The testing quaternion is generated by two different algorithms. The first algorithm chooses a random quaternion in close vicinity to the last by doing a small step. If the new quaternion renders a smaller error it is kept, otherwise discarded. Then it iterates over decreasing step sizes to increase the possibility of a better match. When a sufficient number of iterations have been performed it exits. The other solution chooses the new test quaternions with a method similar to gradient descent. The test quaternion is modified with a step in one of the principal directions. If one of these gives a smaller error it is accepted and then the algorithm proceeds with the next iteration. If none of the directions yields a better result the step size is halved and the algorithm runs again. The algorithm completes when the step size is sufficiently small.

The latter algorithm is much faster but has a higher risk of getting stuck in a local optimum far from the global optimum. Therefore both algorithms are used and the first algorithm creates an initial point for the second algorithm.

When the relations between all connected camera views are known an algorithm finds the way between all unconnected camera views through connected views yielding the least error. A master camera view, usually the first camera, is chosen. This view defines the forward and up direction but can be altered later. All projectors' centre points are expressed with the master view as baseline. All pixels of the camera view are converted using each projector's center point.This is done so that all projector pixels have the same transform and can be represented from a single viewport in a 3D graphics environment. The data points for each projector are collected and approximated by a 2D spline in the same way as described earlier. This spline is then applied as the real-time warping of the projector image.

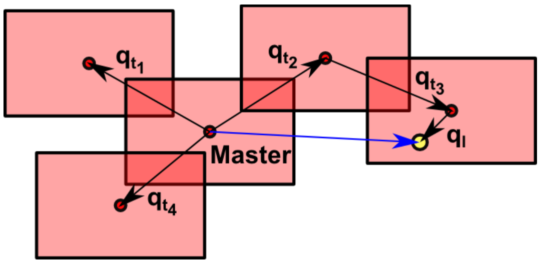

Figure 5, Relations of projector images (red rectangles). Each image has a relation (q_t) to another image through overlap. A local point (yellow), described as a local quaternion(q_l), is later described relative the master image (blue arrow), as each image is transformed relative the master image.

3.2 Pixel Attenuation

After the picture has been placed on the intended projection surface it is important to adjust each pixel in intensity and colour, to achieve an evenly lit image without colour tints. For this we have developed several methods which are, to a high degree, automated to increase performance.

3.2.1 Calibration of joint surfaces between projecting images

Overlapping projector image creates unwanted areas of too high intensity. Usual edge blending takes a portion of the overlapping surface and tries to fade those overlapping parts so that each pixel has the intensity of the original picture pixel. Our proposed method is automatic and uses the entire overlap.

The advantage of the geometrical calibration developed in this report is that it produces a higher degree of precision. Giving more accurate calculations to locate which pixels that overlap and how much they need to be faded, resulting in a better joint between the projector images.

For each projector a weight map is created. The weight map describes the intensity adjustment of the projector pixels (alpha blending). The weight decreases from the centre of the map and increases from the edges of the map having zero weight at the edge. More precise, the weight is calculated as seen in Eq. (3),

$$w(x,y) = \frac{1}{c+(x-x_0)^2}\frac{1}{c+(y-y_0)^2}\frac{1}{c+|(x-x_0)(y-y_0)|}f(x,y) \qquad (3)$$

Where c is a parameter and $f(x,y)$ is the $L2$ distance to the closest zero pixel (i.e. the distance to the edge) in the interpolation mask created for spline interpolation.

For each pixel in the camera view the corresponding projector pixels seen in that pixel are compared. The intensity in each projector is then calculated as Eq. (4) and (5) show.

$$I_i(x,y) = \frac{w_i(x,y)}{S(x,y)} \qquad (4)$$

$$S(x,y) = \sum_i w_i(x,y) \qquad (5)$$

The subscript i is for the different projectors. This is done and added together for all views and interpolated using Gaussian blur.

3.2.2 Correction of projector colour with regards to light intensity lost to spatial distortion (vignetting)

The perceived colour intensity on a projected surface is dependent on the distance and angle to the surface. Thus, projecting a single colour picture on a non-planar surface will give different intensities on different parts of that surface. This problem is often hardest to neutralize at the edges of a projected picture, unfortunately often where other images are to be fused in.

The solution is to shade the brighter pixels in the projector image so that they are perceived as being as intense as the dullest one. The assessment is made by a camera in the viewer's intended position. The camera provides feedback to the compensation algorithm and a measure of the overall residual error. When the projector intensities are automatically controlled the camera has the role of reference/actual value. It is therefore important that the camera measures correctly. Firstly, the camera needs to be placed in the intended viewing position and secondly, it needs compensation for its own vignette effect. The method for anti-vignetting chosen measures the camera's response to a single colored input image. The single colour image is simply a depiction of a evenly lit, diffuse and smooth surface. To avoid picking up imperfections from the surface, form the average of a series of pictures where the camera is being translated, keeping a fixed distance to the smooth surface. The image is finally scaled so that the maximum intensity has the value of 1.

Then there is a need to identify which projector pixels are covered by which camera pixels as has been described before. (See section 3.1.1)

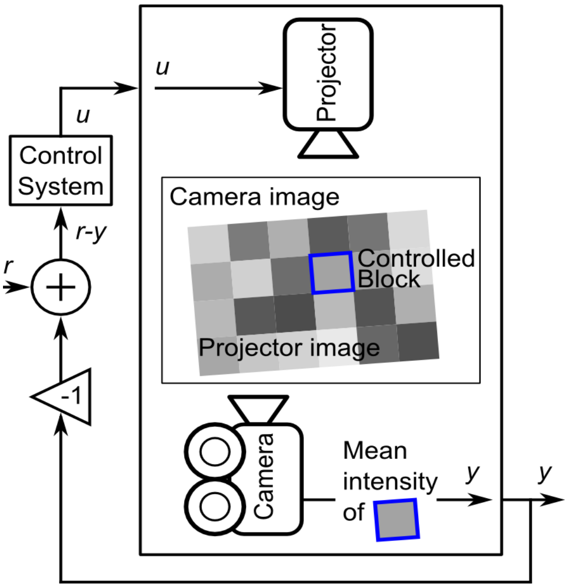

Figure 6, The control system of the pixel blocks (each controlled separately). Where *r* is the desired value, *u* is the controlled value and *y* is the actual value of a particular block. In the controlled system, a camera reads the projector image and the mean intensity of all blocks are fed back.

The projector pixels are controlled so that the camera perceives them as of the same intensity. The desired intensity value is measured as the average of the 5% faintest pixels when the projector emits bright white. To minimize the amount of erroneous readings, the mask where the camera makes its measurements is shrunk. Blocks are created in the projector image, together with the belonging camera pixels, so that errors in the mapping between the projector and camera are minimized. These blocks are then controlled separately so that the intensity in each block is approaching the desired value.

A compensation image for real-time application is created with the found intensity levels for each block. The block image is then gauss filtered with a filter size that allows the block structure to vanish. The final compensation image is created by scaling the filtered block image so that the brightest pixel reaches maximum intensity. Finally the compensation image is applied to the image sent to the projector. This is done through a multiplication, with the compensation image in the pixel / fragment shader. The compensated image is often heavily quantified for low intensities. This is remedied by adding virtual noise, whose expected value is the compensated value, in the shader.

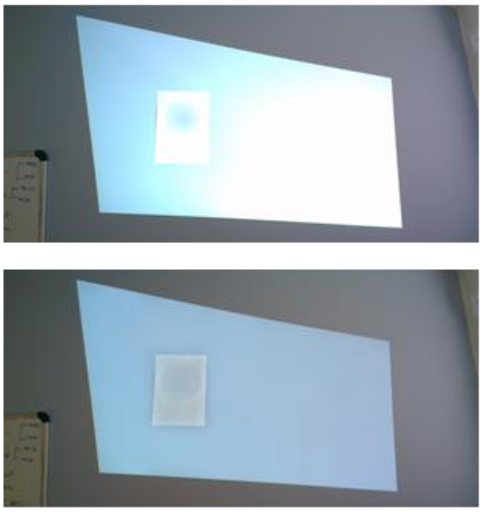

Figure 7, Projector image before and after intensity compensation. Note how the paper's edges stands out, while the large gradient of the surface disappears. This is because only details larger than the control blocks are neutralized, i.e. a high-pass filtering

4 Future work

Some unresolved problems remain to get a completely fused and seamless multi-projector image. Most significant is the problem that a projector's colour transfer function is not linear. Commercial products' that partially solves the problem exists, but these usually focus on an image being perceived in the same way in any medium. The problem regarding multi-projector displays may be defined as:

- A projector image for a given input shall look the same as the sum of two projector images with half of the same input signal.

A possible solution is to first measure the transfer function from input to perceived output for a number of colours. The largest axis aligned volume that is enclosed by measured outputs is found. The intersection of all projectors' colour volumes is the sought common colour volume. Then fit a transfer function, in the form of a 3D spline, within the common colour volume, from the measured signals to the inputs. Images shown by the projectors can now be described as an output instead of an input signal.

5 Conclusion

At Sjöland & Thyselius we have developed several methods to deal with the problem of projecting a picture onto any smooth surface and still get the right perceived picture. With a higher degree of automation the results from these methods are of a higher quality, with less time required for calibration, than with the manual methods used previously. The methods give a better surface fit with less distortion and other defects which greatly enhance experience of the simulations. The methods also give the advantage of a greater adaptability when projecting pictures onto a new surface shape.

References

[1] G. Bradski. The OpenCV Library. Dr. Dobb's Journal of Software Tools, 2000. URL opencv.org.

[2] Zhengyou Zhang. A flexible new technique for camera calibration. Pattern Analysis and Machine Intelligence, IEEE Transactions on, 22(11):1330-1334, 2000. ISSN 0162-8828. doi: 10.1109/34.888718

[3] Ramesh Raskar, Greg Welch, Matt Cutts, Adam Lake, Lev Stesin, and Henry Fuchs. The office of the future: a united approach to imagebased modeling and spatially immersive displays. In Proceedings of the 25th annual conference on Computer graphics and interactive techniques, SIGGRAPH '98, pages 179{188, New York, NY, USA, 1998. ACM. ISBN 300-89791-999-8. doi: 10.1145/280814.280861. URL http://doi.acm.org/ 10.1145/280814.280861.

[4] Samuel J. Jordan. Projector-camera calibration using Gray code patterns, 2010. URL http://hdl.handle.net/1974/5911. 0984: Computer science; Applied sciences; 66569; 9780494700280; n/a; English; Copyright ProQuest, UMI Dissertations Publishing 2010; 2274186791; Jordan, Samuel James; 2010; 55155111; 853293426; 2012-07-06; MR70028; M1: M.A.Sc.; M3: MR70028.

4:th CEAS Air & Space Conference
FTF Congress: Flygteknik 2013

Demonstration of Satellites Enabling the Insertion of Remotely Piloted Aircraft Systems in Europe

H. H. Hesselink, D.-R. Schmitt F. Morlang
AT-One, Germany and The Netherlands

Keywords: *Unmanned Aircraft Systems, Remotely Piloted Aircraft Systems, UAS, RPAS, airspace*

Keywords: *Unmanned Aircraft, UAS, RPAS, Remotely Piloted Aircraft System, Simulation, Airspace*

Abstract

Unmanned Aircraft Systems (UAS) are presently deployed in segregated airspace; passage though controlled airspace is taking place only through segregated corridors. With the increased use and the growing size of Unmanned Aircraft (UA), the need for insertion in non-segregated airspace increases, with first steps being taken in environments with air traffic control services in normal density traffic situations (en-route and not too busy TMA's). Already, civil UAS are flying in segregated airspace to carry out maritime surveillance missions and their insertion in ATC can be expected to be requested soon to increase their operational scope. The European Commission (EC), European Space Agency (ESA), and the European Defence Agency (EDA) have established a European Framework Cooperation (EFC) in which UAS air traffic insertion is identified as major topic to be addressed. We will describe the results of two experiments with real-time, man-in-the-loop air traffic control simulations to support UAS air traffic insertion.

1 Introduction

Several studies investigate UAS air traffic insertion, mostly addressing Detect And Avoid (DAA), safety of the operations (related to the aircraft, other airspace users, and population on the ground), architectures for data link communication, and definition of standards for certification. However, little effort is currently dedicated to performing actual flight trials and preparatory simulations for actually achieving the ultimate goal: air traffic insertion.

The major work so far in air traffic insertion is the European Civil UAV Roadmap defined by the European Commission funded UAVNet consortium [1] . A further roadmap was defined by a consortium called Air4All [2] The document defines six consecutive steps until full integration is achieved in step 6, where civil type certified UAS fly Instrument Flight Rules (IFR) and Visual Flight Rules (VFR) across national borders routinely in controlled and uncontrolled airspace (airspace classes A, B, C, D, E, F, and G). Based on the results from Air4All, a consortium of research centers (E4U, [7) has set up a detailed business case for the prioritization of actions for insertion of UAS in air traffic.

In this paper, we present the set-up and results of simulations for UAS in order to prepare for full flights in the near future. Actual flights cannot be carried out before the full set of routine and emergency procedures has been evaluated in a simulated environment [6].

In order to evaluate and validate routes, procedures, and emergency situations, we have set up simulations in a real-time man-in-the-loop Air Traffic Control (ATC) environment, including UAS, which were piloted from a realistic Remote Pilot Station (RPS). In two projects, USICO (Unmanned Aerial Vehicle Safety Issues for Civil Operations, in 2007) and SINUE (Satellites enabling the integration in Non-segregated airspace of UAS in Europe, simulations have been organized, where real air traffic controllers participated to experiments for the introduction of UAS in non-segregated airspace.

For the USICO, a dense traffic sample of the Frankfurt Flight Information Region (FIR) was chosen. For SINUE, we have chosen to set up a radar simulation facility which has been configured for running the scenarios around the Canary Islands in Spain. For this, the Spanish airspace was set up and a representative traffic sample with flights from and to Gran Canarias was implemented.

2 Research question

To bring air traffic insertion of UAS further, we start with simulating the environments in which the aircraft will fly. It will be possible to set up the necessary architecture in a network of simulators, for the air traffic control station, the unmanned aircraft, and a communication link. In a real-time simulation environment, air traffic controllers will be able to experience without risk, the aircraft in operation in their sector and experience themselves the aircraft's characteristics, the use of emergency routes and procedures, communication with a remote pilot, and the interaction with other traffic. Our research question was to

1) Identify a suitable architecture for BLOS operations with UAS.

2) Examine the effects on ATC of UAS in their airspace.

3 The architecture set-up

In most scenarios, the aircraft will fly en route their missions in a remote area and will therefore be flying Beyond Line of Sight (BLOS). Communication between the pilot and the aircraft will have to take place through satellite communication. Just as well, communication between the ATC centre and the RPS will be relayed over satellite. Therefore, the architecture proposed must at least enable the Command and Control (C2) link between the UAS pilot and the UA and the ATC link between the UAS pilot and the ATC center, see the functional decomposition in figure 2 (from [2]) below.

Figure 2 Functional set-up

In the simulation experiment, the architecture as depicted in figure 3 was chosen.

In the center of figure 3, the UA is flying a mission in controlled airspace. The UAS pilot has no line of sight with the aircraft, so command and control will be relayed over satellite. This already is a standard operating procedure for UAS that fly BLOS operations.

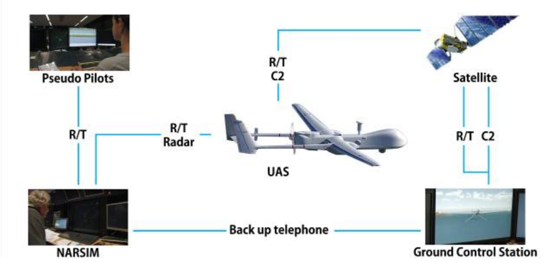

Figure 3 Functional set-up

Specific attention has been paid to VHF R/T communication between ATC and the UAS pilot. In our set up, the aircraft will receive all R/T on the frequency and relays this signal on a dedicated channel to the satellite. This set up requires significant bandwidth hence operating costs, but our calculations do show that bandwidth does not form a limitation here. A back up for R/T communication is available through a standard telephone line.

A pseudo pilot had to control the other traffic in the simulation. In a typical simulation, depending on the intensity of the required actions, pseudo pilots are capable of dealing with 10 to 20 aircraft at the same time.

4 Emergency situations/procedures

The mission of the European Aviation Safety Agency (EASA) is to promote and maintain the highest common standards of safety and environmental protection for civil aviation in Europe and worldwide. EASA performed a study for an impact analysis on safety of communication for unmanned aircraft systems [5].

From this study, through a functional hazard analysis, the following list of relevant emergency situations needs to be covered during experimental simulations and flights:

- Loss of voice communications between UAV/S pilot and ATC
- Interruptions to voice communications between UAV pilot and ATC
- Intelligibility and latency of voice communications between UAV pilot and ATC
- Loss of command and control link between UAV and GCS
- Interruption of command and control link between UAV and ATC (due to system reliability or satcom coverage)
- Loss of surveillance information feed to ATC
- Interruption of surveillance information feed to ATC (due to system reliability or radar coverage)
- Loss of surveillance information to other airspace users
- Interruption of surveillance information to other airspace users (due to system reliability or coverage)

With the exception of the “loss of surveillance information”, all events were considered in the experiments to cover all emergency situations emerging from the use of UAS. As the C2 and ATC signals are relayed through different channels on board the aircraft, the “loss off”- emergency situations can occur for either one of them or for the both simultaneously.

For the design of emergency procedures, three aspects need to be considered: a home area, an emergency route, cleared from the other airspace routes, and a procedure to fly from the current location (where the emergency occurs) to the emergency route.

4.1 Home Area

The home area is a base, where the UA will fly to when an emergency occurs. The aircraft will land there or perform a maneuver which will destroy the aircraft without risk of casualties. For each flight and for each experiment, the home area needs to be defined, depending on the local situation. For the two experiments mentioned in this paper, USICO [4] and SINUE [3], two distinct procedures were defined.

In the SINUE set up, a home area above sea was defined, where the aircraft would fly a circular pattern and be climbing in order to try to re-establish communication with a land based station that would be within line of sight. In USICO, an emergency airport was identified.

4.2 Emergency route

An emergency route must be designed that is fully separated from other air traffic routes, so that the UA can follow a path separated from all other traffic. For every flight with a UAS, the route must be carefully evaluated in order to check whether it is easily and safely reachable from the mission area.

Figure 4 shows the route used in the Spanish experiments, where one route was sufficient for all experiments performed. This route was designed in cooperation with air traffic controllers and was designed such that several entry points were defined towards which the aircraft would fly in case of an emergency. The points were chosen so that the aircraft would never fly over inhabited areas in case of an emergency and was vertically separated from other crossing air routes. The figure below shows the emergency route in red. The home-area is located at the bottom in the middle of the figure.

One special situation is when the aircraft is on final approach. In this case, the UA would fly the standard missed approach procedure to avoid it flying through other aircraft on approach, see the "hook"–pattern on the bottom of the picture.

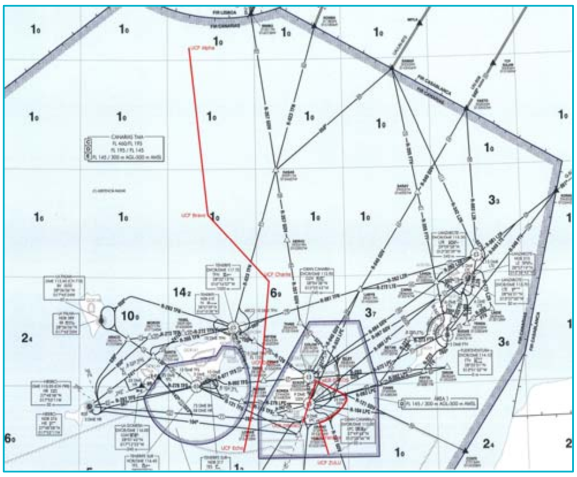

Figure 4 Design of emergency routes

For USICO, the simulated airspace is the TMA Frankfurt controlled by Frankfurt Arrival and the western sector controlled by Langen Radar. Controller working positions of the ATC center (Frankfurt Arrival and Langen Radar) are provided by the employed ATMOS. The simulated traffic in these two sectors is piloted by the pseudo pilots. The traffic in the northern and southern sector is navigating fully autonomously, i.e. it is so called dummy traffic. See figure below. For the emergency, the airport of Hahn was planned as alternate.

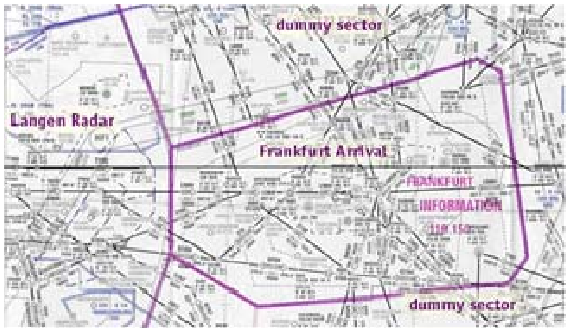

Figure 5 USICO TMA Frankfurt

4.3 Towards the emergency route

To reach the emergency route, the UAS follows a standard procedure which is known to the controller and the remote pilot. The procedure chosen in the SINUE study follows the procedure that has to be followed by other aircraft as well: the UA will abort its flight path by turning towards the closest way point on the emergency route and maintain its current altitude for two minutes. After the two minutes the aircraft would climb or descent towards the altitude of the closest way point on the emergency route.

5 Experiments

In the simulations we carried out experiments in air traffic control simulation facilities, where real air traffic controllers participated to carry out the simulation and to evaluate the proposed concept and procedures.

We used an air traffic control simulator, which resembles the airspace where the aircraft is flying as much as possible. Experienced air traffic controller and pseudo pilots were running the experiments, which were briefed at the beginning of the day and were given the possibility for training.

Through questionnaires directly after each run and at the end of a simulation day a directed list of questions was handled. Just as well, at the end of the day, a discussion session was held with all participants of the simulations

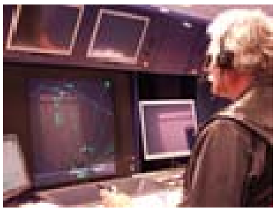

6 Results

The goal of the two studies was to examine the effects on ATC of UAS in their airspace. From the simulations, questionnaires, and debriefings, we obtain results for the sessions that were held.

Separation and collision avoidance. In the simulations, we did not use different separation criteria than those currently in use. The aim was to see if current separation can be maintained, even though there is no pilot on board the aircraft. We instructed controllers to use current separation criteria for the UAS, which they were able to maintain. In initial practical trials with real aircraft, for safety, the separation between a UA and a piloted aircraft will be increased in actual air traffic insertion experiments. The exact separation will need to be decided by the regulatory authority.

Communication. Communication delay because of the satellite connection will not be an issue when high quality bands are used. For SINUE we have chosen to perform the mission around the Canary Islands, where coverage of the Hispasat satellite system can be ensured. The satellite gives a delay in voice communication of around two seconds. In the scenario (no dense traffic), this was rated acceptable by the air traffic controllers.

ATC interface. We investigated the interface with ATC with respect to these aspects. New special squawk codes are proposed:

7600: comm loss
7660: datalink loss, proceed as planned
7661: datalink loss, return home
7662: datalink loss, fly to emergency field
7700: emergency

Although controllers have indicated that they do not particularly require specific terminology or symbols for UAS guidance. Either they do not feel comfortable with more information, or they expect that more information will not help them in solving the issues at hand.

Dependable emergency recovery In the simulations, we have defined a “home”-zone, to which the aircraft will fly following a standard route which is separated from other airspace routes. The procedure for flying towards the standard route follows common practice.

Controllers in all cases indicated they felt comfortable with the procedures defined, even where the emergency situation would occur at the “most inconvenient moment”. In our case an UA was flying without control through an arrival stream and in another situation straight towards two low flying IFR aircraft. As long as emergency situations are defined similar to those of manned aircraft, controllers are well trained for emergency situations.

Situational awareness. It is important for all parties to have a good overview of the traffic situation and to have the same mental picture of a traffic situation. This implies that there is a need for a good situational awareness for air traffic controllers, UA pilots, and pilots of other traffic.

The air traffic controller will need to know that he is dealing with an unmanned aircraft in an instance. Already at any existing ATCo’s (Air Traffic Controller) display, the aircraft type is indicated in the aircraft label. The aircraft types need to be known to controllers. Other options to give more recognition to the UAS can be:

- A special convention for the use of callsigns can be arranged for UAS.
- A dedicated UAS symbol can be used to depict the aircraft.
- The UA label at the ATCo’s display can be made more explicit, e.g. by use of a special colour.

The unmanned aircraft must be easily visible by eye for controllers in the control tower, which implies that the colour coding of the aircraft bodies and liveries must be carefully designed.

During the introduction phase of UAS into air traffic control, other pilots will need to be aware of the flying objects around them. Air traffic control must play a role in this, through informing pilots that an unmanned aircraft is flying ahead of them. This can be quite easily accommodated through informing other traffic over the R/T that a special aircraft is flying in their vicinity. This is already common practice, e.g. with hot air balloons and glider traffic.

Just like for air traffic controllers in the tower, the aircraft must be easily visually recognizable for other pilots.

Emergency procedures. In the experiments, all emergency situations as identified by EASA were tested.

We observed that controllers were not always fully aware of the aircraft's behavior at the moment that it was flying towards the emergency route. This was partly due to the fact that they used it for the first time.

From the discussions with controllers, it is suggested to define and discuss the emergency routes in advance of any simulation or real flight trial, based on the planned flight of the UA. The altitude of the points on the route must be defined such that the aircraft will make as little as possible a vertical movement on its way towards the route. Just as well, the route must also be defined as high as possible, to increase the possibility for re-establishing communication, either through satellite or via direct line-of-sight.

The emergency route can be displayed at the controller's display, either at all times or only at request of the controller.

Back up phone. One specific back up element was introduced in the experiments. The air traffic controller was able to contact the UAS pilot directly by phone. This possibility is especially interesting in case of R/T failure between ATCo and UAS.Recommendations.

We asked the controllers whether they would assign a different priority to unmanned aircraft over manned traffic. Interestingly, they considered UA traffic lower priority than commercial traffic and would treat it as small VFR traffic. This needs to be taken into consideration with assigning routes and sequences to the UA.

From the results of the simulations, the following recommendations are given:

- When operating over satellite, keep the UAS on the party line. The UA pilot and the pilots of other traffic must be able to hear each other and hear the instructions given to each of them.
- Dedicated R/T must be developed or existing R/T must be adapted to inform other pilots of the UA in their vicinity.
- The UA does not require new symbology on the ATCo's display, but the ATCo must be able to see in a glance that the aircraft on his display is unmanned. A simple indication by using a dedicated type of call sign will do.
- The ATCo does not require more information on emergency transponder codes.
- ATCo's need good training of emergency situations.
- Benefit can be taken from the fact that communication with the UA pilot can be established over a high quality land line.

Acknowledgments

Project USICO was co-funded by the European Commission, SINUE and DESIRE funded by the European Space Angency in co-operation with the European Defence Agency.

References

[1] European Civil Unmanned Air Vehicle Roadmap, 25 Nations for an Aerospace Breakthrough, Volume 1 – 3, UAVNet, editor, 2005

[2] Air4All, UAS Insertion into General Air Traffic, Final Study Report, Document No. BAES-AS&FC-BDEV-GEN-RP-005564 Issue 1, June 2008

[3] SINUE, Satellites for the Integration in Non-segregated airspace of UAS in Europe, Final Report, Document No. SINUE_EID_00035_FINAL REPORT, January 2011

[4] [2] Lemmers A, Valens M, Beemster T, Adam V, Keck B, Klostermann E, Evaluation of ATC/ATM integra-tion concepts for civil UAV operations. in: Unmanned Aerial Vehicle Safety Issues for Civil Operations (USICO), Report D4.1, European Project

funded within the GROWTH Aeronautical Part of the 5th Framework Programme of the European Com-mission, Contract G4RD-CT-2002-00635, 2004

[5] EASA, Preliminary Impact Assessment on the Safety of Communications for Unmanned Aircraft Systems, Final Report, volume 1, European Aviation Safety Agency, Research Project EASA.2008/8

[6] Hesselink, H., Schmitt, D.-R., UAS Air Traffic Insertion Starts Now (Real-time simulation of UAS in ATC), Proc. CEAS 2011, The International Conference of the European Aerospace Societies, Venice, 24.- 28. October 2011.

[7] Le Tallec, Claude, Results and Conclusions of the Erea for UAS Study (E4U), Proc. 5th joint workshop on R&D on Unmanned Aerial Systems, Brussels, EDA (editor)

Design of A Small Air Data and MEMS INS/GPS Integrated Navigation System for Wing-in-ground Effect Vehicles

Rongbing Li, Jianye Liu, Yongrong Sun, and Ling Zhang
Navigation Research Center, Nanjing University of Aeronautics and Astronautics, China

Keywords: *wing-in-ground effect, Air data system, MEMS, INS/GPS navigation*

Abstract

Wing-in-ground (WIG) effect vehicles are a kind of crafts that have been designed specifically to utilize the benefits of the ground effect and that fly near to the ground. It is widely believed that the potential exists for the WIG craft to have practical transport applications over water for its more efficiency than the aircrafts and more rapid than ships.

For the greater safety and efficiency of a WIG effect vehicle, it is important to measure the flight air data and to determine navigation parameter that includes air speed, baro-height, attitude, ground velocity and position. All that parameters can be provided by an air data and navigation system which is one of the most important avionics electronic systems.

The motivation of this paper is the design and implementation of a small and low cost air data and MEMS INS/GPS integrated navigation system for a wing-in-ground effect vehicle. The air data and MEMS INS/GPS integrated navigation system provide air data and navigation parameters to the cockpit display with a large LCD screen by which aircrew manage the WIG effect vehicle.

The configuration of the air data and MEMS INS/GPS integrated navigation system includes a pitot probe, two pressure sensors, a small GPS receiver, a MEMS IMU and an embedded air data and navigation processor PCB based on an ARM chip..

A modified Kalman filter is designed to integrated MEMS-INS, GPS and barometer. The objective of the modification of the filter is to deal with GPS delay. A dynamic state recognizer based on the raw output of MEMS IMU was designed and a method that modifies the observation matrix R with an exponential decay role of R was presented to improve robustness in the dynamics of the vehicle.

The prototype of the air data and MEMS INS/GPS integrated navigation system was built. And the demonstration flight test in a WIG vehicle is in progress after the finish of performance test in the laboratory.

1 General Introduction

Wing-in-ground (WIG) effect (or surface effect) vehicles are a kind of crafts that have been designed specifically to utilize the benefits of the ground effect[1,2,3] and that fly near to the ground which may refer to land, water, ice, snow, sand, and so on. Although it has been released almost one century that the ground effect phenomenon which means an increase of the Lift to Drag ratio because the wing compress air against the surface when the wing of a craft flies in close proximity of the ground. The technology of WIG vehicles is not mature enough so that WIG craft can't make big commercial success. However, it is widely believed that the potential exists for the WIG craft to have practical transport applications over water for its more efficiency than the aircrafts and more rapid than ships.

For the greater safety and efficiency of a WIG effect vehicle, it is extremely important to measure the flight air data and to determine navigation parameter that includes air speed, baro-height, attitude, ground velocity and position. All that parameters can be provided by an air data system and the navigation system which is one of the most important avionics electronic systems.

The Navigation Research Center (NRC), Nanjing University of Aeronautics and Astronautics (NUAA), is engaged in the research of navigation technology. Strapdown inertial navigation system, GNSS, inertial integrated navigation theory and application, mini navigation system and air data system for air vehicles are all included.

The motivation of this paper is the design and implementation of a small and low cost air data and MEMS INS/GPS integrated navigation system (abbreviated to ADMIGINS) for a wing-in-ground effect vehicle. The air data and MEMS INS/GPS integrated navigation system provide air data and navigation parameters to the cockpit display with a large LCD screen by which aircrew manage the WIG effect vehicle.

2 The WIG vehicle and Requirement

The WIG vehicle that need equip an ADMIGINS to indicate flight conditions is a seven seat craft named as XZ-1. XZ-1 WIG vehicle is illustrated as Fig.1. The vehicle characteristic of WIG vehicle is shown in Table 1. It can be used in many field such as sightseeing, official business and short distance carriage.

Fig. 1 .XZ-1 WIG vehicle

Table 1 characteristic of WIG vehicle

Vehicle characteristic	Parameter
Length	12m
Wing span	11m
Height	4m
cruising speed	140～160km/h
range	400km
flight altitude	0.5～30m

From the view of the purpose, the air data and MEMS INS/GPS integrated navigation system used in the WIG vehicle should offer the function listed below:

1) Read the output of pressure sensors, calculate air speed and baro-height;
2) Read the output of MEMS inertial sensors and GPS Receiver, calculate attitude, ground velocity, position and acceleration overload based on the integration of MEMS INS and GPS;
3) Package the air data and navigation data and send them to LCD cockpit display.

The ADMIGINS specifications required for the XZ-1 WIG vehicle are listed in Table 2.

Table 2 ADMIGINS specifications

	range	Error limits
Baro-height	-200~+200m	/
Air speed	0~220km/h	±5km/h
Roll	-40°~+40°	±1°
Pitch	-20°~+20°	±1°
Heading	0°~360°	±1°
Ground speed	0~200km/h	±3km/h
Longitude, latitude	/	15m
Acceleration overload	-3~+3g	0.2g

3 System hardware Design and Implementation

The configuration of the air data and MEMS INS/GPS integrated navigation system includes a pitot probe, two Honeywell precision pressure sensors, a small u-Blox GPS receiver, a MEMS IMU and an embedded air data and navigation processor PCB based on an ARM chip. The system hardware architecture is illustrated as Fig 2 and the layout of the sensors and PCB is shown in fig 3.

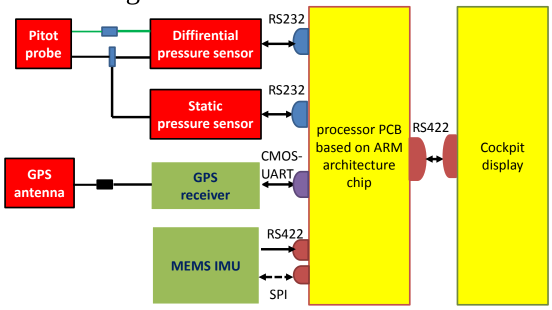

Fig.2 system hardware architecture

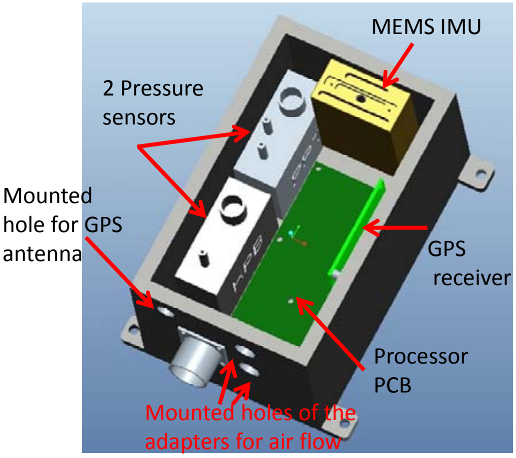

Fig.3 layout of the sensors and PCB

In air data and MEMS INS/GPS integrated navigation system, processor PCB is designed to communicate with the pressure sensor, GPS receiver, MEMS IMU and to collect the sensors data and then to complete the calculations of air data, MEMS-INS and the integration of MEMS INS/GPS. The STM32F4 chip based on ARM architecture has 6 UART interfaces, 2 of them are designed as RS232 to connect with 2 pressure sensors respectively, 1 of them is configured in UART mode and 2 of them are designed to extend with a 422 chip to communicate with the self-designed MEMS-IMU and exchange data with the cockpit display instrument. The SPI interface is also used to suit for some commercial MEMS IMU.

Before the self-designed MEMS IMU is applied, the small MEMS IMU (Fig 4) with volume of about 72 cu cm and with a shape of cuboids, whose height should not be larger than 2.5cm should be designed and integrated.

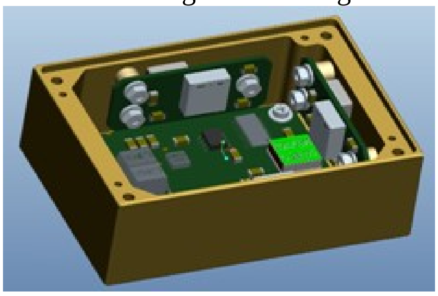

Fig.4 the structure of MEMS-IMU

A single-axis MEMS gyroscope chip and a single-axis MEMS accelerometer chips were integrated into an inertial measurement module by multi-layer PCB process. Three inertial measurement modules is placed and mounted along orthogonally each other in a metal box based on accurate machining. The package of the chips has influence on the PCB design and the volume of the IMU, so the minimum packages of chips were used in our design if the chips are available. The DSP chip with BGA package was placed on the multi-layer PCB. Many decoupling capacitors and resistors with 0402 package were selected and lay out around the ICs. In order to guarantee the quality, an automatic high precision chip mounter was used to place the chips and then finish the chips soldering by reflow soldering process.

In the MEMS IMU, the DSP is the most energy-consuming chip and the DSP and power management IC are the main heat source. The layout of the chips must be optimized in the view of thermal distribution. In the IMU, digital signal condition chips were around the DSP chip and the analog circuit and sensors should be far away the heat source and the optimized layout of the sensors and IC chips is illustrated as fig 5. In fig.5, the dashed lines around accelerometer, DSP and power management IC are used to indicate the chips are on the reverse sides of the PCBs. Another consideration of this design is that the heat chips can conduct the heat to the aluminium box by thermal pads between the chips and the box. The design can reduce the gradient of the temperature field.

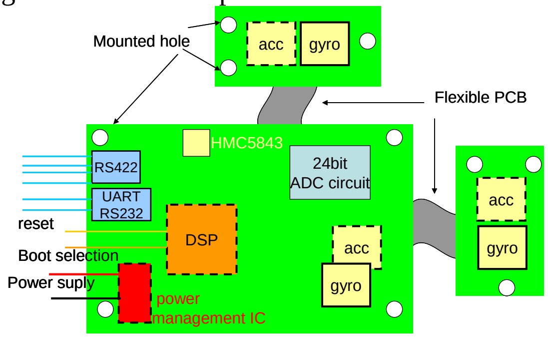

Fig 5. Unfolded layout drawing of the MEMS IMU

4 Design of Air data and MEMS INS/GPS integrated navigation algorithm

4.1 Air data System Configuration and Algorithm

A fully functional air data computer can measure total pressure, static pressure, total temperature, angles of attack (AOA) and slip side (AOSS). The air data that can be calculated by the fully functional air data computer are:

a) Airspeed (indicated, true and Mach number)
b) Altitude and climbing velocity
c) Static Temperature

In some ADC, AOA and AOSS are calculated based on airstream measurements.

According to the characteristic of WIG vehicle and its requirement for air data, the air data system which consists of a pitot-static probe, a total pressure sensor, a static pressure and ADC can measure the essential raw data, complete the air data parameters computations and output the air data by computation based on the raw measurements. The simplified air data system architecture can be illustrated as Fig. 6.

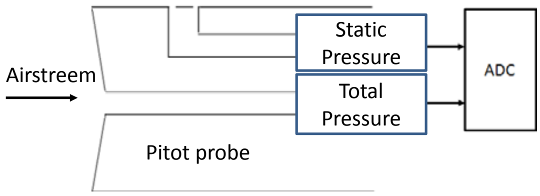

Fig. 6. Schematic diagram of simplified ADS

Altitude is calculated using the static pressure measurement only since external pressure decreases with increasing altitude. The relationship between pressure and altitude is defined by the ICAO standard atmosphere.

This is a fictitious atmosphere defined as follows:

Temperature at sea level: 15 °C（288.15K）

Sea level pressure: 101325 Pa

Under the condition of standard atmosphere，Altitude can be calculated using equation (1).

$$H_p = 44331.5 \times \left[1 - \left(\frac{p_s}{101325} \right)^{0.190263} \right] \qquad (1)$$

H_p is the baro-Altitude in meters and p_s is static pressure in Pascals.

Since the local pressure varies from standard atmosphere, altimeter setting is essential to make a correction to read correctly. Considering that WIG vehicles fly near water surface Most of the time, the altimeter setting for the ADS in this paper can be done by a pilot instructions when the WIG vehicles is very close to the water.

Airspeed the speed of an aircraft relative to the air and can be measured using a pitot tube and a static vent. The pitot tube is a tube that is open at the front end and closed at the rear and facing the on-coming air flow to measure total pressure (also called stagnation/pitot pressure). The pitot tube and the static vent are built into the form of the pitot-static probe.

Airspeed can be classified as indicated airspeed (IAS), calibrated airspeed (CAS), true airspeed (TAS), equivalent airspeed (EAS) and density airspeed. Indicated airspeed (IAS), and true airspeed (TAS) are essential for XZ-1 WIG vehicle.

In compressible subsonic flow, the relationship of the total pressure p_t and the static pressure p_s is

$$p_t = p_s \left[1 + \frac{\gamma - 1}{\gamma} \cdot \frac{\rho V^2}{2 p_s} \right]^{\gamma/\gamma-1} \qquad (2)$$

In equation (2) γ is specific heat ratio of air (= 1.4) ,V is indicated airspeed and ρ is free-stream air density. At low speeds, Equation (3) reduces to:

$$p_t = p_s + \frac{\rho V^2}{2} \tag{3}$$

So the indicated airspeed can be calculated using equation (4).

$$V_{ind} = \sqrt{\frac{2(p_t - p_s)}{\rho}} \tag{4}$$

True airspeed (TAS) is the true measure of aircraft performance in cruise. TAS is usually derived from the Mach number and static air temperature.

Mach number at subsonic speeds can be derived from ratio of the total pressure and static pressure as shown in the equation

$$Ma = \sqrt{5\left[\left(\frac{p_t}{p_s}\right)^{2/7} - 1\right]} \tag{5}$$

In the air data system for XZ-1 WIG vehicle, static air temperature is replaced by the temperature sensed by the temperature sensor integrated in the static pressure sensor. And the true airspeed can be calculated using equation (6).

$$V_t = 38.967\sqrt{T}\,Ma \tag{6}$$

The true airspeed from equation (6) is in knots and temperature is in ° Kelvin.

4.2 MEMS INS/GPS Integration Algorithm

Inertial Navigation System (INS) is a well-known and well-defined technology, having been used in many types of equipment such as ships, submarines, and aircraft. The basic idea of an INS is to track some coordinate system using the gyro stabilized physical or mathematic platform, and to integrate accelerometer signals to determine velocity and position in the desired coordinate system. A strapdown INS works by measuring acceleration and rotation in all three dimensions[4,5]. By knowing its starting position, velocity and attitude, it can determine its present location, velocity and attitude.

Gyros and accelerometers are the only source of measurement information for SINS. Three orthogonal gyroscopes are mounted in a supporting frame to form the Gyroscopes assembly. And three accelerometers are mounted in the direction of the measurement of gyros to form accelerometers assembly. The gyros and accelerometers is the most important conclusive factor to the system performance.

In our navigation system, the strapdown INS mechanization is based on the local level local north coordinates system. The attitude matrix, velocity, position and can be calculated by equation (7), (8) and (9).

$$\dot{C}_n^b = C_n^b \cdot \omega\times \tag{7}$$

$$\begin{bmatrix} \dot{V}_N \\ \dot{V}_E \\ \dot{V}_D \end{bmatrix} = \begin{bmatrix} f_N \\ f_E \\ f_D \end{bmatrix} - [(2\omega_{ie} + \omega_{en})\times] \cdot \begin{bmatrix} V_N \\ V_E \\ V_D \end{bmatrix} + \begin{bmatrix} 0 \\ 0 \\ g \end{bmatrix} \tag{8}$$

$$\begin{bmatrix} \dot{L} \\ \dot{\lambda} \\ \dot{h} \end{bmatrix} = \begin{bmatrix} V_N/(R_m + h) \\ V_E/(R_n + h)\cos L \\ -V_D \end{bmatrix} \tag{9}$$

In equation (9), (10) and (11), C_n^b denotes the strapdown attitude matrix, also called direction cosine matrix, $V, f, \omega, L, \lambda, h$ denote respectively velocity, specific force, angle rate, longitude, latitude and height, R_m, R_n denote the main radius of the curvature of the reference ellipsoid, subscript N, E, D denote North, East and Down. $\omega\times$ is a skew symmetric matrix generated from the vector $\bar{\omega} = [\omega_{ibx}^b, \omega_{iby}^b, \omega_{ibz}^b]$, and it can be written as equation (11)

$$\omega\times = \begin{bmatrix} 0 & -\omega_{nbz}^b & \omega_{nby}^b \\ \omega_{nbz}^b & 0 & -\omega_{nbx}^b \\ -\omega_{nby}^b & \omega_{nbx}^b & 0 \end{bmatrix} \tag{11}$$

$(2\omega_{ie} + \omega_{en})\times$ is skew symmetric matrix generated from the vector of rotation angle rate of the earth and the angle rate of the navigation frame rotating around the ECEF.

Inertial navigation system is a completely self-contained system with a time dependent growth of the navigation errors. The GNSS/SINS integration navigation system makes use of independent sources of information with complementary characteristics from GNSS and SINS. SINS provides navigation data with good short-term accuracy and GNSS provides good long-term and time independent stability. The couple of GPS (GNSS) and SINS is one of the most important modes and is widely used.

A significant large amount of literatures is about the integration of GNSS and SINS[6]. Although different algorithms were applied to GNSS/SINS integrated navigation system, it can be summarized that the GNSS/SINS in literatures can be classified into three categories, loose couple, tight couple and deep couple. Loosely coupled GNSS/SINS systems have been used very widely.

The MEMS INS/GPS integrated navigation system is a loosely coupled GPS/SINS. A classical kalman filter is employed. The kalman filter is implemented in the way of "error state" estimation. This means that the filter estimates the errors in the INS indicated position, velocity, and attitude. The error-state model is a linearized model.

In this paper, 12 states used in the Kalman filter are:

- Error angle vector of INS attitudes (3-states)
- Error vector in INS velocities (3-states)
- Error vector in INS position (3-states)
- Gyroscopes random bias vector (3-states)

The position and level velocity from GPS and vertical velocity calculated by the difference of altitude from ADS are used to compare with that respective parameters from MEMS INS and then to estimate the error in MEMS INS and do the calibration online.

In the software, the Kalman filter is a modified to integrated MEMS-INS, GPS and barometer. The objective of the modification of the filter is to deal with GPS delay. A dynamic state recognizer based on the raw output of MEMS IMU was designed and a method that modifies the observation matrix R with an exponential decay role of R was presented to improve robustness in the dynamics of the vehicle. The adjusting process is illustrated as Fig. 7.

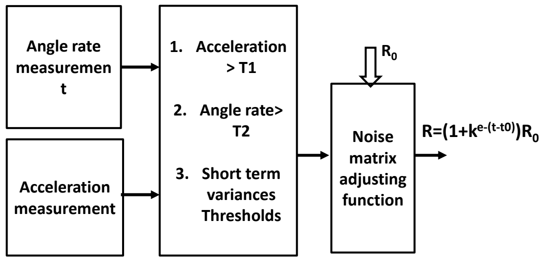

Fig 7. Schematic diagram of adaptive adjusting process of kalman filter

5 Performance test

The prototype of the air data and MEMS INS/GPS integrated navigation system (Fig.8) was built in the beginning of 2013. The prototype consists of a pitot-static probe, a GPS antenna and the collection of the sensors and the processor. The pitot-static probe mounted on the top of vehicle is connected to the pressure sensors by Swagelok tube fittings and the GPS antenna is connected to the GPS receiver by a pair of BNC RF connector assembly.

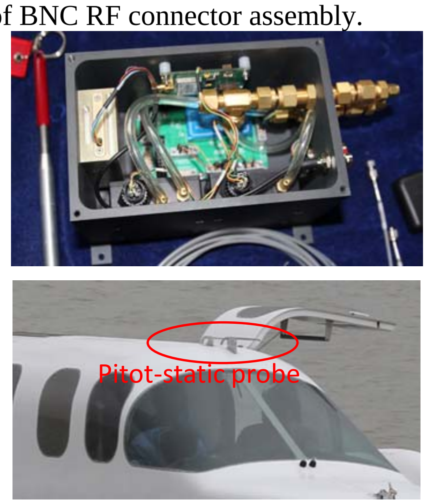

Fig.8 photo of the prototype

The performance test for the prototype was undertaken in NUAA NRC.A commercial FOG SINS/GPS integrated system is used as reference system and the land dynamic performance test was excited by a car.

Figure 9 shows the attitude errors in the car test condition. Based on the experimental data, RMS errors can be calculated and the results is shown in Table 3.

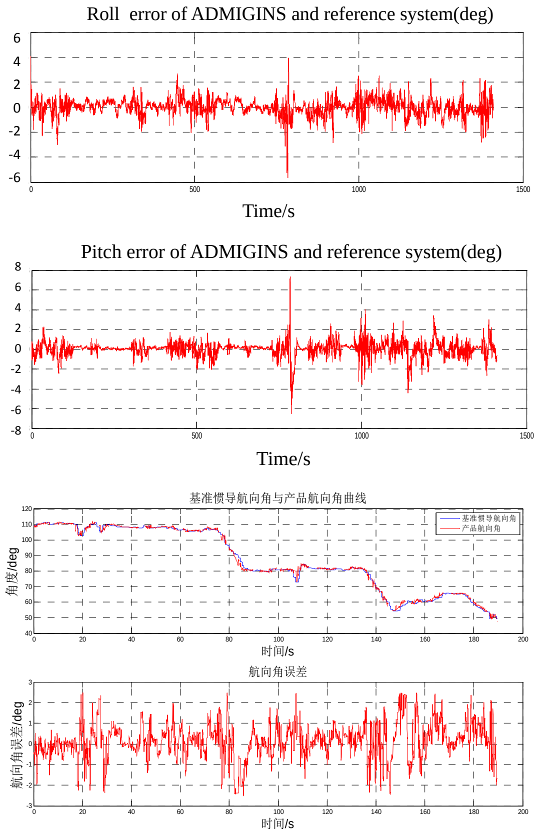

Fig 9. Attitude errors of ADMIGINS

Figure 10 shows the velocity data from GPS receiver and ADMIGINS under static condition. The result can be obtained by statistical computation and has been shown in table 3.

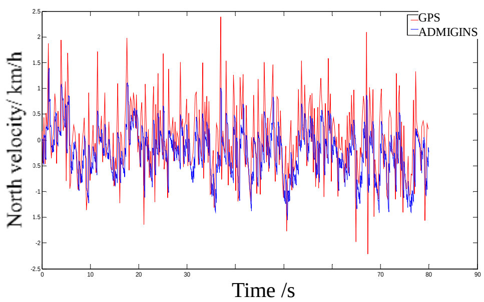

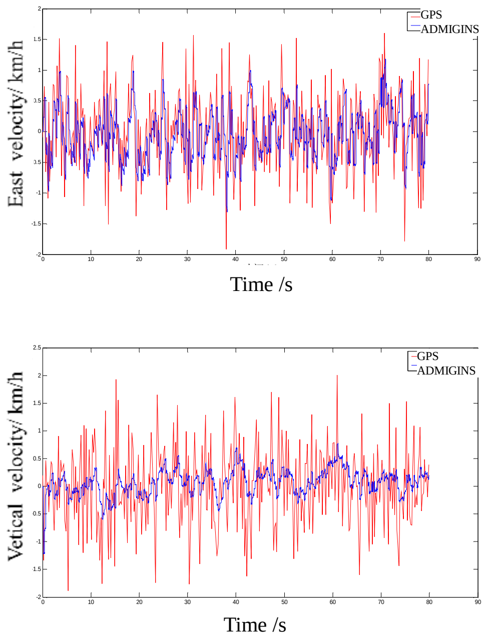

Fig 10. Velocity results of ADMIGINS

Table 3 RMS errors of ADMIGINS

attitude	**error**
Roll	0.8°
Pitch	0.6°
Heading	0.9
East velocity	0.5 km/h
North velocity	0.5 km/h
Vertical velocity	0.3 km/h

The test result in NUAA NRC validate the navigation performance of ADMIGINS. Although the air data system was tested incompletely for the lack of a practicable reference system, the altitude and airspeed outputted by the air data system is stable and sensitively correspond to the atmospheric environment around the air data probe.

Since May of 2013, the air data and MEMS-INS/GPS integrated navigation system has been integrated into the XZ-1 WIG vehicle. Up to the August of 2013, ten flight test was carried out and some system parameters corresponding to the vehicle maneuverability was optimized. The flight tests demonstrated preliminary serviceability.

6 Conclusion

This paper presented the design of a low cost air data and MEMS inertial integrated navigation system and preliminary test result. The further important work test its specifications term by term under flight condition to verify its airworthiness.

References

[1] Halloran M., O'Meara S., "Wing in Ground Effect Craft Review", DSTO Aeronautical and Maritime Research Laboratory, February 1999.

[2] Suh S., Jung K. Chun H., "Numerical And Experimental Studies On Wing In Ground Effect", *International Journal of Ocean System Engineering* Vol. 2, No. 1, 2011, pp. 110-119.

[3] Nebylov A., Daniel D., Sharan S., Nebylov V.,"Flight Automatic Control Systems For THE Wing-In-Ground Effect Craft BUCHON-1", *3rd International Conference Physics AND Control,* Potsdam, GERMANY, September 3-7, 2007.

[4] Neil B., "Inertial Navigation Sensors", Charles Stark Draper Laboratory (P-5286), Cambridge, MA 02139, USA

[5] Hopkins B., Kourepenis A., "Inertial MEMS Systems and Applications", The Charles Stark Draper Laboratory (P-5325),555 Technology Square Cambridge, MA 02139-3563,USA

[6] Schmidt T., Philips T. "INS/GPS Integration Archtechtures", *NATO Report, RTO-EN-SET-116(2011)-06*

4:th CEAS Air & Space Conference
FTF Congress: Flygteknik 2013

CFD sensitivity analysis on bumped airfoil characteristics for inflatable winglet

P. Caso, E. Daniele, P. Della Vecchia and A. De Fenza
University of Naples Federico II, Department of Industrial Engineering
Via Claudio 21, 80125, Naples, Italy

Keywords: CFD, Winglet, Inflatable, Pollution Reduction, Bumped Airfoil

Abstract

The new aerospace technological milestone is aimed to reducing direct operating costs and pollution. In order to obtain pollution reductions via high aerodynamic efficiency, a performance analysis for bumped airfoil based winglet has been proposed. Most conventional aircrafts are equipped with fixed winglets to decrease the induced drag; thus, saving more fuel. New projects point towards advanced smart materials and telescopic wing tip devices to obtain an adaptive morphing shape that gives, through performance improvement, a fuel consumption reduction resulting in less pollutants. The focus of this paper is to evaluate the aerodynamic performance, in terms of lift, drag and moment coefficient for a bumped airfoil in climb/descent flight condition at 5000 meters altitude. The performance analysis has been conducted via a numerical investigation of the effects of bumps number, height and width for inflatable winglet airfoil, a system that would guarantee a more comfortable arrangement of extraction system and just minor surplus of weight compared to classical winglet solutions, with all the subsequent advantages.

1 Introduction

This paper presents a CFD sensitivity analysis on the aerodynamic characteristics of a bumped airfoil at medium Mach number ($M = 0.5$) and high Reynolds number ($Re = 1.37 \times 10^7$). The work aims to continue a previous paper carried out by the AELAB and ADAG research groups of the Department of Industrial Engineering of University of Naples during 2012 [1]. The conceptual design, proposed by Daniele et alii in Ref. [1] involves the design of a telescopic inflatable variable height wing-tip device for long range jet transport aircraft. The span variation is pursued toward a telescopic device moved by an electrical engine. The inflatable system is distributed chord wise and along the base of a tip and it assures the elastic stiffness, while preserving the aerodynamics shape. This conceptual design, with a schematic

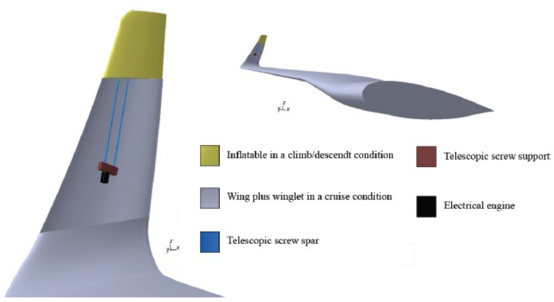

Figure 1: Telescopic device concept

sketch of the main components, is shown in Fig. 1. The main goal of the design proposed in Ref. [1] was to optimize the aircraft aerodynamic efficiency during the whole flight envelope in such a manner to reduce the environmental footprint as well as DOCs without wing span increments (due to the ICAO limitations as shown in Ref. [2][3] and [4]). During the conceptual design, the wingtip device was assumed to be rigid and based on smooth airfoils also in the inflatable zone. Creating an inflatable device, the baseline airfoil for the mobile winglet could not be a smooth airfoil as for the fixed wingtip device; for these reasons, it has been thought to incorporate the bumps on smooth airfoil in order to take into account of all the problems caused by the inflation mode, especially to take into account the aerodynamic losses. In the literature the aerodynamic analysis of the bumped wings regarded originally flight tests on aircraft models with inflatable wings, as shown in Ref. [5]. Subsequently wind tunnel testing and computational fluid dynamics simulations were also used in the prediction of the aerodynamic performance of wings and airfoils as shown in Ref. [6, 7, 8]. Reasor and LeBeau compared two-dimensional CFD simulations of a smooth Eppler 398 wing airfoil with those of an inflatable Eppler 398 wing airfoil. Their results agree with experimental studies which suggest that the bumpy airfoil experiences less flow separation than the smooth airfoil for low Reynolds numbers. They also show that flow is more unsteady over the bumpy airfoil over a range of angles of attack, leading to an increase in drag and a decrease in lift [7]. Le Beau et alii have investigated the effects of a bumpy surface on two different inflatable airfoils. One is based on the Eppler 398 while the other is based on the NACA 4318 airfoil. Two-dimensional CFD simulations have shown that bumpiness has a considerable effect on performance but the effects appear to depend significantly on the baseline airfoil shape [9]. Tao et alii discussed on the stress and on the aerodynamic design of an inflatable wing, highlighting the airfoil performance with and without bumps [10]. Hui and Masatoshi [11] conducted and numerical and experimental investigation on a corrugated airfoil compared to a streamlined airfoil and a flat plate, founding that the corrugated cross section provide sufficient kinetic energy for the boundary layer to overcome adverse pressure gradients, thus discouraging large-scale flow separations and airfoil stall. All the above mentioned research works regard the numerical or experimental aerodynamic analysis in flight regimes of low Reynolds number. The present paper deals with the aerodynamic analysis at high Reynolds number where typical phenomena of low Reynolds (such as bubble formation and separation) are not present.

The principal goal of the aerodynamic sensitivity analysis is to highlight the bump's shape influence on airfoil aerodynamics performance; the sensitivity analysis results could be used, in future works, to help the designer engineer both for structural and aerodynamic design. In this work technological and constructive aspects have not been treated about the bumped airfoil, the materials choosing, the inflation system and all the problems linked to structural aspects. ADAG and AELAB groups are still working to validate and verify the feasibility of this device. In section 2 the approach to parametrization and the computational domain and solver settings are explained. Section 3 summarizes aerodynamic sensitivity analysis results, highlighting the the main effects of the geometrical bumps on the airfoil performance. Finally conclusions are given, looking at future perspectives and developments.

2 Approach

The methodology used to achieve the goals described in the introduction follows these steps:

- geometry parametrization for bumped airfoil;
- CFD Mesh set-up in STARCCM+ solver;
- CFD analysis and relative evaluation about drag, lift, pitching moment coefficients and pressure distribution for each test case;
- results correlation to understand how the aerodynamic parameters change with respect to the bumps characteristics.

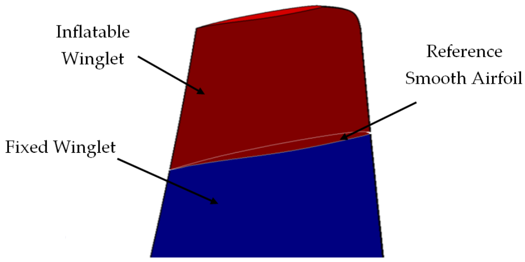

(a) Conceptual design, fixed and inflatable zones [1]

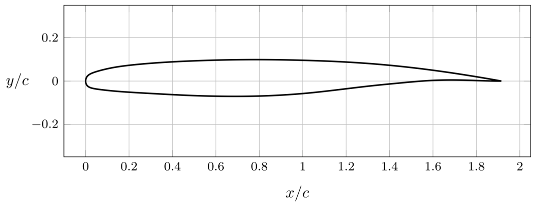

(b) Extracted smooth airfoil

Figure 2: Reference smooth airfoil

2.1 Geometry Parametrization

The first step is characterized by the extraction of baseline smooth airfoil used in the conceptual inflatable winglet design proposed in Ref. [1]. The smooth airfoil has been extracted at the base of the inflatable zone, as it can be seen in Fig. 2. The chord of the smooth airfoil taken is about 1.915 m, which has been normalized to one for the subsequent aerodynamic analysis. The coordinates of the smooth airfoil have been used as reference starting point to create the bumped geometries and compare the aerodynamic results. The main limit in the corrugation process with the incorporation of the bumps is to preserve the geometric airfoil characteristics (camber, maximum thickness and so on). The design process needs to automatically generate multiple corrugated geometry for the aerodynamic analysis. In the literature several method are available to generate bumped airfoils [8], which use circular arc and tangential distribution of the coordinates. In order to match the original airfoil as nearly as possible, a novel geometry parametrization technique has been implemented, based on sinusoidal function. This function uses three bumps characteristics to parametrize an airfoil. Starting from the original smooth airfoil coordinates (x,y), a semi-automated script code gives back a transformed airfoil with corrugated surface defined by a number of bumps N, height H and width W of bumps in unit chord. The output is a corrugated airfoil defined by (xC, yC) coordinates. The method consists into divide the smooth airfoil in N (number of bumps) independent sectors as shown in Fig. 3.

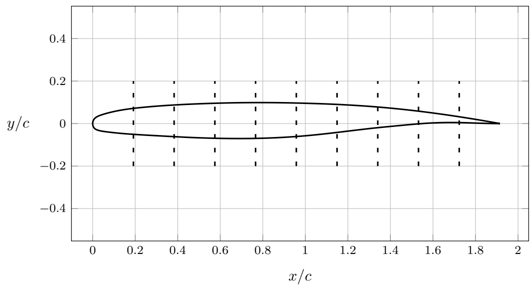

Figure 3: Smooth airfoil : bump's cells separation

This step defines the bump location points as the intersection points between the outlines and separation lines (in dashed line) where the bumping function will be applied, while the formula used in this parametrization shape is

$$b_f = H \left[-1 + sin^2 \left(\frac{S - S_{bf}(i)}{0.2\pi \left(\frac{W}{2} \right)} \right) \right] \quad (1)$$

where the S is curvilinear abscissa, S_{bf} is the bump location, H is bump's height and W is the bump's width. The choice to use sin^2 function, instead of the sin function, is due that the geometry of the bump makes it more realistic, especially in the interconnection region between adjacent bumps. A detail of the bump's height and width is shown in Fig. 5. As it can be seen corrugated airfoil is divided into independent cells, similar to shell structure. Each cell is bounded by one bumped edge on both the upper and lower surface. The edge cell has a particular shape in order to preserve the smooth airfoil edges, especially leading and trailing edges.

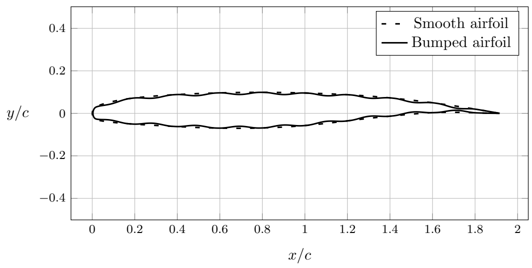

Figure 4: Smooth and bumped airfoils comparison

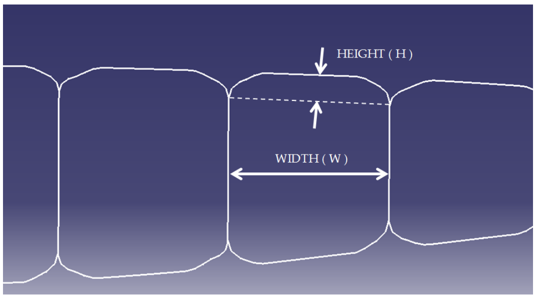

Figure 5: Detail of bum's height and width

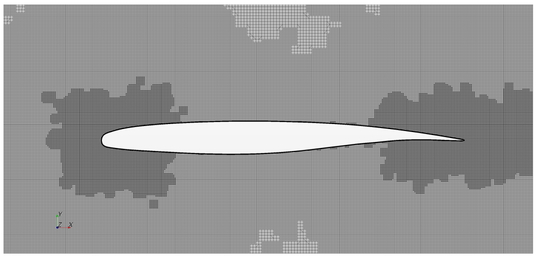

Figure 6: Smooth airfoil mesh grid: volumetric control detail

Table 1: Physics data for the simulation.

Parameter	Value
p (hPa)	540.48
T (K)	291
ν $(Pa * s)$	1.63E-5
M (-)	0.5
Re (-)	1.37×10^7
h (m)	5000
ρ (kg/m^3)	0.7364
a (m/s)	320.5
α (deg)	0.0

2.2 Mesh Set-up

A two-dimensional, viscous, compressible, finite volume method CFD model by using STAR-CCM+ software has been built in order to solve the flow field around the smooth and bumped airfoil via Reynolds Averaged Navier-Stokes equations (RANS) with Spalart-Allmaras turbulence model[12, 13]. The computational domain is a rectangular geometry of 50 × 40 airfoil chord dimensions. A trimmer, prism layer, surface remesher meshing model with volume refinements has been chosen as discretization scheme. Fifty near walls layers have been imposed in the boundary layer with a thickness of near wall cells of 3.9×10^{-6} in order to have a $y^+ \approx 1$. A detail of the airfoil zone mesh, volumetric control is shown in Fig. 6. All the test case analysis has been performed imposing the needed fluid dynamic properties summarized in Table 1 In order to obtain a reliable CFD model, a sensitivity analysis on mesh grid has been performed. Computational domain cells have been globally increased through the base size parameters. Results are summarized in Table. 2. As it can be seen the aerodynamic coefficients change with the mesh base size; as it is expected the more sensible coefficient is the drag coefficient, while lift and pitching moment coefficient have negligible differences (lower than 5%). However a mesh refinement allows to better describe the continuous airfoil geometry and minimizing the variation of the coefficients. In this work the lower base size value of 0.5 has been chosen in order to also have reliable simulations on the drag coefficient. During the grid sensitivity analysis other very important futures have been monitored, which are the equations residuals and wall y^+. Residuals have been all lower than 10^{-6} and $y^+ < 1.0$ along the entire airfoil. In the following aerodynamic analysis, the same mesh setup parameters have been adopted for all the bumped airfoils. A detail of the boundary layer mesh on a bumped geometry is shown in Fig. 7.

Table 2: Mesh sensitivity on smooth airfoil

b. s. (m)	C_d	C_l	C_m	Cells
0.5	0.0072	0.2663	-0.0737	371403
1.0	0.0074	0.2720	-0.0750	142775
2.0	0.0103	0.2790	-0.0759	61648

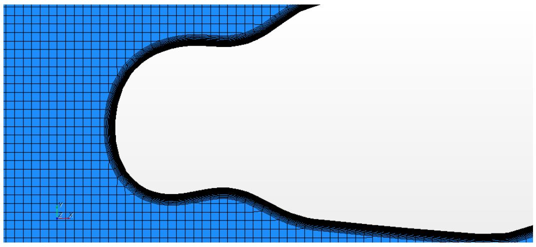

Figure 7: Prism layer detail for bumped airfoil

2.3 CFD analyzed bumped geometry

Twenty-seven test case analysis on bumped airfoils have been executed in parallel mode on SCoPE grid infrastructure of the University of Naples Federico II [14]. As described in Section 2.1, parameters involved in the bumped airfoil design are numbers of bump (N), bump's width (W) and bump's height (H). By combining these parameters in Eq. 1, it is possible to formulate infinite solutions; however in the practice there are several limits: the bump's height and the number of bumps acted together in a way that introduced limits on the range of geometries that could be created. If there are too many bumps and the bump height is too high near the leading and trailing edges of the airfoil, the radius of the bumps could be smaller than the bump height; this causes the bumps to invert and create cavities and on the surface of the airfoil instead of bumps protruding from it. To prevent them, some limits have been imposed on the number of bumps and on the bump height. Three different number of bumps (10, 13, 16) have been combined with three bump's height and width as shown in Table 3. Finally the total of 27 analyzed geometry have been then obtained by combining the three parameters (see Table 3). In Section 3 the aerodynamic results on these bumped airfoils are described, compared to the smooth reference airfoil solution.

Table 3: Parameter's values.

Parameter	Value		
	N10	N13	N16
Number	10	13	16
	W1	W2	W3
Width	$\frac{c}{5N}$	$\frac{c}{2N}$	$\frac{c}{N}$
	H1	H2	H3
Height	$0.001c$	$0.0025c$	$0.0050c$

3 Results

This section summarizes all the results of the bumped airfoil analysis. All the simulations have been performed at flow field conditions of Table 1. In Table 4 the results of the simulations in terms of lift coefficient, drag coefficient, pitching moment coefficient (with the axis of rotation located at 25% of the chord of the airfoil) and relative aerodynamic efficiency (E) computed at zero angle of attack, according to the parameters combination shown in Table 3, are shown. The zero angle of attack has been considered in order to check the CFD capability to appreciate the differences between smooth and bumped airfoil especially on the drag coefficient. Of course the winglet airfoils works at an angle of attack range which only includes the zero angle of attack and further analysis are still in progress to evaluate the bumps' effect at operating angles of attack. All the analysis performed have shown a good convergence characteristics. Results summarized in Table 4 globally show a worsening of the aerodynamic performance of bumped airfoils respect to the smooth airfoil. As it can be seen in the Table 4, the configuration closer to the smooth airfoil in terms of aerodynamic coefficients is the N10W3H1. This geometry has a number of bumps equal to $N = 10$ (which is the lower ones), a bump's width of $\frac{c}{N}$ (which is the higher ones) and the lower bump's height equal to $0.001c$. This result could be expected, because it means that the bumped airfoil closer to the smooth one has a limited number

Table 4: Smooth and Bumped airfoil: results

Name	C_d	C_l	C_m	$E = \frac{C_l}{C_d}$
$SMOOTH$	0.0072	0.2663	-0.0737	36.98
N10W1H1	0.0080	0.2525	-0.0718	31.66
N10W1H2	0.0121	0.1993	-0.0635	16.50
N10W1H3	0.0220	0.1201	-0.0470	5.45
N10W2H1	0.0083	0.2338	-0.0723	28.23
N10W2H2	0.0100	0.2273	-0.0682	22.67
N10W2H3	0.0161	0.1708	-0.0566	10.61
N10W3H1	0.0076	0.2541	-0.0733	33.45
N10W3H2	0.0087	0.2410	-0.0706	27.83
N10W3H3	0.0102	0.2167	-0.0619	21.29
N13W1H1	0.0088	0.2167	-0.0726	24.59
N13W1H2	0.0118	0.1962	-0.0638	16.66
N13W1H3	0.0226	0.0703	-0.0390	3.12
N13W2H1	0.0086	0.2302	-0.0713	26.82
N13W2H2	0.0109	0.2242	-0.0661	20.64
N13W2H3	0.0187	0.1295	-0.0477	6.93
N13W3H1	0.0081	0.2494	-0.0731	30.97
N13W3H2	0.0106	0.2283	-0.0690	21.47
N13W3H3	0.0157	0.1754	-0.0546	11.15
N16W1H1	0.0089	0.2131	-0.0715	23.97
N16W1H2	0.0143	0.1837	-0.0589	12.86
N16W1H3	0.0226	0.1207	-0.0417	5.35
N16W2H1	0.0088	0.2392	-0.0712	27.15
N16W2H2	0.0131	0.1980	-0.0611	15.06
N16W2H3	0.0180	0.1412	-0.0479	7.84
N16W3H1	0.0086	0.2466	-0.0721	28.72
N16W3H2	0.0115	0.2218	-0.0657	19.33
N16W3H3	0.0179	0.1754	-0.0502	9.78

of bumps which reduces the geometry discontinuities, avoiding multiple compressions and expansions on the surface (see also Figure 8). Accordingly, a higher bump's width and lower height are desirable which imply a minor penalty in terms of drag coefficient. Pressure coefficient distribution between smooth and best bumped airfoil is shown in Figure 8. The bumps' effect is clearly visible as a sequence of expansions and compressions (blue) around the smooth points (red ones). Globally the best bumped configuration leads to an airfoil efficiency drop of about 10%, equally distributed between drag coefficient increment (about 4 drag counts) and lift coefficient reduction (about 5%), while the pitching moment coefficient is almost the same, which is an indication of a well described airfoil camber. In order to give a more comprehensive description of the obtained results, in the following Section 3.1 results of Table 4 are reported in several graphs, very useful also in a design phase.

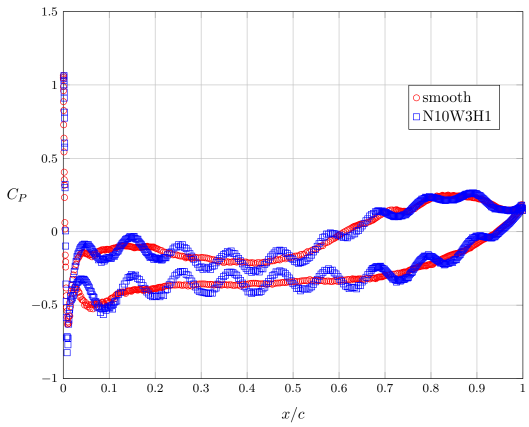

Figure 8: C_P comparison: smooth and bumped airfoil

3.1 Sensitivity analysis on bumped airfoils

Typical design methodologies are related to the definition of dimensionless parameters that allow to separate the dependency from geometry dimension and to use the results in general manner. Two dimensionless parameters have been defined to completely describe the bumps effects on the airfoil performance. These parameters are $R_W = \frac{W}{H}$ which is the ratio between the bump's width and bump's height and $R_C = \frac{W}{c}$ which represents the ratio between the bump's width and chord length. The R_H parameter directly correlates the two main parameters of the bumped airfoil (width and height) highlighting the effect of the ratio between them. The R_C parameter gives the effect of bump's width and, in a such manner, the effect of the number of bumps on the airfoil. From Figure 9 to Figure 16, results

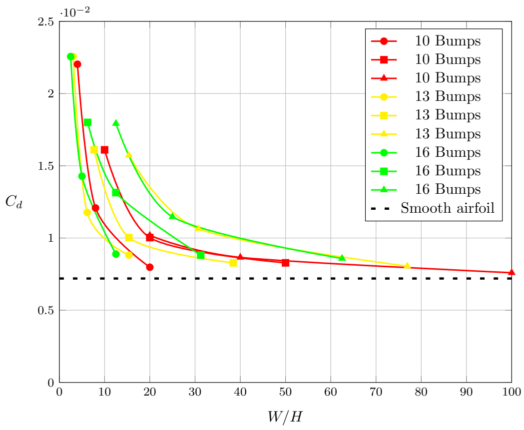

Figure 9: Sensitivity analysis : C_d versus R_H

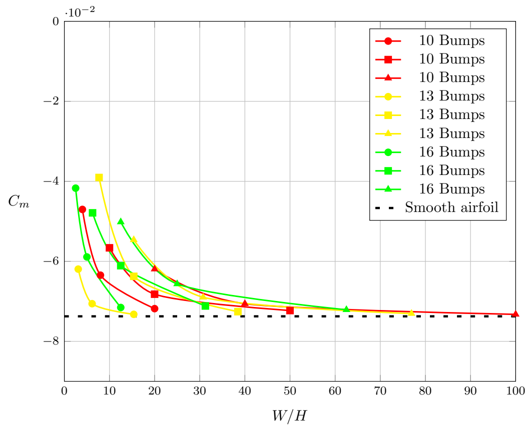

Figure 11: Sensitivity analysis : C_m versus R_H

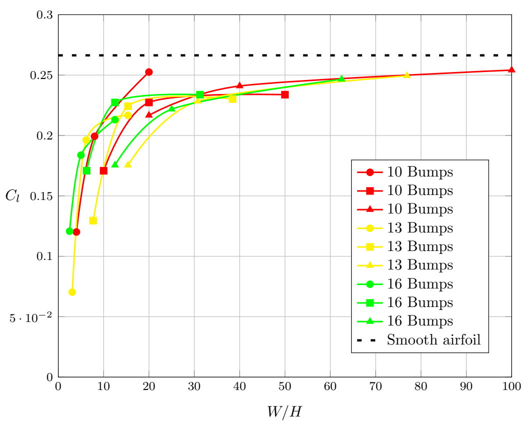

Figure 10: Sensitivity analysis : C_l versus R_H

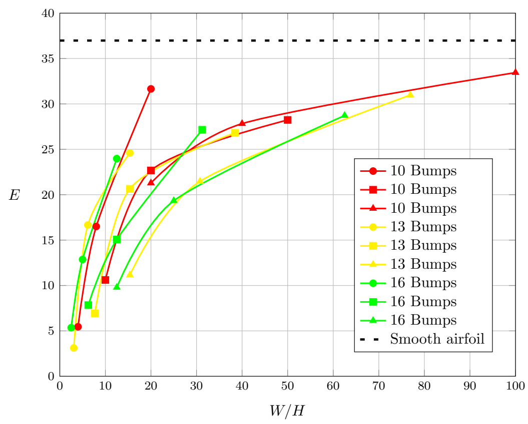

Figure 12: Sensitivity analysis : E versus R_H

of sensitivity analysis are summarized as function of the two dimensionless parameters. Results are divided in terms of number of bumps (red curves=10 bumps, yellow curves=13 bumps and green curves=16 bumps). As it can be seen in the figures, three curve groups can be identified, defined with the same markers. For example, considering the circle marker curves (equivalently the square or triangle marker curves), when the $\frac{W}{H}$ or $\frac{W}{c}$ increases the aerodynamic coefficients have almost the same magnitude independently from the number of bumps. This effect is mainly due to the bump's height: as a matter of fact the bumped airfoils with almost the same aerodynamic coefficients have an equal values of the bump's height while the number of bumps vary from 10 to 16. Looking to the R_H effect, in Figure 9 to Figure 12 is clearly visible a trend of the aerodynamic coefficients with this parameter. When R_H increases, the aerodynamic coefficients tend asymptotically to the smooth airfoil value. As it is expected, the drag coefficients is always higher than the smooth one, due to the perturbations introduced by the bumps, while the lift coefficient is lower than that of the smooth airfoil. Pitching moment coefficient (see Figure 11) clearly shows the difficulty to well

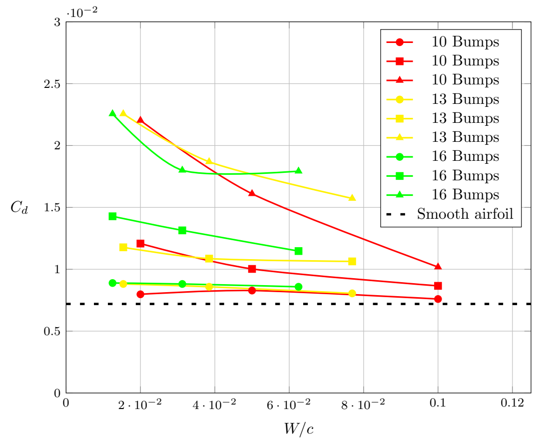

Figure 13: Sensitivity analysis : C_d versus R_C

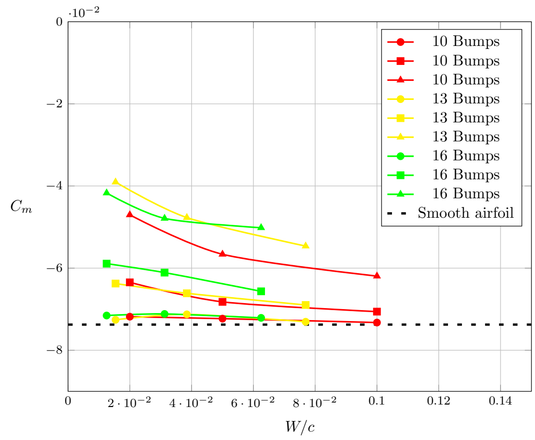

Figure 15: Sensitivity analysis : C_m versus R_C

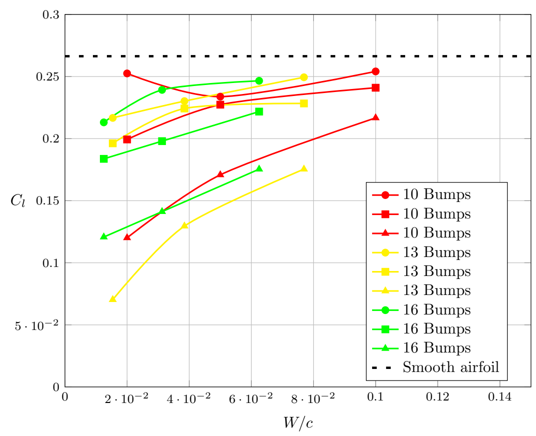

Figure 14: Sensitivity analysis : C_l versus R_C

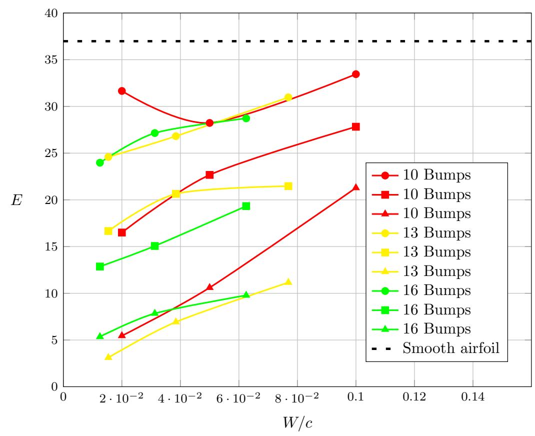

Figure 16: Sensitivity analysis : E versus R_C

reproduce the airfoil curvature of the smooth one with bumps.

The effect of the R_C dimensionless parameter is shown from Figure 13 to Figure 16. As it has been said before, the above mentioned three zones are clearly visible in these figures too. In particular, the curves with the same markers (which are the same height values) unambiguously highlight the bump's height effect: by reducing this value, the aerodynamic coefficients tend to the smooth airfoil values. Moreover Figure 13 to Figure 16 indicate that by increasing the bump's width the corrugated airfoils aerodynamic coefficients tend to those of the smooth airfoil. Main results can be summarized in the following sentences:

- increase W_H : all the aerodynamic performance tend to the smooth airfoil behavior.
- fixed W_C : the best performance are reached for airfoils with ten bumps.
- fixed N, increase W : all the aerodynamic performance tend to the smooth airfoil behavior.
- fixed N and W, increase H : there is a worsening of all the aerodynamic performance.

- fixed H and W, increase N : there is a worsening of all the aerodynamic performance.
- increase W_C : all the aerodynamic performance tend to the smooth airfoil behavior.

4 Conclusion

Bumped airfoils aerodynamic analysis have been performed comparing results with smooth airfoil analysis at medium Mach number and high Reynolds number value. A sinusoidal function based parametrization has been used to well reproduce a supercritical airfoil. Results have been proposed in order to give a more comprehensive and organized representation of the bumps' effect on the airfoil aerodynamic performance. In particular two dimensionless parameters (R_H and R_C) have been defined, also useful in a design process. The analysis have highlighted that a bumped airfoil introduces a global worsening of the all aerodynamic coefficients. The main effect is due to the bump's height which is responsible of the airfoil performance degradations: when this height increases the aerodynamic coefficients worsen. A second effect is due to the bump's width: by increasing the width airfoil aerodynamic performance improve. Final there is the number of bumps effect: the increment of this number gives a performance deterioration, due to the increase of the expansion-compression sequence.

Future analysis will be performed to verify the bumped airfoil performance at several attitude angles, especially those where a winglet works. Others structural and aerodynamic analysis are in progress to demonstrate the feasibility and to well predict loads and aerodynamic performance of inflatable wing-tip device.

References

[1] Daniele E., Della Vecchia P. and De Fenza A., *"Conceptual adaptive wing-tip design for pollution reductions"*, Journal of Intelligent Material System and Structures, 2012, pp. 1197-1212.

[2] Ruijgrok G.J.J. and Van Paassen D.M., *"Elements of Aircraft Pollution"*, Delft: Delft University Press, 2005.

[3] Volders M. and Slingerland R., *"Environmental Harm Minimization during cruise-flight for long-range Preliminary Aircraft Design"*, AIAA Paper 2003-6803.

[4] Dalhuijsen J.L. and Slingerland R., *"Preliminary Wing Optimization for every large Transport Aircraft"*, AIAA Paper 2004-0699.

[5] Brown G., Haggard R. and Norton B., *"Inflatable structures for deployable wings"*, AIAA Paper A01-29254.

[6] LeBeau R.P., Reasor D.A. and Jacob J.D., *"Numerical Investigation of the Effects of Bumps on Inflatable Wing Profiles"*, 18th AIAA CFD Conference, Miami, FL, 2007, pp. 1-8.

[7] Reasor D. A. and LeBeau R. P. *"Numerical Study of Bumpy Airfoil Flow Control for Low Reynolds Numbers"*, 37th AIAA Fluid Dynamics Conference, June 25-28 2007, Miami, FL

[8] Johansen T. A. *"Optimization of a low Reynold's number 2-D inflatable airfoil section"*, A thesis submitted in partial fulllment of the requirements for the degree of master of science in Mechanical Engineering, Utah State University, Logan, 2011

[9] LeBeau R. P., Gilliam, T. D. Schloemer A., Reasor D. A. Hauser, T., and Johansen T. A., *"Numerical comparison of flow over bumpy inflatable airfoils"*, In 47th AIAA Aerospace Science Meeting and Exhibit, Orlando, FL, AIAA 2009-1478.

[10] Jun-Tao Z., Zhong-xi H., Zheng G., Li-li C. *"Analysis and Flight Test for Small Inflatable Wing Design"*, World Academy of Science, Engineering and Technology, Vol. 69, 2012.

[11] Hui H. and Masatoshi T. *"Bioinspired Corrugated Airfoil at Low Reynolds Numbers"*,

Journal of Aircraft, Vol. 45, No. 6, November-December 2008.

[12] Spalart P. R. and Allmaras S. R., *" A One-Equation Turbulence Model for Aerodynamic Flows, "*, Recherche Aerospatiale, pp. 5-21, 1994.

[13] Anderson Jr D.J., *"Fundamentals of Aerodynamics"*, 3^{rd} ed., McGraw-Hill Higher Education (New York), 1991, Chaps. 1, 2,15.

[14] Merola L., *"The SCoPE project"*,University of Naples Federico II (2006).

A Case Study in Aeronautical Engineering Education

Adson Agrico de Paula
Department of Mechanical Engineering, Polytechnic School , University of São Paulo , 05508-900 São Paulo, Brazil
Email: aapaula@usp.br

Keywords: *education; pedagogical methodology; aeronautical engineering; aerodynamics; aircraft design.*

Abstract

The great interest of students in aeronautics gives singular characteristics on teaching-learning process that involves this subject. The pedagogical creation is well-suited for this environment. This work presents and analyses the pedagogical implementation of case study in the aerodynamic design course of mechanical engineering from University of São Paulo. A case study was structured in order to develop all concepts of aerodynamics and aerodynamic design as well as the practical issues that involve the aeronautical engineering environment. It was carried out a case study for aerodynamic design development of the aircrafts Douglas DC-9 and Boeing 737 embryonic mark of commercial aviation. The case study involved students in the real design environment. The discussions concerned historical facts, aerodynamic concepts, requirements, design philosophy and technology development. All of them enriched the educational environment and contributed definitely to education in aeronautical engineering.

1 Introduction

The great interest of engineering students in aeronautics, particularly in aerodynamics, gives singular characteristics on teaching-learning process that involves this subject (figure 1). Understand how flying machines fly is an initial motivation for engineering students. The childhood desire can be a potential to learn on present. In the sense, the engineering professor must know this potential and makes it in learning tool. Teaching of aerodynamics is a great pedagogical opportunity to awaken the reminiscent knowledge that is on natural curiosity of people.

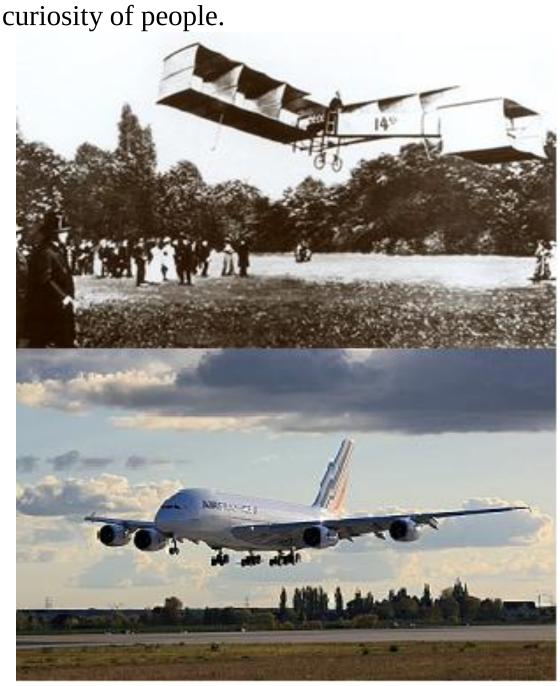

Fig 1. More than a century of interesting in aeronautical since 14-bis until Airbus A380

In aeronautics, the professor must stimulate the curiosity and pleasure in discovering “the secrets of flight”. This is the main pedagogical strategy for education on aerodynamics and aeronautics. Example of this approach can be seen in many aeronautical and mechanical engineering schools where professors motivate students in activities that develop curiosity and creativity such as airplane building competition and tests of experimental aircrafts in wind tunnel and flight. Additionally, these practices give strong aeronautical culture for school.

The mechanical engineering of polytechnic school at University of São Paulo has four lectures related to aeronautical engineering. The aeronautical lectures are composed by Aeronautical Structures Introduction (PME2554), Aerodynamics (PME2557), Computational Fluid Dynamic (PME2556) and Elements of Aircraft and Flight Dynamic (PME2553). These aeronautical lectures were implemented on this mechanical engineering school in order to establish culture in aeronautics, and build a prepared critical mass to give support for challenges of the national aeronautic engineering.

In this context of pedagogical innovation and aeronautical culture, the lecture Elements of Aircraft and Flight Dynamic focus its content in order to offer for student familiarization and understanding with fundamental aerodynamic concepts such as boundary layer, shock wave, lift and drag as well as essential aspects involved in aerodynamic design. These aspects are related to high and low speed issues. Additionally, a multidisciplinary approach conducted during each single class gives a realistic view about all design details that concerns about aeronautical industry environment.

In order to improve the teaching-learning process of the lecture Elements of Aircraft and Flight Dynamic, a case study, as pedagogical innovation, was introduced in 2011. This article discusses about the experience on a case study as learning tool on aeronautical education.

2 Case study on engineering education

Case studies have been increasingly used as learning tool in different knowledge areas such as medicine, nursing, business and engineering. Scholars in these areas recognize that it is not enough to teach generic principles in most cases disconnect among them. In addition, teach about some professional practices, on job, do not give students enough knowledge on balance between theory and practice that they need on their professional life to deal with problems. Besides, the traditional education does not allow students to get in touch with wide range of work situations.

When the case studies have success, they bring a problem from the real life into the classroom to be discussed by students and educators. The academic background will be used to give support to solve the real problem stressing parts and the whole problem. Aspects of real problem can be faced by students, differently from traditional classes, bringing into the classroom a practical thinking that deal suitably with the balance between theory and practice exploring a realistic scenario that might be found by them.

The engineering schools need to prepare future engineers with strong academic background in science to solve complex problems. However, this education is not enough, since wide engineering problem scenario requires not only strong academic background but also understanding and attitude to deal with different engineering situations.

So, engineering case study is appropriated to support academic education on different engineering situations. In this sense, Anwar & Ford [1] define engineering case study as an account of an engineering activity, event, or problem containing some of the background and complexities usually encountered by an engineer. They also say that engineering case presents a scenario that practicing engineers are likely to encounter in the workplaces.

Engineering case study can introduce engineering students in a real design situation in order to practice conceptions, learned previously, as well as propose appropriate solutions for design exerting their own critical analysis. The educator can potentiate, during the practice of case study, development of certain skills in the future engineers such as interdisciplinary view, capability to relate theory and practice and work in group.

In order to show how case study can contribute on aeronautical education, follow the main goals of case study on teaching-learning process indicated by [1, 2]. In addition, they are related to applications for aeronautical engineering environment:

- *Involve in real or simulated situation in your profession area identifying and recognizing problems to figure out solutions*. The aeronautical engineering has many particular characteristics. Involving students in this environment, they might realise typical problems and possible solutions. For instance, how to deal with unexpected wind tunnel results on design schedule.

- *Make diagnostic analyzes for situation considering the variables involved exercising and making judgments.* Simulate the aeronautical environment is important to learn how to consider direct (aerodynamics) and indirect (weight, loads, structural) variables to make decisions.

- *Understanding and recognizing assumptions and inferences, as opposed to concrete facts.* The aerodynamic theory in class gives freedom to design airfoils and wings. On the other hand, the concrete facts have restrictions from multidisciplinary areas. Other example comes from wind tunnel data. Sometimes similarity assumption from wind tunnel data to flight is not true in the real world.

- *Find out necessary information, understanding and interpreting data, to solve problem-situation.* In order to solve a design problem, it is important to investigate aerodynamic data combining with performance and flight mechanics results.

- *Thinking analytically and critically.* Mathematical models used in the aeronautical industry to simulate the aircraft give support to develop analytical thinking. Thus, from many possibilities in the simulation models come up critical analysis. An example from this learning is the development of fly-by-wire laws

- *Apply information at real situation relating theory and practice.* Understanding aerodynamic concepts such as boundary layer, Reynolds number, stall behaviors, shock wave, tip vortices and their relationship with aerodynamic design and aircraft performance.

- *Be able to work in group including discussion between colleagues to solve problems. Understanding and assessing interpersonal relationships, communicating ideas and opinions, making and defending decisions.* It is important to understand an aerodynamic group of design and its structure. Engineers must be clear in technical ideas, and have good interpersonal relationship.

- *Development skills to analyze problems and propose solution and prepare to deal with real and complex situations in non-threatening environment (class room).* Simulate problems during the design development, such as change of take-off requirement during development, it is important to improve proactivity and creativity.

3 A case study in aeronautical engineering education

Case studies can be applied at room class in different ways. The pedagogical approach will depend on many factors such as matter, student knowledge, data and time available.

Motivated by lecture Elements of Aircraft and Flight Dynamic be related to design and the great learning possibilities of case study, it was introduced a case study of aerodynamic design for two of the most classics aircraft in the world, Douglas DC-9 and Boeing 737. The case study was planned in order to exercise concepts of aerodynamic and aerodynamic design as well as practical issues involved on aeronautical engineering environment. The discussions for case study are based on scientific articles: aerodynamic design philosophy of the Boeing 737 [3] and Aerodynamic Design Features of the Douglas DC-9 [4]. The case study activities were developed in the end of course. After learning the most course content, the engineering students had basic information to analyze and apply studied theory on case study. This approach is referenced by [2] as a pedagogical possibility on case study. In the following items, it will be discussed the case study structure.

3.1 Motivation and scenario for case study

The reason to choose as case study the aerodynamics design development of Douglas DC-9 and Boeing 737 is due to both aircrafts be embryonic mark of commercial aviation and compete in the aeronautical market based on similar engineering requirements with different philosophies (figure 2). In the sense, the case study of the Douglas DC-9 and Boeing 737 conducts engineering students to experiment discussions about issues related to historical facts, aerodynamics concepts, requirements, design philosophy, technologic and development. This real situation of aerodynamic design enriches the educational environment and contributes for graduation of professional in aeronautical engineering.

3.2 Educational goals

The educational goals in this case study in aeronautical engineering focus on discussions of following main issues of aerodynamic design:

- Requirements and their importance on design
- Design philosophy and airplane configuration choice
- Multidisciplinary view on design

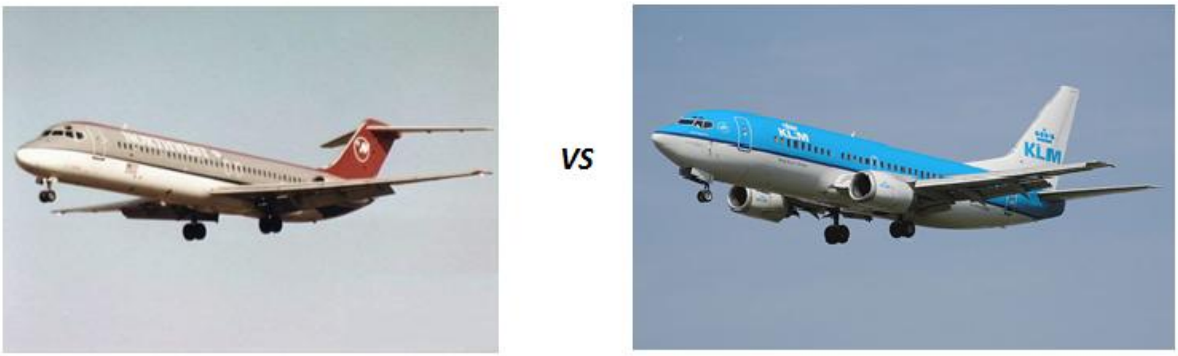

Fig 2. Case study proposed for engineering students. Different design philosophies for Douglas DC-9 and Boeing 737.

3.3 Discussion Groups

The class room was arranged in order to take place discussions to give students autonomy having opportunity to research, work in groups and propose design solutions. The students were divided into two groups of five members. Each group debated as design group about aerodynamic design development of Douglas DC-9 or Boeing 737.

The groups were organized as a typical aerodynamic team in aeronautical industry. There was a team leader, choose by group, two aerodynamicists, and one flight mechanics and one performance member to establish goals of requirements.

Before starting the discussions, the students read the specific article for each group and took notes of the main characteristics of each design. In Addition, flight mechanics and performance members research about theory and requirements in their respectively areas.

After previous preparatory work in advance of discussion in later class, the students performed the case study. Each group took discussions concerning about educational goals indicated by professor and mentioned, in this article, previously. During these discussions a student of each group took notes of main points. After this active, the professor questioned each group about perceptions of the main points on design development analyzed.

Next step it was a “cross-dynamic”, each team leader went to other group. Then each group established discussions about comparisons between Douglas DC-9 and Boeing 737 design with external team leader.

Finally, as last active in class, the professor pointed out most relevant aspects during discusses about aerodynamic development of both aircrafts such as design philosophy and problems during development. Moreover, the educator stimulated engineering students for last discussions and questions. After all, students wrote down a review about the aerodynamic design development of the aircrafts DC-9 and B737, and handed in it as assessment. The figure 3 shows the case study structure.

4 Case study results

In the first moment, the engineering students were apprehensive with the proposal to study the aerodynamics design of the Douglas DC-9 and Boeing 737, since they did not know the practical of aeronautical design. However, the professor establishes a dialogue about the details of the pedagogical task. Besides, the educator explained that the necessary content in aerodynamics to perform the case study had been learned during the lectures. The gains that would be reached with the task were posted by professor giving motivation for group. After all, the groups conducted discussions, in a confident and autonomous way, to good results. In the following items will be described results from engineering case study.

4.1 Preparatory work

It could be realised that students prepared themselves, previously, studying the referenced articles about aerodynamic design of the Douglas DC-9 and Boeing 737. In Addition, members of performance and flight mechanics researched about theirs respectively requirements. Printed documents, notes and discussions in class evidenced the whole preparatory work.

4.2 Group-Dynamic

The students, in an uninhibited way, kept discussing about design issues making remarks related to education goals in according to individual technical area (aerodynamic, performance or flight mechanics), characteristics and perceptions. Besides, they practiced the proactivity, individual respect and work in group. It was possible to realise the following main results from discussions:

Fig 3. **Structure of case study applied for aeronautical engineering education**

Requirements and their importance on design

The preparatory work and discussions on group gave students support to understand that design requirements are well-defined, and determine aerodynamic characteristics that aerodynamicists need to achieve. It was clear to them that requirements of Boeing 737 established an airplane to operate from short runways and over relatively short distances. The group compared requirements from Boeing 707, 727 and 737 helped by performance member. They realised that commercial aviation started with design requirements that involve flights for long range at great Mach number. However, the Boeing 737 represented a new step on commercial aviation, ie, short range and less Mach number. Some Geometric differences among Boeing 707, 727 and 737 show students the importance of requirements on design. The Boeing 737 was designed with a wing less swept and thicker aerodynamic profile. Thus, this design had focus on low speed requirement. The students understood that the Boeing 737 needed high maximum lift to short take-off and landing-filed-length requirements. Because this, besides wing less swept and thicker profile, the entire wing leading incorporates slats and Krugger flaps, whereas the trailing edge has large triple-slotted flaps with extensive Fowler-type motion out to 74% span.

The discussions about Douglas DC-9 show requirements to satisfy short range and runway. The students realised that aerodynamicists optimized the wing design for the lowest operating cost for a given cruise speed, payload-range ability, and field-length requirement. Related to historical and technological issues, it was debated that DC-9 derived from DC-8 but with regional requirements justifying geometric difference. After comparing both aircrafts, the group made a parallel in terms of focus on design. While cruise condition was important for DC-8, second-segment climb on take-off was critical for DC-9.

Design philosophy and airplane configuration choice

Some examples of Boeing 737 development gave students opportunity to understand that when it is established a final airplane configuration, some inherent engineering problems will take place, and aerodynamicists need to solve. The nacelle configuration under-wing on 737 can be a potential problem in high speed. When the nacelles are tucked in closely under the wing can create unfavourable interference effects due to local pressure peak resulting in shocks and high drag. In order to avoid interference effects, aerodynamicists need to optimize the join structure of wing-nacelle arrangement. For 737, many wind tunnel tests are carried out to achieve a desirable shape. The students understood the particular problem related to configuration. In addition, they suggested CFD analysis for new design as engineering tool possible.

Even though 737 has T-tail configuration, In terms of stability and control, students could discuss the well-known phenomenon in aeronautics "deep stall", and they claim that conventional tail configuration of Boeing 737 do not have this problem, but can increase in size and drag . The tail is below the wing wake during stalls and produces a strong recovery pitching moment. Although the article in discussion did not mention possible problems for conventional tail configuration, the flight mechanic member explained that this configuration is favourable to have vibration problems on horizontal tail at high speed because the tail is on line of wing wake during shock wave conditions on wing. Thus, they conclude that aerodynamicists need to design wing to minimize or eliminate the vibration of wake.

Considering directional stability, the group understood that a configuration as 737 is more critical than 707, since the engines are mounted in an outboard position when compared engine-fuselage configuration, and the vertical tail is design to maintain stability in heading for one engine out at low speed. The flight mechanics member mentioned official criterion from FAA for different categories of airplanes. Thus, students could understand the relationship between take-off speeds and vertical tail sizing.

For Douglas DC-9, the students realised that choices in terms of airplane configuration on conceptual design followed the main requirements of the specific design. The fuselage-mounted engines configuration from DC-9 shows many advantages over wing-mounted engines such as less cruise drag, and reduction in the asymmetric-thrust yawing moment that exists when one engine is out. However, the low pylon interference drag for this configuration at second-segment climb condition was determinate to choose the specific configuration. The performance member discussed how critical is the second-segment climb for twin-engine configuration. So, it is important minimize drag on this segment.

The tail configuration was extensive discussed on group. They compared T-Tail configuration to conventional configuration. They understood the benefits of this configuration such as vertical tail more efficiently, and minor horizontal tail because of downwash decrease. In order to minimize weight and drag the group justify T-tail choice. On the other hand, discussions were conducted to understand how “deep stall” is a problem. Once more, there is an inherent problem from a configuration choice to solve. This example from DC-9 was appropriated to engineering students realise how to dial with critical aerodynamic problems on design. It was discussed wind tunnel campaign, and analysis solution for “deep stall” problem. They realised that vortilon and greater horizontal tail solutions for deep stall came from exhausted analysis of wing wake and its influence on horizontal tail effectiveness. In addition, they noted that others airplanes had the same solution for deep stall such as EMBRAER145. Moreover, stall characteristics requirement are debated widely. After that, they noted how critical is this requirement on design.

Multidisciplinary view on design

Usually is hard, in aircraft design, to satisfy disciplines such as aerodynamics, aeroelasticity, performance, structure and weight at same time. During the development of both aircraft Boeing 737 and Douglas DC-9 took place multidisciplinary problems, and the students could realise solutions for these situation. For instance, the group of 737 discussed that an outboard aileron could be used over the entire flight regime without aeroelastic problems. On the other hand, they realised a different solution for Boeing 707 and 727 to avoid aeroelastic problems because of a thinner and more swept wing than 737. In the case of DC-9, deep stall solutions for stall requirements, vortilon and tail extended, increased drag and weight having adverse effect on climb. The aerodynamicists fixed this problem with wing-tip extension.

4.3 Cross-dynamic

During discussions on cross-dynamic, students could understand better an airplane design for commercial jet with requirement of short range and runways. They could realise that Boeing 737 and Douglas DC-9 have similar requirements. It was also commented the similar aerodynamic solutions (thicker profile and less swept wing) to satisfied requirements. However, the designers conducted design philosophy in a different way with distinct airplane configuration choice. So, as a result of these choices engineers need to deal with characteristic problems of configuration. In addition, it was mentioned by most students the importance of high-device systems for short runways requirements in both airplanes.

4.4 Discussions between educator and students

After students put effort into preparatory work and discussions about both design of Boeing 737 and Douglas DC-9, the educator conducted the group to point out on a final conversation the main points of both Design.

First of all, they indicated requirements as “the guide of aerodynamicists”. Aerodynamicists need to follow this guide during the whole design. In addition, requirements determine which performance is more critical. For both airplanes, short runways requirements established importance for take-off and climb segment on design with a specific aerodynamic response for these conditions.

Secondly, design philosophy determines airplane configuration, and when it is established, there are many benefits to achieve the requirements, but some collateral effects will take place, and aerodynamicists need to prepare to solve it.

They also point out the importance of investigation on wind tunnel to solve aerodynamic problems on design development. Besides, it was mentioned that nowadays CFD tools work helping investigation in wind tunnel to fix design problems.

Technology could be realised for students as progressive development. They indicated that aeronautical companies build up technology and know-how during their historical development. Both Douglas and Boeing anticipated design problems and fixed them because took place similar problems in others previous designs. In addition, high-lift devices were referenced as a strong technology solution on design to solve restricted take-off requirement.

They claim that multidisciplinary view on design is very important, and it can affect the development of design unbalancing areas such as aerodynamic, aeroelastic and structure. They understood that this subject is a good point to realise airplane design, since they never had experimented a multidisciplinary view on design. Finally, students wrote down a report that they mention main perceptions described above.

5 Conclusion

After applying a case study in aeronautical education, it is possible to evaluate its benefits. First of all, the aerodynamic concepts such as stall, shock wave and high-lift devices could be better understood using a case study when compared with traditional teaching. The reason for this is the "problematization of concepts". To solve design problems, students needed to understand concepts gave in class but now in different contexts reinforcing them. The "deep stall" was a good example. Secondly, about multidisciplinary view on design, it is clear that lectures of design need to simulate engineering environment, because only this way students can realise some modification on design affecting different areas. In the end, the different design philosophies of the airplanes gave students a wide variety of situations to deal with aerodynamic issues on design. Regard to these aspects of case study, students could construct an engineering world that does not exist on class. Preparing future engineers with concerning reinforcing in concepts, multidisciplinary view and wide variety of scenario case study contributes strongly for aeronautical engineering education.

References

[1] Anwar S. and Ford P., "Use of a case study approach to teach engineering technology students", *International Journal of Electrical Engineering Education*, Vol. 38, No.1, 2001, pp. 1-10.

[2] Masseto M.T., *Competência pedagógica do professor universitário*, 4th ed., Summus editorial,2003,Chap.8

[3] Olason M. L. and Norton D. A. "Aerodynamic Design Philosophy of the Boeing 737", *Journal Aircraft,* Vol. 3, No. 6, 1966.

[4] Shevell R. S. and Schaufele R.D. "Aerodynamic Design Features of the DC-9", *Journal Aircraft*, Vol. 3, No. 6, 1966.

4:th CEAS Air & Space Conference
FTF Congress: Flygteknik 2013

Astrium perspective on space debris mitigation & remediation

P. Voigt*, D. Alary, C. Cougnet**, M. Oswald*, J. Utzmann***
**Astrium GmbH*
Claude Dornier Straße, 88090 Immenstaad, Germany
***Astrium SAS*
31 rue des Cosmonautes, 31402 Toulouse Cedex 4, France

Keywords*: space debris, prevention, avoidance, survival, remediation*

Abstract

The density of space debris has been increasing for decades. The situation is critical especially in LEO. Astrium is aware of the space debris problem and proposes a four-pillar debris mitigation approach containing prevention of debris generation by new launches, avoidance of debris by active spacecraft, removal of debris (large and small) and the survival of in-orbit objects. There is a long-term experience in all these four pillars of mitigation as well as on system and architecture level. The paper will describe the overall mitigation strategy and the different approaches in the four pillars to avoid further debris.

1 Introduction

The density of space debris has been increasing for decades, with the rising number of satellites, rocket bodies and mission-related debris, and with the fragmentation events. The situation is critical especially in LEO. The destruction of one object yields an additional set of debris, and hence a significant increase of the collision probability for many other objects finally resulting in a chain reaction. Experts predict one large collision every 5 years in 2050 and an acceleration of the chain reaction. This would have a severe impact to the LEO domain as useful regime for satellite operations. Already today space debris is a serious problem which is visible through the regular avoidance manoeuvers of the ISS, the threat for sun-synchronous orbits due to the potential destruction of de-functional large Earth observation satellites but also the risk on the safety of ground population due to uncontrolled re-entries (Rosat).

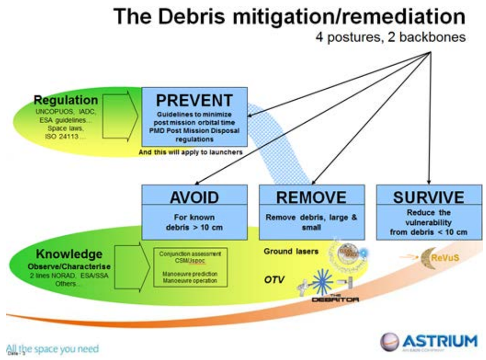

Fig. 1 The Astrium four-pillar debris mitigation approach

Astrium is aware of the space debris problem and proposes a four-pillar debris mitigation approach as drafted in Fig. 1 containing prevention of debris generation by new launches (mainly covered by internal analyses), avoidance of debris by active spacecraft (S/C) (mainly covered by [1]), removal of debris (large and small, mainly covered by internal studies and [2]) and the survival of in-orbit objects (mainly covered by [3]). There is a long-term experience in all these four pillars of mitigation as well as on system and architecture level.

2 Prevention

The generation of additional debris shall be prevented by Post Mission Disposals (PMD) of satellites and launchers to reduce the maximum lifetime in operational orbits to 25 years after the end of operations, by transferring them into graveyard orbits according to the IADC guidelines or by directly re-entering into the Earth atmosphere. The PMD shall be ensured by on-board capabilities after passivation of the system to avoid any explosion. This has an impact on the system itself. It may also be provided by a special de-orbit kit attached into the satellite by an external removal service. In all cases the cost of the solutions is a strong driver. So it has to be required by regulation and license issues.

In general the PMD requirements are similar, beginning with the fundamental IADC regulations, followed by the code of conducts, guidelines, recommendations, standards (Europe, ESA, NASA, UNCOPUOS, ITU, ISO) and the laws at national levels.

Besides all their communalities there are a few subtle differences in the PMD requirements. This has to be considered already at the design stage, sometimes before knowing from where the satellite is going to be launched. Especially the casualty risk is a driver for the design because for larger objects it may be above 10-4 [4] making a controlled re-entry mandatory.

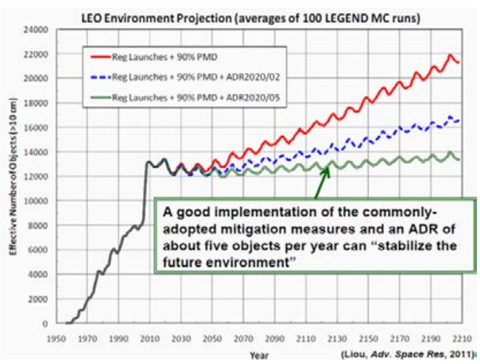

Fig. 2 Development of space debris population depending on different PMD and removal strategies [6]

The success rate of PMD is very often taken at 90% as required by the regulations. This is far away from the real world: for example only 76% (13 out of 17) GEO satellites have succeeded their PMD in 2011 [5] in LEO the success rate is even lower. But even for a PMD success rate of 90% the number of objects will increase as shown by the red graph in Fig. 2. To stabilize the future environment current analyses show that 5 large objects have to be removed per year additionally, beginning in 2020 [6].

The effort for a typical LEO PMD is equivalent to a significant part of the orbit control budget. So with this amount of fuel the mission time could be extended. Thus deciding to stop the operational life of a satellite, and start the passivation and manoeuvers is not an easy decision when the satellite is still providing the operator with significant income.

The reasons for a satellite operator to consider the PMD are

- Risk/liability in case the S/C could cause damage
- Regulation
- Scarcity (e.g. slots in GEO)
- Penalty.

For LEO the main reasons are regulation and license issues. Scarcity is an additional important factor for GEO. Penalty, risk and liability are less strong reasons to perform a PMD.

So depending on the additional value of the mission extension an external PMD service through a piggy back might be beneficial. This shall be an autonomous device, fully qualified, that would enable a full compliance with the law with zero impact on the client design. Several packs would be available, depending on the orbit and size of the client, e.g.:

- Small satellite LEO 600-800 km; drag augmentation balloon 20m²
- Large satellite LEO 600-800 km; drag augmentation sail 100m²
- Large satellite LEO 800-1200 km; Electrodynamic tether
- Large satellite LEO >1200 km; solar sails

A de-orbit pack to be embarked as a piggy back is also a building block of an active debris removal (ADR) mission.

3 Avoidance

To avoid objects the debris situation must be known. Currently LEO-objects larger than ca. 10 cm are tracked by the US SSN so that avoidance manoeuvers can be carried out by operational satellites. Also national means (German TIRA or French GRAVES) exist for surveillance and tracking, however additional sensors are needed with improved capabilities in order to tackle the debris problem. In the future, debris location could be known better through a Space Situation Awareness system(s). Astrium has been and is involved in several system studies in this regard, e.g. the current "CO-II SSA Architectural Design" ESA study [1] and the "Assessment Study for Space Based Space Surveillance Demonstration Mission".

From a system point of view the necessary capabilities should be derived from a chain of requirements, beginning from high level mission or customer requirements and flown down to system level. Examples are the high level requirements “reduction of lethal collision risk” and “reduction of catastrophic collision risk”. For both requirements, the to be defined SSA system should reduce collision risk by a TBD amount.

One example for this chain of requirements down to the system capabilities are the current high level ESA SST requirements. Simulations show [1], that in order to reduce the probability of lethal collision by the required 90% compared with the probability without a system, LEO objects of the size of about 5.7 mm must be catalogued. Feasibility of mass cataloguing of the lethal debris is clearly questioned by the tremendous sensing sensitivity required and the subsequent amount of detections to be processed and further correlated. The second example is the reduction of catastrophic collision risk. A catastrophic collision is defined as a collision with Energy to Mass Ratio (EMR) greater than 40 J/g. In LEO, these are objects with a size of a few centimetres which significantly reduces the technical effort compared to the detection of mm-sized objects.

Given the high number of objects to be detected and tracked, an effective surveillance system within the SST segment is expected to:

- Detect new objects in space,
- Set-up a data base containing the orbit of all known objects,
- Re-detect already seen objects, and
- Maintain the objects orbital data base while meeting the accuracy envelope requirement.

3.1 General characteristics of Space Situation Awareness sensor network architecture elements

A possible sensor network is comprised of both ground- and space-based assets. The proposed ground sensors include a surveillance radar, an optical surveillance system and a tracking network (radar and optical). A space-based telescope system may provide significant performance and robustness for the surveillance and tracking of beyond-LEO target objects. In addition to the sensors on-ground infrastructure is required, e.g. data centers for the data processing. All these components have to be linked to support the whole chain from the detection of an object with the sensors, the downlink and processing of the data on ground and the command for a collision avoidance maneuver [1].

In order to perform the surveillance of objects in LEO orbits (up to 2000 km), the most suitable option is to use **ground-based radar**. Radar assets are insensitive to weather outage effects and can be operated continuously on a 7d/24h basis. However, the required transmitting power limits the range for reasonably sized surveillance radar to the LEO region. A joint surveillance and tracking phased array radar seems beneficial with a fence based surveillance & tracking radar operating principle. An object is detected when it crosses the radar fence. Then, it is immediately tracked in order to support initial orbit determination respectively the orbital parameters' refinement process.

Ground based telescopes are especially suited for the detection of objects beyond LEO. For surveillance the telescopes are moved in a step-and-stare fashion to cover a stripe in a particular direction. This approach is particularly suited for the observation of GEO and to less extent MEO orbits, as the field-of-view crossing times are long, which allows observing the same object several times with the same telescope. For such orbits, the coverage of a fence in declination ensures even the coverage of objects with large inclinations.

However the above approach may have some gaps in the observability of specific orbits. Depending on timeliness and revisit requirements, additional telescopes could be required for the surveillance of non-GEO orbits (e.g. MEO). Additional tracking telescopes may also be required to improve the catalogue accuracy of such orbits. An optical surveillance system (4 sites distributed at different longitudes near the equator) to cover beyond-LEO orbits is recommended.

Space-based telescopes seem especially suitable for the surveillance and tracking of beyond-LEO objects. Especially for GEO, an SBSS (Space-Based Space Surveillance) satellite can play out its advantages just as radar does for the LEO population:

- An SBSS makes the optical SST system robust, as it is insensitive to weather, atmospheric conditions and the day/night cycle.
- Full longitudinal GEO belt coverage and high availability are obtained along with
- Favorable properties w.r.t. catalogue generation and maintenance due to very good observation timeliness and re-visit times.
- And: no geographical and geopolitical restrictions as for multiple ground-based optical sites have to be considered.

These advantages have been already demonstrated, e.g. by SBV, US SBSS and Sapphire. Analyses [1] point strongly towards a telescope in sun-synchronous LEO for comprehensive GEO surveillance and significant collateral detections and cataloguing of objects in other orbital regimes such as MEO as drafted in Fig. 3. Similar to the ground-based fence concept, the complete GEO belt can be covered with frequent follow-ups. The orbital dynamics of the GEO population carries the objects through SBSS' observation fence within 24 hours, just as the Earth carries the surveillance radar fence through the LEO population once per day. This is at the same time the reason why only one sensor can achieve comprehensive GEO coverage, with enhanced follow-up performance and thus orbit determination accuracy via an optional second S/C. As an alternative, only one S/C could be used for performing both observation and follow-up, resulting in a somewhat reduced total coverage but higher accuracy.

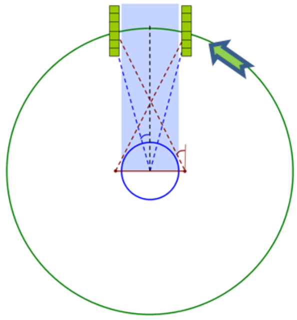

Fig. 3 GEO surveillance fence strategy via step-and-stare pattern [1]

Two fences are shown, which could be covered either by a constellation of two S/C or by one S/C only with reduced declination coverage. Besides the nominal surveillance mode, the tasked tracking of specific objects is possible. The operational flexibility of the SBSS will also allow a significant contribution w.r.t. other mission goals such as the detection of maneuver's and break-up events, object characterization, special mission support (e.g. for LEOP), timely reaction w.r.t. collision risk assessment and will also potentially contribute to the characterization of the sub-catalogue small debris population. In addition, an SBSS could host further secondary payloads, e.g. Space Weather sensors.

Especially for GEO one SBSS satellite covers already many objects of the GEO population with full coverage if two satellites are available. All required basic technologies exist already and are proven. Many advantages have been already demonstrated.

3.2 Phased approach

A phased approach is proposed for the implementation of an independent European space debris knowledge and collision prediction, e.g. consisting of short-term, mid-term and long-term measures. For the **short-term**

- existing capabilities like Graves and TIRA are used and
- a European Space Situation Awareness center can be implemented.

Early performance based on existing assets will show large gaps. The chain from the detection of an object, the data processing until the command of a collision avoidance maneuver can be implemented and tested.

For the **mid-term**

- existing capabilities are updated to increase the performance,
- new elements with higher performance for additional improvement are developed and implemented, e.g. high sensitivity radar for ground based radar (for LEO objects), a space based space surveillance demonstrator and a ground-based optical telescopes close to the equator (initial deployment).

For the **long-term** the system shall be completed for a total coverage with a high accuracy. That includes

- further improved ground based radar for LEO objects and
- a fully operational optical space based surveillance component for GEO (and MEO) objects
- ground-based optical telescopes (full deployment).

Astrium expects a high potential in the development of observation strategies and the combination of different sensor data. Astrium can significantly support the collision avoidance, beginning with the modeling and simulations of the debris population, the development of observation strategies up to the design and construction of a ground- and space based SST infrastructure.

4 Survival

The vulnerability of satellites for untracked debris between 1 mm and 10 cm shall be reduced to survive an impact. Larger objects can be detected and avoided; smaller objects can be absorbed by the structure materials. Different solutions are considered to reduce the vulnerability of satellites in LEO, both at system and satellite architecture levels. In particular, new concepts of shielding are proposed to protect critical equipment against particles of up to 4 mm size. Indeed, it appears that the particles of 2 to 4 mm size are the most significant group contributing to damage of satellites as shown in the EC FP7 study ReVuS (Reducing the Vulnerability of Space Systems to small debris) currently led by Astrium Satellites (see [3]). This section is mainly based on the results of this study.

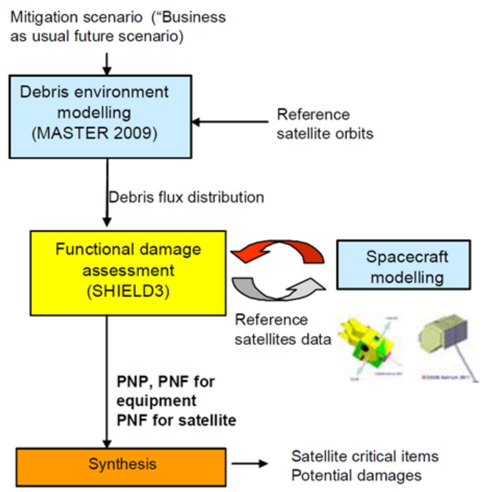

Fig. 4 Approach of the vulnerability analysis in ReVuS [3]

The following three steps approach was the basis of the analyses:

- Vulnerability analysis to evaluate the effects of a collision of a satellite in LEO with small size debris, the potential damage and the critical parts of the satellite, the risk of mission degradation
- the identification and analysis of potential solutions at system level, and at satellite architecture level, with a focus on the shielding concepts and shielding materials

- the resiliency analysis, aiming at evaluating the resiliency of the selected solutions with respect to debris impact and at proposing design rules and standards.

The vulnerability analysis evaluates the effects of a collision of a satellite in LEO with small debris, the potential damages and the critical parts of the satellite as drafted in Fig. 4, supported by the tools MASTER 2009 (ESA Meteoroid and Space Debris Terrestrial Environment Reference Model) for the simulation of the debris environment and SHIELD3

- to evaluate the probabilities of penetration of small debris particles for the satellite and in the equipment
- to determine the failure probability for all equipment parts considered.

The analyses show that debris below 1mm has a high density impact probability of impacts, but only a few penetrate the satellite. Effects on equipment are very low. There is a very high ratio (>= 100) between the density of debris in the range (1-10 mm) and in the range (10-50mm). The risk of being impacted or penetrated by small debris is much higher at 800 km than at 500 km. The radar satellite TerraSAR-X satellite evaluated presents a very low vulnerability to impacts small debris, with a high probability of non-failure (PNF), due to its cylindrical shape along the velocity axis, the rigid body mounted solar arrays and its low altitude (515 km) outside the main density of debris particles.

There are three kinds of potential damages identified:

- First the most critical case is the loss of mission which could result from penetration of debris in the tanks and non-externally redundant equipment. In case of internally redundant equipment the level of failure depends on the internal architecture.
- Second the performance of the satellite could be degraded due to the loss or degradation of the energy supply (solar cells, batteries), the radiators, payload equipment, etc.
- Third the satellite reliability could be reduced due to the loss of redundant equipment.

Based on the results of the vulnerability analysis, solutions at system level and solutions at satellite architecture level (which include the shielding solutions) have been defined.

The system level solutions aim at mitigating the risk at system level. Such solutions can take into account the full range of debris size. An example is the fractionated satellite concept, which consists in sharing some functions of a satellite (communications with ground, computing capability, payloads, etc.) on modules forming a cluster, based on wireless communications and interconnecting network. With an adequate distance between the modules, a collision with debris could lead to the loss of a module, but not the complete mission. Another example is the distributed system concept, which will adapt the principles of existing terrestrial wireless to distributed space system architectures. Possible concepts of operations are also part of the system level solutions.

At spacecraft architecture level, several axes of solutions can be considered, such as:

- Adequate equipment location and physical segregation of the redundancies
- Review of architecture of subsystems, such as solar arrays electrical architecture, propulsion configuration, harness configuration, etc.
- Shielding of the spacecraft: different strategies of shielding can be considered. However, their impact on the spacecraft is different in terms of accommodation and satellite performance (mass, thermal behavior, electrical properties, RF properties), and is a criterion of evaluation of the shielding strategies.

These solutions will be evaluated with respect to their accommodation on the spacecraft and the impacts on the spacecraft configuration in terms of mass, launcher interface, propellant budget, thermal behavior, etc.

The shielding solution will have a significant impact on the mass and on the layout of the satellite. Thus, the shielding solution will be rather used at equipment level, for those items experiencing the highest risk. The analysis of the reference satellites, and more generally of the current and future LEO satellites, show that various basic configurations of equipment can be defined according to their location in the satellite for equipment having a risk of failure due to debris. Tens of configurations have been identified, e.g. to mount equipment behind a radiator or MLI.

A review of the occurrence of such configurations on various current LEO satellites to identify and select the most frequently used has been done in the scope of ReVuS. Still specific analyses for each spacecraft may be beneficial due to the very different design.

A typical shielding has a multi-layer configuration with an outer layer (bumper) to fragment the debris into the smallest possible particles, an intermediate layer to increase the fragmentation and absorb most of the energy of and some particles and an equipment wall to absorb remaining particles.

In general a multi-wall is a better protection against debris than thicker walls because the debris is fragmented which decreases the final impact energy for the equipment wall. A combination of different shielding bricks (e.g. reinforced MLI + reinforced panel) means an additional reduction of the vulnerability. That includes also the use of different materials (e.g. aluminum or carbon-fiber-reinforced plastic) and thicknesses. Each shielding concept has an impact on the performance of the satellite, again especially w.r.t. mass and volume and the effort for the design which drives directly the costs.

Several tests of the material and different bricks shall be performed to evaluate and optimize the selected shielding concepts. Finally design rules and new guidelines for debris impact mitigation shall be proposed.

5 Remediation

5.1 General Considerations

The challenge is to remove 5 to 10 large debris per year in order to stabilize the debris situation. To achieve that goal a wide range of different concepts have been analyzed for single- and multi-target missions, based on new technologies such as sensors to detect the target and evaluate the tumbling rate, systems for capture and stabilization of targets and systems for de-orbiting. The aim was to develop a vehicle able to remove several debris objects and thus hosting several capture systems and de-orbit packs (Debritor). Such a vehicle should be made of off-the-shelf subsystems or equipment in order to lower the development cost at maximum and thus the cost of a mission. In addition concepts to remove small debris (e.g. by laser) have been analyzed. The main part of this section focuses on general aspects and the general Debritor concept and is based on the results of [2].

Four main critical points have been identified:

- the feasibility of such mission with a non-cooperative target; many studies have been performed; many innovative concepts have been presented and analyzed. A few have been tested on ground such as a capture with a net or a harpoon (Astrium); a few have performed an IOV such as a de-orbitation with a sail (NASA). A lot remains to be done (e.g. DEOS, led by Astrium).
- the selection of the debris to remove; this is about selecting the most dangerous debris first. This means in particular targets with enhanced probability of suffering a catastrophic collision, producing a large number of new potential impactors [7]. It could be done for example by using a combined factor made of the mass of the debris together with the collision probability on this particular orbit and its remaining lifetime.
- legal aspects; as soon as a debris removal spacecraft will approach an object, legal question will be raised. Obviously the debris owner will have to accept the removal, but this is not as simple. This is about liability, property transfer, risk transfer, insurance, and

casualties on ground. This is currently analyzed in detail by Astrium in an ESA funded study about an ADR service.

- the cost of removal; no doubt that it has to be low, but how low? This is currently analyzed in detail by Astrium in an ESA funded study about an ADR service.

Amongst these four critical points, the cost of removal is possibly the strongest because such missions bring no intrinsic value on ground, no new applications, no new services, no science, not even any law compliance. So reducing the cost is of paramount importance. The cost of removal per debris is dependent of a lot of inputs. Basically, the equation can be simplified along the mission/system/equipment level with major recommendations.

- At mission level; consider a multi-target mission, where several targets will be processed by the same spacecraft. The alternative launcher solutions could be traded off with respect to the different mission size (number of target to be processed).
- At system level; reduce/cancel the cost driving requirements: autonomy, redundancies... limit on board hardware and involve ground as deeply as possibly, use as far as possible the simplification brought by a relaxed timeline since debris is passive and thus is not sensitive to the duration of the rendezvous and capture.
- At equipment/sub assembly level; reduce the non-recurrent, use off the shelf existing devices.
- At component level; lower the grade of the components down to an acceptable minimum.

Obviously all these levels are linked, and a continuous feedback loop needs to be implemented to define the most efficient and less expensive solution for each function.

The main design drivers of a debris removal system are a strong propulsion capability, relative navigation with and identification of a debris target, capture and de-orbit systems, compatibility with a given launcher. Astrium has a huge expertise in all these segments on programmatic, system and architecture level. W.r.t. space debris Astrium is involved in studies and programs like the ADR service study, DEOS, OTV, a patent for a harpoon to capture objects, internal studies on ion-beam shepherd, passive devices etc.

Hosted Payloads

Additional possibilities to reduce the costs are hosted payloads. The following two concepts are proposed:

- Hosted payloads as a piggy back on the Debritor
- ADR hosted payloads as a piggy back of a common LEO mission

In case of the hosted payloads on the Debritor a multi-purpose mission is possible. The hosted payloads can e.g. use the transfer time from one target to the next target to accomplish a variety of mission goals (e.g. space weather sensors). That adds an additional benefit to the mission, could reduce the costs and offers opportunities for hosted payloads in LEO. Due to its mission profile the orbit control and the orbit drift might not be acceptable by many payloads. To avoid that the hosted payload becomes a driver a trade-off between the effort of adding hosted payloads and the expected cost benefit is mandatory.

Earth observation missions in LEO are especially interesting for ADR devices as hosted payloads as a piggy back because these satellites are already in the orbit regions with potential high valuable targets for removal. Once the nominal mission is over the satellite will approach a target and remove it with a direct re-entry (e.g. by capturing it with a harpoon). Of course a case by case analysis is necessary if such a concept is feasible. But in the end it could become a mandatory option for satellites to host such ADR devices to implement a frequent ADR service.

5.2 The Debritor concept

Capturing and de-orbiting large debris is a complex mission, with a variety of options; they depend on the mode and type of capture, the type of de-orbiting, the use of a single or two active bodies, etc.

The approach that has been followed consisted in defining a family of concept, based on a common platform, and on set of capture/deorbit systems (one per target) to take into account diversity of targets. Indeed, the targets mainly located above 70° up to SSO inclination and between 600 and 1000 km as analyzed in [7], could be upper stages or satellites with different configuration (long cylinder versus target with deployed appendages) and different constraints for capture systems. They could have different masses, different requirements in terms of de-orbiting (e.g. some target require a direct re-entry), etc.

The Debritor is a multi-mission vehicle: during its mission, it will be able to de-orbit several targets, in order to reduce the cost of for a target. Its mission defined a priori: all its targets are selected and known before launch. Thus, the mission of one Debritor vehicle could gather similar targets with respect to type or inclination to optimize the vehicle mass at launch, but the mass of these targets can be different, even if they are preferably around the same average value. Another vehicle mission could gather other types of target.

The type of the capture system could vary between the missions of two vehicles, and even inside the mission of one vehicle. Likewise, the mass of deorbit system (mainly propellant if active) could vary between two missions (target not the same range of mass) and even from one target to the other in a given mission. Therefore, the vehicle configuration should be flexible to implement different types of capture/de-orbit systems, or even different size of de-orbit system in a same mission. The Debritor concept is made of:

- A platform with large propellant capability (including possibly plasmic propulsion) for the transfer to several targets, the proximity operations, and de-orbiting at end of mission.
- Several set of capture systems and de-orbit packs. At least two types of capture system could be implemented to cover the range of targets. Selected capture systems have a flexible link. Active and passive packs could be implemented.

Family concept allows to size the vehicle for a single mission if needed or to a given class of launcher by adapting the number of targets. A platform version could be designed for each class of launcher, by implementing different capacity in propellant mass and thus different types of tanks.

To cope with cost issues, the Debritor concept will benefit to the maximum extend from heritage. For propulsion, existing modules are adequate (E3000, Mars Express) and provide an enough propellant capability (up to more than 3.2t). Avionics, power, communications system from existing platform (LEO platform) could be used as needs in terms of data processing, comms, power generation and distribution are similar. However, the use of electrical propulsion system could lead to a much higher required power (possibly in the order of telecommunications satellites power).

In terms of operation, the vehicle has time to fulfill its mission, so that a timeline at minimal cost will be defined. The system will rely as much as possible on the ground control center, in order to reduce the requirements on the on-board autonomy, and thus the costs. To that aim, the use of GEO communications relay (EDRS, or Inmarsat SBSat for instance) during the rendezvous, capture and de-orbiting of a target will allow an adequate ground involvement.

A description of the Debritor configuration and development approach can be found in [2].

6 Conclusion

Astrium is fully aware of the potential threat of space debris to the infrastructure in space and its impact to every-day life. We propose a four pillar approach, considering the prevention of debris generation, the avoidance of debris by active S/C, the removal of debris and the survival of in-orbit objects.

The first aspect is the necessity of **Post Mission Disposal** which has a huge impact on the design of each satellite. The different requirements w.r.t. the disposal are compared (e.g. maximum acceptable casualty risk) and it is highlighted that the required 90% success rate for a Post Mission Disposal is currently not kept. Solutions are suggested to implement an external Post Mission Disposal Service through an autonomous piggy back pack or to use such a pack for an active debris removal. But even a 90% success rate is not sufficient to stop the generation of debris without the removal of additional debris objects.

The second aspect is the **avoidance of debris by active S/C**. This is only possible if the debris situation is known. Several studies have been and are performed by Astrium to implement a space surveillance and tracking component. Based on the results a first approach for a sensor network is proposed of both ground- and space-based assets.

Astrium proposes a phased approach (e.g. short-term, mid-term and long-term measures) to implement a European Space Situation Awareness system based on existing equipment, its upgrades and the development and implementation of new equipment. For the cataloguing of GEO objects a space-based telescope is recommended because it will already build up a core catalogue with a stand-alone demonstrator.

The third aspect is the **survival of in-orbit objects**. First the debris population of 2 to 4 mm objects is identified to have the highest probability to cause severe damage. Based on the results of the vulnerability analysis, two main categories of solutions have been defined: solutions at system level, and solutions at satellite architecture level, which include the shielding solutions. An example for the system level solution is the fractionated satellite concept, which consists in sharing some functions of a satellite on modules forming a cluster. With an adequate distance between the modules, a collision with debris could lead to the loss of a module, but not the complete mission. At spacecraft architecture level, several axes of solutions are considered, e.g. different shielding solutions.

The fourth aspect is the **remediation of objects**. A general analysis about the main critical points highlights the cost of removal as the possibly strongest aspect. The main technical drivers are the strong propulsion capability, relative navigation with and identification of a debris target, capture and de-orbit systems and the compatibility with a given launcher. To reduce the costs we propose a multi-mission vehicle, called the Debritor, with a simple but robust design which can be adapted for different kinds of removal missions.

Additional benefits may arise from hosted payloads on the Debritor because the available time (e.g. during the transfer from one target to the next target) can be used for other purposes (e.g. space weather sensors). Another possibility is to implement ADR devices as hosted payloads as a piggy back on common LEO satellites (e.g. Earth observation satellites) to remove another object after the end of the nominal mission.

Due to its leading role in many studies and projects related to the space debris topic and its general long-term experience in space business Astrium is able to cover the full spectrum of the space debris challenge as shown in this paper.

References

[1] J. Utzmann et al, 2013, Architectural design for a European SST system, Astrium GmbH, 6th European Conference On Space Debris 2013

[2] C. Cougnet et al, 2012, The Debritor: an "off the shelf" based multi-mission vehicle for large space debris removal, Astrium SAS, IAC 2012

[3] C. Cougnet et al, 2012, Solutions to reduce the vulnerability of space systems to impacts of small debris particles, Astrium SAS, IAC 2012

[4] X. Barbier, 2013, Clean Space – Compendium of Potential Activities for 2013 & 2014, GSTP-6 Element 1, ESA, 2013

[5] H. Klinkrad, T. Flohrer, 2012, Status of the catalogued population in the GEO vicinity, ESA, GEO End of life CNES Workshop, 24th January 2012.

[6] J.C. Liou, 2012, The LEO environment projection, NASA, ADR CNES Workshop 18th june 2012

[7] J. Utzmann, 2012, Ranking and characterization of heavy debris for active removal, Astrium GmbH, IAC 2012

4:th CEAS Air & Space Conference
FTF Congress: Flygteknik 2013

Fostering the Evolution of Systems Thinking in Space Industry with the WAVES Strategy

H. A. Moser
LuxSpace Sàrl, SES Business Center, Betzdorf, GD Luxembourg

Keywords: *Systems engineering; systems thinking; learning*

Abstract

Systems engineering is performed in multi-disciplinary teams involving disciplinary specialists such as in space projects, software engineers, mechanical engineers, and radiofrequency engineers. This activity requires interaction across disciplinary boundaries. Systems thinking, a prerequisite for systems engineering, is learned in interaction. The evolution, i.e. learning, of systems thinking is not sufficiently understood. To improve this understanding, a comprehensive empirical study comprising four cases from space industry within four years has been performed. The analytical framework for this empirical study is presented.

Based on the findings of the empirical study, a strategy to foster the evolution of systems thinking in practice was developed. The identified key factor is the multi-disciplinary quality of interaction. This key factor is influenced by the WAVES (Work Activity for a Versatile Evolution of Systems engineering and thinking) strategy. This strategy comprises two paths. One path focuses on the introduction and entry into entities (professional life, space industry, an organization, a team, and a task). The second path focuses on the continuous improvement of the multi-disciplinary quality of interaction. The overall objectives of WAVES and exemplary instruments addressing these objectives are presented, as well as an overview of the implementation and evaluation approach. Finally, examples of the implementation of WAVES within a small space systems company are provided.

1 Systems Engineering and Systems Thinking

Creating and operating a space mission is a complex activity. It is complex, as a complicated technical system has to be managed by humans. Systems engineering is an approach to product development that has been developed to master this complexity [1]. Systems engineering is a management and engineering effort, considering more than the sum of its elements throughout the lifecycle involving multiple disciplines in a continuous iterative process. A pre-requisite of systems engineering is systems thinking, which is defined as doing something with knowledge of components, context, relationships, and dynamics of a system-of-interest. Systems thinking is expected to evolve within systems engineering interaction. How systems thinking is learned in detail, i.e. how knowledge relevant for systems thinking changes, is not sufficiently understood.

2 Research Approach

Before the evolution of systems thinking can be improved, the current situation (how does systems thinking evolve in practice?) has to be better understood. This requires an empirical study in order to identify factors which can be impacted.

The performed empirical study comprises four separate studies. Study 1 (S1) was a ten-days-study in a European summer school with four student projects in the concept exploration stage of a space mission that focused on detection and characterization of extra-solar planets [2]. Study 2 (S2) was a three-days-study in a concurrent design facility with a project in the concept exploration stage of a space mission that focused on Earth observation [3]. Study 3 (S3) was a longitudinal study of four years with five projects in the space-based maritime surveillance sector, in a small space systems integrator company, and in different lifecycle stages (concept exploration to operations) [4]. Study 4 (S4) was a four-days-study in the same concurrent design facility as in S2 but with different participants and a different project in the concept exploration stage, a space mission focusing on the observation of the solar magnetosphere [5].

Different data collection methods were applied in the four studies. Audio and video records, project journals, and email collection were identified as major data collection methods. These were complemented by data collection methods of second priority, e.g. research journal, documentation collection, interviews, and physical artefacts.

The analysis comprises two methods: an activity-theoretical analysis and a theme-and-key-event analysis. The first method, the activity-theoretical analysis is based on a network of activity systems. A zooming in the network allows for focusing on different details, relations, and particularly, on contradictions with learning potential. The activity-theoretical analysis includes a description of the activity systems networks and an identification of the contradictions. These contradictions, as well as identified critical interaction instances motivate the selection of themes and key events used in the second analysis method, the theme-and-key-event analysis.

The second method, the theme-and-key-event analysis is performed on three levels of analysis (macro, meso, micro). The macrolevel analysis is an ethnographic description of a theme. Themes are key events that are linked in time. The mesolevel analysis is performed with a dual categorisation scheme based on discourse features and systems thinking content. The microlevel analysis is based on multimodal interaction analysis and focuses on critical instances in interaction [6].

This analysis approach allows to identifying contradictions in the work activity of the four studies and factors influencing the evolution of systems thinking. A detailed description of the performed analyses is provided in [7]. The focus of this article is on the interventionist parts of the research project, i.e. how the evolution of systems thinking can be improved based on the findings of the empirical study.

3 The evolution of systems thinking in practice

Knowledge changes within multi-disciplinary discussions (duration between seconds and minutes) [8], across multi-disciplinary discussions (duration between days and years) [9], and in two directions: vertically as a change of competence within a distinct discipline, and horizontally as a change across disciplines. The change across disciplines includes change of extra-disciplinary knowledge (outside one's own discipline) and change of knowledge about relationship between disciplines. This interactional change of knowledge relevant for systems thinking is influenced by a quality, which has been defined as multi-disciplinary quality of interaction.

3.1 Multi-disciplinary quality of interaction as key factor to be influenced

An interaction of high multi-disciplinary quality involves diverse (at least two) disciplinary perspectives with interactors being aware of their diversity (of perspectives, languages, cultures, assumptions, etc.) and orienting towards each other while explaining their point of view. All interactors are comfortable with the required interactional responsiveness (time between initiation, response, and feedback in an interaction), e.g. issues, which cannot be directly solved, can be postponed after the meeting or a first guess within the meeting is followed by a more exhaustive explanation afterwards. In addition o being an improved environment for learning of systems thinking, such an interaction is more likely to reduce unintended design iterations and therefore leads to a shorter development time.

Influencing this key factor multi-disciplinary quality of interaction is the major aim of the intervention focusing on the improvement of the evolution of systems thinking in practice.

4 Fostering the evolution of systems thinking

The evolution of systems thinking is influenced by following the WAVES (Work Activity for a Versatile Evolution of Systems engineering and thinking) strategy. The acronym implies the main goal of the strategy, i.e. a work activity (systems engineering) that supports a manifold (versatile) evolution of systems thinking and of the work activity (systems engineering) itself. Objectives to be achieved for reaching this goal are presented in the following section.

4.1 Objectives of the WAVES strategy

Addressing factors identified in the empirical study result in the following objectives:

- Promote *regular team meetings*
- Promote and support *storytelling*
- Provide consultancy for the work *and task selection*
- Increase the *awareness of others' multiple perspectives*
- Increase *access to multiple perspectives*
- Increase *awareness and appreciation of questions and advice*
- Increase *possibilities for questioning work practice*
- Promote and support *project work at universities*
- Valorise *learning in practice*
- Valorise *multi-disciplinary quality of interaction*
- Valorise *sharing of experiences and extra-disciplinary questioning*

To achieve these objectives, actors on different levels of an organisation such as executive management, project management, and project engineers have to be influenced.

4.2 Structure of the WAVES strategy

Contrary to knowledge management strategies, which focus on the final transfer of knowledge before the retirement and on elicitation and storage of knowledge, the WAVES strategy follows two paths (see Figure 1).

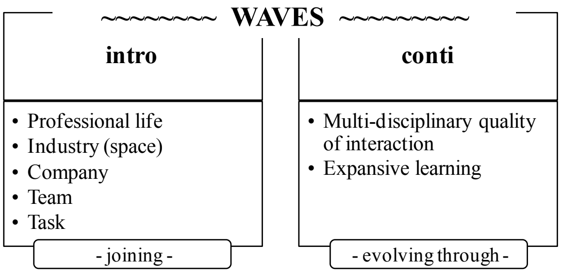

Figure 1: The two paths of the WAVES strategy

The first path is an improvement of introduction, i.e. joining an entity. This encompasses entering into:

- professional life, i.e. professional newcomer, first job after graduation,
- space industry, e.g. a computer specialist, a mechanical specialists, or a geographer with no expertise about the special requirements and challenges of the space environment and regulations,
- an organisation, e.g. new in a company, division, department,

- a team, e.g. new formed team, new team member in a pre-existing team, and
- a task, e.g. doing a radiation analysis for the first time.

Whilst the first path is thought to ease the start of working within a multi-disciplinary work environment, the second path aims on fostering learning of multi-disciplinary engineering teams in general. This includes the way the teams are working, the way they are interacting, and in particular discussing.

Both paths are addressed by instruments, which have been developed or already existed within other human resource development or knowledge management strategies. Additional instruments have been developed and modified to complete the set of instruments used to achieve the objectives of WAVES.

4.3 Instruments of the WAVES strategy

As an example of how objectives are intended to be achieved within the two paths, selected WAVES instruments are presented. Here, three instruments are presented. These three instruments are post-project reviews, Pause and Learn (PaL) sessions [10][11], and storytelling. These instruments have shown their potential for initiating multi-disciplinary discussions. The related objectives of WAVES are: promote and support regular team meetings, promote and support storytelling, and increase possibilities for questioning current work practice.

Two types of regular team meetings are supported: post-project reviews and PaL sessions. Both types of meetings are opportunities for storytelling in addition to ad-hoc storytelling.

Post-project reviews are meetings conducted at the end or close to the end of a project. These meetings provide the possibility to reflect on the accomplished project, i.e. the period from the start of the project which might be in the range of several years, even decades. Therefore, these meetings cover a large scope, which leads to a significant required time commitment. A formal report is generated, which mainly serves as repository of discussed issues, in particular interesting for non-participants.

PaL sessions are adapted After Action Reviews (AAR) of the US Army [12]. Pause and Learn sessions facilitate "local learning loops" and go further than after project reflection [13] or reflection on action [14]. The goal is to have these sessions as close as possible to significant events within the projects, e.g. at project milestones.

Questions asked by a PaL facilitator are of interest as they are regarded as initiators for discussions, in particular discussions on the work approach. The second part of interest is the suggested facilitation of war story exchange. Telling stories can be regarded as a sort of teaching. Learning by teaching is a phenomenon that describes the feedback loop from the receiver (the listener) to the sender (the storyteller) [16]. The promotion of telling and appreciating stories is one of the objectives of WAVES.

A PaL report is prepared by the facilitator and provided to the participants. This report contains the following major components [15]:

- A brief project summary
- The project event or milestone in focus
- Preliminary information and assumptions
- PaL synopsis
- Insights and recommendations
- Action items and proposed follow-up (if applicable)

Table 1 shows basic distinctions between post-project reviews and PaL sessions [15].

Table 1: Post-project vs. PaL sessions

Post-project	PaL session
Conducted at the end of project	Conducted through-out project
Used after a project has finished	Used after any event-team success or challenge
Large scope - all past events	Small scope - one recent event
Large time commitment	Small time commitment
Formal report	PaL report
Benefits mainly others who read the report	Benefits team members who participate

Both, post-project reviews and PaL sessions provide a more formal opportunity to question current practices. In introducing these meetings one increases the possibilities for questioning current work practices.

This questioning is the initiating action of an expansive learning cycle of communities [17]. This action is a major distinction to the SECI (Socialisation, Externalisation, Combination, and Integration) cycle [18]. Figure 2 shows the entire expansive learning cycle where the questioning action is followed by analysing the situation, modelling new solutions, examining these solutions, implementing selected solutions, reflecting on this process of change, and finally consolidating the new practice.

Figure 2: Expansive learning cycle according to [17]

A detailed analysis of a multi-disciplinary engineering team (within S4) identified the importance of questioning and collective analysing of the current and envisioned work approach [9]. As aforementioned, the PaL sessions support this initiation phase.

The third instrument, storytelling is supported and promoted to tellers of stories as well as to listeners. Therefore, WAVES aims on convincing the management of the need to reserve time for sharing these stories. Creating special opportunities for sharing stories is another aim of WAVES. As mentioned before, regular meetings such as PaL sessions are possible opportunities. Having the stories told in the PaL sessions increases the probability of sharing as they will be stored in the PaL report and distributed to the team members (also to those who could not participate). Other possibilities of sharing stories are the coffee machine, lunch break, et cetera.

All three presented instruments focus on improving the awareness of diversity and the orientation towards extra-disciplinary interactors. This is a major constituent of the multi-disciplinary quality of interaction of which the improvement and maintenance on a high level is a continuous effort.

5 Combined approach of implementation and evaluation

A dedicated approach to implement WAVES in space industry has been developed. As the evaluation is linked to the implementation, a combined implementation and evaluation approach has been defined. This approach includes an iterative implementation and evaluation starting on team level and extending to company level, before implementing WAVES within other companies. Continuous assistance and maintenance is an additional part of the implementation and evaluation strategy. This approach is depicted in Figure 3.

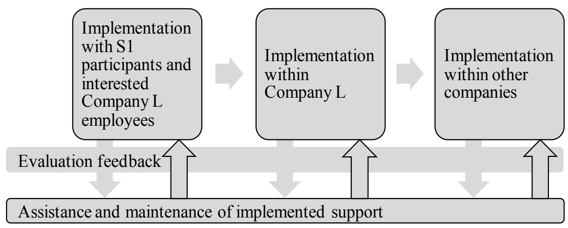

Figure 3: Combined implementation and evaluation approach

6 Implementation and Evaluation within a small space system company

Implementation of WAVES in the company where S3 was conducted has started and is ongoing. This company, LuxSpace, is a small space systems integrator created in 2004 and employs 40 employees from twelve different countries. LuxSpace activities are focussed on four main technological areas: microsatellites, satellite software and simulators, payloads and antennas, as well as Earth observation and telecommunication applications and services.

The addressees of the WAVES instruments are members of the multi-disciplinary engineering teams and the company management. In addition to starting the use of certain WAVES instruments a general introduction of the WAVES strategy was given to senior staff and company management in order to provide a first overview and gather feedback for the iterative evaluation.

Implemented instruments of WAVES are for instance: raising the awareness of the diversity of interactors, which was performed by presentations of exemplary data excerpts and highlighting the importance of taking less for granted. Furthermore, a database of skills and competencies has been developed and implemented based on the need identified by employees and the suggested WAVES instrument. Within S4, an initial PaL session was promoted. The author promoted this session without explicitly mentioning the goal of implementing a WAVES instrument as the entire strategy was not yet developed. This initial implementation was a trial based on an upcoming opportunity. The PaL session was performed after environmental tests of an experiment for human spaceflight and a microsatellite.

Post-project reviews have been performed as collaborative lessons learned workshop directly after successful project completion. One outcome of this workshop was a document that was written collaboratively during the workshop and reviewed by the participants afterwards. Participants were project team members and selected employees who were not part of the team. The idea of having shorter meetings at higher frequency, in particular the PaL sessions was appreciated. The skills database suggested by WAVES was identified as useful as the need for it also emerged from the employees themselves.

7 Conclusion

As systems thinking is learned in interaction, the quality of this multi-disciplinary interaction is of essential interest for improving the process of learning in practice. Awareness of the others diversity and orientation towards the extra-disciplinary interactors is a key constituent of this multi-disciplinary quality. Creating this awareness and orientation and maintaining it is achieved by a set of instruments in two paths of a human resource development strategy.

This strategy, WAVES, is a strategy for fostering the evolution of systems thinking. It is tailored for small and medium sized companies but also applicable for systems engineering departments and teams in larger organisations. It has been developed based on four case studies in different organisations in space industry and its implementation and evaluation is on-going.

Acknowledgements

Thanks to all the participants of the study, the organisations LuxSpace and the Institute of Space Systems of the German Aerospace Center (DLR), Prof. Dr. Charles Max and Prof. Dr. Gudrun Ziegler, the members of DICA-lab, Prof. Dr. Lucienne Blessing, and the Engineering Design & Methodology research group at the University of Luxembourg, Simone Klumpp, and to all others who contributed to this article. In addition, thanks to the National Research Fund of Luxembourg (FNR) for financing the research project within the AFR-PPP programme.

References

[1] Elliott, C. and Deasley, P., *Creating systems that work. Principles of engineering systems for the 21st century.* Royal Academy of Engineering, London, 2007.

[2] Eybl, V., Xiang-Grüß, M., Lammer, et al. "A new approach to investigating star-planet-interaction based on UV transit observations of terrestrial planets around M-dwarfs." In *European Planetary Science Congress.* Vol. 5. 2010.

[3] Bauer, W., Quantius, D., Romberg, O., and Dumont, E. "CarbonSat/C Low-cost satellite mission designed at CEF for Greenhous Gas Detection." In *38th Scientific Assembly of the Committee on space research*, 2010.

[4] Buursink, J., Ruy, G., Schwarzenbarth, K. van Schie, B., Frappé, J.-B., Ries, P., and Moser , H. A. "Vesselsat: Building Two Microsatellites in

One Year." In *Small Satellites, Services & Systems: The 4S Symposium*, 2012.

[5] Quantius, D., Maiwald, V., Schubert, D., Romberg, O., Schlotterer, M., and Hardi P. "The concurrent engineering approach applied on the solar magnetism explorer (SOLMEX) concept." *62nd International Astronautical Congress*, Capetown, 2011.

[6] Ziegler G., Song J.Y., Kracheel M., and Moser H.A., "Analysing critical interaction instances in collaborative concurrent engineering: satellite development", *International Journal of Product Development*, Vol. 17, No. 1/2, 2012, pp. 153-169.

[7] Moser H.A., "*Systems Engineering, System Thinking, and Learning - a Case Study in Space Industry*," Ph.D. Dissertation, Research Unit in Engineering Sciences, University of Luxemburg, Luxemburg, 2013.

[8] Moser H.A., Ziegler G.D.S., Blessing, L.T.M., and Braukhane, A., "Development of systems thinking in multi-disciplinary team interaction: two cases from space industry," *12th International Design Conference - DESIGN*, Zagreb, 2012, pp. 1929-1940.

[9] Moser H.A., Max C.J., and Blessing, L.T.M., "Team learning in space projects - insights from a small satellite integrator," In *62nd International Astronautical Congress*, Capetown, 2011.

[10] Filip, B. "Mapping to support organizational learning: Integrating multiple KM practices." In *3rd International Conference on Managing Knowledge for Space Missions: Knowledge Management at ESA - Knowledge for Mission Success*. Noordwijk, 2010.

[11] Rogers, E. W. and Milam, J. "Pausing for Learning: Applying the After Action Review process at the NASA Goddard Space Flight Center." In *IEEE Aerospace Conference,* 2005.

[12] Headquarters Department of the US Army. "A leader's guide to after-action reviews." 1993

[13] Lawson, B., and Dorst, K. *Design expertise*. Oxford, [UK]: Architectural Press, 2009.

[14] Schön, D. A. *The reflective practitioner: How professionals think in action.* New York: Basic Books, 1983.

[15] Rogers, E. W. "Introducing the Pause and Learn (PaL) process: Adapting the Army After Action Review Process to the NASA Project World at the Goddard Space Flight Center," 2004.

[16] Chen, F., Bapuji, H., Dyck, B., and Wang, X. "I learned more than I taught: the hidden dimension of learning in intercultural knowledge transfer." *The Learning Organization* 19, No. 2, 2012, pp. 109–120.

[17] Engeström, Y. Learning by expanding: An activity theoretical approach to developmental research. Helsinki: Orienta Konsultit Oy, 1987.

[18] Nonaka, I., and Takeuchi, H. *The knowledge creating company: How Japanese companies create the dynamics of innovation.* New York: Oxford Univ. Press, 1995.

4:th CEAS Air & Space Conference
FTF Congress: Flygteknik 2013

Application of the Mixed H2/H$_{oo}$ Method to Design the Microsatellite Attitude Control System

Erberson Rodrigues Pinheiro, Luiz Carlos Gadelha de Souza.
Instituto Nacional de Pesquisas Espaciais, INPE,
Av. dos Astronautas, 1758, 12227-101- São José Dos Campos, SP, Brasil
gadelha@dem.inpe.br

Keywords: *microsatellite, robust control, uncertainty model*

Abstract

Due to the space missions' limited budget, small satellite cluster or constellation would be an economical choice. From risk-sharing viewpoint, a number of smaller satellites have a significant reliability advantage over a bigger one. By and large, artificial satellites are subject to two kinds of uncertainty: structure uncertainty that represent some satellite parameter variation and the unstructured uncertainty, which represent some kind of the satellite model error. On the other hand, the Satellite Attitude Control (SAC) design becomes more vulnerable to uncertainty disturbances like model error and moment-of-inertia variation as the satellite has great decrease in size and weight. This is the case for a microsatellite with mass less than 100kg where the ACS performance and robustness becomes very sensitive to both kinds of uncertainties. Therefore, the design of the SAC has to deal with the drawback between controller performance and robustness. The purpose of this work is to model a microsatellite and to perform a mixed Control via LMI optimization.

1 Introduction

Microsatellites play important role in space missions, such as position location, Earth observation, atmospheric data collection, space science and communication. Some spacecraft used to observation need high-accuracy performance on pointing requirement, so it's necessary to apply a three-axis attitude control, leading a multivariable control system [1]. In the face of disturbance and uncertainty, it's necessary to design a robust control for analysis and synthesis of attitude control system. Examples of satellite robust control system design using multi-objective and nonlinear approaches can be found in [2] and [3], respectively. Low orbit spacecraft are under a more strong influence of gravity gradient torque, aerodynamic torque and magnetic torque. Some equipment on the microsatellite like cameras, telescopes and solar array can move causing change on moment of inertia. Microsatellites with mass less than 100kg are more sensitive to moment of inertia variation and disturbances like external torques. In this work will be use a kind of robust control called mixed control. This combination was introduced by Bernstein and Haddad [4], the idea is to minimize a norm of a transfer function subjected a constraint given by a H_∞ norm of another transfer function. In the paper [5] was considered state and output-feedback control of the mixed H_2/H_∞control and to solve the non-linear Riccati equation was used convex optimization. As for vibration control of rigid-flexible satellite an alternative approach is to use piezoelectric shunt damping technique as has been done in [6]. In this work one uses the mixed H_2/H_∞control via the LMI approach [7] to design an attitude control of a microsatellite subjected an external disturbances and uncertainty in the moment of inertia.

2 Microsatellite Attitude Dynamics

It is defined a body-fixed reference frame B with its origin located in the center of mass of a microsatellite and is given the unit vectors being along the principal axes. The Euler's equations of a microsatellite is given by [8]

$$
\begin{aligned}
I_x\dot{\omega_x} - (I_y - I_z)\omega_y\omega_z &= T_{ex} + T_{gx} + u_x, \\
I_y\dot{\omega_y} - (I_z - I_x)\omega_z\omega_x &= T_{ey} + T_{gy} + u_y, \\
I_z\dot{\omega_z} - (I_x - I_y)\omega_x\omega_y &= T_{ez} + T_{gz} + u_z,
\end{aligned} \tag{1}
$$

where I_x, I_y and I_z are the principal moments of inertia, ω_x, ω_y and ω_z are the body-axis components of angular velocity, T_{ex}, T_{ey} and T_{ez} are the no modelled external torques, T_{gx}, T_{gy} and T_{gz} are the components of gravity gradient torques that will be inserted into the equations and u_x, u_y and u_z are the control torques.

It's necessary to consider another reference system, called local-vertical-local-horizontal (LVLH) with its origin at the center of mass of the microsatellite. The LVLH frame has the following unitary vectors $\{a_1, a_2, a_3\}$, with a_1 in the direction of the microsatellite velocity in the orbital plane, a_3 pointing to the Earth, and a_2 normal to the orbit plane.

To describe the orientation of the body-fixed frame B with respect of LVLH frame in terms of Euler angles, is used the following coordinate transformation

$$
\begin{bmatrix} \mathrm{i} \\ \mathrm{j} \\ \mathrm{k} \end{bmatrix} = \begin{bmatrix} c\theta c\psi & c\theta s\psi & -s\theta \\ s\phi s\theta c\psi - c\phi s\psi & s\phi s\theta s\psi + c\phi c\psi & s\phi c\theta \\ c\phi s\theta c\psi + s\phi s\psi & c\phi s\theta s\psi - s\phi c\psi & c\phi c\theta \end{bmatrix} \begin{bmatrix} a_1 \\ a_2 \\ a_3 \end{bmatrix}. \tag{2}
$$

The angular velocity of the body fixed frame B relative to the LVLH is given by

$$
\vec{\omega}^{B/A} = \omega_x^{B/A}\mathbf{i} + \omega_y^{B/A}\mathbf{j} + \omega_z^{B/A}\mathbf{k}, \tag{3}
$$

where

$$
\begin{bmatrix} \omega_x^{B/A} \\ \omega_y^{B/A} \\ \omega_z^{B/A} \end{bmatrix} = \begin{bmatrix} 1 & 0 & -s\theta \\ 0 & c\phi & s\phi c\theta \\ 0 & -s\phi & c\phi c\theta \end{bmatrix} \begin{bmatrix} \dot{\phi} \\ \dot{\theta} \\ \dot{\psi} \end{bmatrix}. \tag{4}
$$

The angular velocity of the body fixed frame B relative to the inertial frame N fixed in the Earth center becomes

$$
\vec{\omega} = \vec{\omega}^{B/N} = \vec{\omega}^{B/A} + \vec{\omega}^{A/N} = \vec{\omega}^{B/A} - n\vec{a}_2 \tag{5}
$$

where

$$
\begin{bmatrix} \omega_x \\ \omega_y \\ \omega_z \end{bmatrix} = \begin{bmatrix} 1 & 0 & -s\theta \\ 0 & c\phi & s\phi c\theta \\ 0 & -s\phi & c\phi c\theta \end{bmatrix} \begin{bmatrix} \dot{\phi} \\ \dot{\theta} \\ \dot{\psi} \end{bmatrix} - n \begin{bmatrix} c\theta s\psi \\ s\phi s\theta s\psi + c\phi c\psi \\ c\phi s\theta s\psi - s\phi c\psi \end{bmatrix}. \tag{6}
$$

n is the orbital frequency of the microsatellite.

For small attitude deviation from LVLH orientation, the following linearized attitude dynamics can be obtained

$$
\begin{aligned}
\omega_x &= \dot{\phi} - n\psi, \\
\omega_y &= \dot{\theta} - n, \\
\omega_z &= \dot{\psi} + n\phi
\end{aligned} \tag{7}
$$

2.1 Gravity Gradient Torque

In the space, the gravitational field is not uniform, so the variation in the gravitational field over the body yields the gravitational torque about of the center of mass of the body. On the assumption that the microsatellite center of mass is in a Keplerian circular orbit and the Earth is spherical, the gravity gradient torque along the body axes become

$$\begin{aligned} T_{gx} &= 3n^2(I_z - I_y)\phi, \\ T_{gy} &= 3n^2(I_z - I_x)\theta, \\ T_{gz} &= 0. \end{aligned} \quad (8)$$

Inserting the gravity gradient equations (8) into the Euler equations (1) and making a linearization, one has

$$\begin{aligned} I_x\ddot{\phi} - n(I_x - I_y + I_z)\dot{\psi} + 4n^2(I_y - I_z)\phi &= T_{ex} + u_x, \\ I_y\ddot{\theta} + 3n^2(I_x - I_z)\theta &= T_{e2} + u_y, \\ I_z\ddot{\psi} + n(I_{-}I_y + I_z)\dot{\phi} + n^2(I_y - I_x)\psi &= T_{e3} + u_z. \end{aligned} \quad (9)$$

These equations are the Euler equations for the microsatellite, from which one observes that the pitch axis is decoupled from the row and yaw axes.

3 Structured uncertainty

To represent the system uncertainty Δ it will be used Linear Fractional Transformation (LFT) [9]. As showed in Figure 1, using the LFT procedure the block transfer function from the perturbation signal w to error signal z is given by

$$z = [M_{22} + M_{21}\Delta(I - M_{11}\Delta)^{-1}M_{12}]\omega, \quad (10)$$

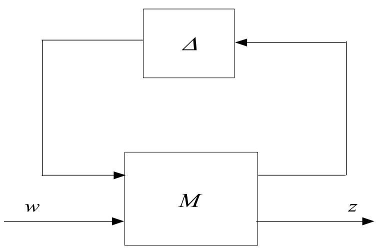

Figure 1. Uncertainty representation in LFT block diagram

The plant of the system can be represented by the block M which is given by

$$M = \begin{bmatrix} M_{11} & M_{12} \\ M_{21} & M_{22} \end{bmatrix}, \quad (11)$$

Considering that there is uncertainty in the principal moment of inertia of the microsatellite, it can be expressed as a nominal value plus a perturbation [7] given by

$$I_i = \bar{I}_i + p_i\delta_i, \qquad i = 1,2,3, \quad (12)$$

where p_i is the variation and δ_i the normalized uncertainty. Inserting it into the Euler equations, one has the dynamic equation with uncertainty. This uncertainty can be pulled out of the system and it can be considered like a disturbance.

Let´s do this calculation, initially, for pitch axis of the microsatellite which is decouple, d is the disturbing torque. As result, the equation of motion is given by

$$I_y\ddot{\theta} + 3n^2(I_x - I_z)\theta = u_y + d, \quad (13)$$

This equation of motion can be put in the block diagram as showed by Figure 2.

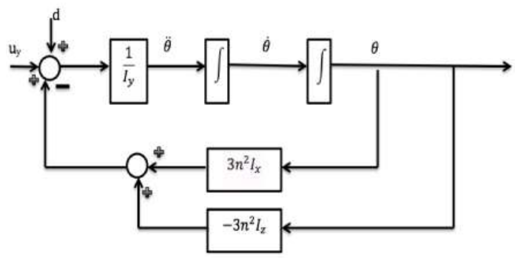

Figure 2. Block diagram of the pitch axis.

Using the Linear Fractional Transformation (LFT), the first block of the Figure 2 can be represented by

$$\begin{aligned} \frac{1}{I_y} &= \frac{1}{\bar{I}_y + p_y\delta_y}, \\ &= \frac{1}{\bar{I}_y} - \frac{p_y}{\bar{I}_y}\delta_y\left(1 + \frac{1}{\bar{I}_y}\delta_y\right)^{-1}\frac{1}{\bar{I}_y}, \end{aligned} \quad (14)$$

Comparing this equation with the LFT Equation (11) the first block will be

$$M_1 = \begin{bmatrix} -\frac{p_y}{\bar{I}_y} & \frac{1}{\bar{I}_y} \\ -\frac{p_y}{\bar{I}_y} & \frac{1}{\bar{I}_y} \end{bmatrix}. \quad (15)$$

Doing the same procedure for the second and the third block are given by

$$3n^2 I_x = 3n^2(\bar{I}_x + p_x\delta_x),$$

$$M_2 = \begin{bmatrix} 0 & 1 \\ 3n^2 p_x & 3n^2 \bar{I}_x \end{bmatrix}, \tag{16}$$

$$3n^2 I_z = 3n^2(\bar{I}_z + p_x\delta_z),$$

$$M_3 = \begin{bmatrix} 0 & -1 \\ 3n^2 p_z & -3n^2 \bar{I}_z \end{bmatrix} \tag{17}$$

As a result, the new block diagram for the pitch axis taking into account the uncertainty is as showed in Figure 3.

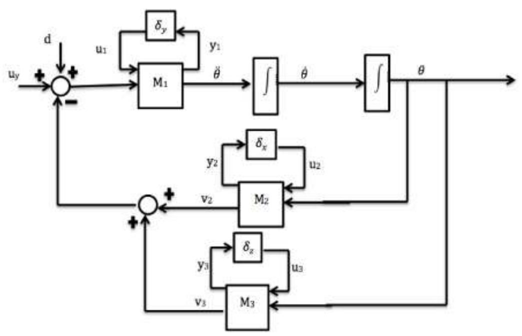

Figure 3. Pitch axis block diagram with uncertainty.

This representation helps to understand how the uncertainty acts in the system and how it can be lumped out of the system like a perturbation. Usually, the uncertainty is incorporated in the generalized plant in the diagonal form as it will be showed later.

The mixed design H_2/H_∞ approach [5] consist, initially, minimizing the perturbation effect of moment of inertia uncertainty (structured) by the H_∞ norm. On the other hand, the external disturbance uncertainty (unstructured) will be minimized by the H_2 norm. As a result, the closed loop system remains stable for external perturbation, which is associated with good performance, for example, quick time response and small overshot.

In order to include both kinds of uncertainties so as the controller designed presents good robustness and adequate performance the new generalized plant must has both signals that will be minimized. Here the generalized plant in matrix form is given by

$$\begin{bmatrix} \dot{\theta} \\ \ddot{\theta} \\ z_\infty \\ z_2 \\ y \end{bmatrix} = \begin{bmatrix} 0 & 1 & 0 & 0 & 0 & 0 & 0 \\ \frac{-3n^2(I_x-I_z)}{I_y} & 0 & -\frac{p_y}{I_y} & -\frac{3n^2 p_x}{I_y} & -\frac{3n^2 p_z}{I_y} & -\frac{1}{I_y} & -\frac{1}{I_y} \\ \frac{-3n^2(I_x-I_z)}{I_y} & 0 & -\frac{p_y}{I_y} & -\frac{3n^2 p_x}{I_y} & -\frac{3n^2 p_z}{I_y} & -\frac{1}{I_y} & -\frac{1}{I_y} \\ 1 & 0 & 0 & 0 & 0 & 0 & 0 \\ -1 & 0 & 0 & 0 & 0 & 0 & 0 \\ Q_1 & 0 & 0 & 0 & 0 & 0 & 0 \\ 0 & Q_2 & 0 & 0 & 0 & 0 & 0 \\ 0 & 0 & 0 & 0 & 0 & 0 & R \\ 1 & 0 & 0 & 0 & 0 & 0 & 0 \end{bmatrix} \begin{bmatrix} \theta \\ \dot{\theta} \\ u_1 \\ u_2 \\ u_3 \\ d \\ u \end{bmatrix} \tag{18}$$

In that case, one has the inputs (u1, u2, u3, u), the outputs (z_{oo}, z_2 , y), the state's x (θ, dθ/dt) and the perturbation d=w. As a result, the new state space model that include both kinds of design requirements is given by

$$\begin{aligned} \dot{x} &= Ax + B_1 w + B_2 u, \\ z_\infty &= C_1 x + D_{11} w + D_{12} u. \\ z_2 &= C_2 x + D_{22} u. \end{aligned} \tag{19}$$

As a result, the generalized plant P is given by

$$P = \begin{bmatrix} A & B_1 & B_2, \\ C_1 & D_{11} & D_{12}, \\ C_2 & D_{21} & D_{22} \end{bmatrix}, \tag{20}$$

4 The Mixed H_2/H_∞ Controller Theory

Figure 4 shows the block diagram of the mixed H_2/H_∞ control approach [5], where the above block represents the uncertainty, the medium block is the generalized plant and the below block is the controller to designed.

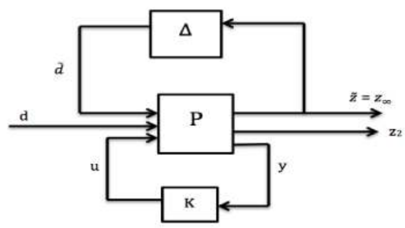

Figure 4. Block diagram of the general configuration.

As showed in [7] the mixed H_2/H_∞ control problem is equivalent to minimize Trace $T_r(Q)$ over the matrices $X=X^T$, $Q=Q^T$ and Y satisfying the Linear Matrix Inequalities [9] given by

$$\begin{bmatrix} AX-B_2+(AX-B_2Y)^T & B_1 & (C_1X-D_{12}Y)^T \\ B_1^T & -I & D_{11}^T \\ C_1X-D_{12}Y & D_{11} & \gamma^2 I \end{bmatrix} < 0,$$

$$\begin{bmatrix} Q & C_2X-D_{22}Y \\ (C_2X-D_{22}Y)^T & X \end{bmatrix} > 0.$$

Assuming that the LMIs above equations have solutions Y*, X*, Q*, the mixed H_2/H_∞ controller K* is given by

$$K^*=Y^*(X^*)^{-1} \qquad (21)$$

As a result, the mixed H_2/H_∞ controller design is a multi-objective control problem where the goal is to minimize the H_2 norm in order to improve performance subjected to the minimization of H_∞ norm to guaranty robustness requirement [9], which results in the two following expressions

$$Min. \|T_{z2w}\|_2 \leq \sqrt{trace(Q^*)} \qquad (22)$$

$$Subject \ \ \|T_{z\infty w}\|_\infty = \gamma \qquad (23)$$

4 Simulations and Results

The microsatellite used in the simulation has inertia moment I_x = 18.4 Kgm^2 , I_x = 18.2 Kgm^{2,} I_z = 6.8Kgm^2, its mass m = 60Kg and dimension = 50x50x60 cm. In the simulations, the initial attitude in roll, pitch, yaw are (10,10,10) degree and the initial angular velocity in roll, pitch , yaw are (0.6, 0.6, 0.6) degree/s.

In the mixed H_2/H_∞ controller design a key point is to find the appropriate values of γ. Besides, one must keep in mind that for $\gamma = \gamma_{min}$ one has the pure H_∞ control problem and $\gamma = \gamma_{max}$ one has the pure H_2 control problem. Here, just for simulations propose one decides to begin using $\gamma = 2$ to perform a comparative study.

As for the uncertainty, one assumes that the variation on the moment of inertia is about 10%. In order to obtain the maximum and the minimum uncertainty variations, one considers two kind of plant, given by:

Plant with uncertainty 1: $\Delta I_x = +10\% I_x$, $\Delta I_y = -10\% I_y$ and $\Delta I_z = -10\% I_z$

Plant with uncertainty 2: $\Delta I_x = -10\% I_x$, $\Delta I_y = +10\% I_y$ and $\Delta I_z = +10\% I_z$

Figures 5 shows the Euler angle of roll, pitch and yaw with uncertainty, where the dashed line represents the plant with uncertainty variation and the continues line the nominal plant without uncertainty. One can see that for pure H_∞ control ($\gamma = \gamma_{min} = 0.2 - blue\ line$) the controller is very robust with respect to uncertainty, because there is no difference between the nominal plant and the plant with uncertainty. On the other hand, it's noted that difference between the nominal plant and the plant with uncertainty increase for pure H_2 control ($\gamma = \gamma_{max} = 100 - red\ line$).

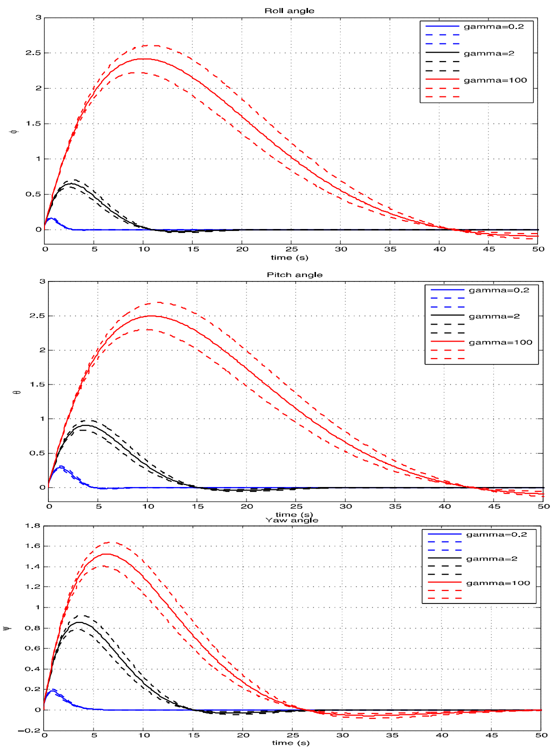

Figure 5. The mixed H_2/H_∞ controller for Euler angle of roll, pitch and yaw with uncertainty.

Figure 6 shows the mixed H_2/H_∞ controller signal for roll, pitch and yaw axes, where for pure H_∞ control (*blue line*), the controller signal has bigger overshot than for pure H_2 control (*red line*), which represents the drawback between its robustness and performance. Considering that the microsatellite actuator must have small torque the mixed H_2/H_∞ control with $\gamma = 2$ is a good choice to design the controller, because it is not so slow like pure H_2 and the control signal is not so strong like pure H_∞ control.

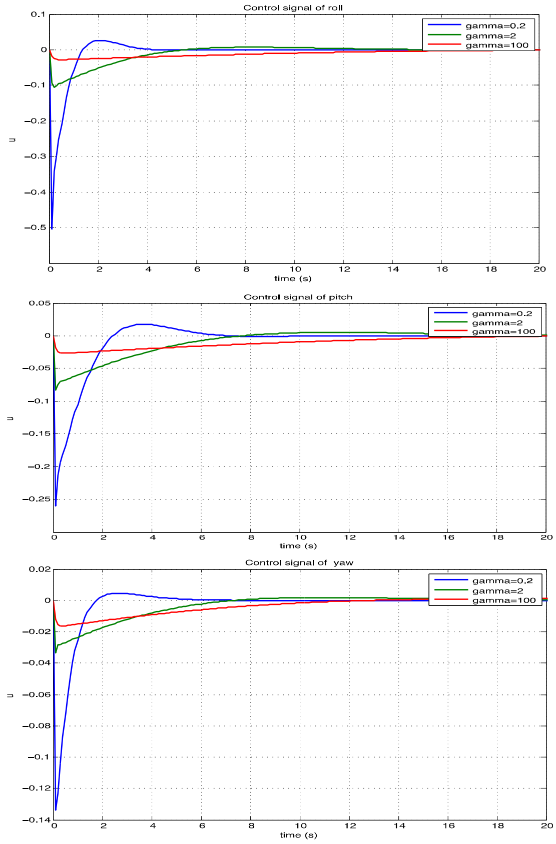

Figure 6 – The mixed H_2/H_∞ controller signal for the roll, pitch and yaw axes

Spacecraft is subjected to small disturbances on the space, and these disturbances can be persistent. In the case of a low orbit the microsatellite is more subject to disturbances due to the gravity gradient, magnetic and aerodynamic torques. The gravity gradient torque is included into the equations, the magnetic torque is cyclic and can be approximated by sinusoids with different frequencies and the aerodynamic torque is cumulative and can be approximated to a step. As result, one has assume that these torque can be represented by the following equation [8]

$$T_{ext} = \sum_k 10^{-5}\mathrm{sen}(knt) + 3\times 10^{-5}[\sigma(t-1000) - \sigma(t-4000)] \quad (24)$$

Figure 7 shows the Euler angles (roll, pitch, yaw) for pure H_∞ control (*blue line*), the mixed control H_2/H_∞ ($\gamma = 2$ – black *line*) and the pure H_2 control (*red line*). One observes that the pure H_∞ control has the best capacity of attenuation with respect to a sinusoidal disturbance. The pure H_2 control is not robust with respect to a sinusoidal disturbance. In order to have a good balance control between robustness and performance it's necessary choose some values of γ such that the mixed control H_2/H_∞ provide a good performance even with the perturbation of the external torques. Again the best mixed control H_2/H_∞ controller value for γ *is* 2.

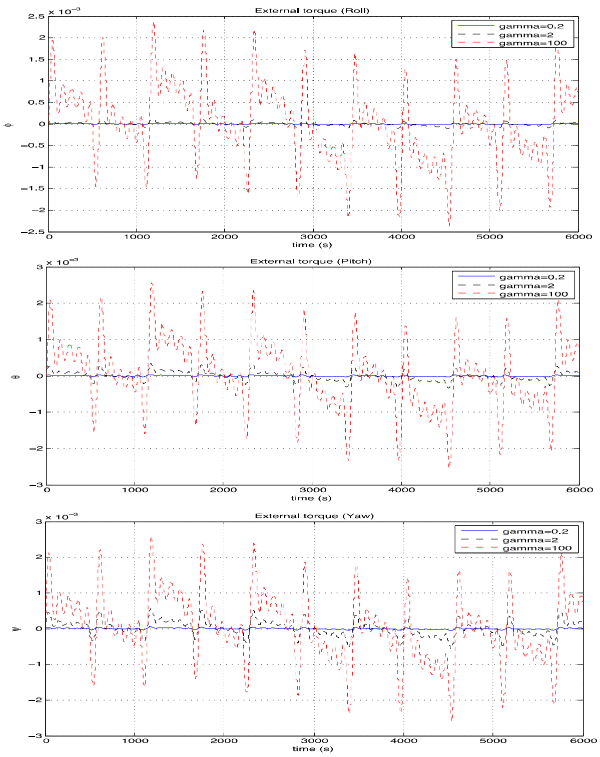

Figure 7. The mixed H_2/H_∞ controller response to external torques for roll, pitch and yaw axes.

5 Conclusion

This paper presents a microsatellite model taking into account the uncertainties and the design of the satellite control system based on the mixed H_2/H_∞ methodology via LMI optimization. This control technique is used to design the microsatellite attitude control system in the face of environmental disturbance (unstructured uncertainty) and moment of inertia variation (structured uncertainty). It is well know that the H_∞ controller provides robust stability with respect to structured uncertainty while the H_2 controller provides good performance with a respect to unstructured uncertainty. Here, one investigates the conjunction of the both methods in order to improve the performance and robustness of the SAC system. To do this, one assumes that the microsatellite is subjected to uncertainty in the moment of inertia variation of about 10% and environmental disturbances were approximated to sinusoidal function plus a step function. The simulations have shown that the H_∞ controller has presented best robustness and performance than the H_2 controller with respect to uncertainty due to inertia moment variation and due external disturbance. However, in all simulations the H_∞ controller signal was bigger than the H_2 controller, which can cause bigger overshot and can saturate the actuator, once microsatellite usually need small actuator. As a result, the way to achieve robustness stability and good performance was to design the controller using the mixed H_2/H_∞ control, because in this procedure one can choose an adequate value for the tuning parameter γ so as one can have robust control and with low control signal.

Referencies

[1] Cubillos, X. C. M. ; Souza, L. C. G. Using of H-Infinity Control Method in Attitude Control System of Rigid-Flexible Satellite. Mathematical Problems in Engineering, v. 2009, p. 1-10, 2009.

[2] Mainenti, I ; Souza, L. C. G. ; Souza, F L . Design of a nonlinear controller for a rigid-flexible satellite using multi-objective Generalized Extremal Optimization with real codification. Shock and Vibration, v. 19, p. 1-10, 2012.

[3] Souza, L. C. G. ; Gonzalez, R G. Application of the state-dependent Riccati equation and Kalman filter techniques to the design of a satellite control system. Shock and Vibration, v. 19, p. 22-28, 2012.

[4] D. S Bernstein. and W. M. Haddad, LQG control with an H_∞ performance bound: A Riccati equation approach. IEEE Transac- tions on Automatic Control, 34(3), 293–305, 1989.

[5] P. P. Khargonekar and M. A. Rotea, Mixed H_2/ H_∞ control: A convex optimization approach. IEEE Transactions on Automatic Control, 36(7), 824–837, 1991.

[6] Sales, T.P. ; Rade, D.A. ; Souza, L.C.G. . Passive vibration control of flexible spacecraft using shunted piezoelectric transducers. Aerospace Science and Technology, v. 1, p. 12-26, 2013.

[7] C. Yanga and P. Sun, Mixed H_2/ H_∞ state-feedback design for microsatellite attitude control, Control Engineering Practice, Vol 10, pp. 951–970, 2002.

[8] J. R. Wertz and W.J. Larson, Space Mission Analysis and Design, Microcosm Press, California. 1989.

[9] S. Boyd, L. El Ghaoui, E. Feron, V. Balakrishnan, Linear matrix inequalities in system and control theory, SIAM studies in applied mathematics. Philadelphia, PA: SIAM. 1994.

4:th CEAS Air & Space Conference
FTF Congress: Flygteknik 2013

The Effect of Engine Dimensions on Supersonic Aircraft Performance

Alvaro Abdalla
USP/Sao Carlos, Brazil

Henrique Gazetta
ITA, Brasil

Tomas Grönstedt
Chalmers Technical University, Sweden

Petter Krus
Linköping University, Sweden

Keywords: *aircraft design, engine design, co-design, system simulation*

Abstract

In aircraft design a critical part of the design is the engine selection. This is typically making a selection from exiting engines. Looking at a next generation future fighters, however, where the time of deployment may be 20-30 years in the future this is not a valid approach as there will be an evolution in the engine designs. E.g. a new European fighter aircraft will most likely be a collaborative project also involving the development of an engine for that aircraft. In this study conceptual engine-airframe co-design is demonstrated, using models of comparable fidelity for both the engine design and the aircraft design. This co-design leads to a deeper understanding of the tradeoffs from both sides, and means that also more radical designs and innovations can be evaluated in a fair way.

1 Introduction

When it comes to an aircraft, the important characteristics of an engine are the thrust, the specific fuel consumption, the dimensions and the weight. One parameter of critical importance is the engine diameter [5]. This will have a great influence on trust and fuel consumption. At the same time the engine diameter influence the maximum cross section area of the aircraft; this in turns has a strong influence on the wetted area and on the wave drag in supersonic flight.

As a baseline for this study the GE F100-129 is used. The aircraft under study is a representation of the F-16, since a lot of data are available in the open literature.

2 Estimation of Engine Performance

In order to support the aircraft aerodynamics evaluation a model was generated to provide engine performance, weight and main dimensions to the aircraft design tool. The baseline engine model was developed in GasTurb software from GasTurb Gmbh, using the GE F110-129 public information (mainly at sea level static condition). The main objective of the baseline engine model was to be representative of the selected engine in terms of performance, weight and dimensions in order to able to reproduce, along with an accurate aerodynamic aircraft model, the F16 performance, weight and dimensions. Once the performance, geometry (max diameter and length) and weight matched satisfactorily (within 3% from the real engine public data) a set of performance data was generated containing engine thrust and fuel flow for all the different engine ratings to be considered during a mission fuel burn evaluation: Max (afterburner on and off), idle and intermediary thrust tables for interpolation.

Two other sets of performance tables were generated similarly to the previously described ones, but with different inlet mass flow and, therefore, different fan sizes. The baseline engine model was modified to run one bigger and one smaller engine (plus and minus 5% in fan diameter). All the others engine parameters were kept constant, so the engine thermodynamic cycle is exactly the same in the three data packages. This two additional data packages were generated in order to feed the aircraft design tool with different size engines and the tool would be able to run new designs and evaluate effects of the different engines in the aircraft design, weight and performance.

The thrust and specific fuel consumption (SFC) without afterburners for the different diameters at Mach 1.2 are shown below at some representative points.

Altitude	Mach	Fan speed	Net Thrust	SFC
10000	1.2	100%	34.5669	26.25763
10000	0.8	60%	6.781307	33.66098
10000	1.2	100%	38.16762	26.25763
10000	0.8	60%	7.487693	33.66098
10000	1.2	100%	31.25424	26.25763
10000	0.8	60%	6.131432	33.66098

Table 1. Net thrust and SFC for two representative operating points and with different diameters.

3 Aerodynamic Performance Estimation.

3.1 Geometric modeling

In order to have a representative 3D model it is necessary to present in detail all parts and components such as an aircraft fuselage, wings, aerodynamic surfaces of lift and control, landing gear and other parts.

Concerning the representation of an existing aircraft such as the F-16, which is the case study of this work, also the engine inside the fuselage is included, and the geometry of the fuselage in the region jet engine must be able to vary to follow variations in the engine diameter.

For a fast and efficient establishment of the complete F-16 configurations, a software was developed to interface between Microsoft Visual Basic and Dassault System Solid Works, and also to the Hopsan simulation software. This software can quickly generate various aircraft configurations to capture the geometry and inertial characteristics.

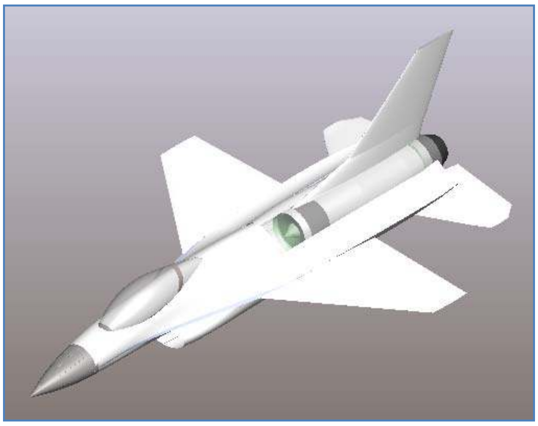

Figure 1. Geometric model of F-16.

3.2 Aerodynamic Drag Estimation

The aircraft cross-sectional distribution areas are calculated of each F-16 aircraft component and are exported automatically to an Excel spreadsheet tables and corresponding graph.

To obtain supersonic drag, three different analytical methods where used. They are described in references [1], [3], [3]. Induced drag and supersonic lift is calculated using approaches in [8], [9], [10] and [11]. Figure 1 shows the parts of the aircraft, designed by the program.

The diameter of the GE F110-129 afterburning turbofan was changed to plus five percent and minus five percent of the original engine diameter. This resulted in the parameters below.

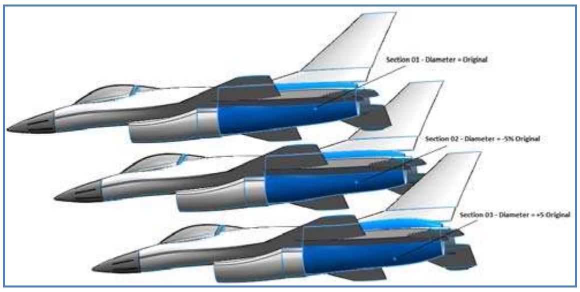

Figure 2. Fuselage with varying diameter for the engine section.

3.3 Wave Drag Coefficient

The drag coefficient for supersonic flight regime corresponding to the Mach numbers 1.05, 1.20 and 2.00, are shown in Table 2. The nominal value could be validated against the actual F-16 configuration from reference [7].

	M = 1.05	M = 1.2	M = 2.0
CDO nominal aircraft	0.047621	0.043627	0.032913
CDO +5% Diameter fuselage	0.049013	0.045027	0.03432
CDO -5% Diameter fuselage	0.046241	0.04224	0.031518

Table 2. Drag coefficients for different engine diameters and Mach numbers.

4 Mission Simulation

For evaluating the performance of the aircraft in a realistic scenario a system simulation model was built that could be used in a mission simulation. The flight dynamics model is here based on a 6 degree of freedom rigid body model that is connected to an aerodynamic model. The aerodynamic model can have different number of wings, with an arbitrary number of control surfaces, and a body with its characteristics. It is here based on a static version of the model presented in [9], although the unsteady effects can of course also be included.

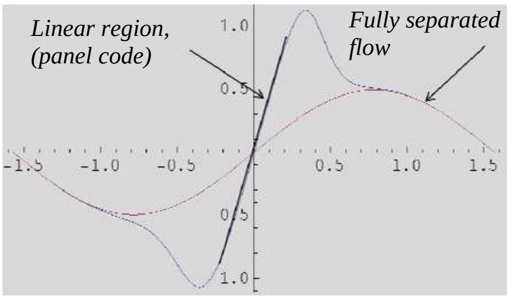

Figure 3. Non-linear aerodynamic model.

The control surfaces are modeled both with a linear increase of lift force with deflection and the corresponding increase in induced drag. There is also a cross coupling effect of drag for control surfaces on the same wing e.g. ailerons and flaps. In this way also the effect of trim drag on performance is automatically included, and the effect of reduced weight as fuel is consumed.

The engine model is essentially a look up table that interpolate between the calculated values delivered from the engine model in the GasTurb software. An intake loss of 5% was also added.

The simulated is a high altitude intercept mission with a minimum load out. The outgoing leg is at maximum throttle without afterburner. Since the engine is the most powerful version of the GE F110 this results in a supersonic cruise at about Mach 1.2. The F16 is not normally considered to have very limited supersonic cruise capability, and even this combination would have difficulty to have the capability with a reasonable load out. However, it makes it interesting as this study is used to give some validation for a conceptual tool that will be used to study future aircraft that are likely to be required to have super cruise capability.

The simulation model was built in the free Hopsan simulation software [3] that is being developed at Linköping University. It is an object oriented system where hierarchical system models can be build an connected to each other using power ports.

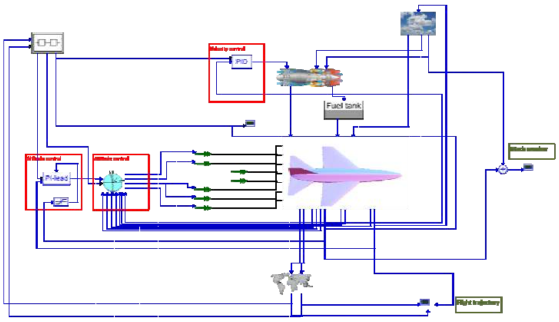

Figure 4. System simulation model in Hopsan.

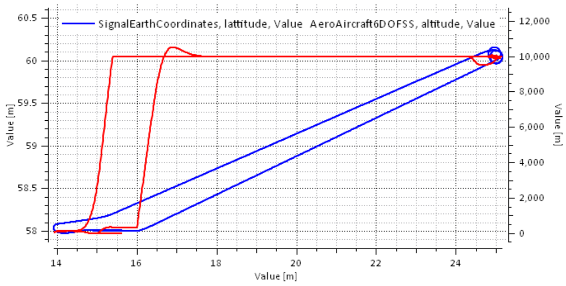

Figure 5. Simulated combat mission with high speed outgoing and subsonic cruise to return.

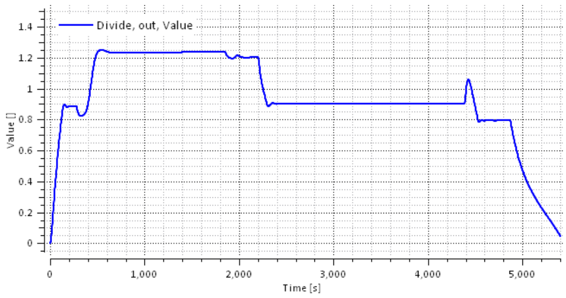

Figure 6. Speed profile (Mach number) for F-15 baseline configuration.

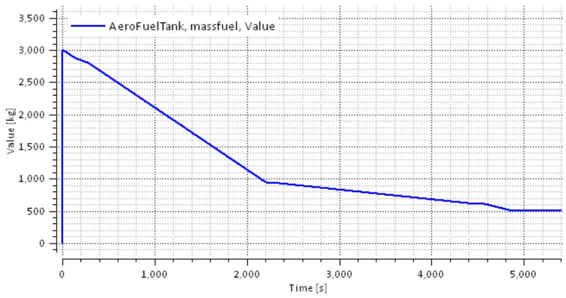

Figure 7. Fuel mass for F-16 baseline configuration.

By simulating the mission for the three cases the variations in functional characteristics can be studied. Of particular interest in this case is the speed of the outgoing leg at maximum throttle in the mission, and the consumed fuel during the whole mission.

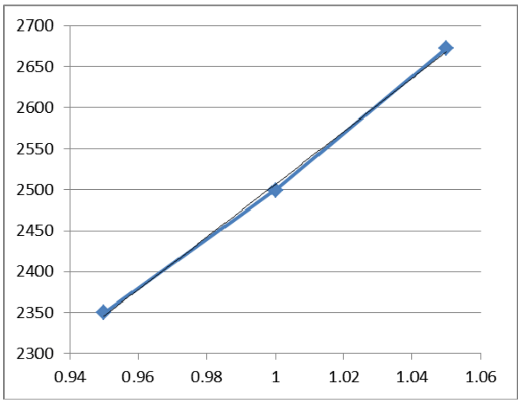

Figure 8. The mission fuel (kg) as a function of normalized engine diameter.

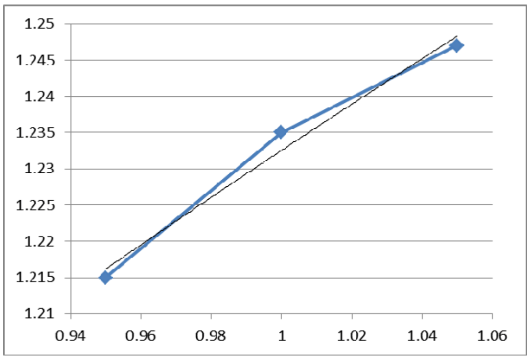

Figure 9. Max Mach number as a function of normalized engine diameter.

Making a curve based on the diagrams above yields

$$m_{fc} = 2506 d^{1.286} \quad (1)$$

$$M = 1.232 d^{0.26} \quad (2)$$

Combinng these the consumed fuel can be obtained as a function of the Mach number as:

$$m_{fc} = 891.8 M^{4.942} \quad (3)$$

This curve is plotted in Figure 10.

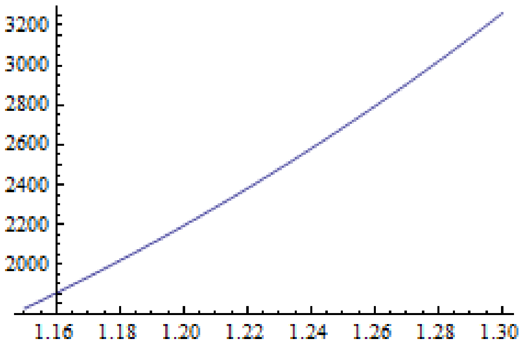

Figure 10. Consumed fuel over the mission as a function of maximum dry Mach number.

This means that the fuel consumption is proportional to almost the power of five of the Mach number, in this nominal point. The reason is probably that an increase of the cross section area of the aft body is very unfavorable to the area distribution and therefore has a detrimental effect on wave drag.

5 Discussion

The results from the variation of engine diameter shows that the maximum speed increase if the diameter increases. The corresponding increase in drag is not enough to offset that. However, looking at the fuel consumption it is apparent that this increases a lot more than the speed. A reduction of engine diameter therefore yields a substantial improvement in fuel economy and range, at the cost of a marginal decrease in performance.

It should be noted, however, that the mission presented here is hardly the design mission as there is a minimal load out, and this particular configuration with the clean airframe with the GE F110-129 does not represent to our knowledge represent an existing aircraft as the only F-16 block 60 using this engine also have conformal fuel tanks that would give a substantial increase in drag and wave drag in particular. Furthermore, the relationship derived here is very much depending on the geometry of the aircraft, e.g. the area distribution and does not necessarily apply to other aircraft. What is demonstrated here is a methodology to arrive at these relations.

6 Conclusions

The study demonstrates, however, that it is useful and possible to consider engine airframe co-design in preliminary design in order to have an estimate of the best engine dimensions already in conceptual design.

7 Acknowledgements

This study was partly funded through CISB/CNPq-Brazil scholarships.

8 Conclusion

The results of this study show that it should be possible to design a aircraft comparable to the F-16 with increased supercruise capability if the engine diameter is increased. Although this has negative effects on the increased wetted area and increased wave drag in supersonic flight, and hence dramatically increased fuel consumption. The study shows, however, that it is very important to optimize the engine parameters together with the airframe.

References

[1] Raymer, D. P., Aircraft Design: A Conceptual Approach, AIAA Series, Third Edition 1999.

[2] R. Stiles, and J. Bertin, United States Air Force Academy S. Brandt, Cranfield Institute of Technology and R. Whitford. Introduction to Aeronautics: A Design Perspective, 2nd Edition, AIAA Education Series.

[3] Roskam, J., Airplane Design Part IV Preliminary Calculation of Aerodynamic, Thrust and Power Characteristics, The University of Kansas, Lawrence 2000.

[4] Krus, P., Braun, R. & Nordin, P., 2012. Aircraft System Simulation for Preliminary Design. In *28th International Congress of the Aeronautical Sciences*. Brisbane: ICAS. Available at: http://www.icas.org/ICAS_ARCHIVE/ICAS2012/.

[5] Jouannet C., Krus P. ‘Unsteady aerodynamic modelling: a simple state-space approach’. *AIAAA Aerospace sciences meeting and exhibit*,2005 Reno, USA.

[6] David L. Daggett, Stephen T. Brown, Ron T. Kawai, Ultra-Efficient Engine Diameter Study, NASA/CR—2003-212309, Boeing Commercial Airplane Group, Seattle, Washington.

[7] D. Boucher, H. Guillot, Experimental Drag Polar of the F-16 Falcon Using Wind Tests, Ecole de l'Air, Salon-de-Provence, F-133001, Ecole de l'Air, Salon-de-Provence, F-133002.
[8] Mike C. Fox, Dana K. Forrest, Supersonic Aerodynamic Characteristics of an Advanced F-16 Derivative Aircraft Configuration, NASA Technical Paper 3355, June 1993.
[9] Raymond L. Barger, Mary S. Adams, Fuselage Design for a Specified Mach-Sliced Area Distribution, NASA Technical Paper 2975, Langley Research Center, Hampton, Virginia.
[10] Robert M. Hall, Impact of Fuselage Cross Section on the Stability of a Generic Fighter, NASA Langley Research Center, Virginia
[11] Whitcomb, R.T., A Study of the Zero-Lift Drag-Rise Characteristics of Wing-Body Combinations Near the Speed of Sound, NACA Rept. 1273, 1956.

4:th CEAS Air & Space Conference
FTF Congress: Flygteknik 2013

Finite Element Model Correlations and Response Predictions of Spacecraft Structure

K.K. Sairajan, G.S. Aglietti, and Scott JI Walker
University of Southampton, Southampton, England

Keywords: *Finite Element Model, Structural Dynamics, Model Correlation, Frequency Response, Base Force Assurance Criterion.*

1 Abstract

Finite Element Models (FEMs) are widely used to predict the behaviour of a complex structure such as a spacecraft before its realization. The capability of the model to accurately predict the performance of the actual system is vital for the successful completion of the mission and hence it is assessed by comparing the analytical results with the experimental data. Modal Assurance Criterion (MAC) and Normalised Cross Orthogonality (NCO) check are the most commonly employed methods in the space industry for the validation of FEMs. In order to match the degrees of freedom of analytical and experimental models, a test-analysis model is used in the NCO.

In this study, Monte Carlo simulations were used to determine the robustness of a System Equivalent Reduction Expansion Process (SEREP) based test-analysis model when experimental and analytical modes of different spacecraft contain various levels of inaccuracy. It has been observed that, the probability to clear the NCO check is determined mainly by the number of modes used in the SEREP reduction.

The effectiveness of MAC and NCO criteria on the response prediction of spacecraft models under the base excitation is also carried out. It is observed that neither MAC nor NCO is suitable to predict the forced response characteristics such as the peak acceleration response. Then, a criterion termed as Base Force Assurance Criterion (BFAC) is defined using the experimentally determined dynamic force at the base and the finite element predicted force in a similar way as MAC was defined. In this study, the results obtained from the real FEM of the spacecraft were taken as the experimental results and those obtained from intentionally erroneous FEMs were considered as the analytical results. The method is applied to assess the performance of different spacecraft models under base excitation and observed that BFAC can correlate the acceleration error in a better way than MAC or NCO.

2 Introduction

The modal assurance criterion [1] and normalised cross orthogonality [2] check are the accepted criteria in the space industry to assess the accuracy of the finite element model of the spacecraft [3, 4]. An accurate FEM is required as these FEMs are used in the coupled load analysis of the spacecraft and the launch vehicle, to determine the accurate loading on the structure. In addition, the dynamic testing of the coupled system in practice is limited due to the problems in representing the actual loading condition and the large size of the launch vehicle [5]. Hence, the analytical calculated coupled analysis results using the FEMs of spacecraft and launch vehicle are the primary option to verify the design margins.

Typically, launch agencies gives the minimum thresholds for the parameters of the correlation and a mathematical model that satisfies these specifications is deemed to be validated and assumed to give predictions that are sufficiently accurate and fit for purpose. If the FEM does not comply with the requirement, a model updating procedure is initiated to modify the FEM until it meets the requirement. This procedure can be quite time consuming and expensive. Hence, it is necessary to make sure that, the correlation method is meaningful for the required purpose; otherwise, model updating may improve the validation, but produce an inferior FEM in terms of the capability to predict the important characteristics such as responses.

Although there are response correlation methods such as frequency response assurance criterion [2, 6] and frequency domain assurance criterion [7], these correlation methods directly compares the frequency responses; typically in the spacecraft industry, modal reductions and mode superposition techniques are used in the analyses, therefore the quality of the FEM is generally verified using a modal approach. In addition, performing these response assurance criteria at many locations, as in the case of spacecraft structure, is a tedious task and the results of the correlation are highly affected with the shift in the natural frequencies, which are very common in complex structures.

In this paper, the usefulness of the MAC and NCO check for the prediction of forced response under base excitation is evaluated using two spacecraft models. To perform the NCO check, a System Equivalent Reduction Expansion Process (SEREP) [8] reduced mass matrix is used. The effect of number of modes on the SEREP reduction is performed using Monte Carlo simulations. To perform the base excitation analysis, the results obtained from the nominal FEM is taken as 'true' or experimentally determined data set and those obtained from the intentionally erroneous FEMs were considered as the analytical data set. The erroneous FEMs were generated from the nominal FEMs by changing the number of joints and stiffness, which simulates the common modelling inaccuracies. The total mass of the system is unaltered. The usefulness of the Base Force Assurance Criterion (BFAC) for correlating FEMs of the spacecraft for base excitation is also investigated.

3 Theoretical Aspects

The MAC and the NCO check can be performed using the nominal or 'true' mode, $\boldsymbol{\psi}$ and erroneous finite element mode, $\boldsymbol{\phi}$ using the equations [2]:

$$MAC_{lm} = \frac{\left|\boldsymbol{\psi}_l^T \boldsymbol{\phi}_m\right|^2}{(\boldsymbol{\psi}_l^T \boldsymbol{\psi}_l)(\boldsymbol{\phi}_m^T \boldsymbol{\phi}_m)} \qquad (0)$$

$$NCO_{lm} = \frac{\left|\boldsymbol{\psi}_l^T \boldsymbol{M}_{TAM} \boldsymbol{\phi}_m\right|^2}{(\boldsymbol{\psi}_l^T \boldsymbol{M}_{TAM} \boldsymbol{\psi}_l)(\boldsymbol{\phi}_m^T \boldsymbol{M}_{TAM} \boldsymbol{\phi}_m)} \qquad (0)$$

respectively. Here, $\boldsymbol{M}_{TAM}$ is the SEREP reduced Test Analysis Model (TAM), superscript T represents the transpose and the subscripts l and m varies from one to the number of target modes. The SEREP TAM can be computed using the normalized modal matrix, $\boldsymbol{\psi}$ as:

$$\boldsymbol{M}_{TAM} = (\boldsymbol{\Psi}^{\dagger})^T \boldsymbol{\Psi}^{\dagger} \qquad (0)$$

where $\boldsymbol{\psi}^{\dagger}$ is the generalized inverse [9] of the modal matrix $\boldsymbol{\Psi}$.

Generally, the spacecraft structure is qualified by fixing the base of the structure to a shaker or slip table and exciting the base with a sine sweep. The response at the important locations on the spacecraft and the natural frequencies of the system are observed during the dynamic test. The transmitted force to the base can also be measured during the test using a force measuring device and this force can be analytically determined using the Craig-Bampton method [10, 11]. Then, the transmitted force, $\boldsymbol{F}$ to the base, by neglecting the shaker and the rigid body motion, can be computed as:

$$\boldsymbol{F} = (\boldsymbol{M}_{Bm}\ddot{\boldsymbol{q}}_m)^T \qquad (0)$$

where $\boldsymbol{M}_{Bm}$ is the Craig-Bampton reduced couple mass matrix and $\ddot{\boldsymbol{q}}$ is the modal acceleration.

The base force assurance criterion is defined using the nominal transmitted force to the base, $\boldsymbol{P}$ and the corresponding absolute analytical value, $\boldsymbol{F}$ using the equation [12]:

$$BFAC_{jk} = \frac{\left(P_j^T F_k\right)^2}{\left(P_j^T P_j\right)\left(F_k^T F_k\right)}. \qquad (0)$$

It should be noted that both $\boldsymbol{P}$ and $\boldsymbol{F}$ are functions of frequency and their absolute values are used in the computation. In this work, a statically determinate structure (single or rigidly connected boundary) is considered, and hence, the subscripts j and k varies from 1 to 6 and this gives a square BFAC matrix of size six. Each diagonal term in the BFAC matrix corresponds to the respective DOF in the boundary set and can be observed that the diagonal values vary between 0.0 and 1.0. A diagonal value of 1.0 indicates a perfect correlation between the experimentally determined and the analytically predicted base or transmitted force in the corresponding direction. The transmitted force can be experimentally determined using a base shake test using the force measuring devices.

4 Results and Discussions

4.1 Spacecraft Models

Two different classes of spacecraft models were considered in this study and these models are shown in Fig. 1. The figure also shows the axis system, seven response locations and the relative sizes of two structures. Spacecraft 1 represents a mini spacecraft with a mass of 75.7 kg whereas Spacecraft 2 represents a medium size spacecraft and has a mass of 300 kg. This FEM was developed by Surrey Satellite Technology Limited (SSTL), UK.

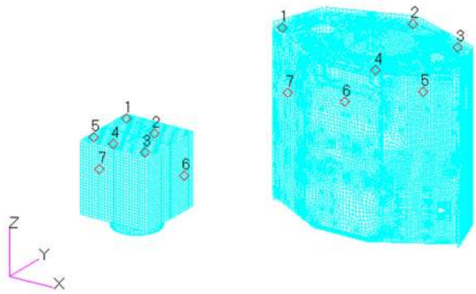

a) Spacecraft 1 **b) Spacecraft 2 (SSTL UK Ltd)**

Fig. 1 Spacecraft Finite Element Models and Axis System.

4.2 Effect of Number Modes in the SEREP Reduction

The robustness of the SEREP to the inaccuracies in the mode shapes have been performed using different spacecraft models [13]. When inaccuracies are present in both experimental and analytical modes, the probability of passing the NCO check is shown in Fig. 2. These probabilities were computed using 1000 Monte-Carlo simulations using the mode shapes of Spacecraft 1 with a simple multiplicative noise in the mode shapes. Eleven target modes in the 0.0-150 Hz were used in this analysis and each mode shape had 99 elements, representing 33 txi-axial accelerometer locations.

It can be seen that, as the Number of Modes in the Reduction (NMR), increase from the minimum number (11 target modes) to the maximum (99), the probability of passing the NCO drastically reduces. A value of NMR=99, even for a very small inaccuracy (0.1%), leads to a complete failure of the NCO check. It should be noted that such a low inaccuracy is very difficult to avoid in practical situations. Hence, it will be better to include only the target modes in the SEREP reduction for the NCO check.

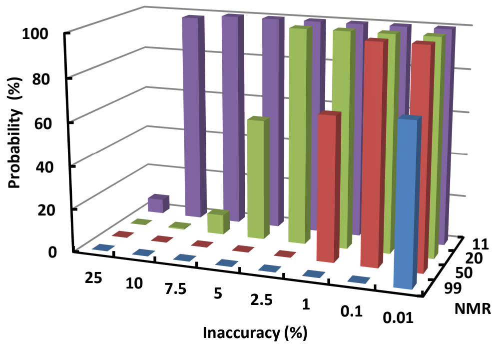

Fig. 2 Probability of NCO check success when inaccuracies are present in both FEM and experimental modes.

4.3 Standard Correlation Methods and Response Predictions of Spacecraft Structure

Generally, the MAC and NCO check are performed to qualify the FEMs of spacecraft structures [3, 4]. The usefulness of these criteria on the prediction of the base excitation response is studied using two spacecraft models (shown in Fig. 1). The peak absolute acceleration in the *Y* direction at seven different locations of both the spacecraft has been computed using the nominal and 12 erroneous FEMs of each spacecraft whilst the structure is excited at the base with *1g* acceleration. Here, g is acceleration due to gravity (9.81 m/s^2).

The percentage error in the acceleration, $Error_{Acc}$ with respect to the nominal value is calculated using the equation:

$$Error_{Acc} = \left| \frac{acc_{Nom} - acc_{FEM}}{acc_{Nom}} \right| 100 \qquad (0)$$

where, acc_{Nom} is the peak value of the nominal absolute acceleration in the 0.0-100 Hz range and acc_{FEM} is the peak value of the absolute acceleration in the frequency range calculated using the intentionally erroneous FEM. The average error in peak acceleration is then computed based on the values observed at the seven different locations. Based on the analysis of the nominal FEM, it was observed that there are three target modes for Spacecraft 1 and seven for Spacecraft 2 in the frequency range of 0.0-100.0 Hz. The target modes were selected based on the criteria specified by Chung and Sernaker [14]. The average MAC values of these target modes were determined for both nominal and erroneous FEMs.

The variation of the average acceleration error in the *Y* direction with average MAC values of the target modes for Spacecraft 1 and 2 are shown in Fig. 3. The average MAC values of Spacecraft 1 are higher than that of Spacecraft 2. This shows that, Spacecraft 2 models have more deviations in the mode shapes from the nominal modes than the other model. It should also be noted that there were seven target modes for Spacecraft 2 and hence correlations will be difficult than the Spacecraft 1. Fig. 3 also shows that, a specific value of MAC unable to indicate the possible error in the acceleration. A small change in the MAC value (0.1) may result in drastic change (as high as two times in Spacecraft 2) in the acceleration response. It can also be seen that, sometimes models with lower MAC values are better in predicting the response than the model having higher MAC. Thus, meeting the MAC specification need not always guaranty that such FEM can reasonably well predict the acceleration response under base excitation.

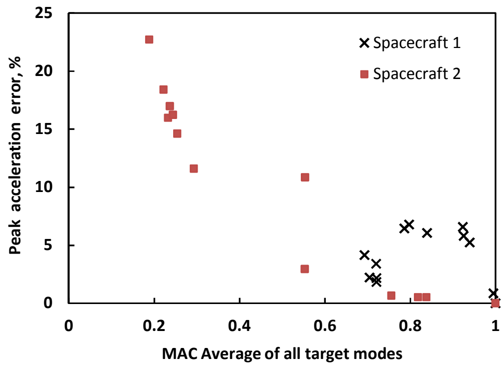

Fig. 3 Variation of the peak acceleration error with MAC values for two spacecraft models.

The variations of the average peak acceleration response error with the NCO diagonal average values are shown in Fig. 4. It can be observed that, occasionally models with almost the same NCO value can give different levels of accuracy in the response predictions. As in the case of MAC, the NCO check also fails to give a good indication about the FEM capability to represents the response characteristics.

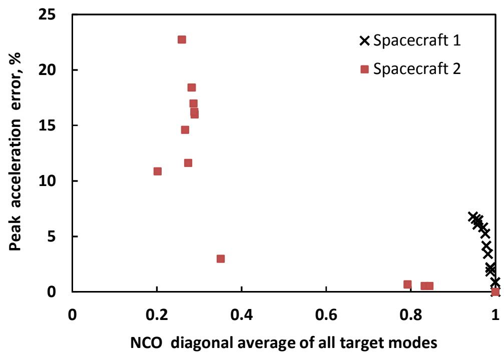

Fig. 4 Variation of peak acceleration error with NCO values for two spacecraft models.

4.4 Base Force Assurance Criterion and Frequency Response

It has shown that the MAC and NCO check are not suitable to represent the FEM's capability of predicting the response. This is primarily because, these are mode shape (vector) correlation methods and sometimes even if the mode shapes remain same, the frequency of vibration and the effective mass of the modes differ. This leads to the change in the structural response, but both MAC and NCO may indicate a high correlation. However, the force transmitted to the base depends on the effective mass of the modes and vary with the frequency. The variation of the average peak response in the *Y* direction with the BFAC diagonal average for both the structures is shown in Fig. 5.

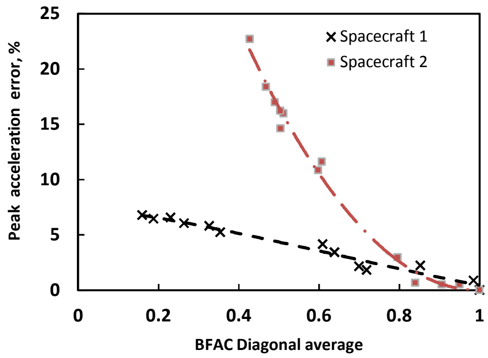

Fig. 5 Variation of peak acceleration error with the BFAC average values for the excitation in Y direction.

It can be observed that a specific value of BFAC always indicates a particular percentage of error in the acceleration response (Fig. 5). Also, for the examples considered, a BFAC value of 0.8 or above ensures that the error in the acceleration response is less than 5%.

The BFAC values and the absolute acceleration response in the *X* direction at the same seven locations shown in Fig. 1, were also calculated whist the spacecraft models are excited with *1g* in the *X* direction. The corresponding plot is shown in Fig. 6 for both the spacecraft models. It can be seen that BFAC gives a reasonably good correlation with the acceleration response irrespective of the direction of excitation. Hence, BFAC can be used as a correlation method for spacecraft structures under base excitation.

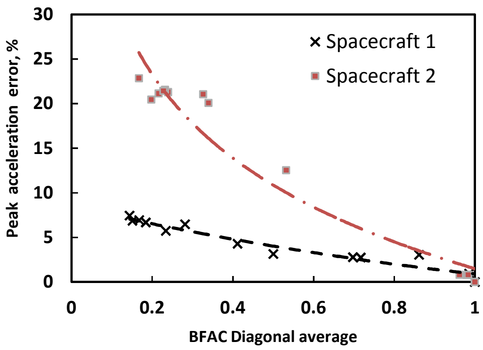

Fig. 6 Variation of peak acceleration error with the BFAC average values for the excitation in X direction.

5 Conclusion

The FEM of a spacecraft structure is conventionally correlated using MAC and NCO checks and it is considered that if the model reaches or exceeds a threshold value, it is a suitable representation of the actual system. For the NCO check, only the target modes were used in the SEREP TAM as more modes in the SEREP deteriorate the NCO correlation. It is shown that using nominal and intentionally erroneous FEMs of two different classes of spacecraft structures; neither the MAC nor NCO check ensures the capability of the model to predict the structural response under base excitation. The base force assurance criterion is found to be a useful tool to correlate the FEMs under base excitation and for the examples considered in this study, a BFAC average value of 0.8 or above always ensures that the error in the acceleration response is within 5%, which is an acceptable value for most practical applications.

Acknowledgment

The authors gratefully acknowledge G. Richardson, Surrey Satellite Technology Limited, UK for providing the spacecraft FEM for this study.

References

[1] Allemang, R. J., and Brown, D. L., "A Correlation Coefficient for Modal Vector Analysis", Proceedings of *1st International Modal analysis Conference*, Society for Experimental Mechanics, Connecticut, USA, Nov. 1982, pp. 110-116.

[2] Ewins, D. J., "Modal Testing Theory, Practice and Application", *Engineering Dynamics Series*, *2* ed., Research Studies Press Ltd, Baldock, England, 2000.

[3] "Loads Analysis of Spacecraft and Payloads", NASA-STD-5002, URL: https://standards.nasa.gov/training/nasa-std-5002/index.html [cited 23/03/2011].

[4] "Modal Survey Assessment", ECSS-E-ST-32-11C, European Space Agency, July 2008, p. 49.

[5] Hasselman, T. K., Coppolino, R. N., and Zimmerman, D. C., "Criteria for Modeling Accuracy: A State-of-the-Practice Survey", Proceedings of *18th International Modal Analysis Conference,* Vol. 1-2, Society for Experimental Mechanics, Connecticut, USA, Feb. 2000, pp. 335-341.

[6] Nefske, D., Sung, S.,. "Correlation of a Coarse Mesh Finite Element Model Using Structural System Identification and a Frequency Response Criterion", Proceedings of *14th International Model Analysis Conference*, Society for Experimental Mechanics, Connecticut, USA, Feb. 1996, pp. 597-602.

[7] Pascual, R., Golinval, J. C., and Razeto, M., "A Frequency Domain Correlation Technique for Model Correlation and Updating", Proceedings of *15th International Modal Analysis Conference* Society for Experimental Mechanics, Connecticut, USA, Feb. 1997, pp. 587-592.

[8] O'callahan, J., Avitabile, P., and Riemer, R., "System Equivalent Reduction Expansion Process (Serep)", Proceedings of *7th International Modal Analysis Conference*, Society for Experimental Mechanics, Connecticut, USA, Jan. 1989, pp. 29-37.

[9] Penrose, R., "A Generalised Inverse for Matrices", *Mathematical Proceedings of the Cambridge Philosophical Society,* Vol. 51, No. 03, 1955, pp. 406-413.
doi: 10.1017/S0305004100030401

[10] Craig, R. R., and Bampton, M. C., "Coupling of Substructures for Dynamic Analyses", *AIAA Journal,* Vol. 6, No. 7, 1968, pp. 1313-1319. doi: 10.2514/3.4741

[11] Young, J. T., "Primer on the Craig-Bampton Method", URL: http://femci.gsfc.nasa.gov/craig_bampton/Primer_on_the_Craig-Bampton_Method.pdf, [cited 23/09/2011].

[12] Sairajan, K. K., and Aglietti, G. S., " Study of the Correlation Criteria for Base Excitation of Spacecraft Structures", *Journal of Spacecraft and Rockets (Paper accepted)* . doi: 10.2514/1.A32457

[13] Sairajan, K. K., and Aglietti, G. S., "Robustness of System Equivalent Reduction Expansion Process on Spacecraft Structure Model Validation", *AIAA Journal,* Vol. 50, No. 11, 2012, pp. 2376-2388. doi: 10.2514/1.J051476

[14] Chung, Y. T., and Sernaker, M. L., "Assessment of Target Mode Selection Criteria for Payload Modal Survey", Proceedings of *12th International Modal Analysis Conference*, Society for Experimental Mechanics, Connecticut, USA, Jan. 1994, pp. 272-279.